# Methods and Tools for Biochemical and Functional Characterization of Plant Immunity

Hsuan Pai
SID 100502529

PhD by Publication

University of East Anglia
School of Biological Sciences
The Sainsbury Laboratory

November 2025

Supervised by:

Prof. Sophien Kamoun
Primary Supervisor

Dr. Phil Carella
Secondary Supervisor

Dr. Eunyoung Chae
Dr. Isabel Monte
External Examiners

©This copy of the thesis has been supplied on condition that anyone who consults it is understood to recognise that its copyright rests with the author and that use of any information derived there from must be in accordance with current UK copyright law. In addition, any quotation or extract must include full attribution.

## Access Condition and Agreement

Each deposit in UEA Digital Repository is protected by copyright and other intellectual property rights, and duplication or sale of all or part of any of the Data Collections is not permitted, except that material may be duplicated by you for your research use or for educational purposes in electronic or print form. You must obtain permission from the copyright holder, usually the author, for any other use. Exceptions only apply where a deposit may be explicitly provided under a stated licence, such as a Creative Commons licence or Open Government licence.

Electronic or print copies may not be offered, whether for sale or otherwise to anyone, unless explicitly stated under a Creative Commons or Open Government license. Unauthorised reproduction, editing or reformatting for resale purposes is explicitly prohibited (except where approved by the copyright holder themselves) and UEA reserves the right to take immediate ‘take down’ action on behalf of the copyright and/or rights holder if this Access condition of the UEA Digital Repository is breached. Any material in this database has been supplied on the understanding that it is copyright material and that no quotation from the material may be published without proper acknowledgement.

# Abstract

This thesis presents a critical analysis of my research from 2019 to 2024, with a primary focus on the development of experimental methods for deciphering the molecular mechanisms underlying plant immunity. Plants exist within complex microbial environments and are continuously exposed to pathogenic threats. To survive, they have evolved sophisticated immune systems that detect invading microbes and activate robust defense responses. Understanding the mechanisms of pathogen recognition and immune signalling is a central goal of plant science with major implications for crop improvement and disease resistance breeding.

The research presented here integrates functional genomics, biochemical approaches, and structural biology to establish versatile platforms for studying plant nucleotide-binding leucine-rich repeat (NLR) immune receptors. By combining methodological innovation with biological discovery, this thesis highlights how advances in experimental pipelines can accelerate mechanistic insights into immune receptor activation and signalling.

In parallel, I extended these approaches to a non-model system, *Phalaenopsis* orchids, where I deciphered the synergistic interaction between two commercially devastating viruses. My work led to the establishment of molecular tools for orchid research, the development of virus-resistant transgenic lines, and the generation of new experimental resources for studying plant–virus interactions in ornamentals.

Finally, the Appendix Chapter presents my outreach work in scientific illustration as a complementary tool for science communication. Through curated case studies, I outline a practical framework for transforming complex scientific concepts into clear and engaging visual narratives.

Together, this thesis demonstrates how integrated method development across functional assays, biochemistry, structural biology, and communication can drive both mechanistic discovery and translational impact in plant science.

# Contents


Abstract ..... 1
Acknowledgements ..... 5
Introduction ..... 7

Chapter 1. Our Understanding of Plant Immunity

- 1.1 Overview of plant immunity mechanisms ..... 9
- 1.2 Timelines of key advances in molecular-plant-microbe-interactions and How molecular biology methods helped these discoveries ..... 13

Chapter 2. Complementation Assays – From Sequence to Functional Verification

- 2.1 Structural, Genomic, and Evolutionary Perspectives on Plant NLRs ..... 19
- 2.2 General Methods for NLR Identification and Functional Characterization ..... 23
- 2.3 Functional and Evolutionary Dissection of Plant NLRs Using Comparative Genomics and Transient Expression ..... 26
- 2.4 Summary ..... 37

Chapter 3. Probing NLR Immune Receptor Complexes with Blue Native Polyacrylamide Gel Electrophoresis (BN-PAGE)

- 3.1 Foundations, Development, and Applications of BN-PAGE in Plant Research ..... 42
- 3.2 General Methods for BN-PAGE–Based Analysis of Plant NLR Activation ..... 45
- 3.3 Application of BN-PAGE for visualizing NLR oligomerization ..... 48
- 3.4 Summary ..... 66

Chapter 4. Fast-forward pipeline for cryo-EM structural analysis of native plant protein complexes

- 4.1 Foundations and Advances of Electron Microscopy in Plant Studies ..... 68
- 4.2 IP-EM and BN-EM Workflows for rapid cryo-EM sample preparation ..... 72
- 4.3 Revealing structural insights into NRC resistosomes and RuBisCO by IP-EM and BN-EM ..... 75
- 4.4 Summary ..... 82

Chapter 5. Engineering Crop Species for Broad-Spectrum Viral Resistance

- 5.1 Antiviral RNA Silencing: Mechanisms and Applications ..... 85
- 5.2 Dissecting Viral Synergism and Establishing Genetic Tools for Orchid Virus Research ..... 92
- 5.3 Summary ..... 105

References ..... 106

Appendix. Illustrated Science: My Journey and Toolkit for Communicating Research by Visuals

- I. Early Inspirations and the Roots of My Sci-Comm Journey ..... 126
- II. Design Principles and Workflow for Sci-Comm Illustration ..... 131
- III. Case Studies ..... 136
- IV. Personal Explorations in Sci-art ..... 144
- V. Digital Tools That Expand and Accelerate the Illustration Process ..... 146
- VI. Summary ..... 150

Appendix: Letter of Support ..... 153

Appendix: Submitted Publications ..... 163

# Acknowledgements // Preface

So, where should I start?

When looking back at my journey at **TSL**, I sometimes feel like *Alice in Wonderland* — as if it's all a dream that might vanish the moment I open my eyes. Five or ten years ago, I couldn't have imagined I would pursue a PhD and/or be on a path as an illustrator; now I have both. None of this would be possible without the Kamoun lab, especially my supervisor **Sophien**. He enrolled me into the group. He values my contribution as more than just a technician. He connected me to my first couple of sci-comm opportunities at the NBI. He promotes my work more than I do. And he still offered his full support even after I switched to another group. Thank you, Sophien, for leading the Kamounity that I am so honoured to be a part of.

My second BIG THANK YOU goes to **Mau.** He was the first person to tell me about the PhD by Publication program and urged me to apply. He believed in the projects we worked on together as Team PAU. He has been a continuous support during my study, acting as both a role model for my research career and a friend.

And of course I cannot thank the scientific community enough for their continuous support. Thank you to **JJ** for the initial opportunity to join TSL, to my current boss **Tatsuya**, and to the Institute for funding my studies. It is a great honour to be the first 'PhD by Publication' from TSL; I hope this inspires others to see this path as a meaningful part of technician commitment. Thank you to **Phil**, **Eunyoung**, and **Isabel** for supervising my PhD and for your encouraging words. I am so glad it was actually my artwork that connected us in the first place!

Life is a series of coincidences ("…and decisions!" said Mau.), and I couldn't think of a better combination of both that could have landed me here. I feel extremely lucky to have worked with **Aki**, **Lida**, **Jiorgos**, **Clem**, **AmirAli**, **Selvaraj**, **Madhu**, **Daniel-san**, and so many others in **the Kamoun lab**. 'Thank you' isn't enough to express my appreciation for **Adeline**; thank you for orienting me to the group, for believing in my potential, for being there through the good and not-so-good times, and for being my best friend here. Life in Norwich wouldn't have been the same without my labmates **Andy**, **Mr. Yu**, **Nutt**, **Aoi**, 岳陽, the Taiwanese group (**Walter**, 辰昀, 皓貞, 孟婷, **Jason**, **Maggie**), friends from CSACBI (**Circle**, **Leman**, **Ales**, **Anastasia**) and later on **the Nobori group**. I am also grateful for the invaluable support during thesis writing (and everything!) from my wifies 斯雨子 and **Diana**; my writing pal **Kim Ku**; my office mates **Phon** & **Vangeli**; the foodies

group **Andrew**, **Julie**, **Ruth** & **Alf**, **Dave**; and my art house buddy **Nick D**. Thank you to everyone surrounding me, you have made all my decisions turned out to be the best decisions.

It was fun revisiting the orchid virus works during this phD – it reminds me of my time at Academia Sinica, and how I first stepped into the world of MPMI. Thank you to my former supervisors **Na-Sheng** and **Yao-Chien Alex**, my first mentor **全哥**, and my orchid team members/colleagues/friends **婷玉** & **淑娟**. The orchid virus chapter is dedicated to you. It also reminds me of my initial enthusiasm for research – I'll keep it up and keep moving on.

Special thanks to **GJ**, for bringing me to the UK and for the time we've spent together. I know you'll shine in your new chapter.

Finally, a big thank you to **my family and friends in Taiwan**, for their unconditional love and support. Even though I have never clearly explained what I am doing in the labs (or even in life), I know I always have their trust, a place of shelter, and someone to share my ups and downs.

Sometimes I think studying biology is a privilege. Even without my gaze, the leaves would still grow, the flowers would bloom, and microbes would continue to bustle in their phyllo-universe, just as they did long before humans arrived. The mechanisms of life have always been there; I am simply trying to understand a tiny fraction of them, purely to satisfy my own curiosity. We are all invited to a party that's been going on for 4 billion years, and I hope this party will never end.

*and I had some regrets,*
*but if I had to do it all again*
*well, that's something I'd like to do.*

Mark Oliver Everett

# Introduction

This thesis provides a critical analysis of my publications from 2019 to 2024, focusing primarily on the methods I developed in deciphering molecular mechanisms of plant immunity.

Plants are constantly challenged by a biotic environment filled with microbes. To prevent microbial colonization and pathogenic disease, plants have evolved multifaceted defense barriers. The outcomes of plant-microbe interactions have profound impacts on human life, particularly because plant diseases pose ongoing threats to ecological stability and agricultural systems. Identifying pathogen resistance traits and advancing the understanding of plant immunity have long been central to research in this field, with significant implications for crop breeding. Recent advances have provided critical insights into pathogen recognition and immune signalling, offering opportunities to develop biotechnological solutions for enhancing crop protection.

In this thesis, I bring together my peer-reviewed studies that investigate how we can understand and enhance plant disease resistance by harnessing plant immune receptors and pathogen-derived resistance from orchid viruses. By combining functional genomics, biochemical assays, and structural biology, the research advances understanding of plant immunity and establishes innovative methodological frameworks. Throughout the chapters, I will discuss the potential impact of these tools on various research projects, as well as explore future applications and possible developments.

Chapter 1 provides an overview of our current knowledge about the multifaceted plant immune mechanisms, and an historical context of how molecular biology methods helped these investigations.

Chapters 2-4 collectively describe the establishment of a series of experimental pipelines designed to bridge gene discovery, functional validation, and structural characterization of plant immune receptors. In Chapter 2, I present a standardized high-throughput pipeline using the model plant *Nicotiana benthamiana* as a heterologous host for transient gene expression to assess Nucleotide-binding leucine-rich repeat (NLR) immune receptor structure and function. This platform integrates sequence-based NLR prediction, modular cloning, hypersensitive cell death assays, and mutational analyses to identify functional receptor–effector pairs. This workflow is also

transferable to non-model plants, forming the foundation for downstream biochemical and structural studies.

Chapter 3 focuses on biochemical methods for probing NLR complex formation through blue native polyacrylamide gel electrophoresis (BN-PAGE). I optimized BN-PAGE to visualize native protein assemblies directly from leaf tissue extracts, revealing how receptors transition from inactive monomers or dimers to active oligomeric resistosomes.

In Chapter 4, I describe the development of two rapid cryogenic electron microscope (cryo-EM) pipelines — immunoprecipitation-EM (IP-EM) and BN-PAGE EM (BN-EM) — that enable structural characterization of plant protein complexes from small-scale samples. These pipelines enable rapid transition from *in planta* purification to high-resolution visualization, capturing immune complexes in distinct activation states.

While the above chapters concentrate on plant immune receptors, in Chapter 5 I conclude my work on deciphering the synergistic interaction between two distantly related orchid viruses in *Phalaenopsis* orchids, leading to the development of transgenic lines with dual virus resistance and new molecular tools for orchid research.

Alongside my research, I am passionate about using illustrations to communicate scientific ideas. In the Appendix Chapter, I present a collection of my science-inspired artworks, which I developed for journal covers, commentary articles, review papers, and events like the Norwich Science Festival. Through these case studies, I outlined the principles and process behind creating effective scientific illustrations, offering insights into how to design visuals that bridge the gap between complex research and storytelling.

# Chapter 1

# Our Understanding of Plant Immunity

## 1.1 Overview of plant immunity mechanisms

Life on earth often exists in close association, like the plant holobiont consisting of a complex system balancing beneficial and pathogenic interactions between plants and microbes (Mannaa M and YS Seo, 2021). In contrast to animals, the non-mobile property makes plants more resilient to the surrounding environment. The crosstalk between host plants and microbes shaped today's plant biology, ecology, and evolution (Mesny et al., 2023).

To achieve successful colonization, microbes utilize diverse strategies to infect plants. Some pathogens actively invade and infiltrate plant tissues, whereas others enter through wounds or natural openings. **Oomycetes and fungal pathogens** use special structures like appressoria and haustoria to penetrate host cells and to release effectors (Pélissier et al., 2021; Wang et al., 2022). Depending on the nutritional lifestyles, biotrophic, hemi biotrophic, and necrotrophic fungal pathogens have different modes to infect plants. Necrotrophic fungal pathogens obtain nutrients from deteriorating cells, whereas biotrophs live on living cells. In contrast, hemibiotrophs first infiltrate living cells before switching to a necrotrophic way of life in order to harvest nutrients from the dead tissues (Jian et al., 2024; Pélissier et al., 2021). **Bacterial pathogens** usually enter plant tissues through natural openings, such as hydathodes and especially stomata, which are the essential pores for gas exchange (Ikram et al., 2024). Wounds caused by physical damage, insect vectors, or adverse weather conditions could also serve as entry points. Some bacteria may also actively penetrate by producing enzymes that degrade the cell wall (Mukhtar, 2025; Ogbonna and Umunna, 2017). Although different pathogens possess diverse lifestyles, they are commonly equipped with an extensive **repertoire of effectors**. These effector molecules, often proteins, are secreted by pathogens to manipulate host cells and facilitate infection. They suppress host defenses, interfere with cellular functions such as gene expression and metabolism, and alter cell structure to benefit the pathogen. Pathogens deliver these effectors into host cells or tissues through various mechanisms, like the type III secretion system (T3SS) in bacteria or specialized structures in fungi (Guerreiro and Stukenbrock, 2025; Ikram et al., 2024). On the other hand, **viruses are obligatory parasites** that serve as a unique case of plant pathogens. Since viruses rely on resources from host cells to proliferate, it's essential for viruses to hijack the host's life machinery, leading to metabolic, physiological, molecular, and morphological alterations in plants (Lozano-

Durán, 2024; Roossinck, 2019). Particularly, viral proteins often have multiple functions in pathogenesis alongside replication, encapsidation, and transmission (Lozano-Durán, 2024; Mannaa and Seo, 2021).

To stay resilient, **plants have developed constitutive (pre-existing) and inducible defense systems.** Pre-existing defenses include both physical and chemical barriers that operate constitutively, even before infection occurs. General **structural defense features such as the cell wall, cuticle, and bark**, restrict pathogen entry and spread. The cell wall's components — cellulose, lignin, and pectins — provide mechanical strength and impermeability, while cuticular waxes and suberin enhance resistance to microbial penetration and water-dependent pathogens (Molina et al., 2024). Some plant species also equipped with specialized structures like trichomes, thorns, and idioblasts that deter insects and grazers (Underwood, 2012). Complementing these physical barriers are **chemical defenses** providing preformed antimicrobial compounds, including terpenoids, phenolics, alkaloids, and glycosides. Many of these secondary metabolites are stored as inactive phytoanticipins and become active upon tissue damage or infection, providing rapid biochemical protection against a broad range of pathogens (Zaynab et al., 2018).

When the initial defenses are breached, plants activate **inducible immune responses in two tiers: Pattern-triggered immunity (PTI)**, which provides broad-spectrum resistance against diverse pathogens, and the more specific **Effector-triggered immunity (ETI)**, which detects pathogen-injected effector molecules inside plant cells (Jones & Dangl, 2006; Jones et al, 2016; Ngou et al, 2022).

**Pattern-triggered immunity (PTI)** represents the first layer of inducible defense. It is initiated when plant cell surface pattern-recognition receptors (PRRs) detect conserved microbial molecules, collectively termed microbe- or pathogen-associated molecular patterns (MAMPs/PAMPs), such as bacterial flagellin, fungal chitin, or lipopolysaccharides (Dodds et al., 2024; Jones et al., 2024; Ngou et al, 2022). In addition, plant-derived damage-associated molecular patterns (DAMPs), including cell wall fragments released during infection, can also activate PTI. The PRRs responsible for MAMP/DAMP perception are typically receptor-like kinases (RLKs) or receptor-like proteins (RLPs) anchored in the plasma membrane (De Lorenzo and Cervone 2022; Macho & Zipfel, 2014; Ngou et al, 2022a). Upon ligand binding, these receptors form active complexes that trigger intracellular signalling cascades, including calcium ion fluxes, the generation of reactive oxygen species (ROS), and the activation of mitogen-activated protein kinase (MAPK) cascades. These early events lead to transcriptional reprogramming and defense responses, including cell wall reinforcement through callose deposition and lignification, stomatal closure to prevent pathogen entry, and the production of antimicrobial secondary metabolites and pathogenesis-related (PR) proteins (Cui et al, 2015; DeFalco & Zipfel, 2021).

Effector-triggered immunity (ETI) constitutes the second layer of defense and is triggered upon pathogens deliver effectors into host cells to suppress immune response (Couto & Zipfel, 2016; Jones and Dangl 2006). ETI is activated when these effectors are recognized, either directly or indirectly, by intracellular receptors, predominately the nucleotide-binding/leucine-rich-repeat receptor (NB-LRR or NLR) family encoded by resistance (*R*) genes (Dodds et al., 2024; Jones et al., 2024; Ngou et al., 2022). NLR activation triggers potent defense responses, including their oligomerization into higher-order immune complexes termed the 'resistosome' (Wang et al., 2019; Förderer et al. 2022; Zhao et al., 2022). The formation of resistosomes often lead to localized programmed cell death known as the hypersensitive response (HR), which confines the pathogen to the infection site by depriving it of nutrients and living tissue (Bi et al., 2021; Wang et al., 2019). ETI shares many signalling components with PTI — including calcium and ROS bursts, MAPK activation, and salicylic acid (SA) accumulation — but typically results in a faster and stronger response (Cui et al, 2015; Spoel and Dong, 2024).

PTI and ETI are highly interconnected, engaging overlapping signalling components and reinforcing each other to ensure durable resistance. Recent studies demonstrate that ETI activation upregulates the expression or stability of key PTI signalling components, and PTI primes cellular signalling pathways that facilitate faster and stronger ETI responses (Ngou et al., 2021; Ngou et al., 2022). Together, PTI and ETI produce amplified defense outputs — elevated ROS, sustained MAPK activation, enhanced defense gene expression, and robust systemic acquired resistance (SAR), a long-lasting and broad-spectrum defense state that primes protection against subsequent infections (Ngou et al., 2021; Ngou et al., 2022).

Beyond PTI and ETI, since viruses possess a fundamentally different lifestyle from bacterial and fungal pathogens, plants employ RNA silencing (or RNA interference, RNAi) to eliminate these obligate intracellular parasites (Jing et al., 2020; Yang and Li, 2018). Initially identified as a post-transcriptional process activated during viral infection or transgene expression, this pathway provides sequence-specific defense by recognizing and degrading viral RNAs. Upon virus infection, RNA silencing is initiated when viral double-stranded RNA (dsRNA), produced during replication or from structured viral regions, is recognized and processed by Dicer-like (DCL) enzymes into 21-24 nucleotide virus-derived small interfering RNAs (vsiRNAs). These vsiRNAs are incorporated into Argonaute (AGO) proteins within the RNA-induced silencing complex (RISC), which uses them as guides to cleave complementary viral RNAs, suppressing replication (Huang et al., 2023; Jing et al., 2020; Yang and Li, 2018). This pathway not only acts locally but also mediates systemic immunity through the movement of small RNAs between cells to prime uninfected distal tissues. Furthermore, RNA-dependent RNA polymerases (RDRs) can amplify the response by generating additional dsRNA and vsiRNAs, reinforcing antiviral activity. In addition to antiviral defense, RNA silencing also

plays major roles in regulating plant endogenous gene expression, influencing the activity of immune receptors such as NLRs (Fick et al., 2022; Ramesh et al., 2021). As a counter-defense, viruses have evolved viral suppressors of RNA silencing (VSRs) that block key steps in this process, driving an evolutionary arms race between viral effectors and host silencing machinery (Burgyán and Havelda, 2011; Daròs 2017).

**In summary, PTI, ETI, and RNA silencing operate as interconnected layers of a unified plant immune network.** PTI provides broad recognition of conserved microbial patterns, ETI delivers strong intracellular responses to specific effectors, and RNA silencing defends primarily against viral pathogens through targeted RNA degradation. Despite distinct recognition mechanisms, these systems share overlapping signalling components such as $Ca^{2+}$ influxes, ROS, and coordinated by key phytohormones like SA, jasmonic acid (JA), and ethylene (ET) (Leonetti et al., 2021; Ngou et al., 2022). Their extensive cross-talk ensure that plants can rapidly detect diverse pathogens and deploy tailored defenses, equipping plants with flexible and durable protection against a wide range of pathogens.

## 1.2 Timelines of key advances in molecular-plant-microbe-interactions and How molecular biology methods helped these discoveries

The scientific understanding of plant immunity has evolved over a century, progressing from descriptive studies of infectious plant diseases to a molecular-level understanding of immune signalling, receptor activation, and host-pathogen coevolution (Ngou et al., 2021; Jones et al., 2024). This progression has been driven not only by **conceptual advances but also by the development of increasingly sophisticated molecular biology methods**, which have transformed our understanding of plant immunity from a largely genetic discipline into a mechanistic, structure-guided science.

**Early Discoveries and the Birth of Plant Virology (Late 1800s–1930s)**

The modern study of plant immunity began with the **discovery of plant viruses** in the late nineteenth century. In 1892, Ivanovsky et al. demonstrated that the infectious agent causing tobacco mosaic disease could pass through filters that retained bacteria, and a few years later, Beijerinck et al. coined the term "virus", identifying it as a new class of infectious entity smaller than any known microorganism (Scholthof 2004; Van der Want and Dijkstra, 2006). These early filtration and transmission experiments established the concept of submicroscopic pathogens and laid the groundwork for virology. In 1935, ***Tobacco mosaic virus*** **(TMV) particle** was crystallized, demonstrating its proteinaceous nature (Okada, 1999). This was one of the earliest molecular characterizations of a biological macromolecule and a landmark achievement for biochemistry and structural biology.

These foundational discoveries inspired the development of **techniques for purifying, visualizing, and characterizing pathogens** at the molecular level. The advent of electron microscopy in the mid-twentieth century further enabled the visualization of virus particles, revealing their defined shapes and sizes (Scholthof, 2004; Van der Want and Dijkstra, 2006). Together, these advances linked structure to function and catalyzed the study of how plants recognize and defend against pathogens.

**The Gene-for-Gene Model and the Genetic Era (before 1980s)**

By the 1940s, plant pathologists observed that pathogen populations could be divided into "**physiologic races**," each specialized to infect certain host genotypes, suggesting a genetic interplay between host and pathogen (Habgood 1970; Stackman 1947). The genetic basis of plant disease resistance was articulated by Flor, whose

work on flax and its fungal pathogen *Melampsora lini* led to the **gene-for-gene model**, proposing that disease resistance requires a matching pair of **plant *Resistance (R)* and pathogen *Avirulence (Avr)* genes** (Dodds 2023; Flor 1971; Kaur et al., 2021). This model provided a simple yet profound explanation for host specificity and established a framework for studying plant-pathogen interactions genetically.

The following decades saw the rise of classical genetics and biochemical methods to investigate plant immunity. In the 1960s and 1970s, parallel advances in **genetic mapping, protein biochemistry, and serological assays**, enabled the identification of **more traits of *R* genes**, such as the *N* gene in tobacco that confers resistance to TMV (Kaur et al., 2021). Physiological studies identified **elicitor molecules** such as bacterial lipopolysaccharides and fungal cell wall components capable of inducing defense responses in plant tissues, foreshadowing the later discovery of immune receptors.

Around the 1980s, the molecular biology revolution brought key tools — **restriction enzymes, cloning vectors, DNA sequencing**, and most importantly **Agrobacterium-mediated transformation** — that allowed isolation and manipulation of plant genes (Ngou et al., 2021; Jones et al., 2024). Combined with Klement's observation of **HR cell death** of tobacco leaves inoculated with pathogenic *Pseudomonas* strains (Atkinson et al., 1985; Klement, 1984), the **first bacterial and fungal *Avr* genes were then cloned**, demonstrating that they encode effectors – the virulence factors secreted by pathogens to manipulate host physiology (De wit et al., 2009; Mansfield, 2009).

## Immune Receptors and The Two-Tiered Immunity Model (1990s – 2000s)

The 1990s marked a turning point, as **molecular cloning** made it possible to isolate and characterize corresponding plant *R* genes of the identified pathogen *Avr* genes. Among these, ***Hm1* from maize was the first cloned *R* gene** (Johal and Briggs, 1992; Chen et al., 2024), which is a NADPH-dependent reductase that detoxifies toxins from the fungal pathogen *Cochliobolus carbonum* (Sindhu et al., 2008). The use of **model plants *Arabidopsis thaliana*, genome analysis, map-based cloning, transposon tagging and other tools** propelled the isolation of several *R* genes: including *Arabidopsis RPS2*, *RPM1*, *RPS5*, and the *RPS4-RRS1* pair; tomato *Pto*, rice *Xa21*, flax *L6*, and tobacco *N* that confer resistance to a diverse range of pathogens. Protein sequence analysis revealed that **many R proteins share a conserved nucleotide-binding leucine-rich repeat (NLR) architecture.** From 1994, the **cloning of PRRs** such as *Cf-9* (Jones et al., 1994) and *flagellin-sensing 2* (*FLS2*) (Chinchilla et al., 2006; Gómez-Gómez and Boller, 2000), and a series of PRR-associated signalling components, including BAK1 as an

essential co-receptor, BIK1 as a receptor-like cytoplasmic kinase (RLCK) linking perception to reactive oxygen species (ROS) generation, and RbohD/F as NADPH oxidases driving the oxidative burst (Kadota et al., 2014; Macho & Zipfel, 2014; Zhang et al., 2010). Molecular assays — such as **yeast two-hybrid screening**, **co-immunoprecipitation**, and **transient expression in *N. benthamiana*** — enabled direct investigation of receptor–ligand interactions, collectively revealing how extracellular perception initiates intracellular signalling cascades (Kourelis and Van der Hoorn, 2018; Ngou et al., 2021).

These discoveries linked multiple forms of pathogen resistance under a protein family class and led to the formulation of the **two-layered PTI-ETI network and "zig-zag" model** between 2006-2010, which illustrates the dynamic interaction between plants and pathogens through four phases: PRR-mediated recognition triggers PTI; effectors then suppress PTI; NLRs detect these effectors to activate ETI; and pathogens subsequently modify or lose effectors to evade recognition (Jones and Dangl, 2006; Ngou et al., 2022). The framework of ongoing cycle of adaptation and counter-adaptation established the foundation for understanding the **coevolutionary relationship between plants and their pathogens**.

Around the same time, another revolutionary discovery shaped the understanding of antiviral defense: **RNA silencing (RNA interference)**. Initially observed during transgene silencing experiments, RNA silencing was soon recognized as a sequence-specific antiviral mechanism in which dsRNA is processed into siRNAs by DCL proteins, as described in the previous section 1.1. Molecular techniques such as **northern blotting, RT-PCR**, and later **small RNA sequencing** were instrumental in uncovering these pathways (Ramesh et al., 2021; Huang et al., 2023).

## Structural and Systems Biology in Plant Immunity (2010s–Present)

More recently, the discovery of **mutual potentiation between PTI and ETI** — where activation of one pathway strengthens the other (Ngou et al., 2021) — has refined the classical hierarchical model of plant immunity into a dynamic, interconnected system. In line with these, from around the 2010s witnessed transformative progress driven by advances in **structural biology**, **genomics**, and **systems-level analyses**. High-throughput sequencing of oomycete and fungal genomes enabled genome-wide identification of RXLR, CRN, and MAX effectors (Soanes et al., 2007; Wilson and McDowell, 2022), revealing conserved structural folds despite rapid sequence diversification driven by host adaptation (Chepsergon, 2020). Followed by comparative genomics around 2016-2020, diverse **NLR architectures — singleton, paired, and network types** — were uncovered from the host side, demonstrating modular

cooperation and lineage-specific expansion (Adachi et al, 2019; Feehan et al, 2020; Wu et al., 2018). Together, these studies established **effectoromics and NLR diversity as co-evolving systems**. More recently, the application of **cryo-electron microscopy** (cryo-EM) with the aid of **AI-based prediction** tools led to atomic-resolution structures of resistosomes (Wang et al. 2019; Förderer et al. 2022; Zhao et al. 2022; Liu et al. 2024). These findings provided direct visualization of immune receptor activation and signalling, bridging decades of genetic and biochemical data.

In parallel, research into **viral suppressors of RNA silencing (VSRs)** elucidated how viruses counter host immunity by inhibiting small RNA biogenesis or ARGONAUTE activity (Burgyán and Havelda, 2011; Daròs 2017). The development of high-throughput sequencing allowed genome-wide profiling of defense gene expression and small RNA populations, revealing **extensive crosstalk between PTI, ETI, and RNA silencing pathways** (Leonetti et al., 2021; Yang and Li, 2018). **Hormonal signalling**, particularly involving salicylic acid (SA), jasmonic acid (JA), and ethylene (ET), was shown to integrate these pathways into coordinated defense networks (Huang et al., 2023).

From the discovery of viruses and the gene-for-gene hypothesis to the molecular dissection of PRRs, NLRs, and RNA-silencing machinery, **the field of plant immunity exemplifies the power of technological innovation in driving conceptual breakthroughs**. In combination with the rise of **synthetic biology** and **gene-editing** technologies, we're now entering a future that designing synthetic immune receptors, NLR chimeras, and engineered small RNAs that enhance resistance against diverse pathogens are made possible (Cao et al., 2025; Contreras et al., 2023; Ngou et al., 2025). Advances in molecular genetics, biochemistry, and structural biology have not only successively unveiled the layers of plant defense — from perception to signalling and execution — but will continue to inspire both basic and applied research in plant biology.

# Chapter 2

# Complementation Assays – From Sequence to Functional Verification

In earlier years, resistance (*R*) genes were discovered through classical genetic approaches, such as forward genetic screens and positional cloning — methods that were crucial for establishing the foundations of plant immunity but slow, labour-intensive and limited in scale (Jones et al., 2024; Ngou et al., 2022). Today, **advances in genome sequencing and computational tools enable high-throughput identification of NLR genes from the genome sequences of diverse plant species**. Combined with phylogenomic analyses, these approaches have deepened our understanding of the evolutionary origins, diversification, and functional versatility of plant immune receptors, **bringing the study of NLR biology to a systems-level perspective** (Barragan et al., 2021; Kourelis et al., 2021).

In this chapter, I outline **the core workflow we use to identify and functionally validate NLR immune receptors**. This pipeline spans from cloning candidate genes for Agrobacterium-mediated transient expression to interpreting hypersensitive (HR) cell death as a measurable output of immune activation. **This framework was established through collective efforts of the Kamoun lab and has since been applied in multiple studies.** Across the five publications presented here, my contribution primarily focused on experimental validation, data generation, and collaborative analyses of NLR evolution, in close collaborations with Hiroaki Adachi, Toshiyuki Sakai, AmirAli Toghani, Mauricio Contreras, and Adeline Harant. Collectively, these studies demonstrate how our unified experimental platform can uncover both mechanistic and evolutionary principles of plant immunity.

**Key Publications in Chapter 2:**

1. Harant A, H Pai, T Sakai, S Kamoun, and H Adachi. (2022) A vector system for fast-forward studies of the *HOPZ-ACTIVATED RESISTANCE1 (ZAR1)* resistosome in the model plant *Nicotiana benthamiana*. Plant Physiology 188:70-80.

2. Adachi H, T Sakai, J Kourelis, H Pai, JL Gonzalez Hernandez, Y Utsumi, M Seki, A Maqbool, and S Kamoun. (2023) Jurassic NLR: Conserved and dynamic evolutionary features of the atypically ancient immune receptor ZAR1. The Plant Cell 35:3662-3685.

3. Kourelis J, MP Contreras, A Harant, H Pai, D Lüdke, H Adachi, L Derevnina, CH Wu, and S Kamoun. (2022) The helper NLR immune protein NRC3 mediates the hypersensitive cell death caused by the cell-surface receptor Cf-4. PLoS Genetics 18:e1010414.

4. Contreras MP, H Pai, C Marchal, R Thompson, J Claeys; H Adachi, and S Kamoun. (2024) The nucleotide binding domain of NRC-dependent disease resistance proteins is sufficient to activate downstream helper NLR oligomerization and immune signaling. New Phytologist (2024) 243:345-361.

5. Pai H, T Sakai, A Posbeyikian, R Frijters, Y Sugihara, MP Contreras, J Kourelis, H Adachi, S Kamoun, and AA Toghani. (2025) A hierarchical immune receptor network in lettuce reveals contrasting patterns of evolution in sensor and helper NLRs. bioRxiv 2025.02.25.639832.

## 2.1 Structural, Genomic, and Evolutionary Perspectives on Plant NLRs

**Overview of Plant NLR Immune Receptors**

**Nucleotide-binding leucine-rich repeat (NLR) proteins** are intracellular immune receptors that sit at the core of the second layer of plant innate immunity (Jones and Dangl 2006; Kourelis and van der Hoorn 2018). NLR detect pathogen-derived effector proteins either directly through physical interaction, or indirectly by monitoring perturbations in host proteins that known as guardees or decoys (Dodds et al., 2024; Jones et al., 2024). This detection triggers a robust immune response, often culminating in a **localized programmed cell death known as the hypersensitive response** (Jones et al. 2016; Contreras et al. 2023). These receptors form one of the largest and most evolutionarily dynamic gene families in plants, with copy numbers ranging from fewer than 100 in *Arabidopsis thaliana* to over 1,000 in complex genomes such as wheat or potato (Lee and Chae 2020; Reyes-Herrera et al., 2024; Toghani and Kamoun 2024; Yang et al., 2017).

**Structurally**, plant NLRs are typically composed of **(i)** a variable N-terminal signalling domain, **(ii)** a central nucleotide-binding and oligomerization domain (nucleotide-binding domain shared with *APAF-1*, various *R*-proteins and *CED-4*, **NB-ARC**) responsible for ATP/ADP exchange and activation, and **(iii)** a C-terminal **leucine-rich repeat (LRR)** domain that mediates effector perception and autoregulation. Based on the N-terminal domain architecture, NLRs are classified into three major subfamilies: **TIR-NLRs** containing a Toll/interleukin-1 receptor domain, **CC-NLRs** carrying a coiled-coil domain, and **RPW8-type CC ($CC_R$) or $CC_{G10}$-type CC** domains define smaller subclasses (Andolfo et al, 2019; Chia et al, 2022; Kourelis & Van Der Hoorn, 2018). In addition to the canonical tripartite NLR structure, certain receptors possess unconventional **integrated domains (IDs)** such as WRKY, BED, HMA, or kinase-like regions. These domains are thought to have evolved through domain fusions and act as decoys that mimic authentic effector targets that trap pathogen effectors, thereby broadening recognition specificity (Cesari et al. 2014; Maqbool et al. 2015; Baggs et al. 2017; Grund et al. 2019).

**Functionally**, NLRs can be categorized as **singletons, paired receptors, or networked systems**. **Singleton** NLRs such as ZAR1 integrate sensing and signalling within a single molecule, forming resistosomes upon activation (Adachi et al, 2019; Feehan et al, 2020; Wu et al, 2017; Wu et al, 2018). **Paired NLRs**, such as Pik-1/Pik-2 in rice or RRS1/RPS4 in *Arabidopsis*, exhibit division of labour, with the "sensor" for detection, and the "helper" as signalling executor (Narusaka et al., 2016; Zhai et al., 2011). Networked NLRs, exemplified by the **NLR required for cell death (NRC) network** in Solanaceae, consist of multiple sensor and helper components forming hierarchical immune modules. Helper NLRs such as NRC2, NRC3, and NRC4 mediate signal

transduction downstream of diverse sensors (Wu et al, 2017; Wu et al, 2018), while $CC_R$ type helpers (e.g., NRG1, ADR1) function downstream of TIR-domain sensors. This **modular architecture of NLR networks and signalling pathways enables redundancy and robustness** in defense signalling (Kourelis et al., 2021).

The architectural and functional diversity of NLRs underpins the adaptability of plant immune systems and provides a molecular basis for the rapid coevolution between host and pathogen. **The understanding of NLR domain organization and their signalling mechanisms therefore provides an essential framework to identify and functionally characterize** these receptors across plant lineages (Kourelis et al., 2021; Prigozhin and Krasileva 2021; Van de Weyer et al. 2019).

## Genome Resources and Bioinformatics Pipelines for NLR Identification

Advances in genome sequencing and computational biology have fundamentally transformed how researchers annotate NLR immune receptors from diverse plant species. With the increasing availability of high-quality genome assemblies across major angiosperm lineages, researchers can **systematically explore "NLRomes" and trace their evolutionary diversification** (Lee and Chae, 2020; Kourelis et al., 2021; Prigozhin and Krasileva 2021; Van de Weyer et al. 2019). Comparative analyses reveal that the **size and organization of NLR repertoires vary dramatically across taxa** — ranging from the compact sets in *Arabidopsis* to the expanded NRC superclades in *Solanaceae* and the complex paired systems of cereal crops (Goh et al., 2024; Kourelis et al., 2021). These variations highlight the **dynamic evolutionary plasticity of immune gene families shaped by ecological and pathogen-driven pressures**.

Bioinformatic identification of NLRs relies primarily on **detecting conserved sequence signatures** that define this receptor family. The hallmark **NB-ARC domain is the most conserved region** among distant related NLRs and can be used to determine evolutionary relationships. Diagnostic motifs within NB-ARC followed a tripartite structure, consist of nucleotide binding (NB) domain, the helix domain-1 (HD1) and the winged-helix domain (WHD) (Figure 1) (Duxbury et al, 2021; Gao et al, 2022; Kibby et al, 2023; Uehling et al, 2017). Hidden Markov Models (HMMs) trained on curated NB-ARC alignments are used to scan predicted proteomes or transcriptomes for these motifs. Such probabilistic models capture both the conserved catalytic residues and the tolerated sequence variability, enabling sensitive detection even in large or fragmented genomes (Baggs et al, 2017; Barragan & Weigel, 2021; Clark et al, 2007).

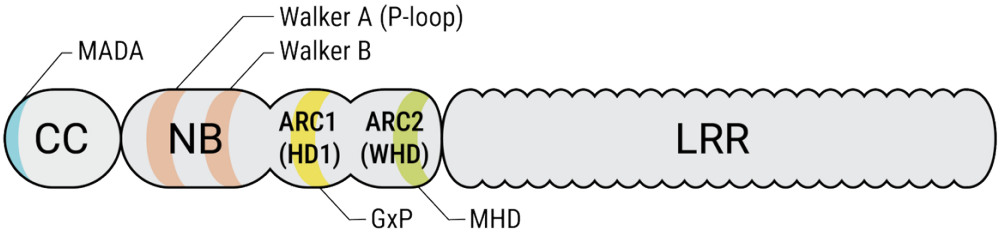


**Figure 1. Schematic domain organization of a typical plant nucleotide-binding leucine-rich repeat (NLR) protein (in this case a CC-NLR, modified from Van Ooijen et al., 2007).** Plant NLRs generally consist of three principal modules: a nucleotide-binding domain shared with APAF-1, various R-proteins and CED-4 (NB-ARC) domain, and a C-terminal leucine-rich repeat (LRR) domain. The identity of the N-terminal domain (e.g. CC, TIR, or related variants) defines the major NLR subclasses. A MADA or MADA-like motif found in the N-terminal α1-helices of many CC-NLRs is crucial for cell death initiation (Adachi et al., 2019). The NB-ARC region is composed of the nucleotide-binding (NB) subdomain, helix domain 1 (HD1 or ARC1), and the winged-helix domain (WHD or ARC2). Within the NB subdomain, the Walker A (P-loop; GxxxxGK[T/S]) and Walker B (hhhDD/E) motifs mediate ATP/ADP binding and hydrolysis. The HD1 domain contains a conserved GxP (GLPL) motif, while the WHD harbours the conserved MHD (methionine–histidine–aspartate) motif, which is critical for regulating nucleotide binding and NLR activation state (Bonardi et al., 2012; Takken et al., 2006; Van Ooijen et al., 2008).

Several specialized **bioinformatics tools** such as NLRtracker, NLR-Parser, NLR-Annotator, and more recent deep-learning-based methods like Helixer and NLRexpress — combine HMM domain searches with motif order recognition, structural prediction, and cross-referencing to reference NLR databases (Kourelis et al., 2021; Martin et al., 2022; Stiehler et al., 2021). These pipelines not only improve prediction accuracy but also distinguish full-length receptors from pseudogenized or truncated gene fragments. After initial identification, candidate proteins are classified by their domain architecture: whether they encode the canonical NB-ARC core, contain LRRs with characteristic LxxLxLxx motifs, or carry additional ID that may function in effector recognition.

The increasing integration of genomic and transcriptomic resources allows these computational predictions to be refined by expression profiling and ortholog detection. activation interfaces, complementing sequence-based annotations. **Curated reference databases** such as PlantNLRatlas and NLRscape now harmonize annotations across hundreds of plant species, serving as repositories for both domain- and sequence-based NLR discovery (Li et al., 2023; Martin et al., 2023). These comprehensive datasets form the basis for comparative and evolutionary analyses, linking molecular sequence features with functional diversification.

## Phylogenetic and Evolutionary Insights from NLRome Analyses

Beyond NLR identification, **phylogenetic reconstruction** provides insight into the evolution of plant immune systems. Sequence alignment of the conserved NB-ARC domains enables classification of NLRs into three monophyletic clades — TIR, CC, and

RPW8-NLRs — and further subdivision into lineage-specific groups. Phylogenetic inference using maximum likelihood or Bayesian approaches allows identification of conserved receptors, such as ZAR1, which is present across most angiosperms, and reveals lineage-specific expansions like the NRC and RGA clades in *Solanaceae* and rice (Goh et al., 2024; Kourelis et al., 2021).

Phylogenomic studies reveal NLR diversification is driven by tandem and segmental duplications, gene conversion, and domain shuffling, producing gene clusters and novel variants. Pathogen-driven selection accelerates sequence turnover in recognition domains such as LRRs and integrated domains. In functional evolution, phylogenomic frameworks also illuminate contrasting evolutionary rates: conserved helper NLRs evolve slowly, while variable sensor NLRs diversify rapidly in response to pathogen pressure (Kourelis et al., 2021; Prigozhin and Krasileva 2021; Van de Weyer et al. 2019). At a broader scale, NLRome evolution mirrors ecological adaptation. Species in pathogen-rich environments maintain expanded, diverse repertoires, whereas specialized or clonally propagated crops lose receptor diversity, highlighting a trade-off between immune complexity and growth efficiency (Barragan et al., 2021; Goh et al., 2024).

Together, these evolutionary studies transform raw genomic data into mechanistic understanding. By integrating HMM-based detection, structural modelling, and phylogenomics, modern NLR research not only reconstructs the history of immune innovation but also provides practical guidance for engineering durable disease resistance in crops.

## 2.2 General Methods for NLR Identification and Functional Characterization

Across my studies, I employed a **standardized workflow that integrates bioinformatic identification of NLR genes, modular cloning of candidate receptors, and transient cell death assays for functional validation** (Figure 2). This approach enables rapid testing of immune receptor activity and sensor–helper specificity across species.

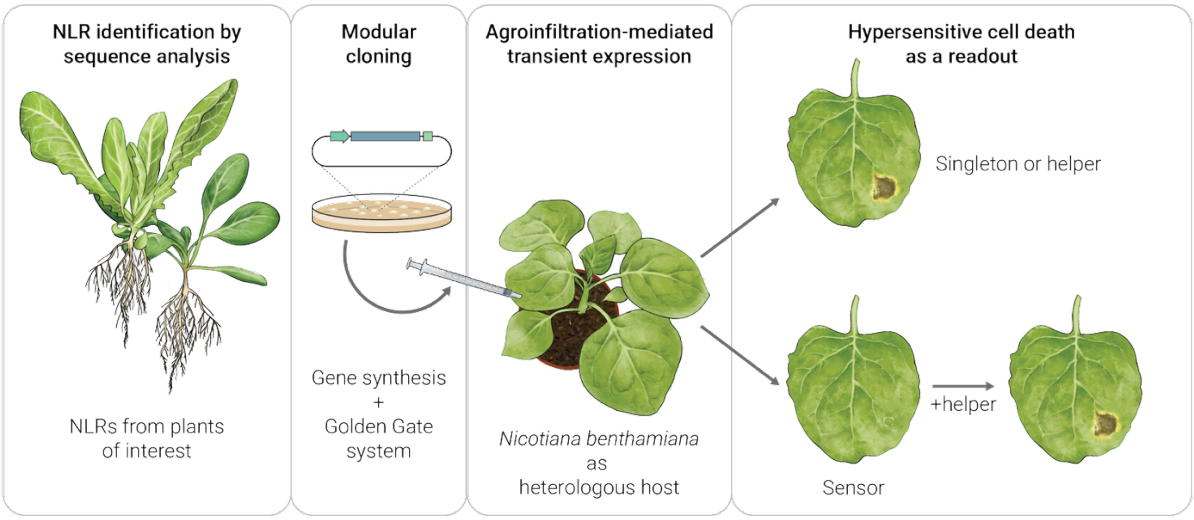


**Figure 2. Workflow for NLR identification and functional characterization.** Candidate NLR genes are first identified by sequence analysis from plant species of interest. Potential NLR genes are then cloned using a modular cloning system and transiently expressed in the heterologous host *Nicotiana benthamiana* via Agrobacterium-mediated infiltration. Functional activity is assessed using hypersensitive cell death as a readout. Cell death can be triggered either by singleton/autoactive helper NLRs alone or by co-expression of activated sensor–helper NLR pairs, enabling discrimination between different modes of NLR function.

### (1) NLR Identification and Sequence Analyses

Putative NLR sequences were first identified from available genome and transcriptome assemblies using HMM-based and motif-guided searches. **Protein sequences were screened for conserved NLR signatures**, including the NB-ARC domain (PF00931) and characteristic motifs such as the P-loop, GLPL, and MHD motifs. The receptor types such as CC-NLRs, TIR-NLRs, $CC_R$-NLRs were annotated based on InterProScan. Bioinformatic packages such as NLR-Parser and NLRtracker were used to automate the searches.

For phylogenetic analyses, **multiple sequence alignments** were generated with MAFFT, and phylogenetic trees were constructed using FastTree and IQtree (Kalyaanamoorthy et al. 2017; Minh et al., 2020; Standley, 2013). Phylogenetic and

synteny analyses guided the identification of orthologs, allelic variants, and conserved clades (for example, the NRC network or the ancient ZAR1 lineage). Sequence conservation and polymorphisms were further analyzed in sequence analysis software such as Geneious Prime and MEGA for residue mapping and motif visualization.

## (2) Construct Generation Using Modular Cloning, Tagging and Variant Design

The **Golden Gate Modular Cloning (MoClo)** systems (Weber et al., 2011) and the MoClo Plant Parts kit (Engler et al., 2014) are foundations in our cloning pipeline, ensuring a rapid "plug-and-play" generation of candidate gene expression cassettes. By using this system, candidate NLRs, effectors, and their variants were cloned into binary vectors (typically pJK268c/pICH series, Kourelis et al., 2020) under 35S promoters, with C-terminal epitope/fluorescent tags. All parts were domesticated to remove internal *Bsa*I/*Bpi*I sites and standardized to the MoClo syntax.

Where necessary, **mutants or chimeric constructs** were generated to dissect NLR activation mechanisms. Examples include:

- Introduce point mutations within conserved motifs (e.g., MHD, P-loop) or predicted effector-binding interfaces to test activation requirements. **Mutations in the conserved residues of the MHD motif often cause constitutive autoactivity** (Bendahmane et al., 2002; Van Ooijen et al., 2008), providing a useful strategy to assess the functional integrity of candidate NLRs without requiring activation by their cognate effectors—particularly when these effectors are unknown or difficult to express.
- Ortholog swaps or truncations to assess **domain compatibility** across species.
- **MADA motif** mutations within the N'-terminus α1 helix to abolish HR while preserving activation capacity (Adachi et al., 2019). This is of great importance in conducting biochemical assays and more details are described in the next Chapter 3.

## (3) Transient Expression and Cell Death Assays

**Constructs are delivered by *Agrobacterium*** to test accumulation and function. We extensively used ***N. benthamiana* as an assay host**, taking the advantage that transient expression via agroinfiltration enables rapid, high throughput testing of candidate NLRs without generating stable transgenic lines. **HR (cell-death) gives robust readouts for immune response** and is quantified visually following a scoring chart (Figure 3). Combined with the *nrc2/3/4* CRISPR knockout lines in hand (Kourelis et al.,

2022), this system provides an efficient, standardized platform to dissect helper–sensor relationships and verify NLR functionality in heterologous hosts.

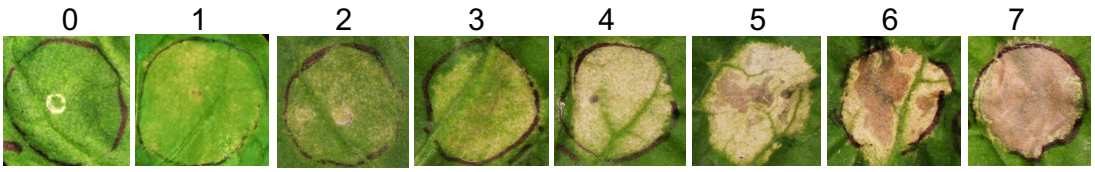


**Figure 3. Hypersensitive response (HR) cell-death scoring chart.** Cell death triggered by transient expression of HR-inducing NLRs is classified into seven severity levels and typically scored at 4–5 days post agroinfiltration. Score 1 indicates mild chlorosis in the infiltrated area. Score 2 shows pronounced yellowing with occasional mild tissue desiccation. Score 3 represents visible but patchy cell death within the infiltrated region. Score 4 corresponds to uniform mild cell death across the entire infiltrated area, appearing as white, desiccated tissue. Scores 5–7 indicate progressively severe tissue collapse manifested as browning necrotic patches, covering <30% (score 5), ~50% (score 6), or >90% (score 7) of the infiltrated area.

The core rationale of co-infiltration combinations was designed to test:

- Autoactivity: NLR expressed alone, comparing WT and autoactive MHD variants.
- Effector activation: NLR + effector pair.
- Helper dependency: effector + sensor ± helper combinations. Mutant background (eg. *nrc2/3/4* CRISPR lines) were used for complementation assays.

This standardized pipeline — combining computational identification, modular cloning, and transient functional assays — provides a rapid and flexible framework for dissecting NLR immune receptor function. By enabling comparative analyses of orthologs, mutants, and chimeras under consistent experimental conditions, it established the foundation for the subsequent biochemical and structural studies presented in later chapters. Together, this integrated workflow links sequence prediction, cloning, and biochemical validation, allowing experimental evidence to refine phylogenetic insights and build a coherent understanding of NLR evolution across plant lineages.

## 2.3 Functional and Evolutionary Dissection of Plant NLRs Using Comparative Genomics and Transient Expression

### (1) A Modular System for Studying ZAR1 Resistosome Assembly in *N. benthamiana*

The **structural discovery of the Arabidopsis ZAR1 resistosome** revolutionized our understanding of NLR receptor activation. Building on this breakthrough, we established the **pZA modular cloning toolkit**—an open-source system of 72 plasmids optimized for rapid assembly and transient expression of NLR-partner-effector modules (Publication 1; Harant et al., 2022). This toolkit laid the foundation for the core experimental pipeline now used in our lab for systematic NLR functional verification and comparative resistosome studies. Using this platform, we identified NbZAR1 as the ortholog of AtZAR1. I confirmed that **NbZAR1 reconstitutes cell death responses dependent on its conserved MADA motif and the RLCK partner JIM2**, recapitulating the AtZAR1 activation mechanism. To further verify the requirement of this cofactor, I performed **JIM2 RNAi assays**, which demonstrated that silencing NbJIM2 abolished NbZAR1-mediated cell death, confirming its functional dependency (Figure 4). Together, the development of the pZA toolkit and functional validation of NbZAR1-JIM2 interaction established a robust and versatile experimental framework for dissecting resistosome activation and exploring the evolutionary diversification of plant immune receptors.

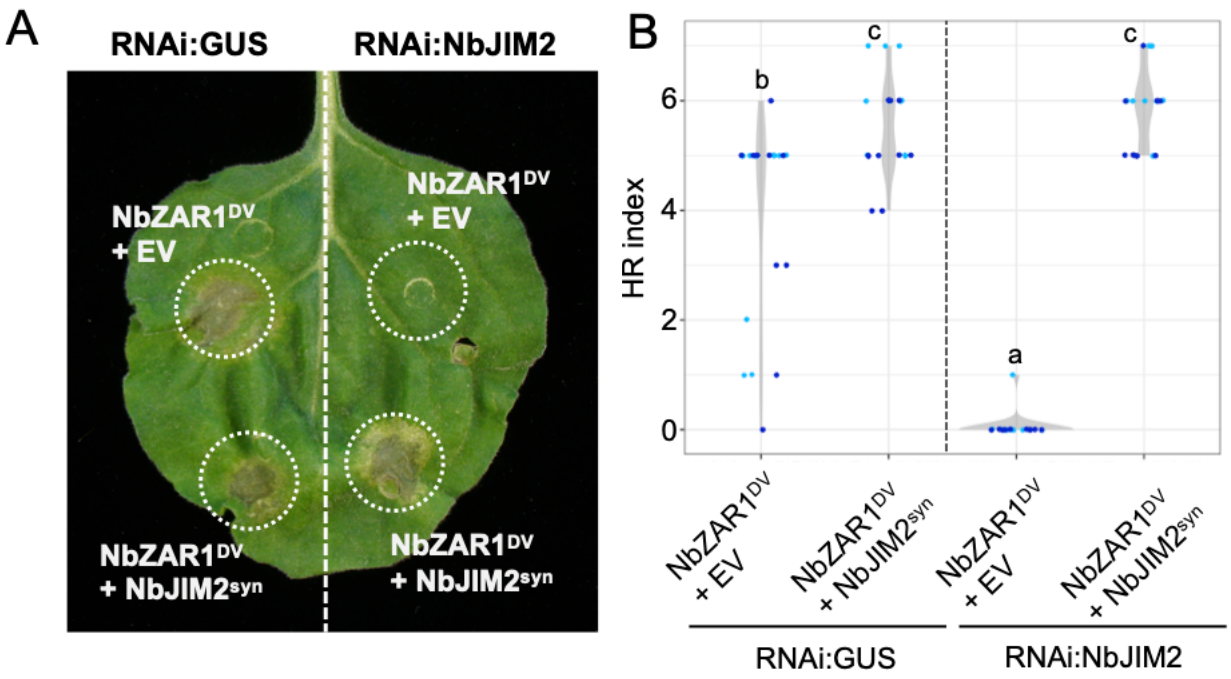


**Figure 4. NbJIM2 is required for autoactive NbZAR1-mediated cell death in *Nicotiana benthamiana*.** (A) Representative leaf showing hypersensitive cell death following co-expression of NbJIM2 and autoactive NbZAR1. Leaves were first infiltrated with Agrobacterium carrying RNAi (NbJIM2-silencing) constructs and subsequently infiltrated 1 day later with strains carrying NbJIM2$^{syn}$ and NbZAR1$^{DV}$ overexpression constructs. NbJIM2$^{syn}$ is a synonymous, RNAi-resistant variant engineered to bypass gene silencing. Photos were taken at 5 days after the second agroinfiltration. (B) Violin plots showing HR index scores compiled from three independent biological experiments. Statistical differences were analysed using Tukey's HSD test ($p < 0.01$). [Adapted from Harant et al., 2022.]

## (2) Evolutionary Conservation and Functional Diversification of ZAR1 Across Angiosperms

Building upon the methodological framework described above, we further explored the **evolutionary history and functional conservation of ZAR1 across the angiosperms** (Publication 2; Harant et al., 2023). By mining more than 120 plant genomes spanning monocots, magnoliids, and eudicots, we identified hundreds of ZAR1 orthologs and reconstructed their evolutionary trajectory. Sequence and structural analyses revealed exceptional conservation of diagnostic motifs — including the P-loop, MHD, and MADA α1 helix — underscoring the ancient origin of ZAR1, estimated to date back over 150 million years. Using the modular cloning toolkit, I cloned and transiently expressed selected orthologs in *N. benthamiana*, demonstrating that **many retained ZRK-dependent activation and cell death induction** (Figure 5), mirroring the *Arabidopsis* system. Interestingly, we also uncovered two divergent clades, ZAR1-SUB and ZAR1-CIN that have acquired thioredoxin-like integrated domains, indicating lineage-specific adaptation. Together, these findings demonstrate that ZAR1 as one of the most ancient and functionally stable immune receptors throughout flowering plant evolution.

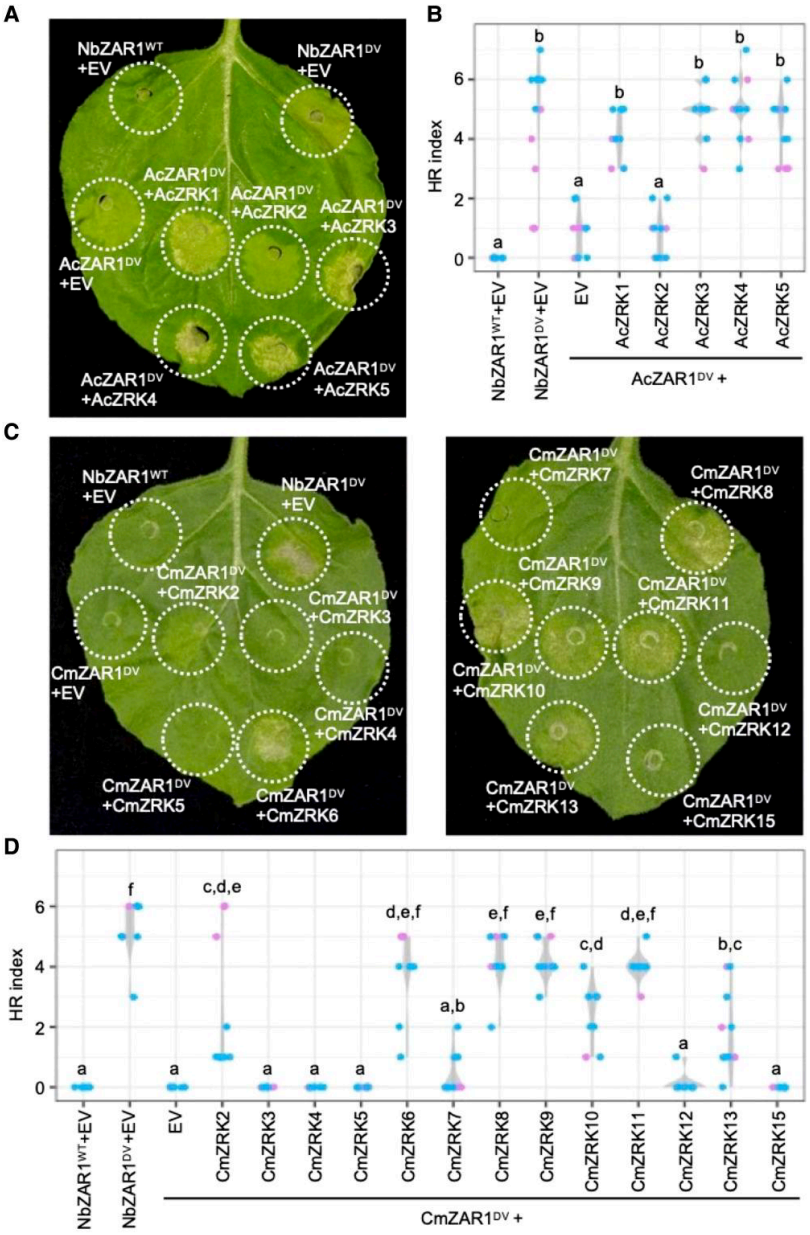


**Figure 5. ZRK family proteins positively regulate autoimmune cell death mediated by *Aquilegia coerulea* AcZAR1 and *Cinnamomum micranthum* CmZAR1 in *Nicotiana benthamiana*.** (A, C) Representative leaves showing cell death after agroinfiltration with wild-type or autoactive ZAR1 variants expressed with or without wild-type ZRKs. Leaves expressing NbZAR1$^{WT}$, NbZAR1$^{D481V}$, AcZAR1$^{D489V}$, and CmZAR1$^{D488V}$ were photographed at 4 days post agroinfiltration. (B, D) Violin plots showing AcZAR1- and CmZAR1-mediated cell death intensity, scored as an HR index from 12 and 9 biological replicates, respectively, across two independent experiments. Statistical significance was determined using Tukey's HSD test ($P < 0.01$). [Adapted from Adachi et al., 2023]

### (3) NRC3 as a Convergence Point Between Cell-Surface and Intracellular Immunity

Using our core experimental framework, we extended our analyses to the **interface between cell-surface and intracellular immune signalling**. This work (Publication 3; Kourelis et al., 2022) investigated how helper NLRs integrate with pattern-recognition receptor (PRR)-mediated defense. Through *N. benthamiana nrc2/3/4* knockout lines, transient co-expression assays, and MADA motif mutagenesis, I confirmed that NRC3 is essential for Cf-4-triggered hypersensitive cell death upon recognition of the fungal effector Avr4. Chimeric constructs swapping the NRC3 α1 helix with that of ZAR1 retained full function, confirming mechanistic conservation among MADA motif of certain CC-NLRs (Figure 6). Furthermore, effectors that suppress NRC3 activity inhibited Cf-4–triggered responses, revealing **NRC3 as a central signalling hub connecting cell-surface and intracellular immune layers**. This work redefined helper NLRs as bridges coordinating distinct tiers of plant immunity.

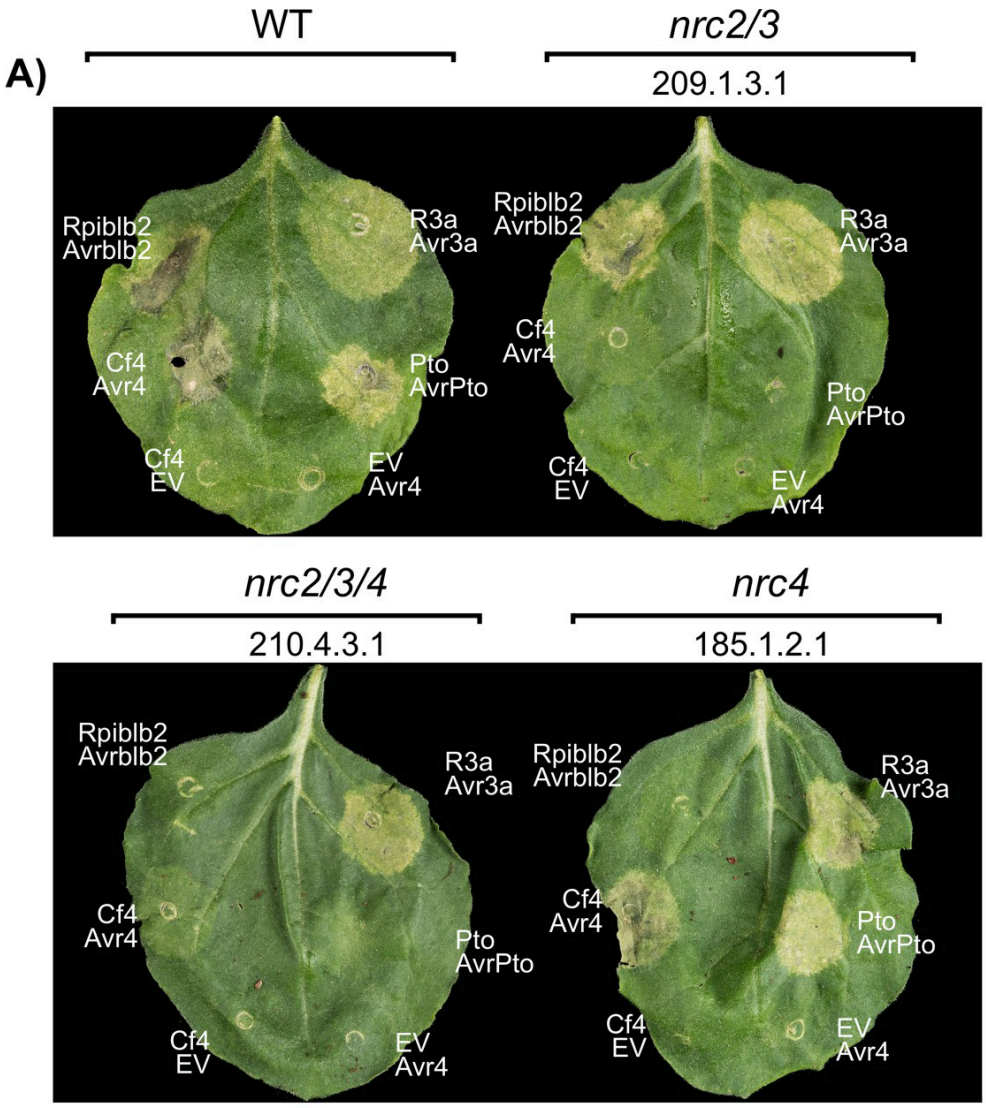


**Figure 6. Cf-4/Avr4-triggered hypersensitive cell death requires NRC2 and NRC3.** Representative *Nicotiana benthamiana* leaves showing hypersensitive cell death triggered by Cf-4/Avr4 in wild-type and NRC CRISPR knockout backgrounds. Cell death is abolished in *nrc2/3* and *nrc2/3/4* lines but retained in the *nrc4* line. Leaves were photographed 7–10 days after agroinfiltration. The NRC knockout lines (*nrc2/3* – 209.1.3.1, *nrc2/3/4* – 210.4.3.1, and *nrc4* – 185.1.2.1) are indicated above each panel. Receptor-effector pairs (Cf-4/Avr4, Prf/Pto-AvrPto, Rpi-blb2/AVRblb2, or R3a/Avr3a) are indicated on the images. Cf-4/EV (empty vector) and EV/Avr4 served as negative controls. [Adapted from Kourelis et al., 2022]

**(4) Defining the Minimal Activation Domain in Sensor–Helper NLR Signalling**

We next examined how sensor NLRs transmit activation signals to their downstream helpers (Publication 4; Contreras, Pai et al., 2024). This study revealed that the **nucleotide-binding (NB) domain of sensor NLR Rx is sufficient to activate downstream helper NLR NRC2 and immune signalling**. Using *N. benthamiana* as an assay system, I generated a series of constructs expressing truncated or domain-swapped variants of NRC-dependent sensor NLRs. Each construct was assembled using our modular Golden Gate toolkit and transiently expressed in *N. benthamiana nrc2/3/4* mutant plants. Through HR cell death assays, I confirmed the **NB domain as the minimal signalling module** (Figure 7). Parallel assays showed that NB domains from other NRC-dependent sensors — such as Gpa2, Rpi-amr1e, Rpi-amr3, and Sw-5b — retained their respective helper specificities and triggered comparable cell death responses. In addition, I further **reproduced cell death phenotypes by transient co-expression of Rx-NB and NRC2 in lettuce (*Lactuca sativa*), establishing that this two-component module is transferable across taxa** (Figure 8). Together, these results define the NB domain as a conserved signalling element for helper activation, refining our mechanistic model of NLR signalling networks and demonstrating how modular domain design and transient assays can uncover universal immune signalling logic in plants.

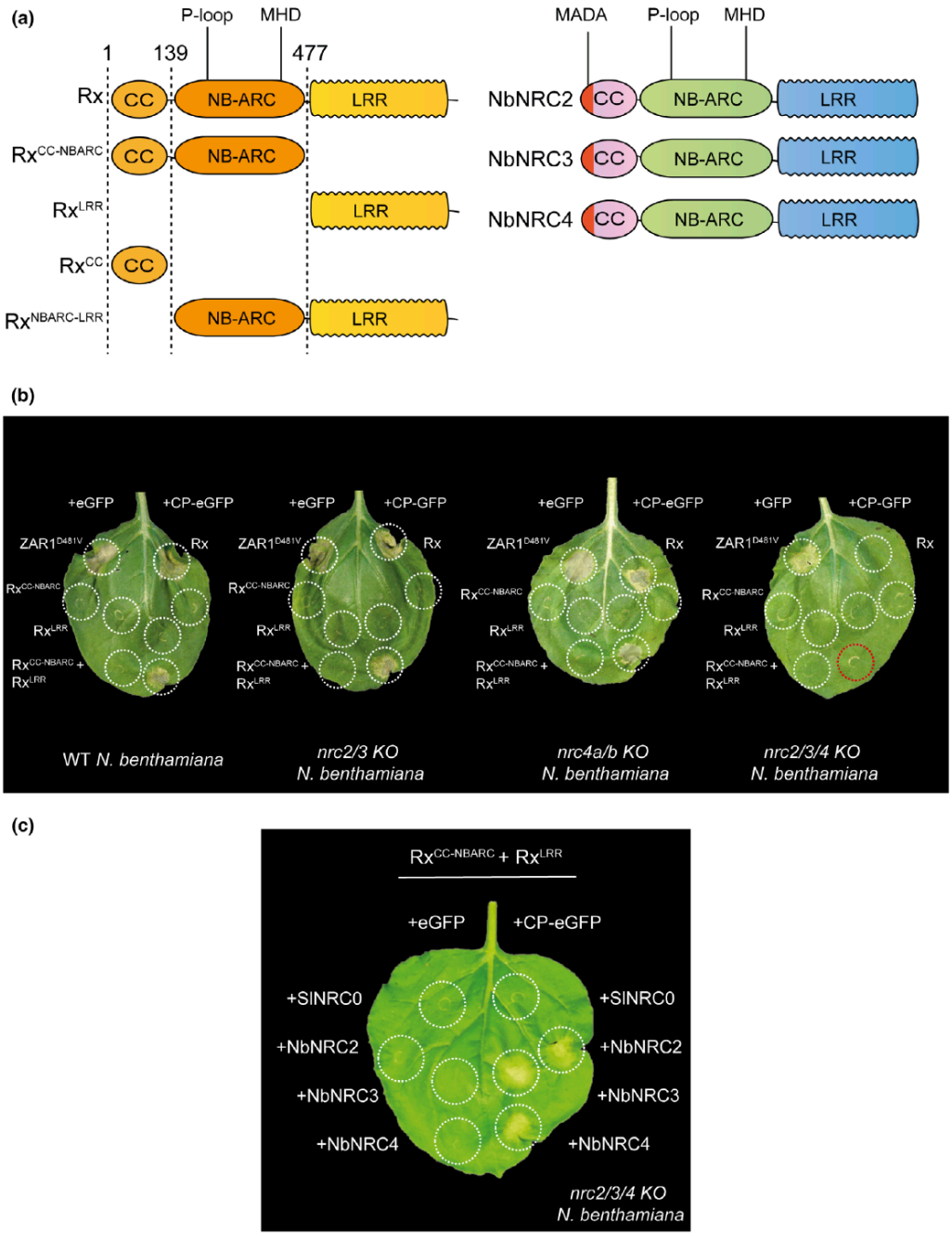


**Figure 7. Cell death triggered by trans-complemented Rx halves upon perception of *Potato virus X* (PVX) coat protein (CP) depends on NRC2, NRC3, or NRC4.** (A) Schematic representation of Rx halves and NRC constructs used in the assay. Domain boundaries and approximate positions of the MADA, P-loop, and MHD motifs are indicated. Presence of the N-terminal MADA motif is shown in red. (B, C) Representative *Nicotiana benthamiana* knockout line leaves agroinfiltrated with the indicated constructs and photographed 5–7 days post infiltration. (B) Cell death mediated by RxCC-NBARC and RxLRR expressed *in trans* is abolished only in the *nrc2/3/4* knockout background (highlighted by red dotted circle). Wild-type Rx and NbZAR1$^{D481V}$ were included as controls for NRC-dependent and NRC-independent cell death, respectively. (C) Cell death mediated by PVX CP–activated Rx halves is restored in nrc2/3/4 plants by co-expression of NbNRC2, NbNRC3, or NbNRC4. Free eGFP served as a negative control for C-terminally eGFP-tagged PVX CP, and SlNRC0 was included as a non-functional helper control. All experiments were repeated three times with at least six technical replicates per experiment, yielding similar results. [Adapted from Contreras and Pai et al., 2024]

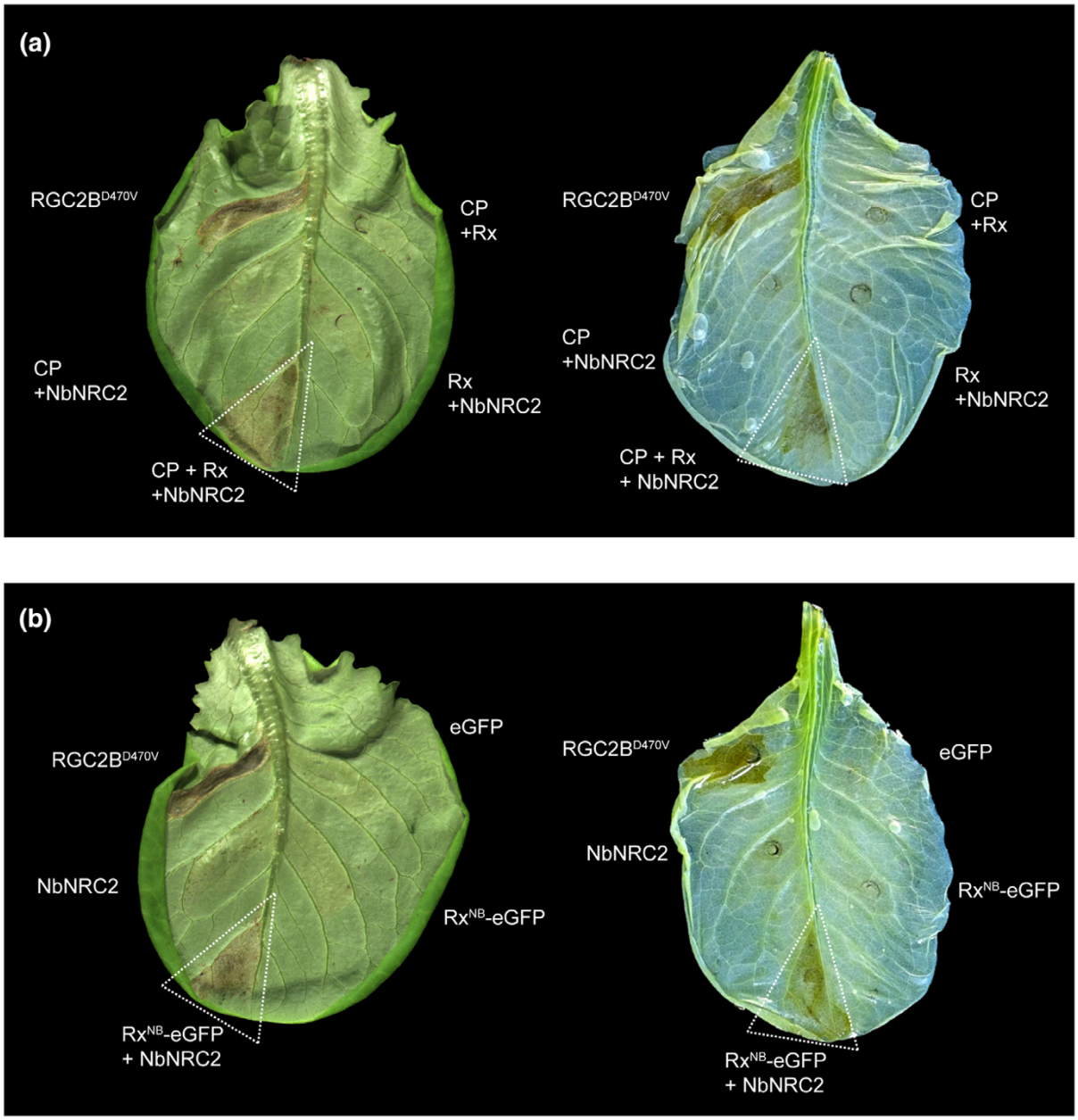


**Figure 8. Rx, Rx$^{NB}$, and the helper NRC2 constitute a minimal transferable immune unit in lettuce (*Lactuca sativa*).** Representative leaves of *L. sativa* var. 'Fenston' showing hypersensitive cell death following agroinfiltration. (A) Cell death observed only when *Potato virus X* (PVX) coat protein (CP), Rx, and NbNRC2 were co-expressed. Omission of any single component abolished the response. (B) Cell death induced by co-expression of Rx$^{NB}$-eGFP and NbNRC2. No cell death was observed with eGFP alone or when Rx$^{NB}$-eGFP and NbNRC2 were expressed individually. For both (A) and (B), left panels show the abaxial side of leaves imaged directly, and right panels show ethanol-bleached leaves to enhance visualization of cell death. Images were taken 5-7 days post agroinfiltration. HR is more visible on the abaxial surface. The constitutively active lettuce NLR RGC2B$^{D470V}$ was used as a positive control. Experiments were repeated three times with similar results. [Adapted from Contreras and Pai et al., 2024]

**(5) Evolutionary Architecture and Functional Validation of Hierarchical NLR Networks in Lettuce**

To broaden our understanding of how NLR signalling networks evolved across angiosperms, we investigated the **organization and evolution of NRC network beyond *Solanaceae*** (Pai et al., 2025, bioRxiv). This work combined phylogenomics with functional assays to uncover the evolutionary organization of the NRC network in *Lactuca sativa*. Comparative analysis across 69 genomes from *Solanales* and *Asterales* revealed that **lettuce maintains a minimal NRC network comprising two helper NLRs and several diversified sensor clades**. To test the predicted network hierarchy, I used our modular cloning and transient expression system in *N. benthamiana* to co-express lettuce sensor–helper pairs. These assays confirmed that distinct groups of lettuce sensors depend on specific helpers (LsatNRC0 or Ast-LsatNRC1) to trigger cell death (Figure 9). Integrating these results with evolutionary rate and structural modelling analyses, we found that **helper NLRs remain highly conserved, whereas sensor NLRs diversify rapidly under positive selection**, particularly in the LRR domain. This study demonstrates how combining large-scale phylogenomics with standardized functional assays reveals the contrasting evolutionary pressures that shape stable signalling cores and diversifying pathogen recognition modules across plant lineages.

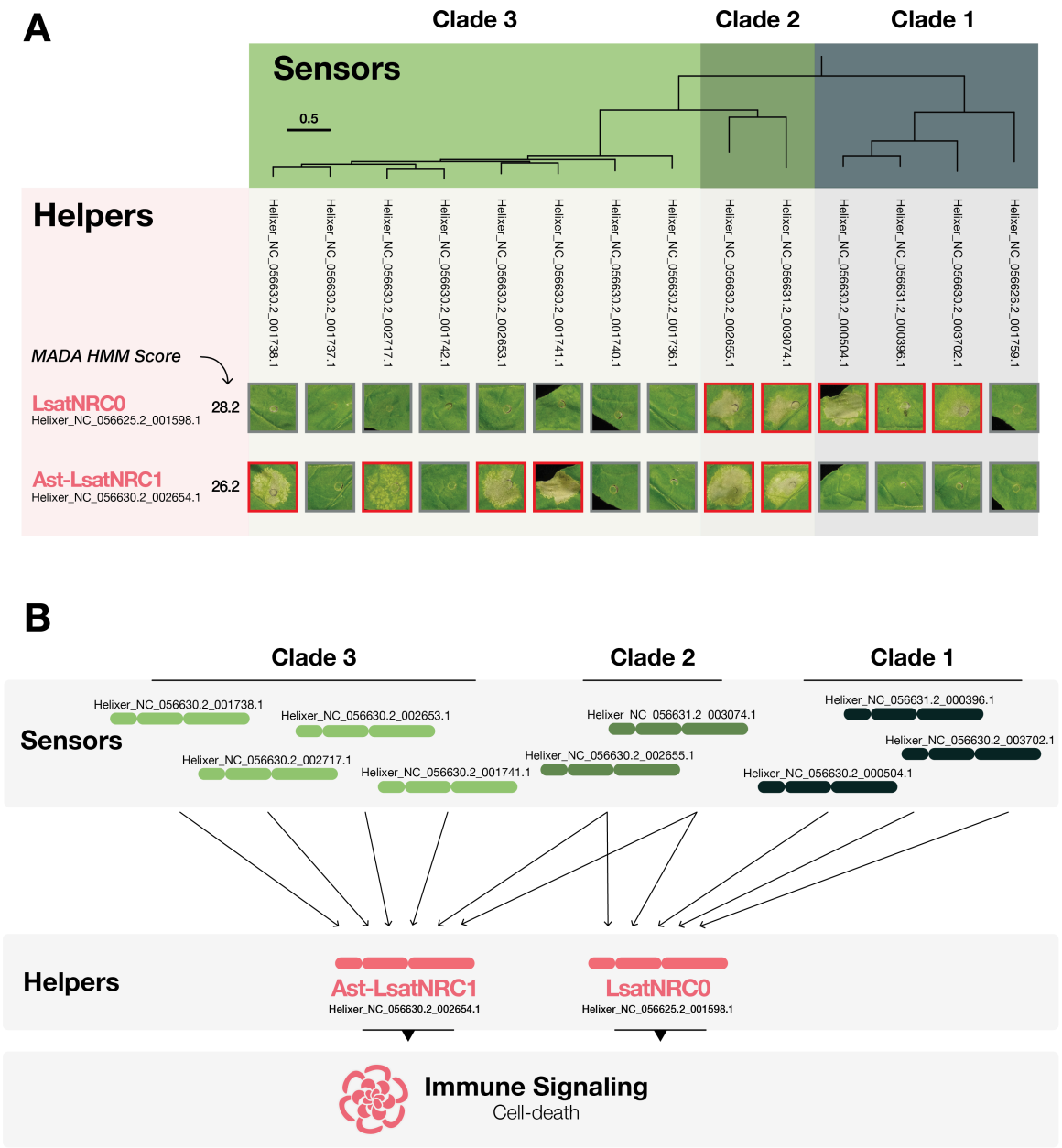


**Figure 9. LsatNRC0 and Ast-LsatNRC1 mediate cell death signalling of distinct NRC-S phylogenetic clades.** (A) Co-agroinfiltration cell death assays of NRC helper (NRC-H) and NRC sensor (NRC-S) proteins. NRC-S proteins were expressed as autoactive mutants together with wild-type NRC helpers. Hypersensitive cell death was observed when autoactive NRC-S was co-expressed and activated NRC-H proteins that possess HR-inducing signalling capacity. (B) Model of the lettuce NRC signalling network, showing that validated NRC-S proteins signal cell death through NRC-Hs LsatNRC0 and Ast-LsatNRC1 in a partially redundant manner. [Adapted from Pai et al., 2025]

## 2.4 Summary

This chapter presented a **standardized workflow for high-throughput identification and functional analysis of plant NLR immune receptors, integrating computational prediction, modular cloning, and transient assays.** Leveraging ***N. benthamiana* as a versatile assay host** underpins the robustness of this system in testing NLR activation: its rapid growth, exceptional compatibility with Agrobacterium-mediated transformation, advanced genomic resources, susceptibility to a broad range of pathogens, and availability of defined mutant lines such as *nrc2/3/4*. These features make it an **ideal model for reconstituting NLR signalling and effector recognition from diverse plant lineages**, enabling functional validation of immune receptors that cannot easily be assayed in their native species. Furthermore, my work showed that this pipeline is readily **transferable to other systems**. For example, the same modular cloning and HR assay framework has been successfully adapted for lettuce, allowing comparative evaluation of NLR signalling networks in distantly related taxa. Such flexibility highlights the pipeline's potential as a generalizable platform for broad phylogenetic and translational studies in plant immunity, transforming the pace at which NLR biology can be studied.

Despite these advantages, further optimization of expression levels and environmental conditions would be helpful to minimize artefacts and the effects of other factors on hypersensitive responses. Future directions will also focus on improving assay throughput and automation. Streamlining HR-based readouts through protoplast assays or suspension cell cultures could enable quantitative and automated screening of large NLR–effector libraries (Danon, 2014; Miebach et al., 2022). Parallel advances in high-content imaging and fluorescence-based viability assays will facilitate real-time monitoring of immune activation, expanding the capacity for functional screening beyond traditional visual scoring of hypersensitive cell death.

Another emerging opportunity lies in **integrating AI and machine learning to enhance genome annotation and NLR gene prediction** (Toghani et al. 2025). AI-assisted approaches, such as domain-aware neural networks and structure-informed classifiers, promise to improve the precision of NLR annotation and prioritize candidates for experimental testing (Li et al., 2023; Martin et al., 2023). Coupling these AI-driven tools with modular cloning and functional assays would create a closed-loop discovery pipeline — from *in silico* identification to *in vivo* verification.

Finally, by linking this workflow to downstream biochemical and structural analyses such as BN-PAGE and cryo-EM (introduced in the next Chapters 3 and 4), it becomes possible to **follow NLRs from sequence to structure, elucidating how evolutionary diversification translates into molecular function**. By connecting

computational prediction with mechanistic insight, it advances our capacity to dissect and engineer plant immune receptor diversity.

# Chapter 3

# Probing NLR Immune Receptor Complexes with Blue Native Polyacrylamide Gel Electrophoresis (BN-PAGE)

NLRs can function as individual singletons or in higher-order configurations, such as pairs, or networks, where they often exhibit a **sensor-helper dynamic** (Adachi et al, 2019; Feehan et al, 2020; Wu et al, 2017; Wu et al, 2018). The structural elucidation of *Arabidopsis* ZAR1 was a groundbreaking discovery that revealed how NLR activation involves the **oligomerization of these receptors into multiprotein complexes known as resistosomes**, a key feature of immune response. While studies of ZAR1 demonstrated how a singleton NLR transitions from a resting monomer to an active pentameric resistosome (Wang et al., 2019; Förderer et al. 2022; Zhao et al., 2022), the biochemical mechanisms governing paired and networked NLR activation remain unclear.

Compared to chromatography and other fractionation methods, non-denaturing PAGE especially **blue native polyacrylamide gel electrophoresis (BN-PAGE)** offers an efficient approach for analyzing multimeric protein complexes using small amount of input samples, enabling the study of protein complexes in their *in vivo* state (Eubel et al., 2005; Na Ayutthaya et al., 2020). In this chapter, I demonstrate **the use of BN-PAGE in uncovering diverse activation mechanisms of NLR resistosomes beyond the canonical ZAR1 model.** In **networked NLRs such as Rx–NRC2**, effector recognition triggers oligomerization of the helper NRC2 while the sensor remains monomeric, supporting an activation-and-release model. In contrast, the **paired NLRs Pikm-1/Pikm-2** exist as a constitutive hetero-complex prior to activation (Figure 10). Further extending the approach, we found that the nematode effector SS15 inhibits immunity by binding NRC2 and blocking its oligomerization, with naturally evolved NRC variants escaping suppression. Together, these findings highlight the versatility of BN-PAGE in dissecting NLR activation, effector interference, and evolutionary adaptation.

## Key Publications in Chapter 3:


1. Contreras MP, H Pai, Y Tumtas, C Duggan, ELH Yuen, A Vergara Cruces, J Kourelis, HK Ahn, KT Lee, CH Wu, TO Bozkurt, L Derevnina, and S Kamoun. (2023c) Sensor NLR immune proteins activate oligomerization of their NRC helpers in response to plant pathogens. EMBO Journal 42:e111519.

2. Contreras MP, H Pai, M Selvaraj, A Toghani, DM Lawson, Y Tumtas, C Duggan, ELH Yuen, CEM Stevenson, A Harant, CH Wu, TO Bozkurt, S Kamoun, and L Derevnina. (2023b) Resurrection of plant disease resistance proteins via helper NLR bioengineering. Science Advances 9:3861.

3. Sugihara Y, J Kourelis, MP Contreras, H Pai, M Selvaraj, A Toghani, C Martínez-Anaya, and S Kamoun. (2025) Helper NLR immune protein NRC3 evolved to evade inhibition by a cyst nematode virulence effector. PLoS Genet. 21:e1011653.

4. Pai H, MP Contreras, J Salguero Linares, D Lüdke, A Posbeyikian, J Kourelis, S Kamoun, and C Marchal. (2025). The Pik NLR pair accumulates at the plasma membrane as a hetero oligomeric sensor-helper immune protein complex prior to activation. bioRxiv DOI: 10.64898/2025.11.30.691369.

5. Pai H, MP Contreras, C Marchal, J Kourelis, A Posbeyikian, and S Kamoun. (2023) Probing the oligomeric state of activated NLR immune receptors by blue native-polyacrylamide gel electrophoresis (BN-PAGE). Zenodo DOI: 10.5281/zenodo.8146428.

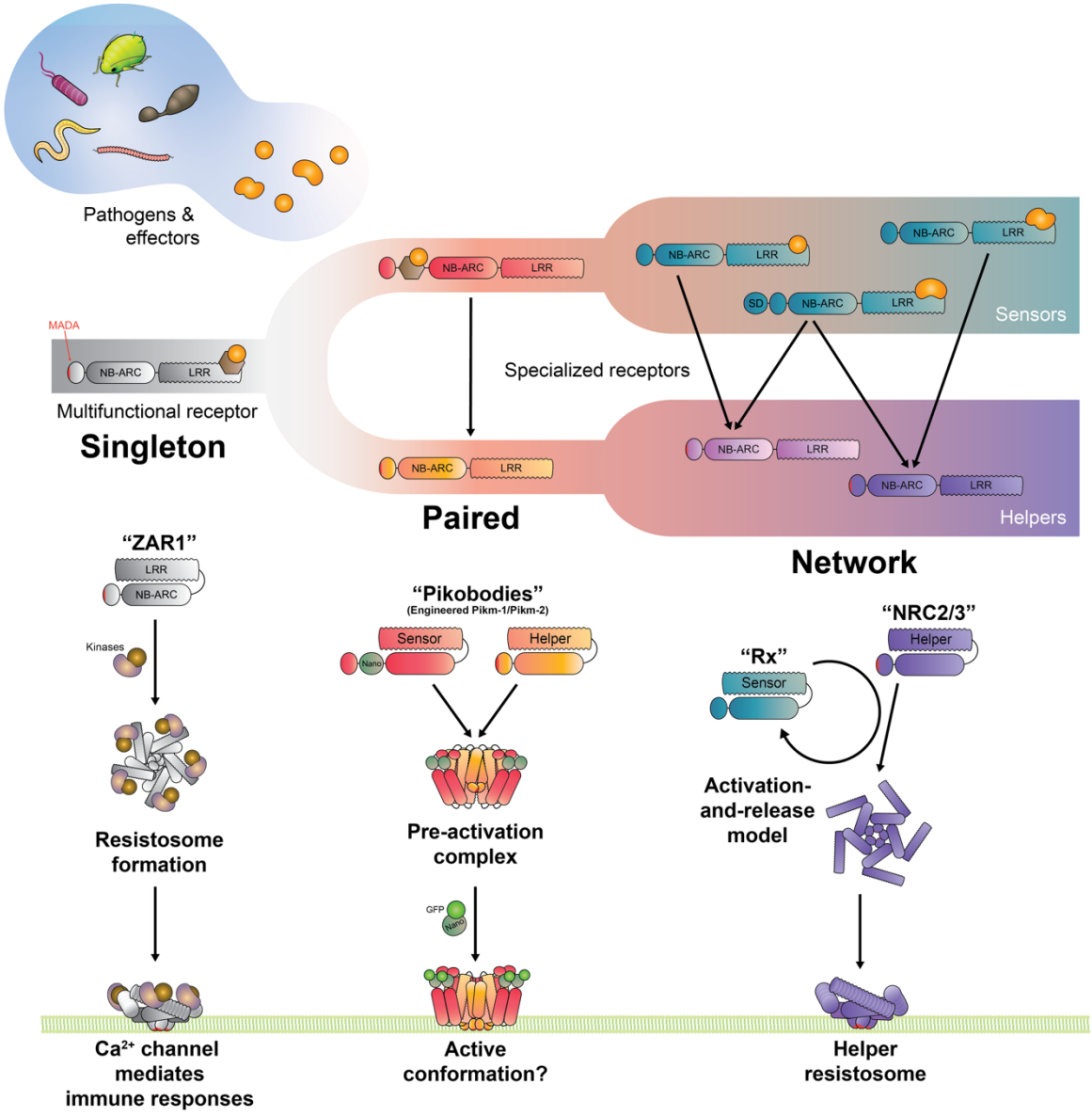


**Figure 10. Proposed models of resistosome activation in singleton, paired, and networked NLR systems.**

**Upper panel:** Evolutionary diversification of plant NLRs into functional singletons, pairs, and networks. While singleton NLRs retain both sensing and signalling capacities, gene duplication and specialization over evolutionary time have led to the emergence of distinct "sensor" and "helper" receptors that function as paired units or as components of complex signalling networks.

**Lower panel:** Distinct activation mechanisms of NLR systems. (Left) Upon direct or indirect effector recognition, singleton CC-NLRs such as ZAR1 assemble into homo-pentameric resistosomes that localize to the plasma membrane and initiate immune signalling, likely through calcium-permeable channel activity. (Middle) Proposed pre-activation assembly model for paired NLRs exemplified by Pikm-1/Pikm-2, in which sensor and helper form a stable hetero-oligomeric complex at the plasma membrane prior to effector perception. An engineered Pikm-1/Pikm-2 pair ("pikobodies") that recognizes GFP was used to validate this model. (Right) The NRC network operates via an "activation-and-release" mechanism, in which activated sensor NLRs transmit a signal to downstream NRC helpers, triggering their oligomerization into resistosome-like complexes that accumulate at the plasma membrane independently of the sensors. [Modified from Contreras et al., 2023a]

## 3.1 Foundations, Development, and Applications of BN-PAGE in Plant Research

### The Principles of BN-PAGE

BN-PAGE is a **non-denaturing technique that enables separation of intact protein complexes according to their molecular weight** while preserving their native structures and interactions. Unlike SDS-PAGE, which denatures proteins through detergent binding, **BN-PAGE employs Coomassie Brilliant Blue G-250** as a charge-shifting dye. The dye binds to proteins and confers a uniform negative charge without disrupting their quaternary structure, allowing migration in an electric field according to molecular size and shape (Na Ayutthaya et al., 2020; Reisinger and Eichacker, 2006). **Mild, non-ionic detergents** such as digitonin, DDM, or Triton X-100 are typically used to solubilize membrane-associated or multimeric complexes while maintaining native interactions (Eubel et al., 2005; Ma and Chia, 2008). As proteins migrate through the gradient polyacrylamide matrix, they resolve into discrete bands representing intact assemblies, oligomeric states, or intermediate complexes. **BN-PAGE can be further combined with SDS-PAGE in a two-dimensional format** (2D BN/SDS-PAGE) to resolve subunit composition after denaturation (Ahn et al., 2023; Klepsch et al., 2008). Owing to its simplicity and ability to preserve native conformation, BN-PAGE has become an indispensable method for analyzing oligomerization, supercomplex formation, and assembly dynamics of both soluble and membrane-bound protein complexes.

### Development of BN-PAGE and Its Application in Plant Research

BN-PAGE was **first introduced in 1991** by Schägger and von Jagow as a powerful non-denaturing technique for resolving mitochondrial membrane protein complexes. Initially designed for mammalian systems, it allowed intact macromolecular assemblies — especially large, hydrophobic complexes — to migrate according to their native size and charge while maintaining biological activity (Fiala et al., 2011; Schägger and von Jagow, 1991). This innovation marked a turning point in structural biochemistry, enabling **visualization of functional complexes** that had previously been intractable to denaturing methods.

The **adoption of BN-PAGE in plant research began in the early 2000s**, when investigators sought to resolve native protein complexes involved in photosynthesis and respiration. Early landmark studies (2003-2005) successfully separated mitochondrial respiratory chain components such as complexes I, III, and V, as well as

chloroplast thylakoid membrane assemblies (Järvi et al., 2011; Ma and Xia, 2008; Nijtmans et al., 2002; Reisinger and Eichacker, 2006). These initial applications in maize, *Arabidopsis*, and potato demonstrated that BN-PAGE could retain the structural integrity of highly hydrophobic photosynthetic and respiratory proteins, establishing it as an indispensable method in plant biochemistry.

A major leap occurred in 2005 with the influential review and methodological synthesis by Eubel and colleagues, which **standardized BN-PAGE protocols for plant organelles.** Their work expanded the technique beyond mitochondria and chloroplasts to encompass plasma-membrane, stromal, and cytosolic complexes. Eubel et al. also introduced practical refinements, including the use of mild detergents such as digitonin to stabilize fragile supercomplexes, and the combination of BN-PAGE with SDS-PAGE in two-dimensional separations (Eubel et al., 2005; Klepsch et al., 2008). This 2D-BN/SDS-PAGE approach enabled detailed subunit mapping, revealing the modular organization of plant respiratory and photosynthetic machinery and promoting widespread adoption across plant proteomics laboratories (Klepsch et al., 2008; Na Ayutthaya et al., 2020).

**Through the 2010s, BN-PAGE became a cornerstone of functional plant proteomics.** Advances in **gel chemistry, gradient optimization, and detergent selection** improved resolution across a broad molecular weight range, allowing detection of small soluble assemblies and multi-megadalton supercomplexes alike (Ball and Roulhac, 2010; Wittig et al., 2010). **Coupled with mass spectrometry and immunoblotting**, BN-PAGE facilitated systematic studies of protein–protein interactions, post-translational modifications, and dynamic complex remodelling in response to stress, development, and environmental cues (Järvi et al., 2011; Woods et al., 2011). Specialized variants even preserved metal cofactors and enzymatic activity, broadening the method's utility for metalloproteomics and enzymology (Nolte and Langer, 2021; Tanambell et al., 2025).

By the 2020s, BN-PAGE had matured into a fully standardized, reproducible platform integral to modern plant structural biology. Protocols tailored for model species such as *A. thaliana* provided detailed guidance on sample preparation, detergent choice, and gel conditions, ensuring consistency across laboratories (Ahn and Jones, 2023; Na Ayutthaya et al., 2020). **The method now underpins investigations ranging from chloroplast ATP synthase assembly to NLR resistosome formation**, serving as a bridge between biochemical fractionation and high-resolution cryo-EM.

## BN-PAGE in the Studies of Plant Resistosomes

The use of BN-PAGE in plant immunity research was catalyzed by the landmark studies on *Arabidopsis* ZAR1 (Li et al., 2019; Bi et al., 2019), which demonstrated that the receptor undergoes an **activation-dependent transition from a monomeric to an ~800 kDa oligomeric complex** — providing the first direct biochemical evidence of resistosome formation (Li et al., 2019; Bi et al., 2019). Subsequent applications rapidly expanded to diverse immune systems, including **TIR-type NLRs such as NRG1.1** (Jacob et al., 2021), the ***Solanaceae* NRC network** (Contreras et al., 2023b, 2023c; Contreras and Pai et al., 2024), and the **visualization of effector-mediated inhibition** (Contreras et al., 2023b; Sugihara et al., 2024).

Through these advances, BN-PAGE emerged as a key method for dissecting NLR activation pathways. It provides a rapid and sensitive means to monitor resistosome formation directly from plant tissues and paving the way for downstream characterization by cryo-EM and functional assays.

## 3.2 General Methods for BN-PAGE–Based Analysis of Plant NLR Activation

Across the studies, I developed and applied a **standardized workflow combining modular cloning, targeted mutagenesis, and BN-PAGE to investigate NLR activation and resistosome formation** in *N. benthamiana* (Figure 11).

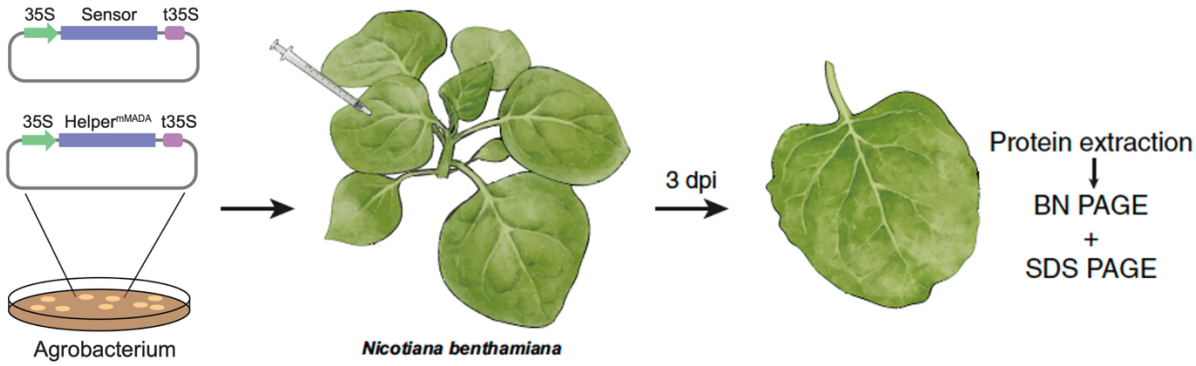


**Figure 11. Workflow of protein PAGE–based analysis of NLR resistosome activation in *Nicotiana benthamiana*.** Sensor and helper NLR constructs driven by the CaMV 35S promoter are cloned into binary vectors and transformed into *Agrobacterium tumefaciens*. Agrobacteria carrying the indicated constructs are co-infiltrated into *N. benthamiana* leaves for transient expression. At 2-3 days post-infiltration (dpi), infiltrated leaf tissue is harvested for protein extraction. Native protein complexes are analyzed by blue native polyacrylamide gel electrophoresis (BN-PAGE), followed by SDS–PAGE for subunit resolution. This workflow enables visualization of NLR complex assembly and resistosome formation *in vivo*. [Adapted from Contreras et al., 2023c]

### (1) Construct Generation Using Modular Cloning

Following the same principles described in Chapter 2, I generated all constructs for BN-PAGE assays using Golden Gate Modular Cloning (MoClo) systems (Weber et al., 2011) and the MoClo Plant Parts kit (Engler et al., 2014). I assembled multigene expression cassettes containing a 2×35S promoter, the synthesized coding sequence of the gene of interest, a C-terminal tag, and a 35S terminator. These constructs were cloned into the binary vector pJK268c (Kourelis et al., 2020), which carries the *Tomato bushy stunt virus* silencing suppressor p19 to enhance transient expression and includes a kanamycin resistance cassette for selection.

### (2) Tagging and Heavy/Light Tag Strategy

To visualize and characterize protein complexes, I **fused each NLR or effector with a C-terminal epitope or fluorescent tag**. Standard tags included 6×HA, 4×Myc,

3×FLAG, and 2×V5. To distinguish the composition of oligomeric complexes, I used a **"heavy/light" tagging strategy** by generating "heavy" versions of selected proteins with larger tandem tags (for example, mCherry-6×HA compared with 6×HA) on one component of a complex, enabling molecular weight shifts to be detected by BN-PAGE. Applications of this approach are described in Section 3.3.

## (3) Mutagenesis for HR Suppression and Biochemical Analysis

To study activated complexes without HR-induced tissue collapse, I introduced targeted mutations in the conserved N-terminal α1 helix (MADA motif) of helper NLRs (Figure 12). The **MADA motif is essential for HR execution but dispensable for effector perception and signalling** (Adachi et al., 2019; Kourelis et al., 2021). Mutations such as NRC2$^{L9/13/17E}$ (NRC2$^{EEE}$), NRC4$^{L9A/V10A/L14A}$ (NRC4$^{AAA}$), and Pikm-2$^{L19/23E}$ (Pikm-2$^{EE}$) abolished HR while preserving stable protein expression and activation. Equivalent mutants (e.g., CaNRC3$^{EEE}$, StNRC3$^{EEE}$, SlNRC3$^{EEE}$) were generated for comparative biochemical analyses across Solanaceae species. These mutants provided an ideal system for biochemical investigation of NLR activation and resistosome formation under native conditions.

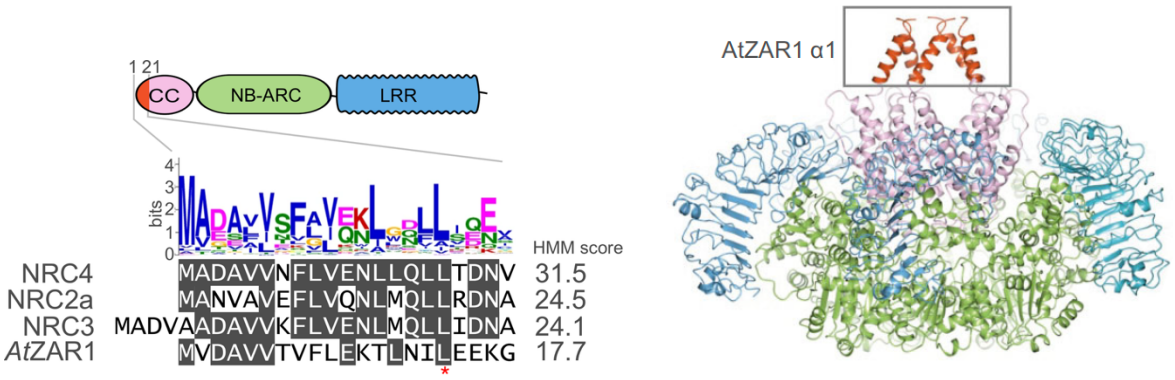


**Figure 12. Conservation and structural localization of the N-terminal MADA motif in CC-NLRs.** (Left) Sequence alignment of the N-terminal MADA motifs from NRC2a, NRC3, NRC4, and *Arabidopsis thaliana* ZAR1 (AtZAR1) shows the consensus MADA motif. Corresponding hidden Markov model (HMM) scores for each sequence are indicated. (Right) Structure of AtZAR1 resistosome highlighting the N-terminal α1 helix that harbours the MADA motif. [Adapted from Adachi et al., 2019 and Kourelis et al., 2022]

## (4) BN-PAGE Workflow

To assess the oligomeric state of transiently expressed proteins, I employed **BN-PAGE as the central technique to directly visualize NLR oligomerization**. I infiltrated four- to five-week-old *N. benthamiana* plants with *A. tumefaciens* strains carrying the

constructs of interest at final $OD_{600}$ = 0.3 for NLRs and 0.2 for effectors. Leaf tissue was collected three days post-infiltration (or two days for NRC4 experiments). I collected six 8-mm leaf discs, snap-froze them in liquid nitrogen, and stored the samples at −80°C until use.

I performed BN-PAGE using the Bis-Tris NativePAGE system (Invitrogen), and the same protein extract was used to run parallel SDS-PAGE assays under denaturing conditions to verify protein expression. On the day of analysis, I ground the frozen leaf tissue into a fine powder using a GenoGrinder (1500 rpm, 55 s). The tissue powder was mixed with 200 µL of freshly prepared ice-cold BN extraction buffer (50 mM Tris-HCl (pH 7.5), 50 mM NaCl, 5 mM $MgCl_2$, 10% glycerol) supplemented with 0.2–0.5% detergent (Triton X-100, IGEPAL, or digitonin depending on protein solubility), 1% DTT, and 1x protease inhibitor cocktail (Sigma). Samples were vortexed intermittently during a 10-min incubation on ice and centrifuged at 13,000 rpm for 15 min at 4°C.

The clarified supernatant was mixed 1:1 with 4x NativePAGE sample buffer and 5% G-250 additive (Invitrogen) before loading 10 µL per lane onto a 3–12% Bis-Tris NativePAGE gel (Invitrogen). Gels were run in XCell SureLock Mini-Cells using the manufacturer's dark and light cathode buffer system (BN2001 and BN2002, Invitrogen) with an initial phase of 150 V for 40 min, followed by 200 V for 90 min at 4°C.

After electrophoresis, proteins were transferred onto PVDF membranes using a semi-dry system (Bio-Rad, 25 V, 1 A, 30 min) in NuPAGE transfer buffer (Invitrogen). Membranes were incubated in 8% acetic acid for 15 min to fix proteins, rinsed thoroughly with water, and air-dried. Marker bands were activated with 100% ethanol and annotated. Blots were then rehydrated in TBST, blocked, and probed with the appropriate primary antibodies overnight at 4°C, followed by standard chemiluminescent detection.

This workflow enabled systematic analysis of NLR activation and resistosome formation under native conditions, providing a robust methodological foundation for the comparative studies summarized in the next section.

## 3.3 Application of BN-PAGE for visualizing NLR oligomerization

**(1) Validation of helper resistosome formation and sensor-helper specificity**

As introduced in Chapter 2, the NRC immune receptor network exemplifies a modular signalling architecture, where helper NLRs NRC2/3/4 mediate defense activation downstream of multiple sensor NLRs. This networked immune signalling system enhances robustness and evolutionary flexibility against pathogens. Building on the genetic framework established by Wu et al. (2017), which revealed that NRC2/3/4 redundantly support Rx-, Bs2-, R8-, and Sw5b-mediated immunity while NRC4 is specifically required for Rpi-blb2 signalling (Publication 1, Figure 13), **I investigated whether these sensor–helper signal transduction could be recapitulated biochemically through BN-PAGE assays.**

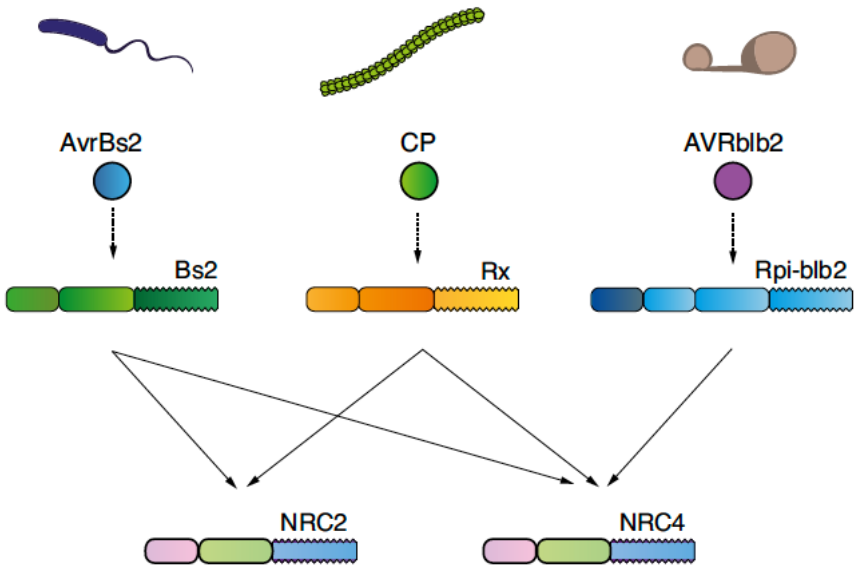


**Figure 13. Schematic representation of helper NLR utilization by different sensor NLRs.** The bacterial effector AvrBs2 is perceived by the sensor NLR Bs2, which signals through both NRC2 and NRC4. Similarly, *Potato virus X* (PVX) coat protein (CP) is recognized by the sensor NLR Rx and activates immune signalling via both NRC2 and NRC4. In contrast, the phytophthora effector AVRblb2 is perceived by the sensor NLR Rpi-blb2, which signals exclusively through NRC4. Arrows indicate functional genetic dependencies between sensors and their downstream helper NRCs. [Adapted from Contreras et al., 2023c]

Using the **cell-death–abolished MADA motif mutants** NRC2$^{EEE}$ and NRC4$^{AAA}$, I expressed the NRC helpers with their upstream sensor NLRs in *nrc2/3/4* CRISPR *N. benthamiana* lines, and visualize NRC oligomerization by BN-PAGE following effector-triggered activation. Firstly, upon activation (e.g., NRC2$^{EEE}$ co-expressed with Rx and PVX CP, Figure 14), the **helper NRC2$^{EEE}$ shifts from a fast-migrating band (~200 kDa)**

to a high-molecular-weight complex (in the 720 to 1,048 kDa range), resembling ZAR1 resistosome formation (Li et al., 2019; Bi et al., 2019). This demonstrated NRC2 oligomerization and resistosome formation.

Consistent with prior reports, activation of Rx or Bs2 induced NRC2 oligomerization into a high-molecular-weight complex, while Rpi-blb2 did not, confirming its NRC4 dependency. Conversely, NRC4 formed oligomers upon activation by all three sensors (Figure 15). These findings bridge genetic and biochemical evidence, demonstrating that helper resistosome formation reflects the established sensor-helper specificities within the NRC network.

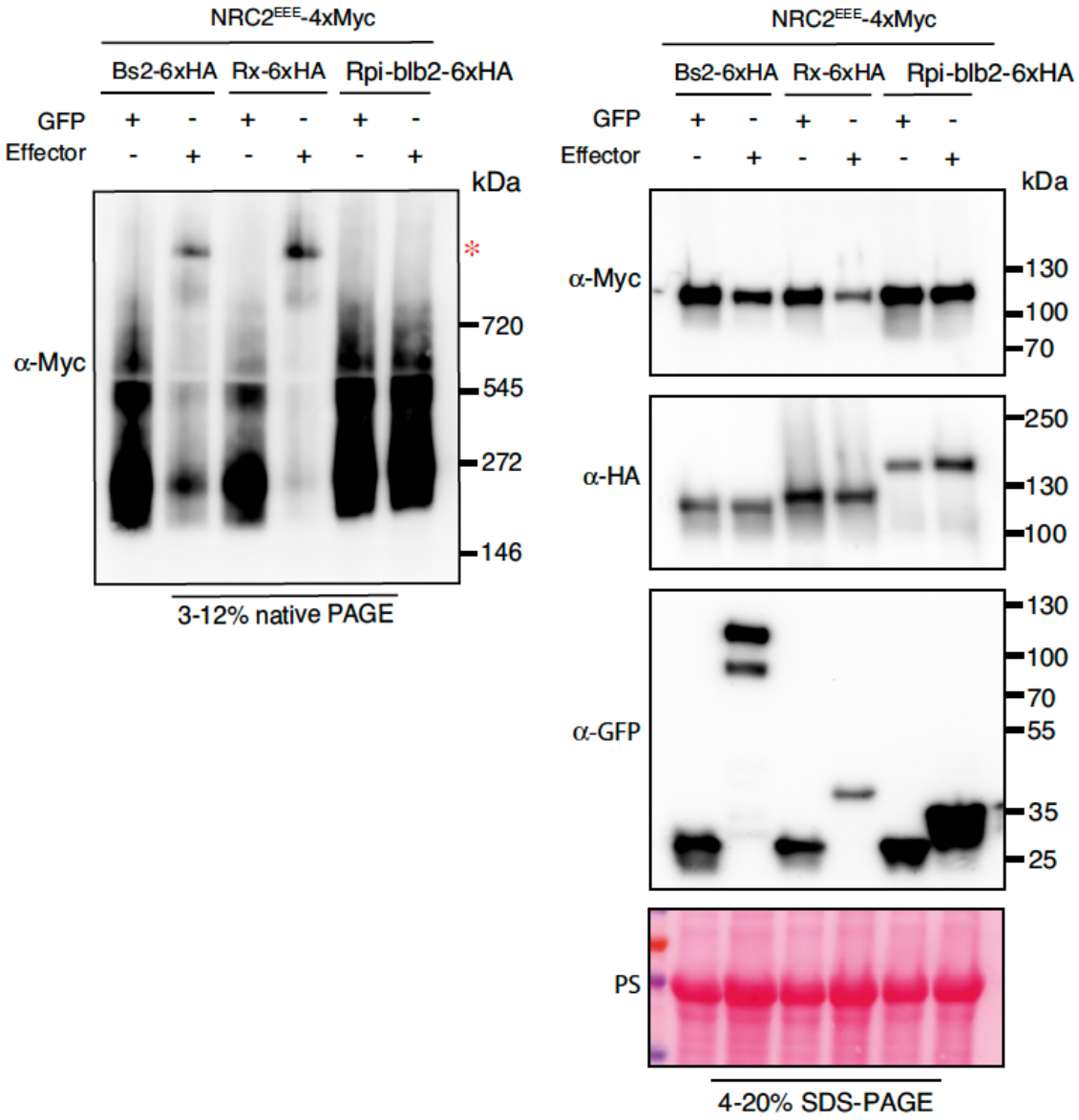


**Figure 14. NRC2-dependent sensor NLRs Bs2 and Rx trigger oligomerization of NRC2$^{EEE}$.** Blue native PAGE (BN-PAGE) and SDS–PAGE analyses showing the oligomerization status of NRC2$^{EEE}$ in the presence of inactive or activated NRC-dependent sensors. Total protein was analyzed on native and denaturing gels before immunoblotting with the indicated antisera. Approximate protein molecular weights (kDa) are shown. Red asterisks mark the bands corresponding to activated NRC2$^{EEE}$ oligomeric complexes. Ponceau S (PS) staining of Rubisco served as a loading control. [Adapted from Contreras et al., 2022]

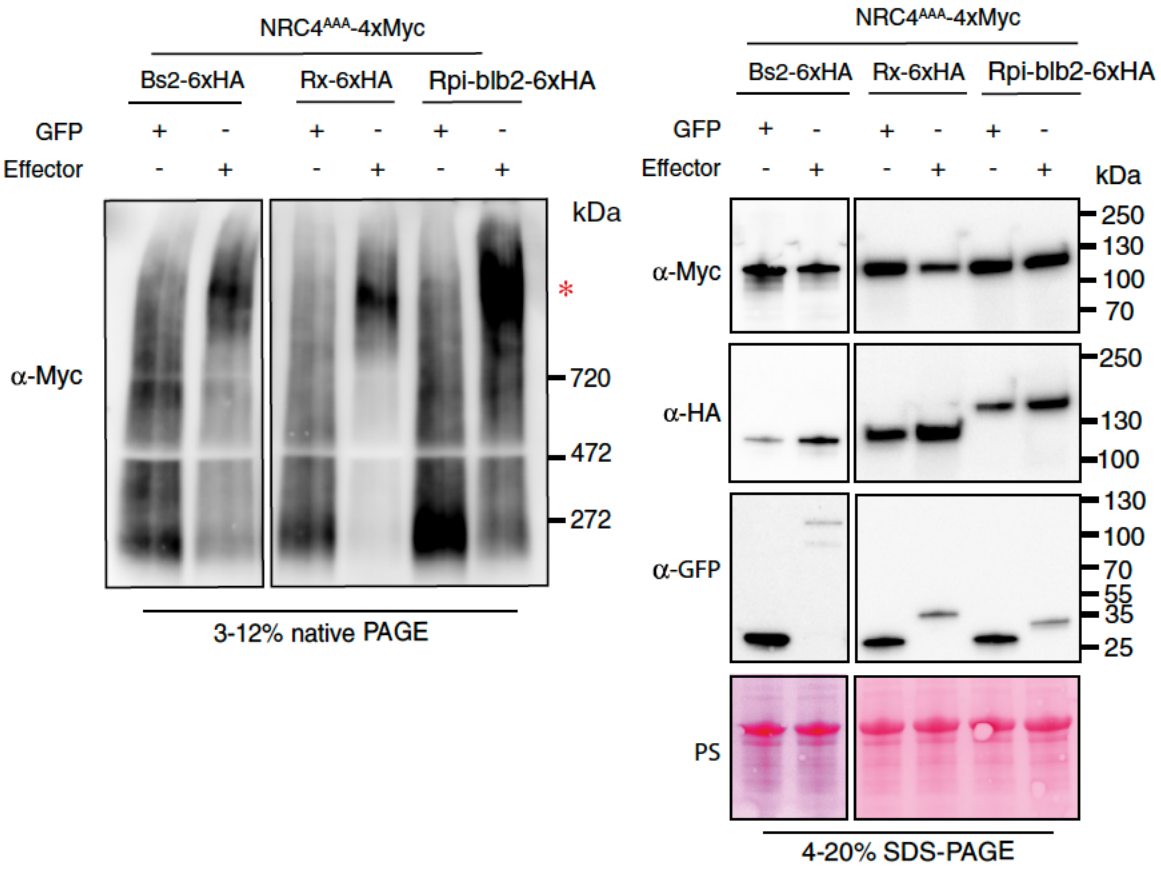


**Figure 15. NRC4-dependent sensor NLRs Bs2, Rx and Rpi-blb2 trigger oligomerization of NRC4$^{AAA}$.** Blue native PAGE (BN-PAGE) and SDS–PAGE analyses showing the oligomerization status of NRC4$^{AAA}$ in the presence of inactive or activated NRC-dependent sensors. Total protein extracts were analyzed on native and denaturing gels followed by immunoblotting with the indicated antisera. Approximate protein molecular weights (kDa) are shown. Red asterisks mark the bands corresponding to activated NRC4$^{AAA}$ oligomeric complexes. Ponceau S (PS) staining of Rubisco served as a loading control. [Adapted from Contreras et al., 2022]

## (2) Determining complex composition and sensor-helper activation models

While structural and biochemical studies have established that singleton NLRs such as ZAR1 and Sr35 form homo-oligomeric resistosomes (Wang et al., 2019; Bi et al., 2021; Förderer et al., 2022) (Figure 16), the **composition of paired or networked NLR complexes remains unresolved.** To clarify whether sensor and helper NLRs form joint heterocomplexes or independent homo-oligomers, **I investigated two representative systems: the Rx-NRC2-PVX CP network and the Pikm-1/Pikm-2 pair.**

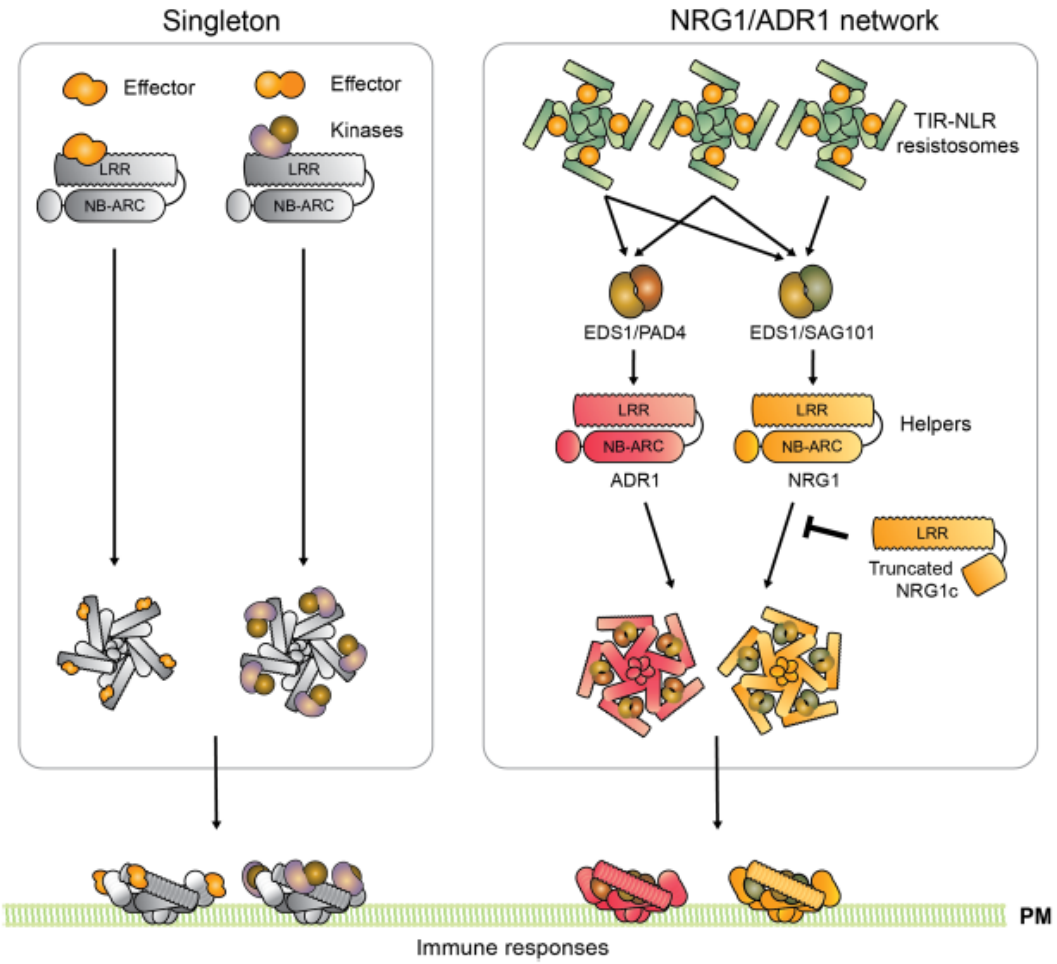


**Figure 16. Reported plant NLR activation models.** (Left) Upon direct or indirect effector perception, singleton CC-NLRs such as ZAR1 and Sr35 activate by forming homo pentameric complexes termed resistosomes. Resistosomes accumulate at the plasma membrane to initiate immune signaling and mediate programmed hypersensitive cell death, presumably by acting as calcium channels. (Right) TIR-NLR singletons and pairs form tetrameric resistosomes upon activation. These resistosomes act as holoenzymes, producing a range of small molecules that are perceived by downstream lipase-like protein dimers EDS1-PAD4 and EDS1-SAG101. These activated EDS1-PAD4 and EDS1-SAG101 complexes can interact with the helper CCR-NLRs ADR1 and NRG1, respectively, leading to their oligomerization into CCR-NLR resistosomes. Following their activation and oligomerization, the ADR1 and NRG1 resistosomes accumulate on the PM to act as calcium-permeable channels, leading to immune signaling and hypersensitive cell death. This network also features an atypical modulator NLR, NRG1c, which can negatively regulate immune signaling by full-length NRG1. [Adapted from Contreras, 2023a]

**The "Activate-and-Release" Model: Rx-NRC2 Network**

Using the Rx (sensor)-NRC2 (helper)-PVX CP (effector) system, I co-expressed Rx-6×HA and NRC2$^{EEE}$-4×Myc in *nrc2/3/4 N. benthamiana*. Upon co-expression with PVX CP, NRC2 shifted from a ~200 kDa monomeric form to a high-molecular-weight complex (~750–900 kDa), consistent with resistosome formation. The **band size shift was observed only when both Rx and PVX CP were co-expressed, indicating that NRC2 activation depends on its upstream sensor.** In contrast, **Rx consistently migrated as a ~400 kDa band regardless of activation or helper presence, indicating that it does not oligomerize or stably associate with NRC2 in the active state** (Publication 1, Figures 17 and 18).

To determine whether the NRC2 complex is composed solely of NRC2 units or involves additional components, I generated **"light" (FLAG-tagged) and "heavy" (mCherry-Myc–tagged) NRC2 variants**. When co-expressed, these variants produced an intermediate-sized complex, confirming that the **NRC2 resistosome consists of multiple NRC2 molecules** (Publication 1, Figures 17 and 19).

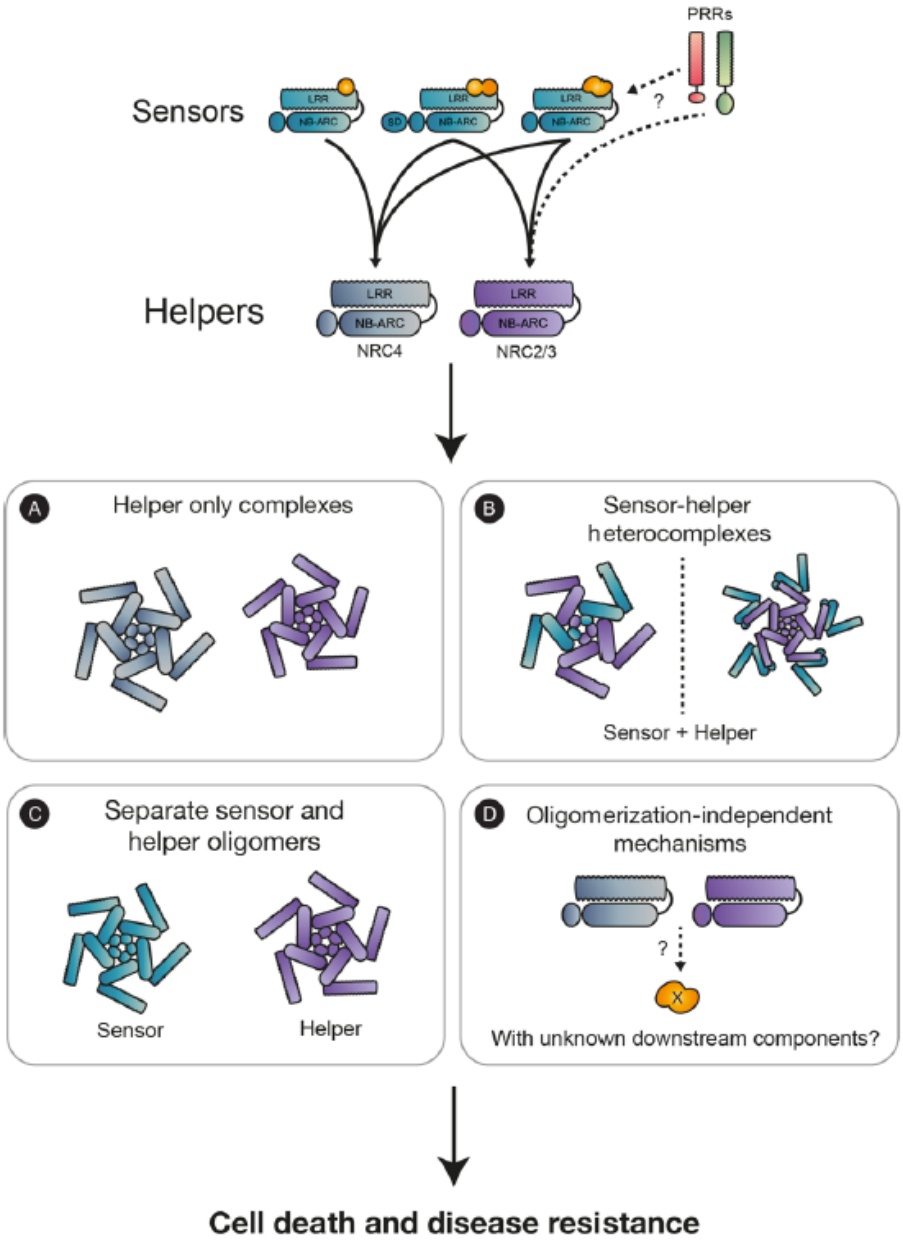


**Figure 17. Proposed activation mechanisms in the NRC immune receptor network.** Activated sensor NLRs (and in some cases pattern-recognition receptors (PRRs)) transmit immune signals to downstream helper NLRs (NRC2/3 and NRC4), resulting in hypersensitive cell death and disease resistance. Several mechanistic models have been proposed: (A) helpers form homo-oligomeric complexes independent of sensors; (B) sensors and helpers assemble into mixed sensor–helper hetero-oligomeric complexes; (C) sensors and helpers oligomerize separately into distinct complexes; and (D) sensors and helpers transmit signals to unknown downstream components without forming resistosome-like oligomers themselves. [Adapted from Contreras, 2023]

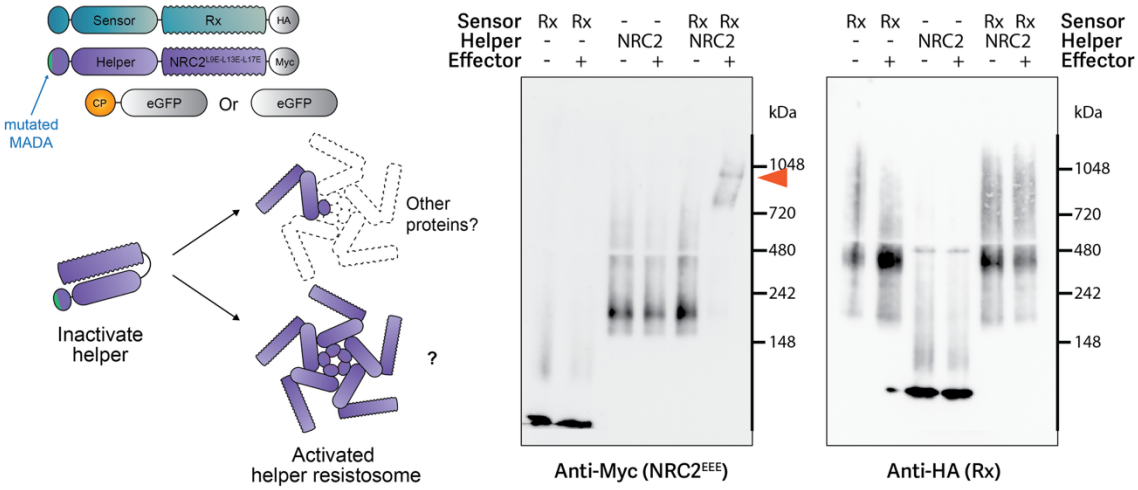


**Figure 18. BN-PAGE reveals that the sensor NLR Rx is not a component of the NRC2 resistosome.**

**(Left)** Schematic representation of the sensor NLR Rx, the helper NLR NRC2$^{EEE}$, and the *Potato virus X* coat protein (CP) effector constructs used in this assay. Upon activation, NRC2$^{EEE}$ is proposed to form homo-oligomeric resistosomes or, alternatively, hetero-oligomeric complexes with interacting partners such as Rx. C-terminal HA, Myc, and eGFP tags were fused to the constructs to enable immunodetection.

**(Right)** BN-PAGE analysis of inactive and activated Rx–NRC2 combinations. Immunoblots probed with anti-Myc and anti-HA antisera detect NRC2$^{EEE}$–Myc and Rx–HA, respectively. Approximate protein molecular weights (kDa) are indicated. The red arrowhead indicates the band corresponding to the activated NRC2EEE oligomeric complex. [Modified from Contreras et al., 2023c]

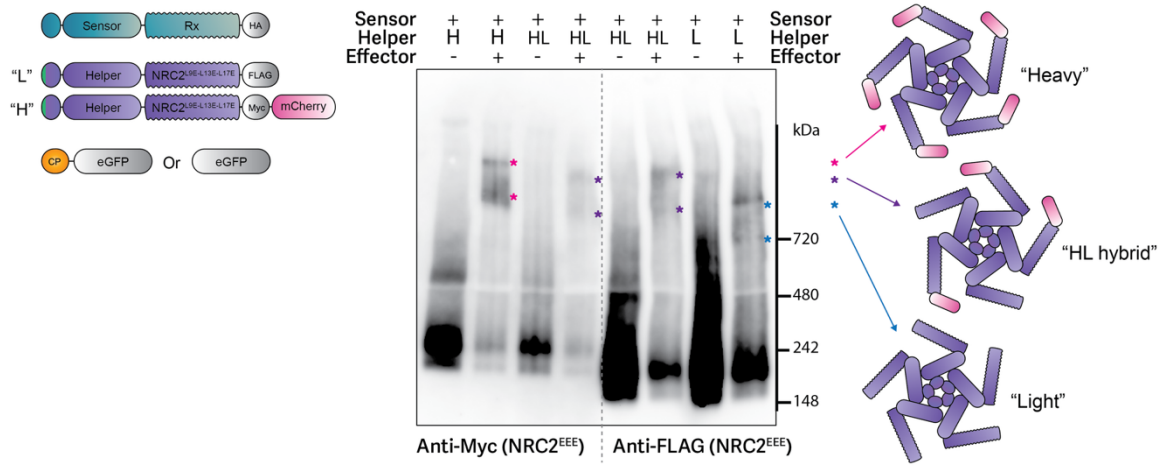


**Figure 19. BN-PAGE demonstrates that the activated NRC2 resistosome is a homo-oligomer.**

**(Left)** Schematic representation of NRC2$^{EEE}$ variants carrying different-sized C-terminal tags. The C-terminal 3XFLAG-tagged NRC2$^{EEE}$ is referred to as the "light (L)" version, whereas the C-terminal mCherry–4XMyc–tagged NRC2$^{EEE}$ is referred to as the "heavy (H)" version. If NRC2 forms homo-oligomers, activated complexes containing different ratios of "heavy" and "light" monomers are expected to migrate at distinct molecular weights.

**(Right)** BN-PAGE analysis of inactive and activated Rx–NRC2 combinations using different "heavy" and "light" helper pairings. Immunoblots probed with anti-Myc antiserum reveal the oligomerization status of NRC2$^{EEE}$. Approximate protein molecular weights (kDa) are indicated. Red asterisks denote activated "heavy" NRC2$^{EEE}$ complexes, blue asterisks denote activated "light" NRC2$^{EEE}$ complexes, and purple asterisks indicate intermediate-molecular-weight complexes containing mixed "heavy" and "light" NRC2$^{EEE}$ subunits. [Modified from Contreras et al., 2023c]

Together, these findings support an **activation-and-release model** in which the **sensor Rx detects the effector, transiently activates NRC2, and dissociates, allowing NRC2 to form a multimeric resistosome independently**. This model contrasts with mammalian NAIP/NLRC4 inflammasomes, where the sensor remains part of the final complex (Vance, 2015), and suggests potential for signal amplification through multiple helper activations by a single active sensor.

## The Pre-Assembled Pair of Pik Sensor-Helper NLRs

To test **whether other NLR pairs follow different activation logic, I examined the rice Pikm-1/Pikm-2 pair,** which confers resistance to *Magnaporthe oryzae* strains producing AVR-Pik effectors (Publication 4). **Previous co-immunoprecipitation assays showed Pikm-1 and Pikm-2 associate both before and after activation** (Zdrzałek et al., 2020), but their oligomeric state remained unknown.

Using the **engineered Pikm-1$^{Enhancer}$ variant, which recognizes GFP** as an activation ligand and exhibits enhanced stability, I co-expressed Pikm-1$^{Enhancer}$ with Pikm-2 in *N. benthamiana* and performed BN-PAGE. **When Pikm-1$^{Enhancer}$ was co-expressed with Pikm-2, a ~1 MDa complex formed even in the absence of GFP, suggesting a pre-assembled hetero-oligomeric complex** (Figure 20). To confirm its composition, I applied the **heavy/light tagging strategy** using V5- ("light") and mCherry-V5–tagged ("heavy") versions of Pikm-1$^{Enhancer}$. The corresponding shift in Pikm-2 band size **confirmed that both sensor and helper are components of the same oligomer** (Figure 21).

Furthermore, using the MADA mutant Pikm-2$^{EE}$, I showed that this hetero-oligomer persists before and after GFP perception by Pikm-1$^{Enhancer}$, and that **GFP is incorporated into the complex**. Membrane fractionation further revealed that Pikm-1, normally cytosolic, is recruited to the plasma membrane when co-expressed with Pikm-2.

Together, these data support a **pre-assembled model for the Pikm-1/Pikm-2 pair**: the sensor and helper form a stable hetero-oligomeric complex at the plasma membrane before effector perception, this may enable rapid immune activation upon effector recognition.

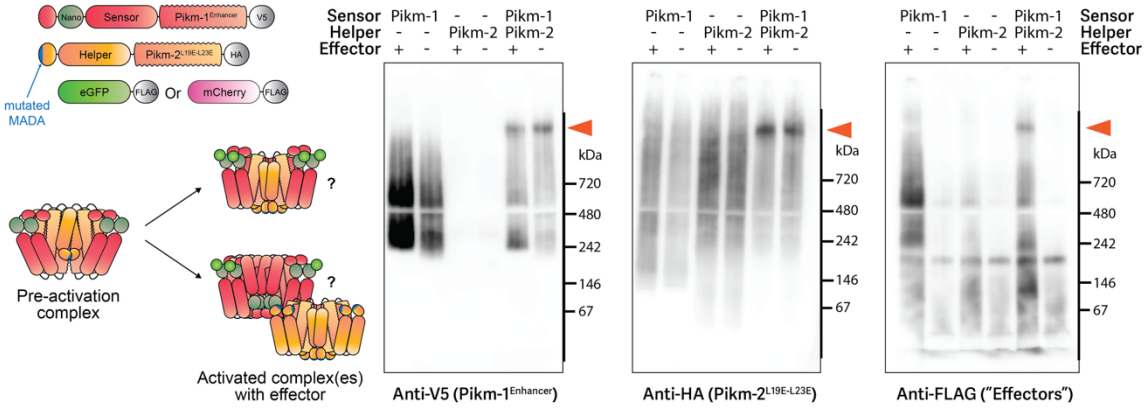


**Figure 20. BN-PAGE reveals a pre-assembled Pikm1$^{Enhancer}$–Pikm2$^{EE}$ heterocomplex that persists before and after activation.**

**(Left)** Schematic representation of the constructs used in the assay. Pikm1$^{Enhancer}$ (V5-tagged) and the autoactivation-enabled helper Pikm2$^{EE}$ (HA-tagged) were co-expressed with the effector ligand eGFP–FLAG, which is specifically recognized by Pikm1$^{Enhancer}$. C-terminal epitope tags (V5, HA, and FLAG) were used for immunodetection. The potential Pikm1–Pikm2 heterocomplex and homocomplexes with the presence of effector are illustrated.

**(Right)** BN-PAGE analyses of Pikm1Enhancer, Pikm2$^{EE}$, and the effector eGFP–FLAG before and after activation. Immunoblots were probed with anti-V5 (Pikm1$^{Enhancer}$), anti-HA (Pikm2$^{EE}$), and anti-FLAG (effector) antisera, respectively. A high–molecular-weight band is detected both prior to and following activation, indicating the presence of a pre-assembled complex. In the presence of the effector, this band is also detected by anti-FLAG immunoblotting, demonstrating that the effector associates with the pre-existing complex upon recognition. However, because Pikm1$^{Enhancer}$ and Pikm2$^{EE}$ are of similar molecular weights, this assay cannot distinguish whether the observed complex represents a sensor–helper heterocomplex or homomeric assemblies of Pikm1Enhancer and/or Pikm2$^{EE}$. Approximate molecular weights (kDa) are indicated.

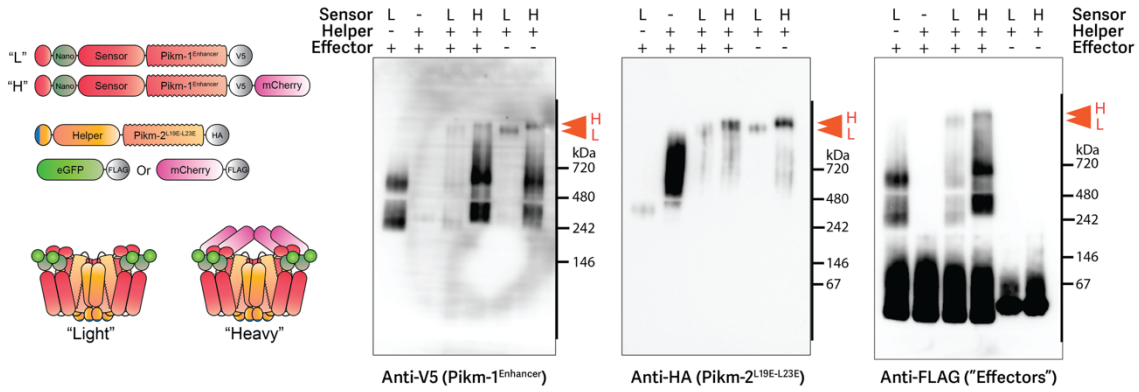


**Figure 21. BN-PAGE revealed Pikm-1Enhancer and Pikm-2EE form heterooligomer.**

**(Left)** Schematic representation of Pikm-$1^{Enhancer}$ variants carrying different-sized C-terminal tags. Pikm-$1^{Enhancer}$-V5 is designated the "light (L)" form, whereas Pikm-$1^{Enhancer}$-V5-mCherry is designated the "heavy (H)" form. If Pikm-$2^{EE}$ participates in heteromeric assemblies with Pikm-$1^{Enhancer}$, the Pikm-$2^{EE}$ band are expected to migrate with complexes containing different "heavy" or "light" sensor subunits.

**(Right)** BN-PAGE analysis of Pikm-$1^{Enhancer}$-Pikm-$2^{EE}$ complexes using different combinations of "heavy" and "light" Pikm-1Enhancer. Immunoblots were probed with anti-V5 antiserum to visualize Pikm-$1^{Enhancer}$ -containing complexes. Approximate molecular weights (kDa) are indicated. The band size shift of the Pikm-$2^{EE}$ complexes indicated Pikm-$1^{Enhancer}$ and Pikm-$2^{EE}$ form heteromeric sensor-helper complexes.

### (3) Effector-Mediated Suppression and Evolutionary Diversification of Helper NLRs

#### Direct Visualization of SS15-Mediated Inhibition in *N. benthamiana*

**Pathogens have evolved effector proteins that suppress NLR-mediated immunity.** A prime example is the **potato cyst nematode effector SPRYSEC15 (SS15)**. By mutational analysis, HR assay and yeast-two-hybrid validation, previous studies have shown that SS15 binds and inhibits tomato NRC1 and N. benthamiana NRC2/3, but not NRC4 (Derevnina et al., 2021).

To dissect at which step SS15 exerts its interference to NRC signalling, I used BN-PAGE to directly visualize this inhibition in *N. benthamiana*. **In the presence of SS15, formation of NRC2 resistosome by Rx and PVX CP was abolished**; the NRC2 resistosome (~1 MDa) band was replaced by a ~240 kDa NRC2–SS15 complex, confirming direct binding. **In contrast, NRC4 oligomerized normally** in the presence of SS15 (Publication 2, Figure 22).

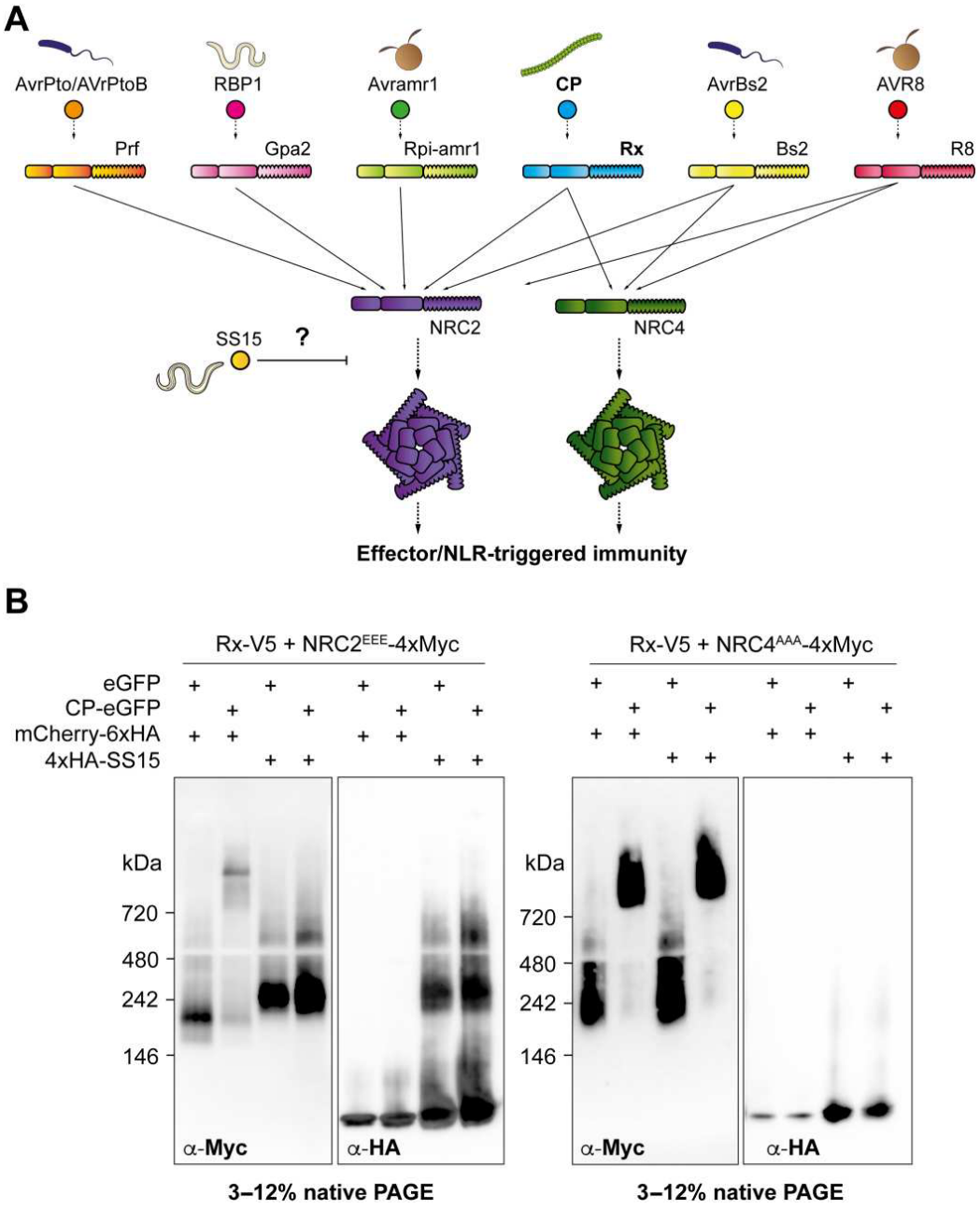


**Figure 22. The nematode effector SS15 selectively inhibits NRC2 but not NRC4 oligomerization.**

(A) Schematic representation of the NRC immune receptor network, in which multiple sensor NLRs signal through downstream helper NLRs. The SPRYSEC effector SS15 specifically interferes with NRC2-mediated signalling but does not affect NRC4.

(B) Blue native PAGE (BN-PAGE) analysis of inactive and activated Rx in combination with NRC2 or NRC4, in the absence or presence of SS15. The left panels show that NRC2 oligomerization is abolished upon SS15 co-expression, whereas the right panels show that NRC4 oligomerization remains unaffected by SS15. Immunoblotting with anti-HA antiserum further reveals that SS15 associates with NRC2 during the inhibitory interaction. Approximate molecular weights (kDa) are indicated. [Adapted from Contreras et al., 2023b]

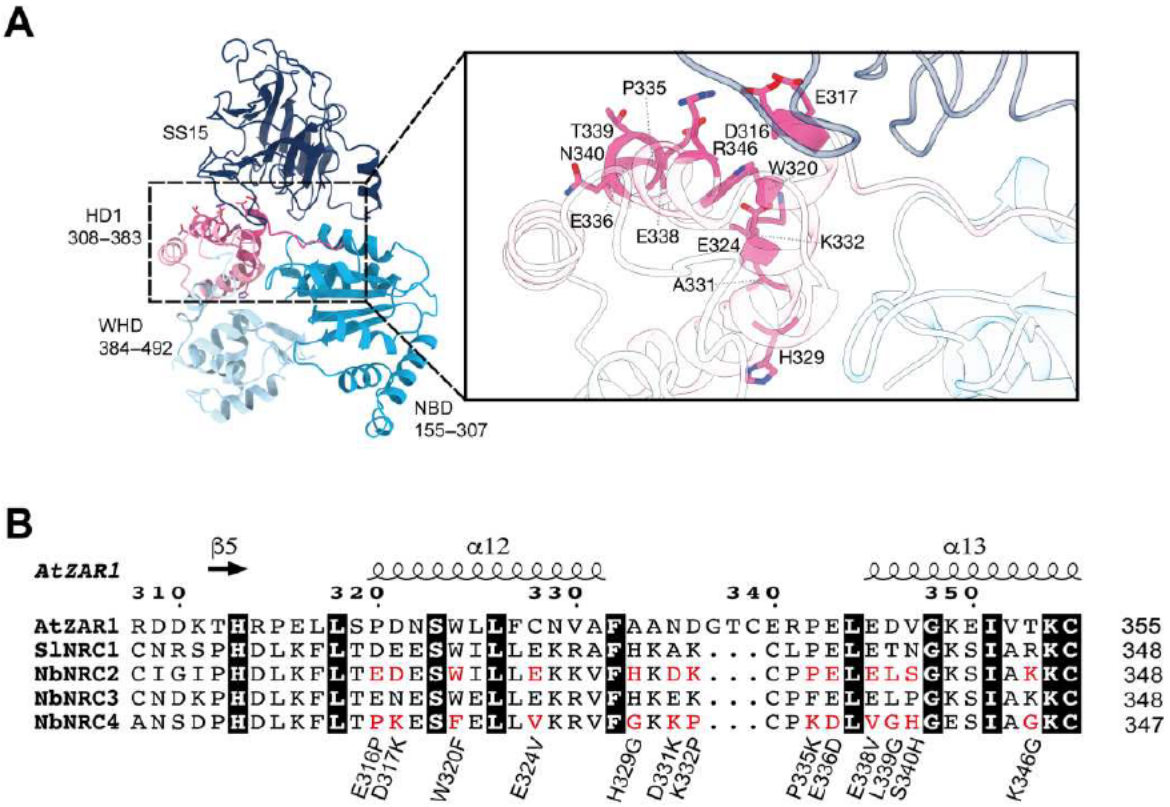


**Figure 23. SS15–NRC binding interface enables bioengineering NRC2 variants that evade suppression.**

(A) Crystal structure of the SS15–SlNRC1NB–ARC complex. The NB, HD1, and WHD domains of *Solanum lycopersicum* NRC1 (SlNRC1) NB–ARC are shown in cyan, pale blue, and magenta, respectively; SS15 is in dark blue. The inset displays a close-up image of the SS15–SlNRC1NB–ARC HD1 domain interface, with the residues corresponding to those selected for mutagenesis in NRC2 highlighted in stick representation. (B) Alignment of the HD1-1 region of *Arabidopsis thaliana* ZAR1 (AtZAR1), SlNRC1, NRC2, NRC3, and NRC4. Candidate residues (highlighted in red) were shortlisted on the basis of the interface identified in the co-crystal structure of SS15 and the SlNRC1 NB–ARC domain, as well as being conserved in SlNRC1, NRC2, and NRC3 but not NRC4 and AtZAR1.Thirteen NRC2 variants were generated by mutating individual candidate positions to the corresponding amino acid in NRC4 (detailed underneath the alignment). [Adapted from Contreras et al., 2023b]

Guided by sequence alignment and structural data, I introduced the D317K mutation within the HD1-WHD interface of NRC2 (Figure 23), predicted to disrupt SS15 binding. BN-PAGE confirmed that this engineered variant restored oligomerization in the presence of SS15, forming a normal resistosome and demonstrating that a single point mutation can confer resistance to effector suppression (Figure 24).

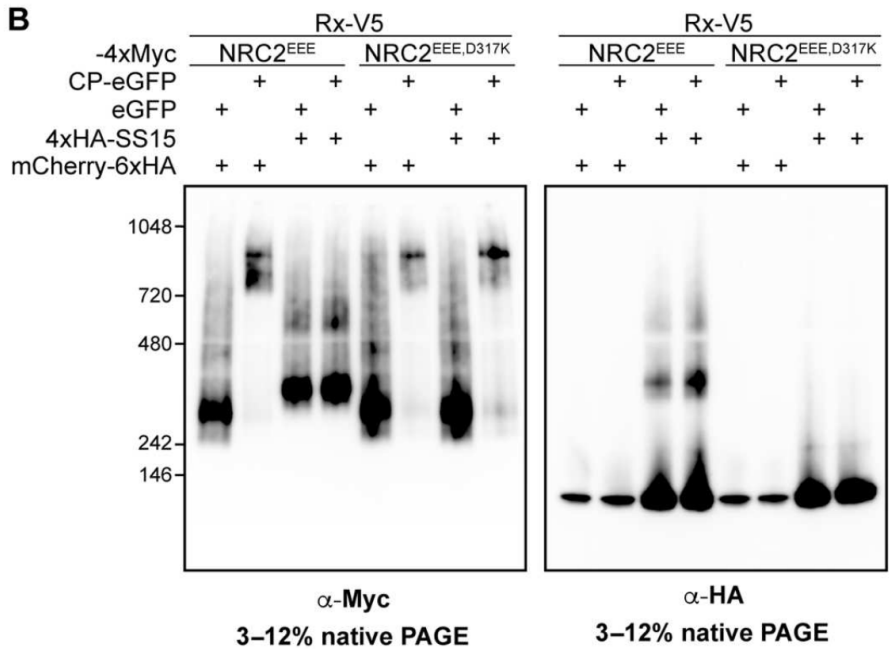


**Figure 24. The NRC2$^{D317K}$ helper variant restores immune signalling by evading SS15-mediated inhibition.** Blue native polyacrylamide gel electrophoresis (BN-PAGE) analysis of inactive and activated Rx co-expressed with either NRC2$^{EEE}$ or NRC2$^{EEE,D317K}$, in the presence or absence of the nematode effector SS15. Immunoblots show that, unlike wild-type NRC2$^{EEE}$, the NRC2$^{EEE,D317K}$ variant retains oligomerization in the presence of SS15. Probing with anti-HA antiserum further demonstrates that SS15 no longer associates with NRC2$^{EEE,D317K}$. [Adapted from Contreras et al., 2023b]

## Evolutionary Diversification of SS15 Sensitivity Across *Solanaceae*

To **broaden this analysis to evolutionary scope, I examined NRC1, NRC2, and NRC3 orthologs across *Solanaceae* species** (including *N. benthamiana*, tomato, potato, and pepper) to assess **natural variation in SS15 sensitivity** (Publication 3). Interestingly, while all NRC2 orthologs were inhibited by SS15, certain NRC1 and NRC3 variants were naturally resistant (Figure 25). **Specifically, SS15 blocked oligomerization of potato NRC3 (StNRC3, E316), but not pepper or tomato NRC3s (CaNRC3 and SlNRC3, K316)**. Reciprocal point mutations confirmed that residue E316 determines SS15 sensitivity, while K316 confers insensitivity (Figure 26).

These results indicate that *Solanaceae* NRCs have diversified at the SS15-binding interface through lineage-specific amino acid substitutions. Phylogenetic analysis suggests that **NRC3 acquired insensitivity to SS15 approximately 19 million years ago, representing an evolutionary adaptation to evade pathogen immunosuppression**. Collectively, these findings uncover a new layer of gene-for-gene coevolution, where helper NLRs evolve to counteract pathogen suppressors, offering valuable insights for engineering more resilient plant immune receptors.

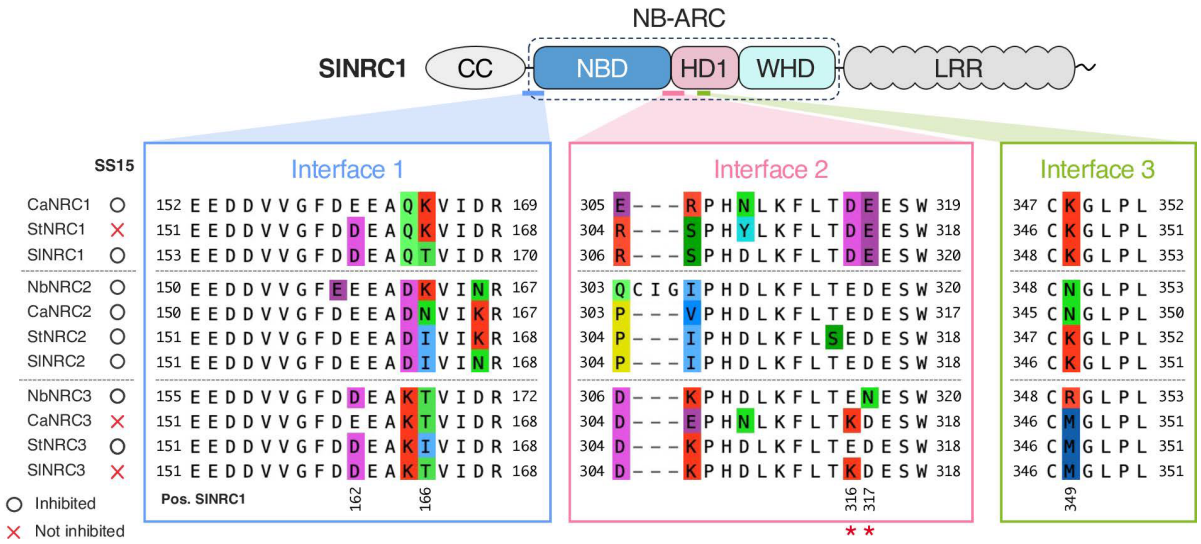


**Figure 25. NRC3 variants from different Solanaceae species are polymorphic at key residues at SS15 binding interface.** Alignment of NRC1, NRC2 and NRC3 interfaces for SS15, two previously identified key residues for SS15 inhibition (D316 and E317 of SlNRC1) are highlighted with red asterisks. Nb: *Nicotiana benthamiana*; Ca: *Capsicum annuum*; Sl: *Solanum lycopersicum*, St: *Solanum tuberosum*. [Adapted from Sugihara et al., 2025]

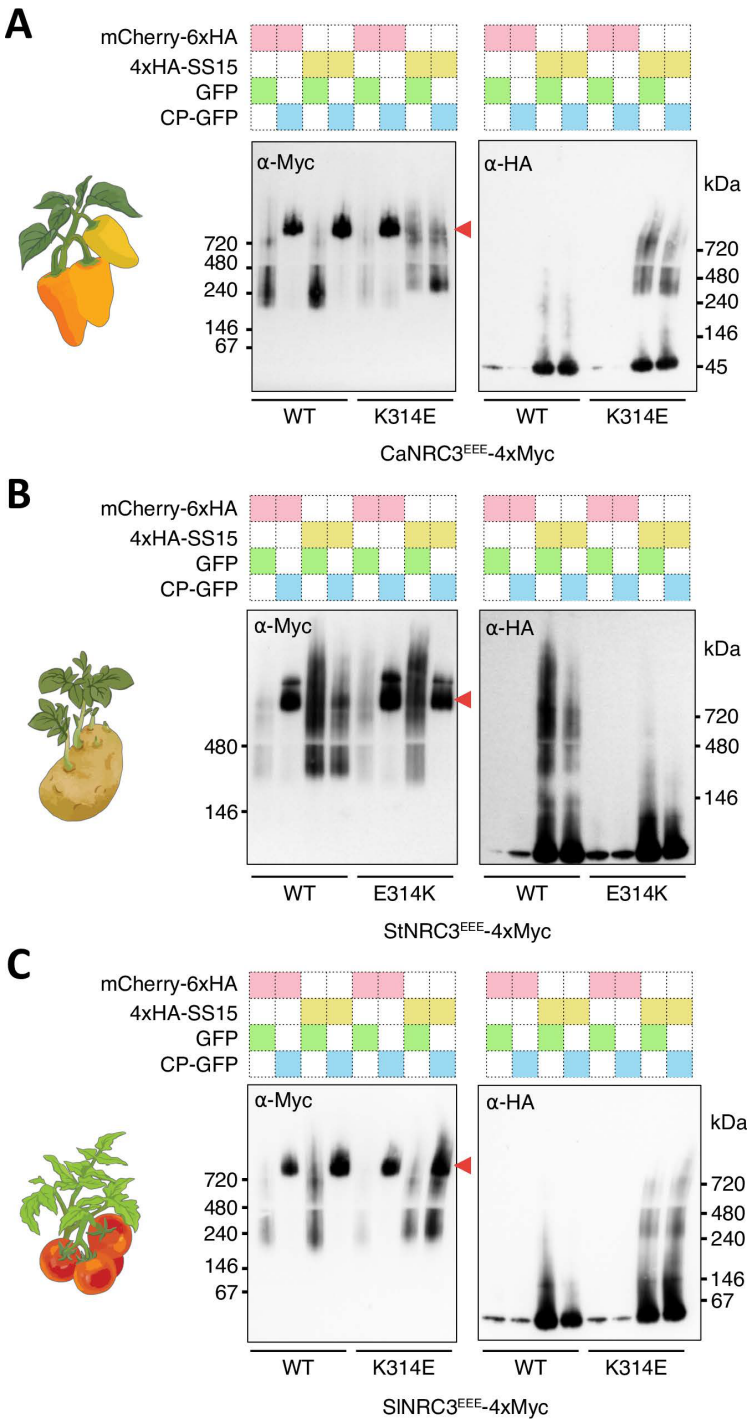


**Figure 26. Polymorphisms at position E316 of NbNRC3 determine oligomerisation in the presence of SS15.** Blue native polyacrylamide gel electrophoresis (BN-PAGE) assays were conducted for *Capsicum annuum* CaNRC3EEE (A), *Solanum tuberosum* StNRC3EEE (B) and *Solanum lycopersicum* SlNRC3EEE (C) with their respective single-point mutations at position matching *Nicotiana benthamiana* NbNRC3 residue 316. These effector-sensor-helper combinations were co-expressed either with mCherry-6xHA fusion protein or N-terminally 4xHA-tagged SS15 in the leaves of nrc2/3/4 N. benthamiana. Red arrowheads indicate resistosome bands. The oligomerization status confirmed that residue E316 determines SS15 sensitivity. [Adapted from Sugihara et al., 2025]

## 3.4 Summary and future perspectives

In this chapter, I have outlined the principles, methodological development, and applications of BN-PAGE in studying plant immune receptor complexes. Originating from plant organelle biochemistry, **BN-PAGE has become a central tool for investigating macromolecular assemblies in plants, providing a direct window into protein complex formation under native conditions**. In my work, I applied BN-PAGE to **visualize the oligomerization of paired and network NLRs** and to study how the **pathogen effector inhibits resistosome formation**. Together, these works demonstrated the versatility of BN-PAGE for monitoring distinct activation states, effector interactions, and evolutionary diversification among NLR immune complexes.

While powerful, BN-PAGE remains an empirical technique that **often requires extensive optimization for each protein complex**. The choice of detergent, extraction buffer, and gel gradient must typically be adjusted case by case, creating a bottleneck for systematic analysis. A key goal for future improvement is to develop a streamlined, predictive framework—a practical "BN-PAGE cookbook"—linking the physicochemical properties of a protein complex (such as size, hydrophobicity, and subcellular localization) to suitable solubilization and electrophoresis conditions. Such a system would greatly accelerate the identification and characterization of new immune complexes.

Looking ahead, **integrating BN-PAGE with complementary methods such as crosslinking mass spectrometry and high-resolution cryo-EM** will enable a more comprehensive understanding of plant immune receptors (Gong et al., 2022; Lundquist et al., 2017; Vincis Pereira Sanglard and Colas des Francs-Small, 2022). From bioinformatic identification and cloning of candidate NLRs to structural characterization, **BN-PAGE serves as a central link in this workflow—providing a rapid means to probe the oligomeric state** of receptors and assess activation-dependent changes. The insights gained from BN-PAGE not only guide the design of constructs and experimental conditions for downstream structural analyses, bridging biochemical assays with high-resolution visualization. In this way, BN-PAGE functions as both a diagnostic tool and a conceptual bridge, connecting molecular biochemistry with systems-level exploration of NLR evolution and immune signalling.

# Chapter 4

# Fast-forward pipeline for cryo-EM structural analysis of native plant protein complexes

Understanding how plant immune receptors assemble and activate at the molecular level requires visualization beyond sequence and biochemical analyses. Recent breakthroughs in **cryo–electron microscopy (cryo-EM) enable near-atomic resolution imaging of protein complexes in native conformations** (Nagaraj, 2024; Wightman, 2022), offering unprecedented insight into dynamic assemblies such as NLR resistosomes. Building on the landmark structural elucidation of the *Arabidopsis* ZAR1 resistosome (Wang et al., 2019), we focused on capturing the conformational transitions and networked interactions of NLRs in their native context.

In collaboration with structural biologists Muniyandi Selvaraj and Jogi Madhuprakash, I developed **rapid sample preparation methods that integrate into EM-based workflows to accelerate structural studies** of plant protein complexes. Specifically, I implemented two approaches — **immunoprecipitation electron microscopy (IP-EM)** and **BN-PAGE electron microscopy (BN-EM)** — that enable small-scale protein purification and direct cryo-EM visualization of protein assemblies. These techniques capture protein complexes at defined activation states, linking cellular assays to molecular architectures.

In this chapter, I outline the development of electron microscopy in studying plant protein complexes, describe our optimized sample preparation pipelines, and highlight key structural discoveries derived from these techniques.

**Key Publications in Chapter 4:**


1. Selvaraj, M, A Toghani, H Pai, Y Sugihara, J Kourelis, ELH Yuan, T Ibraham, H Zhao, RR Xie,A Maqbool, JC De la Concepcion, MJ Banfield, L Derevnina, B Petre, DM Lawson, TO Bozjurt, CH Wu, S Kamoun, and MP Contreras. (2023) Activation of plant immunity through conversion of a helper NLR homodimer into a resistosome. PLoS Biol. 22: e3002868.

2. Pai H, C Marchal, J Sklenar, MP Contreras, D Lưdke, S Kamoun, and M Selvaraj. (In preparation) Atomic model of protein complexes electroeluted from Blue-Native PAGE.

3. Selvaraj M, H Pai, J Madhuprakash, A Toghani, M Webster, S Kamoin, and MP Contreras. (2024) Fast-forward pipeline for cryo-EM structural analysis of native plant protein complexes. Zenodo DOI: 10.5281/zenodo.13768552.

**Supporting Publication in Chapter 4:**

1. Madhuprakash, J, A Toghani, MP Contreras, A Posbeyikian, J Richardson, J Kourelis, TO Bozkurt, M Webster, and S Kamoun. (2024) A disease resistance protein triggers oligomerization of its NLR helper into a hexameric resistosome to mediate innate immunity. Sci. Adv. 10: eadr2594.

## 4.1 Foundations and Advances of Electron Microscopy in Plant Studies

### Historical development and application of EM in plant immunity research

Unveiling structural insights of protein complexes is crucial for comprehending the molecular mechanisms that underlie plant biology. The advent of electron microscopy (EM) has been a cornerstone of structural biology. While the overall design of EM is similar to a light microscope, it **visualizes the sample by using a high-voltage beam of electrons instead of light**. With the much shorter wavelength of electrons compared to visible light, EM can achieve about 2 nm for biological samples — roughly 100 times better—compared to the routine 200 nm resolution of light microscopy (Benjing and Lin, 2020; Fawke, 1995; Wightman, 2022). **The superior resolution allowing visualization of organization of organelles and establishing direct links between ultrastructure and function.**

The application of EM in plant research began over 80 years ago. Not long after Ruska built the first transmission EM (TEM) in 1931, the team then achieved direct visualization of plant viruses, notably Tobacco mosaic virus (TMV) by 1939 (Fawke, 1995; Knapp and Lewandowski, 2001). The trend was then followed by a burst in revealing cellular structures like mitochondria and chloroplasts in the 1940s-1950s. These observations provided crucial insights into photosynthesis, nutrient uptake and distribution (Dudkina et al., 2010; Hoefnagel et al., 1998).

**In plant immunity studies, the first visualization of viral particulate** nature already revolutionized previous fluid-based theories. Continued application of TEM in diagnosing plant virus diseases facilitated the morphological classification of plant viruses, and from the 1970s EM helped elucidate **ultrastructural changes during plant-virus infection**, including observations of virus distribution within different leaf tissues and the impact on organelles (Goldsmith and Miller, 2009; Hitchborn and Hills, 1965; Steere, 1964). Similarly, early TEM studies revealed the detailed internal structure of fungal pathogens including filamentous rusts and powdery mildews. These biotrophic fungi studies contributed to the understanding of how pathogens establish infection

interfaces within plant cells (Harder and Chong, 1968; Mares 1979). The foundational studies shaped new instrumentation and methodology in EM techniques, which themselves enabled further discoveries in plant–pathogen interactions. These include improvements in fixation methods, reconstruction techniques and the development of variations of EM techniques.

From the 2000s, the emergence of **cryogenic EM (cryo-EM)** opens the possibility of imaging large biomolecular assemblies. Initial breakthroughs came from studies of ribosomes—massive, stable complexes composed of proteins and RNA—which became ideal candidates for cryo-EM analysis and sparked the so-called "ribosomania" that rapidly produced dozens of ribosome structures from diverse organisms (Callaway, 2015; Staehelin and Paolillo, 2020). **A landmark application of cryo-EM in the field of plant immunity was the determination of the ZAR1 resistosome** structure, representing the first plant NLR complex resolved in both its inactive and active states (Wang et al., 2019). These studies revealed how ZAR1, in complex with RKS1 and the uridylated RLCK effector PBL2, undergoes dramatic conformational rearrangements into a pentameric ring functioning as a calcium-permeable channel, providing the first direct visualization of receptor activation at the molecular level (Locci and Parker, 2024; Wang et al., 2019).

Subsequent studies have expanded this framework, solving the structures of additional immune receptors, including the CC-NLR Sr35 from wheat, the TIR-NLR receptors RPP1 and Roq1 from *N. benthamiana*, and several helper NLRs such as ADR1s and NRG1s, as well as immune regulators including NPR1 (Huang et al., 2025; Martin et al., 2020; Zhao et al., 2022). These studies collectively revealed that TNL resistosomes expose TIR-domain catalytic sites with NADase activity, producing small signalling molecules such as v-cADPR that activate downstream complexes like EDS1-PAD4-ADR1, bridging cell-surface and intracellular immunity. Structural and biochemical analyses further demonstrated that ADR1s and NRG1s also function as calcium channels, linking receptor activation to ion fluxes and defense gene expression (Locci and Parker, 2024). Together, these structural insights not only illuminate how plants detect and respond to pathogen invasion but also underscore striking evolutionary and mechanistic parallels between plant and animal NLR systems, advancing a unified view of innate immune activation across kingdoms.

## Comparison of different type of structural biology methods

The primary techniques in structural biology include **X-ray crystallography, nuclear magnetic resonance (NMR), and cryo-EM** (Callaway, 2015; Staehelin et al., 2020). Each method has distinct strength and limitations, making it essential to choose

the most suitable approach according to the research question and the properties of the target molecule. In recent years, hybrid strategies that integrate multiple structural methods greatly expands the horizon of structural biology, enabling near-atomic resolution of large biological assemblies (Lv et al., 2024). This section provides an overview of the principles, advantages, and limitations of these major techniques to guide their appropriate application in structural studies.

### (1) X-ray crystallography

X-ray crystallography has long been the **predominant method in structural biology** for resolving macromolecular structures at atomic resolution (Callaway, 2015; Castón and Luque, 2024). Its principle relies on the **hitting X-rays to crystals**: By exposing crystalline lattice to an X-ray beam, the interaction with electron clouds generates a diffraction pattern, which can be analyzed through Bragg's Law to encode the spatial arrangement of atoms (Castón and Luque, 2024; Tatkiewicz et al., 2015). Its key advantages include **(i)** the ability to deliver **atomic-level resolution**, **(ii)** applicability across a **broad spectrum of biological molecules**, and **(iii)** provision of **detailed insights** into molecular interactions and binding sites essential for mechanistic understanding. However, several limitations also exist, foremost is the **requirement for high-quality three-dimensional crystals**, particularly for large, flexible, or membrane-associated proteins. Additional challenges include **(i)** the need for substantial sample quantities, **(ii)** the inherent complexity of phase determination, and **(iii)** the fact that **crystallized molecules may not fully represent their dynamic states** *in vivo*. **(iv)** Furthermore, exposure to X-rays can induce radiation damage, potentially compromising structural accuracy (Dobson, 2019; Miranda et al., 2015; Parent et al., 2018; Vénien-Bryan et al., 2017).

### (2) Nuclear magnetic resonance (NMR)

NMR is especially useful for **determining the 3D structures of biomolecules in solution**, providing both structural and dynamic information. The technique **exploits the magnetic properties of nuclei**, which, when placed in a strong external magnetic field, resonate at frequencies influenced by their chemical environment (Dobson, 2019; Reichhardt et al., 2019). By isotopically labelling biomolecules and recording signals from radiofrequency perturbations, NMR generates data that can be used to calculate detailed information on atomic environments, interatomic distances, and molecular motion. The major strength of NMR lies in **(i)** its ability to **analyze proteins and nucleic acids in solution**, closely approximating physiological conditions, while also **capturing conformational flexibility** and binding interactions over multiple timescales. **(ii)** it does

not require crystallization and is especially **useful for smaller proteins and nucleic acids**. However, NMR is limited by **(i)** molecular size (typically <50 kDa), **(ii) requirement of high concentrations of pure sample**, and **(iii)** involves complex, time-intensive data analysis (Bax and Clore, 2019; Reichhardt et al., 2019; Tatkiewicz et al., 2015). As a result, it contributes a relatively small fraction of deposited protein structures in the database (Geraets et al., 2020).

### (3) Cryogenic electron microscopy (Cryo-EM)

The principle of EM **utilizes a beam of high-energy electrons to illuminate the samples**. Electromagnetic lenses focus this electron beam onto the specimen, and the interactions are detected and transformed into a high-resolution image. Depends on the type of interactions between the electron beam and the specimen — transmitted electrons for **transmission electron microscopy (TEM)**, or scattered electrons for **scanning electron microscopy (SEM)**, the sample's internal structure or surface, respectively, are revealed (Castón and Luque, 2024). While conventional TEM and SEM typically rely on chemical fixation and staining agents (such as heavy metal salts or polymers) to immobilize samples and enhance contrast, **cryo-electron microscopy (cryo-EM) represents a distinct subdivision of EM** that overcomes these preparative limitations. In cryo-EM, **samples are rapidly frozen in liquid ethane** to produce a vitrified ("glass-like") ice layer, **preserving macromolecules in a near-native, hydrated state** without the need for chemical fixatives or staining (Burton-Smith and Murata, 2023; Carroni and Saibil, 2015; Castón and Luque, 2024). Therefore cryo-EM overcomes several limitations of traditional methods: **(i)** It does not require crystallization, thus eliminates the difficulties for large, complicated, or flexible molecules, and those associated with lipid membranes. **(ii) Samples are imaged in a near-native state**, avoiding the artificial constraints imposed by crystal packing. This is also ideal for studying complex and heterogeneous structures, such as membrane proteins and large macromolecular assemblies. **(iii)** It typically **requires a much smaller amount of sample** compared to the quantity needed for crystallization screening. Furthermore, sample **purity is not as critically essential** as individual molecular assemblies can be selected from micrographs, even if mixed with other molecules. While certain challenges remain for cryo-EM, including **(i)** the **high cost** due to the requirement of advanced instrumentation and cryo-sample preparation, and **(ii) limited resolution** because conformational flexibility can complicate image classification (Benjin and Ling, 2020; Carroni and Saibil, 2015; Ignatiou et al., 2024). Nevertheless, the advantages have made cryo-EM a transformative tool for elucidating the architecture and conformational dynamics of protein complexes central to cellular processes, including plant immunity.

## 4.2 IP-EM and BN-EM Workflows for rapid cryo-EM sample preparation

Although cryo-EM can alleviate partial sample heterogeneity through three-dimensional single-particle classification and generally requires less protein than other structural methods, **maintaining biochemical purity and stability remains essential for achieving high-resolution reconstructions** (Czarnocki-Cieciura and Nowotny, 2016; Stark and Chari, 2016). As a starting point for sample preparation, recombinant protein expression systems are widely used in structural biology. These involve introducing target gene sequences into expression vectors and expressing them in host organisms such as bacteria (e.g. *Escherichia coli*), yeast, insect, or mammalian cells. While these systems enable efficient and cost-effective production, they have limitations in reproduce functional folding, assembly, or post-translational modifications, particularly for multi-subunit complexes (Arnold et al., 2018; Passmore and Russo, 2016). In contrast, **native complex purification preserves physiological assembly**, as it maintains the native chaperones and modification pathways necessary for proper complex formation (Klebl et al., 2023; Weissenberger et al., 2021; Xu andf Dang, 2022). Consequently, purification from native sources remains the most reliable strategy for obtaining fully assembled and functional macromolecular complexes.

Here, I present two simple cryo-EM sample preparation strategies — IP-EM and BN-EM — that enables robust structural analysis of plant protein complexes in its native conformation (Figure 27).

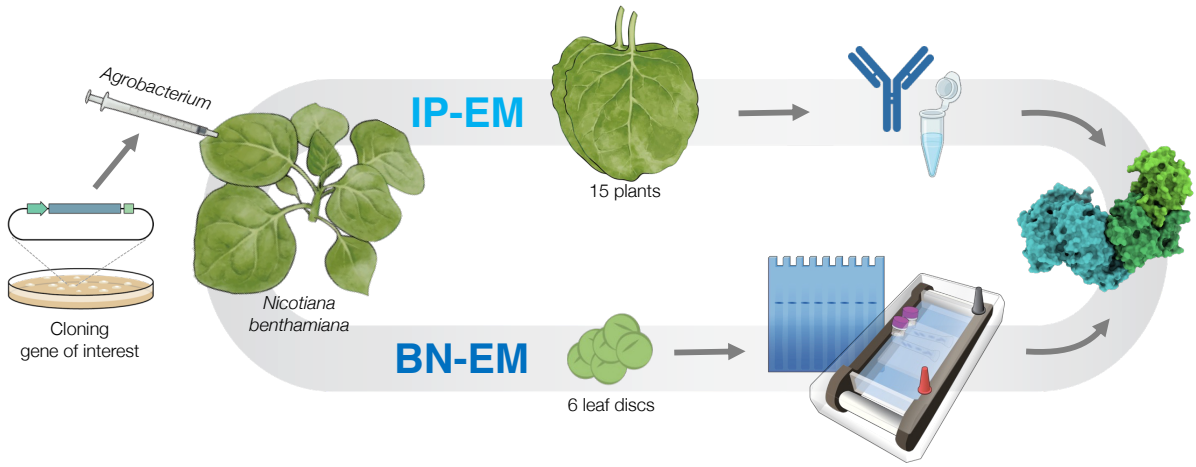


**Figure 27. Schematic overview of immunoprecipitation electron microscopy (IP-EM) and blue-native electron microscopy (BN-EM).**

Immunoprecipitation-electron microscopy (IP-EM)

In general, this method is a large-scale immunoprecipitation approach designed to isolate 3×FLAG-tagged target proteins using anti-FLAG agarose beads. To begin, I agroinfiltrated approximately 30 *N. benthamiana* leaves to transiently express the constructs, all of which were assembled through the modular cloning pipeline described in Chapters 2 and 3. For each purification, I harvested infiltrated leaves three days post-agroinfiltration and immediately snap-froze them in liquid nitrogen. Samples were stored at −80°C until protein extraction.

On the day of purification, I ground about 20 g of frozen leaf tissue into a fine powder using a pre-chilled mortar and pestle with liquid nitrogen. The powder was mixed with 80 ml of ice-cold isolation buffer containing 100 mM Tris–HCl (pH 7.5), 150 mM NaCl, 1 mM $MgCl_2$, 1 mM EDTA, 10% glycerol, 10 mM DTT, 0.4% (v/v) IGEPAL, and 1× cOmplete EDTA-free protease inhibitor (Roche). The homogenate was incubated on ice for 10 min with intermittent vortexing, then centrifuged at 12,000 rpm for 10 min at 4°C to remove debris.

While the sample was centrifuging, I prepared 200 µl of anti-FLAG M2 affinity gel (Sigma) per 20 g of starting tissue. The beads were washed twice with 1 ml of isolation buffer and briefly centrifuged at 800 × g to remove ethanol and activate its binding affinity. I then filtered the clarified leaf extract through Miracloth (Merck) and incubated the supernatant with the prepared beads for 90 min at 4°C with gentle rotation to prevent sedimentation.

After incubation, I collected the protein-bound beads on an open gravity column and washed them with 10 ml of wash buffer (identical to the isolation buffer but without DTT). The bound proteins were eluted in 200 µl of isolation buffer supplemented with 0.3 mg/ml 3×FLAG peptide by incubation for 1 h at 4°C with gentle rotation. Binding to the agarose matrix was competitively replaced by the FLAG peptide, releasing the tagged proteins into the supernatant. After centrifugation at 800 × g for 1 min at 4°C to pellet the beads, I collected the supernatant as the purified protein fraction.

The isolated proteins were analyzed by SDS-PAGE to assess purity and integrity. Typical yields ranged from 1.2 to 1.5 mg/ml for NRC2, RxNB-eGFP, and eGFP, as determined by absorbance at 280 nm. These FLAG-eluted proteins were subsequently used for in vitro assays and structural analyses by cryo-EM.

**BN-PAGE EM (BN-EM)**

To prepare samples for electron microscopy, I followed the BN-PAGE workflow described in Chapter 3.2 with some modifications to accommodate protein recovery for structural analysis. In brief, I ground frozen leaf tissues into fine powder and perform protein extraction with BN extraction buffer. The supernatant was mixed 1:1 with 4× NativePAGE sample buffer and 5% G-250 additive (Invitrogen). The first major difference was, I **loaded up to 30 µL (instead of 10 µL) of the mixture per lane** onto a 3-12% Bis-Tris NativePAGE gel (Invitrogen), **allowing one 10-well gel to be filled with extract derived from six 8-mm leaf discs**. Gels were run at 150 V for 40 min, followed by 200 V for 90 min at 4 °C, using the manufacturer's dark/light cathode buffer system (BN2001/BN2002, Invitrogen).

After electrophoresis, I **excised the gel bands** corresponding to the desired protein complexes. Gel slices from one gel (10-wells) was placed into a **3 kDa dialysis tube**. The **tubes were submerged in an electrophoresis tank containing the light cathode buffer** (BN2002, Invitrogen) and **run overnight at 70 V at 4°C** to electro-elute the proteins from the gel. Following elution, the protein-containing solution was recovered from the dialysis tube, briefly centrifuged to remove residual gel debris, and concentrated as needed for downstream negative staining or cryo-EM grid preparation. This modified workflow preserves the native state of plant protein complexes and enables structural visualization directly from gel-purified samples without extensive biochemical purification.

**The protein samples isolated by IP or BN methods were used immediately for EM analyses without further purification**. Negative stain EM was used as a quality control to assess protein complex integrity and gaining a primary insight of homogenousity. Samples with appropriate quality were then submitted to cryo-EM analysis. The EM procedures, downstream image processing and 3D reconstruction were performed in cooperation with Muniyandi Selvaraj and Jogi Madhuprakash, and the experimental details are as described in Selvaraj et al. (2024) and Madhuprakash et al. (2024) for the NRC2 studies.

## 4.3 Revealing structural insights into NRC resistosomes and RuBisCO by IP-EM and BN-EM

By applying IP-EM and BN-EM pipelines, we successfully resolve structures of NLR proteins and the abundant photosynthetic enzyme ribulose-1,5-bisphosphate carboxylase/oxygenase (RuBisCO), highlighting the methods as versatile tools for quickly elucidating a wide range of plant protein complexes.

### Diverse Structural States of NRC2 Highlight Evolutionary Plasticity in NLR Complexes

**Using IP-EM, we resolved the structures of the helper NLR NRC2** from *N. benthamiana* in both its **resting and activated states**. In the absence of effector stimulation, NRC2 exists as a **homodimer stabilized by three distinct inter-protomer interfaces involving its NB-ARC and LRR domains** (Publication 1, Figure 28). This dimeric configuration maintains the receptor in an autoinhibited state. Upon perception of the PVX CP by the upstream sensor Rx, NRC2 undergoes a dramatic **conformational rearrangement from a compact dimer to a homohexameric resistosome**, distinct from the pentameric architecture of singleton resistosomes such as ZAR1 (Wang et al., 2019). This **structural divergence** suggests that helper NLRs evolved a unique assembly logic to accommodate their role within signalling networks. Furthermore, **by IP-EM we also revealed the cyst nematode effector SS15 binds directly to the NRC2 resting dimer**, locking it in its inactive conformation and preventing oligomerization into the hexameric resistosome (Figure 29). Collectively, these findings reveal that NLR complexes can adopt strikingly different architectures in both their resting and active states, underscoring the **structural and mechanistic diversity that underpins immune signalling across plant NLR** families.

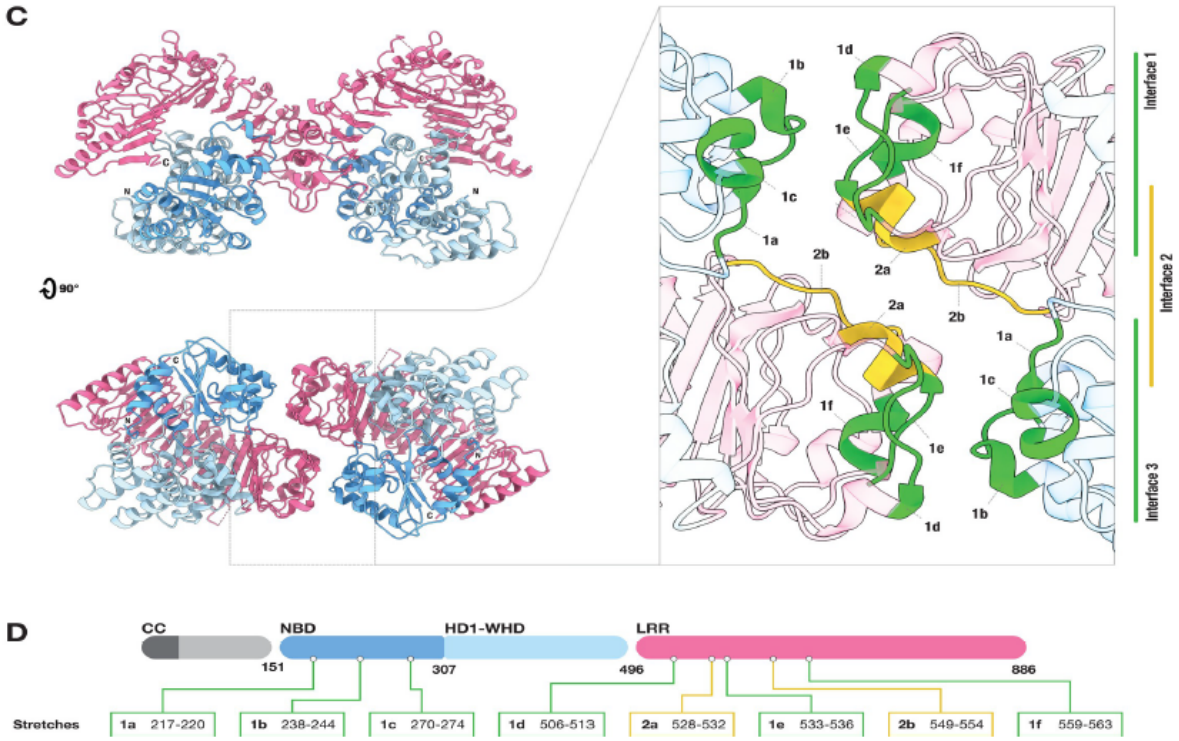


**Figure 28. Atomic model of NRC2 dimers reconstructed from cryo-EM data, with resolved NB domain (NBD), HD1-WHD, and LRR domains.**

**(Upper)** Cryo-EM structure of resting state of NRC2 dimers. Colour coding is corresponding to the lower panel. Atomic model corresponding to NRC2 homodimer shown in two orthogonal views, with resolved NB domain (NBD), HD1-WHD, and LRR domains. Notably, the N-terminal CC domain of NbNRC2 was absent from the cryo-EM density. Inset shows details of interfaces between the two NbNRC2 protomers, highlighting amino acid stretches corresponding to three contact interfaces.

**(Lower)** Colour coding of the domains is shown in the schematic representation of the domain architecture and boundaries of NRC2, which includes the exact boundaries of the amino acid stretches at the dimerization interfaces. [Adapted from Selvaraj et al., 2023]

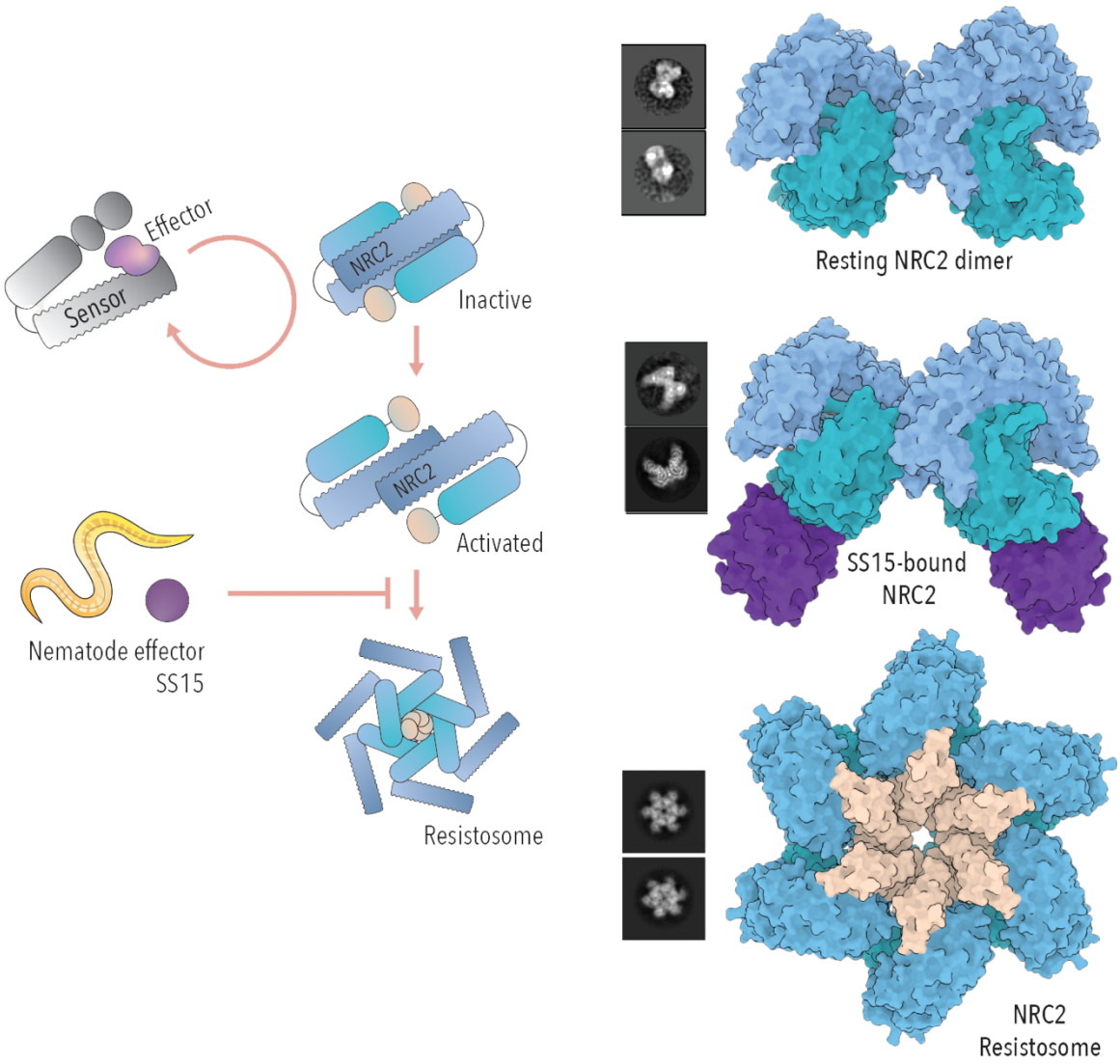


**Figure 29. Cryo-EM structure and a schematic model of how SS15 arresting NRC2 dimer in preventing the hexameric resistosome formation.** Representative electron microscopy images from 2D classification analyses are shown.

## Structural Reconstruction of Plant RuBisCO and Native Complexes Using BN-EM

In contrast to the IP-EM workflow, **BN-EM does not require epitope tagging** or prior knowledge of the protein identity. Any visibly enriched band from a BN-PAGE gel can be analyzed directly by cryo-EM. This feature greatly broadens the applicability of the method, allowing structural exploration of native protein assemblies even when specific antibodies or cloning constructs are unavailable.

As a proof of concept, I applied BN-EM to leaf extracts from *N. benthamiana* and rice. Distinct bands corresponding **RuBisCO** (~550 kDa) were excised, electroeluted, and analyzed by cryo-EM. The reconstructed maps reached **near-atomic resolutions of 3.4 Å for *N. benthamiana*** (Figures 30 and 31) and **3.0 Å for rice** (Figure 32), faithfully preserving secondary-structure elements and side-chain orientations compared to previously reported crystal structures. These results demonstrate that BN-EM preserves native protein conformation throughout electrophoretic separation and electroelution.

To test the generality of this approach, I **extended the analysis to additional plant materials**, including wheat (*Triticum aestivum*) and the early-diverging land plant *Marchantia polymorpha*. Negative-stain EM of electroeluted samples revealed well-defined RuBisCO complexes in both species (Figure 33), supporting the robustness of the pipeline across evolutionary lineages and diverse tissue types. **Beyond the dominant RuBisCO band, we also targeted a minor gel band** from rice extracts. Negative-stain imaging revealed discrete particle populations (Figure 34), suggesting successful recovery of other native complexes and highlighting the potential of BN-EM for exploratory structural studies of low-abundance or previously uncharacterized assemblies.

Collectively, these results establish BN-EM as a versatile, purification-free pipeline for structural investigation of plant macromolecular complexes directly from native tissue extracts. The method bridges traditional biochemistry and high-resolution cryo-EM, expanding the accessible landscape of plant structural biology to include protein assemblies that were previously intractable for conventional purification-based approaches.

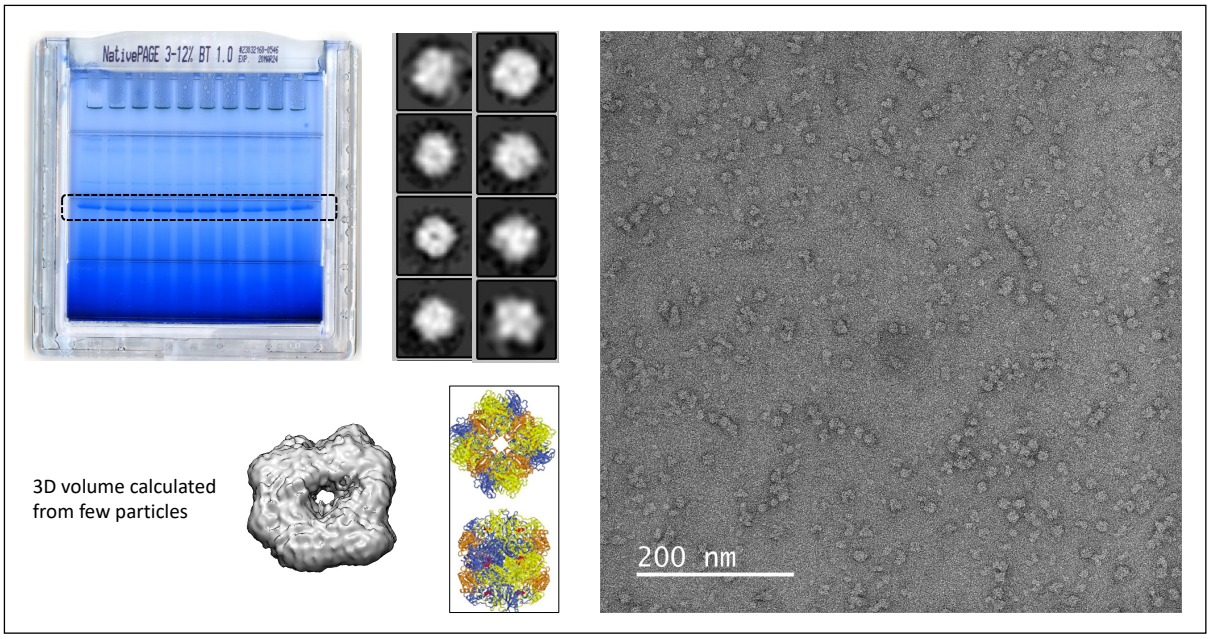


Figure 30. The BN-PAGE gel for electroelution and negative staining pre-screen for *Nicotiana benthamiana* RuBisCO.

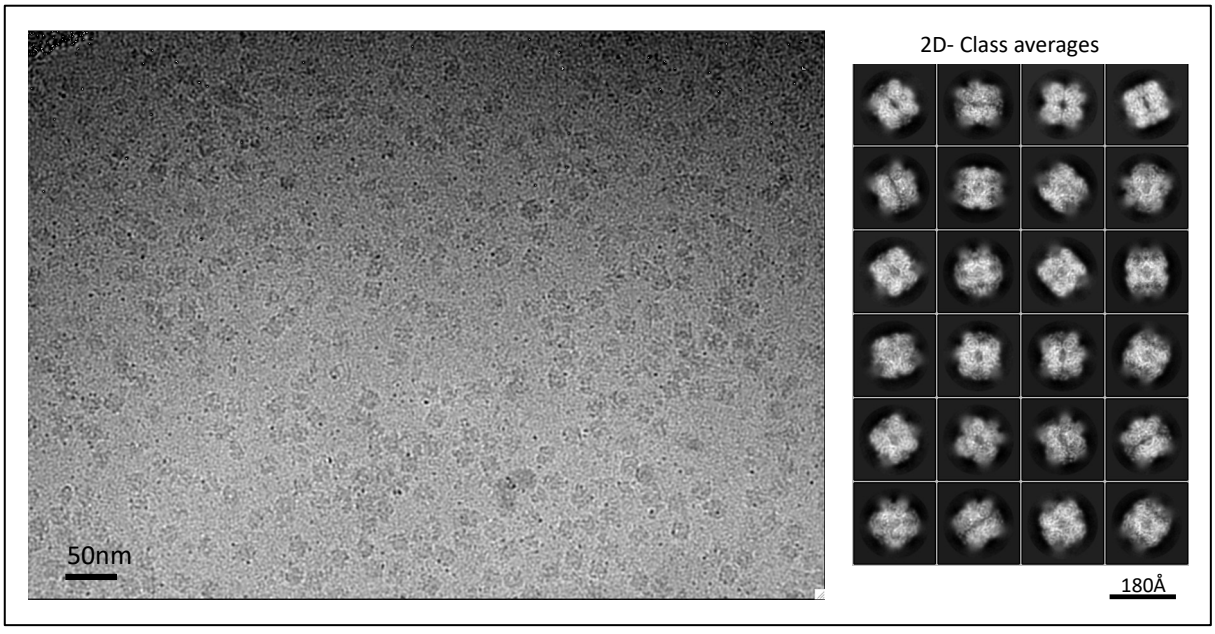


Figure 31. *Nicotiana benthamiana* RuBisCO structure under cryo-EM analysis.

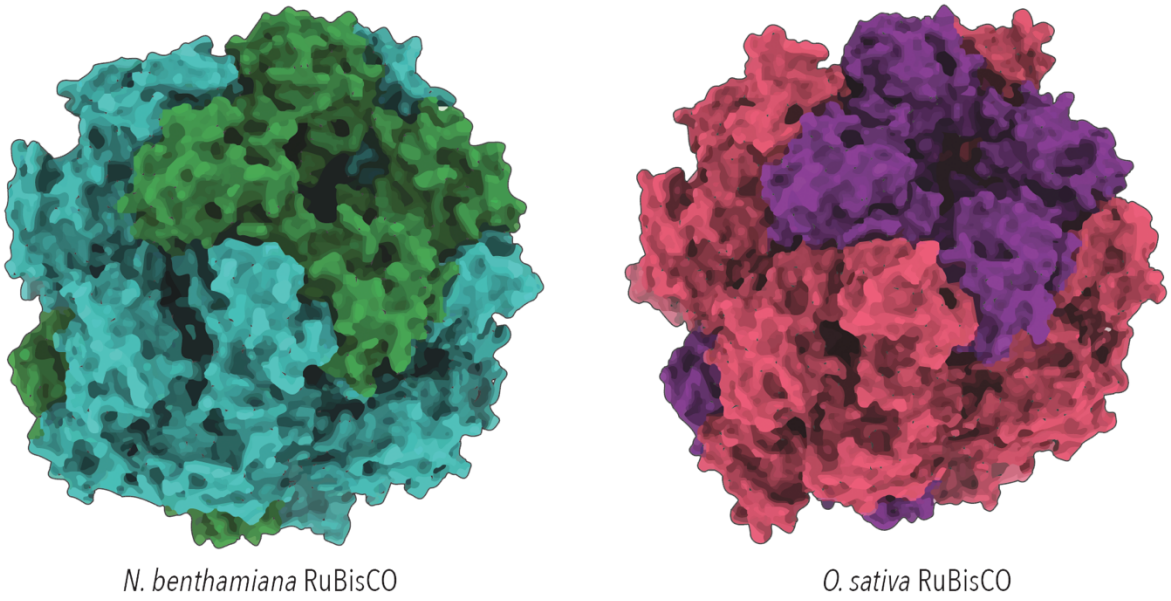


Figure 32. *Nicotiana benthamiana* and rice RuBisCO structures resolved by cryo-EM.

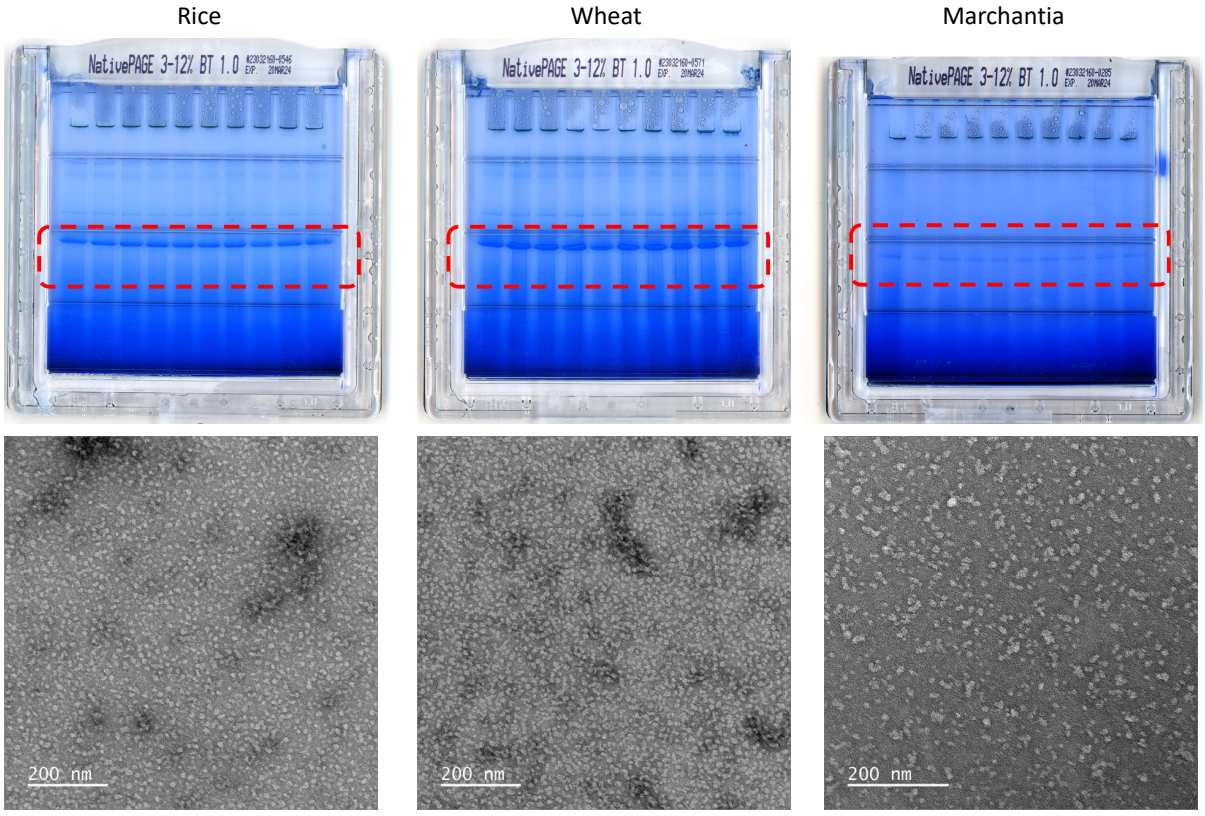


**Figure 33. BN-PAGE and negative-stain EM pre-screening for BN-EM analysis of RuBisCO from multiple plant species.** BN-PAGE gels showing native protein separation from rice, wheat, and Marchantia extracts prior to electroelution. The RuBisCO bands selected for electroelution are indicated by dashed red rectangles. Corresponding negative-stain EM pre-screening images confirm the presence of intact RuBisCO particles following electroelution.

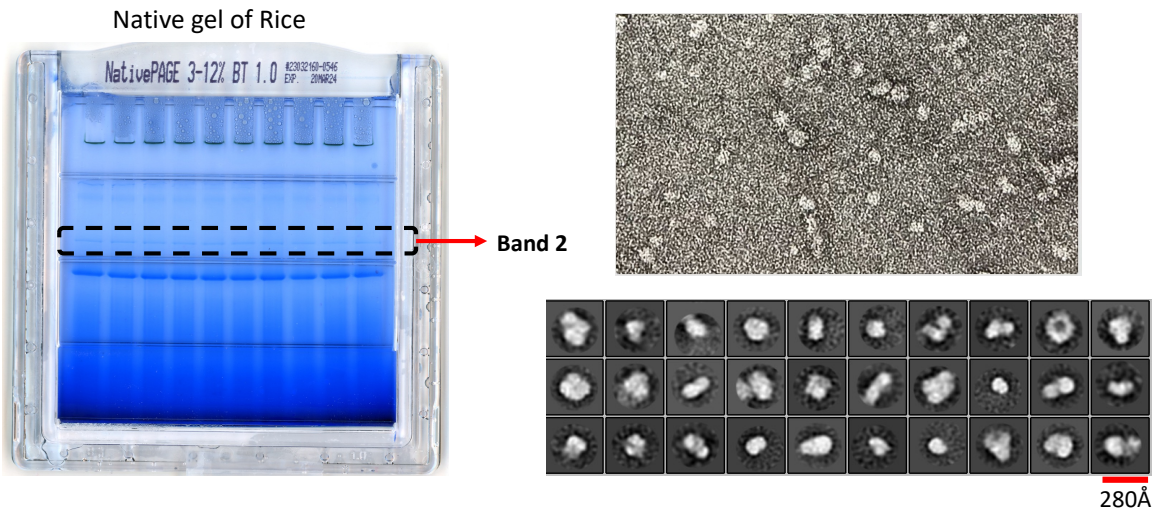


**Figure 34. Extension of BN-EM to non-RuBisCO protein bands. Blue native PAGE (BN-PAGE) gel used for electroelution of a protein band distinct from RuBisCO.** The targeted band is indicated by the dashed black rectangle and red arrow. The electroeluted sample was subjected to negative-stain electron microscopy, revealing heterogeneous protein particles (top right). Representative 2D class averages obtained from the same sample are shown below, demonstrating that BN-EM can be applied to protein complexes beyond RuBisCO.

## 4.4 Summary and Future Perspectives

In this chapter, I established two pipelines — IP-EM and BN-EM that enable rapid isolation of native plant protein complexes for structural characterization. **Through IP-EM, we resolved both the inactive dimeric and active hexameric states of the helper NLR NRC2, plus uncovering how pathogen effectors SS15 can inhibit NRC2 activation** by arresting the resting conformation. **Using BN-EM, I demonstrated a purification-free workflow that successfully reconstructed RuBisCO complexes from diverse plant species**, showcasing the versatility of the approach for studying native assemblies without the need for genetic tagging.

Looking forward, **refining these methods for higher throughput and reproducibility** will be essential, particularly when applied to transient, low-abundance, or unstable complexes (Klebl et al., 2023; Xu and Dang, 2022). For instance, I've observed RuBisCO complexes isolated from Marchantia was unstable in the -80$^{o}$C freezer, fine scheduling immediate cryo-EM grid preparation of employ certain storage buffer might be helpful for resolving this problem. In line with this, each protein assembly possesses distinct biochemical stability and solubility properties, optimization of sample storage condition, incubation time, and buffer additives will be crucial to minimize aggregation or dissociation prior to imaging (Vénien-Bryan and Fernandes, 2023; Weissenberger et al., 2021) — challenges reminiscent of optimizing BN-PAGE sample preparation described in the previous Chapter.

Recent advances in AI-guided tools have dramatically accelerated structural biology, transforming the pace and precision of protein complex studies. In my studies, our team has incorporated tools such as **AlphaFold3 for rapid prediction of protein folds and multimeric assemblies directly from sequence data**, providing valuable hypotheses about domain organization, potential oligomerization interfaces, and critical residues mediating protein–protein interactions (Abramson et al., 2024; Ibrahim et al., 2024; Madhuprakash et al., 2024). By **pre-screening multiple conformations *in silico***, AI modelling guides the rational design of constructs for biochemical and cryo-EM analyses narrowing down targets, optimizing domain boundaries, and predicting stabilizing mutations to facilitate structure determination. However, **current AI algorithms are largely limited to static predictions**, and they cannot yet fully capture the dynamic conformational transitions that underpin NLR activation, signalling, and complex assembly (Madhuprakash et al., 2024; Zhao et al., 2024). This highlights the **continued importance of integrating biochemical approaches in the workflow, which probes structural rearrangements and validate computational models under physiological conditions**. Together, AI-driven modelling and experimental structural biology form a synergistic framework: computational predictions accelerate hypothesis

generation, while experimental validation provides the empirical feedback necessary to refine and train more accurate AI models. This iterative cycle ultimately advancing a **systems-level understanding of plant immune receptor assembly, activation, and evolution**, with unprecedented speed and detail.

# Chapter 5
# Engineering Crop Species for Broad-Spectrum Viral Resistance

Orchids are among the most popular and economically valuable ornamental crops worldwide, driving a thriving global floriculture industry. However, the large-scale cultivation is threatened by viral diseases, which cause irreversible damage to plant health, flower quality, and market value (Sun et al., 2023; Tsai et al., 2022). Among these, *Cymbidium mosaic virus* (CymMV) *and Odontoglossum ringspot virus* (ORSV) are the two most prevalent orchid viruses, frequently occurring as mixed infections that exacerbate symptoms and lead to economic losses (Ajjikuttira et al., 2009). Both viruses spread rapidly through mechanical transmission during propagation and nursery handling. In addition, while some orchid genera (e.g., *Pecteilis* and *Liparis* species) have shown resistance to certain viruses like ORSV, there's **no known genetic resistance in the major marketing varieties** such as *Dendrobium*, *Cymbidium*, *Cattleya*, and especially *Phalaenopsis*, leaving the industry vulnerable to recurring outbreaks (Ryu and Park, 1995；Tsai et al., 2022; Wong et al., 1994).

Towards a sustainable orchid production, my projects published between 2018-2021 focus on **engineering virus-resistant orchids by harnessing the natural mechanism of RNA silencing** — a fundamental antiviral defense system in plants. By understanding and leveraging this pathway, the series of works aim to establish a deeper understanding of host-virus interactions and develop *Phalaenopsis* lines with stable and broad-spectrum resistance to CymMV and ORSV, providing a practical and long-term solution to safeguard orchid cultivation and strengthen the resilience of the global ornamental plant industry.

**Key Publications in Chapter 5:**


1. Pai H, WH Jean, YS Lee, YCA Chang, and NS Lin. (2019) Genome wide analysis of small RNAs from *Odontoglossum ringspot virus* and *Cymbidium mosaic virus* synergistically infected *Phalaenopsis*. Molecular Plant Pathology 21:188-205.

2. Lee SC, H Pai, YW Huang, MH He, YL Song, SY Kuo, WC Chang, YH Hsu, and NS Lin. (2021) Exploring the multifunctional roles of *Odontoglossum ringspot virus* P126 in facilitating *Cymbidium mosaic virus* cell-to-cell movement during mixed Infection. Viruses 13:1552.

3. Chen TY, H Pai, LY Hou, SC Lee, TT Lin, CH Chang, FC Hsu, YH Hsu and NS Lin. (2019) Dual resistance of transgenic plants against *Cymbidium mosaic virus* and *Odontoglossum ringspot virus*. Scientific Reports 9:10230.

**Supporting Publications in Chapter 5:**

4. Tseng KC, YF Chiang-Hsieh, H Pai, NY Wu, HQ Zheng, CN Chow, TY Lee, SB Chang, NS Lin, and WC Chang. (2020) sRIS: A small RNA illustration system for plant next-generation sequencing data analysis. Plant Cell Physiology 61: 1204–1212.

5. Tseng KC, YF Chiang-Hsieh, H Pai, CN Chow, SC Lee, HQ Zheng, PL Kuo, GZ Li, YC Hung, NS Lin, and WC Chang. (2018) MicroRPM: A microRNA prediction model based only on plant small RNA sequencing data. Bioinformatics 34:1108-1115.

## 5.1 Antiviral RNA Silencing: Mechanisms and Applications

### Viral Diseases and Synergistic Infections in Orchids

More than 50 viruses have been reported to infect orchids, and about 30 of them have been described in detail (Ajjikuttira et al., 2009; Cheng et al., 2008; Zettler et al., 1990). Viral infections in orchids typically result in chlorotic or necrotic streaks, ringspots, mosaic and mottled patterns, leaf or floral discoloration, and growth retardation, with symptom severity varying among cultivars and environmental conditions. Among these, CymMV and ORSV are the most prevalent and damaging viruses associated with cultivated orchids worldwide (Ajjikuttira et al., 2009; Li et al., 2011; Sun et al., 2024), both have been widely detected in *Phalaenopsis* and other genera, including *Cymbidium*, *Cattleya*, *Dendrobium*, *Epidendrum*, and *Oncidium*. Although CymMV and ORSV belong to distinct viral families, their co-infection in the same host frequently results in synergistic interactions, producing intensified symptoms compared to single infections, leading to severe tissue damage and floral deformation (Ajjikuttira et al., 2009; Chen et al., 2006; Lan et al., 2019).

CymMV is a member of the genus *Potexvirus* (family *Alphaflexiviridae*) with a monopartite, positive-sense single-stranded RNA [(+)-ssRNA] genome of approximately 6.2 kb. It encodes an RNA-dependent RNA polymerase (RdRp), three movement-associated triple gene block proteins (TGBps), and a 24 kDa coat protein (CP). The non-enveloped, filamentous virions measure about 480 nm in length and are highly stable, facilitating mechanical transmission through contaminated tools and contact between plants (Wong et al., 1997; Tsai et al., 2022). In contrast, ORSV, belongs to the genus *Tobamovirus* (family *Virgaviridae*) and was formerly regarded as the orchid strain of TMV. Its (+)-ssRNA genome (~6.6 kb) contains three open reading frames encoding two RdRp variants, a 34 kDa movement protein (MP), and an 18 kDa CP. The rigid, rod-shaped virions (~300 nm) are remarkably resistant to degradation and can remain

infectious for years in the environment (Chng et al., 1996; Edwardson and Zettler, 1988; Navalinskienë et al., 2005; Ryu and Park, 1995).

Several studies have documented the **synergistic interaction between CymMV and ORSV at both physiological and molecular levels**. Co-infected orchids exhibit **higher viral titers and accelerated viral RNA accumulation** compared to single infections (Ajjikuttira et al., 2009; Chen et al., 2006; Tsai et al., 2022). Studies in transfected *Dendrobium* protoplasts revealed that co-infection increases both positive- and negative-strand RNA levels several-fold, suggesting enhanced replication efficiency (Hu et al., 1994). Functional analyses have demonstrated **reciprocal complementation between viral proteins: the ORSV MP can restore cell-to-cell movement in CymMV** mutants lacking movement function, while CymMV CP can partially complement ORSV transport (Ajjikuttira et al., 2005). However, these explorations are yet to reveal detailed molecular mechanisms and pathogenic processes underlying CymMV and ORSV synergism.

## Viral Suppressors of RNA Silencing and the Basis of Synergism

Similar to the case of CymMV and ORSV, **viral synergism is a common phenomenon in which co-infection by two or more distinct viruses leads to more severe disease symptoms**, increased viral titers, or expanded host range compared with single infections. In cellular level, the synergistic effects often include accelerated replication and enhanced systemic movement in one or both viruses.

Earlier studies revealed **synergism can be due to trans-complementation**, in which viral proteins from one virus compensate for defective or missing functions in another, allowing non-systemic viruses to move through plasmodesmata or replicate in additional tissues (Cooper et al., 1996; Morozov et al., 1997; Solovyev et al., 1996; Syller, 2012). For example, the MP of TMV can facilitate the systemic spread of unrelated viruses, while potyvirus NIaPro and P1 proteins can enhance replication of heterologous viruses through replication-complex interactions (Hýsková et al., 2024; Syller, 2012; Vogler et al., 2008). **Viral synergism also frequently involves suppression or manipulation of the host's immune signalling networks**, including SA and JA pathways, and NLR signalling cascades. By downregulating SA-dependent defense genes and weaken both PTI and ETI, mixed-infected host plants are more susceptible to secondary infection (Alazem and Lin, 2017; Palukaitis and Yoon, 2020; Verma et al., 2016). **Synergistic interactions can also affect virus transmission dynamics**. Insect vectors may acquire and transmit viruses more efficiently during mixed infections, aided by helper virus proteins that enhance viral accumulation in feeding tissues (Ray and Castel, 2022; Tamborindeguy et al., 2023). This cooperative transmission contributes to the co-

evolutionary success of synergistic virus pairs across diverse plant families and ecological contexts.

With the discovery of VSRs, now we know **the above mechanisms are largely due to the suppression of antiviral RNA silencing**, and are tightly linked to each other. VSRs achieve the immune **disruption at multiple levels—by sequestering vsiRNAs, preventing AGO loading, or interfering with small RNA biogenesis** (Burgyán and Havelda, 2011). At the initiation phase of RNA silencing, certain VSRs including cysteine-rich protein of Potato virus M and P14 of *Pothos latent virus* protects long dsRNA from DCL cleavage, allowing early viral replication to proceed unimpeded (Mérai et al., 2006; Qu and Morris, 2005). Another group of VSRs sequesters siRNA duplexes, preventing their incorporation into RISCs. Well-characterized examples include HC-Pro of potyviruses, P19 of tombusviruses, and P21 from *Beet yellows virus* (Roth et al., 2004; Teixeira et al., 2021). In PVX and *Potato virus Y* (PVY) co-infections, PVY-derived HC-Pro sequesters vsiRNAs from both viruses, leading to a dramatic increase in PVX accumulation and symptom intensity (Ghosh et al., 2021; Hýsková et al., 2024; Pruss et al., 1997). In addition to sequestering vsiRNAs, the 2b protein of *Cucumber mosaic virus* (CMV) binds AGO1 to inhibit its slicing activity, while the p0 protein of *Poleroviruses* induces AGO1 degradation via the ubiquitin–proteasome pathway. Other suppressors such as *Turnip crinkle virus* p38 and *Sweet potato mild mottle virus* P1 interfere with AGO1's catalytic function (Atabekova et al., 2023; Baulcombe, 2022; Zhang et al., 2006). Collectively, these mechanisms inhibit antiviral RNA silencing function and in turn enhance co-infecting virus accumulation.

Overall, plant viral synergism represents a multi-layered molecular phenomenon driven primarily by VSR-mediated suppression of RNA silencing and manipulation of host's normal growth. The asymmetric nature of most synergistic relationships — where one virus acts as a "helper" enhancing another's infection — further illustrates the dynamic complexity of plant-virus-host interactions.

## vsiRNAs as Modulators of Host Gene Expression

In contrast to the viral RNA clearance activity of plant RNA silencing pathways, studies have demonstrated that **mRNAs of host genes can conversely be targeted by vsiRNAs** when high sequence complementarity exists between viral and host transcripts (Llave, 2004; Wang et al., 2004). This redirection of the host's antiviral machinery represents a molecular "hijacking" of RNA silencing, whereby vsiRNAs act not only in viral RNA degradation but also in modulating host gene expression—often to the pathogen's advantage.

The earliest evidence came from viroid and satellite RNA systems. Expression of *Potato spindle tuber viroid* (PSTVd)-derived hairpin RNAs in transgenic tomato induced characteristic viroid symptoms, demonstrating that viroid-derived siRNAs can directly trigger pathogenic effects (Wang et al., 2004). Similarly, CMV Y-satellite (Y-sat) produces vsiRNAs complementary to a 22-nt region of the chlorophyll biosynthetic gene *ChlI* in *N. benthamiana*, leading to chlorosis through targeted mRNA cleavage and impaired chlorophyll accumulation (Shimura et al., 2011; Smith et al., 2011). In another case, *Peach latent mosaic viroid* (PLMVd)-derived siRNAs repress a chloroplastic heat-shock protein 90, producing the "peach-calico" phenotype (Navarro et al., 2012).

Beyond these specific examples, degradome and transcriptomic studies have revealed that **vsiRNAs can regulate numerous host transcripts involved in defense, metabolism, and development**. In *Arabidopsis* infected with TMV-Cg, vsiRNAs were shown to interfere genes that involve in mRNA pre-processing and membrane protein secretion systems (Qi et al., 2009). Genome-wide analyses in grapevine (Miozzi et al., 2013), rice, and watermelon (Sun et al., 2017; Xu and Zhou 2017) further identified dozens of host targets related to NLR-mediated immunity, receptor-like kinases, chloroplast function, and stress signalling. Notably, some vsiRNAs target RNA silencing components themselves, including DCL and AGO genes, thereby weakening antiviral defenses and promoting viral persistence (Ramesh et al., 2021).

## Profiling vsiRNA Populations to Decode Host–Virus Interactions

As summarized in the above sections, studies re-define vsiRNAs as dual-function molecules, which is exploited by viruses as defensive agents in antiviral RNA silencing and regulatory tools to manipulate host gene expression. **Profiling vsiRNAs thus offers critical insights into the molecular interplay between plants and viruses**.

Profiling studies by high-throughput sequencing consistently reveal that **vsiRNAs are enriched in the 21- and 22-nt size classes**, reflecting DCL4 and DCL2 activity. This predominance is observed across diverse virus–host systems, including TMV, CMV, *Turnip mosaic virus* (TuMV), PVX, and other sviruses (Donaire et al., 2009; Lin et al., 2010; Pantaleo et al., 2010; Qi et al., 2009). An exception is *Cymbidium ringspot virus* (CymRSV), which accumulates more 22-nt vsiRNAs, likely due to sequestration of 21-nt molecules by its silencing suppressor P19 (Donaire et al., 2009). **The 5'-terminal nucleotide bias of vsiRNAs is another defining characteristic that influences AGO sorting and downstream silencing mode**. Most RNA viruses produce vsiRNAs enriched for 5'-uridine (U) or adenine (A), which preferentially load into AGO1, AGO10, or AGO2 complexes responsible for post-transcriptional silencing (Donaire et al., 2009; Mi et al.,

2008; Pantaleo et al., 2010; Yan et al., 2010). Across all systems, vsiRNAs rarely start with 5'-guanine (G), a conserved bias reflecting AGO loading constraints.

In addition to size and 5' bias, **vsiRNAs display distinct strand polarity and genomic hotspot distributions**. Because viral dsRNA intermediates contain both positive- and negative-strand templates, vsiRNAs are usually produced from both polarities, often in near-equal proportions — as seen in TuMV, PVX, WMV, and TYLCV infections (Donaire et al., 2009). However, polarity bias and distribution patterns can vary across hosts and virus strains, as seen for (-)-strand preference of BaMV vsiRNAs in *N. benthamiana* but slightly (+)-biased vsiRNAs in *Arabidopsis* (Lin et al., 2010), and RSV vsiRNAs are mainly (+)-strand in both rice and tobacco but arise preferentially from RNA segments 3 and 4. Seminal works such as Molnár et al. (2005) and Gago-Zachert et al. (2019) demonstrated that **vsiRNAs arise from highly structured single-stranded viral regions and reflect the activity of Dicer processing during replication**. Deep sequencing studies (Verdin et al., 2017; Wu et al., 2010) further established vsiRNA profiling as a tool not only for dissecting antiviral immunity but **also for identifying novel viruses and reconstructing their genomes from infected plant material**. Methodological advances, including optimized size-selection and computational pipelines (Donaire and Aranda, 2024; Zheng et al., 2017), now enable high-resolution mapping of vsiRNA populations and their strand polarity.

In synergistic systems such as *Bean pod mottle virus* (BPMV) and *Soybean mosaic virus* (SMV), RNA sequencing studies have further shown that **synergism alters vsiRNA profiles and DCL processing efficiency** (Alazem et al., 2023). In co-infections of *Brassica yellows virus* (BrYV) and *Pea enation mosaic virus 2* (PEMV-2), vsiRNAs derived from BrYV increased up to 26-fold compared with single infections, accompanied by modified size distributions and mapping patterns (Zhou et al., 2017). These findings indicate that synergistic interference with RNA silencing changes the balance of antiviral small RNAs, leading to over-replication and altered host gene regulation.

**Collectively, vsiRNA profiles serve not only as diagnostic markers for viral infection but also as mechanistic readouts of antiviral silencing efficiency and virus-encoded suppressor activity across plant lineages**. The profiles can help us identify **(i)** active RNA silencing pathways and viral genomic regions most susceptible to RNA interference in various host-virus systems, **(ii)** potential vsiRNA targets in host genes, **(iii)** the inference of VSRs in the interactions, and **(iv)** serving as a powerful tool for virus discovery and evolutionary studies in plant virology (Deng et al., 2022; Elvira-Gonzalez et al., 2025).

## Pathogen-Derived Resistance: From Concept to RNAi-Based Engineering

**Pathogen-derived resistance (PDR)**, first proposed by Sanford and Johnston (1985), is founded on the principle of "self-interference" — **using genetic elements from a pathogen to disrupt its own infection cycle when expressed in the host**. This strategy revolutionized plant virology by demonstrating that transgenic expression of viral genes could confer resistance against homologous or related viruses (Zhou et al., 2020).

The mechanism of PDR operates through both **protein-based and RNA-based** interference (Beachy, 1997; Zhou et al., 2020). Some other PDR strategies exploit the concept of **biocontrol**, introducing **defective interfering (DI) RNAs**, which are truncated viral RNA variants that compete for replication of the full virus; or cross-protection—where mild strains confer protection against more virulent strains via priming effect (Budzyńska et al., 2022). These are not of the main focus here and are described in reviews.

In protein-mediated PDR, expressing viral CP hinder key infection processes such as uncoating or encapsidation, while expression truncated version of MP and RdRp can interfere with viral replication via **dominant-negative competition**, thereby reducing infectivity or slowing systemic spread (Gottula, and Fuchs, 2009). Classical examples include TMV and CMV CP transgenes in tobacco, PVY or *Potato leafroll virus* (PLRV) CP and defective replicase cassettes in potato (Jahromi et al., 2022; Powell et al., 1989; Van der Wilk et al., 1991).

Along with the discoveries of RNA interference pathways, new PDR concept arises, and the **designs rely on antisense transcripts, untranslatable sense transcripts, or inverted repeat forming hairpin structures that generate siRNAs targeting viral genes** via gene silencing (Majumdar et al., 2023; Weiberg and Jin, 2015) (Figure 35). Successful resistant crops include transgenic papaya against Papaya ringspot virus and Cucurbita lines conferring multi-virus protection. The strategy also extends beyond RNA viruses to DNA viruses, fungi, nematodes, and insects, through host-delivered RNAi constructs targeting essential pathogen or pest genes (Schaefer et al., 2020; Wang et al., 2017).

Together, PDR represents a promising strategy for engineering virus-resistant plants by exploiting viral components to disrupt infection. Insights from vsiRNA profiling and VSR characterization would deepen our understanding of host-virus interactions, strengthen the design of precise and durable resistance strategies.

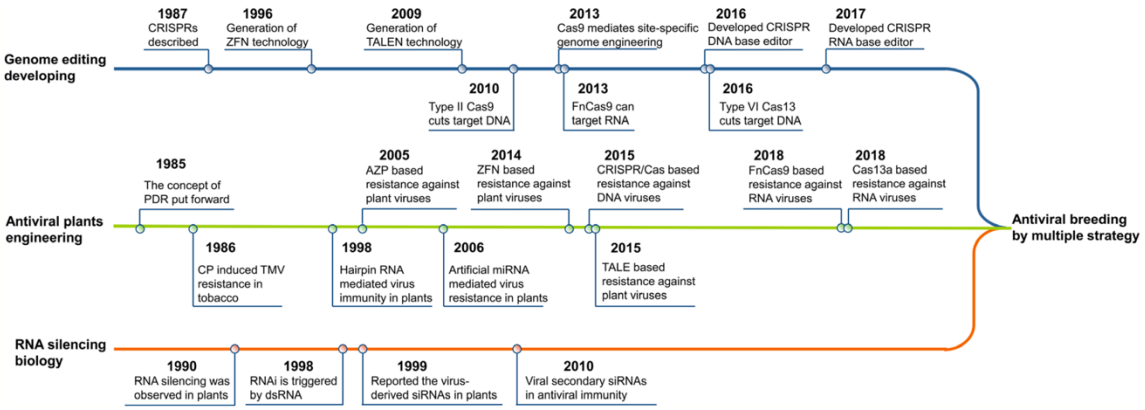


**Figure 35. Timeline of antiviral plant engineering, genome editing and RNA silencing technology developing research fields.** [adapted from Zhao et al., 2020].

## 5.2 Dissecting Viral Synergism and Establishing Genetic Tools for Orchid Virus Research

In this section, I outlined the **findings and experimental tools** I developed to **investigate the molecular mechanisms of CymMV and ORSV co-infection in *Phalaenopsis amabilis*.** This work encompasses analyses of viral infection dynamics, RNA silencing responses, identification of viral suppressors, and the establishment of functional genomics and resistance systems in orchids.

### 5.2.1 Molecular Characterization of CymMV and ORSV Co-Infection in *Phalaenopsis amabilis*

(1) Dynamics of Viral Infection and Synergistic Spread

To investigate the infection dynamics of ORSV and CymMV in orchids, I conducted a **time-course assay to characterize the early progression of viruses in *Phalaenopsis amabilis*.** Previous studies have detected these viruses in systemically infected leaves between two and eight weeks post inoculation (Liu, 2000; Yang, 2008; Lu et al., 2007; Lu et al., 2009), but the precise timeline and spatial distribution of infection in the initial inoculated tissues had not been established. To address this gap, I inoculated virus-free *P. amabilis* plants with purified virions, and I used tissue-blotting to monitor virus infection at defined time points within one month.

In ORSV-inoculated leaves, virus accumulation was first evident around 7–11 days post inoculation (dpi), restricted to the inoculated region. Over a longer period, infection spread basipetally from the leaf tip, with systemic spread observed after 10 dpi, reaching all tested leaves by 20–30 dpi. In contrast, CymMV infection appeared weak and uneven, detectable only at early time points in a subset of plants. Strikingly, when I **co-inoculated plants with both viruses, CymMV accumulation and spread were markedly accelerated with widespread infection** throughout the leaf by 11–20 dpi, whereas ORSV retained its localized pattern (Figure 36).

These observations revealed distinct infection kinetics between the two viruses and highlight the synergistic enhancement of CymMV spread by ORSV co-infection. Based on these results, **I selected 10 dpi as the representative stage for established local infection in subsequent assays**.

(2) Profiling CymMV/ORSV vsiRNAs in Single and Mixed Infections

Following the determination of virus infection time course, I generated eight **small RNA sequencing libraries** from *P. amabilis* leaves collected 10 dpi to profile vsiRNAs under different infection conditions. Libraries were defined by inoculation type — **mock (M), ORSV (O), CymMV (C), or double infection (D)** — and tissue location: **inoculated (i, late stage) or adjacent non-inoculated (n, early stage) areas**, yielding Mi, Mn, Oi, On, Ci, Cn, Di, and Dn (Publication 1, Figure 37). This design captures small RNA populations associated with both localized and a potentially primed antiviral response.

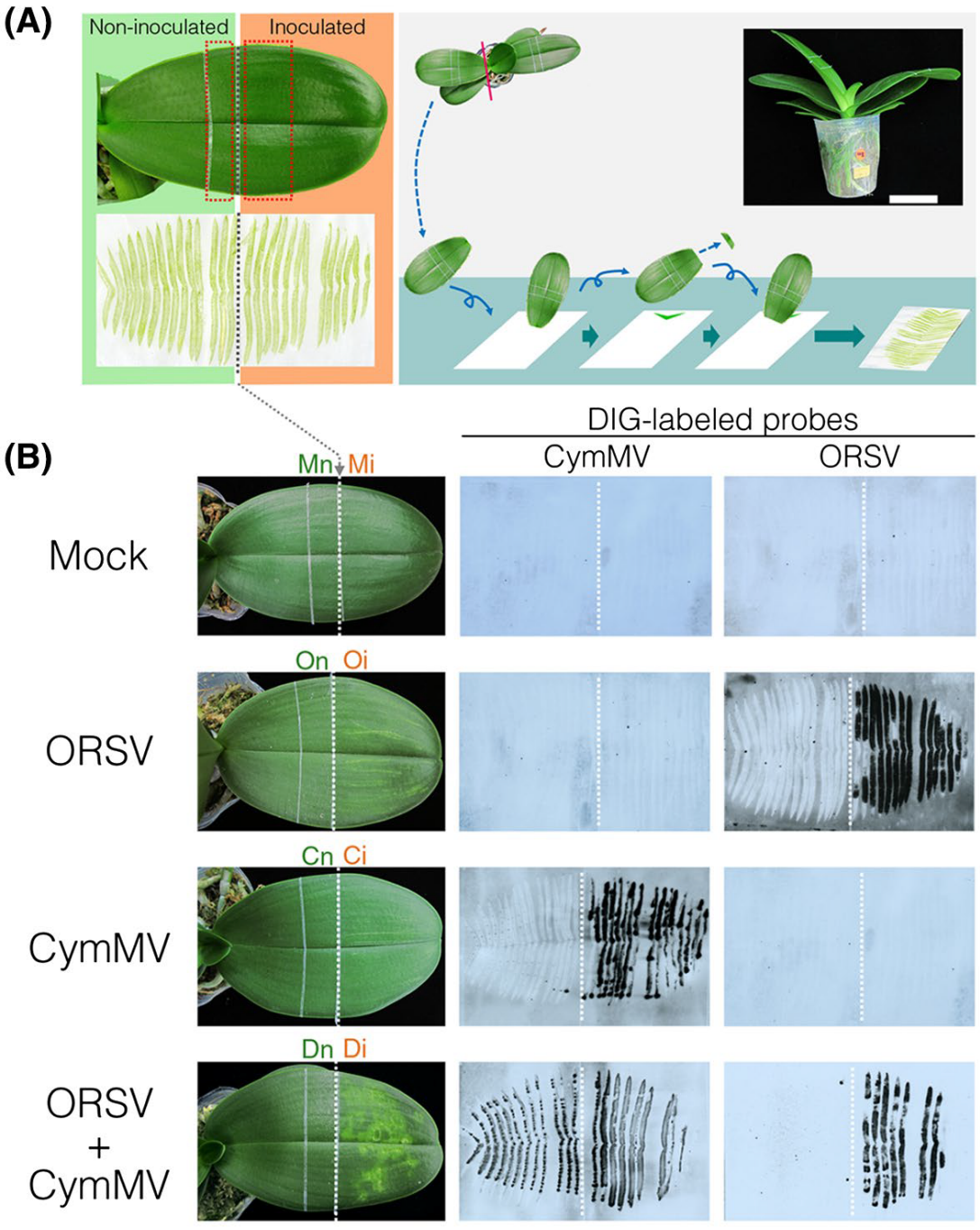

**Figure 37. Symptom development and tissue blot detection of *Odontoglossum ringspot virus* (ORSV) and/or *Cymbidium mosaic virus* (CymMV) infection in *Phalaenopsis*.** (A) Schematic of the leaf-tip inoculation and tissue-blotting strategy used in the infection assays. *Phalaenopsis amabilis* leaves were inoculated with virions on the distal (tip) half of the leaf. Red rectangles indicate the regions used for sampling inoculated and non-inoculated tissues. The right panel illustrates the tissue-blotting procedure: the entire inoculated leaf was excised and sequentially sectioned from the base (non-inoculated) to the tip (inoculated), and each cross-section was pressed onto nylon membranes. (B) Representative leaf phenotypes and corresponding tissue-blot hybridization results at 10 days post-inoculation (dpi) for mock- and virus-inoculated leaves. Mock (M) buffer-inoculated tissues and their adjacent non-inoculated regions were designated Mi and Mn, respectively. Dashed lines indicate the boundary between inoculated (right) and non-inoculated (left) regions as defined in (A). Labels denote inoculated (i, orange) or non-inoculated (n, green) tissues of mock (M), ORSV (O), CymMV (C), or double-infected CymMV + ORSV (D) leaves. Tissue blots were hybridized with digoxigenin (DIG)-labelled probes specific for the CymMV and ORSV coat protein (CP) genes. [Adapted from Pai et al., 2019]

The CymMV and ORSV vsiRNA profiles revealed distinct yet inter-related features that reflect antiviral RNA silencing dynamics and viral synergism in *P. amabilis*. Across all infections, **vsiRNAs were predominantly 21–22 nucleotides** in length, with 21-nt species being most abundant, indicating the involvement of DCL4 and DCL2 in their biogenesis. **Both viruses produced sense-strand–biased vsiRNAs with under-represented 5′-G nucleotides**. However, their genomic origins differed: **CymMV vsiRNAs mainly mapped to the RdRp region, whereas ORSV vsiRNAs concentrated around the CP gene and 3′-untranslated region (3′-UTR)**, particularly a hotspot within the 3′-terminal pseudoknot.

**During double infection**, vsiRNA accumulation and distribution shifted markedly, reflecting asymmetric viral synergism. **CymMV vsiRNAs increased more than five-fold** relative to single infections, while ORSV vsiRNAs occupied a small proportion and exhibited a reorganization of hotspot regions. **The dominant 3′-UTR hotspot in ORSV single infections was replaced by multiple new hotspots in the negative-strand RdRp regions**. Concurrently, **ORSV vsiRNAs shifted from a 5′-A to a 5′-U/C preference**, consistent with up-regulation of AGO1 and AGO5. Together, these results indicate that ORSV-mediated synergism alters vsiRNA biogenesis, enhancing CymMV replication while modifying ORSV silencing profiles.

(3) Phalaenopsis Transcriptomic and microRNA Responses Under Co-Infection

Alongside vsiRNA profiling, I analyzed the **transcriptome and microRNA expression of *P. amabilis* infected with CymMV and ORSV** to identify host genes involved in viral infection, defense, and synergism. Using the same sample framework as for vsiRNA libraries, I focused on mixed-infected leaves to examine host gene reprogramming. While in most mixed-inoculated leaves CymMV spread systemically, **there was a smaller subset where both CymMV and ORSV remained confined to the inoculated area** with lower viral accumulation. I designated leaves showing systemic

CymMV spread as Di/Dn (inoculated and adjacent non-inoculated tissues, respectively), and those with localized CymMV + ORSV infections as Dsi/Dsn. **Dsn represents the earliest stage of infection, Di the late and synergistic stage**, with Dn and Dsi reflecting intermediate phases of viral progression (Figure 38). This design enabled a comparative analysis of early and late transcriptional responses associated with infection dynamics and virus-virus synergism.

By RNA-Seq and RT-qPCR validation, I identified several **differentially expressed genes (DEGs)** upregulated during early infection (Dsn), including xyloglucan endotransglycosylase/hydrolase (cell wall remodelling), UDP-glucosyl transferase, E3 ubiquitin ligase, 2OG-Fe(II) oxygenase, and cytochrome P450 genes, suggesting activation of structural defense and secondary metabolism. During the progression of infection (Dn-Dsi-Di), several DEGs including WRKY and bHLH transcription factors, PR proteins, chitinase, and β-glucanase, were strongly induced, whereas expansin and pectinesterase genes linked to cell wall loosening were downregulated. Comparison between Di and Dn tissues highlighted DEGs potentially associating with synergism, including AGO1, AGO5 (key RNA silencing factors), sphinganine C(4)-monooxygenase (lipid signalling/PCD), PME inhibitor (virus movement restriction), and aux/IAA16 (hormone signalling).

For **miRNAs**, Because *P. amabilis* miRNA database was available, I annotated miRNAs by BLASTN searches against miRBase v18.0 (Kozomara and Griffiths-Jones, 2011) with a tolerance of three mismatches, identifying 104,797 unique sequences across 154 families. I then normalized the read counts with miRNA pool sizes and converted it to tags per million (TPM) for calculating fold-change index among mock, single-, and mixed-infected libraries. The analysis revealed distinct regulation patterns. **MiR156, miR168, miR319, and miR5139 were up-regulated, while miR398, miR408, miR528, and miR535 were down-regulated**, particularly in mixed-infection tissues (Di/Dsi). These results suggest that specific miRNAs are differentially expressed during CymMV and ORSV infections and may participate in antiviral defense and synergistic interactions.

Collectively, these results delineate a dynamic virus–host interaction network in orchids and provide candidate genes for improving resistance to CymMV/ORSV coinfection.

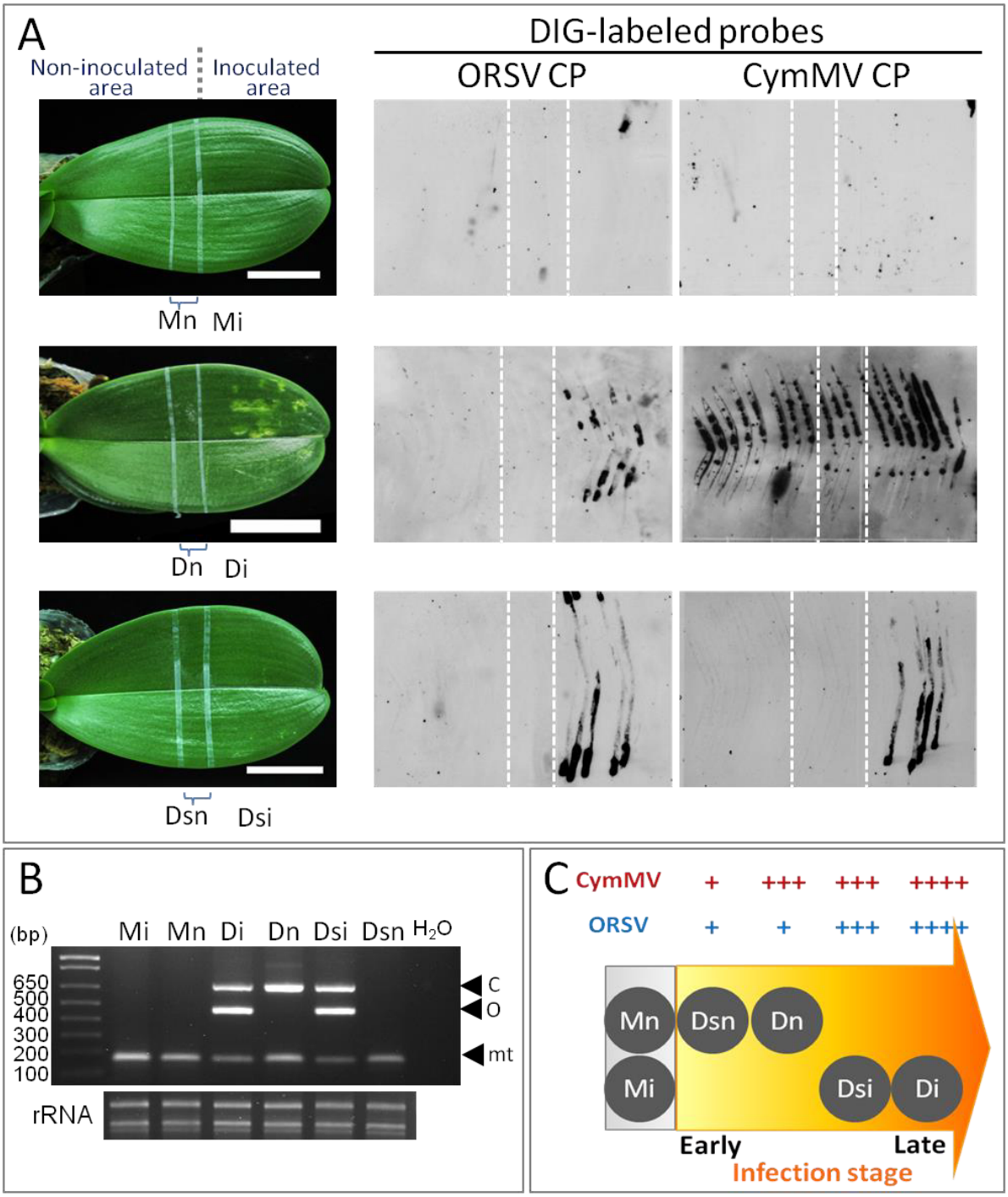


**Figure 38. Classification of mixed *Odontoglossum ringspot virus* (ORSV)-*Cymbidium mosaic virus* (CymMV) infection stages in *Phalaenopsis* based on tissue blotting and RT–PCR analyses.** (A) Leaf phenotypes and tissue-blot detection of CymMV and ORSV accumulation in mixed-inoculated leaves. In most mixed inoculated plants, CymMV spread systemically, whereas ORSV remained largely confined to the inoculated region. A smaller subset of leaves displayed localized co-infection, in which both CymMV and ORSV were restricted to the inoculated area with lower overall viral accumulation. DIG-labelled CP-specific probes were used for detection as in Fig. 37. (B) RT–PCR detection of viral RNA accumulation in inoculated and adjacent non-inoculated tissues. CymMV- and ORSV-specific amplicons confirm differential viral spread and accumulation among the designated sample classes. rRNA serves as the loading control. (C) Schematic representation of infection stages used for downstream host transcriptome and sRNA profiling. Leaves showing systemic CymMV spread were designated as Di (inoculated) and Dn (adjacent non-inoculated),

representing late and intermediate synergistic infection stages, respectively. Leaves with localized co-infection were designated as Dsi (inoculated) and Dsn (adjacent non-inoculated), representing intermediate and earliest infection stages. Dsn corresponds to the earliest detectable stage of infection, while Di represents the late synergistic stage with maximal viral accumulation.

### 5.2.2 Identification and Functional Characterization of CymMV/ORSV Viral Silencing Suppressors (VSRs)

To identify the VSRs from CymMV and ORSV, I used an **GFP reporter assay** in N. *benthamiana*. I cloned individual viral ORFs and co-expressed each viral proteins with a GFP construct (pBIN61-eGFP; Bendahmane et al., 2002) transiently via agroinfiltration, where **suppression of GFP silencing indicated VSR activity**. Known suppressors TBSV P19 and PVX P25 were served as positive controls. Among the ORSV candidates, I found that **only the P126 replicase significantly enhanced GFP fluorescence**, confirming it as the VSR of ORSV, with activity comparable to PVX P25. None of the CymMV proteins (RdRp, TGBp1–3, or CP) exhibited detectable silencing suppression (Publication 2, Figure 39).

To further examine the relationship between replication and VSR function, I generated P126 mutants at residue M1104 (P126R, P126S, P126A) and tested their activity. The P126R mutant lost both VSR function and protein stability, while P126S and P126A retained silencing suppression but failed to replicate, indicating that P126's VSR and replication functions are separable. I confirmed this by testing the full-length mutant clones in *Chenopodium quinoa* and *N. benthamiana*, where all mutants were replication-defective. Together, these results demonstrate that ORSV P126 functions as a bona fide VSR, whereas CymMV lacks detectable silencing suppression activity, likely explaining the asymmetric synergism observed between these two orchid viruses.

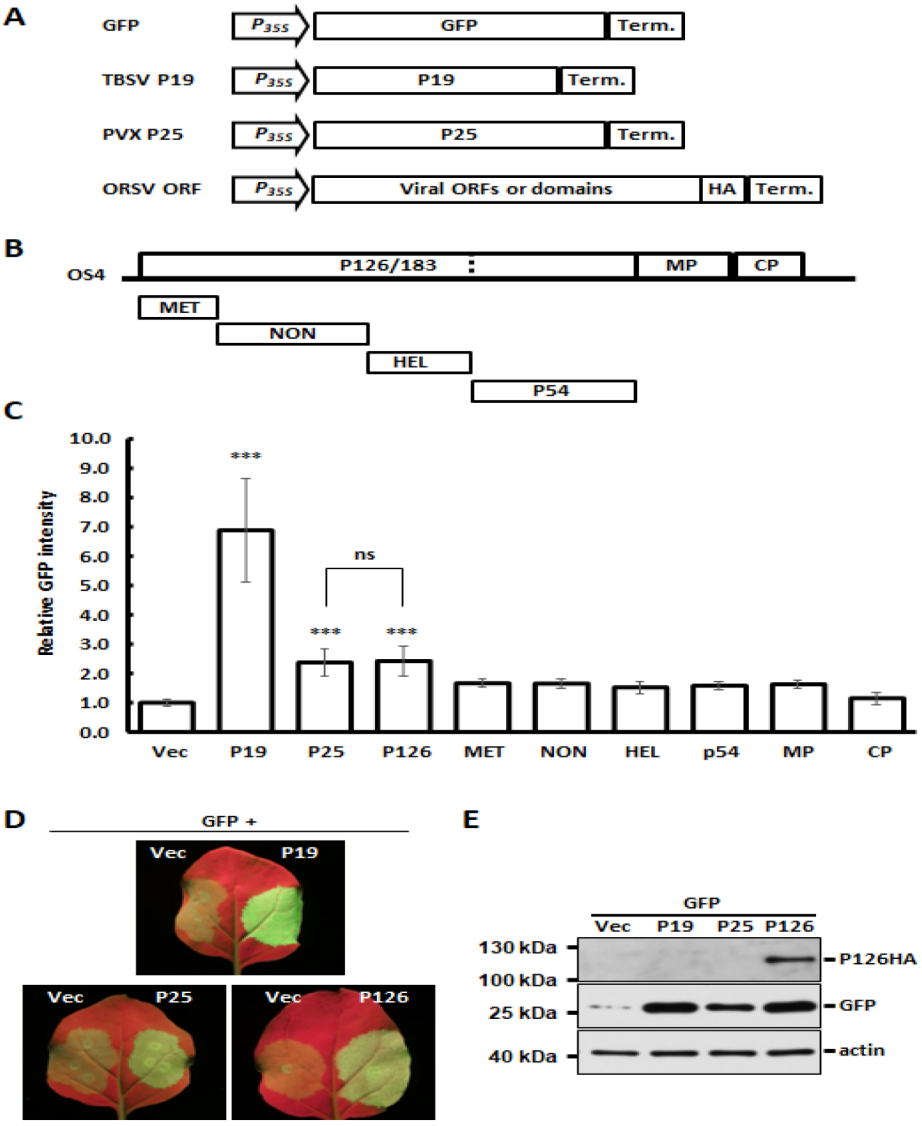


**Figure 39. Viral suppressor of RNA silencing (VSR) activities of *Odontoglossum ringspot virus* (ORSV)-encoded proteins.** VSR activity was assayed based on enhancement of GFP expression in *Nicotiana benthamiana*. (A) Schematic representation of expression cassettes for GFP (reporter), *Tomato bushy stunt virus* (TBSV) P19 and *Potato virus X* (PVX) P25 (positive VSR controls), and the tested ORSV open reading frames (ORFs). (B) Individual ORSV ORFs and protein domains examined in the VSR assay. (C) Quantitative analysis of VSR activity, expressed as a relative index normalized to the empty vector (vec) control. (D) Representative GFP fluorescence signals observed under a hand-held UV lamp. (E) Accumulation of HA-tagged P126, GFP, and actin in the samples shown in (D) was assessed by western blotting. [Adapted from Lee et al., 2021]

### 5.2.3 Development of Molecular Tools for Functional Genomics in Orchids

(1) Establishment of a *Foxtail mosaic virus* (FoMV)-Based VIGS System in *Phalaenopsis*

To establish a functional genomics tool applicable to *Phalaenopsis* and related orchids for validating key factors involved in CymMV and ORSV viral synergism and immune responses, I tested a **virus-induced gene silencing (VIGS) system using distant related FoMV as a vector** (Chang et al., 2013; Huang, 2017). To test the efficiency of FoMV VIGS system, I targeted ***phytoene desaturase*** **(PDS)** ***as a reporter*** gene. Successful silencing would impair chlorophyll biosynthesis and cause visible leaf bleaching. Three months after inoculation with the FoMV-PDS construct (pKF-PaPDS), I observed distinct white patches on the leaves, confirming effective silencing. RT-qPCR analysis further showed that PDS transcript levels were reduced to about 50% of the control during the first month post-infection, and the effect persisted for at least six months (Figure 40).

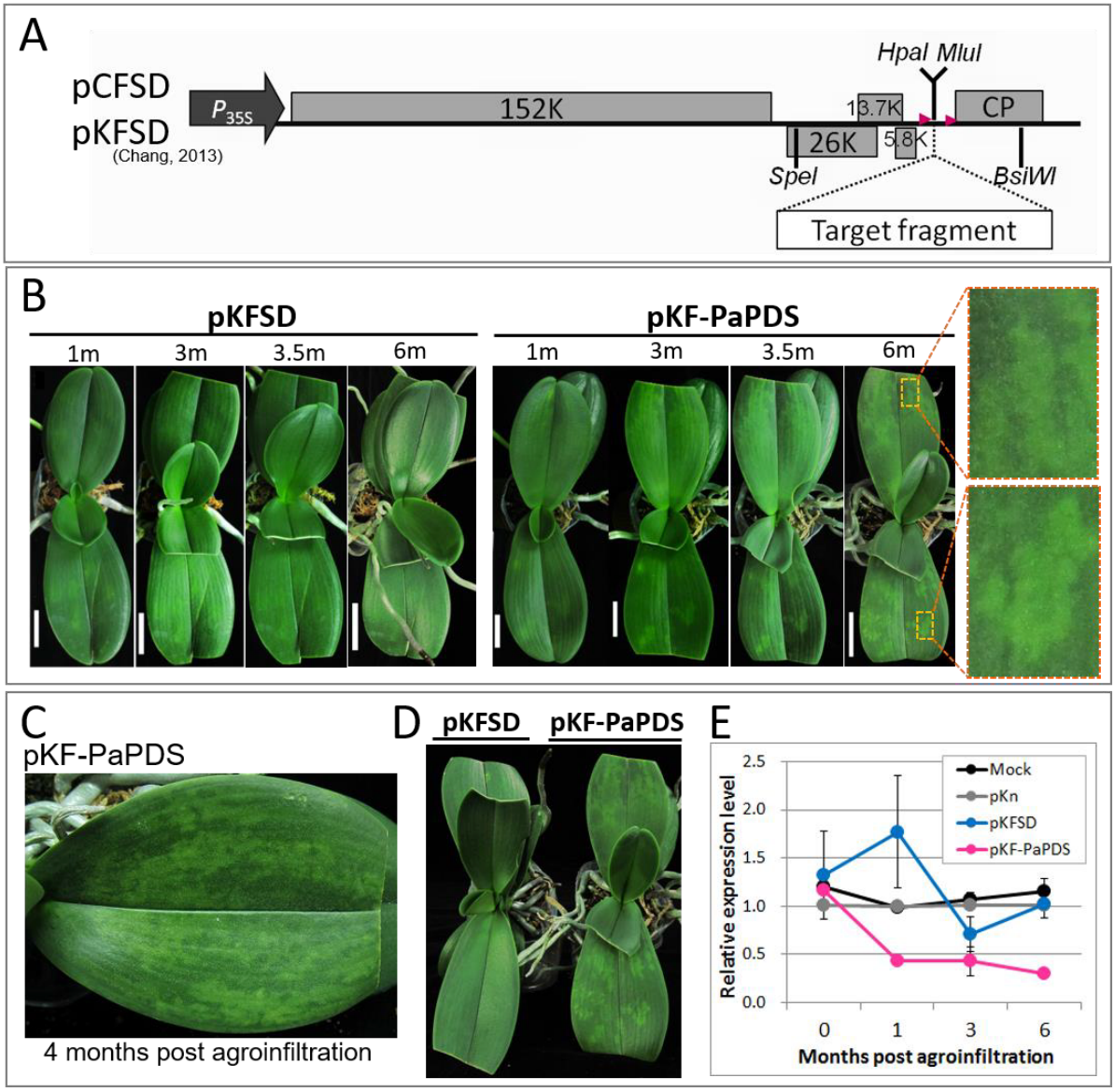


**Figure 40. Development of a *Foxtail mosaic virus* (FoMV)–based virus-induced gene silencing (VIGS) system for functional analysis in *Phalaenopsis*.**

(A) Schematic representation of the FoMV-based VIGS construct (Modified from Huang et al., 2017). An infectious FoMV genome is expressed under the control of the *Cauliflower mosaic virus* (CaMV) 35S promoter. The FoMV genomic structure and open reading frames (ORFs) are indicated. A fragment of the target gene is inserted upstream of the coat protein (CP) ORF via *Hpa*I and *Mlu*I restriction sites. Magenta arrowheads indicate the duplicated CP subgenomic promoter driving expression of the inserted fragment. pKFSD represents the binary vector adapted for Agrobacterium-mediated delivery.

(B) Generation of the pKF-PaPDS construct targeting *Phalaenopsis phytoene desaturase* (PaPDS) gene to evaluate VIGS efficiency. Silencing of PaPDS disrupts chlorophyll biosynthesis, resulting in visible leaf bleaching. Representative phenotypes of plants infiltrated with the empty vector (pKFSD) and the PDS-silencing construct (pKF-PaPDS) are shown from 1 to 6 months post agroinfiltration (mpa).

(C) Close-up view of the leaf-bleaching phenotype in a representative pKF-PaPDS-infiltrated plant.

(D) Side-by-side comparison of pKFSD and pKF-PaPDS-infiltrated plants at 6 mpa.

(E) RT-qPCR analysis of PaPDS transcript levels showing down-regulation beginning 1 month after pKF-PaPDS infiltration and persisting up to the end of monitoring period (6 mpa).

(2) Optimization of Protoplast Isolation from *P. amabilis* Leaves

Protoplasts systems offer an efficient platform for transient analysis of viral replication and host gene function. **While protocols for orchid protoplast isolation have been reported, most use petals or seedlings as starting materials** (Li et al., 2018; Lin et al., 2018; Machmudi et al., 2019; Ren et al., 2021). For our project, **I optimized a method using *P. amabilis* plantlets** at the same developmental stage used in virus inoculation assays.

I incubated approximately 2 g **3-month-old *P. amabilis* leaves** in 15 mL of enzyme solution (1% (w/v) cellulase, 0.2% (w/v) macerozyme in Mannitol-MES buffer). I vacuum-infiltrated the samples for 15 min and then incubated them in the dark for 5 h at room temperature. The digested suspension was filtered through Miracloth and centrifuged at 50xg for 7 min to pellet the protoplasts. I resuspended the pellet in 2 mL of MMC buffer (10 mM MES, 0.47 M mannitol, 10 mM $CaCl_2$, pH 5.8) and **layered 2 mL of 20% (w/v) sucrose beneath the suspension** using a glass dropper to create a cushion. After centrifugation at 50–100 × g for 5 min, I collected the intact protoplasts from the interphase and transferred them to 3 mL of MMC buffer. The cells were centrifuged again at 20 × g for 5 min and washed twice with 3 mL of W5 buffer (2 mM MES, 154 mM NaCl, 125 mM $CaCl_2$, 5 mM KCl, pH 5.7) under the same conditions. Finally, I resuspended the protoplast pellet in MaMg solution (4 mM MES, 0.4 M mannitol, 15 mM $MgCl_2$, pH 5.7) and measured the yield microscopically.

To optimize protoplast recovery, I **tested centrifugation forces between 50 and 120 × g during the sucrose cushion step**. *Phalaenopsis* leaves contain abundant needle-like oxalate crystals that can damage protoplasts if not effectively separated. The results showed that **centrifugation at 70–100 × g yielded the most intact protoplasts**, efficiently removing crystal contaminants without compromising yield and cell viability (Figure 41). The purified *Phalaenopsis* protoplasts obtained using this optimized protocol were successfully used for subsequent viral RNA transfection assays, providing an efficient single-cell system for studying virus replication.

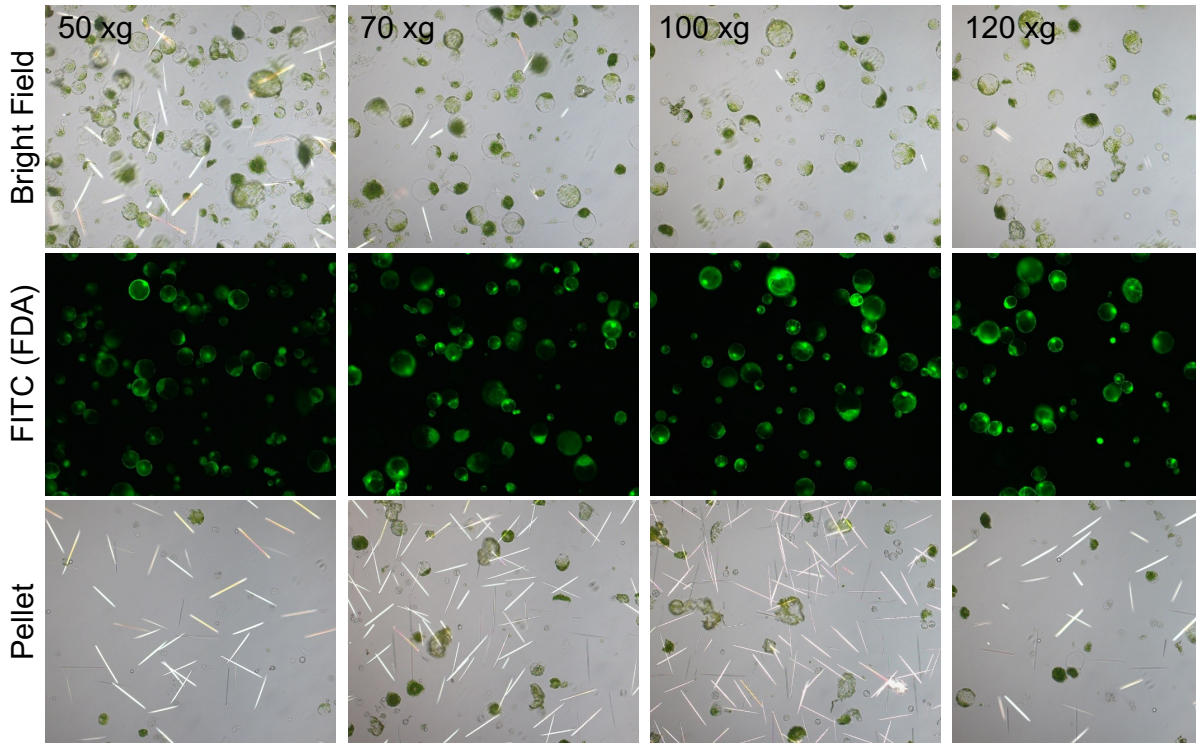


**Figure 41. Optimization of centrifugal force during the sucrose cushion step for *Phalaenopsis* leaf protoplasts isolation.** Protoplast suspensions were subjected to centrifugation at 50 x g, 70 x g, 100 x g, and 120 x g, respectively. **Top row**: Bright-field images showing the morphology and yield of purified protoplasts recovered from the interface. **Middle row**: Fluorescein diacetate (FDA) staining showing the viability of isolated protoplasts at each centrifugal force. **Bottom row**: Bright-field images of the debris pellets after sucrose cushion centrifugation, revealing abundant oxalic acid crystal needles. Increasing centrifugal force resulted in a higher proportion of protoplasts co-pelleting with debris at the bottom layer, indicating reduced recovery efficiency at higher speeds.

### 5.2.4 Engineering Dual Resistance to CymMV and ORSV

Towards our ultimate goal in developing virus-resistant orchids, I first established **a proof-of-concept system in *N. benthamiana* to generate plants with dual resistance to CymMV and ORSV** (Publication 3). Based on PDR strategy, I aim to use transgene-mediated RNA silencing to target viral CP genes. Two binary constructs were engineered: **pCam-COCP, carrying a fused CymMV–ORSV CP fragment** under the 35S promoter, and **pH7W-COCP, which contained the same fragment in sense and antisense orientation to form a hairpin dsRNA** (Figure 42). The hairpin structure was designed to enhance siRNA production and induce stronger antiviral silencing.

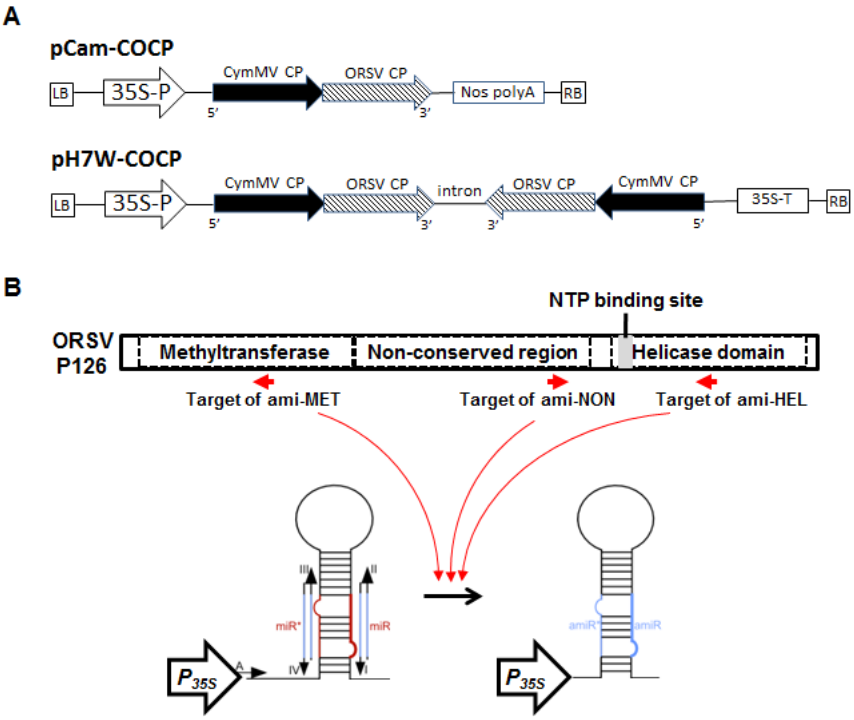


**Figure 42. Schematic design of transgene constructs for conferring resistance to *Cymbidium mosaic virus* (CymMV) and *Odontoglossum ringspot virus* (ORSV) in transgenic plants.** (A) Construction of plasmids containing viral genome fragments as RNA silencing targets. The coat protein (CP) open reading frames (ORFs) of CymMV and ORSV were fused to generate a chimeric fragment (COCP) and cloned under the control of the *Cauliflower mosaic virus* (CaMV) 35S promoter in the binary vectors pCambia (pCam-COCP) and pH7GWIWG2 (pH7W-COCP). (B) Target sites used for artificial microRNA (amiRNA) design are indicated by red arrows. Three amiRNAs were generated by PCR-mediated replacement of the endogenous hairpin region of *Nicotiana benthamiana* miR139a with each selected target sequence. [Adapted from Chen et al., 2019]

In cooperation with my colleague Ting-yu Chen, **transgenic *N. benthamiana* lines were produced via *Agrobacterium tumefaciens*-mediated leaf-disc transformation**, and homozygous T2 plants were selected for virus challenge assays. We then challenged the transformants by mechanical inoculation with CymMV and ORSV virions, and monitor viral accumulation and systemic movement by tissue blotting, ELISA, northern and western blot analyses, and grafting assays.

The **hairpin construct (pH7W-COCP) proved most effective, yielding several highly resistant lines that displayed complete resistance to both viruses**. These plants remained symptomless, with no detectable CymMV or ORSV coat proteins or genomic RNAs in systemic tissues. In protoplast assays, viral RNA accumulation was reduced by 60-90%, and grafting experiments confirmed that virus movement was effectively blocked in resistant scions. In contrast, plants transformed with the simple sense construct (pCam-COCP) showed variable or partial resistance, likely due to less efficient RNA silencing.

Together, these results demonstrate that hairpin-derived RNA interference provides robust and durable dual resistance against CymMV and ORSV in *N. benthamiana*. This approach establishes a validated and efficient model for developing transgene-based virus-resistant orchids, providing a practical framework for engineering *Phalaenopsis* and related ornamental species.

## 5.3 Summary and Future Perspectives

Working with **non-model species** such as orchids presents many challenges — from their long generation times and complex genomes to the limited availability of molecular and genomic tools (Dommes et al., 2019; Ruiz-Bedoya et al., 2023). When I began this project, genomic resources for *Phalaenopsis* were only just being established, and very few experimental systems existed for functional studies. Within this context, my goal was to **build a foundation for understanding viral resistance and synergism in orchids, while developing the molecular tools** necessary to make such studies possible.

Through a combination of infection assays, small RNA and transcriptome profiling, and functional analyses, I characterized the interplay between CymMV and ORSV and revealed **how viral suppressors contribute to viral synergism**. In parallel, I established essential tools for orchid molecular research — including a FoMV-based VIGS system, a refined protoplast isolation protocol, and a transgene-based strategy that achieved robust dual resistance against CymMV and ORSV. Together with my collaborators, we also **(i)** generated **infectious clones for both viruses**, providing a versatile inoculum for infection assays under controlled conditions, **(ii)** tested transient gene expression via **Agrobacterium-mediated infiltration in *Phalaenopsis* leaves**, and **(iii)** developed two **bioinformatic pipelines: microRPM, for identification of mature miRNA sequences** (Tseng et al., 2018), and **sRIS, for inferring the regulatory networks of plant and viral sRNAs** (Tseng et al., 2020) using only small RNA sequencing data. These developments not only enabled the mechanistic discoveries described in this chapter but also provided a foundation for future functional genomics in orchids.

With the rapid advancement of sequencing technologies, gene annotation, and transformation systems, the approaches I developed can now be further refined and extended across species. Likewise, the spatially coarse definition of "infected" versus "neighbouring" tissues in my studies could now be revisited using single-cell or spatial transcriptomics, allowing finer resolution of immune responses (Nobori, 2025; Ko and Brandizzi, 2025). **Looking ahead, integrating these molecular platforms with AI-assisted gene prediction, high-throughput screening, and precision genome editing will transform orchids into a tractable model for plant-virus research**. The tools and insights developed here thus mark not an end, but a beginning — a framework for bridging fundamental discovery with applied resistance engineering in ornamental and other non-model plants.

# References


1. Abramson J, J Adler, J Dunger, R Evans, T Green, A Pritzel, O Ronneberger, L Willmore, AJ Ballard, J Bambrick et al. (2024) Accurate structure prediction of biomolecular interactions with AlphaFold 3. Nature 630: 493–500.
2. Adachi H, M Contreras, A Harant, CH Wu, L Derevnina, T Sakai, C Duggan, E Moratto, TO Bozkurt, A Maqbool, et al. (2019) An N-terminal motif in NLR immune receptors is functionally conserved across distantly related plant species. eLife 8: e49956.
3. Adachi H, T Sakai, J Kourelis, H Pai, JL Gonzalez Hernandez, Y Utsumi, M Seki, A Maqbool, and S Kamoun. (2023) Jurassic NLR: Conserved and dynamic evolutionary features of the atypically ancient immune receptor ZAR1. Plant Cell 35: 3662-3685.
4. Ahn HK, X Lin, AC Olave-Achury, L Derevnina, MP Contreras, J Kourelis, CH Wu, S Kamoun, and JDG Jones. (2023) Effector-dependent activation and oligomerization of plant NRC class helper NLRs by sensor NLR immune receptors Rpi-amr3 and Rpi-amr1. EMBO J. 42: e111484.
5. Ahn HKA and JDG Jones. (2023) Blue native-PAGE of protein complexes in plant cells V.1. Protocols.io. dx.doi.org/10.17504/protocols.io.3byl4jyd8lo5/v1
6. Ajjikuttira P. and SM Wong. (2009) Molecular biology of two orchid infecting viruses: *Cymbidium mosaic potexvirus* and *Odontoglossum ringspot tobamovirus*. p.251-277. In: T. Kull, J. Arditti and S.M. Wong (eds.). Orchid biology: Reviews and perspectives, X. Springer, Netherlands.
7. Ajjikuttira P., CS Loh, and SM Wong. (2005) Reciprocal function of movement proteins and complementation of long distance movement of *Cymbidium mosaic virus* RNA by *Odontoglossum ringspot virus* coat protein. J. Gen. Virol. 86: 1543-1553.
8. Alazem M and NS Lin. (2017) Antiviral roles of abscisic acid in plants. Front. Plant Sci. 8: 1760.
9. Alazem M, J Bwalya, H Pai, J Yu, HC Chu, T Burch-Smith, and KH Kim. (2023) Viral synergism suppresses *R* gene-mediated resistance by impairing downstream defense mechanisms in soybean. Plant Physiol. 192: 3088-3105.
10. Andolfo G, A Di Donato, P Chiaiese, A De Natale, A Pollio, JD Jones, L Frusciante, and MR Ercolano. (2019) Alien domains shaped the modular structure of plant NLR proteins. Genome Biol. Evol. 11: 3466-3477.
11. Arnold SA, SA Müller, C Schmidli, A Syntychaki, L Rima, M Chami, H Stahlberg, KN Goldie, and T Braun. (2018) Miniaturizing EM sample preparation: Opportunities, challenges, and "visual proteomics". Proteomics. 18: e1700176.
12. Atabekova AK, AD Solovieva, DA Chergintsev, AG Solovyev, and SY Morozov. (2023) Role of plant virus movement proteins in suppression of host RNAi defense. Int. J. Mol. Sci. 24: 9049.
13. Atkinson MM, JS Huang , and JA Knopp. (1985) The hypersensitive reaction of tobacco to *Pseudomonas syringae* pv. pisi. Plant Physiol. 79: 843-847.
14. Baggs E, G Dagdas, and KV Krasileva. (2017) NLR diversity, helpers and integrated domains: making sense of the NLR identity. Curr. Opi. Plant Biol. 38: 59-67.
15. Ball CH and PL Roulhac. (2010) Multidimensional techniques in protein separations for neuroproteomics. In: Alzate O, editor. Neuroproteomics. Boca Raton (FL): CRC Press/Taylor & Francis. Chapter 3.

16. Barragan AC and D Weigel. (2021) Plant NLR diversity: the known unknowns of pan-NLRomes Plant Cell 33:814-831.

17. Baulcombe DC. (2022) The role of viruses in identifying and analyzing RNA silencing. Annu. Rev. Virol. 9: 353-373.

18. Bax A and GM Clore. (2019) Protein NMR: Boundless opportunities. J. Magn. Reson. 306: 187-191.

19. Bayguinov PO, MR Fisher, and JAJ Fitzpatrick. (2020) Assaying three-dimensional cellular architecture using X-ray tomographic and correlated imaging approaches. J. Biol. Chem. 295: 15782-15793.

20. Beachy RN. (1997) Mechanisms and applications of pathogen-derived resistance in transgenic plants. Curr. Opin. Biotechnol. 8: 215-220.

21. Bendahmane A, G Farnham, P Moffett, and DC Baulcombe. (2002) Constitutive gain-of-function mutants in a nucleotide binding site–leucine rich repeat protein encoded at the Rx locus of potato. Plant J. 32: 195-204.

22. Benjin X and L Ling. (2020) Developments, applications, and prospects of cryo-electron microscopy. Protein Sci. 29: 872-882.

23. Bi G, M Su, N Li, Y Liang, S Dang, J Xu, M Hu, J Wang, M Zou, Y Deng, et al. (2021) The ZAR1 resistosome is a calcium-permeable channel triggering plant immune signaling. Cell 184: 3528-3541.

24. Bonas U. (1998) 5.4 Avirulence Genes. Method Microbiol. 27: 149-155.

25. Budzyńska D, MP Zwart, and B Hasiów-Jaroszewska. (2022) Defective RNA particles of plant viruses: Origin, structure and role in pathogenesis. Viruses 14: 2814.

26. Burgyán J and Z Havelda. (2011) Viral suppressors of RNA silencing. Trend. Plant Sci. 16: 265-272.

27. Burton-Smith RN and K Murata. (2023) Cryo-electron microscopy of protein cages. Methods Mol. Biol. 2671: 173-210.

28. Calil IP and EPB Fontes. (2016) Plant immunity against viruses: Antiviral immune receptors in focus. Ann. Bot. 119: 711-723.

29. Callway E. (2015) The revolution will not be crystallized: A new method sweeps through structural biology. Nature 525: 172-174.

30. Cao P, Z Sun, S Wang, Q Zhang, Y An, and M Zhang. (2025) The new era of bioengineered plant NLR receptors. Plant Commun. 17: 101567.

31. Carroni M and HR Saibil. (2015) Cryo electron microscopy to determine the structure of macromolecular complexes. Methods 95: 78-85.

32. Castel B, P Ngou, V Cevik, A Redkar, D Kim, Y Yang, P Ding, and JDG Jones. (2019) Diverse NLR immune receptors activate defence via the RPW8-NLR NRG1. New Phytol. 222: 966–980.

33. Castón JR and D Luque. (2024) Conventional electron microscopy, cryogenic electron microscopy, and cryogenic electron tomography of viruses. Subcell. Biochem. 105: 81-134.

34. Cesari S, M Bernoux, P Moncuquet, T Kroj, and P Dodds. (2014) A novel conserved mechanism for plant NLR protein pairs: The 'integrated decoy' hypothesis. Front. Plant Sci. 5: 606.

35. Chen CC, YK Chen YK, WH Ko, and ST Yeh. (2006) Symptomatology and cytopathological studies of *Phalaenopsis* infected with *Odontoglossum ringspot virus* and *Cymbidium mosaic virus*. Research Bulletin of Taichung District Agricultural Improvement Station 93: 15-27. [In Chinese]

36. Chen R, K Gajendiran, and BBH Wulff. (2024) *R* we there yet? Advances in cloning resistance genes for engineering immunity in crop plants. Curr. Opin. Plant Biol. 77: 102489.

37. Chen TY, H Pai, LY Hou, SC Lee, TT Lin, CH Chang, FC Hsu, YH Hsu and NS Lin. (2019) Dual resistance of transgenic plants against *Cymbidium mosaic virus* and *Odontoglossum ringspot virus*. Sci. Rep. 9: 10230.

38. Cheng, YH., CC Chen, and FJ Chan. (2008) Emerging viral diseases of *Phalaenopsis* orchids in Taiwan. pp. 67–82. In Proceedings of the Workshop on Diagnostic and Identification Techniques for Important Plant Quarantine and Protection Diseases (VII). Bureau of Animal and Plant Health Inspection and Quarantine, Council of Agriculture, Executive Yuan, Taiwan; and Department of Plant Pathology, National Chung Hsing University. [In Chinese]

39. Chepsergon J, TE Motaung, D Bellieny-Rabelo, and LN Moleleki. (2020) Organize, don't agonize: Strategic success of phytophthora species. Microorganisms 8: 917.

40. Chia K-S, J Kourelis, M Vickers, T Sakai, S Kamoun, and P Carella. (2024) The N-terminal executioner domains of NLR immune receptors are functionally conserved across major plant lineages. Plant Cell 36: 2491–2511.

41. Chinchilla D, Z Bauer, M Regenass, T Boller, and G Felix. (2006) The *Arabidopsis* receptor kinase FLS2 binds flg22 and determines the specificity of flagellin perception. Plant Cell 18: 465-76.

42. Chng CG, SM Wong, PH Mahtani, CS Loh, CJ Goh, MCC Kao, MCM Chung, and Y Watanabe. (1996) The complete sequence of a Singapore isolate of *Odontoglossum ringspot virus* and comparison with other tobamoviruses. Gene 171: 155–161.

43. Clark RM, G Schweikert, C Toomajian, S Ossowski, G Zeller, P Shinn, N Warthmann, TT Hu, G Fu, and DA Hinds. (2007) Common sequence polymorphisms shaping genetic diversity in *Arabidopsis thaliana*. Science 317: 338-342.

44. Contreras MP, D Lüdke, H Pai, A Toghani, and S Kamoun. (2023a) NLR receptors in plant immunity: making sense of the alphabet soup. EMBO Rep. 24: e57495.

45. Contreras MP, H Pai, C Marchal, R Thompson, J Claeys; H Adachi, and S Kamoun. (2024) The nucleotide binding domain of NRC-dependent disease resistance proteins is sufficient to activate downstream helper NLR oligomerization and immune signaling. New Phytol. 243: 345-361.

46. Contreras MP, H Pai, M Selvaraj, A Toghani, DM Lawson, Y Tumtas, C Duggan, ELH Yuen, CEM Stevenson, A Harant, CH Wu, TO Bozkurt, S Kamoun, and L Derevnina. (2023b) Resurrection of plant disease resistance proteins via helper NLR bioengineering. Sci. Adv. 9: 3861.

47. Contreras MP, H Pai, Y Tumtas, C Duggan, ELH Yuen, A Vergara Cruces, J Kourelis, HK Ahn, KT Lee, CH Wu, TO Bozkurt, L Derevnina , and S Kamoun. (2023c) Sensor NLR immune proteins activate oligomerization of their NRC helpers in response to plant pathogens. EMBO J. 42: e111519.

48. Cooper B, I Schmitz, ALN Rao, RN Beachy, and AJ Dodds. (1996) Cell-to-cell transport of movement-defective cucumber mosaic and tobacco mosaic viruses in transgenic plants expressing heterologous movement protein genes. Virology 216: 208-213.

49. Couto D and C Zipfel. (2016) Regulation of pattern recognition receptor signalling in plants. Nat. Rev. Immunol. 16: 537-552.

50. Cui H, K Tsuda, and JE Parker. (2015) Effector-triggered immunity: from pathogen perception to robust defense. Ann. Rev. Plant Biol. 66: 487-511.

51. Czarnocki-Cieciura M and M Nowotny. (2016) Introduction to high-resolution cryo-electron microscopy. Postepy Biochem. 62: 383-394.

52. Danon A. (2014) Protoplast preparation and determination of cell death. Bio-protocol 4: e1149.

53. Daròs JA. (2017) Viral suppressors: Combatting RNA silencing. Nat. Plants 3: 17098.

54. De Lorenzo G and F Cervone. (2022) Plant immunity by damage-associated molecular patterns (DAMPs). Essays Biochem. 66: 459-469.

55. De Wit PJ, R Mehrabi, HA Van den Burg, and I Stergiopoulos. (2009) Fungal effector proteins: past, present and future. Mol. Plant Pathol. 10: 735-747.

56. DeFalco TA and C Zipfel. (2021) Molecular mechanisms of early plant pattern-triggered immune signaling. Mol. Cell 81: 3449-3467.

57. Deng Z, L Ma, P Zhang, and H Zhu. (2022) Small RNAs participate in plant-virus interaction and their application in plant viral defense. Int. J. Mol. Sci. 23: 696.

58. Derevnina L, MP Contreras, H Adachi, J Upson, A Vergara Cruces, R Xie, J Skłenar, FLH Menke, ST Mugford, D MacLean, W Ma, SA Hogenhout, A Goverse, A Maqbool, CH Wu, and S Kamoun. (2021) Plant pathogens convergently evolved to counteract redundant nodes of an NLR immune receptor network. PLoS Biol. 9: e3001136.

59. Dobson CM. (2019) Biophysical techniques in structural biology. Annu. Rev. Biochem. 88: 25-33.

60. Dodds PN, J Chen, and MA Outram. (2024) Pathogen perception and signaling in plant immunity. Plant Cell 36: 1465–1481.

61. Dodds PN. (2023) From gene-for-gene to resistosomes: Flor's enduring legacy. Mol. Plant Microbe Interact. 36: 461-467.

62. Dommes AB, T Gross, DB Herbert, KI Kivivirta, and A Becker. (2019) Virus-induced gene silencing: Empowering genetics in non-model organisms. J. Exp. Bot. 70: 757-770.

63. Donaire L and MA Aranda. (2024) Computational pipeline for the detection of plant RNA viruses using high-throughput sequencing. Methods Mol. Biol. 2724: 1-20.

64. Donaire L, Y Wang, D Gonzalez-Ibeas, KF Mayer, MA Aranda, and C Llave. (2009) Deep-sequencing of plant viral small RNAs reveals effective and widespread targeting of viral genomes. Virology 392: 203-214.

65. Dudkina NV, R Kouril, JB Bultema, and EJ Boekema. (2010) Imaging of organelles by electron microscopy reveals protein-protein interactions in mitochondria and chloroplasts. FEBS Lett. 584: 2510-2515.

66. Duxbury Z, C Wu, and P Ding. (2021) A comparative overview of the intracellular guardians of plants and animals: NLRs in innate immunity and beyond. Ann. Rev. Plant Biol. 72: 155-184.

67. Edwardson JR and FW Zettler. (1988) *Odontoglossum ringspot virus*. In: The plant viruses. Vol. 2. van Regenmortel, M.H.V. and Fraenkel-Conrat, H. (eds.). Plenum Publishing Corperation, New York, USA. p.233-247.

68. Elvira-Gonzalez L, T Blevins, and M Heinlein. (2025) Small RNA mobility and plant virus diseases. J. Exp. Bot. 21: eraf226.

69. Engler C, M Youles, R Gruetzner, TM Ehnert , S Werner, JD Jones, NJ Patron, and S Marillonnet. (2014) A golden gate modular cloning toolbox for plants. ACS Syn. Biol. 3: 839-843.

70. Eubel H, HP Braun, and AH Millar. (2005) Blue-native PAGE in plants: A tool in analysis of protein-protein interactions. Plant Method. 1: 11.

71. Feehan JM, B Castel, AR Bentham, JD Jones. (2020) Plant NLRs get by with a little help from their friends. Curr. Opi. Plant Biol. 56: 99-108.

72. Fiala GJ, WW Schamel, and B Blumenthal. (2011) Blue native polyacrylamide gel electrophoresis (BN-PAGE) for analysis of multiprotein complexes from cellular lysates. J. Vis. Exp. 48: 2164.

73. Fick A, V Swart, and N van den Berg. (2022) The ups and downs of plant NLR expression during pathogen infection. Front. Plant Sci. 13: 921148.

74. Flor HH (1971) Current status of the gene-for-gene concept. Ann. Rev. Phytopathol. 9: 275-296.

75. Fontes EPB, RM Teixeira, and R Lozano-Durán. (2021) Plant virus-interactions: unraveling novel defense mechanisms under immune-suppressing pressure. Curr. Opi. Plant Biotechnol. 70: 108-114.

76. Förderer A, E Li, AW Lawson, Y Deng, Y Sun, E Logemann, X Zhang, J Wen, Z Han, J Chang, et al. (2022) A wheat resistosome defines common principles of immune receptor channels. Nature 610: 532–539.

77. Fowke LC. (1995) Transmission and scanning electron microscopy for plant protoplasts, cultured cells and tissues. In: Gamborg, O.L., Phillips, G.C. (eds) Plant Cell, Tissue and Organ Culture.

78. Gago-Zachert S, J Schuck, C Weinholdt, M Knoblich, V Pantaleo, I Grosse, T Gursinsky, and SE Behrens. (2019) Highly efficacious antiviral protection of plants by small interfering RNAs identified in vitro. Nucleic Acids Res. 47: 9343-9357.

79. Gao LA, ME Wilkinson, J Strecker, KS Makarova, RK Macrae, EV Koonin, and F Zhang. (2022) Prokaryotic innate immunity through pattern recognition of conserved viral proteins. Science 377: eabm4096.

80. Geraets JA, KR Pothula, and GF Schröder. (2020) Integrating cryo-EM and NMR data. Curr. Opin. Struct. Biol. 61: 173-181.

81. Ghosh D, M Malavika, and S Chakraborty. (2021) Impact of viral silencing suppressors on plant viral synergism: A global agro-economic concern. Appl. Microbiol. Biotechnol. 105: 6301-6313.

82. Goh FJ, CY Huang, L Derevnina, and CH Wu. (2024) NRC Immune receptor networks show diversified hierarchical genetic architecture across plant lineages. Plant Cell 36: 3399-3418.

83. Goldsmith CS and SE Miller. (2009) Modern uses of electron microscopy for detection of viruses. Clin. Microbiol. Rev. 22: 552-63.

84. Gómez-Gómez L and T Boller. (2000) FLS2: An LRR receptor-like kinase involved in the perception of the bacterial elicitor flagellin in *Arabidopsis*. Mol. Cell 5: 1003-1011.

85. Gong J, H Zhang, Y Zeng, Y Cheng, X Sun, and P Wang. (2022) Combining BN-PAGE and microscopy techniques to investigate pigment-protein complexes and plastid transitions in citrus fruit. Plant Methods 18: 124.

86. Gottula J, and M Fuchs. (2009) Toward a quarter century of pathogen-derived resistance and practical approaches to plant virus disease control. Adv. Virus Res. 75: 161-183.

87. Grund E, D Tremousaygue, and L Deslandes. (2019) Plant NLRs with integrated domains: Unity makes strength. Plant Physiol. 179: 1227–1235.

88. Guerreiro MA and Stukenbrock EH. (2025) Fungal plant pathogens. Curr. Biol. 35: R480-R484.

89. Habgood RM. (1970) Designation of physiological races of plant pathogens. Nature 227: 1268-1269.

90. Harant A, H Pai, T Sakai, S Kamoun, and H Adachi. (2022) A vector system for fast-forward studies of the *HOPZ-ACTIVATED RESISTANCE1* (ZAR1) resistosome in the model plant *Nicotiana benthamiana*. Plant Physio. 188: 70-80.

91. Hitchborn JH and GJ Hills. (1965) The use of negative staining in the electron microscopic examination of plant viruses in crude extracts. Virology 27: 528-40.

92. Hoefnagel MHN, OK Atkin, and JT Wiskich. (1998) Interdependence between chloroplasts and mitochondria in the light and the dark. Biochim. Biophys. Acta. 1366: 235-255.

93. Hu JS, S Ferreira, MQ Xu, M Lu, M Iha, E Phlum, and M Wang. (1994) Transmission, movement, and inactivation of *Cymbidium mosaic* and *Odontoglossum ringspot viruses*. Plant Dis. 78: 633-636.

94. Huang IH. (2017) Development of *Foxtail mosaic virus* as a VIGS vector. (Master's thesis, National Chung Hsing University, Taiwan). National Digital Library of Theses and Dissertations, 105NCHU5111019. [In Chinese]

95. Huang M, Z Wu, J Li , Y Ding, S Chen, and X Li. (2023) Plant protection against viruses: An integrated review of plant immunity agents. Int. J. Mol. Sci. 24: 4453.

96. Huang S, J Wang, R Song, A Jia, Y Xiao, Y Sun, L Wang, D Mahr, Z Wu, Z Han, X Li, JE Parker, and J Chai. (2025) Balanced plant helper NLR activation by a modified host protein complex. Nature 639: 447-455.

97. Hýsková V, K Bělonožníková, J Chmelík, H Hoffmeisterová, N Čeřovská, T Moravec, and H Ryšlavá. (2024) Potyviral helper-component protease: Multifaced functions and interactions with host proteins. Plants (Basel). 13: 1236.

98. Ibrahim T, ELH Yuen, HY Wang, FJ King, A Toghani, J Kourelis, C Vuolo, V Adamkova, B Castel, JD Jones. (2024) A helper NLR targets organellar membranes to trigger immunity. bioRxiv. doi: 10.1101/2024.09.19.613839.

99. Ignatiou A, K Macé, A Redzej, TRD Costa, G Waksman, and EV Orlova. (2024) Structural analysis of protein complexes by cryo-electron microscopy. Methods Mol. Biol. 2715: 431-470.

100. Ikram AU, Y Jing, H Chen, and J Chen. (2024) Bacteria deploy water channels to aid infection in plants. Trends Plant Sci. 29: 620-622.

101. Jacob P, NH Kim, F Wu, F El-Kasmi, Y Chi, WG Walton, OJ Furzer, AD Lietzan, S Sunil, K Kempthorn, et al. (2021) Plant "helper" immune receptors are $Ca^{2+}$-permeable nonselective cation channels. Science 373: 420-425.

102. Jahromi MG, H Rahnama, A Mousavi, and MR Safarnejad. (2022) Comparative evaluation of resistance to *Potato virus Y* (PVY) in three different RNAi-based transgenic potato plants. Transgenic Res. 31: 313-323.

103. Järvi S, M Suorsa, V Paakkarinen, and EM Aro. (2011) Optimized native gel systems for separation of thylakoid protein complexes: Novel super- and mega-complexes. Biochem. J. 439: 207–214.

104. Jian Y, D Gong, Z Wang, L Liu, J He, X Han, and K Tsuda. (2024) How plants manage pathogen infection. EMBO Rep. 25: 31-44.

105. Jin Y, JH Zhao, and HS Guo. (2020) Recent advances in understanding plant antiviral RNAi and viral suppressors of RNAi. Curr. Opi. Virol. 46: 65-72.

106. Johal GS and SP Briggs. (1992) Reductase activity encoded by the *HM1* disease resistance gene in maize. Science 258: 985-987.

107. Jones DA, CM Thomas, KE Hammond-Kosack, PJ Balint-Kurti, and JD Jones. (1994) Isolation of the tomato *Cf-9* gene for resistance to *Cladosporium fulvum* by transposon tagging. Science 266: 789-793.

108. Jones JD, RE Vance, and JL Dangl. (2016) Intracellular innate immune surveillance devices in plants and animals. Science 354: aaf6395.

109. Jones JDG and JL Dangl. (2006) The plant immune system. Nature 444: 323–329.

110. Jones JDG, BJ Staskawicz, and JL Dangl. (2024) The plant immune system: From discovery to deployment. Cell 187:2095-2116.

111. Kadota Y, J Sklenar, P Derbyshire, L Stransfeld, S Asai, V Ntoukakis, JD Jones, K Shirasu, F Menke, A Jones, and C Zipfel. (2014) Direct regulation of the NADPH oxidase RBOHD by the PRR-associated kinase BIK1 during plant immunity. Mol. Cell 54: 43-55.

112. Kalyaanamoorthy S, BQ Minh, TKF Wong, A von Haeseler, and LS Jermiin. (2017) ModelFinder: Fast model selection for accurate phylogenetic estimates. Nat. Methods. 14: 587–589.

113. Kaur B, D Bhatia, and GS Mavi. (2021) Eighty years of gene-for-gene relationship and its applications in identification and utilization of R genes. J. Genet. 100: 50.

114. Kibby EM, AN Conte, AM Burroughs, TA Nagy, JA Vargas, LA Whalen, L Aravind, AT Whiteley. (2023) Bacterial NLR-related proteins protect against phage. Cell 186: 2410-2424.

115. Klebl DP, L Aspinall, and SP Muench. (2023) Time resolved applications for Cryo-EM: Approaches, challenges and future directions. Curr. Opin. Struct. Biol. 83: 102696.

116. Klement Z. (1982) Hypersensitivity. n: Mount, M.S. and Lacy, G.H., Eds., Phytopathogenic Prokaryotes, Academic Press, New York. 2: 149-177.

117. Klepsch M, S Schlegel, D Wickström, G Friso, KJ van Wijk, JO Persson, JW de Gier, and S Wagner. (2008) Immobilization of the first dimension in 2D blue native/SDS-PAGE allows the relative quantification of membrane proteomes. Methods 46: 48-53.

118. Knapp E and DJ Lewandowski. (2001) *Tobacco mosaic virus*, not just a single component virus anymore. Mol. Plant Pathol. 2: 117-23.

119. Ko DK and F Brandizzi. (2025) A network-enabled pipeline for gene discovery and validation in non-model plant species. Cell Rep. Methods. 5: 100963.

120. Koh KW, HC Lu, and MT Chan. (2014) Virus resistance in orchids. Plant Sci. 228: 26-38.

121. Kourelis J and H Adachi. (2022) Activation and regulation of NLR immune receptor networks. Plant Cell Physiol. 63: 1366-1377.

122. Kourelis J and RAL van der Hoorn. (2018) Defended to the nines: 25 years of resistance gene cloning identifies nine mechanisms for R protein function. Plant Cell 30: 285–299.

123. Kourelis J, MP Contreras, A Harant, H Pai, D Lüdke, H Adachi, L Derevnina, CH Wu, and S Kamoun. (2022) The helper NLR immune protein NRC3 mediates the hypersensitive cell death caused by the cell-surface receptor Cf-4. PLoS Genet. 18: e1010414.

124. Kourelis J, T Sakai, H Adachi, S Kamoun. (2021) RefPlantNLR is a comprehensive collection of experimentally validated plant disease resistance proteins from the NLR family PLoS Biol. 19: e3001124.

125. Kozomara A and S Griffiths-Jones. (2011) MiRBase: Integrating microRNA annotation and deep-sequencing data. Nucl. Acid. Res. 39: D152-7.

126. Kumar R, and I Dasgupta. (2024) Abscisic acid: An emerging player in plant-virus interactions. Plant Physiol. Biochem. 215: 109046.

127. Lan HH, CM Wang, SS Chen, and JY Zheng. (2019) SiRNAs derived from *Cymbidium mosaic virus* and *Odontoglossum ringspot virus* down-modulated the expression levels of endogenous genes in *Phalaenopsis equestris*. Plant Pathol. J. 35: 508-520.

128. Lapin D, V Kovacova, X Sun, JA Dongus, D Bhandari, P von Born, J Bautor, N Guarneri, J Rzemieniewski, J Stuttmann, et al. (2019) A coevolved EDS1-SAG101-NRG1 module mediates cell death signaling by TIR-domain immune receptors. Plant Cell 31: 2430–2455.

129. Le Roux C, G Huet, A Jauneau, L Camborde, D Trémousaygue, A Kraut, B Zhou, M Levaillant, H Adachi, H Yoshioka, et al. (2015) A receptor pair with an integrated decoy converts pathogen disabling of transcription factors to immunity. Cell 161: 1074–1088.

130. Lee HY, H Mang, E Choi, YE Seo, MS Kim, S Oh, SB Kim, and D Choi. (2021) Genome-wide functional analysis of hot pepper immune receptors reveals an autonomous NLR clade in seed plants. New Phytol. 229: 532–547.

131. Lee RRQ and E Chae. (2020) Variation patterns of NLR clusters in *Arabidopsis thaliana* genomes. Plant Comms. 1: 100089.

132. Lee SC, H Pai, YW Huang, MH He, YL Song, SY Kuo, WC Chang, YH Hsu, and NS Lin. (2021) Exploring the multifunctional roles of *Odontoglossum ringspot virus* P126 infacilitating *Cymbidium mosaic virus* cell-to-cell movement during mixed Infection. Viruses 13: 1552.

133. Lefeuvre P, DP Martin, SF Elena, DN Shepherd, P Roumagnac, and A Varsani. (2019) Evolution and ecology of plant viruses. Nat. Rev. Microbiol. 17: 632–644.

134. Leonetti P, J Stuttmann, and V Pantaleo. (2021) Regulation of plant antiviral defense genes via host RNA-silencing mechanisms. Virol. J. 18: 194.

135. Li J, X Laio, S Zhou, S Liu, L Jiang, and G Wang. (2018) Efficient protoplast isolation and transient gene expression system for *Phalaenopsis* hybrid cultivar 'Ruili Beauty'. In Vitro Cell. Dev. Biol. - Plant 54: 87-93.

136. Li X, L Ma, Y Wang, C Ye, C Guo, Y Li, X Mei, F Du, and H Huang. (2023) PlantNLRatlas: A comprehensive dataset of full- and partial-length NLR resistance genes across 100 chromosome-level plant genomes. Front Plant Sci. 14: 1178069.

137. Lin HY, JC Chen, and SC Fang. (2018) A protoplast transient expression system to enable molecular, cellular, and functional studies in *Phalaenopsis* orchids. Front. Plant Sci. 9: 843.

138. Lin KY, CP Cheng, BCH Chang, WC Wang, YW Huang, YS Lee, HD Huang, YH Hsu, and NS Lin. (2010) Global analyses of small interfering RNAs derived from *Bamboo mosaic virus* and its associated satellite RNAs in different plants. PLoS One 5: e11928.

139. Liu F, Z Yang, C Wang, Z You, R Martin, W Qiao, J Huang, P Jacob, JL Dangl, JE Carette, S Luan, E Nogales, and BJ Staskawicz. (2024) Activation of the helper NRC4 immune receptor forms a hexameric resistosome. Cell 187: 4877-4889.

140. Locci F and JE Parker. (2024) Plant NLR immunity activation and execution: A biochemical perspective. Open Biol. 14: 230387.

141. Lozano-Durán R. (2024) Viral recognition and evasion in plants. Annu. Rev. Plant Biol. 75: 655-677.

142. Lu HC, CE Chen, MH Tsai, HI Wang, HJ Su, and HH Yeh. (2009) *Cymbidium mosaic potexvirus* isolate-dependent host movement systems reveal two movement control determinants and the coat protein is the dominant. Virology 388: 147-159.

143. Lu HC, HH Chen, WC Tsai, WH Chen, HJ Su, DCN Chang, and HH Yeh. (2007) Strategies for functional validation of genes involved in reproductive stages of orchids. Plant Physiol. 143: 558-569.

144. Lu YD, QH Gan, XY Chi, and S Qin. (2008) Roles of microRNA in plant defense and virus offense interaction. Plant Cell Rep. 27: 1571-1579.

145. Lundquist PK, O Mantegazza, A Stefanski, K Stühler, and APM Weber. (2017) Surveying the oligomeric state of *Arabidopsis thaliana* chloroplasts. Mol. Plant. 10: 197-211.

146. Lv M, Y Dai, L Xie, J Guo, Z Liao, W Shang, X Zhao, J Hong, and HM Zhang. (2024) Volume electron microscopy reconstruction uncovers a physical barrier that limits virus to phloem. New Phytol. 241: 343-362.

147. Ma J and D Xia. (2008) The use of blue native PAGE in the evaluation of membrane protein aggregation states for crystallization. J. Appl. Crystallogr. 41(Pt 6): 1150-1160.

148. Machmudi M, H Purnobasuki, and ESW Utami. (2019) The optimization mesophyll protoplast isolation for *Phalaenopsis amboinensis*. Bulgarian J. Agri. Sci. 25: 737-743.

149. Macho AP and C Zipfel. (2014) Plant PRRs and the activation of innate immune signaling. Mol. Cell 54: 263-272.

150. Madhuprakash, J, A Toghani, MP Contreras, A Posbeyikian, J Richardson, J Kourelis, TO Bozkurt, M Webster, and S Kamoun. (2024) A disease resistance protein triggers oligomerization of its NLR helper into a hexameric resistosome to mediate innate immunity. Sci. Adv. 10: eadr2594.

151. Majumdar A, A Sharma A, and R Belludi. (2023) Natural and engineered resistance mechanisms in plants against phytoviruses. Pathogens. 12: 619.

152. Mannaa M and YS Seo. (2021) Plants under the attack of allies: Moving towards the plant pathobiome paradigm. Plants (Basel) 10: 125.

153. Mansfield JW. (2009) From bacterial avirulence genes to effector functions via the *hrp* delivery system: An overview of 25 years of progress in our understanding of plant innate immunity. Mol. Plant Pathol. 10: 721-34.

154. Maqbool A, H Saitoh, M Franceschetti, C Stevenson, A Uemura, H Kanzaki, S Kamoun, R Terauchi, and M Banfield. (2015) Structural basis of pathogen recognition by an integrated HMA domain in a plant NLR immune receptor. eLife 4: e08709

155. Martin EC, CF Ion, F Ifrimescu, L Spiridon, J Bakker, A Goverse, AJ Petrescu. (2023) NLRscape: An atlas of plant NLR proteins. Nucl. Acid. Res. 51: D1470-D1482.

156. Martin EC, L Spiridon, A Goverse, and AJ Petrescu. (2022) NLRexpress-A bundle of machine learning motif predictors-Reveals motif stability underlying plant Nod-like receptors diversity. Front Plant Sci. 13: 975888.

157. Martin R, T Qi, H Zhang, F Liu, M King, C Toth, E Nogales, and BJ Staskawicz. (2020) Structure of the activated ROQ1 resistosome directly recognizing the pathogen effector XopQ. Science 370: eabd9993.

158. Mérai Z, Z Kerényi, S Kertész, M Magna, L Lakatos, and D Silhavy. (2006) Double-stranded RNA binding may be a general plant RNA viral strategy to suppress RNA silencing. J. Virol. 80: 5747-5756.

159. Mesny F, S Hacquard, and BPHJ Thomma. (2023) Co-evolution within the plant holobiont drives host performance. EMBO Rep. 24: e57455.

160. Mi S, T Cai, Y Hu, Y Chen, E Hodges, F Ni, L Wu, S Li, H Zhou, C Long, S Chen, GJ Hannon, and Y Qi. (2008) Sorting of small RNAs into *Arabidopsis* argonaute complexes is directed by the 5' terminal nucleotide. Cell 133: 116-127.

161. Miebach M, R Jiang, PE Jameson, and MNP Remus-Emsermann. (2022) Plant protoplast-based assay to screen for salicylic acid response-modulating bacteria. bioRxiv

162. Minh BQ, HA Schmidt, O Chernomor, D Schrempf, MD Woodhams, A von Haeseler, and R Lanfear. (2020) IQ-TREE 2: New models and efficient methods for phylogenetic inference in the genomic era. Mol. Biol. Evol. 37: 1530-1534.

163. Miozzi L, G Gambino, J Burgyan, and V Pantaleo. (2013) Genome-wide identification of viral and host transcripts targeted by viral siRNAs in *Vitis vinifera*. Mol. Plant Pathol. 14: 30-43.

164. Miranda K, W Girard-Dias, M Attias, W de Souza, and I Ramos. (2015) Three dimensional reconstruction by electron microscopy in the life sciences: An introduction for cell and tissue biologists. Mol. Reprod. Dev. 82: 530-547.

165. Molina A, L Jordá, MÁ Torres, M Martín-Dacal, DJ Berlanga, P Fernández-Calvo, E Gómez-Rubio, and S Martín-Santamaría. (2024) Plant cell wall-mediated disease resistance: Current understanding and future perspectives. Mol. Plant 17: 699-724.

166. Molnár A, T Csorba, L Lakatos, E Varallyaya, C Lacomme, and J Burgyan. (2005) Plant virus-derived small interfering RNAs originate predominantly from highly structured single-stranded viral RNAs. J. Virol. 79: 7812-7818.

167. Morozov SY, ON Fedorkin, G Juttner, J Schiemann, DC Baulcombe, and JG Atabekov. (1997) Complementation of a *Potato virus X* mutant mediated by bombardment of plant tissues with cloned viral movement protein genes. J. Gen. Virol. 78: 2077-2083.

168. Mukhtar T. (2025) Plant immunity and resistance mechanisms: An editorial. Physiol. and Mol. Plant Pathol. 140: 102903.

169. Na Ayutthaya PP, D Lundberg, D Weigel, and L Li. (2020) Blue native polyacrylamide gel electrophoresis (BN-PAGE) for the analysis of protein oligomers in plants. Curr. Protoc. Plant Biol. 5: e20107.

170. Nagaraj PH. (2024) Determining macromolecular structures using cryo-electron microscopy. Methods Mol. Biol. 2787: 315-332.

171. Narusaka M, K Shirasu, Y Noutoshi, Y Kubo, T Shiraishi, M Iwabuchi, and Y Narusaka. (2009) RRS1 and RPS4 provide a dual Resistance-gene system against fungal and bacterial pathogens. Plant J. 60: 218–226.

172. Narusaka M, K Toyoda, T Shiraishi, S Iuchi, Y Takano, K Shirasu, and Y Narusaka. (2016) Leucine zipper motif in RRS1 is crucial for the regulation of *Arabidopsis* dual resistance protein complex RPS4/RRS1. Sci. Rep. 6: 18702.

173. Navalinskienë M, J Raugalas, and M Samuitiene. (2005) Viral diseases of flower plants. 16. Identification of viruses affecting orchids. Biologija 2: 29-34.

174. Navarro B, A Gisel, ME Rodio, S Delgado, R Flores, and F Di Serio. (2012) Small RNAs containing the pathogenic determinant of a chloroplast-replicating viroid guide the degradation of a host mRNA as predicted by RNA silencing. Plant J. 70: 991-1003.

175. Ngou BPM, HK Ahn, P Ding, and JDG Jones. (2021) Mutual potentiation of plant immunity by cell-surface and intracellular receptors. Nature 592: 110–115.

176. Ngou BPM, JDG Jones, and P Ding. (2022) Plant immune networks. Trend. Plant Sci. 27: 255-273.

177. Ngou BPM, M Wyler, MW Schmid, T Suzuki, M Albert, N Dohmae, Y Kadota, and K Shirasu. (2025) Systematic discovery and engineering of synthetic immune receptors in plants. Science 389: eadx2508.

178. Ngou BPM, P Ding, and JDG Jones. (2022) Thirty years of resistance: Zig-zag through the plant immune system. Plant Cell 34: 1447–1478.

179. Nijtmans LG, NS Henderson, and IJ Holt. (2002) Blue Native electrophoresis to study mitochondrial and other protein complexes. Methods 6: 327-334.

180. Nobori T. (2025) Exploring the untapped potential of single-cell and spatial omics in plant biology. New Phytol. 247: 1098-1116.

181. Nolte H and T Langer. (2021) ComplexFinder: A software package for the analysis of native protein complex fractionation experiments. Biochim. Biophys. Acta Bioenerg. 1862: 148444.

182. Ogbonna MJ and OE Umunna. (2017) Pathogen penetration into the host plant tissues: Challenges and obstacles - An overview. Sch. J. Agric. Vet. Sci.

183. Okada Y. (1999) Historical overview of research on the *Tobacco mosaic virus* genome: Genome organization, infectivity and gene manipulation. Philos. Trans. R. Soc. Lond. B. Biol. Sci. 354: 569–582.

184. Pai H, MP Contreras, J Salguero Linares, D Lüdke, A Posbeyikian, J Kourelis, S Kamoun, and C Marchal. (2025). The Pik NLR pair accumulates at the plasma membrane as a hetero oligomeric sensor-helper immune protein complex prior to activation. bioRxiv DOI: 10.64898/2025.11.30.691369.

185. Pai H, T Sakai, A Posbeyikian, R Frijters, Y Sugihara, MP Contreras, J Kourelis, H Adachi, S Kamoun, and AA Toghani. (2025) A hierarchical immune receptor network in lettuce reveals contrasting patterns of evolution in sensor and helper NLRs. bioRxiv 2025.02.25.639832.

186. Pai H, WH Jean, YS Lee, YCA Chang, and NS Lin. (2019) Genome wide analysis of small RNAs from *Odontoglossum ringspot virus* and *Cymbidium mosaic virus* synergistically infected Phalaenopsis. Mol. Plant Pathol. 21:188-205.

187. Palukaitis P and JY Yoon. (2020) R gene mediated defense against viruses. Curr. Opin. Virol. 45: 1-7.

188. Palukaitis P, and JY Yoon. (2024) Defense signaling pathways in resistance to plant viruses: Crosstalk and finger pointing. Adv. Virus Res. 118: 77-212.

189. Pantaleo V, P Saldarelli, L Miozzi, A Giampetruzzi, A Gisel, S Moxon, T Dalmay, G Bisztray, and J Burgyan. (2010) Deep sequencing analysis of viral short RNAs from an infected Pinot Noir grapevine. Virology 408: 49-56.

190. Parent KN, JR Schrad, and G Cingolani. (2018) Breaking symmetry in viral icosahedral capsids as seen through the lenses of x-ray crystallography and cryo-electron microscopy. Viruses 10: 67.

191. Passmore LA and CJ Russo. (2016) Specimen preparation for high-resolution cryo-EM. Methods Enzymol. 579: 51-86.

192. Pélissier R, C Violle, and JB Morel. (2021) Plant immunity: Good fences make good neighbors? Curr. Opin. Plant Biol. 62: 102045.

193. Powell PA, DM Stark, PR Sanders, and RN Beachy. (1989) Protection against *Tobacco mosaic virus* in transgenic plants that express *Tobacco mosaic virus* antisense RNA. Proc. Natl. Acad. Sci. USA. 86: 6949-6952.

194. Prigozhin DM and KV Krasileva. (2021) Analysis of intraspecies diversity reveals a subset of highly variable plant immune receptors and predicts their binding sites. Plant Cell 33: 998–1015.

195. Pruss G, X Ge, XM Shi, JC Carrington, and VB Vance. (1997) Plant viral synergism: The potyviral genome encodes a broad-range pathogenicity enhancer that transactivates replication of heterologous viruses. Plant Cell. 9: 859–868.

196. Qi T, K Seong, DPT Thomazella, JR Kim, J Pham, E Seo, MJ Cho, A Schultink, and BJ Staskawicz. (2018) NRG1functions downstream of EDS1 to regulate TIR-NLR-mediated plant immunity in *Nicotiana benthamiana*. Proc. Natl. Acad. Sci. USA. 115: E10979–E10987.

197. Qi X, FS Bao, and Z Xie. (2009) Small RNA deep sequencing reveals role for *Arabidopsis thaliana* RNA-dependent RNA polymerase in viral siRNA biogenesis. PLoS One 4: e4971.

198. Qu F and TJ Morris. (2005) Suppressors of RNA silencing encoded by plant viruses and their role in viral infections. FEBS Lett. 579: 5958-5964.

199. Ramesh SV, S Yogindran, P Gnanasekaran, S Chakraborty, S Winter, and HR Pappu. (2021) Virus and viroid-derived small RNAs as modulators of host gene expression: molecular insights into pathogenesis. Front. Microbiol. 11: 614231.

200. Ray S and CL Casteel. (2022) Effector-mediated plant-virus-vector interactions. Plant Cell 34: 1514-1531.

201. Reichhardt C, LM Joubert, KV Clemons, DA Stevens, and L Cegelski. (2019) Integration of electron microscopy and solid-state NMR analysis for new views and compositional parameters of Aspergillus fumigatus biofilms. Med. Mycol. 57: S239-S244.

202. Reisinger V and LA Eichacker. (2006) Analysis of membrane protein complexes by blue native PAGE. Proteomics 6 Suppl 2: 6-15.

203. Ren R, J Gao, D Yin, K Li, C Lu, S Ahmad, Y Wei, J Jin, G Zhu, and F Yang. (2021) Highly efficient leaf base protoplast isolation and transient expression systems for orchids and other important monocot crops. Front. Plant Sci. 12: 626015.

204. Reyes-Herrera PH, DA Delgadillo-Duran, M Flores-Gonzalez, LA Mueller, MA Cristancho, and LS Barrero. (2024) Chromosome-scale genome assembly and annotation of the tetraploid potato cultivar Diacol Capiro adapted to the Andean region. G3 (Bethesda) 14: jkae139.

205. Roossinck MJ. (2019) Viruses in the phytobiome. Curr. Opin. Virol. 37: 72-76.

206. Roth BM, GJ Pruss, and VB Vance. (2004) Plant viral suppressors of RNA silencing. Virus Res. 102: 97-108.

207. Ruiz-Bedoya T, KJ McTavish, TV Av-Shalom, D Desveaux, and DS Guttman. (2023) Towards integrative plant pathology. Curr. Opin. Plant Biol. 75: 102430.

208. Ryu KH and WM Park. (1995) The complete nucleotide sequence and genome organization of *Odontoglossum ringspot tobamovirus* RNA. Arch. Virol. 140: 1577-1587.

209. Saile SC, P Jacob, B Castel, LM Jubic, I Salas-Gonzáles, M Bäcker, JDG Jones, JL Dangl, and FE Kasmi. (2020) Two unequally redundant "helper" immune receptor families mediate *Arabidopsis thaliana* intracellular "sensor" immune receptor functions. PLoS Biol. 18: e3000783.

210. Sanford JC and SA Johnston. (1985) The concept of parasite-derived resistance—Deriving resistance genes from the parasite's own genome. J. Theoret. Biol. 113: 395-405.

211. Sarris PF, Z Duxbury, SU Huh, Y Ma, C Segonzac, J Sklenar, P Derbyshire, V Cevik, G Rallapalli, SB Saucet, et al. (2015) A plant immune receptor detects pathogen effectors that target WRKY transcription factors. Cell 161: 1089–1100.

212. Schaefer LK, F Parlange, G Buchmann, E Jung, A Wehrli, G Herren, MC Müller, J Stehlin, R Schmid, T Wicker, B Keller, and S Bourras. (2020) Cross-kingdom RNAi of pathogen effectors leads to quantitative adult plant resistance in wheat. Front. Plant Sci. 11: 253

213. Schägger H and G von Jagow. (1991) Blue native electrophoresis for isolation of membrane protein complexes in enzymatically active form. Anal. Biochem. 199: 223-31.

214. Scholthof KBG. (2004) *Tobacco mosaic virus*: A model system for plant biology. Ann. Rev. Phytopathol. 42: 13-34.

215. Schulze S, L Yu, C Hua, L Zhang, D Kolb, H Weber, A Ehinger, SC Saile, M Stahl, M Franz-Wachtel. (2022) The Arabidopsis TIR-NBS-LRR protein CSA1 guards BAK1-BIR3 homeostasis and mediates convergence of pattern-and effector-induced immune responses. Cell Host Microbe 30: 1717-1731.

216. Selvaraj, M, A Toghani, H Pai, Y Sugihara, J Kourelis, ELH Yuan, T Ibraham, H Zhao, RR Xie,A Maqbool, JC De la Concepcion, MJ Banfield, L Derevnina, B Petre, DM Lawson, TO Bozjurt, CH Wu, S Kamoun, and MP Contreras. (2023) Activation of plant immunity through conversion of a helper NLR homodimer into a resistosome. PLoS Biol. 22: e3002868.

217. Shimizu M, A Hirabuchi, Y Sugihara, A Abe, T Takeda, M Kobayashi, Y Hiraka, E Kanzaki, K Oikawa, H Saitoh, et al. (2022) A genetically linked pair of NLR immune receptors shows contrasting patterns of evolution. Proc. Natl. Acad. Sci. USA. 119: e2116896119.

218. Shimura H, V Pantaleo, T Ishihara, N Myojo, J Inaba, K Sueda, J Burgyan, and C Masuta. (2011) A viral satellite RNA induces yellow symptoms on tobacco by targeting a gene involved in chlorophyll biosynthesis using the RNA silencing machinery. PLoS Pathog. 7:e1002021.

219. Shukla K, Nikita, A Ahmad, MS Noorani, and R Gupta. (2025) Phytohormones and emerging plant growth regulators in tailoring plant immunity against viral infections. Physiologia Plantarum 177: e70171.

220. Sindhu A, S Chintamanani, AS Brandt, M Zanis, SR Scofield, Johal GS. (2008) A guardian of grasses: Specific origin and conservation of a unique disease-resistance gene in the grass lineage. Proc. Natl. Acad. Sci. USA. 105: 1762-1767.

221. Smith NA, AL Eamens, and MB Wang. (2011) Viral small interfering RNAs target host genes to mediate disease symptoms in plants. PLoS Pathog. 7:e1002022.

222. Soanes DM, TA Richards, and NJ Talbot. (2007) Insights from sequencing fungal and oomycete genomes: What can we learn about plant disease and the evolution of pathogenicity? Plant Cell 19: 3318-3326.

223. Solovyev AG, DA Zelenina, EI Savenkov, VZ Grdzelishvili, SY Morozov, DE Lesemann, E Maiss, R Casper, and JG Atabekov. (1996) Movement of Barley stripe mosaic virus chimera with a *Tobacco mosaic virus* movement protein. Virology 217: 435-441.

224. Spoel SH and X Dong. (2024) Salicylic acid in plant immunity and beyond. Plant Cell 36: 1451-1464.

225. Staehelin LA and DJ Paolillo. (2020) A brief history of how microscopic studies led to the elucidation of the 3D architecture and macromolecular organization of higher plant thylakoids. Photosynth. Res. 145: 237-258.

226. Stakman EC. (1947) The nature and importance of physiologic specialization in phytopathogenic fungi. Science 105: 627-632.

227. Stark H and AChari. (2016) Sample preparation of biological macromolecular assemblies for the determination of high-resolution structures by cryo-electron microscopy. Microscopy (Oxf). 65: 23-34.

228. Staskawicz BJ, D Dahlbeck, and NT Keen. (1984) Cloned avirulence gene of *Pseudomonas syringae* pv. glycinea determines race-specific incompatibility on Glycine max (L.) Merr. Proc. Natl. Acad. Sci. USA. 81: 6024-6028.

229. Steere RL. (1964) Electron microscopy of plant viruses. Bot. Rev. 30: 629-666.

230. Stiehler F, M Steinborn, S Scholz, D Dey, APM Weber, and AK Denton. (2021) Helixer: Cross-species gene annotation of large eukaryotic genomes using deep learning. Bioinformatics 36: 5291–5298.

231. Sugihara Y, J Kourelis, MP Contreras, H Pai, M Selvaraj, A Toghani, C Martínez-Anaya, and S Kamoun. (2025) Helper NLR immune protein NRC3 evolved to evade inhibition by a cyst nematode virulence effector. PLoS Genet. 21: e1011653.

232. Sun A, L Wang, Y Zhang, X Yang, Y Su, and X Wu. (2024) Development and application of a duplex RT-RPA assay for the simultaneous detection of *Cymbidium mosaic virus* and *Odontoglossum ringspot virus*. Viruses 16: 543.

233. Sun A, L Wang, Y Zhang, X Yang, Y Wei, D Yang, W Li, and X Wu. (2023) Establishment of a triplex TaqMan quantitative real-time PCR assay for simultaneous detection of *Cymbidium mosaic virus*, *Odontoglossum ringspot virus* and *Cymbidium ringspot virus*. Front. Microbiol. 14: 1129259.

234. Syller J. (2012) Facilitative and antagonistic interactions between plant viruses in mixed infections. Mol. Plant Pathol. 13: 204-16.

235. Tamborindeguy C, FT Hata, RO Molina, and WMC Nunes. (2023) A new perspective on the co-transmission of plant pathogens by hemipterans. Microorganisms 11: 156.

236. Tanambell H, M Danielsen, AH Møller, and TK Dalsgaard. (2025) Proof-of-concept: Ultrafiltration as a pre-treatment for the anion exchange chromatography of RuBisCO from alfalfa. Food Bioproduct. Proc. 154: 440-448.

237. Tatkiewicz W, E Elizondo, E Moreno, C Díez-Gil, N Ventosa, J Veciana, and I Ratera. (2015) Methods for characterization of protein aggregates. Methods Mol. Biol. 1258: 387-401.

238. Teixeira RM, MA Ferreira, GAS Raimundo, and EPB Fontes. (2021) Geminiviral triggers and suppressors of plant antiviral immunity. Microorganisms. 9: 775.

239. Toghani A and S Kamoun. (2024) Functional annotation of 180 RefSeq reference plant proteomes reveals a dataset of 113,684 NLR proteins. Zenodo zenodo: 13627395

240. Toghani A, R Frijters, TO Bozkurt, R Terauchi, S Kamoun, and Y Sugihara. Can AI modelling of protein structures distinguish between sensor and helper NLR immune receptors? New Phytol. 248: 17-23.

241. Tsai CF, CH Huang, FH Wu, CH Lin, CH Lee, SS Yu, YK Chan, and FJ Jan. (2022) Intelligent image analysis recognizes important orchid viral diseases. Front. Plant Sci. 13: 1051348.

242. Tseng KC, YF Chiang-Hsieh, H Pai, CN Chow, SC Lee, HQ Zheng, PL Kuo, GZ Li, YC Hung, NS Lin, and WC Chang. (2018) MicroRPM: A microRNA prediction model based only on plant small RNA sequencing data. Bioinformatics 34: 1108-1115.

243. Tseng KC, YF Chiang-Hsieh, H Pai, NY Wu, HQ Zheng, CN Chow, TY Lee, SB Chang, NS Lin, and WC Chang. (2020) sRIS: A small RNA illustration system for plant next-generation sequencing data analysis. Plant Cell Physiol. 61: 1204–1212.

244. Uehling J, A Deveau, and M Paoletti. (2017) Do fungi have an innate immune response? An NLR-based comparison to plant and animal immune systems. PLoS Pathog. 13: e1006578.

245. Underwood W. (2012) The plant cell wall: A dynamic barrier against pathogen invasion. Front. Plant Sci. 3: 85.

246. Van de Weyer AL, F Monteiro, OJ Furzer, MT Nishimura, V Cevik, K Witek, JDG Jones, JL Dangl, D Weigel, and F Bemm. (2019) A species-wide inventory of NLR genes and alleles in Arabidopsis thaliana. Cell 178: 1260-1272.

247. Van der Want JPH and J Dijkstra. (2006) A history of plant virology. Arch. Virol. 151: 1467-1498.

248. Van der Wilk F, WD Posthumus-Lutke, MJ Huisman, H Huttinga, and R Goldbach. (1991) Expression of the *Potato leafroll luteovirus* coat protein gene in transgenic potato plants inhibits viral infection. Plant Mol. Biol. 17: 431-439.

249. van Kan JA, GF van den Ackerveken, and PJ de Wit. (1991) Cloning and characterization of cDNA of avirulence gene *avr9* of the fungal pathogen *Cladosporium fulvum*, causal agent of tomato leaf mold. Mol. Plant Microbe Interact. 4: 52-59.

250. Van Ooijen G, G Mayr, MM Kasiem, M Albrecht, BJ Cornelissen, and FL Takken. (2008) Structure–function analysis of the NB-ARC domain of plant disease resistance proteins. J. Exp. Bot. 59: 1383-1397.

251. Van Ooijen G, HA van den Burg, BJC Cornelissen, and FLW Takken. (2007) Structure and function of resistance proteins in solanaceous plants Annu. Rev. Phytopathol. 45:43-72

252. Vance RE. (2015) The NAIP/NLRC4 inflammasomes. Curr. Opin. Immunol. 32: 84-89.

253. Vénien-Bryan C, and CAH Fernandes. (2023) Overview of membrane protein sample preparation for single-particle cryo-electron microscopy analysis. Int. J. Mol. Sci. 24: 14785.

254. Vénien-Bryan C, Z Li, L Vuillard, and JA Boutin. (2017) Cryo-electron microscopy and X-ray crystallography: Complementary approaches to structural biology and drug discovery. Acta Crystallogr. F. Struct. Biol. Commun. 73: 174-183.

255. Verdin E, C Wipf-Scheibel, P Gognalons, F Aller, M Jacquemond, and M Tepfer. (2017) Sequencing viral siRNAs to identify previously undescribed viruses and viroids in a panel of ornamental plant samples structured as a matrix of pools. Virus Res. 241: 19-28.

256. Verma V, P Ravindran, and PP Kumar. (2016) Plant hormone-mediated regulation of stress responses. BMC Plant Biol. 16: 86.

257. Vincis Pereira Sanglard L and C Colas des Francs-Small. (2022) High-throughput BN-PAGE for mitochondrial respiratory complexes. Methods Mol. Biol. 2363: 111-119.

258. Vogler H, MO Kwon, V Dang, A Sambade, M Fasler, J Ashby, and M Heinlein. (2008) *Tobacco mosaic virus* movement protein enhances the spread of RNA silencing. PLoS Pathog. 4: e1000038.

259. Wang J, M Hu, J Wang, J Qi, Z Han, G Wang, Y Qi, HW Wang, JM Zhou, and J Chai. (2019) Reconstitution and structure of a plant NLR resistosome conferring immunity Science 364: 6435.

260. Wang M, N Thomas, and H Jin. (2017) Cross-kingdom RNA trafficking and environmental RNAi for powerful innovative pre- and post-harvest plant protection. Curr. Opin. Plant Biol. 38: 133-141.

261. Wang MB, XY Bian, LM Wu, LX Liu, NA Smith, D Isenegger, RM Wu, C Masuta, VB Vance, JM Watson, A Rezaian, ES Dennis, and PM Waterhouse. (2004) On the role of RNA silencing in the pathogenicity and evolution of viroids and viral satellites. Proc. Natl. Acad. Sci. USA. 101: 3275-3280.

262. Wang Y, RN Pruitt, T Nürnberger, and Y Wang. (2022) Evasion of plant immunity by microbial pathogens. Nat. Rev. Microbiol. 20: 449-464.

263. Weber E, C Engler, R Gruetzner, S Werner, and S Marillonnet. (2011) A modular cloning system for standardized assembly of multigene constructs. PLoS One 6: e16765.

264. Weiberg A and H Jin. (2015) Small RNAs: The secret agents in the plant-pathogen interactions. Curr. Opin. Plant Biol. 26: 87-94.

265. Weissenberger G, RJM Henderikx, and PJ Peters. (2021) Understanding the invisible hands of sample preparation for cryo-EM. Nat. Methods. 18: 463-471.

266. Wightman R. (2022) An overview of cryo-scanning electron microscopy techniques for plant imaging. Plants (Basel) 11: 1113.

267. Wilson RA and JM McDowell. (2022) Recent advances in understanding of fungal and oomycete effectors. Curr. Opi. Plant Biol.

268. Wittig I, T Beckhaus, Z Wumaier, M Karas, and H Schägger. (2010) Mass estimation of native proteins by blue native electrophoresis: principles and practical hints. Mol Cell Proteomics. 9: 2149-61.

269. Wong SM, CG Chng, YH Lee, K Tan, and FW Zettler. (1994) Incidence of *Cymbidium mosaic* and *Odontoglossum ringspot viruses* and their significance in orchid cultivation in Singapore. Crop Protect. 13: 235-239.

270. Wong SM, PH Mahtani, KC Lee, HH Yu, Y Tan, KK Neo, Y Chan, M Wu, and CG Chng. (1997) *Cymbidium mosaic potexvirus* RNA: Complete nucleotide sequence and phylogenetic analysis. Arch. Virol. 142: 383-391.

271. Woods AG, I Sokolowska, R Yakubu, M Butkiewicz, M LaFleur, C Talbot, and CC Darie. (2011) Blue native PAGE and mass spectrometry as an approach for the investigation of stable and transient protein-protein interactions. In: Oxidative Stress: Diagnostics, Prevention, and Therapy. Chapter 12, pp. 341-467.

272. Wu CH, A Abd-El-Haliem, TO Bozkurt, K Belhaj, R Terauchi, JH Vossen, and S Kamoun. (2017) NLR network mediates immunity to diverse plant pathogens. Proc. Natl. Acad. Sci. USA. 114: 8113–8118.

273. Wu CH, L Derevnina, and S Kamoun. (2018) Receptor networks underpin plant immunity. Science 360: 1300–1301.

274. Wu HW, SS Lin, KC Chen, SD Yeh, and NH Chua. (2010) Discriminating mutations of HC-Pro of *Zucchini yellow mosaic virus* with differential effects on small RNA pathways involved in viral pathogenicity and symptom development. Mol. Plant Microbe Interact. 23: 17-28.

275. Xu Y, and S Dang. (2022) Recent technical advances in sample preparation for single-particle cryo-EM. Front. Mol. Biosci. 9: 892459.

276. Yan F, H Zhang, MJ Adams, J Yang, J Peng, JF Antoniw, Y Zhou, and J Chen. (2010) Characterization of siRNAs derived from Rice stripe virus in infected rice plants by deep sequencing. Arch. Virol. 155: 935-940.

277. Yang L and Y Li. (2018) Dissection of RNAi-based antiviral immunity in plants. Curr. Opi. Plant Virol. 32: 88-99.

278. Yang RC, FY Peng, and Z Hu. (2017) Inferring defense-related gene families in *Arabidopsis* and wheat. BMC Genomics 18: 980.

279. Yang Z and Y Li. (2018) Dissection of RNAi-based antiviral immunity in plants. Curr. Opi. Virol. 32: 88-99.

280. Yu HH and SM Wong. (1998) Synthesis of biologically active cDNA clones of *Cymbidium mosaic potexvirus* using a population cloning strategy. Arch. Virol. 143: 1617–1620.

281. Yuan M, Z Jiang, G Bi, K Nomura, M Liu, Y Wang, B Cai, JM Zhou, SY He, and XF Xin. (2021) Pattern-recognition receptors are required for NLR-mediated plant immunity. Nature 592: 105-109.

282. Zaynab M, M Fatima, S Abbas, Y Sharif, M Umair, MH Zafar, and K Bahadar. (2018) Role of secondary metabolites in plant defense against pathogens. Microb. Pathog. 124: 198-202.

283. Zdrzałek R, S Kamoun, R Terauchi, H Saitoh, and MJ Banfield. (2020) The rice NLR pair Pikp-1/Pikp-2 initiates cell death through receptor cooperation rather than negative regulation. PLoS One 15: e0238616.

284. Zettler FW, NJ Ko, GC Wisler, MS Elliott, and SM Wong. (1990) Viruses of orchids and their control. Plant Disease 74: 621-626.

285. Zhai C, F Lin, Z Dong, X He, B Yuan, X Zeng, L Wang, and Q Pan. (2011) The isolation and characterization of Pik, a rice blast resistance gene which emerged after rice domestication. New Phytol. 189: 321-34.

286. Zhang J, W Li, T Xiang, Z Liu, K Laluk, X Ding, Y Zou, M Gao, X Zhang, S Chen, T Mengiste, Y Zhang, and JM Zhou JM. (2010) Receptor-like cytoplasmic kinases integrate signaling from multiple plant immune receptors and are targeted by a *Pseudomonas syringae* effector. Cell Host Microbe 7: 290-301.

287. Zhang X, YR Yuan, Y Pei, SS Lin, T Tuschl, DJ Patel, and NH Chua. (2006) Cucumber mosaic virus-encoded 2b suppressor inhibits *Arabidopsis* Argonaute1 cleavage activity to counter plant defense. Genes Dev. 20: 3255-3268.

288. Zhao J, X Yu, X Shentu, and D Li. (2024) The application and development of electron microscopy for three-dimensional reconstruction in life science: A review. Cell Tissue Res. 396: 1-18.

289. Zhao Y, X Yang, G Zhou, and T Zhang. (2020) Engineering plant virus resistance: From RNA silencing to genome editing strategies. Plant Biotechnol. J. 18: 328-336.

290. Zhao YB, MX Liu, TT Chen, X Ma, ZK Li, Z Zheng, SR Zheng, L Chen, YZ Li, LR Tang, Q Chen, P Wang, and S Ouyang. (2022) Pathogen effector AvrSr35 triggers Sr35 resistosome assembly via a direct recognition mechanism. Sci. Adv. 8: eabq5108.

291. Zheng Y, S Gao, C Padmanabhan, R Li, M Galvez, D Gutierrez, S Fuentes, KS Ling, J Kreuze, and Z Fei. (2017) VirusDetect: An automated pipeline for efficient virus discovery using deep sequencing of small RNAs. Virology 500: 130-138.

292. Zhou CJ, XY Zhang , SY Liu , Y Wang, DW Li, JL Yu, and CG Han. (2017) Synergistic infection of BrYV and PEMV 2 increases the accumulations of both BrYV and BrYV-derived siRNAs in *Nicotiana benthamiana*. Sci. Rep. 7: 45132.

293. Zhu M, M Feng, and X Tao. (2025) NLR-mediated antiviral immunity in plants. J. Int. Plant Biol. 67: 786-800.

*Art and science are*
*a sweet pair.*

Kunie Sugiura

# Illustrated Science:

## My Journey and Toolkit for Communicating Research by Visuals

Perhaps echoing the well-known phrase "publish or perish," the essence of scientific research lies not only in uncovering how the world works but also in communicating those discoveries to peers, the public, and future generations. Effective **science communication (sci-comm)** is therefore an indispensable part of scientific research. This broad field encompasses diverse forms of media, among which visual communication plays a particularly powerful role.

**Humans have long used images to interpret and convey their understanding of nature.** As early as 34,000 BCE, prehistoric humans recorded wild mammals by wall paintings in the Chauvet-Pont-d'Arc Cave (Yetisen et al., 2016). Ancient Egyptians illustrated anatomical knowledge and medicinal plants on papyrus for instructional use. During the Renaissance and through the 19th century, scientific illustration flourished as artists and naturalists collaborated to produce exquisitely detailed anatomical and botanical drawings (Ford, 2003). **These works not only disseminated knowledge by making the unseen visible** — from microscopic structures to exotic species — but also **transformed scientific depiction into an art form** combined precision with aesthetic refinement. With the arrival of photography, colour printing, and digital media in the 20th century, scientific illustration has become more accessible than ever (Bucchi and Trench, 2021). No longer limited to trained artists, visual communication has evolved into a universal language through which anyone can observe, interpret, and articulate scientific ideas—continuing its long-standing role as a bridge between observation, understanding, and creative expression.

**For scientists today, visuals are central to how we share our work** — from data visualizations, graphical abstracts to figures for conferences and public outreach. Even within research communities, a well-crafted graphic often conveys the essence of a study more efficiently than text alone (Oska et al., 2020). However, while we understand our science deeply, many of us have little training in visual design and struggle to translate ideas into clear, engaging graphics.

In this chapter, I begin with **my personal journey and early inspirations** in sci-comm illustration, then **outline core principles for creating effective scientific visuals**, and finally **showcase selected case studies** illustrating how these principles shaped my own artwork.

## I. Early Inspirations and the Roots of My Sci-Comm Journey

**Humans are fundamentally visual oriented**, relying heavily on visual cues to navigate, understand, and adapt to the world around us. The familiar notion that "seeing is believing" reflects this deep cognitive bias: visual input often feels more immediate and convincing than abstract verbal descriptions (Smiciklas, 2012). This intuition is well supported by neuroscience: visual information engages powerful processing networks in the human brain, creating both pictorial and verbal memory traces — a phenomenon known as dual coding — whereas text alone typically produces only verbal traces (Ciccione et al., 2025). Moreover, images are processed far more rapidly than written language, bypassing many of the cognitive steps required for reading. As a result, **visuals leave stronger, more durable impressions and enhance recall** across contexts ranging from basic survival to complex communication (Zimmerman et al., 2015).

In science communication, visual displays therefore offer unique advantages. They can distil complex information, transcend language barriers, and improve accessibility for diverse audiences (Woloshin et al., 2023). When browsing digital platforms, our attention often highlights images before text (Figure S1); and on social media, research summaries shared as visual abstracts gain two to five times more engagement than citation-only posts (Oska et al., 2020). My own inspiration to pursue sci-comm illustration began with a memorable example: during a weekly seminar series at Academia Sinica nearly a decade ago, **Professor Keiko Torii concluded her talk with a simple cartoon** illustrating how two peptides, EPF2 and EPFL9, compete for the ERECTA receptor to regulate stomatal patterning (Figure S2; Lee et al., 2015). The single image left a lasting impression — I still remember the talk vividly today. It also opened my eyes that there exists playful way to disseminating scientific findings. Around the same time, I noticed an emergence of scientific journal covers adopting more diverse and creative visual styles. A favourite example is ***Genes to Cells,*** **whose covers features Japanese traditional ukiyo-e woodblock print images but with a contemporary twist**, integrating modern molecular biology concepts in the illustration (Figure S3). These designs showed me that illustrations are not merely decorative — they add conceptual and emotional layers that text alone cannot convey.

*Nicotiana benthamiana*, a solanaceous species native to Australia, is one of the most commonly used model plant organisms. It was initially used by the virology community because of its hypersusceptibility to plant viruses. Later, this feature was exploited with the development of viral vectors that can express foreign genes and the establishment of virus-induced gene silencing (VIGS), which enabled knocking down endogenous plant genes. Benth (or Benthi), as it is colloquially known, was further popularized by the development of agroinfiltration, a method that enabled transient protein expression in plants. Agroinfiltration has been extensively used in cell biology, biochemistry, protein–protein interaction analyses and other *in planta* studies (Goodin *et al.*, 2008). However, genetic analyses of *N. benthamiana* remained limited due to its allotetraploid nature and incomplete sequence of the 3.1 Gb genome. In this issue of *New Phytologist*, Schultink *et al.* (pp. 1001–1009) used a forward genetic screen in *N. benthamiana* to determine that NbZAR1, an orthologue of the *Arabidopsis thaliana* NLR (nucleotide-binding domain and leucine-rich repeat domain-containing) ZAR1, is responsible for the perception of XopJ4 from the tomato bacterial pathogen *Xanthomonas perforans*. Although forward genetic screens using gene silencing have been performed in *N. benthamiana*, Schultink *et al.* are among the first to use a chemical mutagenesis-based screen to dissect plant biological processes. Together with CRISPR genome editing and improved genomics resources, this study ushers in a new era of forward and reverse genetic analyses for this much-cherished model plant system (Fig. 1).

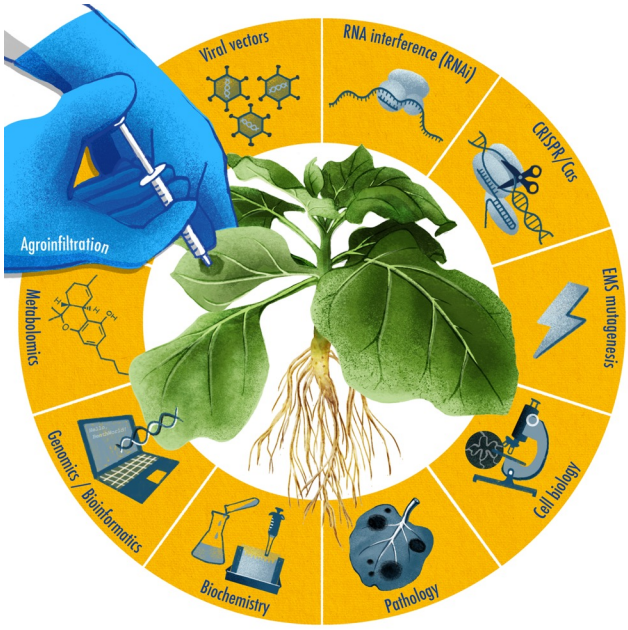


**Figure S1.** Paired written abstract (left) and visual abstract (right) for the article "Dude, where is my mutant? *Nicotiana benthamiana* meets forward genetics" (Derevnina et al., 2019).

**Figure S2.** The cartoon used by Professor Keiko Torii to summarize the study "Competitive binding of antagonistic peptides fine-tunes stomatal patterning (Lee et al., 2015)" during her talk. [Image was downloaded from https://www.plant-stomata.org/]

Figure S3. Example cover images of Genes to Cells journal. From left to right, these images depicted concepts of (1) competition of protein 3D structure prediction pipelines, (2) the Hi-C method charts on Hishimochi rice cakes, and (3) mitotic spindle as cats.
[Images were downloaded from https://www.mbsj.jp/en/gtc/cover_gallery.html]

As a plant scientist, communicating complex ideas clearly is a crucial aspect of my work, and illustration naturally became part of my research practice. This inclination grew from my long-standing hobbies in doodling and handcrafting, and from my fascination with nature—often imagining how organisms perceive their environment (Figure S4). I frequently found myself **sketching diagrams during discussions with colleagues, using visuals to communicate experimental designs or explain technical details.** These informal drawings evolved into my earliest research graphics: graphical abstracts, lab website illustrations, and outreach posters (Figure S5).

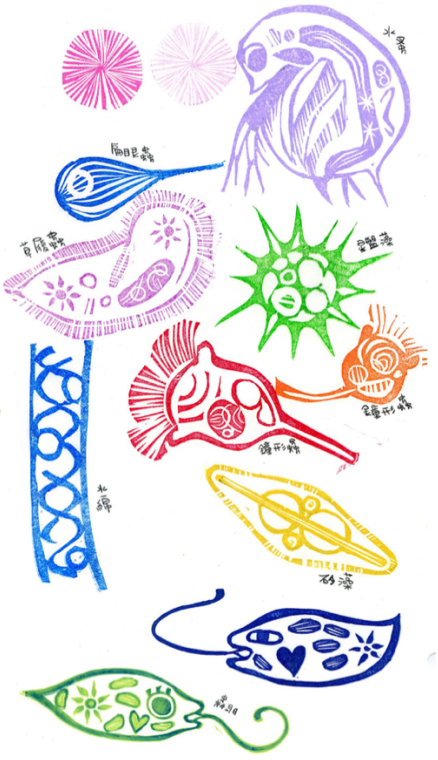

Figure S4. One of my early nature-inspired artwork, depicting planktons in pond water including *Paramecium*, water flea, and slightly anthropomorphic *Euglena*.

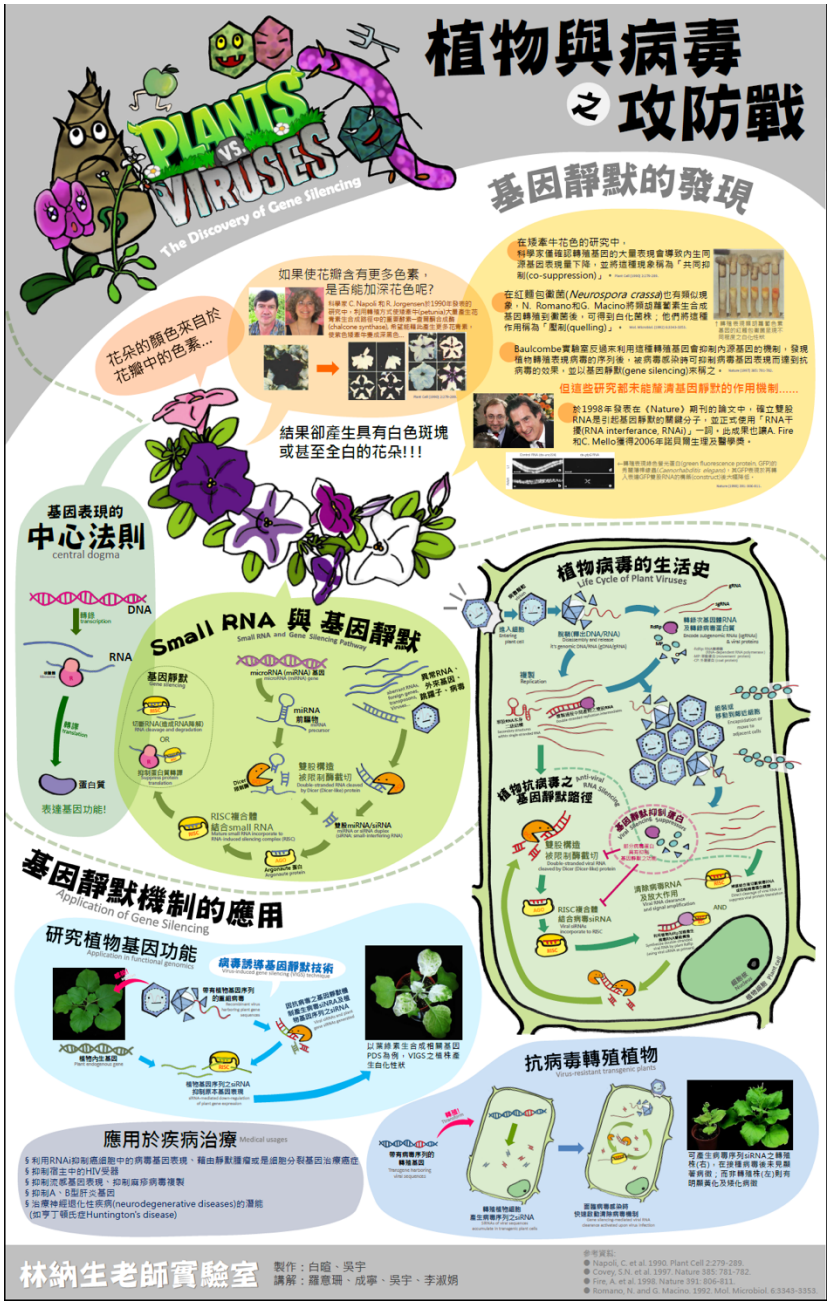


Figure S5. One of my earliest science communication works. This poster is used for outreach events in demonstrating anti-viral RNA silencing and engineering virus resistant plant using RNA interference strategy.

Since joining The Sainsbury Laboratory, I have gained many more opportunities to develop sci-comm illustrations—from **preparing materials for the Norwich Science Festival to collaborative projects that have been published as journal covers** (Figure S6). These experiences have shaped my approach to scientific visualization and gradually led me to articulate a personal framework for designing clear, engaging scientific graphics. The following sections outline this framework and the principles that guide my work.

**Figure S6.** The use of posters, photo booth, and displays I made for science outreach events.

## II. Design Principles and Workflow for Sci-Comm Illustration

**Scientific visualizations integrate information and graphics** to help audiences quickly grasp complex ideas (Smiciklas, 2012). They take many forms—data visualizations (such as Venn diagrams, boxplots, and charts), posters, and graphical abstracts are among the most common in scientific practice. Yet the efficacy of strong visuals in communicating ideas is a principle that applies universally, from scientific concepts to everyday media such as advertisements and event posters (Spence and Doorn, 2022). Fundamentally, **any visual product is a combination of two visible components - text and image - which together convey the information** (Figure S7). When applied to scientific graphics, while the three elements are consistent, their composition differs across graphic types (Figure S8):

- **Data visualization** primarily transforms accurate data into image elements, resulting in a large overlap between image and information.
- **Posters** often combine explanatory text with supporting visuals to guide viewers through a narrative of comprehensive research details.
- **Graphical abstracts** prioritise minimal text and a high proportion of images to highlight key concepts at a glance.

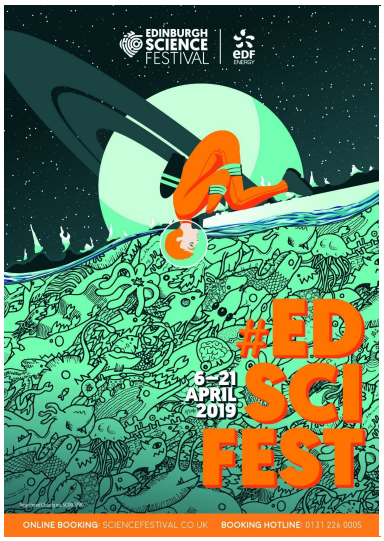


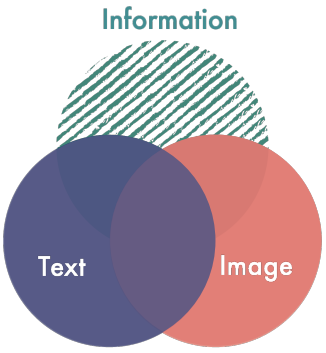


**Figure S7.** A visual display is fundamentally composed of three core elements: image, text, and the underlying information. In this example from the Edinburgh Science Festival poster, illustrations establish the overall theme and visual identity, while the textual elements communicate essential practical details such as the event title, time, and venue. [The poster is downloaded from https://www.acrossthearts.co.uk/review/edfest/6502-edinburgh-science-festival--2019/]

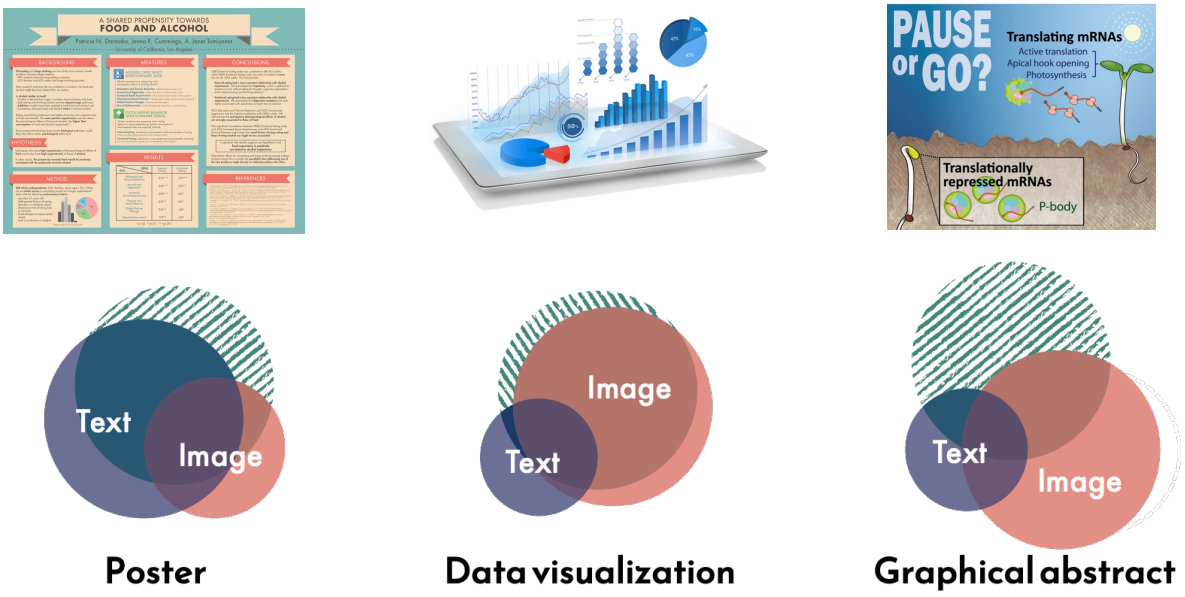


Figure S8. Different compositions of text, image, and information in different types of science communication graphics.

The specific breakdown of these three main elements is further detailed in Figure S9.

The principle of balancing text, image, and information forms only one aspect of the overall design process. To translate the process into practice, I adapted and integrated established frameworks from Perra and Brinkman (2021) and Woloshin et al. (2023) into a **step-by-step workflow** (Figure S10). This workflow moves from conceptual planning to iterative design stages involving discussion and revision. Together, these steps provide a structured approach for transforming scientific concepts into clear and engaging visuals. The steps are:

(i) Identify the target audience, key messages, and available materials
(ii) Decide on the graphic style and review layout options
(iii) Draft the layout
(iv) Apply a colour palette
(v) Discuss, revise, and refine
(vi) Complete and finalise the design

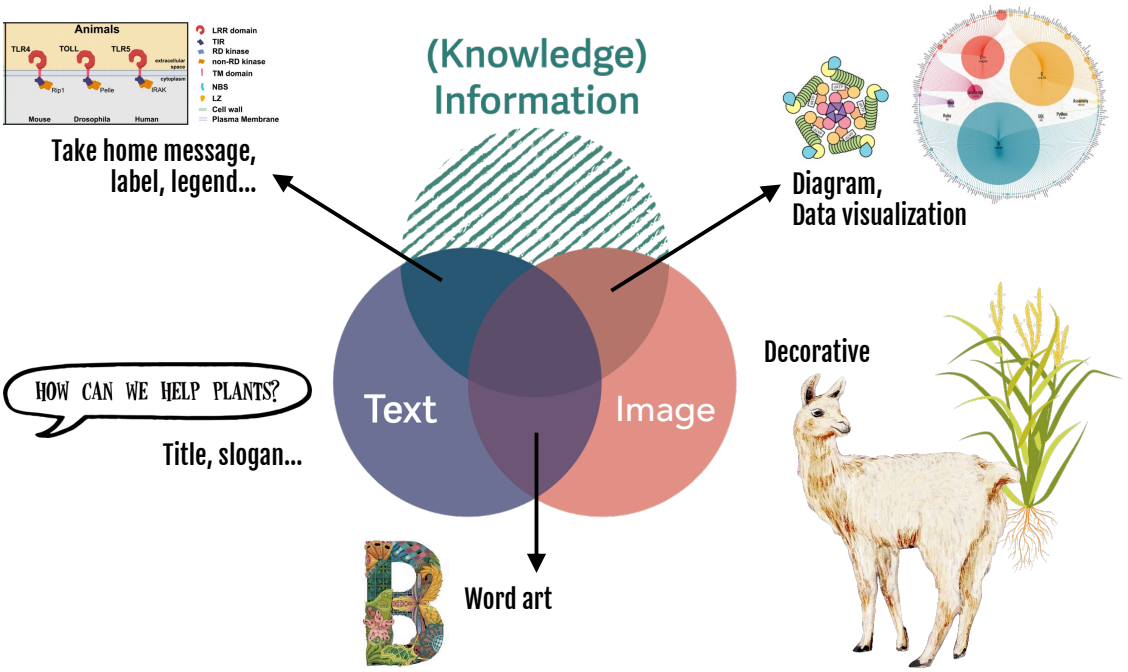


Figure S9. Core components of visual communication in scientific graphics. Schematic illustration showing that effective visual displays are built from the integration of three fundamental elements: text, image, and information. Text provides explicit guidance and contextual cues (e.g., questions, labels, annotations), images offer intuitive and immediate visual representation, and information represents the underlying scientific content or data being conveyed. The surrounding examples illustrate how these elements combine in different scientific visuals.

Figure S10. The workflow for designing science communication graphics.

Step (i): Identify the audience, key messages, and materials

The foundation of any effective illustration is **understanding who the graphic is for and what it needs to communicate.** As scientists, we are deeply familiar with our subjects, which can make it difficult to judge what level of detail is appropriate. Too much information obscures the message; too little risks inaccuracy (Beardsworth, 2020; Vosoughi et al., 2018). The intended audience—experts, interdisciplinary researchers, or the general public—determines the balance.

**Format selection** is equally important: should the message become a poster, an infographic, a data-driven figure, or a conceptual cover image? Once the format is chosen, relevant materials can be assembled: research diagrams, photos of specimens, conceptual sketches, or metaphorical visual elements when artistic interpretation is appropriate.

Together, audience, message, and format form an interconnected triad that anchors the entire design process.

Steps (ii)–(iv): Graphic style, layout, and colour

These steps constitute the core design phase. When collaborating with professional designers or illustrators, much of this work falls to them, but scientists must still make informed and intentional choices.

**Graphic style** may range from fully artistic to strictly vector-based, although research figures generally favour clear vector illustrations over painterly or hand-drawn styles due to readability and consistency. For journal covers, additional stylistic constraints may apply—some journals encourage painterly or 3D-rendered imagery, while others prefer minimalist or photographic styles.

**Layout defines the narrative structure** of a figure or poster. In conceptual graphics, layout directs the viewer's attention and establishes a focal point. In posters or graphical abstracts, layout determines the logical flow, helping readers navigate information naturally, in context to key findings and final takeaway.

**Colour is one of the most influential design elements** and often the most overlooked. A deliberate colour palette enhances readability, draws attention to key elements, and establishes a cohesive visual identity across an entire project. When colour carries meaning—such as distinguishing data groups in a plot, labelling components linked to a figure legend, or highlighting experimental conditions—it

becomes essential to ensure accessibility. Authors should choose **colour-blind-friendly palettes** that remain distinguishable to viewers with common forms of colour vision deficiency (Crameri et al., 2024). Traditional rainbow palettes, once widely used in heatmaps and 3D surface plots, are now discouraged because their endpoints are both dark, their gradients are perceptually uneven, and they perform poorly in colour-blind or monochrome printing contexts (Figure S11). Modern alternatives such as viridis, cividis, or carefully curated discrete palettes provide more uniform contrast and maintain interpretability for all audiences (Crameri et al., 2020). Thoughtful colour usage therefore supports both scientific accuracy and inclusive communication.

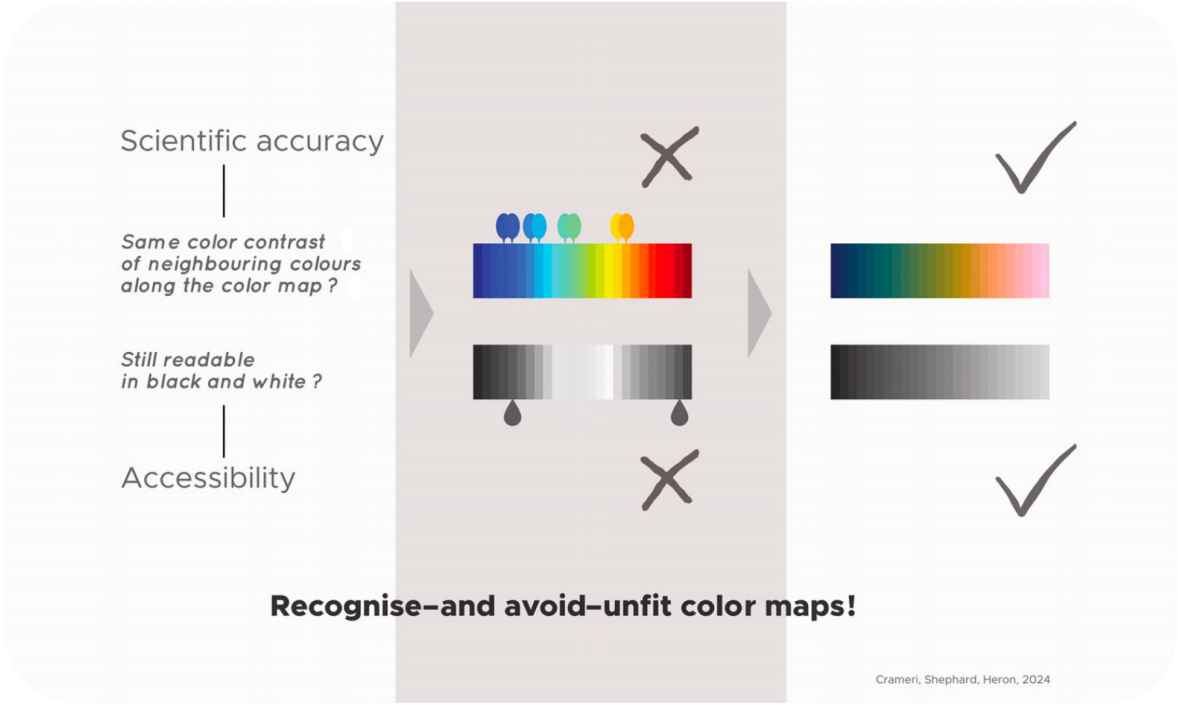


**Figure S11.** Recognising and avoiding unfit colour maps.
The scientific reliability of a colour gradient can be visually assessed by examining contrast between neighbouring colours along the scale. Colour maps in which adjacent values show uneven perceptual differences—appearing artificially closer or farther apart—fail to represent data uniformly and should be avoided (left). Accessibility can be evaluated by converting the colour map to greyscale: if multiple colours collapse into the same grey value after desaturation, the map is not colour-blind– or print-friendly. Well-designed colour maps maintain perceptual uniformity in both colour and greyscale representations (right). [Adapted from Crameri et al., 2024]

## Steps (v)–(vi): Refinement and finalisation

The final stages involve **iterative refinement**—reviewing drafts with collaborators, checking scientific accuracy, adjusting text and visual balance, and ensuring the narrative reads clearly. Finalisation may include polishing details, preparing files in publication-ready formats, and confirming that the visual effectively communicates the intended message.

# III. Case Studies

## III-1. Translating Research into Cover Images

My portfolio of journal cover illustrations began with the artwork created for "*Parasitic modulation of host development by ubiquitin-independent protein degradation*" (Huang et al., 2021). This study uncovered how the phytoplasma effector SAP05 hijacks the host 26S proteasome subunit RPN10 to degrade transcription factors SPL and GATA in a ubiquitin-independent manner, ultimately triggering the dramatic "witches' broom" phenotype. When Weijie and I began our collaboration, we noticed that **phytoplasma study offered a wealth of visually striking material**—phyllody (retrograde development of flowers into leaf-like organs), excessive meristem proliferation, and the evocative term "witches' broom" itself. Therefore, **rather than depicting molecular details, we chose to communicate the core concept:** a tripartite interaction between plant, phytoplasma, and insect vector. In the final composition, a phyllody sunflower occupies the central focus. On the left, I incorporated a visual illusion—sunflower leaves intertwined with a purple ribbon forming the silhouette of a witch's face—subtly reinforcing the theme. On the right, I highlighted the major vector, the aster leafhopper (Macrosteles quadrilineatus) on the leaves, as well phytoplasma cells hidden in the background (Figure S12). Together, these elements created a narrative-rich yet conceptually distilled rendering of the disease system.

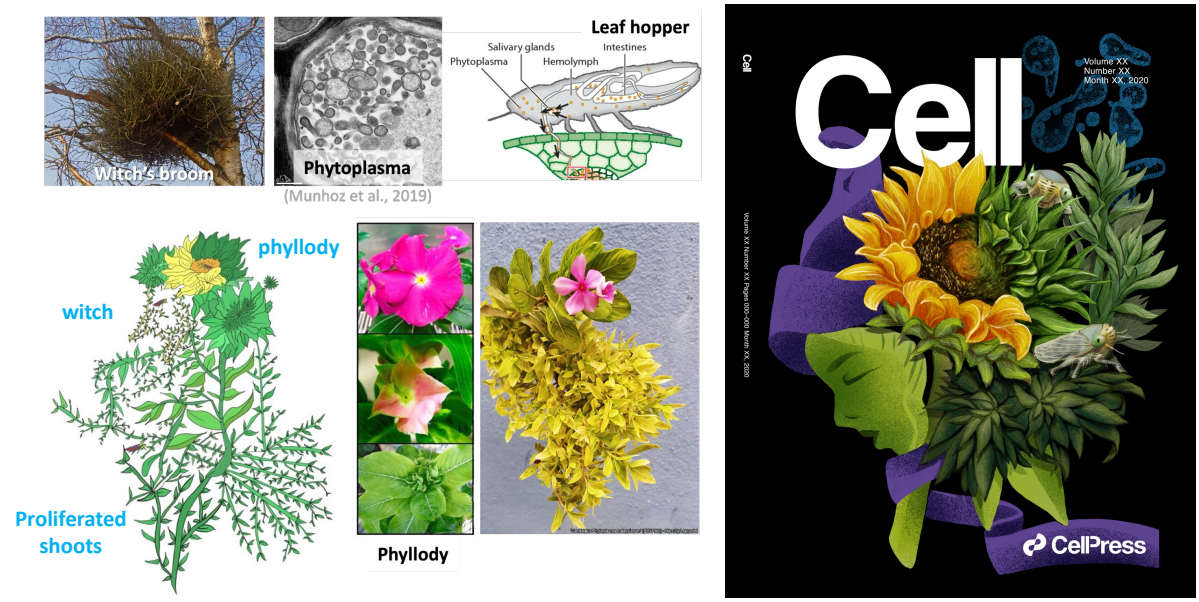


**Figure S12.** The design elements (left panels) and the final artwork (right) for the cover image "Parasitic modulation of host development by ubiquitin-independent protein degradation (Huang et al., 2021)". Bottom left shows an initial concept draft for integrating a witch's face and phytoplasma-induced disease phenotypes.

A second cover artwork was developed for "*Conserved secreted effectors contribute to endophytic growth and multihost plant compatibility in a vascular wilt fungus*" (Redkar et al., 2022). This study identified a suite of conserved early root colonization (ERC) effectors secreted by Fusarium oxysporum during the initial root interaction, determining whether the fungus behaves as a pathogen or as an endophyte across diverse plant hosts. Amey envisioned showcasing a key electron microscopy image representing the earliest colonization stage, which became the conceptual anchor of the illustration. Surrounding this focal image, we incorporated a diagram contrasting pathogenic versus endophytic hyphal behaviour, as well as botanical drawings of the host species (tomato and Marchantia) used in the study. Given The Plant Cell's **preference for photographic aesthetics, we opted for a botanical, photo-realistic style**. After exploring several layouts, we settled on a balanced split: the diagram on one side, botanical illustrations on the other, with the EM micrograph centred to unify the composition (Figure S13). **This arrangement enabled a smooth visual transition between cartoon-like elements and realistic plant imagery**, subtly bridging differences both in scale and style.

**Figure S13.** Some layout ideas (left panels) and the final artwork (right) for the cover image "Conserved secreted effectors contribute to endophytic growth and multihost plant compatibility in a vascular wilt fungus (Redkar et al., 2022)".

III-2. Communicating Science to Non-Specialists - Science Festival and Public Engagement Activities

While journal covers and research diagrams are created for scientific audiences - where the "common language" covers technical concepts and detailed mechanisms; public-facing illustrations require a very different approach (Beardsworth, 2020; Braha, 2017). **Events such as the Norwich Science Festival attract non-specialists, families, and young children, so "accessibility" becomes the primary design principle.** This involves simplifying complex ideas without distorting their meaning, using friendly anthropomorphic characters to create a welcoming tone, and bridging the topic with familiar, everyday concepts.

For the Norwich Science Festival 2021, we designed a **"*Plant Disease Hunt*" activity map** (Figure S14). The team first surveyed Chapel Field Gardens to document the plant diseases naturally present in the park, I then created an illustrated treasure-hunt–style map **encouraging visitors to explore the site and spot symptoms on real plants.** The map was paired with a set of pathogen stickers, each representing the causal agent of a specific disease. Participants could place these stickers on the map once they identified a symptom. Additional facts and explanations were provided on the reverse side. To make the activity more engaging for children, I drew the pathogens with expressive eyes and playful colours (Figure S15). Although these characters were not meant to be scientifically exact, the goal was to spark curiosity, invite participation, and motivate visitors to learn more afterward.

**Figure S14**. *Plant Disease Hunt* activity map. The front side shows a schematic map of Chapelfield Gardens indicating the approximate locations of selected diseased plants. The reverse side presents descriptive information and reference photos of the corresponding plant diseases to aid identification.

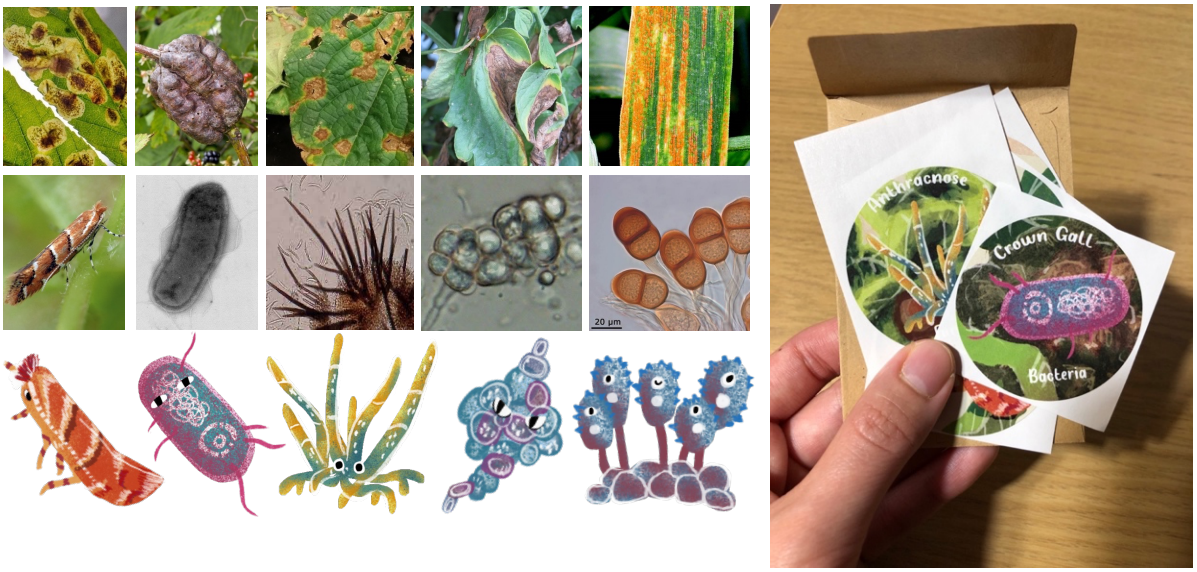


**Figure S15**. Design development for the *Plant Disease Hunt* activity map. Panels show reference photos of disease symptoms and their causal agents, alongside the corresponding cartoon pathogen characters derived from these sources. On the right is the printed plant pathogen stickers distributed to participants to mark observations on the map.

In earlier years of our public-engagement events, we focused heavily on presenting specific plant pathogens studied at the institute. But we gradually realised that many visitors especially children were unfamiliar with even the basic concept of microbes. Recognising this gap, we decided to shift our strategy toward building foundational context that help audiences grasp the unseen microbial world before diving into the details. For the Royal Norfolk Show 2025, I designed a poster that presents a progressive "zoom-in journey" through plant-associated pests and microbes (Figure S16). The illustration begins with familiar scenes - potted dwarf tomato plants and aphids - and gradually transitions into leaf tissue anatomy, microscopic fungal structures, and eventually a single plant cell populated with sub-cellular pathogens such as viruses. By starting from well-known organisms and moving stepwise into progressively smaller scales, the poster helps viewers intuitively grasp the relative size differences and understand how microscopic organisms can produce large and visible disease symptoms.

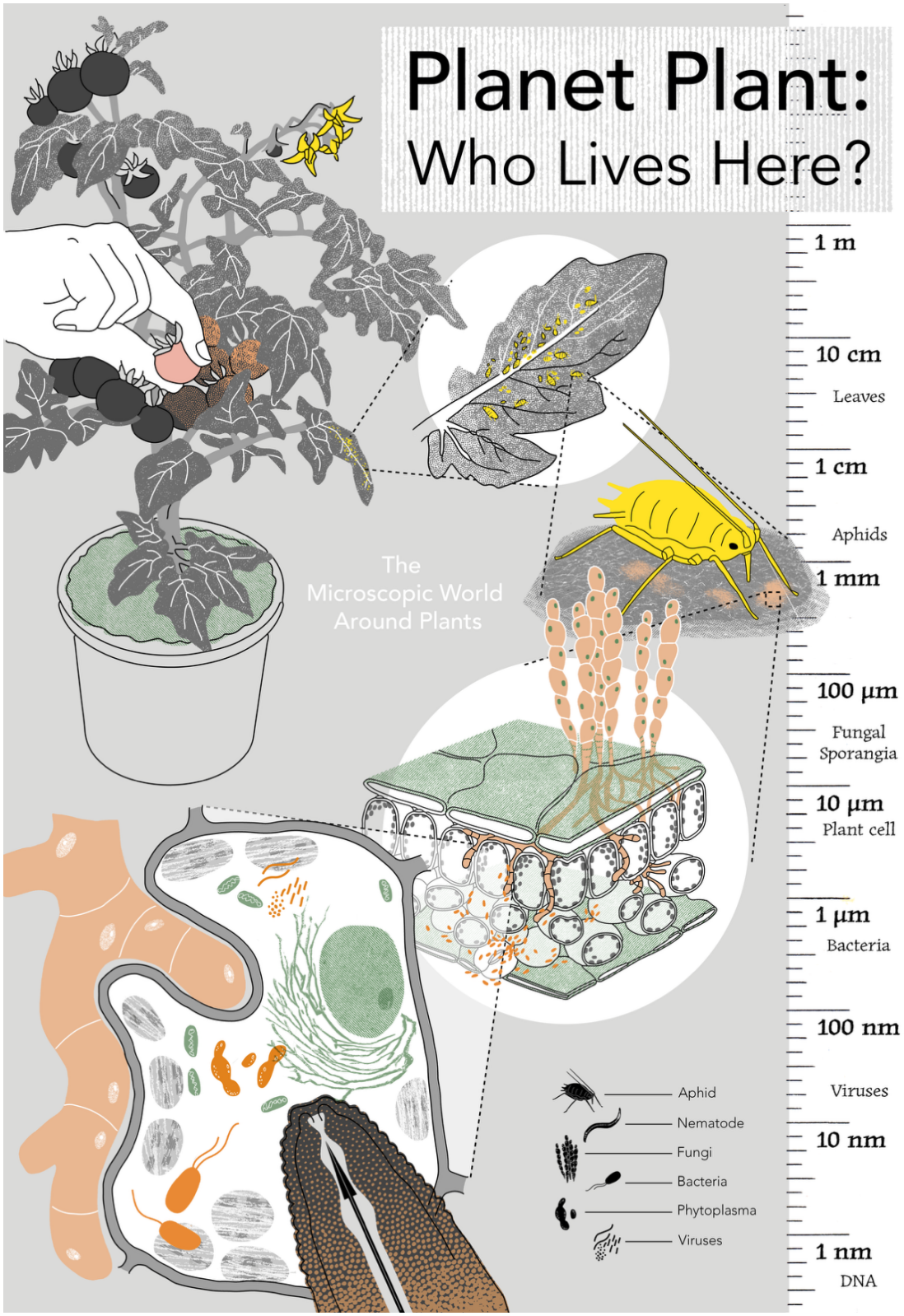


**Figure S16.** *Planet Plant: Who lives here?* A public-engagement poster presented at the Royal Norfolk Show 2025, designed to guide viewers through the diverse size scales of organisms associated with plants—from aphids and fungi to subcellular viral pathogens.

III-3. Building the GetGenome Visual Identity

Among the case studies in this chapter, the GetGenome logo and icon suite stands out as an unique example (Figure S17). Unlike my typical work which leans toward hand-drawn, character-driven illustrations, **this project required a clean, minimalist aesthetic grounded in vector graphics and brand consistency**. GetGenome is a non-profit organization dedicated to expanding equitable access to genomics technologies and training for early career scientists, and the visual identity needed to reflect its ethos of nucleic acid research, empowerment, and collaboration.

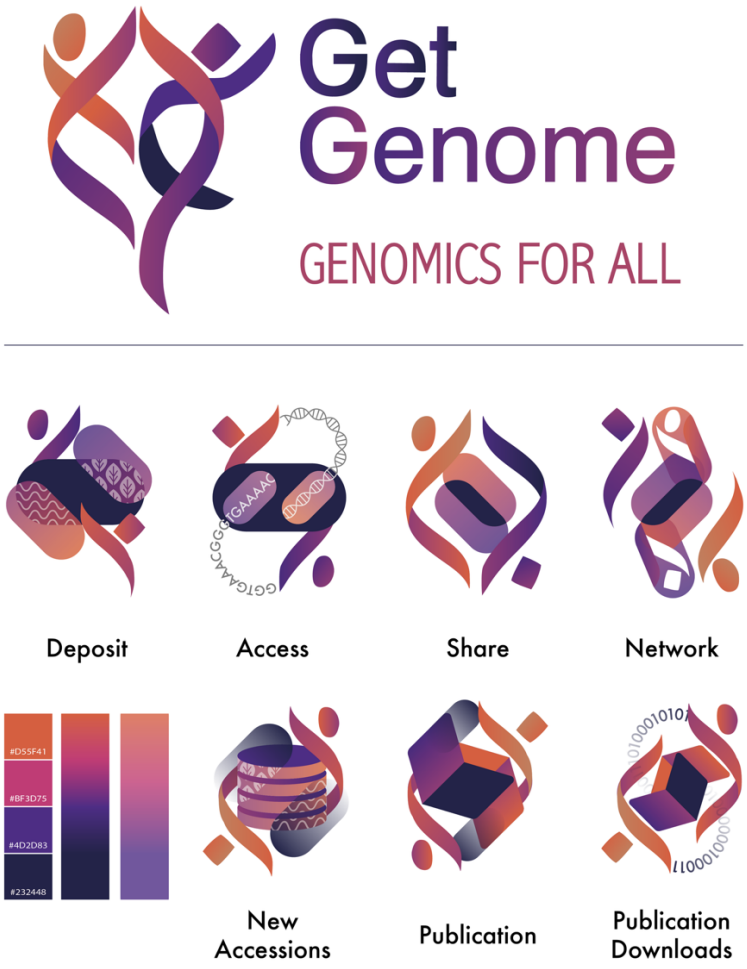


Figure S17. GetGenome logo and visual identity suite.

The design process centred on a paired DNA-helix motif: two stylized double helices integrated with human forms in dynamic poses to symbolize mutual support and growth ethos of the organisation. The name element "GET" was inspired by the app-download button, reflecting the organization's goal of making genome sequencing and data access as easy and approachable as downloading an app. Although the "GET" button was opted in the final logo design, the rounded app-icon shape continues to

appear across the extended infographic set, ensuring visual continuity and reinforcing the organisation's inclusive identity.

Although the conceptual elements of the design are straightforward, **the visual impact relied heavily on consistent colour usage and ensuring that visual rhythm is maintained across modules**. In branding, colour is one of the most powerful tools for recognition and function as immediate associative cues, allows audiences to instantly link an image with a brand. With a small set of bold, intentional hues and repetitive elements (double helices human forms and the oval shape), the approach ensures that GetGenome's visual identity remains coherent across diverse platforms while maintaining a memorable and welcoming aesthetic. Further details on the design rationale are described in Pai et al., 2024.

## IV. Personal Explorations in Sci-art

Alongside commissioned work, I also pursue **personal illustration projects that allow greater creative freedom and expression.** Unlike research-focused graphics, these artworks are not bound to strict scientific messaging; instead, they reflect my own impressions, interpretations, and imaginative responses to the microscopic world.

One example is ***"Fungal Terrarium"*** (Figure S18), which I submitted to the 2023 BSPP T-shirt competition (*https://www.bspp.org.uk/winning-plant-pathology-designs-bspp-t-shirt-competition-2023/*). This piece expresses my fascination with the often-overlooked beauty and diversity of microscopic fungi. While mushrooms are familiar to the general public, the extraordinary architectures of hyphae, conidiophores, and sporangia typically remain hidden from everyday experience. When I look at micrographs of fungal structures, they often resemble miniature forests or fantastical plants sprouting from another world. This inspired me to depict various fungal forms as if they were growing inside a terrarium—inviting viewers to imagine what it would feel like to explore these landscapes at microbial scale. Through this artwork, I hoped to evoke curiosity and appreciation for fungal biology.

Another piece that draws on microscopy is ***"Pathfinder: Phyllo-voyagers"*** (Figure S19). This illustration was inspired by my experiences working in a dark confocal microscopy room, where the fluorescent glow of organelles feels almost cosmic. Peering into plant tissues under the microscope often feels like embarking on a journey through a luminous, extraterrestrial landscape. Microbes live in ways fundamentally from us, they navigate inside other living organisms and make a new home there. With microscopes, we can glimpse into their world. In Pathfinder, I imagined myself viewing this world through the perspective of a microbe—moving through leaf tissues as if exploring an expansive universe, guided by both scientific curiosity and wonder.

Figure S18. *Fungal Terrarium*. The artwork reimagines fungal hyphae, conidiophores, and sporangia growing within a terrarium, inviting viewers to envision the microbial world at an immersive, miniature scale.

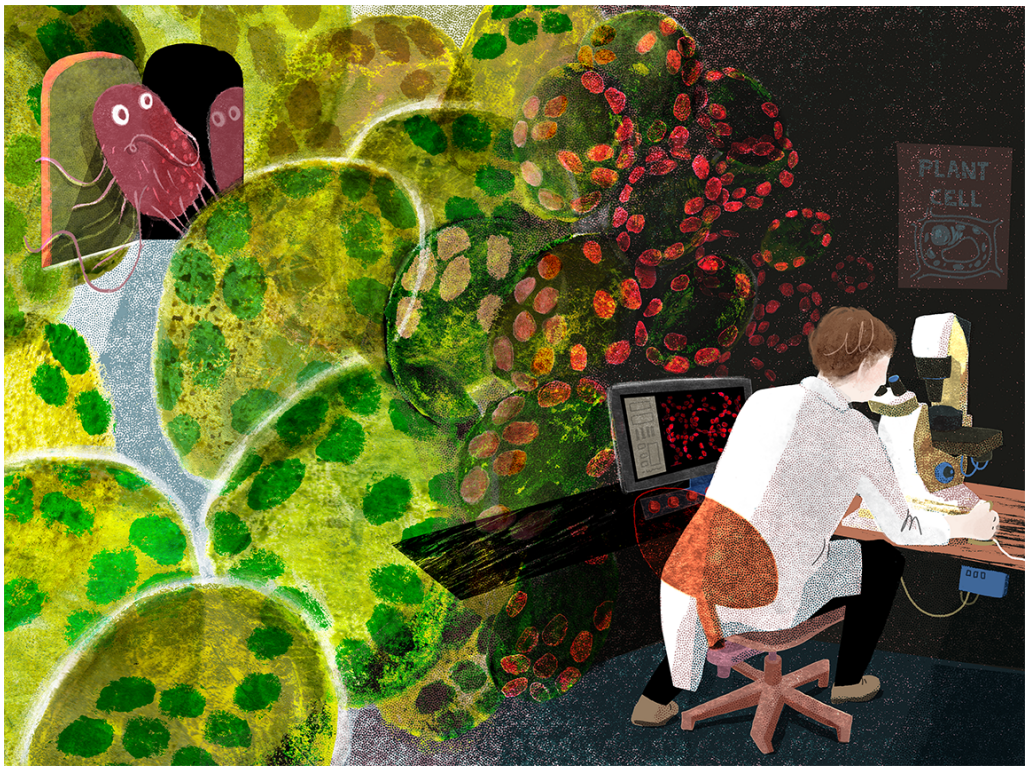


Figure S19. *Pathfinder: Phyllo-voyagers*. Microscopy-inspired illustration reflecting my experience of observing plant tissues under confocal microscopy, inviting the viewers adopting the perspective of a microbe navigating through leaf tissue.

## V. Digital Tools That Expand and Accelerate the Illustration Process

With the rapid advancement of digital and AI-driven tools, visual ideation has become more accessible. While AI still cannot fully replace manual illustration - especially when scientific precision, controlled symbolism, and stylistic consistency are required, we can still benefit from its assistance. Rather than producing final artwork, I use **AI tools to accelerate concept exploration, gathering reference, and refine colour palettes.** Below, I summarize three practical ways in which these tools have enhanced my illustration process.

**AI for rapid concept prototyping**

When preparing the cover image for "*Jurassic NLR: Conserved and dynamic evolutionary features of the atypically ancient immune receptor ZAR1*" (Adachi et al., 2023), I envisioned a playful concept integrating dinosaurs with the ZAR1 resistosome to highlight its deep evolutionary origin (Figure S20). However, it was difficult for other team members to grasp without a concrete visual example. Instead of spending hours producing a polished mock-up, I generated quick compositions combining dinosaurs and plant elements using Midjourney, and manually arranged them into a pentameric structure. **These rough AI prototypes allowed the team to immediately evaluate the direction.** Once approved, I developed the final artwork with precise species selection and curated stylistic choices.

**Figure S20**. AI-assisted rapid concept prototyping. Top left: AI-generated concept images combining dinosaurs and plants produced with Midjourney. Bottom left: manually edited prototype assembling dinosaur–plant elements into a pentameric "resistosome" composition. Right: the final refined artwork published as the journal cover.

## V-1. AI for reference generation

In some cases, illustrations require realistic lighting or three-dimensional rendering that is difficult to conceptualize without physical models. For a commentary illustration accompanying Hui et al., 2023, where we used screwdriver sets as an analogy for the modular LWY-domain architecture of Phytophthora effectors, I wanted to render the host cell background in a semi-realistic, sculptural style. AI tools such as Midjourney and DALL·E 3 helped me **generate conceptual lighting and surface references,** which I then adapted and redrew manually (Figure S21). These AI-generated models served only as guides, but they significantly improved my efficiency in developing consistent forms and spatial depth.

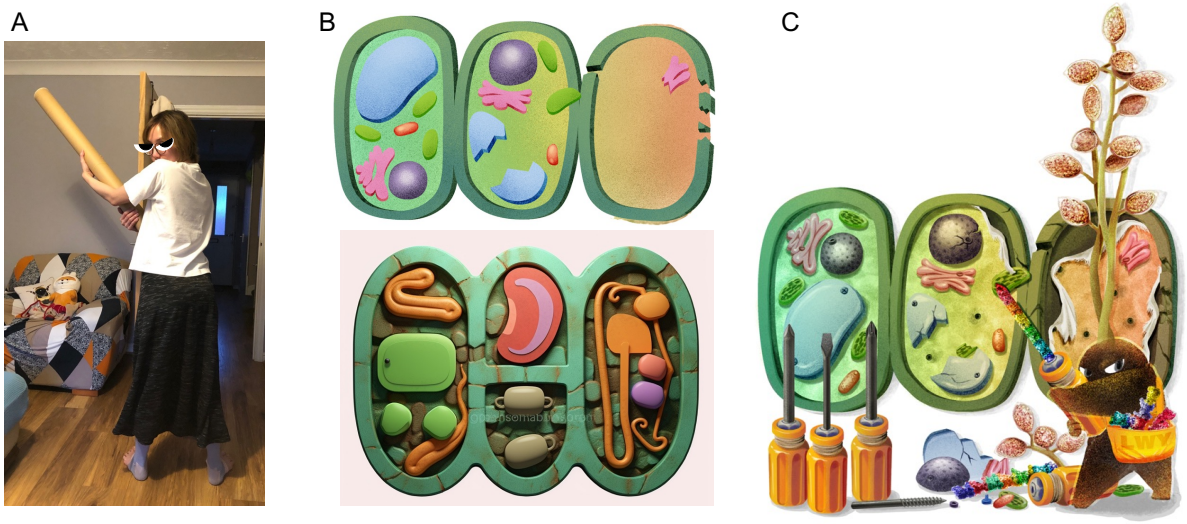


Figure S21. Use of AI tools for generating reference images. (A) Traditional reference collection, including photos sourced online or self-photographed for posture studies. (B) Top: An early illustration draft requiring reference for lighting and shading; Bottom: A corresponding reference image generated using Midjourney to study light and shadow. (C) The final completed artwork incorporating these references.

## V-2. Digital tools for colour exploration and palette extraction

**Colour selection is often subtle yet pivotal** for determining mood, clarity, and visual hierarchy. In addition to colour-blind–friendly design, building harmonious palettes from scratch can be time-consuming. **Colour palette databases** such as Coolors, ColorSpace, and Figma generators, allow quick adaptation of theme colours. Conversely, **colour-extraction tools** (e.g., TinEye, *https://labs.tineye.com/color/*) help derive palettes from reference images (Figure S22). This is not limited to scientific figures, but general photographs, posters, or paintings could all serve as references (Figure S23), providing good examples of balance and proportion of hues. For vector-based projects, **re-colouring tools** in Adobe Illustrator or Adobe Firefly allow even entire

posters to be tested with alternate schemes rapidly (Figures S24 and S25). Raster images can also be automatically traced into vectors for the same purpose. These tools streamline experimentation, ensuring that the final palette is both cohesive and intentional.

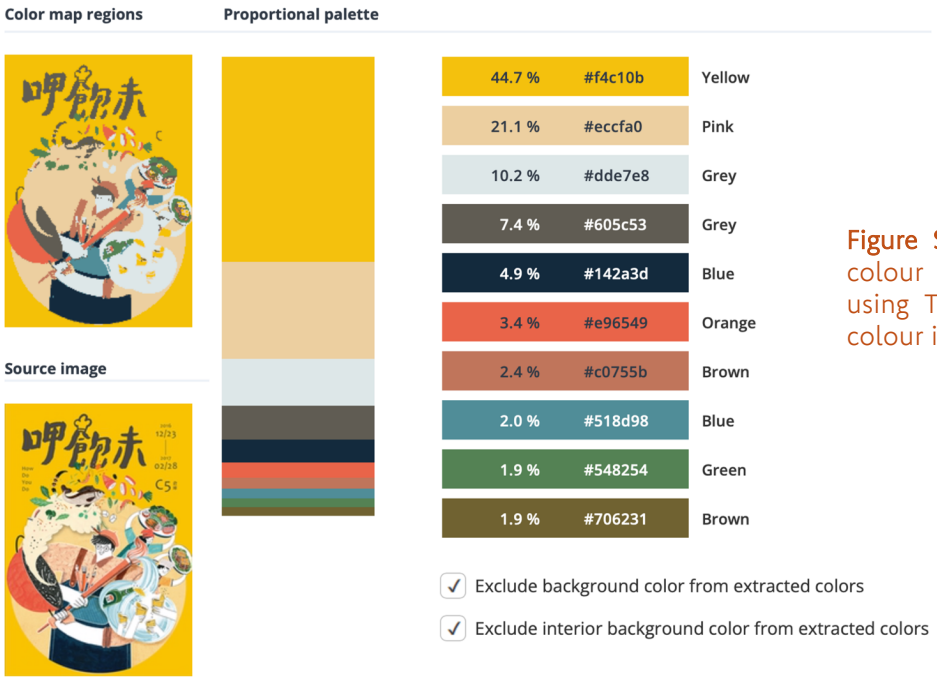


Figure S22. An example of colour extraction result by using TinEye a web-based colour identification tool.

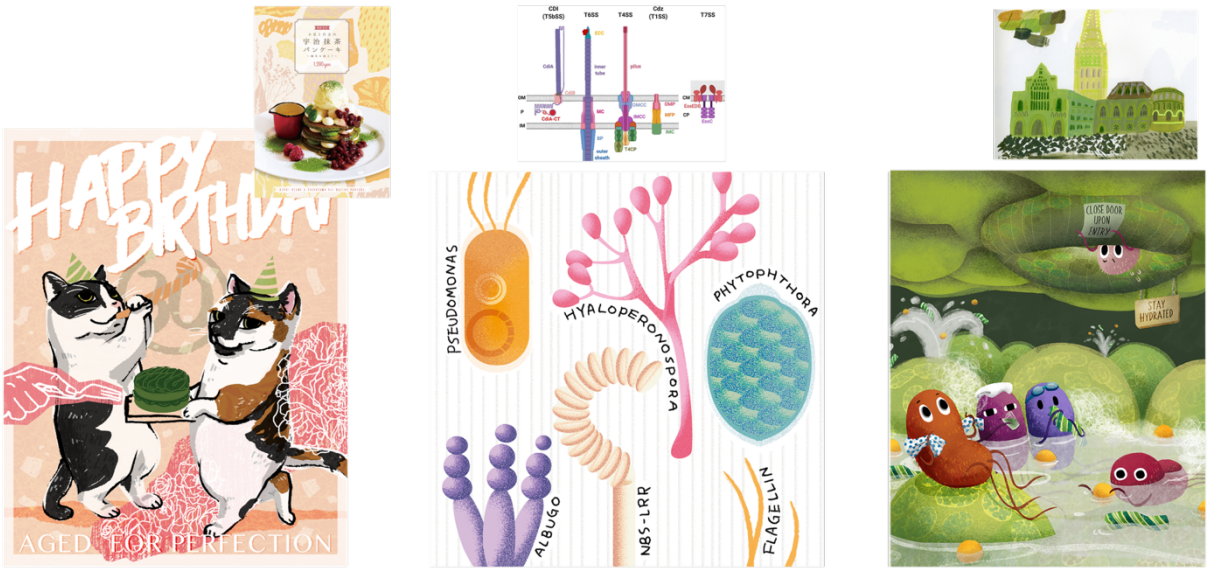


Figure S23. Some examples of my personal colour references and the application in artwork. Smaller panels are the reference images used to extract and study colour schemes, while the larger panels display finished artworks inspired by these palettes.

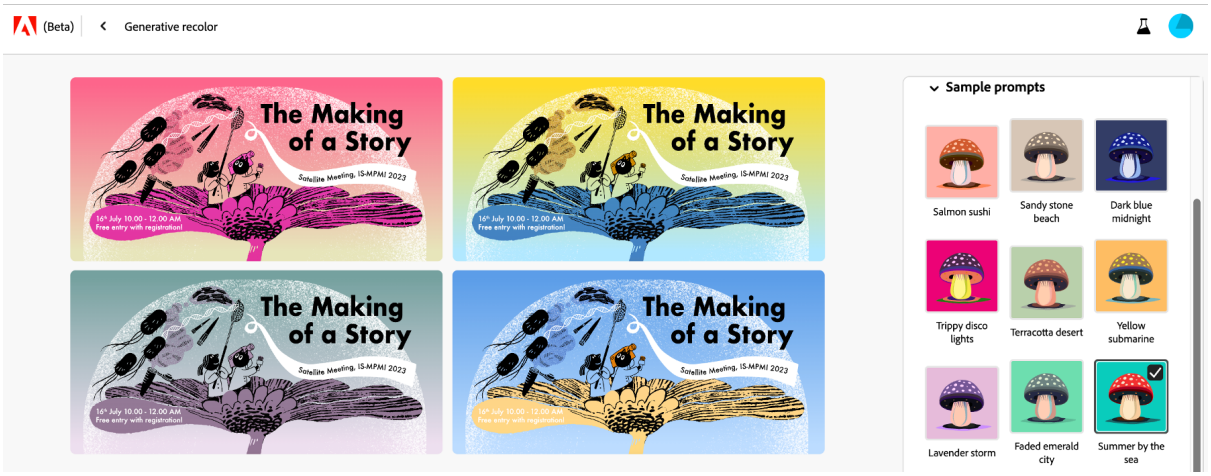


Figure S24. Examples of colour shuffling using the Adobe Firefly re-colouring tool. This tool enables rapid testing and comparison of alternative colour schemes applied to the same artwork.

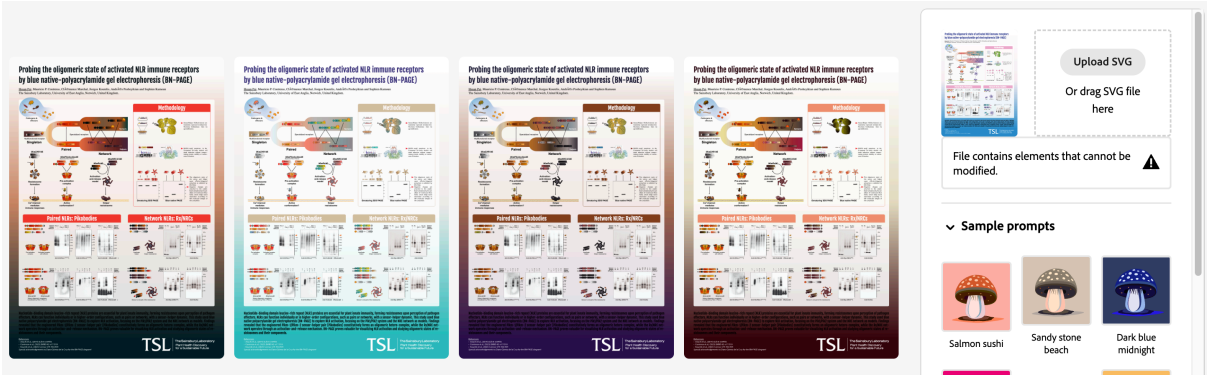


Figure S25. Application of the Adobe Firefly re-colouring tool to an entire poster.

## VI. Summary

From prehistoric cave paintings to Renaissance anatomical drawings, **humans have long used art to interpret and communicate the natural world.** Even the earliest children's picturebooks, such as *Orbis Sensualium Pictus* (Comenius, 1658, cited in Marshall, 2014) and *A Little Pretty Pocket-Book* (Newbery, 1770, cited in Miniature BookCollection), were created explicitly for education, pairing words and images to help the young readers grasp unfamiliar objects and concepts. These examples underscore a principle that has persisted across centuries: **visuals are not mere decoration, but a fundamental vehicle for transmitting knowledge.**

Although the tools and aesthetics of illustration have evolved over time, the core purpose of scientific imagery remains — **to clarify complexity, reveal the unseen, and share discoveries in accessible ways.** Historically, scientific illustrators focused on faithfully representing organisms, anatomical structures, and microscopic worlds that were otherwise inaccessible. Today, scientific illustration has expanded beyond documentation into a versatile creative practice that blends accuracy with narrative, abstraction, and visual metaphor. As Govoni (2020) argues, when an image conveys scientific truth effectively, our brains intuitively perceive it as "beautiful" - revealing an inherent harmony between aesthetics and understanding.

The rapid emergence of **AI-based image-generation tools** in 2022-2023 has further transformed the landscape of visual communication. While AI does not replace scientific illustrators and there's still room to improve for biological accuracy and conceptual nuance, it offers **powerful new ways to brainstorm, prototype, and iterate visual ideas**. As demonstrated throughout this chapter, AI-assisted workflows can accelerate early-stage ideation, provide reference material, streamline colour exploration, and support creative problem-solving, especially for scientists without formal artistic training.

Ultimately, the essence of science communication through illustration lies in its dual power: **to illuminate complexity with clarity, and to connect audiences to scientific ideas.** Whether used in research diagrams, public outreach, branding, or personal creative expression, illustrations form a bridge between scientific knowledge and human curiosity. As visualization tools continue to evolve, scientists are increasingly empowered to craft images that not only inform but inspire — extending the long tradition of using art to understand, explain, and celebrate the natural world.

# References


1. Adachi H, T Sakai, J Kourelis, H Pai, JL Gonzalez Hernandez, Y Utsumi, M Seki, A Maqbool, and S Kamoun. (2023) Jurassic NLR: Conserved and dynamic evolutionary features of the atypically ancient immune receptor ZAR1. Plant Cell 35: 3662-3685.
2. Beardsworth SJ. (2020) Building knowledge bridges through effective science communication. Chemistry 26: 1698-1702.
3. Braha J. (2017) Science communication at scientific societies. Semin. Cell Dev. Biol. 70: 85-89.
4. Bucchi M and B Trench. (2021) Rethinking science communication as the social conversation around science. JCOM 20: Y01.
5. Ciccione L, D Caroti, S Liu, V Giardino, E Pasquinelli, and S Dehaene. (2025) The superiority of graphics over text in long-term memory retention. Psychon Bull Rev. 32: 2322-2330.
6. Crameri F, GE Shephard, and PJ Heron. (2024) Choosing suitable color palettes for accessible and accurate science figures. Curr. Protoc. 4: e1126.
7. Crameri F, GE Shephard, and PJ Heron. (2020) The misuse of colour in science communication. Nat. Commun. 11: 5444
8. Ford B. (2003) Scientific Illustration in the Eighteenth Century. In: Porter R, ed. The Cambridge History of Science. The Cambridge History of Science. Cambridge University Press. 2003:561-583.
9. Govoni P. (2020) Drawing nature, building knowledge: Between beauty and 'gut feelings' in the sciences. In G. Grilli (eds) Non-fiction picturebooks : Sharing Knowledge as an Aesthetic Experience. Pisa: Edizioni ETS. pp. 205-222.
10. Huang W, AM MacLean, A Sugio, A Maqbool, M Busscher, ST Cho, S Kamoun, CH Kuo, RGH Immink, and SA Hogenhout. (2021) Parasitic modulation of host development by ubiquitin-independent protein degradation. Cell 184: 5201-5214.
11. Lee JS, M Hnilova, M Maes, YC Lin, A Putarjunan, SK Han, J Avila, and KU Torii. (2015) Competitive binding of antagonistic peptides fine-tunes stomatal patterning. Nature 522: 439-443.
12. Li H, J Wang, TA Kuan, B Tang, L Feng, J Wang, Z Cheng, J Skłenar, P Derbyshire, M Hulin, Y Li, Y Zhai, Y Hou, FLH Menke, Y Wang, W Ma. (2023) Pathogen protein modularity enables elaborate mimicry of a host phosphatase. Cell 186: 3196-3207.
13. Marshall C. (2014) The First Children's Picture Book, 1658's Orbis Sensualium Pictus. Available at: https://www.openculture.com/2014/05/first-childrens-picture-book-1658s-orbis-sensualium-pictus.html (Accessed 16 February 2023).
14. Miniature Book Collection. (no date) Available at: https://www.loc.gov/item/22005880/ (Accessed 10 April 2023).
15. Oska S, E Lerma E, and J Topf. (2020) A picture is worth a thousand views: A triple crossover trial of visual abstracts to examine their impact on research dissemination. J. Med. Internet Res.
16. Pai H, J Canham J, S Kamoun, and GetGenome. (2024) The story behind GetGenome logo and branding visuals. Zenodo 10950442.
17. Perra M and T Brinkman. (2021) Seeing science: Using graphics to communicate research. Ecosphere 12: e03786.

18. Redkar A, M Sabale, C Schudoma, B Zechmann, YK Gupta, MS López-Berges, G Venturini, S Gimenez-Ibanez, D Turrà, R Solano, A Di Pietro. (2022) Conserved secreted effectors contribute to endophytic growth and multihost plant compatibility in a vascular wilt fungus. Plant Cell 34: 3214-3232.
19. Smiciklas M. (2012) The power of infographics: Using pictures to communicate and connect with your audiences. Indianapolis, IN: Que Biz-Tech.
20. Spence C and G Van Doorn. (2022) Visual communication via the design of food and beverage packaging. Cogn. Res. Princ. Implic. 7:42.
21. Vosoughi S, D Roy, and S Aral. (2018) The spread of true and false news online. Science 359: 1146-1151.
22. Woloshin S, Y Yang, and B Fischhoff. (2023) Communicating health information with visual displays. Nat. Med. 29: 1085-1091.
23. Yetisen AK, AF Coskun, G England, S Cho, H Butt, J Hurwitz, M Kolle, A Khademhosseini, AJ Hart, A Folch, SH Yun. (2015) Art on the Nanoscale and Beyond. Adv. Mater. 28: 1724-42.
24. Zimmerman ME, MJ Katz, C Wang, LC Burns, RM Berman, CA Derby, G L'Italien, D Budd, and RB Lipton. (2015) Comparison of "word" vs. "picture" version of the free and cued selective reminding test (FCSRT) in older adults. Alzheimers Dement (Amst). 1: 94-100.

Appendix

# Letter of Support

北海道大学
HOKKAIDO UNIVERSITY

Faculty of Advanced Life Science,
Hokkaido University,
N10, W8, Kita-ku,
Sapporo 060-0810, Japan
Tel: +81-11-706-3807
Email: hadachi@sci.hokudai.ac.jp

21st November 2025

**Re: Support Letter for Hsuan Pai – PhD by Publication Submission**

To whom it may concern,

I am writing to confirm that I fully support the inclusion of the following publications in Hsuan Pai's PhD by Publication thesis:

> Adachi H, T Sakai, J Kourelis, H Pai, JL Gonzalez Hernandez, Y Utsumi, M Seki, A Maqbool, and S Kamoun. (2023) Jurassic NLR: Conserved and dynamic evolutionary features of the atypically ancient immune receptor ZAR1. The Plant Cell 35:3662-3685.
>
> Harant A, H Pai, T Sakai, S Kamoun, and H Adachi. (2022) A vector system for fast-forward studies of the HOPZ-ACTIVATED RESISTANCE1 (ZAR1) resistosome in the model plant *Nicotiana benthamiana*. Plant Physiology 188:70-80.

Pai was a great colleague when I was a postdoc at the Sainsbury Laboratory. Pai made important contributions to both studies, including performing experiments, data analysis, construct design and method development, all of which were essential to the successful completion of these publications. I am very pleased to support the use of these papers as evidence of Pai's research accomplishments and scholarly contributions.

Without a doubt, I believe that Pai's research experience, technical expertise, and consistent dedication make her a strong candidate for the PhD by Publication program.

Yours sincerely,

**Hiroaki Adachi**
Associate Professor
Faculty of Advanced Life Science,
Hokkaido University

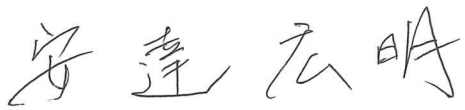

EBERHARD KARLS
UNIVERSITÄT
TÜBINGEN

ZMBP-Pflanzenbiochemie· Auf der Morgenstelle 32 · 72076 Tübingen

**Mathematisch-Naturwissenschaftliche Fakultät**

**Zentrum für MolekularBiologie der Pflanzen (ZMBP)**
**www.zmbp.uni-tuebingen.de**

**Pflanzenbiochemie – Biochemie pflanzlicher Systeme**

**Dr. Mauricio Contreras**
Forschungsgruppenleiter
Telefon +49 7071-29-76657
Telefax +49 7071-29-5226
mauricio.contreras@zmbp.uni-tuebingen.de

**Oxana Bill**
Sekretariat
Telefon +49 7071 29-76657
Telefax +49 7071 29-5226
oxana.bill@zmbp.uni-tuebingen.de

**To whom it may concern,**

I am writing to express my strong support for Ms. Hsuan Pai's application for a PhD by Publication. I worked closely with Hsuan during her time as a research technician in the Kamoun Lab at The Sainsbury Laboratory (TSL), Norwich, where she made substantial contributions to several major research studies focused on the molecular mechanisms of plant innate immunity, particularly the biochemical activation of NLR immune receptors.

Hsuan's technical and scientific contributions were consistently of exceptional quality. She worked across a broad methodological spectrum, including Golden Gate cloning, transient expression assays in *Nicotiana benthamiana*, BN-PAGE biochemical analysis, and early-stage cryo-EM workflows for native protein complexes. Her experimental skill, troubleshooting ability, attention to detail and creative scientific thinking were instrumental to the success of numerous high-impact publications.

One of Hsuan's key breakthroughs in the lab was establishing and optimizing BN-PAGE assays to study plant NLR activation. By leveraging these biochemical readouts, she played a central role in two major publications from the lab in 2023 (*Contreras et al.* 2023a and 2023b). Using BN-PAGE together with complementary biochemical approaches, Hsuan helped develop the "Activation and Release" model for paired NLR signalling and contributed to demonstrating how pathogen effectors interfere with this process by targeting helper NLRs.

Importantly, Hsuan is **co–first author** on *Contreras et al.* (2024), where her contributions were essential to uncovering the minimal domains within sensor NLRs that are sufficient to activate downstream helper NLRs and trigger immune signalling. In this study she:

- produced key BN-PAGE data demonstrating NRC2 oligomerization;
- performed core agroinfiltration assays supporting our sensor–helper activation model;
- generated and optimized constructs used throughout the project;
- contributed to manuscript writing and editing, and prepared draft figures that shaped the structure and presentation of the final paper;
- participated actively in data interpretation and internal review.

Hsuan is also first author of the BN-PAGE methods paper (*Pai et al.*, Zenodo 2023), reflecting her leadership in establishing a robust and widely used pipeline for analysing NLR resistosome states directly from plant tissue as well as her commitment to open science and to sharing her methods with the broader scientific community.

She further contributed substantially to several other peer-reviewed publications, including but not limited to *Adachi et al.* 2023 (ZAR1 evolution), *Kourelis et al.* 2022 (PTI–ETI coordination in the NRC network), and *Harant et al.* 2022 (ZAR1 toolkit development). Across these projects she performed critical cloning work, transient-expression assays, and biochemical analyses.

In addition to her published work, Hsuan is a co-author on a manuscript currently in preparation:

• *Pai H, MP Contreras, J Salguero Linares, D Lüdke, A Posbeyikian, J Kourelis, S Kamoun, and C Marchal.* (In preparation) **The Pik NLR pair accumulates at the plasma membrane as a hetero-oligomeric sensor–helper immune protein complex prior to activation.**

Hsuan contributed BN-PAGE experiments, construct generation, and experimental optimization essential for demonstrating the pre-activation assembly and membrane localization of the Pik NLR pair from rice.

**I also confirm my agreement for Ms. Pai to include the following publications—on which she made significant contributions—in her PhD by Publication thesis:**

1. **Kourelis J, MP Contreras, A Harant, H Pai, D Lüdke, H Adachi, L Derevnina, CH Wu, and S Kamoun. (2022)**
   *The helper NLR immune protein NRC3 mediates the hypersensitive cell death caused by the cell-surface receptor Cf-4.*
   *PLOS Genetics* 18:e1010414.
2. **Contreras MP, H Pai, C Marchal, R Thompson, J Claeys, H Adachi, and S Kamoun. (2024)**
   *The nucleotide binding domain of NRC-dependent disease resistance proteins is sufficient to activate downstream helper NLR oligomerization and immune signaling.*
   *New Phytologist* 243:345–361.
3. **Contreras MP, H Pai, Y Tumtas, C Duggan, ELH Yuen, A Vergara Cruces, J Kourelis, HK Ahn, KT Lee, CH Wu, TO Bozkurt, L Derevnina, and S Kamoun. (2023)**
   *Sensor NLR immune proteins activate oligomerization of their NRC helpers in response to plant pathogens.*
   *EMBO Journal* 42:e111519.
4. **Contreras MP, H Pai, M Selvaraj, A Toghani, DM Lawson, Y Tumtas, C Duggan, ELH Yuen, CEM Stevenson, A Harant, CH Wu, TO Bozkurt, S Kamoun, and L Derevnina. (2023)**
   *Resurrection of plant disease resistance proteins via helper NLR bioengineering.*
   *Science Advances* 9:3861.
5. **Sugihara Y, J Kourelis, MP Contreras, H Pai, M Selvaraj, A Toghani, C Martínez-Anaya, and S Kamoun. (2025)**
   *Helper NLR immune protein NRC3 evolved to evade inhibition by a cyst nematode virulence effector.*
   *PLOS Genetics* 21:e1011653.

Across all projects, Hsuan displayed scientific maturity far exceeding what is typically expected of a research technician. She engaged deeply with conceptual aspects of the work, proposed methodological improvements, documented experiments thoroughly, and consistently generated reproducible, publication-quality data. Her body of work forms a coherent and substantial foundation for a PhD by Publication.

I fully and wholeheartedly support Hsuan's application. Her scientific contributions, independence, and commitment to excellence merit formal recognition through this pathway.

Please feel free to contact me if further information is required.

**Yours sincerely,**
**Dr. Mauricio P. Contreras**
Junior Group Leader
Center for Plant Molecular Biology (ZMBP)
University of Tübingen

植物暨微生物學研究所
Institute of Plant and Microbial Biology

27 November 2025

Ting-Yu Chen
Institute of Plant and Microbial Biology
Academia Sinica
Taipei, Taiwan 115
Tel: +886-2-27899590
tine@as.edu.tw

Re: Letter of Support for Hsuan Pai – PhD by publication

To whom it may concern.

I am writing to confirm that Hsuan Pai played a key role in our research project investigating antiviral mechanisms in *Phalaenopsis*. I have worked closely with Hsuan since she joined my laboratory as a Master's student, during which time she developed and established essential molecular biology methods for orchid research that were critical for the success of the project.

Hsuan was instrumental in the execution of the experimental work, data analysis, and preparation of project reports. The outcomes of this research contributed to several publications, including the paper listed below, for which I served as lead author. Her contributions to this work encompassed experimental design, data curation, data analysis, and visualisation, and her efforts were fundamental to the development of the final manuscript.

Chen TY, H Pai, LY Hou, SC Lee, TT Lin, CH Chang, FC Hsu, YH Hsu and NS Lin. (2019) Dual resistance of transgenic plants against *Cymbidium mosaic virus* and *Odontoglossum ringspot virus*. Scientific Reports 9:10230.

I have no doubt that Hsuan's scientific contributions were central to the successful publication of this work and the associated studies arising from the project. I therefore offer her my full and enthusiastic support as a candidate for a PhD degree at the University of East Anglia.

Yours sincerely,

Ting-Yu Chen ting-yu Chen

Senior Research Assistant

TSL
The Sainsbury Laboratory
Plant Health Discovery
for a Sustainable Future

Norwich Research Park
Norwich NR4 7UH
United Kingdom
+44 (0)1603 450 400
admin@TSL.ac.uk
www.TSL.ac.uk

30 November 2025

Dr Adeline Harant
The Sainsbury Laboratory
Norwich Research Park
Norwich
NR4 7UH
United Kingdom
Tel: 07801493774
adeline.harant@tsl.ac.uk

Re: Letter of Support for Hsuan Pai – PhD by publication

To whom it may concern.

I am writing this letter in support of Hsuan Pai as a candidate for a PhD degree at the University of East Anglia. Hsuan Pai started working with us in 2019 as a laboratory technician.

I can confirm that concerning the following papers, Hsuan Pai contributed to the design of investigation, visualisation, data curation and data analysis. Her work has been instrumental in the developments of these manuscripts.

1. Kourelis J, MP Contreras, A Harant, H Pai, D Lüdke, H Adachi, L Derevnina, CH Wu, and S Kamoun. (2022) The helper NLR immune protein NRC3 mediates the hypersensitive cell death caused by the cell-surface receptor Cf-4. PLoS Genetics 18:e1010414.

2. Harant A, H Pai, T Sakai, S Kamoun, and H Adachi. (2022) A vector system for fast-forward studies of the *HOPZ-ACTIVATED RESISTANCE1 (ZAR1)* resistosome in the model plant *Nicotiana benthamiana*. Plant Physiology 188:70-80.

I have no doubt that the contributions of Hsuan Pai to the above papers was key in getting these papers published. I strongly support her in reaching this recognition of her achievements.

Yours sincerely,

Dr Adeline Harant

Senior Research Assistant

The Sainsbury Laboratory is a registered charity number 1065510, and a registered company limited by guarantee number 03346853 in England & Wales
Registered office: John Innes Centre, Norwich Research Park, Norwich NR4 7UH, United Kingdom
Executive Director: Professor Nick Talbot FRS

Department of Plant Pathology & Crop Physiology
302 Life Science Building
Louisiana State University
Baton Rouge, LA 70803
Telephone: 225-578-1464

25th November 2025

To whom it may concern,

Re: Hsuan Pai - PhD by publication candidate

I am writing this letter to support Hsuan Pai as a candidate for the PhD by publication at the University of East Anglia.

I met Hsuan as a lab mate in Institute of Plant and Microbial Biology, Academia Sinica (Taipei, Taiwan) at the end of 2013. We have worked closely as a team to reveal the pathogenicity and defense mechanism in the pathosystem of plant viruses, *Cymbidium mosaic virus* and *Odontoglossum ringspot virus*, and their hosts, orchids.

Hsuan and I with other team members cooperated to design, perform and execute the experiments, as well as analyzing data. We did solve many issues and difficulties during this project. These have led to two publications listed below.

1. Lee SC, **H Pai**, YW Huang, MH He, YL Song, SY Kuo, WC Chang, YH Hsu, and NS Lin. (2021) Exploring the multifunctional roles of *Odontoglossum ringspot virus* P126 infacilitating *Cymbidium mosaic virus* cell-to-cell movement during mixed Infection. Viruses 13:1552.
2. Chen TY, **H Pai**, LY Hou, SC Lee, TT Lin, CH Chang, FC Hsu, YH Hsu and NS Lin. (2019) Dual resistance of transgenic plants against *Cymbidium mosaic virus* and *Odontoglossum ringspot virus*. Scientific Reports 9:10230.

I am happy to recommend Hsuan Pai as a Ph. D.

Yours Sincerely,

Shu-Chuan Lee

Dr. Shu-Chuan Lee

Postdoctoral Researcher
Department of Plant Pathology and Crop Physiology
302 Life Science Building/ Office LSB 455
Louisiana State University - AgCenter
Baton Rouge, LA 70803
Phone: (225)249-9054

Dr. M. Selvaraj, Ph.D.,
Postdoctoral researcher,
Max Planck Institute of Biochemistry,
Martinsried, Germany
23rd Nov 2025

Subject: Support letter to Hsuan Pai Ph.D thesis:

1. Selvaraj, M, A Toghani, H Pai, Y Sugihara, J Kourelis, ELH Yuan, T Ibraham, H Zhao, RR Xie,A Maqbool, JC De la Concepcion, MJ Banfield, L Derevnina, B Petre, DM Lawson, TO Bozjurt, CH Wu, S Kamoun, and MP Contreras. (2023) Activation of plant immunity through conversion of a helper NLR homodimer into a resistosome. PLoS Biol. 22: e3002868.

Dear Sir/Madam,

I am writing this letter to confirm the key role played by Hsuan Pai in the above manuscript by providing strong technical support in the functional assay involved in this publication. Pai characterized all the mutants discussed in the paper through agroinfiltration, western blots and blue native PAGE assays.

Her experiments helped us to conclude the effect of mutation on the resting state of helper NLR and to device a model for activation. She made clean figures, wrote her experimental sections in manuscript, attended to reviewers comment and submitted the revised version.

Thank you

Yours sincerely,

Selvaraj Muniyandi

TSL The Sainsbury Laboratory

Norwich Research Park
Norwich NR4 7UH
United Kingdom
+44 (0)1603 450 400
admin@TSL.ac.uk
www.TSL.ac.uk

To Whom It May Concern: 24 November 2025

**Re: Request for Letter of Support – Hsuan Pai**

I am writing to confirm Hsuan Pai's contributions to the publications listed below. Over the years I have worked with Pai closely and she has had key roles in all the mentioned papers. The details of her contributions to each publication are available under the "Author Contributions" section for each publication, respectively. Please do not hesitate to contact me should you have any questions.

1. **Pai H**, T Sakai, A Posbeyikian, R Frijters, Y Sugihara, MP Contreras, J Kourelis, H Adachi, S Kamoun, and AA Toghani. (2025) A hierarchical immune receptor network in lettuce reveals contrasting patterns of evolution in sensor and helper NLRs. bioRxiv 2025.02.25.639832.

2. Sugihara Y, J Kourelis, MP Contreras, **H Pai**, M Selvaraj, A Toghani, C Martínez-Anaya, and S Kamoun. (2024) Helper NLR immune protein NRC3 evolved to evade inhibition by a cyst nematode virulence effector. BioRxiv DOI:10.1101/2024.06.16.598756.

3. Selvaraj, M, A Toghani, **H Pai**, Y Sugihara, J Kourelis, ELH Yuan, T Ibraham, H Zhao, RR Xie,A Maqbool, JC De la Concepcion, MJ Banfield, L Derevnina, B Petre, DM Lawson, TO Bozjurt, CH Wu, S Kamoun, and MP Contreras. (2023) Activation of plant immunity through conversion of a helper NLR homodimer into a resistosome. PLoS Biol. 22: e3002868.

With best wishes,

AmirAli Toghani

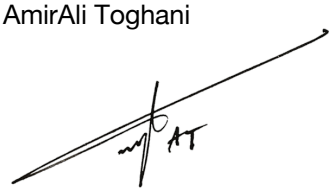

THE SAINSBURY LABORATORY

# Letter of Support

I am writing to confirm my full support for Hsuan Pai's PhD by Publication thesis under the supervision of Professor Sophien Kamoun. I am pleased to grant my permission for the inclusion of the following publications, in which I was a co-author:

1. **Sugihara Y, J Kourelis, MP Contreras, H Pai, M Selvaraj, A Toghani, C Martínez-Anaya, and S Kamoun. (2025)**
   *Helper NLR immune protein NRC3 evolved to evade inhibition by a cyst nematode virulence effector.*
   *PLoS Genet.* 21:e1011653.

2. **Selvaraj M, A Toghani, H Pai, Y Sugihara, J Kourelis, ELH Yuan, T Ibraham, H Zhao, RR Xie, A Maqbool, JC De la Concepcion, MJ Banfield, L Derevnina, B Petre, DM Lawson, TO Bozjurt, CH Wu, S Kamoun, and MP Contreras. (2023)**
   *Activation of plant immunity through conversion of a helper NLR homodimer into a resistosome.*
   *PLoS Biol.* 22:e3002868.

I understand that these works are included in chapters describing the BN-PAGE and cryo-EM methodology pipeline, and I am happy to support their use in her thesis.

Sincerely yours,

**Yu Sugihara**
Team Leader
The Sainsbury Laboratory
Norwich Research Park
NR4 7UH United Kingdom
email: yu.sugihara@tsl.ac.uk

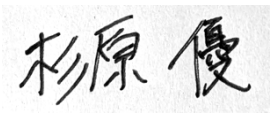

Appendix

# Submitted Publications

bioRxiv preprint doi: https://doi.org/10.1101/2025.02.25.639832; this version posted February 25, 2025. The copyright holder for this preprint (which was not certified by peer review) is the author/funder, who has granted bioRxiv a license to display the preprint in perpetuity. It is made available under aCC-BY 4.0 International license.

# A hierarchical immune receptor network in lettuce reveals contrasting patterns of evolution in sensor and helper NLRs

Hsuan Pai[1], Toshiyuki Sakai[2], Andres Posbeyikian[1], Raoul Frijters[3], Yu Sugihara[1,2], Mauricio P. Contreras[1], Jiorgos Kourelis[4], Hiroaki Adachi[2,5], Sophien Kamoun[1]*, AmirAli Toghani[1]*

1. The Sainsbury Laboratory, University of East Anglia, Norwich Research Park, Norwich, United Kingdom

2. Laboratory of Crop Evolution, Graduate School of Agriculture, Kyoto University, Kyoto, Japan

3. Rijk Zwaan Breeding B.V., Department of Biotechnology, Fijnaart, The Netherlands

4. Department of Life Sciences, Imperial College, London, United Kingdom

5. JST-PRESTO, Saitama, Japan

**Author for correspondence:**

amirali.toghani@tsl.ac.uk (A.T.)

sophien.kamoun@tsl.ac.uk (S.K.)

bioRxiv preprint doi: https://doi.org/10.1101/2025.02.25.639832; this version posted February 25, 2025. The copyright holder for this preprint (which was not certified by peer review) is the author/funder, who has granted bioRxiv a license to display the preprint in perpetuity. It is made available under aCC-BY 4.0 International license.

# ABSTRACT

Nucleotide-binding domain and leucine-rich repeat immune receptors (NLRs) are known for their rapid evolution, even at the intraspecific level, yet the rates of evolution differ significantly across various NLR classes. Within the NRC (NLR Required for Cell Death) network, NLRs operate in complex sensor-helper configurations to confer immunity against a diverse array of pathogens, particularly in Asterids. While helper NLRs are typically conserved and evolve slowly, sensor NLRs tend to evolve more rapidly. However, the functional connections between slow and fast-evolving NLRs remain poorly understood, notably in important crop species. We conducted a comparative analysis of NLRs across 40 Solanales and 29 Asterales genomes to explore NRC network expansion and diversification within the less-studied Asterales order. Our findings reveal that the NRC network has expanded less in Asterales compared to Solanales. We functionally validated a minimal Asterales NRC network with 2 helpers and 9 sensors in common lettuce (*Lactuca sativa*). Through selection and diversification analysis and structural modeling of NRC helper and sensor subclades in the *Lactuca* genus, we found varying evolutionary diversification rates between NRC helpers and sensors. We found a correlation between sensor diversification rates and helper dependency, with sensors reliant on a phylogenetically conserved helpers experiencing limited diversification pressure. Our results highlight the lineage- and function-specific evolution of the NRC network, offering insights into the evolutionary pressures shaping plant immune receptor networks.

bioRxiv preprint doi: https://doi.org/10.1101/2025.02.25.639832; this version posted February 25, 2025. The copyright holder for this preprint (which was not certified by peer review) is the author/funder, who has granted bioRxiv a license to display the preprint in perpetuity. It is made available under aCC-BY 4.0 International license.

# INTRODUCTION

Plants possess a sophisticated innate immune system to defend against a wide array of pathogens (Jones and Dangl 2006; Kourelis and van der Hoorn 2018). A group of intracellular immune receptors, known as nucleotide-binding domain and leucine-rich repeat-containing receptors (NLRs), are essential components of this defense system. These receptors detect pathogen-secreted effector proteins. Upon recognition, NLRs trigger a cascade of defense responses, often culminating in a localized programmed cell death that effectively restricts pathogen spread (Jones et al. 2016; Contreras et al. 2023a). NLR proteins represent one of the most diverse protein families, with different NLR clades evolving at varying rates (Van de Weyer et al. 2019; Prigozhin and Krasileva 2021). However, the relationship between the rate of NLR evolution and their functional roles remains poorly understood.

NLR proteins are typically composed of three main domains: an N-terminal domain, often a coiled-coil (CC) or Toll-interleukin receptor (TIR), which is responsible for signal transduction; a central NB-ARC (nucleotide-binding domain shared with APAF-1, plant R proteins, and CED-4) domain which and plays a role in regulating activation and signaling; and a C-terminal leucine-rich repeat (LRR) domain, which directly or indirectly facilitates pathogen detection (Kourelis and van der Hoorn 2018; Duxbury et al. 2021; Kourelis et al. 2021). Based on their NB-ARC phylogeny, NLRs are classified into four subclades: CC-NLRs (CNLs), $CC_{G10}$-type CC-NLRs, RPW8-type CC-NLRs ($CC_R$-NLRs/RNLs), and TIR-NLRs (TNLs) (Kourelis et al. 2021; Lee et al. 2021). While the tripartite architecture is largely conserved, some NLRs contain additional or non-canonical domains, such as integrated

bioRxiv preprint doi: https://doi.org/10.1101/2025.02.25.639832; this version posted February 25, 2025. The copyright holder for this preprint (which was not certified by peer review) is the author/funder, who has granted bioRxiv a license to display the preprint in perpetuity. It is made available under aCC-BY 4.0 International license.

63 domains (IDs), which contribute to pathogen detection (Cesari et al. 2014; Maqbool
64 et al. 2015; Baggs et al. 2017; Grund et al. 2019). About 20% of CC-NLRs harbor a
65 conserved N-terminal MADA motif essential for triggering cell death (Adachi et al.
66 2019a). Activated CC-NLRs often form higher-order complexes called
67 “resistosome” (Wang et al. 2019; Förderer et al. 2022; Zhao et al. 2022; Liu et al.
68 2024; Madhuprakash et al. 2024), which likely insert into the plasma membrane to
69 act as calcium channels via their N-terminal alpha-helix (Wang et al. 2019; Bi et al.
70 2021; Jacob et al. 2021). Recent advances in computational structural biology have
71 allowed for modeling NLR resistosomes in the presence of simulated plasma
72 membrane with high confidence (Madhuprakash et al. 2024; Toghani et al. 2024).

73 While some NLRs function as independent units, many form pairs or
74 networks of specialized NLRs to enhance evolvability and robustness of immune
75 responses (Wu et al. 2018; Contreras et al. 2023a). NLR pairs, often clustered
76 genetically, work together, such as Pik-1/Pik-2 and RGA5/RGA4 CC-NLR pairs in
77 rice (*Oryza sativa*) and the RPS4/RRS1 TIR-NLR pair in *Arabidopsis thaliana*
78 (Narusaka et al. 2009; Cesari et al. 2014; Le Roux et al. 2015; Maqbool et al. 2015;
79 Sarris et al. 2015; Shimizu et al. 2022; Sugihara et al. 2023). In NLR networks,
80 sensor NLRs depend on helper NLRs for immunity, following one-to-many or many-
81 to-one configurations (Wu et al. 2017, 2018; Adachi et al. 2019b; Contreras et al.
82 2023a). For instance, the $CC_R$-NLRs NRG1 and ADR1 can function downstream of
83 the TIR-NLR signaling pathway (Qi et al. 2018; Castel et al. 2019; Lapin et al. 2019;
84 Saile et al. 2020). The NRC network, first identified in Solanaceae plants like tomato
85 and *Nicotiana benthamiana*, also exemplifies a CC-NLR network, where sensor
86 NLRs rely on NRC helpers (NRC-H) to activate immune responses (Wu et al. 2017,

bioRxiv preprint doi: https://doi.org/10.1101/2025.02.25.639832; this version posted February 25, 2025. The copyright holder for this preprint (which was not certified by peer review) is the author/funder, who has granted bioRxiv a license to display the preprint in perpetuity. It is made available under aCC-BY 4.0 International license.

2018). NRC-dependent sensors (NRC-S) are divided into two subtypes based on domain architecture: Rx-type sensors have a canonical CC-NB-ARC-LRR structure, while SD-type sensors include an additional N-terminal Solanaceous Domain (SD) that contributes to pathogen recognition (Li et al. 2019; Seong et al. 2020; Contreras et al. 2023a; Lüdke et al. 2023). Upon pathogen effector detection, NRC sensors transmit a signal that triggers the assembly of helper NRCs from a homodimer resting state into hexameric resistosomes that induce immune responses and cell death (Contreras et al. 2022; Ahn et al. 2023; Liu et al. 2024; Madhuprakash et al. 2024; Selvaraj et al. 2024). Though the exact mechanism of signal transmission between sensor and helper NRCs remains unclear, it likely involves transient “activation-and-release” interactions (Contreras et al. 2022; Ahn et al. 2023).

The NRC network superclade, consisting of NRC-H and NRC-S, likely originated ~100 million years ago within the superasterid lineage of land plants and has expanded massively in the lamiid lineage (Wu et al. 2017; Goh et al. 2024; Sakai et al. 2024). While particularly prominent in Solanaceae, its expansion and complexity vary across plant families (Goh et al. 2024). *NRC0*, the most conserved and ancient NRC helper in asterids, represents the ancestral state of the NRC network and is frequently genetically linked to its dependent NRC-S (Goh et al. 2024; Sakai et al. 2024). In contrast, other NRC subclades have undergone lineage-specific expansions and exhibit diverse genomic arrangements, with some NRC-H clustered alongside NRC-S, such as *NRC6*, and others dispersed throughout the genome (Wu et al. 2020; Lüdke et al. 2023; Goh et al. 2024). While sensor NLRs evolve rapidly to counter pathogen evolution, helper NLRs are typically more

bioRxiv preprint doi: https://doi.org/10.1101/2025.02.25.639832; this version posted February 25, 2025. The copyright holder for this preprint (which was not certified by peer review) is the author/funder, who has granted bioRxiv a license to display the preprint in perpetuity. It is made available under aCC-BY 4.0 International license.

conserved (Goh et al. 2024). However, recent findings show orthologous helpers also experience diversification pressures to prevent cross-activation and isolate signaling pathways (Selvaraj et al. 2024).

NLR numbers vary widely across species, from a few to over a thousand in some species (Baggs et al. 2020; Lee and Chae 2020; Liu et al. 2021; Goh et al. 2024; Toghani and Kamoun 2024), reflecting the dynamic co-evolutionary arms race between plants and pathogens (Barragan and Weigel 2021). NLR gene evolution follows the birth-and-death model, where gene duplication generates new NLRs—some are maintained and adapt to detect pathogens, while others lose function or are deleted (Michelmore and Meyers 1998; Seong et al. 2020; Barragan and Weigel 2021; Cruz et al. 2024). Recent advances have introduced new evolutionary models, emphasizing the dynamic response of NLRs to pathogen pressure (Barragan and Weigel 2021; Shimizu et al. 2022; Cruz et al. 2024; Sugihara et al. 2024). Pathogen effectors often target NLRs to suppress immunity, but NLRs counteract this through mutations in critical regions or by developing functional redundancy (Wu et al. 2018; Sugihara et al. 2024). For instance, within the NRC network, helpers like NRC2 and NRC3 are suppressed by cyst nematode effector SS15 and oomycete effector AVRcap1b (Derevnina et al. 2021; Contreras et al. 2023b). However, in some species NRC3 has accumulated mutations in its effector-binding region to evade suppression (Sugihara et al. 2024). Additionally, signaling redundancy allows non-suppressed nodes, such as NRC4, to activate immune responses even when parts of the pathway are suppressed (Wu et al. 2018; Contreras et al. 2023b; Huang et al. 2023; Sugihara et al. 2024).

bioRxiv preprint doi: https://doi.org/10.1101/2025.02.25.639832; this version posted February 25, 2025. The copyright holder for this preprint (which was not certified by peer review) is the author/funder, who has granted bioRxiv a license to display the preprint in perpetuity. It is made available under aCC-BY 4.0 International license.

Asterales is one of the most diverse flowering plant orders within the Asterid clade, encompassing several commercially important crops, including the common lettuce (*Lactuca sativa*) (Collinson et al. 2000; Smith and Brown 2018). Lettuce has become a key model for studying genetic resistance to pathogens and NLR evolution (Meyers et al. 1998; Shen et al. 2002; McHale et al. 2009; Truco et al. 2013; Christopoulou et al. 2015; Parra et al. 2016, 2021b, 2021a; Sandoya et al. 2021; Pink et al. 2022). Meyers et al. (1998) categorized the lettuce NLRome into 42 phylogenetic clades, known as Resistance Gene Clusters (RGCs) (Meyers et al. 1998; McHale et al. 2009). These NLR genes were further grouped into eight Major Resistance Clusters (MRCs) based on their locations on chromosomes 1, 2, 3, 4, 8, and 9 (McHale et al. 2009; Truco et al. 2013). In another study, Kuang et al. (2004) reported that genes at the RGC2 locus in lettuce could be categorized into two types: type I (diverse) and type II (conserved), with contrasting patterns of evolution and copy number between them (Kuang et al. 2004). This concept has since been explored in other systems and NLR families, including *Arabidopsis thaliana* and *Zea mays* (maize) (Prigozhin and Krasileva 2021; Prigozhin et al. 2024; Sutherland et al. 2024). Despite extensive functional and genetic research on resistance in lettuce, the evolution of the NRC network in Asterales remain poorly understood.

In this study, we analyzed 40 Solanales and 29 Asterales genomes to investigate the expansion and diversification of the NRC network within the Asterales order. We found that the NRC network in Asterales shows limited expansion compared to Solanales. Notably, NLRs in the Rx-type sensor phylogenetic clade are absent in Asterales, and although NRC-S in Asterales are phylogenetically classified as SD-types based on their NB-ARC, they lack the N-

bioRxiv preprint doi: https://doi.org/10.1101/2025.02.25.639832; this version posted February 25, 2025. The copyright holder for this preprint (which was not certified by peer review) is the author/funder, who has granted bioRxiv a license to display the preprint in perpetuity. It is made available under aCC-BY 4.0 International license.

158 terminal Solanaceous domain. We also confirmed the presence of a functional NRC
159 network in common lettuce (*Lactuca sativa*). Through selection and diversification
160 analyses of NRC helper and sensor subclades within the *Lactuca* genus, we
161 observed distinct patterns of diversification—not only between helpers and sensors
162 but also among different sensor clades. Our results suggest that NRC sensors
163 dependent on the conserved helper NRC0 show limited diversification and
164 expansion, whereas sensors relying on other NRC helpers have undergone greater
165 expansion and display higher rates of diversification. We further showed that unlike
166 NRC helpers, NRC sensors are not predicted to form resistosome-like structures
167 when modeled with AlphaFold 3. These findings provide insights into NRC network
168 evolution and the functional relationships among differentially evolving NLR clades.

169

170

bioRxiv preprint doi: https://doi.org/10.1101/2025.02.25.639832; this version posted February 25, 2025. The copyright holder for this preprint (which was not certified by peer review) is the author/funder, who has granted bioRxiv a license to display the preprint in perpetuity. It is made available under aCC-BY 4.0 International license.

# RESULTS

## The NRC network superclade shows limited expansion in Asterales compared to Solanales

The presence of NLRs in the NRC network superclade across Asterids prompted us to investigate the extent of its expansion in Asterales, a Campanulid order, compared to the well-studied Solanales order from Lamiids (**Figure 1A**) (Wu et al. 2017). For this purpose, we extracted a total number of 21,232 non-redundant NLR sequences from a dataset of de-novo annotated 40 Solanales and 29 Asterales genomes with harmonized annotations, representing a diverse set of species and genera from both orders (**Figure S1**, **Data S1 and S2**) (Toghani et al. 2025a). Based on phylogenetics analysis we then extracted the monophyletic NRC network superclade comprising 7,020 sequences, including the reference NRC-H and NRC-S from RefPlantNLR (**Data S3**) (Kourelis et al. 2021). In Asterales and Solanales, there are on average 300 and 338.6 non-redundant NLRs per genome, respectively. However, NRC superclade NLRs on average only comprise 6.6% of the NLRome in Asterales genomes compared to 50.3% in Solanales (**Figure S2**).

Compared to Solanales, Asterales show a significantly less expanded NRC network, as indicated by the lower copy numbers in both sensor and helper clades (**Figure 1B and S2**). We divided the 88 Asterales NRC helpers into two subclades. One subclade, containing 27 sequences clustered with the conserved NRC0 clade, while the remaining 61 sequences formed a separate clade and clustered with known Solanales NRC helpers, such as NRC2 and NRC4, referred to as Ast-NRCs hereafter (**Figure 1B and S2**) (Wu et al. 2017). All 504 Asterales NRC sensors

bioRxiv preprint doi: https://doi.org/10.1101/2025.02.25.639832; this version posted February 25, 2025. The copyright holder for this preprint (which was not certified by peer review) is the author/funder, who has granted bioRxiv a license to display the preprint in perpetuity. It is made available under aCC-BY 4.0 International license.

194 formed a distinct, well-supported clade that grouped with the Solanales SD-type
195 sensors, but none are phylogenetically clustered with the Rx-type Solanales sensor
196 clade (**Figure 1B**). Although Asterales NRC sensors belong to the SD-type clade,
197 they lack the Solanaceous domain characteristic at their N-termini (**Figure 1B, Data**
198 **S3**) (Seong et al. 2020). These observations suggest a substantial difference in the
199 evolutionary pace and expansion of the NRC network between Solanales and
200 Asterales orders.

201 In common lettuce, the 17 NRC superclade sequences (comprising 2 helpers
202 and 15 sensors) represent only 5% of the total NLRome, which consists of 359
203 sequences. In contrast, TIR-NLRs dominate the NLRome with 206 sequences,
204 making up over 57%. The CC-NLR, $CC_R$-NLR, and $CC_{G10}$-NLR clades contain 97, 9,
205 and 42 sequences, respectively (**Figure S3**). This indicates a disproportionate
206 expansion of different NLR types, with a limited expansion of NRC-H and NRC-S in
207 lettuce.

208

209 **NRC helpers and sensors are often genetically clustered in lettuce and other**
210 **Asterales species**

211 Given the observed differences in the expansion of NRC network superclade
212 between Solanales and Asterales, we further investigated the Asterales NRC
213 network superclade in more detail, focusing on lettuce. We analyzed 40 NRC-H and
214 NRC-S sequences from common lettuce (*Lactuca sativa*) and two wild lettuce
215 species (*Lactuca saligna* and *Lactuca virosa*) (**Data S4**). Phylogenetic analysis
216 revealed four subclades in the *Lactuca* NRC superclade sequences: one helper

bioRxiv preprint doi: https://doi.org/10.1101/2025.02.25.639832; this version posted February 25, 2025. The copyright holder for this preprint (which was not certified by peer review) is the author/funder, who has granted bioRxiv a license to display the preprint in perpetuity. It is made available under aCC-BY 4.0 International license.

clade containing sequences that grouped with either NRC0 or tomato NRC2 (referred to as Ast-NRC1 in each species hereafter), and sensor clades 1, 2, and 3 (**Figure 2A**). These subclades were defined by well-supported branches that form distinct clades in the phylogenetic tree (**Figure 2A and S5**). Based on the previous categorization of NLR families in lettuce, NRC superclade clade sequences are distributed across four RGC groups: (1) the NRC helper clade as RGC7, (2) sensor clade 1 as RGC26, (3) sensor clade 2 as RGC27, and (4) sensor clade 3 as RGC9 (**Figure S3**) (Meyers et al. 1998; McHale et al. 2009).

Based on previous reports of NRC-H and NRC-S being in genetic clusters for NRC0 and NRC6 (Lüdke et al. 2023; Sakai et al. 2024), we examined the physical location of NRC superclade sequences in the lettuce genomes. Unlike previous observations in various Asterid species, lettuce NRC0 (LsatNRC0; Helixer_NC_056625.2_001598.1), on chromosome 3, was not located near any sensor sequences (**Figure 2B**) (Sakai et al. 2024). In contrast, Ast-LsatNRC1 (Helixer_NC_056630.2_002654.1) was found to be in a physical cluster (<100kb) with sensors from clades 2 and 3, all residing on chromosome 8. Notably, all of clade 3 sensors are clustered together on this chromosome. This cluster is part of the previously reported MRC8c (**Figure 2B**) (Meyers et al. 1998; McHale et al. 2009; Christopoulou et al. 2015). The remaining lettuce NRC-S sequences, including those from clade 1, are scattered across chromosomes 4, 8, and 9, as part of MRCs 4, 8a, and 9a, respectively (**Figure 2B**) (Meyers et al. 1998; McHale et al. 2009; Christopoulou et al. 2015). Only LsatNRC0 is not part of any of the reported MRCs (**Figure 2B**).

bioRxiv preprint doi: https://doi.org/10.1101/2025.02.25.639832; this version posted February 25, 2025. The copyright holder for this preprint (which was not certified by peer review) is the author/funder, who has granted bioRxiv a license to display the preprint in perpetuity. It is made available under aCC-BY 4.0 International license.

Due to a lack of chromosome-level assemblies for the wild lettuce species, we could not determine if the NRC-H and NRC-S in these genomes are genetically clustered together. However, our genome analysis revealed Ast-LvirNRC1 (Helixer_CAKMRJ010003334.1_001958.1) positioned near clade 2 and 3 sensors on contig2395 (**Figure 2A and S4**). We further examined five other species across Asterales to investigate whether NRC-S are in genetic clusters with the NRC helpers as a general trend (**Figure S5**). In *Cichorium intybus*, CiNRC0 (Helixer_CM042016.1_001204.1) is located within 500K base pair distance of a clade 1 NRC sensor on chromosome 8 (Helixer_CM042016.1_001201.1), whereas Ast-CiNRC1a (Helixer_CM042010.1_003195.1) and Ast-CiNRC1b (Helixer_CM042010.1_003196.1) are clustered with sensors from clade 2 and 3 on chromosome 3 (**Figure S6 and Data S6**). In *Cynara cardunculus*, CcNRC0 (Helixer_NC_037542.1_000084.1) is in a cluster with a clade 1 sensor (Helixer_NC_037542.1_001617.1) on chromosome 15, and Ast-CcNRC1 is in a genetic cluster with four clade 1 sensors on contig NW_020200580.1 (**Figure S7 and Data S6**). In *Helianthus annuus*, *Chrysanthemum lavandulifolium* and *Codonopsis lanceolata*, none of the helpers are clustered with any sensors (**Figures S6, S7 and Data S6**). These findings suggest variations in the physical clustering of NRC helpers and sensor clades within the *Lactuca* genus and between different Asterales species.

**LsatNRC0 and Ast-LsatNRC1 are required for cell death signaling of distinct NRC sensor phylogenetic clades**

bioRxiv preprint doi: https://doi.org/10.1101/2025.02.25.639832; this version posted February 25, 2025. The copyright holder for this preprint (which was not certified by peer review) is the author/funder, who has granted bioRxiv a license to display the preprint in perpetuity. It is made available under aCC-BY 4.0 International license.

To investigate the functional connections of the lettuce NRC network and to test the phylogeny-based classification of these NLRs into NRC-S and NRC-H, we used Agrobacterium-mediated transient co-expression assays (Agroinfiltration) in an *nrc2/3/4* CRISPR knockout line of *Nicotiana benthamiana* (Wu et al. 2017). We agroinfiltrated autoactive mutants of the putative NRC-S and NRC-H to test their functionality, as the cognate effectors for these sensors remain unidentified. These mutants were generated by introducing a D-to-V mutation within the MHD motif of the NLRs, located near the C-terminus of the NB-ARC domain (Adachi et al. 2019a). We first tested whether transiently expressed NRC-S or NRC-H alone could induce cell death in *N. benthamiana*. While none of the NRC-S triggered cell death on their own, the autoactive mutants of the two lettuce NRC helpers displayed a macroscopic hypersensitive cell death response (**Figure S8A**). We then co-expressed the NRC-S and NRC-H in pairs to assess their potential functional connections and the dependence of lettuce NRC-S on the two NRC helpers. Among the 15 tested NRC-S, 9 displayed HR as autoactive mutants when co-expressed with one or both wild-type NRCs. Three NRC-S induced cell death through only LsatNRC0, while four responded solely through Ast-LsatNRC1. Notably, two sensors were functionally connected with both LsatNRC0 and Ast-LsatNRC1 (**Figure 3, S8B, Data S7**). While both NRC helpers possessed MADA motifs, none of the 15 tested sensors got a hit for MADA HMM profile (**Figure 3, Data S8**) (Adachi et al. 2019a). This was consistent with the cell death assays showing NRC helpers but not NRC sensors are able to cause cell death on their own.

By analyzing the cell death phenotypes alongside the lettuce NRC network superclades' phylogenetic tree, we observed a phylogenetic shift in helper

bioRxiv preprint doi: https://doi.org/10.1101/2025.02.25.639832; this version posted February 25, 2025. The copyright holder for this preprint (which was not certified by peer review) is the author/funder, who has granted bioRxiv a license to display the preprint in perpetuity. It is made available under aCC-BY 4.0 International license.

dependency within the sensor clades. Specifically, all LsatNRC0-dependent sensors belonged to clade 1, while Ast-LsatNRC1-dependent sensors resided in clade 3. Interestingly, NRC-S that functioned with both helpers are clade 2 members positioned between clades 1 and 3 (**Figure 3A**). Taken together these observations indicate the presence of a functional NLR network with partially redundant signaling pathways in lettuce (**Figure 3B**).

## In contrast to NRC helpers, NRC sensors fail to form resistosome-like oligomers when modeled with AlphaFold 3

Recently, we demonstrated that AlphaFold 3 (Abramson et al. 2024) can differentiate between helper and sensor NLRs within pairs by predicting resistosome-like structures for helpers but not for sensors (Toghani et al. 2024). Building on these findings, we applied a similar approach to the lettuce NRC network superclade to investigate potential differences in the *in-silico* oligomerization of NRC-H and NRC-S. Using AlphaFold 3, we modeled five replicates of the two NRC helpers and 16 NRC-S sequences from lettuce as hexamers in the presence of 50 oleic acid molecules, simulating the plasma membrane environment. To evaluate these models, we extracted and analyzed key metrics, including pLDDT (per-residue measure of local confidence), pTM (predicted template modeling score for overall structure), ipTM (interface-specific pTM), and per-chain pTM (**Data S8**). AlphaFold 3 successfully modeled resistosome-like oligomers for both NRC helper sequences, though it was unable to generate a complete N-terminal funnel in any of the LsatNRC0 predicted structures (**Figure 4**).

bioRxiv preprint doi: https://doi.org/10.1101/2025.02.25.639832; this version posted February 25, 2025. The copyright holder for this preprint (which was not certified by peer review) is the author/funder, who has granted bioRxiv a license to display the preprint in perpetuity. It is made available under aCC-BY 4.0 International license.

This was consistent with our previous observations when modeling NRC0 oligomers (Madhuprakash et al. 2024). In contrast, none of the NRC-S from the three sensor subclades formed resistosome-like structures (**Figure 4**). Across all replicates, NRC-S models consistently showed low confidence with high predicted aligned errors (**Figure 4 and S9**). Structurally, NRC-S displayed lower metrics compared to NRC helpers, with pTM and ipTM values below 0.5 and per-chain pTM values below 0.7 (**Figure 4, S9**). Conversely, helpers had consistently higher metrics, with pTM and ipTM exceeding 0.5 in all replicates and an average per-chain pTM of 0.75 (**Figure 4, S9**). These results suggest that AlphaFold 3 can distinguish between NRC-S and NRC-H based solely on sequence and their capacity to form higher-order resistosome-like oligomers.

## Highly variable sites localize to different domains in different NRC-S subclades

Despite having a common evolutionary origin, NRC sensors and helpers exhibit functional diversity (Adachi et al. 2019b; Contreras et al. 2023a). This prompted us to investigate the sequence diversification of NRC-H and NRC-S in the *Lactuca* genus. To test this, we performed Shannon's entropy analysis on each of the helper and sensor clades (Hausser and Strimmer 2009). Shannon's entropy measures the variability of amino acids at a specific position in a protein sequence alignment. A value of 0 indicates only one amino acid is present, while a value of 4.32 signifies all 20 amino acids are present with equal frequency. We used entropy values of 1.5 and higher as a threshold for identifying highly variable residues as reported in previous NLR studies (Prigozhin and Krasileva 2021; Selvaraj et al. 2024). The

bioRxiv preprint doi: https://doi.org/10.1101/2025.02.25.639832; this version posted February 25, 2025. The copyright holder for this preprint (which was not certified by peer review) is the author/funder, who has granted bioRxiv a license to display the preprint in perpetuity. It is made available under aCC-BY 4.0 International license.

*Lactuca* NRC helper clade exhibited minimal variation across its entire length, with only 23 residues exceeding the 1.5 entropy threshold. These variable residues were primarily located within the CC domain. Conserved motifs such as MADA, P-loop, and MHD also had low entropy values (**Figure 5A and 5B, Data S10**). In contrast, the sensor clades displayed significant variations: NRC-S clades 1 and 3 contained a substantially higher number of variable residues (146 and 128, respectively) compared to clade 2 (28 residues) that surpassed the 1.5 entropy threshold. Within clade 1, three clusters of highly variable residues were observed: one in the middle of the CC domain, and two near the N-termini of the NB-ARC and LRR domains, respectively (**Figure 5A and 5B, Data S10**). These findings corroborate the previous report on the presence of variable regions in these domains of NRC0-dependent sensors (Sakai et al. 2024). In clade 2, the few variable residues are scattered throughout the NLR sequence. Interestingly, clade 3 displayed a concentration of variable residues within the concave surface of the LRR domain repeats (**Figure 5A and 5B, Data S10**). As mentioned previously, we did not detect the MADA motif in NRC-S using the MADA HMM. However, despite differences in diversification patterns, all sensors have a conserved "MAYAxVQMFMEKLKQLIYx" N-terminal motif resembling the NRC0-S N-terminal motif reported previously (**Figure 5A**) (Sakai et al. 2024). P-loop and MHD motifs are also highly conserved between all NRC-S (**Figure 5A**). Together these indicated not only helpers and sensors exhibit different patterns of diversification but also NRC-S subclades, compared to each other, have diversified and evolved differently.

bioRxiv preprint doi: https://doi.org/10.1101/2025.02.25.639832; this version posted February 25, 2025. The copyright holder for this preprint (which was not certified by peer review) is the author/funder, who has granted bioRxiv a license to display the preprint in perpetuity. It is made available under aCC-BY 4.0 International license.

356 **Sensors dependent on Ast-LsatNRC1 are under the higher positive selection**
357 **compared to LsatNRC0-dependent sensors**

358 To examine the selection pressures that affected mutations in the NRC helper and
359 NRC-S subclades, we conducted positive selection tests using CodeML in PAML
360 v4.10.7 software (Yang 1997). Six models were evaluated for each NRC subclade
361 (helpers, sensors C1, C2, and C3): M0 (one-ratio), M1 (nearly neutral), M2 (positive
362 selection), M3 (discrete), M7 (beta), and M8 (beta + ω). Likelihood ratio tests (LRT;
363 $2\Delta L = 2(\ln L_{\text{alternative hypothesis}} - \ln L_{\text{null hypothesis}})$) compared M2 vs M1, M3 vs M0, and
364 M8 vs M7 for each clade (**Data S11**). The LRT values were evaluated against the $\chi 2$
365 critical thresholds to assess significance. A higher LRT than the critical value
366 indicates that the alternative hypothesis better fit the data.

367 For the helper clade, the calculated LRT for M2 vs M1 (0) and M8 vs M7
368 (6.379) did not exceed the $\chi 2$ critical threshold (9.21 at 1% significance; degrees of
369 freedom = 2; **Data S11**). Conversely, the LRT for M3 vs M0 (69.097) surpassed the
370 threshold (13.28 at 1% significance; degrees of freedom = 4; **Data S11**),
371 demonstrating that the M3 (discrete) model fit the data significantly better than M0
372 (neutral). The M0 model inherently excludes sites under diversifying selection ($\omega >$
373 1). However, no sites under positive selection were identified in the alternative
374 models (M2, M3, M8) (**Figure 6A; Data S11**).

375 For sensor clade 1, all three LRT comparisons yielded values exceeding the
376 $\chi 2$ thresholds, supporting the alternative models as better fits to the data (M2 vs M1
377 = 22.079, M3 vs M0 = 392.939, M8 vs M7 = 58.949; **Data S11**). Bayes Empirical
378 Bayes (BEB) analysis (Yang et al. 2005) under the M8 (beta + $\omega$) model revealed five

bioRxiv preprint doi: https://doi.org/10.1101/2025.02.25.639832; this version posted February 25, 2025. The copyright holder for this preprint (which was not certified by peer review) is the author/funder, who has granted bioRxiv a license to display the preprint in perpetuity. It is made available under aCC-BY 4.0 International license.

379 sites under positive selection (posterior probability > 0.95). Mapping these to an
380 AlphaFold 3-predicted structure of a representative clade 1 sensor NLR
381 (Helixer_NC_056630.2_000504.1) localized three of these sites to the CC domain
382 (**Figure 6B**).

383 In sensor clade 2, the LRT for M2 vs M1 (6.806) was below the $\chi 2$ critical
384 value. In contrast, LRTs for M3 vs M0 (21.639) and M8 vs M7 (157.960) exceeded
385 the critical thresholds, favoring the alternative models (**Data S11**). Despite this, BEB
386 analysis under the M8 model did not identify any sites under positive selection
387 (posterior probability > 0.95) (**Figure 6A; Data S11**).

388 For sensor clade 3, all three LRT comparisons supported the alternative
389 models (M2 vs M1 = 337.837, M3 vs M0 = 1372.561, M8 vs M7 = 400.550; **Data**
390 **S10**). BEB analysis from the M8 model identified 48 sites under positive selection
391 (posterior probability > 0.95) (**Figure 6A; Data S11**). Mapping these onto an
392 AlphaFold 3-predicted structure of a representative clade 3 sensor NLR
393 (Helixer_NC_056630.2_001736.1) revealed that 33 of the 48 sites were located
394 within the LRR domain (**Figure 6C**). Notably, most of these sites clustered on the
395 concave face of the LRR, a region implicated in effector binding based on previous
396 studies identifying signatures of positive selection and high variability (**Figure 6C**)
397 (Michelmore and Meyers 1998; Prigozhin and Krasileva 2021).

398 Next, we estimated the pairwise nonsynonymous ($d_N$) and synonymous ($d_S$)
399 substitution rates and $d_N/d_S$ ratios ($\omega$) for members of each NRC subclade using the
400 Nei and Gojobori (1986) method (**Data S12**) (Nei and Gojobori 1986; Yang and
401 Nielsen 2000). Analyses were conducted on full-length sequences and individual

bioRxiv preprint doi: https://doi.org/10.1101/2025.02.25.639832; this version posted February 25, 2025. The copyright holder for this preprint (which was not certified by peer review) is the author/funder, who has granted bioRxiv a license to display the preprint in perpetuity. It is made available under aCC-BY 4.0 International license.

402 domains (CC, NB-ARC, and LRR), where $\omega > 1$ implied presence of positive
403 selection. Among full-length and domain-based comparisons, NRC helpers had
404 lower average ω compared to all NRC-S clades (**Figure S11**). While sensor clade 3
405 on average had overall higher ω than the rest of NRC-H and NRC-S clades, the CC
406 domain in clade 1 sensors had $\omega > 1$ values, indicative of positive selection (**Figure**
407 **S11**). Overall, the pairwise $d_N/d_S$ ratios of NRC-H and NRC-S subclades further
408 supported the diversification and positive selection patterns observed in the entropy
409 and CodeML positive selection analyses, respectively.

410

411

bioRxiv preprint doi: https://doi.org/10.1101/2025.02.25.639832; this version posted February 25, 2025. The copyright holder for this preprint (which was not certified by peer review) is the author/funder, who has granted bioRxiv a license to display the preprint in perpetuity. It is made available under aCC-BY 4.0 International license.

# DISCUSSION

The NRC network originated approximately 100 million years ago within the superasterid lineage of land plants (Wu et al. 2017). In this study, we conducted a comparative phylogenetic and diversification analysis of the NRC network superclade in the Asterales and Solanales orders of the Asterid clade. For this purpose, we used a *de novo* generated annotation dataset for 40 Solanales and 29 Asterales genomes using the deep-learning-based Helixer software, ensuring comparable and harmonized gene models across all analyzed genomes (Stiehler et al. 2021; Holst et al. 2023). We then focused on common lettuce as a model Asterales species and experimentally validated a functional and partially redundant NRC network that was identified using phylogenetics analysis. We used this minimal NRC network to study the diversification and evolution of different NRC-H and NRC-S subclades.

The NRC network has expanded significantly in the lamiid lineage of Asterids over tens of millions of years, whereas the campanuliid lineage, including Asterales, has experienced much less expansion (Goh et al. 2024). Our analysis of 40 Solanales and 29 Asterales genomes revealed marked differences in NRC network evolution between these orders. (**Figure 1**). Notably, NRC superclade NLRs make up only 6.6% of the total NLR repertoire in Asterales, compared to 50.3% in Solanales (**Figure S2**). Despite similar average total NLR counts (338.6 in Solanales vs. 300 in Asterales), Asterales appears to have expanded other NLR clades, such as TIR-NLRs. In lettuce, for example, TIR-NLRs comprise a majority of the NLRome (57.4%; 206/359), while NRC superclade sequences represent only 5% (18/359)

bioRxiv preprint doi: https://doi.org/10.1101/2025.02.25.639832; this version posted February 25, 2025. The copyright holder for this preprint (which was not certified by peer review) is the author/funder, who has granted bioRxiv a license to display the preprint in perpetuity. It is made available under aCC-BY 4.0 International license.

(**Figure S2 and S3**). This aligns with previous findings of extensive proliferation of NRC in lamiids versus campanuliids (Goh et al. 2024). Our study found no evidence of Rx-type sensors in Asterales, a class significantly expanded in Solanales and linked to many characterized R-genes in Solanaceous species (Wu et al. 2017). Although Asterales SD-type sensors phylogenetically cluster with their Solanales counterparts, they lack the N-terminal SD-domain. It was previously suggested this is due to a loss of the sensors with SD integration in Asterales (Seong et al. 2020). However, given the presence of SD-type-like sensors in sugarbeet (*Beta vulgaris*), a Caryophyllales species, it's more likely that phylogenetically close sensors, with and without the SD integration, were already present in the common ancestor of superasterids (Seong et al. 2020), but the sensor with the SD integration was possibly lost in the ancestral Asterales species (**Figure 1**). More in-depth phylogenetic analysis across superasterids may provide insights into the origin of SD-type sensors and possible SD integration/emergence events.

In lettuce, NRCs are divided into four distinct phylogenetic subclades: a helper clade and three sensor clades (C1, C2, and C3) (**Figure 2**). Mapping these phylogenetic clades to the classification by Meyers et al. (1998) revealed their alignment with four subclades (RGC7, RGC9, RGC26, and RGC27) (Meyers et al. 1998). Notably, Ast-LsatNRC1 (RGC7), all clade 3 sensors (RGC9), and a single clade 2 sensor (RGC27) are part of MRC8c, which has been linked with QTLs for resistance to *Fusarium oxysporum* and *Verticillium dahliae* (Christopoulou et al. 2015). Other NRC-S from clades 1 and 2 are associated with Major Resistance Clusters (MRC) 4, 8a, and 9a, while *NRC0* is not linked to any known MRC. Although MRC4 and 9a have been implicated in downy mildew resistance, to date,

bioRxiv preprint doi: https://doi.org/10.1101/2025.02.25.639832; this version posted February 25, 2025. The copyright holder for this preprint (which was not certified by peer review) is the author/funder, who has granted bioRxiv a license to display the preprint in perpetuity. It is made available under aCC-BY 4.0 International license.

NRC superclade NLRs have not yet been implicated in resistance to pathogens in common lettuce (Meyers et al. 1998; Christopoulou et al. 2015). However, further investigation into the role of NRC network components classified as MRC8c in resistance against *F. oxysporum* and *V. dahliae* would be valuable, as they represent 12 out of 26 immune receptor genes in this genetic cluster (Christopoulou et al. 2015).

*NRC0* is the most conserved NRC helper across superasterids (Goh et al. 2024; Sakai et al. 2024), while other NRC helpers, such as NRC2, NRC3, and NRC4 in Solanaceae, show lineage-specific expansions (Goh et al. 2024; Selvaraj et al. 2024). Although Asterales have a less extensive overall expansion of NRCs compared to Solanales, many species in Asterales retain an additional NRC helper besides *NRC0*. Previous studies have demonstrated that NRC helpers, including *NRC0* and *NRC6*, can be genetically clustered with NRC sensors in several plant species (Lüdke et al. 2023; Sakai et al. 2024). However, in common lettuce, while Ast-LsatNRC1 is clustered with clade 2 and 3 sensors, *LsatNRC0* is not clustered with any sensor NLRs (**Figure 2B**). Further examination across Asterid species revealed species-specific patterns in the genetic linkage of NRC superclade NLRs. For instance, in *Cichorium intybus* (chicory), *CiNRC0* is proximal to a clade 1 sensor, and both *Ast-CiNRC1* copies cluster with clade 2 and 3 sensors. However, in *Helianthus annuus* (sunflower), no helpers are closely associated with sensors (**Figure S6**). These observations suggest that genetic linkage of *NRC0* with sensors is ancestral (Sakai et al. 2024), but the physical clustering of NRC superclade NLRs may be influenced by species-specific genomic rearrangements.

bioRxiv preprint doi: https://doi.org/10.1101/2025.02.25.639832; this version posted February 25, 2025. The copyright holder for this preprint (which was not certified by peer review) is the author/funder, who has granted bioRxiv a license to display the preprint in perpetuity. It is made available under aCC-BY 4.0 International license.

We expanded Goh et al. (2024) analyses by determining the functional dependency of lettuce NRC sensors on NRC helpers using a transient co-expression system in *N. benthamiana* (Goh et al. 2024). Of the 15 NRC-S tested, 9 triggered hypersensitive cell death when co-expressed with at least one lettuce NRC helper (**Figure 3 and S8**). Phylogenetic analysis revealed a shift in helper dependency among lettuce sensors: Clade 1 sensors exclusively rely on LsatNRC0, while clade 3 sensors depend solely on Ast-LsatNRC1. Clade 2 sensors, an intermediate group between clades 1 and 3, can signal through both LsatNRC0 and Ast-LsatNRC1 (**Figure 3**). This gradual evolutionary shift in helper dependency provides us a simplified system to study the diversification and function of different NRC clades.

Previously, we demonstrated that in monocot NLR pairs, helpers could form resistosome-like oligomers when modeled using AlphaFold 3, whereas sensor NLRs were unable to form similar structures (Toghani et al. 2024). However, whether this finding extends to dicots and NLR networks remained unclear. In this study, none of the tested NRC-S triggered cell death when expressed on its own (**Figure S8**). Multiple studies have also shown that NRC-S cannot independently induce cell death or form higher-order complexes before or after activation (Contreras et al. 2022; Ahn et al. 2023; Selvaraj et al. 2024). Given these observations, we modeled NRC-H and NRC-S as hexameric complexes using AlphaFold 3. Similar to results with sensor-helper pairs in rice, NRC helpers were predicted to form resistosomes, whereas NRC-S failed to yield meaningful or high-confidence structural predictions (**Figure 4**). Combined with our functional data and biochemical evidence from other NRC-S, this finding is consistent with the view that NRC-dependent sensors have

bioRxiv preprint doi: https://doi.org/10.1101/2025.02.25.639832; this version posted February 25, 2025. The copyright holder for this preprint (which was not certified by peer review) is the author/funder, who has granted bioRxiv a license to display the preprint in perpetuity. It is made available under aCC-BY 4.0 International license.

lost the ability to form resistosomes (Contreras et al. 2022; Ahn et al. 2023). However, further structural studies on NRC-S in their resting and active states are needed to elucidate the mechanisms underlying sensor activation and sensor-helper interactions.

Our Shannon entropy and selection analyses revealed that NRC helpers generally show low variability and lack any signatures of positive selection, consistent with helper NLRs like ADR1, which are classified among low-variability NLR clades (**Figures 5, 6, S10, and S11**) (Seong et al. 2020; Prigozhin and Krasileva 2021; Sutherland et al. 2024). In contrast, NRC-S clades demonstrate clade-specific variation patterns. Clade 1 sensors, reliant on NRC0, show high variability in the CC domain and the N-terminal part of the LRR domain, aligning with previous findings by Sakai et al. (2024) (**Figures 5, 6, and S11**) (Sakai et al. 2024). The cause of this diversification—whether due to relaxed selection or co-evolution with pathogens—remains unclear. Clade 2 sensors exhibit generally low variation and can signal through both LsatNRC0 and Ast-LsatNRC1. Clade 3 sensors, dependent on Ast-LsatNRC1, display highly variable regions concentrated on the concave surface of the LRR domain, with numerous sites under positive selection, resembling highly variable NLRs like RPP1 in *Arabidopsis thaliana* (**Figures 5, 6, and S11**) (Prigozhin and Krasileva 2021). The observed genetic clustering within clade 3 suggests that recent tandem duplication events and accelerated co-evolution with pathogens may have driven their diversification (Barragan and Weigel 2021).

Why have NRC network clades evolved differently? The differential evolutionary trajectories of NRC network clades are shaped by their distinct roles, sensor-helper dependencies, and interactions with pathogens. The contrasting

bioRxiv preprint doi: https://doi.org/10.1101/2025.02.25.639832; this version posted February 25, 2025. The copyright holder for this preprint (which was not certified by peer review) is the author/funder, who has granted bioRxiv a license to display the preprint in perpetuity. It is made available under aCC-BY 4.0 International license.

conservation of NRC0 and its functionally connected sensors versus the diversification of other NRC-H and NRC-S highlights varying selective pressures acting on these groups. NRC0 and its dependent sensors are conserved across Asterid lineages (Goh et al. 2024; Sakai et al. 2024) (**Figure 7**). The limited copy number and conservation of NRC0-dependent sensors, particularly in their LRR domains (which usually mediate pathogen recognition), may reflect detection of conserved effector molecules or guarding essential host components that are targeted by effectors, analogous to the ZAR1-ZRK system (Adachi et al. 2023). This conservation may limit the diversification of corresponding plant receptors. Such constraints could also arise from the need to maintain compatibility with NRC0, ensuring that evolutionary changes do not disrupt functional interactions or downstream signaling processes (**Figure 7**). In contrast, other NRC helpers and their associated sensors, especially those in lineages like Solanales, show greater diversification and expansion. This may stem from selective pressures such as detection a broader range of pathogen effectors, evading suppression, or introducing redundancy in signaling pathways (**Figure 7**) (Kamoun 2018; Adachi et al. 2019b; Derevnina et al. 2021; Contreras et al. 2023b; Sugihara et al. 2024). Non-NRC0-dependent sensors, often clustered together, exhibit strong signatures of positive selection, particularly in their LRR domains (**Figure 6C**), which likely reflects their engagement in a faster co-evolutionary arms race with pathogens compared to NRC0-dependent sensors.

In summary, our study highlights the contrasting evolutionary trajectories between helper and sensor NLRs, as well as among distinct sensor NLR clades within the NRC network. The NRC network mediates robust immune responses

bioRxiv preprint doi: https://doi.org/10.1101/2025.02.25.639832; this version posted February 25, 2025. The copyright holder for this preprint (which was not certified by peer review) is the author/funder, who has granted bioRxiv a license to display the preprint in perpetuity. It is made available under aCC-BY 4.0 International license.

554 against a diverse array of pathogens, including bacteria, fungi, oomycetes,
555 nematodes, and viruses. Certain nodes, such as *NRC6*, demonstrate specialization
556 by providing tissue-specific or pathogen-specific resistance (Lüdke et al. 2023). This
557 multi-paced evolution of helpers and sensor clades has likely granted the network
558 the flexibility to diversify and counter a broad spectrum of pathogens while allowing
559 specialization and potential adoption of novel immune functions. The simplified
560 Asterales NRC network in lettuce provided insights into how a shift in helper
561 dependency may have facilitated sensor diversification and expansion distinct from
562 their more conserved ancestral counterparts (**Figure 7**). Furthermore, our findings
563 illustrate how closely related NLRs with a functional connection, such as lettuce
564 NRCs, can exhibit varying diversification patterns, similar to those seen in more
565 distantly related clades or in NLRs displaying allelic diversity within a single locus,
566 such as RGC2 (Kuang et al. 2004). Addressing the molecular mechanisms
567 governing helper specificity and sensor-helper interactions in future studies will
568 illuminate how these immune receptors have adapted and evolved across plant
569 lineages. This will facilitate breeding and immune engineering efforts in Asterid crop
570 species.

571

bioRxiv preprint doi: https://doi.org/10.1101/2025.02.25.639832; this version posted February 25, 2025. The copyright holder for this preprint (which was not certified by peer review) is the author/funder, who has granted bioRxiv a license to display the preprint in perpetuity. It is made available under aCC-BY 4.0 International license.

# METHODS

## Extraction of NRC network superclade

A total number of 29,261 NLRs were compiled from the NLRtracker output of 39 Solanales and 29 Asterales *de-novo* annotated high-quality genome assemblies from NCBI (https://www.ncbi.nlm.nih.gov/datasets/) and a *S. melongena* chromosome-level genome assembly from GWH genome warehouse datasets (Chen et al. 2021) (**Table S1**) (Toghani et al. 2025a, 2025b). Based on the simple domain annotation from NLRtracker we only kept NLRs with "CNL", "CNLO", "CN", "OCNL", "CONL", "NL", "NLO", "ONL", "BCNL", "BNL", "BCN", "BCCNL", "BNLO", "BOCNL", "RNL", "TN", "TNL", "TNLO", "TNLJ" domain architectures. This led to keeping 25,042 NLRs. The remaining NLRs were then deduplicated to keep the 24,518 non-redundant sequences. Finally, based on NLRtracker domain output, any entry with NB-ARC domain shorter than 250 amino acids and longer than 400 amino acids were removed. This led to a final 21,232 sequences that was used for the phylogenetics analysis.

To construct a phylogenetic tree of the extracted NLRs, the NB-ARC domain sequences were aligned with RefPlantNLR NB-ARCs using FAMSA v2.2.2 [default options] (Deorowicz et al. 2016). The alignment was then used to construct a phylogenetic tree using FastTree v2.1.11 [-lg] (Price et al. 2010; Kourelis et al. 2021). The NRC network superclade along with CcRPP1 paraphyletic clade, including 7,040 sequences, was extracted based on the presence of reference sequences from a well-supported branch containing NRC-H and NRC-S. The NB-ARC domain of the extracted sequences were aligned using MAFFT v7.525 (Katoh and Standley

bioRxiv preprint doi: https://doi.org/10.1101/2025.02.25.639832; this version posted February 25, 2025. The copyright holder for this preprint (which was not certified by peer review) is the author/funder, who has granted bioRxiv a license to display the preprint in perpetuity. It is made available under aCC-BY 4.0 International license.

2013). The alignment was used to construct a new phylogenetic tree in the same way as before. The resulting tree was rooted at the CcRPP1 clade.

**Phylogenetics and gene distance analyses**

Plant taxonomy trees and taxa divergence times were obtained from TimeTree 5 database (timetree.org) (Kumar et al. 2022). 122 NRC sequences including helpers and sensors from *Lactuca sativa*, *Lactuca saligna*, *Lactuca virosa*, *Cichorium intybus*, *Helianthus annuus*, *Chrysanthemum lavandulifolium*, *Cynara cardunculus*, and *Codonopsis lanceolata* present in the dataset were extracted based on phylogeny. The NB-ARC sequences of extracted proteins were aligned with AtZAR1, NbZAR1, NbNRC2, SlNRC0, as references, using MAFFT v7.525 [--anysymbol] (Katoh and Standley 2013). FastTree v2.1.11 [-lg] was used to generate the tree of NRC network in the mentioned species (Price et al. 2010). We then used IQtree v2.3.0 [-B 1000 -m MFP] to generate a phylogenetic tree of 40 sequences in the NRC network in the *Lactuca* genus (Kalyaanamoorthy et al. 2017; Minh et al. 2020). The resulting tree was divided to helpers, sensor clade 1, sensor clade 2, and sensor clade 3 subclades based on branch lengths and reference sequences.

To obtain the physical location of the genes on the chromosome, first the GFF output from Helixer was simplified using GffRead [default options] and then imported into R using rtracklayer package (Lawrence et al. 2009; Pertea and Pertea 2020). The physical distances between genes was calculated using a custom R script and gene coordinates were exported to be visualized on chromosomes using MG2C online tool (Chao et al. 2021). The output was then visualized manually.

bioRxiv preprint doi: https://doi.org/10.1101/2025.02.25.639832; this version posted February 25, 2025. The copyright holder for this preprint (which was not certified by peer review) is the author/funder, who has granted bioRxiv a license to display the preprint in perpetuity. It is made available under aCC-BY 4.0 International license.

## Retrieving previous lettuce NLRome classifications

Lettuce NLRome IDs from Christopoulou, et al., 2015, and Lettuce V8 genome assembly from Phytozome 13 were extracted (Goodstein et al. 2012; Christopoulou et al. 2015; Reyes-Chin-Wo et al. 2017). We then used BLASTP as part of BLAST+ v2.16.0 to identify corresponding gene identifiers in the Phytozome 13 annotation to the new Helixer annotation (Camacho et al. 2009). The BLAST output was then processed in R and the gene coordinates, major resistance loci information, and RGC groups were retrieved for the new Helixer annotation.

## Agroinfiltration and cell death assays

To test the functionality of lettuce NRCs, annotated genes were cloned using the Golden Gate Modular Cloning (MoClo) kit (Weber et al. 2011) and the MoClo Plant Parts kit (Engler et al. 2014). In brief, coding sequences were synthesized by GENEWIZ as Golden Gate Level 0 pICH41155 modules and subsequently transferred to the binary vector pICH86988 through *Bsa*I digestion (Weber et al., 2011). Native *Bsa*I sites in the original sequences were domesticated as needed. In addition to wild-type clones, a D-to-V mutation within the MHD motif was introduced to generate autoactive versions (Adachi et al. 2019a) of the lettuce NRCs. Verified clones were transformed into *A. tumefaciens* strain GV3101 pMP90 for ectopic expression in *N. benthamiana*.

For cell death assays, wild-type and nrc2/3/4 *N. benthamiana* plants were grown in a controlled environment growth chamber at 22–25°C with a 16-hour light period and 45%/65% relative humidity during the light/dark cycle. Light intensity

bioRxiv preprint doi: https://doi.org/10.1101/2025.02.25.639832; this version posted February 25, 2025. The copyright holder for this preprint (which was not certified by peer review) is the author/funder, who has granted bioRxiv a license to display the preprint in perpetuity. It is made available under aCC-BY 4.0 International license.

was approximately 200 µmol/m²/s. Four- to five-week-old plants were used for agroinfiltration, following the methods described by Bos et al. (2006) (Bos et al. 2006). The final $OD_{600}$ of all Agrobacterium suspensions was adjusted to 0.5 in infiltration buffer (10mM MES, 10mM $MgCl_2$, and 150µM acetosyringone, pH5.6). This concentration was used for both expressing clones individually and co-expressing NRC-H and NRC-S of interest. The cell death phenotype was imaged 4 to 5 days post-agroinfiltration.

**Sequence polymorphism and selection analyses**

To calculated the Shannon entropy values for each clade, we used the "entropy" R package as part of a custom script as described before (Hausser and Strimmer 2009; Selvaraj et al. 2024). For this purpose, the helper subclade, and all sensor clades from *Lactuca* genus were aligned separately using MAFFT v7.525 [--anysymbol --localpair]. The sensor clade alignment was trimmed with ClipKit v2.0.1 [-m gappy] as described before and the sensor subclades were extracted from the resulting alignment. The entropy values for each clade were then visualized using a ggplot2 (Wickham 2016). Sequence logos for known conserved motifs in helper and sensor clades were generated using ggseqlogo R package (Wagih 2017).

Nucleotide sequence of the NRC superclade sequences were obtained using a custom python script from a compiled CDS file of the annotated genomes. Codon-based nucleotide alignments were generated for each subclade generated using MACSE v2.07 [-prog alignSequences -seq] (Ranwez et al. 2018). Positive selection tests were conducted on resulting alignments using CodeML in PAML

bioRxiv preprint doi: https://doi.org/10.1101/2025.02.25.639832; this version posted February 25, 2025. The copyright holder for this preprint (which was not certified by peer review) is the author/funder, who has granted bioRxiv a license to display the preprint in perpetuity. It is made available under aCC-BY 4.0 International license.

v4.10.7 (Yang 1997). Six models were applied for each subclade: M0 (one-ratio), M1 (nearly neutral), M2 (positive selection), M3 (discrete), M7 (beta), and M8 (beta + $\omega$). Likelihood ratio tests (LRT; $2\Delta L = 2$ ($\ln L_{\text{alternative hypothesis}} - \ln L_{\text{null hypothesis}}$)) were performed to compare M2 vs. M1, M3 vs. M0, and M8 vs. M7 for each clade. LRT values were evaluated against χ2 critical thresholds to assess significance, with higher LRT scores indicating a better fit for the alternative hypothesis. Bayes Empirical Bayes (BEB) analysis under the M8 model, included in the CodeML output, identified sites under positive selection with probabilities higher than 0.95 (Yang et al. 2005).

Pairwise nonsynonymous ($d_N$) and synonymous ($d_S$) substitution rates were estimated for full-length sequences and individual domains (CC, NB-ARC, and LRR) in each clade using the Nei and Gojobori (1986) method (Nei and Gojobori 1986; Yang and Nielsen 2000). These rates were extracted from the “2NG.dN” and “2NG.dS” outputs of CodeML using a custom R script. All figures were generated with the ggplot2 package in R (Wickham 2016).

**Protein structure prediction and mapping Shannon entropy to protein structures**

AlphaFold 3 [Seed=1, Ligand=ADP] was used to predict the monomeric structures of representative sequences from each clade (**Data S9**) (Abramson et al. 2024). The Shannon entropy values for each NRC subclade was mapped to a representative sequence from each clade using a custom R script and ChimeraX (Pettersen et al. 2021). For oligomeric structures, AlphaFold 3 with [Ligand=OLA x 50] was used to

bioRxiv preprint doi: https://doi.org/10.1101/2025.02.25.639832; this version posted February 25, 2025. The copyright holder for this preprint (which was not certified by peer review) is the author/funder, who has granted bioRxiv a license to display the preprint in perpetuity. It is made available under aCC-BY 4.0 International license.

687 model sequences (**Data S9**). First model for each sequence was modeled with Seed
688 = 1. Four other replicates were modeled for each sequence with random seeds.
689 Model confidence and metadata were processed and plotted with R. All scripts
690 available at [https://github.com/amiralito/lettuce_salad].

691

bioRxiv preprint doi: https://doi.org/10.1101/2025.02.25.639832; this version posted February 25, 2025. The copyright holder for this preprint (which was not certified by peer review) is the author/funder, who has granted bioRxiv a license to display the preprint in perpetuity. It is made available under aCC-BY 4.0 International license.

692 # DATA AVAILABILITY

693 Additional supplementary files and material are available at Zenodo repository
694 (https://doi.org/10.5281/zenodo.14544899) (Toghani and Kamoun 2025). Genome
695 annotations and sequence data available at Dryad repository
696 (https://doi.org/10.5061/dryad.sxksn03d6;
697 https://doi.org/10.5281/zenodo.14720919) (Toghani et al. 2025b, 2025a).

698

699 # ACKNOWLEDGMENTS

700 We thank Daniel Lüdke, Joe Win, Jonathan D. G. Jones (The Sainsbury Laboratory,
701 UK), Philip Carella (John Innes Centre, UK), and Chandler Sutherland (University of
702 California, Berkeley, USA) for their valuable and technical feedback. A.T. thanks
703 Josh W. Bennett (John Innes Centre, UK) for insightful scientific discussions and C.
704 Blasco for precision and detailed feedback. We also deeply appreciate the
705 invaluable support and contributions of the TSL community and support groups.

706

707 # FUNDING

708 The Gatsby Charitable Foundation 226 (A.T. and S.K.), Biotechnology and
709 Biological Sciences Research Council (BBSRC) BB/P012574 227 (Plant Health ISP)
710 (AT and SK), BBSRC BBS/E/J/000PR9795 (Plant Health ISP - Recognition) (A.T. and
711 S.K.), BBSRC BBS/E/J/000PR9796 (Plant Health ISP - Response) (A.T. and S.K.),
712 229 BBSRC BBS/E/J/000PR9797 (Plant Health ISP – Susceptibility) (A.T. and S.K.),

bioRxiv preprint doi: https://doi.org/10.1101/2025.02.25.639832; this version posted February 25, 2025. The copyright holder for this preprint (which was not certified by peer review) is the author/funder, who has granted bioRxiv a license to display the preprint in perpetuity. It is made available under aCC-BY 4.0 International license.

BBSRC 230 BBS/E/J/000PR9798 (Plant Health ISP – Evolution) (A.T. and S.K.), European Research Council 231 (ERC) 743165 (S.K.), Engineering and Physical Sciences Research Council EP/Y032187/1 232 (S.K.) H.A. received funding from the Japan Science and Technology Agency (JST), Precursory Research for Embryonic Science and Technology (JPMJPR21D1) and Japan Society for the Promotion of Science (JSPS) (23K20042, 24H00010).

## COMPETING INTEREST STATEMENT

S.K. receives funding from the industry for NLR biology and has co-founded a start-up company (Resurrect Bio Ltd.) related to NLR biology. S.K., J.K., and M.P.C. have filed patents on NLR biology. M.P.C. has received fees from Resurrect Bio Ltd.

bioRxiv preprint doi: https://doi.org/10.1101/2025.02.25.639832; this version posted February 25, 2025. The copyright holder for this preprint (which was not certified by peer review) is the author/funder, who has granted bioRxiv a license to display the preprint in perpetuity. It is made available under aCC-BY 4.0 International license.

# AUTHOR CONTRIBUTIONS

Conceptualization: A.T., S.K., H.A., R.F.

Data Curation: H.P., A.T., T.S., H.A.

Formal Analysis: H.P., A.T., T.S., H.A.

Investigation: H.P., A.T., T.S., H.A.

Methodology: H.P., A.T., A.P., T.S., H.A., Y.S., J.K

Resources: A.T., Y.S., S.K., H.A.

Software: A.T., A.P., T.S., H.A., Y.S.

Supervision: A.T., S.K.

Funding Acquisition: S.K.

Project Administration: A.T., S.K.

Writing Initial Draft: A.T., H.P.

Editing: A.T., S.K., H.A., Y.S., M.P.C

bioRxiv preprint doi: https://doi.org/10.1101/2025.02.25.639832; this version posted February 25, 2025. The copyright holder for this preprint (which was not certified by peer review) is the author/funder, who has granted bioRxiv a license to display the preprint in perpetuity. It is made available under aCC-BY 4.0 International license.

# REFERENCES

**Abramson J, Adler J, Dunger J, Evans R, Green T, Pritzel A, Ronneberger O, Willmore L, Ballard AJ, Bambrick J, et al.** Accurate structure prediction of biomolecular interactions with AlphaFold 3. Nature. 2024:1–3. https://doi.org/10.1038/s41586-024-07487-w

**Adachi H, Contreras M, Harant A, Wu CH, Derevnina L, Sakai T, Duggan C, Moratto E, Bozkurt TO, Maqbool A, et al.** An N-terminal motif in NLR immune receptors is functionally conserved across distantly related plant species. eLife. 2019a:**8**. https://doi.org/10.7554/eLife.49956

**Adachi H, Derevnina L, and Kamoun S**. NLR singletons, pairs, and networks: evolution, assembly, and regulation of the intracellular immunoreceptor circuitry of plants. Current Opinion in Plant Biology. 2019b:**50**:121–131. https://doi.org/10.1016/j.pbi.2019.04.007

**Adachi H, Sakai T, Kourelis J, Pai H, Gonzalez Hernandez JL, Utsumi Y, Seki M, Maqbool A, and Kamoun S**. Jurassic NLR: Conserved and dynamic evolutionary features of the atypically ancient immune receptor ZAR1. The Plant Cell. 2023:koad175. https://doi.org/10.1093/plcell/koad175

**Ahn H-K, Lin X, Olave-Achury AC, Derevnina L, Contreras MP, Kourelis J, Wu C-H, Kamoun S, and Jones JDG**. Effector-dependent activation and oligomerization of plant NRC class helper NLRs by sensor NLR immune receptors Rpi-amr3 and Rpi-amr1. The EMBO Journal. 2023:**n/a**(n/a):e111484. https://doi.org/10.15252/embj.2022111484

**Baggs E, Dagdas G, and Krasileva KV**. NLR diversity, helpers and integrated domains: making sense of the NLR IDentity. Current Opinion in Plant Biology. 2017:**38**(Figure 1):59–67. https://doi.org/10.1016/j.pbi.2017.04.012

**Baggs EL, Monroe JG, Thanki AS, O'Grady R, Schudoma C, Haerty W, and Krasileva KV**. Convergent Loss of an EDS1/PAD4 Signaling Pathway in Several Plant Lineages Reveals Coevolved Components of Plant Immunity and Drought Response[OPEN]. The Plant Cell. 2020:**32**(7):2158–2177. https://doi.org/10.1105/tpc.19.00903

**Barragan AC and Weigel D**. Plant NLR diversity: the known unknowns of pan-NLRomes. The Plant Cell. 2021:**33**(4):814–831. https://doi.org/10.1093/plcell/koaa002

**Bi G, Su M, Li N, Liang Y, Dang S, Xu J, Hu M, Wang J, Zou M, Deng Y, et al.** The ZAR1 resistosome is a calcium-permeable channel triggering plant immune signaling. Cell. 2021:**184**(13):3528-3541.e12. https://doi.org/10.1016/j.cell.2021.05.003

**Bos JIB, Kanneganti T-D, Young C, Cakir C, Huitema E, Win J, Armstrong MR, Birch PRJ, and Kamoun S**. The C-terminal half of Phytophthora infestans RXLR effector AVR3a is sufficient to trigger R3a-mediated hypersensitivity and suppress INF1-induced cell death in Nicotiana benthamiana. The Plant Journal. 2006:**48**(2):165–176. https://doi.org/10.1111/j.1365-313X.2006.02866.x

**Camacho C, Coulouris G, Avagyan V, Ma N, Papadopoulos J, Bealer K, and Madden TL**. BLAST+: architecture and applications. BMC Bioinformatics. 2009:**10**(1):421. https://doi.org/10.1186/1471-2105-10-421

**Castel B, Ngou P, Cevik V, Redkar A, Kim D, Yang Y, Ding P, and Jones JDG**. Diverse NLR immune receptors activate defence via the RPW8-NLR NRG1. New Phytologist. 2019:**222**(2):966–980. https://doi.org/10.1111/nph.15659

**Cesari S, Bernoux M, Moncuquet P, Kroj T, and Dodds P**. A novel conserved mechanism for plant NLR protein pairs: the 'integrated decoy' hypothesis. Frontiers in Plant Science. 2014:**5**.

**Chao J, Li Z, Sun Y, Aluko OO, Wu X, Wang Q, and Liu G**. MG2C: a user-friendly online tool for drawing genetic maps. Molecular Horticulture. 2021:**1**(1):16. https://doi.org/10.1186/s43897-021-00020-x

bioRxiv preprint doi: https://doi.org/10.1101/2025.02.25.639832; this version posted February 25, 2025. The copyright holder for this preprint (which was not certified by peer review) is the author/funder, who has granted bioRxiv a license to display the preprint in perpetuity. It is made available under aCC-BY 4.0 International license.

**Chen M, Ma Y, Wu S, Zheng X, Kang H, Sang J, Xu X, Hao L, Li Z, Gong Z, et al.** Genome Warehouse: A Public Repository Housing Genome-scale Data. Genomics, Proteomics & Bioinformatics. 2021:**19**(4):584–589. https://doi.org/10.1016/j.gpb.2021.04.001

**Christopoulou M, Wo SR-C, Kozik A, McHale LK, Truco M-J, Wroblewski T, and Michelmore RW**. Genome-Wide Architecture of Disease Resistance Genes in Lettuce. G3 Genes|Genomes|Genetics. 2015:**5**(12):2655–2669. https://doi.org/10.1534/g3.115.020818

**Collinson MP, C.A.B. International, and Food and Agriculture Organization of the United Nations eds**. A history of farming systems research (CABI: Rome, Italy Wallingford). https://doi.org/10.1079/9780851994055.0000

**Contreras MP, Lüdke D, Pai H, Toghani A, and Kamoun S**. NLR receptors in plant immunity: making sense of the alphabet soup. EMBO reports. 2023a:**n/a**(n/a):e57495. https://doi.org/10.15252/embr.202357495

**Contreras MP, Pai H, Selvaraj M, Toghani A, Lawson DM, Tumtas Y, Duggan C, Yuen ELH, Stevenson CEM, Harant A, et al.** Resurrection of plant disease resistance proteins via helper NLR bioengineering. Science Advances. 2023b:**9**(18):eadg3861. https://doi.org/10.1126/sciadv.adg3861

**Contreras MP, Pai H, Thompson R, Marchal C, Claeys J, Adachi H, and Kamoun S**. The nucleotide-binding domain of NRC-dependent disease resistance proteins is sufficient to activate downstream helper NLR oligomerization and immune signaling. New Phytologist. **n/a**(n/a). https://doi.org/10.1111/nph.19818

**Contreras MP, Pai H, Tumtas Y, Duggan C, Yuen ELH, Cruces AV, Kourelis J, Ahn H-K, Lee K-T, Wu C-H, et al.** Sensor NLR immune proteins activate oligomerization of their NRC helpers in response to plant pathogens. The EMBO Journal. 2022:**n/a**(n/a):e111519. https://doi.org/10.15252/embj.2022111519

**Cruz DGDL, Zdrzałek R, Banfield MJ, Talbot NJ, and Moscou MJ**. Molecular mimicry of a pathogen virulence target by a plant immune receptor. 2024:2024.07.26.605320. https://doi.org/10.1101/2024.07.26.605320

**Deorowicz S, Debudaj-Grabysz A, and Gudyś A**. FAMSA: Fast and accurate multiple sequence alignment of huge protein families. Sci Rep. 2016:**6**(1):33964. https://doi.org/10.1038/srep33964

**Derevnina L, Contreras MP, Adachi H, Upson J, Cruces AV, Xie R, Sklenar J, Menke FLH, Mugford ST, MacLean D, et al.** Plant pathogens convergently evolved to counteract redundant nodes of an NLR immune receptor network. bioRxiv. 2021:2021.02.03.429184.

**Duxbury Z, Wu C, and Ding P**. A Comparative Overview of the Intracellular Guardians of Plants and Animals: NLRs in Innate Immunity and Beyond. Annual Review of Plant Biology. 2021:**72**(1):155–184. https://doi.org/10.1146/annurev-arplant-080620-104948

**Engler C, Youles M, Gruetzner R, Ehnert T-M, Werner S, Jones JDG, Patron NJ, and Marillonnet S**. A Golden Gate Modular Cloning Toolbox for Plants. ACS Synth Biol. 2014:**3**(11):839–843. https://doi.org/10.1021/sb4001504

**Förderer A, Li E, Lawson AW, Deng Y, Sun Y, Logemann E, Zhang X, Wen J, Han Z, Chang J, et al.** A wheat resistosome defines common principles of immune receptor channels. Nature. 2022:1–8. https://doi.org/10.1038/s41586-022-05231-w

**Goh F-J, Huang C-Y, Derevnina L, and Wu C-H**. NRC immune receptor networks show diversified hierarchical genetic architecture across plant lineages. The Plant Cell. 2024:koae179. https://doi.org/10.1093/plcell/koae179

**Goodstein DM, Shu S, Howson R, Neupane R, Hayes RD, Fazo J, Mitros T, Dirks W, Hellsten U, Putnam N, et al.** Phytozome: a comparative platform for green plant genomics. Nucleic Acids Research. 2012:**40**(D1):D1178–D1186. https://doi.org/10.1093/nar/gkr944

**Grund E, Tremousaygue D, and Deslandes L**. Plant NLRs with integrated domains: Unity makes strength. Plant Physiology. 2019:**179**(4):1227–1235. https://doi.org/10.1104/pp.18.01134

bioRxiv preprint doi: https://doi.org/10.1101/2025.02.25.639832; this version posted February 25, 2025. The copyright holder for this preprint (which was not certified by peer review) is the author/funder, who has granted bioRxiv a license to display the preprint in perpetuity. It is made available under aCC-BY 4.0 International license.

826 **Hausser J and Strimmer K**. Entropy inference and the James-Stein estimator, with application to nonlinear
827 gene association networks. 2009. https://doi.org/10.48550/arXiv.0811.3579

828 **Holst F, Bolger A, Günther C, Maß J, Triesch S, Kindel F, Kiel N, Saadat N, Ebenhöh O, Usadel B, et al.**
829 Helixer–de novo Prediction of Primary Eukaryotic Gene Models Combining Deep Learning and a
830 Hidden Markov Model. 2023:2023.02.06.527280. https://doi.org/10.1101/2023.02.06.527280

831 **Huang C-Y, Huang Y-S, Sugihara Y, Wang H-Y, Huang L-T, Lopez-Agudelo JC, Chen Y-F, Lin K-Y, Chiang**
832 **B-J, Toghani A, et al.** Functional divergence shaped the network architecture of plant immune
833 receptors. 2023:2023.12.12.571219. https://doi.org/10.1101/2023.12.12.571219

834 **Jacob P, Kim NH, Wu F, El-Kasmi F, Chi Y, Walton WG, Furzer OJ, Lietzan AD, Sunil S, Kempthorn K, et**
835 **al.** Plant "helper" immune receptors are Ca 2+ -permeable nonselective cation channels. Science.
836 2021:**7917**(June):eabg7917. https://doi.org/10.1126/science.abg7917

837 **Jones JDG and Dangl JL**. The plant immune system. Nature. 2006:**444**(7117):323–329.
838 https://doi.org/10.1038/nature05286

839 **Jones JDG, Vance RE, and Dangl JL**. Intracellular innate immune surveillance devices in plants and animals.
840 Science. 2016:**354**(6316):aaf6395. https://doi.org/10.1126/science.aaf6395

841 **Kalyaanamoorthy S, Minh BQ, Wong TKF, von Haeseler A, and Jermiin LS**. ModelFinder: fast model
842 selection for accurate phylogenetic estimates. Nat Methods. 2017:**14**(6):587–589.
843 https://doi.org/10.1038/nmeth.4285

844 **Kamoun S**. Wu, C.-H., Derevnina, (2018). Receptor networks underpin plant immunity. 2018.

845 **Katoh K and Standley DM**. MAFFT Multiple Sequence Alignment Software Version 7: Improvements in
846 Performance and Usability. Molecular Biology and Evolution. 2013:**30**(4):772–780.
847 https://doi.org/10.1093/molbev/mst010

848 **Kourelis J and van der Hoorn RAL**. Defended to the Nines: 25 Years of Resistance Gene Cloning Identifies
849 Nine Mechanisms for R Protein Function. The Plant Cell. 2018:**30**(2):285–299.
850 https://doi.org/10.1105/TPC.17.00579

851 **Kourelis J, Sakai T, Adachi H, and Kamoun S**. RefPlantNLR is a comprehensive collection of experimentally
852 validated plant disease resistance proteins from the NLR family. PLOS Biology. 2021:**19**(10):e3001124.
853 https://doi.org/10.1371/JOURNAL.PBIO.3001124

854 **Kuang H, Woo S-S, Meyers BC, Nevo E, and Michelmore RW**. Multiple Genetic Processes Result in
855 Heterogeneous Rates of Evolution within the Major Cluster Disease Resistance Genes in Lettuce[W].
856 The Plant Cell. 2004:**16**(11):2870–2894. https://doi.org/10.1105/tpc.104.025502

857 **Kumar S, Suleski M, Craig JM, Kasprowicz AE, Sanderford M, Li M, Stecher G, and Hedges SB**. TimeTree
858 5: An Expanded Resource for Species Divergence Times. Molecular Biology and Evolution.
859 2022:**39**(8):msac174. https://doi.org/10.1093/molbev/msac174

860 **Lapin D, Kovacova V, Sun X, Dongus JA, Bhandari D, von Born P, Bautor J, Guarneri N, Rzemieniewski J,**
861 **Stuttmann J, et al.** A Coevolved EDS1-SAG101-NRG1 Module Mediates Cell Death Signaling by TIR-
862 Domain Immune Receptors. The Plant Cell. 2019:**31**(10):2430–2455.
863 https://doi.org/10.1105/tpc.19.00118

864 **Lawrence M, Gentleman R, and Carey V**. rtracklayer: an R package for interfacing with genome browsers.
865 Bioinformatics. 2009:**25**(14):1841–1842. https://doi.org/10.1093/bioinformatics/btp328

866 **Le Roux C, Huet G, Jauneau A, Camborde L, Trémousaygue D, Kraut A, Zhou B, Levaillant M, Adachi H,**
867 **Yoshioka H, et al.** A Receptor Pair with an Integrated Decoy Converts Pathogen Disabling of
868 Transcription Factors to Immunity. Cell. 2015:**161**(5):1074–1088.
869 https://doi.org/10.1016/j.cell.2015.04.025

bioRxiv preprint doi: https://doi.org/10.1101/2025.02.25.639832; this version posted February 25, 2025. The copyright holder for this preprint (which was not certified by peer review) is the author/funder, who has granted bioRxiv a license to display the preprint in perpetuity. It is made available under aCC-BY 4.0 International license.

**Lee HY, Mang H, Choi E, Seo YE, Kim MS, Oh S, Kim SB, and Choi D**. Genome-wide functional analysis of hot pepper immune receptors reveals an autonomous NLR clade in seed plants. New Phytologist. 2021:**229**(1):532–547. https://doi.org/10.1111/nph.16878

**Lee RRQ and Chae E**. Variation Patterns of NLR Clusters in Arabidopsis thaliana Genomes. Plant Communications. 2020:**1**(4):100089. https://doi.org/10.1016/j.xplc.2020.100089

**Li J, Huang H, Zhu M, Huang S, Zhang W, Dinesh-Kumar SP, and Tao X**. A Plant Immune Receptor Adopts a Two-Step Recognition Mechanism to Enhance Viral Effector Perception. Molecular Plant. 2019:**12**(2):248–262. https://doi.org/10.1016/j.molp.2019.01.005

**Liu F, Yang Z, Wang C, You Z, Martin R, Qiao W, Huang J, Jacob P, Dangl JL, Carette JE, et al.** Activation of the helper NRC4 immune receptor forms a hexameric resistosome. Cell. 2024:S0092867424007736. https://doi.org/10.1016/j.cell.2024.07.013

**Liu Y, Zeng Z, Zhang Y-M, Li Q, Jiang X-M, Jiang Z, Tang J-H, Chen D, Wang Q, Chen J-Q, et al.** An angiosperm NLR Atlas reveals that NLR gene reduction is associated with ecological specialization and signal transduction component deletion. Molecular Plant. 2021:**14**(12):2015–2031. https://doi.org/10.1016/j.molp.2021.08.001

**Lüdke D, Sakai T, Kourelis J, Toghani A, Adachi H, Posbeyikian A, Frijters R, Pai H, Harant A, Ernst K, et al.** A root-specific NLR network confers resistance to plant parasitic nematodes. 2023:2023.12.14.571630. https://doi.org/10.1101/2023.12.14.571630

**Madhuprakash J, Toghani A, Contreras MP, Posbeyikian A, Richardson J, Kourelis J, Bozkurt TO, Webster MW, and Kamoun S**. A disease resistance protein triggers oligomerization of its NLR helper into a hexameric resistosome to mediate innate immunity. Science Advances. 2024:**10**(45):eadr2594. https://doi.org/10.1126/sciadv.adr2594

**Maqbool A, Saitoh H, Franceschetti M, Stevenson C, Uemura A, Kanzaki H, Kamoun S, Terauchi R, and Banfield M**. Structural basis of pathogen recognition by an integrated HMA domain in a plant NLR immune receptor. eLife. 2015:**4**:e08709. https://doi.org/10.7554/eLife.08709

**McHale LK, Truco MJ, Kozik A, Wroblewski T, Ochoa OE, Lahre KA, Knapp SJ, and Michelmore RW**. The genomic architecture of disease resistance in lettuce. Theor Appl Genet. 2009:**118**(3):565–580. https://doi.org/10.1007/s00122-008-0921-1

**Meyers BC, Chin DB, Shen KA, Sivaramakrishnan S, Lavelle DO, Zhang Z, and Michelmore RW**. The Major Resistance Gene Cluster in Lettuce Is Highly Duplicated and Spans Several Megabases. The Plant Cell. 1998:**10**(11):1817–1832. https://doi.org/10.1105/tpc.10.11.1817

**Michelmore RW and Meyers BC**. Clusters of Resistance Genes in Plants Evolve by Divergent Selection and a Birth-and-Death Process. Genome Res. 1998:**8**(11):1113–1130. https://doi.org/10.1101/gr.8.11.1113

**Minh BQ, Schmidt HA, Chernomor O, Schrempf D, Woodhams MD, von Haeseler A, and Lanfear R**. IQ-TREE 2: New Models and Efficient Methods for Phylogenetic Inference in the Genomic Era. Molecular Biology and Evolution. 2020:**37**(5):1530–1534. https://doi.org/10.1093/molbev/msaa015

**Narusaka M, Shirasu K, Noutoshi Y, Kubo Y, Shiraishi T, Iwabuchi M, and Narusaka Y**. RRS1 and RPS4 provide a dual Resistance-gene system against fungal and bacterial pathogens. The Plant Journal. 2009:**60**(2):218–226. https://doi.org/10.1111/j.1365-313X.2009.03949.x

**Nei M and Gojobori T**. Simple methods for estimating the numbers of synonymous and nonsynonymous nucleotide substitutions. Mol Biol Evol. 1986:**3**(5):418–426. https://doi.org/10.1093/oxfordjournals.molbev.a040410

**Parra L, Maisonneuve B, Lebeda A, Schut J, Christopoulou M, Jeuken M, McHale L, Truco M-J, Crute I, and Michelmore R**. Rationalization of genes for resistance to Bremia lactucae in lettuce. Euphytica. 2016:**210**(3):309–326. https://doi.org/10.1007/s10681-016-1687-1

bioRxiv preprint doi: https://doi.org/10.1101/2025.02.25.639832; this version posted February 25, 2025. The copyright holder for this preprint (which was not certified by peer review) is the author/funder, who has granted bioRxiv a license to display the preprint in perpetuity. It is made available under aCC-BY 4.0 International license.

**Parra L, Nortman K, Sah A, Truco MJ, Ochoa O, and Michelmore R**. Identification and mapping of new genes for resistance to downy mildew in lettuce. Theor Appl Genet. 2021a:**134**(2):519–528. https://doi.org/10.1007/s00122-020-03711-z

**Parra L, Simko I, and Michelmore RW**. Identification of Major Quantitative Trait Loci Controlling Field Resistance to Downy Mildew in Cultivated Lettuce (Lactuca sativa). Phytopathology®. 2021b:**111**(3):541–547. https://doi.org/10.1094/PHYTO-08-20-0367-R

**Pertea G and Pertea M**. GFF Utilities: GffRead and GffCompare. 2020. https://doi.org/10.12688/f1000research.23297.1

**Pettersen EF, Goddard TD, Huang CC, Meng EC, Couch GS, Croll TI, Morris JH, and Ferrin TE**. UCSF ChimeraX: Structure visualization for researchers, educators, and developers. Protein Science. 2021:**30**(1):70–82. https://doi.org/10.1002/pro.3943

**Pink H, Talbot A, Graceson A, Graham J, Higgins G, Taylor A, Jackson AC, Truco M, Michelmore R, Yao C, et al.** Identification of genetic loci in lettuce mediating quantitative resistance to fungal pathogens. Theor Appl Genet. 2022:**135**(7):2481–2500. https://doi.org/10.1007/s00122-022-04129-5

**Price MN, Dehal PS, and Arkin AP**. FastTree 2 – Approximately Maximum-Likelihood Trees for Large Alignments. PLOS ONE. 2010:**5**(3):e9490. https://doi.org/10.1371/journal.pone.0009490

**Prigozhin DM and Krasileva KV**. Analysis of intraspecies diversity reveals a subset of highly variable plant immune receptors and predicts their binding sites. The Plant Cell. 2021. https://doi.org/10.1093/plcell/koab013

**Prigozhin DM, Sutherland CA, Rangavajjhala S, and Krasileva KV**. Majority of the Highly Variable NLRs in Maize Share Genomic Location and Contain Additional Target-Binding Domains. MPMI. 2024:MPMI-05-24-0047-FI. https://doi.org/10.1094/MPMI-05-24-0047-FI

**Qi T, Seong K, Thomazella DPT, Kim JR, Pham J, Seo E, Cho M-J, Schultink A, and Staskawicz BJ**. NRG1 functions downstream of EDS1 to regulate TIR-NLR-mediated plant immunity in Nicotiana benthamiana. Proceedings of the National Academy of Sciences. 2018:**115**(46):E10979–E10987. https://doi.org/10.1073/pnas.1814856115

**Ranwez V, Douzery EJP, Cambon C, Chantret N, and Delsuc F**. MACSE v2: Toolkit for the Alignment of Coding Sequences Accounting for Frameshifts and Stop Codons. Molecular Biology and Evolution. 2018:**35**(10):2582–2584. https://doi.org/10.1093/molbev/msy159

**Reyes-Chin-Wo S, Wang Z, Yang X, Kozik A, Arikit S, Song C, Xia L, Froenicke L, Lavelle DO, Truco M-J, et al.** Genome assembly with in vitro proximity ligation data and whole-genome triplication in lettuce. Nat Commun. 2017:**8**(1):14953. https://doi.org/10.1038/ncomms14953

**Saile SC, Jacob P, Castel B, Jubic LM, Salas-Gonzáles I, Bäcker M, Jones JDG, Dangl JL, and Kasmi FE**. Two unequally redundant "helper" immune receptor families mediate Arabidopsis thaliana intracellular "sensor" immune receptor functions. PLOS Biology. 2020:**18**(9):e3000783. https://doi.org/10.1371/journal.pbio.3000783

**Sakai T, Contreras MP, Martinez-Anaya C, Lüdke D, Kamoun S, Wu C-H, and Adachi H**. The NRC0 gene cluster of sensor and helper NLR immune receptors is functionally conserved across asterid plants. The Plant Cell. 2024:koae154. https://doi.org/10.1093/plcell/koae154

**Sandoya GV, Truco MJ, Bertier LD, Subbarao KV, Simko I, Hayes RJ, and Michelmore RW**. Genetics of Partial Resistance Against Verticillium dahliae Race 2 in Wild and Cultivated Lettuce. Phytopathology®. 2021:**111**(5):842–849. https://doi.org/10.1094/PHYTO-09-20-0396-R

**Sarris PF, Duxbury Z, Huh SU, Ma Y, Segonzac C, Sklenar J, Derbyshire P, Cevik V, Rallapalli G, Saucet SB, et al.** A Plant Immune Receptor Detects Pathogen Effectors that Target WRKY Transcription Factors. Cell. 2015:**161**(5):1089–1100. https://doi.org/10.1016/j.cell.2015.04.024

bioRxiv preprint doi: https://doi.org/10.1101/2025.02.25.639832; this version posted February 25, 2025. The copyright holder for this preprint (which was not certified by peer review) is the author/funder, who has granted bioRxiv a license to display the preprint in perpetuity. It is made available under aCC-BY 4.0 International license.

960 **Selvaraj M, Toghani A, Pai H, Sugihara Y, Kourelis J, Yuen ELH, Ibrahim T, Zhao H, Xie R, Maqbool A, et**
961 **al.** Activation of plant immunity through conversion of a helper NLR homodimer into a resistosome.
962 PLOS Biology. 2024:**22**(10):e3002868. https://doi.org/10.1371/journal.pbio.3002868

963 **Seong K, Seo E, Witek K, Li M, and Staskawicz B**. Evolution of NLR resistance genes with noncanonical N-
964 terminal domains in wild tomato species. New Phytologist. 2020:**227**(5):1530–1543.
965 https://doi.org/10.1111/nph.16628

966 **Shen KA, Chin DB, Arroyo-Garcia R, Ochoa OE, Lavelle DO, Wroblewski T, Meyers BC, and Michelmore**
967 **RW**. Dm3 Is One Member of a Large Constitutively Expressed Family of Nucleotide Binding Site—
968 Leucine-Rich Repeat Encoding Genes. MPMI. 2002:**15**(3):251–261.
969 https://doi.org/10.1094/MPMI.2002.15.3.251

970 **Shimizu M, Hirabuchi A, Sugihara Y, Abe A, Takeda T, Kobayashi M, Hiraka Y, Kanzaki E, Oikawa K,**
971 **Saitoh H, et al.** A genetically linked pair of NLR immune receptors shows contrasting patterns of
972 evolution. Proceedings of the National Academy of Sciences. 2022:**119**(27):e2116896119.
973 https://doi.org/10.1073/pnas.2116896119

974 **Smith SA and Brown JW**. Constructing a broadly inclusive seed plant phylogeny. American Journal of Botany.
975 2018:**105**(3):302–314. https://doi.org/10.1002/ajb2.1019

976 **Stiehler F, Steinborn M, Scholz S, Dey D, Weber APM, and Denton AK**. Helixer: cross-species gene
977 annotation of large eukaryotic genomes using deep learning. Bioinformatics. 2021:**36**(22–23):5291–
978 5298. https://doi.org/10.1093/bioinformatics/btaa1044

979 **Sugihara Y, Abe Y, Takagi H, Abe A, Shimizu M, Ito K, Kanzaki E, Oikawa K, Kourelis J, Langner T, et al.**
980 Disentangling the complex gene interaction networks between rice and the blast fungus identifies a
981 new pathogen effector. PLOS Biology. 2023:**21**(1):e3001945.
982 https://doi.org/10.1371/journal.pbio.3001945

983 **Sugihara Y, Kourelis J, Contreras MP, Pai H, Selvaraj M, Toghani A, Martínez-Anaya C, and Kamoun S**.
984 Helper NLR immune protein NRC3 evolved to evade inhibition by a cyst nematode virulence effector.
985 2024:2024.06.16.598756. https://doi.org/10.1101/2024.06.16.598756

986 **Sutherland CA, Prigozhin DM, Monroe JG, and Krasileva KV**. High allelic diversity in Arabidopsis NLRs is
987 associated with distinct genomic features. EMBO reports. 2024:1–17. https://doi.org/10.1038/s44319-
988 024-00122-9

989 **Toghani A, Frijters R, Bozkurt TO, Terauchi R, Kamoun S, and Sugihara Y**. Can AI modelling of protein
990 structures distinguish between sensor and helper NLR immune receptors? 2024:2024.11.24.625045.
991 https://doi.org/10.1101/2024.11.24.625045

992 **Toghani A and Kamoun S**. Functional annotation of 180 RefSeq reference plant proteomes reveals a dataset of
993 113,684 NLR proteins. 2024. https://doi.org/10.5281/ZENODO.13627394

994 **Toghani A and Kamoun S**. Supporting material for "A hierarchical immune receptor network in lettuce reveals
995 contrasting patterns of evolution in sensor and helper NLRs." 2025.
996 https://doi.org/10.5281/zenodo.14544899

997 **Toghani A, Sugihara Y, and Kamoun S**. Deep-learning-based annotation of 230 superasterid genomes reveals
998 a harmonized dataset of 91,366 NLRs (v250214_91366). 2025a.
999 https://doi.org/10.5281/zenodo.14720919

1000 **Toghani A, Sugihara Y, and Kamoun S**. Deep-learning-based annotation of 230 superasterid genomes reveals
1001 a harmonized dataset of 91,366 NLRs (v250214_91366). 2025b.
1002 https://doi.org/10.5061/dryad.sxksn03d6

1003 **Truco MJ, Ashrafi H, Kozik A, van Leeuwen H, Bowers J, Wo SRC, Stoffel K, Xu H, Hill T, Van Deynze A, et**
1004 **al.** An Ultra-High-Density, Transcript-Based, Genetic Map of Lettuce. G3 Genes|Genomes|Genetics.
1005 2013:**3**(4):617–631. https://doi.org/10.1534/g3.112.004929

bioRxiv preprint doi: https://doi.org/10.1101/2025.02.25.639832; this version posted February 25, 2025. The copyright holder for this preprint (which was not certified by peer review) is the author/funder, who has granted bioRxiv a license to display the preprint in perpetuity. It is made available under aCC-BY 4.0 International license.

**Van de Weyer A-L, Monteiro F, Furzer OJ, Nishimura MT, Cevik V, Witek K, Jones JDG, Dangl JL, Weigel D, and Bemm F**. A Species-Wide Inventory of NLR Genes and Alleles in Arabidopsis thaliana. Cell. 2019:**178**(5):1260-1272.e14. https://doi.org/10.1016/j.cell.2019.07.038

**Wagih O**. ggseqlogo: a versatile R package for drawing sequence logos. Bioinformatics. 2017:**33**(22):3645–3647. https://doi.org/10.1093/bioinformatics/btx469

**Wang J, Hu M, Wang J, Qi J, Han Z, Wang G, Qi Y, Wang HW, Zhou JM, and Chai J**. Reconstitution and structure of a plant NLR resistosome conferring immunity. Science. 2019:**364**(6435). https://doi.org/10.1126/science.aav5870

**Weber E, Engler C, Gruetzner R, Werner S, and Marillonnet S**. A Modular Cloning System for Standardized Assembly of Multigene Constructs. PLOS ONE. 2011:**6**(2):e16765. https://doi.org/10.1371/journal.pone.0016765

**Wickham H**. ggplot2: Elegant Graphics for Data Analysis 2nd ed. 2016. (Springer International Publishing : Imprint: Springer: Cham). https://doi.org/10.1007/978-3-319-24277-4

**Wu C-H, Abd-El-Haliem A, Bozkurt TO, Belhaj K, Terauchi R, Vossen JH, and Kamoun S**. NLR network mediates immunity to diverse plant pathogens. Proceedings of the National Academy of Sciences. 2017:**114**(30):8113–8118. https://doi.org/10.1073/pnas.1702041114

**Wu CH, Adachi H, De La Concepcion JC, Castells-Graells R, Nekrasov V, and Kamoun S**. NRC4 gene cluster is not essential for bacterial flagellin-triggered immunity. Plant Physiology. 2020:**182**(1):455–459. https://doi.org/10.1104/pp.19.00859

**Wu C-H, Derevnina L, and Kamoun S**. Receptor networks underpin plant immunity. Science. 2018:**360**(6395):1300–1301. https://doi.org/10.1126/science.aat2623

**Yang Z**. PAML: a program package for phylogenetic analysis by maximum likelihood. Bioinformatics. 1997:**13**(5):555–556. https://doi.org/10.1093/bioinformatics/13.5.555

**Yang Z and Nielsen R**. Estimating synonymous and nonsynonymous substitution rates under realistic evolutionary models. Mol Biol Evol. 2000:**17**(1):32–43. https://doi.org/10.1093/oxfordjournals.molbev.a026236

**Yang Z, Wong WSW, and Nielsen R**. Bayes Empirical Bayes Inference of Amino Acid Sites Under Positive Selection. Molecular Biology and Evolution. 2005:**22**(4):1107–1118. https://doi.org/10.1093/molbev/msi097

**Zhao Y-B, Liu M-X, Chen T-T, Ma X, Li Z-K, Zheng Z, Zheng S-R, Chen L, Li Y-Z, Tang L-R, et al.** Pathogen effector AvrSr35 triggers Sr35 resistosome assembly via a direct recognition mechanism. Science Advances. 2022:**8**(36):eabq5108. https://doi.org/10.1126/sciadv.abq5108

bioRxiv preprint doi: https://doi.org/10.1101/2025.02.25.639832; this version posted February 25, 2025. The copyright holder for this preprint (which was not certified by peer review) is the author/funder, who has granted bioRxiv a license to display the preprint in perpetuity. It is made available under aCC-BY 4.0 International license.

# SUPPLEMENTARY MATERIAL

**Data S1.** List of genome assemblies and species used in this study.

**Data S2.** List of NLR sequences and metadata used for the phylogenetic analysis.

**Data S3.** List of NRC helper and sensor sequences used for the phylogenetic analysis.

**Data S4.** List of *Lactuca* NRC helper and sensor sequences and metadata.

**Data S5.** List of selected Asterales NRC helper and sensor sequences and metadata.

**Data S6.** Gene-distance matrix of NRC helpers and sensors.

**Data S7.** Raw cell death scores of tested lettuce NRC helpers and sensors in *Nicotiana benthamiana*.

**Data S8.** HMMsearch output of MADA motif for NRC superclade sequences in *Lactuca* genus.

**Data S9.** Model confidences for the predicted models used in different analysis.

**Data S10.** Entropy values for NRC subclades.

**Data S11.** PAML results tables for the NRC subclades.

**Data S12.** Pairwise $d_N$ and $d_S$ values for the four NRC subclades.

bioRxiv preprint doi: https://doi.org/10.1101/2025.02.25.639832; this version posted February 25, 2025. The copyright holder for this preprint (which was not certified by peer review) is the author/funder, who has granted bioRxiv a license to display the preprint in perpetuity. It is made available under aCC-BY 4.0 International license.

# FIGURES

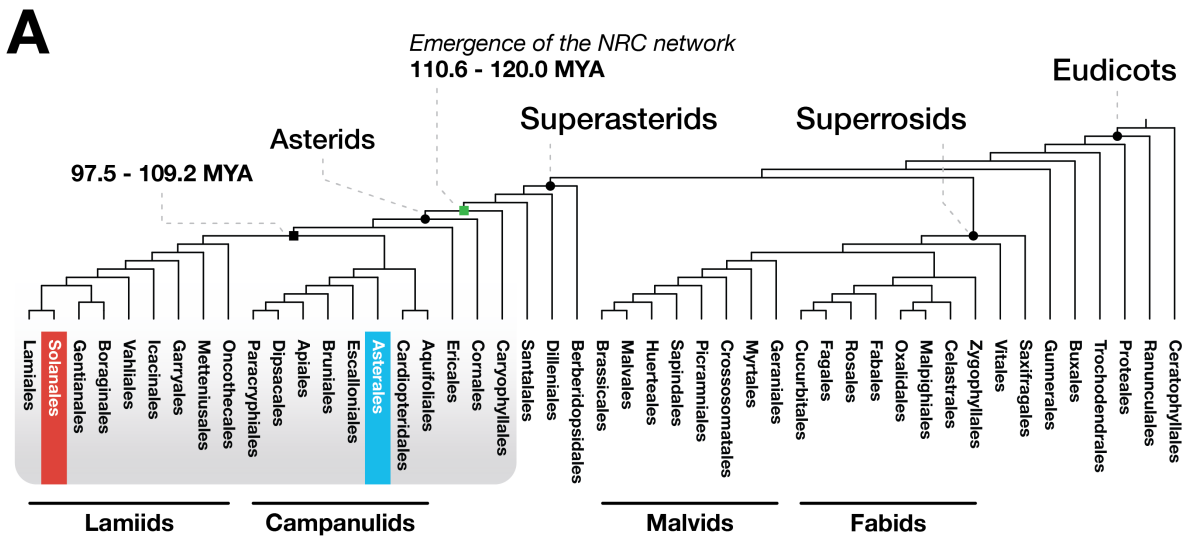


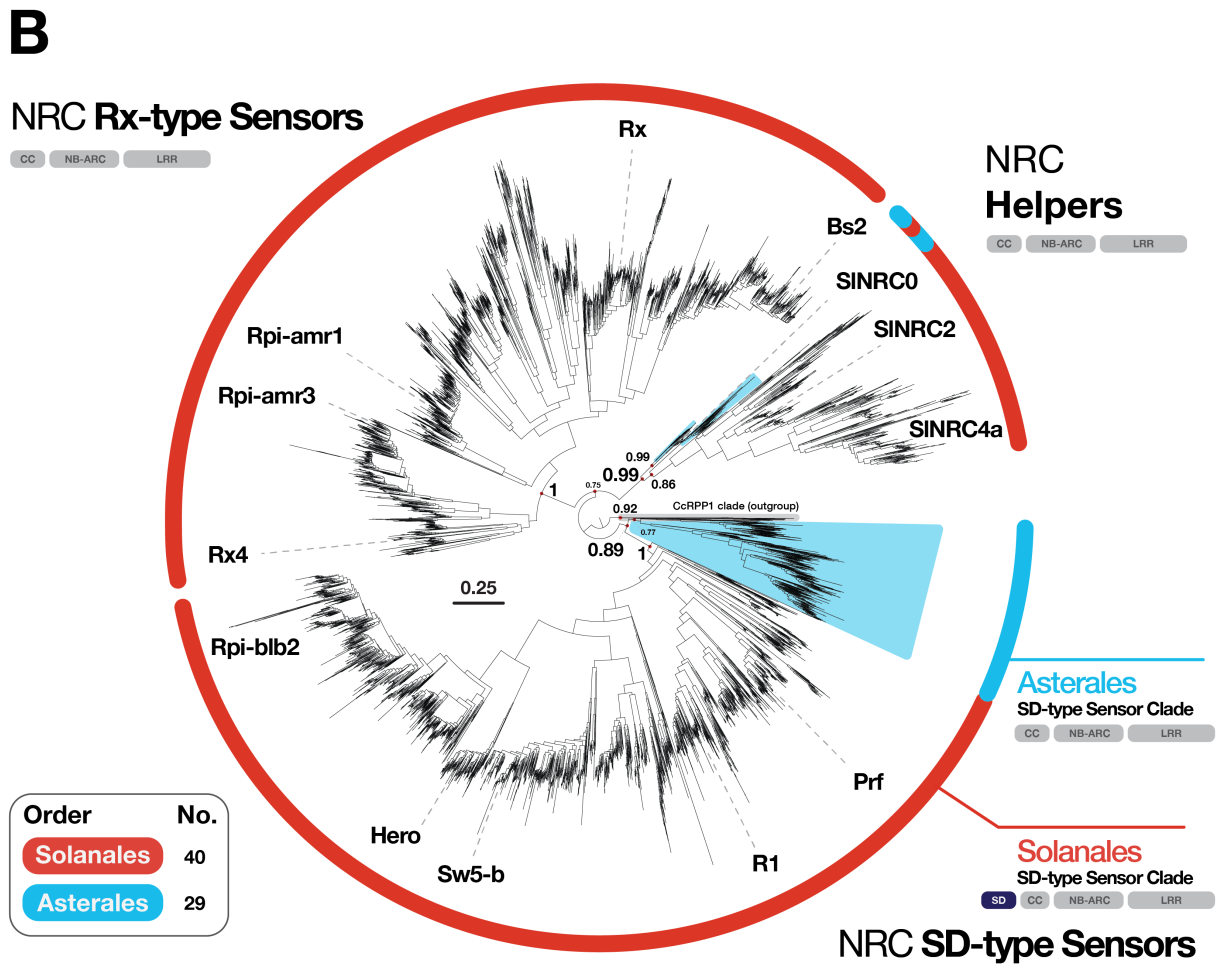

bioRxiv preprint doi: https://doi.org/10.1101/2025.02.25.639832; this version posted February 25, 2025. The copyright holder for this preprint (which was not certified by peer review) is the author/funder, who has granted bioRxiv a license to display the preprint in perpetuity. It is made available under aCC-BY 4.0 International license.

**Figure 1. The NRC network superclade has expanded less in Asterales compared to Solanales.** (A) Taxonomic tree of eudicots with NRC network superclade timeline in Asterids. Phylogenetic tree of plant orders and divergence time estimates obtained from TimeTree 5 (Kumar et al. 2022). (B) Phylogenetics tree of 7,040 NRC network superclade and CcRPP1 paraphyletic clade sequences from 40 Solanales and 29 Asterales genomes. Asterales' clades and branches are highlighted in blue.

bioRxiv preprint doi: https://doi.org/10.1101/2025.02.25.639832; this version posted February 25, 2025. The copyright holder for this preprint (which was not certified by peer review) is the author/funder, who has granted bioRxiv a license to display the preprint in perpetuity. It is made available under aCC-BY 4.0 International license.

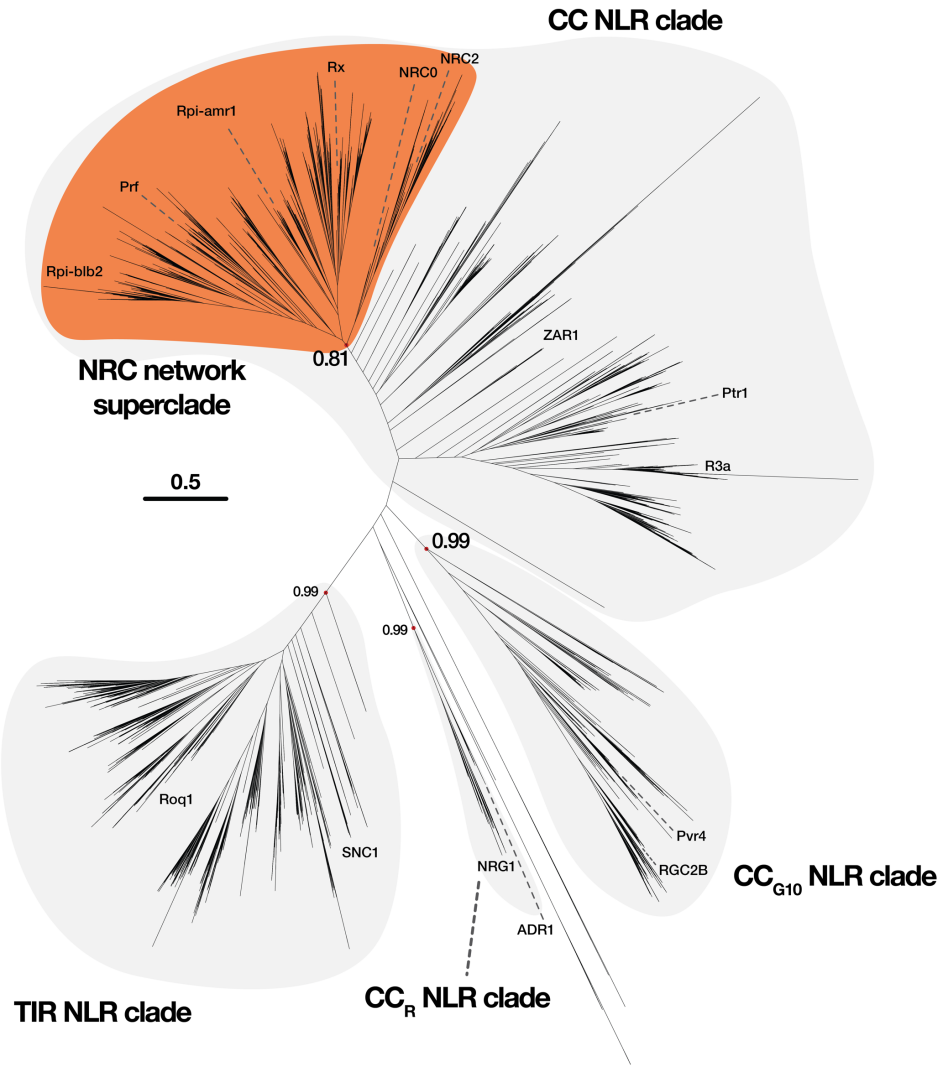


1067

1068 **Figure S1. Phylogenetics tree of 21,645 Solanales and Asterales NLRs with RefPlantNLR as the**

1069 **reference.** NRC network superclade, consisting of NRC helpers (NRC-H) and sensors (NRC-S),

1070 forms a well-supported clade within the CC-NLR clade.

1071

bioRxiv preprint doi: https://doi.org/10.1101/2025.02.25.639832; this version posted February 25, 2025. The copyright holder for this preprint (which was not certified by peer review) is the author/funder, who has granted bioRxiv a license to display the preprint in perpetuity. It is made available under aCC-BY 4.0 International license.

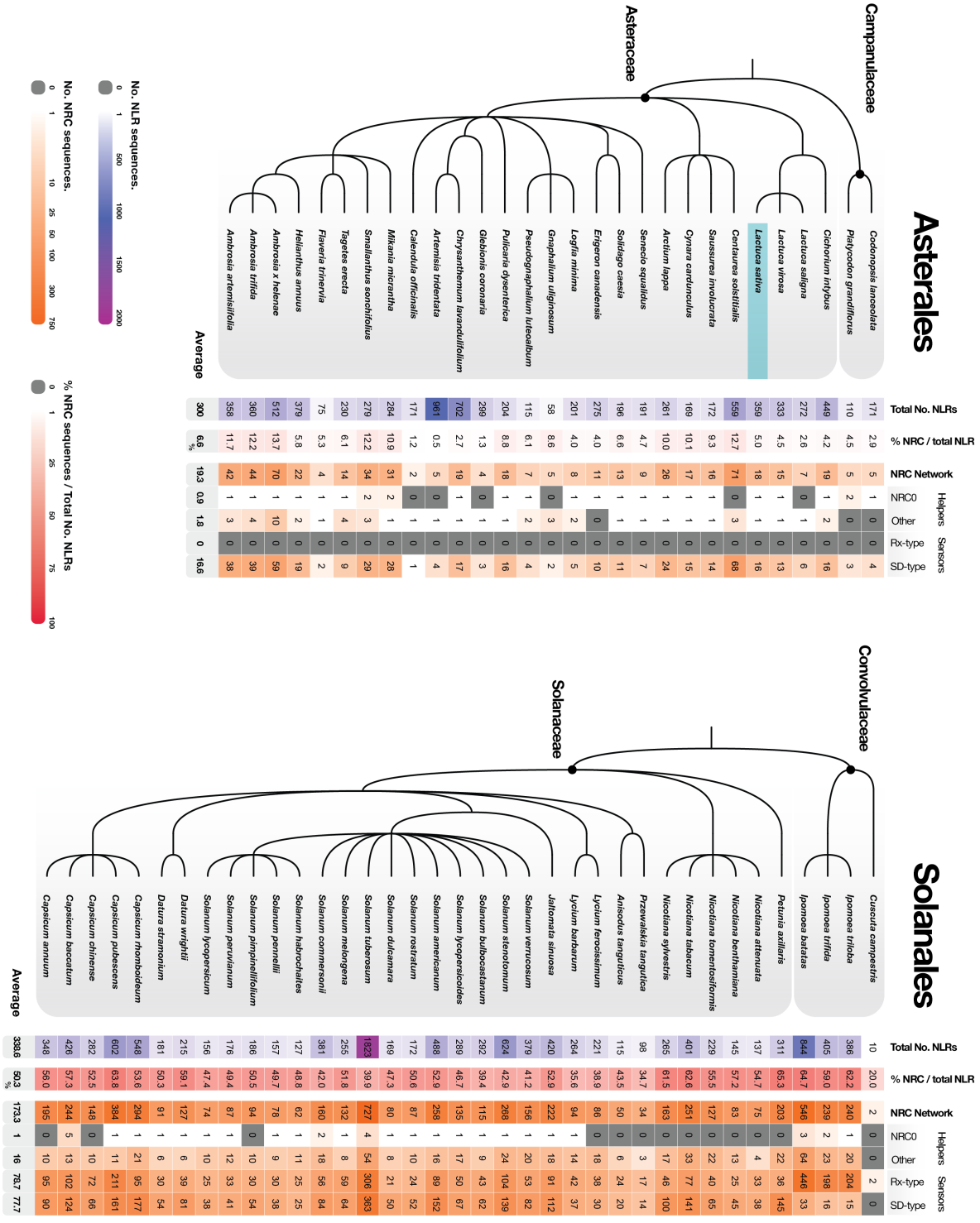


**Figure S2. Total number of NLRs, NRC network superclade sequences, NRC0s, other NRC helpers, Rx-type sensors, SD-type sensors, and percentage of NRC superclade sequences out of total number of NLRs in studied Asterales and Solanales species.** *Lactuca sativa* (common lettuce) is highlighted in blue.

bioRxiv preprint doi: https://doi.org/10.1101/2025.02.25.639832; this version posted February 25, 2025. The copyright holder for this preprint (which was not certified by peer review) is the author/funder, who has granted bioRxiv a license to display the preprint in perpetuity. It is made available under aCC-BY 4.0 International license.

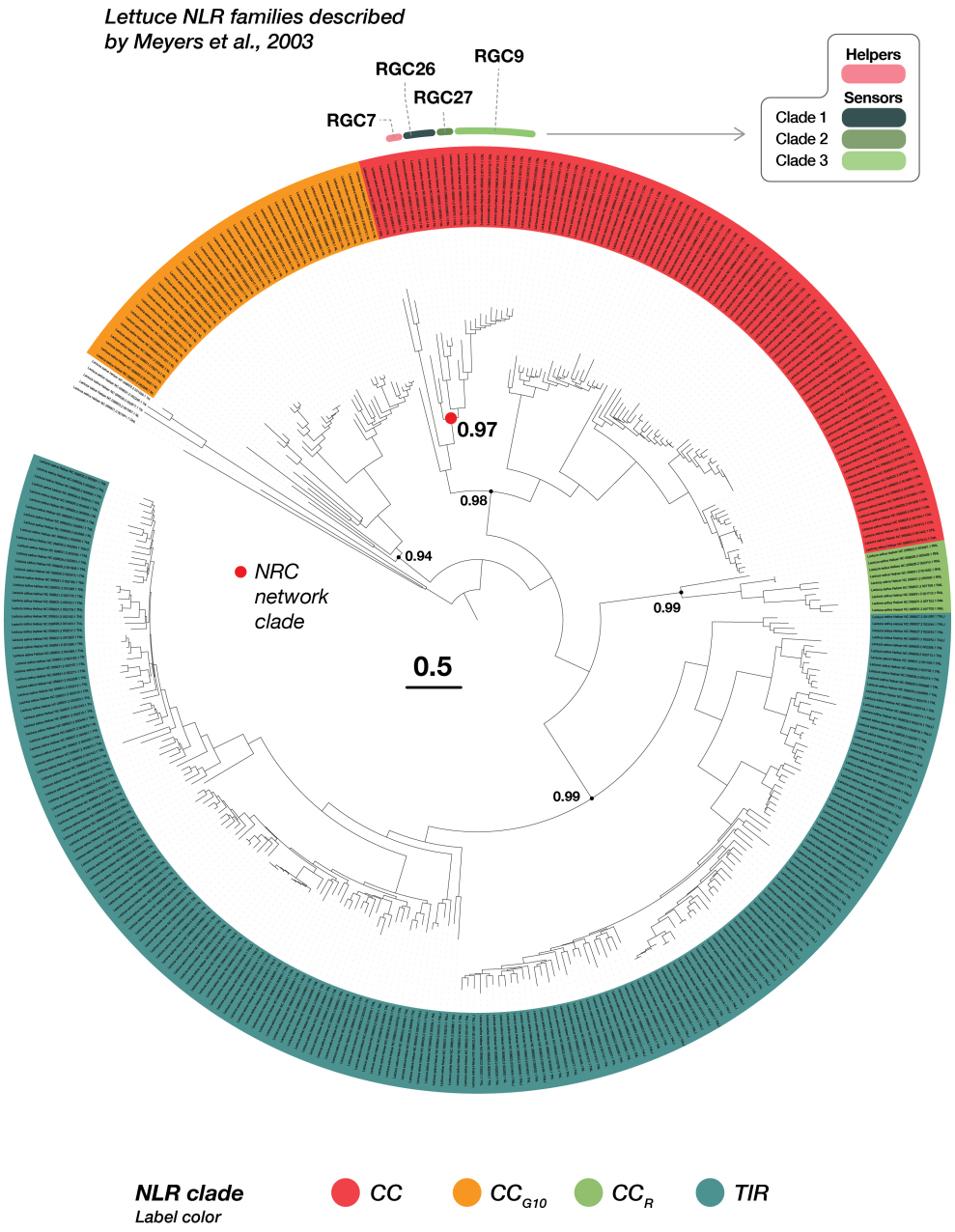


**Figure S3. Phylogenetic tree of common lettuce (*Lactuca sativa*) NLRome featuring 359 sequences.** Different NLR clades are highlighted in color. Numbers on tree nodes indicate bootstrap values. Phylogenetic tree was made based on NB-ARC domains and rooted at midpoint. NRC network superclade is highlighted with the red dot. NLR family classification by Meyers et al. (1998) is shown for the NRC network superclade (Meyers et al. 1998; Christopoulou et al. 2015).

bioRxiv preprint doi: https://doi.org/10.1101/2025.02.25.639832; this version posted February 25, 2025. The copyright holder for this preprint (which was not certified by peer review) is the author/funder, who has granted bioRxiv a license to display the preprint in perpetuity. It is made available under aCC-BY 4.0 International license.

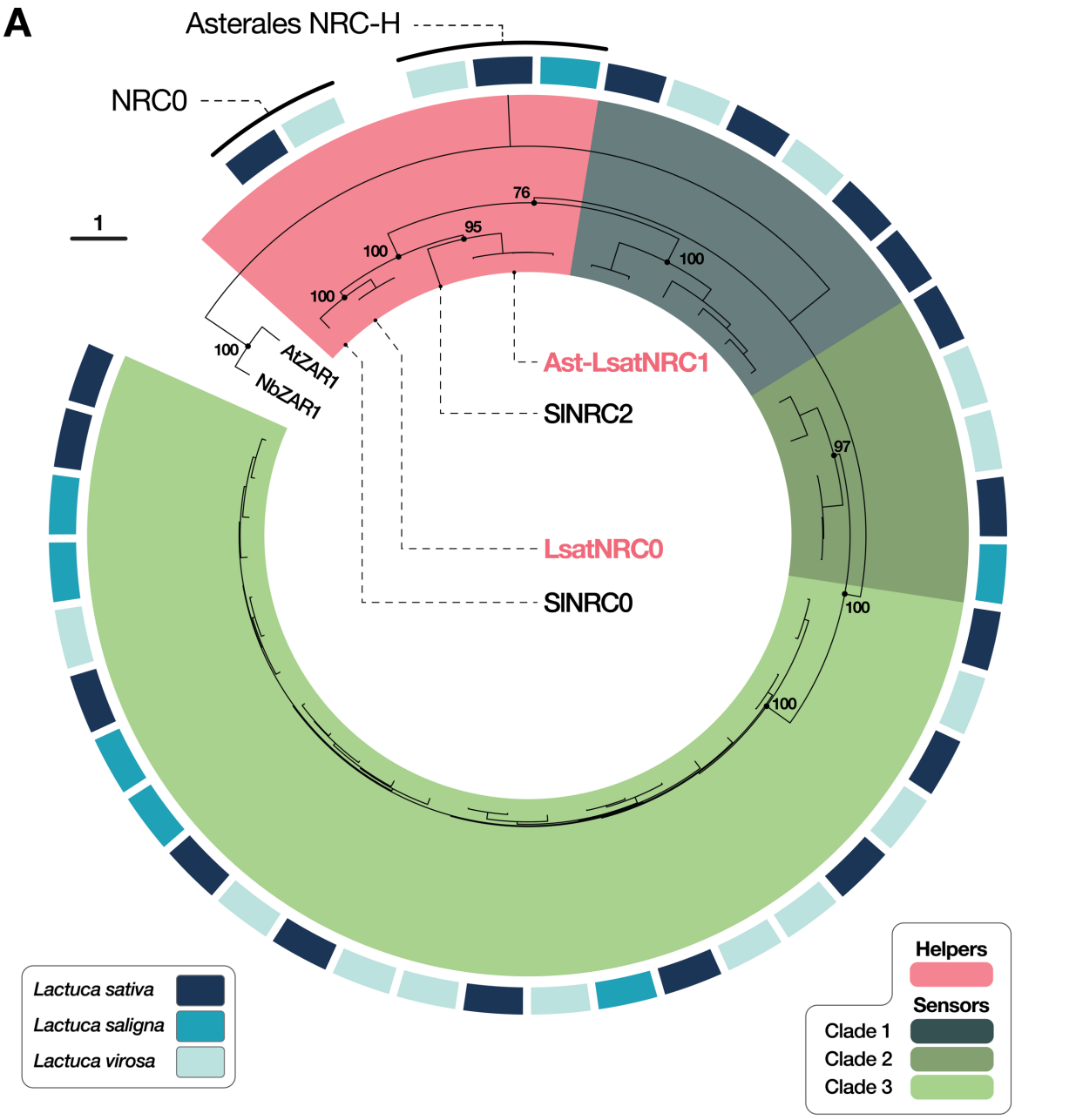


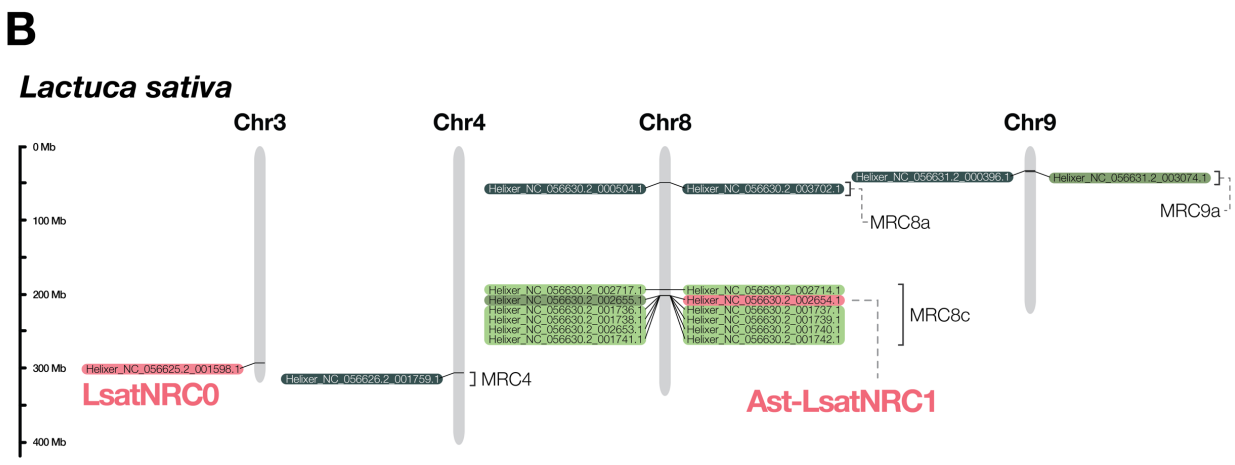


1083

bioRxiv preprint doi: https://doi.org/10.1101/2025.02.25.639832; this version posted February 25, 2025. The copyright holder for this preprint (which was not certified by peer review) is the author/funder, who has granted bioRxiv a license to display the preprint in perpetuity. It is made available under aCC-BY 4.0 International license.

**Figure 2. Unlike LsatNRC0, Ast-LsatNRC1 is genetically linked to sensor NLRs in lettuce.** (A) Phylogenetic tree of NRC superclade sequences of three *Lactuca* species (*Lactuca sativa*, *Lactuca saligna*, and *Lactuca virosa*). NRC-S are divided in three well-supported phylogenetic subclades. Numbers on tree nodes indicate bootstrap values. AtZAR1 and NbZAR1 were used as outgroup sequences. SlNRC0 and SlNRC2 were used as reference sequences. (B) Physical map of *Lactuca sativa* NRC superclade sequences on the chromosomes. Previously described Major Resistance Clusters (MRCs) are shown for NRCs (McHale et al. 2009; Truco et al. 2013).

bioRxiv preprint doi: https://doi.org/10.1101/2025.02.25.639832; this version posted February 25, 2025. The copyright holder for this preprint (which was not certified by peer review) is the author/funder, who has granted bioRxiv a license to display the preprint in perpetuity. It is made available under aCC-BY 4.0 International license.

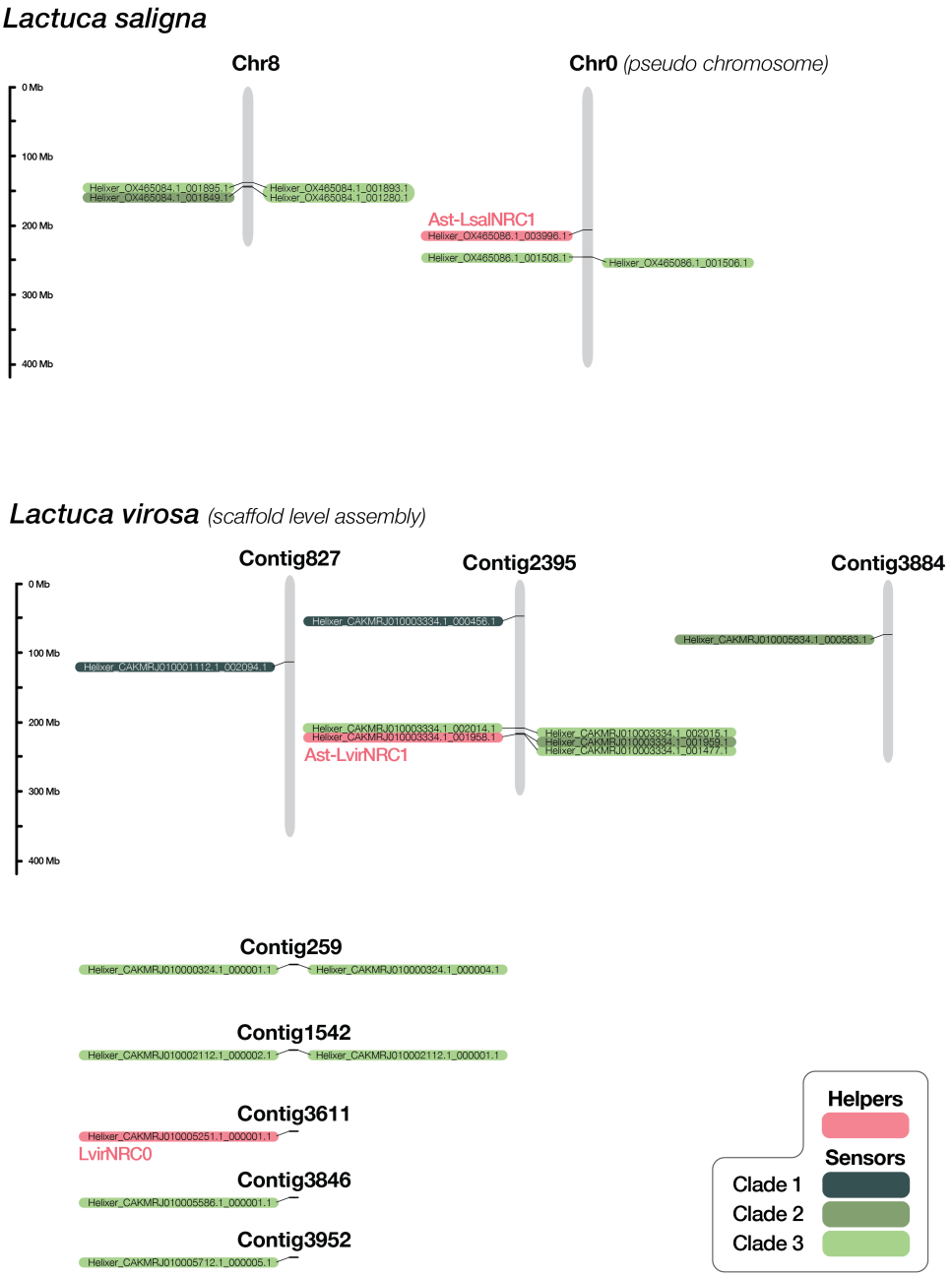


**Figure S4. Physical map of *Lactuca saligna* and *Lactuca virosa* NRC superclade sequences.**

bioRxiv preprint doi: https://doi.org/10.1101/2025.02.25.639832; this version posted February 25, 2025. The copyright holder for this preprint (which was not certified by peer review) is the author/funder, who has granted bioRxiv a license to display the preprint in perpetuity. It is made available under aCC-BY 4.0 International license.

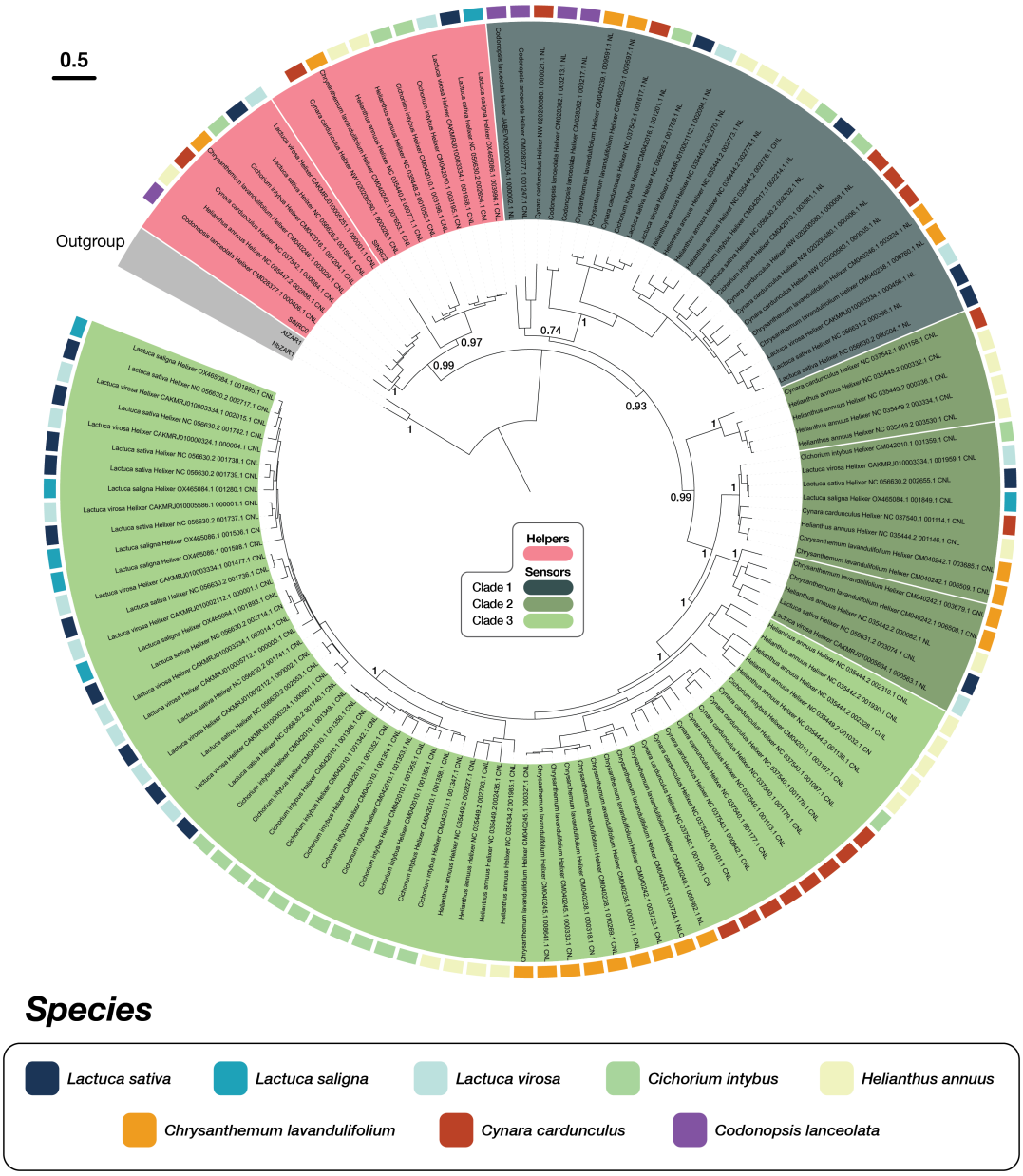


1093

1094 **Figure S5. Phylogenetic tree of NRC superclade sequences of *Lactuca* species (*Lactuca***
1095 ***sativa*, *Lactuca saligna*, and *Lactuca virosa*), *Codonopsis lanceolata*, *Helianthus annuus*,**
1096 ***Cichorium intybus*, *Chrysanthemum lavandulifolium*, and *Cynara cardunculus*.** NRC-S are
1097 divided in three phylogenetic categories based on previous classification in the *Lactuca* genus.
1098 Numbers on tree nodes indicate bootstrap values. AtZAR1 and NbZAR1 were used as outgroup
1099 sequences. SlNRC0 and SlNRC2 were used as reference sequences.

bioRxiv preprint doi: https://doi.org/10.1101/2025.02.25.639832; this version posted February 25, 2025. The copyright holder for this preprint (which was not certified by peer review) is the author/funder, who has granted bioRxiv a license to display the preprint in perpetuity. It is made available under aCC-BY 4.0 International license.

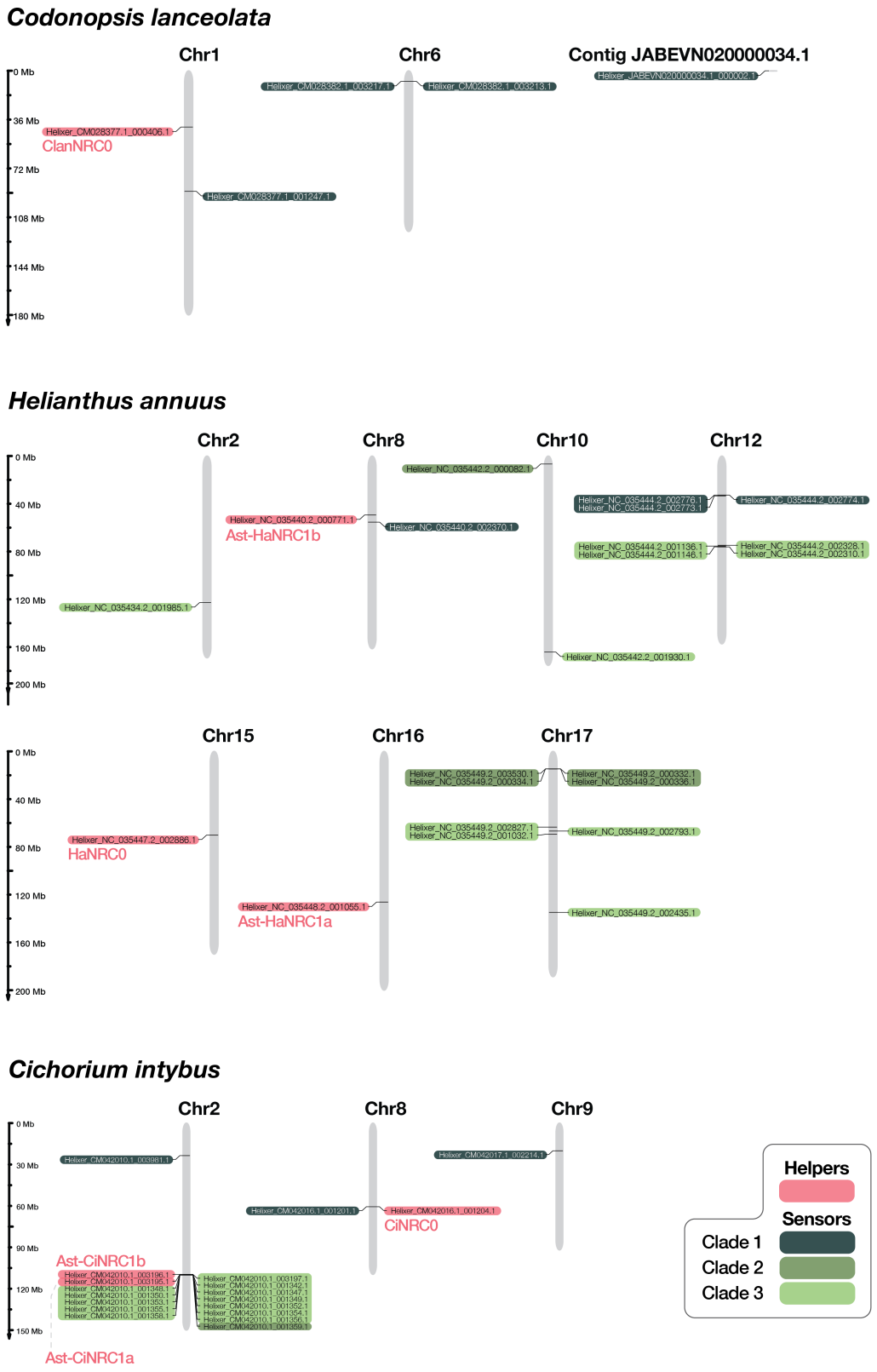


**Figure S6. Physical map of *Codonopsis lanceolata*, *Helianthus annuus*, and *Cichorium intybus* NRC superclade sequences.**

bioRxiv preprint doi: https://doi.org/10.1101/2025.02.25.639832; this version posted February 25, 2025. The copyright holder for this preprint (which was not certified by peer review) is the author/funder, who has granted bioRxiv a license to display the preprint in perpetuity. It is made available under aCC-BY 4.0 International license.

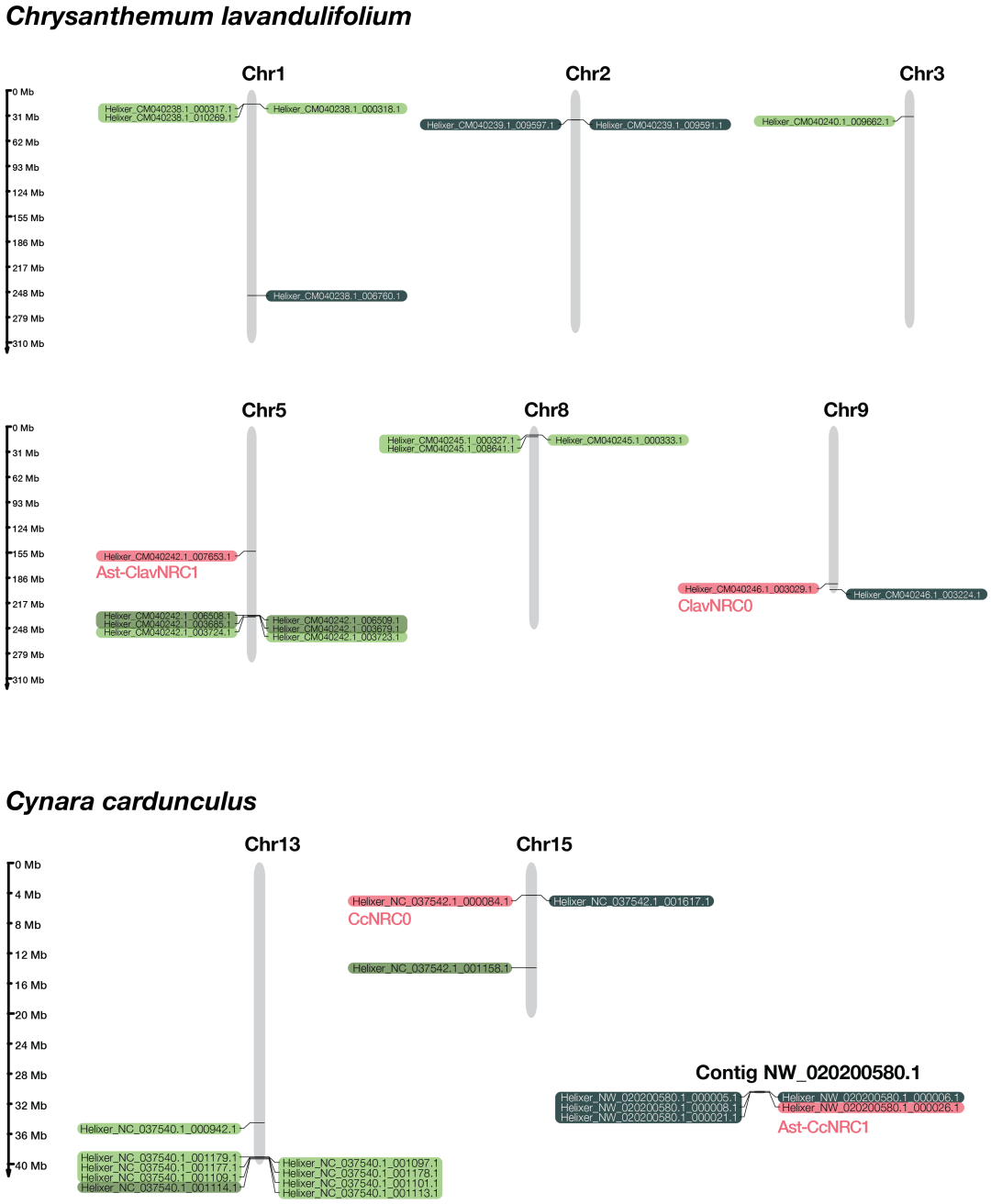


**Figure S7. Physical map of *Chrysanthemum lavandulifolium* and *Cynara cardunculus* NRC superclade sequences.**

bioRxiv preprint doi: https://doi.org/10.1101/2025.02.25.639832; this version posted February 25, 2025. The copyright holder for this preprint (which was not certified by peer review) is the author/funder, who has granted bioRxiv a license to display the preprint in perpetuity. It is made available under aCC-BY 4.0 International license.

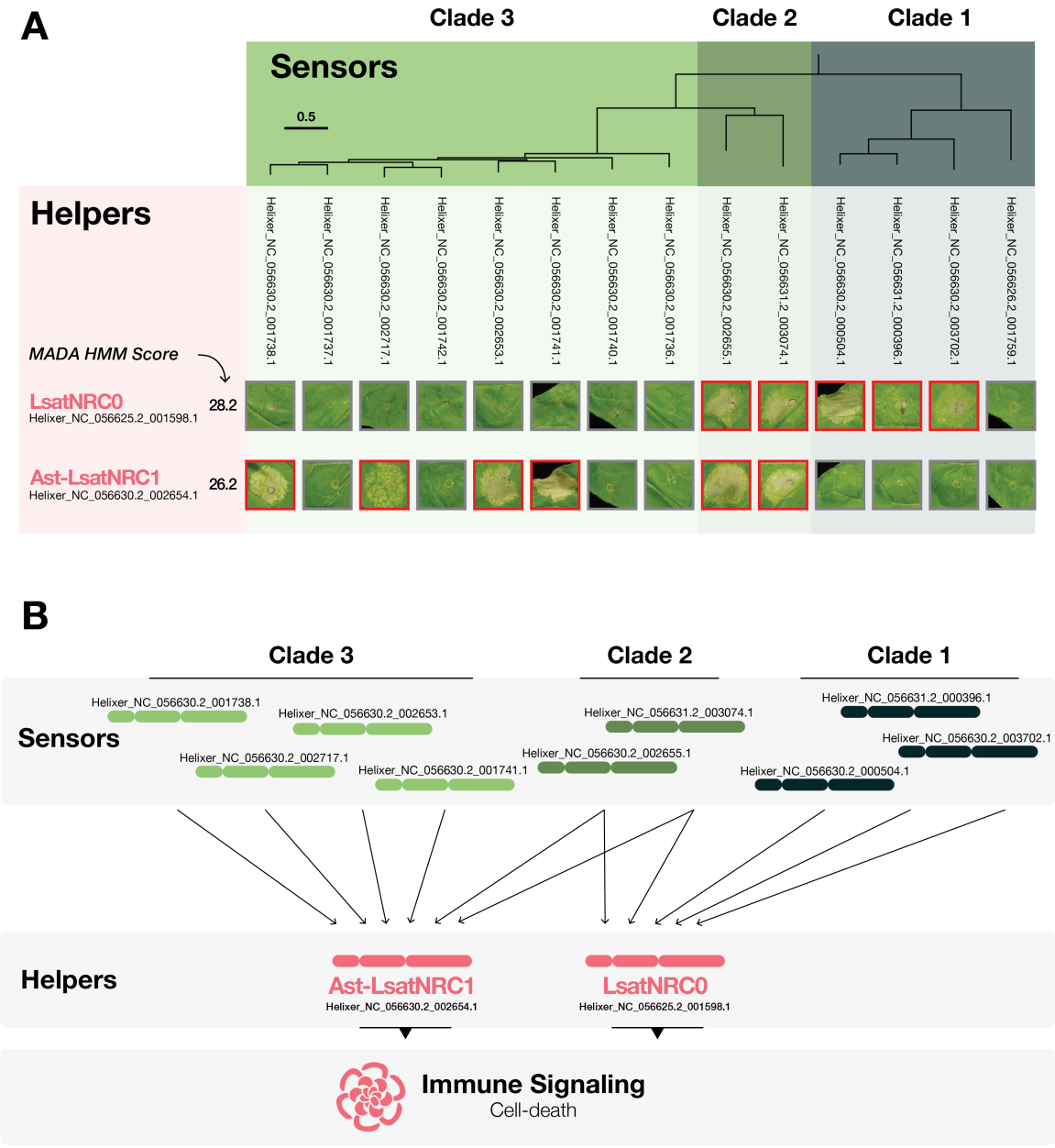


1107

1108 **Figure 3. LsatNRC0 and Ast-LsatNRC1 mediate the cell death signaling of distinct NRC-S**

1109 **phylogenetic clades.** (A) Co-agroinfiltration cell death assays of NRC-H and NRC-S. NRC-S

1110 expressed as autoactive mutants with wild-type NRC helpers. (B) Lettuce NRC network model. The 9

1111 validated NRC-S can cause cell death through LsatNRC0 and Ast-LsatNRC1 in a partially redundant

1112 manner.

1113

bioRxiv preprint doi: https://doi.org/10.1101/2025.02.25.639832; this version posted February 25, 2025. The copyright holder for this preprint (which was not certified by peer review) is the author/funder, who has granted bioRxiv a license to display the preprint in perpetuity. It is made available under aCC-BY 4.0 International license.

**A**

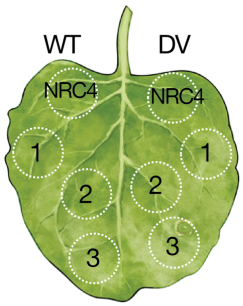


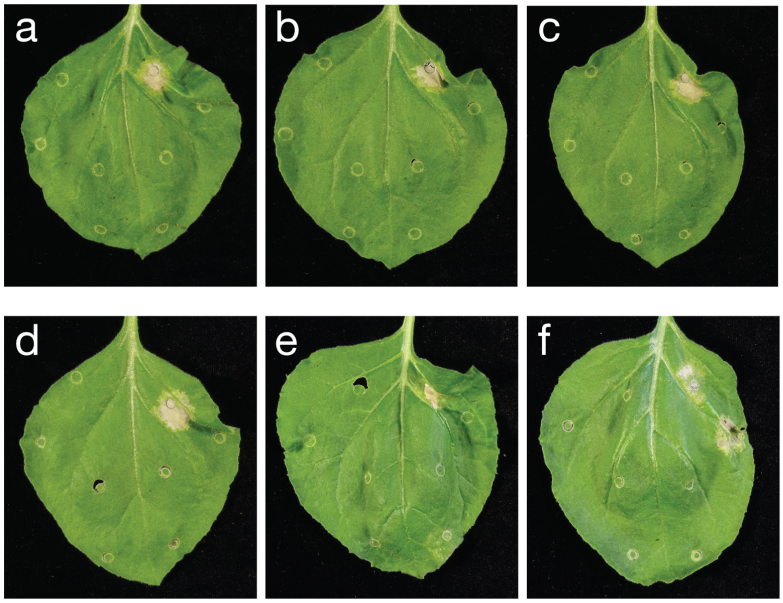


**a**
1: Helixer_NC_056631.2_003074.1(Lt48)
2: Helixer_NC_056630.2_001738.1(L432)
3: Helixer_NC_056630.2_001737.1(Lt34)

**b**
1: Helixer_NC_056630.2_002717.1(Lt36)
2: Helixer_NC_056630.2_001741.1(Lt38)
3: Helixer_NC_056630.2_001742.1(Lt40)

**c**
1: Helixer_NC_056630.2_002653.1(Lt42)
2: Helixer_NC_056630.2_001740.1(Lt44)
3: Helixer_NC_056630.2_001736.1(Lt46)

**d**
1: Helixer_NC_056630.2_002655.1(Lt50)
2: Helixer_NC_056630.2_000504.1(Lt52)
3: Helixer_NC_056631.2_000396.1(Lt54)

**e**
1: Helixer_NC_056630.2_003702.1(Lt56)
2: Helixer_NC_056626.2_001759.1(Lt58)
3: Helixer_NC_056625.2_001598.1(Lt60)

**f**
1: Helixer_NC_056630.2_002654.1(Lt62)
2: Lsat_1_v5_gn_9_45540.1(Lt64)
3: Lsat_1_v5_gn_9_45620.1(Lt66)

**B**

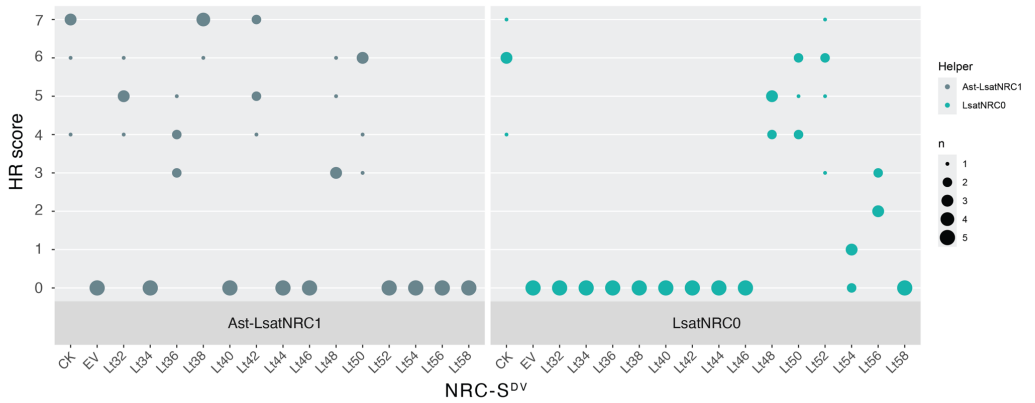


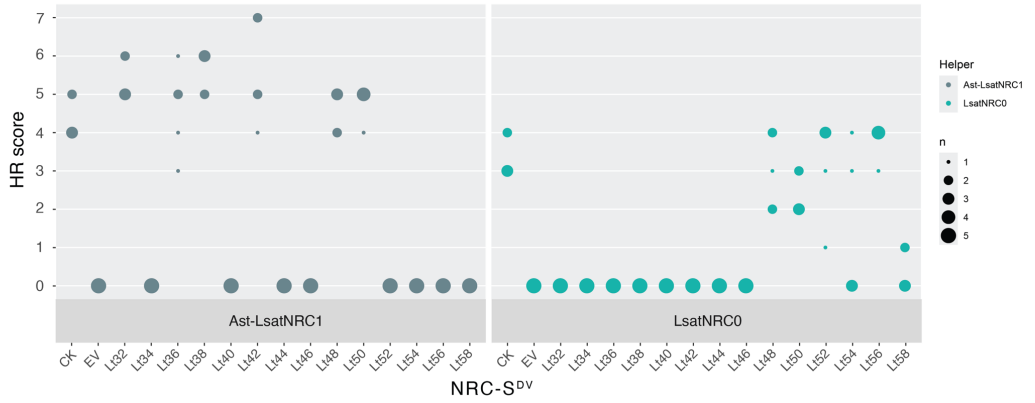


1114

bioRxiv preprint doi: https://doi.org/10.1101/2025.02.25.639832; this version posted February 25, 2025. The copyright holder for this preprint (which was not certified by peer review) is the author/funder, who has granted bioRxiv a license to display the preprint in perpetuity. It is made available under aCC-BY 4.0 International license.

**Figure S8. Hypersensitive response (HR) assays of NRC-H and NRC-S.** (A) Representative *N. benthamiana* leaves expressing wild-type (WT) or MHD mutated (DV) NRC-H and NRC-S, photographed at 5 days post agroinfiltration. $NRC4^{WT}$ and $NRC4^{DV}$ were infiltrated here as negative and positive controls for HR, respectively. (B) Quantification of co-agroinfiltration HR assays of NRC-H and NRC-S. NRC-S expressed as autoactive mutants with wild-type NRC helpers. CK: $NRC4^{DV}$ infiltrated alone as positive control of HR. EV: NRC-H co-infiltrated with empty vector, as a negative control. Number (n) of data points are reflected as different sized circles. Two biological replicates are displayed as independent panels.

bioRxiv preprint doi: https://doi.org/10.1101/2025.02.25.639832; this version posted February 25, 2025. The copyright holder for this preprint (which was not certified by peer review) is the author/funder, who has granted bioRxiv a license to display the preprint in perpetuity. It is made available under aCC-BY 4.0 International license.

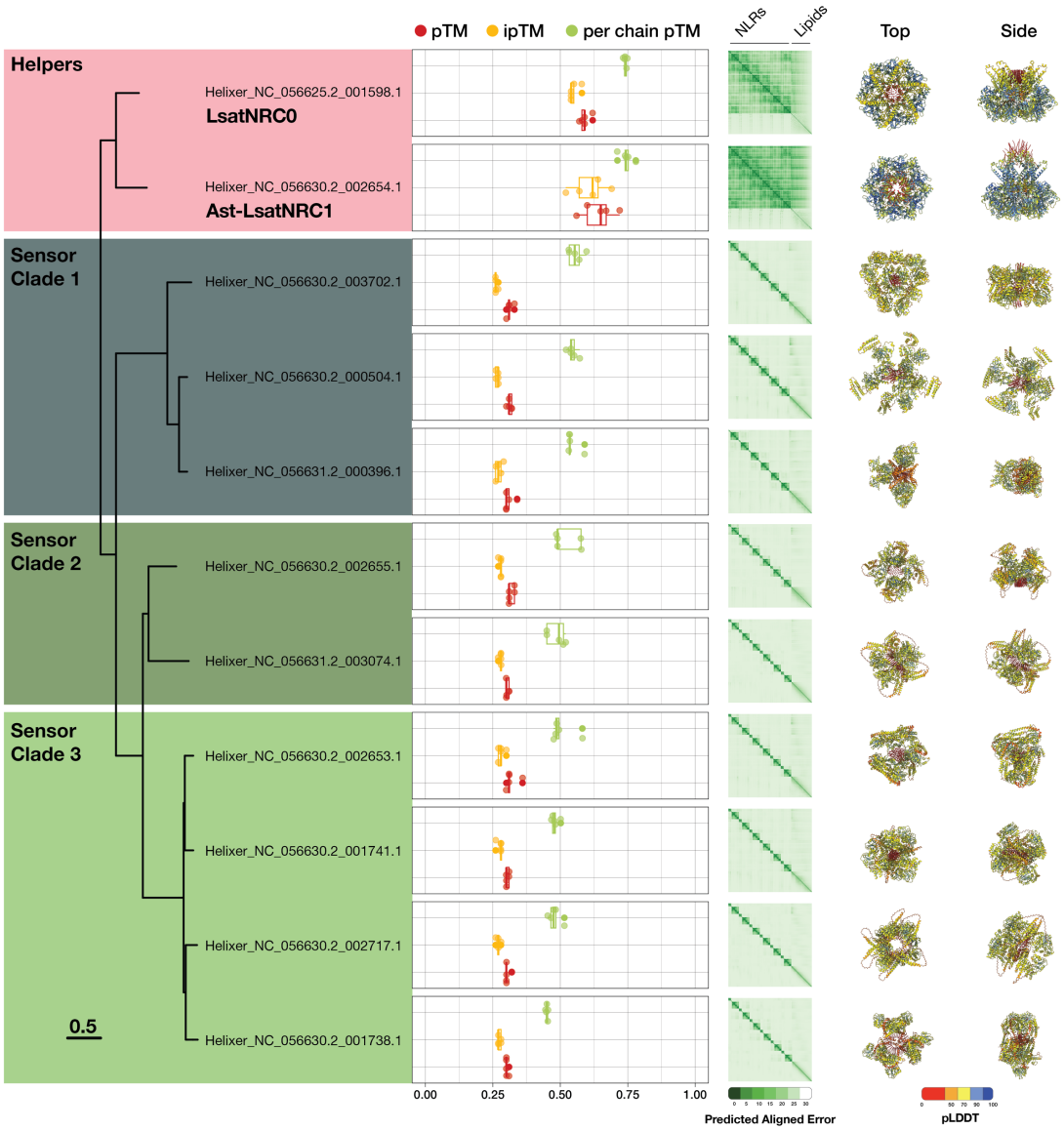


**Figure 4. In contrast to NRC helpers, NRC-S failed to form resistosome-like structures when modeled with AlphaFold 3.** Structural modeling with AlphaFold 3 was used to predict the ability of the tested lettuce NRC-H and NRC-S to form resistosome-like hexameric oligomers. Simulations included 50 oleic acid molecules to approximate the plasma membrane. Key structural metrics, including pLDDT (per-residue measure of local confidence), pTM (predicted template modeling score for overall structure), ipTM (interface-specific pTM), and per-chain pTM, are plotted for each protein (n=5). Example predicted structures from the fourth replicate are displayed in top and side views, colored with the pLDDT color scale indicating local confidence levels.

bioRxiv preprint doi: https://doi.org/10.1101/2025.02.25.639832; this version posted February 25, 2025. The copyright holder for this preprint (which was not certified by peer review) is the author/funder, who has granted bioRxiv a license to display the preprint in perpetuity. It is made available under aCC-BY 4.0 International license.

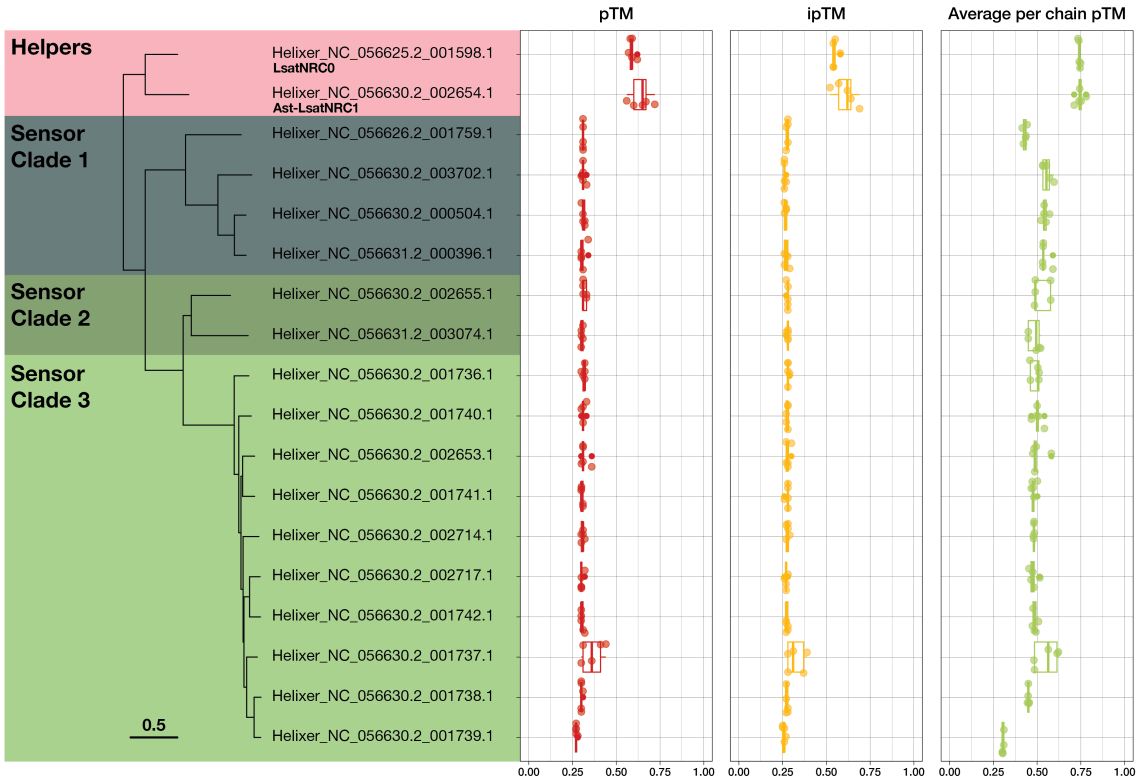


**Figure S9. Structural modeling of lettuce NRC-H and NRC-S clade sequences with AlphaFold 3.** Simulations included 50 oleic acid molecules to approximate the plasma membrane. Key structural metrics, including pTM (predicted template modeling score for overall structure), ipTM (interface-specific pTM), and per-chain pTM, are plotted for each protein (n=5).

bioRxiv preprint doi: https://doi.org/10.1101/2025.02.25.639832; this version posted February 25, 2025. The copyright holder for this preprint (which was not certified by peer review) is the author/funder, who has granted bioRxiv a license to display the preprint in perpetuity. It is made available under aCC-BY 4.0 International license.

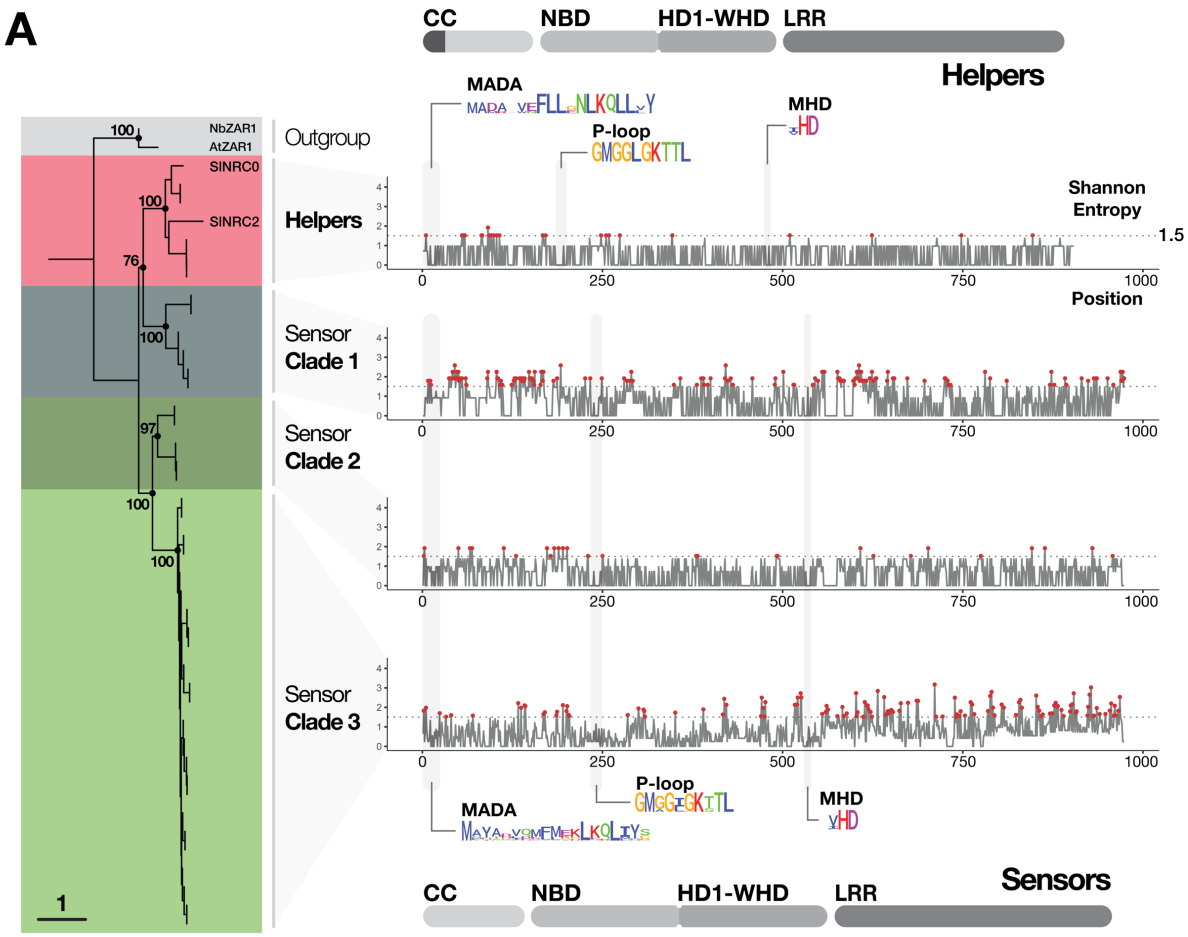


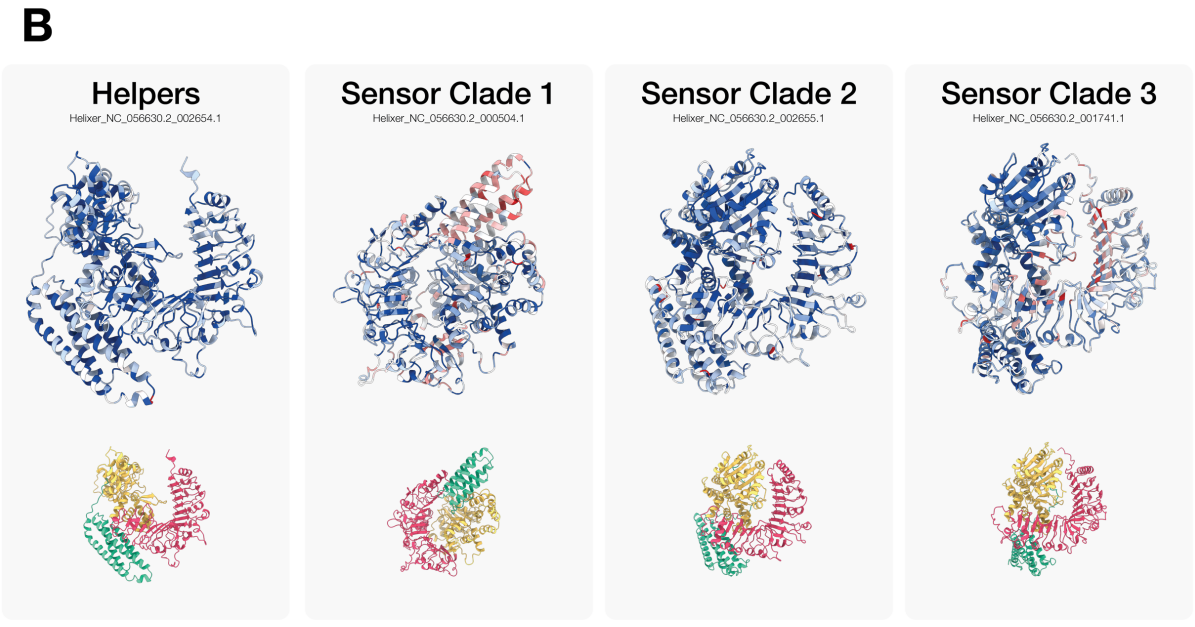


1138

bioRxiv preprint doi: https://doi.org/10.1101/2025.02.25.639832; this version posted February 25, 2025. The copyright holder for this preprint (which was not certified by peer review) is the author/funder, who has granted bioRxiv a license to display the preprint in perpetuity. It is made available under aCC-BY 4.0 International license.

1139 **Figure 5. Lettuce NRC helpers and sensors have differential patterns of diversification.** (A)
1140 Shannon entropy plots of the full-length NLR sequences calculated within each NRC subclade.
1141 Highly variable residues with Shannon entropy values of 1.5 and higher are highlighted by red dots.
1142 (B) Predicted AlphaFold 3 structures of representative sequences from each NRC subclade colored
1143 by Shannon entropy values (top) and domains (bottom).

1144

bioRxiv preprint doi: https://doi.org/10.1101/2025.02.25.639832; this version posted February 25, 2025. The copyright holder for this preprint (which was not certified by peer review) is the author/funder, who has granted bioRxiv a license to display the preprint in perpetuity. It is made available under aCC-BY 4.0 International license.

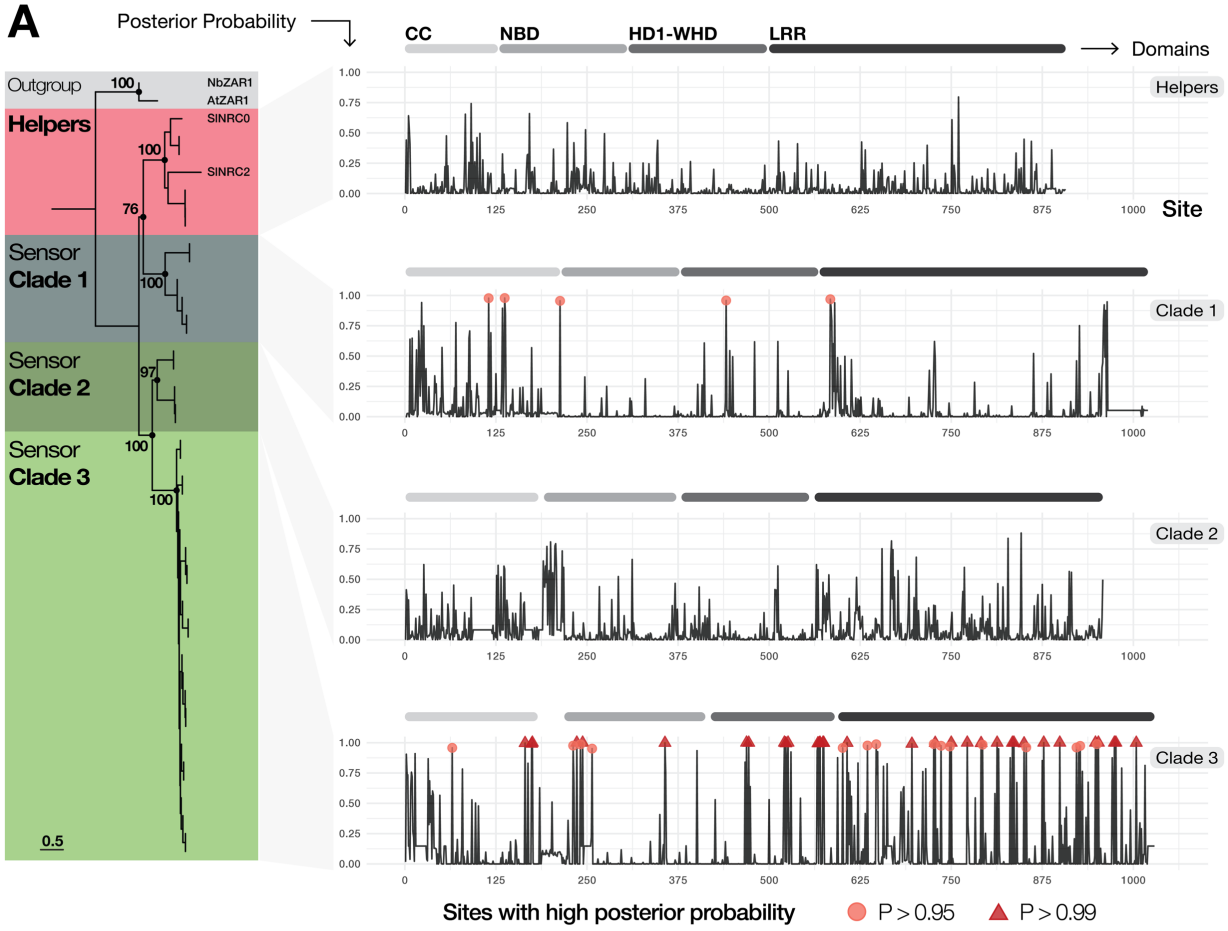


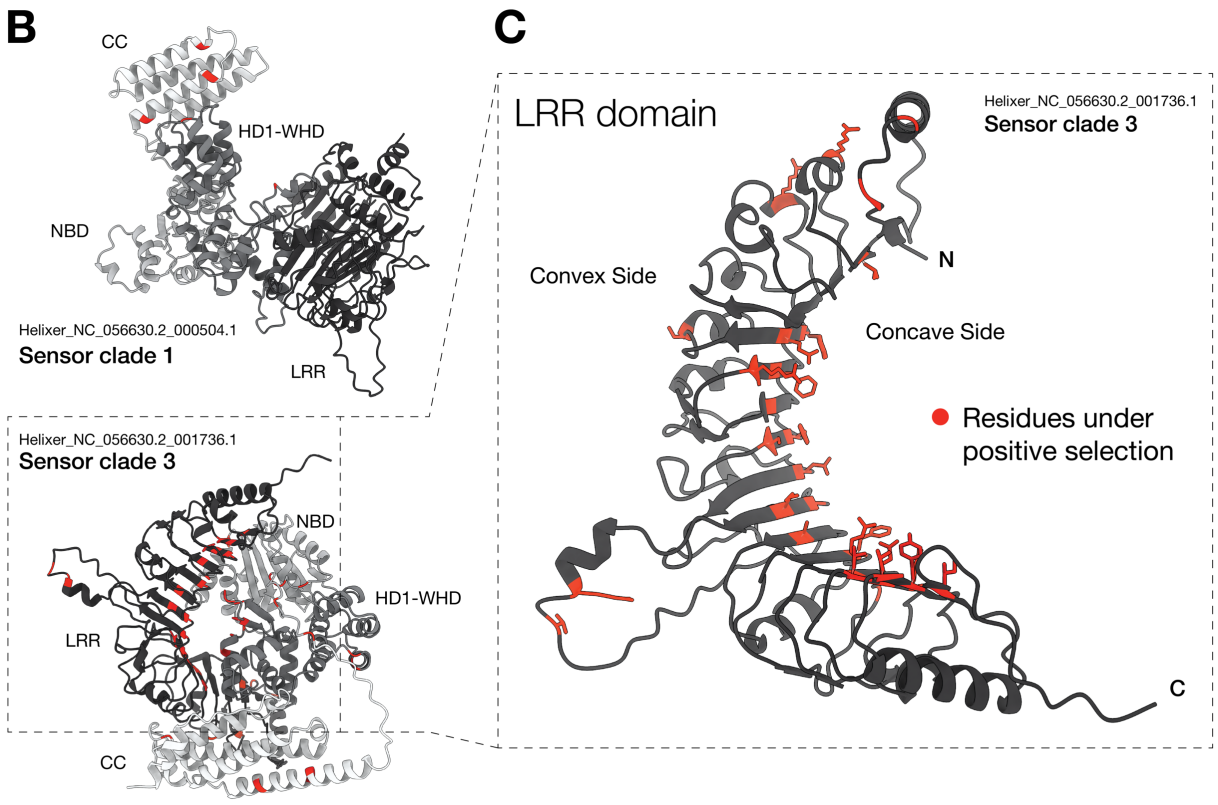


1145

bioRxiv preprint doi: https://doi.org/10.1101/2025.02.25.639832; this version posted February 25, 2025. The copyright holder for this preprint (which was not certified by peer review) is the author/funder, who has granted bioRxiv a license to display the preprint in perpetuity. It is made available under aCC-BY 4.0 International license.

**Figure 6. Ast-LsatNRC1-dependent sensors are under more positive selection compared to NRC0-dependent sensors and NRC helpers.** (A) Posterior probabilities for full-length NLRs in each NRC clade, estimated using the M8 (beta + $\omega$) model from the CodeML package in PAML. Sites with posterior probabilities (P) > 0.95 and > 0.99 are marked by circles and triangles, respectively (Yang 1997). (B) Sites under positive selection (red) mapped onto predicted structures of representative sensor NLRs from clades 1 and 3, generated using AlphaFold 3. (C) Zoomed-in view of the LRR domain from a representative clade 3 sensor NLR, highlighting sites under positive selection (red).

bioRxiv preprint doi: https://doi.org/10.1101/2025.02.25.639832; this version posted February 25, 2025. The copyright holder for this preprint (which was not certified by peer review) is the author/funder, who has granted bioRxiv a license to display the preprint in perpetuity. It is made available under aCC-BY 4.0 International license.

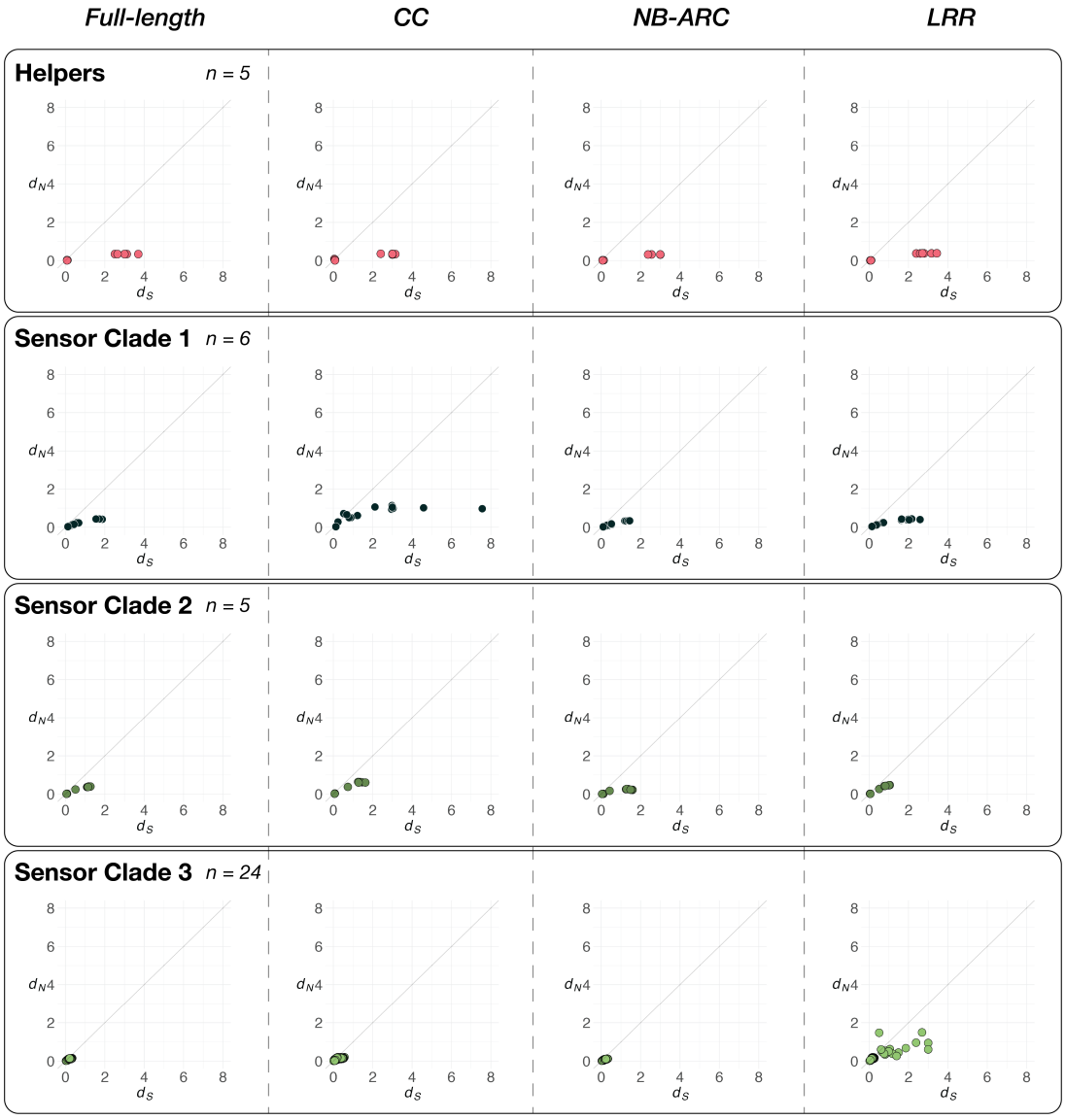


**Figure S10. Pairwise $d_N$ and $d_S$ values for full-length, and CC, NB-ARC, and LRR domains of NLRs within the *Lactuca* NRC clades.** The nonsynonymous (dN) and synonymous (dS) substitution rates were estimated using the approximate method of Nei and Gojobori (1986), implemented in the PAML software (Nei and Gojobori 1986; Yang 1997). A diagonal line represents $d_N = d_S$, indicating neutral selection. Points above this line correspond to positive selection ($\omega = d_N / d_S > 1$).

bioRxiv preprint doi: https://doi.org/10.1101/2025.02.25.639832; this version posted February 25, 2025. The copyright holder for this preprint (which was not certified by peer review) is the author/funder, who has granted bioRxiv a license to display the preprint in perpetuity. It is made available under aCC-BY 4.0 International license.

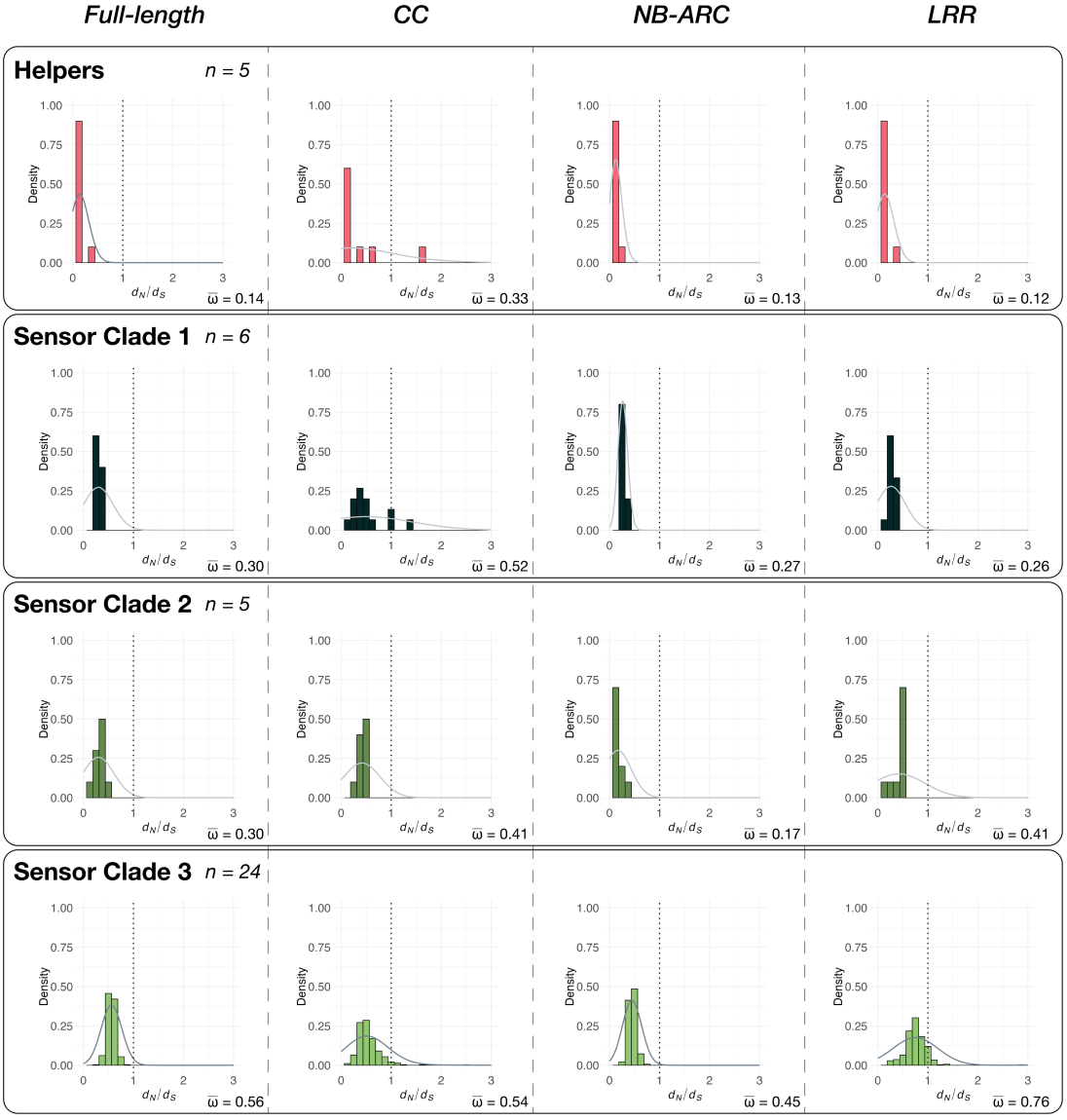


**Figure S11. Histogram of pairwise $d_N/d_S$ ratios for full-length, and CC, NB-ARC, and LRR domains of NLRs within the *Lactuca* NRC clades.** The nonsynonymous (dN) to synonymous (dS) substitution rate ratios were estimated using the approximate method of Nei and Gojobori (1986), implemented in the PAML software (Nei and Gojobori 1986; Yang 1997). $d_N/d_S$ ($\omega$) = 1 is highlighted with dotted line. Average $\omega$ for each graph is displayed at the bottom right corner.

bioRxiv preprint doi: https://doi.org/10.1101/2025.02.25.639832; this version posted February 25, 2025. The copyright holder for this preprint (which was not certified by peer review) is the author/funder, who has granted bioRxiv a license to display the preprint in perpetuity. It is made available under aCC-BY 4.0 International license.

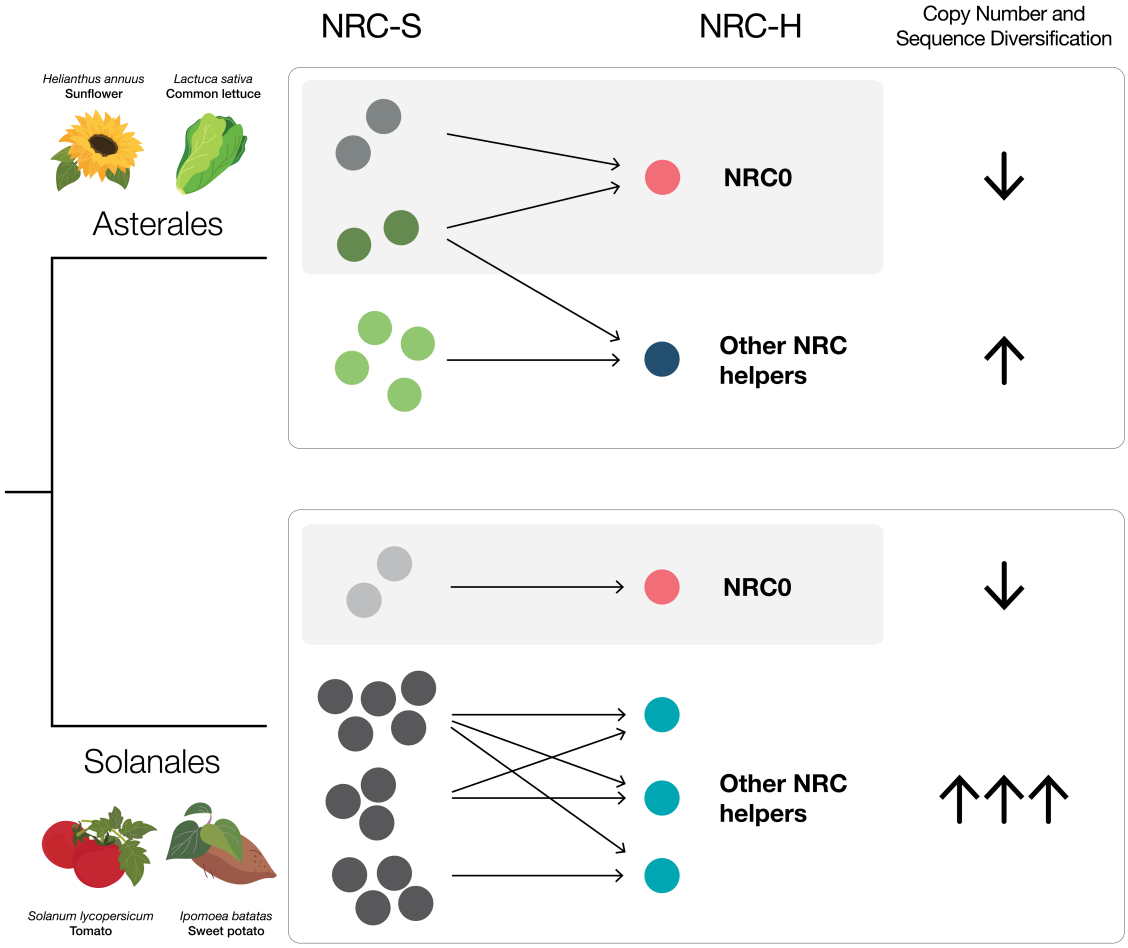


1167

1168 **Figure 7. Evolutionary constraints and diversification patterns in NRC helpers and sensors.**

1169 Sensors dependent on NRC0 are characterized by lower copy number and are under lower positive

1170 selection, likely due to evolutionary constraints associated with their dependency on NRC0. In

1171 contrast, other NRC helpers and the sensors depending on them have undergone significant

1172 expansions, exhibiting higher copy numbers and diversification rates. Representative species from

1173 each order are shown.

1174

https://doi.org/10.1093/plcell/koad175 THE PLANT CELL 2023: 35: 3662–3685

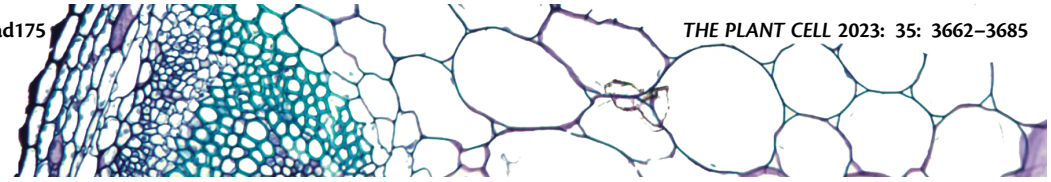

Large-Scale Biology

# Jurassic NLR: Conserved and dynamic evolutionary features of the atypically ancient immune receptor ZAR1

Hiroaki Adachi [1,2,3] Toshiyuki Sakai [1,2] Jiorgos Kourelis [1] Hsuan Pai [1] Jose L. Gonzalez Hernandez [4] Yoshinori Utsumi [5] Motoaki Seki [5,6,7] Abbas Maqbool [1] and Sophien Kamoun [1,*]

1 The Sainsbury Laboratory, University of East Anglia, Norwich Research Park, Norwich NR4 7UH, UK
2 Laboratory of Crop Evolution, Graduate School of Agriculture, Kyoto University, Mozume, Muko, Kyoto 617-0001, Japan
3 PRESTO, Japan Science and Technology Agency, 4-1-8, Honcho, Kawaguchi, Saitama 332-0012, Japan
4 Agronomy, Horticulture and Plant Sciences Department, South Dakota State University, Brookings, SD 57007, USA
5 Plant Genomic Network Research Team, RIKEN Center for Sustainable Resource Science, 1-7-22 Suehiro-cho, Tsurumi-ku, Yokohama, Kanagawa 230-0045, Japan
6 Plant Epigenome Regulation Laboratory, RIKEN Cluster for Pioneering Research, 2-1 Hirosawa, Wako, Saitama 351-0198, Japan
7 Kihara Institute for Biological Research, Yokohama City University, 641-12 Maioka-cho, Totsuka-ku, Yokohama, Kanagawa 244-0813, Japan

*Author for correspondence: sophien.kamoun@tsl.ac.uk
The author responsible for distribution of materials integral to the findings presented in this article in accordance with the policy described in the Instructions for Authors (https://academic.oup.com/plcell/pages/General-Instructions) is: Sophien Kamoun (sophien.kamoun@tsl.ac.uk).

## Abstract

Plant nucleotide-binding leucine-rich repeat (NLR) immune receptors generally exhibit hallmarks of rapid evolution, even at the intraspecific level. We used iterative sequence similarity searches coupled with phylogenetic analyses to reconstruct the evolutionary history of HOPZ-ACTIVATED RESISTANCE1 (ZAR1), an atypically conserved NLR that traces its origin to early flowering plant lineages ~220 to 150 million yrs ago (Jurassic period). We discovered 120 ZAR1 orthologs in 88 species, including the monocot *Colocasia esculenta*, the magnoliid *Cinnamomum micranthum*, and most eudicots, notably the Ranunculales species *Aquilegia coerulea*, which is outside the core eudicots. Ortholog sequence analyses revealed highly conserved features of ZAR1, including regions for pathogen effector recognition and cell death activation. We functionally reconstructed the cell death activity of ZAR1 and its partner receptor-like cytoplasmic kinase (RLCK) from distantly related plant species, experimentally validating the hypothesis that ZAR1 evolved to partner with RLCKs early in its evolution. In addition, ZAR1 acquired novel molecular features. In cassava (*Manihot esculenta*) and cotton (*Gossypium* spp.), ZAR1 carries a C-terminal thioredoxin-like domain, and in several taxa, *ZAR1* duplicated into 2 paralog families, which underwent distinct evolutionary paths. *ZAR1* stands out among angiosperm NLR genes for having experienced relatively limited duplication and expansion throughout its deep evolutionary history. Nonetheless, ZAR1 also gave rise to noncanonical NLRs with integrated domains and degenerated molecular features.

## Introduction

Plant immune receptors, often encoded by disease resistance (*R*) genes, detect invading pathogens and activate innate immune responses that can limit infection (Jones and Dangl 2006). A major class of immune receptors is formed by intracellular proteins of the nucleotide-binding leucine-rich repeat (NLR) family (Dodds and Rathjen 2010; Jones et al. 2016; Kourelis and van der Hoorn 2018). NLRs detect host-translocated pathogen effectors either by directly binding them or by indirectly monitoring proteins known as guardees or decoys.

NLRs are arguably the most diverse protein family in flowering plants (angiosperms) with many species having large (>100) and diverse repertoires of NLR genes in their genomes (Shao et al. 2016; Baggs et al. 2017; Kourelis et al. 2021). NLR genes typically exhibit hallmarks of rapid evolution even at the intraspecific level (Van de Weyer et al. 2019; Lee and

Received January 17, 2023. Accepted June 02, 2023. Advance access publication July 19, 2023
© American Society of Plant Biologists 2023. All rights reserved. For permissions, please e-mail: journals.permissions@oup.com

Downloaded from https://academic.oup.com/plcell/article/35/10/3662/7226528 by guest on 02 August 2025

## IN A NUTSHELL

**Background:** In plants, nucleotide-binding leucine-rich repeat (NLR) immune receptors generally exhibit hallmarks of rapid evolution even at the intraspecific level. NLRs evolve primarily through a birth-and-death process: new NLRs emerge by recurrent cycles of gene duplication and loss—some genes are maintained in the genome and acquire new pathogen detection specificities, whereas others are deleted or become nonfunctional through the accumulation of deleterious mutations. Such dynamic patterns of evolution enable the NLR immune system to keep up with fast-evolving effector repertoires of pathogenic microbes. Unlike typical NLRs, HOPZ-ACTIVATED RESISTANCE1 (ZAR1) is conserved across angiosperms.

**Question:** Can we use a molecular evolution framework to determine the critical features of a conserved plant NLR?

**Findings:** We performed iterative sequence similarity searches coupled with phylogenetic analyses to reconstruct the evolutionary history of ZAR1. ZAR1 is an atypically conserved NLR that traces its origin to early flowering plant lineages ~220 to 150 million yrs ago (Jurassic period). Ortholog sequence analyses revealed highly conserved features of ZAR1, including regions for pathogen recognition and immune activation. We functionally reconstructed the immune activity of ZAR1 and its host partner receptor-like cytoplasmic kinases (RLCKs) from distantly related plant species, supporting the hypothesis that ZAR1 has evolved to partner with RLCKs early in its evolution. ZAR1 stands out among angiosperm NLRs for having experienced relatively limited gene duplication and expansion throughout its deep evolutionary history.

**Next steps:** Further comparative analyses, combining molecular evolution and structural biology of plant and animal NLR systems will yield experimentally testable hypotheses for NLR research.

Chae 2020; Prigozhin and Krasileva 2020). Towards the end of the 20th century, Michelmore and Meyers (1998) proposed that NLRs evolve primarily through the birth-and-death process. In this model, new NLRs emerge by recurrent cycles of gene duplication and loss—some genes are maintained in the genome and acquire new pathogen detection specificities, whereas others are deleted or become nonfunctional through the accumulation of deleterious mutations. Such dynamic patterns of evolution enable the NLR immune system to keep up with fast-evolving effector repertoires of pathogenic microbes.

However, as noted over 20 yrs ago by Michelmore and Meyers (1998), a subset of NLR proteins is slow evolving and has remained fairly conserved throughout evolutionary time (Wu et al. 2017; Stam et al. 2019). These "high-fidelity" NLRs (per Lee and Chae 2020) offer unique opportunities for comparative analyses, providing a molecular evolution framework to reconstruct key transitions and reveal functionally critical biochemical features (Delaux et al. 2019). Nonetheless, comprehensive evolutionary reconstructions of conserved NLR proteins remain limited despite the availability of a large number of plant genomes across the breadth of plant phylogeny. One of the reasons is that the great majority of NLRs lack clear-cut orthologs across divergent plant taxa. Here, we address this gap in knowledge by investigating the macroevolution of ZAR1 (HOPZ-ACTIVATED RESISTANCE1), an atypically ancient NLR, and asking fundamental questions about the conservation and diversification of this immune receptor throughout its deep evolutionary history.

NLRs generally function in nonself perception and innate immunity in plants and animals (Jones et al. 2016; Uehling et al. 2017). In the broadest biochemical definition, plant NLRs share a multidomain architecture typically consisting of a NB-ARC (nucleotide-binding domain shared with APAF-1, various R-proteins, and CED-4) followed by a leucine-rich repeat (LRR) domain. Angiosperm NLRs form several major monophyletic groups with distinct N-terminal domain fusions (Shao et al. 2016; Kourelis et al. 2021). These include the subclades TIR-NLR with the Toll/interleukin-1 receptor (TIR) domain, CC-NLR with the Rx-type coiled-coil (CC) domain, $CC_R$-NLR with the RPW8-type CC ($CC_R$) domain (Tamborski and Krasileva 2020), and the more recently defined $CC_{G10}$-NLR with a distinct type of CC ($CC_{G10}$) (Lee H-Y et al. 2020). In addition to the canonical tripartite domain architecture, up to 10% of NLRs carry unconventional "integrated" domains. Integrated domains (IDs) are thought to generally function as decoys to bait pathogen effectors and enable pathogen detection (Cesari et al. 2014; Wu et al. 2015; Sarris et al. 2016; Kourelis and van der Hoorn 2018). They include dozens of different modules indicating that novel domain acquisitions have repeatedly taken place throughout the evolution of plant NLRs (Kroj et al. 2016; Sarris et al. 2016). To date, over 400 NLRs from 31 genera in 11 orders of flowering plants have been experimentally validated as reported in the RefPlantNLR reference dataset (Kourelis et al. 2021). Several of these NLRs are coded by *R* genes that function against economically important pathogens and contribute to sustainable agriculture (Dangl et al. 2013).

In recent years, the research community has gained a better understanding of the structure/function relationships of plant NLRs and the immune receptor circuitry they form (Wu et al. 2018; Adachi et al. 2019a; Burdett et al. 2019; Jubic et al. 2019;

Downloaded from https://academic.oup.com/plcell/article/35/10/3662/7226528 by guest on 02 August 2025

Bayless and Nishimura 2020; Feehan et al. 2020; Mermigka et al. 2020; Wang and Chai 2020; Xiong et al. 2020; Zhou and Zhang 2020). Some NLRs, such as ZAR1, form a single functional unit that carries both pathogen sensing and immune signaling activities in a single protein (termed "singleton NLR" per Adachi et al. 2019a). Other NLRs function together in pairs or more complex networks, where connected NLRs have functionally specialized into sensor NLRs dedicated to pathogen detection or helper NLRs that are required for sensor NLRs to initiate immune signaling (Feehan et al. 2020). Paired and networked NLRs are thought to have evolved from multifunctional ancestral receptors through asymmetrical evolution (Adachi et al. 2019a, 2019b). As a result of their direct coevolution with pathogens, NLR sensors tend to diversify faster than helpers and can be dramatically expanded in some plant taxa (Wu et al. 2017; Stam et al. 2019). For instance, sensor NLRs often exhibit noncanonical biochemical features, such as degenerated functional motifs and unconventional domain integrations (Adachi et al. 2019b; Seong et al. 2020).

The elucidation of plant NLR structures by cryo-electron microscopy has significantly advanced our understanding of the biochemical events associated with the activation of these immune receptors (Wang et al., 2019a, 2019b; Ma et al. 2020; Martin et al. 2020). The CC-NLR ZAR1, the TIR-NLRs RPP1 and Roq1 oligomerize upon activation into a multimeric complex known as the resistosome. In the case of ZAR1, recognition of bacterial effectors occurs through its partner receptor-like cytoplasmic kinases (RLCKs), which are encoded by genes that occur in a genomic cluster; this cluster encodes multiple RLCK-type pseudokinases that vary depending on the pathogen effector and host plant (Lewis et al. 2013; Wang et al., 2015; Seto et al. 2017; Schultink et al. 2019; Laflamme et al. 2020). Activation of ZAR1 induces conformational changes in the nucleotide-binding domain resulting in ADP release, dATP/ATP binding, and pentamerization of the ZAR1–RLCK complex into the resistosome. The ZAR1 resistosome exposes a funnel-shaped structure formed by the N-terminal α1 helices, which translocates into the plasma membrane, and the resistosome itself acts as a $Ca^{2+}$ channel (Wang et al., 2019b; Bi et al. 2021). The ZAR1 N-terminal α1 helix matches the MADA consensus sequence motif that is functionally conserved in ∼20% of CC-NLRs including NLRs from dicot and monocot plant species (Adachi et al. 2019b). This suggests that the biochemical "death switch" mechanism of the ZAR1 resistosome may apply to a significant fraction of CC-NLRs. Interestingly, unlike singleton and helper CC-NLRs, sensor CC-NLRs often carry degenerated MADA α1 helix motifs and/or N-terminal domain integrations, which would preclude their capacity to trigger cell death according to the ZAR1 model (Adachi et al. 2019b; Seong et al. 2020).

Comparative sequence analyses based on a robust evolutionary framework can yield insights into molecular mechanisms and help generate experimentally testable hypotheses. ZAR1 was previously reported to be conserved across multiple dicot plant species but whether it occurs in other angiosperms hasn't been systematically studied (Lewis et al. 2010; Baudin et al. 2017; Schultink et al. 2019; Harant et al. 2022). Here, we used a phylogenomic approach to investigate the molecular evolution of ZAR1 across flowering plants (angiosperms). We discovered 120 ZAR1 orthologs in 88 species, including monocot, magnoliid, and eudicot species indicating that ZAR1 is an atypically conserved CC-NLR that traces its origin to early angiosperm lineages ∼220 to 150 million yrs ago (Jurassic period). We took advantage of this large collection of orthologs to identify highly conserved features of ZAR1, revealing regions for effector recognition, intramolecular interactions, and cell death activation. We showed that the cell death activity of ZAR1 from distantly related plant species can be dependent of its partner RLCKs, therefore experimentally validating the hypothesis that ZAR1 has evolved to be a partner with RLCKs early in its evolution. Throughout its evolution, ZAR1 also acquired features, including the C-terminal integration of a thioredoxin-like domain and duplication into 2 paralog families ZAR1-SUB and ZAR1-CIN. Members of the ZAR1-SUB paralog family have highly diversified in eudicots and often lack conserved ZAR1 features. We conclude that ZAR1 has experienced relatively limited gene duplication and expansion throughout its deep evolutionary history but still did give rise to noncanonical NLR proteins with IDs and degenerated molecular features.

## Results

### ZAR1 is widely conserved across angiosperms

To determine the distribution of ZAR1 across plant species, we applied a computational pipeline based on iterated BLAST searches of plant genome and protein databases (Fig. 1A). These comprehensive searches were seeded with previously identified ZAR1 sequences from Arabidopsis (*Arabidopsis thaliana*), *Nicotiana benthamiana*, tomato (*Solanum lycopersicum*), sugar beet (*Beta vulgaris*), and cassava (*Manihot esculenta*) (Baudin et al. 2017; Schultink et al. 2019; Harant et al. 2022). We also performed iterated phylogenetic analyses using the NB-ARC domain of the harvested ZAR1-like sequences and obtained a well-supported clade that includes the previously reported ZAR1 sequences, as well as new clade members from more distantly related plant species, notably *Colocasia esculenta* (taro, Alismatales), *Cinnamomum micranthum* (Syn. *Cinnamomum kanehirae*, stout camphor, Magnoliidae), and *Aquilegia coerulea* (columbine, Ranunculales; Supplemental Data Set 1).

In total, we identified 120 *ZAR1* genes from 88 angiosperm species that tightly clustered in the ZAR1 phylogenetic clade (Fig. 1B and Supplemental Data Set 1). Among the 120 genes, 108 code for canonical CC-NLR proteins with 52.0% to 97.0% similarity to Arabidopsis ZAR1, whereas another 9 carry the 3 major domains of CC-NLR proteins but have a C-terminal integrated domain (ZAR1-ID, see below). The remaining 3 genes code for 2 truncated NLRs and a potentially misannotated coding sequence due to a gap in the genome sequence. In summary, we propose that the identified clade

Downloaded from https://academic.oup.com/plcell/article/35/10/3662/7226528 by guest on 02 August 2025

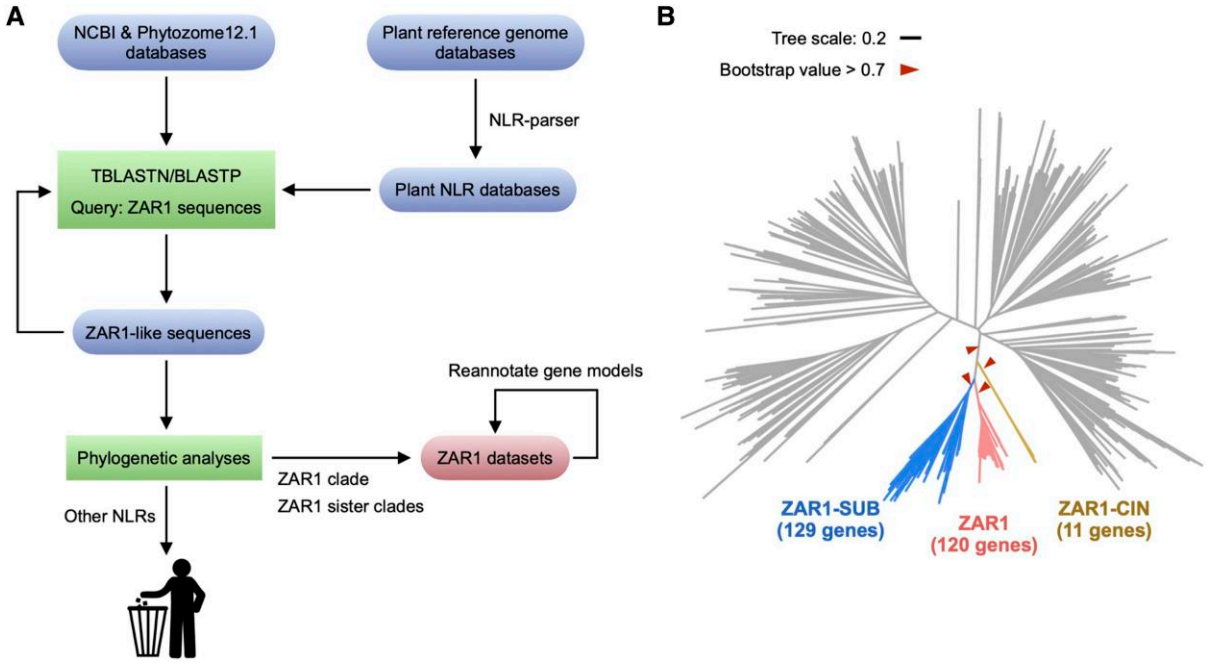


**Figure 1.** Comparative sequence analyses identify and classify ZAR1 sequences from angiosperms. **A)** Workflow for computational analyses in searching for *ZAR1* orthologs. We performed TBLASTN/BLASTP searches and subsequent phylogenetic analyses to identify *ZAR1* ortholog genes from plant genome/proteome datasets. **B)** ZAR1 forms a clade with 2 closely related sister subclades. The phylogenetic tree was generated in MEGA7 by the neighbor-joining method using NB-ARC domain sequences of ZAR1-like proteins identified from the prior BLAST searches and 1,019 NLRs identified from 6 representative plant species, taro, stout camphor, columbine, tomato, sugar beet, and Arabidopsis. Red arrowheads indicate bootstrap support > 0.7 and is shown for the relevant nodes. The scale bar indicates the evolutionary distance in amino acid substitution per site.

consists of ZAR1 orthologs from a diversity of angiosperm species. Our analyses of ZAR1-like sequences also revealed 2 well-supported sister clades of the ZAR1 ortholog clade (Fig. 1B). We named these subclades ZAR1-SUB and ZAR1-CIN (referred to as ZAR1-sis and ZAR1-basal in Gong et al. (2022), respectively), and we describe them in more detail below.

We have recently proposed that ZAR1 is the most conserved CC-NLR between rosid and asterid plants (Harant et al. 2022). To further evaluate ZAR1 conservation relative to other CC-NLRs across angiosperms, we used a phylogenetic tree of 1,475 NLRs from the monocot taro, the magnoliid stout camphor, and 6 eudicot species (columbine, Arabidopsis, cassava, sugar beet, tomato, and *N. benthamiana*) to calculate the phylogenetic (patristic) distance between each of the 49 Arabidopsis CC-NLRs and their closest neighbor from each of the other plant species. As shown in Harant et al. (2022), ZAR1 stands out for having the shortest phylogenetic distance to its orthologs relative to other CC-NLRs in this diverse angiosperm species set (Supplemental Fig. S1). A similar analysis where we plotted the phylogenetic distance between each of the 159 *N. benthamiana* CC-NLRs to their closest neighbor from the other species also revealed ZAR1 as displaying the shortest patristic distance across all examined species (Supplemental Fig. S2). These analyses revealed that ZAR1 is possibly the most widely conserved CC-NLR in flowering plants (angiosperms).

## Phylogenetic distribution of *ZAR1* in angiosperms

Although *ZAR1* is distributed across a wide range of angiosperms, we noted particular patterns in its phylogenetic distribution. Supplemental Data Set 1 describes the gene identifiers and other features of ZAR1 orthologs sorted based on the phylogenetic clades reported by Smith and Brown (2018). Sixty-eight of the 88 plant species have a single copy of *ZAR1* whereas 20 species have 2 or more copies (Supplemental Data Set 2). *ZAR1* is primarily a eudicot gene, but we identified 3 *ZAR1* orthologs outside the eudicots, 2 in the monocot taro, and another 1 in the magnoliid stout camphor. We failed to detect *ZAR1* orthologs in 39 species among the 127 species we examined (Supplemental Data Set 1). Except for taro, *ZAR1* is missing in monocot species (17 examined), including in the well-studied *Hordeum vulgare* (barley), *Oryza sativa* (rice), *Triticum aestivum* (wheat), and *Zea mays* (maize). *ZAR1* is also missing in all examined species of the eudicot Fabales, Cucurbitales, Apiales, and Asterales. However, we found a *ZAR1* ortholog in columbine (a eudicot outside the monophyletic clade of core eudicots) and *ZAR1* is widespread in other eudicots, including in 63 rosid, 4 Caryophyllales, and 18 asterid species.

Downloaded from https://academic.oup.com/plcell/article/35/10/3662/7226528 by guest on 02 August 2025

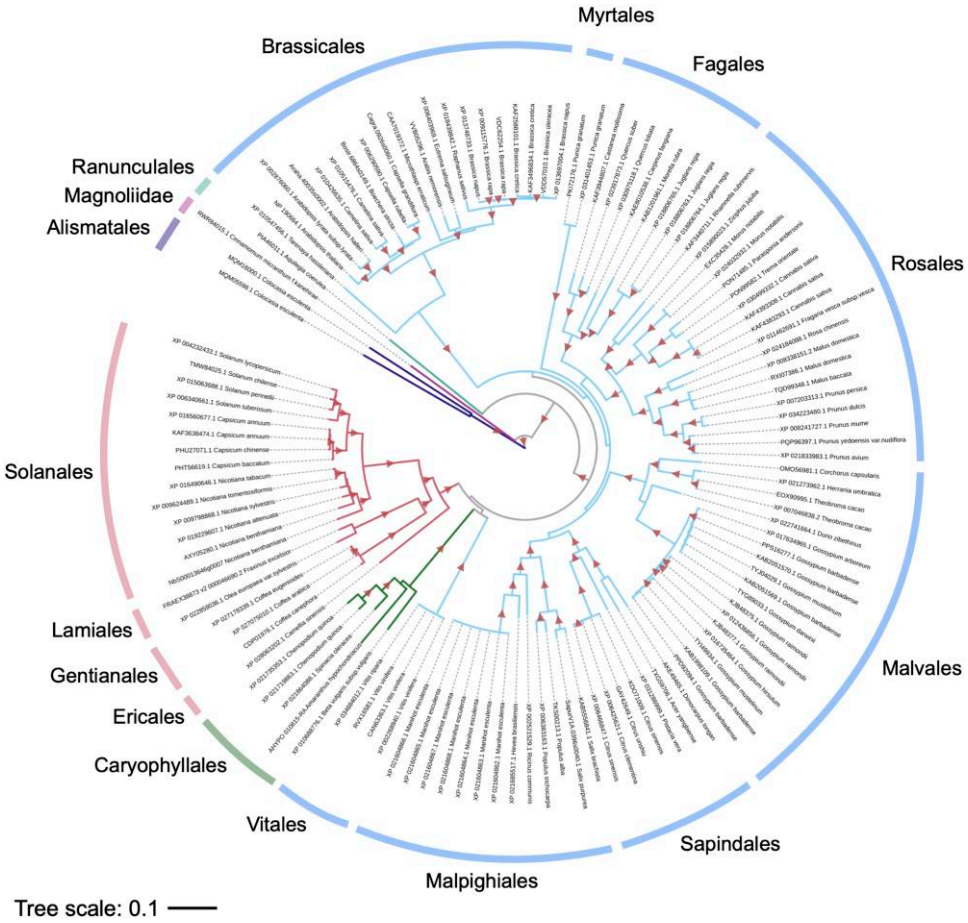


**Figure 2.** The *ZAR1* gene is distributed across angiosperms. The phylogenetic tree was generated in MEGA7 by the neighbor-joining method using full-length amino acid sequences of 120 ZAR1 orthologs identified in Fig. 1. Red triangles indicate bootstrap support > 0.7. The scale bar indicates the evolutionary distance in amino acid substitution per site.

## *ZAR1* is an ancient Jurassic gene that predates the split between monocots, magnoliids, and eudicots

The overall conservation of the 120 ZAR1 orthologs enabled us to perform phylogenetic analyses using the full-length protein sequence and not just the NB-ARC domain as generally done with NLRs (Fig. 2 and Supplemental Fig. S3). These analyses yielded a robust ZAR1 phylogenetic tree with well-supported branches that generally mirrored established phylogenetic relationships between the examined plant species (Smith and Brown 2018; Chaw et al. 2019). For example, the ZAR1 tree matched a previously published species tree of angiosperms based on 211 single-copy core ortholog genes (Chaw et al. 2019). We conclude that the origin of the *ZAR1* gene predates the split between monocots, magnoliids, and eudicots and its evolution traced species divergence ever since. We postulate that ZAR1 probably emerged in the Jurassic era ~220 to 150 million yrs ago (Mya) based on the species divergence time estimate of Chaw et al. (2019) and consistent with the latest fossil evidence for the emergence of flowering plants (Fu et al. 2018; Cui et al. 2022).

## *ZAR1* is a genetic singleton in a locus that exhibits gene colinearity across eudicot species

NLR genes are often clustered in loci that are thought to accelerate sequence diversification and evolution (Michelmore and Meyers 1998; Lee and Chae 2020). We examined the genetic context of ZAR1 genes using available genome assemblies of taro, stout camphor, columbine, Arabidopsis, cassava, sugar beet, tomato, and *N. benthamiana*. The *ZAR1* locus is generally devoid of other NLR genes as the closest NLR is found in the Arabidopsis genome 183 kb away from *ZAR1* (Supplemental Data Set 3). We conclude that *ZAR1* has probably remained a genetic singleton NLR gene throughout its evolutionary history in angiosperms.

Next, we examined the *ZAR1* locus for gene colinearity across the examined species. We noted a limited degree of gene colinearity between Arabidopsis vs. cassava, cassava vs. tomato, and tomato vs. *N. benthamiana* (Supplemental Fig. S4). Flanking conserved genes include the ATPase and protein kinase genes that are present at the *ZAR1* locus in both rosid and asterid eudicots. In contrast, we didn't observe conserved gene blocks at the *ZAR1* locus of taro, stout

Downloaded from https://academic.oup.com/plcell/article/35/10/3662/7226528 by guest on 02 August 2025

camphor, and columbine, indicating that this locus is divergent in these species. Overall, although limited, the observed gene colinearity in eudicots is consistent with the conclusion that *ZAR1* is a genetic singleton with an ancient origin.

## ZAR1 orthologs carry sequence motifs known to be required for Arabidopsis ZAR1 resistosome function

The overall sequence conservation and deep evolutionary origin of ZAR1 orthologs combined with the detailed knowledge of the ZAR1 structure and function provide a unique opportunity to explore the evolutionary dynamics of this ancient immune receptor in a manner that cannot be applied to more rapidly evolving NLRs. We used MEME (Multiple EM for Motif Elicitation; Bailey and Elkan 1994) to search for conserved sequence patterns among the 117 ZAR1 orthologs (ZAR1 and ZAR1-ID) that encode full-length CC-NLR proteins. This analysis revealed several conserved sequence motifs that span across the ZAR1 orthologs (range of protein lengths: 753–1,132 amino acids; Fig. 3A and Supplemental Table S1). In Fig. 3A, we described the major 5 sequence motifs or interfaces known to be required for Arabidopsis ZAR1 function that are conserved across ZAR1 orthologs.

Effector recognition by ZAR1 occurs indirectly via binding to RLCKs through the LRR domain. Key residues in the Arabidopsis ZAR1–RLCK interfaces are highly conserved among ZAR1 orthologs and were identified by MEME as conserved sequence patterns (Fig. 3A). Valine (V) 544, histidine (H) 597, glycine (G) 645, proline (P) 816, tryptophan (W) 825, and phenylalanine (F) 839 in the Arabidopsis ZAR1 LRR domain were validated by mutagenesis as important residues for RLCK binding whereas isoleucine (I) 600 was not essential (Wang et al., 2015; Baudin et al. 2017; Wang et al., 2019a; Hu et al. 2020). In the 117 ZAR1 orthologs, V544, H597, G645, P816, W825, and F839 are conserved in 88% to 100% of the proteins compared to only 63% for I600.

After effector recognition, Arabidopsis ZAR1 undergoes conformational changes from the monomeric inactive form to the oligomeric active state. This is mediated by ADP release from the NB-ARC domain and subsequent ATP binding, which triggers further structural remodeling in ZAR1 leading to the formation of the activated pentameric resistosome (Wang et al., 2019b). NB-ARC sequences that coordinate binding and hydrolysis of dATP, namely, P-loop and MHD motifs, are highly conserved across ZAR1 orthologs (Fig. 3A). Histidine (H) 488 and lysine (K) 195, located in the ADP/ATP-binding pocket (Wang et al., 2019a, 2019b), are invariant in all 117 orthologs. In addition, 3 NB-ARC residues, W150, S152, and V154, known to form the NBD–NBD oligomerization interface for resistosome formation (Wang et al., 2019b; Hu et al. 2020), are present in 82% to 97% of the ZAR1 orthologs and were also part of a MEME motif (Fig. 3A).

The N-terminal CC domain of Arabidopsis ZAR1 mediates cell death signaling thorough the N-terminal α1 helix/MADA motif that becomes exposed in activated ZAR1 resistosome to form a funnel-like structure (Baudin et al. 2017, 2019; Wang et al., 2019b; Adachi et al. 2019b). We detected an N-terminal MEME motif that matches the α1 helix/MADA motif (Fig. 3A). We also used the HMMER software (Eddy 1998) to query the ZAR1 orthologs with a previously reported MADA motif–hidden Markov model (HMM; Adachi et al. 2019b). This HMMER search detected a MADA-like sequence at the N-terminus of all 117 ZAR1 orthologs (Supplemental Data Set 1).

Taken together, based on the conserved motifs depicted in Fig. 3A, we propose that angiosperm ZAR1 orthologs share the main functional features of Arabidopsis ZAR1: (i) effector recognition via RLCK binding, (ii) remodeling of intramolecular interactions via ADP/ATP switch, (iii) oligomerization via the NBD–NBD interface, and (iv) α1 helix/MADA motif–mediated activation of hypersensitive cell death.

## ZAR1 resistosome displays conserved surfaces on RLCK binding sites and the inner glutamate ring

To identify additional conserved and variable features in ZAR1 orthologs, we used ConSurf (Ashkenazy et al. 2016) to calculate a conservation score for each amino acid and generate a diversity barcode for ZAR1 orthologs (Fig. 3B). We then used the cryo-EM structures of Arabidopsis ZAR1 to determine how the ConSurf score maps onto the 3D structures (Figs. 3, C and D, and 4). First, we found 5 major variable surfaces (VS1 to VS5) on the inactive ZAR1 monomer structure (Fig. 3, C and D), as depicted in the ZAR1 diversity barcode (Fig. 3B). VS1 comprises α2/α4 helices and a loop between α3 and α4 helices of the CC domain. VS2 and VS3 corresponds to α1/α2 helices of NBD and a loop between α2 and α3 helices of HD1, respectively. VS4 comprises a loop between WHD and LRR and first 3 helices of the LRR domain. VS5 is mainly derived from the last 3 helices of the LRR domain and the loops between these helices (Fig. 3, B and D).

Next, we examined highly conserved surfaces on inactive and active ZAR1 structures (Fig. 4, A and B). Consistent with the MEME analyses, we confirmed that highly conserved surfaces match to the RLCK binding interfaces (Fig. 4, A and B). We also confirmed that the N-terminal α1 helix/MADA motif is conserved on the resistosome surfaces, although the first 4 N-terminal amino acids are missing from the N terminus of the active ZAR1 cryo-EM structures (Fig. 4, B and C). We also noted sequence conservation at the glutamate rings (comprised of E11, E18, E130, and E134) inside the Arabidopsis ZAR1 resistosome (Supplemental Fig. S5). Glutamic acid (E) 11 is conserved in 94% of ZAR1 orthologs, whereas only 3% to 18% retain E18, E130, and E134 in the same positions as Arabidopsis ZAR1. Interestingly, mutation of E11 to alanine (A) impaired Arabidopsis ZAR1–mediated cell death but the E18A, E130A, and E134A mutants were capable of inducing cell death (Bi et al. 2021). Furthermore, the E11A mutation impaired $Ca^{2+}$ channel activity of the ZAR1 resistosome in vitro and in vivo (Bi et al. 2021). Therefore, our motif and structure analyses suggest that RLCK-mediated effector recognition and E11-dependent $Ca^{2+}$ influx are key functional features conserved across the great majority of ZAR1 orthologs.

Downloaded from https://academic.oup.com/plcell/article/35/10/3662/7226528 by guest on 02 August 2025

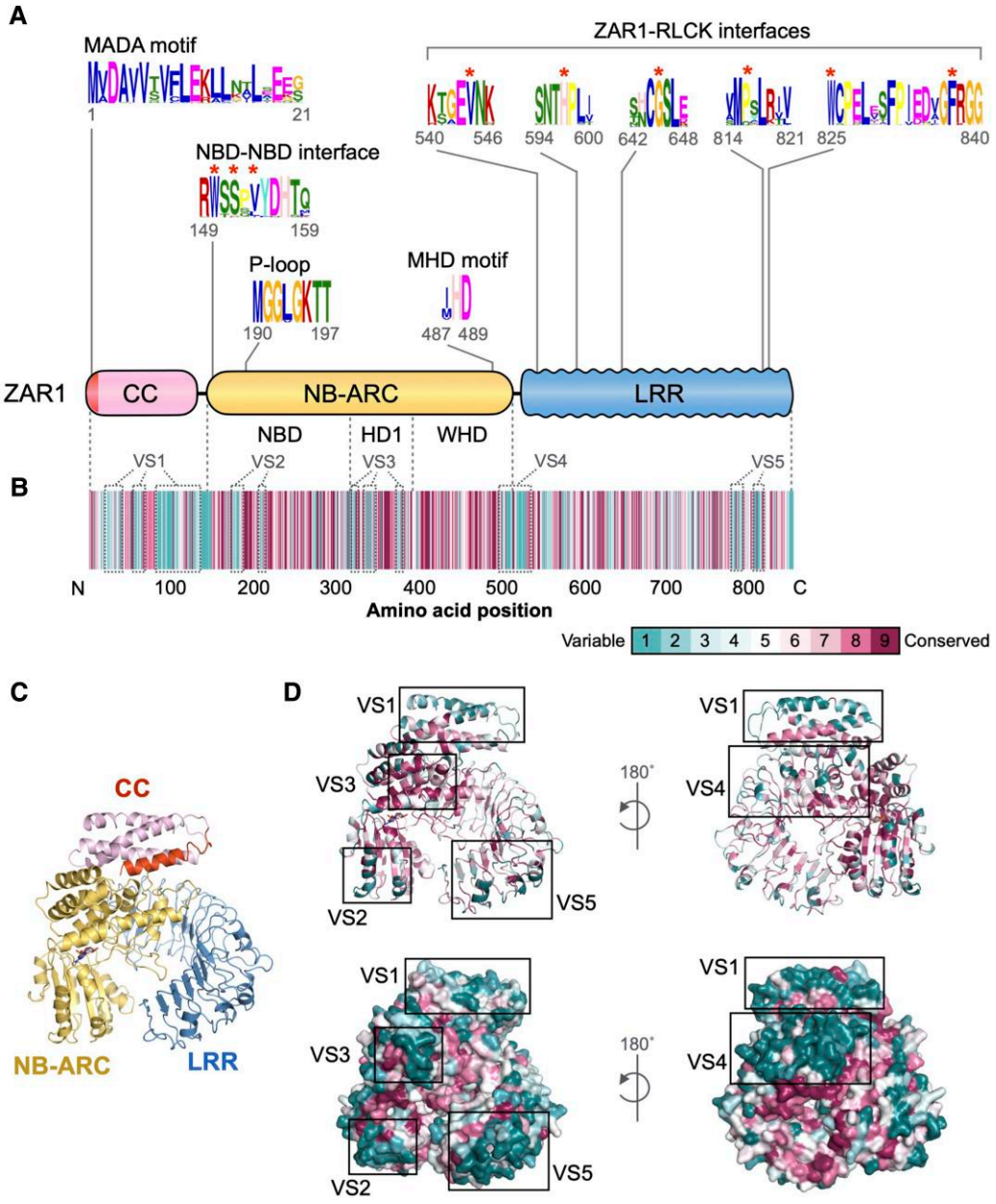


**Figure 3.** ZAR1 orthologs carry conserved sequence patterns required for Arabidopsis ZAR1 resistosome function. **A)** Schematic representation of the Arabidopsis ZAR1 protein highlighting the position of conserved sequence patterns across ZAR1 orthologs. Consensus sequence patterns were identified by MEME using 117 ZAR1 ortholog sequences. Raw MEME motifs are listed in Supplemental Table S1. Red asterisks indicate residues functionally validated in Arabidopsis ZAR1 for NBD–NBD and ZAR1–RLCK interfaces. **B)** Conservation and variation of each amino acid among ZAR1 orthologs across angiosperms. Amino acid alignment of 117 ZAR1 orthologs was used for conservation score calculation via the ConSurf server (https://consurf.tau.ac.il). The conservation scores are mapped onto each amino acid position in Arabidopsis ZAR1 (NP_190664.1). **C, D)** Distribution of the ConSurf conservation score on the Arabidopsis ZAR1 structure. The inactive ZAR1 monomer is illustrated in cartoon representation with domain architecture **C)** and conservation score **D)**. Major 5 variable surfaces (VS1 to VS5) on the inactive ZAR1 monomer structure are described in gray dot or black boxes in panel B or D, respectively.

## ZAR1 interaction sites are conserved in ZED1-related kinase (ZRK) family proteins across distantly related plant species

We endeavored to experimentally test the hypothesis that ZAR1 ortholog proteins across angiosperm species require RLCKs to activate their molecular switch. First, we searched for RLCK XII-2 subfamily genes in the distantly related plant species, taro, stout camphor, and columbine. The BLAST searches of protein databases were seeded with previously identified RLCK ZED1-related kinase (ZRK) sequences from Arabidopsis and *N. benthamiana* (Lewis et al. 2013; Schultink et al. 2019). We also performed iterated phylogenetic analyses

Downloaded from https://academic.oup.com/plcell/article/35/10/3662/7226528 by guest on 02 August 2025

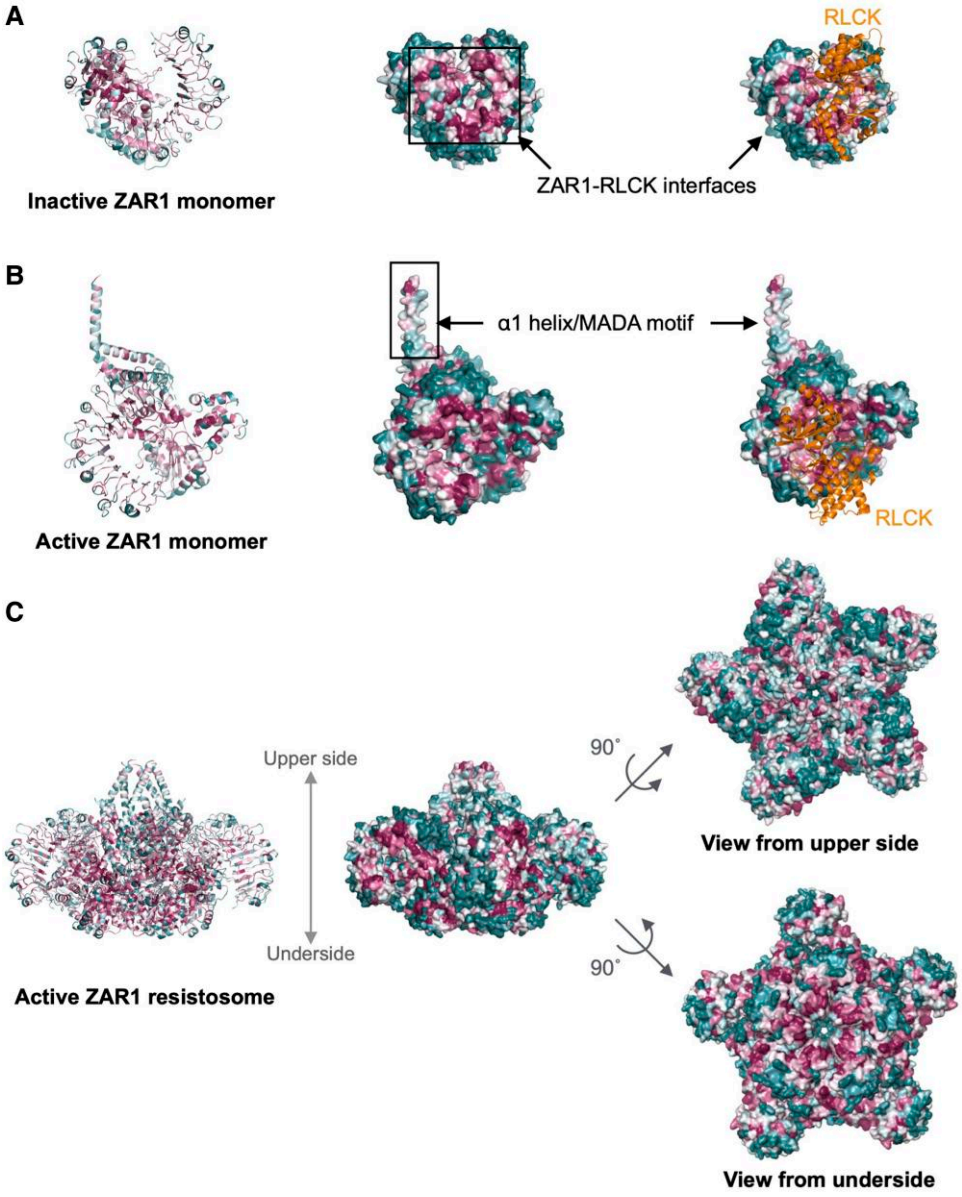


**Figure 4.** ZAR1 orthologs across angiosperms display multiple conserved surfaces on the resistosome structure. Distribution of the ConSurf conservation score was visualized on the inactive monomer **A)**, active monomer **B)**, and resistosome **C)** structures of Arabidopsis ZAR1. Each structure and cartoon representation are illustrated based on the conservation score shown in Fig. 3.

using the kinase domain of the harvested ZRK-like sequences and obtained a well-supported clade that includes previously reported ZRK from Arabidopsis (ZRK1∼7, 10∼15) and *N. benthamiana* (JIM2) as well as additional clade members from taro, stout camphor, and columbine (Fig. 5A). In total, we identified 21 *ZRK* genes in these species, which include 1 *ZRK* gene (*CeZRK1*) from taro, 15 *ZRK* genes (*CmZRK1∼15*) from stout camphor, and 5 *ZRK* genes (*AcZRK1∼5*) from columbine (Fig. 5A; Supplemental Data Set 4).

Remarkably, similar to Arabidopsis *ZRKs* (Lewis et al. 2013), a number of the identified *ZRKs* are located in genomic clusters. 13 *ZRK* genes in stout camphor and 4 *ZRK* genes in columbine form gene clusters on scaffold QPKB01000003.1 and contig KZ305039.1, respectively (Fig. 5B). All of the identified *ZRK* genes are located on a different scaffold or contig to the *ZAR1* gene in taro, stout camphor, and columbine, whereas Arabidopsis *ZAR1* and the 9 *ZRK* genes occur on the same chromosome (Supplemental Data Set 4).

The 21 *ZRK* genes code for proteins of 277 to 452 amino acids, similar to Arabidopsis and *N. benthamiana ZRKs*, which code for 269 to 396 amino acid proteins (Supplemental File 1). ZRK family proteins from taro, stout camphor, and columbine show 20.8% to 42.2% similarity to Arabidopsis RKS1/ZRK1 (Supplemental File 2). Although the sequence similarity is low across the ZRK proteins in angiosperms, ZAR1 interaction sites are highly conserved in the ZRKs (Supplemental

Downloaded from https://academic.oup.com/plcell/article/35/10/3662/7226528 by guest on 02 August 2025

Fig. S6; Wang et al., 2019a; Hu et al. 2020). Notably, functionally validated residues for ZAR1–RLCK interactions (G27 and leucine 31 [L31] in Arabidopsis RKS1/ZRK1; G29 and aspartic acid [D] 231 in Arabidopsis ZED1/ZRK5) are conserved in 81% to 100% of the 21 ZRKs. Moreover, 90% of the 21 ZRKs have a hydrophobic V or I residue at the same position to V35 in Arabidopsis RKS1/ZRK1 (corresponding to I24 in Arabidopsis ZED1/ZRK5). This sequence conservation supports our hypothesis that ZRK family proteins function together with ZAR1 across distantly related plant species.

## Heterologous expression of *ZAR1* and *ZRK* orthologs from flowering plant species in *N. benthamiana*

To validate functional connections between ZAR1 orthologs and their partner ZRKs across angiosperm diversity, we cloned wild-type *ZAR1* and *ZRK* genes from taro, stout camphor, and columbine. We also generated autoactive ZAR1 mutants by introducing a D to V mutation in the MHD motif following the approach we previously used for NbZAR1 ($NbZAR1^{D481V}$; Harant et al. 2022). In a series of experiments, we expressed the *ZAR1* and *ZRK* genes separately or in combination.

First, we examined whether wild-type and MHD mutants of ZAR1 are autoactive in *N. benthamiana*. We expressed wild-type and MHD mutant of taro ZAR1 ($CeZAR1^{WT}$, $CeZAR1^{D487V}$), stout camphor ZAR1 ($CmZAR1^{WT}$, $CmZAR1^{D488V}$), and columbine ZAR1 ($AcZAR1^{WT}$, $AcZAR1^{D489V}$) to determine whether wild-type and MHD mutant of these ZAR1 orthologs cause autoactive cell death in *N. benthamiana*. The 3 orthologs behaved differently in these assays. Whereas both $AcZAR1^{WT}$ and $AcZAR1^{D489V}$ induced autoactive cell death in *N. benthamiana* leaves, only the D to V mutant of CeZAR1 ($CeZAR1^{D487V}$) elicited cell death and neither 1 of $CmZAR1^{WT}$ and $CmZAR1^{D488V}$ caused a cell death response (Supplemental Fig. S7). As controls, we expressed wild-type and D to V mutant of Arabidopsis ZAR ($AtZAR1^{WT}$, $AtZAR1^{D489V}$) and *N. benthamiana* ZAR1 ($NbZAR1^{WT}$, $NbZAR1^{D481V}$). As reported previously (Baudin et al. 2019; Harant et al. 2022), $NbZAR1^{D481V}$ triggered autoactive cell death in *N. benthamiana* leaves but $AtZAR1^{D489V}$ did not (Supplemental Fig. S7).

Next, to determine whether wild-type ZRKs from taro, stout camphor, and columbine trigger autoactive cell death in *N. benthamiana*, we screened 19 ZRKs from taro (CeZRK1), stout camphor (CmZRK2, CmZRK3, CmZRK4, CmZRK5, CmZRK6, CmZRK7, CmZRK8, CmZRK9, CmZRK10, CmZRK11, CmZRK12, CmZRK13, and CmZRK15), and columbine (AcZRK1, AcZRK2, AcZRK3, AcZRK4, and AcZRK5; Pai et al. 2023). None of the tested ZRKs triggered macroscopic cell death response when expressed in *N. benthamiana* leaves (Supplemental Fig. S8; Pai et al. 2023). These results indicate that taro, stout camphor, and columbine ZRKs do not have autoactivity in *N. benthamiana*. This provides an opportunity to investigate functional connection between cospecific ZAR1 and ZRK orthologs by determining the effect of ZRK expression on ZAR1-mediated cell death response.

## Stout camphor and columbine ZED1-related kinase (ZRK) proteins positively regulate the autoactive cell death of their cospecific ZAR1

To determine ZRK function in ZAR1-mediated cell death, we coexpressed D to V mutant versions of ZAR1 orthologs, $CeZAR1^{D487V}$, $CmZAR1^{D488V}$, and $AcZAR1^{D489V}$ with ZRK genes from each species. In these assays, CeZRK1 expression did not enhance cell death autoactivity of $CeZAR1^{D487V}$, whereas AcZRK1, AcZRK3, AcZRK4, and AcZRK5, but not AcZRK2, enhanced the cell death response of $AcZAR1^{D489V}$ (Fig. 6, A and B, and Supplemental Fig. S8). Coexpression of $CmZAR1^{D488V}$ together with CmZRK2, CmZRK6, CmZRK8, CmZRK9, CmZRK10, CmZRK11, or CmZRK13 caused macroscopic cell death in *N. benthamiana* leaves even though $CmZAR1^{D488V}$ itself did not trigger visible cell death (Fig. 6, C and D).

We further conducted side-by-side experiments coexpressing ZAR1 D to V mutants and ZRKs in comparison with single gene expression of either ZAR1 D to V mutants or ZRKs (Supplemental Fig. S9). This confirmed that 4 columbine ZRKs (AcZRK1, AcZRK3, AcZRK4, and AcZRK5) and 7 stout camphor ZRKs (CmZRK2, CmZRK6, CmZRK8, CmZRK9, CmZRK10, CmZRK11, and CmZRK13) positively regulate cell death activity of their cospecific ZAR1, although the ZRKs themselves did not show autoactivity in *N. benthamiana* (Supplemental Fig. S9). These results indicate that the ZAR1 orthologs of these species are functionally associated with ZRKs as previously shown for Arabidopsis ZAR1 and *N. benthamiana* ZAR1. We conclude that ZAR1 has been partnering with RLCKs for over 150 Mya of angiosperm evolution.

Considering that the interaction surfaces between ZAR1 and ZRKs are well conserved (Fig. 4A), we hypothesized that ZAR1 and ZRK proteins may be functionally interchangeable between different plant species. To test this, we coexpressed Arabidopsis RKS1/ZRK1 with D to V mutant of Arabidopsis ZAR1 (AtZAR1), AcZAR1, and CmZAR1 in the *N. benthamiana zar1-1* mutant line. As observed in the original ZAR1–ZRK experiments (Fig. 6), RKS1/ZRK1 positively regulated autoactive cell death by $CmZAR1^{D488V}$ (Supplemental Fig. S10). In the control experiment expressing $AtZAR1^{D489V}$ and RKS1/ZRK1, RKS1/ZRK1 conferred autoactivity to the AtZAR1 MHD mutant in the *N. benthamiana zar1-1* line (Supplemental Fig. S10). These experiments further confirm that the immune function of ZAR1 and ZRK family proteins is conserved across different flowering plant species.

Our observation that the CeZAR1 autoactive mutant triggered cell death regardless of CeZRK1 raised the possibility that CeZAR1 functions together with the endogenous JIM2 RLCK in *N. benthamiana*. To test this, we used a hairpin-silencing construct of *JIM2* (RNAi:JIM2) that mediates silencing of *JIM2* when transiently expressed in *N. benthamiana* leaves (Harant et al. 2022). Silencing of endogenous *JIM2* did not affect the cell death activity of $CeZAR1^{D487V}$, although it suppressed cell death triggered by $NbZAR1^{D481V}$ (Supplemental Fig. S11). This result indicates that unlike *N. benthamiana* ZAR1, taro ZAR1 triggers autoactive cell death independently of JIM2.

Downloaded from https://academic.oup.com/plcell/article/35/10/3662/7226528 by guest on 02 August 2025

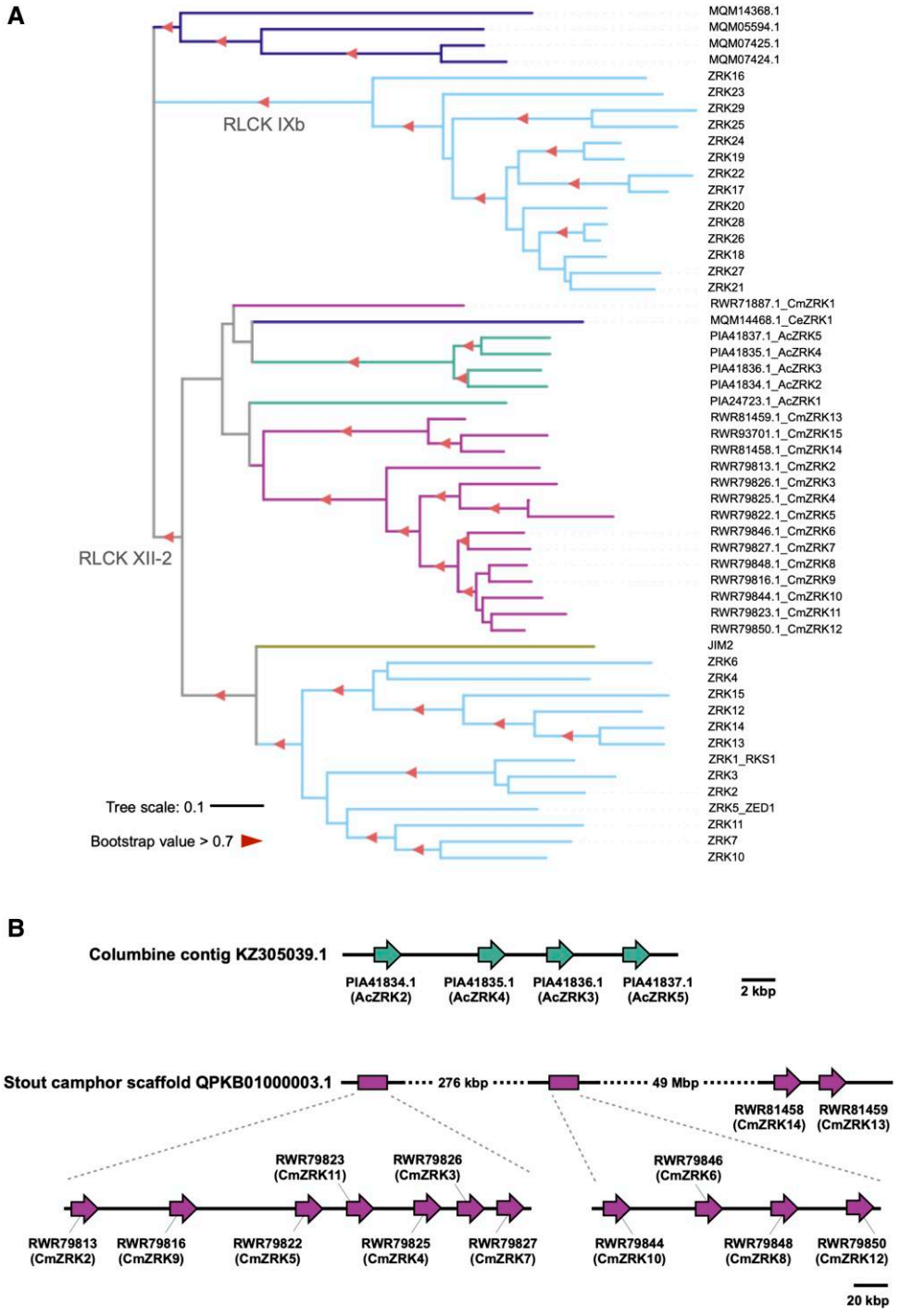


**Figure 5.** *ZRK* gene clusters occur in *A. coerulea* and *C. micranthum*. **A)** The phylogenetic tree was generated in MEGA7 by the neighbor-joining method using full-length amino acid sequences of 39 ZRK proteins. Red triangles indicate bootstrap support > 0.7. The scale bar indicates the evolutionary distance in amino acid substitution per site. **B)** Schematic representation of the *ZRK* gene clusters on an *A. coerulea* (columbine) contig and a *C. micranthum* (Stout camphor) scaffold.

## Integration of a PLP3a thioredoxin-like domain at the C-termini of cassava and cotton ZAR1

As noted earlier, 9 ZAR1 orthologs carry an ID at their C-termini (Supplemental Data Set 1). These ZAR1-ID include 2 predicted proteins (XP_021604862.1 and XP_021604864.1) from *M. esculenta* (cassava) and 7 predicted proteins (KAB1998109.1, PPD92094.1, KAB2051569.1, TYG89033.1, TYI49934.1, TYJ04029.1, and KJB48375.1) from the cotton plant species *Gossypium barbadense*, *Gossypium darwinii*, *Gossypium mustelinum*, and *Gossypium raimondii* (Supplemental Data Set 1). The integrations follow an intact LRR domain, and the IDs vary in length from 108 to 266 amino acids (Fig. 7A). We

Downloaded from https://academic.oup.com/plcell/article/35/10/3662/7226528 by guest on 02 August 2025

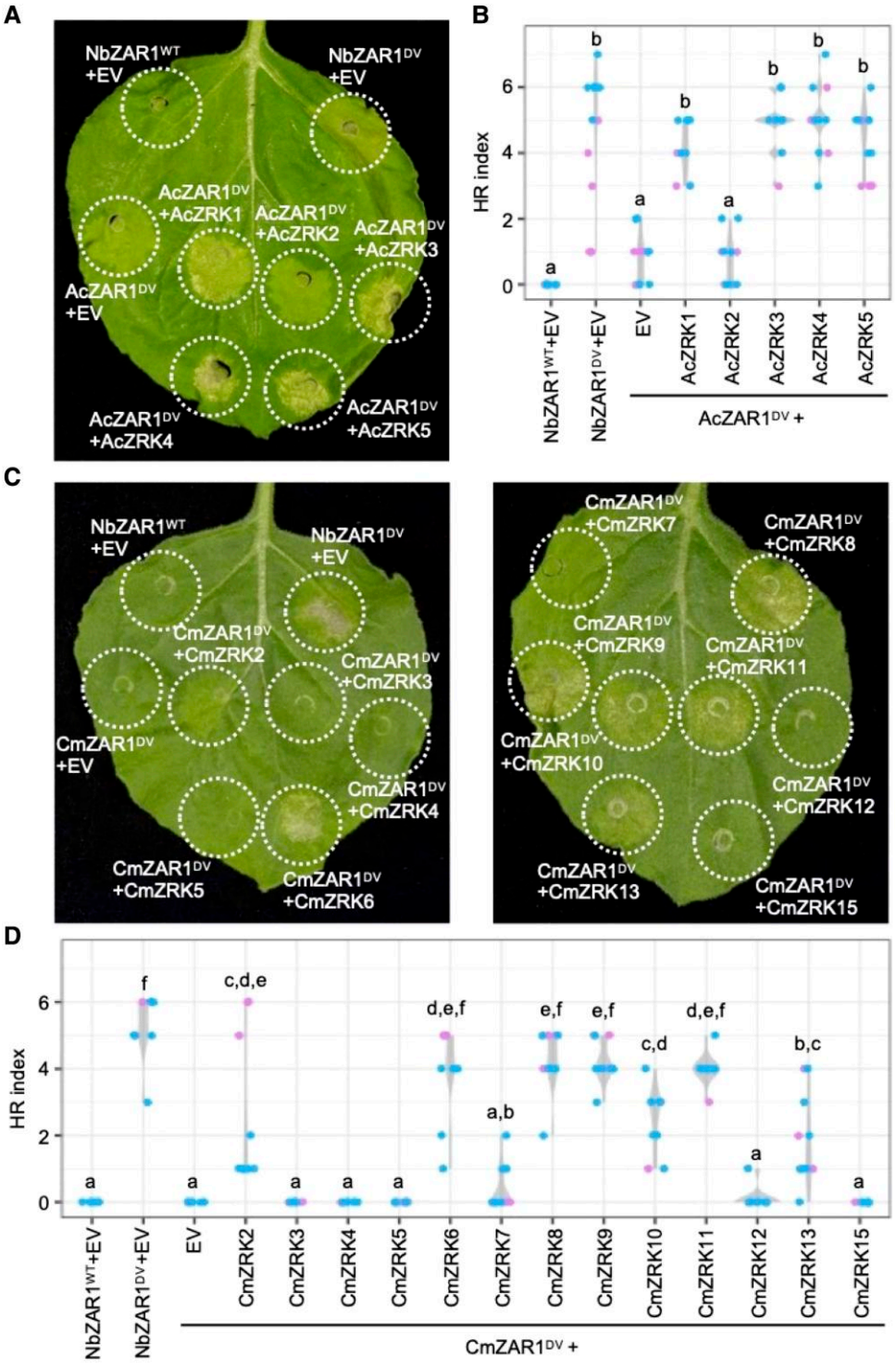


**Figure 6.** ZRK family proteins positively regulate *A. coerulea* AcZAR1 and *C. micranthum* CmZAR1 autoimmune cell death in *N. benthamiana*. **A, C)** Cell death observed in *N. benthamiana* after expression of ZAR1 mutants with or without wild-type ZRKs. *N. benthamiana* leaf panels expressing wild-type NbZAR1 ($NbZAR1^{WT}$), $NbZAR1^{D481V}$ ($ZAR1^{D481V}$), $AcZAR1^{D489V}$ ($AcZAR1^{DV}$), and $CmZAR1^{D488V}$ ($CmZAR1^{DV}$) with or without wild-type ZRKs, were photographed at 4 d after agroinfiltration. **B, D)** Violin plots show AcZAR1 and CmZAR1 cell death intensity scored as an HR index based on 12 and 9 replicates (different leaves from independent plants) in 2 independent experiments. Statistical differences among the samples were analyzed with Tukey's HSD test ($P < 0.01$).

Downloaded from https://academic.oup.com/plcell/article/35/10/3662/7226528 by guest on 02 August 2025

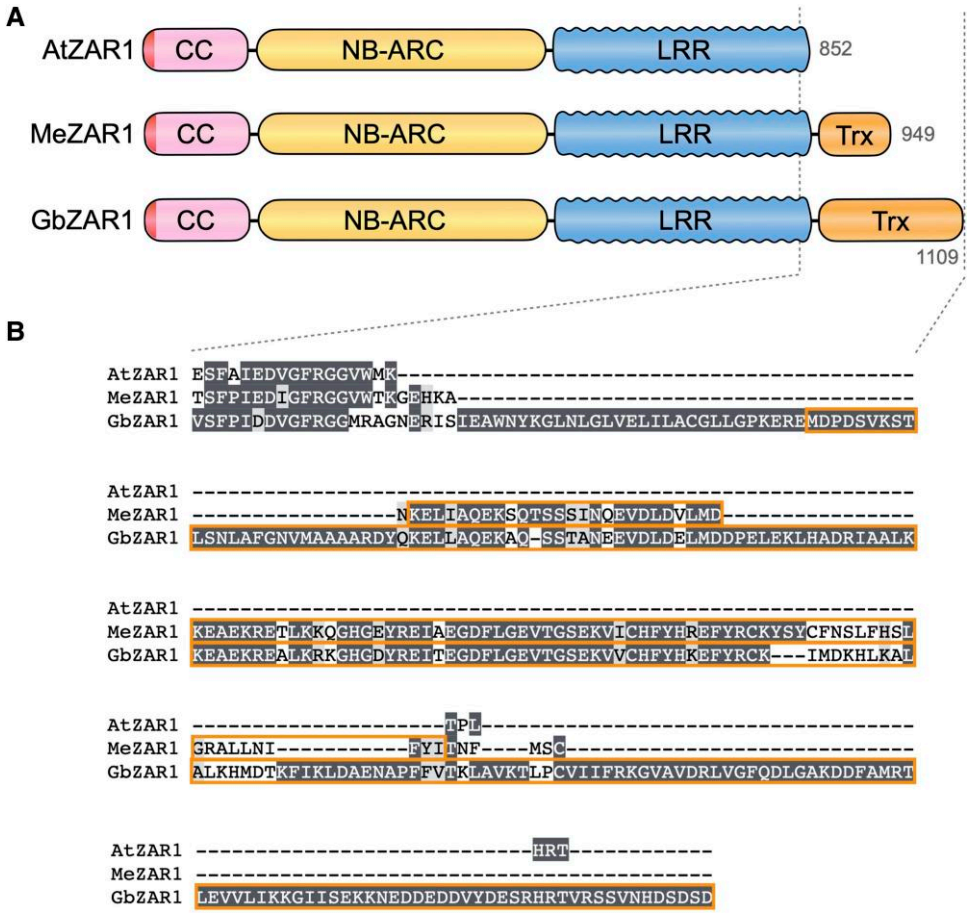


**Figure 7.** Cassava and cotton ZAR1-ID carry an additional Trx domain at the C terminus. **A)** Schematic representation of NLR domain architecture with C-terminal Trx domain. **B)** Description of Trx domain sequences on amino acid sequence alignment. Cassava XP_021604862.1 (MeZAR1) and cotton KAB1998109.1 (GbZAR1) were used for MAFFT version 7 alignment as representative ZAR1-ID. Arabidopsis ZAR1 (AtZAR1) was used as a control of ZAR1 without ID.

confirmed that the ZAR1-ID gene models of cassava XP_021604862.1 and XP_021604864.1 are correct based on RNA sequencing (RNA-seq) exon coverage in the NCBI database (database ID: LOC110609538). However, cassava *ZAR1-ID* XP_021604862.1 and XP_021604864.1 are isoforms encoded by transcripts from a single locus on chromosome LG2 (RefSeq sequence NC_035162.1) of the cassava RefSeq assembly (GCF_001659605.1) which also produces transcripts encoding isoforms lacking the C-terminal ID (XP_021604863.1, XP_021604865.1, XP_021604866.1, XP_021604867.1, and XP_021604868.1). Thus, cassava *ZAR1-ID* are probably splicing variants from a unique cassava *ZAR1* gene locus.

To determine whether the *ZAR1-ID* transcript is expressed in cassava, we analyzed public RNA-seq data from cassava samples in detail (BioSample IDs in NCBI database: SAMN02950671, SAMN02950673, SAMN02950674, SAMN02950672 SAMN02444910, SAMN02444915, AMN02444919, and SAMN05208186). We confirmed that RNA-seq reads detected from leaf and stem samples of 60,444 and MCOL1522 cassava cultivars span between the end of LRR and beginning of Trx domain regions (Supplemental Fig. S12). Notably, those reads are detected in the samples inoculated with the bacteria *Xanthomonas euvesicatoria* or *Xanthomonas axonopodis*, but not in their control samples (Supplemental Fig. S12). Furthermore, 3 reads spanning LRR and Trx regions are detected in RNA-seq data from a lateral bud of the TME204 cultivar (Supplemental Fig. S12). This suggests that ZAR1-ID is a splicing variant produced in cassava leaves and stems during *Xanthomonas* infection or in the specific tissue like the lateral bud.

To determine the phylogenetic relationship between ZAR1-ID and canonical ZAR1, we mapped the domain architectures of ZAR1 orthologs on the phylogenetic tree shown in Fig. 2 (Supplemental Fig. S13). Cassava and cotton *ZAR1-ID* occur in different branches of the ZAR1 rosid clade indicating that they may have evolved as independent integrations although alternative evolutionary scenarios such as a common origin followed by subsequent deletion of the ID or lineage sorting remain possible (Supplemental Fig. S13).

We annotated all the C-terminal extensions as thioredoxin-like using InterProScan (Trx, IPR036249; IPR013766; cd02989). The integrated Trx domain sequences are similar to Arabidopsis AT3G50960 (phosphoducin-like PLP3a; 34.8% to

Downloaded from https://academic.oup.com/plcell/article/35/10/3662/7226528 by guest on 02 August 2025

90% similarity to integrated Trx domains), which is located immediately downstream of *ZAR1* in a tail-to-tail configuration in the Arabidopsis genome (Supplemental Fig. S14). We also noted additional genetic linkage between *ZAR1* and *Trx* genes in other rosid species, namely, field mustard, orange, cacao, grapevine, and apple, and in the asterid species coffee (Supplemental Data Set 5). We conclude that *ZAR1* is often genetically linked to a PLP3a-like Trx domain gene and that the ID in *ZAR1-ID* has probably originated from a genetically linked sequence.

## The *ZAR1-SUB* clade emerged early in eudicot evolution from a single *ZAR1* duplication event

Phylogenetic analyses revealed *ZAR1-SUB* as a sister clade of the *ZAR1* ortholog clade (Figs. 1B and 8). The *ZAR1-SUB* clade comprises 129 genes from a total of 55 plant species (Supplemental Data Set 6). Twenty-one of the 55 plant species carry a single copy of *ZAR1-SUB* whereas 34 species have 2 or more copies (Supplemental Data Set 2). Of the 129 genes, 122 code for canonical CC-NLR proteins (692 to 1,038 amino acid length) with shared sequence similarities ranging from 36.5% to 99.9% (Supplemental Data Set 6).

Unlike *ZAR1*, *ZAR1-SUB* NLRs are restricted to eudicots (Supplemental Fig. S15 and Supplemental Data Set 6). Three out of 129 genes are from eudicot clade Ranunculales species outside the core eudicots, namely, columbine, *Macleaya cordata* (plume poppy) and *Papaver somniferum* (opium poppy). The remaining ZAR1-SUB are spread across rosid and asterid species. We found that 11 species have *ZAR1-SUB* genes but lack a *ZAR1* ortholog (Supplemental Data Set 2). These 11 species include 2 of the early diverging eudicots plume poppy and opium poppy, and the Brassicales *Carica papaya* (papaya). Interestingly, papaya is the only Brassicales species carrying a *ZAR1-SUB* gene, whereas the 16 other Brassicales species have *ZAR1* but lack *ZAR1-SUB* genes (Supplemental Data Set 2). In total, we didn't detect *ZAR1-SUB* genes in 44 species that have *ZAR1* orthologs and these 44 species include the monocot taro, the magnoliid stout camphor, and 42 eudicots, such as Arabidopsis, sugar beet, and *N. benthamiana* (Supplemental Data Set 2).

In summary, given the taxonomic distribution of the *ZAR1-SUB* clade genes, we propose that *ZAR1-SUB* has emerged from a single duplication event of *ZAR1* prior to the split between Ranunculales and other eudicot lineages about ∼120 to 130 Mya based on the species divergence time estimate of Chaw et al. (2019).

## *ZAR1-SUB* paralogs have significantly diverged from *ZAR1*

We investigated the sequence patterns of ZAR1-SUB proteins and compared them to the sequence features of canonical ZAR1 proteins that we identified earlier (Fig. 3A). MEME analyses revealed several conserved sequence motifs (Supplemental Table S2). Especially, the MEME motifs in the ZAR1-SUB NB-ARC domain were similar to ZAR1 ortholog motifs (Supplemental Table S3). These include P-loop and MHD motifs, which are broadly conserved in NB-ARC of 97% and 100% of the ZAR1-SUB NLRs, respectively (Fig. 9A). MEME also revealed sequence motifs in the ZAR1-SUB LRR domain that partially overlaps in position with the conserved ZAR1–RLCK interfaces (Fig. 9A and Supplemental Fig. S16). However, the ZAR1-SUB MEME motifs in the LRR domain were variable at the ZAR1–RLCK interface positions compared to ZAR1 and the motif sequences were markedly different between ZAR1-SUB and ZAR1 proteins (Figs. 3A and 9A).

Remarkably, unlike ZAR1 orthologs, MEME did not predict the conserved sequence pattern from a region corresponding to the MADA motif, indicating that these sequences have diverged across ZAR1-SUB proteins (Fig. 9A). We confirmed the low frequency of MADA motifs in ZAR1-SUB proteins using HMMER searches with only ∼30% (38 out of 129) of the tested proteins having a MADA-like sequence (Supplemental Data Set 6; Fig. 8). Moreover, conserved sequence patterns were not predicted for the NBD–NBD interface of the ZAR1 resistosome (Fig. 9A and Supplemental Fig. S16).

We generated a diversity barcode for ZAR1-SUB proteins using ConSurf as we did earlier with ZAR1 orthologs (Fig. 9B). This revealed that there are several conserved sequence blocks in each of the CC, NB-ARC, and LRR domains, such as the regions corresponding to P-loop, MHD motif, and the equivalent of the ZAR1–RLCK interfaces.

Next, we mapped the ConSurf conservation scores onto a homology model of a representative ZAR1-SUB protein (XP_004243429.1 from tomato) built based on the Arabidopsis ZAR1 cryo-EM structures (Supplemental Fig. S17). As highlighted in Supplemental Fig. S17B and C, conserved residues, such as the MHD motif region in the WHD, are located inside of the monomer and resistosome structures. Interestingly, although the prior MEME prediction analyses revealed conserved motifs in positions matching the ZAR1–RLCK interfaces in the LRR domain, the ZAR1-SUB structure homology models displayed variable surfaces in this region (Supplemental Fig. S17A). This indicates that the variable residues within these sequence motifs are predicted to be on the outer surfaces of the LRR domain and may reflect interaction with different ligands.

Taken together, these results suggest that unlike ZAR1 orthologs, the ZAR1-SUB paralogs have divergent molecular patterns for regions known to be involved in effector recognition, resistosome formation, and activation of hypersensitive cell death.

## Eleven tandemly duplicated *ZAR1-CIN* genes occur in a 500-kb cluster in the *C. micranthum* (stout camphor) genome

The *ZAR1-CIN* clade, identified by phylogenetic analyses as a sister clade to *ZAR1* and *ZAR1-SUB*, consists of 11 genes from the magnoliid species stout camphor (Figs. 1B and 8 and Supplemental Data Set 7). Eight of the 11 *ZAR1-CIN* genes code for canonical CC-NLR proteins with 63.8% to 98.9% sequence similarities to each other, whereas the remaining 3 genes code for truncated

Downloaded from https://academic.oup.com/plcell/article/35/10/3662/7226528 by guest on 02 August 2025

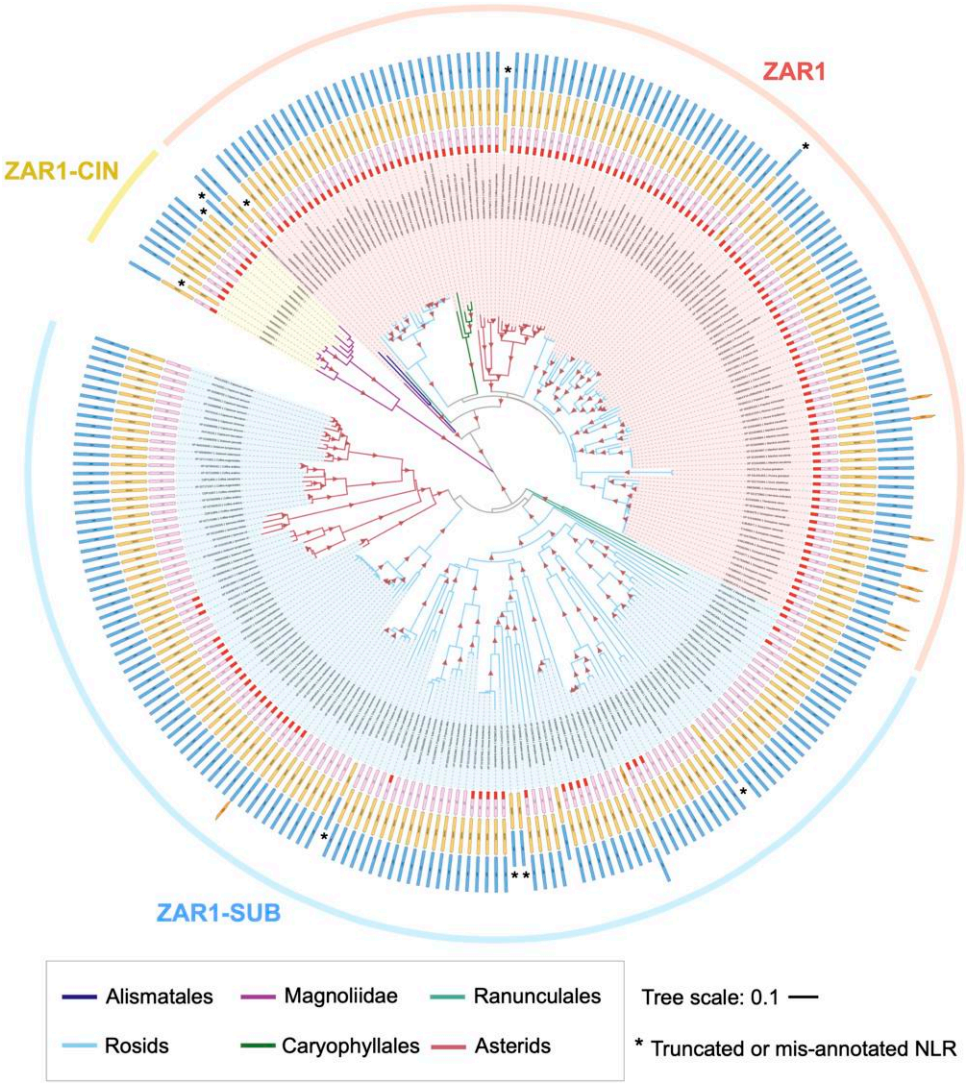


**Figure 8.** ZAR1-SUB has emerged early in eudicots and diverged at MADA motif sequence. The phylogenetic tree was generated in MEGA7 by the neighbor-joining method using full-length amino acid sequences of 120 ZAR1, 129 ZAR1-SUB, and 11 ZAR1-CIN identified in Fig. 1. Red triangles indicate bootstrap support > 0.7. The scale bar indicates the evolutionary distance in amino acid substitution per site. NLR domain architectures are illustrated outside of the leaf labels: MADA is red, CC is pink, NB-ARC is yellow, LRR is blue, and other domain is orange. Black asterisks on domain schemes describe truncated NLRs or potentially misannotated NLR.

NLR proteins. Interestingly, all *ZAR1-CIN* genes occur in a ~500-kb cluster on scaffold QPKB01000005.1 of the stout camphor genome assembly (GenBank assembly accession GCA_003546025.1) (Supplemental Fig. S18, A and B). This scaffold also contains the stout camphor *ZAR1* ortholog (*CmZAR1*, RWR84015), which is located 48 Mb from the *ZAR1-CIN* cluster (Supplemental Fig. S18, A and B). Based on the observed phylogeny and gene clustering, we suggest that the *ZAR1-CIN* cluster emerged from segmental duplication and expansion of the ancestral *ZAR1* gene after stout camphor split from the other examined *ZAR1*-containing species.

We examined the expression of the eleven *CmZAR1* and *ZAR1-CIN* genes in 7 tissues of *C. micranthum* based on the data of Chaw et al. (Chaw et al. 2019). The *CmZAR1* gene is relatively highly expressed in 7 different tissues of the stout camphor tree (Supplemental Fig. S18C). In contrast, only 5 of the eleven *ZAR1-CIN* genes displayed detectable expression levels. Of these, 2 *ZAR1-CIN* genes (RWR85656 and RWR85657) had different expression patterns across the tissues. Whereas RWR85657 had the highest expression level in flowers, RWR85656 displayed the highest expression levels in stem and old leaf tissues (Supplemental Fig. S18C). The implications of these observations remain unclear but may reflect different degrees of tissue specialization of the *ZAR1-CIN* genes.

## Tandemly duplicated *ZAR1-CIN* genes display variable ligand-binding interfaces on the LRR domain

We performed MEME and ConSurf analyses of the 8 intact ZAR1-CIN proteins as described above for ZAR1 and

Downloaded from https://academic.oup.com/plcell/article/35/10/3662/7226528 by guest on 02 August 2025

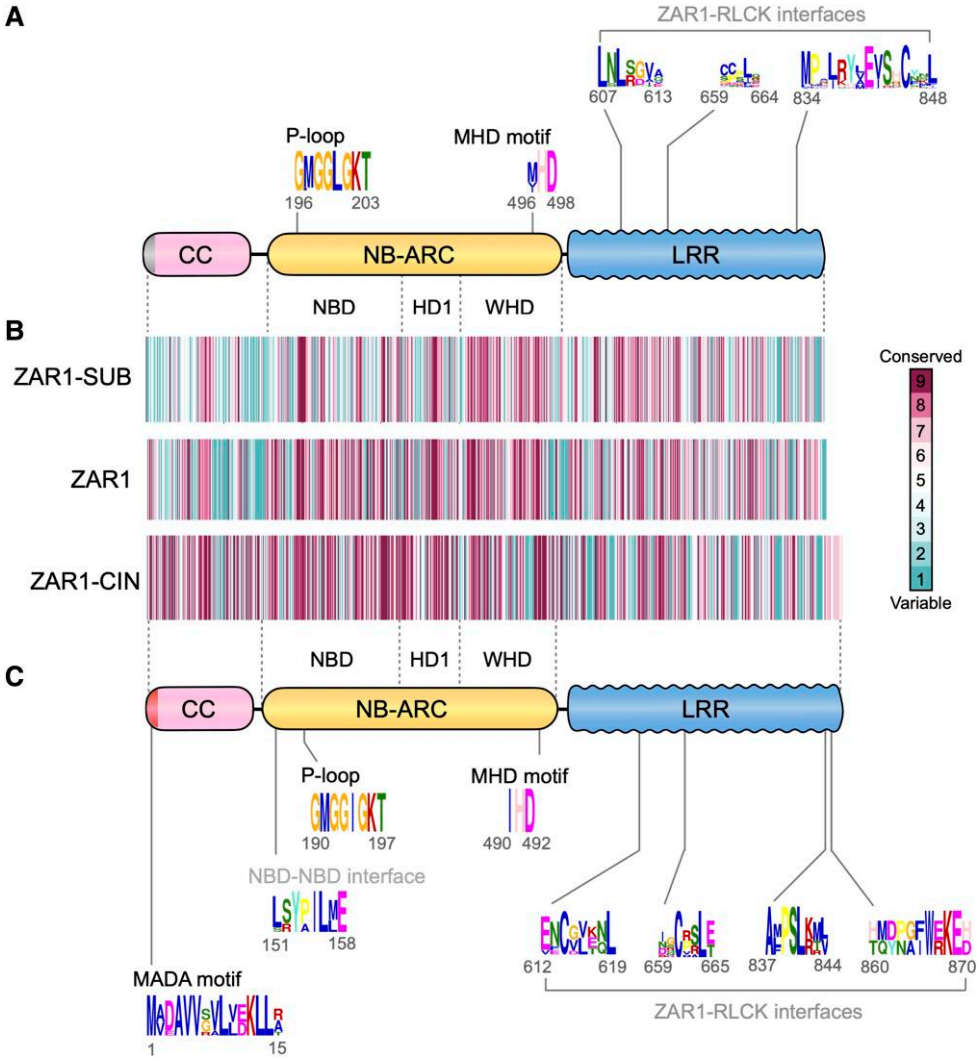


**Figure 9.** Conserved sequence distributions in ZAR1-SUB and ZAR1-CIN. **A)** Schematic representation of the ZAR1-SUB protein highlighting the position of the representative conserved sequence patterns across ZAR1-SUB. Representative consensus sequence patterns identified by MEME are described on the scheme. Raw MEME motifs are listed in Supplemental Tables S2 and S3. **B)** Conservation and variation of each amino acid among ZAR1-SUB and ZAR1-CIN. Amino acid alignment of 129 ZAR1-SUB or 8 ZAR1-CIN was used for conservation score calculation via the ConSurf server (https://consurf.tau.ac.il). The conservation scores are mapped onto each amino acid position in queries XP_004243429.1 (ZAR1-SUB) and RWR85656.1 (ZAR1-CIN), respectively. **C)** Schematic representation of the ZAR1-CIN protein highlighting the position of the representative conserved sequence patterns across 8 ZAR1-CIN. Raw MEME motifs are listed in Supplemental Tables S4 and S5.

ZAR1-SUB. The ConSurf barcode revealed that although ZAR1-CIN proteins are overall conserved, their WHD region and LRR domain include some clearly variable blocks (Fig. 9B). MEME analyses of ZAR1-CIN sequences revealed that like ZAR1 orthologs, the MADA, P-loop, and MHD motifs match highly conserved blocks of the ZAR1-CIN ConSurf barcode (Fig. 9, B and C, and Supplemental Tables S4 and S5). Consistently, 87.5% (7 out of 8) of the ZAR1-CIN proteins were predicted to have a MADA-type N-terminal sequence based on MADA-HMM analyses (Supplemental Data Set 7 and Fig. 8).

MEME picked up additional sequence motifs in ZAR1-CIN proteins that overlap in position with the NBD–NBD and ZAR1–RLCK interfaces (Fig. 9C and Supplemental Fig. S19). However, the sequence consensus at the NBD–NBD and ZAR1–RLCK interfaces indicated these motifs are more variable among ZAR1-CIN proteins relative to ZAR1 orthologs and the motif sequences at both interfaces were markedly different from the matching region in ZAR1 (Figs. 3A and 9C).

We also mapped the ConSurf conservation scores onto a homology model of a representative ZAR1-CIN protein (RWR85656.1) built based on the Arabidopsis ZAR1 cryo-EM structures (Supplemental Fig. S17). This model revealed several conserved surfaces, such as on the α1 helix in the CC domain and the WHD of the NB-ARC domain (Supplemental Fig. S17, B and C). In contrast, the ZAR1-CIN structure homology models displayed highly varied surfaces especially in the LRR region matching the

Downloaded from https://academic.oup.com/plcell/article/35/10/3662/7226528 by guest on 02 August 2025

RLCK binding interfaces of ZAR1 (Supplemental Fig. S17A). This sequence diversification on the LRR surface suggests that the ZAR1-CIN paralogs may have different host partner proteins and/or effector recognition specificities compared to ZAR1.

## Discussion

This study of ZAR1 macroevolution originated from phylogenomic analyses we initiated during the UK COVID-19 lockdown of March 2020. We performed iterated comparative sequence similarity searches of plant genomes using the CC-NLR immune receptor ZAR1 as a query, and subsequent phylogenetic evaluation of the recovered ZAR1-like sequences. This revealed that *ZAR1* is an ancient gene with 120 orthologs recovered from 88 species including monocot, magnoliid, and eudicot plants. This atypical conservation of *ZAR1* in these species provides the view that *ZAR1* originated early in angiosperms during the Jurassic geologic period ~220 to 150 Mya (Fig. 10A). This evolutionary model of ZAR1 is consistent with a recent study by Gong et al. (2022) that was published 1.5 yrs after we posted a preprint of the present paper (Adachi et al. 2020). The ortholog series enabled us to determine that resistosome sequences that are known to be functionally important and have remained highly conserved throughout the long evolutionary history of ZAR1. In addition, we experimentally validated the model that ZAR1 has partnered with RLCKs for over 150 Mya through functional reconstruction of ZAR1–RLCK pairs from distantly related plant species (Fig. 10B). The main unexpected feature among ZAR1 orthologs is the acquisition of a C-terminal thioredoxin-like domain in cassava and cotton species (Fig. 7). Our phylogenetic analyses also indicated that *ZAR1* duplicated twice throughout its evolution (Fig. 10A). In the eudicots, *ZAR1* spawned a large paralog family, *ZAR1-SUB*, which greatly diversified and often lost the typical sequence features of *ZAR1*. A second paralog, *ZAR1-CIN*, is restricted to a tandemly repeated 11-gene cluster in stout camphor. Overall, our findings map patterns of functional conservation, expansion, and diversification onto the evolutionary history of *ZAR1* and its paralogs.

*ZAR1* most likely emerged prior to the split between monocots, Magnoliids, and eudicots, which corresponds to ~220 to 150 Mya based on the dating analyses of Chaw et al. (2019). The origin of the angiosperms remains hotly debated with uncertainties surrounding some of the fossil record coupled with molecular clock analyses that would benefit from additional genome sequences of undersampled taxa (Coiro et al. 2019). Fu et al. (2018) and Cui et al. (2022) provided credence to an earlier emergence of angiosperms with the discovery of the fossil flowers *Nanjinganthus dendrostyla* and *Florigerminis jurassica*, respectively. These findings place the emergence of flowering plants at the Jurassic. It is tempting to speculate that *ZAR1* emerged among these early flowering plants during the period when dinosaurs dominated planet Earth.

NLRs are notorious for their rapid and dynamic evolutionary patterns even at the intraspecific level. In sharp contrast, *ZAR1* is an atypical core NLR gene conserved in a wide range of angiosperm species (Fig. 2). Nevertheless, Arabidopsis ZAR1 can recognize diverse bacterial pathogen effectors, including 5 different effector families distributed among nearly half of a collection of ~500 *Pseudomonas syringae* strains (Laflamme et al. 2020) and an effector AvrAC from *Xanthomonas campestris* (Wang et al., 2015). How did ZAR1 remain conserved throughout its evolutionary history while managing to detect a diversity of effectors? The answer to the riddle lies in the fact that ZAR1 effector recognition occurs via its partner RLCKs. ZRKs of the RLCK XII-2 subfamily rest in complex with inactive ZAR1 proteins and bait effectors by binding them directly or by recruiting other effector-binding RLCKs, such as family VII PBS1-like protein 2 (PBL2) (Lewis et al. 2013; Wang et al., 2015). These ZAR1-associated RLCKs are highly diversified not only in Arabidopsis (Lewis et al. 2013) but also in stout camphor and columbine, where RLCK XII-2 members occur in expanded ZRK gene clusters (Fig. 5). In the Arabidopsis ZRK cluster, RKS1/ZRK1 is required for recognition of the *X. campestris* effector AvrAC (Wang et al., 2015) and ZRK3 and ZED1/ZRK5 are required for recognition of *P. syringae* effectors HopF2a and HopZ1a, respectively (Lewis et al. 2013; Seto et al. 2017). Therefore, as in the model discussed by Schultink et al. (2019) and Gong et al. (2022), ZRKs appear to have evolved as pathogen "sensors" whereas ZAR1 acts as a conserved signal executor to activate immune response.

The MEME and ConSurf analyses are consistent with the model of ZAR1/RLCK evolution described above. *ZAR1* is not just exceptionally conserved across angiosperms, but it has also preserved sequence patterns that are key to resistosome-mediated immunity (Figs. 3 and 4). Within the LRR domain, ZAR1 orthologs display highly conserved surfaces for RLCK binding (Fig. 4). We conclude that ZAR1 has been guarding host kinases throughout its evolution ever since the Jurassic period. These findings strikingly contrast with observations recently made by Prigozhin and Krasileva (2020) on highly variable Arabidopsis NLRs (hvNLRs), which tend to have diverse LRR sequences. For instance, the CC-NLR RPP13 displays variable LRR surfaces across 62 Arabidopsis accessions, presumably because these regions are effector recognition interfaces that are caught in arms race coevolution with the oomycete pathogen *Hyaloperonospora arabidopsidis* (Prigozhin and Krasileva 2020). The emerging view is that the mode of pathogen detection (direct vs indirect recognition) drives an NLR evolutionary trajectory by accelerating sequence diversification at the effector binding site or by maintaining the binding interface with the partner guardee/decoy proteins (Prigozhin and Krasileva 2020).

Our functional validation of ZAR1 and ZRKs from distantly related plant species supported the model that ZRKs function together with ZAR1 to trigger immune response *in planta* (Fig. 6). Eleven of the 19 tested ZRKs either required or enhanced the autoactivity of their cospecific ZAR1 in *N. benthamiana*. The

Downloaded from https://academic.oup.com/plcell/article/35/10/3662/7226528 by guest on 02 August 2025

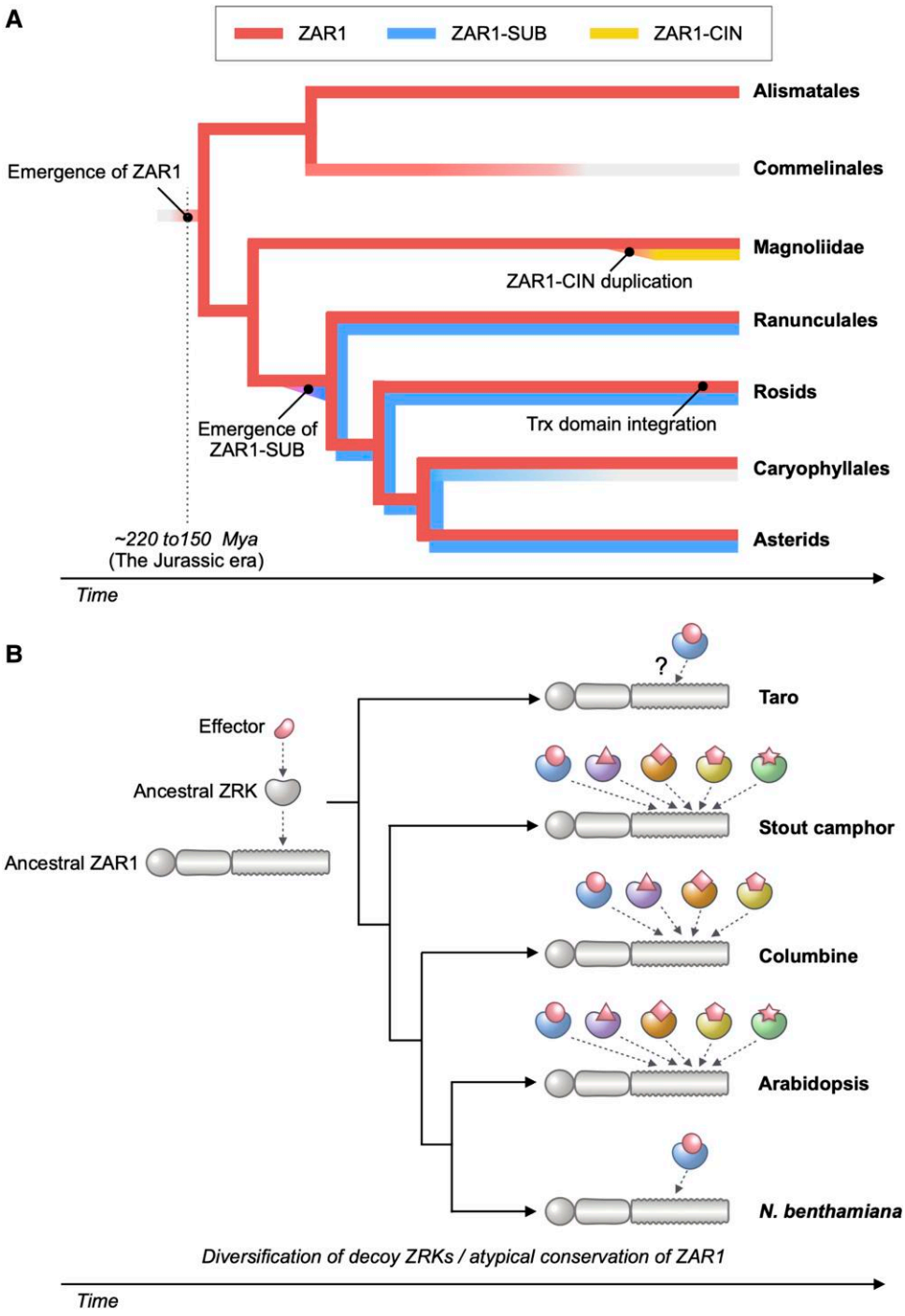


**Figure 10.** Coevolution of *ZAR1* and *ZRK* genes in angiosperms. **A)** We propose that the ancestral *ZAR1* gene has emerged ~220 to 150 million yrs ago (Mya) before monocot and eudicot lineages split. ZAR1 is a widely conserved CC-NLR in angiosperms, but it is likely that *ZAR1* was lost in the monocot lineage, Commelinales. A sister clade paralog *ZAR1-SUB* has emerged early in the eudicot lineages and may have been lost in Caryophyllales. Another sister clade paralog *ZAR1-CIN* was duplicated from the *ZAR1* gene and expanded in the Magnoliidae *C. micranthum*. Trx domain integration to C terminus of ZAR1 has independently occurred in few rosid lineages. **B)** *ZAR1* has coevolved with partner *ZRK* gene for pathogen effector recognition since the Jurassic era. During the coevolution, ZRKs diversified to catch up with fast-evolving effectors.

remaining 8 tested ZRKs, CeZRK1, AcZRK2, CmZRK3, CmZRK4, CmZRK5, CmZRK7, CmZRK12, and CmZRK15 did not alter cell death activity of ZAR1. Notably, CmZRK4, CmZRK5, and CmZRK12 have N-terminal truncation or mutations at the ZAR1 interaction sites identified from the Arabidopsis ZAR1–ZRK studies (Supplemental File 2). Therefore, some of the ZRK members may have lost their association with ZAR1 through deletion or mutations.

Downloaded from https://academic.oup.com/plcell/article/35/10/3662/7226528 by guest on 02 August 2025

Taro and columbine ZAR1 could trigger autoactivated cell death without their partner RLCKs in *N. benthamiana*, whereas stout camphor and *N. benthamiana* ZAR1 proteins require ZRKs to trigger the cell death response (Fig. 6 and Supplemental Fig. S7) (Harant et al. 2022). In the case of taro and columbine, ZRKs may trigger conformational changes of ZAR1 after recognition of cognate pathogen effectors. In this scenario, autoactive ZAR1 could form a resistosome without ZRK proteins, thereby triggering the observed cell death response. In the future, further comparative biochemical studies would further inform our understanding of how ZAR1–ZRK interactions have evolved and contributed to ZAR1 resistosome formation across angiosperms.

*ZAR1* orthologs display a patchy distribution across angiosperms (Supplemental Data Set 1). Given the low number of non-eudicot species with *ZAR1*, it is challenging to develop a conclusive evolutionary model. Nonetheless, the most parsimonious explanation is that *ZAR1* was lost in the monocot Commelinales lineage (Fig. 10A and Supplemental Data Set 1). *ZAR1* is also missing in some eudicot lineages, notably Fabales, Cucurbitales, Apiales, and Asterales (Supplemental Data Set 1). Cucurbitaceae (Cucurbitales) species are known to have reduced repertoires of NLR genes possibly due to low levels of gene duplications and frequent deletions (Lin et al. 2013). *ZAR1* may have been lost in this and other plant lineages as part of an overall shrinkage of their NLRomes or as consequence of selection against autoimmune phenotypes triggered by NLR misregulation (Karasov et al. 2017; Adachi et al. 2019a). Notably, plant linages that don't have a *ZAR1* ortholog also lack *ZRK* family genes, suggesting that ZAR1 and ZRK coevolved to function in resistosome-mediated immunity across angiosperms (Gong et al. 2022).

We unexpectedly discovered that some *ZAR1* orthologs from cassava and cotton species carry a C-terminal thioredoxin-like domain (*ZAR1-ID* in Fig. 7). Although Gong et al. (2022) suggested *ZAR-ID* are annotation errors, we confirmed that at least cassava *ZAR1-Trx* is expressed as a splicing variant in leaf and stem inoculated with *Xanthomonas* bacteria or in lateral bud (Supplemental Fig. S12). What is the function of these IDs? The occurrence of unconventional domains in NLRs is relatively frequent and ranges from 5% to 10% of all NLRs. In several cases, IDs have emerged from pathogen effector targets and became decoys that mediate detection of the effectors (Kourelis and van der Hoorn 2018). Whether or not the integrated Trx domain of ZAR1-ID functions to bait effectors will need to be investigated. Since ZAR1-ID proteins still carry intact RLCK binding interfaces (Supplemental File 3), they may have evolved dual or multiple recognition specificities via RLCKs and the Trx domain. In addition, all ZAR1-ID proteins have an intact N-terminal MADA motif (Supplemental Fig. S13), suggesting that they probably can execute the hypersensitive cell death through their N-terminal CC domains even though they carry a C-terminal domain extension (Adachi et al. 2019b). In the future, it would be intriguing to understand how the ZAR1-ID splicing variant is produced and how the ZAR-ID function comparing to the ZAR1 resistosome model.

Our sequence analyses of *ZAR1-ID* indicate that the integrated Trx domain originates from the *PLP3* phosphoducin gene, which is immediately downstream of *ZAR1* in the Arabidopsis genome and adjacent to *ZAR1* in several other eudicot species (Supplemental Fig. S14). Whether or not PLP3 plays a role in ZAR1 function and the degree to which close genetic linkage facilitated domain fusion between these 2 genes are provocative questions for future studies.

*ZAR1* spawned 2 classes of paralogs through 2 independent duplication events. The *ZAR1-SUB* paralog clade emerged early in the eudicot lineage—most likely tens of millions of years after the emergence of *ZAR1*—and has diversified into at least 129 genes in 55 species (Fig. 10A). ZAR1-SUB proteins are distinctly more diverse in sequence than ZAR1 orthologs and generally lack key sequence features of ZAR1, like the MADA motif and the NBD–NBD oligomerization interface (Fig. 9) (Adachi et al. 2019b; Wang et al., 2019b; Hu et al. 2020). This pattern is consistent with the "use-it-or-lose-it" evolutionary model, in which NLRs that specialize for pathogen detection lose some of the molecular features of their multifunctional ancestors (Adachi et al. 2019b). Therefore, we predict that many ZAR1-SUB proteins evolved into specialized sensor NLRs that require NLR helper mates for executing the hypersensitive response. It is possible that ZAR1-SUB helper mate is ZAR1 itself and that these NLRs evolved into a phylogenetically linked network of sensors and helpers similar to the NRC network of asterid plants (Wu et al. 2017). However, 11 species have a *ZAR1-SUB* gene but lack a canonical *ZAR1* (Supplemental Data Set 2), indicating that these ZAR1-SUB NLRs may have evolved to depend on other classes of NLR helpers.

How would ZAR1-SUB sense pathogens? Given that the LRR domains of most ZAR1-SUB proteins markedly diverged from the RLCK binding interfaces of ZAR1, it is unlikely that all of ZAR1-SUB members bind RLCKs in a ZAR1-type manner (Supplemental Fig. S17). This leads us to draw the hypothesis that ZAR1-SUB proteins have diversified to recognize other ligands than RLCKs. Indeed, Gong et al. (2022) showed that only *Populus trichocarpa* and *Prunus persica* ZAR1-SUB (PtZAR1-SUB and PpZAR1-SUB) out of 6 tested ZAR1-SUB members interacted with ZRK proteins in coimmunoprecipitation experiments. Both PtZAR1-SUB and PpZAR1-SUB did not form ZAR1-like oligomer complexes with RKS1 and did not cause cell death responses. Therefore, ZAR1-SUB may require other components to be activated or execute immune responses. In the future, functional investigations of ZAR1-SUB proteins could provide insights into how multifunctional NLRs, such as ZAR1, evolve into functionally specialized NLRs.

The *ZAR1-CIN* clade consists of 11 clustered paralogs that are unique to the magnoliid species stout camphor as revealed from the genome sequence of the Taiwanese small-flowered camphor tree (also known as *C. kanehirae*,

Downloaded from https://academic.oup.com/plcell/article/35/10/3662/7226528 by guest on 02 August 2025

Chinese name niu zhang 牛樟) (Chaw et al. 2019). This cluster probably expanded from *ZAR1*, which is ~48 Mbp on the same genome sequence scaffold (Supplemental Fig. S18). The relatively rapid expansion of *ZAR1-CIN* into a tandemly duplicated gene cluster is more in line with the classical model of NLR evolution compared to *ZAR1* maintenance as a genetic singleton over tens of millions of years (Michelmore and Meyers 1998). ZAR1-CIN proteins may have neofunctionalized after duplication, acquiring new recognition specificities as consequence of coevolution with host partner proteins and/or pathogen effectors. Consistent with this view, *ZAR1-CIN* exhibit different patterns of gene expression across tissues (Supplemental Fig. S18). Moreover, ZAR1-CIN proteins display distinct surfaces at the ZAR1–RLCK binding interfaces and may bind to other ligands than RLCKs as we hypothesized above for ZAR1-SUB (Supplemental Fig. S16). ZAR1-CIN could be viewed as intraspecific highly variable NLRs (hvNLR) per the nomenclature of Prigozhin and Krasileva (2020).

Unlike ZAR1-SUB, ZAR1-CIN have retained the N-terminal MADA sequence (Fig. 9 and Supplemental Fig. S17). We propose that ZAR1-CIN are able to execute the hypersensitive cell death on their own similar to ZAR1. However, ZAR1-CIN display divergent sequence patterns at NBD–NBD oligomerization interfaces compared to ZAR1 (Fig. 9C and Supplemental Fig. S19). Therefore, ZAR1-CIN may form resistosome-type complexes that are independent of ZAR1. One intriguing hypothesis is that ZAR1-CIN may associate with each other to form heterocomplexes of varying complexity and functionality operating as an NLR receptor network. In any case, the clear-cut evolutionary trajectory from *ZAR1* to the *ZAR1-CIN* paralog cluster provides a robust evolutionary framework to study functional transitions and diversifications in this CC-NLR lineage.

In summary, our phylogenomics analyses raise several intriguing questions about ZAR1 evolution. The primary conclusion we draw is that ZAR1 is an ancient CC-NLR that has been a partner with RLCKs ever since the Jurassic period. We propose that throughout at least 150 million yrs, ZAR1 has maintained its molecular features for sensing pathogens via RLCKs and activating hypersensitive cell death. Further comparative analyses, combining molecular evolution and structural biology, of plant resistosomes and between resistosomes and the apoptosomes and inflammasome of animal NLR systems (Wang and Chai 2020) will yield experimentally testable hypotheses for NLR research.

## Materials and methods

### ZAR1 and ZRK sequence retrieval

We performed BLAST (Altschul et al. 1990) using previously identified ZAR1 and ZRK protein sequences as queries (Lewis et al. 2013; Baudin et al. 2017; Schultink et al. 2019; Harant et al. 2022) to search ZAR1 and ZRK-like sequences in NCBI nr or nr/nt database (https://blast.ncbi.nlm.nih.gov/Blast.cgi) and Phytozome12.1 (https://phytozome.jgi.doe.gov/pz/portal.html#!search? show=BLAST). In the BLAST search, we used cut-offs, percent identity ≥ 30%, and query coverage ≥ 80%. The BLAST pipeline was circulated by using the obtained sequences as new queries to search for *ZAR1* and *ZRK*-like genes over the angiosperm species. We also performed the BLAST pipeline against a plant NLR dataset annotated by the NLR-parser (Steuernagel et al. 2015) from 38 plant reference genome databases (Supplemental Data Set 8).

### Phylogenetic analyses

For the phylogenetic analysis, we aligned NLR and ZRK amino acid sequences (Supplemental Files 1, 4 to 8) using MAFFT v.7 (Katoh and Standley 2013) and manually deleted the gaps in the alignments in MEGA7 (Kumar et al. 2016). Full-length or NB-ARC domain sequences of the aligned NLR datasets were used for generating phylogenetic trees. To generate ZRK phylogenetic trees, we used full-length or kinase domain sequences of the aligned ZRK datasets. The neighbor-joining tree was made using MEGA7 with JTT model and bootstrap values based on 100 iterations. All phylogenetic tree files are in Supplemental Files 9 to 13.

### Patristic distance analyses

To calculate the phylogenetic (patristic) distance, we used Python script based on DendroPy (Sukumaran and Holder 2010). We calculated patristic distances from each CC-NLR to the other CC-NLRs on the phylogenetic tree and extracted the distance between CC-NLRs of Arabidopsis (*A. thaliana*) or *N. benthamiana* to the closest NLR from the other plant species. The script used for the patristic distance calculation is available from GitHub (https://github.com/slt666666/Phylogenetic_distance_plot2).

### Gene colinearity analyses

To investigate genetic colinearity at *ZAR1* loci, we extracted the 3 genes upstream and downstream of *ZAR1* using GFF files derived from reference genome databases (Supplemental Data Set 8). To identify conserved gene blocks, we used gene annotation from NCBI Protein database and confirmed protein domain information based on InterProScan (Jones et al, 2014).

### Sequence conservation analyses

Full-length NLR sequences of each subfamily ZAR1, ZAR1-SUB, or ZAR1-CIN were subjected to motif searches using the MEME (Bailey and Elkan 1994) with parameters "0 or 1 occurrence per sequence, top twenty motifs," to detect consensus motifs conserved in ≥90% of the input sequences. The output data are summarized in Supplemental Tables S1, S2, and S4.

To predict the MADA motif from ZAR1, ZAR1-SUB, and ZAR1-CIN datasets, we used the MADA-HMM previously developed (Adachi et al. 2019b), with the hmmsearch program (hmmsearch –max -o <outputfile> <hmmfile>) implemented in HMMER v2.3.2 (Eddy 1998). We termed sequences over the HMMER cut-off score of 10.0 as the MADA motif and sequences having the score 0-to-10.0 as the MADA-like motif.

Downloaded from https://academic.oup.com/plcell/article/35/10/3662/7226528 by guest on 02 August 2025

To analyze sequence conservation and variation in ZAR1, ZAR1-SUB, and ZAR1-CIN proteins, aligned full-length NLR sequences (Supplemental Files 3, 14, and 15) were used for ConSurf (Ashkenazy et al. 2016). Arabidopsis ZAR1 (NP_190664.1), a tomato ZAR1-SUB (XP_004243429.1), or a Stout camphor ZAR1-CIN (RWR85656.1) was used as a query for each analysis of ZAR1, ZAR1-SUB, or ZAR1-CIN, respectively. The output datasets are in Supplemental Data Sets 9 to 11.

### Protein structure analyses

The atomic coordinate of ZAR1 (protein data bank accession codes; 6J5T) was downloaded from protein data bank for illustration in ccp4mg. We used the cryo-EM structures of ZAR1 as templates to generate homology models of ZAR1-SUB and ZAR1-CIN. Amino acid sequences of a tomato ZAR1-SUB (XP_004243429.1) and a stout camphor ZAR1-CIN (RWR85656.1) were submitted to Protein Homology Recognition Engine V2.0 (Phyre2) for modeling (Kelley et al., 2015). The coordinates of the ZAR1 structure (6J5T) were retrieved from the Protein Data Bank and assigned as the modeling template by using Phyre2 Expert Mode. The resulting models of ZAR1-SUB and ZAR1-CIN and the ZAR1 structures (6J5T) were illustrated with the ConSurf conservation scores in PyMol.

### Plant growth conditions

Wild-type *N. benthamiana* and *zar1-1* mutant plants (Schultink et al. 2019) were grown in a controlled growth chamber with temperature 22 to 25°C, humidity 45% to 65%, and 16/8 hr light/dark cycle. Fluorescent light bulbs (Slyvania Gro—Lux F58W/Gro—T8 and Phillips master TL-D 58W84D) were used, and the light intensity was about 200 $\mu$M/ms$^2$.

### Plasmid construction

The Golden Gate Modular Cloning (MoClo) kit (Weber et al. 2011) and the MoClo plant parts kit (Engler et al. 2014) were used for cloning, and all vectors are from this kit unless specified otherwise. ZAR1 and RLCK homologs identified in the taro (*C. esculenta*; Assembly: ASM944546v1), columbine (*A. coerulea*; Assembly: Aquilegia_coerulea_v1; Filiault et al. 2018), and stout camphor tree (*C. kanehirae*; Assembly: ASBRC_Ckan_1.0; Chaw et al. 2019) genomes were codon optimized for *N. benthamiana* using the ThermoFisher GeneOptimizer tool and synthesized by GENEWIZ as Golden Gate Level 0 modules into pICH41155. Genes were subcloned into the binary vector pICH86988 (Weber et al. 2011) and transformed into *A. tumefaciens* strain GV3101 pMP90. Cloning design and sequence analysis were done using Geneious Prime (v2022.0.1; https://www.geneious.com). Plasmid construction is described in Supplemental Data Set 12.

### Transient gene expression and cell death assay

Transient expression of ZAR1 and RLCK homologs in *N. benthamiana* was performed by agroinfiltration according to methods described by Bos et al. (2006). Briefly, 4-wk-old *N. benthamiana* plants were infiltrated with *Agrobacterium tumefaciens* strains carrying the binary expression plasmids. *A. tumefaciens* suspensions were prepared in infiltration buffer (10 mM MES, 10 mM $MgCl_2$, and 150 $\mu$M acetosyringone, pH 5.6) and were adjusted to appropriate $OD_{600}$ (Supplemental Data Set 12). Macroscopic cell death phenotypes were scored according to Supplemental Fig. 20 and statistical differences among the samples were analyzed with Tukey's HSD test (Supplemental Data Set 13).

### RNA-seq data analyses

Public RNA-seq reads, which were previously obtained with Illumina HiSeq 2000 (Chaw et al. 2019), were used to analyze expression profiles of CmZAR1 and ZAR1-CIN genes in the stout camphor tree (Accession Numbers: SRR7416905, SRR7416906, SRR7416908, SRR7416909, SRR7416910, SRR7416911, and SRR7416918). Reads were mapped to the stout camphor genome assembly (GenBank assembly accession GCA_003546025.1) using HISAT2 (Kim et al. 2019) and transformed into a Transcripts Per Million (TPM) value according to Li et al. (2010). TPM values were visualized by the heatmap. The heatmap was colored by 8 ranges (0, 0–5, 5–20, 20–40, 40–60, 60–80, 80–100, and >100) of TPM values.

RNA-seq reads (Accession Numbers: SRR1538828, SRR1538829, SRR1538848, SRR1538903, SRR1538904, SRR1538905, SRR1538928, SRR1538929, SRR1538930, SRR1538931, SRR1538932, SRR1538933, SRR1050891, SRR1050897, SRR1050892, SRR1050898, and SRR3629840) were used to analyze MeZAR1-ID expression in cassava. RNA-seq reads were filtered and trimmed using fastp (Chen et al. 2018). The quality-trimmed reads were mapped to the cassava genome assembly (GenBank assembly accession GCF_001659605.2) using HISAT2 (Kim et al. 2019). Mapped reads were analyzed using Integrative Genomics Viewer (Robinson et al. 2011).

### Accession numbers

DNA sequence data used in this study can be found from reference genome or GenBank/EMBL databases with accession numbers listed in Supplemental Data Sets 1, 4, 8, and 9.

## Acknowledgments

We are thankful to several colleagues for discussions and ideas. We thank Sebastian Schornack (Sainsbury Laboratory, University of Cambridge, Cambridge, UK) and Kodai Honda (Laboratory of Crop Evolution, Graduate School of Agriculture, Kyoto University) for valuable comments on this paper. We thank the Prime Minister of the United Kingdom for announcing a stay-at-home order on March 23, 2020.

## Author contributions

Conceptualization was done by H.A. and S.K.; data curation was done by H.A., T.S., J.K., H.P., J.L.G.H., and A.M.; formal analysis was done by H.A., T.S., and A.M.; investigation was done

Downloaded from https://academic.oup.com/plcell/article/35/10/3662/7226528 by guest on 02 August 2025

by H.A., T.S., and A.M.; methodology was done by H.A., T.S., J.K., and A.M.; the resources were accumulated by H.A., T.S., J.K., H.P., Y.U., and M.S.; supervision was done by H.A., A.M., and S.K.; funding acquisition was done by S.K.; project administration was done by S.K.; writing the initial draft was done by H.A., J.K., and S.K.; editing was done by H.A., T.S., J.K., J.L.G.H., and S.K.

## Supplemental data

The following materials are available in the online version of this article.

**Supplemental Figure S1.** Arabidopsis ZAR1 is the most conserved CC-NLR across angiosperms, which supports Fig. 1.

**Supplemental Figure S2.** NbZAR1 is highly conserved across angiosperms, which supports Fig. 1.

**Supplemental Figure S3.** Sequence alignment of full-length ZAR1 ortholog proteins across angiosperms, which supports Fig. 2.

**Supplemental Figure S4.** Schematic representation of the intragenomic relationship at ZAR1 loci across angiosperm genomes, which supports Fig. 2.

**Supplemental Figure S5.** E11 on the glutamate ring inside of the Arabidopsis ZAR1 resistosome is conserved across the orthologs, which supports Fig. 4.

**Supplemental Figure S6.** Sequence alignment of full-length ZRK proteins across angiosperms, which supports Fig. 5.

**Supplemental Figure S7.** Heterologous expression of ZAR1 orthologs from flowering plant species in *N. benthamiana*, which supports Fig. 6.

**Supplemental Figure S8.** *C. esculenta* ZRK1 does not alter autoimmune cell death by *C. esculenta* ZAR1 in *N. benthamiana*, which supports Fig. 6.

**Supplemental Figure S9.** Four *A. coerulea* ZRKs and 7 *C. micranthum* ZRKs positively regulate AcZAR1 and CmZAR1 autoactive cell death in *N. benthamiana*, which supports Fig. 6.

**Supplemental Figure S10.** Cell death assay by coexpressing Arabidopsis RKS1 with *A. coerulea* ZAR1 and *C. micranthum* ZAR1 in *N. benthamiana*, which supports Fig. 6.

**Supplemental Figure S11.** Silencing of *JIM2* does not affect CeZAR1 autoactive cell death in *N. benthamiana*, which supports Fig. 6.

**Supplemental Figure S12.** Cassava ZAR1-ID is transcribed as a splicing variant from a single locus on the genome, which supports Fig. 7.

**Supplemental Figure S13.** Trx domain integration occurred in 2 independent rosid ZAR1 subclades, which supports Fig. 7.

**Supplemental Figure S14.** Integrated Trx domains show high sequence similarity to ZAR1-linked PLP3a gene in Arabidopsis, which supports Fig. 7.

**Supplemental Figure S15.** ZAR1-SUB gene is distributed across eudicots, which supports Fig. 8.

**Supplemental Figure S16.** Sequence alignment of full-length ZAR1 and ZAR1-SUB proteins, which supports Fig. 9.

**Supplemental Figure S17.** ZAR1 and the sister subclade NLRs display different conserved surfaces on the resistosome structure, which supports Fig. 9.

**Supplemental Figure S18.** ZAR1-CIN gene cluster occurs in the *C. micranthum* genome, which supports Fig. 8.

**Supplemental Figure S19.** Sequence alignment of full-length ZAR1 and ZAR1-CIN proteins, which supports Fig. 9.

**Supplemental Figure S20.** Representative images for scoring cell death intensity as an HR index, which supports Fig. 6.

**Supplemental Table S1.** List of MEME motifs predicted from ZAR1 in angiosperms.

**Supplemental Table S2.** List of MEME motifs predicted from ZAR1-SUB.

**Supplemental Table S3.** Comparison of MEME motifs between ZAR1-SUB and ZAR1.

**Supplemental Table S4.** List of MEME motifs predicted from ZAR1-CIN.

**Supplemental Table S5.** Comparison of MEME motifs between ZAR1-CIN and ZAR1.

**Supplemental Data Set 1.** List of ZAR1 in angiosperms. "NF" means "not found."

**Supplemental Data Set 2.** List of plant species with the number of ZAR1, ZAR1-SUB, and ZAR1-CIN genes.

**Supplemental Data Set 3.** List of the closest NLR genes to ZAR1 locus.

**Supplemental Data Set 4.** Genome loci of ZAR1 and ZRK genes. "NA" means "not acquired."

**Supplemental Data Set 5.** List of genes genetically linked to ZAR1 in eudicots. "NF" means "not found."

**Supplemental Data Set 6.** List of ZAR1-SUB. "NF" means "not found."

**Supplemental Data Set 7.** List of ZAR1-CIN. "NF" means "not found."

**Supplemental Data Set 8.** Reference genome databases used for NLR annotation with NLR-parser.

**Supplemental Data Set 9.** The ConSurf conservation score among ZAR1 proteins.

**Supplemental Data Set 10.** The ConSurf conservation score among ZAR1-SUB proteins.

**Supplemental Data Set 11.** The ConSurf conservation score among ZAR1-CIN proteins.

**Supplemental Data Set 12.** Plasmid list used in this study.

**Supplemental Data Set 13.** Summary of Tukey's HSD test results in cell death assay.

**Supplemental File 1.** Amino acid sequences of full-length ZRKs.

**Supplemental File 2.** Amino acid alignment file of 35 ZRK in angiosperms.

**Supplemental File 3.** Amino acid alignment file of 120 ZAR1 in angiosperms.

**Supplemental File 4.** Amino acid sequences of full-length NLRs used for phylogenetic analysis in Fig. 1B.

**Supplemental File 5.** Amino acid sequences of full-length NLRs used for phylogenetic analysis in Supplemental Fig. S1.

Downloaded from https://academic.oup.com/plcell/article/35/10/3662/7226528 by guest on 02 August 2025

**Supplemental File 6.** Amino acid sequences of 120 ZAR1 in angiosperms.

**Supplemental File 7.** Amino acid sequences of 129 ZAR1-SUB.

**Supplemental File 8.** Amino acid sequences of 11 ZAR1-CIN.

**Supplemental File 9.** NLR phylogenetic tree file in Fig. 1B.

**Supplemental File 10.** NLR phylogenetic tree file in Supplemental Fig. S1.

**Supplemental File 11.** NLR phylogenetic tree file in Fig. 2.

**Supplemental File 12.** ZRK phylogenetic tree file in Fig. 5A.

**Supplemental File 13.** NLR phylogenetic tree file in Fig. 8.

**Supplemental File 14.** Amino acid alignment file of 129 ZAR1-SUB.

**Supplemental File 15.** Amino acid alignment file of 11 ZAR1-CIN.

## Funding

This work was funded by the Gatsby Charitable Foundation, Biotechnology and Biological Sciences Research Council (BBSRC, UK), and European Research Council (ERC BLASTOFF projects). J.L.G.H. acknowledges support from the South Dakota Agricultural Experiment Station (SD00H605-16). H.A. was funded by the Japan Society for the Promotion of Science (21K20583 and 22K14893) and Japan Science and Technology Agency Precursory Research for Embryonic Science and Technology (JPMJPR21D1).

*Conflict of interest statement.* S.K. receives funding from industry on NLR biology.

## Data availability

Accession numbers for all genes reported and all large-scale data are provided in the manuscript.

## References

**Adachi H, Contreras MP, Harant A, Wu CH, Derevnina L, Sakai T, Duggan C, Moratto E, Bozkurt TO, Maqbool A, et al.** An N-terminal motif in NLR immune receptors is functionally conserved across distantly related plant species. eLife. 2019b:**8**:e49956. https://doi.org/10.7554/eLife.49956

**Adachi H, Derevnina L, Kamoun S**. NLR singletons, pairs, and networks: evolution, assembly, and regulation of the intracellular immunoreceptor circuitry of plants. Curr Opin Plant Biol. 2019a:**50**:121–131. https://doi.org/10.1016/j.pbi.2019.04.007

**Adachi H, Sakai T, Kourelis J, Maqbool A, Kamoun S**. Jurassic NLR: conserved and dynamic evolutionary features of the atypically ancient immune receptor ZAR1. bioRxiv. 2020. https://doi.org/10.1101/2020.10.12.333484

**Altschul SF, Gish W, Miller W, Myers EW, Lipman DJ**. Basic local alignment search tool. J Mol Biol. 1990:**215**(3):403–410. https://doi.org/10.1016/S0022-2836(05)80360-2

**Ashkenazy H, Abadi S, Martz E, et al.** Consurf 2016: an improved methodology to estimate and visualize evolutionary conservation in macromolecules. Nucleic Acids Res. 2016:**44**(W1):W344–W350. https://doi.org/10.1093/nar/gkw408

**Baggs E, Dagdas G, Krasileva KV**. NLR diversity, helpers and integrated domains: making sense of the NLR IDentity. Curr Opin Plant Biol. 2017:**38**:59–67. https://doi.org/10.1016/j.pbi.2017.04.012

**Bailey TL, Elkan C**. Fitting a mixture model by expectation maximization to discover motifs in biopolymers. Proc Int Conf Intell Syst Mol Biol. 1994:**2**:28–36.

**Baudin M, Hassan JA, Schreiber KJ, Lewis JD**. Analysis of the ZAR1 immune complex reveals determinants for immunity and molecular interactions. Plant Physiol. 2017:**174**(4):2038–2053. https://doi.org/10.1104/pp.17.00441

**Baudin M, Schreiber KJ, Martin EC, Petrescu AJ, Lewis JD**. Structure-function analysis of ZAR1 immune receptor reveals key molecular interactions for activity. Plant J. 2020:**101**(2):352–370. https://doi.org/10.1111/tpj.14547

**Bayless AM, Nishimura MT**. Enzymatic functions for Toll/interleukin-1 receptor domain proteins in the plant immune system. Front Genet. 2020:**11**:539. https://doi.org/10.3389/fgene.2020.00539

**Bi G, Su M, Li N, et al.** The ZAR1 resistosome is a calcium-permeable channel triggering plant immune signaling. Cell. 2021:**184**(13):3528–3541.e12. https://doi.org/10.1016/j.cell.2021.05.003

**Bos JI, Kanneganti TD, Young C, Cakir C, Huitema E, Win J, Armstrong MR, Birch PR, Kamoun S**. The C-terminal half of *Phytophthora infestans* RXLR effector AVR3a is sufficient to trigger R3a-mediated hypersensitivity and suppress INF1- induced cell death in *Nicotiana benthamiana*. Plant J. 2006:**48**(2):165–176. https://doi.org/10.1111/j.1365-313X.2006.02866.x

**Burdett H, Bentham AR, Williams SJ, et al.** The plant "resistosome": structural insights into immune signaling. Cell Host Microbe. 2019:**26**(2):193–201. https://doi.org/10.1016/j.chom.2019.07.020

**Cesari S, Bernoux M, Moncuquet P, Kroj T, Dodds PN**. A novel conserved mechanism for plant NLR protein pairs: the "integrated decoy" hypothesis. Front Plant Sci. 2014:**5**:606. https://doi.org/10.3389/fpls.2014.00606

**Chaw SM, Liu YC, Wu YW, et al.** Stout camphor tree genome fills gaps in understanding of flowering plant genome evolution. Nat Plants. 2019:**5**(1):63–73. https://doi.org/10.1038/s41477-018-0337-0

**Chen S, Zhou Y, Chen Y, Gu J**. Fastp: an ultra-fast all-in-one FASTQ preprocessor. Bioinformatics. 2018:**34**(17):i884–i890. https://doi.org/10.1093/bioinformatics/bty560

**Coiro M, Doyle JA, Hilton J**. How deep is the conflict between molecular and fossil evidence on the age of angiosperms? New Phytol. 2019:**223**(1):83–99. https://doi.org/10.1111/nph.15708

**Cui D-F, Hou Y, Yin P, Wang X**. A Jurassic flower bud from China. Geological Society, London. 2022:**521**:81–93. https://doi.org/10.1144/SP521-2021-122

**Dangl JL, Horvath DM, Staskawicz BJ**. Pivoting the plant immune system from dissection to deployment. Science. 2013:**341**(6147):746–751. https://doi.org/10.1126/science.1236011

**Delaux PM, Hetherington AJ, Coudert Y, et al.** Reconstructing trait evolution in plant evo-devo studies. Curr Biol. 2019:**29**(21):R1110–R1118. https://doi.org/10.1016/j.cub.2019.09.044

**Dodds PN, Rathjen JP**. Plant immunity: towards an integrated view of plant-pathogen interactions. Nat Rev Genet. 2010:**11**(8):539–548. https://doi.org/10.1038/nrg2812

**Eddy SR**. Profile hidden Markov models. Bioinformatics. 1998:**14**(9):755–763. https://doi.org/10.1093/bioinformatics/14.9.755

**Engler C, Youles M, Gruetzner R, Ehnert TM, Werner S, Jones JD, Patron NJ, Marillonnet S**. A golden gate modular cloning toolbox for plants. ACS Synth Biol. 2014:**3**(11):839–843. https://doi.org/10.1021/sb4001504

**Feehan JM, Castel B, Bentham AR, Jones JD**. Plant NLRs get by with a little help from their friends. Curr Opin Plant Biol. 2020:**56**:99–108. https://doi.org/10.1016/j.pbi.2020.04.006

**Filiault DL, Ballerini ES, Mandáková T, et al.** The *Aquilegia* genome provides insight into adaptive radiation and reveals an extraordinarily polymorphic chromosome with a unique history. ELife. 2018:**7**:e36426. https://doi.org/10.7554/eLife.36426

Downloaded from https://academic.oup.com/plcell/article/35/10/3662/7226528 by guest on 02 August 2025

**Fu Q, Diez JB, Pole M, et al.** An unexpected noncarpellate epigynous flower from the Jurassic of China. Elife. 2018:**7**:e38827. https://doi.org/10.7554/eLife.38827

**Gong Z, Qi J, Hu M, Bi G, Zhou JM, Han GZ**. The origin and evolution of a plant resistosome. Plant Cell. 2022:**34**(5):1600–1620. https://doi.org/10.1093/plcell/koac053

**Harant A, Pai H, Sakai T, Kamoun S, Adachi H**. A vector system for fast-forward studies of the HOPZ-ACTIVATED RESISTANCE1 (ZAR1) resistosome in the model plant *Nicotiana benthamiana*. Plant Physiol. 2022:**188**(1):70–80. https://doi.org/10.1093/plphys/kiab471

**Hu M, Qi J, Bi G, Zhou JM**. Bacterial effectors induce oligomerization of immune receptor ZAR1 *in vivo*. Mol Plant. 2020:**13**(5):793–801. https://doi.org/10.1016/j.molp.2020.03.004

**Jones P, Binns D, Chang H, Fraser M, Li W, McAnulla C, McWilliam H, Maslen J, Mitchell A, Nuka G, et al.** Interproscan 5: genome-scale protein function classification. Bioinformatics. 2014:**30**(9):1236–1240. https://doi.org/10.1093/bioinformatics/btu031

**Jones JD, Dangl JL**. The plant immune system. Nature. 2006:**444**(7117):323–329. https://doi.org/10.1038/nature05286

**Jones JD, Vance RE, Dangl JL**. Intracellular innate immune surveillance devices in plants and animals. Science. 2016:**354**(6316):aaf6395. https://doi.org/10.1126/science.aaf6395

**Jubic LM, Saile S, Furzer OJ, El Kasmi F, Dangl JL**. Help wanted: helper NLRs and plant immune responses. Curr Opin Plant Biol. 2019:**50**:82–94. https://doi.org/10.1016/j.pbi.2019.03.013

**Karasov TL, Chae E, Herman JJ, Bergelson J**. Mechanisms to mitigate the trade-off between growth and defense. Plant Cell. 2017:**29**(4):666–680. https://doi.org/10.1105/tpc.16.00931

**Katoh K, Standley DM**. MAFFT multiple sequence alignment software version 7: improvements in performance and usability. Mol Biol Evol. 2013:**30**(4):772–780. https://doi.org/10.1093/molbev/mst010

**Kelley LA, Mezulis S, Yates CM, Wass MN, Sternberg MJ**. The Phyre2 web portal for protein modeling, prediction and analysis. Nat Protoc. 2015:**10**(6):845–858. https://doi.org/10.1038/nprot.2015.053

**Kim D, Paggi JM, Park C, Bennett C, Salzberg SL.** Graph-based genome alignment and genotyping with HISAT2 and HISAT-genotype. Nature Biotechnol. 2019:**37**(8):907–915. https://doi.org/10.1038/s41587-019-0201-4

**Kourelis J, Sakai T, Adachi H, Kamoun S**. RefPlantNLR is a comprehensive collection of experimentally validated plant disease resistance proteins from the NLR family. PLoS Biol. 2021:**19**(10):e3001124. https://doi.org/10.1371/journal.pbio.3001124

**Kourelis J, van der Hoorn RAL**. Defended to the nines: 25 years of resistance gene cloning identifies nine mechanisms for R protein function. Plant Cell. 2018:**30**(2):285–299. https://doi.org/10.1105/tpc.17.00579

**Kroj T, Chanclud E, Michel-Romiti C, Grand X, Morel JB**. Integration of decoy domains derived from protein targets of pathogen effectors into plant immune receptors is widespread. New Phytol. 2016:**210**(2):618–626. https://doi.org/10.1111/nph.13869

**Kumar S, Stecher G, Tamura K**. MEGA7: molecular evolutionary genetics analysis version 7.0 for bigger datasets. Mol Biol Evol. 2016:**33**(7):1870–1874. https://doi.org/10.1093/molbev/msw054

**Laflamme B, Dillon MM, Martel A, Almeida RND, Desveaux D, Guttman DS**. The pan-genome effector-triggered immunity landscape of a host-pathogen interaction. Science. 2020:**367**(6479):763–768. https://doi.org/10.1126/science.aax4079

**Lee RRQ, Chae E**. Variation patterns of NLR clusters in *Arabidopsis thaliana* genomes. Plant Communications. 2020:**1**(4):100089. https://doi.org/10.1016/j.xplc.2020.100089

**Lee H-Y, Mang H, Choi E-H, Seo Y-E, Kim M-S, Oh S, Kim S-B, Choi D**. Genome-wide functional analysis of hot pepper immune receptors reveals an autonomous NLR cluster in seed plants. New Phytol. 2021:**229**(1):532–547. https://doi.org/10.1111/nph.16878

**Lewis JD, Lee AH, Hassan JA, et al.** The *Arabidopsis* ZED1 pseudokinase is required for ZAR1-mediated immunity induced by the *Pseudomonas syringae* type III effector HopZ1a. Proc Natl Acad Sci U S A. 2013:**110**(46):18722–18727. https://doi.org/10.1073/pnas.1315520110

**Lewis JD, Wu R, Guttman DS, Desveaux D**. Allele-specific virulence attenuation of the *Pseudomonas syringae* HopZ1a type III effector via the *Arabidopsis* ZAR1 resistance protein. PLoS Genet. 2010:**6**(4):e1000894. https://doi.org/10.1371/journal.pgen.1000894

**Li B, Ruotti V, Stewart RM, Thomson JA, Dewey CN**. RNA-Seq gene expression estimation with read mapping uncertainty. Bioinformatics. 2010:**26**(4):493–500. https://doi.org/10.1093/bioinformatics/btp692

**Lin X, Zhang Y, Kuang H, Chen J**. Frequent loss of lineages and deficient duplications accounted for low copy number of disease resistance genes in Cucurbitaceae. BMC Genomics. 2013:**14**:335. https://doi.org/10.1186/1471-2164-14-335

**Ma S, Lapin D, Liu L, et al.** Direct pathogen-induced assembly of an NLR immune receptor complex to form a holoenzyme. Science. 2020:**370**(6521):eabe3069. https://doi.org/10.1126/science.abe3069

**Martin R, Qi T, Zhang H, Liu F, King M, Toth C, Nogales E, Staskawicz BJ**. Structure of the activated ROQ1 resistosome directly recognizing the pathogen effector XopQ. Science. 2020:**370**(6521):eabd9993. https://doi.org/10.1126/science.abd9993

**Mermigka G, Amprazi M, Mentzelopoulou A, Amartolou A, Sarris PF**. Plant and animal innate immunity complexes: fighting different enemies with similar weapons. Trends Plant Sci. 2020:**25**(1):80–91. https://doi.org/10.1016/j.tplants.2019.09.008

**Michelmore RW, Meyers BC**. Clusters of resistance genes in plants evolve by divergent selection and a birth-and-death process. Genome Res. 1998:**8**(11):1113–1130. https://doi.org/10.1101/gr.8.11.1113

**Pai H, Kourelis J, Adachi H, Kamoun S**. ZED1-related kinases (ZRKs) from *Aquilegia coerulea* and *Cinnamomum micranthum* do not trigger autoactive cell death in *Nicotiana benthamiana*. Zenodo. 2023. https://doi.org/10.5281/zenodo.7844723

**Prigozhin DM, Krasileva KV**. Analysis of intraspecies diversity reveals a subset of highly variable plant immune receptors and predicts their binding sites. Plant Cell. 2021:**33**(4):998–1015. https://doi.org/10.1093/plcell/koab013

**Robinson JT, Thorvaldsdóttir H, Winckler W, Guttman M, Lander ES, Getz G, Mesirov JP**. Integrative genomics viewer. Nat Biotechnol. 2011:**29**(1):24–26. https://doi.org/10.1038/nbt.1754

**Sarris PF, Cevik V, Dagdas G, Jones JD, Krasileva KV**. Comparative analysis of plant immune receptor architectures uncovers host proteins likely targeted by pathogens. BMC Biol. 2016:**14**:8. https://doi.org/10.1186/s12915-016-0228-7

**Schultink A, Qi T, Bally J, Staskawicz B**. Using forward genetics in *Nicotiana benthamiana* to uncover the immune signaling pathway mediating recognition of the *Xanthomonas perforans* effector XopJ4. New Phytol. 2019:**221**(2):1001–1009. https://doi.org/10.1111/nph.15411

**Seong K, Seo E, Witek K, Li M, Staskawicz B**. Evolution of NLR resistance genes with noncanonical N-terminal domains in wild tomato species. New Phytol. 2020:**227**(5):1530–1543. https://doi.org/10.1111/nph.16628

**Seto D, Koulena N, Lo T, Menna A, Guttman DS, Desveaux D**. Expanded type III effector recognition by the ZAR1 NLR protein using ZED1-related kinases. Nat Plants. 2017:**3**:17027. https://doi.org/10.1038/nplants.2017.27

**Shao ZQ, Xue JY, Wu P, et al.** Large-scale analyses of angiosperm nucleotide-binding site-leucine-rich repeat genes reveal three anciently diverged classes with distinct evolutionary patterns. Plant Physiol. 2016:**170**(4):2095–2109. https://doi.org/10.1104/pp.15.01487

**Smith SA, Brown JW**. Constructing a broadly inclusive seed plant phylogeny. Am J Bot. 2018:**105**(3):302–314. https://doi.org/10.1002/ajb2.1019

**Stam R, Silva-Arias GA, Tellier A**. Subsets of NLR genes show differential signatures of adaptation during colonization of new habitats. New Phytol. 2019:**224**(1):367–379. https://doi.org/10.1111/nph.16017

Downloaded from https://academic.oup.com/plcell/article/35/10/3662/7226528 by guest on 02 August 2025

**Steuernagel B, Jupe F, Witek K, Jones JD, Wulff BB**. NLR-parser: rapid annotation of plant NLR complements. Bioinformatics. 2015:**31**(10): 1665–1667. https://doi.org/10.1093/bioinformatics/btv005

**Sukumaran J, Holder MT**. Dendropy: a Python library for phylogenetic computing. Bioinformatics. 2010:**26**(12):1569–1571. https://doi.org/10.1093/bioinformatics/btq228

**Tamborski J, Krasileva KV**. Evolution of plant NLRs: from natural history to precise modifications. Annu Rev Plant Biol. 2020:**71**:355–378. https://doi.org/10.1146/annurev-arplant-081519-035901

**Uehling J, Deveau A, Paoletti M**. Do fungi have an innate immune response? An NLR-based comparison to plant and animal immune systems. PLoS Pathog. 2017:**13**(10):e1006578. https://doi.org/10.1371/journal.ppat.1006578

**Van de Weyer AL, Monteiro F, Furzer OJ, et al.** A species-wide inventory of NLR genes and alleles in *Arabidopsis thaliana*. Cell. 2019:**178**(5):1260–1272.e14. https://doi.org/10.1016/j.cell.2019.07.038

**Wang J, Chai J**. Structural insights into the plant immune receptors PRRs and NLRs. Plant Physiol. 2020:**182**(4):1566–1581. https://doi.org/10.1104/pp.19.01252

**Wang J, Hu M, Wang J, Qi J, Han Z, Wang G, Qi Y, Wang H-W, Zhou J-M, Chai J**. Reconstitution and structure of a plant NLR resistosome conferring immunity. Science. 2019b:**364**(6435):eaav5870. https://doi.org/10.1126/science.aav5870

**Wang G, Roux B, Feng F, et al.** The decoy substrate of a pathogen effector and a pseudokinase specify pathogen-induced modified-self recognition and immunity in plants. Cell Host Microbe. 2015:**18**(3): 285–295. https://doi.org/10.1016/j.chom.2015.08.004

**Wang J, Wang J, Hu M, Shan W, Qi J, Wang G, Han Z, Qi Y, Gao N, Wang H-W, et al.** Ligand-triggered allosteric ADP release primes a plant NLR complex. Science. 2019a:**364**(6435):eaav5868. https://doi.org/10.1126/science.aav5868

**Weber E, Engler C, Gruetzner R, Werner S, Marillonnet S**. A modular cloning system for standardized assembly of multigene constructs. PLoS One. 2011:**6**(2):e16765. https://doi.org/10.1371/journal.pone.0016765

**Wu CH, Abd-El-Haliem A, Bozkurt TO, et al.** NLR network mediates immunity to diverse plant pathogens. Proc Natl Acad Sci U S A. 2017:**114**(30):8113–8118. https://doi.org/10.1073/pnas.1702041114

**Wu CH, Derevnina L, Kamoun S**. Receptor networks underpin plant immunity. Science. 2018:**360**(6395):1300–1301. https://doi.org/10.1126/science.aat2623

**Wu CH, Krasileva KV, Banfield MJ, Terauchi R, Kamoun S**. The "sensor domains" of plant NLR proteins: more than decoys? Front Plant Sci. 2015:**6**:134. https://doi.org/10.3389/fpls.2015.00134

**Xiong Y, Han Z, Chai J**. Resistosome and inflammasome: platforms mediating innate immunity. Curr Opin Plant Biol. 2020:**56**:47–55. https://doi.org/10.1016/j.pbi.2020.03.010

**Zhou JM, Zhang Y**. Plant immunity: danger perception and signaling. Cell. 2020:**181**(5):978–989. https://doi.org/10.1016/j.cell.2020.04.028

Downloaded from https://academic.oup.com/plcell/article/35/10/3662/7226528 by guest on 02 August 2025

PLOS GENETICS

RESEARCH ARTICLE

# The helper NLR immune protein NRC3 mediates the hypersensitive cell death caused by the cell-surface receptor Cf-4

**Jiorgos Kourelis, Mauricio P. Contreras, Adeline Harant, Hsuan Pai, Daniel Lüdke, Hiroaki Adachi[¤a], Lida Derevnina[¤b], Chih-Hang Wu[¤c]*, Sophien Kamoun***

The Sainsbury Laboratory, University of East Anglia, Norwich Research Park, Norwich, United Kingdom

¤a Current address: Laboratory of Crop Evolution, Graduate School of Agriculture, Kyoto University, Mozume, Muko, Kyoto, Japan
¤b Current address: Crop Science Centre, Department of Plant Sciences, University of Cambridge, Lawrence Weaver Road, Cambridge, United Kingdom
¤c Current address: Institute of Plant and Microbial Biology, Academia Sinica, Nankang, Taipei, Taiwan
* wuchh@gate.sinica.edu.tw (CHW); sophien.kamoun@tsl.ac.uk (SK)

Check for updates

OPEN ACCESS

**Citation:** Kourelis J, Contreras MP, Harant A, Pai H, Lüdke D, Adachi H, et al. (2022) The helper NLR immune protein NRC3 mediates the hypersensitive cell death caused by the cell-surface receptor Cf-4. PLoS Genet 18(9): e1010414. https://doi.org/10.1371/journal.pgen.1010414

**Editor:** Tiancong Qi, Tsinghua University, CHINA

**Received:** February 19, 2022

**Accepted:** September 6, 2022

**Published:** September 22, 2022

**Peer Review History:** PLOS recognizes the benefits of transparency in the peer review process; therefore, we enable the publication of all of the content of peer review and author responses alongside final, published articles. The editorial history of this article is available here: https://doi.org/10.1371/journal.pgen.1010414

**Copyright:** © 2022 Kourelis et al. This is an open access article distributed under the terms of the Creative Commons Attribution License, which permits unrestricted use, distribution, and reproduction in any medium, provided the original author and source are credited.

**Data Availability Statement:** All data is included in the manuscript and in supporting information.

**Funding:** This work has been supported by the Gatsby Charitable Foundation (MPC, HP, DL, SK), Biotechnology and Biological Sciences Research

## Abstract

Cell surface pattern recognition receptors (PRRs) activate immune responses that can include the hypersensitive cell death. However, the pathways that link PRRs to the cell death response are poorly understood. Here, we show that the cell surface receptor-like protein Cf-4 requires the intracellular nucleotide-binding domain leucine-rich repeat containing receptor (NLR) NRC3 to trigger a confluent cell death response upon detection of the fungal effector Avr4 in leaves of *Nicotiana benthamiana*. This NRC3 activity requires an intact N-terminal MADA motif, a conserved signature of coiled-coil (CC)-type plant NLRs that is required for resistosome-mediated immune responses. A chimeric protein with the N-terminal α1 helix of Arabidopsis ZAR1 swapped into NRC3 retains the capacity to mediate Cf-4 hypersensitive cell death. Pathogen effectors acting as suppressors of NRC3 can suppress Cf-4-triggered hypersensitive cell-death. Our findings link the NLR resistosome model to the hypersensitive cell death caused by a cell surface PRR.

## Author summary

Just like humans, plants get sick. They get infected by parasites as diverse as fungi, bacteria, viruses, nematodes and insects. And just like humans, plants have an immune system that helps them defend against these parasites. Their first line of defence are disease resistance genes. When a resistance gene in the plant matches a gene in the parasite, the plant immune system is activated and the parasite invasion is restricted. Here, we show that one type of disease resistance gene that functions as a sensor on the cell surface requires other components inside the cell to execute the immune response. Pathogens evolved to suppress this type of immune networks by targeting the hub that connects different types of immune pathways.

Council (BBSRC) (BB/P012574 (Plant Health ISP)) (SK), European Research Council (ERC) (Retooling plant immunity for resistance to blast fungi, grant number 743165) (AH, SK), Japan Society for the Promotion of Plant Science (JSPS) Overseas Research Fellowships (grant number 1040031) (HA), Deutsche Forschungsgemeinschaft (DFG) Walter Benjamin Program (project number 464864389) (DL), and BASF Plant Science (BASF Plant Science) (JK, SK). The funders had no role in study design, data collection and analysis, decision to publish, or preparation of the manuscript.

**Competing interests:** I have read the journal's policy and the authors of this manuscript have the following competing interests: JK and SK receive funding from industry and have filed patents on NLR biology.

## Introduction

Recognition of pathogens by the plant innate immune system predominantly relies on cell surface immune receptors and intracellular nucleotide-binding and oligomerization domain (NOD)-like leucine-rich repeat receptors (NLRs). The activation of these receptors upon recognition of their cognate ligands triggers specific responses which ultimately result in activation of downstream immune pathways and disease resistance. The ligand sensing mechanisms are either by direct binding of a pathogen-derived or pathogen-induced ligand to the receptor, or by indirect recognition requiring additional host proteins [1]. Once cell-surface receptors and intracellular NLRs are activated, both classes of receptors induce common outputs, such as $Ca^{2+}$ influx, reactive oxygen species (ROS) production and mitogen activated protein kinase (MAPK) activation. However, the molecular mechanisms by which receptor activation results in common downstream immune signaling are not as well understood. The extent to which the downstream signaling of cell surface immune receptors and intracellular NLRs differs and converges is one of the main open questions in the field of plant immunity [2].

The plant NLR family is defined by a central NB-ARC (nucleotide-binding domain shared with APAF-1, various R-proteins and CED-4) domain and at least one other domain [3]. Plant NLRs can be subdivided in four main subclades characterized by distinct N-terminal domains. TIR-NLRs contain a catalytically active N-terminal Toll/interleukin-1 receptor (TIR) domain, while $CC_R$-NLRs, $CC_{G10}$-NLRs, and CC-NLRs contain distinct RPW8-type, G10-type, or Rx-type coiled coil (CC) domains, respectively. Several breakthroughs have been made in recent years in understanding the molecular mechanisms of recognition and signaling of plant NLRs [4]. NLR activation upon ligand recognition can result in an exchange of adenosine diphosphate (ADP) to adenosine triphosphate (ATP) in the NB-ARC domain and the formation of an oligomeric complex, termed a "resistosome". The Arabidopsis CC-NLR HOPZ-ACTIVATED RESISTANCE 1 (ZAR1) forms a pentameric resistosome structure in which the N-terminal α1 helix extends out to form a funnel which acts as a $Ca^{2+}$-permeable channel [5–7]. Likewise, upon activation the wheat CC-NLR Sr35 also forms a pentameric resistosome structure which acts as a $Ca^{2+}$-permeable channel, highlighting a common mechanism by which CC-NLRs function [8]. Like CC-NLRs, the $CC_R$-type helper-NLRs N REQUIREMENT GENE 1.1 (NRG1.1) and ACTIVATED DISEASE RESISTANCE 1 (ADR1) also generate $Ca^{2+}$-permeable channels upon activation [9]. The TIR-NLRs RECOGNITION OF PERONOSPORA PARASITICA 1 (RPP1) and RECOGNITION OF XopQ1 (Roq1) form tetrameric resistosome complexes upon activation [10,11]. The oligomerization of the TIR domain results in nicotinamide adenine dinucleotide nucleosidase (NADase) activity and the release of a plant-specific variant cyclic ADP-ribose (v-cADPR) [12,13]. In addition, some plant TIR domains can form a distinct oligomeric form with 2′,3′-cyclic adenosine monophosphate (cAMP)/cyclic guanosine monophosphate (cGMP) synthetase activity by hydrolyzing dsRNA/dsDNA and this activity is also required for immune signaling [14]. A subset of NLRs, known as functional singletons, combine pathogen detection and immune signaling activities into a single protein [15]. In contrast, many NLRs have functionally specialized over evolutionary time in "sensor" or "helper" NLRs dedicated to pathogen recognition or immune signaling, respectively [15]. Sensor and helper NLRs function together and can form receptor networks with a complex architecture [16,17].

Cell surface receptors are typically divided into two categories: the receptor-like kinases (RKs, also known as RLKs) and the receptor-like proteins (RPs, also known as RLPs). RKs contain a C-terminal intracellular kinase domain for downstream signaling, while RPs contain a small cytoplasmic tail and lack a C-terminal kinase domain. Both RKs and RPs have a single-pass transmembrane domain and a variety of extracellular ligand-binding domains [18]. Upon

ligand perception, RKs typically hetero-oligomerize with other RKs which act as co-receptors. For example, binding of chitin by the Arabidopsis LysM-RK LYSM-CONTAINING RECEPTOR-LIKE KINASE 5 (LYK5) induces hetero-oligomerization with the LysM-RK co-receptor CHITIN ELICITOR RECEPTOR KINASE 1 (CERK1) [19]. Furthermore, recognition of the flg22 peptide of bacterial flagellin by the leucine-rich repeat (LRR)-RK FLAGELLIN-SENSITIVE 2 (FLS2) induces hetero-oligomerization with the LRR-RK co-receptor SOMATIC EMBRYOGENESIS RECEPTOR-LIKE KINASE 3 (SERK3, also known as BRASSINOSTEROID INSENSITIVE 1-ASSOCIATED RECEPTOR KINASE (BAK1)) [20]. Similarly, most LRR-RPs constitutively interact with the LRR-RK SUPPRESSOR OF BAK1-INTERACTING RECEPTOR-LIKE KINASE 1 1 (SOBIR1), and activation upon ligand binding induces the hetero-oligomerization with the LRR-RLK co-receptor SERK3/BAK1 [21–27]. These activated complexes in turn phosphorylate specific downstream receptor-like cytoplasmic kinases (RLCKs) which ultimately relay the immune response [2,28].

While the signaling cascades downstream of cell surface immune receptors and NLRs were thought to be distinct [29], it is now becoming clear that in fact these signaling modules intertwine at different points [30–32]. Cell surface immune signaling was recently shown to be required for the hypersensitive cell death immune response triggered by a variety of NLRs [30,31]. Specifically, in the absence of cell surface immune signaling, the activation of the TIR-NLR pair RESISTANT TO RALSTONIA SOLANACEARUM 1 (RRS1)/RESISTANT TO P. SYRINGAE 4 (RPS4) by the effector AvrRps4 does not result in hypersensitive cell death [30]. Moreover, activation of the $CC_{G10}$-NLRs RESISTANT TO P. SYRINGAE 2 (RPS2) and RESISTANT TO P. SYRINGAE 5 (RPS5) by AvrRpt2 [30,31] and AvrPphB [30], respectively, or the CC-NLR RESISTANCE TO P. SYRINGAE PV MACULICOLA 1 (RPM1) by AvrRpm1 [30] results in diminished hypersensitive cell death in the absence of cell surface immune signaling. The emerging model is that cell surface immune signaling and intracellular NLR signaling mutually potentiate each other by enhancing transcription of the core signaling components of these pathways [30,31]. However, the mechanistic links between cell surface immune receptors and NLRs are not yet known [33]. Additionally, there is a tendency in the field to view cell surface and NLR receptors through a unified lens despite their huge structural and functional diversity [3,18]. The degree to which distinct classes of cell surface and intracellular receptors engage in signaling networks remains unclear.

In addition to their potentiation of cell surface immune signaling, NLRs can also be genetically involved downstream of cell surface immune receptor activation. The lipase-like protein ENHANCED DISEASE SUSCEPTIBILITY 1 (EDS1) forms mutually exclusive receptor complexes with either the related protein PHYTOALEXIN DEFICIENT 4 (PAD4) or SENESCENCE-ASSOCIATED GENE 101 (SAG101) to perceive small molecules produced by activated TIR-NLRs [34,35]. The ligand-bound EDS1/SAG101 and EDS1/PAD4 complexes in turn activate the $CC_R$-type helper-NLRs NRG1 and ADR1 to initiate immune signaling downstream of TIR-NLRs [34–36]. In Arabidopsis, the EDS1/PAD4/ADR1 and, to a lesser extent, EDS1/SAG101/NRG1 modules are also genetically required for a subset of the immune responses triggered by LRR-RPs [32,37] and LRR-RKs [37]. However, a subset of LRR-RPs can trigger hypersensitive cell death upon activation, and this hypersensitive cell death is not affected in mutants of the EDS1/PAD4/ADR1 and EDS1/SAG101/NRG1 pathway [32]. Indeed, the extent to which the subset of LRR-RPs that trigger hypersensitive cell death require NLRs warrants further investigation. Previously, the NLR protein NRC1 (NLR protein required for hypersensitive-response (HR)-associated cell death 1) was implicated in the cell death mediated by the LRR-RLPs Cf-4 [38], LeEIX2 [39], and Ve1 [40]. However, these studies were based on virus-induced gene silencing and, therefore, off-target effects on other NLR genes cannot be ruled out. Indeed, the silencing experiments performed in *Nicotiana benthamiana* were based on a

fragment sequence corresponding to the LRR domain of tomato NRC1 and predated the sequencing of the *N. benthamiana* genome [41]. The sequencing of the *N. benthamiana* genome revealed that *N. benthamiana* does not encode a functional ortholog of the tomato NRC1 gene [41–44]. Instead, the *N. benthamiana* genome contains homologs of NRC1, namely NRC2, NRC3, and NRC4 [16]. Therefore, the precise contribution of NLRs to the hypersensitive response mediated by Cf-4 type receptors has remained unclear, in part due to incomplete silencing of the various *N. benthamiana* NRCs using previously reported constructs [41,45].

The NRC superclade is a subclade of CC-NLRs that has massively expanded in some asterid plants, including the Solanaceae [16]. The NRC superclade consists of sensor NLRs encoded by *R* genes which confer resistance to diverse pathogens, and the NRC (NLR required for cell death) helper CC-NLRs, which mediate immune signaling and the hypersensitive cell death response downstream of effector recognition by the sensor NLRs. NRCs form redundant nodes in complex receptor networks, with different NRCs exhibiting different specificities for their sensor NLRs. Much like ZAR1, the N-terminal α1 helix of NRCs is defined by a molecular signature called the "MADA motif" [46]. NRCs and ZAR1 are therefore classified as MADA-CC-NLRs, a class that includes ~20% of all CC-NLRs in angiosperms [3,46]. In solanaceous species, the NRC network comprises up to half of the NLRome and can be counteracted by pathogen effectors. Recently, Derevnina *et al*., [47] showed that effector proteins from the cyst nematode *Globodera rostochiensis* and the oomycete *Phytophthora infestans* specifically suppress the activity of NRC2 and NRC3, independently of their sensor NLR partners.

In this study, we took advantage of various combinations of CRISPR/Cas9-induced loss-of-function mutations in the *N. benthamiana* NRCs to revisit the connection between NRCs and cell surface receptors [46,48,49]. We hypothesized that an activated NRC resistosome is required for downstream signaling upon LRR-RP activation in order to produce hypersensitive cell death. To challenge this hypothesis, we used the LRR-RP Cf4 [50], which upon recognition of the fungal pathogen *Cladosporium fulvum* (Syn. *Passalora fulva*) apoplastic effector Avr4 triggers hypersensitive cell death [51]. Using a combination of reverse genetics and complementation, we determined that Cf-4/Avr4-triggered cell death is largely mediated by the *N. benthamiana* NRC3 homolog, thereby clearly defining the contributions of *N. benthamiana* NRC homologs to pathways downstream of the Cf-4 LRR-RP. By using defined mutations in the MADA motif and generating swaps with the Arabidopsis ZAR1 α1 helix, we show that NRC resistosome function is potentially downstream of Cf-4 activation by Avr4. Finally, we show that divergent pathogen-derived suppressors of NRC activity suppress Cf-4/Avr4-triggered cell death. We conclude that Cf-4/Avr4-triggered hypersensitive cell death is mediated by the MADA-CC-NLR NRC3. Divergent pathogens target this node, thereby suppressing both intracellular and cell surface triggered immune responses. NRC3 is conserved in the Solanaceae and likely mediates hypersensitive cell death triggered by a variety of leucine-rich repeat receptor-like proteins. We propose that NRC3 is a core node that connects cell surface and intracellular immune networks.

## Results

### Cf-4/Avr4-triggered hypersensitive cell death is compromised in the *N. benthamiana nrc2/3* CRISPR mutant line

We previously generated multiple mutant lines of *N. benthamiana* that carry CRISPR/Cas9-induced premature termination mutations in various combinations of the *NRC2* (*NRC2a* and *NRC2b*), *NRC3* and *NRC4* (*NRC4a*, *NRC4b*, and *NRC4c*) genes [46,48,49]. These lines (*nrc2/3*, *nrc4*, and *nrc2/3/4*) enabled us to revisit the contribution of NRC helper NLRs to the

hypersensitive cell death caused by the receptor-like protein Cf-4. To do this, we quantified the cell death response following transient expression of Cf-4/Avr4 by agroinfiltration, or as controls the receptor/effector pairs Pto/AvrPto (mediated by Prf; NRC2/3-dependent), Rpi-blb2/AVRblb2 (NRC4-dependent), or R3a/Avr3a (NRC-independent) (**Figs 1** and **S1**) [16]. Cf-4/Avr4-triggered cell-death was significantly reduced in both the *nrc2/3*, and *nrc2/3/4* CRISPR mutant lines as compared to wild-type (**Fig 1A**). By contrast, even though the lipase-like protein EDS1 and the $CC_R$-type helper-NLRs NRG1 and ADR1 are implicated in mediating some responses downstream of cell-surface receptors in Arabidopsis [32,37], Cf-4/Avr4-triggered cell-death was not affected in *N. benthamiana eds1* CRISPR lines (**S2 Fig**) [52]. Cf-4 protein accumulation was not affected in the *nrc2/3/4* CRISPR lines (**Fig 1B**), indicating that the reduction in cell death is not due to differences in Cf-4 protein accumulation between these lines. While Pto/AvrPto-triggered cell death is completely abolished in the *nrc2/3* and *nrc2/3/4* CRISPR lines (**Figs 1A**, **1C** and **S1B**), Cf-4/Avr4 expression resulted in chlorosis in the *nrc2/3* and *nrc2/3/4* lines which did not develop into confluent cell death (**Figs 1C** and **S1B**). These results indicate that the Cf-4/Avr4-triggered hypersensitive cell death requires NRC2/3.

## NRC3 mediates Cf-4/Avr4-triggered hypersensitive cell death in *N. benthamiana*

Next, we determined the individual contribution of NRC2 and NRC3 to Cf-4/Avr4-triggered cell death. To do this, we transiently complemented the *nrc2/3/4* CRISPR lines with either NRC2 or NRC3 in addition to expressing Cf-4/Avr4 (**Fig 2A**). As a control, we used Pto/AvrPto, which can utilize either NRC2 or NRC3 for Prf-mediated hypersensitive cell death signalling in *N. benthamiana* [41]. In addition to NRC2 and NRC3, we used NRC4 which is not expected to complement the Cf-4/Avr4 or Pto/AvrPto-triggered cell death in the *N. benthamiana nrc2/3/4* lines. Although it was previously reported that NRC1 is required for Cf-4/Avr4 hypersensitive cell death [38], *N. benthamiana* and other species in the *Nicotiana* genus lack *NRC1* (**S3 Fig**). Thus, we decided to use tomato NRC1 (*Sl*NRC1) to test whether *Sl*NRC1 can also complement Cf-4/Avr4-triggered cell death in *N. benthamiana*. All tested NRCs accumulate, however NRC3 accumulates to lower levels as compared to *Sl*NRC1, NRC2, or NRC4 (**Fig 2B**). In the *nrc2/3/4* lines, Cf-4/Avr4 and Pto/AvrPto-triggered cell death responses were complemented by NRC3 compared to the empty vector (EV) or NRC4 control (**Figs 2C** and **2D**, **S4A** for statistical analysis). NRC2 complemented Pto/AvrPto cell death in the *nrc2/3/4* lines, but only partially complemented Cf-4/Avr4-triggered cell death as compared to NRC3 (**Fig 2C** and **2D**). Finally, *Sl*NRC1 partially complemented Pto/AvrPto cell death, but not Cf-4/Avr4 cell death (**Figs 2C** and **2D**, **S4A** for statistical analysis). This difference is not due to differential protein accumulation, as NRC3 protein accumulates less than *Sl*NRC1 or NRC2 and NRC4 (**Fig 2C**). Whereas NRC1 is pseudogenized in the *Nicotiana* genus with only small fragments corresponding to the LRR being found in the genome assemblies, NRC2 and NRC3 are conserved in all Solanaceous species investigated (**S3 Fig**). Indeed, both tomato and pepper NRC3 (*Sl*NRC3 and *Ca*NRC3, respectively) can complement Cf-4/Avr4-triggered cell death in the *nrc2/3/4* lines, but not tomato or pepper NRC1 (*Sl*NRC1 and *Ca*NRC1) or pepper NRC2 (*Ca*NRC2) (**S5 Fig**). Tomato NRC2 (*Sl*NRC2) can partially complement Cf-4/Avr4-triggered cell death as compared to tomato NRC3 (**S5 Fig**). Furthermore, NRC3 can complement Cf-2/Rcr3/Avr2-, Cf-5/Avr5-, and Cf-9/Avr9-triggered cell death in the *nrc2/3/4* lines, while NRC2 can partially complement Cf-9/Avr9-triggered cell death as observed for Cf-4/Avr4 (**S6 Fig**). We conclude that NRC3 is the main NRC helper node contributing to cell-surface receptor-triggered hypersensitive cell death in the Solanaceae.

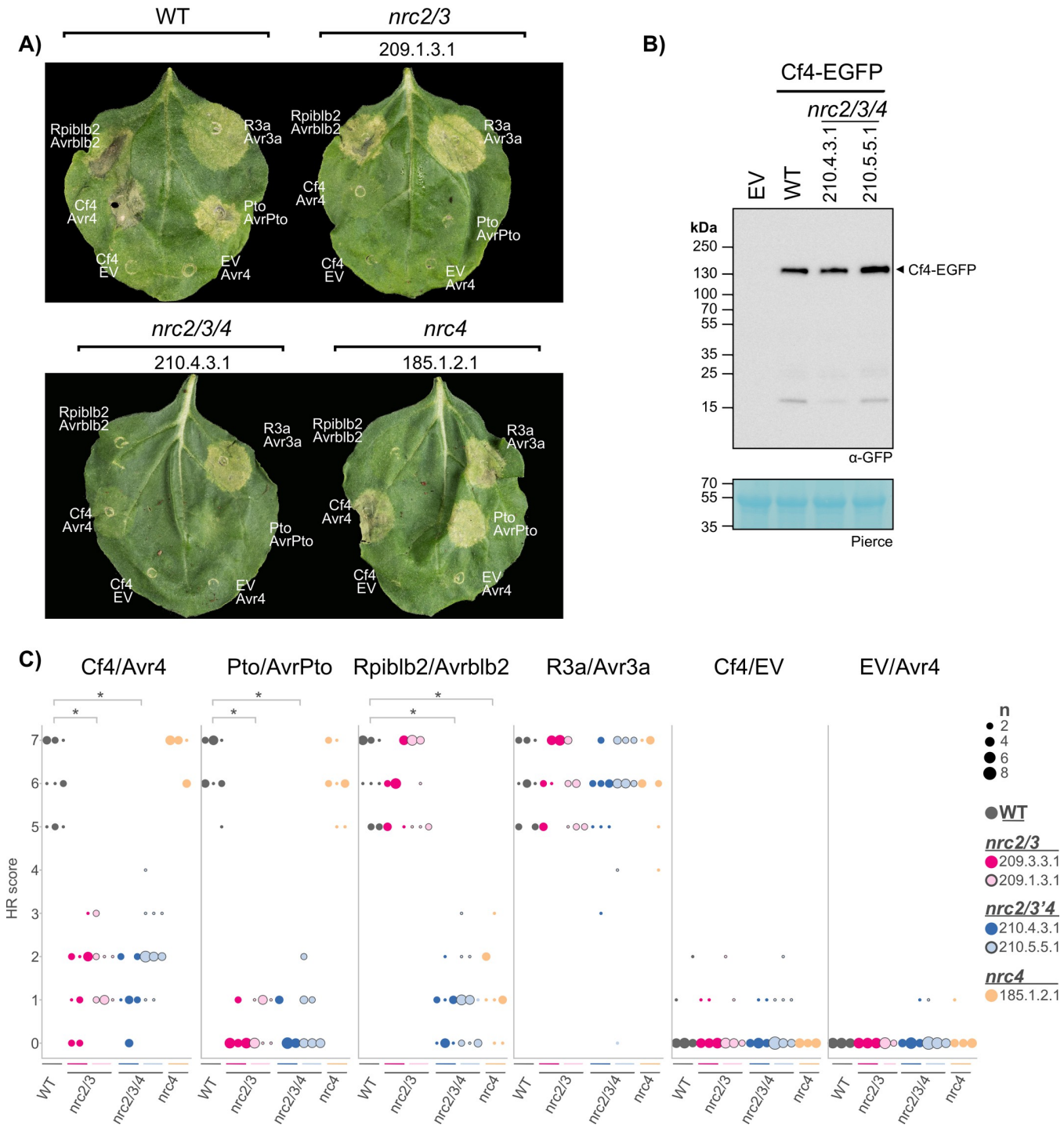


**Fig 1. Cf-4/Avr4-triggered hypersensitive cell death requires NRC2/3. A**) Cf-4/Avr4-triggered hypersensitive cell death is lost in the *nrc2/3* and *nrc2/3/4* knock-out lines, but not in the *nrc4* line. Representative *N. benthamiana* leaves infiltrated with appropriate constructs photographed 7–10 days after infiltration. The NRC CRISPR lines, *nrc2/3*-209.1.3.1, *nrc2/3/4*-210.4.3.1, and *nrc4*-185.1.2.1, are labelled above the leaf and the receptor/effector pair tested, Cf-4/Avr4, Prf (Pto/AvrPto), Rpi-blb2/AVRblb2 or R3a/Avr3a, are labelled on the leaf image. Cf-4/EV and EV/Avr4 were also included as negative controls. A representative leaf of the independent *nrc2/3*-209.3.3.1, and *nrc2/3/4*-210.5.5.1 CRISPR line are shown in S1B Fig) Cf-4 protein accumulation is not affected in the *nrc2/3/4* lines. For the immunoblot analysis, total protein was extracted 5 days after transient expression of Cf-4-EGFP by agroinfiltration in wild-type, *nrc2/3/4*-210.4.3.1 and *nrc2/3/4*-210.5.5.1 *N. benthamiana* leaves. Cf-4-EGFP accumulation was detected using anti-GFP antibody. **C**) Quantification of hypersensitive cell death. Cell death was scored based on a 0–7 scale (S1 Fig) between 7–10 days post infiltration. The results are presented as a dot plot, where the size of each dot is proportional to the count of the number of samples with the same score within each biological replicate. The experiment was

independently repeated three times. The columns correspond to the different biological replicates. Significant differences between the conditions are indicated with an asterisk (*). Details of statistical analysis are presented in S1 Fig.

https://doi.org/10.1371/journal.pgen.1010414.g001

## The NRC3 N-terminal MADA motif is required for Cf-4-triggered hypersensitive cell death

The NRC-helper clade is characterized by a N-terminal MADA-type α1 helix diagnostic of ZAR1-type CC-NLRs [46]. In order to determine whether the N-terminal MADA motif of NRC3 is required for the Cf-4/Avr4-triggered hypersensitive cell death, we took advantage of recently described cell death abolishing "MADA" mutations in this motif [46]. Like ZAR1 and NRC4, both NRC2 and NRC3 have an N-terminal MADA-type α1 helix (**Fig 3A**). Mutating leucine 17 to glutamic acid (L17E) abolishes NRC4-mediated cell death and immunity [46]. L17E and L21E mutations in NRC2 ($NRC2^{L17E}$) and NRC3 ($NRC3^{L21E}$) correspond to the L17E mutation in NRC4 ($NRC4^{L17E}$) (**Fig 3A and 3B**). To establish whether these mutations affect NRC2- or NRC3-mediated cell death, we conducted a complementation assay of Cf-4/Avr4 or Pto/AvrPto cell death in *N. benthamiana nrc2/3/4* lines with either wild-type NRC2 or NRC3, or their respective MADA mutants (**Fig 3B**). The MADA mutation did not affect protein accumulation, as both NRC2, NRC3, and their respective MADA mutants accumulated to similar levels (**Fig 3C**). Unlike wild-type NRC3, $NRC3^{L21E}$ didn't complement either Cf-4/Avr4 or Pto/AvrPto-triggered cell death in the *nrc2/3/4* lines (**Fig 3D and 3E**). As previously noted, NRC2 only partially complemented Cf-4/Avr4-triggered cell-death as compared to NRC3 (**Figs 2** and **S4**), but the $NRC2^{L17E}$ failed to complement either Cf-4/Avr4-triggered cell-death or Pto/AvrPto-triggered cell death (**Figs 3D** and **3E**, **S7A** for the statistical analysis). We conclude that the N-terminal α1 helix of NRC2 and NRC3 is required for their function as helper-NLRs downstream of Cf-4 activation.

## A chimeric protein fusion of the Arabidopsis ZAR1 α1 helix to NRC2/3 can complement loss of Cf-4-triggered hypersensitive cell death

In the activated ZAR1 resistosome, the N-terminal α1 helix of the CC domain is an important determinant for cell death induction [7]. In order to determine whether the N-terminal α1 helix of the ZAR1 CC domain could substitute for the NRC2/NRC3 predicted α1 helix in Cf-4/Avr4-triggered hypersensitive cell death, we generated chimaeras of NRC2 or NRC3 ($NRC2^{ZAR1\alpha1}$ and $NRC3^{ZAR1\alpha1}$), where the first 17 amino acids of ZAR1 corresponding to the α1 helix (**Fig 4A**) substitute the first 17 amino acids of NRC2 or the first 21 amino acids of NRC3. To test whether these chimaeras can complement Cf-4/Avr4 or Pto/AvrPto-triggered cell death, we transiently expressed these receptor/effector pairs with either wild-type NRC2 or NRC3, or their respective ZAR1 α1 helix chimaeras in *N. benthamiana nrc2/3/4* lines (**Fig 4B**). The chimeric proteins expressed and accumulated to similar level as both wild-type NRC2 and NRC3 proteins (**Fig 4C**). Like wild-type NRC3, $NRC3^{ZAR1\alpha1}$ complemented both Cf-4/Avr4 or Pto/AvrPto-triggered cell death in the *N. benthamiana nrc2/3/4* CRISPR lines (**Fig 4D and 4E**). Surprisingly, the $NRC2^{ZAR1\alpha1}$ chimaera complemented Cf-4/Avr4-triggered cell death to a similar extent as NRC3 (**Fig 4D and 4E**). The $NRC2^{ZAR1\alpha1}$ chimaera also complemented Pto/AvrPto-triggered cell death to a greater extent than wild-type NRC2 (**Figs 4D and 4E**, **S8A** for the statistical analysis). Importantly, this was not because the NRC ZAR1 α1 helix chimaeras are autoactive, as expressing them with either Cf-4 or Pto and an EV control did not result in cell death (**Fig 4D and 4E**). Furthermore, while NRC3 with the NRC2 α1 helix ($NRC3^{NRC2\alpha1}$) can complement Cf-4/Avr4- and Pto/AvrPto-triggered cell death, NRC2 with the NRC3 α1 helix ($NRC2^{NRC3\alpha1}$) cannot (**S9 Fig**). In ZAR1 E11 is required to generate a

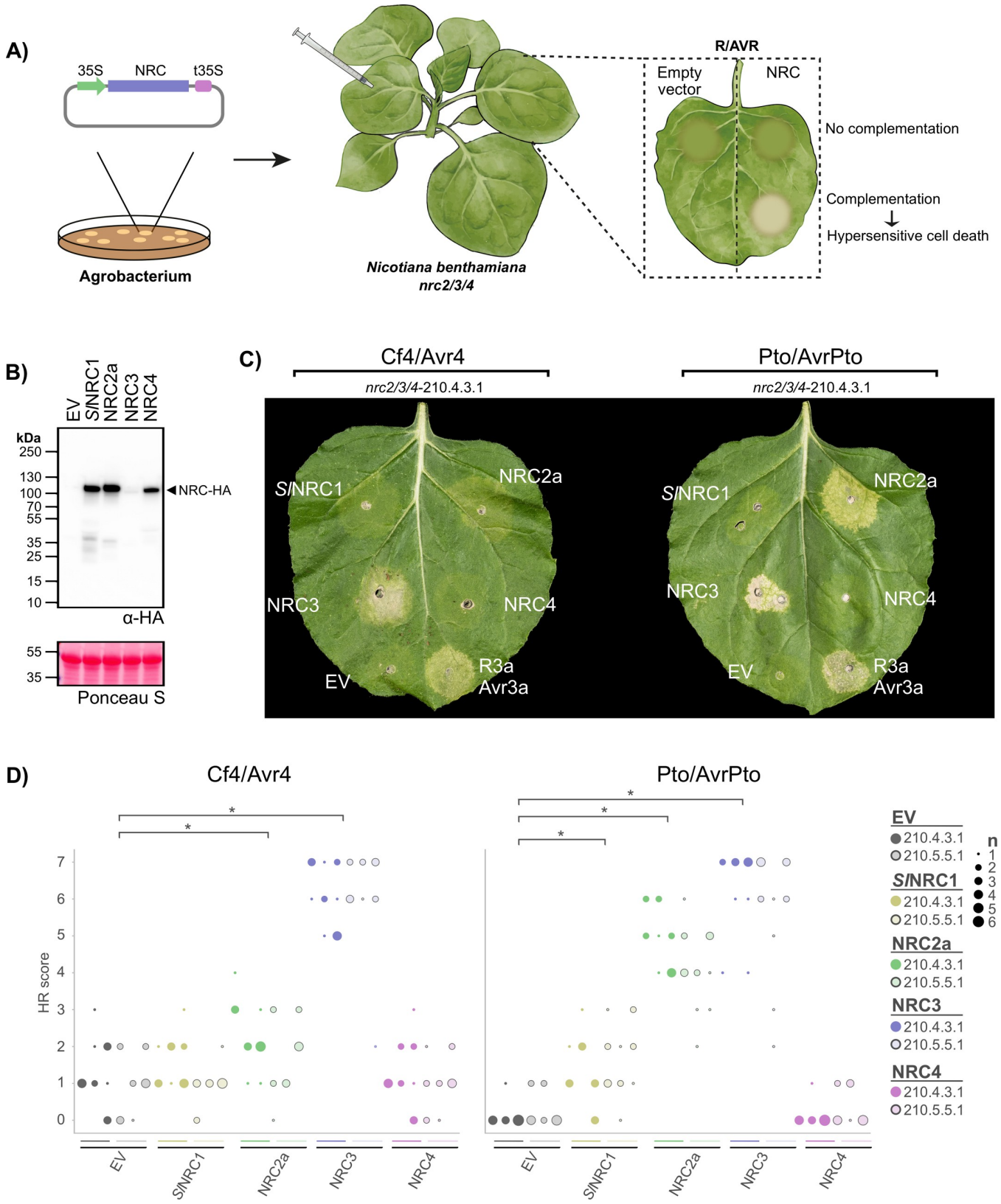


**Fig 2. NRC3 complements Cf-4/Avr4-triggered hypersensitive cell death in the *nrc2/3/4* knock-out lines. A**) A schematic representation of the cell death complementation assay. NRCs and empty vector (EV) were transformed into *A. tumefaciens*, and transiently co-expressed *in N. benthamiana* plants with either

Cf-4/Avr4 or Pto/AvrPto. Hypersensitive cell death was scored based on a modified 0–7 scale between 7–10 days post infiltration (S1A Fig). **B**) *Sl*NRC1, NRC2, NRC3, and NRC4 protein accumulation. Immunoblot analysis of transiently expressed C-terminally 6xHA-tagged NRCs 5 days after agroinfiltration in wild-type *N. benthamiana* plants. **C**) Cf-4/Avr4-triggered hypersensitive cell death is complemented in the *nrc2/3/4* lines with NRC3 and to a lesser extent NRC2, but not *Sl*NRC1 or NRC4. Representative *N. benthamiana* leaves infiltrated with appropriate constructs were photographed 7–10 days after agroinfiltration. The receptor/effector pair tested, Cf-4/Avr4 and Prf (Pto/AvrPto), are labelled above the leaf of *nrc2/3/4*-210.4.3.1. The NRC used for complementation or EV control are labelled on the leaf image. A representative leaf of the independent *nrc2/3/4*-210.5.5.1 line is shown in S4D Fig) Quantification of hypersensitive cell death. Cell death was scored based on a 0–7 scale between 7–10 days post infiltration. The results are presented as a dot plot, where the size of each dot is proportional to the count of the number of samples with the same score within each biological replicate. The experiment was independently repeated three times. The columns correspond to the different biological replicates. Significant differences between the conditions are indicated with an asterisk (*). Details of statistical analysis are presented in S4 Fig.

https://doi.org/10.1371/journal.pgen.1010414.g002

$Ca^{2+}$-permeable membrane-permeable pore and induce cell death [7]. However, this residue is not required for the wheat NLR Sr35 to generate a $Ca^{2+}$-permeable membrane-permeable pore and induce cell death [8], and is similarly also not required for NRC4-mediated cell-death [46]. Mutating the equivalent glutamic acid residue in NRC3 to glutamine (E14Q) does not impair complementation of Cf-4/Avr4- or Pto/AvrPto-triggered cell death in the *nrc2/3/4* CRISPR lines (S10 Fig). We conclude that the α1 helix of ZAR1 can replace the NRC2 and NRC3 α1 helix for hypersensitive cell death signaling, and even enhances the NRC-dependent hypersensitive cell-death response. Why the $NRC2^{ZAR1\alpha1}$ chimaera, but not the $NRC2^{NRC3\alpha1}$ chimaera, can complement Cf-4/Avr4-triggered cell death to a similar extent as NRC3 is not clear. We conclude that modifications of the α1 helix of NRCs can sometimes expand their role as helper-NLRs.

## Pathogen effectors can suppress Cf4-triggered hypersensitive cell death in a NRC3-dependent manner

We recently showed that plant pathogens have converged on suppressing the NRC network to prevent immune responses [47]. NRC3, for example, is suppressed by both the cyst nematode *Globodera rostochiensis* effector SPRYSEC15, as well as the oomycete *Phytophthora infestans* effector AVRcap1b [47]. Since Cf-4/Avr4-triggered cell death requires NRC3, we reasoned that these effectors could also suppress cell death triggered by Cf-4 and similar LRR-RPs. To test this hypothesis, we generated heterologous expression constructs containing both NRC3 and either SPRYSEC15, AVRcap1b, or mCherry (control). We then co-expressed these NRC3/suppressor combinations together with Cf-4/Avr4 in *N. benthamiana nrc2/3/4* lines (Fig 5A). As controls, we used either autoactive $NRC3^{D480V}$, or the receptor/effector pair Pto/AvrPto, both of which are suppressed by SPRYSEC15 and AVRcap1b [47]. The receptor/effector pair R3a/Avr3a, which is not affected by SPRYSEC15 or AVRcap1b, was used as a control combination [47]. These experiments revealed that both AVRcap1b and SPRYSEC15 suppress Cf-4/Avr4-triggered cell death (**Figs** 5B and 5C, S11A for the statistical analysis). As expected, AVRcap1b and SPRYSEC15 suppressed autoactive $NRC3^{D480V}$ and Pto/AvrPto-triggered cell death, but not R3a/Avr3a-triggered cell death (Fig 5B and 5C). As previously noted, transient expression of Cf-4/Avr4 results in a NRC3-independent chlorosis (Fig 1), and this phenotype was not suppressed by either SPRYSEC15 or AVRcap1b (Fig 5B and 5C). We conclude that divergent pathogen effectors, acting as suppressors of NRC3-mediated cell death, can suppress the hypersensitive cell death induced by the cell-surface receptor Cf-4.

## Discussion

Cell surface receptor-mediated immunity and intracellular NLR-mediated immunity are viewed as the main innate immune responses in plants. Although their signaling pathways were initially thought to be qualitatively distinct, recent findings point to a degree of cross-talk

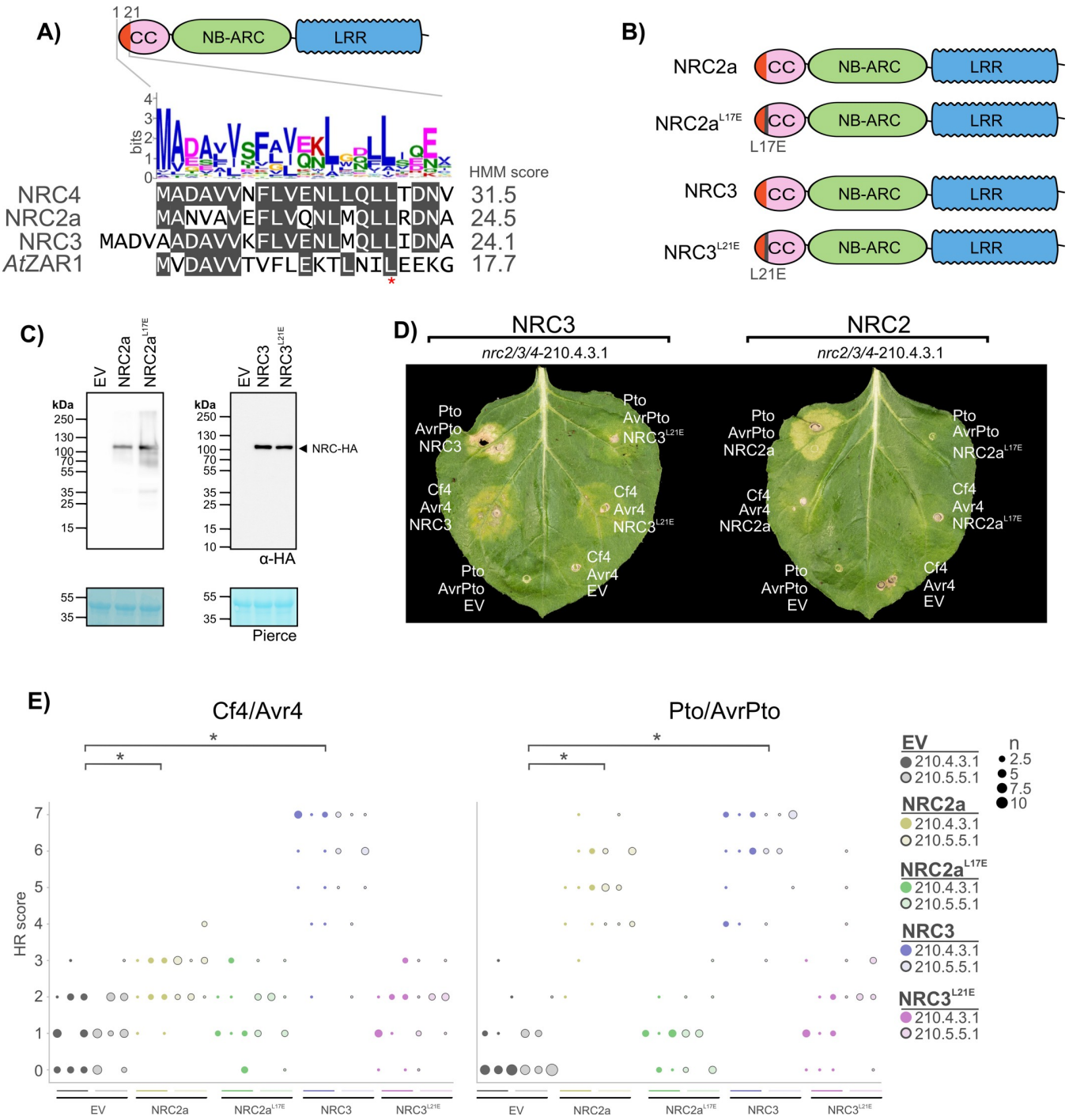


**Fig 3. The N-terminal MADA motif of NRC3 is required for Cf-4/Avr4-triggered hypersensitive cell death. A**) NRC3 has an N-terminal MADA motif. Alignment of NRC2, NRC3, NRC4 and ZAR1 N-terminal MADA motif with the consensus sequence pattern of the MADA motif and the HMM score for each sequence. **B**) Schematic representation of NRC2, NRC3, and the respective NRC2$^{L17E}$ and NRC3$^{L21E}$ MADA mutants. **C**) NRC2 and NRC3 MADA mutants accumulate to similar levels as wild-type proteins. Immunoblot analysis of transiently expressed C-terminally 6xHA-tagged NRCs 5 days after agroinfiltration in wild-type *N. benthamiana* plants. **D**) NRC MADA mutants do not complement Cf-4/Avr4 or Pto/AvrPto-triggered hypersensitive cell death in the *N. benthamiana nrc2/3/4* lines. Representative *N. benthamiana* leaves infiltrated with appropriate constructs were photographed 7–10 days after infiltration. The NRCs tested, NRC2 and NRC3, are labelled above the leaf of *nrc2/3/4*-210.4.3.1. The receptor/effector pair tested, Cf-4/Avr4 and Prf (Pto/AvrPto), are labelled on the leaf image. A representative leaf of the independent *nrc2/3/4*-210.5.5.1 line is shown in S7E Fig) Quantification of hypersensitive cell death. Cell death was scored based on a 0–7 scale between 7–10 days post infiltration. The results are presented as a dot plot, where the size of each dot is proportional to the count of the number of samples with the same score within each biological replicate. The experiment was independently repeated three times. The columns

correspond to the different biological replicates. Significant differences between the conditions are indicated with an asterisk (*). Details of statistical analysis are presented in S7 Fig.

https://doi.org/10.1371/journal.pgen.1010414.g003

[30–32,37]. Here we show that the cell-surface leucine-rich repeat receptor-like protein Cf-4 taps into the NRC helper NLR network to trigger hypersensitive cell death upon recognition of the apoplastic fungal *Cladosporium fulvum* effector Avr4. We propose that NRC3 is a core node that connects cell surface and intracellular immune networks, which may involve uncharacterized sensor-NLRs (Fig 6). Divergent plant pathogens have convergently evolved to target the NRC3 node, thereby suppressing both intracellular and cell surface triggered immune responses (Fig 6).

The hypersensitive cell death elicited by Cf-4/Avr4 is abolished in *N. benthamiana nrc2/3* and *nrc2/3/4*, but not *nrc4* lines (Fig 1). Interestingly, transient expression of Cf-4/Avr4 triggers a NRC2/3/4-independent chlorosis (Fig 1) indicating that there are probably both NRC-dependent and -independent responses triggered by Cf-4, possibly mediated by the complex and dynamic association of RPs such as Cf-4 with partner RKs and RLCKs [21]. Although complementation using *N. benthamiana* or tomato NRC2, but not pepper NRC2, only partially rescues the phenotype, complementation using *N. benthamiana*, tomato, and pepper NRC3 significantly restores Cf-4/Avr4-triggered hypersensitive cell death in the *nrc2/3* and *nrc2/3/4* CRISPR lines (Fig 2). Since NRC3 is conserved in all solanaceous species investigated (S3 Fig) it may mediate cell death responses triggered by cell-surface receptors in these species as well. When in evolutionary time this member of the NRC helper NLR family evolved to connect to the signaling pathway triggered by pattern recognition receptors remains to be elucidated.

Previously, NRC1 was implicated in the cell death mediated by the cell surface receptors Cf-4 [38], LeEIX2 [39] and Ve1 [40] in *N. benthamiana*. Here we show that NRC3, rather than NRC1, links cell-surface immune receptors to intracellular immunity in the *N. benthamiana* experimental system (**Figs** 1 and 2). Additionally, *Sl*NRC1 cannot complement Cf-4/Avr4-triggered hypersensitive cell death in the *N. benthamiana* experimental system (Fig 2). Unlike *Sl*NRC1, NRC3 is conserved in all Solanaceous species (S3 Fig), indicating that this link between cell surface immune receptors and intracellular immunity may be conserved in the Solanaceae. In addition to the NRC-dependent hypersensitive cell death, NRC-independent responses are also activated by these cell surface immune receptors. It may be that for some pathogens the NRC-independent response is sufficient to result in immunity, while for other pathogens the NRC-dependent response is also required. Which genetic components are involved in the NRC-independent response downstream of cell surface receptors remains a topic of further study.

NRC3 requires an intact MADA motif to mediate Cf-4/Avr4-triggered hypersensitive cell death (Fig 3). This is similar to intracellular activation of NRCs, where NRC4-mediated Rpi-blb2/AVRblb2-triggered cell death and immunity require an intact NRC4 MADA motif [46]. Additionally, the ZAR1 α1 helix can functionally substitute for the N-terminal equivalent sequence of NRC3. This observation suggests that the hypersensitive cell death response downstream of Cf-4/Avr4 immune signaling could involve an activated resistosome. Indeed, NRC2 was recently shown to oligomerize into a resistosome-like structure upon activation by multiple sensor NLRs, indicating that NRC-type helper NLRs are likely to function like ZAR1 [53,54].

Surprisingly, swapping the ZAR1 α1 helix into NRC2 resulted in a stronger cell death response as compared to the native NRC2. In contrast to the native NRC2, this chimeric protein could efficiently complement Cf-4/Avr4-triggered hypersensitive cell death (Fig 4). Given

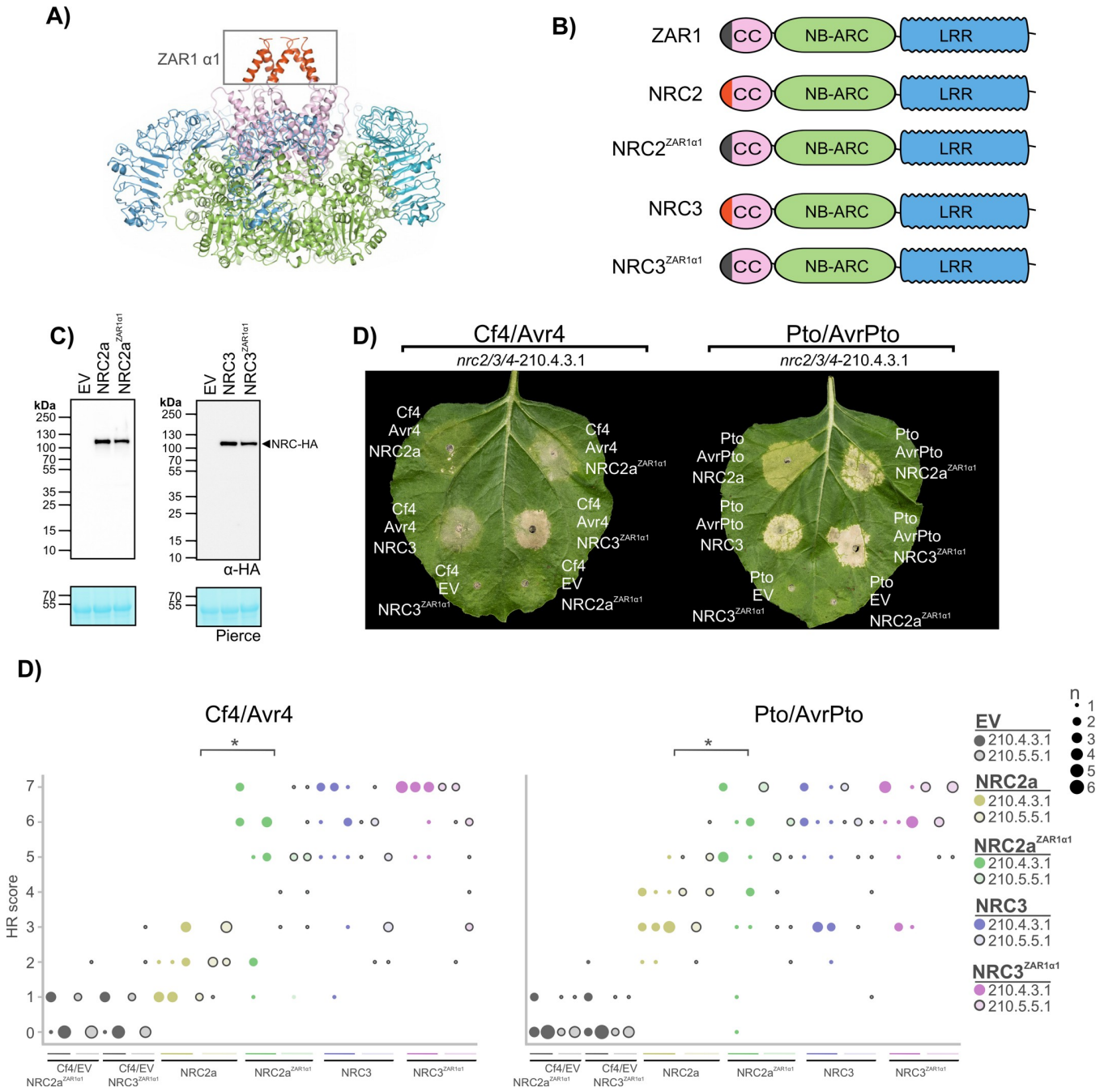


**Fig 4. The ZAR1 α1 helix can functionally replace the NRC2 and NRC3 α1 helix for Cf-4/Avr4-triggered hypersensitive cell death. A**) Structure of the ZAR1 resistosome with the N-terminal α1 helix highlighted. **B**) Schematic representation of ZAR1, NRC2, NRC3, and the respective NRC2$^{ZAR1α1}$ and NRC3$^{ZAR1α1}$ chimaeras in which residues 1–17 and 1–21 are replaced by residues 1–17 from ZAR1, respectively. **C**) NRC ZAR1 α1 helix chimaeras accumulate to similar levels as wild-type NRC proteins. Immunoblot analysis of transient NRC-6xHA accumulation 5 days after agroinfiltration in wild-type *N. benthamiana* plants. **D**) NRC ZAR1 α1 helix chimaeras can complement Cf-4/Avr4 and Pto/AvrPto-triggered hypersensitive cell death in the *N. benthamiana nrc2/3/4* CRISPR lines. Representative *N. benthamiana* leaves infiltrated with appropriate constructs were photographed 7–10 days after infiltration. The receptor/effector pair tested, Cf-4/Avr4 and Prf (Pto/AvrPto), are labelled above the leaf of NRC CRISPR line *nrc2/3/4*-210.4.3.1. The NRC tested, NRC2 and NRC3, are labelled on the leaf image. To ensure the NRC ZAR1 α1 helix chimaeras were not autoactive when expressed with either Cf-4 or Pto an EV control was taken along. A representative leaf of the independent *nrc2/3/4*-210.5.5.1 CRISPR line is shown in S8E Fig) Quantification of hypersensitive cell death. Cell death was scored based on a 0–7 scale between 7–10 days post infiltration. The results are presented as a dot plot, where the size of each dot is proportional to the count of the number of samples with the same score within each biological replicate. The experiment was independently repeated three times. The columns correspond to the different biological replicates. Significant differences between the conditions are indicated with an asterisk (*). Details of statistical analysis are presented in S8 Fig.

https://doi.org/10.1371/journal.pgen.1010414.g004

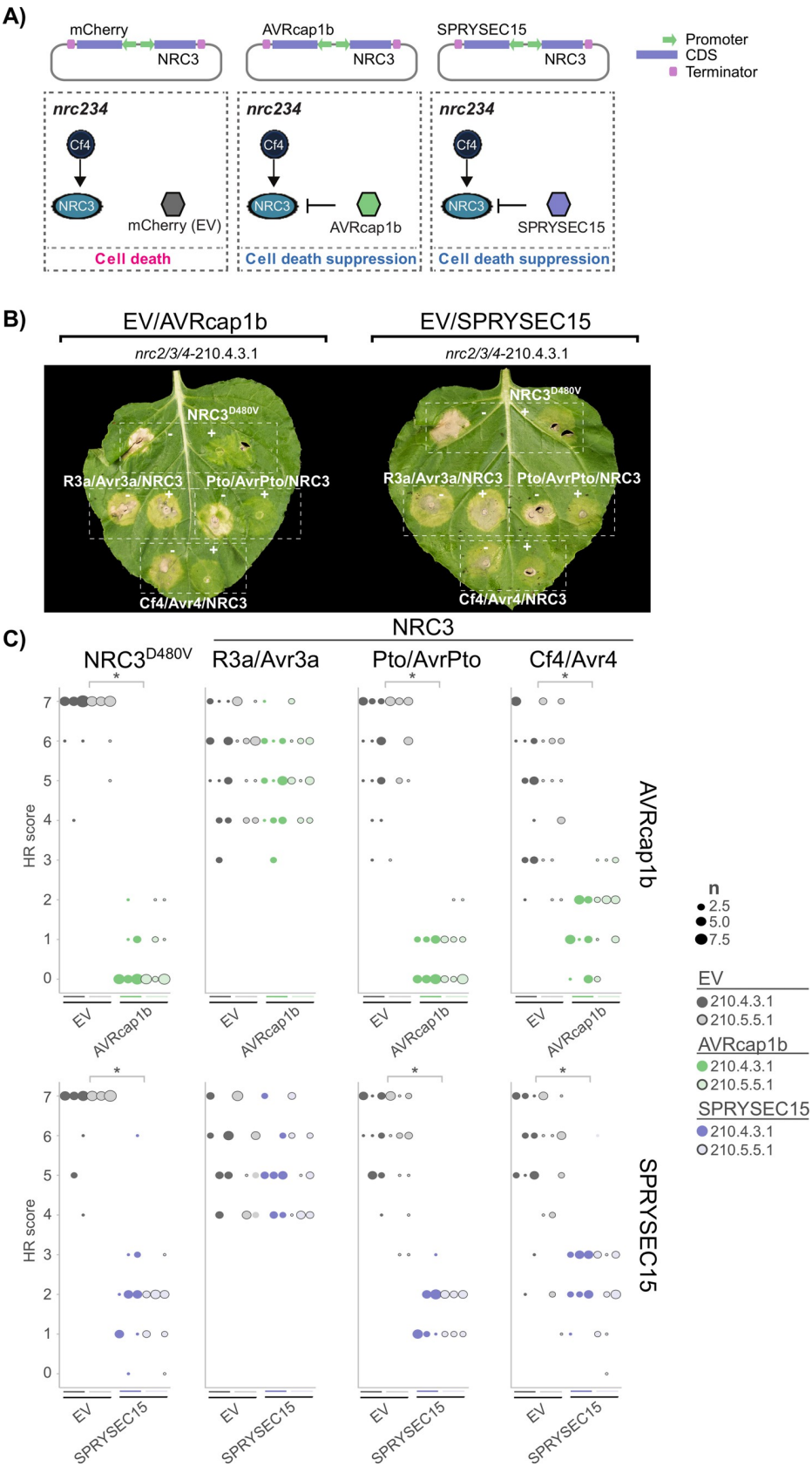
A)
mCherry
NRC3
AVRcap1b
NRC3
SPRYSEC15
NRC3
Promoter
CDS
Terminator
nrc234
Cf4
NRC3
mCherry (EV)
Cell death
nrc234
Cf4
NRC3
AVRcap1b
Cell death suppression
nrc234
Cf4
NRC3
SPRYSEC15
Cell death suppression
B)
EV/AVRcap1b
EV/SPRYSEC15
nrc2/3/4-210.4.3.1
nrc2/3/4-210.4.3.1
NRC3D480V
R3a/Avr3a/NRC3
Pto/AvrPto/NRC3
Cf4/Avr4/NRC3
NRC3D480V
R3a/Avr3a/NRC3
Pto/AvrPto/NRC3
Cf4/Avr4/NRC3
C)
NRC3
NRC3D480V
R3a/Avr3a
Pto/AvrPto
Cf4/Avr4
HR score
EV
AVRcap1b
SPRYSEC15
n
2.5
5.0
7.5
EV
210.4.3.1
210.5.5.1
AVRcap1b
210.4.3.1
210.5.5.1
SPRYSEC15
210.4.3.1
210.5.5.1

**Fig 5. Cf-4/Avr4-triggered hypersensitive cell death can be suppressed by divergent pathogen effectors. A**) A schematic representation of cell death suppression assay. *A. tumefaciens* containing vectors carrying both NRC3 and either SPRYSEC15, AVRcap1b, or mCherry as empty vector control, were co-expressed in *N. benthamiana nrc2/3/4* CRISPR lines, with the effectors suppressing the cell death response. **B**) Cf-4/Avr4-triggered hypersensitive cell death is suppressed by SPRYSEC15 and AVRcap1b, but not the EV control. Representative image of *N. benthamiana nrc2/3/4*-210.4.3.1 CRISPR line leaves which were agroinfiltrated with NRC3/suppressor constructs, as indicated above the leaf, and either autoactive $NRC3^{D480V}$, Prf (Pto/AvrPto), R3a/Avr3a, or Cf-4/Avr4 as labelled on the leaf image, photographed 7–10 days after infiltration. A representative leaf of the independent *nrc2/3/4*-210.5.5.1 CRISPR line is shown in **S11C Fig**) Quantification of hypersensitive cell death. Cell death was scored based on a 0–7 scale between 7–10 days post infiltration. The results are presented as a dot plot, where the size of each dot is proportional to the count of the number of samples with the same score within each biological replicate. The experiment was independently repeated three times. The columns correspond to the different biological replicates. Significant differences between the conditions are indicated with an asterisk (*). Details of statistical analysis are presented in **S11 Fig**.

https://doi.org/10.1371/journal.pgen.1010414.g005

that the stronger immune responses triggered by the $NRC2^{ZAR1\alpha1}$ chimaera are not due to enhanced protein accumulation, the specific mechanisms that explain these differences remain unclear (**Fig 4**). It may be that this chimeric protein is more "trigger-happy", either due to reduced autoinhibition or enhanced capacity to generate the resistosome funnel. Often trigger-happy mutations give increased autoimmune responses [55–57]. However, we did not observe autoimmune responses with the $NRC2^{ZAR1\alpha1}$ chimaera. Alternatively, the ZAR1 α1 helix may stabilize activated NRC2. It may also be involved in subcellular localization and targeting either prior to, or after activation, and this localization could affect the strength of the immune response. Regardless of the mechanism, this chimeric approach has biotechnological implications and may be useful in engineering trigger-happy helper NLRs, such as the NRCs, that can mediate more potent immune responses.

The recent observation that the ZAR1 α1 helix forms a resistosome that acts as a $Ca^{2+}$-permeable membrane-permeable pore [7] raises the possibility that a similar mechanism mediates Cf-4/Avr4-triggered cell death. This signaling could be either a cell autonomous response directly downstream of activated cell surface receptors, or a response involved in amplification of the initial signaling response in either a cell autonomous or non-autonomous fashion. Genetic dissection of the NRC-independent responses may yield answers to these questions. It could very well be that upon activation of PRRs by pathogen molecules, multiple $Ca^{2+}$ channels are activated during various stages in the signaling cascade, thereby explaining previous difficulties in genetically dissecting this response [9,32,58–60].

We recently discovered that two effectors from unrelated pathogens suppress NRC3-mediated immune responses [47]. Here, we found that these two effectors can also suppress cell surface immune signaling through acting on NRC3 (**Fig 6**). In the case of SPRYSEC15 this suppression involves direct binding of the effector to the NB-ARC domain of NRC proteins, while the suppression mediated by AVRcap1b is indirect [47]. Therefore, in addition to suppressing intracellular immune activation, SPRYSEC15 and AVRcap1b can also suppress immune activation triggered by cell-surface receptors. Perhaps this is a more common approach by pathogens. We hypothesize that various cell surface receptors that are involved in nematode and oomycete immunity would also be dependent on helper NLRs of the NRC family similar to the fungal resistance protein Cf-4.

We have previously shown that the leucine-rich repeat receptor-like kinase FLS2 does not require NRC2/3/4 for triggering MAPK phosphorylation and a ROS burst upon recognition of the bacterial flagellin epitope flg22 [48]. Furthermore, Suppressor of the G2 allele of skp1 (SGT1)-a core component of the CC-NLR-mediated hypersensitive cell death-is not required for receptor-like kinase signaling in *N. benthamiana* or Arabidopsis [61], further confirming that NRCs are not always downstream of leucine-rich repeat receptor kinases. It therefore

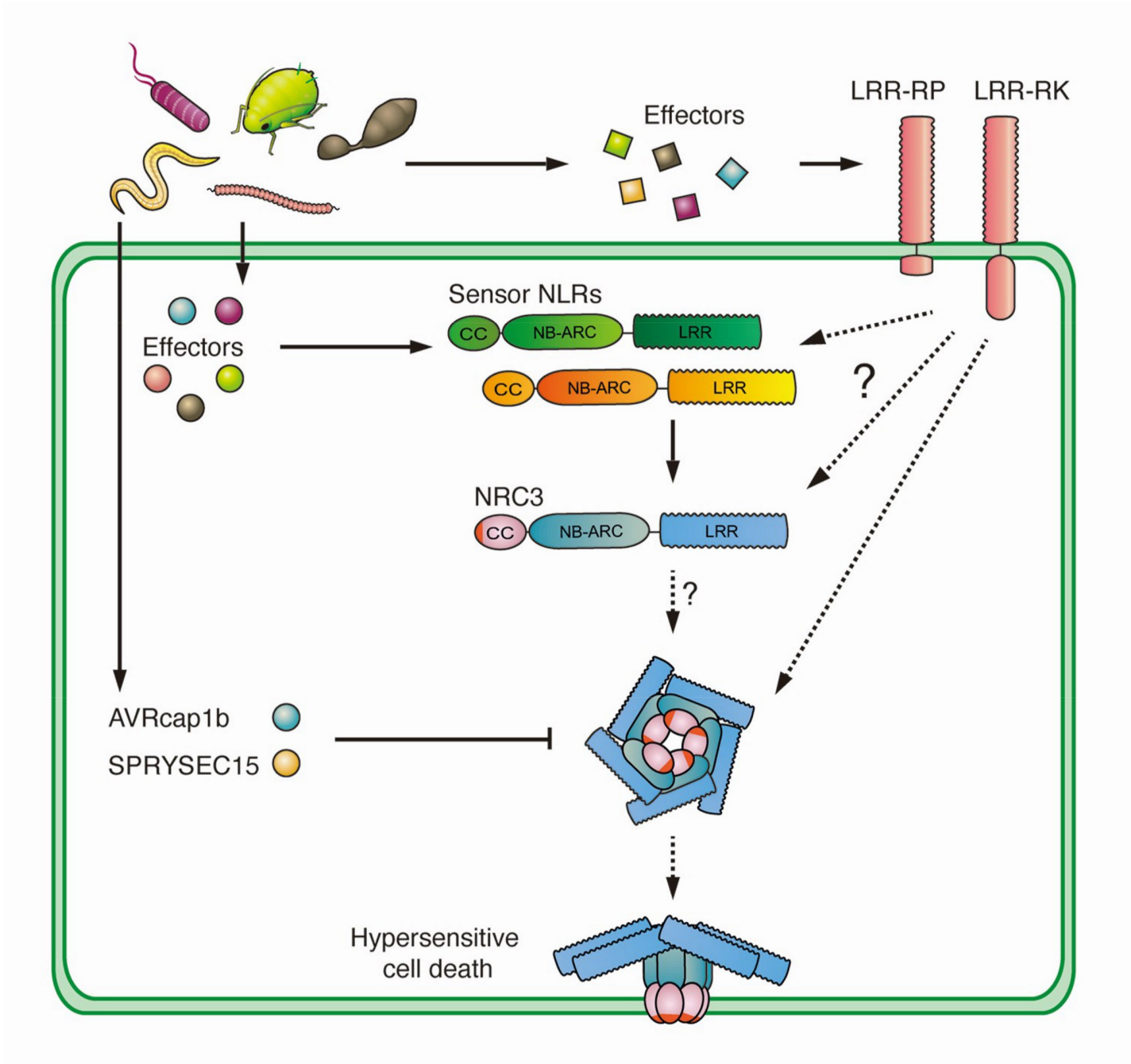


**Fig 6. Hypersensitive cell death triggered by activation of cell-surface immune receptors requires the NRC network in Solanaceae.** Recognition of apoplastic effectors and translocated intracellular effectors by cell-surface leucine-rich repeat receptor proteins and intracellular NRC-type sensor-NLRs, respectively, results in NRC3-mediated hypersensitive cell death. This cell death requires an intact α1 helix of NRC3 indicating the possible formation of an activated NRC3 resistosome. Divergent pathogen effectors converge on this node to suppress both NLR triggered as well as cell-surface receptor triggered immune recognition.

https://doi.org/10.1371/journal.pgen.1010414.g006

seems likely that NRC3 is only required for full activation of the subset of cell surface receptors that can trigger hypersensitive cell death. Since NRCs are transcriptionally upregulated upon activation of Cf-4, FLS2 and other cell surface immune receptors [38] it may be that Cf-4 activation results in transcriptional upregulation of NRC3 in a NRC-independent manner, to

amplify the immune response and trigger hypersensitive cell death in a second phase in a NRC3-dependent manner.

Intracellular NLR immune receptors were recently shown to require intact cell surface immune signaling in order to efficiently trigger hypersensitive cell death [30,31]. However, the mechanistic links between cell surface immune signaling and the activation of intracellular immune receptors remain unclear [33]. Here we show that intracellular NLR immune receptors are also required for hypersensitive cell death induction by a cell surface receptor. In addition, we show that this hypersensitive cell death likely requires activation of a MADA-CC-NLR type resistosome. Understanding how these signaling modules intertwine and have evolved and how pathogens suppress these responses can be leveraged to guide new approaches for breeding disease resistance.

## Material and methods

### Plant material and growth conditions

Wild-type and mutant *N. benthamiana* were propagated in a glasshouse and, for most experiments, were grown in a controlled growth chamber with temperature 22–25˚C, humidity 45–65% and 16/8 hr light/dark cycle. The CRISPR lines used have been previously described: *nrc2/3*-209.1.3.1 and *nrc2/3*-209.3.3.1 [49], *nrc2/3/4*-210.4.3.1 and *nrc2/3/4*-210.5.5.1 [48], *nrc4*-185.1.2.1 [46], and *eds1* [62].

### Plasmid constructions

The Golden Gate Modular Cloning (MoClo) kit [63] and the MoClo plant parts kit [64] were used for cloning, and all vectors are from this kit unless specified otherwise. Effectors, receptors and NRCs were cloned into the binary vector pJK268c, which contains the Tomato bushy stunt virus silencing inhibitor p19 in the backbone [65]. Cloning design and sequence analysis were done using Geneious Prime (v2021.2.2; https://www.geneious.com). Plasmid construction is described in **S1 Table**.

### Transient gene-expression and cell death assays

Transient gene expression in *N. benthamiana* were performed by agroinfiltration according to methods described by van der Hoorn *et al*., [66]. Briefly, *A. tumefaciens* strain GV3101 pMP90 carrying binary vectors were inoculated from glycerol stock in LB supplemented with appropriate antibiotics and grown O/N at 28˚C until saturation. Cells were harvested by centrifugation at 2000 × *g*, RT for 5 min. Cells were resuspended in infiltration buffer (10 mM $MgCl_2$, 10 mM MES-KOH pH 5.6, 200 μM acetosyringone) to the appropriate $OD_{600}$ (see **S1 Table**) in the stated combinations and left to incubate in the dark for 2 h at RT prior to infiltration into 5-week-old *N. benthamiana* leaves. HR cell death phenotypes were scored in a range from 0 (no visible necrosis) to 7 (fully confluent necrosis) according to Adachi *et al*., [46] (**S1A Fig**).

### Protein immunoblotting

Six *N. benthamiana* leaf discs (8 mm diameter) taken 5 days post agroinfiltration were homogenised in extraction buffer [10% glycerol, 25 mM Tris-HCl, pH 7.5, 1 mM EDTA, 150 mM NaCl, 1% (w/v) PVPP, 10 mM DTT, 1x protease inhibitor cocktail (SIGMA), 0.2% IGEPAL CA-630 (SIGMA)]. The supernatant obtained after centrifugation at 12,000 x g for 10 min 4 ˚C was used for SDS-PAGE. Immunoblotting was performed with rat monoclonal anti-HA antibody (3F10, Roche) or mouse monoclonal anti-GFP antibody conjugated to HRP (B-2, Santa Cruz Biotech) in a 1:5000 dilution. Equal loading was validated by staining the PVDF

membranes with Pierce Reversible Protein Stain Kit (#24585, Thermo Fisher) or using Ponceau S (SIGMA).

### Bioinformatic and phylogenetic analyses of the NRC-helper family

NRC sequences were retrieved by BLASTP against the NCBI RefSeq proteomes using the tomato and *N. benthamiana* NRC proteins (*Sl*NRC1, *Sl*NRC2, *Sl*NRC3, *Sl*NRC4a, *Sl*NRC4b, *Nb*NRC2a, *Nb*NRC2b, *Nb*NRC3, *Nb*NRC4a, *Nb*NRC4b, *Nb*NRC4c) as a query. A single representative splice-variant was selected per gene. Full-length amino acid sequences were aligned using MAFFT (v7.450; [67]) (**S1 dataset**). FastTree (v2.1.11; [68]) was used to produce a phylogeny of the NRCs which were rooted on XP_00428175 (**S2 Dataset**). The NRC phylogeny was edited using the iTOL suite (6.3; [69]).

## Supporting information

**S1 Fig. Statistical analysis of Cf-4/Avr4-triggered cell death in different *N. benthamiana nrc* mutant lines. A**) Cf-4/Avr4-triggered cell death was scored on a scale of 0–7, with 0 being no response, and 7 being fully confluent cell-death in the entire infiltrated sector. Visible cell death starts appearing at a score of 4. **B**) Statistical analysis was conducted using the besthr R package. The dots represent the ranked data and their corresponding means (dashed lines), with the size of each dot proportional to the number of observations for each specific value (count key below each panel). The panels on the right show the distribution of 100 bootstrap sample rank means, where the blue areas under the curve illustrate the 0.025 and 0.975 percentiles of the distribution. A difference is considered significant if the ranked mean for a given condition falls within or beyond the blue percentile of the mean distribution of the wild-type control. **C**) Cf-4/Avr4-triggered hypersensitive cell death is lost in the *nrc2/3* and *nrc2/3/4* CRISPR lines. Representative *N. benthamiana* leaves infiltrated with appropriate constructs were photographed 7–10 days after infiltration. The NRC CRISPR lines, *nrc2/3*-209.3.3.1, *nrc2/3/4*-210.5.5.1, are labelled above the leaf and the receptor/effector pair tested, Cf-4/Avr4, Prf (Pto/AvrPto), Rpi-blb2/AVRblb2 or R3a/Avr3a, are labelled on the leaf image. Cf-4/EV and EV/Avr4 were also included.
(TIF)

**S2 Fig. Cf-4/Avr4-triggered hypersensitive cell death does not require EDS1. A**) Cf-4/Avr4-triggered hypersensitive cell death is lost in the *nrc2/3/4* knock-out lines, but not in the *eds1* line. Representative *N. benthamiana* leaves infiltrated with appropriate constructs photographed 7–10 days after infiltration. The CRISPR lines, *nrc2/3/4*-210.4.3.1, and *eds1*, are labelled above the leaf and the receptor/effector pair tested, Cf-4/Avr4 (NRC2/3-depedent), Rx/CP (NRC2/3/4-dependent) or XopQ (Roq1, EDS1-dependent), are labelled on the leaf image. As noticed previously, transient XopQ expression gives a mild chlorotic response which is absent in the *eds1* CRISPR line [70]. Cf-4/EV and EV/Avr4 were also included as negative controls. **B**) Quantification of hypersensitive cell death. Cell death was scored based on a 0–7 scale (**S1 Fig**) between 7–10 days post infiltration. The results are presented as a dot plot, where the size of each dot is proportional to the count of the number of samples with the same score within each biological replicate. The experiment was independently repeated three times. The columns correspond to the different biological replicates. Significant differences between the conditions are indicated with an asterisk (*). **C**) Statistical analysis was conducted using the besthr R package. The dots represent the ranked data and their corresponding means (dashed lines), with the size of each dot proportional to the number of observations for each specific value (count key below each panel). The panels on the right show the distribution of

100 bootstrap sample rank means, where the blue areas under the curve illustrate the 0.025 and 0.975 percentiles of the distribution. A difference is considered significant if the ranked mean for a given condition falls within or beyond the blue percentile of the mean distribution of the wild-type control.
(TIF)

**S3 Fig. In contrast to the widely conserved NRC3, NRC1 is not present in *N. benthamiana*.** Phylogenetic tree of the NRC-helper NLR family based on the full-length protein sequences was inferred using an approximately Maximum Likelihood method as implemented in FastTree [68] based on the Jones-Taylor-Thornton (JTT) model [71]. The tree was rooted on XP_00428175. The different NRC subfamilies are indicated. Domain architecture was determined using NLRtracker [3]. Probable pseudogenes or partial genes, including *Nicotiana* NRC1 are indicated.
(TIF)

**S4 Fig. Statistical analysis of NRC complementation of Cf-4/Avr4-triggered cell death *N. benthamiana nrc2/3/4* CRISPR lines. A**) Statistical analysis was conducted using besthr R package [72]. The dots represent the ranked data and their corresponding means (dashed lines), with the size of each dot proportional to the number of observations for each specific value (count key below each panel). The panels on the right show the distribution of 100 bootstrap sample rank means, where the blue areas under the curve illustrate the 0.025 and 0.975 percentiles of the distribution. A difference is considered significant if the ranked mean for a given condition falls within or beyond the blue percentile of the mean distribution of the wild-type control. **B**) Cf-4/Avr4-triggered hypersensitive cell death is complemented in the *nrc2/3/4* CRISPR lines with NRC3 and to a lesser extent NRC2, but not NRC1 or NRC4. Representative *N. benthamiana* leaves infiltrated with appropriate constructs were photographed 7–10 days after infiltration. The receptor/effector pair tested, Cf-4/Avr4 and Prf (Pto/AvrPto), are labelled above the leaf of NRC CRISPR line *nrc2/3/4*-210.5.5.1. The NRC used for complementation or EV control are labelled on the leaf image.
(TIF)

**S5 Fig. Tomato and pepper NRC3 complement Cf-4/Avr4-triggered hypersensitive cell death in the *nrc2/3/4* knock-out lines. A**) Cf-4/Avr4-triggered hypersensitive cell death is complemented in the *nrc2/3/4* lines with tomato and pepper NRC3 (*Sl*NRC3 and *Ca*NRC3), but not tomato or pepper NRC1 (*Sl*NRC1 and *Ca*NRC1), or NRC2 (*Sl*NRC2 and *Ca*NRC2). Representative *N. benthamiana* leaves infiltrated with appropriate constructs were photographed 7–10 days after agroinfiltration. The receptor/effector pair tested, Cf-4/Avr4 or Cf-4/Avr2 as a negative control, and the NRC used for complementation are labelled on the leaf image. Hypersensitive cell-death is indicated by magenta circles, whereas combinations not displaying hypersensitive cell-death are marked with cyan circles. **B**) *Sl*NRC1, *Sl*NRC2, and *Sl*NRC3 and *Ca*NRC1, *Ca*NRC2, and *Ca*NRC3 protein accumulation. Immunoblot analysis of transiently expressed C-terminally mEGFP-tagged NRCs together with the p19 silencing inhibitor 5 days after agroinfiltration in wild-type *N. benthamiana* plants detected using anti-GFP antibody. P19 alone was used as an empty vector control. **C**) Quantification of hypersensitive cell death. Cell death was scored based on a 0–7 scale between 7–10 days post infiltration. The results are presented as a dot plot, where the size of each dot is proportional to the count of the number of samples with the same score within each biological replicate. The experiment was independently repeated three times. The columns correspond to the different biological replicates. Significant differences between the conditions are indicated with an asterisk (*). Some of the codon-optimized NRC constructs display weak autoactivity. **D**) Statistical analysis

was conducted using besthr R package [72]. The dots represent the ranked data and their corresponding means (dashed lines), with the size of each dot proportional to the number of observations for each specific value (count key below each panel). The panels on the right show the distribution of 100 bootstrap sample rank means, where the blue areas under the curve illustrate the 0.025 and 0.975 percentiles of the distribution. A difference is considered significant if the ranked mean for a given condition falls within or beyond the blue percentile of the mean distribution of the wild-type control.
(TIF)

**S6 Fig. NRC3 complements Cf-2/Rcr3/Avr2-, Cf-5/Avr5-, and Cf-9/Avr9-triggered hypersensitive cell death in the *nrc2/3/4* knock-out lines. A**) Cf-2/Rcr3/Avr2-, Cf-5/Avr5-, and Cf-9/Avr9-triggered hypersensitive cell death is complemented in the *nrc2/3/4* lines with NRC3, while Cf-9/Avr9-triggered hypersensitive cell death is partially complemented with NRC2. Representative *N. benthamiana* leaves infiltrated with appropriate constructs were photographed 7–10 days after agroinfiltration. The receptor/effector pair tested, Cf-2/Rcr3/Avr2, Cf-5/Avr5, and Cf-9/Avr9, are labelled above the leaf of *nrc2/3/4*-210.4.3.1. The NRC used for complementation or EV control are labelled on the leaf image, R3a/Avr3a was used as a positive control. **B**) Quantification of hypersensitive cell death. Cell death was scored based on a 0–7 scale between 7–10 days post infiltration. The results are presented as a dot plot, where the size of each dot is proportional to the count of the number of samples with the same score within each biological replicate. The experiment was independently repeated three times. The columns correspond to the different biological replicates. Significant differences between the conditions are indicated with an asterisk (*). **C**) Statistical analysis was conducted using besthr R package [72]. The dots represent the ranked data and their corresponding means (dashed lines), with the size of each dot proportional to the number of observations for each specific value (count key below each panel). The panels on the right show the distribution of 100 bootstrap sample rank means, where the blue areas under the curve illustrate the 0.025 and 0.975 percentiles of the distribution. A difference is considered significant if the ranked mean for a given condition falls within or beyond the blue percentile of the mean distribution of the wild-type control.
(TIF)

**S7 Fig. Statistical analysis of NRC MADA mutant complementation of Cf-4/Avr4-triggered cell death *N. benthamiana nrc2/3/4* CRISPR lines. A**) Statistical analysis was conducted using besthr R package [72]. The dots represent the ranked data and their corresponding means (dashed lines), with the size of each dot proportional to the number of observations for each specific value (count key below each panel). The panels on the right show the distribution of 100 bootstrap sample rank means, where the blue areas under the curve illustrate the 0.025 and 0.975 percentiles of the distribution. A difference is considered significant if the ranked mean for a given condition falls within or beyond the blue percentile of the mean distribution of the wild-type control. **B**) NRC MADA mutants cannot complement Cf-4/Avr4 or Pto/AvrPto-triggered hypersensitive cell death in the *N. benthamiana nrc2/3/4* CRISPR lines. Representative *N. benthamiana* leaves infiltrated with appropriate constructs were photographed 7–10 days after infiltration. The NRCs tested, NRC2 and NRC3, are labelled above the leaf of NRC CRISPR line *nrc2/3/4*-210.5.5.1. The receptor/effector pair tested, Cf-4/Avr4 and Prf (Pto/AvrPto), are labelled on the leaf image. To ensure the NRC MADA mutants were not autoactive they were expressed with either Cf-4 or Pto and an EV control was taken along.
(TIF)

**S8 Fig. Statistical analysis of NRC ZAR1 α1 helix chimaera complementation of Cf-4/Avr4-triggered cell death *N. benthamiana nrc2/3/4* CRISPR lines. A**) Statistical analysis was conducted using besthr R package [72]. The dots represent the ranked data and their corresponding means (dashed lines), with the size of each dot proportional to the number of observations for each specific value (count key below each panel). The panels on the right show the distribution of 100 bootstrap sample rank means, where the blue areas under the curve illustrate the 0.025 and 0.975 percentiles of the distribution. A difference is considered significant if the ranked mean for a given condition falls within or beyond the blue percentile of the mean distribution of the wild-type control. **B**) NRC ZAR1 α1 helix chimaeras can complement Cf-4/Avr4 and Pto/AvrPto-triggered hypersensitive cell death in the *N. benthamiana nrc2/3/4* CRISPR lines. Representative *N. benthamiana* leaves infiltrated with appropriate constructs were photographed 7–10 days after infiltration. The receptor/effector pair tested, Cf-4/Avr4 and Prf (Pto/AvrPto), are labelled above the leaf of NRC CRISPR line *nrc2/3/4*-210.5.5.1. The NRCs tested, NRC2 and NRC3, are labelled on the leaf image. To ensure the NRC ZAR1 α1 helix chimaeras were not autoactive they were expressed with either Cf-4 or Pto and an EV control was taken along.
(TIF)

**S9 Fig. The NRC2 α1 helix can functionally replace the NRC3 α1 helix for Cf-4/Avr4-triggered hypersensitive cell death. A**) Residues 1–17 of NRC2 and 1–21 of NRC3 were replaced with residues 1–21 of NRC3 and 1–17 of NRC2 to generate the $NRC2^{NRC3\alpha1}$ and $NRC3^{NRC2\alpha1}$ chimaeras. NRC3 with the NRC2 α1 helix ($NRC3^{NRC2\alpha1}$) can complement Cf-4/Avr4 and Pto/AvrPto-triggered hypersensitive cell death in the *N. benthamiana nrc2/3/4* CRISPR lines, while NRC2 with the NRC3 α1 helix ($NRC2^{NRC3\alpha1}$) cannot. Representative *N. benthamiana* leaves infiltrated with appropriate constructs were photographed 7–10 days after infiltration. The receptor tested, Cf-4 and Prf (Pto), is labelled above the leaf of NRC CRISPR line *nrc2/3/4*-210.4.3.1. The NRC and NRC chimaeras tested as well as the effectors are labelled on the leaf image. To ensure the NRC α1 helix chimaeras were not autoactive when expressed with either Cf-4 or Pto and an Avr2 or EV control was taken along, respectively. **B)** Quantification of hypersensitive cell death. Cell death was scored based on a 0–7 scale between 7–10 days post infiltration. The results are presented as a dot plot, where the size of each dot is proportional to the count of the number of samples. Significant differences between the conditions are indicated with an asterisk (*). **C**) Statistical analysis was conducted using besthr R package [72]. The dots represent the ranked data and their corresponding means (dashed lines), with the size of each dot proportional to the number of observations for each specific value (count key below each panel). The panels on the right show the distribution of 100 bootstrap sample rank means, where the blue areas under the curve illustrate the 0.025 and 0.975 percentiles of the distribution. A difference is considered significant if the ranked mean for a given condition falls within or beyond the blue percentile of the mean distribution of the wild-type control.
(TIF)

**S10 Fig. NRC3 E15Q can complement Cf-4/Avr4-triggered hypersensitive cell death. A**) NRC3 and the NRC3 E15Q mutant can complement Cf-4/Avr4 and Pto/AvrPto-triggered hypersensitive cell death in the *N. benthamiana nrc2/3/4* CRISPR lines. Representative *N. benthamiana* leaves infiltrated with appropriate constructs were photographed 7–10 days after infiltration. The receptor/effector pair tested, Cf-4/Avr4 and Prf (Pto/AvrPto), as well as the NRC and NRC mutants used are labelled on the leaf image. To ensure the NRC3 E15Q mutant was not autoactive we expressed it with either Cf-4 or Pto and an EV control. **B)** Quantification of hypersensitive cell death. Cell death was scored based on a 0–7 scale between 7–10 days post infiltration. The results are presented as a dot plot, where the size of each dot is

proportional to the count of the number of samples with the same score. Significant differences between the conditions are indicated with an asterisk (*). **C**) Statistical analysis was conducted using besthr R package [72]. The dots represent the ranked data and their corresponding means (dashed lines), with the size of each dot proportional to the number of observations for each specific value (count key below each panel). The panels on the right show the distribution of 100 bootstrap sample rank means, where the blue areas under the curve illustrate the 0.025 and 0.975 percentiles of the distribution. A difference is considered significant if the ranked mean for a given condition falls within or beyond the blue percentile of the mean distribution of the wild-type control.
(TIF)

**S11 Fig. Statistical analysis of Cf-4/Avr4-suppression mediated by divergent pathogen effectors. A**) Statistical analysis was conducted using besthr R library [72]. The dots represent the ranked data and their corresponding means (dashed lines), with the size of each dot proportional to the number of observations for each specific value (count key below each panel). The panels on the right show the distribution of 100 bootstrap sample rank means, where the blue areas under the curve illustrates the 0.025 and 0.975 percentiles of the distribution. A difference is considered significant if the ranked mean for a given condition falls within or beyond the blue percentile of the mean distribution of the wild-type control. **B**) Cf-4/Avr4-triggered hypersensitive cell death is suppressed by SPRYSEC15 and AVRcap1b, but not the EV control. Representative image of *N. benthamiana nrc2/3/4*-210.5.5.1 CRISPR line leaves which were agroinfiltrated with NRC3/suppressor constructs, as indicated above the leaf, and either autoactive NRC3$^{D480V}$, Prf (Pto/AvrPto), R3a/Avr3a, or Cf-4/Avr4 as labelled on the leaf image, photographed 7–10 days after infiltration.
(TIF)

**S1 Table. Description of constructs and *Agrobacterium* strains.**
(XLSX)

**S1 Dataset. MAFFT alignment of the unique full-length NCBI RefSeq NRCs (Fasta format).** This file contains the MAFFT alignment of 134 unique NRCs found in the NCBI RefSeq database. XP_00428175 was added as an outgroup.
(FASTA)

**S2 Dataset. Approximately maximum likelihood phylogenetic tree of the NCBI RefSeq NRCs (Nexus format).** This file contains the phylogenetic analysis of the full-length NRCs found in the NCBI RefSeq database using the JTT method.
(NEX)

## Acknowledgments

We thank Aleksandra Białas, Ana Cristina Barragan Lopez, Clémence Marchal, Paul Crosnier, and Thorsten Langner for their helpful comments on the figures, and Phil Robinson for photography.

## Author Contributions

**Conceptualization:** Jiorgos Kourelis, Daniel Lüdke, Hiroaki Adachi, Chih-Hang Wu, Sophien Kamoun.

**Data curation:** Jiorgos Kourelis, Mauricio P. Contreras, Chih-Hang Wu.

**Formal analysis:** Jiorgos Kourelis.

**Funding acquisition:** Sophien Kamoun.

**Investigation:** Jiorgos Kourelis, Mauricio P. Contreras, Adeline Harant, Hsuan Pai, Daniel Lüdke, Chih-Hang Wu.

**Project administration:** Sophien Kamoun.

**Visualization:** Jiorgos Kourelis, Hsuan Pai.

**Writing – original draft:** Jiorgos Kourelis, Sophien Kamoun.

**Writing – review & editing:** Jiorgos Kourelis, Mauricio P. Contreras, Adeline Harant, Daniel Lüdke, Hiroaki Adachi, Lida Derevnina, Chih-Hang Wu, Sophien Kamoun.

## References

1. Kourelis J, van der Hoorn RAL. Defended to the nines: 25 years of resistance gene cloning identifies nine mechanisms for R protein function. Plant Cell. 2018; 30: 285–299. https://doi.org/10.1105/tpc.17.00579 PMID: 29382771
2. Lu Y, Tsuda K. Intimate association of PRR- and NLR-mediated signaling in plant immunity. Mol Plant Microbe Interact. 2021; 34: 3–14. https://doi.org/10.1094/MPMI-08-20-0239-IA PMID: 33048599
3. Kourelis J, Sakai T, Adachi H, Kamoun S. RefPlantNLR: a comprehensive collection of experimentally validated plant NLRs. Cold Spring Harbor Laboratory; 2021. https://doi.org/10.1101/2020.07.08.193961
4. Duxbury Z, Wu C-H, Ding P. A comparative overview of the intracellular guardians of plants and animals: NLRs in innate immunity and beyond. Annu Rev Plant Biol. 2021; 72: 155–184. https://doi.org/10.1146/annurev-arplant-080620-104948 PMID: 33689400
5. Wang J, Hu M, Wang J, Qi J, Han Z, Wang G, et al. Reconstitution and structure of a plant NLR resistosome conferring immunity. Science. 2019; 364: eaav5870. https://doi.org/10.1126/science.aav5870 PMID: 30948527
6. Wang J, Wang J, Hu M, Wu S, Qi J, Wang G, et al. Ligand-triggered allosteric ADP release primes a plant NLR complex. Science. 2019; 364: eaav5868. https://doi.org/10.1126/science.aav5868 PMID: 30948526
7. Bi G, Su M, Li N, Liang Y, Dang S, Xu J, et al. The ZAR1 resistosome is a calcium-permeable channel triggering plant immune signaling. Cell. 2021; 184: 3528–3541.e12. https://doi.org/10.1016/j.cell.2021.05.003 PMID: 33984278
8. Förderer A, Li E, Lawson A, Deng Y, Sun Y, Logemann E, et al. A wheat resistosome defines common principles of immune receptor channels. 2022. https://doi.org/10.1101/2022.03.23.485489
9. Jacob P, Kim NH, Wu F, El-Kasmi F, Chi Y, Walton WG, et al. Plant "helper" immune receptors are Ca2+-permeable nonselective cation channels. Science. 2021; 373: 420–425. https://doi.org/10.1126/science.abg7917 PMID: 34140391
10. Ma S, Lapin D, Liu L, Sun Y, Song W, Zhang X, et al. Direct pathogen-induced assembly of an NLR immune receptor complex to form a holoenzyme. Science. 2020; 370: eabe3069. https://doi.org/10.1126/science.abe3069 PMID: 33273071
11. Martin R, Qi T, Zhang H, Liu F, King M, Toth C, et al. Structure of the activated ROQ1 resistosome directly recognizing the pathogen effector XopQ. Science. 2020; 370: eabd9993. https://doi.org/10.1126/science.abd9993 PMID: 33273074
12. Horsefield S, Burdett H, Zhang X, Manik MK, Shi Y, Chen J, et al. $NAD^+$ cleavage activity by animal and plant TIR domains in cell death pathways. Science. 2019; 365: 793–799. https://doi.org/10.1126/science.aax1911 PMID: 31439792
13. Wan L, Essuman K, Anderson RG, Sasaki Y, Monteiro F, Chung E-H, et al. TIR domains of plant immune receptors are $NAD^+$-cleaving enzymes that promote cell death. Science. 2019; 365: 799–803. https://doi.org/10.1126/science.aax1771 PMID: 31439793
14. Yu D, Song W, Tan EYJ, Liu L, Cao Y, Jirschitzka J, et al. TIR domains of plant immune receptors are 2′,3′-cAMP/cGMP synthetases mediating cell death. 2021. https://doi.org/10.1101/2021.11.09.467869
15. Adachi H, Derevnina L, Kamoun S. NLR singletons, pairs, and networks: evolution, assembly, and regulation of the intracellular immunoreceptor circuitry of plants. Curr Opin Plant Biol. 2019; 50: 121–131. https://doi.org/10.1016/j.pbi.2019.04.007 PMID: 31154077

16. Wu C-H, Abd-El-Haliem A, Bozkurt TO, Belhaj K, Terauchi R, Vossen JH, et al. NLR network mediates immunity to diverse plant pathogens. Proc Natl Acad Sci U S A. 2017; 114: 8113–8118. https://doi.org/10.1073/pnas.1702041114 PMID: 28698366

17. Wu C-H, Derevnina L, Kamoun S. Receptor networks underpin plant immunity. Science. 2018; 360: 1300–1301. https://doi.org/10.1126/science.aat2623 PMID: 29930125

18. Zipfel C. Plant pattern-recognition receptors. Trends Immunol. 2014; 35: 345–351. https://doi.org/10.1016/j.it.2014.05.004 PMID: 24946686

19. Cao Y, Liang Y, Tanaka K, Nguyen CT, Jedrzejczak RP, Joachimiak A, et al. The kinase LYK5 is a major chitin receptor in Arabidopsis and forms a chitin-induced complex with related kinase CERK1. Nürnberger T, editor. eLife. 2014; 3: e03766. https://doi.org/10.7554/eLife.03766 PMID: 25340959

20. Sun Y, Li L, Macho AP, Han Z, Hu Z, Zipfel C, et al. Structural basis for flg22-induced activation of the Arabidopsis FLS2-BAK1 immune complex. Science. 2013; 342: 624–628. https://doi.org/10.1126/science.1243825 PMID: 24114786

21. Liebrand TWH, Berg GCM van den, Zhang Z, Smit P, Cordewener JHG, America AHP, et al. Receptor-like kinase SOBIR1/EVR interacts with receptor-like proteins in plant immunity against fungal infection. Proc Natl Acad Sci. 2013; 110: 10010–10015. https://doi.org/10.1073/pnas.1220015110 PMID: 23716655

22. Zhang L, Kars I, Essenstam B, Liebrand TWH, Wagemakers L, Elberse J, et al. Fungal endopolygalacturonases are recognized as microbe-associated molecular patterns by the Arabidopsis receptor-like protein RESPONSIVENESS TO BOTRYTIS POLYGALACTURONASES1. Plant Physiol. 2014; 164: 352–364. https://doi.org/10.1104/pp.113.230698 PMID: 24259685

23. Albert I, Böhm H, Albert M, Feiler CE, Imkampe J, Wallmeroth N, et al. An RLP23–SOBIR1–BAK1 complex mediates NLP-triggered immunity. Nat Plants. 2015; 1: 15140. https://doi.org/10.1038/nplants.2015.140 PMID: 27251392

24. Bi G, Liebrand TWH, Bye RR, Postma J, van der Burgh AM, Robatzek S, et al. SOBIR1 requires the GxxxG dimerization motif in its transmembrane domain to form constitutive complexes with receptor-like proteins. Mol Plant Pathol. 2016; 17: 96–107. https://doi.org/10.1111/mpp.12266 PMID: 25891985

25. Postma J, Liebrand TWH, Bi G, Evrard A, Bye RR, Mbengue M, et al. Avr4 promotes Cf-4 receptor-like protein association with the BAK1/SERK3 receptor-like kinase to initiate receptor endocytosis and plant immunity. New Phytol. 2016; 210: 627–642. https://doi.org/10.1111/nph.13802 PMID: 26765243

26. van der Burgh AM, Postma J, Robatzek S, Joosten MHAJ. Kinase activity of SOBIR1 and BAK1 is required for immune signalling. Mol Plant Pathol. 2019; 20: 410–422. https://doi.org/10.1111/mpp.12767 PMID: 30407725

27. Huang WRH, Schol C, Villanueva SL, Heidstra R, Joosten MHAJ. Knocking out *SOBIR1* in *Nicotiana benthamiana* abolishes functionality of transgenic receptor-like protein Cf-4. Plant Physiol. 2021; 185: 290–294. https://doi.org/10.1093/plphys/kiaa047 PMID: 33721902

28. DeFalco TA, Zipfel C. Molecular mechanisms of early plant pattern-triggered immune signaling. Mol Cell. 2021; 81: 3449–3467. https://doi.org/10.1016/j.molcel.2021.07.029 PMID: 34403694

29. Jones JDG, Dangl JL. The plant immune system. Nature. 2006; 444: 323–329. https://doi.org/10.1038/nature05286 PMID: 17108957

30. Ngou BPM, Ahn H-K, Ding P, Jones JDG. Mutual potentiation of plant immunity by cell-surface and intracellular receptors. Nature. 2021; 1–6. https://doi.org/10.1038/s41586-021-03315-7 PMID: 33692545

31. Yuan M, Jiang Z, Bi G, Nomura K, Liu M, Wang Y, et al. Pattern-recognition receptors are required for NLR-mediated plant immunity. Nature. 2021; 1–5. https://doi.org/10.1038/s41586-021-03316-6 PMID: 33692546

32. Pruitt RN, Locci F, Wanke F, Zhang L, Saile SC, Joe A, et al. The EDS1–PAD4–ADR1 node mediates *Arabidopsis* pattern-triggered immunity. Nature. 2021; 1–5. https://doi.org/10.1038/s41586-021-03829-0 PMID: 34497423

33. Bjornson M, Zipfel C. Plant immunity: Crosstalk between plant immune receptors. Curr Biol. 2021; 31: R796–R798. https://doi.org/10.1016/j.cub.2021.04.080 PMID: 34157265

34. Huang S, Jia A, Song W, Hessler G, Meng Y, Sun Y, et al. Identification and receptor mechanism of TIR-catalyzed small molecules in plant immunity. Science. 2022; 0: eabq3297. https://doi.org/10.1126/science.abq3297 PMID: 35857645

35. Jia A, Huang S, Song W, Wang J, Meng Y, Sun Y, et al. TIR-catalyzed ADP-ribosylation reactions produce signaling molecules for plant immunity. Science. 2022; 0: eabq8180. https://doi.org/10.1126/science.abq8180 PMID: 35857644

36. Sun X, Lapin D, Feehan JM, Stolze SC, Kramer K, Dongus JA, et al. Pathogen effector recognition-dependent association of NRG1 with EDS1 and SAG101 in TNL receptor immunity. Nat Commun. 2021; 12: 3335. https://doi.org/10.1038/s41467-021-23614-x PMID: 34099661

37. Tian H, Wu Z, Chen S, Ao K, Huang W, Yaghmaiean H, et al. Activation of TIR signalling boosts pattern-triggered immunity. Nature. 2021; 1–7. https://doi.org/10.1038/s41586-021-03987-1 PMID: 34544113

38. Gabriëls SHEJ Takken FLW, Vossen JH, de Jong, Liu Q, Turk SCHJ, et al. cDNA-AFLP combined with functional analysis reveals novel genes involved in the hypersensitive response. Mol Plant Microbe Interact. 2006; 19: 567–576. https://doi.org/10.1094/MPMI-19-0567 PMID: 16776290

39. Gabriëls SHEJ Vossen JH, Ekengren SK, van Ooijen G, Abd-El-Haliem AM, van den Berg GCM, et al. An NB-LRR protein required for HR signalling mediated by both extra- and intracellular resistance proteins. Plant J. 2007; 50: 14–28. https://doi.org/10.1111/j.1365-313X.2007.03027.x PMID: 17346268

40. Fradin EF, Zhang Z, Ayala JCJ, Castroverde CDM, Nazar RN, Robb J, et al. Genetic dissection of *Verticillium* wilt resistance mediated by tomato *Ve1*. Plant Physiol. 2009; 150: 320–332. https://doi.org/10.1104/pp.109.136762 PMID: 19321708

41. Wu C-H, Belhaj K, Bozkurt TO, Birk MS, Kamoun S. Helper NLR proteins NRC2a/b and NRC3 but not NRC1 are required for Pto-mediated cell death and resistance in *Nicotiana benthamiana*. New Phytol. 2016; 209: 1344–1352. https://doi.org/10.1111/nph.13764 PMID: 26592988

42. Bombarely A, Rosli HG, Vrebalov J, Moffett P, Mueller LA, Martin GB. A draft genome sequence of *Nicotiana benthamiana* to enhance molecular plant-microbe biology research. Mol Plant Microbe Interact. 2012; 25: 1523–1530. https://doi.org/10.1094/MPMI-06-12-0148-TA PMID: 22876960

43. Naim F, Nakasugi K, Crowhurst RN, Hilario E, Zwart AB, Hellens RP, et al. Advanced engineering of lipid metabolism in *Nicotiana benthamiana* using a draft genome and the V2 viral silencing-suppressor protein. PLOS ONE. 2012; 7: e52717. https://doi.org/10.1371/journal.pone.0052717 PMID: 23300750

44. Nakasugi K, Crowhurst R, Bally J, Waterhouse P. Combining transcriptome assemblies from multiple de novo assemblers in the allo-tetraploid plant *Nicotiana benthamiana*. PLOS ONE. 2014; 9: e91776. https://doi.org/10.1371/journal.pone.0091776 PMID: 24614631

45. Brendolise C, Montefiori M, Dinis R, Peeters N, Storey RD, Rikkerink EH. A novel hairpin library-based approach to identify NBS–LRR genes required for effector-triggered hypersensitive response in *Nicotiana benthamiana*. Plant Methods. 2017; 13: 32. https://doi.org/10.1186/s13007-017-0181-7 PMID: 28465712

46. Adachi H, Contreras MP, Harant A, Wu C-H, Derevnina L, Sakai T, et al. An N-terminal motif in NLR immune receptors is functionally conserved across distantly related plant species. eLife. 2019; 8: e49956. https://doi.org/10.7554/eLife.49956 PMID: 31774397

47. Derevnina L, Contreras MP, Adachi H, Upson J, Cruces AV, Xie R, et al. Plant pathogens convergently evolved to counteract redundant nodes of an NLR immune receptor network. PLOS Biol. 2021; 19: e3001136. https://doi.org/10.1371/journal.pbio.3001136 PMID: 34424903

48. Wu C-H, Adachi H, De la Concepcion JC, Castells-Graells R, Nekrasov V, Kamoun S. *NRC4* gene cluster is not essential for bacterial flagellin-triggered immunity. Plant Physiol. 2020; 182: 455–459. https://doi.org/10.1104/pp.19.00859 PMID: 31712307

49. Witek K, Lin X, Karki HS, Jupe F, Witek AI, Steuernagel B, et al. A complex resistance locus in *Solanum americanum* recognizes a conserved *Phytophthora* effector. Nat Plants. 2021; 7: 198–208. https://doi.org/10.1038/s41477-021-00854-9 PMID: 33574576

50. Thomas CM, Jones DA, Parniske M, Harrison K, Balint-Kurti PJ, Hatzixanthis K, et al. Characterization of the tomato *Cf-4* gene for resistance to *Cladosporium fulvum* identifies sequences that determine recognitional specificity in Cf-4 and Cf-9. Plant Cell. 1997; 9: 2209–2224. https://doi.org/10.1105/tpc.9.12.2209 PMID: 9437864

51. Joosten MHAJ Cozijnsen TJ, de Wit PJGM. Host resistance to a fungal tomato pathogen lost by a single base-pair change in an avirulence gene. Nature. 1994; 367: 384–386. https://doi.org/10.1038/367384a0 PMID: 8114941

52. Zönnchen J, Gantner J, Lapin D, Barthel K, Eschen-Lippold L, Zantop S, et al. Differential requirement for the EDS1 catalytic triad in *A. thaliana* and *N. benthamiana*. bioRxiv; 2021. p. 2021.12.15.472806. https://doi.org/10.1101/2021.12.15.472806

53. Contreras MP, Pai H, Tumtas Y, Duggan C, Yuen ELH, Cruces AV, et al. Sensor NLR immune proteins activate oligomerization of their NRC helper. 2022. https://doi.org/10.1101/2022.04.25.489342

54. Ahn H-K, Lin X, Olave-Achury AC, Derevnina L, Contreras MP, Kourelis J, et al. Effector-dependent activation and oligomerization of NRC helper NLRs by Rpi-amr3 and Rpi-amr1. 2022. https://doi.org/10.1101/2022.04.25.489359

55. Segretin ME, Pais M, Franceschetti M, Chaparro-Garcia A, Bos JIB, Banfield MJ, et al. Single amino acid mutations in the potato immune receptor R3a expand response to *Phytophthora* effectors. Mol Plant Microbe Interact. 2014; 27: 624–637. https://doi.org/10.1094/MPMI-02-14-0040-R PMID: 24678835

56. Chapman S, Stevens LJ, Boevink PC, Engelhardt S, Alexander CJ, Harrower B, et al. Detection of the virulent form of AVR3a from *Phytophthora infestans* following artificial evolution of potato resistance gene R3a. PLOS ONE. 2014; 9: e110158. https://doi.org/10.1371/journal.pone.0110158 PMID: 25340613

57. Giannakopoulou A, Steele JFC, Segretin ME, Bozkurt TO, Zhou J, Robatzek S, et al. Tomato I2 immune receptor can be engineered to confer partial resistance to the oomycete *Phytophthora infestans* in addition to the fungus *Fusarium oxysporum*. Mol Plant Microbe Interact. 2015; 28: 1316–1329. https://doi.org/10.1094/MPMI-07-15-0147-R PMID: 26367241

58. Tian W, Hou C, Ren Z, Wang C, Zhao F, Dahlbeck D, et al. A calmodulin-gated calcium channel links pathogen patterns to plant immunity. Nature. 2019; 572: 131–135. https://doi.org/10.1038/s41586-019-1413-y PMID: 31316205

59. Thor K, Jiang S, Michard E, George J, Scherzer S, Huang S, et al. The calcium-permeable channel OSCA1.3 regulates plant stomatal immunity. Nature. 2020; 585: 569–573. https://doi.org/10.1038/s41586-020-2702-1 PMID: 32846426

60. Bjornson M, Pimprikar P, Nürnberger T, Zipfel C. The transcriptional landscape of *Arabidopsis thaliana* pattern-triggered immunity. Nat Plants. 2021; 7: 579–586. https://doi.org/10.1038/s41477-021-00874-5 PMID: 33723429

61. Yu G, Xian L, Zhuang H, Macho AP. SGT1 is not required for plant LRR-RLK-mediated immunity. Mol Plant Pathol. 2021; 22: 145–150. https://doi.org/10.1111/mpp.13012 PMID: 33174685

62. Ordon J, Gantner J, Kemna J, Schwalgun L, Reschke M, Streubel J, et al. Generation of chromosomal deletions in dicotyledonous plants employing a user-friendly genome editing toolkit. Plant J. 2017; 89: 155–168. https://doi.org/10.1111/tpj.13319 PMID: 27579989

63. Weber E, Engler C, Gruetzner R, Werner S, Marillonnet S. A modular cloning system for standardized assembly of multigene constructs. PLOS ONE. 2011; 6: e16765. https://doi.org/10.1371/journal.pone.0016765 PMID: 21364738

64. Engler C, Youles M, Gruetzner R, Ehnert T-M, Werner S, Jones JDG, et al. A Golden Gate modular cloning toolbox for plants. ACS Synth Biol. 2014; 3: 839–843. https://doi.org/10.1021/sb4001504 PMID: 24933124

65. Kourelis J, Malik S, Mattinson O, Krauter S, Kahlon PS, Paulus JK, et al. Evolution of a guarded decoy protease and its receptor in solanaceous plants. Nat Commun. 2020; 11: 4393. https://doi.org/10.1038/s41467-020-18069-5 PMID: 32879321

66. van der Hoorn RAL, Laurent F, Roth R, de Wit PJGM. Agroinfiltration is a versatile tool that facilitates comparative analyses of *Avr9/Cf-9*-induced and *Avr4/Cf-4*-induced necrosis. Mol Plant Microbe Interact. 2000; 13: 439–446. https://doi.org/10.1094/MPMI.2000.13.4.439 PMID: 10755307

67. Katoh K, Misawa K, Kuma K, Miyata T. MAFFT: a novel method for rapid multiple sequence alignment based on fast Fourier transform. Nucleic Acids Res. 2002; 30: 3059–3066. https://doi.org/10.1093/nar/gkf436 PMID: 12136088

68. Price MN, Dehal PS, Arkin AP. FastTree 2 –approximately maximum-likelihood trees for large alignments. PLOS ONE. 2010; 5: e9490. https://doi.org/10.1371/journal.pone.0009490 PMID: 20224823

69. Letunic I, Bork P. Interactive Tree Of Life (iTOL) v4: recent updates and new developments. Nucleic Acids Res. 2019; 47: W256–W259. https://doi.org/10.1093/nar/gkz239 PMID: 30931475

70. Schultink A, Qi T, Lee A, Steinbrenner AD, Staskawicz B. Roq1 mediates recognition of the *Xanthomonas* and *Pseudomonas* effector proteins XopQ and HopQ1. Plant J. 2017; 92: 787–795. https://doi.org/10.1111/tpj.13715 PMID: 28891100

71. Jones DT, Taylor WR, Thornton JM. The rapid generation of mutation data matrices from protein sequences. Bioinformatics. 1992; 8: 275–282. https://doi.org/10.1093/bioinformatics/8.3.275 PMID: 1633570

72. MacLean D. besthr—Generating Bootstrap Estimation Distributions of HR Data. Team MacLean Bioinformatics; 2020. Available from: https://github.com/TeamMacLean/besthr.

doi:10.1093/plphys/kiab471 PLANT PHYSIOLOGY 2022: 188: 70–80

Plant Physiology®

Breakthrough Tech

# A vector system for fast-forward studies of the HOPZ-ACTIVATED RESISTANCE1 (ZAR1) resistosome in the model plant *Nicotiana benthamiana*

**Adeline Harant ,[1] Hsuan Pai ,[1] Toshiyuki Sakai ,[1,2] Sophien Kamoun [1,*,†] and Hiroaki Adachi[1,3,*,†]**

1 The Sainsbury Laboratory, University of East Anglia, Norwich Research Park, Norwich NR4 7UH, UK
2 Laboratory of Crop Evolution, Graduate School of Agriculture, Kyoto University, Mozume, Muko, Kyoto 617-0001, Japan
3 Graduate School of Biological Sciences, Nara Institute of Science and Technology, Ikoma 630-0192, Japan

*Author for communication: adachi.hiroaki@bs.naist.jp
†Senior authors

S.K. and H.A. designed the research, supervised the work, and wrote the manuscript. A.H., H.P., T.S., and H.A. performed the experiments and analyzed the data. All authors read and edited the manuscript.
The author responsible for distribution of materials integral to the findings presented in this article in accordance with the policy described in the Instructions for Authors (https://academic.oup.com/plphys/pages/General-Instructions) is Hiroaki Adachi (adachi.hiroaki@bs.naist.jp).

## Abstract

*Nicotiana benthamiana* has emerged as a complementary experimental system to *Arabidopsis thaliana*. It enables fast-forward in vivo analyses primarily through transient gene expression and is particularly popular in the study of plant immunity. Recently, our understanding of nucleotide-binding leucine-rich repeat (NLR) plant immune receptors has greatly advanced following the discovery of the Arabidopsis HOPZ-ACTIVATED RESISTANCE1 (ZAR1) resistosome. Here, we describe a vector system of 72 plasmids that enables functional studies of the ZAR1 resistosome in *N. benthamiana*. We showed that ZAR1 stands out among the coiled coil class of NLRs (CC-NLRs) for being highly conserved across distantly related dicot plant species and confirmed NbZAR1 as the *N. benthamiana* ortholog of Arabidopsis ZAR1. Effector-activated and autoactive NbZAR1 triggers the cell death response in *N. benthamiana* and this activity is dependent on a functional N-terminal α1 helix. C-terminally tagged NbZAR1 remains functional in *N. benthamiana*, thus enabling cell biology and biochemical studies in this plant system. We conclude that the NbZAR1 open source pZA plasmid collection forms an additional experimental system to Arabidopsis for in planta resistosome studies.

## Introduction

*Nicotiana benthamiana* has developed into a popular model system in plant biology, particularly for the study of plant immunity. The appeal of *N. benthamiana* as an experimental system is primarily due to agroinfiltration, a rapid transient protein expression method that enables cell biology, biochemistry, protein–protein interaction analyses, and other in vivo experiments (Goodin et al., 2008). In addition, *N. benthamiana* is a member of the asterid group of flowering plants and as such is relatively distant from the classic model plant *Arabidopsis thaliana*, which belongs to the rosid group. Therefore, *N. benthamiana* is a complementary experimental system to Arabidopsis that also allows for a broader perspective into the evolution of molecular mechanisms in dicot plants.

Plants use nucleotide-binding leucine-rich repeat (NLR) proteins to mount innate immunity against invading

Received June 07, 2021. Accepted September 08, 2021. Advance access publication October 11, 2021
© American Society of Plant Biologists 2021. All rights reserved. For permissions, please email: journals.permissions@oup.com

Downloaded from https://academic.oup.com/plphys/article/188/1/70/6388044 by guest on 02 August 2025

pathogens. NLRs are intracellular receptors that detect host cell-translocated pathogen effectors and activate a hypersensitive cell death response that is a hallmark of plant immunity. The recent elucidation of the structures of the inactive and active complexes formed by the Arabidopsis NLR protein ZAR1 (HOPZ-ACTIVATED RESISTANCE1) with its partners receptor-like cytoplasmic kinases (RLCKs) is a major breakthrough in understanding how these immune receptors are activated and function. Activated ZAR1 forms a wheel-like pentamer, termed a resistosome, that undergoes a conformational switch—the death switch—to expose a funnel-shaped structure formed by the N-terminal α1 helices (Wang et al., 2019a, 2019b). The funnel of the ZAR1 resistosome forms a pore on the plasma membrane and the resistosome itself acts as a $Ca^{2+}$ channel (Bi et al., 2021). The N-terminal α1 helix matches a sequence motif known as MADA motif that is functionally conserved across ∼20% of coiled-coil (CC)-type plant NLRs (Adachi et al., 2019). This indicates that the ZAR1 death switch mechanism may be widely conserved across plant species. Mutations in surface-exposed residues within the α1 helix/MADA motif impair cell death and disease resistance mediated by ZAR1 and other MADA-CC-NLRs (Adachi et al., 2019; Wang et al., 2019b; Hu et al., 2020).

Here, we describe a Golden Gate compatible vector system (pZA) that enables functional studies of the ZAR1 resistosome in *N. benthamiana*. Golden Gate enables modular cloning through assembly of DNA fragments in one-step Type IIS restriction enzyme reactions. Consistent with previous reports (Baudin et al., 2017, 2019; Schultink et al., 2019), we confirmed that Arabidopsis ZAR1 (AtZAR1) does not cause hypersensitive cell death in *N. benthamiana* when expressed on its own and that *N. benthamiana* carries an ortholog of ZAR1 (NbZAR1). We developed and validated the pZA plasmid collection and share it as an open source resource that should prove useful for functional and comparative studies of NLR resistosomes in plants.

## Results and discussion

### ZAR1 is conserved across distantly related dicot plant species

Baudin et al. (2017) previously reported two orthologs of Arabidopsis ZAR1 and named them NbZAR1 and NbZAR2. We confirmed their findings by performing phylogenetic analyses of NLR proteins using the NB-ARC (nucleotide-binding adaptor shared by APAF-1, certain *R* gene products and CED-4) domain from five dicot plant species (Arabidopsis, cassava [*Manihot esculenta*], sugar beet [*Beta vulgaris* ssp. *vulgaris* var. *altissima*], tomato [*Solanum lycopersicum*], and *N. benthamiana*) representing three major clades of dicot plants (rosids, aterids, and Caryophyllales). The resulting phylogenetic tree included 829 NLRs, which expectedly clustered into the well-defined NLR classes (Figure 1, A). Arabidopsis ZAR1 (AtZAR1, AT3G50950) fell within a well-supported CC-NLR subclade that included *NbZAR1* (NbS00000462g0011), *NbZAR2* (NbS00013646g0007), and one gene each from the three other dicot plant species (Figure 1, A). As previously reported (Baudin et al., 2017), *NbZAR2* is truncated in the reference *N. benthamiana* genome (Supplemental Figure S1). The other four genes, *NbZAR1*, Manes.02G097400 (*MeZAR1*), Bv9 203570 geqf.t1 (*BvZAR1*), and Solyc02g084890 (*SlZAR1*), code for CC-NLR proteins of similar length to AtZAR1, suggesting them as ZAR1 orthologs in each dicot plant species (Supplemental Figure S1).

Based on our experience, ZAR1 seemed atypical among NLRs for having well-defined orthologs across unrelated dicot species. To directly evaluate ZAR1 conservation relative to other CC-NLRs, we calculated the phylogenetic (patristic) distance between each of the 47 Arabidopsis CC-NLRs and their closest gene from the other plant species based on the phylogenetic tree (Figure 1, A). Interestingly, AtZAR1 stood out among the CC-NLRs as having the shortest phylogenetic distance to its four orthologs (Figure 1, B). Similarly, in a reverse analysis where we plotted the phylogenetic distance between each of the 153 *N. benthamiana* CC-NLRs to their closest gene from the other species, NbZAR1 again stood out as being exceptionally conserved across all five examined species relative to other *N. benthamiana* CC-NLRs (Supplemental Figure S2). Multiple alignments of the ZAR1 orthologs from the examined species confirmed the relatively high conservation of ZAR1 with pair-wise sequence similarities ranging from 58% to 86% across the full NLR protein (Supplemental Figure S1). Overall, these analyses confirm NbZAR1 as the *N. benthamiana* ortholog of AtZAR1 and reveal ZAR1 as possibly the most widely conserved CC-NLR in dicot plants.

### Golden Gate compatible plasmids for in vivo ZAR1 resistosome studies

The Golden Gate cloning system enables rapid and high-throughput assembly of multiple sequence modules, such as promotor, terminator, or tags into a common vector (Patron et al., 2015). To facilitate in vivo resistosome studies using this cloning strategy, we first introduced synonymous mutations to *Bpi*I restriction enzyme sites in the coding sequence of *AtZAR1* and *NbZAR1* to make them both Golden Gate compatible. Next, we generated a synthetic version of *NbZAR1*, termed *NbZAR1*$^{syn}$, for genetic complementation assays in *NbZAR1* silencing plants. Shuffled synonymous codon sequences can avoid virus-induced and hairpin RNA-mediated gene silencing (Wu et al., 2016; Derevnina et al., 2021). We cloned the genes into Golden Gate compatible vectors (see Level 0 in Table 1). Each coding sequence was flanked by *Bsa*I restriction enzyme sites and overhang sequences for optimal Golden Gate reactions (Supplemental Figure S3). Therefore, the Level 0 vectors can be used to transfer genes into a variety of *Agrobacterium tumefaciens* binary vectors for in planta protein expression.

To activate ZAR1 in the *N. benthamiana* system, we cloned an RLCK XII protein *NbJIM2* (XOPJ4 IMMUNITY 2) and *Xanthomonas perforans* effector *XopJ4* with Golden Gate compatible sequences (Table 1). NbJIM2 is an

Downloaded from https://academic.oup.com/plphys/article/188/1/70/6388044 by guest on 02 August 2025

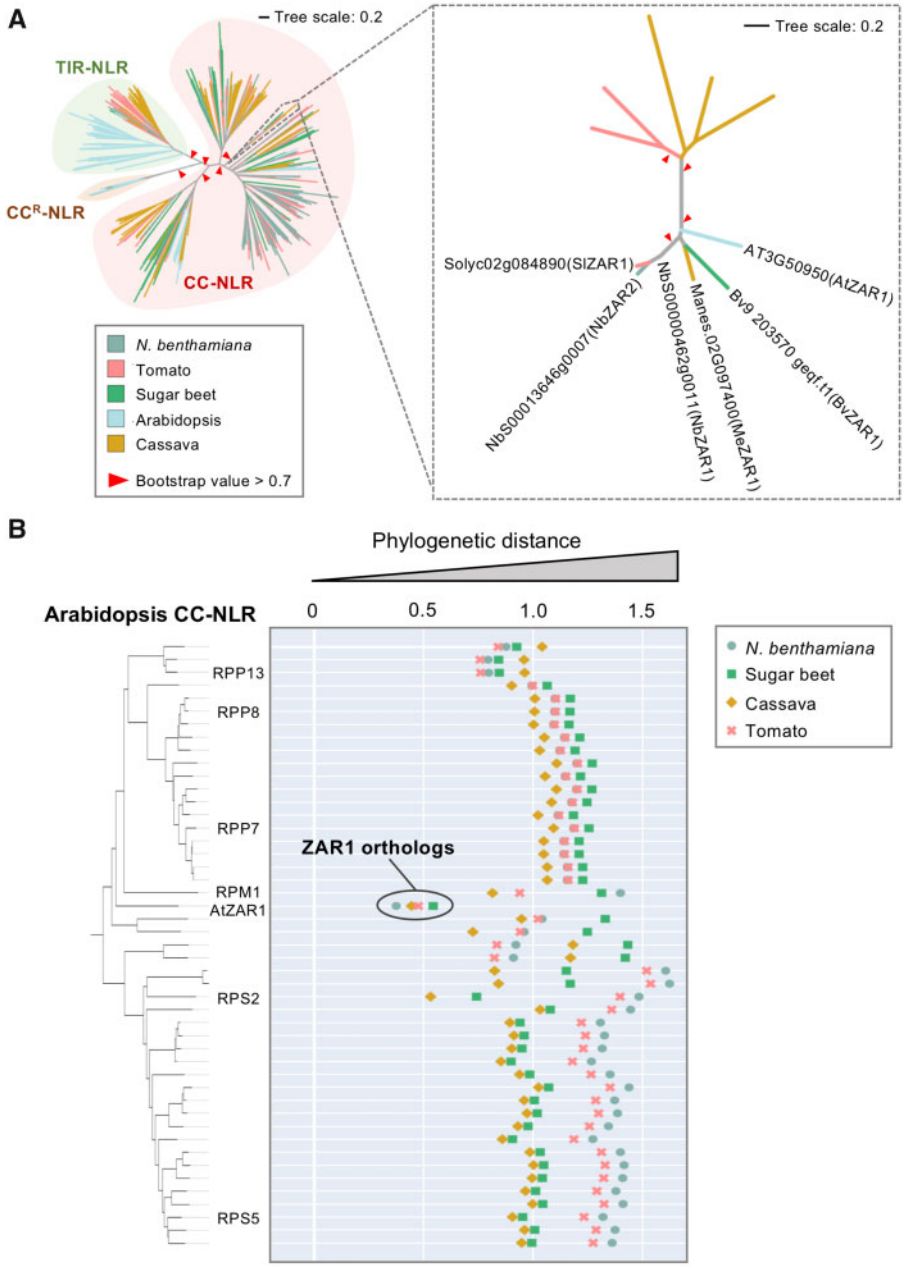


**Figure 1** ZAR1 is a conserved CC-NLR across distantly related dicot plant species. A, ZAR1 forms a small subclade that is composed of orthologous genes from distantly related dicot plant species. The phylogenetic tree was generated in MEGA7 by the neighbor-joining method using NB-ARC domain sequences of 829 NLRs identified from *N. benthamiana* (NbS-), tomato (Solyc-), sugar beet (Bv-), Arabidopsis (AT-), and cassava (Manes-) (left panel). The ZAR1 subclade phylogenetic tree is shown on the right panel. Each branch is marked with different colors based on plant species. Red arrow heads indicate bootstrap support $>0.7$ and are shown for the relevant nodes. The scale bars indicate the evolutionary distance in amino acid substitution per site. Amino acid sequences of the full-length ZAR1 orthologs can be found in Supplemental Figure S1. B, AtZAR1 is highly conserved among dicot CC-NLRs. The phylogenetic (patristic) distances of two CC-NLR nodes between Arabidopsis and other plant species were calculated from the NB-ARC phylogenetic tree in A. The closest patristic distances are plotted with different colors based on plant species. Representative Arabidopsis NLRs are highlighted. The closest patristic distances of two CC-NLR nodes between *N. benthamiana* and other plant species can be found in Supplemental Figure S2.

endogenous partner RLCK associating with NbZAR1 and is required for XopJ4 recognition in *N. benthamiana* (Schultink et al., 2019). As an alternative strategy for activating ZAR1, we generated autoactive ZAR1 by mutating the MHD motif, which is conserved across ZAR1 orthologs (Supplemental Figure S1). Substitution from aspartic acid (D) to valine (V) in the MHD motif generally makes full-length NLRs autoactive (Tameling et al., 2006). MHD mutants of *AtZAR1*, *NbZAR1*, and *NbZAR1*$^{syn}$ (*AtZAR1*$^{D489V}$, *NbZAR1*$^{D481V}$, and *NbZAR1*$^{syn\text{-}D481V}$) were cloned into Level 0 vectors (Table 1).

We also generated an inactive version of ZAR1 by substituting leucine 17 to glutamic acid mutation (L17E) in

Downloaded from https://academic.oup.com/plphys/article/188/1/70/6388044 by guest on 02 August 2025

**Table 1** Golden Gate plasmid resources prepared in this study

| Plasmids | Relevant features | Bacterial selection | Usage |
|---|---|---|---|
| pZA1 | Golden Gate compatible (GG_) wild-type AtZAR1 with STOP codon | $Spc^r$ | Level 0 |
| pZA2 | GG_AtZAR1$^{D489V}$ with STOP codon | $Spc^r$ | Level 0 |
| pZA3 | GG_AtZAR1$^{L17E}$ with STOP codon | $Spc^r$ | Level 0 |
| pZA4 | GG_AtZAR1$^{L17E/D489V}$ with STOP codon | $Spc^r$ | Level 0 |
| pZA5 | GG_wild-type NbZAR1 with STOP codon | $Spc^r$ | Level 0 |
| pZA6 | GG_NbZAR1$^{D481V}$ with STOP codon | $Spc^r$ | Level 0 |
| pZA7 | GG_NbZAR1$^{L17E}$ with STOP codon | $Spc^r$ | Level 0 |
| pZA8 | GG_NbZAR1$^{L17E/D481V}$ with STOP codon | $Spc^r$ | Level 0 |
| pZA9 | GG_wild-type AtZAR1 without STOP codon | $Spc^r$ | Level 0 |
| pZA10 | GG_AtZAR1$^{D489V}$ without STOP codon | $Spc^r$ | Level 0 |
| pZA11 | GG_AtZAR1$^{L17E}$ without STOP codon | $Spc^r$ | Level 0 |
| pZA12 | GG_AtZAR1$^{L17E/D489V}$ without STOP codon | $Spc^r$ | Level 0 |
| pZA13 | GG_wild-type NbZAR1 without STOP codon | $Spc^r$ | Level 0 |
| pZA14 | GG_NbZAR1$^{D481V}$ without STOP codon | $Spc^r$ | Level 0 |
| pZA15 | GG_NbZAR1$^{L17E}$ without STOP codon | $Spc^r$ | Level 0 |
| pZA16 | GG_NbZAR1$^{L17E/D481V}$ without STOP codon | $Spc^r$ | Level 0 |
| pZA17 | GG_wild-type AtZAR1, $Km^r$ plant selection marker | $Km^r$ | Level 2 |
| pZA18 | GG_AtZAR1$^{D489V}$, $Km^r$ plant selection marker | $Km^r$ | Level 2 |
| pZA19 | GG_AtZAR1$^{L17E}$, $Km^r$ plant selection marker | $Km^r$ | Level 2 |
| pZA20 | GG_AtZAR1$^{L17E/D489V}$, $Km^r$ plant selection marker | $Km^r$ | Level 2 |
| pZA21 | GG_wild-type NbZAR1, $Km^r$ plant selection marker | $Km^r$ | Level 2 |
| pZA22 | GG_NbZAR1$^{D481V}$, $Km^r$ plant selection marker | $Km^r$ | Level 2 |
| pZA23 | GG_NbZAR1$^{L17E}$, $Km^r$ plant selection marker | $Km^r$ | Level 2 |
| pZA24 | GG_NbZAR1$^{L17E/D481V}$, $Km^r$ plant selection marker | $Km^r$ | Level 2 |
| pZA25 | GG_wild-type AtZAR1-4xMyc, $Km^r$ plant selection marker | $Km^r$ | Level 2 |
| pZA26 | GG_AtZAR1$^{D489V}$-4xMyc, $Km^r$ plant selection marker | $Km^r$ | Level 2 |
| pZA27 | GG_AtZAR1$^{L17E}$-4xMyc, $Km^r$ plant selection marker | $Km^r$ | Level 2 |
| pZA28 | GG_AtZAR1$^{L17E/D489V}$-4xMyc, $Km^r$ plant selection marker | $Km^r$ | Level 2 |
| pZA29 | GG_wild-type NbZAR1-4xMyc, $Km^r$ plant selection marker | $Km^r$ | Level 2 |
| pZA30 | GG_NbZAR1$^{D481V}$-4xMyc, $Km^r$ plant selection marker | $Km^r$ | Level 2 |
| pZA31 | GG_NbZAR1$^{L17E}$-4xMyc, $Km^r$ plant selection marker | $Km^r$ | Level 2 |
| pZA32 | GG_NbZAR1$^{L17E/D481V}$-4xMyc, $Km^r$ plant selection marker | $Km^r$ | Level 2 |
| pZA33 | GG_wild-type AtZAR1-6xHA, $Km^r$ plant selection marker | $Km^r$ | Level 2 |
| pZA34 | GG_AtZAR1$^{D489V}$-6xHA, $Km^r$ plant selection marker | $Km^r$ | Level 2 |
| pZA35 | GG_AtZAR1$^{L17E}$-6xHA, $Km^r$ plant selection marker | $Km^r$ | Level 2 |
| pZA36 | GG_AtZAR1$^{L17E/D489V}$-6xHA, $Km^r$ plant selection marker | $Km^r$ | Level 2 |
| pZA37 | GG_wild-type NbZAR1-6xHA, $Km^r$ plant selection marker | $Km^r$ | Level 2 |
| pZA38 | GG_NbZAR1$^{D481V}$-6xHA, $Km^r$ plant selection marker | $Km^r$ | Level 2 |
| pZA39 | GG_NbZAR1$^{L17E}$-6xHA, $Km^r$ plant selection marker | $Km^r$ | Level 2 |
| pZA40 | GG_NbZAR1$^{L17E/D481V}$-6xHA, $Km^r$ plant selection marker | $Km^r$ | Level 2 |
| pZA41 | GG_wild-type AtZAR1-eGFP, $Km^r$ plant selection marker | $Km^r$ | Level 2 |
| pZA42 | GG_AtZAR1$^{D489V}$-eGFP, $Km^r$ plant selection marker | $Km^r$ | Level 2 |
| pZA43 | GG_AtZAR1$^{L17E}$-eGFP, $Km^r$ plant selection marker | $Km^r$ | Level 2 |
| pZA44 | GG_AtZAR1$^{L17E/D489V}$-eGFP, $Km^r$ plant selection marker | $Km^r$ | Level 2 |
| pZA45 | GG_wild-type NbZAR1-eGFP, $Km^r$ plant selection marker | $Km^r$ | Level 2 |
| pZA46 | GG_NbZAR1$^{D481V}$-eGFP, $Km^r$ plant selection marker | $Km^r$ | Level 2 |
| pZA47 | GG_NbZAR1$^{L17E}$-eGFP, $Km^r$ plant selection marker | $Km^r$ | Level 2 |
| pZA48 | GG_NbZAR1$^{L17E/D481V}$-eGFP, $Km^r$ plant selection marker | $Km^r$ | Level 2 |
| pZA49 | GG_synthesized NbZAR1 (NbZAR1$^{syn}$) with STOP codon | $Spc^r$ | Level 0 |
| pZA50 | GG_NbZAR1$^{syn\text{-}D481V}$ with STOP codon | $Spc^r$ | Level 0 |
| pZA51 | GG_NbZAR1$^{syn\text{-}L17E}$ with STOP codon | $Spc^r$ | Level 0 |
| pZA52 | GG_NbZAR1$^{syn\text{-}L17E/D481V}$ with STOP codon | $Spc^r$ | Level 0 |
| pZA53 | GG_NbZAR1$^{syn}$ without STOP codon | $Spc^r$ | Level 0 |
| pZA54 | GG_NbZAR1$^{syn\text{-}D481V}$ without STOP codon | $Spc^r$ | Level 0 |
| pZA55 | GG_NbZAR1$^{syn\text{-}L17E}$ without STOP codon | $Spc^r$ | Level 0 |
| pZA56 | GG_NbZAR1$^{syn\text{-}L17E/D481V}$ without STOP codon | $Spc^r$ | Level 0 |
| pZA57 | GG_NbZAR1$^{syn}$-4xMyc, $Km^r$ plant selection marker | $Km^r$ | Level 2 |
| pZA58 | GG_NbZAR1$^{syn\text{-}D481V}$-4xMyc, $Km^r$ plant selection marker | $Km^r$ | Level 2 |
| pZA59 | GG_NbZAR1$^{syn\text{-}L17E}$-4xMyc, $Km^r$ plant selection marker | $Km^r$ | Level 2 |
| pZA60 | GG_NbZAR1$^{syn\text{-}L17E/D481V}$-4xMyc, $Km^r$ plant selection marker | $Km^r$ | Level 2 |
| pZA61 | GG_NbZAR1$^{syn}$-6xHA, $Km^r$ plant selection marker | $Km^r$ | Level 2 |
| pZA62 | GG_NbZAR1$^{syn\text{-}D481V}$-6xHA, $Km^r$ plant selection marker | $Km^r$ | Level 2 |
| pZA63 | GG_NbZAR1$^{syn\text{-}L17E}$-6xHA, $Km^r$ plant selection marker | $Km^r$ | Level 2 |

(continued)

Downloaded from https://academic.oup.com/plphys/article/188/1/70/6388044 by guest on 02 August 2025

Table 1 Continued

| Plasmids | Relevant features | Bacterial selection | Usage |
|---|---|---|---|
| pZA64 | GG_NbZAR1$^{syn\text{-}L17E/D481V}$-6xHA, Km$^r$ plant selection marker | Km$^r$ | Level 2 |
| pZA65 | GG_NbZAR1$^{syn}$-eGFP, Km$^r$ plant selection marker | Km$^r$ | Level 2 |
| pZA66 | GG_NbZAR1$^{syn\text{-}D481V}$-eGFP, Km$^r$ plant selection marker | Km$^r$ | Level 2 |
| pZA67 | GG_NbZAR1$^{syn\text{-}L17E}$-eGFP, Km$^r$ plant selection marker | Km$^r$ | Level 2 |
| pZA68 | GG_NbZAR1$^{syn\text{-}L17E/D481V}$-eGFP, Km$^r$ plant selection marker | Km$^r$ | Level 2 |
| pZA69 | Intron-containing hairpin RNA (ihpRNA)-NbZAR1 | Km$^r$ | RNAi |
| pZA70 | ihpRNA-NbJIM2 | Km$^r$ | RNAi |
| pZA71 | GG_synthesized NbJIM2 (NbJIM2$^{syn}$)-3xFLAG, Km$^r$ plant selection marker | Km$^r$ | Level 2 |
| pZA72 | GG_XopJ4, Km$^r$ plant selection marker | Km$^r$ | Level 2 |

Spc$^r$, spectinomycin-resistant; Km$^r$, kanamycin-resistant.

the N-terminal MADA motif, since mutations in the N-terminal MADA motif often impair NLR cell death activity (Supplemental Figure S1; Adachi et al., 2019; Wang et al., 2019b). We generated a MADA-mutant series in wild-type and MHD-mutant backgrounds, namely MADA mutants (*AtZAR1*$^{L17E}$, *NbZAR1*$^{L17E}$, and *NbZAR1*$^{syn\text{-}L17E}$) and MADA/MHD mutants (*AtZAR1*$^{L17E/D489V}$, *NbZAR1*$^{L17E/D481V}$, and *NbZAR1*$^{syn\text{-}L17E/D481V}$) (Level 0 in Table 1).

We assembled all of the *ZAR1* genes into binary vector plasmids without epitope tags or with the C-terminal tags 4xMyc, 6xHA, and eGFP (pZA17-48 and pZA57-68 in Table 1). We provide this collection of 72 plasmids (Table 1) as an open access resource for in planta ZAR1 resistosome studies.

## Golden Gate-based genetic complementation assay evaluates effector-activated ZAR1 cell death in *N. benthamiana*

To validate constructs generated by the Golden Gate assembly, we first tested whether XopJ4-triggered cell death is dependent on NbZAR1 in the *N. benthamiana* transient expression system. We used a hairpin-silencing construct (RNAi:NbZAR1) that mediates silencing of *NbZAR1* when transiently expressed in *N. benthamiana* leaves (Supplemental Figure S4). Silencing of *NbZAR1* suppressed cell death triggered by XopJ4, compared with the RNAi:GUS silencing control (Figure 2, A and B). We further performed an agroinfiltration complementation assay using a silencing-resilient version of NbZAR1 (NbZAR1$^{syn}$). Unlike the original NbZAR1, NbZAR1$^{syn}$ complemented the cell death response triggered by XopJ4 in *NbZAR1* silencing leaves (Figure 2, A and B). Consistent with this genetic complementation phenotype, NbZAR1$^{syn}$ was expressed in the RNAi:NbZAR1 background at a similar level to the RNAi:GUS control (Figure 2, C). These results indicate that our construct series enables functional studies of the ZAR1 resistosome in the *N. benthamiana* transient expression system.

## L17E mutation in NbZAR1 N-terminal α1 helix impairs XopJ4-triggered cell death in *N. benthamiana*

Given that mutations in surface-exposed residues within the N-terminal α1 helix/MADA motif impair cell death by Arabidopsis ZAR1 (Wang et al., 2019b), we hypothesized that the intact α1 helix is required for NbZAR1-mediated cell death in response to XopJ4. To test this hypothesis, we used a MADA-mutant NbZAR1$^{syn\text{-}L17E}$ in the complementation assay of RNAi:NbZAR1. Unlike NbZAR1$^{syn}$, NbZAR1$^{syn\text{-}L17E}$ did not complement the XopJ4-triggered cell death response in RNAi:NbZAR1 leaves (Figure 2, A and B). We confirmed that NbZAR1$^{syn\text{-}L17E}$ protein was expressed in *NbZAR1* silencing leaves (Figure 2, C). Thus, we conclude that similar to Arabidopsis ZAR1, the N-terminal α1 helix/MADA motif in activated NbZAR1 mediates the cell death response in *N. benthamiana*.

## Unlike Arabidopsis ZAR1, NbZAR1 triggers autoimmune cell death in *N. benthamiana*

Next, we investigated the effect of a MHD mutation on AtZAR1 and NbZAR1 autoimmunity in the *N. benthamiana* system (Figure 3, A). As recently reported by Baudin et al. (2019), AtZAR1 did not trigger macroscopic cell death in *N. benthamiana* leaves even when the full-length protein carries the D489V mutation in the MHD motif (Figure 3, B and C). In contrast, NbZAR1 caused macroscopic cell death when the MHD mutant NbZAR1$^{D481V}$ was expressed in *N. benthamiana* leaves (Figure 3, D and E). NRC4 (NLR required for cell death 4) was used as a control MADA-CC-NLR, because its MHD mutant NRC4$^{D478V}$ causes autoactive cell death in *N. benthamiana* leaves (Adachi et al., 2019). Our results indicate that unlike Arabidopsis ZAR1, full-length NbZAR1 can be made autoactive in *N. benthamiana* through mutation of the MHD motif. These results are consistent with a previous report that AtZAR1 does not complement NbZAR1 cell death activity when co-expressed with XopJ4/JIM2 (Schultink et al., 2019). We conclude that unlike AtZAR1, NbZAR1 is probably compatible with endogenous RLCK and can therefore display autoactivity when expressed on its own in *N. benthamiana* leaves.

## The endogenous RLCK partner JIM2 is required for NbZAR1 autoimmune cell death

To test the hypothesis that the endogenous RLCK partner is required for NbZAR1 autoactivity (Schultink et al., 2019), we used RNAi:NbJIM2 (Supplemental Figure S4) and coexpressed the hairpin silencing construct with autoactive

Downloaded from https://academic.oup.com/plphys/article/188/1/70/6388044 by guest on 02 August 2025

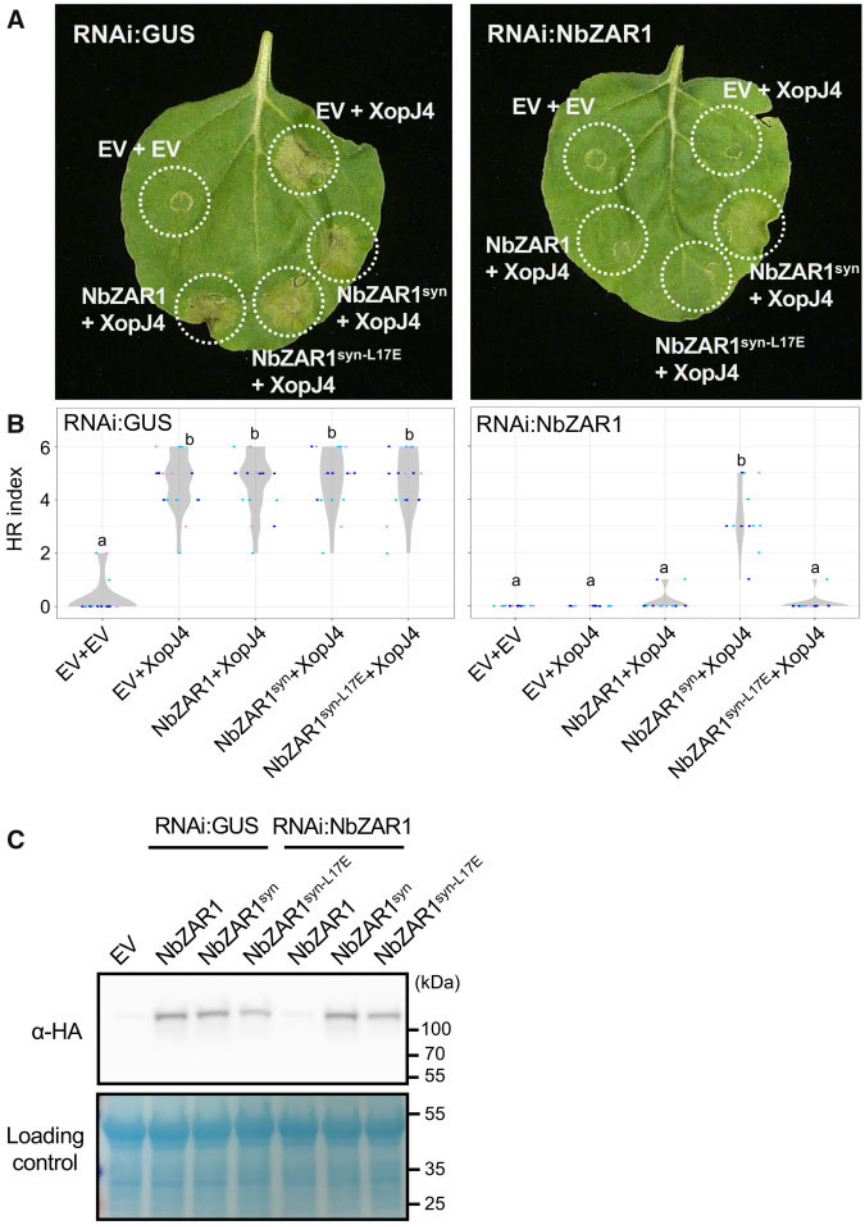


**Figure 2** The NbZAR1 MADA motif mediates XopJ4-triggered cell death in *N. benthamiana*. A, Cell death observed in *N. benthamiana* leaves after expression of *ZAR1* and *XopJ4*. The leaves were infiltrated with Agrobacterium strains carrying *ZAR1* and *XopJ4* overexpression constructs at 1 d after initial agroinfiltration of RNAi constructs. *Nicotiana benthamiana* leaf panels expressing non-epitope-tagged wild-type and variant proteins of NbZAR1 were photographed at 5 d after the second agroinfiltration. B, Violin plots showing cell death intensity scored as an HR index based on three independent experiments. Statistical differences among the samples were analyzed with Tukey's HSD test ($P < 0.01$). C, In planta protein accumulation of wild-type NbZAR1 and the variant. For anti-HA immunoblot, total proteins were prepared from *N. benthamiana* leaves at 2 d after the second agroinfiltration. Empty vector control is described as EV. Equal loading was checked with Reversible Protein Stain Kit (Thermo Fisher Scientific).

NbZAR1$^{D481V}$. Compared with the RNAi:GUS silencing control, RNAi:NbJIM2 significantly reduced cell death by NbZAR1$^{D481V}$ (Supplemental Figure S5). Moreover, a synthetic version of NbJIM2 with a codon shuffled sequence (NbJIM2$^{syn}$) restored the NbZAR1$^{D481V}$ autoimmune cell death response (Supplemental Figure S5). Although a pathogen effector was not used to activate NbZAR1, this experiment shows that autoactive NbZAR1 is dependent on its partner RLCK NbJIM2. This indicates that NbZAR1$^{D481V}$ may require an RLCK to form a signaling competent conformation like the AtZAR1 resistosome (Wang et al., 2019a, 2019b).

## NbZAR1 autoimmune cell death is dependent on its N-terminal α1 helix

Next, we tested whether NbZAR1 requires an intact N-terminal α1 helix/MADA motif for triggering autoactive cell death. We expressed the double MADA/MHD mutant NbZAR1$^{L17E/D481V}$ in *N. benthamiana* leaves using

Downloaded from https://academic.oup.com/plphys/article/188/1/70/6388044 by guest on 02 August 2025

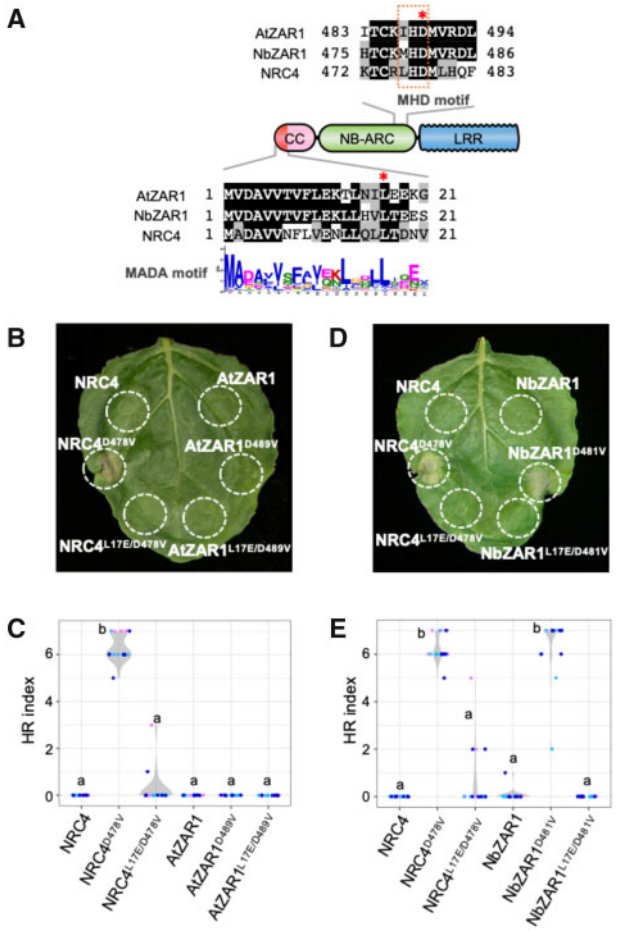


**Figure 3** NbZAR1 triggers autoimmune cell death in *N. benthamiana* leaves and requires an intact MADA motif for autoactivity. A, Schematic representation of substitution sites in AtZAR1, NbZAR1, and NRC4. Mutated sites are shown with red asterisks on the sequence alignment. B and D, Cell death observed in *N. benthamiana* leaves after expression of ZAR1 mutants. *Nicotiana benthamiana* leaf panels expressing non-epitope-tagged wild-type and variant proteins of AtZAR1 and NbZAR1 were photographed at 5 d after agroinfiltration. C and E, Violin plots showing cell death intensity scored as an HR index based on three independent experiments. Statistical differences among the samples were analyzed with Tukey's HSD test ($P < 0.01$).

agroinfiltration and observed that the L17E mutation significantly reduced the cell death activity compared with NbZAR1$^{D481V}$ (Figure 3, D and E). This result indicates that an intact N-terminal α1 helix is necessary for NbZAR1$^{D481V}$ autoactivity. Given that the α1 helix forms a funnel-shaped structure that is a key structural component of the activated ZAR1 resistosome and its translocation into the plasma membrane (Wang et al., 2019b), we conclude that the NbZAR1$^{D481V}$ experimental system recapitulates the resistosome model in *N. benthamiana*.

## C-terminally tagged NbZAR1 is functional in *N. benthamiana*

*Nicotiana benthamiana* agroinfiltration is a powerful method for in vivo cell biology, biochemistry, and protein–protein interaction analyses, but this experimental system requires that the target protein remains functional and intact after fusion to an epitope or fluorescent tag (Goodin et al., 2008; Bally et al., 2018). We therefore set out to determine the degree to which NbZAR1 can tolerate protein tags (Table 1). We focused on C-terminal tags, given that N-terminal tag fusion is known to interfere with the AtZAR1 cell death activity (Wang et al., 2019b). We tested NbZAR1$^{D481V}$ constructs fused to three different tags, 4xMyc, 6xHA, and eGFP by agroinfiltration. In all three cases, NbZAR1$^{D481V}$ retained the capacity to trigger autoactive cell death although the response was weaker than the non-epitope-tagged NbZAR1 positive control (Figure 4, A–F). We also showed by western blot analyses that these C-terminally tagged NbZAR1 accumulated at detectable levels in *N. benthamiana* leaves and generally formed a single band indicative of minimal protein degradation (Figure 4, G–I). We conclude that C-terminal tagging of NbZAR1 doesn't dramatically interfere with the activity and integrity of this NLR protein.

## Toward in vivo studies of the ZAR1 resistosome

We conclude that the open source pZA plasmid resource we developed can serve as valuable reagents for in vivo resistosome studies in *N. benthamiana* that complements the Arabidopsis system and provides a foundation for future studies. Effector-activated and autoactive NbZAR1 can be readily tested by agroinfiltration in *N. benthamiana* leaves and assayed for cell death activity. This indicates the effectiveness of our plasmid resource to monitor the activated state of ZAR1 in the *N. benthamiana* system. We also note one advantage of the ZAR1 MADA mutants, which are presumably activated but unable to trigger cell death. This mutation strategy enables protein purification or microscopic observation of effector-activated/autoactive ZAR1 using plant tissues without cell death response that generally perturbs biochemical and cell biology studies. Since NbZAR1$^{D481V}$ tolerates different C-terminal tags and each variant protein expresses well in *N. benthamiana*, the pZA plasmid resource can be applied for in planta cell biology, biochemical, and protein–protein interactions studies of the ZAR1 resistosome.

The pZA toolkit complements existing resources in Arabidopsis. Of particular interest is the visualization of activated NLR oligomers in vivo. Recently, an ~900 kDa complex associated with activated AtZAR1 was detected in Blue Native polyacrylamide gel electrophoresis (BN-PAGE) analysis using Arabidopsis protoplasts (Hu et al., 2020). Bi et al. (2021) monitored subcellular dynamics of AtZAR1 resistosomes on the plasma membrane in Arabidopsis protoplasts under total internal reflection fluorescence microscopy. *Nicotiana benthamiana* agroinfiltration offers a rapid and effective alternative expression system to the Arabidopsis protoplast system used by Hu et al. (2020) and Bi et al. (2021) that can be explored in the future.

*Nicotiana benthamiana* is rapidly developing as an excellent experimental system to study oligomeric complexes by different types of NLRs. Jacob et al. (2021) detected oligomer formation of a CC$_R$-NLR (RPW8-type CC-NLR) AtNRG1.1

Downloaded from https://academic.oup.com/plphys/article/188/1/70/6388044 by guest on 02 August 2025

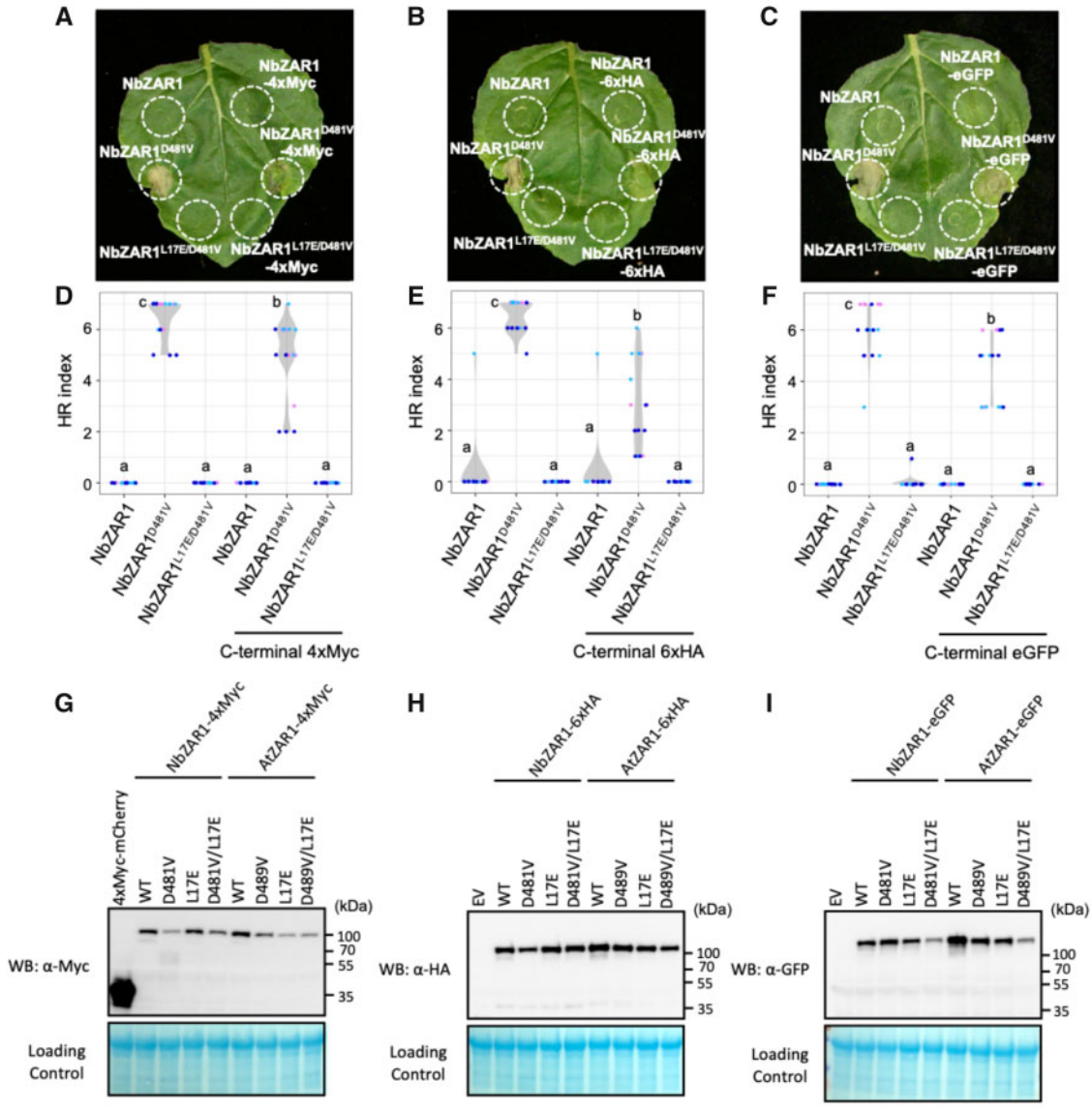


**Figure 4** C-terminal tagged NbZAR1 triggers autoimmune cell death in *N. benthamiana* leaves. A–C, Cell death observed in *N. benthamiana* leaves after expression of *ZAR1* mutants. *Nicotiana benthamiana* leaf panels expressing wild-type and variant proteins of NbZAR1 with C-terminal 4xMyc, 6xHA, or eGFP tag were photographed at 5 d after agroinfiltration. D–F, Violin plots showing cell death intensity scored as an HR index based on three independent experiments. Statistical differences among the samples were analyzed with Tukey's HSD test ($P < 0.01$). G–I, In planta protein accumulation of AtZAR1 and NbZAR1 variants. For anti-Myc, anti-HA, and anti-GFP immunoblots of AtZAR1, NbZAR1, and the mutant proteins, total proteins were prepared from *N. benthamiana* leaves at 2 d after agroinfiltration. Empty vector control is described as EV. Equal loading was checked with Reversible Protein Stain Kit (Thermo Fisher).

(N REQUIREMENT GENE 1.1) in BN-PAGE when they expressed an AtNRG1.1 autoactive MHD mutant in *N. benthamiana* leaves. Imaging analysis showed AtNRG1.1 MHD mutant forms punctate structures on the plasma membrane of *N. benthamiana* epidermal cells (Jacob et al., 2021). Martin et al. (2020) solved a cryo-electron microscopy structure of activated TIR-NLR (Toll/interleukin-1 receptor-NLR) ROQ1 (RECOGNITION OF XOPQ 1) by purifying activated ROQ1 protein from *N. benthamiana* leaves. Therefore, the *N. benthamiana* system has potential as a protein expression platform for structural studies of both resting and activated states of NLRs in vivo.

Here, we describe that ZAR1 stands out among CC-NLRs for being widely conserved across dicot plants. Recently, we expanded on these analyses and reconstructed the evolutionary history of ZAR1 across angiosperms (Adachi et al., 2021). Notably, ZAR1 orthologs were identified not only from dicot plant species but also from a monocot, taro (*Colocasia esculenta*). Thus, we conclude that the origin of ZAR1 traces back to early flowering plant linages ~220 to 150 million years ago (Jurassic period). However, it still remains unknown how ZAR1 orthologs vary in their molecular and biochemical activities among flowering plant species. The pZA system enables evolutionary studies of the

Downloaded from https://academic.oup.com/plphys/article/188/1/70/6388044 by guest on 02 August 2025

ZAR1 resistosome. Further comparative analyses between AtZAR1, NbZAR1, and other orthologs would help answer questions about the molecular evolution of the resistosome as a mechanism to trigger NLR-mediated immunity.

## Materials and methods

### Plant growth conditions

Wild-type *N. benthamiana* was propagated in a glasshouse and, for most experiments, grown in a controlled growth chamber with temperatures of 22°C–25°C, humidity 45%–65%, and a 16/8-h light/dark cycle.

### Bioinformatic and phylogenetic analyses

We used NLR-parser (Steuernagel et al., 2015) to identify NLR sequences from the protein databases of tomato (Sol Genomics Network, Tomato ITAG release 2.40), *N. benthamiana* (Sol Genomics Network, *N. benthamiana* Genome v0.4.4), *A. thaliana* (https://www.araport.org/, Araport11), cassava (*M. esculenta*) (https://phytozome-next.jgi.doe.gov/, Phytozome v13, Manihot esculenta v7.1), and sugar beet (*B. vulgaris* ssp. *vulgaris* var. *altissima*) (http://bvseq.molgen.mpg.de/index.shtml, RefBeet-1.2). The obtained NLR sequences from NLR-parser were aligned using MAFFT v. 7 (Katoh and Standley, 2013), and the protein sequences that lacked the p-loop motif were discarded to make the NLR dataset (Supplemental File S1). The gaps in the alignments were deleted manually in MEGA7 (Kumar et al., 2016) and the NB-ARC domains were used for generating phylogenetic trees (Supplemental File S2). The neighbor-joining tree was made using MEGA7 with JTT model and bootstrap values based on 100 iterations (Supplemental File S3). Amino acid sequences of ZAR1 orthologs and the percent identity are listed in Supplemental Files S4, S5.

To calculate the phylogenetic (patristic) distance, we used Python script based on DendroPy (Sukumaran and Holder, 2010). We calculated patristic distances from each CC-NLR to the other CC-NLRs on the phylogenetic tree (Supplemental File S3) and extracted the distance between CC-NLRs of Arabidopsis or *N. benthamiana* to the closest NLR from the other plant species. The script used for the patristic distance calculation is available from GitHub (https://github.com/slt666666/Phylogenetic_distance_plot).

### Plasmid constructions

For Golden Gate cloning system, wild-type and MHD-mutant clones of *AtZAR1* and *NbZAR1* were synthesized through GENEWIZ Standard Gene Synthesis with synonymous mutations to *Bpi*I restriction enzyme sites. The synthetic fragment of *NbZAR1* was designed manually to introduce synonymous substitution by following *N. benthamiana* codon usage. The fragment was synthesized through GENEWIZ Standard Gene Synthesis and then subcloned into pICSL01005 (Level 0 acceptor for CDS no stop modules, Addgene no.47996) or pICH41308 (Level 0 acceptor for CDS modules, Addgene no.47998) together with the remaining *NbZAR1* fragment to generate full-length *NbZAR1*$^{syn}$. Primers used for amplifying the *NbZAR1* fragment are listed in Supplemental Table S1.

To generate MADA motif mutants of *AtZAR1* and *NbZAR1*, the leucine (L) 17 in the MADA motif was substituted to glutamic acid (E) by site-directed mutagenesis using Phusion High-Fidelity DNA Polymerase (Thermo Fisher Scientific). To make *AtZAR1* and *NbZAR1* clones for C-terminal tagging, the stop codons were removed by PCR using Phusion High-Fidelity DNA Polymerase (Thermo Fisher Scientific). All wild-type and mutant cording sequences of *AtZAR1* and *NbZAR1* were cloned into pCR8/GW/D-TOPO (Invitrogen) as level 0 modules (Weber et al., 2011). Primers used for the site-directed mutagenesis and removing the stop codon are listed in Supplemental Table S1.

The level 0 plasmids of *AtZAR1*, *NbZAR1*, and *NbZAR1*$^{syn}$ were used for Golden Gate assembly with or without C-terminal tag modules, pICSL50009 (6xHA, Addgene no. 50309), pICSL50010 (4xMyc, Addgene no. 50310), or pICSL50034 (eGFP, TSL SynBio) into the binary vector pICH86988 (Engler et al., 2014).

Golden Gate compatible *XopJ4* and *NbJIM2*$^{syn}$ clones were synthesized through GENEWIZ Standard Gene Synthesis and were subcloned into the pICH86988 vector. pICSL50007 (3xFLAG, Addgene no. 50308) was used to make the C-terminal 3xFLAG fusion construct of NbJIM2$^{syn}$.

To prepare the RNAi construct, the silencing fragments were amplified from *NbZAR1* and *NbJIM2* cDNA by Phusion High-Fidelity DNA Polymerase (Thermo Fisher Scientific) using primers listed in Supplemental Table S1. The purified amplicons were cloned into the pRNAi-GG vector (Yan et al., 2012).

### Transient gene-expression and cell death assays

Transient gene expression in *N. benthamiana* was performed by agroinfiltration according to methods described by Bos et al. (2006). Briefly, 4-weeks old *N. benthamiana* plants were infiltrated with *A. tumefaciens* Gv3101 strains carrying the binary expression plasmids. *Agrobacterium tumefaciens* suspensions were prepared in infiltration buffer (10 mM MES, 10 mM $MgCl_2$, and 150 μM acetosyringone, pH5.6) and were adjusted to $OD_{600}$ = 0.5. Macroscopic cell death phenotypes were scored according to the scale of Segretin et al. (2014) modified to range from 0 (no visible necrosis) to 7 (fully confluent necrosis).

To perform genetic complementation assays in RNAi:NbZAR1 and RNAi:NbJIM2 backgrounds, we initially infiltrated *A. tumefaciens* strains carrying RNAi constructs ($OD_{600}$ = 0.5). At 1 d after the first agroinfiltration, we performed second agroinfiltration using mixtures of two different *A. tumefaciens* strains to complement NbZAR1/NbJIM2 expression and overexpress cell death triggering genes. In this second agroinfiltration, we adjusted the final concentration of each *A. tumefaciens* suspension to $OD_{600}$ = 0.3.

Downloaded from https://academic.oup.com/plphys/article/188/1/70/6388044 by guest on 02 August 2025

### RNA extraction and semi-quantitative RT-PCR

Plant total RNA was extracted using RNeasy Mini Kit (Qiagen). A total of 500 ng RNA of each sample was subjected to reverse transcription using SuperScript IV Reverse Transcriptase (Thermo Fisher Scientific). Semi-quantitative reverse transcription PCR (RT-PCR) was performed using DreamTaq (Thermo Fisher Scientific) with 22, 32, and 36 amplification cycles for *EF-1α*, *NbJIM2*, and *NbZAR1*, respectively. Primers used for RT-PCR are listed in Supplemental Table S1.

### Protein immunoblotting

Protein samples were prepared from six discs (8 mm diameter) cut out of *N. benthamiana* leaves at 2 d after agroinfiltration and were homogenized in extraction buffer (10% [v/v] glycerol, 25 mM Tris–HCl, pH 7.5, 1 mM EDTA, 150 mM NaCl, 2% [w/v] PVPP, 10 mM DTT, 1× protease inhibitor cocktail [SIGMA], 0.5% [v/v] IGEPAL [SIGMA]). The supernatant obtained after centrifugation at 12,000 × *g* for 10 min was used for SDS-PAGE. Immunoblotting was performed with HA-probe (F-7) HRP (Santa Cruz Biotech), c-Myc (9E10) HRP (Santa Cruz Biotech), or GFP (B-2) HRP (Santa Cruz Biotech) in a 1:5,000 dilution. Equal loading was checked by taking images of the stained PVDF (polyvinylidene difluoride) membranes with Pierce Reversible Protein Stain Kit (#24585, Thermo Fisher Scientific).

### Plasmid distribution

All pZA plasmids are available through Addgene through the Kamoun Lab page https://www.addgene.org/Sophien_Kamoun/.

### Statistical analyses

HR indexes were visualized as a violin plot using the "ggplot2" package (Wickham, 2016). Tukey's HSD test was applied to HR indexes using the "TukeyHSD" function in R (version 3.6).

## Accession numbers

DNA sequence data used in this study can be found in reference genome or GenBank/EMBL databases under the following accession numbers: AtZAR1 (AT3G50950, NP_190664.1), NbZAR1 (NbS00000462g0011, AXY05280.1), NbZAR2 (NbS00013646g0007), SlZAR1 (Solyc02g084890, XP_004232433.1), MeZAR1 (Manes.02G097400, P_02160 4862.1), BvZAR1 (Bv9_203570_geqf.t1, XP_010688776.1), NbJIM2 (NbS00009407g0011, MH532571.1), and XopJ4 (AF221058.1).

## Supplemental data

**Supplemental Figure S1.** Sequence alignment of full-length ZAR1 ortholog proteins.

**Supplemental Figure S2.** NbZAR1 is highly conserved across dicot species.

**Supplemental Figure S3.** Golden Gate level 0 modules of AtZAR1 and NbZAR1 genes.

**Supplemental Figure S4.** *NbZAR1* and *NbJIM2* silencing in *N. benthamiana*.

**Supplemental Figure S5.** NbJIM2 is required for NbZAR1 autoactive cell death in *N. benthamiana*.

**Supplemental Table S1.** Primers used for generating Golden Gate constructs in this study.

**Supplemental File S1.** Amino acid sequences of full-length NLRs in the NLR dataset.

**Supplemental File S2.** Amino acid sequences for NLR phylogenetic tree.

**Supplemental File S3.** NLR phylogenetic tree file.

**Supplemental File S4.** Amino acid sequences of ZAR1 orthologs.

**Supplemental File S5.** Percent identity matrix of ZAR1 orthologs by Clustal2.1.

## Acknowledgments

We are thankful to several colleagues especially Sophien Kamoun's group members for discussions and ideas. We also thank Mark Youles of TSL SynBio for invaluable technical support and Mauricio Contreras for suggesting the pZA name.

## Funding

This work was funded by the Gatsby Charitable Foundation (S.K., TSL), Biotechnology and Biological Sciences Research Council (S.K., BBS/E/J/000PR9795 and BB/V002937/1), and European Research Council (S.K., NGRB and BLASTOFF).

*Conflict of interest statement.* S.K. receives funding from industry on NLR biology.

## References

**Adachi H, Contreras MP, Harant A, Wu CH, Derevnina L, Sakai T, Duggan C, Moratto E, Bozkurt TO, Maqbool A, et al.** (2019) An N-terminal motif in NLR immune receptors is functionally conserved across distantly related plant species. eLife **8:** e49956

**Adachi H, Sakai T, Kourelis J, Gonzalez Hernandez JL, Maqbool A, Kamoun S** (2021) Jurassic NLR: conserved and dynamic evolutionary features of the atypically ancient immune receptor ZAR1. bioRxiv preprint 10.1101/2020.10.12.333484

**Bally J, Jung H, Mortimer C, Naim F, Philips JG, Hellens R, Bombarely A, Goodin MM, Waterhouse PM** (2018) The rise and rise of *Nicotiana benthamiana*: a plant for all reasons. Annu Rev Phytopathol **56:** 405–426

**Baudin M, Hassan JA, Schreiber KJ, Lewis JD** (2017) Analysis of the ZAR1 immune complex reveals determinants for immunity and molecular interactions. Plant Physiol **174:** 2038–2053

**Baudin M, Schreiber KJ, Martin EC, Petrescu AJ, Lewis JD** (2019) Structure–function analysis of ZAR1 immune receptor reveals key molecular interactions for activity. Plant J **101:** 352–370

**Bi G, Su M, Li N, Liang Y, Dang S, Xu J, Hu M, Wang J, Zou M, Deng Y, et al.** (2021) The ZAR1 resistosome is a calcium-permeable channel triggering plant immune signaling. Cell **184:** 1–14

**Bos JI, Kanneganti TD, Young C, Cakir C, Huitema E, Win J, Armstrong MR, Birch PR, Kamoun S** (2006) The C-terminal half of *Phytophthora infestans* RXLR effector AVR3a is sufficient to trigger R3a-mediated hypersensitivity and suppress INF1-induced cell death in *Nicotiana benthamiana*. Plant J **48:** 165–176

Downloaded from https://academic.oup.com/plphys/article/188/1/70/6388044 by guest on 02 August 2025

**Derevnina L, Contreras MP, Adachi H, Upson J, Cruces AV, Xie R, Sklenar J, Menke FLH, Mugford ST, MacLean D, et al.** (2021) Plant pathogens convergently evolved to counteract redundant nodes of an NLR immune receptor network. bioRxiv preprint 10.1101/2021.02.03.429184

**Engler C, Youles M, Gruetzner R, Ehnert TM, Werner S, Jones JD, Patron NJ, Marillonnet S** (2014) A golden gate modular cloning toolbox for plants. ACS Synth Biol **3:** 839–843

**Goodin MM, Zaitlin D, Naidu RA, Lommel SA** (2008) *Nicotiana benthamiana*: its history and future as a model for plant–pathogen interactions. Mol Plant Microbe Interact **21:** 1015–1026

**Hu M, Qi J, Bi G, Zhou JM** (2020) Bacterial effectors induce oligomerization of immune receptor ZAR1 in vivo. Mol Plant **13:** 793–801 (pii: S1674-2052(20)30066-6)

**Jacob P, Kim NH, Wu F, El-Kasmi F, Chi Y, Walton WG, Furzer OJ, Lietzan AD, Sunil S, Kempthorn K, et al.** (2021) Plant "helper" immune receptors are $Ca^{2+}$-permeable nonselective cation channels. Science **17:** eabg7917.

**Katoh K, Standley DM** (2013) MAFFT multiple sequence alignment software version 7: improvements in performance and usability. Mol Biol Evol **30:** 772–780

**Kumar S, Stecher G, Tamura K** (2016) MEGA7: molecular evolutionary genetics analysis version 7.0 for bigger datasets. Mol Biol Evol **33:** 1870–1874

**Martin R, Qi T, Zhang H, Liu F, King M, Toth C, Nogales E, Staskawicz BJ** (2020) Structure of the activated ROQ1 resistosome directly recognizing the pathogen effector XopQ. Science **370:** eabd9993

**Patron NJ, Orzaez D, Marillonnet S, Warzecha H, Matthewman C, Youles M, Raitskin O, Leveau A, Farré G, Rogers C, et al.** (2015) Standards for plant synthetic biology: a common syntax for exchange of DNA parts. New Phytol **208:** 13–19

**Schultink A, Qi T, Bally J, Staskawicz B** (2019) Using forward genetics in *Nicotiana benthamiana* to uncover the immune signaling pathway mediating recognition of the *Xanthomonas perforans* effector XopJ4. New Phytol **221:** 1001–1009

**Segretin ME, Pais M, Franceschetti M, Chaparro-Garcia A, Bos JI, Banfield MJ, Kamoun S** (2014) Single amino acid mutations in the potato immune receptor R3a expand response to Phytophthora effectors. Mol Plant Microbe Interact **27:** 624–637

**Steuernagel B, Jupe F, Witek K, Jones JD, Wulff BB** (2015) NLR-parser: rapid annotation of plant NLR complements. Bioinformatics **31:** 1665–1667

**Sukumaran J, Holder MT** (2010) DendroPy: a Python library for phylogenetic computing. Bioinformatics **26:** 1569–1571

**Tameling WI, Vossen JH, Albrecht M, Lengauer T, Berden JA, Haring MA, Cornelissen BJ, Takken FL** (2006) Mutations in the NB-ARC domain of I-2 that impair ATP hydrolysis cause autoactivation. Plant Physiol **140:** 1233–1245

**Wang J, Wang J, Hu M, Shan W, Qi J, Wang G, Han Z, Qi Y, Gao N, Wang H-W, et al.** (2019a) Ligand-triggered allosteric ADP release primes a plant NLR complex. Science **364:** eaav5868

**Wang J, Hu M, Wang J, Qi J, Han Z, Wang G, Qi Y, Wang H-W, Zhou J-M, Chai J** (2019b) Reconstitution and structure of a plant NLR resistosome conferring immunity. Science **364:** eaav5870

**Weber E, Engler C, Gruetzner R, Werner S, Marillonnet S** (2011) A modular cloning system for standardized assembly of multigene constructs. PLoS ONE **6:** e16765

**Wickham H** (2016) ggplot2: Elegant Graphics for Data Analysis. Springer-Verlag, New York. ISBN 978-3-319-24277-4

**Wu CH, Belhaj K, Bozkurt TO, Birk MS, Kamoun S** (2016) Helper NLR proteins NRC2a/b and NRC3 but not NRC1 are required for Pto-mediated cell death and resistance in *Nicotiana benthamiana*. New Phytol **209:** 1344–1352

**Yan P, Shen W, Gao X, Li X, Zhou P, Duan J** (2012) High-throughput construction of intron- containing hairpin RNA vectors for RNAi in plants. PLoS ONE **7:** e38186

Downloaded from https://academic.oup.com/plphys/article/188/1/70/6388044 by guest on 02 August 2025

Check for updates

New Phytologist

Research

# The nucleotide-binding domain of NRC-dependent disease resistance proteins is sufficient to activate downstream helper NLR oligomerization and immune signaling

**Mauricio P. Contreras*, Hsuan Pai*, Rebecca Thompson, Clemence Marchal, Jules Claeys, Hiroaki Adachi and Sophien Kamoun**

The Sainsbury Laboratory, University of East Anglia, Norwich Research Park, Norwich, NR4 7UH, UK

Author for correspondence:
*Sophien Kamoun*
*Email:* sophien.kamoun@tsl.ac.uk

Received: *3 December 2023*
Accepted: *23 April 2024*

*New Phytologist* (2024) **243:** 345–361
**doi**: 10.1111/nph.19818

**Key words:** helper NLR, immunology, innate immunity, NB-LRR, NOD, oligomerization, plant immunity.

## Summary

- Nucleotide-binding domain and leucine-rich repeat (NLR) proteins with pathogen sensor activities have evolved to initiate immune signaling by activating helper NLRs. However, the mechanisms underpinning helper NLR activation by sensor NLRs remain poorly understood. Although coiled coil (CC) type sensor NLRs such as the *Potato virus X* disease resistance protein Rx have been shown to activate the oligomerization of their downstream helpers NRC2, NRC3 and NRC4, the domains involved in sensor–helper signaling are not known.
- Here, we used *Agrobacterium tumefaciens*-mediated transient expression in *Nicotiana benthamiana* to show that the nucleotide-binding (NB) domain within the NB-ARC of Rx is necessary and sufficient for oligomerization and immune signaling of downstream helper NLRs. In addition, the NB domains of the disease resistance proteins Gpa2 (cyst nematode resistance), Rpi-amr1, Rpi-amr3 (oomycete resistance) and Sw-5b (virus resistance) are also sufficient to activate their respective downstream NRC helpers.
- Using transient expression in the lettuce (*Lactuca sativa*), we show that Rx (both as full length or as NB domain truncation) and its helper NRC2 form a minimal functional unit that can be transferred from solanaceous plants (lamiids) to Campanulid species.
- Our results challenge the prevailing paradigm that NLR proteins exclusively signal via their N-terminal domains and reveal a signaling activity for the NB domain of NRC-dependent sensor NLRs. We propose a model in which helper NLRs can perceive the status of the NB domain of their upstream sensors.

## Introduction

Nucleotide-binding and leucine-rich repeat proteins (NLRs) are intracellular innate immune receptors of eukaryotes and prokaryotes (Chou *et al.*, 2023; Contreras *et al.*, 2023a). In plants, they directly or indirectly sense pathogen virulence proteins, termed effectors, and mediate robust immune signaling and disease resistance (Duxbury *et al.*, 2021; Contreras *et al.*, 2023a). Plant NLRs exhibit a conserved domain architecture, consisting of an N-terminal domain, a central NB-ARC (nucleotide-binding domain shared by APAF1, R gene product and CED-4) and a C-terminal leucine-rich repeat (LRR) region (Kourelis *et al.*, 2021). The NB-ARC can be subdivided into a nucleotide-binding (NB) domain, a helical domain 1 (HD1) and a winged-helix domain (WHD) (Chou *et al.*, 2023; Förderer & Kourelis, 2023). Based on their N-terminal domain features, angiosperm NLRs can be broadly categorized into Toll/Interleukin-1 receptor (TIR) type, coiled coil (CC) type, G10 subclade coiled coil ($CC_{G10}$) type and RPW8 coiled coil ($CC_R$) type, which follow the NB-ARC-based NLR phylogeny (Kourelis *et al.*, 2021). Some NLRs can function as individual units, termed singletons, mediating both pathogen perception and immune signaling (Adachi *et al.*, 2019b). However, coevolution with pathogens has led to functionally specialized NLRs, where pathogen perception and immune signaling become uncoupled. In these cases, one NLR acts as a pathogen sensor and relies on a downstream helper NLR to mediate immune signaling and disease resistance. Sensors and helpers can function as genetically linked pairs or in higher order configurations that can include genetically unlinked receptor networks (Wu *et al.*, 2018; Adachi & Kamoun, 2022). However, in contrast to singleton NLRs (Contreras *et al.*, 2023a), the activation mechanisms of paired and networked NLRs are less understood. In particular, the molecular mechanisms underpinning CC-NLR sensor–helper communication are not known.

The current paradigm for NLR activation is that effector perception leads to oligomerization and induced-proximity of the N-terminal domains (Duxbury *et al.*, 2021; Contreras

*These authors contributed equally to this work.

© 2024 The Authors
*New Phytologist* © 2024 New Phytologist Foundation
This is an open access article under the terms of the Creative Commons Attribution License, which permits use, distribution and reproduction in any medium, provided the original work is properly cited.

*et al.*, 2023a). For CC-NLRs such as Arabidopsis ZAR1 and wheat Sr35, effector recognition triggers conformational changes in inactive NLR monomers which lead to the assembly of a pentameric resistosome complex (Wang *et al.*, 2019; Förderer *et al.*, 2022; Zhao *et al.*, 2022). In the resistosome, the first α-helices (α1-helices) of the CC domains come together to form a funnel-like structure that inserts into the plasma membrane, presumably to perturb membrane integrity and act as a calcium channel (Wang *et al.*, 2019; Bi *et al.*, 2021). The α1-helices of ZAR1, Sr35 and *c.* 20% of all angiosperm CC-NLRs are defined by the MADA motif, which is crucial for cell death induction (Adachi *et al.*, 2019a). In some cases, the CC domain or the α1-helix on their own are sufficient to initiate cell death induction, presumably via the assembly of a resistosome-like structure that retains the capacity to de-stabilize the plasma membrane and mediate calcium influx (Bentham *et al.*, 2018; Adachi *et al.*, 2019a; Bi *et al.*, 2021; Förderer *et al.*, 2022). The CC domain is, therefore, considered as the executor domain of downstream signaling in singleton or helper CC-NLRs. By contrast, sensor NLRs have lost this activity throughout evolution due to degeneration of the MADA motif and even acquisition of novel N-terminal domains upstream of the CC domain (Adachi *et al.*, 2019b; Contreras *et al.*, 2023a). How sensor–helper sub-functionalization shaped the activities of paired and networked CC-NLR domains is not well understood. In particular, the domains of sensor NLRs that mediate signal transduction and communication with downstream helper NLRs are largely unknown.

In the Solanaceae, the NLRs required for cell death (NRC) network is composed of multiple sensor CC-NLRs and cell-surface receptors which genetically require downstream helper CC-NLRs, known as NRCs (Wu *et al.*, 2017; Kourelis *et al.*, 2022). This immune receptor network is of great agronomical importance, mediating immunity to diverse plant pathogenic oomycetes, fungi, nematodes, viruses, bacteria, and insects (Wu *et al.*, 2017; Derevnina *et al.*, 2021; Kourelis *et al.*, 2022). All NRC-dependent sensors fall into an expanded phylogenetic clade that includes many well-known disease resistance proteins while the NRC helpers form a tight and well-supported sister clade (Wu *et al.*, 2017). The NRC-dependent sensor NLRs themselves cluster into two distinct phylogenetic groups, the Rx type and the Solanaceous domain (SD) type clade (Contreras *et al.*, 2023a). Interestingly, not all NRC-dependent sensors can activate all helpers, reflecting a degree of specificity that has probably resulted from sensor-effector and sensor–helper coevolution (Adachi *et al.*, 2019b; Contreras *et al.*, 2023a). For instance, the disease resistance sensor NLRs Rx, Sw-5b, Gpa2, Bs2 and Rpi-amr3 can signal interchangeably through NRC2, NRC3 or NRC4, whereas Rpi-amr1e signals through NRC2 and NRC3 but not NRC4 and Rpi-blb2 and Mi-1.2 signal through NRC4 but not NRC2 or NRC3 (Wu *et al.*, 2017; Derevnina *et al.*, 2021; Witek *et al.*, 2021; Lin *et al.*, 2022; Ahn *et al.*, 2023; Contreras *et al.*, 2023c). This complex configuration of many-to-one and one-to-many functional sensor-helper connections likely contributes to increased robustness and evolvability of the NRC immune network (Wu *et al.*, 2018; Adachi *et al.*, 2019b; Contreras *et al.*, 2023a).

Phylogenomic analyses revealed that the NRC superclade emerged from a pair of genetically linked NLRs before the split between the asterid and Caryophyllales lineages over 100 million years ago (Ma) (Wu *et al.*, 2017). Two recent studies on NRC network diversity and macroevolution across asterid plants mapped out massive expansions of family-specific NRC sensors and helpers in the Lamiid lineage within asterids, which include the Solanaceae, in contrast to the more broadly conserved NRC0 helpers and their genetically linked sensors (Goh *et al.*, 2023; Sakai *et al.*, 2023). These studies also highlighted an overall lack of sensor–helper interchangeability across taxa (Goh *et al.*, 2023; Sakai *et al.*, 2023). How sensor–helper compatibility and specificity have evolved is not understood, given that the molecular determinants for sensor–helper specificity are not known.

In previous studies, we proposed an activation-and-release biochemical model for sensor–helper activation in the NRC network: pathogen-activation of NRC-dependent sensor NLRs leads to homo-oligomerization of their NRC helpers into resistosome complexes which accumulate at the plasma membrane, separate from the sensors that activated them (Contreras *et al.*, 2023c). Specifically, the sensor NLR proteins Rx (virus resistance), Bs2 (bacterial resistance) and Rpi-amr3 (oomycete resistance) can trigger oligomerization of NRC2 and NRC4 (Ahn *et al.*, 2023; Contreras *et al.*, 2023b,c). By contrast, Rpi-amr1e (oomycete resistance) can oligomerize NRC2 but not NRC4, and Rpi-blb2 (oomycete resistance) can oligomerize NRC4 but not NRC2 (Ahn *et al.*, 2023; Contreras *et al.*, 2023c). In addition, this activation mechanism appears to be conserved in the tomato (*Solanum lycopersicum*) NRC0 helper and its genetically linked sensor (Sakai *et al.*, 2023). This indicates that the activation-and-release mechanism is likely conserved across the NRC superclade. More recently, two publications on NRC2 and NRC4, respectively, provided structural and biochemical insights into the resting state and activated forms of NRC helpers. Selvaraj *et al.* (2023) showed that resting state NRC2 exists as a homodimer which converts into a higher order oligomer after activation. Parallelly, Liu *et al.* (2023) showed that the constitutively active NRC4 variant $NRC4^{D478V}$ forms a hexameric resistosome. However, the nature of the signal relayed by sensor NLRs to initiate NRC oligomerization is unknown.

The NRC-dependent sensor NLR Rx mediates extreme immunity to *Potato virus X* (PVX) by recognizing its coat protein (CP) via an unknown mechanism (Bendahmane *et al.*, 1995, 1999; Tameling & Baulcombe, 2007). In a study published over 20 yr ago, Moffett *et al.* (2002) showed that Rx can perceive PVX CP and cause hypersensitive cell death when expressed *in trans* as two separate halves in the model plant *Nicotiana benthamiana*. This work resulted in a highly influential mechanistic model, which postulated that multiple intramolecular interactions maintain Rx in an inactive state. Upon effector perception, these intramolecular interactions are relieved via conformational changes within the NLR protein, resulting in dissociation of the Rx halves and initiation of immune signaling (Moffett *et al.*, 2002). In a follow up study, Rairdan *et al.* (2008) went further, demonstrating that a *c.* 150 amino acid region of Rx corresponding to the NB domain ($Rx^{NB}$) is sufficient to



© 2024 The Authors
*New Phytologist* © 2024 New Phytologist Foundation

14698137, 2024, 1, Downloaded from https://nph.onlinelibrary.wiley.com/doi/10.1111/nph.19818 by Test, Wiley Online Library on [02/08/2025]. See the Terms and Conditions (https://onlinelibrary.wiley.com/terms-and-conditions) on Wiley Online Library for rules of use; OA articles are governed by the applicable Creative Commons License

14698137, 2024, 1, Downloaded from https://nph.onlinelibrary.wiley.com/doi/10.1111/nph.19818 by Test, Wiley Online Library on [02/08/2025]. See the Terms and Conditions (https://onlinelibrary.wiley.com/terms-and-conditions) on Wiley Online Library for rules of use; OA articles are governed by the applicable Creative Commons License

trigger the hypersensitive cell death when expressed in *N. benthamiana*. They proposed that upon activation, intramolecular rearrangements in the Rx protein release the NB domain from negative regulation by the CC and LRR domains to enable signaling and cell death induction. More recently, Chen *et al.* (2016) and De Oliveira *et al.* (2016) showed that the central NB-ARC domain of Sw-5b is capable of triggering effector-independent cell death when expressed in *N. benthamiana*. However, these findings have remained puzzling, considering that the prevailing models of CC-NLR activation assign the signaling activity to the very N-terminal CC and not the NB domain as discussed above. Moreover, the work by Moffett *et al.* and Rairdan *et al.* predates the discovery of Rx dependence on the NRC2, NRC3 or NRC4 helpers to cause the hypersensitive cell death and confer immunity and resistance to *Potato virus X* (Wu *et al.*, 2017; Derevnina *et al.*, 2021). Whether the deconstructed and minimal Rx domains signal via the NRC helpers is unknown.

In this study, we revisited the work of Moffett *et al.* and Rairdan *et al.* on Rx in the context of the NRC immune receptor network. We show that the Rx halves expressed *in trans* as well as $Rx^{NB}$-eGFP can activate downstream helper NLR oligomerization and immune signaling. We also show that the Rx halves expressed *in trans* are capable of mediating resistance to PVX. In addition, the NB domain truncations of the Rx type sensors Gpa2, Rpi-amr1e and Rpi-amr3 as well as the SD type sensor Sw-5b can also activate NRC-dependent cell death, and exhibit the same downstream helper specificities of their full-length counterparts. Finally, we show that full-length PVX CP-activated Rx and $Rx^{NB}$-eGFP both trigger cell death when co-expressed with NRC2 in the unrelated Campanulid lettuce, suggesting that $Rx^{NB}$ and NRCs are likely a minimal two-component system that can be transferred across plant taxa. Our findings reveal a novel signaling role for the NB domain in NRC-dependent sensor NLRs, serving as a minimal signal for helper activation. We suggest a model where sensor NLRs undergo conditional NB-ARC domain rearrangements upon effector perception, exposing the NB domain to activate their downstream NRC helpers and triggering oligomerization into resistosomes.

## Materials and Methods

### Plant growth conditions

Wild-type, *nrc2/3*, *nrc4a/b* and *nrc2/3/4* KO *Nicotiana benthamiana* D. lines as well as lettuce (*Lactuca sativa* L.) var. 'Fenston' were grown in a controlled environment growth chamber with a humidity of 45–65% and a 16 h : 8 h, 22°C : 25°C, light : dark cycle.

### Plasmid construction

The Golden Gate Modular Cloning (MoClo) kit (Weber *et al.*, 2011) and the MoClo plant parts kit (Engler *et al.*, 2014) were used for cloning, and all vectors are from this kit unless specified otherwise. Cloning design and sequence analysis were done using Geneious Prime (v.2021.2.2; https://www.geneious.com). Rx, $Rx^{D460V}$, CP-eGFP and $NRC2^{EEE}$ constructs used were previously described (Contreras *et al.*, 2023c). $NbZAR1^{D481V}$ construct was previously described (Harant *et al.*, 2022). All NRC constructs used were previously described (Derevnina *et al.*, 2021; Sakai *et al.*, 2023). Rx halves were cloned into pICH86988 acceptor with integrated 35S promoter and OCS terminator. All NB domain constructs and their corresponding eGFP controls were cloned into the pJK268c vector with pICSL51288 (2×35S promoter) and pICSL41414 (35S terminator), which includes the silencing suppressor P19 in the same backbone to enhance protein accumulation levels. Domain boundaries for all sensor NB domains were based on amino acid sequence alignment to the original $Rx^{NB}$ domain boundaries reported by Rairdan *et al.* (2008) (Supporting Information Fig. S6), and subsequently ordered as synthetic gene fragments (Azenta/Genewiz). $RGC2B^{D470V}$ construct was synthesized and cloned into pJK001c acceptor with pICSL51288 (2×35S promoter) and pICSL41414 (35S terminator). C-terminal tag modules used were pICSL50012 (V5), pICSL5007 (3×FLAG), pICSL50034 (eGFP), pICSL5009 (6×HA) or pICSL50010 (4×Myc), as indicated.

### Cell death assays by agroinfiltration

Proteins of interest were transiently expressed in *N. benthamiana* and lettuce according to previously described methods (Bos *et al.*, 2006). Briefly, leaves from 4 to 5-wk-old plants were infiltrated with suspensions of *Agrobacterium tumefaciens*, using the GV3101 pM90 strain for *N. benthamiana* and the C58C1 strain for lettuce. Strains were transformed with expression vectors coding for different proteins indicated. Final $OD_{600}$ of all *A. tumefaciens* suspensions were adjusted in infiltration buffer (10 mM MES, 10 mM $MgCl_2$, and 150 μM acetosyringone (pH 5.6)). Final $OD_{600}$ used was 0.3 for each construct. Whenever multiple constructs were co-infiltrated into an individual spot, the total concentration of bacteria was kept constant across treatments by adding untransformed *A. tumefaciens* when necessary. This was to avoid an effect from differences in the total $OD_{600}$ of bacteria in each treatment. For better visualization of cell death on lettuce, infiltrated leaves were bleached by 70% ethanol in 90°C water bath for 15 min.

### Extraction of total proteins for BN-PAGE and SDS-PAGE assays

Four- to five-wk-old plants were agroinfiltrated as described above with constructs of interest and leaf tissue was collected 3 d post agroinfiltration. Final $OD_{600}$ used was 0.3 for each NLR immune receptor, Rx halves or NB domain, and 0.2 for eGFP or CP-eGFP. BN-PAGE was performed using the Bis–Tris Native PAGE system (Invitrogen) according to the manufacturer's instructions. Leaf tissue was ground using a Geno/Grinder tissue homogenizer and total protein was subsequently extracted and homogenized extraction buffer. GTMN extraction buffer was used (10% glycerol, 50 mM Tris–HCl (pH 7.5), 5 mM $MgCl_2$

© 2024 The Authors
*New Phytologist* © 2024 New Phytologist Foundation

and 50 mM NaCl), supplemented with 10 mM DTT, 1× protease inhibitor cocktail (Sigma) and 0.2% Triton X-100 (Sigma). Samples were incubated in extraction buffer on ice for 10 min with short vortex mixing every 2 min. Following incubation, samples were centrifuged at 5000 ***g*** for 15 min and the supernatant was used for BN-PAGE and SDS-PAGE assays.

### BN-PAGE assays

BN-PAGE assays were done as described previously (Ahn *et al.*, 2023; Contreras *et al.*, 2023c). Briefly, samples extracted as detailed above were diluted as per the manufacturer's instructions by adding NativePAGE 5% G-250 sample additive, 4× Sample Buffer and water. After dilution, samples were loaded and run on Native PAGE 3–12% Bis–Tris gels alongside either NativeMark unstained protein standard (Invitrogen) or SERVA Native Marker (SERVA). The proteins were then transferred to polyvinylidene difluoride membranes using NuPAGE Transfer Buffer using a Trans-Blot Turbo Transfer System (Bio-Rad) as per the manufacturer's instructions. Proteins were fixed to the membranes by incubating with 8% acetic acid for 15 min, washed with water and left to dry. Membranes were subsequently reactivated with methanol to correctly visualize the unstained native protein marker. Membranes were immunoblotted as described below.

### SDS-PAGE assays

For SDS-PAGE, samples were diluted using a 3 : 1 ratio of sample to SDS loading dye and denatured at 72°C for 10 min. Denatured samples were spun down at 5000 ***g*** for 3 min and supernatant was run on 4–20% Bio-Rad 4–20% Mini-PROTEAN TGX gels alongside a PageRuler Plus prestained protein ladder (Thermo Scientific). The proteins were then transferred to polyvinylidene difluoride membranes using Trans-Blot Turbo Transfer Buffer using a Trans-Blot Turbo Transfer System (Bio-Rad) as per the manufacturer's instructions. Membranes were immunoblotted as described below.

### Immunoblotting and detection of BN-PAGE and SDS-PAGE assays

Blotted membranes were blocked with 5% milk in Tris-buffered saline plus 0.01% Tween 20 (TBS-T) for an hour at room temperature and subsequently incubated with desired antibodies at 4°C overnight. Antibodies used were anti-GFP (B-2) HRP (Santa Cruz Biotechnology, Dallas, TX, USA), anti-HA (3F10) HRP (Roche), anti-Myc (9E10) HRP (Roche), anti-FLAG (M2) HRP (Sigma), and anti-V5 (V2260) HRP (Roche), all used in a 1 : 5000 dilution in 5% milk in TBS-T. To visualize proteins, we used Pierce ECL Western (32 106; Thermo Fisher Scientific, Waltham, MA, USA), supplementing with up to 50% SuperSignal West Femto Maximum Sensitivity Substrate (34 095; Thermo Fisher Scientific) when necessary. Membrane imaging was carried out with an ImageQuant LAS 4000 or an ImageQuant 800 luminescent imager (GE Healthcare Life Sciences, Piscataway, NJ, USA). Rubisco loading control was stained using Ponceau S (Sigma) or Ponceau 4R (Irn Bru; AG Barr, Cumbernauld, UK).

### PVX infection assays by agroinfiltration

PVX infection assays were carried out as described previously (Kourelis *et al.*, 2023). Four- to five-wk-old *N. benthamiana* plants were inoculated with Potato virus X (PVX) strains expressing eGFP by agroinfiltration as described above. Two leaves from three plants were inoculated per experiment ($n = 6$) and the experiment was repeated three times in transient expression assays. GFP fluorescence was measured 4 d postinfiltration using an Amersham™ ImageQuant™ 800 biomolecular imager (Cy2 450 nm for GFP). The mean fluorescence intensity per cm2 in each infiltration site was measured using FIJI (IMAGEJ v.2.1.0). We conducted an ANOVA and Tukey HSD *post hoc* test using the R package agricolae to compare mean fluorescence intensity $cm^{-2}$ across all treatments (v.1.3-5). The data was visualized using GGPLOT2 (v.3.3.4) (61). We used GFP as a proxy for PVX load. For these experiments, six leaf discs from the same infiltration site at the same time-point were taken and processed as detailed above. Samples were used for SDS-PAGE assays and probed with mouse monoclonal anti-GFP antibody conjugated to HRP (B-2; Santa Cruz Biotech).

## Results

### The hypersensitive response caused by expression of Rx halves *in trans* with the coat protein (CP) of *Potato virus X* (PVX) is dependent on NRC helpers

To test whether the Rx halves expressed *in trans* activate cell death via NRC-dependent pathways, we expressed $Rx^{CC\text{-}NBARC}$ and $Rx^{LRR}$ or full-length Rx with or without PVX CP in leaves of WT, *nrc2/3*, *nrc4a/b* or *nrc2/3/4* KO *N. benthamiana* (Fig. 1a). We also tested the other combination of Rx halves previously reported by Moffett *et al.* to trigger PVX CP-dependent cell death, $Rx^{CC}$ and $Rx^{NBARC\text{-}LRR}$ in WT and *nrc2/3/4* KO *N. benthamiana* (Figs 1a, S1A). The constitutively active $NbZAR1^{D481V}$ variant was used as a control for NRC-independent cell death (Harant *et al.*, 2022). Like full-length Rx, cell death mediated by $Rx^{CC\text{-}NBARC}$ and $Rx^{LRR}$ expressed *in trans* was only abolished in the *nrc2/3/4* KO *N. benthamiana* background but not in the *nrc2/3* or *nrc4a/b* KO backgrounds, suggesting that it is also NRC2/3/4-dependent (Fig. 1b). The $Rx^{CC}$ and $Rx^{NBARC\text{-}LRR}$ halves also triggered PVX CP-dependent cell death which was abolished in *nrc2/3/4* KO *N. benthamiana* (Fig. S1A). We also carried out complementation assays in *nrc2/3/4* KO *N. benthamiana* lines to further confirm the NRC-dependency of cell death mediated by both sets of Rx halves. In each case, we co-expressed the two Rx halves with PVX CP in the *nrc2/3/4* background and complemented with NbNRC2, NbNRC3 and NbNRC4. We included tomato (*S. lycopersicum*) SlNRC0, an NRC that full-length Rx is unable to signal through, as an independent negative control for complementation (Sakai *et al.*, 2023). Like full-length Rx, the cell death in response to PVX CP mediated by both $Rx^{CC\text{-}NBARC}$ with $Rx^{LRR}$ and $Rx^{CC}$ with



© 2024 The Authors
*New Phytologist* © 2024 New Phytologist Foundation

14698137, 2024, 1, Downloaded from https://nph.onlinelibrary.wiley.com/doi/10.1111/nph.19818 by Test, Wiley Online Library on [02/08/2025]. See the Terms and Conditions (https://onlinelibrary.wiley.com/terms-and-conditions) on Wiley Online Library for rules of use; OA articles are governed by the applicable Creative Commons License

14698137, 2024, 1, Downloaded from https://nph.onlinelibrary.wiley.com/doi/10.1111/nph.19818 by Test, Wiley Online Library on [02/08/2025]. See the Terms and Conditions (https://onlinelibrary.wiley.com/terms-and-conditions) on Wiley Online Library for rules of use; OA articles are governed by the applicable Creative Commons License

$Rx^{NBARC-LRR}$ halves expressed *in trans* was restored upon complementation with NbNRC2, NbNRC3 and NbNRC4, but not SlNRC0 (Figs 1c, S1B).

## Rx halves mediate PVX disease resistance to levels similar to Rx

We next decided to assay the Rx halves in the context of pathogen infection rather than with activation using heterologously expressed PVX CP. To this end, we performed PVX infection assays with the Rx halves system. We infected leaf tissue with a GFP-tagged PVX variant (pGR106::PVX::GFP) as described previously (Derevnina *et al.*, 2021; Kourelis *et al.*, 2023) (Fig. 2), using GFP accumulation as a proxy for viral load. In these infection assays, we tested both the $Rx^{CC-NBARC}$/$Rx^{LRR}$ and $Rx^{CC}$/$Rx^{NBARC-LRR}$ halves, with Rx being included as a control for disease resistance. Both $Rx^{CC-NBARC}$/$Rx^{LRR}$ and $Rx^{CC}$/$Rx^{NBARC-LRR}$ halves could reduce viral load, with cell death being observed in conjunction with the reduction in viral load (Fig. 2). Each half on its own was insufficient to mediate resistance to PVX, leading to viral accumulation comparable to the EV control. We conclude that Rx can confer resistance to PVX when its domains are expressed *in trans*, and that all domains are required for both of PVX CP-triggered cell death and PVX disease resistance.

## Rx halves mediate coat protein (CP)-dependent oligomerization of their NRC2 helper

We previously reported that Rx can mediate NRC2 oligomerization and resistosome formation upon PVX CP recognition, without forming part of the activated NRC2 oligomer (Contreras *et al.*, 2023b,c). To test whether the activation of the Rx halves expressed *in trans* also leads to oligomerization of NRC2, we leveraged previously established blue-native polyacrylamide gel electrophoresis (BN-PAGE)-based readouts for NRC resistosome formation. We co-expressed the inactive or PVX CP-activated $Rx^{CC-NBARC}$ and $Rx^{LRR}$ halves in leaves of *nrc2/3/4* KO *N. benthamiana* plants, complementing with the previously characterized $NbNRC2^{EEE}$ MADA motif mutant to abolish cell death induction without compromising helper activation (Contreras *et al.*, 2023c). In these assays, $Rx^{CC-NBARC}$ and $Rx^{LRR}$ expressed *in trans* mediated NRC2 oligomerization in a PVX CP-dependent manner, with both Rx halves being required. Notably, the NRC2 oligomer formed upon activation by $Rx^{CC-NBARC}$ and $Rx^{LRR}$ migrates at the same height as the NRC2 oligomer formed upon activation by full-length Rx. The absence of a shift in size of the NRC2 oligomer in the Rx compared to the $Rx^{CC-NBARC}$/$Rx^{LRR}$ treatments suggests that the PVX CP-activated Rx halves do not form part of the mature NRC2 oligomer, much like full-length Rx (Fig. 3).

In previously published BN-PAGE assays, Rx is visualized as a complex of *c.* 400 kDa regardless of its activation state (Contreras & Kamoun, 2022; Contreras *et al.*, 2023c). When probing for the Rx halves expressed *in trans* in BN-PAGE assays, we observed that $Rx^{CC-NBARC}$ also migrates as a band of *c.* 400 kDa, although this band migrates comparatively faster than full-length Rx indicating a lower molecular weight (Fig. 3). $Rx^{LRR}$, by contrast, is visualized as a high molecular weight smear covering molecular weights from *c.* 400 to 1000 kDa. Like full-length Rx, we did not observe any change in the migration pattern of $Rx^{CC-NBARC}$ or $Rx^{LRR}$ upon activation of the system with PVX CP. Although we can detect signal for $Rx^{LRR}$ at a molecular weight that overlaps with the molecular weight of the NRC2 resistosome, this signal is also present in the treatments without PVX CP activation, suggesting that it is unlikely to correspond to a pool of $Rx^{LRR}$ that is integrated into the NRC2 oligomer. We also noted that the migration pattern of $Rx^{CC-NBARC}$ is independent of the presence of $Rx^{LRR}$, and vice-versa (Fig. 3). We also did not observe a distinct band for $Rx^{LRR}$ co-migrating with $Rx^{CC-NBARC}$ in BN-PAGE. The lack of co-migration in our BN-PAGE assays suggest that these two domains are not forming stable complexes and likely only associate transiently. Alternatively, the sub-pool of Rx halves that are forming a stable complex before activation is not highly abundant and cannot easily be detected in BN-PAGE.

## The effector-independent cell death triggered by the 154 amino acid nucleotide-binding domain of Rx ($Rx^{NB}$) is dependent on NRC2, NRC3 or NRC4

Previously, Rairdan *et al.* (2008) showed that a truncated version of the NRC-dependent sensor Rx encoding only the 154 amino acid NB domain region of the NB-ARC fused to eGFP ($Rx^{NB}$-eGFP) was capable of constitutively triggering cell death in *N. benthamiana* and *N. tabacum*. Based on these results, we hypothesized that the NB domain could encode the minimal signal for NRC helper activation. To test this hypothesis, we performed cell death assays with $Rx^{NB}$-eGFP in WT and *nrc2/3/4* KO *N. benthamiana* plants. We included the constitutively active $ZAR1^{D481V}$ and $Rx^{D460V}$ variants as controls for NRC-independent and NRC-dependent cell death, respectively, and eGFP as a negative control for cell death (Fig. 4a). We were able to reproduce the previously reported cell death triggered by $Rx^{NB}$-eGFP in WT *N. benthamiana*. This cell death was abolished in leaves of *nrc2/3/4* KO *N. benthamiana*, indicating that $Rx^{NB}$-eGFP activates NRC-dependent hypersensitive cell death. This suggests that the NB domain of Rx is necessary and sufficient to activate downstream NRC helpers (Fig. 4a).

Mutating a highly conserved K residue in the p-loop motif typically makes NLRs nonfunctional (Mestre & Baulcombe, 2006). To test the p-loop dependency of $Rx^{NB}$-eGFP-mediated activation of NRCs, we generated $Rx^{NB}$-eGFP p-loop mutants (K to R substitution in position 176, as per numbering in full-length Rx, Fig. 4b) and expressed them in leaves of WT and *nrc2/3/4* KO *N. benthamiana*. Interestingly, much like $Rx^{NB}$-eGFP, the $Rx^{NB}$-eGFP p-loop mutants triggered NRC-dependent cell death. This indicates that unlike full-length Rx and the Rx halves expressed *in trans* (Moffett *et al.*, 2002), cell death triggered by $Rx^{NB}$-eGFP does not require an intact p-loop (Fig. S3).

To further test the NRC-dependency of $Rx^{NB}$-eGFP triggered cell death, we carried out complementation assays in leaves of *nrc2/3/4* KO *N. benthamiana*. We co-expressed $Rx^{NB}$-eGFP with NbNRC2, NbNRC3 and NbNRC4 or SlNRC0, a tomato NRC

© 2024 The Authors
*New Phytologist* © 2024 New Phytologist Foundation

that full-length Rx is unable to signal through (Sakai *et al.*, 2023). The cell death mediated by the $Rx^{NB}$-eGFP was restored upon complementation with NbNRC2, NbNRC3 and NbNRC4, but not SlNRC0 (Fig. 4c). We conclude that $Rx^{NB}$-eGFP is indeed activating cell death via NRC-dependent pathways and that it retains the specificity to activate the same set of NRC helpers that full-length Rx signals through in *N. benthamiana*.

To investigate the contributions of the C-terminal eGFP tag to the cell death mediated by $Rx^{NB}$-eGFP, we generated $Rx^{NB}$-mCherry-6×HA fusions and tested them for NRC-

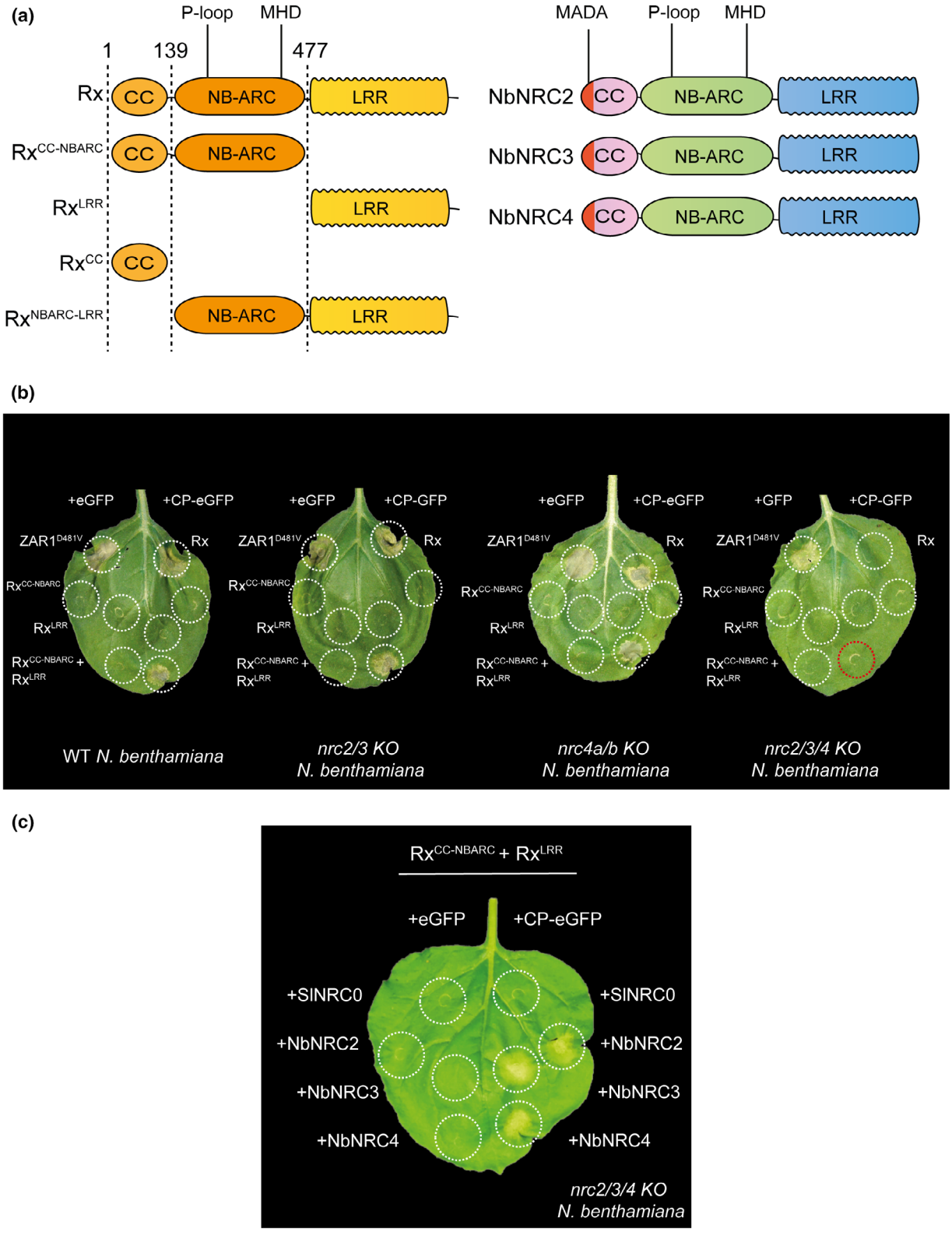




© 2024 The Authors
*New Phytologist* © 2024 New Phytologist Foundation

14698137, 2024, 1, Downloaded from https://nph.onlinelibrary.wiley.com/doi/10.1111/nph.19818 by Test, Wiley Online Library on [02/08/2025]. See the Terms and Conditions (https://onlinelibrary.wiley.com/terms-and-conditions) on Wiley Online Library for rules of use; OA articles are governed by the applicable Creative Commons License

**Fig. 1** The cell death triggered by expression of Rx halves *in trans* upon perception of the coat protein (CP) of *Potato virus X* is dependent on NRC2, NRC3 or NRC4. (a) Schematic representation of Rx halves and NRC constructs used. Domain boundaries for Rx halves are indicated above. Approximate position of MADA, p-loop and MHD motifs are indicated above. Presence of an N-terminal MADA motif is indicated in dark red. (b, c) Representative leaves of different *Nicotiana benthamiana* KO lines agroinfiltrated to express constructs shown and photographed 5–7 d after infiltration. The experiments were repeated three times with at least 6 technical replicates per repeat, with similar results in all cases. (b) Cell death mediated by $Rx^{CC\text{-}NBARC}$ and $Rx^{LRR}$ complemented *in trans* is only abolished in *nrc2/3/4* KO *N. benthamiana* plants. Red dotted circle highlights absence of hypersensitive cell death in *nrc2/3/4* KO background. Wild-type Rx was included for comparison. $NbZAR1^{D481V}$ was included as a control for NRC-independent cell death. (c) Cell death mediated by PVX CP-activated $Rx^{CC\text{-}NBARC}$ and $Rx^{LRR}$ is complemented by NbNRC2, NbNRC3 and NbNRC4 in leaves of *nrc2/3/4* KO *N. benthamiana* lines when activated by co-expression of PVX CP. Free eGFP was used as a negative control for C-terminally eGFP-tagged PVX CP. SlNRC0 was used as a negative control as a helper NRC that does not get activated by Rx. Experiments were repeated 3 times with similar results. Equivalent cell death assays for the other set of Rx halves, $Rx^{CC}$ and $Rx^{NBARC\text{-}LRR}$ can be found in Supporting Information Fig. S1.

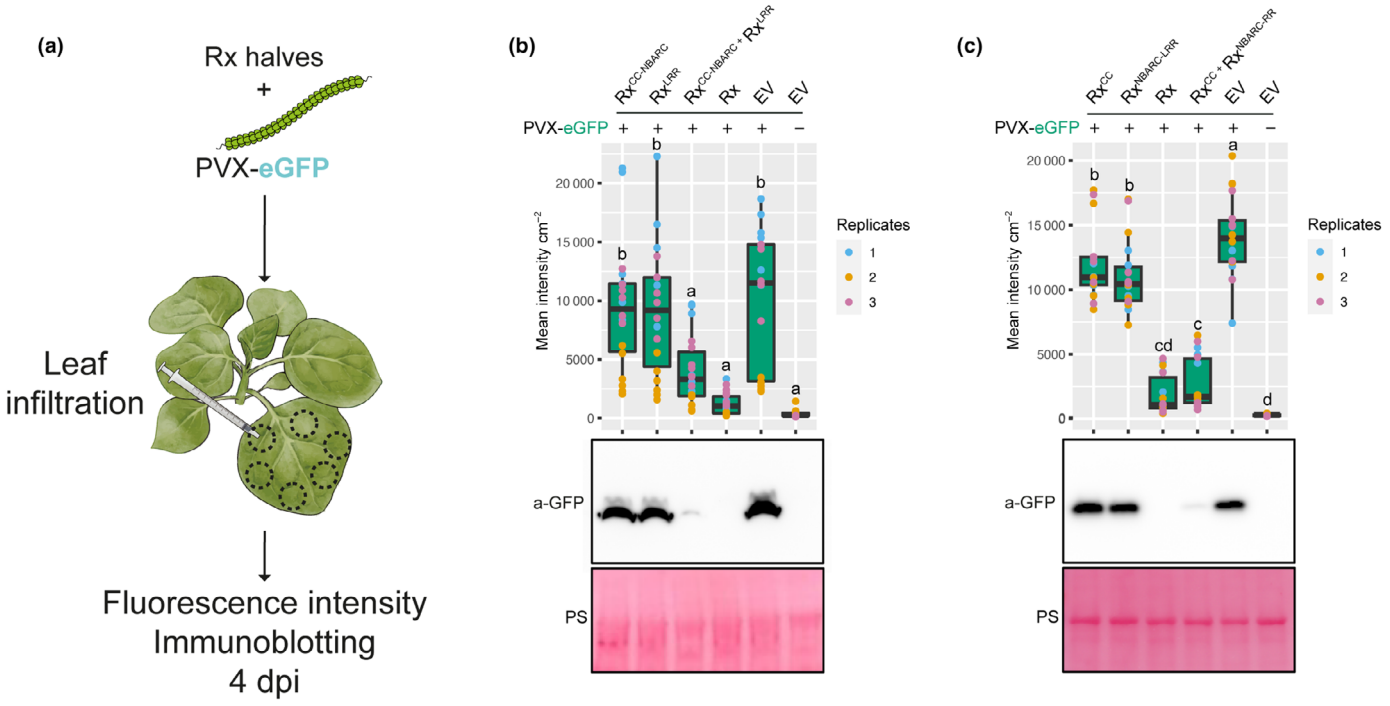


**Fig. 2** The Rx halves expressed *in trans* confer PVX disease resistance to levels comparable to full-length Rx. (a) Schematic representation of the experimental design used. Briefly, the Rx halves were expressed on their own or co-expressed, together with a PVX strain carrying eGFP (pGR106::PVX::eGFP). GFP fluorescence intensity and accumulation were determined 4 d post infiltration as a proxy for viral accumulation. Rx was included as a positive control for PVX resistance. EV was included as a susceptible control. An additional treatment with just agroinfiltration buffer and no PVX infection was used to determine the background fluorescence intensity. (b, c) $Rx^{CC\text{-}NBARC}$/$Rx^{LRR}$ (b) and $Rx^{CC}$/$Rx^{NBARC\text{-}LRR}$ (c) reduce viral accumulation to levels comparable to Rx. Mean fluorescence per square centimeter was measured in *Nicotiana benthamiana* leaves 4 d after infiltration and used as a proxy for PVX viral load. Boxplots summarize the results of three independent replicates with six internal replicates. Each individual dot represents a measurement, color coded by replicate (legend on the right of each boxplot). In each green box, the top, middle and lower horizontal lines correspond to the upper quartile, median and lower quartile values. Vertical line (whiskers) in each treatment depicts the maximum and minimum values, with dots either above or below this line being considered outliers. Letters depict significant differences between treatments as determined by analysis of variance (ANOVA) followed by Tukey's honestly significant difference (HSD) test ($P < 0.05$). Specific reduction of PVX-expressed GFP accumulation was also used as a proxy to evaluate viral load in the presence of the Rx halves. Total protein was extracted from the same PVX-infected areas used to determine fluorescence intensity and used for Western blot analysis. GFP was detected by probing with the appropriate antibodies. Ponceau staining (PS) was used to show equal protein loading across samples. Experiments were repeated 3 times with similar results. dpi, days post inoculation.

dependent cell death. These $Rx^{NB}$-mCherry-6×HA fusions also triggered NRC-dependent cell death, although this cell death was weaker than that triggered by $Rx^{NB}$-eGFP (Fig. S4A). In complementation assays carried out in leaves of *nrc2/3/4* KO *N. benthamiana*, cell death triggered by $Rx^{NB}$-mCherry-6×HA was also complemented by NbNRC2, NbNRC3 and NbNRC4 but not SlNRC0 (Fig. S4B). We used western blot analysis to test for $Rx^{NB}$-mCherry-6×HA protein accumulation levels in *nrc2/3/4* KO *N. benthamiana*. Strikingly, although this construct triggers NRC-dependent cell death in WT *N. benthamiana*, we were unable to detect any signal for $Rx^{NB}$-mCherry-6×HA (Fig. S4C). Based on these results, we conclude that the cell death triggered by the $Rx^{NB}$ truncations is not specific to $Rx^{NB}$-eGFP. Since $Rx^{NB}$-eGFP-triggered cell death is much stronger and easier to detect *in planta*, we decided to proceed with C-terminally eGFP-tagged variants for all subsequent experiments.

© 2024 The Authors
*New Phytologist* © 2024 New Phytologist Foundation



14698137, 2024, 1, Downloaded from https://nph.onlinelibrary.wiley.com/doi/10.1111/nph.19818 by Test, Wiley Online Library on [02/08/2025]. See the Terms and Conditions (https://onlinelibrary.wiley.com/terms-and-conditions) on Wiley Online Library for rules of use; OA articles are governed by the applicable Creative Commons License

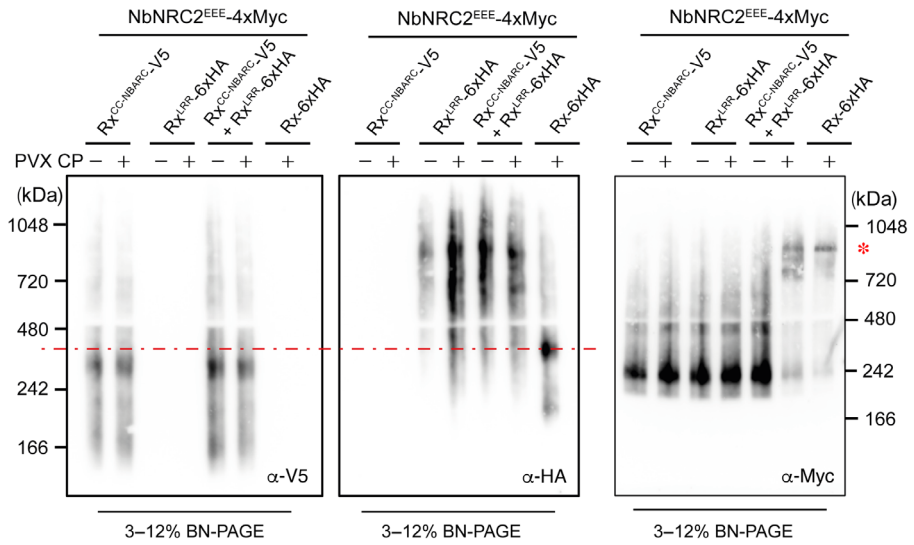


**Fig. 3** Rx halves expressed *in trans* mediate PVX CP-dependent oligomerization of their NRC2 helper. BN-PAGE assays with the inactive and PVX CP-activated $Rx^{CC\text{-}NBARC}$ and $Rx^{LRR}$ halves co-expressed with $NRC2^{EEE}$. C-terminally V5-tagged $Rx^{CC\text{-}NBARC}$, 6×HA-tagged $Rx^{LRR}$ and 4×Myc-tagged $NbNRC2^{EEE}$ were co-expressed with either free GFP or C-terminally GFP-tagged PVX CP. Full-length Rx was included for comparison and as a positive control for NRC2 oligomerization. Protein extracts were run on BN-PAGE and SDS-PAGE assays in parallel and immunoblotted with the appropriate antisera labelled on the lower right corner of each blot. Red asterisks on the right indicates size of bands corresponding to the activated NRC2 complex. Red dotted lines indicate the molecular weight at which the full-length Rx complex migrates. V5 and HA blots were run on the same gel to allow for precise comparison of molecular weights. Approximate molecular weights (kDa) of the proteins are shown on the left for V5 and HA blots (run on the same gel), and on the right for Myc. SDS-PAGE accompanying BN-PAGE can be found in Supporting Information Fig. S2. Experiments were repeated 3 times with similar results.

## $Rx^{NB}$ mediates effector-independent oligomerization of the NRC2 helper

We next sought to investigate if $Rx^{NB}$ is sufficient to trigger NRC2 oligomerization. To this end, we co-expressed $Rx^{NB}$ and $NbNRC2^{EEE}$ in leaves of *nrc2/3/4* KO *N. benthamiana* and performed BN-PAGE assays at different timepoints, with Rx/PVX CP as a positive control for NRC2 oligomerization. Interestingly, expression of $Rx^{NB}$-eGFP was sufficient to mediate the formation of NRC2 high molecular weight complexes of a similar size as the NRC2 oligomers formed upon activation with full-length Rx/PVX CP. Importantly, the absence of a shift in size of the NRC2 oligomers triggered by $Rx^{NB}$-eGFP compared to those triggered by Rx/PVX CP suggests that, much like full-length Rx, $Rx^{NB}$-eGFP does not form part of the mature NRC2 oligomer (Fig. 4d). We noted that compared to the treatments with full-length Rx and PVX CP activation, $Rx^{NB}$-eGFP-activated NRC2 treatments also showed a weak signal of a size that matches to inactive NRC2 in all timepoints analyzed, indicating that $Rx^{NB}$-eGFP mediated helper oligomerization may be less efficient, or that the RxNB-eGFP-activated NRC2 oligomers are less stable than their full-length Rx-activated counterparts (Fig. 4d). We did not observe any signal for $Rx^{NB}$-eGFP at a molecular weight matching that of the NRC2 oligomer, which further suggests that the mature NRC2 resistosome does not include $Rx^{NB}$-eGFP (Fig. 4d).

## The nucleotide-binding (NB) domains of the sensor NLRs Gpa2, Rpi-amr1e, Rpi-amr3 and Sw-5b are sufficient to activate downstream NRC helpers

To what degree does the activation of NRC helpers by the NB domain of sensor NLRs apply to other disease resistance proteins? We investigated this by generating NB domain-eGFP

**Fig. 4** The NB domain of Rx ($Rx^{NB}$) constitutively induces NRC2/NRC3/NRC4-dependent cell death and formation of the helper NRC2 oligomer. (a) Photo of a representative leaves from WT and *nrc2/3/4* KO *Nicotiana benthamiana* plants expressing $Rx^{NB}$-eGFP. $NbZAR1^{D481V}$ and $Rx^{D460V}$ were included as controls for NRC-independent and NRC-dependent cell death, respectively. eGFP was included as a negative control for cell death. Leaves were agroinfiltrated to express the constructs indicated and photographed 5–7 d after infiltration. The experiment was repeated three times with at least 6 technical replicates per repeat, with similar results in all cases. (b) Schematic representation of $Rx^{NB}$-eGFP construct. Domain boundaries used are indicated above, and were the same as reported previously by Rairdan *et al*. (2008). Position of highly conserved lysine (K) residue of the p-loop is indicated, with numbering corresponding to its position in full-length Rx. (c) Representative leaf of *nrc2/3/4* KO *N. benthamiana* expressing $Rx^{NB}$-eGFP complemented with NbNRC2, NbNRC3 or NbNRC4. SlNRC0 was included as a negative control for complementation. $NbZAR1^{D481V}$ and $Rx^{D460V}$ were included as controls for NRC-independent and NRC-dependent cell death, respectively. A quantitative analysis of the cell death can be found in Supporting Information Fig. S7. (d) BN-PAGE assays with inactive and activated C-terminally 4×Myc-tagged $NRC2^{EEE}$. $NRC2^{EEE}$ was activated either with Rx-6×HA/PVX CP-eGFP or $Rx^{NB}$-eGFP. Total protein extracts were run on native and denaturing PAGE assays in parallel and immunoblotted with the appropriate antisera labelled in the lower left corner of each blot. Approximate molecular weights (kDa) of the proteins are shown on the right. Accompanying SDS-PAGE assays can be found in Fig. S5. The experiment was repeated 3 times with similar results.



© 2024 The Authors
*New Phytologist* © 2024 New Phytologist Foundation

14698137, 2024, 1, Downloaded from https://nph.onlinelibrary.wiley.com/doi/10.1111/nph.19818 by Test, Wiley Online Library on [02/08/2025]. See the Terms and Conditions (https://onlinelibrary.wiley.com/terms-and-conditions) on Wiley Online Library for rules of use; OA articles are governed by the applicable Creative Commons License

14698137, 2024, 1, Downloaded from https://nph.onlinelibrary.wiley.com/doi/10.1111/nph.19818 by Test, Wiley Online Library on [02/08/2025]. See the Terms and Conditions (https://onlinelibrary.wiley.com/terms-and-conditions) on Wiley Online Library for rules of use; OA articles are governed by the applicable Creative Commons License

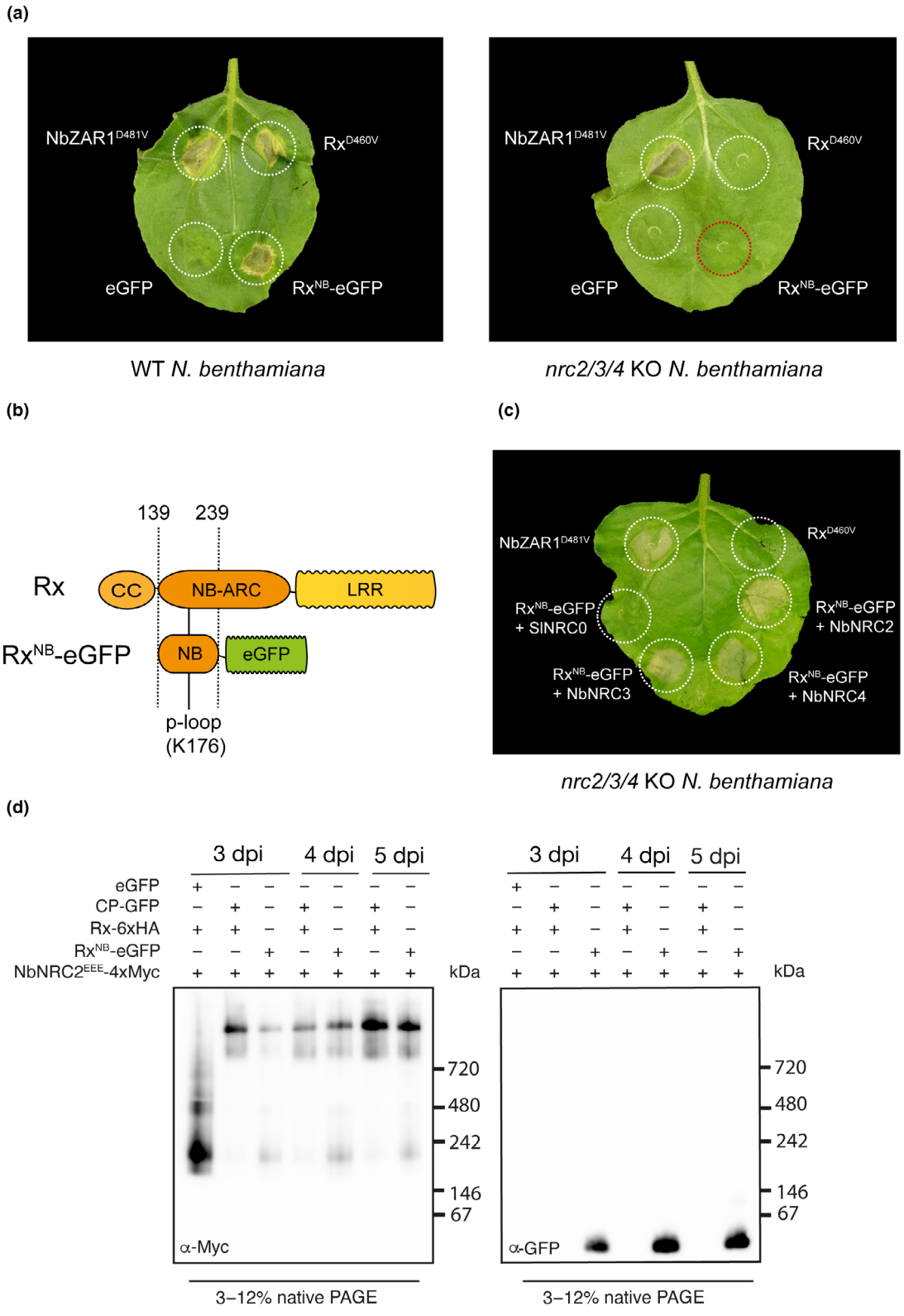


fusions of 8 well-studied disease resistance NLR proteins that are dependent on NRC helpers in the immune receptor network (Figs 5, S6). This panel covered the phylogenetic diversity of NRC-dependent sensors and was composed of the Rx type sensors Gpa2, Rpi-amr1e, Rpi-amr3 and Bs2, and the SD type sensors Mi-1.2, Rpi-blb2 and Sw-5b (Contreras *et al.*, 2023a). Gpa2$^{NB}$-eGFP, Rpi-amr1e$^{NB}$-eGFP and Sw-5b$^{NB}$-eGFP triggered NRC-dependent cell death to levels comparable to

© 2024 The Authors
*New Phytologist* © 2024 New Phytologist Foundation

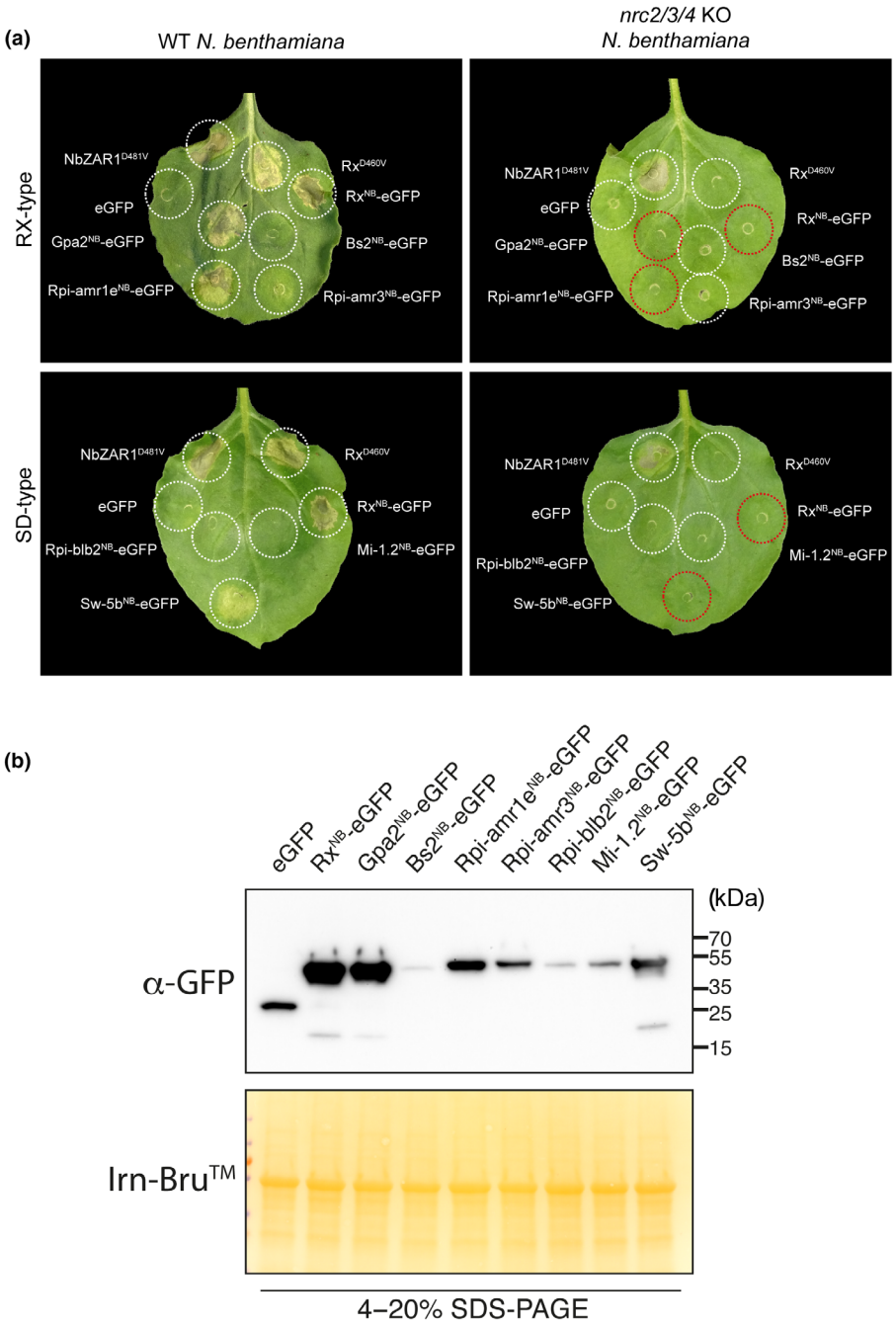


**Fig. 5** The NB domains of the sensor NLRs Gpa2, Rpi-amr1e, Rpi-amr3 and Sw-5b are sufficient to activate downstream NRC helpers. (a) Representative photos of cell death assays with the constructs indicated in leaves of either WT or *nrc2/3/4* KO *Nicotiana benthamiana*. NbZAR1$^{D481V}$ and eGFP were included as positive and negative controls for cell death, respectively. Rx$^{D460V}$ was included as a control for NRC-dependent cell death. Leaves were agroinfiltrated to express the constructs indicated and photographed 5–7 d after infiltration. One representative leaf is shown. A quantitative analysis of the cell death assays can be found in Supporting Information Fig. S7. All NB domain constructs and relevant controls were co-expressed with the silencing suppressor P19 in order to boost expression. (b) Protein extracts from leaves of *nrc2/3/4* KO *N. benthamiana* expressing proteins of interest were run on SDS-PAGE assays and immunoblotted with the appropriate antisera labelled on the left. Approximate molecular weights (kDa) of the proteins are shown on the right. Rubisco loading control was carried out using Ponceau 4R staining (Irn-Bru™). Experiment was repeated two times with similar results. All NB domain constructs and relevant controls were co-expressed with the silencing suppressor P19 in order to boost expression.

Rx$^{NB}$-eGFP (Figs 5a, S7). Rpi-amr3$^{NB}$-eGFP triggered weak NRC-dependent cell death in a subset of the leaves tested (6 out of 18 total infiltration spots) (Figs 5a, S7). By contrast, Bs2$^{NB}$-eGFP, Rpi-blb2$^{NB}$-eGFP and Mi-1.2$^{NB}$-eGFP did not trigger cell death (Figs 5a, S7). In parallel, we determined the protein accumulation levels of each NB domain-eGFP fusion *in planta*. All of the sensor NLR NB domains that induced cell death accumulated *in planta* (Rx, Gpa2, Rpi-amr1e and Sw-5b). By contrast, the NB domain truncations that triggered weak or no cell death accumulated to comparatively lower levels (Rpi-amr3, Bs2, Rpi-blb2 and Mi-1.2) (Fig. 5b). We conclude that NB domain-mediated activation of downstream NRC helpers is not exclusive to Rx and can also be triggered by other Rx type and SD type sensors of the NRC network.

## The nucleotide-binding (NB) domains of the sensor NLRs Gpa2, Rpi-amr1e and Sw-5b retain the NRC helper specificities of their full-length counterparts

Sensor NLRs in the NRC network can signal via different subsets of downstream NRC helpers. For example, PVX CP-activated Rx, Ran-binding protein 1 (RBP1)-activated Gpa2 and Tospovirus movement protein NSm-activated Sw-5b can signal interchangeably via NRC2, NRC3 and NRC4, whereas AVRamr1-



© 2024 The Authors
*New Phytologist* © 2024 New Phytologist Foundation

14698137, 2024, 1, Downloaded from https://nph.onlinelibrary.wiley.com/doi/10.1111/nph.19818 by Test, Wiley Online Library on [02/08/2025]. See the Terms and Conditions (https://onlinelibrary.wiley.com/terms-and-conditions) on Wiley Online Library for rules of use; OA articles are governed by the applicable Creative Commons License

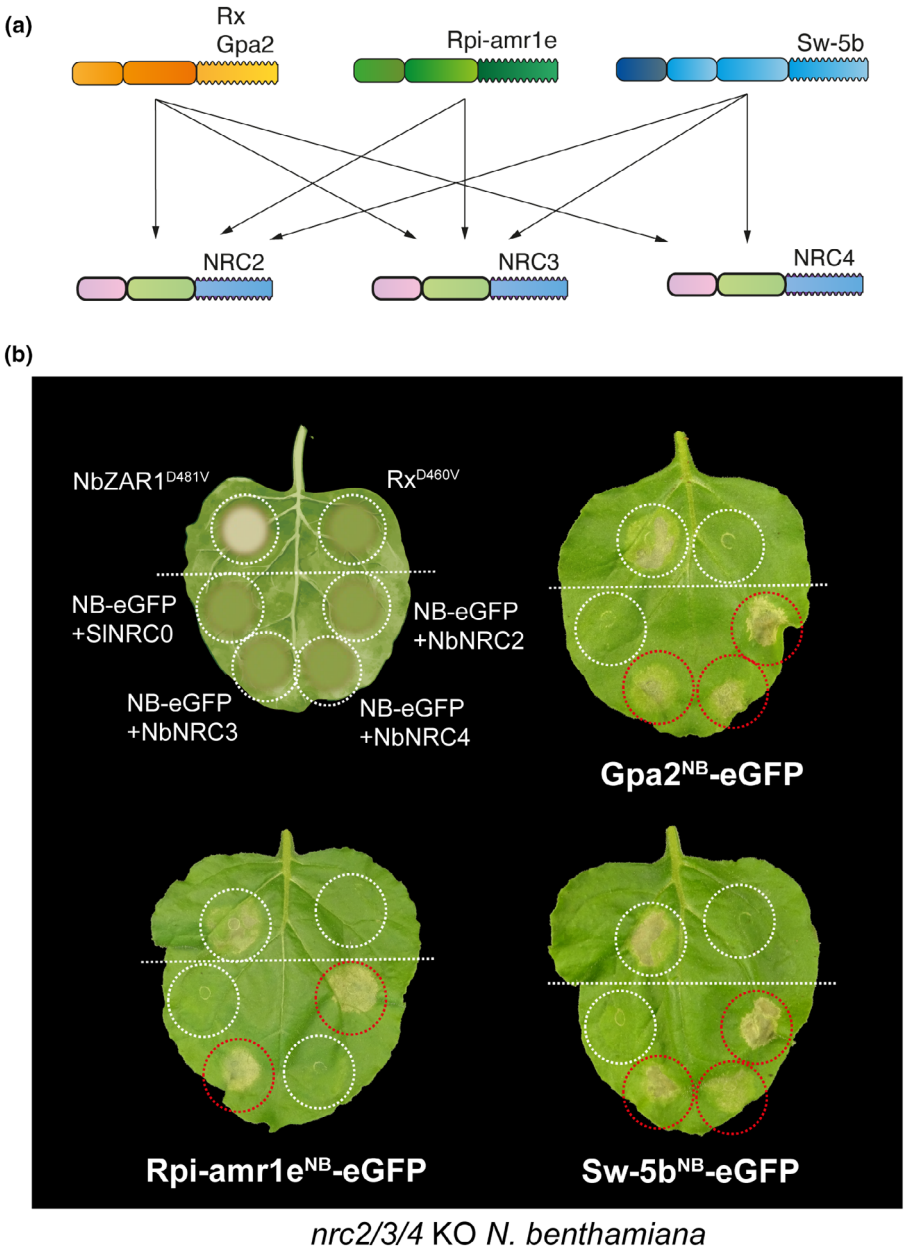


**Fig. 6** The NB domains of the sensor NLRs Gpa2, Rpi-amr1e, and Sw-5b retain the same NRC helper specificity as their full-length counterparts. (a) Schematic representation of helper signaling specificities of the NRC-dependent sensors tested. Rx type sensors Rx, Gpa2 and Rpi-amr1e are represented with three domains whereas the SD type sensor Sw-5b is represented with four domains (SD, CC, NB-ARC and LRR). (b) Representative photos of cell death assays with the constructs indicated in leaves of *nrc2/3/4* KO *Nicotiana benthamiana*. Upper left schematic of a *N. benthamiana* leaf indicates the treatment in each position. NB-eGFP refers to NRC-dependent sensor NB domain-eGFP fusions. The NB-eGFP fusions tested in each case are indicated underneath each leaf. NbZAR1$^{D481V}$ and Rx$^{D460V}$ were included as positive and negative controls for cell death, respectively. Leaves were agroinfiltrated to express the constructs indicated and photographed 5–7 d after infiltration. One representative leaf is shown. A quantitative analysis of the cell death assays can be found in Supporting Information Fig. S7. All NB domain constructs and relevant controls were co-expressed with the silencing suppressor P19 in order to boost expression.

activated Rpi-amr1e can signal via NRC2 and NRC3 but not NRC4 (Figs 6a, S8) (Wu *et al.*, 2017; Derevnina *et al.*, 2021; Witek *et al.*, 2021; Lin *et al.*, 2022; Contreras *et al.*, 2023b,c). We next sought to determine whether, Gpa2$^{NB}$-eGFP, Rpi-amr1e$^{NB}$-eGFP and Sw-5b$^{NB}$-eGFP retained the same downstream NRC specificities of their full-length counterparts, similar to Rx$^{NB}$-eGFP. To this end, we performed complementation assays in leaves of *nrc2/3/4* KO *N. benthamiana* co-expressing each of these NB domains together with NbNRC2, NbNRC3 or NbNRC4, respectively. We included SlNRC0 as a negative control for complementation. We did not include Rpi-amr3 in these experiments as Rpi-amr3$^{NB}$-eGFP accumulated poorly *in planta* and triggered comparatively weaker cell death, making it harder to draw robust conclusions (Figs 5, S7). The cell death triggered by Gpa2$^{NB}$-eGFP and Sw-5b$^{NB}$-eGFP was restored upon co-expression with NbNRC2, NbNRC3 and NbNRC4. Rpi-amr1e$^{NB}$-eGFP cell death was restored upon co-expression with NbNRC2 and NbNRC3 but not with NbNRC4 (Fig. 6b). None of the NB domains were complemented by SlNRC0. This indicates that NB domain-eGFP fusions retain the same helper NRC specificity profiles of their full-length counterparts.

## Rx$^{NB}$ and its helper NRC2 form a minimal functional unit that can be transferred from Solanaceae to the Asteraceae plant lettuce

We leveraged transient expression in lettuce (*Lactuca sativa*) by agroinfiltration (Wróblewski *et al.*, 2018) to investigate the

© 2024 The Authors
*New Phytologist* © 2024 New Phytologist Foundation



14698137, 2024, 1, Downloaded from https://nph.onlinelibrary.wiley.com/doi/10.1111/nph.19818 by Test, Wiley Online Library on [02/08/2025]. See the Terms and Conditions (https://onlinelibrary.wiley.com/terms-and-conditions) on Wiley Online Library for rules of use; OA articles are governed by the applicable Creative Commons License

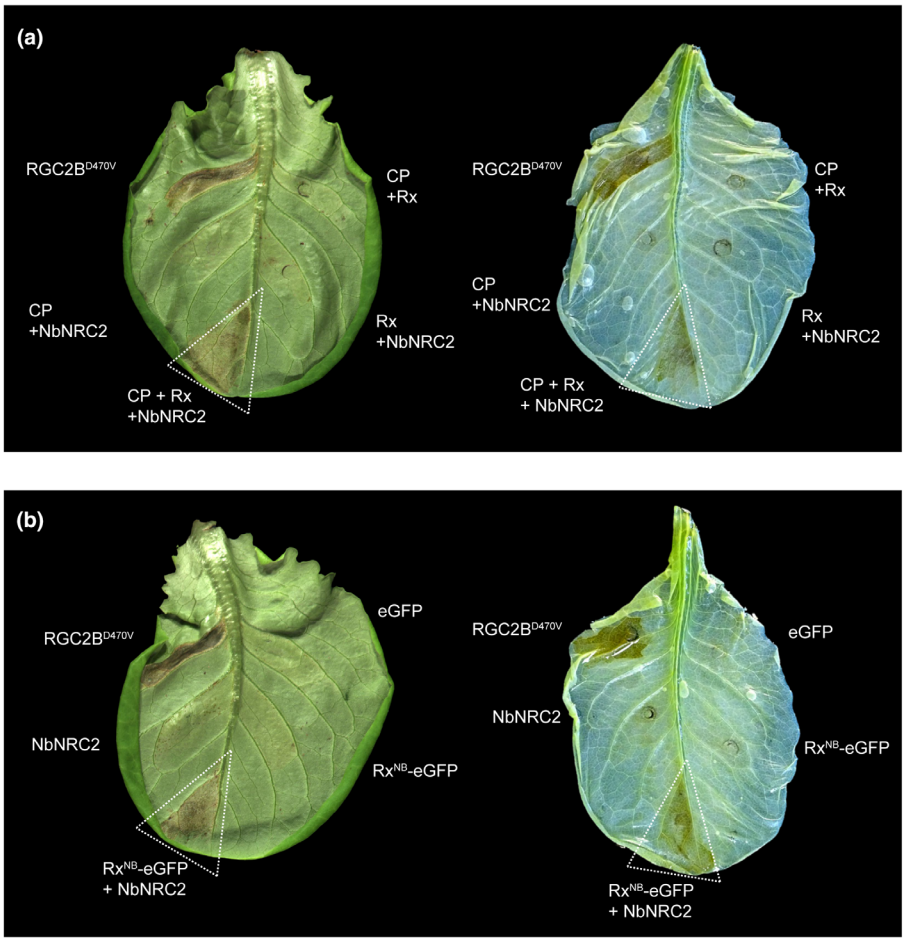


**Fig. 7** Rx, Rx$^{NB}$ and their helper NRC2 form a minimal functional unit that can be transferred to the Asteraceae plant lettuce. Photo of representative leaves of lettuce (*L. sativa*) var. 'Fenston'. (a) Lettuce leaf showing cell death after co-expression of PVX CP, Rx and NbNRC2. No cell death was observed when any one of the three components (PVX CP, Rx or NbNRC2) was absent. Left side of the panel shows abaxial side of a representative leaf, imaged after 5–7 d post agroinfiltration. Ride side of the panel shows abaxial side of a different representative leaf, bleached with ethanol and imaged after 5–7 d post agroinfiltration to enhance visualization of cell death. (b) Photo of representative leaves of lettuce (*L. sativa*) var. 'Fenston' showing cell death after co-expression of Rx$^{NB}$-eGFP and NbNRC2. No cell death was observed with eGFP or with Rx$^{NB}$-eGFP and NbNRC2 when expressed individually. (a, b) Images were taken 5–7 d after agroinfiltration. Left side of the panels show abaxial side of a representative leaf, imaged after 5–7 d post agroinfiltration. Ride side of the panel shows abaxial side of a different representative leaf, bleached with ethanol and imaged after 5–7 d post agroinfiltration to enhance visualization of cell death. Images were taken from abaxial side as HR cell death in lettuce is more visible on abaxial than adaxial sides. The constitutively active variant of the lettuce NLR RGC2B (RGC2B$^{D470V}$) was used as a positive control for cell death in lettuce. Experiments were repeated three times with similar results.

capacity of the Rx/NRC2 pair to function in a species distantly related to the Solanaceae. Lettuce is an Asteraceae in the Campanulid lineage and is estimated to have split from *Nicotiana* (Solanaceae, Lamiid) *c.* 102 Ma (Zeng *et al.*, 2014). Lettuce predates the expansion of the NRC helpers that occurred in Solanaceae and other lamiids and therefore lacks orthologs of NRC2, NRC3 and NRC4 and other Solanaceae NRCs (Goh *et al.*, 2023; Sakai *et al.*, 2023). We first determined whether Rx/CP and NRC2 can trigger cell death in lettuce by co-expressing these three proteins in lettuce leaves. We included an autoactive variant of the previously published lettuce CC$_{G10}$-NLR RGC2B (RGC2B$^{D470V}$) as a positive control for cell death (Meyers *et al.*, 1998; Shen *et al.*, 2002). We observed a cell death response indicative of immune activation when all three components, CP, Rx and NRC2 were co-expressed in leaves of lettuce. This cell death was abolished when any one of these three components was missing (Fig. 7a).

Next, we tested whether Rx$^{NB}$-eGFP and NRC2 were also capable of mediating cell death in lettuce. We included RGC2B$^{D470V}$ and eGFP as positive and negative controls for cell death, respectively. Co-expression of Rx$^{NB}$-eGFP and NbNRC2 triggered cell death in lettuce, whereas expression of either Rx$^{NB}$-eGFP or NbNRC2 alone did not (Fig. 7b). This result suggests that no additional proteins are required for Rx$^{NB}$-eGFP to activate NRC2. Alternatively, additional proteins that may be required are conserved between *N. benthamiana* (Lamiid) and



© 2024 The Authors
*New Phytologist* © 2024 New Phytologist Foundation

14698137, 2024, 1, Downloaded from https://nph.onlinelibrary.wiley.com/doi/10.1111/nph.19818 by Test, Wiley Online Library on [02/08/2025]. See the Terms and Conditions (https://onlinelibrary.wiley.com/terms-and-conditions) on Wiley Online Library for rules of use; OA articles are governed by the applicable Creative Commons License

lettuce (Campanulid). We conclude that $Rx^{NB}$-eGFP and NRC2 are most likely a minimal two-component system that can be transferred from *N. benthamiana* to lettuce.

## Discussion

In this study, we build upon findings by Moffett *et al.* (2002) and Rairdan *et al.* (2008) regarding the ability of individual domains of the virus disease resistance protein Rx to activate immunity *in trans*, or as a nucleotide-binding (NB) domain. We revisited this work within the framework of the activation-and-release biochemical model for sensor–helper activation in the NRC network of CC-NLRs (Contreras *et al.*, 2023c). Our findings demonstrate that the domains of Rx can trigger NRC-dependent cell death and oligomerization as well as mediate PVX disease resistance when expressed *in trans* (Figs 1–3). We also show that the effector-independent cell death mediated by $Rx^{NB}$-eGFP, is dependent on NRC helpers and involves the formation of NRC2 resistosomes. Similar to the full-length Rx, the Rx halves and $Rx^{NB}$-eGFP do not integrate into the mature NRC2 helper oligomer (Figs 3, 4). Furthermore, our work reveals that the *c.* 150 amino acid NB domain fragments of other sensor NLRs, such as Gpa2, Rpi-amr1e, Rpi-amr3 and Sw-5b, also induce constitutive cell death. Importantly, $Rx^{NB}$, $Gpa2^{NB}$, $Rpi\text{-}amr1e^{NB}$, and $Sw\text{-}5b^{NB}$ maintain the downstream helper specificity profiles of their full-length counterparts (Figs 5, 6). Finally, we demonstrate that both full-length PVX CP-activated Rx and $Rx^{NB}$-eGFP can initiate cell death in lettuce when co-expressed with NRC2, suggesting that this represents a minimal, two-component system transferable to unrelated plant taxa (Fig. 7). Our data support a working model in which the conditional exposure of sensor NLR NB domains upon pathogen perception serves as a signal for downstream NRCs that triggers helper oligomerization and resistosome formation (Fig. 8).

The prevailing paradigm for NLR activation is that their N-terminal domains mediate immune signaling upon resistosome assembly. This is the case for the N-terminal CC domains of singleton and helper CC-NLRs and for the N-terminal TIR domains of sensor TIR-NLRs (Bentham *et al.*, 2018; Contreras *et al.*, 2023a). Based on our data, we propose that for some NRC-dependent sensor NLRs, the NB domain region of the central NB-ARC, not the N-terminal CC domain, executes signaling to downstream helpers. How does the NB domain of sensor NLRs initiate the activation of NRC helpers? Is this activation achieved through direct binding or does it necessitate enzymatic activity, as is the case for TIR-NLRs and their downstream $CC_R$-NLR helpers (Ma *et al.*, 2020; Huang *et al.*, 2022)? Interestingly, while the activation of full-length Rx and the Rx halves expressed *in trans* requires an intact p-loop (Moffett *et al.*, 2002), $Rx^{NB}$ activation of NRCs is p-loop independent (Fig. S3). This observation indicates that while ATP-binding is required for conditional NB domain exposure, it does not play a role in the recognition of the sensor NB domain by the helper once the NB domain is exposed, making sensor NB domain-catalyzed ATP hydrolysis an improbable mechanism of helper activation.

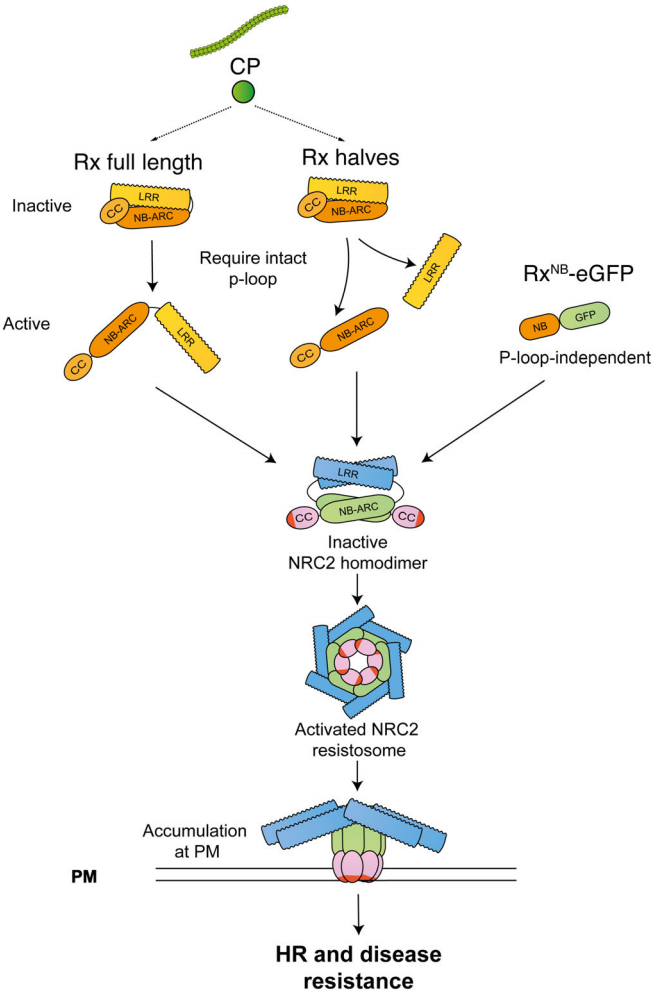


**Fig. 8** Proposed working model for NRC activation by Rx halves expressed *in trans* and $Rx^{NB}$-eGFP. Schematic representation of full-length Rx, Rx halves and $Rx^{NB}$-eGFP-mediated NRC activation. before effector-triggered activation, NRC-dependent sensors such as Rx are held in an inactive conformation by intramolecular interactions. These intramolecular interactions between the different Rx domains hide the sensor NLR NB domain, preventing its signaling, and contribute to the previously reported association of the $Rx^{CC\text{-}NBARC}$/$Rx^{LRR}$ and $Rx^{CC}$/$Rx^{NBARC\text{-}LRR}$ halves (Moffett *et al.*, 2002). Upon perception of PVX CP, Rx undergoes a series of p-loop dependent conformational changes that expose the NB domain and lead to dissociation of the Rx halves expressed *in trans* (Moffett *et al.*, 2002). This conditional NB domain exposure allows it to signal to downstream helpers such as NRC2, which exist as homodimers in their resting state, leading to its homo-oligomerization and resistosome formation. The activated NRC2 resistosome may be hexameric, based on the recently reported $NRC4^{D478V}$ structure (Liu *et al.*, 2023). Following activation by their upstream sensor, NRC helper oligomers signal via their N-terminal CC domain. In the case of the $Rx^{NB}$-eGFP and other sensor NB domain-eGFP fusions, the NB domain is exposed and therefore constitutively activates downstream helpers. Because no intramolecular rearrangements are required to relieve autoinhibitory intramolecular interactions, the p-loop mutation does not abolish this cell death.

How do the Rx halves convert PVX CP perception into NRC activation? Our data support a model in which the Rx halves, which constitutively associate at resting state, undergo a series of

© 2024 The Authors
*New Phytologist* © 2024 New Phytologist Foundation



14698137, 2024, 1, Downloaded from https://nph.onlinelibrary.wiley.com/doi/10.1111/nph.19818 by Test, Wiley Online Library on [02/08/2025]. See the Terms and Conditions (https://onlinelibrary.wiley.com/terms-and-conditions) on Wiley Online Library for rules of use; OA articles are governed by the applicable Creative Commons License

p-loop dependent conformational changes that lead to their dissociation, as reported previously (Moffett *et al.*, 2002). These conformational changes would then expose the NB domain, allowing it to signal to downstream helpers and trigger the formation of an NRC resistosome, potentially via transient interactions. In the case of Sw-5b, it was previously shown that the NB-ARC domain on its own also triggers cell death, suggesting that the CC and LRR are negatively regulating the NB-ARC domain but that intra NB-ARC domain interactions are not sufficient to prevent the NB domain from signaling. Further work is required to understand the dynamic intramolecular interactions that NRC-dependent sensor NLRs undergo when transitioning from the inactive to the active state. Understanding the structural details of sensor NLR activation will shed light on the molecular mechanisms underpinning sensor–helper communication.

Our transient expression assays in lettuce, along with recently published data demonstrating that Campanulid NRC sensor–helper pairs can initiate immune signaling in *N. benthamiana* (Goh *et al.*, 2023; Sakai *et al.*, 2023), lead us to favor a model in which sensor NB domains and NRC helpers directly interact, with no additional components required for sensor–helper communication. While it remains possible that additional conserved components exist between *N. benthamiana* and lettuce, the evolutionary divergence between these two plant species – estimated at 102 million years – makes this hypothesis less likely (Zeng *et al.*, 2014). Indeed, in another recent publication from our group, the NB domain of Rx was shown to mediate conversion of the resting state NRC2 homodimer into a resistosome when both proteins were combined *in vitro*, providing further evidence that this is a two-component system (Selvaraj *et al.*, 2023). The fact that the NB domain alone is sufficient to activate NRCs suggests that sensor NLRs are unlikely to be required as scaffolds for helper NLR polymerization during sensor–helper activation, as is the case for the mammalian NAIP/NLRC4 sensor–helper pairs (Zhang *et al.*, 2015). Moreover, the recent structure of the activated NRC4 homo-hexamer revealed that the activated NRC4 resistosome does not include a sensor, which would support our previously postulated activation-and-release model. It should be noted that this structure corresponded to the constitutively active $NRC4^{D478V}$ variant and not to a sensor or NB domain–activated helper (Liu *et al.*, 2023). Further biochemical and structural analyses will provide insights into the precise dynamics of sensor–helper interactions during activation.

To date, conclusive evidence that NRC-dependent sensors and their NRC helpers form stable complexes has not been obtained. This is largely due to sensor–helper co-immunoprecipitation studies being notoriously difficult to control properly, as was shown recently by Huang et al. in their recent study (Huang *et al.*, 2023). In this same study, however, Huang *et al.* leveraged Turbo-ID to reveal that NRC-dependent sensors specifically show enhanced interactions with their corresponding downstream helpers following activation, in support of a model in which NRC activation is mediated by transient sensor–helper interactions.

The discovery that Rx and NRC2 can effectively function in lettuce carries significant implications for disease resistance breeding and bioengineering (Marchal *et al.*, 2022). These findings raise the possibility of transferring NRC sensor–helper pairs across crop species at least within asterid plants. This potential transfer may even extend to agronomically important species outside of the Asteraceae, such as soybean, wheat, or rice, which lack NRCs altogether (Wu *et al.*, 2017). Furthermore, it opens the door to the prospect of transferring entire networks of NRC sensors and helpers across species boundaries, capitalizing on the resilience that networked signaling architectures offer to immune systems (Wu *et al.*, 2018). The transfer of the NRC network across species is particularly exciting given that it confers resistance to multiple species of pathogens and pests (Wu *et al.*, 2017; Derevnina *et al.*, 2021; Kourelis *et al.*, 2022).

Additionally, the observation that Rx can recognize PVX CP in lettuce, triggering cell death, prompts important inquiries about the recognition mechanism of PVX CP. Previous work suggested that Rx indirectly recognizes PVX CP and that this recognition necessitates the host component RanGAP2 (Moffett *et al.*, 2002; Sacco *et al.*, 2007; Tameling & Baulcombe, 2007). The fact that Rx can still respond to PVX CP in lettuce raises the possibility that either Rx retains its proper functionality with the lettuce RanGAP2 ortholog or that Rx recognition of PVX CP might involve direct, albeit transient, interactions. Further research is required to elucidate the precise role of RanGAP2 in Rx functionality and to unravel the specific mechanism by which Rx perceives PVX CP.

According to a well-established paradigm of plant immunity, NLRs are known to guard critical host components, known as guardees or decoys, that are perturbed during pathogen infection (Van Der Biezen & Jones, 1998; Dangl & Jones, 2001; van der Hoorn & Kamoun, 2008). We propose that helper NLRs, such as the NRCs, may have evolved to guard the conformational state of the NB-ARC domains in their upstream sensors, enabling them to detect any pathogen-triggered modifications. The NB-ARC domain stands out as the most conserved feature within the NLR protein family, and NB-ARC rearrangements have been demonstrated as critical for NLR activation across various life forms (Duxbury *et al.*, 2021; Chou *et al.*, 2023). It is plausible that NRC helpers have evolved to perceive the activation status of the NB-ARC domains of their upstream sensors, recognizing NB-ARC conformational states indicative of effector perception and immune activation. This concept is reminiscent of how $CC_R$-NLR helpers, such as NRG1 and ADR1, have evolved to sense the activation of their upstream TIR-NLR sensors by detecting the formation of EDS1-SAG101/PAD4 heterodimers induced following TIR-NLR resistosome assembly and small molecule production (Huang *et al.*, 2022; Jia *et al.*, 2022; Feehan *et al.*, 2023). We propose that helper NLRs in the NRC family function as 'guards of sensors', perceiving sensor NLR activation. In this model, sensor NLRs could even be considered as decoys, as they have degenerated features such as nonfunctional MADA motifs and N-terminal domain integrations (SD) and have lost the capacity to trigger cell death on their own (Adachi *et al.*, 2019b; Contreras *et al.*, 2023a).

A significant, unresolved question is deciphering the molecular basis of sensor–helper specificity, a fundamental characteristic of the NRC network. While certain sensors can activate multiple



© 2024 The Authors
*New Phytologist* © 2024 New Phytologist Foundation

14698137, 2024, 1, Downloaded from https://nph.onlinelibrary.wiley.com/doi/10.1111/nph.19818 by Test, Wiley Online Library on [02/08/2025]. See the Terms and Conditions (https://onlinelibrary.wiley.com/terms-and-conditions) on Wiley Online Library for rules of use; OA articles are governed by the applicable Creative Commons License

helpers within a given host, others selectively activate a subset of the NRC helper repertoire. Furthermore, across evolutionary timescales, sensors from one species can lose the ability to communicate with NRC helpers from distantly or even closely related species, as is the case of species-specific sensor–helper NRC pairs in lamiids (Goh *et al.*, 2023; Sakai *et al.*, 2023). Our data suggests that the NB domain plays a crucial role as a molecular determinant for sensor–helper specificity on the sensor side. However, although the sensor NB is necessary and sufficient for NRC activation, the contributions of other sensor NLR domains to downstream helper activation remain unclear. Furthermore, the domains within the helper proteins involved in perceiving sensor NLR activation are yet to be identified. Understanding the domains and interfaces involved in sensor and helper protein interactions, and their evolutionary dynamics, will provide additional insights into the mechanisms through which paired and networked CC-NLRs activate. Identifying the precise molecular communication between sensors and helpers could have substantial implications for disease resistance engineering, potentially enabling the synthetic expansion and optimization of sensor–helper interactions, resulting in more robust and efficient immune receptor networks.

## Acknowledgements

We thank D. Lüdke for valuable comments on this article. We thank members of the Jones lab (The Sainsbury Laboratory), including Camille-Madeleine Szymansky, Hee-Kyung Ahn and Jonathan Jones, for valuable scientific discussions. We thank Tania Toruño and Peter-Paul Damen (Rijk Zwaan, Netherlands) for providing seeds of lettuce (*L. sativa*) var. 'Fenston' and valuable scientific discussions. We thank all members of the TSL Support Services for their invaluable assistance. MPC thanks S. Scorza for support and L. A. 'El Flaco' Spinetta for inspiration. The Kamoun Lab is funded primarily from the Gatsby Charitable Foundation, Biotechnology and Biological Sciences Research Council (BBSRC, UK, BB/WW002221/1, BB/V002937/1, BBS/E/J/000PR9795 and BBS/E/J/000PR9796) and the European Research Council (BLASTOFF).

## Competing interests

SK receives funding from industry on NLR biology and has cofounded a start-up company (Resurrect Bio Ltd.) related to NLR biology. SK, CM and MPC have filed patents on NLR biology. MPC has received fees from Resurrect Bio Ltd.

## Author contributions

MPC was involved in conceptualization; data curation; formal analysis; supervision; validation; investigation; visualization; methodology; project administration; and writing – original draft, review and editing. HP was involved in conceptualization, data curation, formal analysis, supervision, validation, investigation, methodology, and writing – review and editing. RT provided the data curation, formal analysis, validation, investigation, and visualization. CM provided the data curation, formal analysis, investigation, and visualization. JC provided the data curation, formal analysis, validation, and investigation. HA provided the conceptualization, investigation, and writing – review and editing. SK provided the conceptualization; resources; supervision; funding acquisition; visualization; project administration; and writing – original draft, review and editing. MPC and HP contributed equally to this work.

## ORCID

Hiroaki Adachi https://orcid.org/0000-0002-7184-744X
Jules Claeys https://orcid.org/0000-0001-8397-2822
Mauricio P. Contreras https://orcid.org/0000-0001-6002-0730
Sophien Kamoun https://orcid.org/0000-0002-0290-0315
Clemence Marchal https://orcid.org/0000-0003-1669-3270
Hsuan Pai https://orcid.org/0000-0002-7284-6131
Rebecca Thompson https://orcid.org/0009-0006-6734-2138

## Data availability

All relevant data are within the article and in the Supporting Information. This study includes no data that would need to be deposited in external repositories.

## References

**Adachi H, Contreras MP, Harant A, Wu C-h, Derevnina L, Sakai T, Duggan C, Moratto E, Bozkurt TO, Maqbool A *et al.* 2019a.** An N-terminal motif in NLR immune receptors is functionally conserved across distantly related plant species. *eLife* **8**: e49956.

**Adachi H, Derevnina L, Kamoun S. 2019b.** NLR singletons, pairs, and networks: evolution, assembly, and regulation of the intracellular immunoreceptor circuitry of plants. *Current Opinion in Plant Biology* **50**: 121–131.

**Adachi H, Kamoun S. 2022.** NLR receptor networks in plants. *Essays in Biochemistry* **66**: 541–549.

**Ahn HK, Lin X, Olave-Achury AC, Derevnina L, Contreras MP, Kourelis J, Wu CH, Kamoun S, Jones JD. 2023.** Effector-dependent activation and oligomerization of plant NRC class helper NLRs by sensor NLR immune receptors Rpi-amr3 and Rpi-amr1. *EMBO Journal* **42**: e111484.

**Bendahmane A, Kanyuka K, Baulcombe DC. 1999.** The Rx gene from potato controls separate virus resistance and cell death responses. *Plant Cell* **11**: 781–791.

**Bendahmane A, Köhm BA, Dedi C, Baulcombe DC. 1995.** The coat protein of *potato virus X* is a strain-specific elicitor of Rx1-mediated virus resistance in potato. *The Plant Journal* **8**: 933–941.

**Bentham AR, Zdrzałek R, De la Concepcion JC, Banfield MJ. 2018.** Uncoiling CNLs: structure/function approaches to understanding CC domain function in plant NLRs. *Plant and Cell Physiology* **59**: 2398–2408.

**Bi G, Su M, Li N, Liang Y, Dang S, Xu J, Hu M, Wang J, Zou M, Deng Y. 2021.** The ZAR1 resistosome is a calcium-permeable channel triggering plant immune signaling. *Cell* **184**: 3528–3541.

**Chen X, Zhu M, Jiang L, Zhao W, Li J, Wu J, Li C, Bai B, Lu G, Chen H *et al.* 2016.** A multilayered regulatory mechanism for the autoinhibition and activation of a plant CC-NB-LRR resistance protein with an extra N-terminal domain. *New Phytologist* **212**: 161–175.

**Chou W-C, Jha S, Linhoff MW, Ting JP-Y. 2023.** The NLR gene family: from discovery to present day. *Nature Reviews Immunology* **23**: 1–20.

**Contreras MP, Kamoun S. 2022.** The high molecular weight complex formed by the plant immune receptor Rx does not contain host protein RanGAP2. *Zenodo*. doi: 10.5281/zenodo.7398800.

© 2024 The Authors
*New Phytologist* © 2024 New Phytologist Foundation



14698137, 2024, 1, Downloaded from https://nph.onlinelibrary.wiley.com/doi/10.1111/nph.19818 by Test, Wiley Online Library on [02/08/2025]. See the Terms and Conditions (https://onlinelibrary.wiley.com/terms-and-conditions) on Wiley Online Library for rules of use; OA articles are governed by the applicable Creative Commons License

**Contreras MP, Lüdke D, Pai H, Toghani A, Kamoun S. 2023a.** NLR receptors in plant immunity: making sense of the alphabet soup. *EMBO Reports* **24**: e57495.

**Contreras MP, Pai H, Selvaraj M, Toghani A, Lawson DM, Tumtas Y, Duggan C, Yuen ELH, Stevenson CEM, Harant A *et al.* 2023b.** Resurrection of plant disease resistance proteins via helper NLR bioengineering. *Science Advances* **9**: eadg3861.

**Contreras MP, Pai H, Tumtas Y, Duggan C, Yuen ELH, Cruces AV, Kourelis J, Ahn HK, Lee KT, Wu CH *et al.* 2023c.** Sensor NLR immune proteins activate oligomerization of their NRC helpers in response to plant pathogens. *EMBO Journal* **42**: e111519.

**Dangl JL, Jones JD. 2001.** Plant pathogens and integrated defence responses to infection. *Nature* **411**: 826–833.

**De Oliveira AS, Koolhaas I, Boiteux LS, Caldararu OF, Petrescu AJ, Oliveira Resende R, Kormelink R. 2016.** Cell death triggering and effector recognition by Sw-5 SD-CNL proteins from resistant and susceptible tomato isolines to Tomato spotted wilt virus. *Molecular Plant Pathology* **17**: 1442–1454.

**Derevnina L, Contreras MP, Adachi H, Upson J, Vergara Cruces A, Xie R, Skłenar J, Menke FL, Mugford ST, MacLean D *et al.* 2021.** Plant pathogens convergently evolved to counteract redundant nodes of an NLR immune receptor network. *PLoS Biology* **19**: e3001136.

**Duxbury Z, Wu C-h, Ding P. 2021.** A comparative overview of the intracellular guardians of plants and animals: NLRs in innate immunity and beyond. *Annual Review of Plant Biology* **72**: 155–184.

**Engler C, Youles M, Gruetzner R, Ehnert T-M, Werner S, Jones JD, Patron NJ, Marillonnet S. 2014.** A golden gate modular cloning toolbox for plants. *ACS Synthetic Biology* **3**: 839–843.

**Feehan JM, Wang J, Sun X, Choi J, Ahn H-K, Ngou BPM, Parker JE, Jones JDG. 2023.** Oligomerization of a plant helper NLR requires cell-surface and intracellular immune receptor activation. *Proceedings of the National Academy of Sciences, USA* **120**: e2210406120.

**Förderer A, Kourelis J. 2023.** NLR immune receptors: structure and function in plant disease resistance. *Biochemical Society Transactions* **51**: 1473–1483.

**Förderer A, Li E, Lawson AW, Deng Y-n, Sun Y, Logemann E, Zhang X, Wen J, Han Z, Chang J *et al.* 2022.** A wheat resistosome defines common principles of immune receptor channels. *Nature* **610**: 532–539.

**Goh F-J, Huang C-Y, Derevnina L, Wu C-H. 2023.** NRC immune receptor networks show diversified hierarchical genetic architecture across plant lineages. *BioRxiv*. doi: 10.1101/2023.10.25.563953.

**Harant A, Pai H, Sakai T, Kamoun S, Adachi H. 2022.** A vector system for fast-forward studies of the HOPZ-ACTIVATED RESISTANCE1 (ZAR1) resistosome in the model plant *Nicotiana benthamiana*. *Plant Physiology* **188**: 70–80.

**Huang C-Y, Huang Y-S, Sugihara Y, Wang H-Y, Huang L-T, Lopez-Agudelo JC, Chen Y-F, Lin K-Y, Chiang B-J, Toghani A. 2023.** Functional divergence shaped the network architecture of plant immune receptors. *BioRxiv*. doi: 10.1101/2023.12.12.571219.

**Huang S, Jia A, Song W, Hessler G, Meng Y, Sun Y, Xu L, Laessle H, Jirschitzka J, Ma S. 2022.** Identification and receptor mechanism of TIR-catalyzed small molecules in plant immunity. *Science* **377**: eabq3297.

**Jia A, Huang S, Song W, Wang J, Meng Y, Sun Y, Xu L, Laessle H, Jirschitzka J, Hou J *et al.* 2022.** TIR-catalyzed ADP-ribosylation reactions produce signaling molecules for plant immunity. *Science* **377**: 8180.

**Kourelis J, Contreras MP, Harant A, Pai H, Lüdke D, Adachi H, Derevnina L, Wu C-H, Kamoun S. 2022.** The helper NLR immune protein NRC3 mediates the hypersensitive cell death caused by the cell-surface receptor Cf-4. *PLoS Genetics* **18**: e1010414.

**Kourelis J, Marchal C, Posbeyikian A, Harant A, Kamoun S. 2023.** NLR immune receptor–nanobody fusions confer plant disease resistance. *Science* **379**: 934–939.

**Kourelis J, Sakai T, Adachi H, Kamoun S. 2021.** RefPlantNLR is a comprehensive collection of experimentally validated plant disease resistance proteins from the NLR family. *PLoS Biology* **19**: e3001124.

**Lin X, Olave-Achury A, Heal R, Pais M, Witek K, Ahn H-K, Zhao H, Bhanvadia S, Karki HS, Song T *et al.* 2022.** A potato late blight resistance gene protects against multiple Phytophthora species by recognizing a broadly conserved RXLR-WY effector. *Molecular Plant* **15**: 1457–1469.

**Liu F, Yang Z, Wang C, Martin R, Qiao W, Carette JE, Luan S, Nogales E, Staskawicz B. 2023.** The activated plant NRC4 immune receptor forms a hexameric resistosome. *BioRxiv*. doi: 10.1101/2023.12.18.571367.

**Ma S, Lapin D, Liu L, Sun Y, Song W, Zhang X, Logemann E, Yu D, Wang J, Jirschitzka J *et al.* 2020.** Direct pathogen-induced assembly of an NLR immune receptor complex to form a holoenzyme. *Science* **370**: eabe3069.

**Marchal C, Pai H, Kamoun S, Kourelis J. 2022.** Emerging principles in the design of bioengineered made-to-order plant immune receptors. *Current Opinion in Plant Biology* **10**: 102311.

**Mestre P, Baulcombe DC. 2006.** Elicitor-mediated oligomerization of the tobacco N disease resistance protein. *Plant Cell* **18**: 491–501.

**Meyers BC, Shen KA, Rohani P, Gaut BS, Michelmore RW. 1998.** Receptor-like genes in the major resistance locus of lettuce are subject to divergent selection. *Plant Cell* **10**: 1833–1846.

**Moffett P, Farnham G, Peart J, Baulcombe DC. 2002.** Interaction between domains of a plant NBS–LRR protein in disease resistance-related cell death. *EMBO Journal* **21**: 4511–4519.

**Rairdan GJ, Collier SM, Sacco MA, Baldwin TT, Boettrich T, Moffett P. 2008.** The coiled-coil and nucleotide binding domains of the potato Rx disease resistance protein function in pathogen recognition and signaling. *Plant Cell* **20**: 739–751.

**Sacco MA, Mansoor S, Moffett P. 2007.** A RanGAP protein physically interacts with the NB-LRR protein Rx, and is required for Rx-mediated viral resistance. *The Plant Journal* **52**: 82–93.

**Sakai T, Martinez-Anaya C, Contreras MP, Kamoun S, Wu C-H, Adachi H. 2023.** The NRC0 gene cluster of sensor and helper NLR immune receptors is functionally conserved across asterid plants. *BioRxiv*. doi: 10.1101/2023.10.23.563533.

**Selvaraj M, Toghani A, Pai H, Sugihara Y, Kourelis J, Yuen ELH, Ibrahim T, Zhao H, Xie R, Maqbool A *et al.* 2023.** Activation of plant immunity through conversion of a helper NLR homodimer into a resistosome. *BioRxiv*. doi: 10.1101/2023.12.17.572070.

**Shen KA, Chin DB, Arroyo-Garcia R, Ochoa OE, Lavelle DO, Wroblewski T, Meyers BC, Michelmore RW. 2002.** Dm3 is one member of a large constitutively expressed family of nucleotide binding site—leucine-rich repeat encoding genes. *Molecular Plant–Microbe Interactions* **15**: 251–261.

**Tameling WI, Baulcombe DC. 2007.** Physical association of the NB-LRR resistance protein Rx with a Ran GTPase–activating protein is required for extreme resistance to *Potato virus X*. *Plant Cell* **19**: 1682–1694.

**Van Der Biezen EA, Jones JD. 1998.** Plant disease-resistance proteins and the gene-for-gene concept. *Trends in Biochemical Sciences* **23**: 454–456.

**van der Hoorn RA, Kamoun S. 2008.** From guard to decoy: a new model for perception of plant pathogen effectors. *Plant Cell* **20**: 2009–2017.

**Wang J, Hu M, Wang J, Qi J, Han Z, Wang G, Qi Y, Wang H-W, Zhou J-M, Chai J. 2019.** Reconstitution and structure of a plant NLR resistosome conferring immunity. *Science* **364**: eaav5870.

**Weber E, Engler C, Gruetzner R, Werner S, Marillonnet S. 2011.** A modular cloning system for standardized assembly of multigene constructs. *PLoS ONE* **6**: e16765.

**Witek K, Lin X, Karki HS, Jupe F, Witek AI, Steuernagel B, Stam R, Van Oosterhout C, Fairhead S, Heal R. 2021.** A complex resistance locus in *Solanum americanum* recognizes a conserved Phytophthora effector. *Nature Plants* **7**: 198–208.

**Wróblewski T, Spiridon L, Martin EC, Petrescu A-J, Cavanaugh K, Truco MJ, Xu H, Gozdowski D, Pawłowski K, Michelmore RW. 2018.** Genome-wide functional analyses of plant coiled–coil NLR-type pathogen receptors reveal essential roles of their N-terminal domain in oligomerization, networking, and immunity. *PLoS Biology* **16**: e2005821.

**Wu C-H, Abd-El-Haliem A, Bozkurt TO, Belhaj K, Terauchi R, Vossen JH, Kamoun S. 2017.** NLR network mediates immunity to diverse plant pathogens. *Proceedings of the National Academy of Sciences, USA* **114**: 8113–8118.

**Wu C-H, Derevnina L, Kamoun S. 2018.** Receptor networks underpin plant immunity. *Science* **360**: 1300–1301.

**Zeng L, Zhang Q, Sun R, Kong H, Zhang N, Ma H. 2014.** Resolution of deep angiosperm phylogeny using conserved nuclear genes and estimates of early divergence times. *Nature Communications* **5**: 4956.



© 2024 The Authors
*New Phytologist* © 2024 New Phytologist Foundation

14698137, 2024, 1, Downloaded from https://nph.onlinelibrary.wiley.com/doi/10.1111/nph.19818 by Test, Wiley Online Library on [02/08/2025]. See the Terms and Conditions (https://onlinelibrary.wiley.com/terms-and-conditions) on Wiley Online Library for rules of use; OA articles are governed by the applicable Creative Commons License

**Zhang L, Chen S, Ruan J, Wu J, Tong AB, Yin Q, Li Y, David L, Lu A, Wang WL. 2015.** Cryo-EM structure of the activated NAIP2-NLRC4 inflammasome reveals nucleated polymerization. *Science* **350**: 404–409.

**Zhao Y-B, Liu M-X, Chen T-T, Ma X, Li Z-K, Zheng Z, Zheng S-R, Chen L, Li Y-Z, Tang L-R. 2022.** Pathogen effector AvrSr35 triggers Sr35 resistosome assembly via a direct recognition mechanism. *Science Advances* **8**: eabq5108.

## Supporting Information

Additional Supporting Information may be found online in the Supporting Information section at the end of the article.

**Fig. S1** The cell death triggered by expression of Rx halves *in trans* upon perception of the coat protein (CP) of *Potato virus X* is dependent on NRC2, NRC3 or NRC4.

**Fig. S2** SDS-PAGE blots accompanying BN-PAGE assays in Fig. 2.

**Fig. S3** Cell death triggered by $Rx^{NB}$-eGFP does not require an intact p-loop.

**Fig. S4** $Rx^{NB}$-mCherry-6xHA also triggers NRC2/3/4-dependent cell death.

**Fig. S5** SDS-PAGE blots accompanying BN-PAGE assays in Fig. 3.

**Fig. S6** Amino acid sequence alignment of the NB domains of the sensor NLRs Rx, Gpa2, Bs2, Rpi-amr1e, Rpi-amr3, Rpi-blb2, Mi-1.2 and Sw-5b.

**Fig. S7** The NB domains of the sensor NLRs Gpa2, Rpi-amr1e, Rpi-amr3 and Sw-5b are sufficient to activate downstream NRC helpers.

**Fig. S8** The full-length sensor NLR Gpa2 can signal through NRC2 and NRC4.

Please note: Wiley is not responsible for the content or functionality of any Supporting Information supplied by the authors. Any queries (other than missing material) should be directed to the *New Phytologist* Central Office.

© 2024 The Authors
*New Phytologist* © 2024 New Phytologist Foundation



14698137, 2024, 1, Downloaded from https://nph.onlinelibrary.wiley.com/doi/10.1111/nph.19818 by Test, Wiley Online Library on [02/08/2025]. See the Terms and Conditions (https://onlinelibrary.wiley.com/terms-and-conditions) on Wiley Online Library for rules of use; OA articles are governed by the applicable Creative Commons License

Check for updates

Article

SOURCE DATA | TRANSPARENT PROCESS | OPEN ACCESS

THE EMBO JOURNAL

# Sensor NLR immune proteins activate oligomerization of their NRC helpers in response to plant pathogens

Mauricio P Contreras[1], Hsuan Pai[1], Yasin Tumtas[2], Cian Duggan[2], Enoch Lok Him Yuen[2], Angel Vergara Cruces[1,†], Jiorgos Kourelis[1], Hee-Kyung Ahn[1], Kim-Teng Lee[3], Chih-Hang Wu[3], Tolga O Bozkurt[2], Lida Derevnina[1,*,‡] & Sophien Kamoun[1,**]

## Abstract

**Nucleotide-binding domain leucine-rich repeat (NLR) immune receptors are important components of plant and metazoan innate immunity that can function as individual units or as pairs or networks. Upon activation, NLRs form multiprotein complexes termed resistosomes or inflammasomes. Although metazoan paired NLRs, such as NAIP/NLRC4, form hetero-complexes upon activation, the molecular mechanisms underpinning activation of plant paired NLRs, especially whether they associate in resistosome hetero-complexes, is unknown. In asterid plant species, the NLR required for cell death (NRC) immune receptor network is composed of multiple resistance protein sensors and downstream helpers that confer immunity against diverse plant pathogens. Here, we show that pathogen effector-activation of the NLR proteins Rx (confers virus resistance), and Bs2 (confers bacterial resistance) leads to oligomerization of their helper NLR, NRC2. Activated Rx does not oligomerize or enter into a stable complex with the NRC2 oligomer and remains cytoplasmic. In contrast, activated NRC2 oligomers accumulate in membrane-associated puncta. We propose an activation-and-release model for NLRs in the NRC immune receptor network. This points to a distinct activation model compared with mammalian paired NLRs.**

**Keywords** immune receptor; inflammasome; NB-LRR; NOD-like receptor; resistosome

**Subject Category** Plant Biology

**DOI** 10.15252/embj.2022111519 | Received 26 April 2022 | Revised 25 November 2022 | Accepted 2 December 2022 | Published online 29 December 2022

**The EMBO Journal (2023) 42: e111519**

## Introduction

A class of intracellular immune receptors, known as NLRs (nucleotide-binding domain and leucine-rich repeat receptors), are key components of the innate immune systems of plants and metazoan. NLRs play an important role in mediating pathogen recognition and subsequent immune responses (Jones *et al*, 2016; Duxbury *et al*, 2021). In plants, NLRs can activate host defense by recognizing pathogen secreted virulence proteins, termed effectors. This recognition leads to immune signaling, often culminating in a form of programmed cell death known as the hypersensitive response (Jones & Dangl, 2006; Kourelis & Van Der Hoorn, 2018; Ngou *et al*, 2022). Similarly, metazoan NLRs are capable of sensing pathogen effectors and other classes of pathogen derived molecules, ultimately leading to a form of programmed cell death known as pyroptosis (Maekawa *et al*, 2011; Duxbury *et al*, 2016). Some plant and metazoan NLRs can function as single units, with one NLR protein mediating both effector/elicitor perception and subsequent downstream signaling. These are referred to as functional singleton NLRs (Adachi *et al*, 2019a, 2019b). However, NLRs can also function as genetically linked receptor pairs or in higher order configurations that can include genetically unlinked receptor networks (Wu *et al*, 2017, 2018). In these cases, the sensing and signaling functions are uncoupled in two distinct proteins. One NLR acts as the pathogen sensor, requiring a second NLR which acts as a helper (or executor) to mediate immune activation and disease resistance (Wu *et al*, 2018; Adachi *et al*, 2019b; Feehan *et al*, 2020). Although much progress has been made in recent years regarding the biochemical mechanisms of how singleton NLRs activate and signal (Wang *et al*, 2019a; Ma *et al*, 2020; Martin *et al*, 2020; preprint: Förderer *et al*, 2022), our understanding of how paired and networked NLRs operate remains limited.

1 The Sainsbury Laboratory, University of East Anglia, Norwich, UK
2 Department of Life Sciences, Imperial College, London, UK
3 Institute of Plant and Microbial Biology, Academia Sinica, Taipei, Taiwan
*Corresponding author. Tel: +44 0 1223 342200; E-mail: ld645@cam.ac.uk
**Corresponding author. Tel: +44 0 1603 450410; E-mail: sophien.kamoun@tsl.ac.uk
†Present Address: John Innes Centre, University of East Anglia, Norwich, UK
‡Present Address: Department of Plant Sciences, Crop Science Centre, University of Cambridge, Cambridge, UK

© 2022 The Authors. Published under the terms of the CC BY 4.0 license.



Downloaded from https://www.embopress.org on August 2, 2025 from IP 78.145.55.37.

Plant and metazoan NLRs belong to the signal transduction ATPases with numerous domains (STAND) superfamily. They usually exhibit a modular, tri-partite structure with an N-terminal signaling domain, a central nucleotide binding domain and a C-terminal domain with superstructure forming repeats (Kim *et al*, 2016; Duxbury *et al*, 2021; Kourelis *et al*, 2021b). The N-terminal domains of NLRs can broadly be used to classify these receptors into distinct groups which, in plants, tend to also cluster together in phylogenetic analyses. Plant NLR N-terminal domains can be either coiled-coil-type (CC) NLRs, G10-type CC ($CC_{G10}$) NLRs, RPW8-type CC ($CC_R$) NLRs or toll/interleukin-1 receptor-type (TIR) NLRs, whereas metazoan NLRs usually exhibit either N-terminal PYRIN or caspase recruitment domains (CARD) (Lechtenberg *et al*, 2014; Kim *et al*, 2016; Lee *et al*, 2021; Kourelis *et al*, 2021b). The central nucleotide binding domain is the defining feature of NLRs and is typically a nucleotide-binding adaptor shared by APAF-1, plant R proteins and CED-4 (NB-ARC) domain in plants, while metazoan NLRs can have either an NB-ARC or a NAIP, C2TA, HET-E and TP1 (NACHT) domain. As for their superstructure forming repeats, these can be either leucine-rich repeats (LRR) or tetratricopeptide repeats (TPR) (Duxbury *et al*, 2021; Kourelis *et al*, 2021b).

While the general principles of how NLRs sense their ligands are well-understood (Kourelis & Van Der Hoorn, 2018; Ngou *et al*, 2022), our knowledge of the molecular mechanisms that underpin NLR activation and signaling are more limited. In the case of mammalian NLRs, activation leads to oligomerization and formation of higher order wheel-like complexes, termed inflammasomes. Inflammasomes ultimately recruit caspases which act as the final executors of programmed cell-death (Lechtenberg *et al*, 2014; Kim *et al*, 2016). In contrast, the mechanisms of plant NLR activation were not well understood until the recent elucidation of the structure of inactive and activated ZAR1, a conserved singleton CC-NLR from Arabidopsis (Wang *et al*, 2019a, 2019b; preprint: Adachi *et al*, 2022). The activation of ZAR1 upon recognition of its cognate effectors both *in vitro* and *in vivo* leads to its oligomerization and formation of a higher-order pentameric homo-complex analogous to the inflammasome and coined as the resistosome (Wang *et al*, 2019a, 2019b; Hu *et al*, 2020). Oligomerization based activation mechanisms have also been observed *in vivo* for the plant singleton CC-NLR RPP7 and the $CC_R$-NLR helper NRG1.1 (Li *et al*, 2020; preprint: Jacob *et al*, 2021). More recently, the structure of the activated wheat CC-NLR Sr35 pentameric resistosome suggests that this activation strategy is likely evolutionarily conserved across plant CC-NLRs (preprint: Förderer *et al*, 2022). The activated complexes of CC-NLRs and $CC_R$-NLRs act as $Ca^{2+}$-permeable membrane-associated pores upon complex formation, an activity that is required for the hypersensitive cell death (Bi *et al*, 2021; Duggan *et al*, 2021; preprint: Jacob *et al*, 2021; Ngou *et al*, 2021; preprint: Förderer *et al*, 2022). Despite these advances, the molecular mechanisms of paired and networked plant CC-NLR activation are poorly understood. In the case of Pia (RGA4 and RGA5), immune signaling is activated through release of negative regulation (Césari *et al*, 2014). In contrast, the Pik-1 and Pik-2 pair is activated via receptor cooperation by forming a tri-partite complex with the pathogen effector (Zdrzałek *et al*, 2020; De la Concepcion *et al*, 2021). However, whether sensor and helper NLRs engage in heteromeric resistosome complexes is unknown.

Networked NLR immune signaling architectures present many advantages to plant and metazoan immune systems, likely contributing to their robustness and enhancing their evolvability in the face of highly adaptable pathogens (Wu *et al*, 2018). In mammals, multiple different NAIP sensor NLRs can perceive distinct immune elicitors and switch to an active conformation, contributing to immunity. Following activation, NAIPs require the helper NLR NLRC4 to mediate downstream signaling (Kofoed & Vance, 2011; Zhao *et al*, 2011; Vance, 2015). NAIP2 is one of these sensors. Upon perception of its cognate effector, NAIP2 initiates sensor-helper signaling via the formation of a heterocomplex with NLRC4 (Qu *et al*, 2012). This NAIP2/NLRC4 heterocomplex acts as a nucleation point for multiple NLRC4 monomers that leads to the formation of a NAIP/NLRC4 inflammasome with multiple additional NLRC4 units (Hu *et al*, 2015; Zhang *et al*, 2015). Similar networked signaling architectures have also been described in plants. In asterid flowering plants, a major phylogenetic cluster of CC-NLRs known as the NRC superclade comprises an immune receptor network with multiple sensor NLRs and downstream helper NLRs (Wu *et al*, 2017). This network mediates immunity against a wide array of plant pathogens including oomycetes, nematodes, aphids, bacteria and viruses and includes many well characterized and agronomically important sensor NLRs (Wu *et al*, 2017; Derevnina *et al*, 2021). All sensors in the NRC network signal, often redundantly, through a downstream hub of helper NRCs to mediate cell death and disease resistance. NRC helpers contain a key signature in the α-1 helix of their N-termini known as the MADA motif, which is crucial for mediating cell death. This motif is conserved in around 20% of angiosperm CC-NLRs and is functionally conserved between ZAR1, Sr35 and the NRCs, which suggests that the "death switch mechanism" characterized for the ZAR1 resistosome may apply to NRCs as well (Adachi *et al*, 2019a; Kourelis *et al*, 2021a; preprint: Förderer *et al*, 2022). Considering how widespread and vital this immune network is for several crop species, developing a better mechanistic understanding of how it functions is critical. However, how sensor and helper NLR pairs communicate and initiate immune responses is not understood.

In this study, we explore the mechanism of activation of a sensor/helper CC-NLR pair. We selected the NRC-dependent sensor CC-NLR Rx as a model experimental system. Rx is an agronomically important sensor NLR from potato (*Solanum tuberosum)* that confers resistance to *Potato virus X* (PVX), a single-stranded RNA filamentous plant virus, by recognizing its coat protein (CP) (Bendahmane *et al*, 1995, 1999; Grinzato *et al*, 2020). Prior to activation, Rx is held in an inactive state by intramolecular autoinhibitory interactions between its LRR domain and its CC and NB-ARC domains (Moffett *et al*, 2002; Rairdan & Moffett, 2006). Upon CP-triggered activation, Rx undergoes intramolecular rearrangements that include the release of LRR autoinhibition and the exposure of its NB-ARC domain, leading to its activation (Moffett *et al*, 2002). We previously showed that in order to mediate hypersensitive cell death and disease resistance, Rx and other sensors in the NRC network genetically require their downstream NRC helpers, with different sensors exhibiting different NRC helper specificities (Wu *et al*, 2017; Derevnina *et al*, 2021). Rx and the wild pepper (*Capsicum chacoense*) NLR Bs2, for example, can signal interchangeably via NRC2, NRC3 or NRC4. In contrast, the *Solanum bulbocastanum* NLR Rpi-blb2 which confers resistance to *Phytophthora*

Downloaded from https://www.embopress.org on August 2, 2025 from IP 78.145.55.37.

 © 2022 The Authors

*infestans* strains carrying AVRblb2, can only signal through NRC4 (Appendix Fig S1A). However, the mechanisms by which sensor NLRs signal through NRCs are still not understood. Similar to the mammalian NAIP/NLRC4 system, Rx could be forming distinct Rx/NRC higher order hetero-resistosomes with each of its three NRC helpers, reminiscent of the NAIP/NLRC4 inflammasomes (Adachi *et al*, 2019b). Alternatively, plants may feature distinct activation mechanisms for paired and networked NLRs than those previously shown in mammalian paired systems. How activation of sensor NLRs translates into helper activation, immune signaling and disease resistance remains an important question in plant immunology.

To dissect the biochemical mechanisms that underpin Rx and NRC activation, we established a resistosome formation assay using Blue Native polyacrylamide gel electrophoresis (BN-PAGE) by taking advantage of NRC proteins mutated in the MADA motif that are activated without triggering plant cell death. We demonstrate Rx-mediates oligomerization of its NRC2 helper in *Nicotiana benthamiana* following virus perception. Our data suggest that the activated NRC2 complex is an NRC2 resistosome that does not include Rx. Confocal live cell imaging and membrane fractionation assays reveal a sub-cellular shift in localization for NRC2 upon resistosome formation, moving from the cell cytoplasm to the plasma membrane to form membrane-associated punctate structures. This points to an activation-and-release model for sensor-helper signaling in the NRC network, whereby Rx can trigger NRC oligomerization without stably forming part of the activated helper complex. Notably, this model is distinct from the hetero-complexes shown for mammalian NLR paired systems, such as NAIP/NLRC4, implying that plant and metazoan NLR pairs exhibit different activation strategies.

## Results

### Activation of Rx with *Potato virus X* coat protein leads to oligomerization of its helper NRC2

Prior biochemical *in vivo* studies of activated NLRs have been hampered by the cell death response initiated upon receptor activation. We hypothesized that we could leverage MADA motif mutations in the very N-terminal α1 helix which abolish cell death induction without compromising resistosome formation (Adachi *et al*, 2019a; Hu *et al*, 2020; Duggan *et al*, 2021; preprint: Förderer *et al*, 2022) (Fig 1A). We previously showed that NRC2 is a MADA-type NLR with a conserved motif in its N-terminus, which is required for the execution of cell death and immune signaling. Making mutations in the N-terminal MADA motif of NRC4 completely abolishes NRC4 mediated cell death without affecting protein stability (Adachi *et al*, 2019a; Kourelis *et al*, 2021a). To this end, we created MADA mutations in NRC2 analogous to those previously made in NRC4, to generate an NRC2$^{L9/13/17\ E}$ MADA motif mutant (NRC2$^{EEE}$) (Fig 1A). Like the previously characterized NRC4 mutants, NRC2$^{EEE}$ is unable to functionally complement hypersensitive cell death upon co-expression of effector-activated NRC2-dependent sensors in *nrc2/3/4 N. benthamiana* CRISPR lines (Appendix Fig S1B).

We subsequently leveraged Rx and NRC2$^{EEE}$ to determine the oligomeric state of the sensor and helper upon effector-triggered activation *in vivo*. To achieve this, we transiently expressed these proteins by agroinfiltration in the absence or presence of PVX CP in leaves of *nrc2/3/4 N. benthamiana* CRISPR lines and subjected total protein extracts to BN-PAGE assays (Fig 1B). In its inactive state NRC2$^{EEE}$ appears as a fast-migrating band of ~ 200 kDa, regardless of the presence or absence of Rx (Fig 1C). Upon activating the system by co-expressing Rx and NRC2$^{EEE}$ together with C-terminally tagged CP-GFP, but not upon co-expression of free GFP as a negative control, NRC2 shifts to a slower-migrating, high-molecular-weight complex with two bands in the 720 to 1,048 kDa range (Fig 1C). While we consistently observe this two-band pattern, with a lower molecular weight band of ~ 750 kDa and a higher molecular weight band of ~ 900 kDa, the ~ 900 kDa band is more abundant. This shift to a higher molecular weight complex upon activation of the system is reminiscent of the ZAR1 resistosome formation documented *in vivo* (Hu *et al*, 2020), suggesting that NRC2 may exhibit a similar mechanism of oligomerization and resistosome formation upon activation. The formation of this higher order NRC2 complex is dependent on the presence of Rx, as in the absence of the upstream sensor, co-expression with CP does not result in oligomerization of NRC2$^{EEE}$ or any other apparent change in molecular weight when compared with in the absence of CP (Fig 1C). We conclude that Rx is able and required to mediate NRC2 oligomerization upon CP-triggered activation.

We reproduced the BN-PAGE assays as described above with the wild-type NRC2 carrying an intact N-terminal α1 helix. Because of

**Figure 1. Activation of Rx with *Potato virus X* coat protein leads to NRC2 oligomerization.**

A Structure of the AtZAR1 resistosome, highlighting the N-terminal α1 helix. Much like AtZAR1 and NRC4, the N-terminal α1 helix encodes a MADA motif. Alignment of NRC2, NRC4 and AtZAR1 N-terminal MADA motifs along with the consensus sequence pattern for the motif and the HMM score for MADA prediction of each sequence. Residues mutated in NRC2$^{EEE}$ mutant are highlighted with red asterisks (positions 9, 13 and 17, respectively).

B Schematic representation of the experimental pipeline used. *Agrobacterium tumefaciens* strains were used to transiently express proteins of interest in leaves of *nrc2/3/4 Nicotiana benthamiana* CRISPR mutant lines by agroinfiltration. Leaf tissue was harvested 3 days post-infiltration and total protein extracts were used for BN and SDS–PAGE assays.

C BN-PAGE and SDS–PAGE assays with inactive and activated Rx-NRC2. C-terminally 6xHA tagged Rx and C-terminally 4xMyc-tagged NRC2$^{EEE}$ were co-expressed with either free GFP or C-terminally GFP-tagged CP. Free mCherry-4xMyc and mCherry-6xHA fusions were used as controls in the treatments without NRC2 and Rx, respectively. Total protein was extracted with a Tris–HCl-based buffer, as described in materials and methods. Extracts were run on native and denaturing PAGE assays in parallel and immunoblotted with the appropriate antisera labeled on the left. Approximate molecular weights (kDa) of the proteins are shown on the right. Red asterisks indicate bands corresponding to the activated NRC2 complex. Rubisco loading control was carried out using Ponceau stain (PS). The experiment was repeated three times.

Source data are available online for this figure.

Downloaded from https://www.embopress.org on August 2, 2025 from IP 78.145.55.37.

© 2022 The Authors

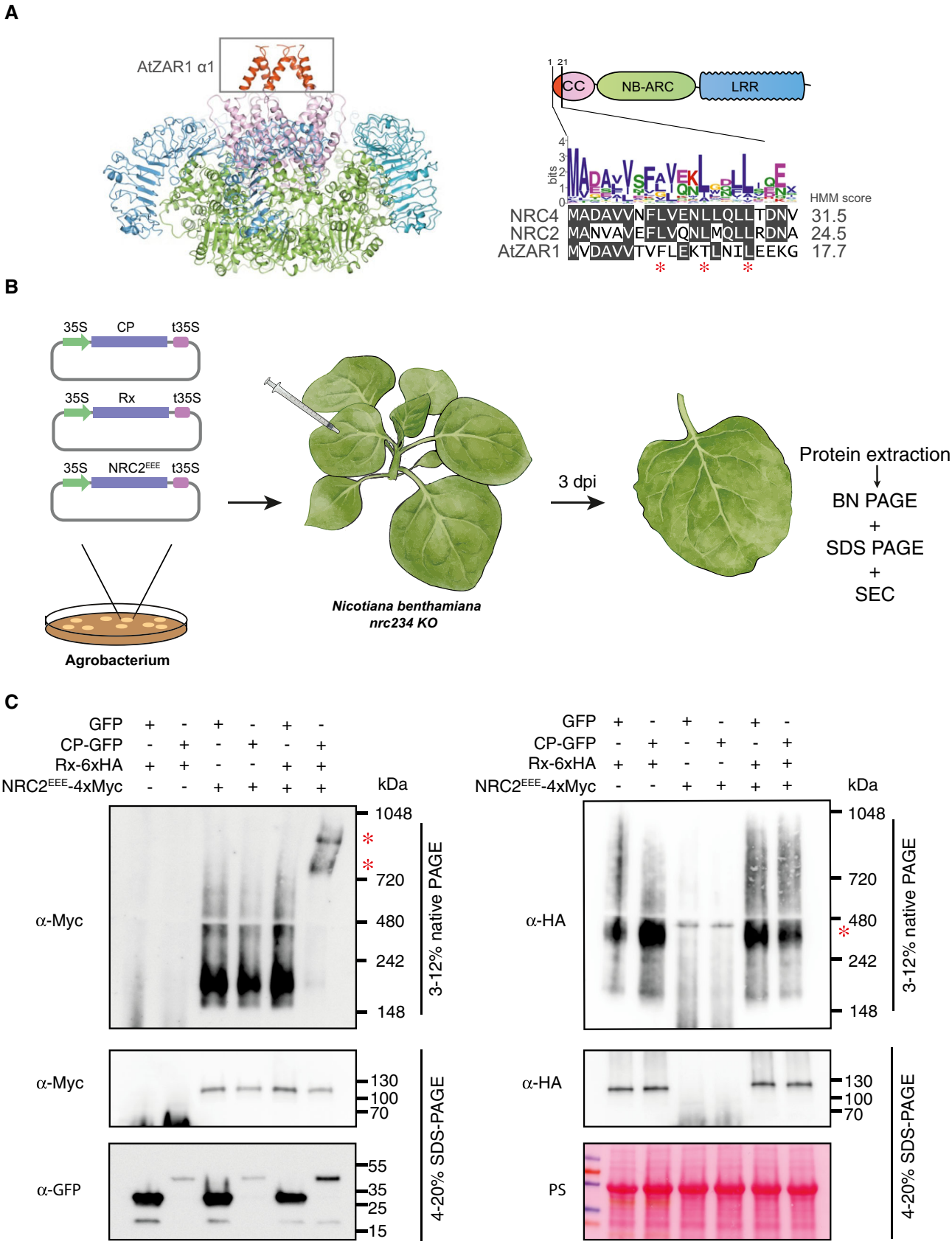


**Figure 1.**

Downloaded from https://www.embopress.org on August 2, 2025 from IP 78.145.55.37.


© 2022 The Authors

the early onset of cell death triggered upon NRC2 activation, we harvested tissue at the latest timepoint possible before confluent necrosis is observed (38 h post infiltration). Probing for NRC2 in these assays revealed a similar oligomerization pattern to what we observed for NRC2$^{EEE}$ (Fig EV1). However, likely due to the ongoing cell death, protein accumulation of NRC2, Rx and CP was reduced compared with the NRC2$^{EEE}$ treatments. Therefore, we decided to move forward with NRC2$^{EEE}$ for subsequent experiments to mitigate the effects of cell death.

#### Rx does not oligomerize following activation by CP

In the BN-PAGE assays performed above, we observed that the sensor Rx constitutively migrates as a band of ~ 400 kDa, regardless of its activation state (Figs 1B and EV1). Interestingly, the presence of this ~ 400 kDa band does not depend on the presence of NRC2$^{EEE}$ in *N. benthamiana nrc2/3/4* CRISPR lines, suggesting that it is unlikely to be a preformed complex between Rx or any endogenous NRC2, NRC3 or NRC4. Considering that the size of a single Rx-6xHA monomer is expected to be ~ 115 kDa, we hypothesized that the ~ 400 kDa band observed for Rx in BN-PAGE assays could correspond to a preformed Rx complex with additional host proteins, such as RanGAP2, as has been previously reported (Tameling & Baulcombe, 2007). Rx could also potentially constitutively self-associate, forming a larger complex of multiple sensor units. We did not observe any shifts in size for Rx upon activation of the system with CP (Fig 1C). This is in line with previous reports that CP and Rx do not form a stable complex (Tameling & Baulcombe, 2007). Furthermore, we were unable to detect any signal for Rx at a size matching the activated higher molecular weight NRC2$^{EEE}$ complex described above, suggesting that Rx does not form a stable part of this activated NRC2 complex (Fig 1C). This implies an activation mechanism that differs from the hetero-oligomeric inflammasome previously reported for mammalian paired NLRs.

To independently validate the BN-PAGE experiments using a different analytical method, we performed gel filtration assays on protein extracts from leaves of *nrc2/3/4 N. benthamiana* CRISPR lines expressing Rx and NRC2$^{EEE}$ in the absence or presence of PVX CP. Proteins of interest were detected in the resulting fractions by SDS–PAGE analysis and immunoblotting with corresponding antibodies. Inactive NRC2$^{EEE}$ migrated mostly as a small molecular mass complex, eluting at around 15 mL, while Rx migrated at a slightly higher molecular weight, with most signal eluting at 13 mL (Fig EV2). Consistent with the BN-PAGE assays, upon activation of the system by co-expressing CP-GFP, almost all NRC2$^{EEE}$ exhibited a shift in elution volume, migrating as a large complex. This complex eluted at a size between ~ 440 kDa and ~ 669 kDa, which would be consistent with a pentameric NRC2$^{EEE}$ resistosome complex (~ 550 kDa) (Fig EV2). Rx did not exhibit a shift in elution volume upon activation. We also did not observe an increase in signal for Rx in any of the fractions corresponding to the activated NRC2$^{EEE}$ complex. Our results in both BN-PAGE and gel filtration assays suggest that upon effector perception, Rx can mediate oligomerization of NRC2 into a higher order complex of ~ 550 kDa without stably associating with this complex. As both techniques yielded similar results and given that gel filtration required long sample handling times, we decided to use BN-PAGE as a readout for the remainder of the study.

#### Rx does not form a stable complex with NRC2

To further test the hypothesis that Rx does not form part of the activated NRC2 complex, we decided to use different molecular weight tags to study Rx-NRC2 interactions with size shifts. In previous experiments, we employed C-terminally tagged Rx-6xHA and NRC2$^{EEE}$-4xMyc (from here onwards termed "light" versions) (Fig 2A). We then generated C-terminal tandem tag constructs to generate Rx-mCherry-6xHA and NRC2$^{EEE}$-mCherry-4xMyc (termed "heavy" versions) (Fig 2A). We used these higher molecular weight versions to determine whether the addition of a larger molecular weight tag in one of the Rx-NRC2 system components could induce a shift in size of the other in BN-PAGE assays. We first confirmed that these new "heavy" versions retained the ability to correctly mediate hypersensitive cell death (Appendix Fig S2). When complementing leaves of *nrc2/3/4 N. benthamiana* CRISPR mutant lines with light NRC2$^{EEE}$-4xMyc together with the heavy Rx-mCherry-6xHA, BN-PAGE assays showed no shift in size for NRC2$^{EEE}$, either in the inactive or activated states, relative to light NRC2$^{EEE}$-4xMyc co-expressed with light Rx-6xHA (Fig 2B). Heavy Rx-mCherry-6xHA, in contrast, exhibited a shift in size both on BN-PAGE and SDS–PAGE (Fig 2B). Similarly, co-expression of heavy NRC2$^{EEE}$-mCherry-4xMyc with light Rx-6xHA does not result in a size-shift for Rx in BN-PAGE relative to light NRC2$^{EEE}$-4xMyc co-expressed with light Rx-6xHA. Again, a clear shift in size was observed in both the inactive and activated states for heavy NRC2$^{EEE}$-mCherry-4xMyc relative to light NRC2$^{EEE}$-4xMyc both in BN-PAGE and SDS–PAGE (Fig 2B). All in all, these data suggest that Rx and NRC2 likely do not form stable complexes with each other at resting state, and that following activation by its upstream sensor, NRC2 oligomerizes and forms a higher order complex that does not include Rx.

#### The activated NRC2 complex is composed of multiple NRC2 proteins

Considering that our findings are in line with the hypothesis that Rx does not form part of the active NRC2 complex, we next sought to further characterize the nature of this high-molecular-weight NRC2 complex. To do so, we leveraged the previously used heavy and light tag approach. We postulated that if NRC2 monomers were indeed forming a complex upon activation, a heterogeneous mixture of differently sized NRC2 molecules would lead to a shift in size of the activated complex, relative to homogeneous heavy or light NRC2 complexes. To test this hypothesis, we co-expressed Rx-6xHA with either light NRC2$^{EEE}$-3xFLAG (104 kDa), heavy NRC2$^{EEE}$-mCherry-4xMyc (133 kDa) or a mixture of heavy and light NRC2 variants in leaves of *nrc2/3/4 N. benthamiana* CRISPR mutant lines (Fig 3A). As expected, both the inactive and activated heavy NRC2$^{EEE}$-mCherry-4xMyc exhibited a higher molecular weight than the inactive and activated light NRC2$^{EEE}$-3xFLAG complexes, respectively (Fig 3B). However, upon co-expressing both heavy NRC2$^{EEE}$-mCherry-4xMyc and light NRC2$^{EEE}$-3xFLAG, the activated NRC2 complex was of intermediate molecular weight, relative to either light NRC2$^{EEE}$-3xFLAG or heavy NRC2-mCherry-4xMyc complexes (Fig 3B). The observation that combining differently sized NRC2 variants results in an intermediate molecular weight activated complex suggests that upon activation by Rx, both NRC2 versions are entering a complex. Interestingly, we were unable to see any change in size for inactive NRC2$^{EEE}$ when mixing the two molecular weight variants (Fig 3B).

Downloaded from https://www.embopress.org on August 2, 2025 from IP 78.145.55.37.

© 2022 The Authors

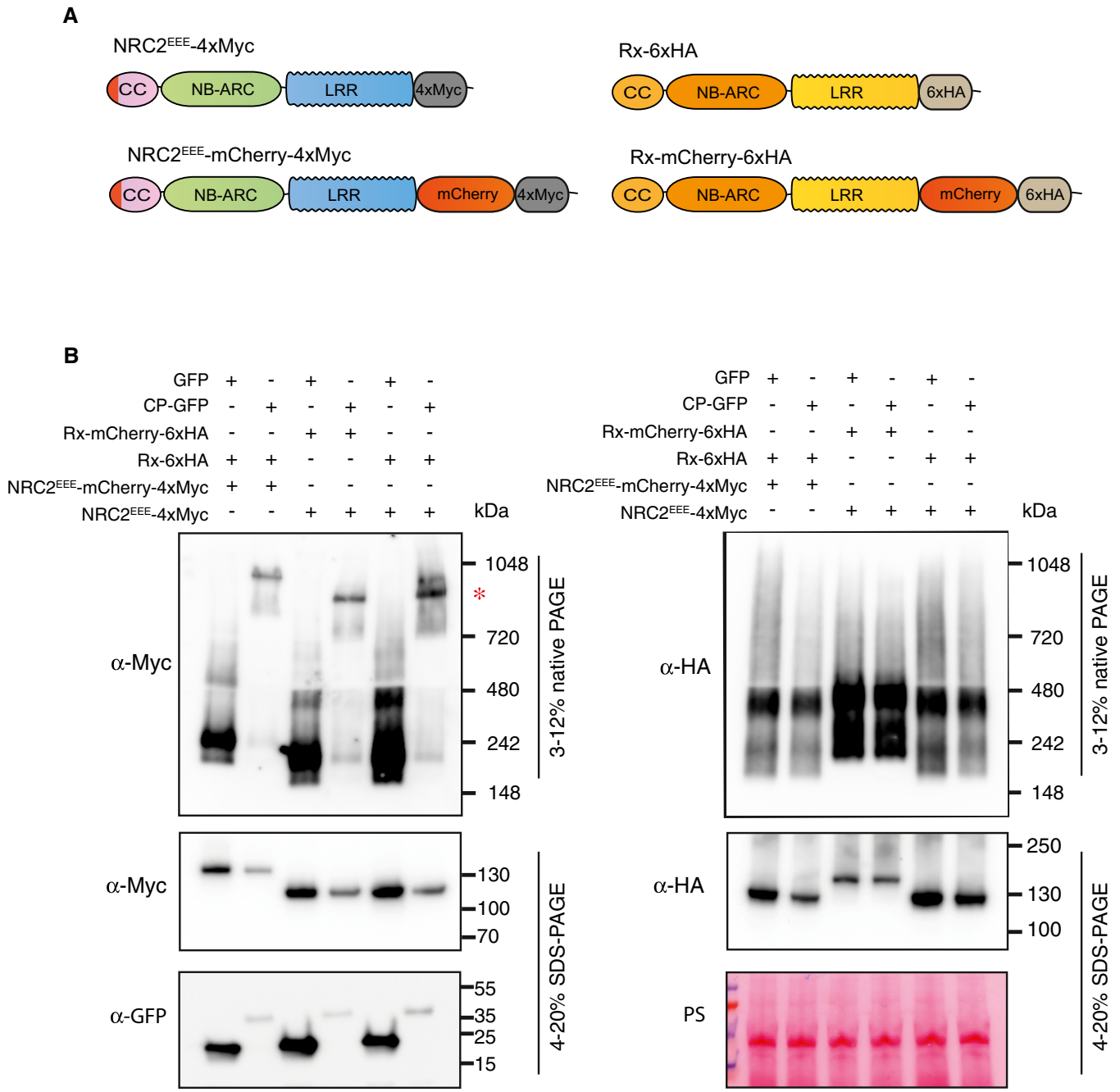


**Figure 2. Rx and NRC2 do not form a stable complex upon activation.**

A Schematic representation of NRC2$^{EEE}$ and Rx with differently sized tags. The C-terminally 4xMyc-tagged NRC2$^{EEE}$ and C-terminally 6xHA tagged Rx used in previous experiments were termed "light" versions, while the new C-terminally tandem mCherry-4xMyc-tagged NRC2$^{EEE}$ and C-terminally mCherry-6xHA-tagged Rx variants were termed "heavy" versions.

B BN-PAGE and SDS–PAGE assays with inactive and activated Rx-NRC2 using different heavy and light sensor-helper combinations. Total protein was extracted with a Tris–HCl-based buffer, as described in materials and methods. Extracts were run on native and denaturing PAGE assays in parallel and immunoblotted with the appropriate antisera labeled on the left. Approximate molecular weights (kDa) of the proteins are shown on the right. Red asterisk indicates bands corresponding to the activated NRC2 complex. Rubisco loading control was carried out using Ponceau stain (PS). The experiment was repeated three times.

Source data are available online for this figure.

We conclude that the fast-migrating lower molecular weight band observed for inactive NRC2 is likely not a complex of multiple NRC2 molecules. This allows us to draw a model for Rx-NRC2 activation in which, following effector-triggered activation, Rx leads to activation of its downstream helper NRC2, which oligomerizes and forms a resistosome complex that includes multiple NRC2 units.

Downloaded from https://www.embopress.org on August 2, 2025 from IP 78.145.55.37.

 © 2022 The Authors

### Bs2, another NRC2-dependent sensor NLR, also triggers oligomerization of NRC2

Since Rx is able to trigger oligomerization of the downstream helper NRC2, we tested whether this applies to other NRC-dependent sensors. We performed complementation assays co-expressing NRC2$^{EEE}$ in leaves of *nrc2/3/4 N. benthamiana* CRISPR mutants along with the inactive or activated NRC2/3/4-dependent sensor Bs2, or Rpi-blb2, an NRC4-dependent sensor that is unable to signal through NRC2 (Fig 4A) (Wu *et al*, 2017; Duggan *et al*, 2021). In addition, all three C-terminally 6xHA-tagged sensors were tested in cell death assays to ensure that tagging did not interfere with effector-triggered

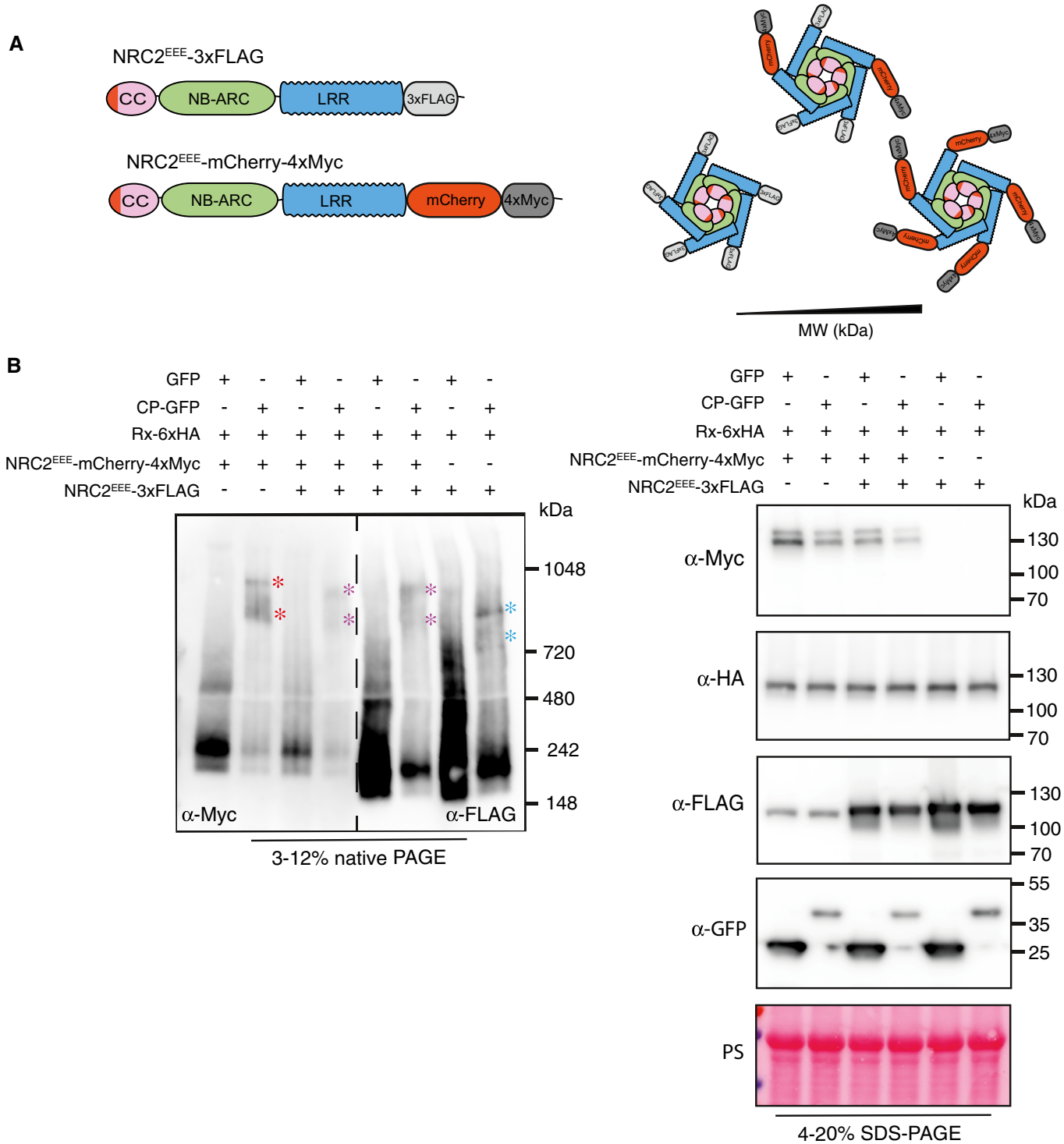


**Figure 3.**

Downloaded from https://www.embopress.org on August 2, 2025 from IP 78.145.55.37.

**Figure 3. The activated NRC2$^{EEE}$ complex is composed of multiple NRC2 units.**

A Schematic representation of NRC2$^{EEE}$ with differently sized tags. The C-terminally 3xFLAG-tagged NRC2$^{EEE}$ was termed the "light" version and C-terminally mCherry-4xMyc tagged NRC2$^{EEE}$ was termed the "heavy" variant. If NRC2 forms homo-oligomers, active complexes with different proportions of "heavy" and "light" NRC2 monomers should in theory exhibit different molecular weights.

B BN-PAGE and SDS–PAGE assays with inactive and activated Rx-NRC2 using different "heavy" and "light" helper combinations. Total protein was extracted with a Tris–HCl-based buffer, as described in materials and methods. Extracts were run on native and denaturing PAGE assays in parallel and immunoblotted with the appropriate antisera labeled on the left. Approximate molecular weights (kDa) of the proteins are shown on the right. A non-specific band was observed at ~ 110 kDa for the anti-FLAG antibody. Red asterisks indicate bands corresponding to the activated "heavy" NRC2 complexes. Blue asterisks indicate bands corresponding to "light" NRC2 complexes. Purple bands indicate intermediate molecular weight complexes combining "heavy" and "light" NRC2. Rubisco loading control was carried out using Ponceau stain (PS). The experiment was repeated three times.

Source data are available online for this figure.

signaling (Appendix Fig S3). Our BN-PAGE assays revealed that while Bs2 activation with AvrBs2 was able to trigger NRC2$^{EEE}$ resistosome formation in a similar fashion to Rx, Rpi-blb2 activation with AVRblb2 did not lead to the formation of a NRC2$^{EEE}$ resistosome (Fig 4B). This suggests that sensor-mediated NRC2 oligomerization applies to another NRC2 dependent sensor. Moreover, the observation that only sensors that genetically require NRC2 can trigger its oligomerization shows that previously genetically characterized sensor-helper specificities in the NRC network can be recapitulated biochemically by helper oligomerization in BN-PAGE.

### Bs2, Rx and Rpi-blb2 can trigger oligomerization of their helper NRC4

We next tested whether the NRC2 activation mechanism also applies to another NRC helper, NRC4, which can support signaling by the three previously tested sensors, Bs2, Rx and Rpi-blb2 (Fig 4A). We leveraged a previously published NRC4 variant with L9A/V10A/L14A mutations in its N-terminal MADA motif (NRC4$^{AAA}$) (Adachi *et al*, 2019a) that does not cause hypersensitive cell death and enables *in planta* biochemical analyses. We performed complementation assays by co-expressing NRC4$^{AAA}$ in leaves of *nrc2/3/4 N. benthamiana* CRISPR mutants along with the inactive or effector-activated sensors mentioned previously. All three sensor NLRs were able to trigger NRC4$^{AAA}$ oligomerization (Fig 5). This suggests that sensor-mediated NRC helper oligomerization upon effector perception applies to another helper NLR in the NRC network.

### Activated NRC2 oligomers accumulate in membrane-associated puncta, whereas Rx remains cytoplasmic

The cellular biology of activated NLRs remains poorly understood. We previously showed that the NRC helper NLR NRC4 exhibits dynamic spatiotemporal changes in subcellular localization following effector-triggered activation of its upstream sensor NLR Rpi-blb2 (Duggan *et al*, 2021). We applied similar methods to study the sub-cellular dynamics of the Rx-NRC2 system by transiently co-expressing fluorescently tagged versions of Rx-RFP and NRC2$^{EEE}$-GFP in leaves of *nrc2/3/4 N. benthamiana* CRISPR mutants. We activated the Rx-NRC2 system by expressing 4xMyc-tagged CP or a 4xMyc-tag empty vector (EV) control and monitored sensor and helper localization using confocal live-cell imaging (Fig 6). As a plasma membrane (PM) marker, we co-expressed RPW8.2-BFP (Duggan *et al*, 2021). In parallel, protein was extracted from the same leaf tissue used for microscopy to confirm that the tags do not interfere with Rx-mediated NRC2 cell death and oligomerization by BN-PAGE assays (Appendix Fig S4). In their inactive state, both Rx-RFP and NRC2$^{EEE}$-GFP co-localize to the cytoplasm in 100% of observations (N = 16 images) (Fig 6A; Movie EV1). Strikingly, when co-expressing CP, activated NRC2$^{EEE}$-GFP predominantly localizes to puncta which frequently co-localize with the PM, marked by RPW8.2-BFP. In contrast, Rx-RFP does not exhibit major changes in subcellular localization. The sensor remains in the cytoplasm and does not concentrate in the NRC2 puncta (15/16 images taken). These puncta are uniformly distributed throughout the PM (Fig 6B; Movie EV1). To investigate the membrane association of the activated oligomeric NRC2 complex, we obtained protein extracts from the same tissues used for microscopy and carried out membrane fractionation assays in nondenaturing conditions using the same experimental setup described above and performed SDS–PAGE assays using the different fractions (Fig 6C). In line with what we previously observed in live-cell imaging experiments, we found that in the inactive state, both Rx and NRC2$^{EEE}$ are mainly present in the soluble fraction. Following activation, NRC2$^{EEE}$ is equally distributed between the soluble and membrane fractions, indicating a shift in subcellular localization and increased membrane-association. Rx, however, exhibits no such shift upon activation and remains predominantly in the soluble fraction. We conclude that upon effector-triggered activation of Rx, the sensor subsequently mediates activation of its helper NRC2$^{EEE}$ in the cytoplasm. The activated NRC2 units form oligomeric resistosomes that dynamically relocalize and form membrane-associated puncta that are separate from the sensor.

**Figure 4. Bs2, another NRC2-dependent sensor NLR, triggers oligomerization of NRC2$^{EEE}$.**

A Schematic representation of the NRC genetic dependencies of sensors used in this experiment.

B BN-PAGE and SDS–PAGE assays with inactive and activated NRC-dependent sensors and NRC2. Total protein was extracted with a Tris–HCl-based buffer, as described in materials and methods. Extracts were run on native and denaturing PAGE assays in parallel and immunoblotted with the appropriate antisera labeled on the left. Approximate molecular weights (kDa) of the proteins are shown on the right. Red asterisk indicates bands corresponding to the activated NRC2 complexes. Rubisco loading control was carried out using Ponceau stain (PS). The experiment was repeated three times.

Source data are available online for this figure.

Downloaded from https://www.embopress.org on August 2, 2025 from IP 78.145.55.37.

 © 2022 The Authors

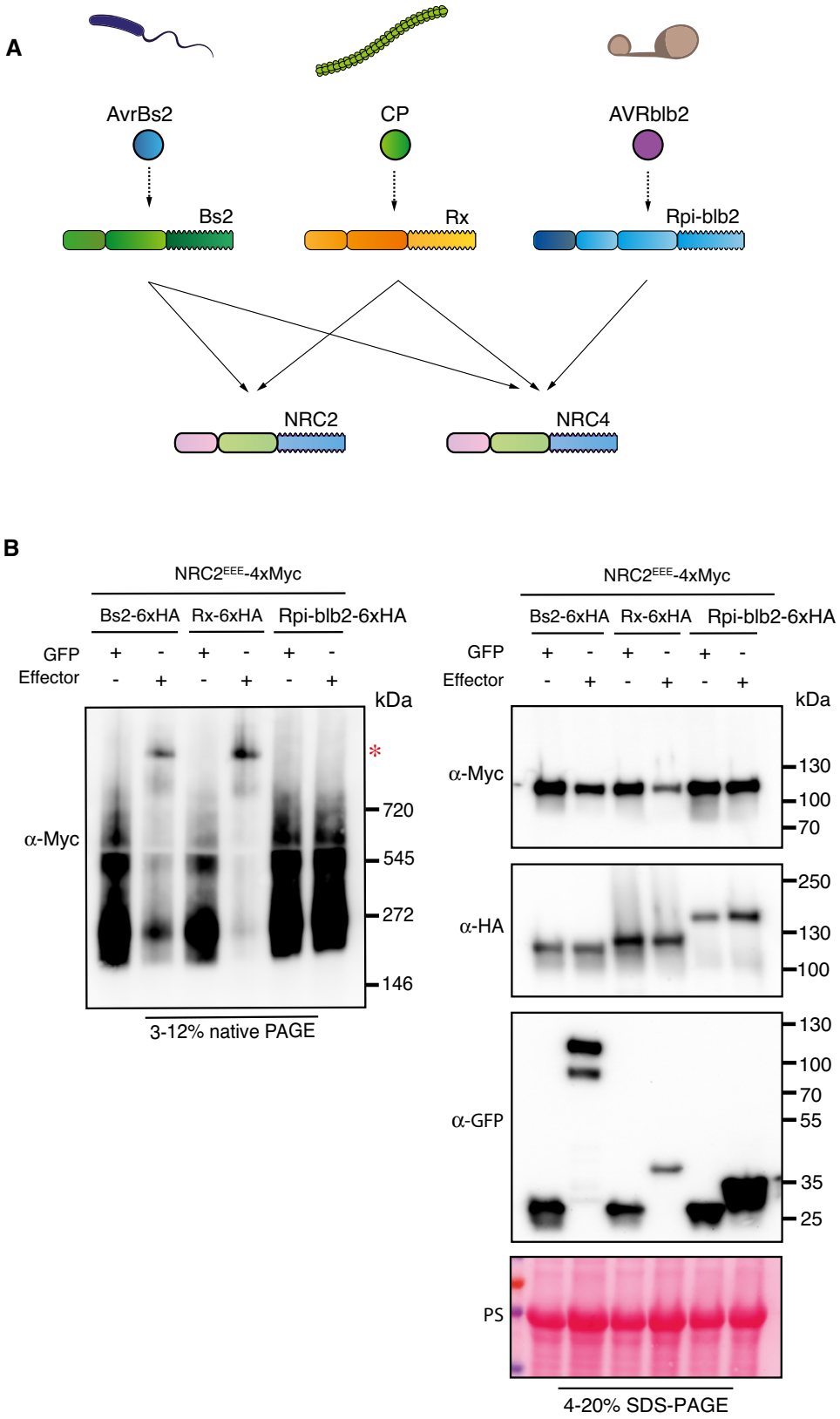


**Figure 4.**

Downloaded from https://www.embopress.org on August 2, 2025 from IP 78.145.55.37.

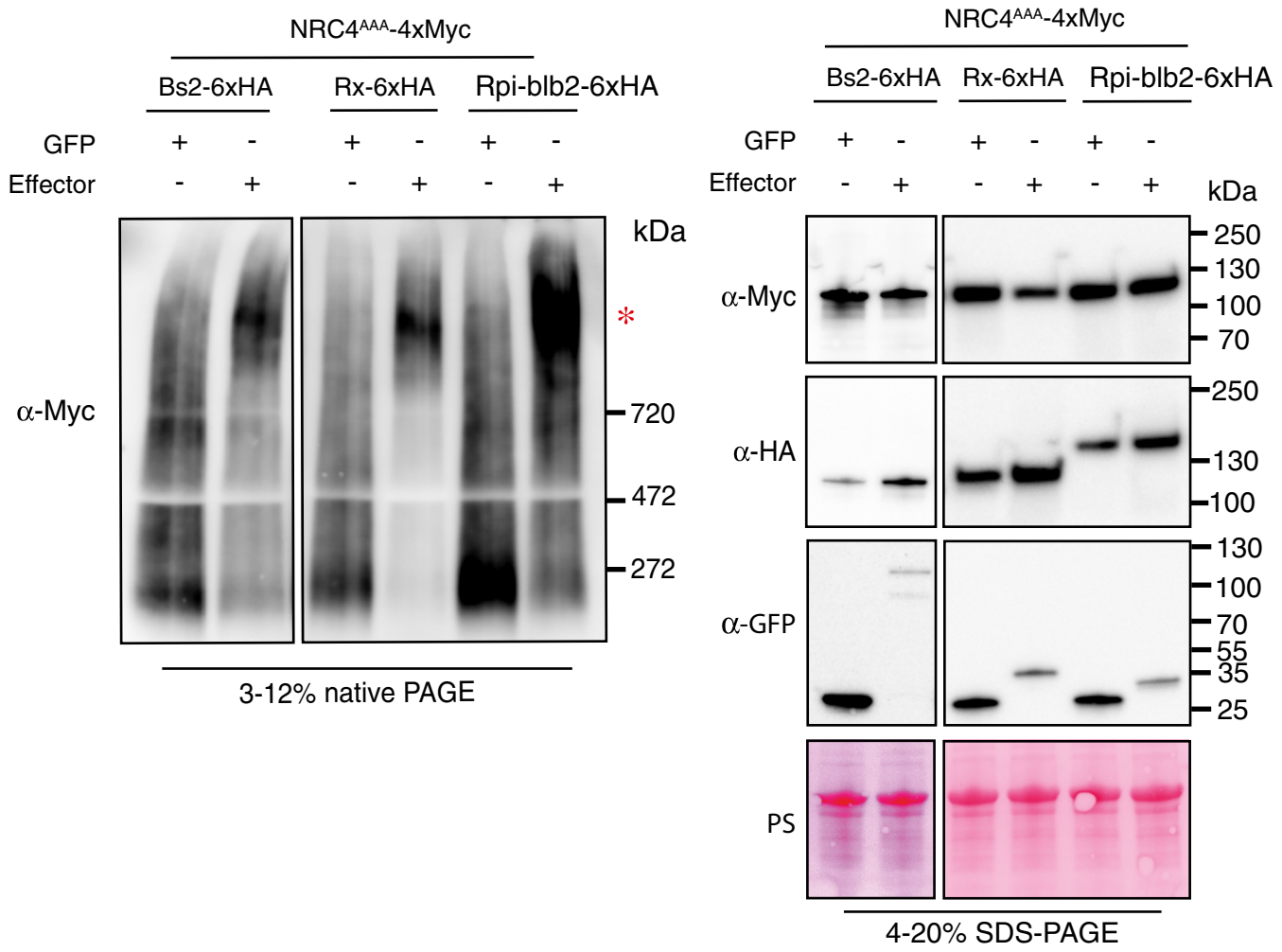


**Figure 5. Bs2, Rx and Rpi-blb2 trigger oligomerization of another helper NLR, NRC4.**

BN-PAGE and SDS–PAGE assays with inactive and activated NRC-dependent sensors and NRC4$^{AAA}$. Total protein was extracted with a HEPES-based buffer, as described in materials and methods. Extracts were run on native and denaturing PAGE assays in parallel and immunoblotted with the appropriate antisera labeled on the left. Approximate molecular weights (kDa) of the proteins are shown on the right. Red asterisk indicates bands corresponding to the activated NRC4 complexes. Rubisco loading control was carried out using Ponceau stain (PS). The experiment was repeated three times.
Source data are available online for this figure.

### *Potato virus X* infection triggers Rx-mediated oligomerization of NRC2

To confirm our previous results in the context of pathogen infection rather than with activation using heterologously expressed effectors, we used BN-PAGE to study the activation of NRC2 in the context of viral infection. We transiently co-expressed Rx and NRC2$^{EEE}$ in leaves of *nrc2/3/4 N. benthamiana* CRISPR mutant lines and activated the system by infecting leaf tissues with PVX via co-expressing a GFP tagged PVX variant (pGR106::PVX::GFP), as

**Figure 6. *Potato virus X* coat protein activated NRC2 forms plasma membrane-associated puncta, unlike Rx.**

C-terminally GFP-tagged NRC2$^{EEE}$ and C-terminally RFP-tagged Rx were co-expressed either with an EV-4xMyc construct or a CP-4xMyc construct in leaves of *nrc2/3/4 N. benthamiana* CRISPR mutant lines.

A, B Single-plane confocal micrographs show the localization of both components of the inactive and active Rx-NRC2 system, together with PM marker RPW8.2-BFP. Scale bars represent 10 μm. (A) NRC2$^{EEE}$-GFP and Rx-RFP co-localize in the cytoplasm prior to activation. (B) Upon co-expression of CP and activation of the system, NRC2$^{EEE}$ forms puncta associated with the PM while Rx remains in the cytoplasm.

C Membrane enrichment assays are consistent with microscopy, showing that inactive NRC2$^{EEE}$-GFP is mostly present in the soluble (cytoplasmic) fraction, whereas activated NRC2$^{EEE}$-GFP exhibits equal distribution across soluble and membrane fractions. Rx is mostly present in the soluble fraction and exhibits no change upon activation of the system with CP. T = total, S = soluble, M = membrane. ATPase was used as a membrane marker. Rubisco was used as a marker for total and soluble fractions and visualized by Ponceau staining (PS). Red asterisks indicate bands matching the expected MW for each protein. The experiment was repeated two times.

Source data are available online for this figure.

Downloaded from https://www.embopress.org on August 2, 2025 from IP 78.145.55.37.

 © 2022 The Authors

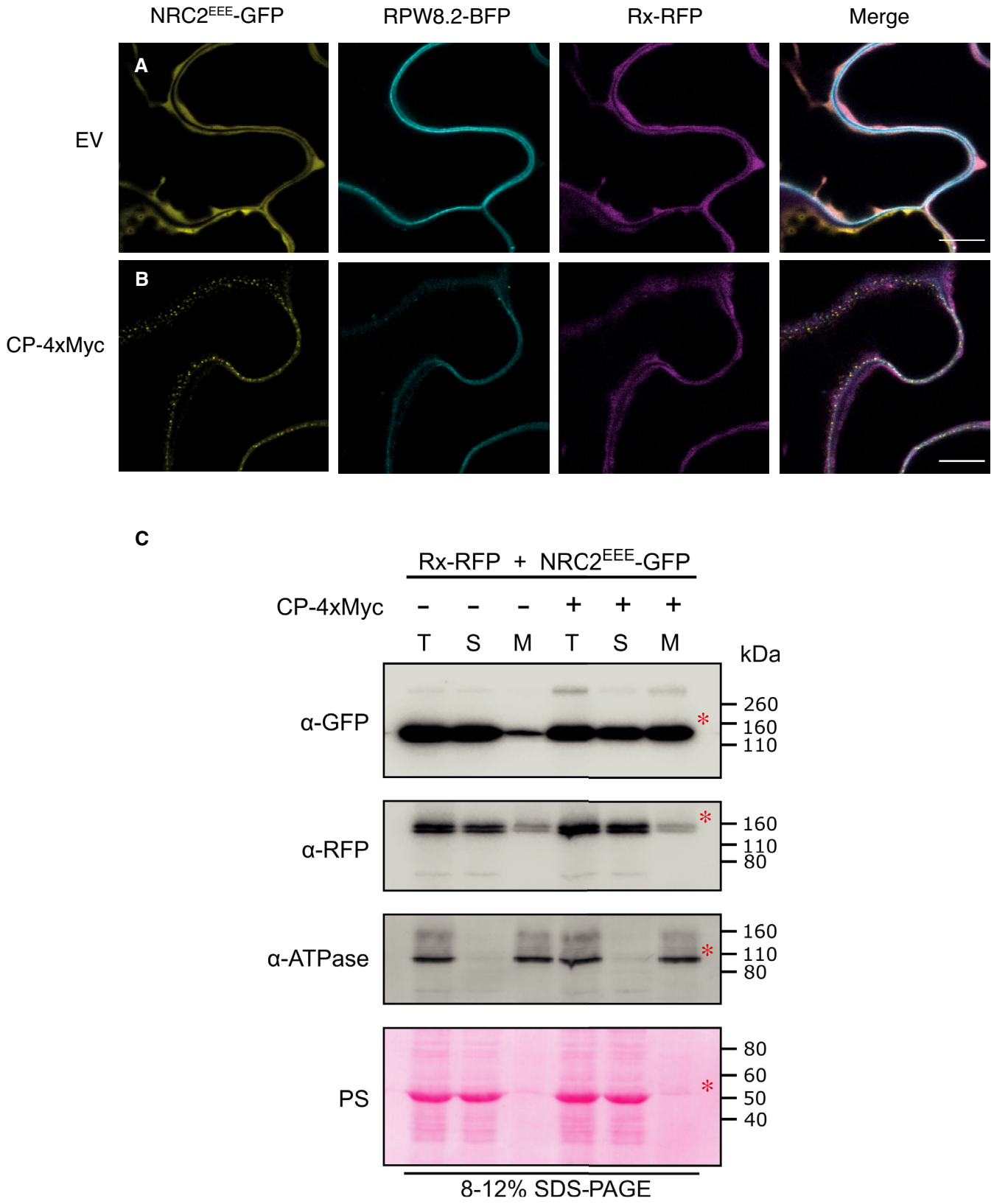


**Figure 6.**

Downloaded from https://www.embopress.org on August 2, 2025 from IP 78.145.55.37.

© 2022 The Authors

described previously (Derevnina *et al*, 2021). Transient expression of free GFP was used as a negative control for infection. After 3 days, protein extracts from infected or uninfected leaf tissues were used for BN-PAGE assays (Fig 7A). Consistent with previous results, infection with PVX led to sensor-dependent oligomerization of NRC2$^{EEE}$ (Fig 7B). Interestingly, in the SDS–PAGE, a very strong GFP signal was observed in all PVX treatments, suggesting that the virus is able to replicate in the presence of Rx and NRC2$^{EEE}$. This implies that, while the leucine to glutamic acid mutations in the N-terminal MADA motif of NRC2 do not prevent resistosome formation mediated by Rx, the NRC2$^{EEE}$ mutant is both unable to trigger hypersensitive cell death and mediate Rx-dependent PVX resistance (Fig 7B). We conclude that for sensor-helper pairs in the NRC network, the sensor NLR is activated following pathogen recognition and subsequently signals to its downstream NRC helper, leading to its oligomerization and resistosome formation. We also conclude that an NRC helper with a functional MADA-motif is necessary for the Rx-NRC2 system to mediate full PVX resistance.

### *Potato virus X* infection triggers Rx-dependent formation of membrane-associated NRC2 puncta

We next sought out to study the sensor-dependent subcellular reorganization of NRC2 described above in the context of pathogen infection. To this end, we transiently co-expressed NRC2$^{EEE}$ either with Rx-RFP or free RFP in leaves of *nrc2/3/4 N. benthamiana* CRISPR mutant lines and activated the system by infecting leaf tissues with PVX (pGR106::PVX), as described previously (Derevnina *et al*, 2021). After 3 days, we monitored sensor and helper localization using confocal live-cell imaging (Fig 8). Under these infection conditions, the helper NRC2$^{EEE}$-GFP remains in the cytoplasm in the absence of its upstream sensor Rx (18/18 images taken) (Fig 8A). Consistent with previous results, when co-expressing NRC2$^{EEE}$-GFP together with Rx-RFP and infecting with PVX, the helper predominantly localizes to PM-associated puncta. In contrast, Rx remains in the cytoplasm during PVX infection and does not exhibit co-localization with NRC2 (18/18 images taken) (Fig 8B). Our data indicate that the dynamic re-localization and PM-association of NRC2 we observed following treatment with CP (Fig 6) also occurs during pathogen infection.

## Discussion

The aim of this study was to develop a better understanding of the molecular mechanisms that underpin activation of paired and networked plant NLR immune receptors. Such *in planta* studies were previously hampered by the cell death response associated with activated NLRs. The capacity to make mutations in the N-terminal MADA motif of CC-NLR helper proteins that abolish elicitation of cell death without affecting activation enabled us to develop readouts for the formation of resistosome-like oligomers and address several questions related to NRC activation. We used biochemical and cellular biology techniques to develop a working model for activation of the NRC network sensors NLRs Rx, Bs2, Rpi-blb2 and their helpers NRC2 and NRC4 (Wu *et al*, 2017; Derevnina *et al*, 2021). Our data demonstrate that these sensor NLRs can mediate NRC oligomerization (Figs 1, 4, 5, and EV1) upon activation with their corresponding effectors and in the case of Rx, during pathogen infection (Fig 7). For NRC2, we show that sensor activation also mediates helper re-localization to PM during pathogen infection (Figs 6 and 8). This activated NRC2 complex appears to be an oligomer containing multiple NRC2 units, which excludes the sensor NLR (Figs 1, 2, 3, and EV2), suggesting a model for sensor-helper activation that differs from mammalian paired NLR systems, such as NAIP/NLRC4 (Vance, 2015; Zhang *et al*, 2015). These findings and those of a co-published study on oligomerization of NRC2 after activation of the oomycete resistance proteins Rpi-amr1 and Rpi-amr3 (preprint: Ahn *et al*, 2022) have led us to develop an activation-and-release working model for NLRs in the NRC network (Fig 9).

The N-terminal α1-helices of ZAR1, Sr35 and the NRCs are defined by a molecular signature called the "MADA motif" (Adachi *et al*, 2019a; Kourelis *et al*, 2021a). This motif can be found in ~ 20% of angiosperm CC-NLRs and is essential for immune signaling and disease resistance. For TIR-NLR biology, multiple essential downstream components for immune signaling, such as the EDS1 signaling hub and the CC$_R$ NLRs NRG1 and ADR1 have been identified, which enabled the generation of genetic backgrounds with which to study TIR-NLR activities in the absence of immune signaling (preprint: Gantner *et al*, 2019; Lapin *et al*, 2019; Martin *et al*, 2020; Saile *et al*, 2020; Sun *et al*, 2021). Unlike TIR-NLRs, approaches to study activated CC-NLRs in the absence of a plant cell death response were not available until recently (Adachi *et al*, 2019a; Duggan *et al*, 2021). The availability of MADA mutant variants that no longer trigger cell death, but retain the capacity to activate, oligomerize and re-localize enabled us to study the cellular and biochemical mechanisms of CC-NLR activation.

MADA motif mutants of NRCs are unable to mediate cell death yet they can still oligomerize and relocalize to the PM upon activation by their upstream sensors. How does this fit with current models of CC-NLR execution of the hypersensitive cell death? Our work complements existing studies that show how MADA mutants can be leveraged to shed light on the diversity of molecular mechanisms that underpin CC-NLR activation (Adachi *et al*, 2019a; Hu *et al*, 2020; preprint: Kourelis *et al*, 2021a; preprint: Förderer *et al*, 2022). Two studies on NRC4 and ZAR1, respectively, showed that mutations in the N-terminal MADA-motif containing α1-helices abolished cell death triggered by these NLRs but had no effect on PM localization (Hu *et al*, 2020; Duggan *et al*, 2021). Similar to NRC2$^{EEE}$ and NRC4$^{AAA}$, ZAR1 and Sr35 with mutated N-termini were still able to form resistosomes (Hu *et al*, 2020; preprint: Förderer *et al*, 2022). Resistosome assembly and PM localization are, therefore, required but not sufficient to mediate cell death. In the case of Sr35, mutations in the MADA motif even abolished the capacity of this NLR to trigger cell death in insect cells (preprint: Förderer *et al*, 2022), suggesting that no further downstream components are required or that the signaling initiated by these resistosomes can engage with highly conserved pathways present across the plant and animal kingdoms. How do MADA motif mutations interfere with cell death? One possibility is that the MADA mutations interfere with the $Ca^{2+}$ channel activity that was recently assigned to activated CC and CC$_R$-NLR proteins (Bi *et al*, 2021; preprint: Jacob *et al*, 2021; preprint: Förderer *et al*, 2022). Alternatively, N-terminal α1-helices in CC-NLRs with mutated MADA motifs may result in resistosomes that associate with the plasma membrane but are unable to fully penetrate the lipid bilayer to form a functional pore or channel. Further

Downloaded from https://www.embopress.org on August 2, 2025 from IP 78.145.55.37.

 © 2022 The Authors

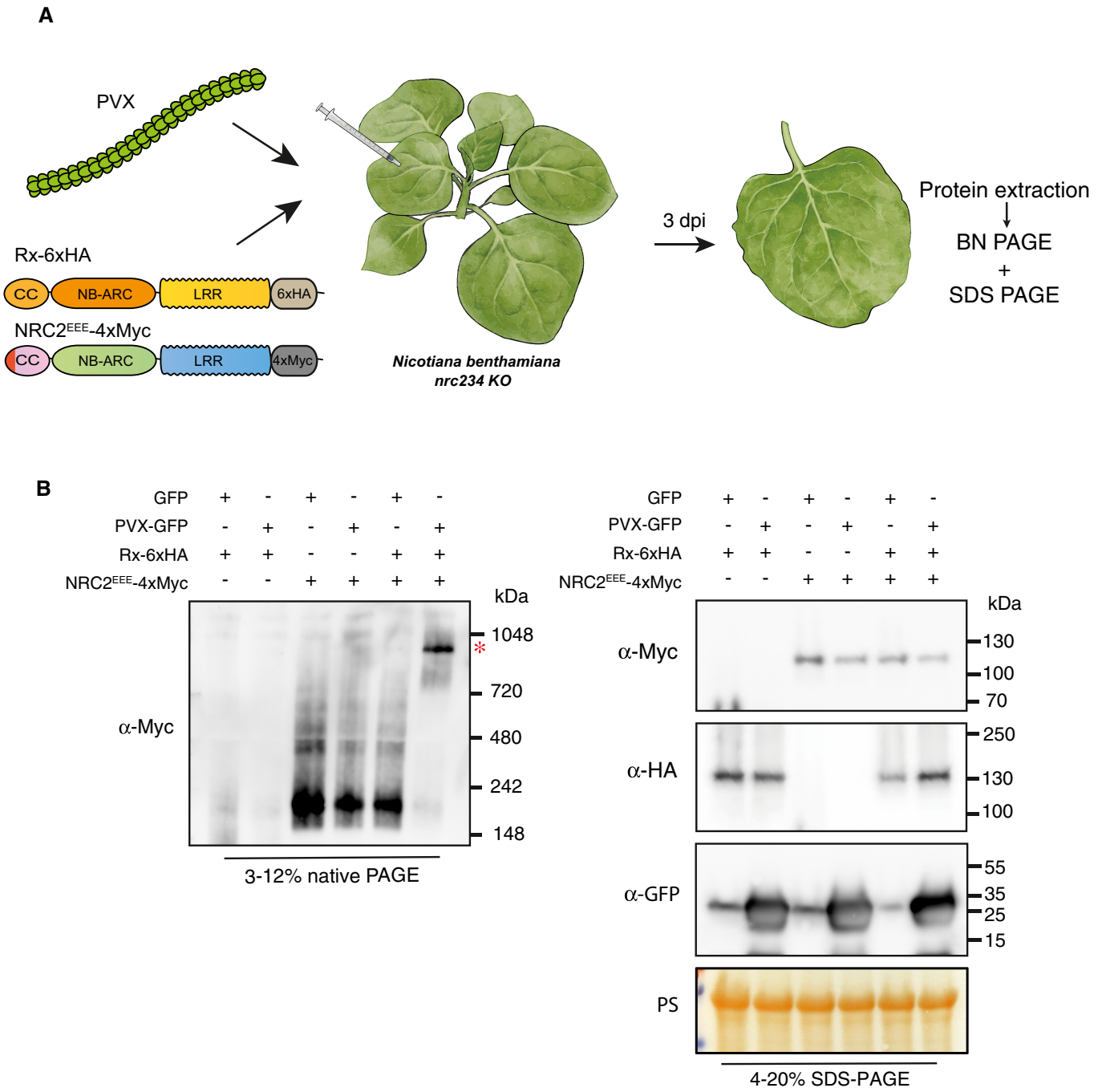


**Figure 7. *Potato virus X* infection triggers Rx-mediated oligomerization of NRC2.**

A Schematic representation of the experimental pipeline used. *A. tumefaciens* strains were used to transiently express proteins of interest in leaves of *nrc2/3/4 N. benthamiana* CRISPR mutant lines by agroinfiltration. Simultaneously, the same leaves were infected with PVX by using an *A. tumefaciens* carrying GFP expressing PVX. Free GFP was used as a negative control for PVX-GFP infection. Free mCherry-4xMyc and mCherry-6xHA fusions were used as controls in the treatments without NRC2 and Rx, respectively. Leaf tissue was harvested 3 days post-infiltration and total protein extracts were used for BN and SDS–PAGE assays.

B BN-PAGE and SDS–PAGE assays with infected and uninfected leaves expressing Rx and NRC2. Total protein was extracted with a Tris–HCl-based buffer, as described in materials and methods. Extracts were run on native and denaturing PAGE assays in parallel and immunoblotted with the appropriate antisera labeled on the left. Approximate molecular weights (kDa) of the proteins are shown on the right. Red asterisks indicate bands corresponding to the activated NRC2 complexes. Rubisco loading control was carried out using Ponceau stain (PS). The experiment was repeated three times.

Source data are available online for this figure.

Downloaded from https://www.embopress.org on August 2, 2025 from IP 78.145.55.37.

© 2022 The Authors

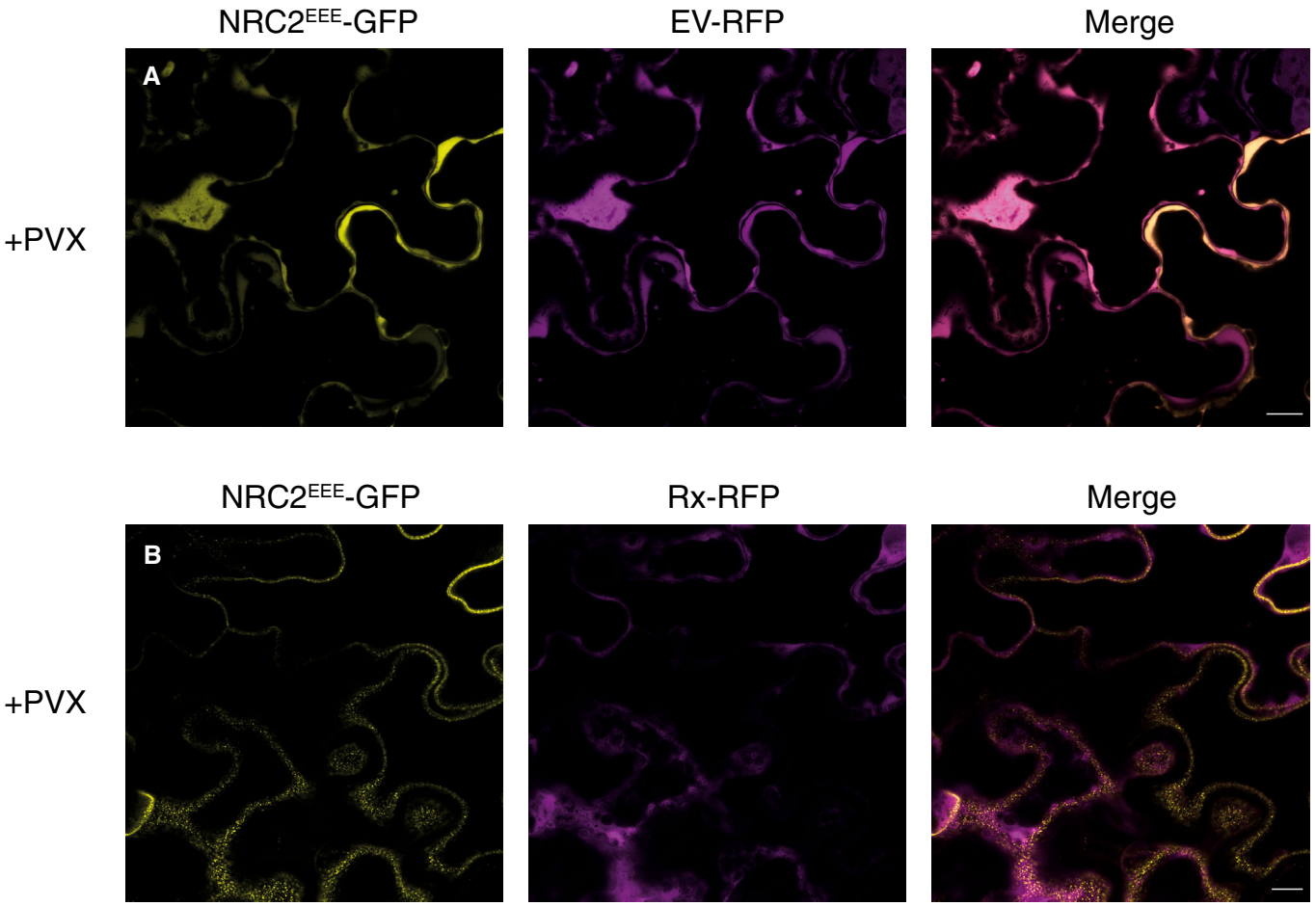


**Figure 8. *Potato virus X* infection triggers Rx-dependent NRC2 membrane-associated puncta.**

A, B Single-plane confocal micrographs show the localization of NRC2 together with Rx or free RFP during PVX infection. C-terminally GFP-tagged NRC2$^{EEE}$ was co-infiltrated with either EV-RFP or Rx-RFP in leaves of *nrc2/3/4 N. benthamiana* CRISPR mutant lines and infected with PVX by agroinfection. Scale bars represent 10 μm. (A) In the absence of Rx, NRC2$^{EEE}$-GFP is localized to the cytoplasm during PVX infection. (B) When Rx is present, NRC2$^{EEE}$ forms puncta associated with the PM during PVX infection.

research will dissect the precise role of this N-terminal motif in NRC and CC-NLR-mediated cell death.

The recent elucidation of multiple plant NLR structures has demonstrated that plant and metazoan NLRs exhibit functional differences despite several commonalities. In this work, we propose an activation-and-release working model for sensor-helper pairs in the NRC network (Fig 9). In this working model, effector-triggered activation of a sensor NLR leads to conformational changes, which relay a signal to downstream helpers, potentially via transient interactions. These helpers subsequently activate, oligomerize and form resistosomes. The activated helper complexes then part ways with their sensors and re-localize to the plasma membrane where they trigger cell death. It is possible that transient intermediates exist where sensors interact with their helpers to trigger their activation. However, BN-PAGE assays with differently sized versions of Rx and NRC2 and confocal microscopy suggest that a stable hetero-complex scenario is unlikely for the mature activated Rx-NRC2 system. This points to a biochemical model for plant paired NLR activation that differs from activation processes previously characterized for metazoan NLR pairs. We conclude that these plant and metazoan paired and networked NLRs exhibit distinct activation mechanisms and biochemical processes. Whether this activation-and-release model applies to other paired plant CC-NLRs or even other paired metazoan NLRs remains to be tested.

**Figure 9. An activation-and-release working model for sensor-helper pairs in the NRC network.**

Prior to effector-triggered activation, NRC-dependent sensors such as Rx and Bs2 are held in an inactive conformation by intramolecular interactions. Upon perceiving their cognate effectors, the sensors undergo a series of conformational changes that allow them to signal to NRC2 and mediate its homo-oligomerization and resistosome formation. The activated NRC2 resistosome separates from the sensors and accumulates at the PM. The sensors remain in the cytoplasm, separate from the activated helper.

Downloaded from https://www.embopress.org on August 2, 2025 from IP 78.145.55.37.

 © 2022 The Authors

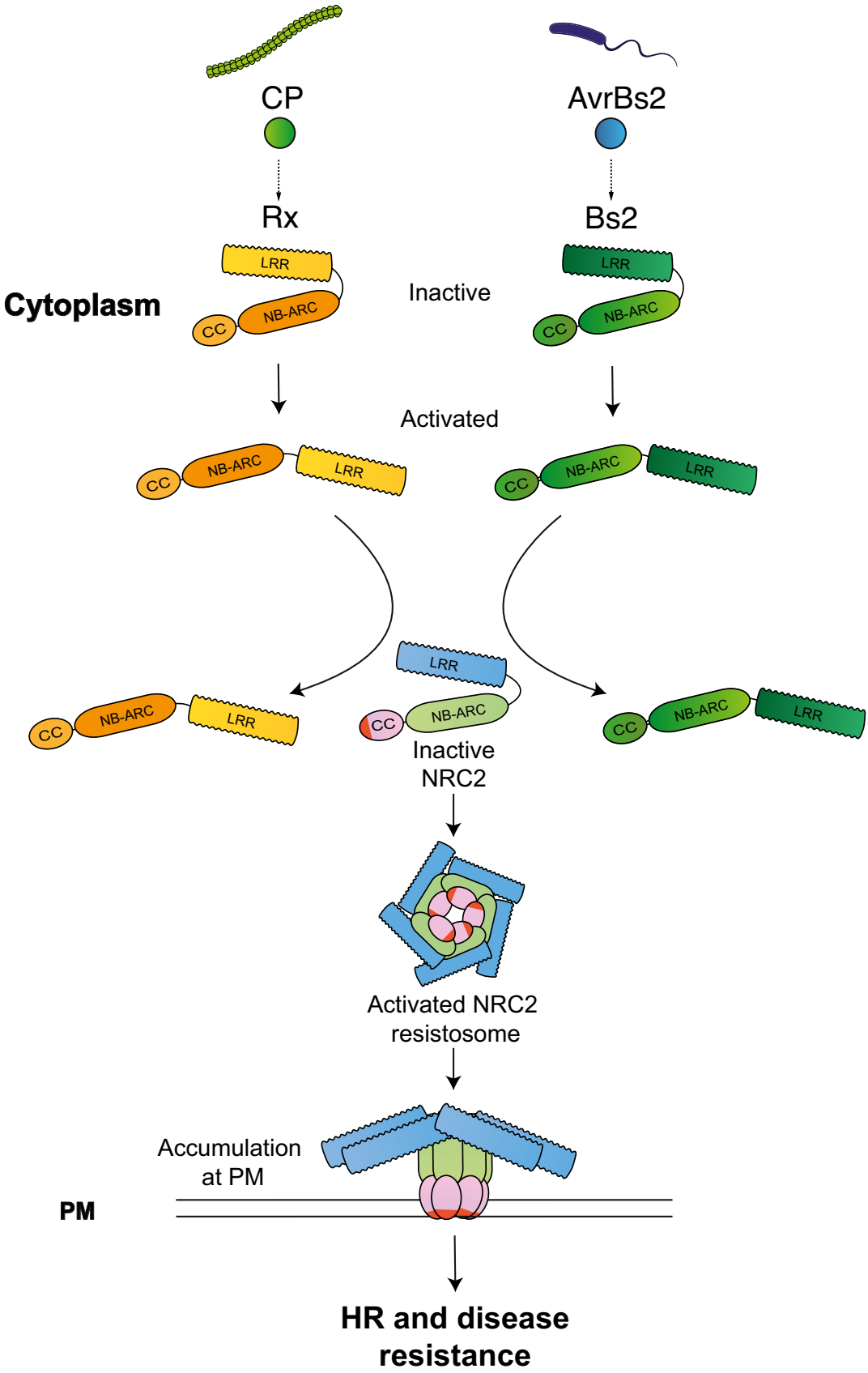


**Figure 9.**

Downloaded from https://www.embopress.org on August 2, 2025 from IP 78.145.55.37.

Previous work has shown that following CP-triggered activation, Rx undergoes a series of conformational changes that lead to cell death and immune activation (Moffett *et al*, 2002; Rairdan & Moffett, 2006). Nonetheless, how a signal is relayed from sensor to helper remains unknown. While Rx does not oligomerize upon activation, the conformational switch may allow Rx to interact transiently with NRC2 in order to mediate its activation. To date, conclusive evidence that NRC-dependent sensors and their NRC helpers form stable complexes has not been obtained, possibly because the complexes are transient. Regardless of whether a direct or indirect interaction between sensor and helper mediates NRC activation, these findings and those of the companion study (preprint: Ahn *et al*, 2022) indicate that the mature NRC2 resistosome is released from the activated sensor. In this scenario, one Rx or Bs2 could potentially activate multiple NRC2 molecules, possibly triggering an NRC2 oligomerization cascade independent of the sensor. Alternatively, NRCs may form transient sensor-helper heterocomplexes with their sensor, which could act as an intermediate polymerization scaffold for the putative NRC resistosome, reminiscent of the first stages of NAIP/NLRC4 inflammasome maturation. A mechanism in which one sensor molecule can activate multiple NRC resistosomes would be much more efficient in amplifying immune signals as opposed to an activated sensor stably engaging in a sensor-helper heterocomplex. Such an amplification would be analogous to the working model for TIR-NLR/$CC_R$-NLR sensor-helper pairs, where small molecules produced by activated TIR-NLR sensors lead to downstream helper activation via the EDS1 signaling hub, triggering $CC_R$-NLR resistosome formation (preprint: Jacob *et al*, 2021; Sun *et al*, 2021; preprint: Huang *et al*, 2022). Further studies will shed more light on the dynamics of NRC resistosome assembly.

The PVX system allowed us to study paired NLR activation during pathogen infection, taking the state-of-the-art beyond activation with effector proteins (Figs 7 and 8). This work complements previous studies on NLR oligomerization upon heterologous expression of cognate effectors (Williams *et al*, 2014; Duxbury *et al*, 2020; Hu *et al*, 2020; Li *et al*, 2020; Ma *et al*, 2020; Martin *et al*, 2020), showing that the same mechanism likely applies during infection by pathogenic organisms. Investigating the oligomeric state and subcellular localization of paired/networked NLRs upon infection will provide further insights into the mechanisms that underpin NLR-mediated immunity. In the case of NRC4, this helper can focally accumulate at the interface between *P. infestans* and the host plant at the site where effectors are delivered before re-localizing and forming discrete puncta at the PM following activation (Duggan *et al*, 2021). Interestingly, the puncta observed for activated NRC2 and NRC4 are distributed throughout the cell PM. What is the exact nature of these puncta, how many resistosomes accumulate in the observed PM micro-domains and whether they form macro-complexes remain open questions.

A multitude of structural, biochemical and cell biology studies have contributed to our mechanistic understanding of NLR activation and signaling (Kourelis & Van Der Hoorn, 2018; Duxbury *et al*, 2021; Ngou *et al*, 2022). Our work expands on the current conceptual mechanistic framework of NLR activation by incorporating the higher order of genetic complexity presented by plant immune receptor networks (Wu *et al*, 2017, 2018). In the case of singleton NLRs, an individual protein can perceive effectors and subsequently form a resistosome to execute cell death. We previously proposed that in plant NLR networks, sensors have specialized over evolutionary time to perceive effectors and have lost the biochemical features required for executing cell death (Adachi *et al*, 2019a, 2019b). Based on our current working model (Fig 9), sensor NLRs have lost the capacity to oligomerize into resistosomes and have specialized in pathogen perception and helper activation. In contrast, activated NRC2 and NRC4 behave similarly to other MADA-CC-NLRs by forming resistosome-like homo-oligomers that translocate to the PM. Nonetheless, the many-to-many sensor-helper connections in the NRC network raise further questions. What is the precise nature of the activation signal relayed from sensor to helper? What are the precise dynamics of NRC resistosome assembly? How do the molecular determinants for sensor-helper specificity translate into resistosome formation? Addressing these questions holds the potential to advance our understanding of the diversity of plant NLR immune activation beyond functional singleton NLRs.

## Materials and Methods

### Plant growth conditions

Wild-type and *nrc2/3/4* CRISPR mutant *N. benthamiana* lines were grown in a controlled environment growth chamber with a temperature range of 22–25°C, humidity of 45–65% and a 16/8-h light/dark cycle.

### Plasmid constructions

The Golden Gate Modular Cloning (MoClo) kit (Weber *et al*, 2011) and the MoClo plant parts kit (Engler *et al*, 2014) were used for cloning, and all vectors are from this kit unless specified otherwise. Effectors, receptors and NRCs were cloned into the binary vector pJK268c, which contains the Tomato bushy stunt virus silencing inhibitor p19 in the backbone (Kourelis *et al*, 2020). Cloning design and sequence analysis were done using Geneious Prime (v2021.2.2; https://www.geneious.com). Plasmid construction is described in Appendix Table S1.

### Cell death assays by agroinfiltration

Effectors and NLR immune receptors of interest were transiently expressed according to previously described methods (Bos *et al*, 2006). Briefly, leaves from 4–5-week-old plants were infiltrated with suspensions of *A. tumefaciens* GV3101 pM90 strains transformed with expression vectors coding for different proteins indicated. Final $OD_{600}$ of all *A. tumefaciens* suspensions were adjusted in infiltration buffer (10 mM MES, 10 mM $MgCl_2$, and 150 μM acetosyringone (pH 5.6)). Final $OD_{600}$ used was 0.3 for each NLR immune receptor and 0.2 for all effectors, adding up to a total $OD_{600}$ of 0.8.

### Extraction of total proteins for BN-PAGE and SDS–PAGE assays

Four to five-week-old plants were agroinfiltrated as described above with constructs of interest and leaf tissue was collected 3 days post agroinfiltration or 2 days post agroinfiltration in experiments with NRC4 (Fig 5). Final $OD_{600}$ used was 0.3 for each NLR immune

Downloaded from https://www.embopress.org on August 2, 2025 from IP 78.145.55.37.

 © 2022 The Authors

receptor used and 0.2 for all effectors for a total $OD_{600}$ of 0.8. BN-PAGE was performed using the Bis-Tris Native PAGE system (Invitrogen) according to the manufacturer's instructions. Leaf tissue was ground using a Geno/Grinder tissue homogenizer and total protein was subsequently extracted and homogenized extraction buffer. For NRC2, GTMN extraction buffer was used (10% glycerol, 50 mM Tris–HCl (pH 7.5), 5 mM $MgCl_2$ and 50 mM NaCl) supplemented with 10 mM DTT, 1x protease inhibitor cocktail (SIGMA) and 0.2% Nonidet P-40 Substitute (SIGMA). For NRC4, GHMN buffer (10% glycerol, 50 mM HEPES (pH 7.4), 5 mM $MgCl_2$ and 50 mM NaCl) buffer supplemented with 10 mM DTT, 1x protease inhibitor cocktail (SIGMA) and 1% Digitonin (SIGMA) was used for extraction. Samples were incubated in extraction buffer on ice for 10 min with short vortex mixing every 2 min. Following incubation, samples were centrifuged at 5,000 *g* for 15 min and the supernatant was used for BN-PAGE and SDS–PAGE assays.

#### BN-PAGE assays

For BN-PAGE, samples extracted as detailed above were diluted as per the manufacturer's instructions by adding NativePAGE 5% G-250 sample additive, 4x Sample Buffer and water. After dilution, samples were loaded and run on Native PAGE 3–12% Bis-Tris gels alongside either NativeMark unstained protein standard (Invitrogen) or SERVA Native Marker (SERVA). The proteins were then transferred to polyvinylidene difluoride membranes using NuPAGE Transfer Buffer using a Trans-Blot Turbo Transfer System (Bio-Rad) as per the manufacturer's instructions. Proteins were fixed to the membranes by incubating with 8% acetic acid for 15 min, washed with water and left to dry. Membranes were subsequently re-activated with methanol in order to correctly visualize the unstained native protein marker. Membranes were immunoblotted as described below.

#### SDS–PAGE assays

For SDS–PAGE, samples were diluted in SDS loading dye and denatured at 72 °C for 10 min. Denatured samples were spun down at 5,000 *g* for 3 min and supernatant was run on 4–20% Bio-Rad 4–20% Mini-PROTEAN TGX gels alongside a PageRuler Plus prestained protein ladder (Thermo Scientific). The proteins were then transferred to polyvinylidene difluoride membranes using Trans-Blot Turbo Transfer Buffer using a Trans-Blot Turbo Transfer System (Bio-Rad) as per the manufacturer's instructions. Membranes were immunoblotted as described below.

#### Immunoblotting and detection of BN-PAGE and SDS–PAGE assays

Blotted membranes were blocked with 5% milk in Tris-buffered saline plus 0.01% Tween 20 (TBS-T) for an hour at room temperature and subsequently incubated with desired antibodies at 4°C overnight. Antibodies used were anti-GFP (B-2) HRP (Santa Cruz Biotechnology), anti-HA (3F10) HRP (Roche), anti-Myc (9E10) HRP (Roche), and anti-FLAG (M2) HRP (Sigma), all used in a 1:5,000 dilution in 5% milk in TBS-T. To visualize proteins, we used Pierce ECL Western (32106, Thermo Fisher Scientific), supplementing with up to 50% SuperSignal West Femto Maximum Sensitivity Substrate (34095, Thermo Fishes Scientific) when necessary. Membrane imaging was carried out with an ImageQuant LAS 4000 or an ImageQuant 800 luminescent imager (GE Healthcare Life Sciences, Piscataway, NJ). Rubisco loading control was stained using Ponceau S (Sigma) or Ponceau 4R (AG Barr).

#### Gel filtration assays

Protein was extracted as described above. Protein extracts were filtered through a 0.45 μm filter (Sartorius) and 200 μl of filtered extract were analyzed by gel filtration. Extracts were run on a Superdex 200 Increase 10/300 GL column (GE Healthcare) connected to an AKTA Pure system (GE Healthcare), with samples being run at a flow rate of 0.4 ml/min. The buffer used for elution was GTMN extraction buffer (10% glycerol, 50 mM Tris–HCl (pH 7.5), 5 mM $MgCl_2$ and 50 mM NaCl) supplemented with 1 mM DTT, to match the extraction buffer used for NRC2. The eluted fractions were analyzed by SDS–PAGE as described above and immunoblotted with the corresponding antibodies.

#### BN and SDS–PAGE assays with PVX infection (agroinfection)

Four to five-week-old plants were agroinfiltrated as described above with constructs of interest. Simultaneously, PVX was delivered by agroinfection using an *A. tumefaciens* strain carrying GFP-labeled PVX (pGR106-PVX-GFP). Final $OD_{600}$ used was 0.3 for each NLR immune receptor used and 0.05 for the *A. tumefaciens* strain carrying PVX or free GFP for a total $OD_{600}$ of 0.65. Leaf tissue was collected 3 days post agroinfiltration. BN-PAGE and SDS–PAGE assays were carried out as described above.

#### Confocal microscopy

Three to four-week-old plants were agroinfiltrated as described above with constructs of interest. PVX was delivered as before, or the coat protein CP-4xMyc or EV control at $OD_{600}$ 0.1; Rx-RFP at $OD_{600}$ of 0.25 and $NRC2^{EEE}$-GFP at $OD_{600}$ of 0.25. Leaf tissue was prepared for imaging by sectioning of desired area surrounding an infection spot using a cork borer size 4, and were mounted, live, in wells containing dH2O made in Carolina Observation Gel to enable diffusion of gasses. The abaxial of the leaf tissue was imaged using a Leica SP8 with 40x water immersion objective. Laser excitations for fluorescent proteins were used as described previously (Duggan *et al*, 2021), namely 488 nm (Argon) for GFP, 561/594 nm (Diode) for RFP and 405 nm (Diode) for BFP.

#### Membrane enrichment assays

Membrane enrichment was carried out by slightly modifying a previously described protocol (Abas & Luschnig, 2010). In brief, leaf material was ground to fine powder using liquid nitrogen and 2x volume of extraction buffer was added. Extraction buffer consisted of 0.81 M sucrose, 5% (v/v) glycerol, 10 mM EDTA, 10 mM EGTA, 5 mM KCl, and 100 mM Tris–HCl (pH 7.5) supplemented with 5 mM DTT, 1% Sigma Plant Protease Inhibitor Cocktail, 1 mM PMSF and 0.5% PVPP. After addition of the buffer, the samples were vortexed for a minute and the cell debris was cleared out by two subsequent centrifugation steps at 1,000 *g* for 5 min. The supernatant was diluted 1:1 using distilled water and an aliquot of the

Downloaded from https://www.embopress.org on August 2, 2025 from IP 78.145.55.37.

© 2022 The Authors

supernatant was separated as the total fraction (T). The remaining supernatant (200–300 µl) was further centrifuged at 21,000 *g* for 90 min at 4°C. This centrifugation yielded the supernatant (soluble fraction, S) and membrane enriched pellet (membrane fraction, M). After separating the soluble fraction, the pellet was resuspended in diluted extraction buffer (without PVPP). All the fractions were diluted with SDS loading dye, and proteins were denatured by incubating at 50°C for 15 min. Western blotting was performed as previously described following SDS–PAGE. Endogenous plasma membrane ATPase was detected using anti-H + ATPase (AS07 260) antibody (Agrisera) as a marker to show the success of membrane enrichment.

## Data availability

All relevant data are within the article, in the Appendix and in the Source Data files. This study includes no data that would need to be deposited in external repositories.

**Expanded View** for this article is available online.

### Acknowledgements
We are very thankful to several colleagues for discussions and ideas. We thank Daniel Lüdke (The Sainsbury Laboratory, Norwich, UK) for valuable comments on this article. We thank all members of the TSL Support Services for their invaluable assistance. We thank S. Hrek. M.C. and S.K. dedicate this article to the memory of Diego A. Maradona. A.V.C. was funded by the John Innes Foundation and TSL. The Kamoun Lab is funded primarily from the Gatsby Charitable Foundation, Biotechnology and Biological Sciences Research Council (BBSRC, UK, BB/WW002221/1, BB/V002937/1, BBS/E/J/000PR9795 and BBS/E/J/000PR9796) and the European Research Council (BLASTOFF).

### Author contributions
**Mauricio P Contreras:** Conceptualization; data curation; formal analysis; supervision; validation; investigation; visualization; methodology; writing – original draft; project administration; writing—review and editing. **Hsuan Pai:** Data curation; formal analysis; validation; investigation; methodology. **Yasin Tumtas:** Data curation; formal analysis; validation; investigation; visualization; methodology; writing—review and editing. **Cian Duggan:** Data curation; formal analysis; validation; investigation; visualization; methodology; writing—review and editing. **Enoch Lok Him Yuen:** Data curation; validation; investigation; visualization; writing—review and editing. **Angel Vergara Cruces:** Data curation; formal analysis; validation; investigation; visualization; writing—review and editing. **Jiorgos Kourelis:** Resources; writing—review and editing. **Hee-Kyung Ahn:** Conceptualization; methodology; writing—review and editing. **Kim-Teng Lee:** Investigation. **Chih-Hang Wu:** Conceptualization; methodology; writing—review and editing. **Tolga O Bozkurt:** Resources; supervision; funding acquisition; project administration. **Lida Derevnina:** Conceptualization; resources; supervision; project administration; writing—review and editing. **Sophien Kamoun:** Conceptualization; resources; supervision; funding acquisition; visualization; writing—original draft; project administration; writing—review and editing.

### Disclosure and competing interest statement
C.D., T.O.B and S.K. receive funding from industry on NLR biology. S.K. has filed patents on NLR biology.

## References

Abas L, Luschnig C (2010) Maximum yields of microsomal-type membranes from small amounts of plant material without requiring ultracentrifugation. *Anal Biochem* 401: 217 – 227

Adachi H, Contreras MP, Harant A, Wu C-h, Derevnina L, Sakai T, Duggan C, Moratto E, Bozkurt TO, Maqbool A *et al* (2019a) An N-terminal motif in NLR immune receptors is functionally conserved across distantly related plant species. *Elife* 8: e49956

Adachi H, Derevnina L, Kamoun S (2019b) NLR singletons, pairs, and networks: evolution, assembly, and regulation of the intracellular immunoreceptor circuitry of plants. *Curr Opin Plant Biol* 50: 121 – 131

Adachi H, Sakai T, Kourelis J, Pai H, Gonzalez Hernandez JL, Maqbool A, Kamoun S (2022) Jurassic NLR: conserved and dynamic evolutionary features of the atypically ancient immune receptor ZAR1. *bioRxiv* https://doi.org/10.1101/2020.10.12.333484 [PREPRINT]

Ahn H-K, Lin X, Olave-Achury AC, Derevnina L, Contreras MP, Kourelis J, Kamoun S, Jones JDG (2022) Effector-dependent activation and oligomerization of NRC helper NLRs by Rpi-amr3 and Rpi-amr1. *bioRxiv* https://doi.org/10.1101/2022.04.25.489359 [PREPRINT]

Bendahmane A, Köhm BA, Dedi C, Baulcombe DC (1995) The coat protein of potato virus X is a strain-specific elicitor of Rx1-mediated virus resistance in potato. *Plant J* 8: 933 – 941

Bendahmane A, Kanyuka K, Baulcombe DC (1999) The Rx gene from potato controls separate virus resistance and cell death responses. *Plant Cell* 11: 781 – 791

Bi G, Su M, Li N, Liang Y, Dang S, Xu J, Hu M, Wang J, Zou M, Deng Y (2021) The ZAR1 resistosome is a calcium-permeable channel triggering plant immune signaling. *Cell* 184: 3528 – 3541.e12

Bos JI, Kanneganti TD, Young C, Cakir C, Huitema E, Win J, Armstrong MR, Birch PR, Kamoun S (2006) The C-terminal half of Phytophthora infestans RXLR effector AVR3a is sufficient to trigger R3a-mediated hypersensitivity and suppress INF1-induced cell death in Nicotiana benthamiana. *Plant J* 48: 165 – 176

Césari S, Kanzaki H, Fujiwara T, Bernoux M, Chalvon V, Kawano Y, Shimamoto K, Dodds P, Terauchi R, Kroj T (2014) The NB-LRR proteins RGA 4 and RGA 5 interact functionally and physically to confer disease resistance. *EMBO J* 33: 1941 – 1959

De la Concepcion JC, Benjumea JV, Bialas A, Terauchi R, Kamoun S, Banfield MJ (2021) Functional diversification gave rise to allelic specialization in a rice NLR immune receptor pair. *eLife* 10: e71662

Derevnina L, Contreras MP, Adachi H, Upson J, Vergara Cruces A, Xie R, Skłenar J, Menke FLH, Mugford ST, MacLean D *et al* (2021) Plant pathogens convergently evolved to counteract redundant nodes of an NLR immune receptor network. *PLoS Biol* 19: e3001136

Duggan C, Moratto E, Savage Z, Hamilton E, Adachi H, Wu C-H, Leary AY, Tumtas Y, Rothery SM, Maqbool A *et al* (2021) Dynamic localization of a helper NLR at the plant–pathogen interface underpins pathogen recognition. *Proc Natl Acad Sci* 118: 118

Duxbury Z, Ma Y, Furzer OJ, Huh SU, Cevik V, Jones JD, Sarris PF (2016) Pathogen perception by NLRs in plants and animals: parallel worlds. *Bioessays* 38: 769 – 781

Duxbury Z, Wang S, MacKenzie CI, Tenthorey JL, Zhang X, Huh SU, Hu L, Hill L, Ngou PM, Ding P *et al* (2020) Induced proximity of a TIR signaling domain on a plant-mammalian NLR chimera activates defense in plants. *Proc Natl Acad Sci* 117: 18832 – 18839

Downloaded from https://www.embopress.org on August 2, 2025 from IP 78.145.55.37.

 © 2022 The Authors

Duxbury Z, Wu C-h, Ding P (2021) A comparative overview of the intracellular guardians of plants and animals: NLRs in innate immunity and beyond. *Annu Rev Plant Biol* 72: 155 – 184

Engler C, Youles M, Gruetzner R, Ehnert T-M, Werner S, Jones JD, Patron NJ, Marillonnet S (2014) A golden gate modular cloning toolbox for plants. *ACS Synth Biol* 3: 839 – 843

Feehan JM, Castel B, Bentham AR, Jones JDG (2020) Plant NLRs get by with a little help from their friends. *Curr Opin Plant Biol* 56: 99 – 108

Förderer A, Li E, Lawson A, Deng Y-n, Sun Y, Logemann E, Zhang X, Wen J, Han Z, Chang J *et al* (2022) A wheat resistosome defines common principles of immune receptor channels. *bioRxiv* https://doi.org/10.1101/2022.03.23.485489 [PREPRINT]

Gantner J, Ordon J, Kretschmer C, Guerois R, Stuttmann J (2019) An EDS1-SAG101 complex functions in TNL-mediated immunity in Solanaceae. *bioRxiv* https://doi.org/10.1101/511956 [PREPRINT]

Grinzato A, Kandiah E, Lico C, Betti C, Baschieri S, Zanotti G (2020) Atomic structure of potato virus X, the prototype of the Alphaflexiviridae family. *Nat Chem Biol* 16: 564 – 569

Hu Z, Zhou Q, Zhang C, Fan S, Cheng W, Zhao Y, Shao F, Wang H-W, Sui S-F, Chai J (2015) Structural and biochemical basis for induced self-propagation of NLRC4. *Science* 350: 399 – 404

Hu M, Qi J, Bi G, Zhou J-M (2020) Bacterial effectors induce oligomerization of immune receptor ZAR1 in vivo. *Mol Plant* 13: 793 – 801

Huang S, Jia A, Song W, Hessler G, Meng Y, Sun Y, Xu L, Laessle H, Jirschitzka J, Ma S *et al* (2022) Identification and receptor mechanism of TIR-catalyzed small molecules in plant immunity. *bioRxiv* https://doi.org/10.1101/2022.04.01.486681 [PREPRINT]

Jacob P, Kim NH, Wu F, El-Kasmi F, Walton WG, Furzer OJ, Lietzan AD, Sunil S, Kempthorn K, Redinbo MR *et al* (2021) The plant immune receptors NRG1. 1 and ADR1 are calcium influx channels. *bioRxiv* https://doi.org/10.1101/2021.02.25.431980 [PREPRINT]

Jones JD, Dangl JL (2006) The plant immune system. *Nature* 444: 323 – 329

Jones JD, Vance RE, Dangl JL (2016) Intracellular innate immune surveillance devices in plants and animals. *Science* 354: aaf6395

Kim YK, Shin J-S, Nahm MH (2016) NOD-like receptors in infection, immunity, and diseases. *Yonsei Med J* 57: 5 – 14

Kofoed EM, Vance RE (2011) Innate immune recognition of bacterial ligands by NAIPs determines inflammasome specificity. *Nature* 477: 592 – 595

Kourelis J, Van Der Hoorn RA (2018) Defended to the nines: 25 years of resistance gene cloning identifies nine mechanisms for R protein function. *Plant Cell* 30: 285 – 299

Kourelis J, Malik S, Mattinson O, Krauter S, Kahlon PS, Paulus JK, van der Hoorn RA (2020) Evolution of a guarded decoy protease and its receptor in solanaceous plants. *Nat Commun* 11: 1 – 15

Kourelis J, Contreras MP, Harant A, Adachi H, Derevnina L, Wu C-H, Kamoun S (2021a) The helper NLR immune protein NRC3 mediates the hypersensitive cell death caused by the cell-surface receptor Cf-4. *bioRxiv* https://doi.org/10.1101/2021.09.28.461843 [PREPRINT]

Kourelis J, Sakai T, Adachi H, Kamoun S (2021b) RefPlantNLR is a comprehensive collection of experimentally validated plant disease resistance proteins from the NLR family. *PLoS Biol* 19: e3001124

Lapin D, Kovacova V, Sun X, Dongus JA, Bhandari D, von Born P, Bautor J, Guarneri N, Rzemieniewski J, Stuttmann J (2019) A coevolved EDS1-SAG101-NRG1 module mediates cell death signaling by TIR-domain immune receptors. *Plant Cell* 31: 2430 – 2455

Lechtenberg BC, Mace PD, Riedl SJ (2014) Structural mechanisms in NLR inflammasome signaling. *Curr Opin Struct Biol* 29: 17 – 25

Lee HY, Mang H, Choi E, Seo YE, Kim MS, Oh S, Kim SB, Choi D (2021) Genome-wide functional analysis of hot pepper immune receptors reveals an autonomous NLR clade in seed plants. *New Phytol* 229: 532 – 547

Li L, Habring A, Wang K, Weigel D (2020) Atypical resistance protein RPW8/HR triggers Oligomerization of the NLR immune receptor RPP7 and autoimmunity. *Cell Host Microbe* 27: 405 – 417.e6

Ma S, Lapin D, Liu L, Sun Y, Song W, Zhang X, Logemann E, Yu D, Wang J, Jirschitzka J *et al* (2020) Direct pathogen-induced assembly of an NLR immune receptor complex to form a holoenzyme. *Science* 370: eabe3069

Maekawa T, Kufer TA, Schulze-Lefert P (2011) NLR functions in plant and animal immune systems: so far and yet so close. *Nat Immunol* 12: 817 – 826

Martin R, Qi T, Zhang H, Liu F, King M, Toth C, Nogales E, Staskawicz BJ (2020) Structure of the activated ROQ1 resistosome directly recognizing the pathogen effector XopQ. *Science* 370: eabd9993

Moffett P, Farnham G, Peart J, Baulcombe DC (2002) Interaction between domains of a plant NBS–LRR protein in disease resistance-related cell death. *EMBO J* 21: 4511 – 4519

Ngou BPM, Ding P, Jones JD (2021) Channeling plant immunity. *Cell* 184: 3358 – 3360

Ngou BPM, Ding P, Jones JDG (2022) Thirty years of resistance: zig-zag through the plant immune system. *Plant Cell* 34: 1447 – 1478

Qu Y, Misaghi S, Izrael-Tomasevic A, Newton K, Gilmour LL, Lamkanfi M, Louie S, Kayagaki N, Liu J, Kömüves L *et al* (2012) Phosphorylation of NLRC4 is critical for inflammasome activation. *Nature* 490: 539 – 542

Rairdan GJ, Moffett P (2006) Distinct domains in the ARC region of the potato resistance protein Rx mediate LRR binding and inhibition of activation. *Plant Cell* 18: 2082 – 2093

Saile SC, Jacob P, Castel B, Jubic LM, Salas-Gonzáles I, Bäcker M, Jones JD, Dangl JL, El Kasmi F (2020) Two unequally redundant "helper" immune receptor families mediate *Arabidopsis thaliana* intracellular "sensor" immune receptor functions. *PLoS Biol* 18: e3000783

Sun X, Lapin D, Feehan JM, Stolze SC, Kramer K, Dongus JA, Rzemieniewski J, Blanvillain-Baufumé S, Harzen A, Bautor J *et al* (2021) Pathogen effector recognition-dependent association of NRG1 with EDS1 and SAG101 in TNL receptor immunity. *Nat Commun* 12: 1 – 15

Tameling WI, Baulcombe DC (2007) Physical association of the NB-LRR resistance protein Rx with a ran GTPase–activating protein is required for extreme resistance to potato virus X. *Plant Cell* 19: 1682 – 1694

Vance RE (2015) The NAIP/NLRC4 inflammasomes. *Curr Opin Immunol* 32: 84 – 89

Wang J, Hu M, Wang J, Qi J, Han Z, Wang G, Qi Y, Wang H-W, Zhou J-M, Chai J (2019a) Reconstitution and structure of a plant NLR resistosome conferring immunity. *Science* 364: eaav5870

Wang J, Wang J, Hu M, Wu S, Qi J, Wang G, Han Z, Qi Y, Gao N, Wang H-W *et al* (2019b) Ligand-triggered allosteric ADP release primes a plant NLR complex. *Science* 364: eaav5868

Weber E, Engler C, Gruetzner R, Werner S, Marillonnet S (2011) A modular cloning system for standardized assembly of multigene constructs. *PloS One* 6: e16765

Williams SJ, Sohn KH, Wan L, Bernoux M, Sarris PF, Segonzac C, Ve T, Ma Y, Saucet SB, Ericsson DJ *et al* (2014) Structural basis for assembly and function of a heterodimeric plant immune receptor. *Science* 344: 299 – 303

Wu C-H, Abd-El-Haliem A, Bozkurt TO, Belhaj K, Terauchi R, Vossen JH, Kamoun S (2017) NLR network mediates immunity to diverse plant pathogens. *Proc Natl Acad Sci USA* 114: 8113 – 8118

Downloaded from https://www.embopress.org on August 2, 2025 from IP 78.145.55.37.

© 2022 The Authors 

Wu C-H, Derevnina L, Kamoun S (2018) Receptor networks underpin plant immunity. *Science* 360: 1300 – 1301

Zdrzałek R, Kamoun S, Terauchi R, Saitoh H, Banfield MJ (2020) The rice NLR pair Pikp-1/Pikp-2 initiates cell death through receptor cooperation rather than negative regulation. *PloS One* 15: e0238616

Zhang L, Chen S, Ruan J, Wu J, Tong AB, Yin Q, Li Y, David L, Lu A, Wang WL *et al* (2015) Cryo-EM structure of the activated NAIP2-NLRC4 inflammasome reveals nucleated polymerization. *Science* 350: 404 – 409

Zhao Y, Yang J, Shi J, Gong Y-N, Lu Q, Xu H, Liu L, Shao F (2011) The NLRC4 inflammasome receptors for bacterial flagellin and type III secretion apparatus. *Nature* 477: 596 – 600

**License:** This is an open access article under the terms of the Creative Commons Attribution License, which permits use, distribution and reproduction in any medium, provided the original work is properly cited.

Downloaded from https://www.embopress.org on August 2, 2025 from IP 78.145.55.37.



© 2022 The Authors

Check for updates



PLANT SCIENCES

# Resurrection of plant disease resistance proteins via helper NLR bioengineering

**Mauricio P. Contreras[1], Hsuan Pai[1], Muniyandi Selvaraj[1], AmirAli Toghani[1], David M. Lawson[2], Yasin Tumtas[3], Cian Duggan[3], Enoch Lok Him Yuen[3], Clare E. M. Stevenson[2], Adeline Harant[1], Abbas Maqbool[2], Chih-Hang Wu[4], Tolga O. Bozkurt[3], Sophien Kamoun[1]*, Lida Derevnina[1]†***

Copyright © 2023 The Authors, some rights reserved; exclusive licensee American Association for the Advancement of Science. No claim to original U.S. Government Works. Distributed under a Creative Commons Attribution License 4.0 (CC BY).

**Parasites counteract host immunity by suppressing helper nucleotide binding and leucine-rich repeat (NLR) proteins that function as central nodes in immune receptor networks. Understanding the mechanisms of immunosuppression can lead to strategies for bioengineering disease resistance. Here, we show that a cyst nematode virulence effector binds and inhibits oligomerization of the helper NLR protein NRC2 by physically preventing intramolecular rearrangements required for activation. An amino acid polymorphism at the binding interface between NRC2 and the inhibitor is sufficient for this helper NLR to evade immune suppression, thereby restoring the activity of multiple disease resistance genes. This points to a potential strategy for resurrecting disease resistance in crop genomes.**

## INTRODUCTION

The nucleotide binding and leucine-rich repeat (NLR) class of intracellular immune receptors is an important component of innate immunity in plants and animals. They mediate intracellular recognition of pathogens and subsequently initiate an array of immune responses to counteract infection (*1*, *2*). NLRs can be activated by pathogen-secreted virulence proteins, termed effectors, which pathogens deliver into host cells to modulate host physiology (*2*). A hallmark of plant and animal NLR activation is their oligomerization into higher-order immune complexes termed resistosomes or inflammasomes, respectively (*3*–*9*). These complexes initiate immune signaling via diverse mechanisms, often leading to a form of programmed cell death, termed hypersensitive response (HR) in plants or pyroptosis in animals (*10*, *11*). Recent studies have reported NLR-like proteins mediating antiviral immunity and programmed cell death in prokaryotes via mechanisms analogous to those found in eukaryotic NLRs, suggesting that this is a conserved defense mechanism across all three domains of life (*12*). Pathogen effectors can act both as triggers and suppressors of NLR-mediated immunity (*13*). In some cases, adapted pathogens deploy effectors that directly or indirectly interfere with NLR signaling to suppress immune activation (*12*, *14*–*17*). However, the exact biochemical mechanisms by which pathogen effectors compromise NLR-mediated immunity to promote disease remain largely unknown. Moreover, whereas multiple strategies to bioengineer effector recognition specificities in NLRs have been proposed in recent years (*18*), approaches to mitigate the impact of effector-mediated immune suppression of NLRs are lacking.

NLRs belong to the signal adenosine triphosphatases (ATPases) with numerous domains (STAND) superfamily. They typically exhibit a tripartite domain architecture consisting of an N-terminal signaling domain, a central nucleotide binding domain, and C-terminal superstructure forming repeats (*2*). The central domain, termed NB-ARC (nucleotide binding adaptor shared by APAF-1, plant R proteins, and CED-4) in plant NLRs, is a hallmark of this protein family and plays a key role as a molecular switch, mediating conformational changes required for activation. NB-ARC domains consist of a nucleotide binding domain (NB), a helical domain (HD1), and a winged helix domain (WHD) (*2*, *19*). Diverse NLR activation and signaling strategies are found in nature. In some cases, one NLR protein, termed a singleton, can mediate both elicitor perception and subsequent immune signaling (*20*). However, some NLRs can function as receptor pairs or, in higher-order configurations, termed immune receptor networks (*13*, *21*). In these cases, one NLR acts as a pathogen sensor, requiring a second helper NLR to initiate immune signaling. Such is the case in the solanaceous NRC immune receptor network, which is composed of multiple sensor NLRs that require an array of downstream helper NLRs termed NRCs (NLRs required for cell death) to successfully initiate immune signaling. Upon perception of their cognate effectors, sensors in this network activate oligomerization of their downstream NRC helpers into a putative NRC resistosome, without stably forming part of the mature complex. This has been termed the activation and release model (*4*). The NRC network can encompass up to half of the NLRome in some solanaceous plant species and plays a key role in mediating immunity against a variety of plant pathogens including oomycetes, bacteria, viruses, nematodes, and insects (*15*, *21*).

Plant and metazoan parasites have evolved effectors that interfere with host NLR signaling to promote disease. Parasite effectors can suppress NLR-mediated immunity indirectly by interfering with host proteins that act downstream of NLR signaling (*15*, *17*, *22*, *23*) or directly by interacting with NLRs to inhibit their functions (*15*, *16*, *24*). One such example is the potato cyst nematode (*Globodera rostochiensis*) effector, SPRYSEC15 (SS15), which can suppress signaling mediated by *Nicotiana benthamiana* helper NLRs NRC2 and NRC3 and tomato (*Solanum lycopersicum*) helper NLR NRC1, by binding to their central NB-ARC domains.

[1]The Sainsbury Laboratory, University of East Anglia, Norwich, UK. [2]Department of Biochemistry and Metabolism, John Innes Centre, Norwich, UK. [3]Department of Life Sciences, Imperial College, London, UK. [4]Institute of Plant and Microbial Biology, Academia Sinica, Taipei, Taiwan.
*Corresponding author. Email: sophien.kamoun@tsl.ac.uk (S.K.); ld645@cam.ac.uk (L.D.)
†Present address: Crop Science Centre, Department of Plant Sciences, University of Cambridge, Cambridge, UK.



Downloaded from https://www.science.org on August 02, 2025

In contrast, another *N. benthamiana* helper NLR NRC4, a paralog of NRC2/3, cannot be suppressed by SS15 (Fig. 1A and fig. S1A) (*15*). In this study, we reasoned that mapping the binding interface between SS15 and its target helper NLRs combined with leveraging NRC4 resilience to inhibition would enable us to bioengineer NLR variants that evade pathogen suppression, therefore resurrecting the immune signaling activity of upstream sensors in the NRC network.

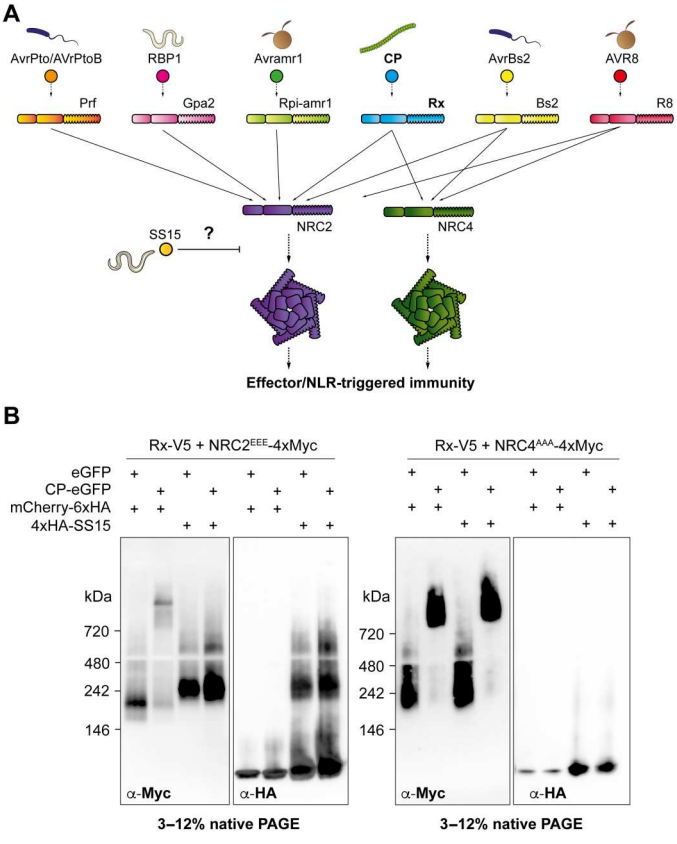


**Fig. 1. SS15 directly inhibits NRC2 but not NRC4 oligomerization.** (**A**) Schematic representation of the NRC immune receptor network, consisting of multiple sensor NLRs and their downstream helper NLRs, NRC2 and NRC4 (in purple and green, respectively). Potato virus X (PVX) capsid protein (CP) and Rx are in boldface as they are used for most of the experiments in this study. Effector-triggered activation of a sensor leads to downstream helper oligomerization and resistosome formation. The *G. rostochiensis* effector SS15 (in yellow) can directly bind to the NB-ARC domain of NRC2 but not NRC4, thereby inhibiting signaling by directly binding to the NB-ARC domain of this helper NLR. (**B**) Blue native polyacrylamide gel electrophoresis (BN-PAGE) assays with inactive and activated Rx together with NRC2 or NRC4, in the absence or presence of SS15. C-terminally V5-tagged Rx and C-terminally 4xMyc-tagged NRC2$^{EEE}$ or NRC4$^{AAA}$ were coexpressed with either free green fluorescent protein (GFP) or C-terminally GFP-tagged PVX CP. These effector-sensor-helper combinations were coinfiltrated together with a 6xHA-mCherry fusion protein or with N-terminally 6xHA-tagged SS15. Total protein extracts were run in parallel on native and denaturing PAGE assays and immunoblotted with the appropriate antisera labeled below. Approximate molecular weights (in kilodalton) of the proteins are shown on the left. Corresponding SDS-PAGE assays can be found in fig. S1. The experiment was repeated three times with similar results.

## RESULTS

### SS15 blocks NRC2 but not NRC4 oligomerization and resistosome formation

First, we investigated how SS15 binding to NRC2 prevents immune signaling, notably whether SS15 prevents oligomerization of NRC following sensor NLR activation. To test this hypothesis, we transiently coexpressed NRC2 or NRC4 with their upstream sensor NLR Rx and the effector SS15 in leaves of *nrc2/3/4* CRISPR knockout (KO) *N. benthamiana* plants and leveraged previously established blue native polyacrylamide gel electrophoresis (BN-PAGE)–based readouts for NRC resistosome formation (*4*). For biochemical analyses, we used previously described NRC2 and NRC4 variants with mutations in their N-terminal MADA motifs (NRC2$^{EEE}$ and NRC4$^{AAA}$, respectively), which abolish cell death induction without compromising receptor activation, oligomerization, or localization (*4*, *25*, *26*). We activated the sensor helper Rx-NRC system by coexpressing the potato virus X (PVX) capsid protein (CP) fused to green fluorescent protein (GFP) or free GFP as an inactive control. In the absence of SS15, both NRC2 and NRC4 oligomerize upon effector-triggered activation mediated by their upstream sensor Rx. However, when SS15 is present, Rx/CP-activated NRC2 is unable to oligomerize and appears as a band of ~240 kDa, which co-migrates with SS15. Inactive NRC2 coexpressed with SS15 also migrates as a band of ~240 kDa, which is slower-migrating relative to inactive NRC2 in the absence of SS15, indicative of in vivo NRC2-SS15 complex formation (Fig. 1B and fig. S1). We also observed that SS15 coexpression not only blocks NRC2 oligomerization but also prevents the previously reported shift of NRC2 from cytoplasm to plasma membrane (PM) as well as the formation of NRC2 PM-associated puncta upon Rx/CP activation (fig. S2) (*4*). In contrast, NRC4 oligomerization is not affected in the presence of SS15, which is in line with previous findings that NRC4 immune signaling is not suppressed by SS15 (*15*). We conclude that SS15 can suppress immune signaling by acting as a direct proteinaceous inhibitor of NRC2, but not NRC4, by directly binding to its NB-ARC domain to block the formation of a signal-competent oligomeric resistosome.

### SS15 binds and immobilizes a critical "hinge" in the NB-ARC domain

Given that NRC4 retains the capacity to oligomerize in the presence of SS15, we leveraged this differential SS15 sensitivity between NRC2 and NRC4 to identify the domain that determines SS15 association and inhibition. We generated a series of NRC2-NRC4 chimeric proteins (Fig. 2, A and B, and fig. S3), which we subsequently assayed for SS15 association via in planta co-immunoprecipitation. We identified one chimeric variant of NRC4, carrying the HD1-1 region of NRC2 (NRC4$^{2HD1-1}$), which gains association to SS15 (Fig. 2C). Unlike NRC4, NRC4$^{2HD1-1}$ is susceptible to inhibition by SS15 and is unable to oligomerize and trigger cell death in the presence of SS15 (Fig. 2, D and E, and figs. S3 and S4). We conclude that the HD1-1 region is important for association to SS15 and for the effector to directly inhibit NRC oligomerization and programmed cell death.

To further define the interface between SS15 and NRC proteins, we attempted to crystallize SS15 in complex with the NB-ARC domain of several NRC proteins. We obtained crystals of SS15 in complex with the NB-ARC domain of SlNRC1, a tomato NRC

Downloaded from https://www.science.org on August 02, 2025

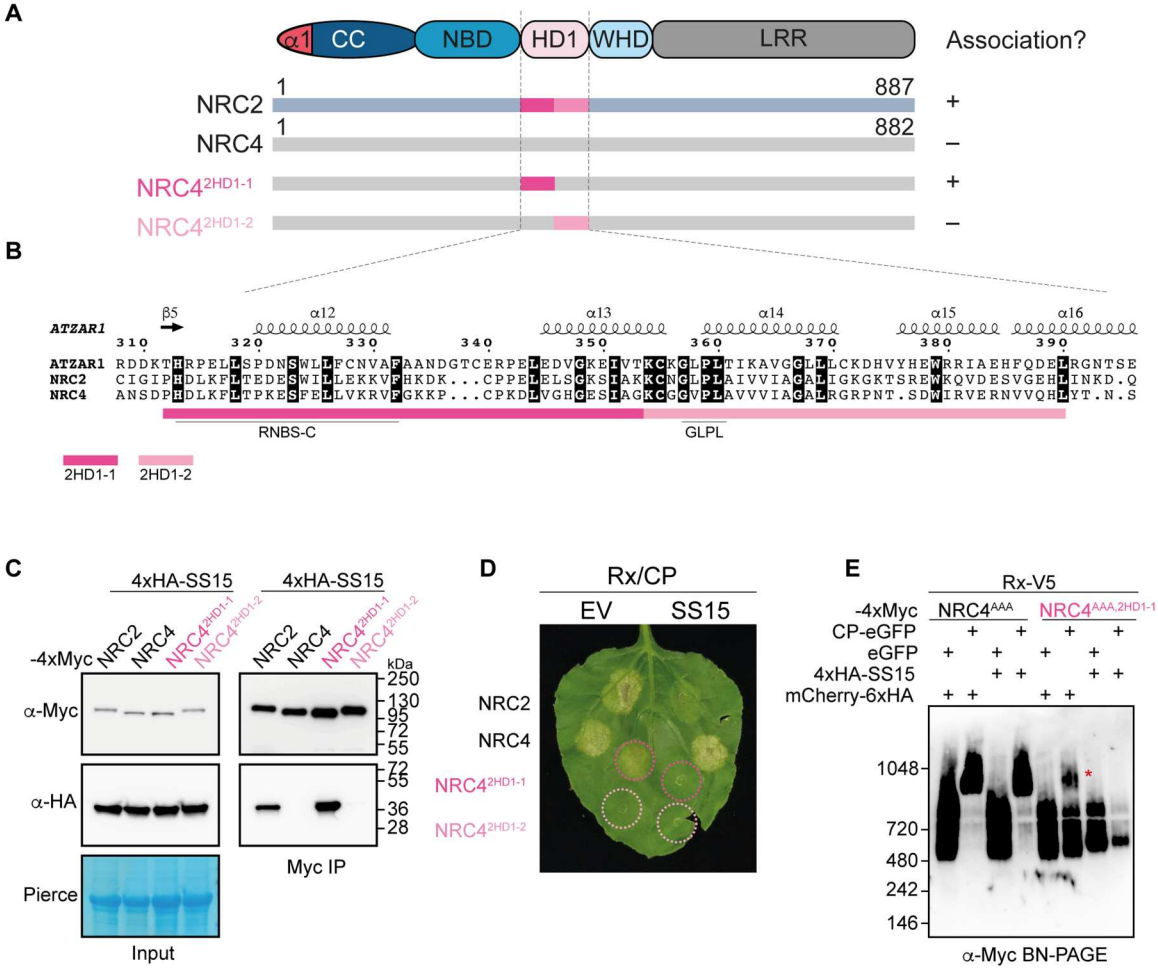


**Fig. 2. The HD1-1 region of NRC NB-ARC domain determines sensitivity to SS15.** (**A**) Schematic representation of the NRC domain architecture, highlighting regions within the NB-ARC domain swapped between NRC2-NRC4 chimeric proteins. Association (+) or lack thereof (–) between these NLR immune receptors and SS15 determined by in planta co-immunoprecipitation (Co-IP) is detailed on the right. (**B**) Amino acid sequence alignment of the HD1 region of the NB-ARC domains of AtZAR1, NRC2, and NRC4. Predicted secondary structure is shown above. Well-characterized motifs within this region are underlined below. (**C**) Co-IP assays between SS15 and chimeric NRC2-NRC4 variants. C-terminally 4xMyc-tagged NRC proteins were coexpressed with N-terminally 4xHA-SS15. IPs were performed with agarose beads conjugated to Myc antibodies (Myc IP). Total protein extracts were immunoblotted with the antisera labeled on the left. Approximate molecular weights (in kilodalton) of the proteins are shown on the right. Rubisco loading control was carried out using Ponceau stain (PS). The experiment was repeated three times with similar results. (**D**) Photo of representative leaves from *N. benthamiana nrc2/3/4* KO plants showing HR after coexpression of Rx/PVX CP with NRC2/NRC4 and the two NRC2-NRC4 chimeras. Combination shown were coexpressed with mCherry-6xHA (EV) or 4xHA-SS15. Three biological replicates with at least six technical replicates each are shown. Quantitative analyses of the HR phenotypes are found in fig. S4. (**E**) BN-PAGE assay with inactive and activated Rx with NRC4 or an NRC2-NRC4 chimeric protein in the absence or presence of SS15. Effector-sensor-helper combinations shown were coinfiltrated together with mCherry-6xHA or with 4xHA-SS15. Total protein extracts were run in parallel on native and denaturing PAGE and immunoblotted with the antisera labeled on the left. SDS-PAGE blots are found in fig. S3. Approximate molecular weights (in kilodalton) of the proteins are shown on the left. The experiment was repeated three times with similar results.

that is inhibited by the nematode effector. Because purification and crystallization trials of SS15 in complex with $NRC2^{NB\text{-}ARC}$ and $NRC3^{NB\text{-}ARC}$ were unsuccessful, we moved forward with the $SlNRC1^{NB\text{-}ARC}$-SS15 crystals. We subsequently solved the structure using x-ray diffraction data collected to 4.5-Å resolution (Fig. 3A, fig. S5, and table S3), which allowed us to determine that SS15 binds to a loop in the HD1-1 region of NRCs that connects the NB domain to the HD1 and WHD domains. This provides orthogonal evidence that the SS15-NRC interactions are mediated by this region as shown with the chimera experiments (Fig. 2). This loop was previously shown to act as a "hinge," allowing the NB domain to rotate relative to the HD1 and WHD domains following activation (fig. S5 and movie S1) (*27*). We propose that SS15 prevents conformational changes that are critical for NLR activation by binding and immobilizing the NB-HD1 hinge.

## Single amino acid variants of NRC2 evade suppression by SS15

Given that SS15 suppresses cell death induction mediated by SlNRC1, NRC2, and NRC3 but not NRC4 or other well-characterized NLRs such as ZAR1 (fig. S1) (*15*), we leveraged the high degree of conservation that is characteristic of plant NB-ARC domains to narrow down residues within the binding interface that underpin this interaction. We shortlisted residues within the HD1-1 region

Downloaded from https://www.science.org on August 02, 2025

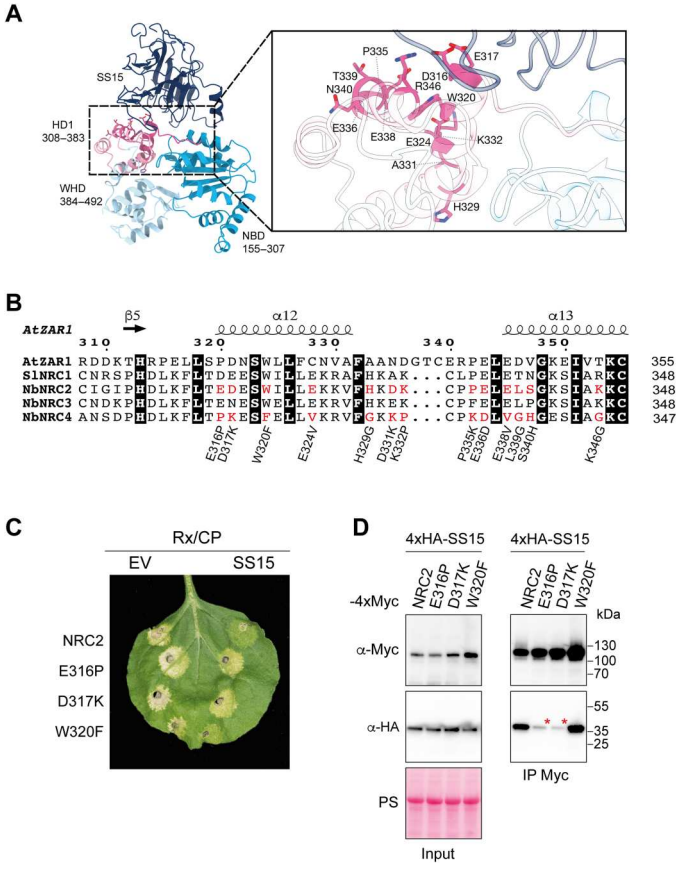


**Fig. 3. SS15-NRC binding interface enables bioengineering NRC2 variants that evade suppression.** (**A**) Crystal structure of the SS15-SlNRC1$^{NB-ARC}$ complex. The NB, HD1, and WHD domains of SlNRC1$^{NB-ARC}$ are shown in cyan, pale blue, and magenta, respectively; SS15 is in dark blue. The inset displays a close-up image of the SS15-SlNRC1$^{NB-ARC}$ HD1 domain interface, with the residues corresponding to those selected for mutagenesis in NRC2 highlighted in stick representation. (**B**) Alignment of the HD1-1 region of AtZAR1, SlNRC1, NRC2, NRC3, and NRC4. Candidate residues (highlighted in red) were shortlisted on the basis of the interface identified in the co-crystal structure of SS15 and the SlNRC1 NB-ARC domain, as well as being conserved in SlNRC1, NRC2, and NRC3 but not NRC4 and AtZAR1. Thirteen NRC2 variants were generated by mutating individual candidate positions to the corresponding amino acid in NRC4 (detailed underneath the alignment). (**C**) Photo of representative leaves from *N. benthamiana nrc2/3/4* KO plants showing HR after coexpression of Rx and PVX CP with NRC2, or different NRC2 variants generated. All proteins were coexpressed with a free mCherry-6xHA fusion protein (EV) or with N-terminally 4xHA-tagged SS15. The experiment consisted of three biological replicates. See fig. S7 quantitative analysis of HR phenotypes. (**D**) Co-IP assays between SS15 and NRC2 variants. C-terminally 4xMyc-tagged NRC2 variants were transiently coexpressed with N-terminally 4xHA-tagged SS15. IPs were performed with agarose beads conjugated to Myc antibodies (Myc IP). While only data for E316P, D317K, and W320F NRC2 variants are shown, additional variants were also tested and can be found in fig S6. Total protein extracts were immunoblotted with appropriate antisera labeled on the left. Approximate molecular weights (in kilodalton) of the proteins are shown on the right. Rubisco loading control was carried out using PS. The experiment was repeated three times with similar results.

that are similar in SlNRC1, NRC2, and NRC3 but different in NRC4 or AtZAR1 (Fig. 3B). Combining information from the cocrystal structure and the alignments allowed us to select 13 candidate residues to test by mutagenesis in NRC2 (Fig. 3B). We mutated each of these residues to the corresponding amino acid found in NRC4 and screened these NRC2 variants for susceptibility to SS15 inhibition in cell death assays. This revealed two variants, NRC2$^{E316P}$ and NRC2$^{D317K}$, which triggered cell death when activated by Rx/CP and were no longer inhibited by SS15 (Fig. 3C and figs. S6 and S7). We also tested all 13 single amino acid mutants for association with SS15 by in planta co-immunoprecipitation and found that NRC2$^{E316P}$ and NRC2$^{D317K}$ exhibited reduced association with SS15 relative to NRC2 (Fig. 3D and fig. S6), which is in line with the observation that SS15 is not able to suppress these variants (Fig. 3C). All other NRC2 variants generated were indistinguishable from NRC2 in terms of their capacity to trigger HR when activated by Rx/CP and were all suppressed by SS15, except for NRC2$^{E324V}$, which did not accumulate in planta (fig. S6). We conclude that the E316 and D317 residues are critical for SS15-mediated inhibition of NRC2 and that mutating these residues to their equivalent amino acid in NRC4 allows Rx/CP-activated NRC2 to evade SS15 association and inhibition.

### A bioengineered NRC2$^{D317K}$ variant resurrects the activity of multiple NRC2-dependent sensors in the presence of SS15

We next tested whether these two SS15-evading variants of NRC2 could restore the functionality of NRC2-dependent sensor NLRs that are suppressed by the parasite effector. We tested this by performing complementation assays with NRC2$^{E316P}$ and NRC2$^{D317K}$ in *nrc2/3/4* CRISPR KO *N. benthamiana* plants. We activated the NRC2 variants with a panel of agronomically important sensor NLRs mediating resistance to diverse pathogens, including the potato cyst nematode R protein Gpa2 (an allele of Rx), as well as other well-characterized oomycete and bacterial resistance proteins. NRC2$^{D317K}$ evaded SS15 inhibition with all tested sensor NLRs restoring their capacity to activate immune signaling (Fig. 4A and figs. S8 and S9). In contrast, NRC2$^{E316P}$ could evade SS15 suppression when activated by Rx, but not when activated by other sensors. We therefore selected NRC2$^{D317K}$ for follow-up biochemical studies, using BN-PAGE–based assays. Unlike NRC2, activated NRC2$^{D317K}$ oligomerized even in the presence of SS15 and did not form an in vivo complex with the inhibitor (Fig. 4B). We conclude that NRC2$^{D317K}$ can fully evade SS15-mediated immune suppression, retaining the capacity to oligomerize and mediate cell death when activated by multiple agronomically important sensor NLRs.

## DISCUSSION

Our study reveals how a parasite effector has evolved as an inhibitor of a helper NLR by directly binding its NB-ARC domain to prevent resistosome formation and immune signaling. By binding and immobilizing a critical hinge loop in the HD1 region of the NB-ARC, SS15 restricts movement of the NB domain relative to the HD1 and WHD domains, preventing immune receptor activation. While SS15 can bind and inhibit NRC2, it cannot bind or inhibit the NRC2 paralog NRC4. We exploited NRC4's resilience to SS15 inhibition by making chimeric NRC2-NRC4 variants that, together

Downloaded from https://www.science.org on August 02, 2025

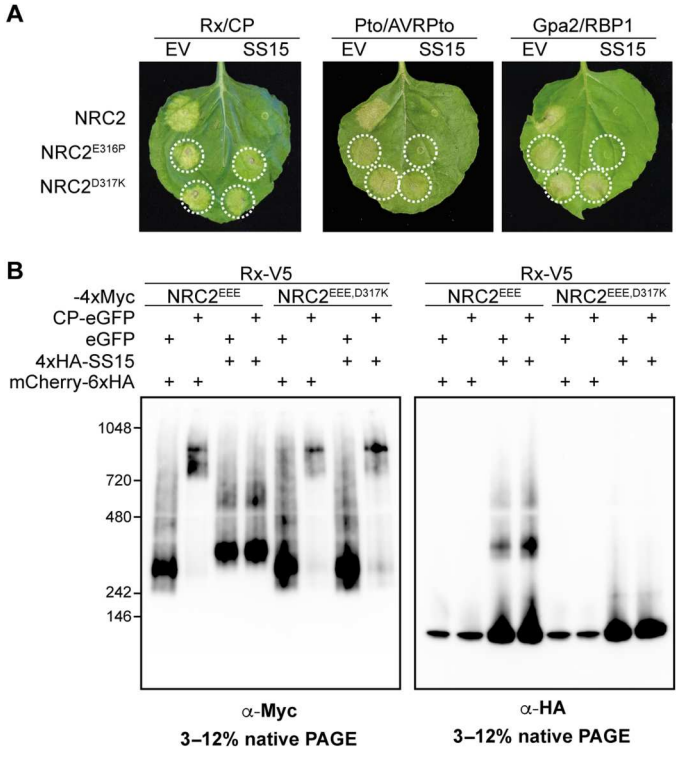


**Fig. 4. NRC2$^{D317K}$ helper restores immune signaling of multiple disease resistance genes in the presence of the effector SS15.** (**A**) Photo of representative leaves from *N. benthamiana nrc2/3/4* KO plants showing HR after coexpression of Rx/CP, Pto/AVRPto, or Gpa2/RBP1 together with NRC2, NRC2$^{E316P}$, or NRC2$^{D317K}$ in the absence or presence of SS15. The experiment consisted of three biological replicates. A quantitative analysis of HR phenotypes can be found in fig. S8. (**B**) BN-PAGE assays with inactive and active Rx together with NRC2 or NRC2$^{D317K}$, in the absence or presence of SS15. C-terminally V5-tagged Rx and C-terminally 4xMyc-tagged NRC2$^{EEE}$ or NRC2$^{EEE,D317K}$ were coexpressed with either free GFP or C-terminally GFP-tagged PVX CP. These effector-sensor-helper combinations were coexpressed together with a 6xHA-mCherry fusion protein or with N-terminally 4xHA-tagged SS15. Total protein extracts were run in parallel on blue native and denaturing PAGE assays and immunoblotted with the appropriate antisera labeled below. Approximate molecular weights (in kilodaltons) of the proteins are shown on the left. Corresponding SDS-PAGE blots can be found in fig. S9. The experiment was repeated three times with similar results.

with structural information, helped us identify the inhibitor binding interface. Mutational studies of this interface allowed us to generate A amino acid variant of NRC2 (NRC2$^{D317K}$) that evades SS15 inhibition without compromising receptor signaling capacity. This NRC2$^{D317K}$ variant can now support signaling by any NRC2-dependent sensor even in the presence of SS15.

In the future, we will address the conservation of the NRC-SS15 interface across NLR proteins. In particular, understanding the degree of conservation of the NRC-SS15 interface across solanaceous NRCs, notably at position 317, can be of great use. This will allow us to determine whether substitutions analogous to NRC2$^{D317K}$ can be effective at evading SS15 suppression when deployed in NRCs from different solanaceous crop species. Moreover, evolutionary analyses coupled with ancestral sequence reconstruction may enable reconstructing the evolutionary trajectory of the NRC-SS15 interface to gain a deeper understanding of the coevolutionary dynamics between NLRs and their pathogen inhibitors.

The existence of plant parasite–secreted NLR inhibitors suggests that suppressed resistance genes may occur in crop genomes. Leveraging the approach detailed in this study, it may be possible to resurrect cryptic or defeated resistance proteins to enhance disease resistance. Moreover, considering that multiple sensors can signal through the same downstream helper, applying this approach to helper NLRs holds potential to simultaneously resurrect multiple upstream sensor NLRs. The single amino acid NRC2 variants we identified could be generated in locus using gene editing technologies in agronomically important crop species, making deployment of this technology viable in countries where transgenic approaches are not feasible. Our work describes a potential approach to achieve robust immunity by engineering NLRs that avoid parasite suppression. This could, in theory, be applied to other plant, metazoan, or even prokaryotic NLR immune receptors that are directly targeted by parasite effectors (*12*, *15*, *16*, *24*). Combined with recent advances in NLR engineering to bioengineer pathogen recognition specificities (*18*, *28*), this technology holds the potential to facilitate synthetic disease resistance breeding.

## MATERIALS AND METHODS

### Plant growth conditions

Wild-type and *nrc2/3/4* CRISPR mutant *N. benthamiana* lines were grown in a controlled environment growth chamber with a temperature range of 22° to 25°C, humidity of 45 to 65%, and a 16-hour light/8-hour dark cycle.

### Plasmid construction

We used the Golden Gate Modular Cloning (MoClo) kit (*29*) and the MoClo plants part kit (*30*) for cloning. All vectors used were generated with these kits unless otherwise stated. Cloning design and sequence analysis were done using Geneious Prime (v2021.2.2; www.geneious.com). Plasmid construction is described in more detail in table S1.

### Cell death assays by agroinfiltration

Proteins of interest were transiently expressed in *N. benthamiana* according to previously described methods (*4*). Briefly, leaves from 4- to 5-week-old plants were infiltrated with suspensions of *Agrobacterium tumefaciens* GV3101 pM90 strains transformed with expression vectors coding for different proteins indicated. The final $OD_{600}$ (optical density at 600 nm) of all *A. tumefaciens* suspensions were adjusted in infiltration buffer [10 mM MES, 10 mM $MgCl_2$, and 150 μM acetosyringone (pH 5.6)]. The final $OD_{600}$ used for each construct is described in table S2.

### Extraction of total proteins for BN-PAGE and SDS-PAGE assays

Four- to 5-week-old *N. benthamiana* plants were agroinfiltrated as described above with constructs of interest, and leaf tissue was collected 3 days after agroinfiltration for NRC2 and 2 days after agroinfiltration for NRC4. The final $OD_{600}$ used for each construct is described in table S2. BN-PAGE was performed using the bis-tris NativePAGE system (Invitrogen) according to the manufacturer's instructions, as described previously (*4*). Leaf tissue was ground using a Geno/Grinder tissue homogenizer. For NRC2, GTMN

Downloaded from https://www.science.org on August 02, 2025

extraction buffer was used [10% glycerol, 50 mM tris-HCl (pH 7.5), 5 mM $MgCl_2$, and 50 mM NaCl] supplemented with 10 mM dithiothreitol (DTT), 1× protease inhibitor cocktail (Sigma-Aldrich), and 0.2% NP-40 substitute (Sigma-Aldrich). For NRC4, GHMN buffer [10% glycerol, 50 mM Hepes (pH 7.4), 5 mM $MgCl_2$, and 50 mM NaCl] buffer supplemented with 10 mM DTT, 1× protease inhibitor cocktail (Sigma-Aldrich), and 1% digitonin (Sigma-Aldrich) was used for extraction. Samples were incubated in extraction buffer on ice for 10 min with short vortex mixing every 2 min. Following incubation, samples were centrifuged at 5000*g* for 15 min, and the supernatant was used for BN-PAGE and SDS-PAGE assays.

### BN-PAGE assays

For BN-PAGE, samples extracted as detailed above were diluted as per the manufacturer's instructions by adding NativePAGE 5% G-250 sample additive, 4× sample buffer, and water. After dilution, samples were loaded and run on NativePAGE 3 to 12% bis-tris gels alongside either NativeMark unstained protein standard (Invitrogen) or SERVA Native Marker (SERVA). The proteins were then transferred to polyvinylidene difluoride membranes using the NuPAGE Transfer Buffer using a Trans-Blot Turbo transfer system (Bio-Rad) as per the manufacturer's instructions. Proteins were fixed to the membranes by incubating with 8% acetic acid for 15 min, washed with water, and left to dry. Membranes were subsequently reactivated with methanol to correctly visualize the unstained native protein marker. Membranes were immunoblotted as described below.

### SDS-PAGE assays

For SDS-PAGE, samples were diluted in SDS loading dye and denatured at 72°C for 10 min. Denatured samples were spun down at 5000*g* for 3 min, and the supernatant was run on Bio-Rad 4 to 20% Mini-PROTEAN TGX gels alongside a PageRuler Plus prestained protein ladder (Thermo Fisher Scientific). The proteins were then transferred to polyvinylidene difluoride membranes using the Trans-Blot Turbo transfer buffer using a Trans-Blot Turbo transfer system (Bio-Rad) as per the manufacturer's instructions. Membranes were immunoblotted as described below.

### Immunoblotting and detection of BN-PAGE and SDS-PAGE assays

Blotted membranes were blocked with 5% milk in tris-buffered saline and 0.01% Tween 20 (TBS-T) for an hour at room temperature and subsequently incubated with desired antibodies at 4°C overnight. Antibodies used were anti-GFP (B-2) horseradish peroxidase (HRP) (Santa Cruz Biotechnology), anti-hemagglutinin (HA) (3F10) HRP (Roche), anti-Myc (9E10) HRP (Roche), and anti-V5 (V2260) HRP (Roche), all used in a 1:5000 dilution in 5% milk in TBS-T. To visualize proteins, we used Pierce ECL Western (32106, Thermo Fisher Scientific), supplementing with up to 50% SuperSignal West Femto Maximum Sensitivity Substrate (34095, Thermo Fisher Scientific) when necessary. Membrane imaging was carried out with an ImageQuant LAS 4000 or an ImageQuant 800 luminescent imager (GE Healthcare Life Sciences, Piscataway, NJ). Rubisco loading control was stained using Ponceau S (Sigma-Aldrich).

### Co-immunoprecipitation assays

Co-immunoprecipitation assays were performed as described previously (*15*). Total soluble protein was extracted as described above from leaves of *N. benthamiana* 3 days after agroinfiltration using the GTEN buffer [10% glycerol, 25 mM tris-HCl (pH 7.5), 1 mM EDTA, and 150 mM NaCl] supplemented with 2% (w/v) polyvinylpolypyrrolidone (PVPP), 10 mM DTT, and 1× protease inhibitor cocktail (Sigma-Aldrich), as well as 0.3% IGEPAL (Sigma-Aldrich). $OD_{600}$ used can be found in table S2. Protein extracts were filtered using Minisart 0.45-μm filters (Sartorius Stedim Biotech, Goettingen, Germany). Part of the extract was set aside before immunoprecipitation and used for SDS-PAGE as described above. These were the inputs. A total of 1.4 ml of the remaining filtered total protein extract was mixed with 30 μl of anti–c-Myc agarose beads (A7470, Sigma-Aldrich) and incubated end over end for 90 min at 4°C. Beads were washed five times with immunoprecipitation wash buffer [GTEN extraction buffer with 0.3% (v/v) IGEPAL (Sigma-Aldrich)] and resuspended in 60 μl of SDS loading dye. Proteins were eluted from beads by heating for 10 min at 72°C. Immunoprecipitated samples were used for SDS-PAGE and immunoblotted as described above and compared to the inputs.

### Confocal microscopy

Three- to 4-week-old plants were agroinfiltrated as described above with constructs of interest. The final $OD_{600}$ used for each construct is described in table S2. Leaf tissue was prepared for imaging by sectioning of the desired area surrounding an infiltration spot using a cork borer size 4 and was mounted, live, in wells containing $dH_2O$ made in Carolina Observation Gel to enable diffusion of gasses. The abaxial of the leaf tissue was imaged using a Leica SP8 with 40× water immersion objective. Laser excitations for fluorescent proteins were used as described previously (*31*), namely, 488 nm (argon) for GFP, 561/594 nm (diode) for red fluorescent protein, and 405 nm (diode) for blue fluorescent protein.

### Membrane enrichment assays

Membrane enrichment was carried out by slightly modifying a previously described protocol (*32*). Briefly, the leaf material was ground to fine powder using liquid nitrogen and 2× volume of extraction buffer was added. Extraction buffer consisted of 0.81 M sucrose, 5% (v/v) glycerol, 10 mM EDTA, 10 mM EGTA, 5 mM KCl, and 100 mM tris-HCl (pH 7.5) supplemented with 5 mM DTT, 1% Sigma-Aldrich plant protease inhibitor cocktail, 1 mM phenylmethylsulfonyl fluoride, and 0.5% PVPP. After addition of the buffer, the samples were vortexed for a minute, and the cell debris was cleared out by two subsequent centrifugation steps at 1000*g* for 5 min. The supernatant was diluted 1:1 using distilled water, and an aliquot of the supernatant was separated as the total fraction (*T*). The remaining supernatant (200 to 300 μl) was further centrifuged at 21,000*g* for 90 min at 4°C. This centrifugation yielded the supernatant (soluble fraction, *S*) and membrane-enriched pellet (membrane fraction, *M*). After separating the soluble fraction, the pellet was resuspended in diluted extraction buffer (without PVPP). All the fractions were diluted with SDS loading dye, and proteins were denatured by incubating at 50°C for 15 min. Western blotting was performed as previously described following SDS-PAGE. Endogenous plasma membrane ATPase was detected using an anti-H + ATPase (AS07 260) antibody (Agrisera) as a marker to show the success of membrane enrichment.

Downloaded from https://www.science.org on August 02, 2025

### Heterologous protein production and purification from *Escherichia coli*

Heterologous production and purification of SS15 was performed as previously described (*15*). Recombinant SS15 protein (lacking signal peptide) was expressed by cloning in pOPIN-S3C plasmid, with an N-terminal tandem 6xHis-SUMO followed by a 3C protease cleavage site. pOPIN-S3C:SS15 was transformed into *Escherichia coli* SHuffle cells. Eight liters of these cells were grown at 30°C in autoinduction medium (*33*) to an $OD_{600}$ of 0.6 to 0.8 followed by overnight incubation at 18°C and harvested by centrifugation. Pelleted cells were resuspended in 50 mM tris-HCl (pH 8), 500 mM NaCl, 50 mM glycine, 5% (v/v) glycerol, and 20 mM imidazole (buffer A) supplemented with cOmplete EDTA-free protease inhibitor tablets (Roche) and lysed by sonication. The clarified cell lysate was applied to a $Ni^{2+}$-NTA column connected to an AKTA pure system. 6xHis-SUMO-SS15 was step eluted with elution buffer (buffer A with 500 mM imidazole) and directly injected onto a Superdex 200 26/600 gel filtration column pre-equilibrated with buffer B [20 mM Hepes (pH 7.5) and 150 mM NaCl]. The fractions containing 6xHis-SUMO-SS15 were pooled, and the N-terminal 6xHis-SUMO tag was cleaved by addition of 3C protease (10 μg/mg of fusion protein), incubating overnight at 4°C. Cleaved SS15 was further purified using a $Ni^{2+}$-NTA column, this time collecting the flow-through to separate the cleaved tag from the SS15 protein. Untagged SS15 was further purified by another round of gel filtration as described above. The concentration of protein was judged by absorbance at 280 nm (using a calculated molar extinction coefficient of 35,920 $M^{-1}$ $cm^{-1}$ for SS15).

Heterologous production and purification of $SlNRC1^{NB\text{-}ARC}$ was performed as previously described (*34*). Recombinant $SlNRC1^{NB\text{-}ARC}$ protein was also expressed cloning in pOPIN-S3C plasmid as described above. pOPIN-S3C:$SlNRC1^{NB\text{-}ARC}$ was transformed into *E. coli* Lemo21 (DE3) cells. Eight liters of these cells were grown at 37°C in autoinduction medium (*33*) to an $OD_{600}$ of 0.6 to 0.8 followed by overnight incubation at 18°C and harvested by centrifugation. Pelleted cells were resuspended in 50 mM tris-HCl (pH 8), 500 mM NaCl, 50 mM glycine, 5% (v/v) glycerol, and 20 mM imidazole (buffer A) supplemented with cOmplete EDTA-free protease inhibitor tablets (Roche) and lysed by sonication. The clarified cell lysate was applied to a $Ni^{2+}$-NTA column connected to an AKTA pure system. 6xHis-SUMO-$SlNRC1^{NB\text{-}ARC}$ was step eluted with elution buffer (buffer A with 500 mM imidazole) and directly injected onto a Superdex 200 26/600 gel filtration column pre-equilibrated with buffer B [20 mM Hepes (pH 7.5) and 150 mM NaCl]. The fractions containing 6xHis-SUMO-$SlNRC1^{NB\text{-}ARC}$ were pooled, and the N-terminal 6xHis-SUMO tag was cleaved by addition of 3C protease (10 μg/mg of fusion protein), incubating overnight at 4°C. Cleaved $SlNRC1^{NB\text{-}ARC}$ was further purified using a $Ni^{2+}$-NTA column, this time collecting the flow-through to separate the cleaved tag from the $SlNRC1^{NB\text{-}ARC}$ protein. Untagged $SlNRC1^{NB\text{-}ARC}$ was further purified by another round of gel filtration as described above. The concentration of protein was judged by absorbance at 280 nm (using a calculated molar extinction coefficient of 63,370 $M^{-1}$ $cm^{-1}$ for $SlNRC1^{NB\text{-}ARC}$).

To obtain $SlNRC1^{NB\text{-}ARC}$ in complex with SS15, both proteins were incubated in a 1:1 molar ratio overnight at 4°C and subjected to gel filtration on a Superdex 200 26/600 gel filtration column as described above. The fractions containing $SlNRC1^{NB\text{-}ARC}$ in complex with SS15 were pooled, concentrated to 10 to 15 mg/ml, and subsequently used for crystallization screens.

### Crystallization, data collection, and structure solution

Crystallization screens were performed at 18°C using the sitting-drop vapor diffusion technique. Drops composed of 0.3 μl of protein solution and 0.3 μl of reservoir solution were set up in MRC 96-well crystallization plates (Molecular Dimensions), which were dispensed using an Oryx Nano or an Oryx8 robot (Douglas Instruments). Crystal growth was monitored using a Minstrel Desktop Crystal Imaging System (Rikagu). Suitable crystals grew after 72 hours in a Morpheus screen crystallization condition containing 0.1 M MES buffer (pH 6.5), 10% (w/v) PEG-8000 (polyethylene glycol, molecular weight 8000), and 20% (v/v) ethylene glycol (Molecular Dimensions) and were harvested by flash-cooling in liquid nitrogen using LithoLoops (Molecular Dimensions). X-ray diffraction data were collected at the Diamond Light Source (Didcot, UK) on beamline I03 using an Eiger2 XE 16M pixel array detector (Dectris) with crystals maintained at 100 K by a Cryojet cryocooler (Oxford Instruments).

X-ray data were integrated and scaled using X-ray Detection Software (XDS) (*35*), as implemented through the XIA2 (*36*) pipeline, and then merged using AIMLESS (*37*), via the CCP4i2 graphical user interface (*38*). The $NRC1^{NB\text{-}ARC}$-SS15 complex crystallized in space group $P6_1$ with cell parameters $a = b = 128.6$ and $c = 170.7$ Å, and the Most Unexceptional crystal yielded diffraction data to 4.5 Å resolution (see table S3 for a summary of data collection and refinement statistics). Given the small size of the dataset, we assigned 10% of the data (883 unique reflections) for the $R_{free}$ calculation, to give a more statistically meaningful metric. The crystal structure of $NRC1^{NB\text{-}ARC}$ alone was already available [Protein Data Bank (PDB) 6S2P], but there was no experimentally determined structure for SS15. Thus, we made use of AlphaFold2 (AF2) multimer (*39*), as implemented through ColabFold (*40*) to generate structural predictions for the complex. There was very good sequence coverage for both proteins, and the five independent models of the individual components were closely similar. The predicted local distance difference test (pLDDT) scores were generally good (e.g., averages of 82 and 75 for $NRC1^{NB\text{-}ARC}$ and SS15 models, respectively, from the rank 1 predictions). However, the relative placement of the two components varied across the five models, and the corresponding predicted aligned error (PAE) scores indicated very low confidence in these predictions. A comparison of the five $NRC1^{NB\text{-}ARC}$ models with the known crystal structure showed a good agreement (e.g., superposition of the rank 1 model gave a root mean square deviation of 1.77 Å). Given that the AF2 model provided starting coordinates for several loops missing from the crystal structure, we decided to use this model in molecular replacement. Templates for both components were prepared using the "Process Predicted Models" CCP4i2 task, which removed low-confidence regions (based on pLDDT) and converted the pLDDT scores in the *B* factor field of the PDB coordinate files to pseudo *B* factors. Analysis of the likely composition of the asymmetric unit (ASU) suggested that it contained two copies of each component, giving an estimated solvent content of ~67%. Phaser (*41*) was able to place the four chains within the ASU, although the second SS15 domain required manual repositioning with respect to its neighboring NRC1 domain to avoid a number of clashes and improve the fit to the density. This was achieved using COOT (*42*) and guided by the arrangement of

Downloaded from https://www.science.org on August 02, 2025

the other NRC1-SS15 complex (fig. S4). The structure was then subjected to jelly body refinement in REFMAC5 (*43*) using ProSMART restraints (*44*) generated from the AF2 models, giving $R_{work}$ and $R_{free}$ values of 0.357 and 0.401, respectively, to a 4.5-Å resolution.

Now, it was possible to generate more complete models for the components by superposing the original unprocessed AF2 models and trimming these with reference to the improved electron density. Furthermore, a substantial region of positive difference density was present at the cores of both NRC1 domains, which corresponded to the adenosine diphosphate (ADP) in the crystal structure; thus, we incorporated ADP into the model. Because of the low resolution of the dataset, only very limited rebuilding was possible in COOT, where Geman-McClure and Ramachandran restraints were used to maintain good stereochemical parameters. After several cycles of restrained refinement in REFMAC5 and editing in COOT, a reasonable model was obtained with $R_{work}$ and $R_{free}$ values of 0.258 and 0.298, respectively. However, there remained a region of positive difference density near the N termini of both SS15 domains that we could not adequately explain. At this point, we reran the AF2 multimer predictions, but this time with one copy of the complex taken from the crystal structure as a reference template. Although these computational predictions did not produce complexes that were consistent with the x-ray data, and the models for the individual components did not appear to be noticeably improved based on pLDDT scores, we used them as starting points to rebuild the x-ray structure.

Notably, for several models, the N-terminal region of SS15 adopted conformations that partially accounted for the region of positive difference electron density, and this could be improved by careful rebuilding and refinement. This "AlphaFold recycling" procedure was repeated a further two times before finalizing the structure, which included residues 153 to 494 for SlNRC1 (numbered with respect to the full-length protein) and residues 18 to 223 for SS15, where residues 33 to 43 in both copies of the latter formed α helices that occupied the regions of positive difference density observed earlier. For the last refinement in REFMAC5, the following options were used: ProSMART restraints generated from the latest AF2 models, overall *B* factor refinement with translation/libration/screw (TLS) restraints (where each protein chain was treated as a separate domain), and noncrystallographic symmetry restraints. The final model gave $R_{work}$ and $R_{free}$ values of 0.237 and 0.275, respectively, to a 4.5-Å resolution (see table S3 for a summary of refinement statistics). All structural figures were prepared using ChimeraX (*45*) and PyMOL (*46*).

## Supplementary Materials

**This PDF file includes:**
Figs. S1 to S9
Legends for tables S1 and S2
Table S3
Legend for movie S1
References

**Other Supplementary Material for this manuscript includes the following:**
Tables S1 and S2
Movie S1

## REFERENCES AND NOTES


1. J. D. Jones, R. E. Vance, J. L. Dangl, Intracellular innate immune surveillance devices in plants and animals. *Science* **354**, aaf6395 (2016).
2. Z. Duxbury, C.-H. Wu, P. Ding, A comparative overview of the intracellular guardians of plants and animals: NLRs in innate immunity and beyond. *Annu. Rev. Plant Biol.* **72**, 155–184 (2021).
3. J. Wang, M. Hu, J. Wang, J. Qi, Z. Han, G. Wang, Y. Qi, H. W. Wang, J. M. Zhou, J. Chai, Reconstitution and structure of a plant NLR resistosome conferring immunity. *Science* **364**, eaav5870 (2019).
4. M. P. Contreras, H. Pai, Y. Tumtas, C. Duggan, E. L. H. Yuen, A. V. Cruces, J. Kourelis, H.-K. Ahn, K.-T. Lee, C.-H. Wu, T. O. Bozkurt, L. Derevnina, S. Kamoun, Sensor NLR immune proteins activate oligomerization of their NRC helpers in response to plant pathogens. *The EMBO Journal* **42**, e111519 (2023).
5. H.-K. Ahn, X. Lin, A. C. Olave-Achury, L. Derevnina, M. P. Contreras, J. Kourelis, S. Kamoun, J. D. G. Jones, Effector-dependent activation and oligomerization of plant NRC class helper NLRs by sensor NLR immune receptors Rpi-amr3 and Rpi-amr1. *The EMBO Journal* **42**, e111484 (2023).
6. A. Förderer, E. Li, A. W. Lawson, Y. Deng, Y. Sun, E. Logemann, X. Zhang, J. Wen, Z. Han, J. Chang, Y. Chen, P. Schulze-Lefert, J. Chai, A wheat resistosome defines common principles of immune receptor channels. *Nature* **610**, 532-539 (2022).
7. R. Martin, T. Qi, H. Zhang, F. Liu, M. King, C. Toth, E. Nogales, B. J. Staskawicz, Structure of the activated ROQ1 resistosome directly recognizing the pathogen effector XopQ. *Science* **370**, eabd9993 (2020).
8. I. V. Hochheiser, M. Pilsl, G. Hagelueken, J. Moecking, M. Marleaux, R. Brinkschulte, E. Latz, C. Engel, M. Geyer, Structure of the NLRP3 decamer bound to the cytokine release inhibitor CRID3. *Nature* **604**, 184–189 (2022).
9. Z. Hu, Q. Zhou, C. Zhang, S. Fan, W. Cheng, Y. Zhao, F. Shao, H. W. Wang, S. F. Sui, J. Chai, Structural and biochemical basis for induced self-propagation of NLRC4. *Science* **350**, 399–404 (2015).
10. Z. Duxbury, S. Wang, C. I. MacKenzie, J. L. Tenthorey, X. Zhang, S. U. Huh, L. Hu, L. Hill, P. M. Ngou, P. Ding, J. Chen, Y. Ma, H. Guo, B. Castel, P. N. Moschou, M. Bernoux, P. N. Dodds, R. E. Vance, J. D. G. Jones, Induced proximity of a TIR signaling domain on a plant-mammalian NLR chimera activates defense in plants. *Proc. Natl. Acad. Sci. U.S.A.* **117**, 18832–18839 (2020).
11. B. P. M. Ngou, P. Ding, J. D. Jones, Thirty years of resistance: Zig-zag through the plant immune system. *Plant Cell* **34**, 1447–1478 (2022).
12. L. A. Gao, M. E. Wilkinson, J. Strecker, K. S. Makarova, R. K. Macrae, E. V. Koonin, F. Zhang, Prokaryotic innate immunity through pattern recognition of conserved viral proteins. *Science* **377**, eabm4096 (2022).
13. C.-H. Wu, L. Derevnina, S. Kamoun, Receptor networks underpin plant immunity. *Science* **360**, 1300–1301 (2018).
14. L. D. Cunha, J. M. Ribeiro, T. D. Fernandes, L. M. Massis, C. A. Khoo, J. H. Moffatt, H. J. Newton, C. R. Roy, D. S. Zamboni, Inhibition of inflammasome activation by *Coxiella burnetii* type IV secretion system effector IcaA. *Nat. Commun.* **6**, 10205 (2015).
15. L. Derevnina, M. P. Contreras, H. Adachi, J. Upson, A. Vergara Cruces, R. Xie, J. Skłenar, F. L. H. Menke, S. T. Mugford, D. MacLean, W. Ma, S. A. Hogenhout, A. Goverse, A. Maqbool, C. H. Wu, S. Kamoun, Plant pathogens convergently evolved to counteract redundant nodes of an NLR immune receptor network. *PLOS Biol.* **19**, e3001136 (2021).
16. H. Yen, N. Sugimoto, T. Tobe, Enteropathogenic Escherichia coli uses NleA to inhibit NLRP3 inflammasome activation. *PLOS Pathog.* **11**, e1005121 (2015).
17. Q. Chai, S. Yu, Y. Zhong, Z. Lu, C. Qiu, Y. Yu, X. Zhang, Y. Zhang, Z. Lei, L. Qiang, B. X. Li, Y. Pang, X. B. Qiu, J. Wang, C. H. Liu, A bacterial phospholipid phosphatase inhibits host pyroptosis by hijacking ubiquitin. *Science* **378**, eabq0132 (2022).
18. C. Marchal, H. Pai, S. Kamoun, J. Kourelis, Emerging principles in the design of bioengineered made-to-order plant immune receptors. *Curr. Opin. Plant Biol.* **70**, 102311 (2022).
19. J. Kourelis, T. Sakai, H. Adachi, S. Kamoun, RefPlantNLR is a comprehensive collection of experimentally validated plant disease resistance proteins from the NLR family. *PLOS Biol.* **19**, e3001124 (2021).
20. H. Adachi, L. Derevnina, S. Kamoun, NLR singletons, pairs, and networks: Evolution, assembly, and regulation of the intracellular immunoreceptor circuitry of plants. *Curr. Opin. Plant Biol.* **50**, 121–131 (2019).
21. C.-H. Wu, A. Abd-el-Haliem, T. O. Bozkurt, K. Belhaj, R. Terauchi, J. H. Vossen, S. Kamoun, NLR network mediates immunity to diverse plant pathogens. *Proc. Natl. Acad. Sci. U.S.A.* **114**, 8113–8118 (2017).
22. C. N. LaRock, B. T. Cookson, The Yersinia virulence effector YopM binds caspase-1 to arrest inflammasome assembly and processing. *Cell Host Microbe* **12**, 799–805 (2012).
23. H. Chen, D. Yang, F. Han, J. Tan, L. Zhang, J. Xiao, Y. Zhang, Q. Liu, The bacterial T6SS effector EvpP prevents NLRP3 inflammasome activation by inhibiting the $Ca^{2+}$-dependent MAPK-Jnk pathway. *Cell Host Microbe* **21**, 47–58 (2017).


Downloaded from https://www.science.org on August 02, 2025

24. H. S. Karki, S. Abdullah, Y. Chen, D. A. Halterman, Natural genetic diversity in the potato resistance gene RB confers suppression avoidance from Phytophthora effector IPI-O4. *Mol. Plant Microbe Interact.* **34**, 1048–1056 (2021).
25. H. Adachi, M. P. Contreras, A. Harant, C. H. Wu, L. Derevnina, T. Sakai, C. Duggan, E. Moratto, T. O. Bozkurt, A. Maqbool, J. Win, S. Kamoun, An N-terminal motif in NLR immune receptors is functionally conserved across distantly related plant species. *eLife* **8**, e49956 (2019).
26. J. Kourelis, M. P. Contreras, A. Harant, H. Pai, D. Lüdke, H. Adachi, L. Derevnina, C.-H. Wu, S. Kamoun, The helper NLR immune protein NRC3 mediates the hypersensitive cell death caused by the cell-surface receptor Cf-4. *PLoS Genetics* **18**, e1010414 (2022).
27. J. Wang, J. Wang, M. Hu, S. Wu, J. Qi, G. Wang, Z. Han, Y. Qi, N. Gao, H. W. Wang, J. M. Zhou, J. Chai, Ligand-triggered allosteric ADP release primes a plant NLR complex. *Science* **364**, eaav5868 (2019).
28. J. Kourelis, C. Marchal, A. Posbeyikian, A. Harant, S. Kamoun, NLR immune receptor-nanobody fusions confer plant disease resistance. *Science* **379**, 934–939 (2023).
29. E. Weber, C. Engler, R. Gruetzner, S. Werner, S. Marillonnet, A modular cloning system for standardized assembly of multigene constructs. *PLOS ONE* **6**, e16765 (2011).
30. C. Engler, M. Youles, R. Gruetzner, T. M. Ehnert, S. Werner, J. D. G. Jones, N. J. Patron, S. Marillonnet, A golden gate modular cloning toolbox for plants. *ACS Synth. Biol.* **3**, 839–843 (2014).
31. C. Duggan, E. Moratto, Z. Savage, E. Hamilton, H. Adachi, C. H. Wu, A. Y. Leary, Y. Tumtas, S. M. Rothery, A. Maqbool, S. Nohut, T. R. Martin, S. Kamoun, T. O. Bozkurt, Dynamic localization of a helper NLR at the plant–pathogen interface underpins pathogen recognition. *Proc. Natl. Acad. Sci. U.S.A.* **118**, e2104997118 (2021).
32. L. Abas, C. Luschnig, Maximum yields of microsomal-type membranes from small amounts of plant material without requiring ultracentrifugation. *Anal. Biochem.* **401**, 217–227 (2010).
33. F. W. Studier, Protein production by auto-induction in high-density shaking cultures. *Protein Expr. Purif.* **41**, 207–234 (2005).
34. J. F. Steele, R. K. Hughes, M. J. Banfield, Structural and biochemical studies of an NB-ARC domain from a plant NLR immune receptor. *PLOS ONE* **14**, e0221226 (2019).
35. W. Kabsch, XDS. *Acta Crystallogr. D Biol. Crystallogr.* **66**, 125–132 (2010).
36. G. Winter, xia2: An expert system for macromolecular crystallography data reduction. *J. Appl. Cryst.* **43**, 186–190 (2010).
37. P. R. Evans, G. N. Murshudov, How good are my data and what is the resolution? *Acta Crystallogr. D Biol. Crystallogr.* **69**, 1204–1214 (2013).
38. M. D. Winn, An overview of the CCP4 project in protein crystallography: An example of a collaborative project. *J. Synchrotron Radiat.* **10**, 23–25 (2003).
39. R. Evans, M. O'Neil, A. Pritzel, N. Antropova, A. Senior, T. Green, A. Žídek, R. Bates, S. Blackwell, J. Yim, O. Ronneberger, S. Bodenstein, M. Zielinski, A. Bridgland, A. Potapenko, A. Cowie, K. Tunyasuvunakool, R. Jain, E. Clancy, P. Kohli, J. Jumper, D. Hassabis, Protein complex prediction with AlphaFold-Multimer. bioRxiv 2021.10.04.463034 [Preprint]. 10 March 2022. https://doi.org/10.1101/2021.10.04.463034.
40. M. Mirdita, K. Schütze, Y. Moriwaki, L. Heo, S. Ovchinnikov, M. Steinegger, ColabFold: Making protein folding accessible to all. *Nat. Methods* **19**, 679–682 (2022).
41. A. J. McCoy, R. W. Grosse-Kunstleve, P. D. Adams, M. D. Winn, L. C. Storoni, R. J. Read, Phaser crystallographic software. *J. Appl. Cryst.* **40**, 658–674 (2007).
42. P. Emsley, B. Lohkamp, W. G. Scott, K. Cowtan, Features and development of Coot. *Acta Crystallogr. D Biol. Crystallogr.* **66**, 486–501 (2010).
43. G. N. Murshudov, P. Skubák, A. A. Lebedev, N. S. Pannu, R. A. Steiner, R. A. Nicholls, M. D. Winn, F. Long, A. A. Vagin, REFMAC5 for the refinement of macromolecular crystal structures. *Acta Crystallogr. D Biol. Crystallogr.* **67**, 355–367 (2011).
44. R. A. Nicholls, M. Fischer, S. McNicholas, G. N. Murshudov, Conformation-independent structural comparison of macromolecules with ProSMART. *Acta Crystallogr. D Biol. Crystallogr.* **70**, 2487–2499 (2014).
45. E. F. Pettersen, T. D. Goddard, C. C. Huang, E. C. Meng, G. S. Couch, T. I. Croll, J. H. Morris, T. E. Ferrin, UCSF ChimeraX: Structure visualization for researchers, educators, and developers. *Protein Sci.* **30**, 70–82 (2021).
46. The PyMOL Molecular Graphics System, Version 1.2r3pre, Schrödinger, LLC.
47. M. E. Segretin, M. Pais, M. Franceschetti, A. Chaparro-Garcia, J. I. B. Bos, M. J. Banfield, S. Kamoun, Single amino acid mutations in the potato immune receptor R3a expand response to Phytophthora effectors. *Mol. Plant Microbe Interact.* **27**, 624–637 (2014).
48.. D. MacLean, Besthr. Zenodo (2019). https://doi.org/10.5281/zenodo.3374507.
49. I. W. Davis, A. Leaver-Fay, V. B. Chen, J. N. Block, G. J. Kapral, X. Wang, L. W. Murray, W. B. Arendall, J. Snoeyink, J. S. Richardson, D. C. Richardson, MolProbity: All-atom contacts and structure validation for proteins and nucleic acids. *Nucleic Acids Res.* **35**, W375–W383 (2007).


**Acknowledgments:** We are very thankful to J. Kourelis, C. Marchal, D. Lüdke, and H.-K. Ahn (The Sainsbury Laboratory, Norwich, UK) for invaluable scientific discussions, ideas, and feedback. We thank J. Mundy for assistance with crystallography experiments. We thank the Diamond Light Source, UK (beamline i03 under proposal MX18565) for access to x-ray data collection facilities. M.P.C. thanks L. Messi for inspiration. We thank all members of the TSL Support Services for their invaluable assistance. **Funding:** The authors received funding from the Gatsby Charitable Foundation (to M.P.C., H.P., M.S., A.T., D.M.L., C.E.M.S., A.H., A.M., C.-H.W., S.K., and L.D.), Biotechnology and Biological Sciences Research Council (BBSRC) BB/P012574 (Plant Health ISP) (to M.P.C., H.P., M.S., A.T., D.M.L., C.E.M.S., A.H., A.M., C.-H.W., S.K., and L.D.), BBSRC BBS/E/J/000PR9795 (Plant Health ISP - Recognition) (to M.P.C., H.P., M.S., A.T., D.M.L., C.E.M.S., A.H., A.M., C.-H.W, S.K., and L.D.), BBSRC BBS/E/J/000PR9796 (Plant Health ISP - Response) (to M.P.C., H.P., M.S., A.T., D.M.L., C.E.M.S., A.H., A.M., C.-H.W., S.K., and L.D.), BBSRC BBS/E/J/000PR9797 (Plant Health ISP – Susceptibility) (to M.P.C., H.P., M.S., A.T., D.M.L., C.E.M.S., A.H., A.M., C.-H.W., S.K., and L.D.), BBSRC BBS/E/J/000PR9798 (Plant Health ISP – Evolution) (to M.P.C., H.P., M.S., A.T., D.M.L., C.E.M.S., A.H., A.M., C.-H.W., S.K., and L.D.), BBSRC BB/V002937/1 (to M.P.C., L.D., and S.K.), BBSRC BB/T006102/1 (to Y.T., C.D., and T.O.B.), BBSRC impact acceleration award BB/X511055/1 (to E.L.H.Y.), Academia Sinica and National Science and Technology Council NSTC-111-2628-B-001-023 (to C.-H.W.), and European Research Council (ERC) 743165 (to S.K.). The funders had no role in the study design, data collection and analysis, decision to publish, or preparation of the manuscript. **Author contributions:** Conceptualization: M.P.C., C.-H.W., S.K., and L.D. Methodology: M.P.C., H.P., M.S., D.M.L., C.E.M.S., A.M., and L.D. Validation: M.P.C., H.P., M.S., Y.T., C.D., E.L.H.Y., and A.H. Formal analysis: M.P.C., H.P., M.S., A.T., D.M.L., Y.T., C.D., C.E.M.S., and L.D. Investigation: M.P.C., H.P., M.S., Y.T., C.D., E.L.H.Y., A.H., A.M., and L.D. Data curation: M.P.C., H.P., M.S., A.T., D.M.L., Y.T., C.D., E.L.H.Y., C.E.M.S., A.M., A.H., and L.D. Visualization: M.P.C., H.P., M.S., A.T., Y.T., C.D., E.L.H.Y., and L.D. Funding acquisition: T.O.B., S.K., and L.D. Project administration: M.P.C., T.O.B., S.K., and L.D. Supervision: M.P.C., T.O.B., S.K., and L.D. Writing—original draft: M.P.C., S.K., and L.D. Writing—review and editing: M.P.C., D.M.L., S.K., and L.D. **Competing interests:** C.D., T.O.B., and S.K. receive funding from industry on NLR biology and cofounded a start-up company (Resurrect Bio Ltd.) on resurrecting disease resistance. M.P.C., S.K., and L.D. have filed patents on NLR biology. M.P.C. and L.D. have received fees from Resurrect Bio Ltd. **Data and materials availability:** All data needed to evaluate the conclusions in the paper are present in the paper and/or the Supplementary Materials. Data relevant to the structure presented in Fig. 3 can be found in PDB 8BV0.

Submitted 20 December 2022
Accepted 30 March 2023
Published 3 May 2023
10.1126/sciadv.adg3861

Downloaded from https://www.science.org on August 02, 2025

PLOS GENETICS

RESEARCH ARTICLE

# Helper NLR immune protein NRC3 evolved to evade inhibition by a cyst nematode virulence effector

**Yu Sugihara[1], Jiorgos Kourelis[1¤], Mauricio P. Contreras[1], Hsuan Pai[1], Adeline Harant[1], Muniyandi Selvaraj[1], AmirAli Toghani[1], Claudia Martínez-Anaya[1,2*], Sophien Kamoun[1*]**

**1** The Sainsbury Laboratory, University of East Anglia, Norwich, United Kingdom, **2** Instituto de Biotecnología, Universidad Nacional Autónoma de México, Cuernavaca, Morelos, México

¤ Current address: Department of Life Sciences, Imperial College London, London, United Kingdom
* sophien.kamoun@tsl.ac.uk (SK); claudia.martinez@ibt.unam.mx (CM-A)

Check for updates

OPEN ACCESS

**Citation:** Sugihara Y, Kourelis J, Contreras MP, Pai H, Harant A, Selvaraj M, et al. (2025) Helper NLR immune protein NRC3 evolved to evade inhibition by a cyst nematode virulence effector. PLoS Genet 21(4): e1011653. https://doi.org/10.1371/journal.pgen.1011653

**Editor:** Tiancong Qi, Tsinghua University, CHINA

**Received:** September 10, 2024

**Accepted:** March 9, 2025

**Published:** April 9, 2025

**Peer Review History:** PLOS recognizes the benefits of transparency in the peer review process; therefore, we enable the publication of all of the content of peer review and author responses alongside final, published articles. The editorial history of this article is available here: https://doi.org/10.1371/journal.pgen.1011653

**Copyright:** © 2025 Sugihara et al. This is an open access article distributed under the terms of the Creative Commons Attribution License, which permits unrestricted use, distribution, and reproduction in any medium, provided the original author and source are credited.

## Abstract

Parasites can counteract host immunity by suppressing nucleotide binding and leucine-rich repeat (NLR) proteins that function as immune receptors. We previously showed that a cyst nematode virulence effector SPRYSEC15 (SS15) binds and inhibits oligomerisation of helper NLR proteins in the expanded NRC1/2/3 clade by preventing intramolecular rearrangements required for NRC oligomerisation into an activated resistosome. Here we examined the degree to which NRC proteins from multiple Solanaceae species are sensitive to suppression by SS15 and tested hypotheses about adaptive evolution of the binding interface between the SS15 inhibitor and NRC proteins. Whereas all tested orthologs of NRC2 were inhibited by SS15, some natural variants of NRC1 and NRC3 are insensitive to SS15 suppression. Ancestral sequence reconstruction combined with functional assays revealed that NRC3 transitioned from an ancestral suppressed form to an insensitive one over 19 million years ago. Our analyses revealed the evolutionary trajectory of an NLR immune receptor against a parasite inhibitor, identifying key evolutionary transitions in helper NLRs that counteract this inhibition. This work reveals a distinct type of gene-for-gene interaction between parasite or pathogen immunosuppressors and host immune receptors that contrasts with the coevolution between AVR effectors and immune receptors.

## Author summary

Plants have immune systems that protect them from various pathogens, including bacteria, fungi and nematodes. This immune system harnesses proteins called NLRs (nucleotide-binding and leucine-rich repeat proteins) to detect and respond to pathogens. However, pathogens often evolve strategies to suppress plant immunity. For example, the cyst nematode *Globodera rostochiensis* produces an effector protein called SPRYSEC15 (SS15) that inhibits certain NLR proteins, suppressing the plant's immune response. In this study, we explored how a group of NLR proteins called NRCs, found in

**Data availability statement:** The datasets used in this study are archived in Zenodo (https://doi.org/10.5281/zenodo.14584438). The ancestral sequence reconstruction pipeline "anceseq" is available on Github (https://github.com/YuSugihara/ancseq) and archived in Zenodo (https://doi.org/10.5281/zenodo.10808871).

**Funding:** 1. This study was supported by The Gatsby Charitable Foundation (YS, JK, MPC, HP, AH, MS, AT, CMA, SK), Biotechnology and Biological Sciences Research Council (BBSRC) BB/P012574 (Plant Health ISP) (YS, JK, MPC, HP, AH, MS, AT, CMA, SK), BBSRC BBS/E/J/000PR9795 (Plant Health ISP - Recognition) (YS, JK, MPC, HP, AH, MS, AT, CMA, SK), BBSRC BBS/E/J/000PR9796 (Plant Health ISP - Response) (YS, JK, MPC, HP, AH, MS, AT, CMA, SK), BBSRC BBS/E/J/000PR9797 (Plant Health ISP – Susceptibility) (YS, JK, MPC, HP, AH, MS, AT, CMA, SK), BBSRC BBS/E/J/000PR9798 (Plant Health ISP – Evolution) (YS, JK, MPC, HP, AH, MS, AT, CMA, SK), BBSRC BB/V002937/1 (SK, MPC), European Research Council (ERC) 743165 (SK). More information about the funding sources can be found at the following websites: the Gatsby Charitable Foundation (https://www.gatsby.org.uk/), BBSRC (https://www.ukri.org/councils/bbsrc/), ERC (https://erc.europa.eu) The funders had no role in the study design, data collection and analysis, decision to publish, or preparation of the manuscript.

**Competing interests:** I have read the journal's policy and the authors of this manuscript have the following competing interests: S.K. receives funding from industry on NLR biology and has cofounded a start-up company (Resurrect Bio Ltd.) related to NLR biology. J.K., M.P.C. and S.K. have filed patents on NLR biology. M.P.C. has received fees from Resurrect Bio Ltd.

the Solanaceae plant family, have evolved to counteract SS15 inhibition. We discovered that while SS15 inhibits all tested NRC2 orthologs, some natural variants of NRC1 and NRC3 are insensitive to its effects. By reconstructing the evolutionary history of NRC3, we found that these proteins acquired insensitivity to SS15 through a specific amino acid substitution about 19 million years ago. Our findings highlight a previously understudied type of evolutionary arms race between plants and pathogens, where plants adapt to evade pathogen-derived suppressors. This research expands our understanding of plant-pathogen coevolution and offers insights that could guide the development of crops with improved disease resistance.

## Introduction

Molecular interactions between plant immune receptors and pathogen effectors drive their coevolution, shaping the dynamics of host-pathogen relationships [1–4]. Harold H. Flor, in 1942, proposed the hypothesis that single genes in plants and pathogens determine the outcome of their interactions; that is, a plant carrying a certain gene displays resistance against a pathogen carrying a corresponding gene [5,6]. In plant-pathogen interactions, Flor's model is generally interpreted as the recognition of pathogen effectors (known as AVR effectors) by plant immune receptors (encoded by disease resistance genes or *R* genes), triggering a robust resistance mechanism. This gene-for-gene model has provided an invaluable conceptual framework and has significantly influenced both applied and basic research in disease resistance [7]. In particular, this model provided a deep understanding of the principles of coevolution between plant immune receptors, encoded by disease resistance (*R*) genes, and pathogen (or parasite) AVR effectors [8–11]. Indeed, the plant pathology community has documented numerous examples of adaptive evolution, notably cases where the pathogen AVR effector has evaded detection by its cognate R immune receptor [11–13]. Despite advancements in our understanding of R-AVR interactions at the mechanistic and evolutionary level, other types of gene-for-gene interactions, notably coevolution between pathogen immunosuppressors and their host targets, remain less understood [14,15] (S1 Fig).

Nucleotide-binding and leucine-rich repeat (NLR) proteins constitute the predominant class of plant disease resistance genes [16–18]. NLRs are intracellular receptors that directly or indirectly recognise pathogen effectors, a molecular event which triggers an immune response [18,19]. A continuous coevolutionary arms race between plants and pathogens has resulted in the diversification and expansion of NLRs in plants [14,20,21]. NLRs have evolved diverse activation mechanisms. Asterid plants, and notably the Solanaceae, have a complex NLR immune receptor network also known as the NRC network [14,16,22]. In this model, a specific phylogenetic clade of coiled-coil (CC)-type NLR proteins, known as NLR REQUIRED FOR CELL DEATH (NRC), function as helper NLRs (NRC-H) genetically downstream of multiple sensor NLRs (NRC-S) to mediate immune responses and to confer disease resistance against diverse pathogens and pests [22–24].

NRC-H and NRC-S are phylogenetically related CC-NLRs that originate from a common ancestor that was present before the split between asterids and Caryophyllales [22]. Recent studies have shown that the NRC0 sensor/helper gene cluster reflects an ancestral state of the NRC network [23,24]. *NRC0* helpers have been genetically and functionally conserved across asterids for more than 100 million years, predating the massive expansion and diversification of NRC-H and NRC-S into lineage- or species-specific NRC networks in lamiids, notably in the Solanaceae family [23–25]. Throughout their expansion and diversification, NRC proteins

have subfunctionalised from the larger NRC network, resulting in organ-specialised subnetworks or in partial genetic redundancy as well as evolving specificity to different sensor NLRs [26,27]. Notably, NRC3 of solanaceous species is required not only by sensor NLRs but also by the tomato cell-surface receptors Cf-2, Cf-4, Cf-5 and Cf-9, which trigger hypersensitive cell death response upon the recognition of the fungal pathogen *Cladosporium fulvum* (syn. *Passalora fulva*) apoplastic effectors [28–30].

Upon perceiving AVR effectors, NRC-S proteins activate their cognate NRC helpers via an 'activate-and-release' mechanism, presumably through the NB-ARC (nucleotide-binding adaptor shared by APAF-1, certain *R* gene products and CED-4) module of the sensor NLR [26,31–33]. The NB-ARC module consists of three domains: a nucleotide binding domain (NBD), a helical domain (HD1) and a winged helix domain (WHD) [34–36]. The current mechanistic model is that activation by NRC-S converts NRC helpers from a resting state homodimer into resistosomes—oligomeric, pore-like complexes that translocate to the plasma membrane [33,37]. These complexes enable immune responses such as calcium influx and hypersensitive cell death, culminating in disease resistance [38]. Oligomerisation into resistosomes has been demonstrated *in planta* for several NRCs using blue native polyacrylamide gel electrophoresis (BN-PAGE) [24,31–33,35]. More recently, the cryogenic electron microscopy (cryo-EM) structures of sensor-activated NRC2 and a constitutively active mutant of NRC4 ($NRC4^{D478V}$) revealed hexameric resistosomes [38,39].

We previously showed that SPRYSEC15 (SS15), a small secreted protein of the cyst nematode *Globodera rostochiensis*, binds and inhibits oligomerisation of NRC2 and NRC3 from the model plant *Nicotiana benthamiana*, as well as NRC1 from tomato (*Solanum lycopersicum*), by preventing intramolecular rearrangements required for NRC oligomerisation into activated resistosomes [35,40,41]. Conversely, SS15 does not inhibit oligomerisation of *N. benthamiana* NRC4 protein, a paralog of NRC2 and NRC3 [35]. Leveraging NRC4 resilience to SS15 inhibition and the crystal structure of SS15 in complex with the NB-ARC module of NRC1, Contreras et al. (2023) mapped two key residues, E316 and D317, on NRC2 that mediate binding to SS15 and showed that NRC2 variants mutated at these positions can evade SS15 suppression without compromising receptor signalling [35]. However, these studies focused mainly on NRC2, NRC3, and NRC4 from *N. benthamiana*, without examining the sensitivity of NRC proteins across Solanaceae to SS15 inhibition. Indeed, Solanaceae species have 7–21 NRC-H paralogs [24], and the phylogenomic analyses of 123 solanaceous genome assemblies from 39 species of the genera *Solanum*, *Physalis*, *Capsicum* and *Nicotiana* revealed 15 phylogenetic clades [37,42]. Ten of the 15 clades include orthologs from at least two genera, therefore representing relatively deep NRC lineages. Of interest to this study, SS15 has only been shown to inhibit members of the NRC1, NRC2, NRC3 clade, a well-supported and deep branch in the Solanaceae NRC tree [37].

The extent to which NLR immune receptors have evolved to counteract pathogen suppressors is unknown. Here we discovered that orthologous NRC proteins from multiple Solanaceae species vary in their sensitivity to suppression by the cyst nematode effector SS15. We found that some natural variants of NRC1 and NRC3 are insensitive to SS15 suppression, whereas all tested NRC2 orthologs are inhibited by SS15. To test hypotheses about adaptive evolution of the NRC-SS15 binding interface, we used ancestral sequence reconstruction to show that NRC3 has transitioned from an ancestral suppressed form to an insensitive one over 19 million years ago. Our analyses reconstructed the evolutionary trajectory of NLRs against their suppressors and identified key evolutionary transitions of solanaceous helper NLRs to counteract the SS15 inhibitor. This work reveals a distinct type of gene-for-gene interaction between host immune receptors and pathogen immunosuppressors that contrasts with R-AVR coevolution.

## Results

### Natural variants of NRC1 and NRC3 but not NRC2 are insensitive to SS15 inhibition

We previously showed that SS15 inhibits NRC1, NRC2 and NRC3 but not NRC4 [35,41]. Given that the homologous NRC1, NRC2, NRC3, along with the NLR modulator NRCX, form a well-supported clade in the Solanaceae NRC tree (Figs 1A and S2) [24,37], we investigated the degree to which NRC orthologs from multiple Solanaceae species are inhibited by SS15. For this purpose, we cloned 11 representative NRC sequences from *Nicotiana benthamiana* (NbNRC2 and NbNRC3), *Capsicum annuum* (pepper; CaNRC1, CaNRC2 and CaNRC3), *Solanum tuberosum* (potato; StNRC1, StNRC2 and StNRC3) and

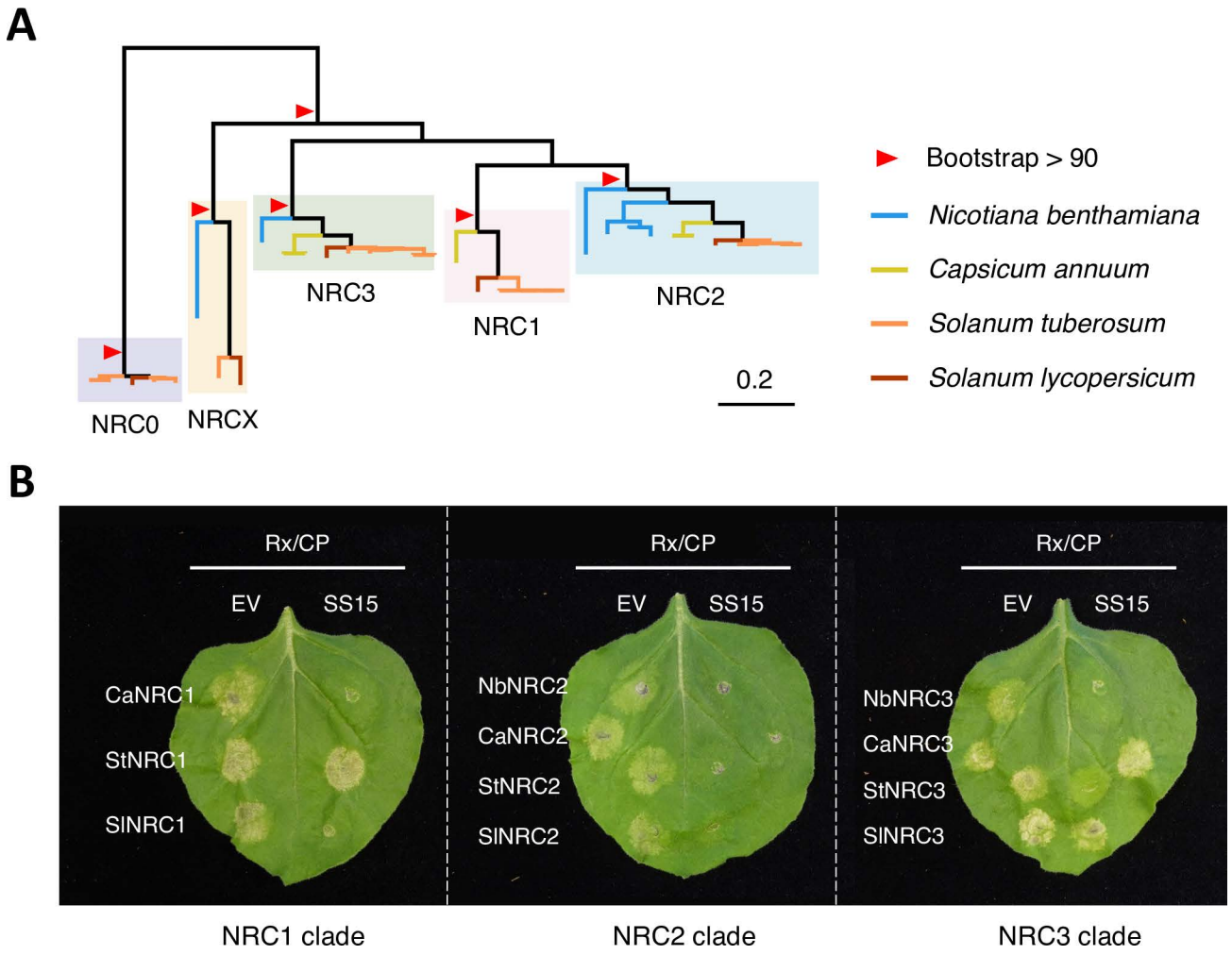


**Fig 1. Natural variants of NRC1 and NRC3 but not NRC2 are insensitive to SS15 inhibition.** (A) Phylogenetic tree of the NRC1/2/3 clade from four different Solanaceae species. We used the full-length NRC sequences of the NRC0, NRC1, NRC2, NRC3 and NRCX clades from four different Solanaceae species (*Nicotiana benthamiana*, *Capsicum annuum*, *Solanum tuberosum* and *Solanum lycopersicum*) to create a phylogenetic tree. The phylogenetic tree was reconstructed by the maximum likelihood method using IQ-TREE with 1,000 bootstrap replicates. The phylogenetic positions of cloned NRCs are indicated in S2 Fig. (B) Representative images of HR cell death assays after transient co-expression of either an empty vector (EV) or SPRYSEC15 (SS15) with the NRC-S sensor NLR, Rx, the *Potato virus X* (PVX) coat protein (CP) and NRCs in the leaves of *N. benthamiana nrc2/3/4* KO plants. Note that, unlike tomato, *N. benthamiana* lacks *nrc1*. Leaves were photographed 5 days after infiltration.

https://doi.org/10.1371/journal.pgen.1011653.g001

*Solanum lycopersicum* (tomato; SlNRC1, SlNRC2 and SlNRC3) from the phylogenetically related NRC1/2/3 clade (Figs 1 and S2). To assess cell death due to hypersensitive response (HR) in the presence of SS15, we transiently co-expressed NRCs with the upstream NRC-S sensor NLR, Rx, along with either an empty vector (EV) or SS15 in the leaves of *nrc2/3/4* CRISPR knock-out (KO) *N. benthamiana* plants. We activated the sensor-helper Rx-NRC system by co-expressing the *Potato virus X* (PVX) coat protein (CP). Whereas all tested NRC2s were inhibited by SS15, some natural variants of NRC1 and NRC3 were insensitive to SS15 inhibition (Fig 1B). For NRC1, pepper NRC1 (CaNRC1) and tomato NRC1 (SlNRC1) were inhibited by SS15, while potato NRC1 (StNRC1) was insensitive to SS15 inhibition (Fig 1B). For NRC3, *N. benthamiana* NRC3 (NbNRC3) and potato NRC3 (StNRC3) were inhibited by SS15, while pepper NRC3 (CaNRC3) and tomato NRC3 (SlNRC3) were insensitive (Fig 1B). These results indicate that some natural variants of NRC1 and NRC3 are insensitive to SS15 and that they might have acquired mutations affecting SS15 binding to their NB-ARC modules.

## NRC3 variants from different Solanaceae species carry key polymorphisms at the SS15 binding interface

Contreras et al. (2023) described the structure of SS15 in complex with the NB-ARC module of SlNRC1 ($SlNRC1^{NB\text{-}ARC}$) revealing three contact interfaces (Fig 2A) [35]. To interpret the results of the cell death assay in Fig 1B, we mapped the NRC polymorphisms at these interfaces (Fig 2B). Among multiple polymorphisms, we focused on positions D316 and E317 of SlNRC1, which are critical to SS15 inhibition in NbNRC2 [35]. In contrast to NRC1 and NRC2, NRC3 is polymorphic at positions matching D316 and E317 (here and below, the position numbers are based on SlNRC1 sequence) (Fig 2B). Remarkably, polymorphism E316K in NRC3 correlated with inhibition phenotypes, with CaNRC3 and SlNRC3 orthologs, carrying lysine at position 316 (K316), being insensitive to SS15 inhibition (Figs 1B and 2B). We therefore hypothesised that this amino acid substitution at position matching 316 affects binding and sensitivity to SS15 in the NRC3 clade.

## Polymorphisms at NRC3 position 316 determine sensitivity to SS15 suppression

Given the findings described in Figs 1 and 2 and since NRC3 is a core helper NLR required not only by sensor NLRs but also by cell surface receptors [28–30], we focused on NRC3 and tested the effect of E316K substitution on SS15 binding. We generated a single-point mutant for each wild type (WT) NRC3 at position matching SlNRC1 amino acid 316 (E316K in NbNRC3, K314E in CaNRC3, E314K in StNRC3 and K314E in SlNRC3; Figs 2B and 3A). We then compared the HR cell death between WT NRC3s and single-point mutants in the presence and absence of SS15 (Fig 3B and 3C). The E-to-K substitutions in NbNRC3 and StNRC3 significantly increased the cell death response in the presence of SS15, while the K-to-E substitutions in CaNRC3 and SlNRC3 significantly reduced it (Fig 3B and 3C). The differences are not due to SS15-mediated destabilization of NRCs as there is no correlation between SS15 suppression levels and protein accumulation levels (S3 Fig). $SlNRC3^{K314E}$ showed statistically reduced HR scores compared with WT SlNRC3 in the presence of SS15, but the difference was not as marked as in the case of other single-point mutants (Figs 3B, 3C and S3). These results indicate that naturally occurring polymorphisms at position 316 of NRC3 are critical for sensitivity to SS15 in line with our previous study on NbNRC2 [35]. Furthermore, our findings indicate that SlNRC3 may contain additional amino acid polymorphisms besides K314 that contribute to its insensitivity to SS15.

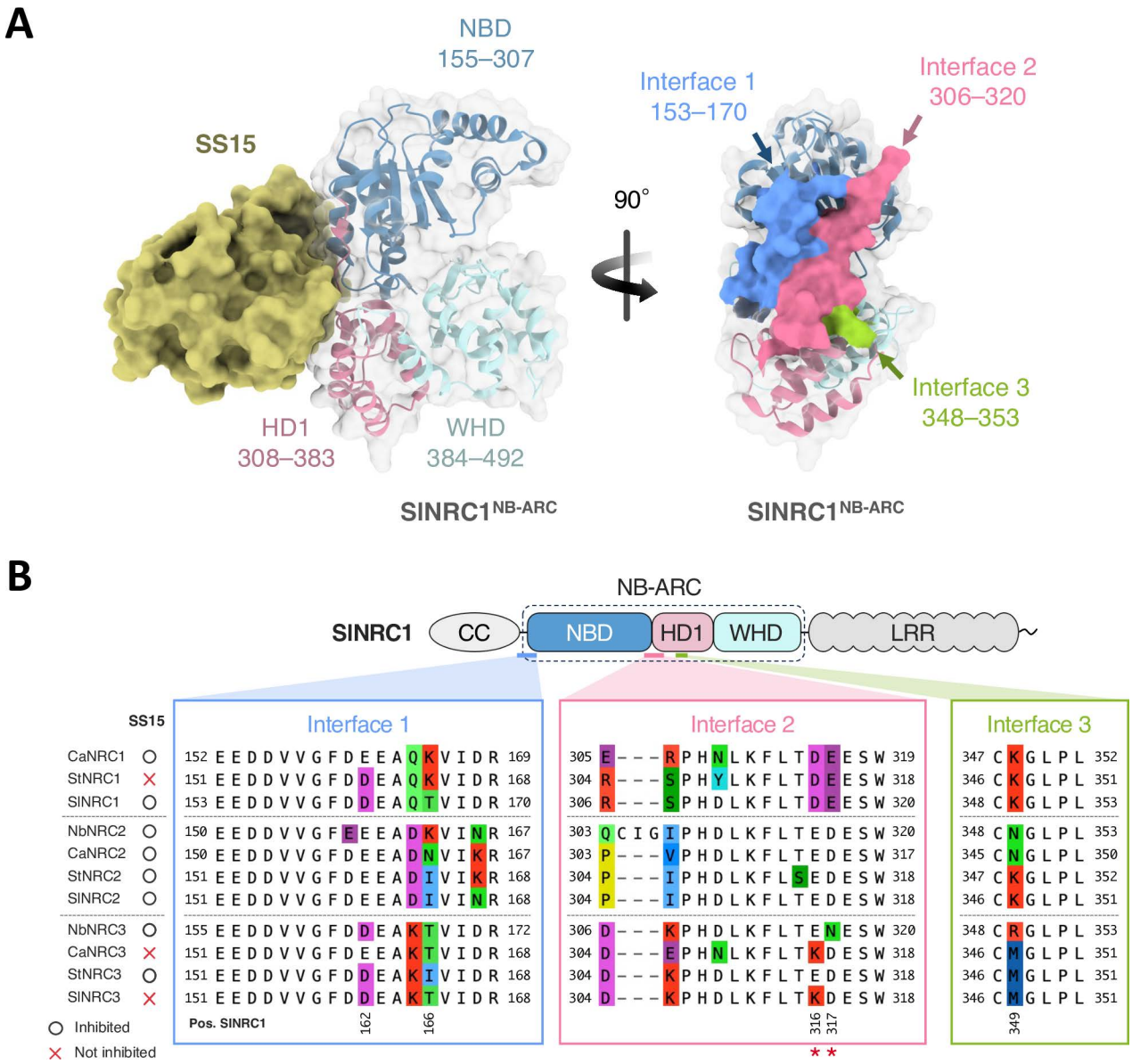


**Fig 2. NRC3 variants from different Solanaceae species are polymorphic at key residues at SS15 binding interface.** (A) Structure of SS15 in complex with the NB-ARC module of SlNRC1 (SlNRC1$^{NB\text{-}ARC}$). The NB-ARC module of SlNRC1 has three different interfaces interacting with SS15. The NB-ARC module consists of a nucleotide binding domain (NBD), a helical domain (HD1) and a winged helix domain (WHD), highlighted in different colours. The structure was published in [35] (PDB: 8BV0). The boundaries between the domains follow those in [35]. The structure is visualized using ChimeraX [43]. (B) Alignment of NRC1, NRC2 and NRC3 interfaces for SS15. The positions of the residues are based on SlNRC1. Whether an NRC is inhibited by SS15 is indicated on the right side of the protein name based on the results in Fig 1B. Two key residues for SS15 inhibition (D316 and E317 of SlNRC1), previously identified in [35], are highlighted with red asterisks.

https://doi.org/10.1371/journal.pgen.1011653.g002

## Polymorphisms at position E316 of NbNRC3 determine oligomerisation in the presence of SS15

Contreras et al. (2023) showed that SS15 blocks NRC2 oligomerisation and resistosome formation following activation by the NRC-S protein Rx and PVX CP [35]. We extended these experiments to NRC3 orthologs from pepper, potato and tomato to determine the effect of SS15 on their oligomerisation following activation (Fig 4). To this end, we used previously

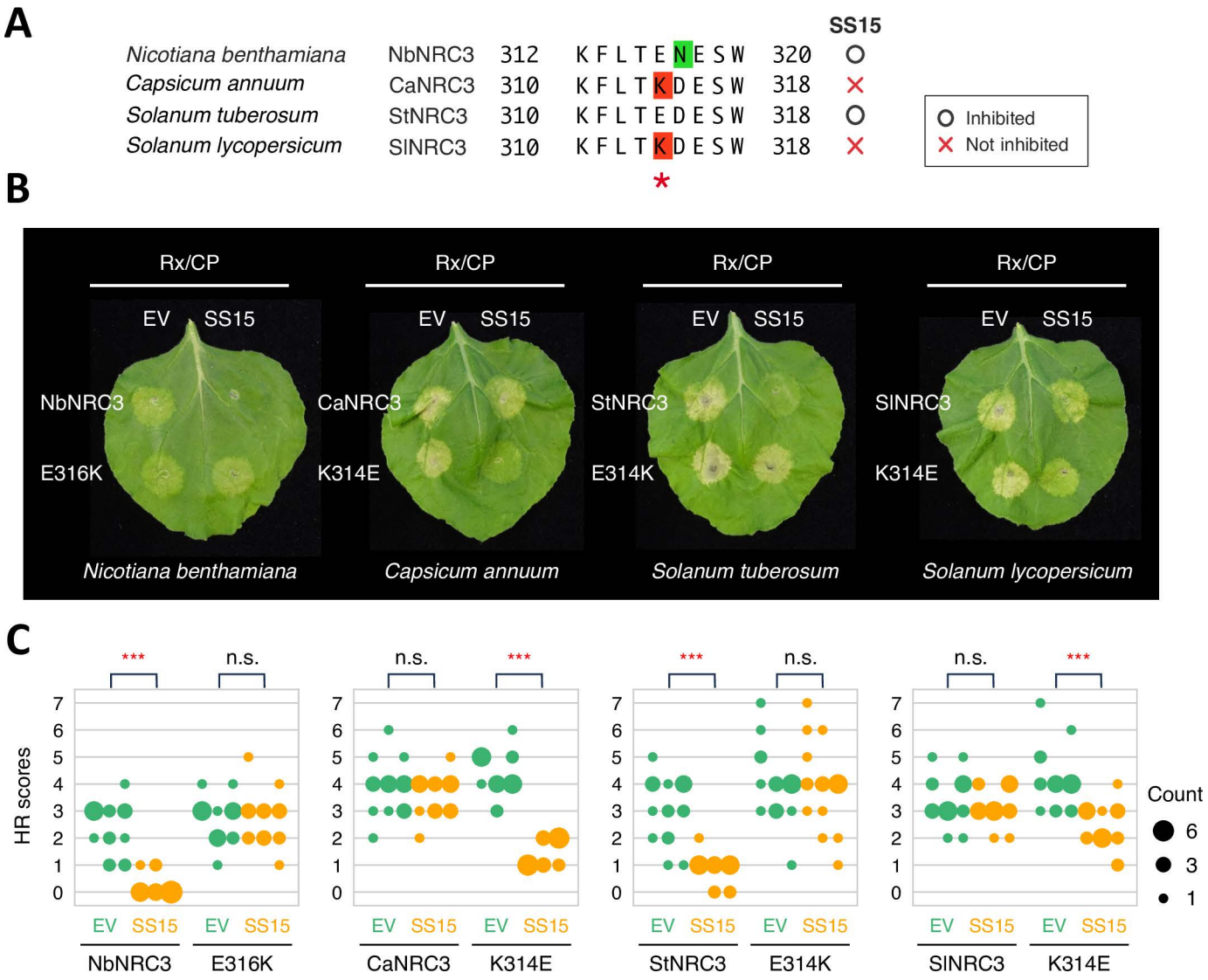


**Fig 3. Polymorphisms at NRC3 position 316 determine sensitivity to SS15 suppression.** (A) Schematic representation of the mutated sites in the multiple sequence alignment of NRC3. The residue matching D316 of SlNRC1 is highlighted with a red asterisk. Whether an NRC is inhibited by SS15 is indicated on the right side of the panel based on Fig 1B. (B) Representative images of HR cell death assays showing the results after transient co-expression of an empty vector (EV) or SS15 with Rx and PVX CP, along with either WT NRC3 or its single-point mutant in the leaves of *N. benthamiana nrc2/3/4* KO plants. Mutations were introduced in NRC3 at the residues matching D316 of SlNRC1. The leaves were photographed 5 days after infiltration. (C) Statistical analysis using a two-sided permutation test with 10,000 replicates. Statistically significant differences are indicated (***: $p < 0.001$; n.s.: not significant). Each column represents an independent experiment. The data underlying Fig 3C can be found in S1 Data.

https://doi.org/10.1371/journal.pgen.1011653.g003

established blue native polyacrylamide gel electrophoresis (BN-PAGE) to assay for NRC resistosome formation [33,35], and NRC3 mutants of the N-terminal MADA motifs (CaNRC3$^{EEE}$, StNRC3$^{EEE}$ and SlNRC3$^{EEE}$ for *C. annuum*, *S. tuberosum* and *S. lycopersicum*, respectively), which abolish cell death without compromising receptor activation [35,44]. To activate NRC3s, we co-expressed 4xMyc-tagged NRC3 MADA mutants (NRC3$^{EEE}$-4xMyc) with V5-tagged sensor NLR Rx (Rx-V5) and either free GFP or GFP-tagged PVX CP (CP-GFP). These effector-sensor-helper combinations were co-expressed either with mCherry-6xHA fusion protein (mCherry-6xHA) as a negative control or 4xHA-tagged SS15 (4xHA-SS15) in

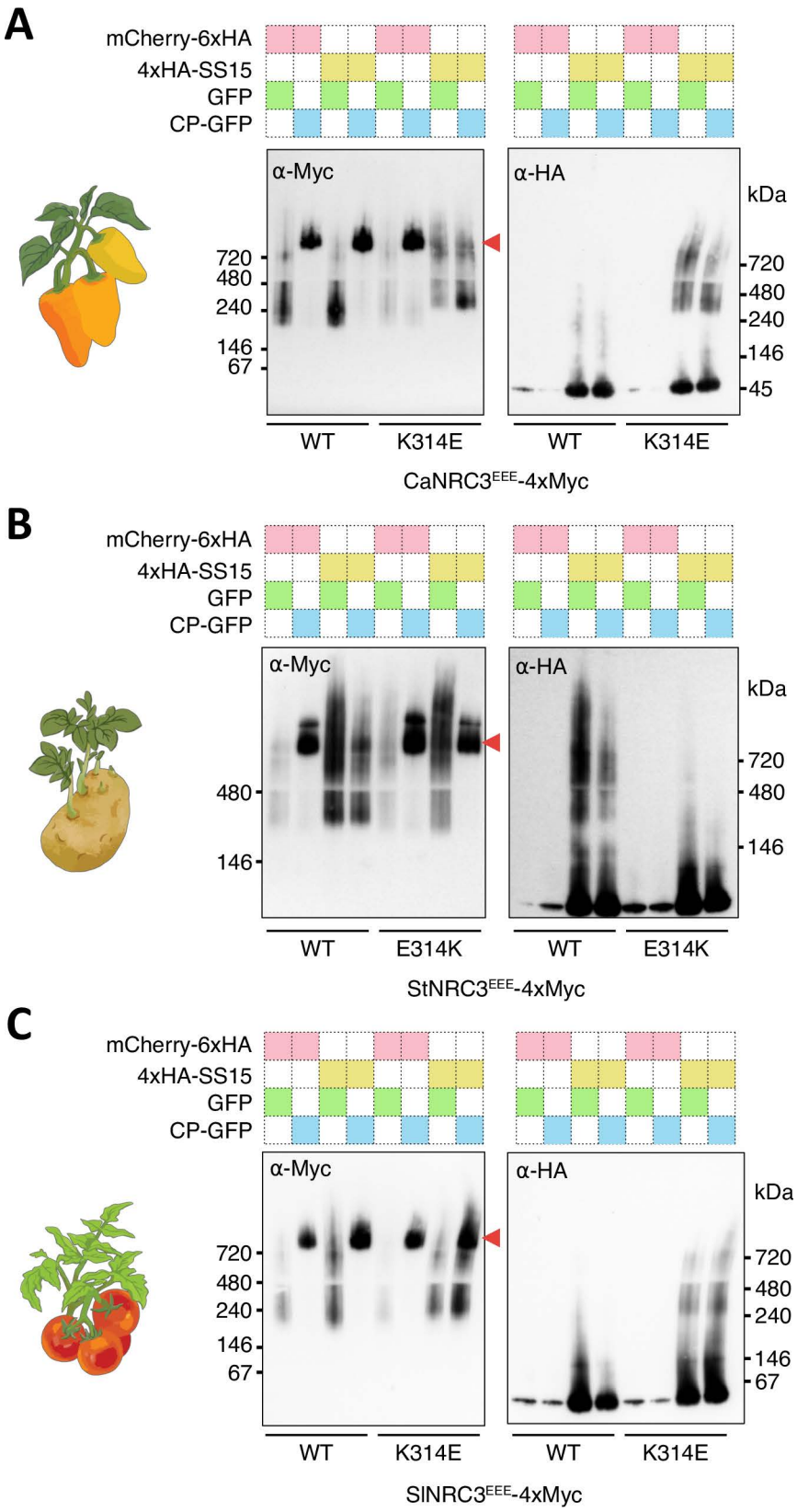


**Fig 4. Polymorphisms at position E316 of NbNRC3 determine oligomerisation in the presence of SS15.** Blue native polyacrylamide gel electrophoresis (BN-PAGE) assays were conducted for CaNRC3$^{EEE}$ (A), StNRC3$^{EEE}$ (B) and

SlNRC3$^{EEE}$ (C) with their respective single-point mutations at position matching NbNRC3 residue 316. CaNRC3$^{EEE}$, StNRC3$^{EEE}$ and SlNRC3$^{EEE}$ are the NRC3 mutants of the N-terminal MADA motifs. C-terminally 4xMyc-tagged NRC3$^{EEE}$ mutants were co-expressed with C-terminally V5-tagged Rx and either free GFP or C-terminally GFP-tagged PVX CP in the leaves of *N. benthamiana nrc2/3/4* KO plants. These effector-sensor-helper combinations were co-expressed either with mCherry-6xHA fusion protein or N-terminally 4xHA-tagged SS15. Red arrowheads indicate resistosome bands. Corresponding SDS-PAGE blots are in S4–S6 Figs.

https://doi.org/10.1371/journal.pgen.1011653.g004

the leaves of *N. benthamiana nrc2/3/4* KO plants (Figs 4 and S4–S6). High molecular weight bands (arrowheads in Fig 4) were visualized when WT NRC3$^{EEE}$ were co-expressed with CP, Rx and mCherry, compared with co-expression with the non-activating genes GFP and mCherry in the presence of Rx (Figs 4 and S4–S6). These results suggest that all tested WT NRC3s oligomerize and form high-order resistosome complexes upon effector-triggered activation mediated by Rx and CP. However, when NRC3$^{EEE}$s were co-expressed with SS15 in the presence of Rx and CP, the resistosome band for StNRC3$^{EEE}$ was considerably reduced in comparison to the absence of SS15, and a smear (also observed in the inactive state) appeared, showing the inhibitory effect of SS15 on StNRC3$^{EEE}$. In contrast, SS15 did not prevent resistosome formation for CaNRC3$^{EEE}$ and SlNRC3$^{EEE}$ (Figs 4 and S4–S6). Due to the low level of protein accumulation observed for NbNRC3 in *N. benthamiana*, we could not analyse the resistosome formation of NbNRC3 [41].

Next, we tested whether mutating NbNRC3 residue 316 (CaNRC3$^{EEE/K314E}$, StNRC3$^{EEE/E314K}$ and SlNRC3$^{EEE/K314E}$) affects SS15 inhibition of NRC3 oligomerization following activation as described in the previous section. Again, high molecular weight bands were visualized after co-expression of Rx and CP in BN-PAGE assays, indicating the capacity of these mutants to form a resistosome (Figs 4 and S4–S6). In contrast, the resistosome formations of CaNRC3$^{EEE/K314E}$ and SlNRC3$^{EEE/K314E}$ were impaired in the presence of SS15. In both cases, the lower molecular weight band of NRC3 exhibited a shift in size, presumably due to NRC3-SS15 complex formation *in planta* (Fig 4A and 4C). Moreover, the anti-HA blots revealed similar migration patterns for SS15 with CaNRC3$^{EEE/K314E}$ and SlNRC3$^{EEE/K314E}$, further suggesting that these mutants are forming a complex with the effector, leading to inhibition. Unlike StNRC3$^{EEE}$, the mutant StNRC3$^{EEE/E314K}$ was capable of oligomerizing in the presence of SS15 (Fig 4B). These results indicate that position E316 of NbNRC3 determines the oligomerisation of NRC3 in the presence of SS15, but in tomato SlNRC3, other residues appear to contribute to the insensitivity to SS15. Overall, these results are consistent with our observations in the HR cell death assays (Figs 1B, 3B and 3C).

## Ancestral sequence reconstruction infers that E316 is ancestral in the NRC3 clade

We revealed that polymorphisms at position 316 determine SS15 sensitivity in natural variants of NRC3. However, polymorphisms E316 of NbNRC3, K314 of CaNRC3, E314 of StNRC3 and K314 of SlNRC3 are phylogenetically discordant in the NRC3 tree (Figs 5 and S2). To clarify the evolutionary history of NRC3, we applied ancestral sequence reconstruction to 314 non-redundant NRC1/2/3/X nucleotide sequences extracted from an NLRome database of 66,665 sequences from 124 genomes in the Solanaceae family (Fig 5A and S1 Table) [42]. Ancestral sequence reconstruction inferred five amino acid substitutions from node 1 to node 6 on the three interfaces defined by the crystal structure of SlNRC1$^{NB\text{-}ARC}$ in complex with SS15 (Figs 2, 5 and S7). Node 1, which predates the divergence between the *Nicotiana* genus and the rest of the taxa, had an ambiguous residue at the position E317 of SlNRC1, resulting in two different ancestral variants anc1.1 and anc1.2 with N317 ($p = 0.45$) and D317 ($p = 0.55$),

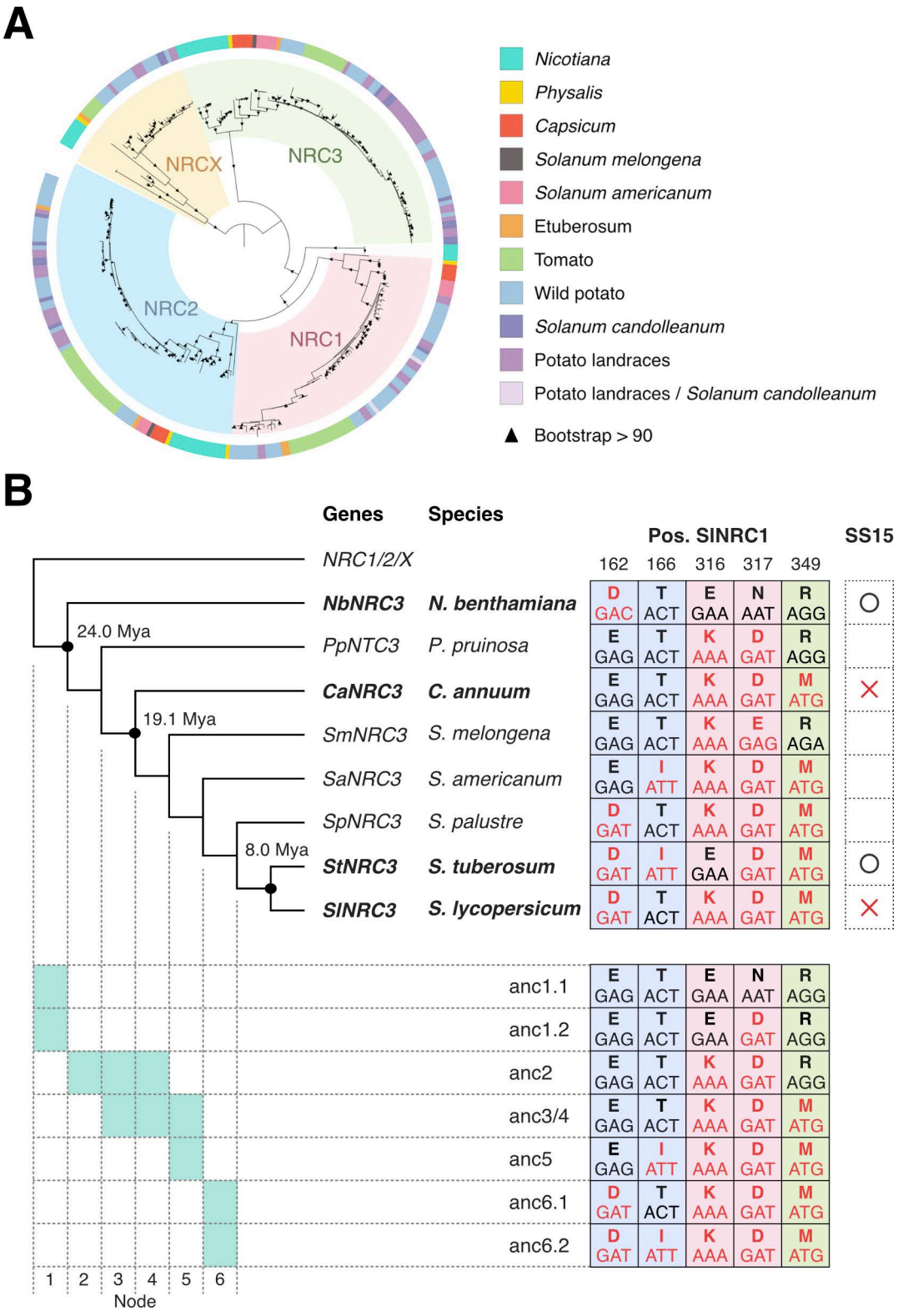


**Fig 5. Ancestral sequence reconstruction infers that E316 is ancestral in the NRC3 clade.** (A) Phylogenetic tree of 314 non-redundant nucleotide sequences from NRC1/2/3/X clade. The 314 non-redundant nucleotide sequences of the NRC1/2/3/X clade were extracted from 124 genomes in the Solanaceae family [42]. The codon-based nucleotide sequence alignment of these sequences was used to reconstruct the phylogenetic tree. The phylogenetic tree was reconstructed by the

maximum likelihood method using IQ-TREE with 1,000 bootstrap replicates. (B) Schematic illustration of the ancestral sequence reconstruction of the NRC3 clade. The ancestral sequences were inferred from a codon-based alignment of 314 sequences from the NRC1/2/3/X clade (A). We focused on the three interfaces interacting with SS15 (Fig 2), and five amino acid substitutions were identified from nodes 1 to 6. The ancestral states of remaining residues for the interfaces are identical to the amino acids of SlNRC3. The positions are based on SlNRC1 in the alignment of Fig 2B. A probability value (*p*) greater than 0.3 was considered as an ambiguous residue, and multiple ancestral states were tested from the same node (S1 Table). The correspondence of the inferred ancestral sequences with the nodes is indicated below the phylogeny. We used the calibration time estimated by [45].

https://doi.org/10.1371/journal.pgen.1011653.g005

respectively (Figs 5 and S7 and S1 Table). Both ancestral variants had E316 as the ancestral state, and the E316K polymorphism is inferred to have arisen during the transition from node 1–2, which are estimated to date to 24.0 (23.0–25.7) and 19.1 (17.0–21.0) million years ago (Mya) with 95% confidence intervals, respectively [45] (Fig 5B). These results indicate that the ancestral state of the NRC3 clade at position 316 was most likely E316 with the E316K polymorphism arising over ~19.1 Mya after the divergence between *Nicotiana* and the other taxa. Moreover, StNRC3 E314 is likely a regressive mutation that occurred after the divergence between *S. lycopersicum* and *S. tuberosum*.

## Ancestral NRC3 variants with E316 are inhibited by SS15, but those with K316 are not

Whereas predicted ancestral sequences at node 1 have E316 (GAA), those at node 2 to node 6 have K316 (AAA) at the key 316 position (Fig 5B). We therefore hypothesised that node 1 ancestral NRC3 is suppressed by SS15, whereas subsequent variants with K316 are not. To test this hypothesis, we swapped the SS15 binding interface of SlNRC3 (K at position 316; insensitive to SS15 inhibition) with the ancestral amino acid combinations we previously inferred (Figs 5B and 6A). Given that SlNRC3 is identical to anc6.1 at the five SS15 binding interface residues, we cloned the remainder six ancestral NRC3 sequences from node 1 to node 6 in SlNRC3 (Figs 5B and 6A), and tested them for SS15 suppression using HR and BN-PAGE assays (Figs 6 and S8–S10). These experiments revealed that SlNRC3 variants with anc1.1 and anc1.2 amino acid combinations (E316) were suppressed by SS15 for induction of HR and NRC3 oligomerisation, whereas anc2, anc3/4, anc5 and anc6.2 (K316) were not (Figs 6 and S8–S10). Overall, the difference between the NRC3 treatments with and without SS15 were clear, however, in the case of the HR assays with the anc2 variant, there was statistically significant difference between the empty vector and SS15 (S8 Fig). Nonetheless, we conclude that the anc2 variant is insensitive to SS15 given that the effector failed to suppress HR cell death and prevent resistosome formation (Figs 6 and S8–S10). These results indicate that ancestral NRC3, at the node predating the divergence between *Nicotiana* and other taxa, was inhibited by SS15. NRC3 evolved to evade SS15 inhibition over 19.1 million years ago through the E316K substitution.

To further challenge our hypothesis, we compared side-by-side anc1.1 and anc1.2 with SlNRC3 (anc6.1) and its single-point mutant (K314E) in HR cell death assays with and without SS15 (S11A and S11B Fig). SlNRC3 variants with anc1.1 and anc1.2 amino acid combinations (E316) were significantly suppressed by SS15 for induction of HR compared to SlNRC3 and the K314E mutant (S11A and S11B Fig). In the BN-PAGE assay, SS15 prevented the formation of the resistosome band for the anc1.1 variant whereas SlNRC3 and SlNRC3$^{K314E}$ were insensitive to SS15 suppression (S11C and S12 Fig). These results indicate that SlNRC3 (anc6.1) possesses additional amino acid polymorphisms besides K314, which contribute to its insensitivity to SS15 (Figs 3, 6, S11 and S12).

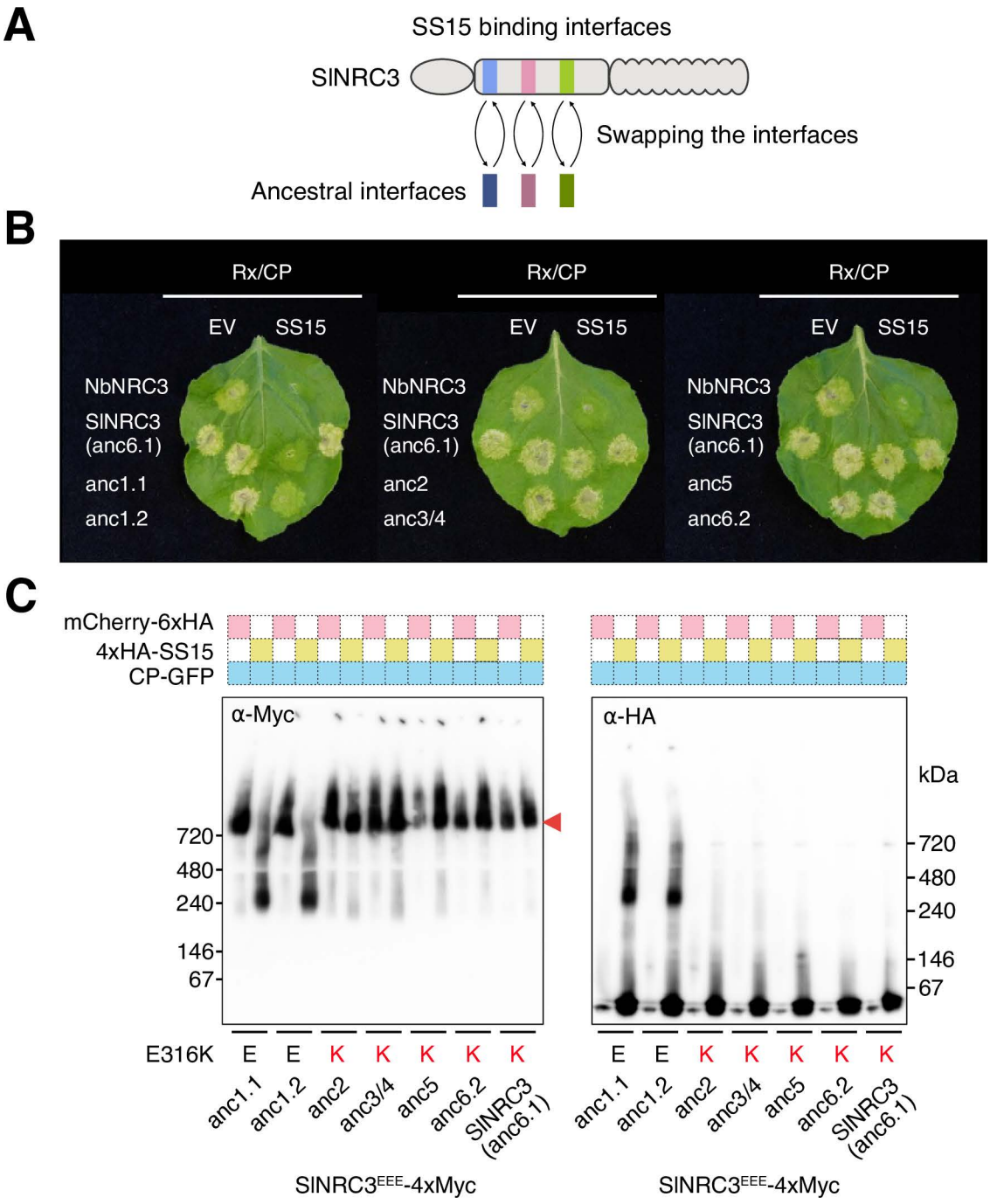


**Fig 6. Ancestral NRC3 variants with E316 are inhibited by SS15, but those with K316 are not.** (A) Overview of the strategy for resurrecting the ancestral interfaces of NRC3 for SS15. The three interfaces are defined as for SS15 in Fig 2. Using SlNRC3 as a backbone, we swapped the interface sequences with the ancestral sequences inferred in Fig 5. (B) Representative images of HR cell death assays showing the results after transient co-expression of either an empty vector (EV) or SS15 with Rx, PVX CP and the ancestral NRC3 variants in the leaves of *N. benthamiana nrc2/3/4* KO plants. NbNRC3 and SlNRC3 are used as negative and positive controls, respectively. The ancestral NRC3 variant for anc6.1 was identical to WT SlNRC3. The leaves were photographed 5 days after infiltration. The statistical analysis is in S8 Fig. (C) BN-PAGE assays for ancestral NRC3$^{EEE}$ variants. BN-PAGE assay was conducted for ancestral NRC3$^{EEE}$ variants. NRC3$^{EEE}$ represents the NRC3 mutant of the N-terminal MADA motif. C-terminally 4xMyc-tagged ancestral NRC3$^{EEE}$ variants were co-expressed with C-terminally V5-tagged Rx and C-terminally GFP-tagged PVX CP in the leaves of *N. benthamiana nrc2/3/4* KO plants. These effector-sensor-helper combinations were co-expressed either with mCherry-6xHA fusion protein or N-terminally 4xHA-tagged SS15. A red arrowhead indicates resistosome bands. Corresponding SDS-PAGE blots are in S10 Fig.

https://doi.org/10.1371/journal.pgen.1011653.g006

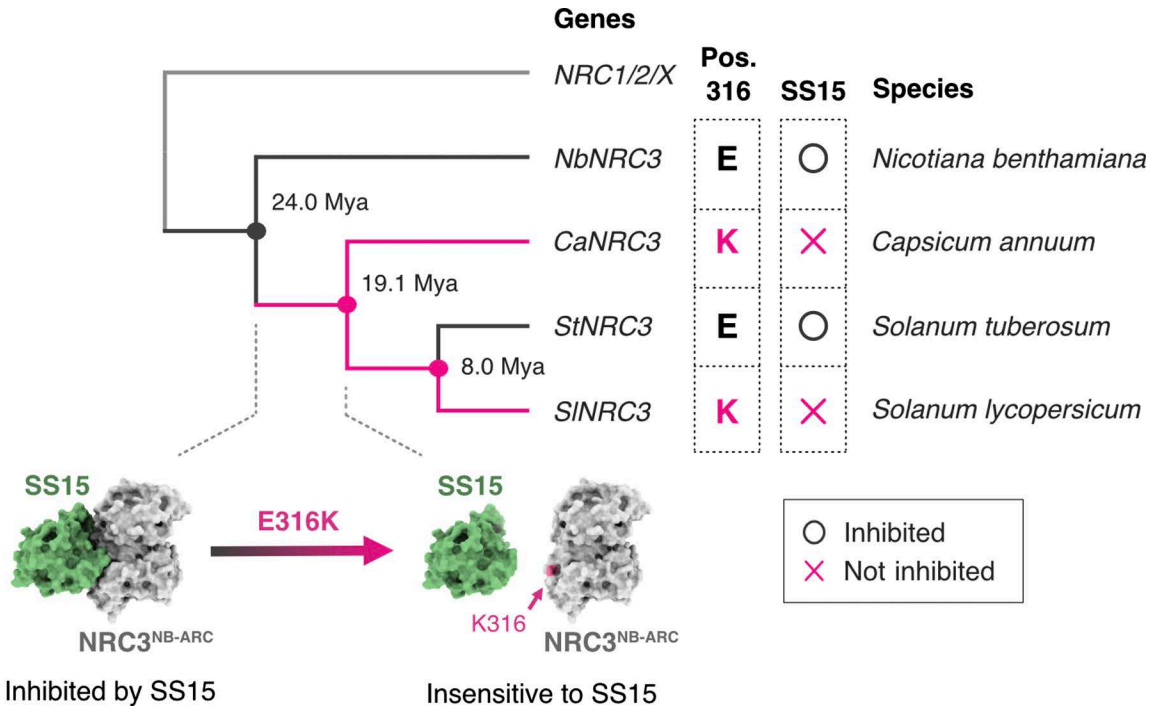


**Fig 7. NRC3 has evolved to evade inhibition by the cyst nematode effector SS15 over 19 Mya.** Polymorphisms at position E316 of NbNRC3 determine sensitivity to the cyst nematode effector SPRYSEC15 (SS15). The ancestral sequence reconstruction inferred that E316 is an ancestral state of the NRC3 clade and that E316K mutation occurred over 19 million years ago before the divergence of *Capsicum* and *Solanum* genus. The E316K mutation has made NRC3 insensitive to SS15, but NRC3 of *S. tuberosum* (StNRC3) acquired a regressive mutation (K316E) and became inhibited by SS15.

https://doi.org/10.1371/journal.pgen.1011653.g007

## Discussion

Plant pathogen effectors can function as suppressors of NLR-mediated immunity [15]. However, the degree to which NLRs have evolved to evade pathogen immunosuppressors has remained unknown. In this study, we discovered that some natural variants of helper NLRs in the NRC family are insensitive to suppression by the cyst nematode effector SS15. We found that some natural variants of NRC1 and NRC3 are insensitive to SS15 suppression, while all tested NRC2s are suppressed by SS15 (Fig 1). These contrasting SS15 inhibition phenotypes enabled us to determine that a single polymorphic amino acid residue at position E316 of NbNRC2 [35] determines sensitivity to SS15 in the NRC3 clade of solanaceous plants (Figs 2–4). We also tested hypotheses about adaptive evolution (from sensitive to insensitive phenotype) of the NRC-SS15 binding interface and used ancestral sequence reconstruction to show that NRC3 has evolved to evade SS15 inhibition over 19 Mya (Figs 5 and 6). These experiments led to an evolutionary model that maps out transitions in the evolution of NRC3 sensitivity to SS15 inhibition (Fig 7) and supports the view that suppressor and their receptor targets are engaged in another layer of gene-for-gene coevolution in addition to classic R-AVR interactions (S1 Fig). Intriguingly, the analyses also indicated regressive evolution (from insensitive to sensitive phenotype) in potato StNRC3 (Figs 5 and 7). Collectively, our study indicates adaptive evolution of NLRs to a pathogen immunosuppressor and identified key evolutionary transitions in a Solanaceae helper NLR that counteract this inhibition.

Our results indicate that position E316 is critical for SS15 inhibition in both NRC2 and NRC3 clades. On the other hand, the same position is not polymorphic in NRC1 sequences

across multiple species, even though they showed varying sensitivities to SS15 (Fig 1). This indicates that different residues contribute to insensitivity to SS15 in the NRC1 clade and that the sensitivity to SS15 has evolved independently in different clades of the NRC family.

Ancestral sequence reconstruction statistically infers intermediate sequences at phylogenetic nodes, enabling the identification of key evolutionary mutations. It is increasingly being applied to plant-pathogen coevolutionary systems [4,26,46–48]. For instance, this method was used to explore when the rice sensor NLR Pik-1 evolved to detect the AVR-PikD effector of the pathogenic fungus *Magnaporthe oryzae* (syn. *Pyricularia oryzae*) [47]. Similarly, ancestral sequence reconstruction was applied to the AVR-Pik effector family to understand the directionality of evolutionary changes, determining whether the effector family expanded host-target binding or host immunity evaded the effector family [46]. Moreover, a recent study employed this technique on NRC3 to examine the evolutionary history of sensor-helper compatibility [26]. In our study, we applied ancestral sequence reconstruction to NRC3 and reconstructed the evolutionary dynamics of NLRs against pathogen immunosuppressors. We analysed six evolutionary intermediate sequences of Solanaceae NRC3 to differentiate their evolutionary trajectories and discovered that SS15 sensitivity had shifted due to the E316K polymorphism that arose approximately 19 million years ago. This finding paves the way for further analyses of NLR-suppressor coevolution, particularly whether ancestral SS15 has bound ancestral NRC3 and has evolved to overcome insensitive NLRs.

Ancestral sequence reconstruction revealed the regressive evolution of potato StNRC3 to becoming sensitive to the nematode effector SS15 (Figs 5 and 7). Why did this seemingly counterintuitive evolutionary transition occur in StNRC3? One possible explanation is a trade-off between functional NLR activation and evasion of pathogen immunosuppression. In NLRs, mutations in the NB-ARC module are known to cause autoimmunity, loss-of-function, or sensor-helper incompatibility [26,49–51]. Since E316K is located in the NB-ARC module, this polymorphism could affect NLR activity, and plants carrying K316 might be subject to negative selection in the absence of parasite pressure. In this scenario, SS15 insensitivity in potato StNRC1 might be a compensating mutation that enhanced the activity of potato StNRC3 (Fig 1). Alternatively, the mutation may reflect a trade-off between SS15 evasion and another, yet unidentified, parasite or pathogen effector that interacts with StNRC3. To address this question, further investigations into the diversity of parasite or pathogen effectors that interact with NRC3 are necessary.

NRC helpers have recently been shown to form homodimers in their resting state [37]. How SS15 prevents a conversion of homodimers into resistosomes remains unclear. Importantly, the SS15-NRC interaction interface does not overlap with the NRC homodimerization interface, and co-expression of NRCs with SS15 does not result in the appearance of lower molecular weight bands of NRCs [35] (Figs 4 and 6C). This suggests that SS15 likely to binds to NRC homodimers. Obtaining structural insights into the NRC homodimer together with SS15 will shed more light on the precise molecular mechanism of SS15 inhibition.

Recent studies have reported bioengineering plant immune receptors to broaden their recognition repertoire for pathogen effectors [52–61]. An alternative bioengineering approach involves designing NLR variants that evade pathogen suppression [35,62]. A previous study utilised the differential SS15 inhibition exhibited by NbNRC2 and NbNRC4 to engineer an SS15-insensitive NRC2 variant. Our study further explored the natural diversity of NRCs within the Solanaceae family, identifying naturally occurring NRC3 variants that have evolved insensitivity to SS15 suppression (Figs 5–7). Notably, the tomato SlNRC3 harbours additional mutations at the interface, besides E314K, which confer robust insensitivity to SS15 (S11 Fig). Identifying these additional mutations could be useful to bioengineer NRC variants with enhanced robustness against SS15 inhibition. Our findings shed light on a previously

overlooked aspect of NLR-suppressor coevolution, underscoring the immune receptors' capacity to adapt to pathogen-mediated immunosuppression.

The suppressor function of the cyst nematode effector SS15 was first identified in *N. benthamiana*, whereas SS15 elicits a defence response in *Nicotiana tabacum* (tobacco), a species which also possesses the NRC network [40]. This observation suggests that SS15 may exhibit AVR activity in some host genetic backgrounds. Similarly, host-dependent AVR/suppressor activities were observed in Avr1 of *Fusarium oxysporum* f. sp. *lycopersici* infecting tomatoes [63] and AvrPtoB and AvrPphB of *Pseudomonas syringae* [64,65]. In tomato and its wild relatives, the *I* gene mediates resistance to Avr1-expressing strains of the fungus, while Avr1 suppresses the resistance mediated by *I-2* and *I-3* genes [63,66–69]. Notably, *I-2* encodes a CC-type NLR, while *I* and *I-3* encode cell-surface receptors [69]. Also, while AvrPtoB is recognised by the tomato NLR receptor complex Prf/Pto, in *Arabidopsis* it acts as a suppressor of the helper NLRs ADR1-L1/L2 [65,70,71]. Interestingly, a recent study showed that this suppression is guarded by the *Arabidopsis* sensor TIR-NLR SNC1 [65,72]. Additionally, in *Arabidopsis*, RPS5 indirectly recognises AvrPphB via PBS1 cleavage and triggers HR, while AvrPphB suppresses AvrB-induced activation of RPM1 (resistance to *P. syringae* pv. *maculicola* protein 1) [64,73]. In the case of SS15, it remains unclear how it elicits a defence response in *N. tabacum*. If an NLR recognises SS15 in *N. tabacum*, it would be interesting to determine whether this NLR binds and detects SS15 through its NB-ARC module, and how evolutionary pressure from SS15 has influenced the evolution of NLR resistance genes. These dual AVR/suppressor activities of effectors add complexity to Flor's gene-for-gene model, introducing layers of conditional coevolution between the interacting genes (S1 Fig).

Elucidating evolutionary pathways is crucial for understanding how genes and proteins have evolved to acquire their current functions [4,74,75]. In plant-pathogen interactions, various modes of gene-for-gene interactions have been proposed [14,15,26,49,76,77]. Deciphering the major evolutionary transitions underlying these gene-for-gene specificities is crucial for understanding the arms race coevolution between plants and pathogens [4,46,47]. This study leveraged natural variants of NLRs that evaded pathogen inhibitors and identified the critical evolutionary transitions that counteract these inhibitors, thereby highlighting the intricate and multilayered coevolutionary dynamics between NLRs and pathogen effectors. A better understanding of NLR-AVR and NLR-suppressor coevolution is critical to inform NLR bioengineering approaches and improve disease resistance.

## Materials and methods

### Plant growth conditions

*N. benthamiana* triple *nrc2/3/4* CRISPR knock-out (KO) mutant line '210.5.5.1' was grown in a controlled environment growth chamber with a temperature range of 22–25°C, 45–65% humidity, and a 16/8 h light/dark cycle.

### Cell death and suppression assays

Four-week-old *nrc2/3/4* KO *N. benthamiana* plants were spot-infiltrated with *Agrobacterium tumefaciens* GV3101 carrying plasmids indicated in S2 Table. Cell death, HR, was photographed 5 days post infiltration and scored according to the 0 (no necrosis) to 7 (confluent necrosis) scale (S13 Fig) as described in previous studies [41,78]. All the HR scores underlying the figures are in S1 Data. The HR scores were statistically analysed using the "permutation_test" function implemented in "SciPy" python library v1.10.0 with the options "n_resamples=10000, vectorized=False, alternative=two-sided, random_state=0". In the "permutation_test" function, we used the difference between two group means as a test statistic.

## Total protein extraction

Four-week-old *nrc2/3/4* KO *N. benthamiana* plants were infiltrated with agrobacterial suspensions as indicated in S2 Table. Leaf tissue was collected 72 h after agroinfiltration in liquid nitrogen and was grounded in a Geno/Grinder homogeniser. Proteins were extracted in GTMN buffer [10% glycerol, 50 mM tris-HCl (pH 7.5), 5 mM MgCl2, and 50 mM NaCl] supplemented with 10 mM dithiothreitol (DTT), 1x protease inhibitor cocktail (Sigma-Aldrich), and 0.2% Triton 100-X (Sigma-Aldrich), and incubated on ice for 10 min with short vortex mixing every 2 min. Debris was removed by centrifugation at 5000 *xg* for 15 min. Supernatant was used for BN-PAGE and SDS-PAGE assays.

## BN-PAGE assays

For BN-PAGE, 25 ul of extracted proteins were combined with NativePAGE 5% G-250 sample additive, NativePAGE 4x sample buffer, and water. Five ul samples were loaded and run on NativePAGE 4–16% bis-tris gels alongside SERVA Native Marker (SERVA). Proteins were transferred to PVDF membranes with NuPAGE Transfer Buffer in a Trans-Blot Turbo transfer apparatus (Bio-Rad) as per the manufacturer's instructions. Proteins were fixed to the membranes incubating with 8% acetic acid for 15 min, washed with water, and left to dry. Activation with ethanol allowed visualising the unstained native protein marker.

## SDS-PAGE assays

Extracted proteins were diluted in SDS loading dye and incubated at 72°C for 10 min and briefly centrifuged. Fifteen ul of supernatant were run on Bio-Rad 4–20% Mini-PROTEAN TGX gels with PageRuler Plus prestained protein ladder (Thermo Fisher Scientific). Proteins were transferred to PVDF difluoride membranes in Trans-Blot Turbo transfer buffer in a Trans-Blot Turbo transfer system (Bio-Rad) as per the manufacturer's instructions.

## Immunoblotting and epitope detection

BN or SDS blotted membranes were blocked with 5% milk in tris-buffered saline and 0.01% Tween 20 (TBS-T) for an hour at room temperature, and subsequently overnight at 4°C with indicated antibodies (S2 Table). Bands were visualised with Pierce ECL Western (32106, Thermo Fisher Scientific), supplementing with up to 50% SuperSignal West Femto Maximum Sensitivity Substrate (34095, Thermo Fisher Scientific) when necessary. Membranes were imaged in an ImageQuant 800 luminescent system (GE Healthcare Life Sciences, Piscataway, NJ). Rubisco loading control was stained using Ponceau S (Sigma) or Ponceau 4R (Irn Bru; AG Barr, Cumbernauld, UK).

## Interface of NRC1 and SS15

The crystal structure of tomato SlNRC1 NB-ARC module ($SlNRC1^{NB\text{-}ARC}$) bound to SS15 effector at 4.5 Å resolution (PDB code 8BV0) was previously resolved [35]. In this structure, SS15 effector approaches the NRC1 between its NBD and HD1 domains. Molecular interactions between $SlNRC1^{NB\text{-}ARC}$ and SS15 were listed using the CONTACT program of CCP4 [79] with a distance cut-off of 2.5 to 3.6 Å. The interacting residues were clustered in three regions in SlNRC1 ranging 153–170, 306–320 and 348–353 and formed the core of the interface between $SlNRC1^{NB\text{-}ARC}$ and SS15 in the crystal structure. These three regions were named interface 1, 2 and 3, respectively. All the interfaces contain a loop region at their centre together, allowing movement of the NBD with respect to HD1 and WHD. The structure was visualized using ChimeraX [43]. To identify the polymorphisms on these interfaces, 11 NRC protein sequences

tested in HR cell death assay were aligned using MAFFT v7.508 with the options "--maxiterate 1000 --localpair" [80]. The regions corresponding to the interfaces 1, 2 and 3 were extracted from the alignment.

## Phylogenetic analyses of helper NRC clades

A previous study reported NRC helper sequences of *N. benthamiana*, *C. annuum* (pepper), *S. tuberosum* (potato) and *S. lycopersicum* (tomato) [37]. The full-length amino acid sequences of the NRC0 (5 sequences), NRC1 (6 sequences), NRC2 (10 sequences), NRC3 (7 sequences) and NRCX (3 sequences) were obtained from this previously published dataset. Exact matches for the NbNRC2, CaNRC3 and StNRC3 sequences used in the HR cell death assay were not found within the dataset. Therefore, they were included in the dataset. The full-length amino acid sequences of helper NRC0/1/2/3/X clades were aligned using MAFFT v7.508 with the options "--maxiterate 1000 --localpair" [80]. This alignment was then trimmed using ClipKIT v1.3.0 with the options "-c -m gappy -g 0.9" [81]. Based on the trimmed alignment, a phylogenetic tree was created using IQ-TREE v1.6.12 [82] with 1,000 ultrafast bootstrap replicates [83]. ModelFinder selected the best-fit model for tree reconstruction, "JTT+G4", according to the Bayesian Information Criterion (BIC) [84]. The resulting tree was visualised using Iroki [85], and the bootstrap values for key nodes were shown in the figures.

## Obtaining codon-based alignment for ancestral sequence reconstruction

Sequences of 2,361 helper NRCs were obtained from a previously published dataset [26]. The dataset was cleaned by removing sequences containing internal stop codons, those lacking a multiple-of-three nucleotide length, and terminal stop codons, resulting in 2,353 sequences. Then, sequences shorter than 2,400 or longer than 2,800 bases were filtered out, resulting in 1,748 sequences. To identify the NRC1/2/3/X clade, the protein sequences of the NB-ARC module were aligned using MAFFT v7.508 with the options "--maxiterate 1000 --localpair" [80]. The alignment was trimmed using ClipKIT v1.3.0 with the options "-c -m gappy -g 0.9" [81]. Based on the trimmed alignment, a phylogenetic tree was created using IQ-TREE v2.2.6 [86] with 1,000 ultrafast bootstrap replicates [83]. ModelFinder selected the best-fit model for tree reconstruction, "JTT+F+R6", according to the BIC [84]. Based on this phylogenetic tree, the 591 full-length nucleotide sequences were obtained from the NRC1/2/3/X clade. These 591 sequences were translated using seqkit v2.3.0 "translate" command [87] and then re-aligned using MAFFT v7.508 with the options "--maxiterate 1000 --localpair" [80]. The position T4 of "Ppr-t_12226" was manually edited in the alignment. To obtain a codon-based nucleotide sequence alignment, the nucleotide sequences were threaded onto the protein alignment using the "thread_dna" command in phykit v1.11.14 [88]. The alignment was trimmed using ClipKIT v1.3.0 with the options "-c -m gappy -g 0.9" [81]. Finally, duplicated sequences were removed using seqkit v2.3.0 "rmdup" command [87] with the -s and -P options. Some duplicated splicing variants were also filtered out, resulting in 314 non-redundant nucleotide sequences.

## Ancestral sequence reconstruction

Based on the codon-based nucleotide alignment, which contains 314 non-redundant nucleotide sequences from the NRC1/2/3/X clade, a phylogenetic tree was created using IQ-TREE v2.2.6 [86] with 1,000 ultrafast bootstrap replicates [83]. ModelFinder selected the best-fit model for tree reconstruction, "TIM3+F+I+R4", according to the BIC [84]. An empirical Bayes method implemented in IQ-TREE was used to infer the ancestral states of the input sequences [86,89,90]. The previously generated alignment and tree files were input to IQ-TREE, specifying the options "-s DNA -o SlNRCX -m TIM3+F+I+R4". Since IQ-TREE does not infer the

ancestral states of insertion and deletion events (indels), the sequence alignment was converted to a simple binary presence-absence alignment file. In this file, "0" and "1" represent non-gap and gap, respectively. The Jukes-Cantor type binary model (JC2) in IQ-TREE was used to infer the ancestral states of this binary data, similar to how a previous study did with RAxML [91,92]. For indel reconstruction, the branch lengths of the tree were fixed with the "-blfix" option. Finally, the results of ancestral sequence reconstruction were combined with those of ancestral indel reconstruction, and the probabilities of each codon were calculated by simply multiplying the probabilities of each nucleotide. A probability value (*p*) greater than 0.3 was considered as an ambiguous residue. Focusing on the three interfaces defined by the crystal structure of SlNRC1$^{NB\text{-}ARC}$ in complex with SS15, six different ancestral variants (anc1.1, anc1.2, anc2, anc3/4, anc5, anc6.2) were cloned and tested (S2 Table). The ancestral interfaces of anc6.1 were identical to those of WT SlNRC3. This programming pipeline was named "ancseq" and deposited on GitHub (https://github.com/YuSugihara/ancseq).

### Consensus sequence analyses

The NRC sequences and alignment in Fig 5A were used as input. The alignments were converted into a matrix using the "alignment_to_matrix" function in logomaker (Tareen and Kinney, 2020) with the options (to_type='information', pseudocount=0), and the logo plots were generated with the "weblogo_protein" color scheme in logomaker. The NRC1/2/3 clade was distinguished from the NRCX clade, where four sequences were not clearly assigned to either the NRC1, NRC2, or NRC3 clades (Fig 5A).

## Supporting information

**S1 Fig. Multiple levels of gene-for-gene interactions between pathogens and plants.** To date, most studies have focused on coevolution between R (immune receptors or *R* genes) and AVR effectors, of which there are numerous examples. On the other hand, coevolution between pathogen effectors with immunosuppression activities (suppressors) and their receptor targets are less understood.
(TIF)

**S2 Fig. Phylogenetic tree of helper NRC0/1/2/3/X clades and sequences used in Fig 1B.** We used the NRC sequences of the NRC0, NRC1, NRC2, NRC3 and NRCX clades from four different Solanaceae species (*Nicotiana benthamiana*, *Capsicum annuum*, *Solanum tuberosum* and *Solanum lycopersicum*) and created a phylogenetic tree. When a cloned sequence is not identical to any sequences in the dataset, we added them to the dataset. Each cloned NRC sequence is highlighted in red. When a cloned sequence is identical to multiple NRC sequences in the tree, they are indicated in the figure. The phylogenetic tree is reconstructed by the maximum likelihood method using IQ-TREE with 1,000 bootstrap replicates.
(TIF)

**S3 Fig. Protein accumulations of NRC3s and their single-point mutants in the presence of SS15.** C-terminally 4xMyc-tagged NRC3s and single-point mutants were expressed with N-terminally StrepII-tagged SS15 in the leaves of *N. benthamiana nrc2/3/4* KO plants. NbNRC3 expressed with EV was used as a negative control for the anti-Strep blot. Rubisco loading control was carried out using Ponceau staining (PS).
(TIF)

**S4 Fig. SDS-PAGE accompanying BN-PAGE shown in Fig 4A.** SDS-PAGE assay was conducted for CaNRC3$^{EEE}$ and its single-point mutant at position matching NbNRC3 residue 316.

CaNRC3$^{EEE}$ represents the CaNRC3 mutant of the N-terminal MADA motif. C-terminally 4xMyc-tagged CaNRC3$^{EEE}$ mutants were co-expressed with C-terminally V5-tagged Rx and either free GFP or C-terminally GFP-tagged PVX CP in the leaves of *N. benthamiana nrc2/3/4* KO plants. These effector-sensor-helper combinations were co-expressed either with mCherry-6xHA fusion protein or N-terminally 4xHA-tagged SS15. Rubisco loading control was carried out using Ponceau staining (PS).
(TIF)

**S5 Fig. SDS-PAGE accompanying BN-PAGE shown in Fig 4B.** SDS-PAGE assay was conducted for StNRC3$^{EEE}$ and its single-point mutant at position matching NbNRC3 residue 316. StNRC3$^{EEE}$ represents the StNRC3 mutant of the N-terminal MADA motif. C-terminally 4xMyc-tagged StNRC3$^{EEE}$ mutants were co-expressed with C-terminally V5-tagged Rx and either free GFP or C-terminally GFP-tagged PVX CP in the leaves of *N. benthamiana nrc2/3/4* KO plants. These effector-sensor-helper combinations were co-expressed either with mCherry-6xHA fusion protein or N-terminally 4xHA-tagged SS15. Rubisco loading control was carried out using Ponceau staining (PS).
(TIF)

**S6 Fig. SDS-PAGE accompanying BN-PAGE shown in Fig 4C.** SDS-PAGE assay was conducted for SlNRC3$^{EEE}$ and its single-point mutant at position matching NbNRC3 residue 316. SlNRC3$^{EEE}$ represents the SlNRC3 mutant of the N-terminal MADA motif. C-terminally 4xMyc-tagged SlNRC3$^{EEE}$ mutants were co-expressed with C-terminally V5-tagged Rx and either free GFP or C-terminally GFP-tagged PVX CP in the leaves of *N. benthamiana nrc2/3/4* KO plants. These effector-sensor-helper combinations were co-expressed either with mCherry-6xHA fusion protein or N-terminally 4xHA-tagged SS15. Rubisco loading control was carried out using Ponceau staining (PS).
(TIF)

**S7 Fig. Consensus sequence patterns for SS15 interface regions of each NRC clade.** The consensus sequence patterns of each NRC clade and the NRC1/2/3 clade were generated using logomaker [93]. We used the NRC sequences and alignment from Fig 5A. The NRC1/2/3 clade was distinguished from the NRCX clade, where four sequences were not clearly assigned to either the NRC1, NRC2, or NRC3 clade (Fig 5A).
(TIF)

**S8 Fig. Statistical analysis of Fig 6B.** We used a two-sided permutation test with 10,000 replicates. Statistically significant differences are indicated (***: $p < 0.001$; n.s.: not significant). Each column represents an independent experiment. The data underlying this figure can be found in S1 Data.
(TIF)

**S9 Fig. Protein accumulations of ancestral NRC3 variants in the presence of SS15.** C--terminally 4xMyc-tagged ancestral NRC3 variants were expressed with N-terminally StrepII-tagged SS15 in the leaves of *N. benthamiana nrc2/3/4* KO plants. The ancestral NRC3 variant for anc6.1 was identical to WT SlNRC3 at the five SS15 binding interface residues. NbNRC3 expressed with EV was used as a negative control for the anti-Strep blot. Rubisco loading control was carried out using Ponceau staining (PS).
(TIF)

**S10 Fig. SDS-PAGE accompanying BN-PAGE shown in Fig 6C.** SDS-PAGE assay was conducted for ancestral NRC3$^{EEE}$ variants. NRC3$^{EEE}$ represents the NRC3 mutant of the N-terminal MADA motif. C-terminally 4xMyc-tagged ancestral NRC3$^{EEE}$ variants were

co-expressed with C-terminally V5-tagged Rx and C-terminally GFP-tagged PVX CP in the leaves of *N. benthamiana nrc2/3/4* KO plants. These effector-sensor-helper combinations were co-expressed either with mCherry-6xHA fusion protein or N-terminally 4xHA-tagged SS15.
(TIF)

**S11 Fig. Tomato NRC3 accumulates mutations that confer robust insensitivity to SS15.** (A) Representative images of HR cell death assays showing the results after transient co-expression of either an empty vector (EV) or SS15 with Rx and PVX CP, along with either WT SlNRC3, SlNRC3$^{K314E}$ or the ancestral NRC3 variants (anc1.1 and anc1.2) in the leaves of *N. benthamiana nrc2/3/4* KO plants. The anc1.1 and anc1.2 are the ancestral NRC3 variants tested in Fig 6. The leaves were photographed 5 days after infiltration. (B) Statistical analysis of S11A Fig using a two-sided permutation test with 10,000 replicates. Statistically significant differences are indicated (***: $p < 0.001$; n.s.: not significant). Each column represents an independent experiment. (C) BN-PAGE assays for WT SlNRC3, SlNRC3$^{K314E}$ and anc1.1. The SlNRC3$^{EEE}$s, the N-terminal MADA motif mutants, were used in this BN-PAGE assay. C-terminally 4xMyc-tagged NRC3s were co-expressed with C-terminally V5-tagged Rx and C-terminally GFP-tagged PVX CP in the leaves of *N. benthamiana nrc2/3/4* KO plants. These effector-sensor-helper combinations were co-expressed either with mCherry-6xHA fusion protein or N-terminally 4xHA-tagged SS15. A red arrowhead indicates resistosome bands. Corresponding SDS-PAGE blots are in S12 Fig. The data underlying S11B Fig can be found in S1 Data.
(TIF)

**S12 Fig. SDS-PAGE accompanying BN-PAGE shown in S11C Fig.** SDS-PAGE assays were conducted for WT SlNRC3, SlNRC3$^{K314E}$ and anc1.1. The SlNRC3$^{EEE}$s, the N-terminal MADA motif mutants, were used in this SDS-PAGE assay. C-terminally 4xMyc-tagged NRC3 variants were co-expressed with C-terminally V5-tagged Rx and either free GFP or C-terminally GFP-tagged PVX CP in the leaves of *N. benthamiana nrc2/3/4* KO plants. These effector-sensor-helper combinations were co-expressed either with mCherry-6xHA fusion protein or N-terminally 4xHA-tagged SS15. Rubisco loading control was carried out using Ponceau staining (PS).
(TIF)

**S13 Fig. HR scale used in this study.** Cell death, HR, was photographed 5 days post infiltration and scored according to the 0 (no necrosis) to 7 (confluent necrosis) scale as described in previous studies [41,78].
(TIF)

**S1 Table. Summary of ancestral sequence reconstruction probabilities.**
(XLSX)

**S2 Table. Cloning details of constructs used in this study.**
(XLSX)

**S1 Data. Underlying numerical data for Figs 3C, S8 and S11B.**
(XLSX)

## Acknowledgements

C.M.-A. is grateful to the DGAPA-PASPA UNAM Program for financing a sabbatical year at TSL. We thank all members of the TSL Support Services for their invaluable assistance.

## Author contributions

**Conceptualization:** Jiorgos Kourelis, Sophien Kamoun.

**Data curation:** Yu Sugihara, Jiorgos Kourelis, AmirAli Toghani, Claudia Martínez-Anaya.

**Formal analysis:** Yu Sugihara, Muniyandi Selvaraj, Claudia Martínez-Anaya.

**Funding acquisition:** Sophien Kamoun.

**Investigation:** Yu Sugihara, Jiorgos Kourelis, Claudia Martínez-Anaya.

**Methodology:** Yu Sugihara, Mauricio P. Contreras, Hsuan Pai.

**Project administration:** Sophien Kamoun.

**Resources:** Jiorgos Kourelis.

**Software:** Yu Sugihara.

**Supervision:** Jiorgos Kourelis, Mauricio P. Contreras, Claudia Martínez-Anaya, Sophien Kamoun.

**Validation:** Yu Sugihara, Mauricio P. Contreras, Adeline Harant, Claudia Martínez-Anaya.

**Visualization:** Yu Sugihara, Mauricio P. Contreras, Hsuan Pai, Muniyandi Selvaraj, AmirAli Toghani, Claudia Martínez-Anaya, Sophien Kamoun.

**Writing – original draft:** Yu Sugihara, Jiorgos Kourelis, Mauricio P. Contreras, Muniyandi Selvaraj, Claudia Martínez-Anaya, Sophien Kamoun.

**Writing – review & editing:** Yu Sugihara, Jiorgos Kourelis, Mauricio P. Contreras, Claudia Martínez-Anaya, Sophien Kamoun.

## References

1. Delaux P-M, Schornack S. Plant evolution driven by interactions with symbiotic and pathogenic microbes. Science. 2021;371(6531):eaba6605. https://doi.org/10.1126/science.aba6605 PMID: 33602828
2. Jones JDG, Dangl JL. The plant immune system. Nature. 2006;444(7117):323–9. https://doi.org/10.1038/nature05286
3. Ngou BPM, Ding P, Jones JDG. Thirty years of resistance: zig-zag through the plant immune system. Plant Cell. 2022;34(5):1447–78. https://doi.org/10.1093/plcell/koac041
4. Schornack S, Kamoun S. EVO-MPMI: from fundamental science to practical applications. Curr Opin Plant Biol. 2023;76:102469. https://doi.org/10.1016/j.pbi.2023.102469 PMID: 37783039
5. Flor HH. Current status of the gene-for-gene concept. Annu Rev Phytopathol. 1971;9(1):275–96. https://doi.org/10.1146/annurev.py.09.090171.001423
6. Flor HH. Inheritance of pathogenicity of Melampsora lini. Phytopathology. 1942;32:653–69.
7. Dodds PN. From gene-for-gene to resistosomes: Flor's enduring legacy. MPMI. 2023;36(8):461–7. https://doi.org/10.1094/mpmi-06-23-0081-hh
8. Białas A, Zess EK, De la Concepcion JC, Franceschetti M, Pennington HG, Yoshida K, et al. Lessons in effector and NLR biology of plant-microbe systems. Mol Plant Microbe Interact. 2018;31(1):34–45. https://doi.org/10.1094/MPMI-08-17-0196-FI PMID: 29144205
9. De la Concepcion JC, Maidment JHR, Longya A, Xiao G, Franceschetti M, Banfield MJ. The allelic rice immune receptor Pikh confers extended resistance to strains of the blast fungus through a single polymorphism in the effector binding interface. PLoS Pathog. 2021;17(3):e1009368. https://doi.org/10.1371/journal.ppat.1009368 PMID: 33647072
10. Dodds PN, Lawrence GJ, Catanzariti A-M, Teh T, Wang C-IA, Ayliffe MA, et al. Direct protein interaction underlies gene-for-gene specificity and coevolution of the flax resistance genes and flax rust avirulence genes. Proc Natl Acad Sci U S A. 2006;103(23):8888–93. https://doi.org/10.1073/pnas.0602577103 PMID: 16731621
11. Kanzaki H, Yoshida K, Saitoh H, Fujisaki K, Hirabuchi A, Alaux L, et al. Arms race co-evolution ofMagnaporthe oryzae AVR-Pik and rice Pik genes driven by their physical interactions. Plant J. 2012;72(6):894–907. https://doi.org/10.1111/j.1365-313x.2012.05110.x

12. Crean EE, Bilstein-Schloemer M, Maekawa T, Schulze-Lefert P, Saur IML. A dominant-negative avirulence effector of the barley powdery mildew fungus provides mechanistic insight into barley MLA immune receptor activation. J Exp Bot. 2023;74(18):5854–69. https://doi.org/10.1093/jxb/erad285 PMID: 37474129

13. Upson JL, Zess EK, Białas A, Wu C-H, Kamoun S. The coming of age of EvoMPMI: evolutionary molecular plant-microbe interactions across multiple timescales. Curr Opin Plant Biol. 2018;44:108–16. https://doi.org/10.1016/j.pbi.2018.03.003 PMID: 29604609

14. Contreras MP, Lüdke D, Pai H, Toghani A, Kamoun S. NLR receptors in plant immunity: making sense of the alphabet soup. EMBO Rep. 2023;24(10):e57495. https://doi.org/10.15252/embr.202357495 PMID: 37602936

15. Wu C-H, Derevnina L. The battle within: how pathogen effectors suppress NLR-mediated immunity. Curr Opin Plant Biol. 2023;74:102396. https://doi.org/10.1016/j.pbi.2023.102396 PMID: 37295294

16. Adachi H, Derevnina L, Kamoun S. NLR singletons, pairs, and networks: evolution, assembly, and regulation of the intracellular immunoreceptor circuitry of plants. Curr Opin Plant Biol. 2019;50:121–31. https://doi.org/10.1016/j.pbi.2019.04.007 PMID: 31154077

17. Araújo AC de, Fonseca FCDA, Cotta MG, Alves GSC, Miller RNG. Plant NLR receptor proteins and their potential in the development of durable genetic resistance to biotic stresses. Biotechnol Res Innov. 2019;3:80–94. https://doi.org/10.1016/j.biori.2020.01.002

18. Kourelis J, van der Hoorn RAL. Defended to the nines: 25 years of resistance gene cloning identifies nine mechanisms for R protein function. Plant Cell. 2018;30(2):285–99. https://doi.org/10.1105/tpc.17.00579 PMID: 29382771

19. Cesari S. Multiple strategies for pathogen perception by plant immune receptors. New Phytol. 2018;219(1):17–24. https://doi.org/10.1111/nph.14877 PMID: 29131341

20. Barragan AC, Weigel D. Plant NLR diversity: the known unknowns of pan-NLRomes. Plant Cell. 2021;33(4):814–31. https://doi.org/10.1093/plcell/koaa002

21. Chia K-S, Carella P. Taking the lead: NLR immune receptor N-terminal domains execute plant immune responses. New Phytol. 2023;240(2):496–501. https://doi.org/10.1111/nph.19170 PMID: 37525357

22. Wu C-H, Abd-El-Haliem A, Bozkurt TO, Belhaj K, Terauchi R, Vossen JH, et al. NLR network mediates immunity to diverse plant pathogens. Proc Natl Acad Sci U S A. 2017;114(30):8113–8. https://doi.org/10.1073/pnas.1702041114 PMID: 28698366

23. Goh F-J, Huang C-Y, Derevnina L, Wu C-H. NRC Immune receptor networks show diversified hierarchical genetic architecture across plant lineages. Plant Cell. 2024;36(9):3399–418. https://doi.org/10.1093/plcell/koae179

24. Sakai T, Contreras MP, Martinez-Anaya C, Lüdke D, Kamoun S, Wu C-H, et al. The NRC0 gene cluster of sensor and helper NLR immune receptors is functionally conserved across asterid plants. Plant Cell. 2024;36(9):3344–61. https://doi.org/10.1093/plcell/koae154 PMID: 38833594

25. Oh S, Kim S, Park H, Kim M, Seo M, Wu C, et al. Nucleotide-binding leucine-rich repeat network underlies nonhost resistance of pepper against the Irish potato famine pathogen Phytophthora infestans. Plant Biotechnol J. 2023;21(7):1361–72. https://doi.org/10.1111/pbi.14039

26. Huang C-Y, Huang Y-S, Sugihara Y, Wang H-Y, Huang L-T, Lopez-Agudelo JC, et al. Subfunctionalization of NRC3 altered the genetic structure of the Nicotiana NRC network. PLoS Genet. 2024;20(9):e1011402. https://doi.org/10.1371/journal.pgen.1011402

27. Lüdke D, Sakai T, Kourelis J, Toghani A, Adachi H, Posbeyikian A, et al. A root-specific NLR network confers resistance to plant parasitic nematodes. bioRxiv; 2023:2023.12.14.571630. https://doi.org/10.1101/2023.12.14.571630

28. Kourelis J. Interplay between cell-surface receptor and intracellular NLR-mediated immune responses. New Phytol. 2023;240(6):2218–26. https://doi.org/10.1111/nph.19212 PMID: 37605623

29. Kourelis J, Contreras MP, Harant A, Pai H, Lüdke D, Adachi H, et al. The helper NLR immune protein NRC3 mediates the hypersensitive cell death caused by the cell-surface receptor Cf-4. PLoS Genet. 2022;18(9):e1010414. https://doi.org/10.1371/journal.pgen.1010414 PMID: 36137148

30. Kourelis J, Adachi H. Activation and regulation of NLR immune receptor networks. Plant Cell Physiol. 2022;63(10):1366–77. https://doi.org/10.1093/pcp/pcac116

31. Ahn H-K, Lin X, Olave-Achury AC, Derevnina L, Contreras MP, Kourelis J, et al. Effector-dependent activation and oligomerization of plant NRC class helper NLRs by sensor NLR immune receptors Rpi-amr3 and Rpi-amr1. EMBO J. 2023;42(5):e111484. https://doi.org/10.15252/embj.2022111484 PMID: 36592032

32. Contreras MP, Pai H, Thompson R, Marchal C, Claeys J, Adachi H, et al. The nucleotide-binding domain of NRC-dependent disease resistance proteins is sufficient to activate downstream helper NLR oligomerization and immune signaling. New Phytol. 2024;243(1):345–61. https://doi.org/10.1111/nph.19818

33. Contreras MP, Pai H, Tumtas Y, Duggan C, Yuen ELH, Cruces AV, et al. Sensor NLR immune proteins activate oligomerization of their NRC helpers in response to plant pathogens. EMBO J. 2022;42(5):e111519. https://doi.org/10.15252/embj.2022111519

34. Bentham A, Burdett H, Anderson PA, Williams SJ, Kobe B. Animal NLRs provide structural insights into plant NLR function. Ann Bot. 2017;119(5):827–702. https://doi.org/10.1093/aob/mcw171 PMID: 27562749

35. Contreras MP, Pai H, Selvaraj M, Toghani A, Lawson DM, Tumtas Y, et al. Resurrection of plant disease resistance proteins via helper NLR bioengineering. Sci Adv. 2023;9(18):eadg3861. https://doi.org/10.1126/sciadv.adg3861 PMID: 37134163

36. Kourelis J, Sakai T, Adachi H, Kamoun S. RefPlantNLR is a comprehensive collection of experimentally validated plant disease resistance proteins from the NLR family. PLoS Biol. 2021;19(10):e3001124. https://doi.org/10.1371/journal.pbio.3001124 PMID: 34669691

37. Selvaraj M, Toghani A, Pai H, Sugihara Y, Kourelis J, Yuen ELH, et al. Activation of plant immunity through conversion of a helper NLR homodimer into a resistosome. PLoS Biol. 2024;22(10):e3002868. https://doi.org/10.1371/journal.pbio.3002868 PMID: 39423240

38. Liu F, Yang Z, Wang C, You Z, Martin R, Qiao W, et al. Activation of the helper NRC4 immune receptor forms a hexameric resistosome. Cell. 2024;187(18):4877-4889.e15. https://doi.org/10.1016/j.cell.2024.07.013

39. Madhuprakash J, Toghani A, Contreras MP, Posbeyikian A, Richardson J, Kourelis J, et al. A disease resistance protein triggers oligomerization of its NLR helper into a hexameric resistosome to mediate innate immunity. Sci Adv. 2024;10(45):eadr2594. https://doi.org/10.1126/sciadv.adr2594 PMID: 39504373

40. Ali S, Magne M, Chen S, Obradovic N, Jamshaid L, Wang X, et al. Analysis of Globodera rostochiensis effectors reveals conserved functions of SPRYSEC proteins in suppressing and eliciting plant immune responses. Front Plant Sci. 2015;6:623. https://doi.org/10.3389/fpls.2015.00623 PMID: 26322064

41. Derevnina L, Contreras MP, Adachi H, Upson J, Vergara Cruces A, Xie R, et al. Plant pathogens convergently evolved to counteract redundant nodes of an NLR immune receptor network. PLoS Biol. 2021;19(8):e3001136. https://doi.org/10.1371/journal.pbio.3001136

42. Sugihara Y, Toghani A, Kamoun S, Kourelis J. NLRome dataset from 124 genomes of plants in the Solanaceae family. Zenodo. 2023 [cited 2023 Dec 12]. https://doi.org/10.5281/zenodo.10354350

43. Meng EC, Goddard TD, Pettersen EF, Couch GS, Pearson ZJ, Morris JH, et al. UCSF ChimeraX: tools for structure building and analysis. Protein Sci. 2023;32(11):e4792. https://doi.org/10.1002/pro.4792 PMID: 37774136

44. Adachi H, Contreras MP, Harant A, Wu C-H, Derevnina L, Sakai T, et al. An N-terminal motif in NLR immune receptors is functionally conserved across distantly related plant species. Elife. 2019;8:e49956. https://doi.org/10.7554/eLife.49956 PMID: 31774397

45. Särkinen T, Bohs L, Olmstead RG, Knapp S. A phylogenetic framework for evolutionary study of the nightshades (Solanaceae): a dated 1000-tip tree. BMC Evol Biol. 2013;13:214. https://doi.org/10.1186/1471-2148-13-214 PMID: 24283922

46. Bentham AR, Petit-Houdenot Y, Win J, Chuma I, Terauchi R, Banfield MJ, et al. A single amino acid polymorphism in a conserved effector of the multihost blast fungus pathogen expands host-target binding spectrum. PLoS Pathog. 2021;17(11):e1009957. https://doi.org/10.1371/journal.ppat.1009957 PMID: 34758051

47. Białas A, Langner T, Harant A, Contreras MP, Stevenson CE, Lawson DM, et al. Two NLR immune receptors acquired high-affinity binding to a fungal effector through convergent evolution of their integrated domain. Elife. 2021;10:e66961. https://doi.org/10.7554/eLife.66961 PMID: 34288868

48. Snoeck S, Abramson BW, Garcia AGK, Egan AN, Michael TP, Steinbrenner AD. Evolutionary gain and loss of a plant pattern-recognition receptor for HAMP recognition. Elife. 2022;11:e81050. https://doi.org/10.7554/eLife.81050 PMID: 36377784

49. De la Concepcion JC, Vega Benjumea J, Bialas A, Terauchi R, Kamoun S, Banfield MJ. Functional diversification gave rise to allelic specialization in a rice NLR immune receptor pair. Elife. 2021;10:e71662. https://doi.org/10.7554/eLife.71662 PMID: 34783652

50. Sueldo DJ, Shimels M, Spiridon LN, Caldararu O, Petrescu A, Joosten MHAJ, et al. Random mutagenesis of the nucleotide-binding domain of NRC1 (NB-LRR Required for Hypersensitive Response-Associated Cell Death-1), a downstream signalling nucleotide-binding, leucine-rich repeat (NB-LRR) protein, identifies gain-of-function mutations in the nucleotide-binding pocket. New Phytol. 2015;208(1):210–23. https://doi.org/10.1111/nph.13459

51. Williams SJ, Sornaraj P, deCourcy-Ireland E, Menz RI, Kobe B, Ellis JG, et al. An autoactive mutant of the M flax rust resistance protein has a preference for binding ATP, whereas wild-type M protein binds ADP. Mol Plant Microbe Interact. 2011;24(8):897–906. https://doi.org/10.1094/MPMI-03-11-0052 PMID: 21539434

52. Bentham AR, De la Concepcion JC, Benjumea JV, Kourelis J, Jones S, Mendel M, et al. Allelic compatibility in plant immune receptors facilitates engineering of new effector recognition specificities. Plant Cell. 2023;35(10):3809–27. https://doi.org/10.1093/plcell/koad204 PMID: 37486356

53. Cesari S, Xi Y, Declerck N, Chalvon V, Mammri L, Pugnière M, et al. New recognition specificity in a plant immune receptor by molecular engineering of its integrated domain. Nat Commun. 2022;13(1):1524. https://doi.org/10.1038/s41467-022-29196-6 PMID: 35314704

54. De la Concepcion JC, Franceschetti M, MacLean D, Terauchi R, Kamoun S, Banfield MJ. Protein engineering expands the effector recognition profile of a rice NLR immune receptor. eLife. 2019;8:e47713 https://doi.org/10.7554/elife.47713

55. Kourelis J, Marchal C, Posbeyikian A, Harant A, Kamoun S. NLR immune receptor–nanobody fusions confer plant disease resistance. Science. 2023;379(6635):934–9. https://doi.org/10.1126/science.abn4116

56. Liu Y, Zhang X, Yuan G, Wang D, Zheng Y, Ma M, et al. A designer rice NLR immune receptor confers resistance to the rice blast fungus carrying noncorresponding avirulence effectors. Proc Natl Acad Sci U S A. 2021;118(44):e2110751118. https://doi.org/10.1073/pnas.2110751118 PMID: 34702740

57. Maidment JHR, Shimizu M, Bentham AR, Vera S, Franceschetti M, Longya A, et al. Effector target-guided engineering of an integrated domain expands the disease resistance profile of a rice NLR immune receptor. Elife. 2023;12:e81123. https://doi.org/10.7554/eLife.81123 PMID: 37199729

58. Marchal C, Pai H, Kamoun S, Kourelis J. Emerging principles in the design of bioengineered made-to-order plant immune receptors. Curr Opin Plant Biol. 2022;70:102311. https://doi.org/10.1016/j.pbi.2022.102311 PMID: 36379872

59. Tamborski J, Seong K, Liu F, Staskawicz BJ, Krasileva KV. Altering specificity and autoactivity of plant immune receptors Sr33 and Sr50 via a rational engineering approach. Mol Plant Microbe Interact. 2023;36(7):434–46. https://doi.org/10.1094/MPMI-07-22-0154-R PMID: 36867580

60. Zdrzałek R, Xi Y, Langner T, Bentham AR, Petit-Houdenot Y, De la Concepcion JC, et al. Bioengineering a plant NLR immune receptor with a robust binding interface toward a conserved fungal pathogen effector. Proc Natl Acad Sci USA. 2024;121(28):e2402872121. https://doi.org/10.1073/pnas.2402872121

61. Zdrzałek R, Stone C, De la Concepcion JC, Banfield MJ, Bentham AR. Pathways to engineering plant intracellular NLR immune receptors. Curr Opin Plant Biol. 2023;74:102380. https://doi.org/10.1016/j.pbi.2023.102380 PMID: 37187111

62. Karki HS, Abdullah S, Chen Y, Halterman DA. Natural genetic diversity in the potato resistance gene RB confers suppression avoidance from phytophthora effector IPI-O4. Mol Plant Microbe Interact. 2021;34(9):1048–56. https://doi.org/10.1094/MPMI-11-20-0313-R PMID: 33970667

63. Houterman PM, Cornelissen BJC, Rep M. Suppression of plant resistance gene-based immunity by a fungal effector. PLoS Pathog. 2008;4(5):e1000061. https://doi.org/10.1371/journal.ppat.1000061

64. Russell AR, Ashfield T, Innes RW. Pseudomonas syringae effector AvrPphB suppresses AvrB-induced activation of RPM1 but not AvrRpm1-induced activation. Mol Plant Microbe Interact. 2015;28(6):727–35. https://doi.org/10.1094/MPMI-08-14-0248-R PMID: 25625821

65. Wang M-Y, Chen J-B, Wu R, Guo H-L, Chen Y, Li Z-J, et al. The plant immune receptor SNC1 monitors helper NLRs targeted by a bacterial effector. Cell Host Microbe. 2023;31(11):1792-1803.e7. https://doi.org/10.1016/j.chom.2023.10.006 PMID: 37944492

66. Catanzariti A-M, Do HTT, Bru P, de Sain M, Thatcher LF, Rep M, et al. The tomato I gene for Fusarium wilt resistance encodes an atypical leucine-rich repeat receptor-like protein whose function is nevertheless dependent on SOBIR1 and SERK3/BAK1. Plant J. 2017;89(6):1195–209. https://doi.org/10.1111/tpj.13458 PMID: 27995670

67. Catanzariti A, Lim GTT, Jones DA. The tomato I-3 gene: a novel gene for resistance to Fusarium wilt disease. New Phytol. 2015;207(1):106–18. https://doi.org/10.1111/nph.13348

68. Houterman PM, Ma L, Van Ooijen G, De Vroomen MJ, Cornelissen BJC, Takken FLW, et al. The effector protein Avr2 of the xylem-colonizing fungus Fusarium oxysporum activates the tomato resistance protein I-2 intracellularly. Plant J. 2009;58(6):970–8. https://doi.org/10.1111/j.1365-313x.2009.03838.x

69. van der Does HC, Constantin ME, Houterman PM, Takken FLW, Cornelissen BJC, Haring MA, et al. Fusarium oxysporum colonizes the stem of resistant tomato plants, the extent varying with the R-gene present. Eur J Plant Pathol. 2018;154(1):55–65. https://doi.org/10.1007/s10658-018-1596-3

70. Sheikh AH, Zacharia I, Pardal AJ, Dominguez-Ferreras A, Sueldo DJ, Kim J-G, et al. Dynamic changes of the Prf/Pto tomato resistance complex following effector recognition. Nat Commun. 2023;14(1):2568. https://doi.org/10.1038/s41467-023-38103-6 PMID: 37142566

71. Zhang N, Gan J, Carneal L, González-Tobón J, Filiatrault M, Martin GB. Helper NLRs Nrc2 and Nrc3 act codependently with Prf/Pto and activate MAPK signaling to induce immunity in tomato. Plant J. 2023;117(1):7–22. https://doi.org/10.1111/tpj.16502

72. Zhang Y, Goritschnig S, Dong X, Li X. A gain-of-function mutation in a plant disease resistance gene leads to constitutive activation of downstream signal transduction pathways in *suppressor of npr1-1*, *constitutive 1*. Plant Cell. 2003;15(11):2636–46. https://doi.org/10.1105/tpc.015842 PMID: 14576290

73. Pottinger SE, Innes RW. RPS5-mediated disease resistance: fundamental insights and translational applications. Annu Rev Phytopathol. 2020;58:139–60. https://doi.org/10.1146/annurev-phyto-010820-012733 PMID: 32284014

74. Kamoun S. Think. Evolutionary. Transitions. Zenodo. 2024 [cited 2024 Feb 26]. https://doi.org/10.5281/zenodo.10653728

75. Siddiq MA, Hochberg GK, Thornton JW. Evolution of protein specificity: insights from ancestral protein reconstruction. Curr Opin Struct Biol. 2017;47:113–22. https://doi.org/10.1016/j.sbi.2017.07.003 PMID: 28841430

76. Brabham HJ, Gómez De La Cruz D, Were V, Shimizu M, Saitoh H, Hernández-Pinzón I, et al. Barley MLA3 recognizes the host-specificity effector Pwl2 from Magnaporthe oryzae. Plant Cell. 2023;36(2):447–70. https://doi.org/10.1093/plcell/koad266

77. Sugihara Y, Abe Y, Takagi H, Abe A, Shimizu M, Ito K, et al. Disentangling the complex gene interaction networks between rice and the blast fungus identifies a new pathogen effector. PLoS Biol. 2023;21(1):e3001945. https://doi.org/10.1371/journal.pbio.3001945 PMID: 36656825

78. Segretin ME, Pais M, Franceschetti M, Chaparro-Garcia A, Bos JIB, Banfield MJ, et al. Single amino acid mutations in the potato immune receptor R3a expand response to Phytophthora effectors. Mol Plant Microbe Interact. 2014;27(7):624–37. https://doi.org/10.1094/MPMI-02-14-0040-R PMID: 24678835

79. Winn MD. An overview of the CCP4 project in protein crystallography: an example of a collaborative project. J Synchrotron Radiat. 2003;10(Pt 1):23–5. https://doi.org/10.1107/s0909049502017235 PMID: 12511787

80. Katoh K, Standley DM. MAFFT multiple sequence alignment software version 7: improvements in performance and usability. Mol Biol Evol. 2013;30(4):772–80. https://doi.org/10.1093/molbev/mst010 PMID: 23329690

81. Steenwyk JL, Buida TJ, Li Y, Shen X-X, Rokas A. ClipKIT: a multiple sequence alignment trimming software for accurate phylogenomic inference. PLoS Biol. 2020;18(12):e3001007. https://doi.org/10.1371/journal.pbio.3001007

82. Nguyen L-T, Schmidt HA, von Haeseler A, Minh BQ. IQ-TREE: a fast and effective stochastic algorithm for estimating maximum-likelihood phylogenies. Mol Biol Evol. 2015;32(1):268–74. https://doi.org/10.1093/molbev/msu300 PMID: 25371430

83. Hoang DT, Chernomor O, von Haeseler A, Minh BQ, Vinh LS. UFBoot2: improving the ultrafast bootstrap approximation. Mol Biol Evol. 2018;35(2):518–22. https://doi.org/10.1093/molbev/msx281 PMID: 29077904

84. Kalyaanamoorthy S, Minh BQ, Wong TKF, von Haeseler A, Jermiin LS. ModelFinder: fast model selection for accurate phylogenetic estimates. Nat Methods. 2017;14(6):587–9. https://doi.org/10.1038/nmeth.4285 PMID: 28481363

85. Moore RM, Harrison AO, McAllister SM, Polson SW, Wommack KE. Iroki: automatic customization and visualization of phylogenetic trees. PeerJ. 2020;8:e8584. https://doi.org/10.7717/peerj.8584

86. Minh BQ, Schmidt HA, Chernomor O, Schrempf D, Woodhams MD, von Haeseler A, et al. IQ-TREE 2: new models and efficient methods for phylogenetic inference in the genomic era. Mol Biol Evol. 2020;37(5):1530–4. https://doi.org/10.1093/molbev/msaa015 PMID: 32011700

87. Shen W, Le S, Li Y, Hu F. SeqKit: a cross-platform and ultrafast toolkit for FASTA/Q file manipulation. PLoS One. 2016;11(10):e0163962. https://doi.org/10.1371/journal.pone.0163962 PMID: 27706213

88. Steenwyk JL, Buida TJ III, Labella AL, Li Y, Shen X-X, Rokas A. PhyKIT: a broadly applicable UNIX shell toolkit for processing and analyzing phylogenomic data. Bioinformatics. 2021;37(16):2325–31. https://doi.org/10.1093/bioinformatics/btab096

89. VanAntwerp J, Finneran P, Dolgikh B, Woldring D. Ancestral sequence reconstruction and alternate amino acid states guide protein library design for directed evolution. In: Traxlmayr MW, editor. Yeast surface display. New York (NY): Springer US; 2022. p. 75–86. https://doi.org/10.1007/978-1-0716-2285-8_4

90. Yang Z, Kumar S, Nei M. A new method of inference of ancestral nucleotide and amino acid sequences. Genetics. 1995;141(4):1641–50. https://doi.org/10.1093/genetics/141.4.1641 PMID: 8601501

91. Aadland K, Pugh C, Kolaczkowski B. High-throughput reconstruction of ancestral protein sequence, structure, and molecular function. In: Sikosek T, editor. Computational methods in protein evolution. New York (NY): Springer; 2019. p. 135–70. https://doi.org/10.1007/978-1-4939-8736-8_8

92. Stamatakis A. RAxML version 8: a tool for phylogenetic analysis and post-analysis of large phylogenies. Bioinformatics. 2014;30(9):1312–3. https://doi.org/10.1093/bioinformatics/btu033 PMID: 24451623

93. Tareen A, Kinney JB. Logomaker: beautiful sequence logos in Python. Bioinformatics. 2019;36(7):2272–4. https://doi.org/10.1093/bioinformatics/btz921

bioRxiv preprint doi: https://doi.org/10.64898/2025.11.30.691369; this version posted December 2, 2025. The copyright holder for this preprint (which was not certified by peer review) is the author/funder, who has granted bioRxiv a license to display the preprint in perpetuity. It is made available under aCC-BY 4.0 International license.

# The Pik NLR pair accumulates at the plasma membrane as a hetero-oligomeric sensor-helper immune protein complex prior to activation

Hsuan Pai[1], Mauricio P. Contreras[1,3], Jose Salguero Linares[1], Daniel Lüdke[1], Andres Posbeyikian[1], Jiorgos Kourelis[1,2], Sophien Kamoun[1]*, Clemence Marchal[1,3]*

[1]The Sainsbury Laboratory, University of East Anglia; Norwich Research Park, Norwich, UK
[2]current affiliation: Department of Life Sciences, Imperial College London, London SW7 2AZ, UK
[3]current affiliation: Department of Plant Biochemistry, Center for Plant Molecular Biology (ZMBP), Eberhard Karls University, Tübingen, Germany

*Corresponding authors

## Abstract

Following the perception of pathogen virulence proteins in plants, nucleotide-binding and leucine-rich repeat immune receptors (NLRs) are activated via a wide range of mechanisms. Singleton NLRs can both perceive effectors and trigger an immune response, whereas other NLRs specialise in either pathogen recognition (sensor NLRs) or activation of the immune response (helper NLRs). Sensor and helper NLRs can function as genetically linked pairs or in unlinked receptor networks. Although growing evidence suggests that NLRs conditionally oligomerise upon activation, our understanding of the resting state of NLRs prior to effector perception remains limited. Here, we investigated the oligomeric state of the genetically linked rice (*Oryza sativa*) sensor Pik-1 and helper Pik-2 NLR pair prior to effector activation when transiently expressed in *Nicotiana benthamiana* leaves. We show that both wild-type Pikm-1 and engineered Pikm-1$^{Enhancer}$ sensors associate with Pikm-2 and form ~1 MDa hetero-complexes in the resting state that accumulate at the plasma membrane. Our findings contribute to the growing evidence that pre-activation mechanisms vary widely across NLRs. This knowledge could be leveraged for disease resistance engineering strategies complementary to approaches focussing solely on effector binding.

## One sentence summary

The Pik sensor-helper pair of rice immune receptor proteins forms a hetero-oligomer that accumulates at the plasma membrane in its resting state.

## Synopsis

Nucleotide-binding and leucine-rich repeat receptors (NLRs) are key players in plant immune systems that recognise and respond to harmful pathogen effector proteins. NLRs can play specialised roles in either detecting effectors (sensor NLRs) or triggering the immune response (helper NLRs) and might function together as pairs or within larger networks. Although many NLRs are known to oligomerise upon the perception of effectors, much less is understood about their resting state prior to pathogen recognition. In this study, we investigated the resting state of a pair of rice

bioRxiv preprint doi: https://doi.org/10.64898/2025.11.30.691369; this version posted December 2, 2025. The copyright holder for this preprint (which was not certified by peer review) is the author/funder, who has granted bioRxiv a license to display the preprint in perpetuity. It is made available under aCC-BY 4.0 International license.

NLRs, Pik-1 and Pik-2, transiently expressed in *Nicotiana benthamiana* leaves. These two proteins formed a sensor/helper complex at the cell membrane even in the absence of the effector protein. This discovery is significant because it reveals a new aspect of how these immune proteins are organised before activation, contributing to our understanding of the diverse ways plants prepare for immune responses. This finding adds to the growing body of evidence that, although many NLR proteins form complexes to respond to pathogens, their resting states and pre-activation mechanisms can vary widely.

## Introduction

Nucleotide-binding and leucine-rich repeat receptors (NLRs) are intracellular immune receptors found across all kingdoms of life[1,2]. In plants, NLRs directly or indirectly detect virulence proteins secreted by pathogens, termed effectors, which leads to the activation of an immune response and disease resistance[3]. Throughout evolution, NLR proteins have diversified from single functional units (functional singletons) capable of sensing pathogen effectors and initiating an immune response into specialised, sub-functionalized units comprising sensor NLRs that sense effectors or helper NLRs that mediate the downstream immune responses[4]. Across plant genomes, sensor and helper NLR genes can be genetically linked and cooperate as pairs, often in head-to-head orientation with a shared promoter sequence[4–12]. Additionally, some sensor and helper NLRs can function as complex receptor networks that are genetically unlinked[13,14].

Plant NLRs exhibit a conserved domain architecture consisting of a variable N-terminal domain, a central nucleotide-binding domain shared by APAF1, certain *R* gene products, and CED-4 (NB-ARC) domain, and a C-terminal leucine-rich repeat region (LRR). Although the majority of NLRs have maintained this canonical domain architecture, they sometimes exhibit diverse modes of activation and signalling. An emerging paradigm in NLR biology is that NLRs conditionally oligomerise into inflammasome-like structures known as resistosomes upon activation[15]. However, our understanding of the resting and autoinhibited states of NLR proteins in plants prior to effector perception is limited. Moreover, much of our knowledge of plant NLRs is derived from the activation mechanisms of singleton and helper NLRs. How paired sensor and helper NLRs mechanistically function remains poorly understood. In this study, we addressed this question using the paired rice (*Oryza sativa*) immune proteins Pik-1 and Pik-2, which confer resistance to the rice blast pathogen *Magnaporthe oryzae* (syn. *Pyricularia oryzae*) and constitute a well-established model system for NLR receptor bioengineering[9,16–21]

NLRs can be phylogenetically classified based on their NB-ARC domains and the nature of their N-terminal domains. In flowering plants (angiosperms), these include Toll/Interleukin-1 receptor (TIR), G10 subclade coiled coil ($CC_{G10}$), RESISTANCE TO POWDERY MILDEW 8 (RPW8) coiled coil ($CC_R$), and coiled coil (CC) domains[22]. Some NLRs carry unconventional integrated domains (IDs) that are generally thought to mediate the detection of pathogen effectors either by directly binding to the effectors or by acting as a substrate for their enzymatic activity[5,6,23–26]. Several characterised sensor NLRs featuring an ID (NLR-IDs) function as a genetically linked pair, with a helper NLR that lacks an ID for immune activation upon effector detection[5,7,9,11,12].

bioRxiv preprint doi: https://doi.org/10.64898/2025.11.30.691369; this version posted December 2, 2025. The copyright holder for this preprint (which was not certified by peer review) is the author/funder, who has granted bioRxiv a license to display the preprint in perpetuity. It is made available under aCC-BY 4.0 International license.

Despite the diversity observed across plant NLRs, a common theme among different classes of NLRs is the formation of higher-order oligomers termed resistosomes upon pathogen-induced activation. These resistosomes exhibit variable stoichiometry, with tetramers, pentamers, hexamers, and octamers described thus far[27–36]. The CC-NLR singletons ZAR1[27,28] and Sr35[29,30] form pentameric resistosomes at the plasma membrane, while $CC_{G10}$-NLR WAI3 forms an octameric resistosome. By contrast, in asterid plants, the NRC (NLR required for cell death) network is composed of functionally specialized sensor and helper NLRs[13], in which activation of sensor NLRs upon detection of pathogen effectors triggers the oligomerisation of helper NLRs and ultimately hypersensitive cell death and disease resistance[37–39]. Notably, NRC-dependent sensors are not part of the activated NRC oligomers and are thought to mediate oligomerisation of the helper NLR through an activate-and-release model via their central nucleotide-binding domain[40]. NRC2, NRC3 and NRC4 form hexameric resistosomes that accumulate at the plasma membrane[31,32,41]. Notably, NRC4, ZAR1, Sr35, and WAI3 display $Ca^{2+}$ channel activity, which contributes to immune activation and cell death[29,31,34,42,43]. In another activation mechanism, TIR-NLRs act as sensors and oligomerise to form tetrameric holo-enzymes that produce nucleotide-derived second messengers upon effector detection. The newly generated small molecules induce heterodimerization of the lipase-like proteins enhanced disease susceptibility 1 (EDS1) with either senescence-associated gene 101 (SAG101) or phytoalexin deficient 4 (PAD4). Formation of EDS1-SAG101 or EDS1-PAD4 hetero-complexes is perceived by the $CC_R$-NLR N REQUIREMENT GENE 1 (NRG1) or ACTIVATED DISEASE RESISTANCE 1 (ADR1) helper NLRs respectively, triggering their oligomerization[14,35]. Like singleton and NRC helpers, NRG1 and ADR1 oligomers show $Ca^{2+}$-permeable cation channel activity at the plasma membrane[43]. Altogether, these findings indicate that the modes of activation of NLR proteins that lead to the formation of higher-order complexes are highly variable.

The diversity of NLR activation mechanisms is also reflected in their resting states. It is becoming increasingly apparent that NLR proteins adopt different conformations to remain in an (auto-)inhibited state and prevent autoactivation. For example, ZAR1 adopts a monomeric conformation in complex with its partner pseudokinase RKS1[27] in its autoinhibited resting state. Interfering with ZAR1-RKS1 resting-state association does not trigger autoimmunity, suggesting that ZAR1 monomers are the minimal autoinhibited unit. Strikingly, the helper NRC2 forms homodimers[33] and dimers of dimers (tetramers) that can assemble to form filament-like structures in its resting state[44]. Furthermore, recent blue native–polyacrylamide gel electrophoresis (BN-PAGE) assays indicated that the TIR-NLR pairs CHS3-CSA1 and RPS4-RRS1 appear to form heterodimers in their resting state, although the structure of the complexes remains to be elucidated[46,47]. Altogether, these observations suggest that oligomerisation is not exclusive to NLR activation and that oligomer formation in the resting state may constitute an additional layer of self-inhibition. Importantly, the diversity observed among the relatively few NLR resting states characterised so far suggests that many more resting-state configurations remain to be identified.

*Pikm-1* and *Pikm-2* are alleles of two genes at the *Pik* locus that encode a CC-NLR pair. This NLR pair confers resistance to strains of the rice blast fungus *M. oryzae* by detecting alleles of the AVR-Pik effector, including AVR-PikD[9,48–50] (Figure 1A). The sensor Pikm-1 contains a non-canonical heavy-metal associated (HMA) integrated domain between its CC and NB-ARC domains that directly binds to AVR-Pik effectors.

bioRxiv preprint doi: https://doi.org/10.64898/2025.11.30.691369; this version posted December 2, 2025. The copyright holder for this preprint (which was not certified by peer review) is the author/funder, who has granted bioRxiv a license to display the preprint in perpetuity. It is made available under aCC-BY 4.0 International license.

The HMA domain is the most variable domain across different Pik-1 alleles, suggesting that this domain is under selection imposed by AVR-Pik[48,51,52]. Given that the effector recognition specificity appears to be largely encoded by the integrated HMA in Pik-1, this integrated domain has been successfully targeted for immune receptor bioengineering to broaden or switch its effector recognition spectrum[19,20,53]. We recently demonstrated that replacing the Pikm-1 HMA domain with a completely unrelated sequence such as that of nanobodies that bind fluorescent proteins (FPs) resulted in a fully functional immune receptor able to sense FPs and trigger an effective immune response when co-expressed with the Pikm-2 helper[21] (Figure 1A). Additionally, Pik-1 and Pik-2 can be successfully transferred from monocot to dicot species without requiring any additional components for the induction of an immune response[21]. Thus, the Pik CC-NLR pair is a highly promising NLR system for disease resistance engineering strategies across multiple crop species.

In a previous study, Zdrzałek et al.[16] used co-immunoprecipitation assays to show that Pikm-1 and Pikm-2 associate *in planta* before and after effector-mediated activation[16]. However, the oligomeric state of such complexes has not been investigated. Determining the oligomeric state of the Pik complexes will deepen our understanding of how cooperating receptors trigger an immune response. Importantly, this would allow fine tuning of this receptor pair for disease resistance and complement current approaches focussing solely on effector binding. Notably, BN-PAGE assays have only recently been used to study plant NLR biochemistry[37,38,54,55]. Here, we used BN-PAGE to show that Pikm-1 and Pikm-2 form hetero-oligomeric complexes prior to effector-mediated activation in *Nicotiana benthamiana* leaves. We show that both wild-type Pikm-1 and Pikm-1$^{\text{Enhancer}}$ [21], a nanobody engineered variant that senses green fluorescent protein (GFP), form hetero-oligomers with Pikm-2 in their resting state. Taking advantage of mutations in the N-terminal domain of helper NLRs that prevent the induction of cell death upon effector activation[56], we demonstrate that GFP, the ligand of Pikm-1$^{\text{Enhancer}}$, is also part of the Pikm-1$^{\text{Enhancer}}$-Pikm-2 hetero-oligomer. Additionally, when both proteins were expressed individually, we detected the helper Pikm-2 in both the membrane and soluble fractions in a membrane fractionation assay, and Pikm-1 mainly in the soluble fraction. Co-expression of the sensor and helper led to a shift in the localisation of Pikm-1 to the membrane and increased the membrane accumulation of Pikm-2. Our work emphasizes that NLR immune receptor proteins have diverse resting states and pre-activation mechanisms, despite their common feature of forming inflammasome-like resistosome oligomers during immune responses. Beyond developing a better understanding of immune receptor function, the details of these mechanisms lay the groundwork for developing new strategies in disease resistance engineering.

## Results

### Pikm-1$^{\text{Enhancer}}$ associates with Pikm-2 prior to effector activation

We previously showed that Pikm-1$^{\text{Enhancer}}$ specifically senses GFP and triggers an immune response in the presence of Pikm-2[21]. However, it is not known whether Pikm-1$^{\text{Enhancer}}$ and Pikm-2 interact in the absence of their ligand in the same manner as Pikm-1 and Pikm-2[16]. To investigate this question, we transiently co-expressed Pikm-1$^{\text{Enhancer}}$ and Pikm-2 in *N. benthamiana* leaves through agroinfiltration and performed co-immunoprecipitation (Co-IP) experiments (Figure 1B-C). Tagged Pikm-2 co-

bioRxiv preprint doi: https://doi.org/10.64898/2025.11.30.691369; this version posted December 2, 2025. The copyright holder for this preprint (which was not certified by peer review) is the author/funder, who has granted bioRxiv a license to display the preprint in perpetuity. It is made available under aCC-BY 4.0 International license.

expressed with either Pikm-1 or Pikm-1$^{Enhancer}$ triggered a hypersensitive response in the presence of the corresponding ligand (AVR-PikD for Pikm-1 and GFP for Pikm-1$^{Enhancer}$, Figure 1B), demonstrating that these receptors are functional and not autoactive in the absence of their ligand under the tested conditions. Pikm-1$^{Enhancer}$ co-immunoprecipitated with Pikm-2 to levels comparable to Pikm-1. By contrast, the negative control Rx (CC-NLR) co-immunoprecipitated only weakly with Pikm-1, Pikm-1$^{Enhancer}$, or Pikm-2 (Figure 1C and Figure S1), corresponding to the background signal of the IP. We thus confirmed that Pikm-1$^{Enhancer}$ and Pikm-2 follow the same interaction pattern as Pikm-1 and Pikm-2 in their resting state.

**The Pik pair forms a ~1 MDa hetero-oligomer prior to activation**

Although we observed an interaction between Pikm-1$^{Enhancer}$-Pikm-2 and Pikm-1-Pikm-2 in their resting state, the oligomerisation state of these complexes is unknown. To examine the oligomerisation state of the Pik pair prior to effector-mediated activation, we co-expressed the Pikm-1+Pikm-2 or Pikm-1$^{Enhancer}$+Pikm-2 pairs in *N. benthamiana* leaves and performed BN-PAGE assays. We observed a high-molecular-weight band at ~1 MDa only in lanes where Pikm-1 or Pikm-1$^{Enhancer}$ were co-expressed with Pikm-2 (Figure 2A, red asterisks). This band migrated at a similar size for both the sensor and helper (V5 and HA antisera blots, respectively). Because Pikm-1 and Pikm-2 are similar in size (~110 kDa), it is impossible to determine whether the bands correspond to separate Pik homo-oligomers (a sensor-only and a separate, helper-only oligomer) or to a hetero-oligomer that includes both subunits (Figure 2B). Each sensor and helper was co-expressed with Rx as a negative control (Figure 2A, Figure S2).

To resolve potential sensor and helper homo- or hetero-oligomers, we leveraged a previously published “heavy/light” tag approach[38]. We generated a C-terminally tagged tandem mCherry-V5 variant of Pikm-1$^{Enhancer}$ termed “heavy”. This variant was functional and triggered a hypersensitive response in the presence of Pikm-2 and GFP, but not mCherry (Figure 2C). We tested whether this heavy variant of the Pikm-1$^{Enhancer}$ sensor would induce a size shift of the Pikm-2 oligomer in BN-PAGE assays (Figure 2D). In the presence of Pikm-2, Pikm-1$^{Enhancer}$ ‘heavy’ migrated as a higher-molecular-weight band in the BN-PAGE blot compared to C-terminally V5-tagged Pikm-1$^{Enhancer}$ (termed ‘light’). Additionally, we observed an identical size shift in the BN-PAGE blot when probing for Pikm-2 (Figure 2D, red asterisks), suggesting that Pikm-1 and Pikm-2 are both part of the pre-activated ~1 MDa oligomer.

We also observed intermediate bands at ~242 and ~480 kDa in the lanes where Pikm-1 or Pikm-1$^{Enhancer}$ were expressed without Pikm-2 (Figure 2A and 2D). This suggests that the Pik sensors may form homo-oligomers in the absence of the corresponding Pik helper and that most of the Pikm-1 sensor pool shifts to the higher-order oligomeric state in the presence of the helper Pikm-2. Based on these results, we conclude that Pikm-1 and Pikm-2, as well as Pikm-1$^{Enhancer}$ and Pikm-2, form a ~1 MDa hetero-oligomer prior to activation that includes both the sensor and helper.

**Pikm-1$^{Enhancer}$ and Pikm-2 preferentially accumulate in the membrane fraction when co-expressed**

bioRxiv preprint doi: https://doi.org/10.64898/2025.11.30.691369; this version posted December 2, 2025. The copyright holder for this preprint (which was not certified by peer review) is the author/funder, who has granted bioRxiv a license to display the preprint in perpetuity. It is made available under aCC-BY 4.0 International license.

Growing evidence suggests that activated CC-NLRs and $CC_R$-NLRs localise to membrane compartments[37,38,42,43,57,58]. Since the Pik sensor-helper pair forms a high-molecular-weight complex prior to activation, we investigated whether the Pik hetero-complex associates with membrane compartments in its resting state by performing membrane fractionation assays under non-denaturing conditions with the same constructs used for Co-IP and BN-PAGE assays. When Pikm-1$^{Enhancer}$ was co-expressed with Rx, we detected Pikm-1$^{Enhancer}$ in both the soluble and membrane fractions, with higher accumulation in the soluble fraction (Figure 3A, Figure S3). By contrast, Pikm-2 was present in comparable amounts in both the soluble and membrane fractions when co-expressed with Rx. Pikm-1$^{Enhancer}$, but not Rx, accumulated in comparable amounts in both the soluble and membrane fractions upon co-expression with Pikm-2 (Figure 3A and S3, red asterisks). When co-expressed with Pikm-1$^{Enhancer}$, Pikm-2 showed slightly stronger accumulation in the membrane fraction compared to co-expression with Rx (Figure 3A and S3, blue asterisks). We conclude that Pikm-1$^{Enhancer}$ and Pikm-2 both accumulate in the soluble and membrane fractions, with preferential accumulation in the membrane fraction upon co-expression.

## Pikm-1$^{Enhancer}$ and Pikm-2 localise to both the cytosol and plasma membrane when co-expressed

To investigate the subcellular localisation of Pikm-1$^{Enhancer}$ and Pikm-2, we used confocal microscopy (Figure 3B). Since Pikm-1$^{Enhancer}$ triggers cell death in the presence of GFP, CFP, YFP and mNeonGreen, we co-expressed Pikm-1$^{Enhancer}$-v5-mCherry (Pikm-1$^{Enhancer}$ 'heavy', Figure 2) with Pikm-2-HA or Rx-HA in *N. benthamiana* leaves to determine its subcellular localisation. For Pikm-2, we generated a C-terminally tagged version with mCherry to track its localisation upon co-expression with Pikm-1$^{Enhancer}$-v5 or Rx-v5. Since Pikm-2-mCherry becomes autoactive at 3 dpi in the presence of Pikm-1$^{Enhancer}$-v5 but not Rx-v5 (Figure 3D), we performed confocal imaging at 2 dpi before cell death was visible, the same time point used for the membrane fractionation assays (Figure 3A). We incubated leaf disks in a 0.5 µM fluorescein diacetate (FDA) solution for 10 minutes prior to imaging. FDA is membrane permeable and accumulates in viable cells as fluorescein, providing a green fluorescent marker for the cytosol.

Pikm-1$^{Enhancer}$ fully co-localised with fluorescein when co-expressed with Rx, as indicated by the presence of cytosolic strands. When co-expressed with Pikm-2, Pikm-1$^{Enhancer}$ remained cytoplasmic, but puncta were occasionally observed. In the absence of Pikm-1$^{Enhancer}$, Pikm-2 co-localised with fluorescein at the cell periphery, with few or no cytosolic strands detected in maximum projection images derived from 10–15 slices. These observations indicate that Pikm-2 associated with the plasma membrane in the presence of both Rx and Pikm-1$^{Enhancer}$ and was also present in the cytosol. By contrast, Pikm-1$^{Enhancer}$ clearly localised to the cytosol when co-expressed with Rx and occasionally formed puncta in the presence of Pikm-2, suggesting that Pikm-2 can alter the subcellular localisation of Pikm-1$^{Enhancer}$.

We then compared the localisation of Pikm-1 and Pikm-2 to that of the plasma membrane marker LTI6B from *Arabidopsis thaliana*[59] (Figure S4). Because Pikm-1$^{Enhancer}$ triggers cell death in the presence of free GFP, CFP, YFP, and mNeonGreen, we used wild-type Pikm-1 fused to mNeonGreen at its C-terminus for these assays.

bioRxiv preprint doi: https://doi.org/10.64898/2025.11.30.691369; this version posted December 2, 2025. The copyright holder for this preprint (which was not certified by peer review) is the author/funder, who has granted bioRxiv a license to display the preprint in perpetuity. It is made available under aCC-BY 4.0 International license.

Pikm-2 was fused to mNeonGreen as well, while LTI6B was fused to mCherry, both at their C-termini. Co-expression of Pikm-1–mNeonGreen or Pikm-2–mNeonGreen with Rx resulted in autoactivity, which was not observed with the Pikm-1–mNeonGreen + Pikm-2–HA or Pikm-2–mNeonGreen + Pikm-1–v5 combinations. Therefore, we performed confocal imaging at 2 dpi, before cell death became apparent.

Consistent with observations for Pikm-1$^{Enhancer}$, Pikm-1 co-localised with cytosolic strands and partially co-localised with the plasma membrane marker LTI6B at the cell periphery when co-expressed with Rx (Figure S4). When co-expressed with Pikm-2, Pikm-1 remained associated with cytosolic strands and co-localised with LTI6B at the cell periphery. Additionally, we detected Pikm-1 puncta in a small proportion of cells when Pikm-1 was co-expressed with Pikm-2, but not with Rx. Pikm-2 co-localised with LTI6B and formed puncta in a small proportion of cells when co-expressed with Pikm-1 or with Rx (Figure S4). Together, these results are consistent with the findings from membrane fractionation assays, supporting the conclusion that the Pikm-1$^{Enhancer}$/Pikm-2 and Pikm-1/Pikm-2 hetero-complexes primarily localise to the plasma membrane, with a pool present in the cytosol.

## GFP associates with the Pikm-1$^{Enhancer}$-Pikm-2 hetero-complex

Finally, we investigated whether the Pik hetero-complex would undergo any changes upon treatment with a ligand that binds to Pik-1. We could not perform these experiments using wild-type Pik proteins because hypersensitive cell death interferes with the biochemical assays. We therefore took advantage of the occurrence of the MADA motif in the N-terminal α1 helix of Pikm-2[56] to introduce two mutations into this motif (Pikm-2$^{L19E,L23E}$, subsequently termed Pikm-2$^{EE}$) that abolished the induction of cell death upon co-expression with Pikm-1$^{Enhancer}$ and GFP (Figure 4A). Mutations in this motif have previously been used to prevent the induction of cell death without compromising NLR activation and resistosome formation, enabling biochemical studies[38,56].

To determine whether treatment with the ligand would alter the Pik hetero-complex, we co-expressed Pikm-1$^{Enhancer}$ and Pikm-2$^{EE}$ with GFP or the negative control mCherry in *N. benthamiana* leaves and performed BN-PAGE assays (Figure 4B and Figure S5). We detected a GFP signal (using anti-FLAG antibodies) at ~1 MDa only when GFP was co-expressed with Pikm-1$^{Enhancer}$ and Pikm-2$^{EE}$. By contrast, mCherry did not yield a signal at the ~1 MDa Pikm-1$^{Enhancer}$ /Pikm-2$^{EE}$ complex. We conclude that GFP was integrated into the ~1 MDa Pikm-1$^{Enhancer}$/Pik-2 hetero-oligomer complex.

Despite these findings, we could not draw any conclusions about the activation state of the Pik NLR pair. Given that the ~1 MDa bands were identical regardless of the presence of GFP, we could not conclude that the Pik pair was activated by GFP or whether Pikm-2$^{EE}$ is a non-functional mutant of Pikm-2 that is blocked in a conformation similar to that of its resting state.

## Discussion

bioRxiv preprint doi: https://doi.org/10.64898/2025.11.30.691369; this version posted December 2, 2025. The copyright holder for this preprint (which was not certified by peer review) is the author/funder, who has granted bioRxiv a license to display the preprint in perpetuity. It is made available under aCC-BY 4.0 International license.

In this study, we investigated the oligomeric state and subcellular localisation of the CC-NLR pair Pikm-1 and Pikm-2 prior to activation. We leveraged a previously described bioengineered Pikm-1 variant, Pikm-1$^{Enhancer}$, which specifically recognises GFP[21] and enhances the accumulation of the Pikm-1/Pikm-2 complex in BN-PAGE assays compared with the wild type in our experimental conditions (Figure 2A). We demonstrated that Pikm-1 and Pikm-2, as well as Pikm-1$^{Enhancer}$ and Pikm-2, form hetero-oligomers in their resting state (Figure 1 and 2). This hetero-oligomer accumulates at the plasma membrane (Figure 3). Furthermore, we generated the Pikm-2$^{EE}$ mutant, which is unable to trigger cell death in the presence of Pikm-1$^{Enhancer}$ and its ligand GFP, to determine whether the ligand is part of the hetero-oligomer. GFP migrated at the same molecular weight as the Pikm-1$^{Enhancer}$-Pikm-2$^{EE}$ hetero-oligomer, indicating that GFP may directly associate with the Pik hetero-complex (Figure 4). Overall, our study revealed that the sensor and helper of the CC-NLR Pik pair accumulate at the plasma membrane in the form of a ~1 MDa hetero-complex in its resting state, highlighting the diversity of NLR activation mechanisms.

**The Pik pair forms a hetero-oligomer in its resting state**

There is growing evidence that CC-NLRs remain autoinhibited in their resting state through a variety of mechanisms. For example, Arabidopsis ZAR1 exists as a monomer in complex with additional host components termed “guardees” prior to activation[27]. Additionally, we previously showed that NRC2 from *N. benthamiana* and tomato (*Solanum lycopersicum*) forms a homodimer in its resting state[33,44]. In its resting state, *Sl*NRC2 also forms higher-order dimer-based oligomers, leading to the formation of homo-tetramers and filaments, although these states are not required for NRC2 activation[44]. High-order oligomeric resting states were also observed for the mammalian NLR protein NLRP3 (NACHT-, leucine-rich-repeat-, and pyrin domain-containing protein 3)[60,61]. Prior to activation, NLRP3 forms oligomeric double-ring cages bound to membranes. Importantly, this conformation is required for the activation of NLRP3[60]. Here, we showed that the Pik sensor-helper pair forms a high-order hetero-oligomer in its resting state. Notably, hetero-oligomeric assembly was also reported for the TIR-NLR sensor pairs CSA1-CHS3 and RPS4-RRS1 in the resting state, which also remained in complex following effector activation[46,47]. Determining whether the Pikm-1-Pikm-2 oligomer changes its conformation or oligomeric state following ligand perception upon activation will require additional experiments, ideally using structural biology approaches. However, determining the structures of NLR pairs has been challenging, and their structures have not yet been resolved.

Although we demonstrated that both the Pikm-1 sensor and the Pikm-2 helper are part of the Pik sensor-helper pre-activation complex, the stoichiometry of the hetero-oligomer remains unclear. In BN-PAGE assays, we observed bands at ~242 kDa and between 480 and 720 kDa when the sensors Pikm-1 or Pikm-1$^{Enhancer}$ were expressed without Pikm-2 (Figure 2, Figure 4, Figure S2), indicating that the sensor alone may either form homo-oligomers of different stoichiometries or associates with unknown host components conserved between the heterologous *N. benthamiana* system and rice. By contrast, we did not consistently observe similar complexes for Pikm-2 in the absence of Pikm-1, although two potential Pikm-2 oligomeric states were visible in the BN-PAGE blots (Figure 2B, Figure S5). These observations raise the question of whether the final Pik resting state hetero-oligomer forms through the association of pre-formed sensor and helper homo-oligomers or through the oligomerisation of

bioRxiv preprint doi: https://doi.org/10.64898/2025.11.30.691369; this version posted December 2, 2025. The copyright holder for this preprint (which was not certified by peer review) is the author/funder, who has granted bioRxiv a license to display the preprint in perpetuity. It is made available under aCC-BY 4.0 International license.

sensor-helper heterodimers. Furthermore, if the GFP-bound Pikm-1$^{Enhancer}$-Pikm-2$^{EE}$ hetero-oligomer reflects the activated state of the Pik pair, how does ligand binding trigger its activation and subsequent cell death? Resolving the structures of the Pik oligomer in both the resting and activated states will be essential to address these questions.

**The Pik hetero-oligomer accumulates at the plasma membrane**

Using both membrane fractionation and confocal microscopy, we observed that Pikm-1 shifted from the cytosol to the plasma membrane when expressed with Pikm-2 (Figure 3, Figure S3 and S4). This indicates that Pikm-2 is the main driver for plasma membrane localization in the complex. This helper protein exhibits similar subcellular dynamics to *At*ADR1, *At*NRG1, and *At*RPM1, which also associate with the plasma membrane in their resting state[62,63]. How does Pikm-2 recruit Pikm-1 to the plasma membrane? Perhaps the two proteins use the plasma membrane as an oligomerisation scaffold, similar to what was observed for the cage-like structures that shield NLRP3 from mis-activation[60]. Further experiments are needed to determine the biological relevance of the plasma membrane association of the Pik complex in the resting state and whether it is required for the activation of the immune response upon effector recognition.

Several studies have shown that effector-activated or autoactive NLRs form puncta that associate with the plasma membrane[38,43,57,64]. These puncta are thought to be resistosomes or aggregates of membrane-associated resistosomes that actively contribute to the onset of cell death upon activation. We observed that both Pik-1 and Pik-2 occasionally formed puncta in *N. benthamiana* cells (Figure 3B, Figure S4). Specifically, only autoactive Pikm-2-mNeonGreen formed puncta in the absence of Pikm-1, while Pikm-2-mCherry did not. Pikm-1 and Pikm-1$^{Enhancer}$ only formed puncta when co-expressed with Pikm-2 (Figure 3B, Figure S4). Given that we only observed puncta in a small fraction of the cells expressing these components and that most of the NLR-fluorescent fusion proteins used in these experiments were autoactive, we cannot draw conclusions about the biological relevance of the Pik puncta at this time. Overall, the biochemical nature of these puncta remains elusive, as they might consist of resistosome foci or clusters of inactive NLR complexes.

**Outlook**

The Pik NLR pair is present as an allelic series in rice cultivars and confers resistance against *M. oryzae*, the causal agent of rice blast disease, by recognising specific alleles of the AVR-Pik effector[9,48–50]. Recent studies have shown that the *Pik-1* and *Pik-2* alleles have co-evolved to tightly control the immune response[20,51]. For instance, mismatching the allelic sensor Pikp-1 with the helper Pikm-2 caused hypersensitive cell death in the absence of the effector, while co-expressing Pikm-1 with Pikp-2 resulted in a weakened immune response[51]. Compatibility between Pik alleles appears to be driven by specific polymorphic residues, such as Glu230 located in the NB-ARC domain of Pik-2[51], and variations within the integrated HMA domain of Pik-1[20]. Notably, allelic mismatching did not prevent hetero-complex formation in Co-IP experiments, although co-evolved pairs showed a preferential association[51]. This raises several important questions: Does the binding affinity of these sensor-helper alleles directly affect their hetero-oligomeric state? Which molecular determinants underlie constitutive cell death or reduced activity in mismatched Pik hetero-oligomers? Can

bioRxiv preprint doi: https://doi.org/10.64898/2025.11.30.691369; this version posted December 2, 2025. The copyright holder for this preprint (which was not certified by peer review) is the author/funder, who has granted bioRxiv a license to display the preprint in perpetuity. It is made available under aCC-BY 4.0 International license.

incompatibility at the sensor-helper hetero-oligomerisation interface lead to autoactivation of the Pik system? Answering these questions will provide insights into how Pik-1 and Pik-2 have co-adapted and how co-evolution influences the oligomerisation abilities of different alleles. Furthermore, a better understanding of the molecular basis of sensor-helper compatibility in this system may guide future Pik bioengineering efforts.

The resting state of the Pik hetero-oligomer adds to the diversity of CC-NLR activation mechanisms characterised to date. It will be interesting to determine whether other genetically linked CC-NLR pairs also form hetero-oligomers in the resting state. It is likely that additional diversity in CC-NLR pairs in the resting state remains to be discovered, especially since not all characterised CC-NLR pairs function cooperatively, as does the Pik system[16]. For instance, unlike Pik-1 and Pik-2, the rice Pia pair (RGA4 and RGA5) appears to function via negative regulation, with the sensor RGA5 maintaining its helper RGA4 in a repressed state. Effector binding by RGA5 is thought to trigger a conformational change in RGA5 and subsequent release of RGA4 inhibition leading to the induction of cell death in *N. benthamiana*[65]. Although RGA4 and RGA5 interact in both the absence and presence of the effector AVR-Pia, whether this negative regulation model influences the resting state or activated oligomerisation profile of this NLR pair remains to be determined.

We propose a model describing the cooperation between a sensor and a helper in a CC-NLR pair via the formation of a large (~1 MDa) membrane-associated hetero-oligomer in the resting state (Figure 5). This work adds to the growing evidence that, while oligomerisation is a hallmark of NLR-mediated immune responses, the resting states and mechanisms leading to NLR assembly into resistosomes exhibit remarkable diversity. These findings should advance the field beyond a uniform view of NLR structure and function and further facilitate comparative analyses of NLRs across diverse plants.

## Material and Methods

### Plant growth conditions

Wild-type *N. benthamiana* plants were grown in a controlled environment growth chamber with a temperature range of 22–25°C, relative humidity of 45–65%, and a 16/8-h light/dark cycle.

### Plasmid construction

The Golden Gate Modular Cloning (MoClo) kit[66] and the MoClo Plant Parts kit[67] were used for cloning unless otherwise specified (Table S1). Cloning design and sequence analysis were performed using Geneious Prime (v2022.2.2; https://www.geneious.com). For the mRFP-Lti6b-TurboID plasma membrane marker, the coding sequence of *LOW-TEMPERATURE-INDUCED6b* from Arabidopsis (*Lti6b*, GenBank accession number AT3G05890) was amplified without the stop codon alongside the TurboID sequence from AT3G05890. Both PCR fragments were ligated using overlapping PCRs. The fusion construct *Lti6b*-TurboID was then cloned into the pENTR/D-TOPO plasmid (Thermo Scientific). The final RFP-Lti6b-TurboID construct was generated via Gateway cloning (LR reaction, Thermo Scientific) of pENTR/D-TOPO into pGWB555[68]. Plasmid construction is described in Table S1.

bioRxiv preprint doi: https://doi.org/10.64898/2025.11.30.691369; this version posted December 2, 2025. The copyright holder for this preprint (which was not certified by peer review) is the author/funder, who has granted bioRxiv a license to display the preprint in perpetuity. It is made available under aCC-BY 4.0 International license.

**Cell death assays in *N. benthamiana***

Transient gene expression in *N. benthamiana* was performed by agroinfiltration as described by van der Hoorn et al. [69]. Briefly, *Agrobacterium tumefaciens* strain GV3101 pMP90 carrying binary vectors was inoculated from glycerol stock in LB medium supplemented with the appropriate antibiotics and grown overnight at 28°C until saturation. The cells were harvested by centrifugation at 2000 × *g* at room temperature for 5 min. The cells were washed once and resuspended in infiltration buffer (10 mM $MgCl_2$, 10 mM MES-KOH pH 5.6, 200 µM acetosyringone) to the appropriate $OD_{600}$ (see Table S1) in various combinations and incubated for 30 min at room temperature prior to infiltration into 4- to 5-week-old *N. benthamiana* leaves. Two leaves from three plants were inoculated per experiment (*N* = 6), and the experiment was repeated three times. In all assays where the original Pikm was co-infiltrated with its cognate effector AVR-PikD, the Tomato bushy stunt virus (TBSV) silencing inhibitor p19[70] was co-infiltrated into the leaves to enhance expression and ensure a reliable hypersensitive response. Hypersensitive cell death phenotypes were visually scored 4–5 days post infiltration in a range from 0 (no visible necrosis) to 7 (fully confluent necrosis) according to Adachi et al.[56].

**Protein extraction for BN- and SDS-PAGE assays**

Six *N. benthamiana* leaf discs (9 mm diameter) collected at 2 days post agroinfiltration were homogenised in 200 µL extraction buffer (10% glycerol, 50 mM Tris-HCl [pH 7.5], 5 mM $MgCl_2$, 50 mM NaCl) supplemented with 10 mM DTT, 1× protease inhibitor cocktail (SIGMA), and 0.5% Triton-X (SIGMA) and incubated on ice for 10 min. The samples were centrifuged at 5,000 × *g* for 15 min at 4°C, and the supernatant was used for BN- and SDS-PAGE assays.

**BN-PAGE assays**

For BN-PAGE, 25 µL of the supernatant obtained from protein extraction described above was diluted as per the manufacturer's instructions by adding NativePAGE 5% G-250 sample additive, 4× Sample Buffer, and water. After dilution, the samples were run on Native PAGE 3–12% Bis-Tris gels alongside a Native Marker (SERVA). The separated proteins were transferred to polyvinylidene difluoride membranes using NuPAGE Transfer Buffer with a Trans-Blot Turbo Transfer System (Bio-Rad) as per the manufacturer's instructions. Proteins were fixed to the membranes by incubating in 8% acetic acid for 15 min, washed with water, and left to dry. The membranes were subsequently re-activated with ethanol to correctly visualise the unstained native protein marker. The membranes were immunoblotted as described below.

**SDS-PAGE assays**

For SDS-PAGE, 25 µL of the supernatant obtained from protein extraction described above was diluted in 75 µL 4× SDS-PAGE sample buffer (final concentration: 50 mM Tris-HCl [pH 6.8], 100 mM DTT, 2% SDS, 0.01% bromophenol blue, 10% glycerol) and incubated at 72°C for 10 min. The samples were centrifuged at 5,600 × *g* for 2 min, and 10 µL of the supernatant was separated on a 10–20% SDS-PAGE gel (Bio-Rad) and transferred onto a polyvinylidene difluoride (PVDF) membrane using a Trans-Blot turbo transfer system (Bio-Rad). The membranes were immunoblotted as described below.

**Co-immunoprecipitation**

bioRxiv preprint doi: https://doi.org/10.64898/2025.11.30.691369; this version posted December 2, 2025. The copyright holder for this preprint (which was not certified by peer review) is the author/funder, who has granted bioRxiv a license to display the preprint in perpetuity. It is made available under aCC-BY 4.0 International license.

Two leaves from the bottom half of a *N. benthamiana* plant (~1 g) collected 2 days post agroinfiltration were homogenised in 2:1 (mL:g) buffer:sample extraction buffer (10% glycerol, 25 mM Tris-HCl, pH 7.5, 1 mM EDTA, 150 mM NaCl, 2% [w/v] PVPP 10 mM DTT, 1× protease inhibitor cocktail [SIGMA], 0.2% IGEPAL® CA-630 [SIGMA]). The samples were incubated on ice for 10 min and centrifuged at 5,000 × *g* for 30 min. The supernatant was passed through a Minisart 0.45 µM filter (Sartorius Stedim Biotech, Goettingen, Germany), and 25 µL of the sample was used for SDS-PAGE as described above. For immunoprecipitation, 1 mL of filtered supernatant was mixed with 60 µL v5 beads (Roche) that had been washed three times and resuspended in immunoprecipitation buffer at a 1:1 ratio (10% glycerol, 25 mM Tris-HCl, pH 7.5, 1 mM EDTA, 150 mM NaCl, 0.2% IGEPAL® CA-630 [SIGMA]). The beads were washed six times with immunoprecipitation buffer and resuspended in 50 µL 4× SDS-PAGE sample buffer. The samples were incubated at 72°C for 10 min to release the proteins from the beads and centrifuged at 5,600 × *g* for 2 min to pellet the beads. Finally, 15 µL of supernatant was loaded on a 10–20% SDS-PAGE gel (Bio-Rad) and transferred onto a PVDF membrane using a Trans-Blot turbo transfer system (Bio-Rad). The membranes were immunoblotted as described below.

**Confocal microscopy**

Transient gene expression in *N. benthamiana* was performed by agroinfiltration as described above. Leaf disks (0.4 mm diameter) were directly mounted in 0.5 µM Fluorescein diacetate (FDA) solution and incubated for 10 min in the dark before imaging for the experiments shown in Figure 3. For Figure S4, LTI6B from Arabidopsis fused to mRFP at its N-terminus was used as a plasma membrane marker. The abaxial epidermal tissue was imaged under a Zeiss LSM880 confocal microscope using a 40× water immersion objective lens. Laser excitation was set to 561 nm (diode) for mCherry and to 488 nm (Argon) for fluorescein (Figure 3) or mNeonGreen (Figure S5). *Z*-stacks were processed in Zen lite (v3.12) to generate maximum projections and the fluorescence intensity profiles shown in Figure 3 and Figure S5. Images shown are representative of three experiments in which two plants per condition were infiltrated, and leaf disk were sampled from two leaves per plant.

**Membrane fractionation assays**

Membrane fractionation assays were performed as previously described[38]. Briefly, leaf material was ground into a fine powder in liquid nitrogen and combined with 2 volumes of extraction buffer (0.81 M sucrose, 5% [v/v] glycerol, 10 mM EDTA, 10 mM EGTA, 5 mM KCl, and 100 mM Tris-HCl [pH 7.5]) supplemented with 5 mM DTT, 1% Sigma Plant Protease Inhibitor Cocktail, 1 mM PMSF, and 0.5% PVPP. The samples were vortexed for 1 min, and cell debris was pelleted via two subsequent centrifugation steps at 1,000 × *g* for 5 min. The supernatant was diluted 1:1 in distilled water, and an aliquot of the diluted sample was separated as the total fraction (T). The remaining supernatant (200–300 µl) was centrifuged at 21,000 × *g* for 90 min at 4°C. This centrifugation step separated the sample into the soluble fraction (S) in the supernatant and the membrane-enriched fraction (M) in the pellet. After the soluble fraction was set aside, the pellet was resuspended in diluted extraction buffer without PVPP. The fractions were diluted with SDS loading dye, and proteins were denatured by incubating at 50°C for 15 min. Immunoblotting was performed as described in the SDS-PAGE section. Endogenous plasma membrane ATPase was detected using anti-H + ATPase (AS07 260) antibody (Agrisera) as a control to confirm successful membrane enrichment.

bioRxiv preprint doi: https://doi.org/10.64898/2025.11.30.691369; this version posted December 2, 2025. The copyright holder for this preprint (which was not certified by peer review) is the author/funder, who has granted bioRxiv a license to display the preprint in perpetuity. It is made available under aCC-BY 4.0 International license.

## Immunoblotting

Membranes were blocked in 3% dried milk dissolved in Tris-buffered saline (50 mM Tris-HCl [pH7.5], 150 mM NaCl) supplemented with 1% Tween® for 20 to 30 min. The membranes were probed with either rat monoclonal anti-HA antibody (3F10, Roche; 1:5000 dilution), mouse monoclonal ANTI-FLAG® antibody conjugated to HRP (M2, Sigma; 1:5000 dilution), or mouse monoclonal anti-V5 antibody (V5-10, Sigma-Aldrich; 1:5000). After adding either Pierce ECL Western Substrate (Thermo Fisher Scientific) or 1/5 to 1/2 (v/v) SuperSignal West Femto Maximum Sensitivity Substrate (34095, Thermo Fisher Scientific), chemiluminescent signals were detected using an Amersham™ ImageQuant™ 800 biomolecular imager. Equal loading was validated by staining the PVDF membranes with Ponceau S.

## Acknowledgments

We thank all members of the TSL Support Services, the Center for Plant Molecular Biology (ZMBP) plant cultivation facilities, and Sandra Richter from the ZMBP microscopy platform for their invaluable assistance. We thank Laura Medina-Puch, Delphine Pott, and Shaojun Pan from the ZMBP for generating the mRFP-Lti6b-TurboID construct used in this study.

## Funding

The authors received funding from the Gatsby Charitable Foundation (C.M., A.P., D.L., and S.K.), Biotechnology and Biological Sciences Research Council (BBSRC) BB/P012574 (Plant Health ISP) (S.K.), European Research Council (ERC) 743165 (S.K.), and BASF Plant Science (J.K. and S.K.). D.L. was funded by the DFG Walter Benjamin Programme (project no. 464864389). The funders had no role in the study design, data collection and analysis, decision to publish, or preparation of the manuscript.

## Author contributions

CM: Conceptualization, Formal analysis, Supervision, Validation, Visualisation, Writing – Original draft, Writing – review and editing, Project administration

SK: Conceptualization, Supervision, Project administration, Funding acquisition, Writing – review and editing

HP: Conceptualization, Investigation, Methodology, Validation, Visualisation, Writing – review and editing

AP: Investigation, Writing – review and editing

MPC: Conceptualization, Data Curation, Investigation, Methodology, Validation, Writing – review and editing.

JS: Investigation, Methodology, Writing – review and editing.

DL: Conceptualization, Investigation, Methodology, Writing – review and editing.

bioRxiv preprint doi: https://doi.org/10.64898/2025.11.30.691369; this version posted December 2, 2025. The copyright holder for this preprint (which was not certified by peer review) is the author/funder, who has granted bioRxiv a license to display the preprint in perpetuity. It is made available under aCC-BY 4.0 International license.

JK: Investigation, Resources, Writing – review and editing

**Competing interests**

J.K, C.M. and M.P.C. received funding from industry to study NLR biology at the time of the study. S.K. receives funding from industry to study NLR biology and co-founded a start-up company (Resurrect Bio Ltd.). C.M., M.P.C., J.K., and S.K. have filed patents on NLR biology. M.P.C. received fees from Resurrect Bio Ltd.

bioRxiv preprint doi: https://doi.org/10.64898/2025.11.30.691369; this version posted December 2, 2025. The copyright holder for this preprint (which was not certified by peer review) is the author/funder, who has granted bioRxiv a license to display the preprint in perpetuity. It is made available under aCC-BY 4.0 International license.

## References

1. Sundaram, B., Tweedell, R. E., Kumar, S. P. & Kanneganti, T.-D. The NLR family of innate immune and cell death sensors. *Immunity* **57**, 674–699 (2024).
2. Chou, W.-C., Jha, S., Linhoff, M. W. & Ting, J. P.-Y. The NLR gene family: from discovery to present day. *Nat Rev Immunol* **23**, 635–654 (2023).
3. Contreras, M. P., Lüdke, D., Pai, H., Toghani, A. & Kamoun, S. NLR receptors in plant immunity: making sense of the alphabet soup. *EMBO reports* **n/a**, e57495 (2023).
4. Adachi, H., Derevnina, L. & Kamoun, S. NLR singletons, pairs, and networks: evolution, assembly, and regulation of the intracellular immunoreceptor circuitry of plants. *Current Opinion in Plant Biology* **50**, 121–131 (2019).
5. Cesari, S., Bernoux, M., Moncuquet, P., Kroj, T. & Dodds, P. N. A novel conserved mechanism for plant NLR protein pairs: The 'integrated decoy' hypothesis. *Frontiers in Plant Science* **5**, 1–10 (2014).
6. Marchal, C., Michalopoulou, V. A., Zou, Z., Cevik, V. & Sarris, P. F. Show me your ID: NLR immune receptors with integrated domains in plants. *Essays in Biochemistry* **66**, 527–539 (2022).
7. Cesari, S. *et al.* The rice resistance protein pair RGA4/RGA5 recognizes the Magnaporthe oryzae effectors AVR-Pia and AVR1-CO39 by direct binding. *Plant Cell* **25**, 1463–1481 (2013).
8. Okuyama, Y. *et al.* A multifaceted genomics approach allows the isolation of the rice Pia-blast resistance gene consisting of two adjacent NBS-LRR protein genes. *The Plant Journal* **66**, 467–479 (2011).

bioRxiv preprint doi: https://doi.org/10.64898/2025.11.30.691369; this version posted December 2, 2025. The copyright holder for this preprint (which was not certified by peer review) is the author/funder, who has granted bioRxiv a license to display the preprint in perpetuity. It is made available under aCC-BY 4.0 International license.

9. Ashikawa, I. *et al.* Two adjacent nucleotide-binding site-leucine-rich repeat class genes are required to confer Pikm-specific rice blast resistance. *Genetics* **180**, 2267–2276 (2008).
10. Kiyosawa, S. Identification of Blast-Resistance Genes in Some Rice Varieties. *Japanese Journal of Breeding* **28**, 287–296 (1978).
11. Narusaka, M. *et al.* RRS1 and RPS4 provide a dual Resistance-gene system against fungal and bacterial pathogens. *The Plant Journal* **60**, 218–226 (2009).
12. Yang, Y. *et al.* Allelic variation in the Arabidopsis TNL CHS3/CSA1 immune receptor pair reveals two functional cell-death regulatory modes. *Cell Host & Microbe* https://doi.org/10.1016/j.chom.2022.09.013 (2022) doi:10.1016/j.chom.2022.09.013.
13. Wu, C. H. *et al.* NLR network mediates immunity to diverse plant pathogens. *Proceedings of the National Academy of Sciences of the United States of America* **114**, 8113–8118 (2017).
14. Gong, Y., Tian, L., Kontos, I., Li, J. & Li, X. Plant immune signaling network mediated by helper NLRs. *Current Opinion in Plant Biology* **73**, 102354 (2023).
15. Hu, Z. & Chai, J. Assembly and Architecture of NLR Resistosomes and Inflammasomes. *Annual Review of Biophysics* **52**, 207–228 (2023).
16. Zdrzałek, R., Kamoun, S., Terauchi, R., Saitoh, H. & Banfield, M. J. The rice NLR pair Pikp-1/Pikp-2 initiates cell death through receptor cooperation rather than negative regulation. *PLOS ONE* **15**, (2020).
17. Kanzaki, H. *et al.* Arms race co-evolution of Magnaporthe oryzae AVR-Pik and rice Pik genes driven by their physical interactions. *The Plant Journal* **72**, 894–907 (2012).

bioRxiv preprint doi: https://doi.org/10.64898/2025.11.30.691369; this version posted December 2, 2025. The copyright holder for this preprint (which was not certified by peer review) is the author/funder, who has granted bioRxiv a license to display the preprint in perpetuity. It is made available under aCC-BY 4.0 International license.

18. Maidment, J. H. R. *et al.* Multiple variants of the fungal effector AVR-Pik bind the HMA domain of the rice protein OsHIPP19, providing a foundation to engineer plant defense. *Journal of Biological Chemistry* **296**, (2021).
19. De La Concepcion, J. C. *et al.* Protein engineering expands the effector recognition profile of a rice NLR immune receptor. *eLife* **8**, (2019).
20. Bentham, A. R. *et al.* Allelic compatibility in plant immune receptors facilitates engineering of new effector recognition specificities. *The Plant Cell* **35**, 3809–3827 (2023).
21. Kourelis, J., Marchal, C., Posbeyikian, A., Harant, A. & Kamoun, S. NLR immune receptor–nanobody fusions confer plant disease resistance. *Science* **379**, 934–939 (2023).
22. Kourelis, J., Sakai, T., Adachi, H. & Kamoun, S. RefPlantNLR is a comprehensive collection of experimentally validated plant disease resistance proteins from the NLR family. *PLOS Biology* **19**, 124–124 (2021).
23. Wu, C.-H., Krasileva, K. V., Banfield, M. J., Terauchi, R. & Kamoun, S. The "sensor domains" of plant NLR proteins: more than decoys? *Frontiers in Plant Science* **6**, 134–134 (2015).
24. Kroj, T., Chanclud, E., Michel-Romiti, C., Grand, X. & Morel, J.-B. Integration of decoy domains derived from protein targets of pathogen effectors into plant immune receptors is widespread. *New Phytologist* **210**, 618–626 (2016).
25. Sarris, P. F., Cevik, V., Dagdas, G., Jones, J. D. G. & Krasileva, K. V. Comparative analysis of plant immune receptor architectures uncovers host proteins likely targeted by pathogens. *BMC Biology* **14**, 8–8 (2016).
26. Eitas, T. K. & Dangl, J. L. NB-LRR proteins: pairs, pieces, perception, partners, and pathways. *Current Opinion in Plant Biology* **13**, 472–477 (2010).

bioRxiv preprint doi: https://doi.org/10.64898/2025.11.30.691369; this version posted December 2, 2025. The copyright holder for this preprint (which was not certified by peer review) is the author/funder, who has granted bioRxiv a license to display the preprint in perpetuity. It is made available under aCC-BY 4.0 International license.

27. Wang, J. J. *et al.* Ligand-triggered allosteric ADP release primes a plant NLR complex. *Science (New York, N.Y.)* **364**, (2019).
28. Wang, J. *et al.* Reconstitution and structure of a plant NLR resistosome conferring immunity. *Science (New York, N.Y.)* **364**, (2019).
29. Förderer, A. *et al.* A wheat resistosome defines common principles of immune receptor channels. *bioRxiv* 2022.03.23.485489-2022.03.23.485489 (2022) doi:10.1101/2022.03.23.485489.
30. Zhao, Y.-B. *et al.* Pathogen effector AvrSr35 triggers Sr35 resistosome assembly via a direct recognition mechanism. *Science Advances* **8**, eabq5108 (2022).
31. Liu, F. *et al.* Activation of the helper NRC4 immune receptor forms a hexameric resistosome. *Cell* **0**, (2024).
32. Madhuprakash, J. *et al.* A disease resistance protein triggers oligomerization of its NLR helper into a hexameric resistosome to mediate innate immunity. 2024.06.18.599586 Preprint at https://doi.org/10.1101/2024.06.18.599586 (2024).
33. Selvaraj, M. *et al.* Activation of plant immunity through conversion of a helper NLR homodimer into a resistosome. *PLOS Biology* **22**, e3002868 (2024).
34. Guo, G. *et al.* An activated wheat CCG10-NLR immune receptor forms an octameric resistosome. 2025.08.26.672026 Preprint at https://doi.org/10.1101/2025.08.26.672026 (2025).
35. Ma, S. *et al.* Direct pathogen-induced assembly of an NLR immune receptor complex to form a holoenzyme. *Science* **370**, (2020).
36. Martin, R. *et al.* Structure of the activated ROQ1 resistosome directly recognizing the pathogen effector XopQ. *Science* **370**, (2020).

bioRxiv preprint doi: https://doi.org/10.64898/2025.11.30.691369; this version posted December 2, 2025. The copyright holder for this preprint (which was not certified by peer review) is the author/funder, who has granted bioRxiv a license to display the preprint in perpetuity. It is made available under aCC-BY 4.0 International license.

37. Ahn, H.-K. *et al.* Effector-dependent activation and oligomerization of plant NRC class helper NLRs by sensor NLR immune receptors Rpi-amr3 and Rpi-amr1. *The EMBO Journal* e111484 (2023) doi:10.15252/embj.2022111484.
38. Contreras, M. P. *et al.* Sensor NLR immune proteins activate oligomerization of their NRC helpers in response to plant pathogens. *The EMBO Journal* **42**, e111519 (2023).
39. Sakai, T. *et al.* The NRC0 gene cluster of sensor and helper NLR immune receptors is functionally conserved across asterid plants. 2023.10.23.563533 Preprint at https://doi.org/10.1101/2023.10.23.563533 (2023).
40. Contreras, M. P. *et al.* The nucleotide binding domain of NRC-dependent disease resistance proteins is sufficient to activate downstream helper NLR oligomerization and immune signaling. 2023.11.30.569466 Preprint at https://doi.org/10.1101/2023.11.30.569466 (2023).
41. Seager, B. A. *et al.* A plant pathogen effector blocks stepwise assembly of a helper NLR resistosome. 2025.07.14.664264 Preprint at https://doi.org/10.1101/2025.07.14.664264 (2025).
42. Bi, G. *et al.* The ZAR1 resistosome is a calcium-permeable channel triggering plant immune signaling. *Cell* **184**, 3528-3541.e12 (2021).
43. Jacob, P. *et al.* Plant “helper” immune receptors are Ca 2+ -permeable nonselective cation channels. *Science* eabg7917–eabg7917 (2021) doi:10.1126/science.abg7917.
44. Ma, S. *et al.* Oligomerization-mediated autoinhibition and cofactor binding of a plant NLR. *Nature* 1–3 (2024) doi:10.1038/s41586-024-07668-7.

bioRxiv preprint doi: https://doi.org/10.64898/2025.11.30.691369; this version posted December 2, 2025. The copyright holder for this preprint (which was not certified by peer review) is the author/funder, who has granted bioRxiv a license to display the preprint in perpetuity. It is made available under aCC-BY 4.0 International license.

45. Liu, F. *et al.* The activated plant NRC4 immune receptor forms a hexameric resistosome. 2023.12.18.571367 Preprint at https://doi.org/10.1101/2023.12.18.571367 (2024).
46. Yang, Y. *et al.* Paired plant immune CHS3-CSA1 receptor alleles form distinct hetero-oligomeric complexes. *Science* **383**, eadk3468 (2024).
47. Ahn, H.-K. *et al.* Recognition-dependent activation of the RRS1-R/RPS4 immune receptor complex. 2025.04.11.646618 Preprint at https://doi.org/10.1101/2025.04.11.646618 (2025).
48. Costanzo, S. & Jia, Y. Sequence variation at the rice blast resistance gene *Pi-km* locus: Implications for the development of allele specific markers. *Plant Science* **178**, 523–530 (2010).
49. Hua, L. *et al.* The isolation of Pi1, an allele at the Pik locus which confers broad spectrum resistance to rice blast. *TAG. Theoretical and applied genetics.* **125**, 1047–1055 (2012).
50. Xu, X. *et al.* Efficient authentic fine mapping of the rice blast resistance gene Pik-h in the Pik cluster, using new Pik-h-differentiating isolates. *Mol Breeding* **22**, 289–299 (2008).
51. De La Concepcion, J. C. *et al.* Functional diversification gave rise to allelic specialization in a rice NLR immune receptor pair. *eLife* **10**, (2021).
52. Zhai, C. *et al.* Function and interaction of the coupled genes responsible for Pik-h encoded rice blast resistance. *PloS one* **9**, (2014).
53. Maidment, J. H. R. *et al.* Multiple variants of the fungal effector AVR-Pik bind the HMA domain of the rice protein OsHIPP19, providing a foundation to engineer plant defense. *Journal of Biological Chemistry* **296**, (2021).

bioRxiv preprint doi: https://doi.org/10.64898/2025.11.30.691369; this version posted December 2, 2025. The copyright holder for this preprint (which was not certified by peer review) is the author/funder, who has granted bioRxiv a license to display the preprint in perpetuity. It is made available under aCC-BY 4.0 International license.

54. Hu, M., Qi, J., Bi, G. & Zhou, J.-M. Bacterial Effectors Induce Oligomerization of Immune Receptor ZAR1 In Vivo. *Molecular Plant* **13**, 793–801 (2020).
55. Li, L., Habring, A. & Wang, K. Atypical Resistance Protein RPW8 / HR Triggers Oligomerization of the NLR Immune Receptor RPP7 Article Atypical Resistance Protein RPW8 / HR Triggers Oligomerization of the NLR Immune Receptor RPP7 and Autoimmunity. *Cell Host and Microbe* 1–13 (2020) doi:10.1016/j.chom.2020.01.012.
56. Adachi, H. *et al.* An N-terminal motif in NLR immune receptors is functionally conserved across distantly related plant species. *eLife* **8**, (2019).
57. Duggan, C. *et al.* Dynamic localization of a helper NLR at the plant–pathogen interface underpins pathogen recognition. *Proceedings of the National Academy of Sciences* **118**, e2104997118–e2104997118 (2021).
58. Ibrahim, T. *et al.* A helper NLR targets organellar membranes to trigger immunity. 2024.09.19.613839 Preprint at https://doi.org/10.1101/2024.09.19.613839 (2024).
59. Cutler, S. R., Ehrhardt, D. W., Griffitts, J. S. & Somerville, C. R. Random GFP::cDNA fusions enable visualization of subcellular structures in cells of Arabidopsis at a high frequency. *Proceedings of the National Academy of Sciences* **97**, 3718–3723 (2000).
60. Andreeva, L. *et al.* NLRP3 cages revealed by full-length mouse NLRP3 structure control pathway activation. *Cell* **184**, 6299-6312.e22 (2021).
61. Hochheiser, I. V. *et al.* Cryo-EM structure of the NLRP3 decamer bound to the cytokine release inhibitory drug CRID3. 2021.07.22.453353 Preprint at https://doi.org/10.1101/2021.07.22.453353 (2021).

bioRxiv preprint doi: https://doi.org/10.64898/2025.11.30.691369; this version posted December 2, 2025. The copyright holder for this preprint (which was not certified by peer review) is the author/funder, who has granted bioRxiv a license to display the preprint in perpetuity. It is made available under aCC-BY 4.0 International license.

62. Wang, Z. *et al.* Plasma membrane association and resistosome formation of plant helper immune receptors. *Proceedings of the National Academy of Sciences* **120**, e2222036120 (2023).
63. El Kasmi, F. *et al.* Signaling from the plasma-membrane localized plant immune receptor RPM1 requires self-association of the full-length protein. *Proceedings of the National Academy of Sciences of the United States of America* **114**, E7385–E7394 (2017).
64. Saile, S. C. *et al.* Arabidopsis ADR1 helper NLR immune receptors localize and function at the plasma membrane in a phospholipid dependent manner. *New Phytologist* https://doi.org/10.1111/NPH.17788 (2021) doi:10.1111/NPH.17788.
65. Césari, S. *et al.* The NB-LRR proteins RGA4 and RGA5 interact functionally and physically to confer disease resistance. *The EMBO Journal* **33**, 1941–1959 (2014).
66. Weber, E., Engler, C., Gruetzner, R., Werner, S. & Marillonnet, S. A modular cloning system for standardized assembly of multigene constructs. *PLoS ONE* **6**, e16765–e16765 (2011).
67. Engler, C. *et al.* A Golden Gate modular cloning toolbox for plants. *ACS Synthetic Biology* **3**, 839–843 (2014).
68. NAKAGAWA, T. *et al.* Improved Gateway Binary Vectors: High-Performance Vectors for Creation of Fusion Constructs in Transgenic Analysis of Plants. *Biosci. Biotechnol. Biochem.* **71**, 2095–2100 (2007).
69. Van der Hoorn, R. A. L., Laurent, F., Roth, R. & De Wit, P. J. G. M. Agroinfiltration Is a Versatile Tool That Facilitates Comparative Analyses of Avr9/Cf-9-Induced and Avr4/Cf-4-Induced Necrosis. *MPMI* **13**, 439–446 (2000).

bioRxiv preprint doi: https://doi.org/10.64898/2025.11.30.691369; this version posted December 2, 2025. The copyright holder for this preprint (which was not certified by peer review) is the author/funder, who has granted bioRxiv a license to display the preprint in perpetuity. It is made available under aCC-BY 4.0 International license.

70. van der Hoorn, R. A. L. *et al.* Structure–Function Analysis of Cf-9, a Receptor-Like Protein with Extracytoplasmic Leucine-Rich Repeats$w. *The Plant Cell* **17**, 1000–1015 (2005).

71. Kirchhofer, A. *et al.* Modulation of protein properties in living cells using nanobodies. *Nat Struct Mol Biol* **17**, 133–138 (2010).

72. Selvaraj, M. *et al.* Activation of plant immunity through conversion of a helper NLR homodimer into a resistosome. 2023.12.17.572070 Preprint at https://doi.org/10.1101/2023.12.17.572070 (2023).

bioRxiv preprint doi: https://doi.org/10.64898/2025.11.30.691369; this version posted December 2, 2025. The copyright holder for this preprint (which was not certified by peer review) is the author/funder, who has granted bioRxiv a license to display the preprint in perpetuity. It is made available under aCC-BY 4.0 International license.

## Figures

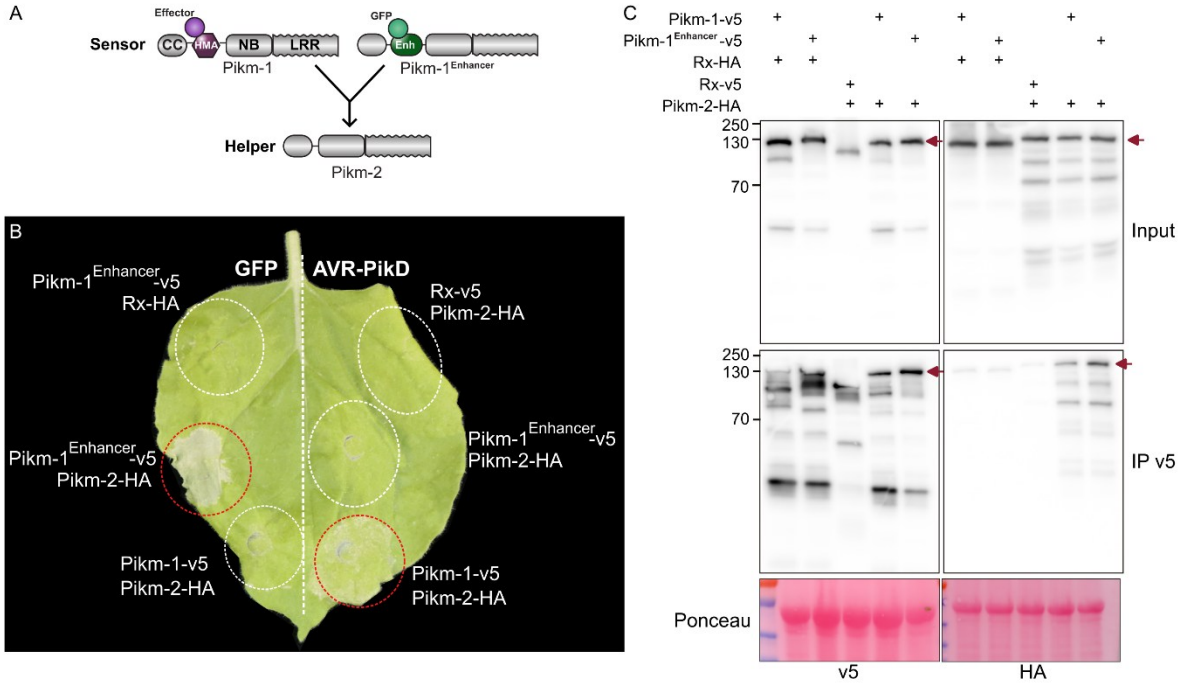


**Figure 1. Pikm-1$^{Enhancer}$ associates with Pikm-2 prior to effector activation.**
A) Diagram of the domain organisation of the sensors Pikm-1 and Pikm-1$^{Enhancer}$ and the helper Pikm-2. Swapping the heavy-metal-associated (HMA) domain of Pikm-1 for the nanobody Enhancer, which binds to GFP[71], leads to a functional receptor able to trigger an immune response in the presence of GFP[21]. Both the Pikm-1 and Pikm-1$^{Enhancer}$ sensors signal through the Pikm-2 helper upon effector or ligand recognition to trigger an immune response.
B) Pikm-2-6xHA, Pikm-1-2xV5, and Pikm-1$^{Enhancer}$-2xV5 are functional in the presence of their ligand when transiently expressed in *N. benthamiana*. The image shows a representative leaf that was infiltrated with the indicated constructs and photographed 5 days after infiltration. Dashed circles indicate the infiltrated areas, and red circles show where a hypersensitive response was observed.
C) Pikm-2 co-immunoprecipitates with both Pikm-1 and Pikm-1$^{Enhancer}$ in the absence of their ligand. Rx-v5 + Pikm-2-HA and Rx-HA + Pikm-1-v5 were used as negative controls, and Pikm-1 + Pikm-2 was used as a positive control[16]. Total protein extracts (input) and proteins immunoprecipitated using v5 beads (IP v5) were immunoblotted with antibodies labelled at the bottom. Approximate molecular weights (kDa) are shown at left, and red arrows indicate bands corresponding to the Pik receptors. Ponceau staining of the membrane is shown below the immunoblots.

bioRxiv preprint doi: https://doi.org/10.64898/2025.11.30.691369; this version posted December 2, 2025. The copyright holder for this preprint (which was not certified by peer review) is the author/funder, who has granted bioRxiv a license to display the preprint in perpetuity. It is made available under aCC-BY 4.0 International license.

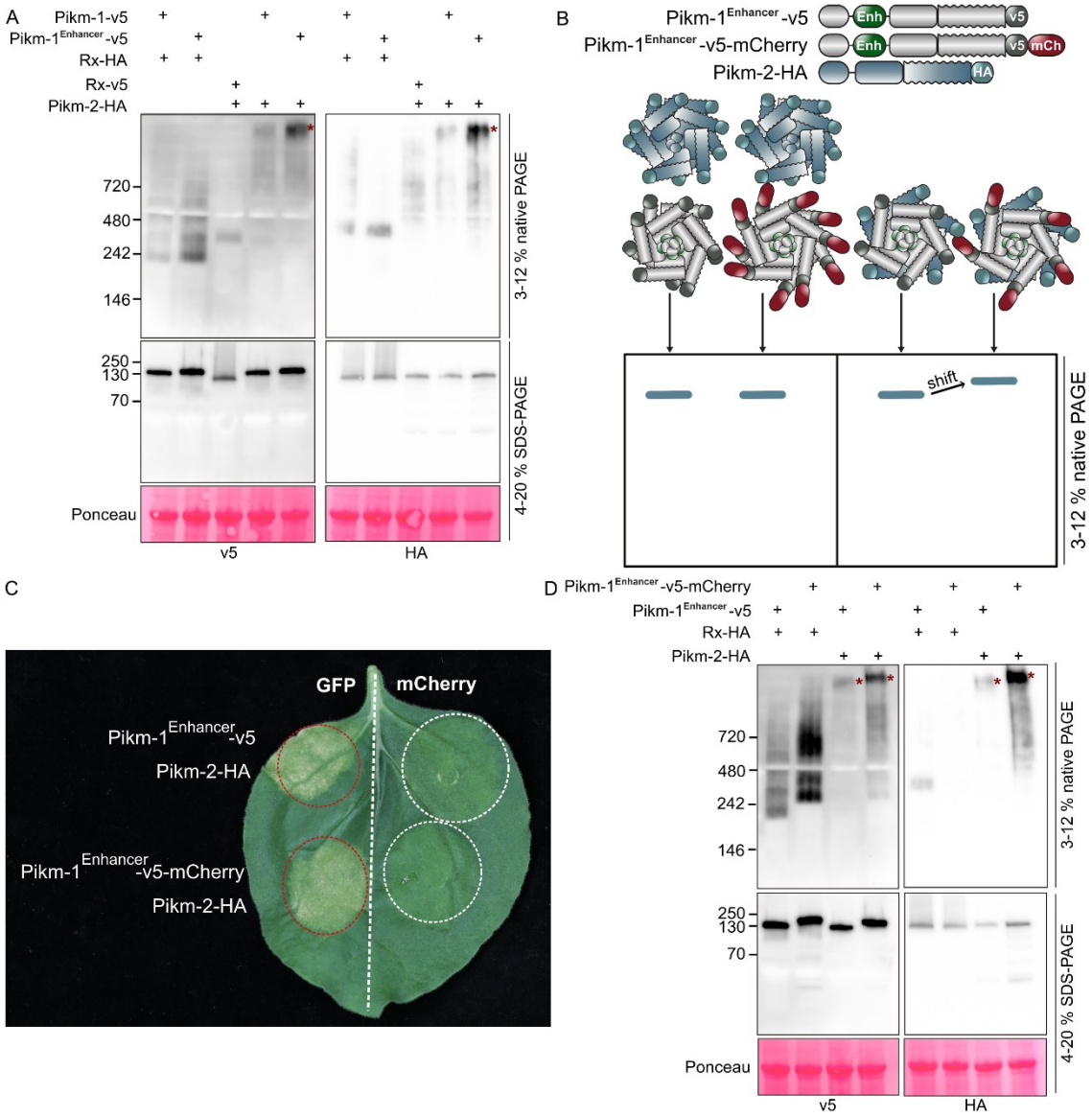


**Figure 2. The Pik pair forms a ~1 MDa hetero-oligomer prior to effector activation.**

A) BN-PAGE (top) and SDS-PAGE (middle) assays using *N. benthamiana* leaves co-expressing Pikm-2 with either Pikm-1 or Pikm-1$^{Enhancer}$. Co-expression of Rx with Pikm-1 variants or Pikm-2 was used as a negative control. BN-PAGE and denaturing SDS-PAGE were run in parallel to verify the expression of all proteins. Approximate molecular weights (kDa) of the proteins are shown at left, and red asterisks indicate bands corresponding to the ~1 MDa Pik oligomer. Bottom, Ponceau staining.

B) Diagrams illustrating the strategy for using a 'heavy' Pikm-1$^{Enhancer}$-2xV5-mCherry or 'light' Pikm-1$^{Enhancer}$-2xV5 version of Pikm-1$^{Enhancer}$. Briefly, a band shift of Pikm-2 in the immunoblot when using the 'heavy' Pikm-1$^{Enhancer}$ variant indicates that both Pikm-2 and Pikm-1$^{Enhancer}$ associate and are part of the same complex.

C) Pikm-2-6xHA, Pikm-1-2xV5, Pikm-1$^{Enhancer}$-2xV5, and Pikm-1$^{Enhancer}$-2xV5-mCherry are functional when transiently co-expressed in the presence of their ligand in *N. benthamiana*. The image shows a representative leaf that was infiltrated with the indicated constructs and photographed 5 days after infiltration. Dashed circles

bioRxiv preprint doi: https://doi.org/10.64898/2025.11.30.691369; this version posted December 2, 2025. The copyright holder for this preprint (which was not certified by peer review) is the author/funder, who has granted bioRxiv a license to display the preprint in perpetuity. It is made available under aCC-BY 4.0 International license.

indicate the infiltrated areas, and red circles show where a hypersensitive response was observed.
D) BN-PAGE (top) and SDS-PAGE (middle) assays using 'heavy' Pikm-1$^{Enhancer}$ and Pikm-2. Co-expression of Rx with Pikm-1 variants was used as a negative control. BN-PAGE and denaturing SDS-PAGE were run in parallel to ensure all components were expressed. Approximate molecular weights (kDa) of the proteins are shown on the left, and red asterisks point to the bands corresponding to ~1 MDa Pik oligomer. Below, Ponceau staining showing Rubisco.

bioRxiv preprint doi: https://doi.org/10.64898/2025.11.30.691369; this version posted December 2, 2025. The copyright holder for this preprint (which was not certified by peer review) is the author/funder, who has granted bioRxiv a license to display the preprint in perpetuity. It is made available under aCC-BY 4.0 International license.

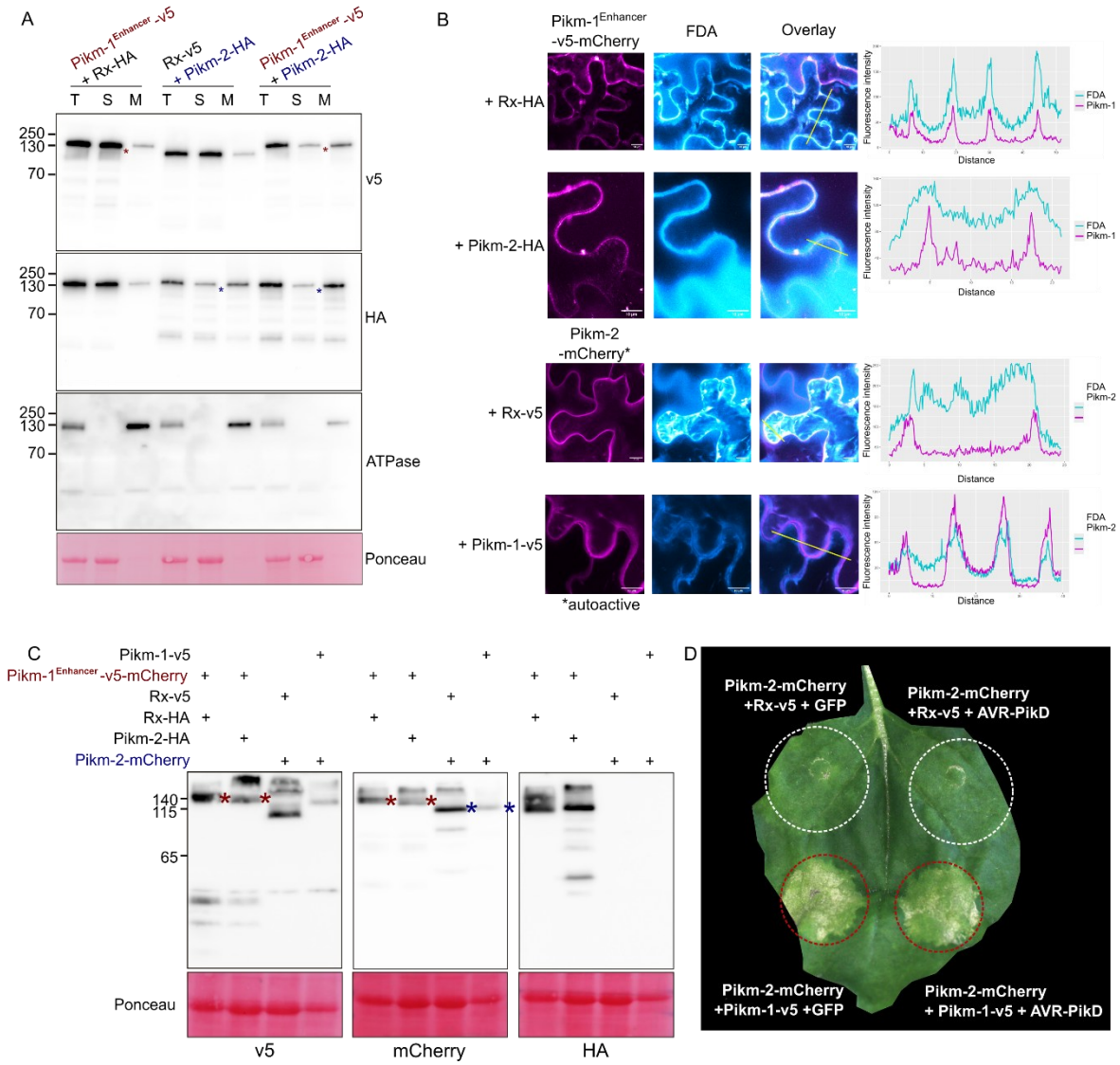


**Figure 3. Pikm-1$^{Enhancer}$ and Pikm-2 preferentially accumulate in the membrane fraction when co-expressed.**

A) Membrane fractionation assay of Pikm-1$^{Enhancer}$ and Pikm-2. Rx was used as a negative control. Fractions: T = total, S = soluble, M = membrane. ATPase was used as a membrane marker. Rubisco was used as a marker for the total and soluble fractions and visualised by Ponceau staining. Red asterisks show the shift of Pikm-1$^{Enhancer}$ from the soluble to the membrane fraction upon co-expression with Pikm-2.

B) Confocal microscopy images of maximum projection of *z*-stacks of 10–25 slides showing the subcellular localisation of Pikm-1$^{Enhancer}$-v5-mCherry or Pikm-2-mCherry co-expressed with Rx or the matching NLR from the Pik pair. Fluorescein was used as a cytosolic marker. The graphs at right depict the fluorescence intensity from each channel across the yellow line shown on the overlay image. All components were transiently expressed in *N. benthamiana* via agroinfiltration, and subcellular localisation was observed at 2 dpi. Laser excitation was set to 561 nm (diode) for mCherry and to 488 nm (argon) for fluorescein, and detection wavelengths were set to 590–660 nm and 500–560 nm for mCherry and fluorescein, respectively.

C) SDS-PAGE assay of the samples used for confocal microscopy. Total protein extracts (input) were immunoblotted with the antibodies labelled at the bottom.

bioRxiv preprint doi: https://doi.org/10.64898/2025.11.30.691369; this version posted December 2, 2025. The copyright holder for this preprint (which was not certified by peer review) is the author/funder, who has granted bioRxiv a license to display the preprint in perpetuity. It is made available under aCC-BY 4.0 International license.

Approximate molecular weight (kDa) of the protein is shown at left. Ponceau staining showing Rubisco is shown below the immunoblots.
D) Cell death assay of *N. benthamiana* leaves co-expressing Pikm-2-mCherry with Pikm-1-v5 or Rx-v5 and GFP (negative control) or AVR-PikD, an effector from *M. oryzae* recognised by the Pikm pair. The image shows a representative leaf that was infiltrated with the indicated constructs and photographed 5 days after infiltration. Dashed circles indicate the infiltrated areas, and red circles show where a hypersensitive response was observed.

bioRxiv preprint doi: https://doi.org/10.64898/2025.11.30.691369; this version posted December 2, 2025. The copyright holder for this preprint (which was not certified by peer review) is the author/funder, who has granted bioRxiv a license to display the preprint in perpetuity. It is made available under aCC-BY 4.0 International license.

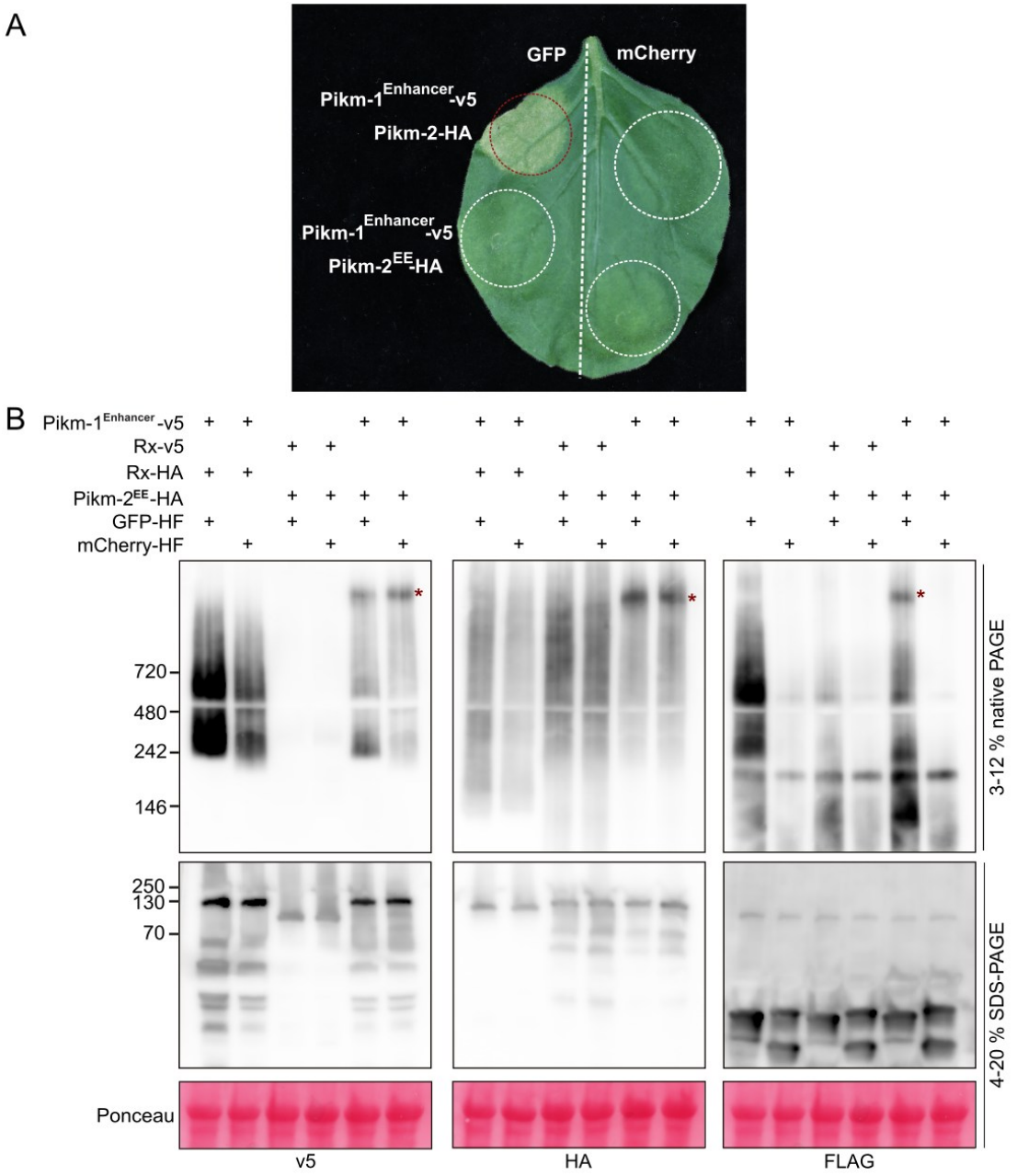


**Figure 4. The GFP ligand associates with the Pikm-1$^{Enhancer}$/Pikm-2 hetero-complex.**

A) Cell death assay of *N. benthamiana* leaves co-expressing Pikm-1 $^{Enhancer}$ with Pikm-2 or Pikm-2$^{EE}$ with GFP (ligand) or mCherry (negative control). The image shows a representative leaf that was infiltrated with the indicated constructs and photographed 5 days after infiltration. Dashed circles indicate the infiltrated areas, and red circles show where a hypersensitive response was observed.

B) BN-PAGE (top) and SDS-PAGE (middle) assays of Pikm-2$^{EE}$ + Pikm-1$^{Enhancer}$. Co-expression of Rx with Pikm-1 $^{Enhancer}$ or Pikm-2$^{EE}$ was used as a negative control for hetero-oligomer formation. mCherry was used as a negative control for the presence of the ligand bound to Pikm-1$^{Enhancer}$. BN-PAGE and SDS-PAGE samples were run in parallel to ensure all components were expressed. Approximate molecular weights (kDa) of the proteins are shown on the left, and red asterisks point to the bands corresponding to the ~1 MDa Pik oligomer. Below, Ponceau staining showing Rubisco.

bioRxiv preprint doi: https://doi.org/10.64898/2025.11.30.691369; this version posted December 2, 2025. The copyright holder for this preprint (which was not certified by peer review) is the author/funder, who has granted bioRxiv a license to display the preprint in perpetuity. It is made available under aCC-BY 4.0 International license.

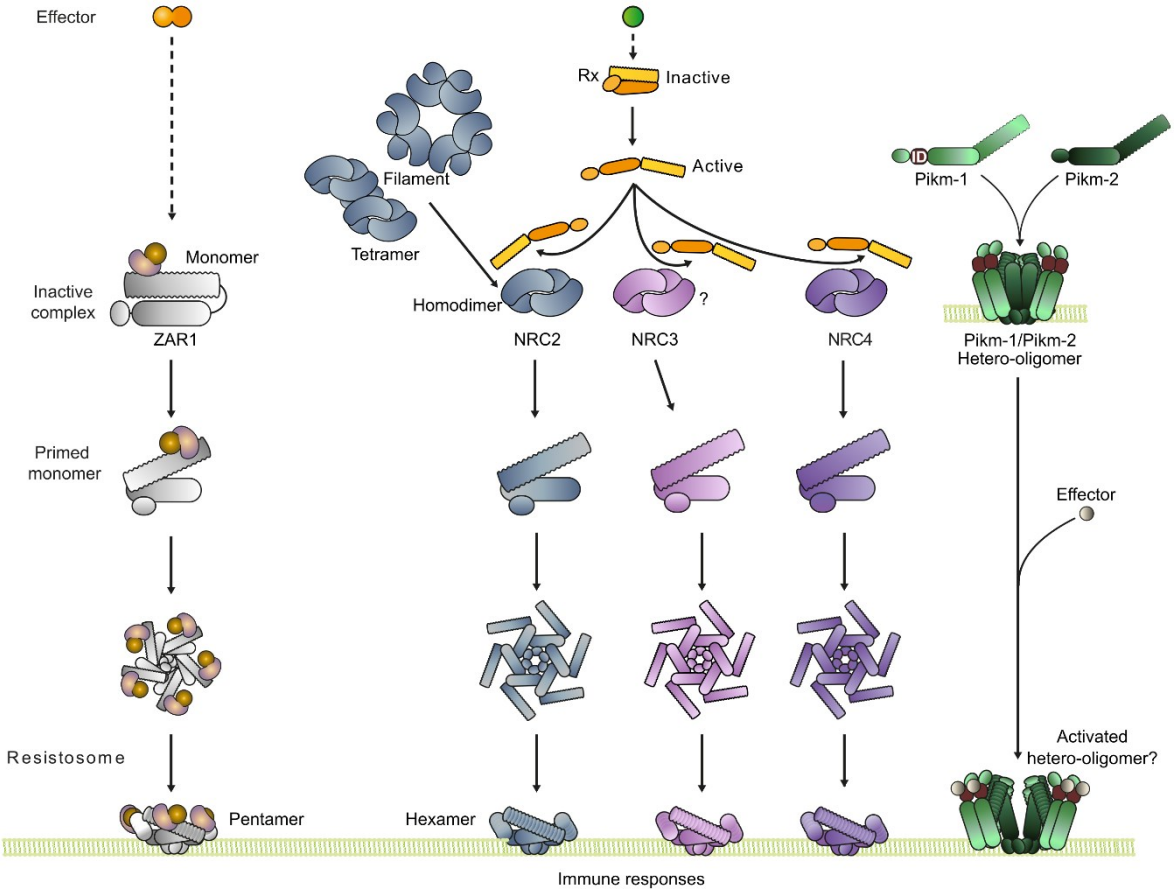


**Figure 5. CC-NLRs exhibit diverse conformations in the resting state.**
Updated figure from Selvaraj et al.[72] depicting different NLR resting and activated states. While ZAR1 exists as a monomer bound to its guardees in its resting state, several forms have been observed for the NRC2 helper[44,72], including dimers, tetramers, and filaments. While filament-like structures were observed via confocal microscopy for NRC2 upon overexpression in planta, these structures were not detected for its paralog NRC4[72], suggesting a potentially different resting state configuration for NRC4. Our work suggests that the Pik CC-NLR pair forms a hetero-complex bound to the plasma membrane in its resting state. How effector binding to the integrated domain (ID) of the Pik-1 sensor leads to the activation of the complex remains to be determined.

bioRxiv preprint doi: https://doi.org/10.64898/2025.11.30.691369; this version posted December 2, 2025. The copyright holder for this preprint (which was not certified by peer review) is the author/funder, who has granted bioRxiv a license to display the preprint in perpetuity. It is made available under aCC-BY 4.0 International license.

## Supplementary tables

## Table S1: Constructs generated or used in this study.

bioRxiv preprint doi: https://doi.org/10.64898/2025.11.30.691369; this version posted December 2, 2025. The copyright holder for this preprint (which was not certified by peer review) is the author/funder, who has granted bioRxiv a license to display the preprint in perpetuity. It is made available under aCC-BY 4.0 International license.

## Supplementary Figures

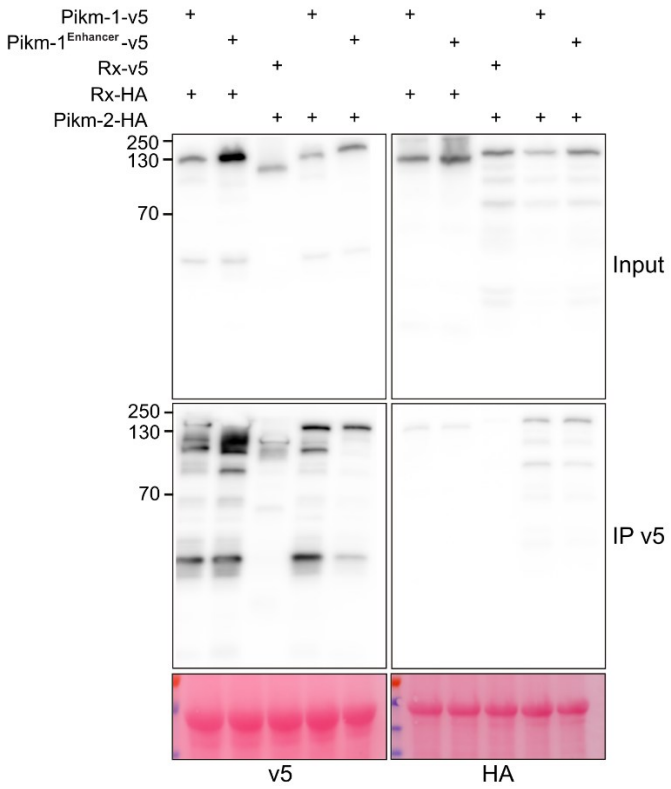


**Figure S1: Pikm-1$^{Enhancer}$ interacts with Pikm-2 prior to effector-mediated activation.**
Replicate of the experiment shown in Figure 1.

bioRxiv preprint doi: https://doi.org/10.64898/2025.11.30.691369; this version posted December 2, 2025. The copyright holder for this preprint (which was not certified by peer review) is the author/funder, who has granted bioRxiv a license to display the preprint in perpetuity. It is made available under aCC-BY 4.0 International license.

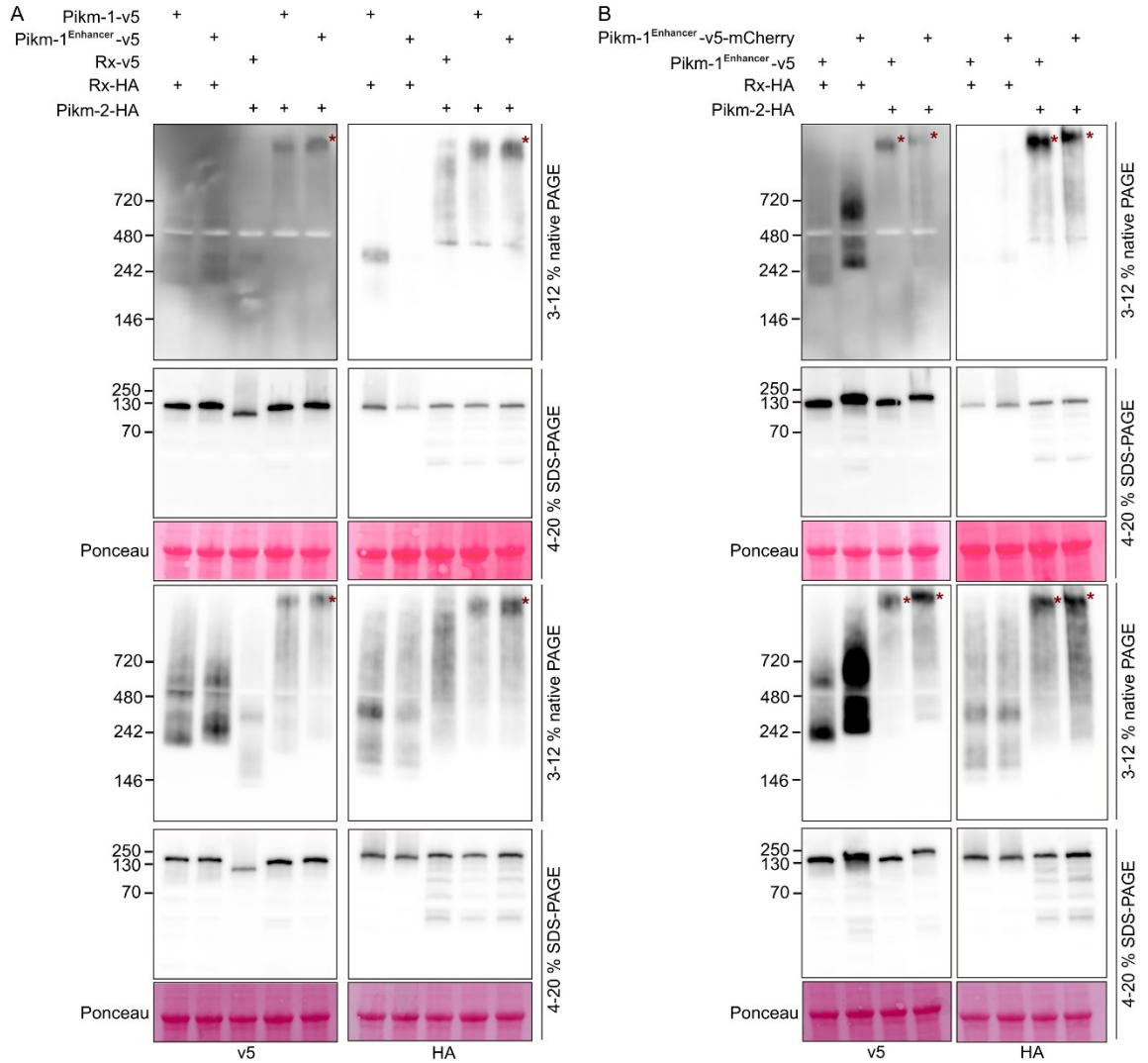


**Figure S2. The Pik pair forms a ~1 MDa hetero-oligomer prior to effector-mediated activation.**

A-B) Replicates of the experiment shown in Figure 2.

bioRxiv preprint doi: https://doi.org/10.64898/2025.11.30.691369; this version posted December 2, 2025. The copyright holder for this preprint (which was not certified by peer review) is the author/funder, who has granted bioRxiv a license to display the preprint in perpetuity. It is made available under aCC-BY 4.0 International license.

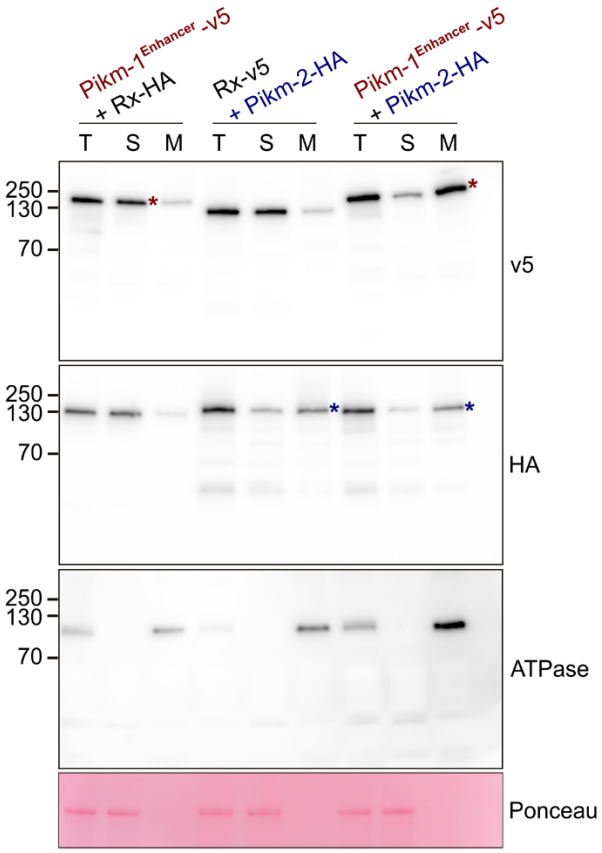


**Figure S3. Pikm-1$^{Enhancer}$ and Pikm-2 preferentially accumulate in the membrane fraction when co-expressed.**
Replicate of the experiment shown in Figure 3.

bioRxiv preprint doi: https://doi.org/10.64898/2025.11.30.691369; this version posted December 2, 2025. The copyright holder for this preprint (which was not certified by peer review) is the author/funder, who has granted bioRxiv a license to display the preprint in perpetuity. It is made available under aCC-BY 4.0 International license.

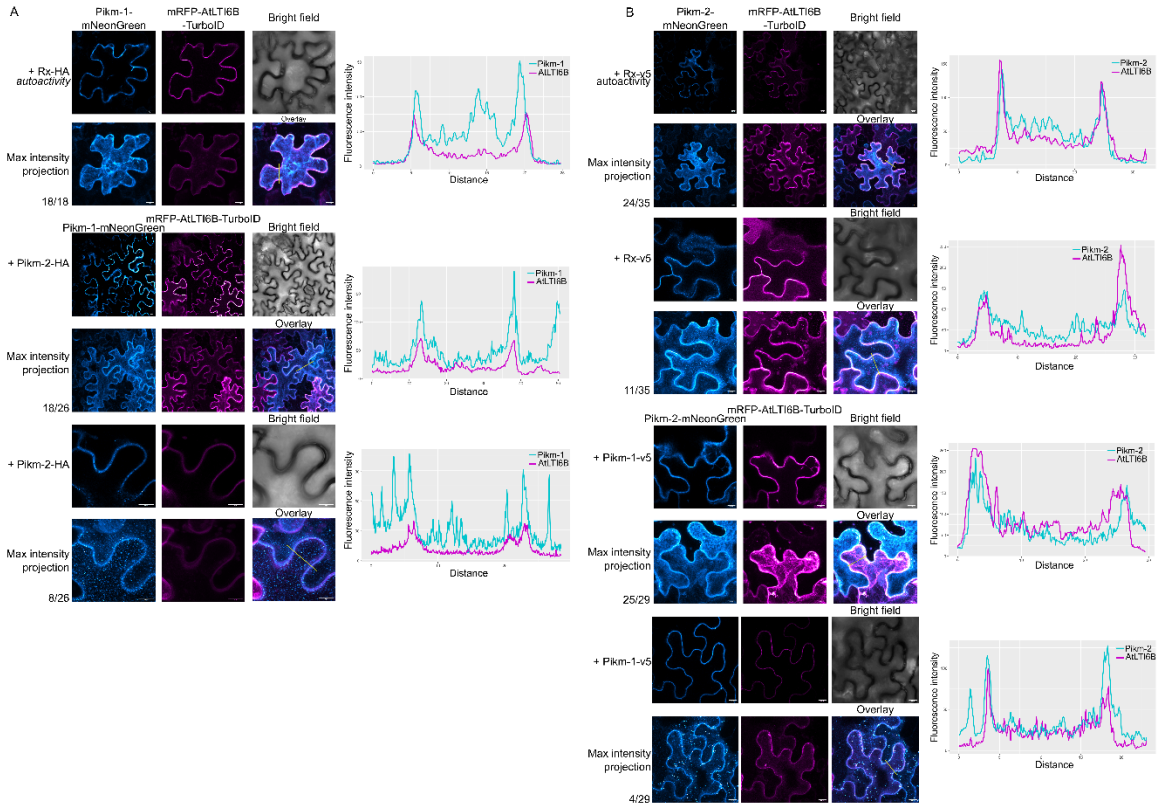


**Figure S4. The Pik hetero-complex localises to the plasma membrane.** Confocal microscopy images (single plane and maximum projection of *z*-stacks of 10–25 slides) showing the subcellular localisation of A) Pikm-1-v5-mNeonGreen or B) Pikm-2-mNeonGreen co-expressed with Rx or the matching NLR from the Pik pair. LTI6B from Arabidopsis was used as a plasma membrane marker. The graphs at right depict the fluorescence intensity from each channel across the yellow line shown on the overlay image. All components were transiently expressed in *N. benthamiana* via agroinfiltration, and subcellular localisation was observed at 2 dpi. Laser excitation was set to 561 nm (diode) for mRFP and to 488 nm (Argon) for mNeonGreen, and detection wavelengths were set to 590–660 nm and 500–550 nm for mCherry and mNeonGreen, respectively.

bioRxiv preprint doi: https://doi.org/10.64898/2025.11.30.691369; this version posted December 2, 2025. The copyright holder for this preprint (which was not certified by peer review) is the author/funder, who has granted bioRxiv a license to display the preprint in perpetuity. It is made available under aCC-BY 4.0 International license.

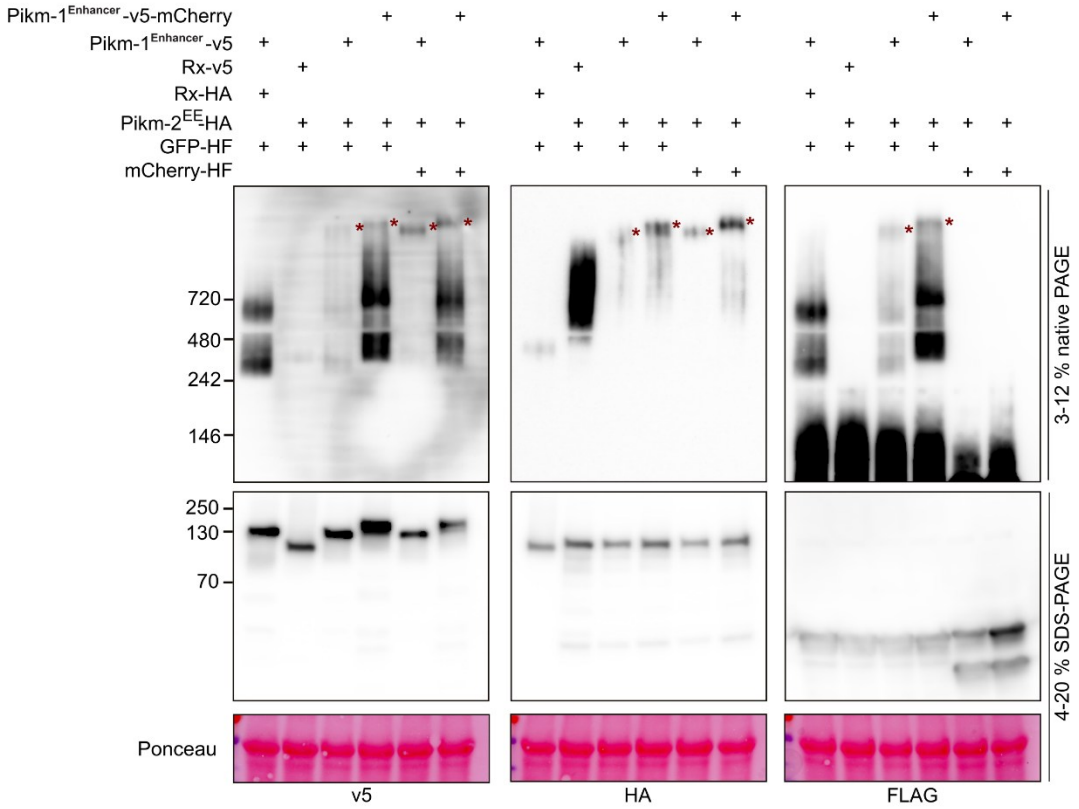


**Figure S5. The ligand bound by Pikm-1$^{Enhancer}$ is part of the Pikm-1$^{Enhancer}$/Pikm-2 hetero-oligomer.**

BN-PAGE (top) and SDS-PAGE (bottom) assays showing that GFP is part of the Pikm-2$^{EE}$ + Pikm-1$^{Enhancer}$ hetero-oligomer and that the corresponding bands shifted when the 'heavy' version of Pikm-1$^{Enhancer}$ was used. Co-expression of Rx with Pikm-1$^{Enhancer}$ or Pikm-2$^{EE}$ was used as a negative control for hetero-oligomer formation. mCherry was used as a negative control for the presence of the ligand bound to Pikm-1$^{Enhancer}$. The samples used for BN-PAGE were run in parallel on a denaturing SDS-PAGE gel to ensure all components were expressed. Approximate molecular weights (kDa) of the proteins are shown at left, and red asterisks point to the bands corresponding to the ~1 MDa Pik oligomer. Ponceau staining showing Rubisco is shown below the immunoblots.

PLOS BIOLOGY

SHORT REPORTS

# Activation of plant immunity through conversion of a helper NLR homodimer into a resistosome

**Muniyandi Selvaraj[1], AmirAli Toghani[1], Hsuan Pai[1], Yu Sugihara[1], Jiorgos Kourelis[1], Enoch Lok Him Yuen[2], Tarhan Ibrahim[2], He Zhao[1], Rongrong Xie[1¤a], Abbas Maqbool[1¤b], Juan Carlos De la Concepcion[3¤c], Mark J. Banfield[3], Lida Derevnina[1¤d], Benjamin Petre[1¤e], David M. Lawson[3], Tolga O. Bozkurt[2], Chih-Hang Wu[1¤f], Sophien Kamoun[1]*, Mauricio P. Contreras[1]***

**1** The Sainsbury Laboratory, University of East Anglia; Norwich Research Park, Norwich, United Kingdom, **2** Imperial College London, London, United Kingdom, **3** Department of Biochemistry and Metabolism, John Innes Centre, Norwich, United Kingdom

¤a Current address: Joint Center for Single Cell Biology, School of Agriculture and Biology, Shanghai Jiao Tong University, Shanghai, China
¤b Current address: Department of Biochemistry and Metabolism, John Innes Centre, Norwich, United Kingdom
¤c Current address: Gregor Mendel Institute, Austrian Academy of Sciences, Vienna BioCenter, Vienna, Austria
¤d Current address: Crop Science Centre, Department of Plant Sciences, University of Cambridge, Cambridge, United Kingdom
¤e Current address: Université de Lorraine, INRAE, IAM, Nancy, France
¤f Current address: Institute of Plant and Microbial Biology, Academia Sinica, Nankang, Taipei, Taiwan
* sophien.kamoun@tsl.ac.uk (SK); mauricio.contreras@tsl.ac.uk (MPC)

## Abstract

Nucleotide-binding domain and leucine-rich repeat (NLR) proteins can engage in complex interactions to detect pathogens and execute a robust immune response via downstream helper NLRs. However, the biochemical mechanisms of helper NLR activation by upstream sensor NLRs remain poorly understood. Here, we show that the coiled-coil helper NLR NRC2 from *Nicotiana benthamiana* accumulates in vivo as a homodimer that converts into a higher-order oligomer upon activation by its upstream virus disease resistance protein Rx. The cryo-EM structure of NbNRC2 in its resting state revealed intermolecular interactions that mediate homodimer formation and contribute to immune receptor autoinhibition. These dimerization interfaces have diverged between paralogous NRC proteins to insulate critical network nodes and enable redundant immune pathways, possibly to minimise undesired cross-activation and evade pathogen suppression of immunity. Our results expand the molecular mechanisms of NLR activation pointing to transition from homodimers to higher-order oligomeric resistosomes.

OPEN ACCESS

**Citation:** Selvaraj M, Toghani A, Pai H, Sugihara Y, Kourelis J, Yuen ELH, et al. (2024) Activation of plant immunity through conversion of a helper NLR homodimer into a resistosome. PLoS Biol 22(10): e3002868. https://doi.org/10.1371/journal.pbio.3002868

**Academic Editor:** Xinnian Dong, Duke University, UNITED STATES OF AMERICA

**Received:** April 2, 2024

**Accepted:** September 30, 2024

**Published:** October 18, 2024

**Peer Review History:** PLOS recognizes the benefits of transparency in the peer review process; therefore, we enable the publication of all of the content of peer review and author responses alongside final, published articles. The editorial history of this article is available here: https://doi.org/10.1371/journal.pbio.3002868

**Copyright:** © 2024 Selvaraj et al. This is an open access article distributed under the terms of the Creative Commons Attribution License, which permits unrestricted use, distribution, and reproduction in any medium, provided the original author and source are credited.

**Data Availability Statement:** All data are available in the main text or the supplementary materials. Data related to the NRC2 structure can be found at PDB/EMDB, with PDB ID 8RFH and EMD-19121,

as well as S1 Table. Datasets and scripts associated to NRC phylogenomics analyses can be accessed on Zenodo (https://zenodo.org/records/10354350 and https://zenodo.org/records/13362063).

**Funding:** The authors received funding from The Gatsby Charitable Foundation (MS, AT, HP, YS, JK, HZ, RX, AM, BP, LD, DML, CHW, SK, MPC); The John Innes Foundation (JCDLC); Biotechnology and Biological Sciences Research Council (BBSRC) BB/P012574 (Plant Health ISP) (MS, AT, HP, YS, JK, HZ, RX, AM, BP, LD, DML, CHW, SK, MPC); BBSRC BBS/E/J/000PR9795 (Plant Health ISP – Recognition) (MS, AT, HP, YS, JK, RX, AM, BP, LD, DML, CHW, SK, MPC); BBSRC BBS/E/J/000PR9796 (Plant Health ISP – Response) (MS, AT, HP, YS, JK, RX, AM, BP, LD, DML, CHW, SK, MPC); BBSRC BBS/E/J/000PR9797 (Plant Health ISP – Susceptibility) (MS, AT, HP, YS, JK, RX, AM, BP, LD, DML, CHW, SK, MPC); BBSRC BBS/E/J/000PR9798 (Plant Health ISP – Evolution) (MS, AT, HP, YS, JK, RX, AM, BP, LD, DML, CHW, SK, MPC); BBSRC BB/V002937/1 (LD, SK, MPC); BBSRC BB/T006102/1 (TI, TOB); BBSRC impact acceleration award BB/X511055/1 (ELHY); Academia Sinica and National Science and Technology Council NSTC-111-2628-B-001-023 (CHW); European Research Council (ERC) 743165 (SK). The funders had no role in the study design, data collection and analysis, decision to publish, or preparation of the manuscript.

**Competing interests:** TOB and SK receive funding from industry on NLR biology and cofounded a start-up company (Resurrect Bio Ltd.) on resurrecting disease resistance. JK, LD, SK and MPC have filed patents on NLR biology. LD and MPC have received fees from Resurrect Bio Ltd.

**Abbreviations:** BN-PAGE, blue native polyacrylamide gel electrophoresis; co-IP, co-immunoprecipitation; NB, nucleotide binding; NLR, nucleotide-binding and leucine-rich repeat; STAND, signal transduction ATPases with numerous domains.

## Introduction

The nucleotide-binding and leucine-rich repeat (NLR) class of intracellular immune receptors is an important component of innate immunity across the tree of life. They mediate intracellular recognition of pathogens and subsequently initiate an array of immune responses in order to counteract infection [1,2]. Plant NLRs can be activated by pathogen-secreted virulence proteins, termed effectors, which pathogens deliver into host cells to modulate host physiology [3]. NLRs belong to the signal transduction ATPases with numerous domains (STAND) superfamily. They typically exhibit a tripartite domain architecture consisting of an N-terminal signalling domain, a central nucleotide-binding domain and C-terminal superstructure forming repeats [4]. The central domain, termed NB-ARC (nucleotide-binding adaptor shared by APAF-1, plant R proteins, and CED-4) in plant NLRs, is a signature feature of this protein family and plays a key role as a molecular switch, mediating conformational changes required for activation [4]. A hallmark of NLR activation in eukaryotes and prokaryotes is their oligomerization into higher-order immune complexes, such as plant resistosomes or mammalian and bacterial inflammasomes. These complexes initiate immune signalling via diverse mechanisms, often leading to a form of programmed cell death [5–11].

NLRs belong to different phylogenetic clades carrying distinct N-terminal domains, with the coiled-coil (CC)-type being the most widespread in plants [12]. A canonical plant CC-NLR is Arabidopsis AtZAR1, which is sequestered in a resting monomeric state in complex with its partner pseudokinase RKS1. Perception of its cognate effector AvrAC primes individual AtZAR1 monomers, which undergo conformational changes and subsequently assemble into pentameric resistosomes [9,13]. Following resistosome assembly, CC-NLR oligomers insert themselves into the plasma membrane and presumably act as calcium channels, initiating immune signalling and cell death, as shown for AtZAR1 and the wheat CC-NLR TmSr35 [7,14]. In previous studies from our group, we showed that NbNRC2 and NbNRC4 form plasma membrane associated oligomers upon activation [15,16]. More recently, cryo-EM based structural studies showed that NbNRC2 and SlNRC4 form inflammasome-like resistosomes upon activation, although unlike AtZAR1 and TmSr35, these NRC assemblies are hexameric [17,18]. However, the extent to which the model of plant NLR activation drawn from CC-NLRs like AtZAR1 or TmSr35 which involves conversion from a monomeric resting state to an oligomer applies to other CC-NLRs, particularly to helper CC-NLRs, remains unknown.

NLR proteins have evolved from multifunctional singletons that can mediate both pathogen effector perception and subsequent immune signalling, as is the case for AtZAR1 [19,20]. However, several NLRs have subfunctionalised throughout evolution into sensors that are dedicated to pathogen perception and helpers that initiate immune signalling. NLR sensors and helpers can function together as receptor pairs or in higher-order configurations termed immune receptor networks [19]. In the NRC immune receptor network of solanaceous plants, multiple sensor CC-NLRs can signal redundantly via an array of downstream paralogous helper CC-NLRs termed NRCs (NLRs required for cell death) to confer disease resistance to a multitude of pathogens and pests [21]. Effector perception by NRC-dependent sensors leads to conformational changes which allow their central nucleotide-binding (NB) domain to signal to downstream helper NRCs and trigger their oligomerization into a helper resistosome [16,22,23]. Although assembly into pentameric or hexameric resistosomes is a shared endpoint between AtZAR1 and NRCs, respectively, the early stages of NRC activation are not understood. Whether the resting form of NRCs exhibits a similar conformation as the monomeric resting state AtZAR1 is not known.

In this work, we used cryo-EM to solve the structure of the helper NLR NbNRC2 purified from the model plant *Nicotiana benthamiana*. We show that unlike the canonical CC-NLR

AtZAR1, NbNRC2 forms a homodimer in its resting state. Mutagenesis of various residues in the NbNRC2 homodimerization interface led to impaired self-association and effector-independent activation, suggesting that homodimerization contributes to immune receptor autoinhibition. We leveraged our recent finding that the NB domains of sensor NLRs are sufficient to activate downstream NRC helpers [22] to study the activation of the NbNRC2 homodimer by the NB domain of the *Potato virus X* disease resistance protein Rx ($Rx^{NB}$). Using in vitro reconstitution assays, we show that $Rx^{NB}$ can trigger formation of a high molecular weight NbNRC2 oligomer. Remarkably, even though NbNRC2, NbNRC3, and NbNRC4 are genetically redundant paralogs for Rx-mediated signalling and disease resistance [21], NbNRC2 does not hetero-associate or co-localise with other NRC paralogs from *N. benthamiana*. These findings were corroborated with phylogenomic analysis of the homodimerization interface across the 15 major clades of NRC proteins found in the Solanaceae family. This interface has diverged within the majority of the individual NRC clades likely leading to molecular insulation of helper nodes in the immune receptor network. We propose that insulation of NRC helper pathways emerged throughout evolution to generate genetic redundancy, minimise undesired cross-activation, and evade pathogen suppression of immunity. Our work expands our understanding of the mechanisms of NLR activation, pointing to helper NLR conformational transitions from homodimers to oligomeric resistosomes.

## Results

### Cryo-EM structure of the NbNRC2 homodimer

Blue native polyacrylamide gel electrophoresis (BN-PAGE) suggests that the helper NLR NbNRC2 accumulates in planta at a higher molecular weight than a monomer [16,22–24]. This prompted us to determine whether this protein self-associates in planta in its resting state. Co-immunoprecipitation assays conducted in the solanaceous model plant *N. benthamiana* revealed that NbNRC2 self-associates, unlike the canonical functional singleton NbZAR1 (**Fig 1A**).

To further investigate the resting form of NbNRC2, we transiently expressed and affinity-purified NbNRC2 from leaves of *N. benthamiana*. Size-exclusion chromatography with this sample revealed elution volumes consistent with a helper NLR homodimer (**S1 Fig**). Subsequent negative-staining imaging of purified NbNRC2 and their class averages also suggested an NRC2 homodimer (**Fig 1B**). Cryo-EM imaging of these particles and single particle reconstruction revealed a homodimer structure at a resolution range of 3.9 to 4.5 Å with C2 symmetry imposed (**Figs 1C and S2, S3 and S4 and S1 Table**). The reconstructed structure contains the NB-ARC and LRR domains of NbNRC2, with the N-terminal CC domain appearing disordered in the density map. Flexible fitting of the AlphaFold2 model of NbNRC2 monomers into the cryo-EM map of the dimeric assembly revealed the relative orientation of the helper NLR protomers as well as the domains responsible for homodimer organisation (**Figs 1C and 1D and S3 and S4 and S1 Movie**).

The dimerization interface can be divided into 3 parts. The NB domain of each NbNRC2 protomer interacts with the LRR region of the other protomer, forming 2 similar interfaces related by 2-fold symmetry of the dimer (interface 1 and interface 3) (**Fig 1C**). The N-terminal LRR region of each NbNRC2 protomer stacks over the equivalent region of the other protomer, at the 2-fold symmetry, forming interface 2 (**Fig 1C**). These 3 interfaces hold the homodimer together with a buried surface area 937 $Å^2$ for each protomer, making the total buried surface 1874 $Å^2$. The residues at the dimerization interface were listed with a distance cut-off of 6 Å (**S2 Table**). Interfaces 1 and 3 are composed of 3 stretches of residues in the NB domain (Stretch 1a-1c, residues 217–220, 238–244, and 270–274, respectively) in 1 protomer and 3 stretches of

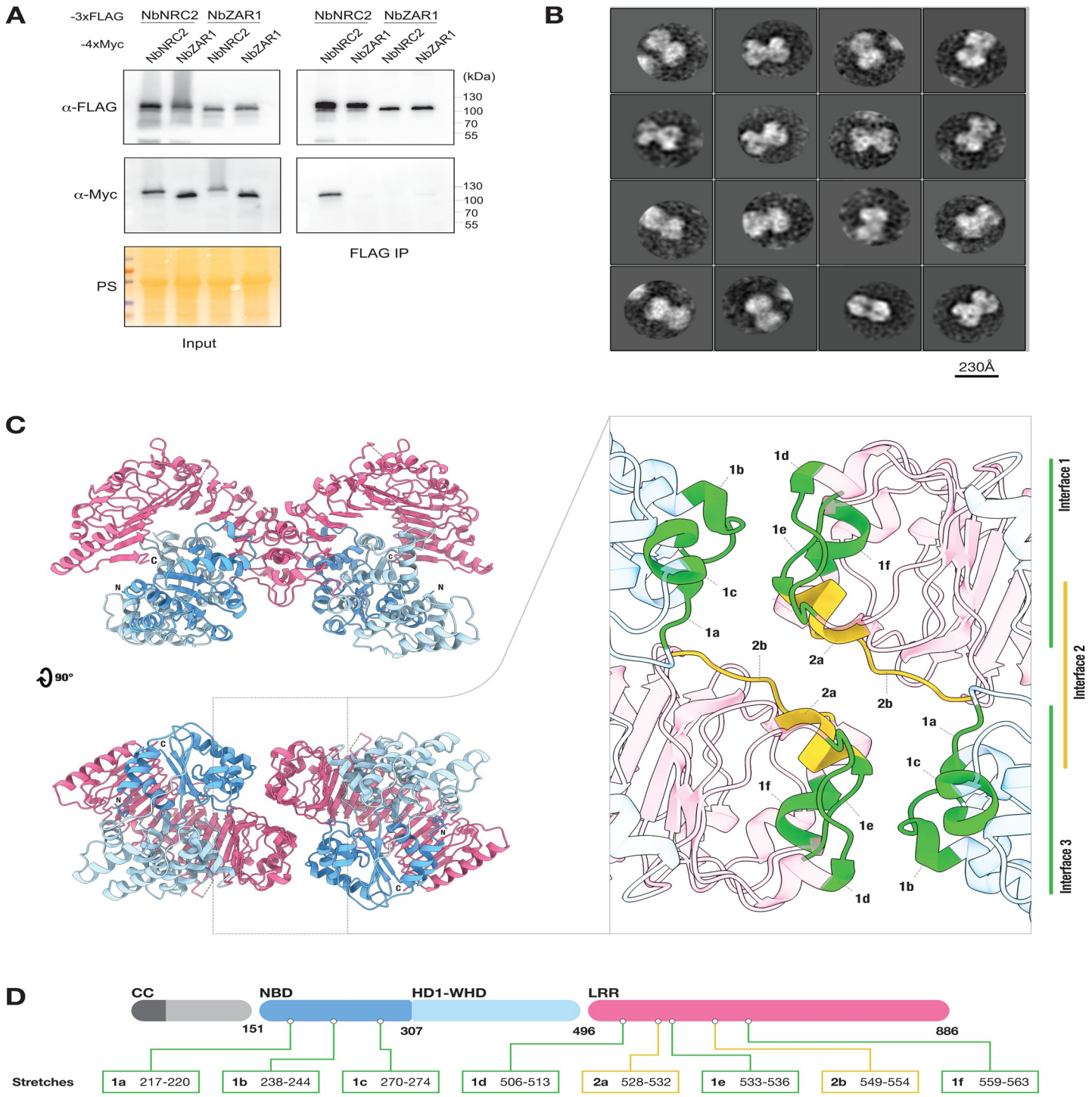


**Fig 1. The helper NLR NRC2 forms a homodimer in planta.** (**A**) Co-immunoprecipitation assays to test self-association of NRC2 and ZAR1 from *N. benthamiana*. C-terminally 3xFLAG-tagged NbNRC2 and NbZAR1 proteins were co-expressed with C-terminally 4xMyc tagged NbNRC2 or NbZAR1. Immunoprecipitations were performed with agarose beads conjugated to FLAG antibodies (FLAG IP). Total protein extracts were immunoblotted with the antisera labelled on the left. Approximate molecular weights (in kDa) of the proteins are shown on the right. Protein loading control was carried out using Ponceau stain (PS). The experiment was performed 3 times with similar results. (**B**) 2D classifications from negative staining transmission electron microscopy images of affinity-purified NbNRC2. NbNRC2 appears as a dimer, with a maximum dimension of approximately 150 Å at its widest point. Scale bar = 230 Å. (**C**) Cryo-EM structure of resting state of NRC2 dimers. Colour coding can be found in (**D**). Atomic model corresponding to NRC2 homodimer shown in 2 orthogonal views, with resolved NB domain (NBD), HD1-WHD, and LRR domains. Notably, the N-terminal CC domain of NbNRC2 was absent from the cryo-EM density. Inset shows details of interfaces between the 2 NbNRC2 protomers, highlighting amino acid stretches corresponding to three contact interfaces. (**D**) Colour coding of the domains is shown in the schematic representation of the domain architecture and

boundaries of NRC2, which includes the exact boundaries of the amino acid stretches at the dimerization interfaces. A schematic representation of the pipeline used for cryo-EM imaging, data processing and model building can be found in **S2 Fig**. Additional views of the structure and dimerization interface can be found in **S3 and S4 Figs and S1 Movie**. Additional information on image processing and model building can be found in **S1 Table**. The full data underlying the structure in this figure can be found in the Protein Data Bank, PDB 8RFH.

https://doi.org/10.1371/journal.pbio.3002868.g001

residues in the LRR (stretches 1d-1f, residues 506–513, 533–536, and 559–563, respectively) from the other protomer (**Fig 1C and 1D**). Two stretches of residues in the LRR (stretches 2a and 2b, residues 528–532 and 549–554, respectively) stack together forming interface 2 (**Fig 1C and 1D**). In the dimer assembly, the C-termini of the LRR domain and the NB domain of each protomer interact *in cis*. The 15 parallel strands of each LRR domain orient antiparallel relative to the other protomer in the dimer. The C-termini of each LRR are found at the periphery of the assembly and do no not contribute to the dimerization interface (**Fig 1C**).

## Homodimerization contributes to autoinhibition of resting state NbNRC2

In order to functionally validate our cryo-EM structure and to gain insights into the biological relevance of NbNRC2 homodimerization, we made 15 NbNRC2 variants with mutations in residues at the inter-protomer interaction interface. All 15 NbNRC2 variants generated accumulated in planta when transiently expressed in leaves of *nrc2/3/4* KO *N. benthamiana* (**S5 Fig**). Strikingly, 1 variant NbNRC2$^{E243R}$ became autoactive, triggering effector-independent cell death at 3 days post-infiltration (**Figs 2A and S6**). Next, we co-expressed all 15 NbNRC2 variants with Rx or with Rx/CP (**Figs 2A and S7**). This revealed 6 additional NbNRC2 variants that triggered effector-independent cell death when Rx was co-expressed. These were NbNRC2$^{C241A}$, NbNRC2$^{Y508A}$, NbNRC2$^{K512A}$, NbNRC2$^{P554E}$, NbNRC2$^{T560F}$, and NbNRC2$^{K563E}$, which we termed sensitised/trigger-happy [25]; 6 out of 7 mutations that led to autoactive or trigger-happy phenotypes were in residues found in interfaces 1 and 3, mediated by NB to LRR inter-protomer interactions. NbNRC2$^{P554E}$ was the only mutant in the LRR-LRR interface 2 region with a trigger-happy phenotype. All variants triggered cell death when co-expressed with Rx and CP except for NbNRC2$^{D239K}$, which did not trigger cell death upon Rx activation. Residue D239 has also been shown to mediate inter-protomer contacts in the active NbNRC2 hexameric resistosome, so the absence of cell death in the NbNRC2$^{D239K}$ may be due to compromised resistosome assembly [17]. We next assessed all 7 autoactive or trigger-happy NbNRC2 variants in co-immunoprecipitation assays to determine whether they were impaired in self-association. Tissue was harvested at 2 days post infiltration, before the onset of visible cell death triggered by NbNRC2$^{E243R}$. Self-association was abolished in all variants tested, except for variant NbNRC2$^{K563E}$ which displayed weak self-association compared to WT NbNRC2 (**Fig 2B**).

## The NbNRC2 homodimer converts into a resistosome upon activation

To further study NRC2 activation, we set up in vitro reconstitution experiments with purified NbNRC2 and carried out BN-PAGE assays. First, to determine the optimal experimental conditions, we incubated purified NbNRC2 with increasing levels of ATP, which is necessary for NLR activation [4,26]. Incubation of NbNRC2 with 15 mM ATP led to the disappearance of the lower molecular weight NRC2 band and appearance of higher molecular weight complexes migrating at a similar size to the NbNRC2 oligomer observed in planta [16,22–24] (**S8 Fig**). This indicates that purified NbNRC2 may get spontaneously activated at 15 mM ATP in vitro. We selected 5 mM ATP for subsequent assays.

Next, we hypothesized that the disease resistance protein Rx disrupts the NbNRC2 homodimer to trigger activation of its helper NLR. To test this, we used Rx$^{NB}$, the 154 amino acid NB

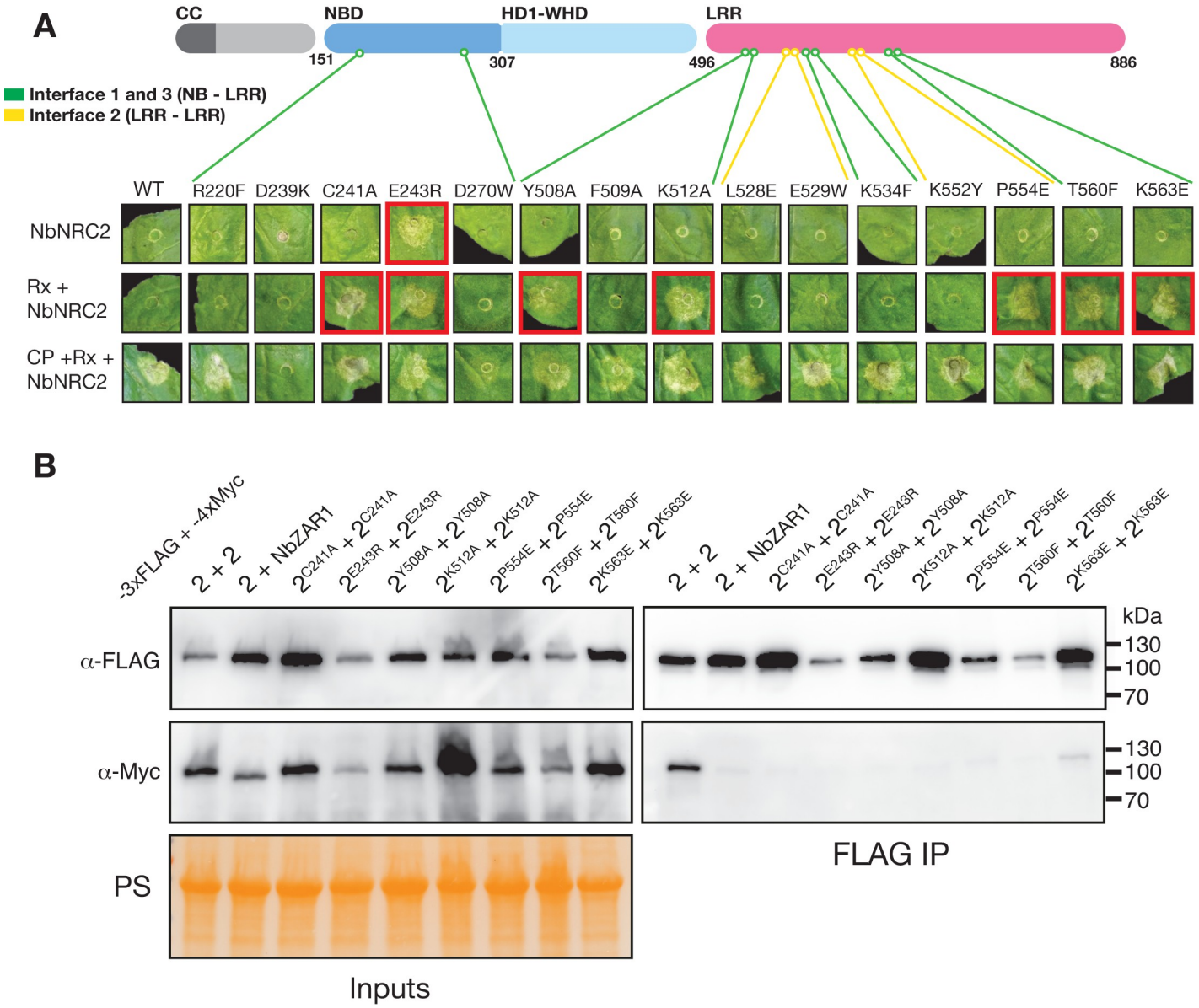


**Fig 2. Homodimerization contributes to autoinhibition of resting state NbNRC2.** Mutagenesis of amino acids found at the NbNRC2 homodimerization interface can lead to autoactivity and impaired self-association. (**A**) Schematic representation of NbNRC2 domain organisation, indicating the approximate position of the mutagenized residues. Green lines indicate residues corresponding to interfaces 1 and 3 (NB domain to LRR domain inter-protomer interface) and yellow lines indicate residues corresponding to interface 2 (LRR to LRR inter-protomer interface). Cell death assays were carried out by transiently expressing each NbNRC2 variant in leaves of *nrc2/3/4* KO *N. benthamiana* either on its own (top row), together with the sensor NLR Rx (middle row) or with the sensor NLR Rx and PVX CP (bottom row). Red outline on boxes indicate effector-independent activation (autoactivation or trigger-happy phenotypes). Quantification of these cell death assays can be found in S6 **and** S7 **Figs**. (**B**) Co-immunoprecipitation assays to test self-association of NbNRC2 and 7 NbNRC2 homodimerization interface mutants with impaired autoinhibition. For each treatment, C-terminally 3xFLAG-tagged NbNRC2 variants indicated (labelled 2) were co-expressed with a C-terminally 4xMyc tagged version of the same variant (also labelled 2). WT NbNRC2 self-association was included as a positive control, and association between NbNRC2 and NbZAR1 was included as a negative control. Immunoprecipitations were performed with agarose beads conjugated to FLAG antibodies (FLAG IP). Total protein extracts were immunoblotted with the antisera labelled on the left. Approximate molecular weights (in kDa) of the proteins are shown on the right. Protein loading control was carried out using Ponceau stain (PS). The experiment was performed three times with similar results.

https://doi.org/10.1371/journal.pbio.3002868.g002

domain of Rx, which is necessary and sufficient to activate NbNRC2 in the absence of a pathogen effector [22,27]. In the presence of 5 mM ATP, these in vitro reconstitution experiments revealed that increasing amounts of $Rx^{NB}$ triggered the appearance of higher order complexes

similar in size to the NbNRC2 resistosome (S8 Fig). We conclude that conversion of the helper NLR homodimer into a resistosome by a sensor NLR is a key step of NbNRC2 activation in a mechanistic model that is different from the activation of the ZAR1/RKS1 complex [9,13].

## NRC paralogs do not associate with each other

Paralogous NRC helpers can form genetically redundant network nodes in the ~100-million-year-old immune receptor network, therefore promoting robustness and evolvability of the plant immune system [3,21,28]. However, the biochemical basis of NRC redundancy is unknown. We hypothesized that NRC paralogs acquired mutations in their dimerization interfaces that insulate them from one another, as predicted from prior theory on the evolution of orthogonal signalling pathways following gene duplication events [29,30]. We investigated the degree to which NRC paralogs form heterodimers with each other using in planta co-immunoprecipitation assays of resting forms of NbNRC2, NbNRC3, and NbNRC4, and used NbZAR1 as a negative control. Our assays confirmed NbNRC2 self-association but yielded weak to non-detectable signal for hetero-association between NbNRC2 and NbNRC3, NbNRC4 or NbZAR1 (Fig 3A). We conclude that NbNRC2 preferentially self-associates in *N. benthamiana* and does not form stable heterocomplexes with its paralogs NbNRC3 and NbNRC4.

We independently corroborated these findings using live-cell confocal microscopy (Fig 3B). NbNRC2 accumulates in filament-like structures in its resting state that do not overlap with the previously reported peripheral subcellular localization of NbNRC4 [15] further supporting the view that these critical network nodes signal via insulated pathways. Overall, these findings are consistent with the distinct sequences of the dimer interfaces of NRC helper NLRs inferred from the NbNRC2 homodimer structure (**Fig 3C and S1 Data**).

## Homodimerization interfaces have diverged throughout NRC evolution

The observation that NbNRC2 does not form heterocomplexes with other NRC paralogs despite their common evolutionary origin prompted us to perform phylogenomic analyses across the highly expanded NRC clade of the Solanaceae family. First, we developed a computational pipeline to extract 1,092 NRC sequences from 6,630,292 predicted proteins from 123 solanaceous genome assemblies representing 38 species of the genera *Solanum*, *Physalis*, *Capsicum*, and *Nicotiana* (S2 Data). We grouped these NRC sequences into 15 phylogenetic clades ranging in size from 31 to 129 sequences (S9 Fig), and 10 of the 15 clades include orthologs from at least 2 genera, therefore representing relatively deep NRC lineages (S10 Fig).

The consensus sequences of the 8 amino acid stretches found in the dimerization interface were, overall, degenerated across all NRC sequences compared to known conserved motifs of CC-NLRs, e.g., P-loop and MHD motifs, suggesting that they have diversified throughout NRC evolution (**Figs** 4A and S10 and S3 Data). However, the dimerization interfaces tended to be conserved within each clade (**Figs** 4B and S10 **and** S11 **and** S4 Data). We identified unique polymorphisms within the major NRC2, NRC3, and NRC4 clades by calculating the relative amino acid ratio for one clade versus the others using a 50-fold cutoff with a minimum frequency of 80% within the query clade (Fig 3B). Using these criteria, the NRC2 and NRC3 clades, which contain representative proteins used in co-immunoprecipitation assays in Fig 3A, had 5 and 3 unique polymorphisms among the 44 amino acids that map to the homodimer interface (Fig 4B and S5 Data).

Next, we corroborated these findings using Shannon's entropy analyses. The entropy of a given amino acid position ranges from zero ($Log_2 1$) for fully conserved residues to a

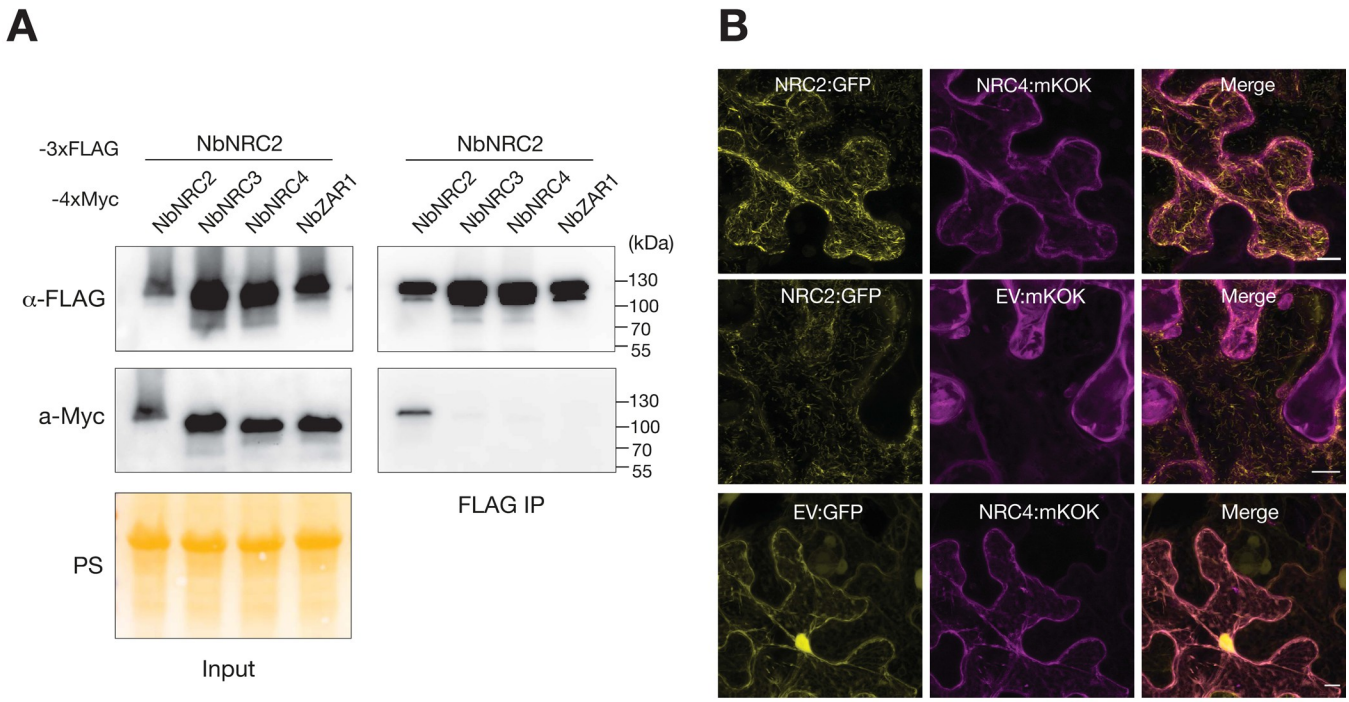

**Fig 3. NRC2 does not hetero-associate or co-localise with other NRC paralogs in its resting state.** (**A**) Co-IP assays to test the association of NRC2 with its paralogs NRC3 and NRC4 from *N. benthamiana*. C-terminally FLAG-tagged NbNRC2 was co-expressed with C-terminally 4xMyc-tagged NbNRC2, NbNRC3, NbNRC4, or NbZAR1 as a negative control. IPs were performed with agarose beads conjugated to FLAG antibodies (FLAG IP). Total protein extracts were immunoblotted with the antisera labelled on the left. Approximate molecular weights (kDa) of the proteins are shown on the right. Protein loading control was carried out using Ponceau stain (PS). The experiment was performed 3 times with similar results. (**B**) Z-stacks of confocal micrographs show the localization of NbNRC2:GFP together with NbNRC4:mKOk or EV:mKOk. C-terminally GFP-tagged NbNRC2 was co-infiltrated with either NbNRC4:mKOk or EV:mKOK in wild-type *N. benthamiana* plants. EV:GFP was co-infiltrated with NbNRC4:mKOk as an additional control. Scale bars represent 10 μm. Images were taken 48 h post-agroinfiltration. (**C**) Amino acid sequence alignment of the 8 stretches identified at the NbNRC2 dimerization interface, comparing NbNRC2, NbNRC3, NbNRC4, and NbZAR1.

https://doi.org/10.1371/journal.pbio.3002868.g003

maximum of 4.32 ($Log_2 20$) when all 20 amino acids are equally found (30). We used a threshold of 1.5 to highlight highly variable positions consistent with previous NLR studies (31). All 8 dimerization stretches scored above 1.5 when all 1,092 NRC helpers were compared but were highly conserved within 11 of the 15 NRC clades (**Figs** 4A and S10 and S11). In 6 clades (NRC0, NRCX, NRC2, NRC3, NRC4a, and NRC4t), all residues across the 8 stretches scored under the 1.5 threshold and showed little to no sequence diversity (S10 and S11 **Figs** and S4 Data). In 5 clades (NRC1, NRC6, NRC7, NRC4b, and $NRC4_{other}$), the 8 stretches were under the 1.5 threshold except for 1 to 3 variable residues within each clade (S10 Fig). In the remainder of the clades (NRC8, NRC9, NRC5, and NRC4c), all 8 stretches had up to 12 variable residues within each clade with entropy values higher than 1.5 indicating higher levels of sequence diversity compared to other clades (S4 Data). In contrast, conserved motifs, such as P-loop and MHD, were consistently under the defined threshold with 13 of the 15 clades scoring under 1.5 and displaying little to no sequence variation (**Figs** 4 and S10 and S11 **and** S4 Data).

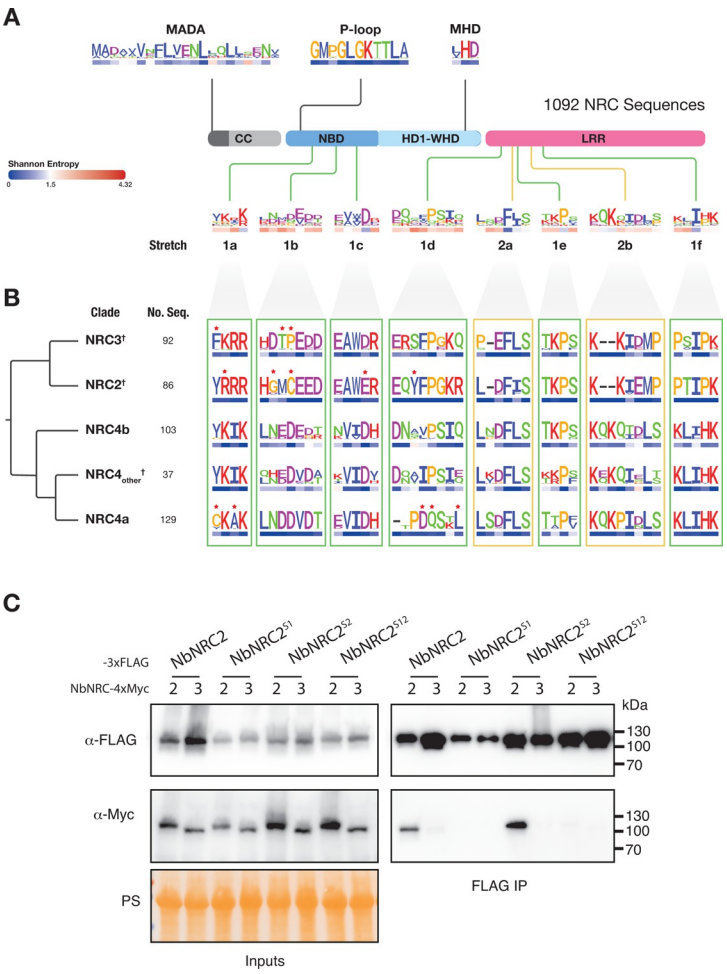


**Fig 4. The NRC homodimerization interface has diversified throughout evolution of NRC clade.** (**A**) Schematic representation of NRC domain architecture, featuring CC, NBD, HD1-WHD, and LRR domains. Approximate position of different previously characterized NLR motifs (MADA, p-loop, MHD) and the 8 amino acid stretches present at the dimerization interface are indicated. A database of 993 unique NRC sequences and 99 reference NRC sequences was compiled from a total of 123 solanaceous genomes (S2 Data) and used to generate consensus sequence patterns for each motif/region (S3 Data). Shannon entropy scores for each amino acid position were calculated using this database and indicated, in bits, below each position in the consensus sequence pattern (S4 Data). A Shannon entropy score of 1.5 was established as a threshold to distinguish between highly variable (>1.5 bits) and non-highly variable (<1.5 bits) amino acids, as established previously [31]. (**B**) All 1,092 NRC sequences were grouped by phylogeny (S8 Fig), and consensus sequence patterns within each clade were generated with sequence logos for each of the 8 amino acid stretches that define the dimerization interface (S9 Fig). NRC clades are ordered by phylogenetic relationship, indicated on the left along with the number of NRC sequences within each clade. Shannon entropy score is indicated below each amino acid in the consensus sequence pattern. Red stars above indicate amino acid polymorphisms that are unique to each clade, as determined by analysing their relative amino acid ratio among NRC clades (S5 Data). †Indicates clades containing *N. benthamiana* NRCs used in the co-immunoprecipitation experiments in Fig 3A. More detailed Shannon entropy plots calculated across all 1,092 NRC sequences and within each individual NRC clade are shown in S10 Fig. (**C**) Co-immunoprecipitation assays to test self-association of NbNRC2 or NbNRC3 with various NbNRC2 variants carrying the homodimerization interface of NbNRC3. We generated swaps at the NB to LRR inter-protomer interface (interfaces 1 and 3, comprised of stretches 1a-f and referred to as NbNRC2$^{S1}$), at the LRR to LRR inter-protomer interface (interface 2, comprised of stretches 2a-b, NbNRC2$^{S2}$) and at both (NbNRC2$^{S12}$). C-terminally 3xFLAG-tagged NbNRC2, NbNRC2$^{S1}$, NbNRC2$^{S2}$, and NbNRC2$^{S12}$ were coexpressed with C-terminally 4xMyc tagged NbNRC2 or NbNRC3. Immunoprecipitations were performed with agarose beads conjugated to FLAG antibodies (FLAG IP). Total protein extracts were immunoblotted with the antisera labelled on the left. Approximate molecular weights (in kDa) of the proteins are shown on the right. Protein loading control was carried out using Ponceau stain (PS). The experiment was performed two times with similar results.

https://doi.org/10.1371/journal.pbio.3002868.g004

To determine the extent to which residues at the homodimerization interface contribute to insulation between NRC paralogs, we swapped residues at the homodimerization interface from NbNRC3 into NbNRC2 (Fig 3C) and tested these chimeric proteins in co-immunoprecipitation assays (Fig 4C). We generated swaps at the NB to LRR inter-protomer interface (interfaces 1 and 3, comprised of stretches 1a-f and referred to as NbNRC2$^{S1}$), at the LRR to LRR inter-protomer interface (interface 2, comprised of stretches 2a-b, NbNRC2$^{S2}$) and at both (NbNRC2$^{S12}$). NbNRC2$^{S1}$ and NbNRC2$^{S12}$ did not associate with NbNRC2. Interestingly, NbNRC2$^{S2}$ associated with NbNRC2. None of the swaps tested gained the capacity to associate with NbNRC3. These results suggest that introducing NbNRC3 residues at the NB to LRR inter-protomer interface (S1) prevents association with NbNRC2, indicating that this interface likely mediates NRC inter-paralog insulation.

## Discussion

### Contrasting activation mechanisms across plant NLRs

To date, our understanding of the structural basis of the resting state of plant NLRs has been limited to that of AtZAR1 [13]. In this study, we show that a CC-NLR helper in the NRC immune network exhibits a distinct mechanism of activation relative to the ZAR1/ZRK system (S12 Fig). Our data is consistent with a model in which exposure of the NB domain of the disease resistance protein Rx converts the homodimer of its downstream helper NbNRC2 into a high molecular weight oligomer. The cryo-EM structure of the NbNRC2 homodimer revealed novel intermolecular interactions that hold this helper NLR in an autoinhibited resting state, which can lead to effector-independent activation when mutagenized. The surfaces involved in NbNRC2 homodimerization are surface exposed in the activated NbNRC2 hexamer structure [17]. This implies that conversion from homodimer to a multimeric resistosome is likely to involve dimer dissociation into monomers or large-scale conformational rearrangements in the dimer, likely with additional intermediate assemblies. Further work will shed light on the precise dynamics underpinning transition from homodimer to higher-order oligomers. In particular, how sensor NLRs trigger homodimer activation and whether primed monomers precede NRC oligomerization remain open questions.

The contrasting models in early steps of activation of NbNRC2 and AtZAR1 indicate that plant NLRs have evolved a diversity of activation and autoinhibition mechanisms possibly associated with their evolutionary transitions from functional singletons to paired and networked immune receptors. Moreover, in another work, we showed that Rx/CP-activated NbNRC2 forms hexameric oligomers, unlike the pentameric assemblies formed by activated AtZAR1, pointing to differing models both at resting state and following activation [17]. Another recently published study on the constitutively active SlNRC4 variant SlNRC4$^{D478V}$ revealed that it also forms hexameric assemblies with calcium channel activity, suggesting that hexamerization applies to other NRCs as well [18]. We propose that AtZAR1 is more likely to reflect the ancestral state of CC-NLRs given that it is present across ancient plant lineages, including dicotyledons, monocotyledons, and magnoliids and has been proposed to guard ZRK proteins since the Jurassic era [32,33]. In contrast, NRC sensor/helper pairing is thought to be a more recent innovation, having emerged in the Caryophyllales and Asterid lineages of dicotyledoneous flowering plants [21,34,35]. It will be interesting to determine the extent to which homodimerization has evolved as a steady state across NLRs. Already, other NLRs including RPM1, a CC-NLR outside the NRC superclade, have been known to self-associate in its resting state, suggesting that resting state self-association is not exclusive to paired or networked NLRs [36,37].

More recently, Ma and colleagues showed that SlNRC2, the *Solanum lycopersicum* ortholog of NbNRC2, also forms homodimers [38]. Interestingly, they report that resting state SlNRC2 homodimers can assemble into tetramers and filaments similar to the mobile filamentous structures identified by Duggan and colleagues using live cell imaging [15,38]. While the SlNRC2 homodimer also appears to be contributing towards helper autoinhibition, mutations in the tetramerization or filament formation interfaces did not lead to effector independent activation, making the biological function of these assemblies unclear [38]. Interestingly, NRC4 does not form filaments at the resting state and instead accumulates at the plasma membrane, shifting to the interface between *Phytophthora infestans* and the host plant at the site where effectors are delivered before re-localising and forming discrete puncta at the plasma membrane following activation [15]. In the future, we need a better understanding of the diversity of resting state oligomeric complexes and subcellular assemblies of NRC helpers and the biological activities associated with this diversity.

How does homodimerization contribute to sensor-helper communication? Interestingly, while the NbNRC2$^{E243R}$ variant triggered effector independent cell death even in the absence of sensor NLR overexpression, several NbNRC2 homodimerization interface mutants tested became autoactive only when the sensor NLR Rx was overexpressed. This suggests that homodimerization also prevents helper mis-activation by resting state sensor NLRs. The observation that NbNRC2 mutants impaired in homodimer formation can spontaneously activate when high doses of resting state sensor NLR are present suggests that sensors and helpers may be capable of engaging in transient, low affinity, interactions even prior to effector perception. We hypothesize that in the case of NbNRC2 these interactions would be of insufficient affinity or stability to lead to helper activation and that when NbNRC2 homodimer stability is compromised, high doses of resting state sensor become sufficient to trigger activation.

Our findings that mutations that compromise homodimerization display effector-independent autoactivity has implications for bioengineering boosted helper NLRs. While several NbNRC2 homodimerization mutants triggered strong cell death upon Rx overexpression, they were not autoactive when expressed in a cell with normal doses of endogenous sensors (**S6 Fig**). It is possible that these homodimerization interface mutants will respond to lower doses of effector-activated sensors, therefore leading to enhanced immune activation dynamics and improved disease resistance. Previous work by Segretin and colleagues identified mutations in the CC-NLR R3a that led to enhanced cell death upon effector perception, also termed sensitised or "trigger-happy" variants [25]. While the precise mechanistic basis for this trigger-happy phenotype in R3a is not known, it is possible that it is due to the disruption of autoinhibitory interactions as is the case for our NbNRC2 homodimerization interface mutants. Whether R3a or other NLRs also form resting state autoinhibitory dimers or oligomers remains to be tested. Nonetheless, we hypothesize that making mutations to alter resting state NLR immune receptor autoinhibition may provide an exciting strategy to bioengineer enhanced disease resistance.

NLRs are generally thought to be hypervariable due to coevolution with rapidly evolving pathogens [39,40]. While the NRC clade of helper NLRs exhibits greater conservation within the Solanaceae compared to NRC-dependent sensors and most other NLRs [21,34,35], these proteins exhibit variable regions across the NRC helper clade (**Figs 4** and **S10 and S11**). Our analyses revealed that distinct NRC clades have diverged from each other in the homodimerization interface and that NRC2 does not associate with its NRC3 and NRC4 paralogs. Swapping the NbNRC3 homodimerization interface into NbNRC2 led to NbNRC2 variants that failed to associate with NbNRC2. We propose that following duplication, NRC paralogs have accumulated mutations in the dimerization interface that prevent them from forming heterodimers, thereby forming insulated pathways in the immune network. The established paradigm is that sequence diversification of plant NLRs is primarily driven by co-evolutionary arms-races with

rapidly evolving pathogens. Here, we show that NRC helpers have rapidly diversified, potentially to prevent hetero-association and form insulated redundant signalling nodes, expanding our understanding of the adaptive drivers of NLR diversification. However, co-evolution with pathogens may have also driven the emergence of insulated NRC pathways given that redundant nodes in this receptor networks may enable the plant to evade suppression by pathogen effectors, contributing to the robustness of the immune system (**S12 Fig**) [20,24,41,42].

## Materials and methods

### Plant growth conditions

Wild-type and *nrc2/3/4* CRISPR mutant [43] *N. benthamiana* lines were grown in a controlled environment growth chamber with a temperature range of 22 to 25˚C, humidity of 45% to 65% and a 16/8-h light/dark cycle.

### Plasmid construction

We used the Golden Gate Modular Cloning (MoClo) kit [44] and the MoClo plants part kit [45] for cloning. All vectors used were generated with these kits unless otherwise stated. Cloning design and sequence analysis were done using Geneious Prime (v2021.2.2; https://www.geneious.com). All NRC and ZAR1 constructs used for co-immunoprecipitation assays were cloned into the pICH86988 level one acceptor with a C-terminal 3xFLAG tag (pICSL5007) or a C-terminal 4xMyc tag (pICSL5010). Constructs for protein purification were cloned into pJK268c-mRFP acceptor with 2 × 35 s promoter (pICSL51288) and terminator (pICSL41414). NbNRC2 was cloned with a C-terminal 6xHis-3xFLAG tag. $Rx^{NB}$-eGFP and eGFP constructs were cloned with an N-terminal 6xHis-3xFLAG tag. Constructs used for cell biology were previously reported [15,16].

### Transient protein expression by agroinfiltration in *Nicotiana benthamiana*

Proteins of interest were transiently expressed in *N. benthamiana* according to previously described methods [16]. Briefly, leaves from 4- to 5-week-old plants were infiltrated with suspensions of *Agrobacterium tumefaciens* GV3101 pM90 strains transformed with expression vectors coding for different proteins indicated. Final $OD_{600}$ of all *A. tumefaciens* suspensions were adjusted in infiltration buffer (10 mM MES, 10 mM $MgCl_2$, and 150 μm acetosyringone (pH 5.6)). Final $OD_{600}$ used for each construct was 0.3.

### Cell death assays by agroinfiltration in *Nicotiana benthamiana*

Strains were transformed with expression vectors coding for different proteins indicated. Final $OD_{600}$ of all *A. tumefaciens* suspensions were adjusted in infiltration buffer (10 mM MES, 10 mM $MgCl_2$, and 150 μm acetosyringone (pH 5.6)). Final $OD_{600}$ used was 0.3 for each NLR construct and 0.1 for CP-eGFP or eGFP. Whenever multiple constructs were co-infiltrated into an individual spot, the total concentration of bacteria was kept constant across treatments by adding untransformed *A. tumefaciens* when necessary. This was to avoid an effect from differences in the total $OD_{600}$ of bacteria in each treatment.

### Co-immunoprecipitation (co-IP) assays

Co-immunoprecipitation assays were performed as described previously [41]. Four- to five-week-old *N. benthamiana* plants were agroinfiltrated as described above with constructs of interest and leaf tissue was collected 3 days post agroinfiltration. Final $OD_{600}$ used for each construct was 0.3. Leaf tissue was ground using a Geno/Grinder tissue homogenizer. GTEN

extraction buffer was used (10% glycerol, 50 mM Tris-HCl (pH 7.5), 5 mM $MgCl_2$, and 50 mM NaCl) supplemented with 10 mM DTT, 1× protease inhibitor cocktail (SIGMA) and 0.2% IGEPAL (SIGMA). Samples were incubated in extraction buffer on ice for 10 min with short vortex mixing every 2 min. Following incubation, samples were centrifuged at 5,000 *xg* for 15 min and the supernatant was collected. This was spun down an additional time at 5,000 *xg* for 15 min and then supernatant was filtered using Minisart 0.45 μm filter (Sartorius Stedim Biotech, Goettingen, Germany).

Part of the extract was set aside prior to immunoprecipitation. These were used as inputs. 1.4 ml of the remaining filtered total protein extract was mixed with 30 μl of anti-FLAG agarose beads (SIGMA) and incubated end over end for 90 min at 4˚C. Beads were washed 5 times with immunoprecipitation wash buffer (GTEN extraction buffer with 0.2% v/v IGEPAL (SIGMA)). Associated plant proteins were competitively eluted by excess of 3xFLAG peptides. Elution was spun down at 1,000 *xg* for 1 min and the supernatant was transferred to a new tube. Inputs and eluted immunoprecipitates were diluted in SDS loading dye and denatured by heating for 10 min at 72˚C. All samples were used for SDS-PAGE. Briefly, they were run on 4% to 20% Bio-Rad Mini-PROTEAN TGX gels alongside a PageRuler Plus prestained protein ladder (Thermo Scientific). The proteins were then transferred to polyvinylidene difluoride membranes using Trans-Blot Turbo Transfer Buffer using a Trans-Blot Turbo Transfer System (Bio-Rad) as per the manufacturer's instructions. Membranes were immunoblotted as described below.

## Immunoblotting and detection of BN-PAGE and SDS-PAGE assays

Blotted membranes were blocked with 5% milk in Tris-buffered saline plus 0.01% Tween 20 (TBS-T) for an hour at room temperature and subsequently incubated with desired antibodies at 4˚C overnight. Antibodies used were anti-GFP (B-2) HRP (Santa Cruz Biotechnology), anti-FLAG (M2) HRP (Sigma), or anti-Myc (9E10) HRP (Roche), as indicated in the figures, all used in a 1:5,000 dilution in 5% milk in TBS-T. To visualise proteins, we used Pierce ECL Western (32106, Thermo Fisher Scientific), supplementing with up to 50% SuperSignal West Femto Maximum Sensitivity Substrate (34095, Thermo Fisher Scientific) when necessary. Membrane imaging was carried out with an ImageQuant LAS 4000 or an ImageQuant 800 luminescent imager (GE Healthcare Life Sciences, Piscataway, New Jersey, United States of America). Rubisco loading control was stained using Ponceau S (Sigma) or Ponceau 4R (A.G. Barr).

## Protein purification from *N. benthamiana*

Around 30 leaves of *nrc2/3/4* KO *N. benthamiana* were agroinfiltrated as described above to transiently express NbNRC2-6xHis-3xFLAG, 6xHis-3xFLAG-$Rx^{NB}$-eGFP, or 6xHis-3xFLAG-eGFP. All constructs were cloned in pJK268c acceptor. Tissue was harvested after 3 days and snap-frozen in liquid nitrogen. All samples were stored at −80˚C until the protein was finally extracted. The entire purification process was completed in the same day for each preparation. On the day of purification, the frozen tissue was ground into fine powder in a mortar and pestle that was pre-cooled with liquid nitrogen, and 20 g of ground powder were resuspended with extraction buffer (100 mM Tris-HCl (pH 7.5), 150 mM NaCl, 1 mM $MgCl_2$ 1 mM EDTA, 10% glycerol, 10 mM DTT, 1× cOmplete EDTA-free protease inhibitor tablets (Sigma) and 0.4% v/v IGEPAL). Approximately 20 g of ground tissue was resuspended in ice-cold extraction buffer at a 1:4 w/v ratio (20 g of powder in 80 ml of extraction buffer). After vortexing and resuspending the powder in this buffer, the crude extract was spun down for 10 min at max. speed. The supernatant was transferred to a new tube and centrifuged again for 10 min at max.

speed. This second supernatant was filtered using Miracloth (Merck), and 200 ml of anti-FLAG beads were added to the supernatant and incubated at 4˚C for 90 min. The tubes were in constant rotation to prevent the beads from sedimenting. The protein-bound beads were collected on an open column and washed with 10 ml of wash buffer (100 mM Tris-HCl (pH 7.5), 150 mM NaCl, 1 mM $MgCl_2$ 1 mM EDTA, 10% glycerol, and 0.4% v/v IGEPAL). The washed beads were collected in an Eppendorf tube and eluted with the final isolation buffer in 200 ml volume (100 mM Tris HCl (pH 7.5), 150 mM NaCl, 1 mM MgCl2, 1 mM EDTA, protease inhibitor cocktail, 5% glycerol, and 0.2% IGEPAL) supplemented with 0.3 mg/ml 3xFLAG peptide. The eluted protein was used for SDS-PAGE to assess sample quality and purity. About 1.2 to 1.5 mg/ml concentration was obtained for NRC2, $Rx^{NB}$-eGFP, and eGFP from each purification, as determined by absorption at 280 nm. FLAG-eluted pure protein samples were used for all in vitro experiments and structural studies.

## Gel filtration assays with purified NbNRC2

C-terminally 6xHis-3xFLAG NbNRC2 was transiently expressed in leaves of nrc2/3/4 KO *N. benthamiana* as described above. C-terminally 6xHis-3xFLAG-tagged NbNRC2 used in gel filtration assays was cloned in pICH86988 acceptor. Extracts were purified as described above and injected onto Superdex 200 Increase 10/300 GL column (GE Healthcare) connected to an AKTA FPLC system (GE Healthcare). The column was pre-equilibrated in buffer containing 25 mM Tris-HCL (pH 8), 500 mM NaCl, 5% glycerol, and 1 mM EDTA. Samples were centrifuged prior to loading. The sample was injected at a flow rate of 0.2 ml/min at 4˚C and 0.5 ml fractions were collected for analysis by SDS-PAGE.

## Negative staining

A total of 3 ml of purified NRC2 sample diluted to 0.3 mg/ml were applied to 400 mesh Copper grids (Agar Scientific) with continuous carbon that was glow discharged using a PELCO Easiglow (Ted Pella) for 30 s at 8 mA. After 30 s, the sample was blotted using Sartorius 292 filter paper and immediately washed with 2 consecutive drops of 100 ml distilled water each. After washing, 10 ml of 2% (w/v) uranyl acetate stain in $H_2O$ was applied. After 20 s, the excess was blotted off. Immediately after this, another 10 ml of 2% (w/v) uranyl acetate stain in $H_20$ was applied for 30 s and then blotted off. The grid was air-dried and examined in a FEI Talos F200C transmission electron microscope (Thermo Fisher Scientific), operated at 200 keV, equipped with a 4k OneView CMOS detector (Gatan), and 15 representative micrographs were recorded with a magnified pixel size 1.7Å (**Fig 1B**) each with a high particle density. Particles were auto-picked from these 15 micrographs using RELION 3.1 without any template. 2D-classification of the auto-picked particles (2,447 particles) from these images revealed particles resembling putative NRC2 as dimers (**Fig 1B**).

## Cryo-EM sample preparation and data collection

Schematic representation of the Cryo-EM structure determination workflow can be found in **S2 Fig**. C-flat grids (Protochips: 1.2/1.3 300 mesh) were used for Cryo-EM grid preparation, and 3 ml of 1.2 mg/ml of full-length NRC2 sample were applied 2 times over negatively glow discharged C-flat grids and coated with graphene oxide. The sample was applied inside the chamber of a Vitrobot Mark IV (Thermo Fisher Scientific) at 4˚C and 90% humidity and vitrified in liquid ethane. Without graphene oxide coating, no particles were observed in vitreous ice, so graphene-coated grids were used. The Cryo-EM images were collected on a FEI Titan Krios (Thermo Fisher Scientific) operated at 300 keV equipped with a K3 direct electron detector (Gatan) after inserting an energy filter with a slit width of 20 eV. Micrographs were

collected with a total dose of 50 $e^{-}/Å^2$, nominal magnification of 105 kx, giving a magnified pixel size of 0.828 Å. Images were collected as movies of 50 fractions with defocus values ranging from −1.5 μm to −2.7 μm with 2 exposures per hole. A total of 6,135 movies were collected for the image processing and 3D reconstruction using RELION 4.0 [46].

The micrograph movies were imported into RELION and subjected to drift correction using MotionCor2 [47] and CTFFIND4.0 was used for fitting of contrast transfer function and defocus estimation. The Laplacian-of-Gaussian auto-picker in RELION 4.0 was used for automatic reference-free particle picking [46]. The particles were extracted in 256-pixel box and subjected to several rounds of 2D classification with a circular mask of 150 Å. The 2D classes revealed a clear dimer with secondary structural features in many views. Clean 2D-classes were selected (664,305 particles) and were subjected to 3D classification using an ab initio 3D model generated by RELION. The best 3D class revealing the protein fold consisted of 229,347 particles and was subjected to 3D refinement using Refine3D using that 3D class as a reference with a circular mask of 180 Å. Following examination of the C1 refined map, a C2 symmetry was applied. After particle polishing, CTF refinement and postprocessing, the final average resolution was 3.9 Å as estimated by the Fourier shell correlation (FSC = 0.143). For post-processing, a solvent mask covering all protein volume was created and was extended by 8 pixels, to which a smooth soft-edge of 11 pixel were added. This mask was visually examined on how it covers the 3D-volume before post-processing to ensure that it is smooth and covers all the volume. The local resolution plot was calculated using PHENIX 3.0 [48]. The final map revealed distinct domain boundaries of the NRC2 protein fold with clear secondary structural features, helical twists, and individual beta strands and allowed us to place each NRC2 protomer and initiate model building at this resolution. A significant number of particle views are down the short dimension, owing to graphene oxide backing. The final map revealed the NB-ARC and LRR domains of the NRC2 molecule, with the N-terminal CC domain not resolved.

## Model building and refinement

The AlphaFold2 model of NRC2 monomer was divided into NB, ARC, and LRR domains. Each of these domains was fitted separately into the Cryo-EM density using UCSF ChimeraX as rigid body units [49]. Significantly, AlphaFold2 multimer was unable to predict the quaternary structure we observed experimentally. The model was then manually adjusted in COOT, combined and refined using the PHENIX real space refinement module and the fit of the atomic model to the features in the Cryo-EM map was evaluated visually (**S3 Fig**) [48,50]. This model was validated using PHENIX and MolProbity [48,51]. Figures were made using ChimeraX. The interface residues and the buried surface area were evaluated using PyMol and the PISA server [52,53]. A distance cut-off 6 Å is used to define residues at the interface to accommodate all short- and long-range interacting residues. These residues compose the 8 dimerization stretches indicated in **Fig 1C** and listed in **S2 Table**. These are the stretches carried for subsequent phylogenetic analyses. Further details on Cryo-EM data processing statistics can be found in **S1 Table**.

## In vitro NRC2 activation assays

To understand the impact of excess ATP on NRC2, 6 ml of 10 mM NbNRC2 were incubated with increasing concentration of ATP (0, 5, 10, and 15 mM, respectively) overnight in a 20 ml reaction volume, in presence of 5 mM $MgCl_2$. The reaction mixture was subjected to BN-PAGE analysis as described below. To test the role of $Rx^{NB}$-eGFP in NRC2 dimer activation in vitro, we expressed and purified both proteins separately from *nrc2/3/4* KO *N. benthamiana*. eGFP was included as a negative control for $Rx^{NB}$-eGFP. C-terminally FLAG-

tagged NbNRC2 and N-terminally FLAG-tagged $Rx^{NB}$-eGFP and eGFP were purified by FLAG affinity purification as described above, and 6 ml of 10 mM NbNRC2 were mixed in a final reaction volume of 20 ml with increasing amounts of $Rx^{NB}$-eGFP (1, 2, and 4 mM, respectively), in the presence of 5 mM ATP and 5 mM $MgCl_2$. Mixtures were incubated on ice overnight and then run on BN-PAGE as described below.

## BN-PAGE assays

For BN-PAGE, samples from in vitro studies described below were diluted as per the manufacturer's instructions by adding NativePAGE 5% G-250 sample additive, 4× Sample Buffer and water. After dilution, samples were loaded and run on Native PAGE 3% to 12% Bis-Tris gels alongside either NativeMark unstained protein standard (Invitrogen) or SERVA Native Marker (SERVA). The proteins were then transferred to polyvinylidene difluoride membranes using NuPAGE Transfer Buffer using a Trans-Blot Turbo Transfer System (Bio-Rad) as per the manufacturer's instructions. Proteins were fixed to the membranes by incubating with 8% acetic acid for 15 min, washed with water and left to dry. Membranes were subsequently re-activated with methanol to correctly visualise the unstained native protein marker. Membranes were immunoblotted as described above.

## Confocal microscopy

Three- to four-week-old plants were agroinfiltrated as described above with constructs of interest. The live cell confocal microscopy analyses were conducted 2 days after agroinfiltration. To image the infiltrated leaf tissue, they were excised using a size 4 cork borer, submerged in $dH_2O$, and live-mounted on glass slides. The imaging of the abaxial side of the leaf tissue was performed using a Leica STELLARIS 5 inverted confocal microscope equipped with a 63× water immersion objective lens. The laser excitations for GFP and mKOk tags were 488 nm and 514 nm, respectively. To prevent spectral mixing from different fluorescent tags when imaging samples with multiple tags, sequential scanning between lines was applied. All confocal images are single plane images.

## Bioinformatic and phylogenetic analyses

NLRtracker [12] output from 123 genome assemblies representing 38 species in 4 genera of the Solanaceae (nightshade) family [54,55] was imported in R, and 66,451 full-length NLR sequences were extracted; 23,872 NLR sequences with domain architectures of "CNL" and "CN" as determined by NLRtracker were retained. The NB-ARC domain (equivalent to NB domain and HD1-WHD domains in **Fig 1**) for these NLRs was also extracted from NLRtracker. Subsequently, the NB-ARC sequences of RefPlantNLR [12], tomato NRC helpers [56], and pepper NRC helpers [57] were added to the extracted NB-ARCs. The NB-ARC domain boundaries were retrieved from NLRtracker output and only sequences with NB-ARC sequences between 300 and 400 amino acids long were kept and truncated or unusually long NB-ARC sequences were discarded. This led to retaining 19,760 sequences. The resulting sequences were aligned using MAFFT v7.505 [--anysymbol] [58]. The alignment was then used to generate a phylogenetic tree using FastTree v2.1.11 [-lg] [59].

The NRC-network superclade containing 10,665 sequences (including helpers and sensors) was extracted from the CC-NLR phylogenetic tree by selecting the major branch containing both NRC reference helpers and sensors using Dendroscope v3.8.10 [Options > Advanced Options > Extract Subnetwork] [60]. The NRC superclade sequences were then realigned and used to create a new phylogenetic tree, from which the NRC helper clade was extracted using the same methods. The resulting 1,796 NRC helper sequences, without the reference

sequences, were deduplicated using CD-HIT v4.8.1 [-c 1.00] [61]. The deduplication was carried out to capture the highest diversity without introducing bias into the analysis due to over-represented sequences.

The resulting sequences were filtered based on length, retaining only sequences between 750 and 950 amino acids long. As a result, 993 sequences were kept. This decision was based on the length distribution within the NRC helper data and the length of the reference NRC sequences. The Geneious prime v2023.2.1 (https://www.geneious.com/) length graph feature was used for this purpose.

The NB-ARC domains from the remaining 993 sequences were combined with length filtered NB-ARCs (300 to 400 amino acids) of the reference NRC helpers from *N. benthamiana* (16 sequences), tomato (13 sequences), pepper (10 sequences), potato (42 sequences), and RefPlantNLR (14 sequences), resulting in 1,088 sequences in total, and aligned using MAFFT. The alignment was used to construct a new phylogenetic tree of deduplicated NRC helpers and reference sequences using FastTree. Finally, NRC helper subclades were extracted based on the presence of reference NRCs in well-supported major branches. Sequences that fell outside or between major clades were not included in the grouping of NRC helpers into subclades. The identified clades were then extracted using Dendroscope in the same way as before.

The full set of 1,092 NRC sequences consists of full-length sequences of the final set (993 sequences) and the unfiltered reference sequences of *N. benthamiana* (16 sequences), tomato (13 sequences), pepper (14 sequences), potato (42 sequences), and RefPlantNLR (14 sequences). These were also aligned using MAFFT [--localpair] to identify the dimer stretches in all NRC helpers. The alignment of the combined 1,092 sequences was trimmed to retain only important and well-aligned regions. This was accomplished using ClipKIT v2.0.1 [-m gappy] to remove sites with 90% gaps [62].

The dimerization stretches and conserved sequence motifs were mapped onto the alignment of all NRC helpers based on NbNRC2 and NLRtracker and extracted using the R scripts available at https://github.com/amiralito/NRC2Dimer [63]. Logo plots for stretches and sequence motifs were generated using the ggseqlogo R package [64].

## Shannon entropy analysis

Shannon Entropy values for all NRC helpers and each NRC clade separately were calculated using the Entropy R package [65] and visualised using the R scripts available at https://github.com/amiralito/NRC2Dimer [63].

## Identification of the unique residues in each NRC clade

To identify the unique residues in the NRC clades, we calculated the relative amino acid ratio among the NRC clades NRC2/3/4a/4b/$4_{other}$. We first divided the sequences into query and subject groups. Based on the trimmed alignment of NRC helpers, we calculated the amino acid frequency at each position in both query and subject groups. We then divided the amino acid frequency of the query group by that of the subject group at the same position. We only retained positions where one of the amino acid frequencies is more than 80% in the query group, and we regarded positions with a relative amino acid ratio of more than 50 as unique residues in the query clade. If an amino acid in the query group does not exist in the subject group, the ratio was output as infinite. The gaps were also ignored in this analysis. If all the query sequences had a gap at a position, the ratio was output as "NA." We iteratively calculated this relative amino acid ratio between an NRC clade and the other NRC clades, by alternating the query NRC clade. The scripts for this analysis are also available at https://github.com/amiralito/NRC2Dimer [63].

## Supporting information

**S1 Fig. NbNRC2 elutes as a dimer in analytical gel filtration assays.** Gel filtration assays with NbNRC2. C-terminally 6xHis-3xFLAG tagged NbNRC2 was expressed and purified from leaves of *nrc2/3/4* KO *N. benthamiana*. Purified protein was run on an S200 10/300 analytical column, and the estimated molecular weight of the NRC2 peak was calculated based on comparison of the elution volume to a protein standard curve ran on the same column. Elution volume (Ve) and molecular weight (Mw) in kDa are shown above the peak. A range of fractions below the peak, marked in green, were ran on SDS-PAGE and visualised using Coomassie Brilliant Blue staining (green panel). Approximate molecular weights (kDa) of the proteins are shown on the left of the green panel. The data underlying this figure can be found in S6 Data.
(EPS)

**S2 Fig. Cryo-EM image processing and 3D-reconstruction of NbNRC2 homodimers.** Schematic representation of cryo-EM data processing and 3D-reconstruction of resting state NRC2 homodimer. Detailed information on the data collection and processing as well as model building can be found in the pertinent Methods section and in S1 Table.
(EPS)

**S3 Fig. Representative map sections of NbNRC2 homodimer.** (**A**) Representative images taken from the map of the NbNRC2 homodimer showing the overall fit of the atomic model of NbNRC2 into the cryo-EM density map. **(B)** The extra density at NB domain which accounts for ADP is circled in red. (**C**) A small unaccounted globular density seen between WHD and LRR is shown in right bottom. This was modelled as IP6 in the recent SlNRC2 resting state structure [38]. (**D**) Closeup view of the post-processed map (left), showing helical grooves and bulk side chains at selected places along with the molecular model (right) fitted into it.
(EPS)

**S4 Fig. The helper NLR NbNRC2 forms a homodimer in planta.** (**A**) Overall molecular architecture and organisation of resting state NRC2 homodimer. Schematic of NbNRC2 domain architecture is shown above. Fit of NRC2 AlphaFold2 model into the cryo-EM density map is shown on the right. (**B**) Overall view of sharpened map by phenix_autosharp.
(EPS)

**S5 Fig. All NbNRC2 homodimerization interface mutants accumulate in planta.** NbNRC2, NbNRC3, and all NbNRC2 variants with mutations in the homodimerization interface were transiently expressed in *nrc2/3/4* KO *N. benthamiana*. Proteins were extracted 2 days post infiltration and run on SDS-PAGE assays and immunoblotted with the appropriate antisera labelled on the left. Approximate molecular weights (kDa) of the proteins are shown on the right.
(EPS)

**S6 Fig. NbNRC2$^{E243R}$ homodimerization interface mutant triggers effector-independent autoactive cell death.** Quantitative analysis of cell death assays shown in Fig 2A, carried out in leaves of *nrc2/3/4* KO *N. benthamiana*. HR cell death was scored based on a modified 0–7 scale [25] at 5–7 days post agroinfiltration. NbNRC2 + Rx + CP was included as a positive control for cell death. HR scores are presented as dot plots, where the size of each dot is proportional to the number of samples with the same score (Count). Results are based on 3 biological replicates. Statistical analysis was carried out in R, using the BestHR package [66]. "a" or "b" on top of each treatment indicate statistically significant differences compared to the negative control NbNRC2. The data underlying this figure can be found in S7 Data.
(EPS)

**S7 Fig. NbNRC2 homodimerization interface mutants triggers effector-independent cell death when co-expressed with Rx.** Quantitative analysis of cell death assays shown in Fig 2A, carried out in leaves of *nrc2/3/4* KO *N. benthamiana*. Top panel shows cell death HR cell death was scored based on a modified 0–7 scale [25] at 5–7 days post agroinfiltration. Top panel features all NbNRC2 homodimerization interface mutants co-expressed with Rx. Top panel features all NbNRC2 homodimerization interface mutants co-expressed with Rx and with CP. In both cases, NbNRC2 + Rx and NbNRC2 + Rx + CP are included as negative and positive controls for cell death, respectively. HR scores are presented as dot plots, where the size of each dot is proportional to the number of samples with the same score (Count). Results are based on 3 biological replicates. Statistical analysis was carried out in R, using the BestHR package [66]. "a" on top of each treatment indicate statistically significant differences, compared to the negative control NbNRC2 + Rx. The data underlying this figure can be found in S8 Data.
(EPS)

**S8 Fig. The nucleotide-binding domain of the sensor NLR Rx converts the NRC2 helper homodimer into a higher order oligomer in vitro.** (**A**) BN-PAGE assay with NRC2 incubated with ATP in vitro. Purified NbNRC2-FLAG (5 mM) was incubated overnight with no ATP or with increasing amounts of ATP (5, 10, or 15 mM). The experiment was repeated 3 times with similar results. (**B**) BN-PAGE assay with NRC2 incubated with $Rx^{NB}$ in vitro. Purified NbNRC2-FLAG (5 mM) was incubated overnight with increasing amounts of purified FLAG-$Rx^{NB}$-eGFP (0, 1, 2, and 4 mM, respectively). eGFP (4 mM) was included as a negative control. The experiment was performed 3 times with similar results. (**A, B**) In vitro reactions were run in parallel on native and denaturing PAGE and immunoblotted with the antisera labelled below each blot. Approximate molecular weights (in kDa) of the proteins are shown on the right. Red asterisk indicates signal at a molecular weight matching the previously reported NRC2 resistosome-like oligomer. (**C**) SDS-PAGE assays accompanying BN-PAGE assays. Affinity-purified proteins were run on SDS-PAGE assays and immunoblotted with the appropriate antisera labelled on the left. Approximate molecular weights (kDa) of the proteins are shown on the right.
(EPS)

**S9 Fig. NRC sequences form a well-supported monophyletic clade within the CC-NLR and NRC superclade phylogenetic trees.** (**A**) NRC superclade including NRC helpers, Rx-type sensors, and SD-type sensors form a distinct, well-supported clade in a phylogenetic tree of 19,760 CC-NLRs from the Solanaceae family (**S9 and S10 Data**). (**B**) NRCs are monophyletic and part of the same well-supported clade inside the NRC superclade phylogenetic tree (**S11 Data**). (**C**) NRC sequences are divided into 15 distinct phylogenetic subclades based on the presence of reference NRC sequences (**S12 and S13 Data**). Numbers next to the major branches indicate bootstrap values.
(EPS)

**S10 Fig. Sequence motif and Shannon entropy plots for 1,092 NRC sequences retrieved from 123 genome assemblies from 4 genera in the Solanaceae family.** Sequence motif and Shannon entropy plots for the MADA, P-loop, MHD motifs, and 8 dimerization stretches of 1,092 NRC sequences grouped into NRC clades based on phylogenetic relationships. The number of sequences and the distribution across the 4 genera within each clade are indicated on the right (S3 and S4 Data).
(EPS)

**S11 Fig. Shannon entropy plots of full-length proteins calculated across all 1,092 NRC sequences and within each individual NRC clade.** The dimer stretches 1 and 2 are coloured by green and yellow, respectively. MADA, P-loop, and MHD motif are coloured by grey. Shannon entropy score of 1.5, indicated by the dotted line, was established as a threshold to distinguish between highly variable (>1.5 bits) and non-highly variable (<1.5 bits) amino acids, as established previously (31) (**S3 and S4 Data**).
(EPS)

**S12 Fig. Contrasting mechanisms of activation between ZAR1 and the helper NLR NbNRC2.** The figure depicts the working model for activation of NRC2 homodimers. Unlike the functional singleton ZAR1, the helper NLR NRC2 exists as an autoinhibited homodimer in its resting form. NbNRC2 carries unique polymorphisms at the interface between its 2 protomers and exclusively associates with itself without hetero-dimerising with its NRC paralogs NbNRC3 or NbNRC4. Activation of upstream sensors and conditional exposure of their nucleotide-binding (NB) domains results in conversion of the NbNRC2 homodimer into a high molecular weight resistosome, presumably via homodimer dissociation into a putative primed monomer which subsequently oligomerizes. Like those observed for activated NRC4, the NRC2 oligomers may be hexameric in nature, which also differs from the pentameric complexes observed for activated ZAR1.
(EPS)

**S1 Table. Cryo-EM data collection, refinement, and validation statistics.**
(DOCX)

**S2 Table. Interface residues at 6 Å cut-off distance and their definition as amino acid stretches.**
(DOCX)

**S1 Movie. 3D view of NRC2 homodimer reconstructed from Cryo-EM micrographs (as separate file).** NB-ARC domain is shown in grey. LRR domain is shown in blue.
(MP4)

**S1 Data. Sequence alignment of NbNRC2, NbNRC3, NbNRC4, and NbZAR1 (as separate file).**
(FASTA)

**S2 Data. Genome metadata used in the phylogenetic analyses (as separate file).**
(XLSX)

**S3 Data. Curated 1,092 NRC sequences in FASTA format (as separate file).**
(FASTA)

**S4 Data. Entropy values for 1,092 NRC sequences and each NRC clade for the analysed dimerization stretches, sequences motifs, and the full-length proteins (as separate file).**
(XLSX)

**S5 Data. Frequencies of each amino acid within the NRC2, NRC3, NRC4other, NRC4a, and NRC4b clades compared to other NRC clades (as separate file).**
(XLSX)

**S6 Data. Numerical data underlying analytical gel filtration trace in S1 Fig.**
(XLS)

**S7 Data. Numerical data underlying cell death quantification in S6 Fig.**
(XLSX)

**S8 Data. Numerical data underlying cell death quantification in S7 Fig.**
(XLSX)

**S9 Data. List of CC-type NLR sequences and associated metadata (as separate file).**
(XLSX)

**S10 Data. Extracted NB-ARC (NBD and HD1-WHD) domain sequences of CC-type and reference NLRs (as separate file).**
(FASTA)

**S11 Data. NB-ARC (NBD and HD1-WHD) domain sequences of NRC superclade and reference NLRs (as separate file).**
(FASTA)

**S12 Data. NB-ARC (NBD and HD1-WHD) domain sequences of curated NRC sequences (as separate file).**
(FASTA)

**S13 Data. NB-ARC (NBD and HD1-WHD) domain sequences of reference NRC sequences from *S. lycopersicum*, *S. tuberosum*, *N. benthamiana*, *C. annuum*, and RefPlantNLR (as separate file).**
(FASTA)

**S1 Raw Images. Uncropped blots and gel scans underlying all figures in the manuscript.**
(PDF)

## Acknowledgments

We are very thankful to D. Lüdke (The Sainsbury Laboratory, Norwich, UK) for valuable discussions and critical reading of this manuscript. We thank C. McClune, (Stanford, California, USA) for useful discussions. We thank J. Richardson (John Innes Centre, Norwich, UK) for support and excellent maintenance of John Innes Centre Bioimaging facility. Negative stain EM data for this investigation were collected at JIC Bioimaging facility, which is supported by the Biotechnology and Biological Sciences Research Council (BB/CCG2240/1). We thank N. Lukoyanova (Birkbeck, University of London, London, UK) for support with Cryo-EM imaging. Cryo-EM data for this investigation were collected at ISMB EM facility, which is supported by the Wellcome Trust (202679/Z/16/Z and 206166/Z/17/Z). SK and MPC thank F. Sinatra and L. Messi for inspiration. We thank all members of the TSL Support Services for their invaluable assistance.

## Author Contributions

**Conceptualization:** Muniyandi Selvaraj, AmirAli Toghani, Chih-Hang Wu, Sophien Kamoun, Mauricio P. Contreras.

**Data curation:** Muniyandi Selvaraj, AmirAli Toghani, Hsuan Pai, Mauricio P. Contreras.

**Formal analysis:** Muniyandi Selvaraj, AmirAli Toghani, Mauricio P. Contreras.

**Funding acquisition:** Tolga O. Bozkurt, Sophien Kamoun.

**Investigation:** Muniyandi Selvaraj, AmirAli Toghani, Hsuan Pai, Yu Sugihara, Jiorgos Kourelis, Enoch Lok Him Yuen, Tarhan Ibrahim, Rongrong Xie, Abbas Maqbool,

Juan Carlos De la Concepcion, Lida Derevnina, David M. Lawson, Chih-Hang Wu, Mauricio P. Contreras.

**Methodology:** Muniyandi Selvaraj, AmirAli Toghani, Hsuan Pai, Yu Sugihara, Jiorgos Kourelis, Enoch Lok Him Yuen, He Zhao, Rongrong Xie, Abbas Maqbool, Juan Carlos De la Concepcion, Benjamin Petre, Mauricio P. Contreras.

**Project administration:** Muniyandi Selvaraj, Sophien Kamoun, Mauricio P. Contreras.

**Supervision:** Mark J. Banfield, Sophien Kamoun, Mauricio P. Contreras.

**Validation:** Muniyandi Selvaraj, Hsuan Pai, Mauricio P. Contreras.

**Visualization:** Muniyandi Selvaraj, AmirAli Toghani, Hsuan Pai, Enoch Lok Him Yuen, Mauricio P. Contreras.

**Writing – original draft:** Muniyandi Selvaraj, AmirAli Toghani, Yu Sugihara, Sophien Kamoun, Mauricio P. Contreras.

**Writing – review & editing:** Muniyandi Selvaraj, Hsuan Pai, Yu Sugihara, Jiorgos Kourelis, Enoch Lok Him Yuen, Tarhan Ibrahim, He Zhao, Abbas Maqbool, Juan Carlos De la Concepcion, Mark J. Banfield, Lida Derevnina, Benjamin Petre, David M. Lawson, Tolga O. Bozkurt, Chih-Hang Wu, Sophien Kamoun, Mauricio P. Contreras.

## References


1. Chou W-C, Jha S, Linhoff MW, Ting JP-Y. The NLR gene family: from discovery to present day. Nat Rev Immunol. 2023:1–20.
2. Duxbury Z, Wu C-h, Ding P. A comparative overview of the intracellular guardians of plants and animals: NLRs in innate immunity and beyond. Annu Rev Plant Biol. 2021; 72:155–184.
3. Contreras MP, Lüdke D, Pai H, Toghani A, Kamoun S. NLR receptors in plant immunity: making sense of the alphabet soup. EMBO Rep. 2023:e57495. https://doi.org/10.15252/embr.202357495 PMID: 37602936
4. Förderer A, Kourelis J. NLR immune receptors: structure and function in plant disease resistance. Biochem Soc Trans. 2023; 51(4):1473–1483. https://doi.org/10.1042/BST20221087 PMID: 37602488
5. Xiao L, Magupalli VG, Wu H. Cryo-EM structures of the active NLRP3 inflammasome disc. Nature. 2023; 613(7944):595–600. https://doi.org/10.1038/s41586-022-05570-8 PMID: 36442502
6. Zhang L, Chen S, Ruan J, Wu J, Tong AB, Yin Q, et al. Cryo-EM structure of the activated NAIP2-NLRC4 inflammasome reveals nucleated polymerization. Science. 2015; 350(6259):404–409. https://doi.org/10.1126/science.aac5789 PMID: 26449474
7. Förderer A, Li E, Lawson AW, Deng Y-n, Sun Y, Logemann E, et al. A wheat resistosome defines common principles of immune receptor channels. Nature. 2022; 610(7932):532–539. https://doi.org/10.1038/s41586-022-05231-w PMID: 36163289
8. Gao LA, Wilkinson ME, Strecker J, Makarova KS, Macrae RK, Koonin EV, et al. Prokaryotic innate immunity through pattern recognition of conserved viral proteins. Science. 2022; 377(6607):eabm4096. https://doi.org/10.1126/science.abm4096 PMID: 35951700
9. Wang J, Hu M, Wang J, Qi J, Han Z, Wang G, et al. Reconstitution and structure of a plant NLR resistosome conferring immunity. Science. 2019; 364(6435):eaav5870. https://doi.org/10.1126/science.aav5870 PMID: 30948527
10. Martin R, Qi T, Zhang H, Liu F, King M, Toth C, et al. Structure of the activated ROQ1 resistosome directly recognizing the pathogen effector XopQ. Science. 2020; 370(6521):eabd9993. https://doi.org/10.1126/science.abd9993 PMID: 33273074
11. Ma S, Lapin D, Liu L, Sun Y, Song W, Zhang X, et al. Direct pathogen-induced assembly of an NLR immune receptor complex to form a holoenzyme. Science. 2020; 370(6521):eabe3069. https://doi.org/10.1126/science.abe3069 PMID: 33273071
12. Kourelis J, Sakai T, Adachi H, Kamoun S. RefPlantNLR is a comprehensive collection of experimentally validated plant disease resistance proteins from the NLR family. PLoS Biol. 2021; 19(10):e3001124. https://doi.org/10.1371/journal.pbio.3001124 PMID: 34669691

13. Wang J, Wang J, Hu M, Wu S, Qi J, Wang G, et al. Ligand-triggered allosteric ADP release primes a plant NLR complex. Science. 2019; 364(6435):eaav5868. https://doi.org/10.1126/science.aav5868 PMID: 30948526
14. Bi G, Su M, Li N, Liang Y, Dang S, Xu J, et al. The ZAR1 resistosome is a calcium-permeable channel triggering plant immune signaling. Cell. 2021; 184(13):3528–3541. PubMed PMID: e12. https://doi.org/10.1016/j.cell.2021.05.003 PMID: 33984278
15. Duggan C, Moratto E, Savage Z, Hamilton E, Adachi H, Wu C-H, et al. Dynamic localization of a helper NLR at the plant–pathogen interface underpins pathogen recognition. Proc Natl Acad Sci U S A. 2021; 118(34):e2104997118. https://doi.org/10.1073/pnas.2104997118 PMID: 34417294
16. Contreras MP, Pai H, Tumtas Y, Duggan C, Yuen ELH, Cruces AV, et al. Sensor NLR immune proteins activate oligomerization of their NRC helpers in response to plant pathogens. EMBO J. 2023; 42(5): e111519. https://doi.org/10.15252/embj.2022111519 PMID: 36579501
17. Madhuprakash J, Toghani A, Contreras MP, Posbeyikian A, Richardson J, Kourelis J, et al. A disease resistance protein triggers oligomerization of its NLR helper into a hexameric resistosome to mediate innate immunity. bioRxiv. 2024: 2024.06. 18.599586.
18. Liu F, Yang Z, Wang C, You Z, Martin R, Qiao W, et al. Activation of the helper NRC4 immune receptor forms a hexameric resistosome. Cell. 2024. https://doi.org/10.1016/j.cell.2024.07.013 PMID: 39094568
19. Adachi H, Derevnina L, Kamoun S. NLR singletons, pairs, and networks: evolution, assembly, and regulation of the intracellular immunoreceptor circuitry of plants. Curr Opin Plant Biol. 2019; 50:121–131. https://doi.org/10.1016/j.pbi.2019.04.007 PMID: 31154077
20. Wu C-H, Derevnina L, Kamoun S. Receptor networks underpin plant immunity. Science. 2018; 360 (6395):1300–1301. https://doi.org/10.1126/science.aat2623 PMID: 29930125
21. Wu C-H, Abd-El-Haliem A, Bozkurt TO, Belhaj K, Terauchi R, Vossen JH, et al. NLR network mediates immunity to diverse plant pathogens. Proc Natl Acad Sci U S A. 2017; 114(30):8113–8118. https://doi.org/10.1073/pnas.1702041114 PMID: 28698366
22. Contreras MP, Pai H, Thompson R, Marchal C, Claeys J, Adachi H, et al. The nucleotide-binding domain of NRC-dependent disease resistance proteins is sufficient to activate downstream helper NLR oligomerization and immune signaling. New Phytol. 2024. https://doi.org/10.1111/nph.19818 PMID: 38757730
23. Ahn HK, Lin X, Olave-Achury AC, Derevnina L, Contreras MP, Kourelis J, et al. Effector-dependent activation and oligomerization of plant NRC class helper NLRs by sensor NLR immune receptors Rpi-amr3 and Rpi-amr1. EMBO J. 2023:e111484. https://doi.org/10.15252/embj.2022111484 PMID: 36592032
24. Contreras MP, Pai H, Selvaraj M, Toghani A, Lawson DM, Tumtas Y, et al. Resurrection of plant disease resistance proteins via helper NLR bioengineering. Sci Adv. 2023; 9(18):eadg3861. doi: https://doi.org/10.1126/sciadv.adg3861 PMID: 37134163
25. Segretin ME, Pais M, Franceschetti M, Chaparro-Garcia A, Bos JI, Banfield MJ, et al. Single amino acid mutations in the potato immune receptor R3a expand response to Phytophthora effectors. Mol Plant Microbe Interact. 2014; 27(7):624–637. https://doi.org/10.1094/MPMI-02-14-0040-R PMID: 24678835
26. Huang S, Jia A, Ma S, Sun Y, Chang X, Han Z, et al. NLR signaling in plants: From resistosomes to second messengers. Trends Biochem Sci. 2023. https://doi.org/10.1016/j.tibs.2023.06.002 PMID: 37394345
27. Rairdan GJ, Collier SM, Sacco MA, Baldwin TT, Boettrich T, Moffett P. The coiled-coil and nucleotide binding domains of the potato Rx disease resistance protein function in pathogen recognition and signaling. Plant Cell. 2008; 20(3):739–751. https://doi.org/10.1105/tpc.107.056036 PMID: 18344282
28. Zhang N, Gan J, Carneal L, González-Tobón J, Filiatrault M, Martin GB. Helper NLRs Nrc2 and Nrc3 act codependently with Prf/Pto and activate MAPK signaling to induce immunity in tomato. Plant J. 2023. https://doi.org/10.1111/tpj.16502 PMID: 37844152
29. Capra EJ, Laub MT. Evolution of two-component signal transduction systems. Annu Rev Microbiol. 2012; 66:325–347. https://doi.org/10.1146/annurev-micro-092611-150039 PMID: 22746333
30. Pereira-Leal JB, Levy ED, Kamp C, Teichmann SA. Evolution of protein complexes by duplication of homomeric interactions. Genome Biol. 2007; 8(4):1–12. https://doi.org/10.1186/gb-2007-8-4-r51 PMID: 17411433
31. Prigozhin DM, Krasileva KV. Analysis of intraspecies diversity reveals a subset of highly variable plant immune receptors and predicts their binding sites. Plant Cell. 2021; 33(4):998–1015. https://doi.org/10.1093/plcell/koab013 PMID: 33561286
32. Adachi H, Sakai T, Kourelis J, Pai H, Gonzalez Hernandez JL, Maqbool A, et al. Jurassic NLR: conserved and dynamic evolutionary features of the atypically ancient immune receptor ZAR1. Plant Cell. 2023;In press:2020. 10. 12.333484.
33. Gong Z, Qi J, Hu M, Bi G, Zhou J-M, Han G-Z. The origin and evolution of a plant resistosome. Plant Cell. 2022; 34(5):1600–1620. https://doi.org/10.1093/plcell/koac053 PMID: 35166827

34. Goh F-J, Huang C-Y, Derevnina L, Wu C-H. NRC immune receptor networks show diversified hierarchical genetic architecture across plant lineages. Plant Cell. 2024; 36(9):3399–3418. https://doi.org/10.1093/plcell/koae179 PMID: 38922300

35. Sakai T, Contreras MP, Martinez-Anaya C, Lüdke D, Kamoun S, Wu C-H, et al. The NRC0 gene cluster of sensor and helper NLR immune receptors is functionally conserved across asterid plants. Plant Cell. 2024; 36(9):3344–3361. https://doi.org/10.1093/plcell/koae154 PMID: 38833594

36. El Kasmi F, Chung E-H, Anderson RG, Li J, Wan L, Eitas TK, et al. Signaling from the plasma-membrane localized plant immune receptor RPM1 requires self-association of the full-length protein. Proc Natl Acad Sci U S A. 2017; 114(35):E7385–E7394. https://doi.org/10.1073/pnas.1708288114 PMID: 28808003

37. Tran DT, Chung E-H, Habring-Müller A, Demar M, Schwab R, Dangl JL, et al. Activation of a plant NLR complex through heteromeric association with an autoimmune risk variant of another NLR. Curr Biol. 2017; 27(8):1148–1160. https://doi.org/10.1016/j.cub.2017.03.018 PMID: 28416116

38. Ma S, An C, Lawson AW, Cao Y, Sun Y, Tan EYJ, et al. Oligomerization-mediated autoinhibition and cofactor binding of a plant NLR. Nature. 2024;1–3. https://doi.org/10.1038/s41586-024-07668-7 PMID: 38866053

39. Jones JD, Vance RE, Dangl JL. Intracellular innate immune surveillance devices in plants and animals. Science. 2016; 354(6316):aaf6395. https://doi.org/10.1126/science.aaf6395 PMID: 27934708

40. Baggs E, Dagdas G, Krasileva KV. NLR diversity, helpers and integrated domains: making sense of the NLR IDentity. Curr Opin Plant Biol. 2017; 38:59–67. https://doi.org/10.1016/j.pbi.2017.04.012 PMID: 28494248

41. Derevnina L, Contreras MP, Adachi H, Upson J, Vergara Cruces A, Xie R, et al. Plant pathogens convergently evolved to counteract redundant nodes of an NLR immune receptor network. PLoS Biol. 2021; 19(8):e3001136. https://doi.org/10.1371/journal.pbio.3001136 PMID: 34424903

42. Wang M-Y, Chen J-B, Wu R, Guo H-L, Chen Y, Li Z-J, et al. The plant immune receptor SNC1 monitors helper NLRs targeted by a bacterial effector. Cell Host Microbe. 2023; 31(11):1792–1803. e7. https://doi.org/10.1016/j.chom.2023.10.006 PMID: 37944492

43. Witek K, Lin X, Karki HS, Jupe F, Witek AI, Steuernagel B, et al. A complex resistance locus in Solanum americanum recognizes a conserved Phytophthora effector. Nat Plants. 2021; 7(2):198–208. https://doi.org/10.1038/s41477-021-00854-9 PMID: 33574576

44. Engler C, Youles M, Gruetzner R, Ehnert T-M, Werner S, Jones JD, et al. A golden gate modular cloning toolbox for plants. ACS Synth Biol. 2014; 3(11):839–843. https://doi.org/10.1021/sb4001504 PMID: 24933124

45. Weber E, Engler C, Gruetzner R, Werner S, Marillonnet S. A modular cloning system for standardized assembly of multigene constructs. PLoS ONE. 2011; 6(2):e16765. https://doi.org/10.1371/journal.pone.0016765 PMID: 21364738

46. Kimanius D, Dong L, Sharov G, Nakane T, Scheres SH. New tools for automated cryo-EM single-particle analysis in RELION-4.0. Biochem J. 2021; 478(24):4169–4185. https://doi.org/10.1042/BCJ20210708 PMID: 34783343

47. Zheng SQ, Palovcak E, Armache J-P, Verba KA, Cheng Y, Agard DA. MotionCor2: anisotropic correction of beam-induced motion for improved cryo-electron microscopy. Nat Methods. 2017; 14(4):331–332. https://doi.org/10.1038/nmeth.4193 PMID: 28250466

48. Afonine PV, Poon BK, Read RJ, Sobolev OV, Terwilliger TC, Urzhumtsev A, et al. Real-space refinement in PHENIX for cryo-EM and crystallography. Acta Crystallogr D Struct Biol. 2018; 74(6):531–544. https://doi.org/10.1107/S2059798318006551 PMID: 29872004

49. Pettersen EF, Goddard TD, Huang CC, Meng EC, Couch GS, Croll TI, et al. UCSF ChimeraX: Structure visualization for researchers, educators, and developers. Protein Sci. 2021; 30(1):70–82. https://doi.org/10.1002/pro.3943 PMID: 32881101

50. Emsley P, Lohkamp B, Scott WG, Cowtan K. Features and development of Coot. Acta Crystallogr D Biol Crystallogr. 2010; 66(4):486–501. https://doi.org/10.1107/S0907444910007493 PMID: 20383002

51. Williams CJ, Headd JJ, Moriarty NW, Prisant MG, Videau LL, Deis LN, et al. MolProbity: More and better reference data for improved all-atom structure validation. Protein Sci. 2018; 27(1):293–315. https://doi.org/10.1002/pro.3330 PMID: 29067766

52. DeLano WL. Pymol: An open-source molecular graphics tool. CCP4 Newsl Protein Crystallogr. 2002; 40(1):82–92.

53. Krissinel E, Henrick K. Inference of macromolecular assemblies from crystalline state. J Mol Biol. 2007; 372(3):774–797. https://doi.org/10.1016/j.jmb.2007.05.022 PMID: 17681537

54. Torres Ascurra YC, Zhang L, Toghani A, Hua C, Rangegowda NJ, Posbeyikian A, et al. Functional diversification of a wild potato immune receptor at its center of origin. Science. 2023; 381(6660):891–897. https://doi.org/10.1126/science.adg5261 PMID: 37616352

55. Sugihara Y, Toghani A, Kamoun S, Kourelis J. NLRome dataset from 124 genomes of plants in the Solanaceae family. Zenodo. 2023. https://doi.org/10.5281/zenodo.10354350

56. Adachi H, Sakai T, Harant A, Pai H, Honda K, Toghani A, et al. An atypical NLR protein modulates the NRC immune receptor network in Nicotiana benthamiana. PLoS Genet. 2023; 19(1):e1010500. https://doi.org/10.1371/journal.pgen.1010500 PMID: 36656829

57. Oh S, Kim S, Park HJ, Kim MS, Seo MK, Wu CH, et al. Nucleotide-binding leucine-rich repeat network underlies nonhost resistance of pepper against the Irish potato famine pathogen Phytophthora infestans. Plant Biotechnol J. 2023. https://doi.org/10.1111/pbi.14039 PMID: 36912620

58. Katoh K, Standley DM. MAFFT multiple sequence alignment software version 7: improvements in performance and usability. Mol Biol Evol. 2013; 30(4):772–780. https://doi.org/10.1093/molbev/mst010 PMID: 23329690

59. Price MN, Dehal PS, Arkin AP. FastTree: computing large minimum evolution trees with profiles instead of a distance matrix. Mol Biol Evol. 2009; 26(7):1641–1650. https://doi.org/10.1093/molbev/msp077 PMID: 19377059

60. Huson DH, Scornavacca C. Software for Systematics and Evolution. Syst Biol. 2012; 61(6):1061–1067.

61. Fu L, Niu B, Zhu Z, Wu S, Li W. CD-HIT: accelerated for clustering the next-generation sequencing data. Bioinformatics. 2012; 28(23):3150–3152. https://doi.org/10.1093/bioinformatics/bts565 PMID: 23060610

62. Steenwyk JL, Buida TJ III, Li Y, Shen X-X, Rokas A. ClipKIT: a multiple sequence alignment trimming software for accurate phylogenomic inference. PLoS Biol. 2020; 18(12):e3001007. https://doi.org/10.1371/journal.pbio.3001007 PMID: 33264284

63. Toghani A, Sugihara Y. amiralito/NRC2Dimer: Repository Release (v1.0.1). Zenodo. 2024. https://doi.org/10.5281/zenodo.13362063

64. Wagih O. ggseqlogo: a versatile R package for drawing sequence logos. Bioinformatics. 2017; 33 (22):3645–3647. https://doi.org/10.1093/bioinformatics/btx469 PMID: 29036507

65. Hausser J, Strimmer K. Entropy inference and the James-Stein estimator, with application to nonlinear gene association networks. J Mach Learn Res. 2009; 10(7).

66. MacLean D. Besthr. Zenodo. 2019.

CORRECTED 27 NOVEMBER 2024; SEE LAST PAGE

Check for updates

SCIENCE ADVANCES | RESEARCH ARTICLE

IMMUNOLOGY

# A disease resistance protein triggers oligomerization of its NLR helper into a hexameric resistosome to mediate innate immunity

**Jogi Madhuprakash[1]*, AmirAli Toghani[1], Mauricio P. Contreras[1], Andres Posbeyikian[1], Jake Richardson[2], Jiorgos Kourelis[1], Tolga O. Bozkurt[3], Michael W. Webster[4]*, Sophien Kamoun[1]***

Copyright © 2024 The Authors, some rights reserved; exclusive licensee American Association for the Advancement of Science. No claim to original U.S. Government Works. Distributed under a Creative Commons Attribution License 4.0 (CC BY).

**NRCs are essential helper NLR (nucleotide-binding domain and leucine-rich repeat) proteins that execute immune responses triggered by sensor NLRs. The resting state of NbNRC2 was recently shown to be a homodimer, but the sensor-activated state remains unclear. Using cryo-EM, we determined the structure of sensor-activated NbNRC2, which forms a hexameric inflammasome-like resistosome. Mutagenesis of the oligomerization interface abolished immune signaling, confirming the functional significance of the NbNRC2 resistosome. Comparative structural analyses between the resting state homodimer and sensor-activated homohexamer revealed substantial rearrangements, providing insights into NLR activation mechanisms. Furthermore, structural comparisons between NbNRC2 hexamer and previously reported CC-NLR pentameric assemblies revealed features allowing an additional protomer integration. Using the NbNRC2 hexamer structure, we assessed the recently released AlphaFold 3 for predicting activated CC-NLR oligomers, revealing high-confidence modeling of NbNRC2 and other CC-NLR amino-terminal α1 helices, a region proven difficult to resolve structurally. Overall, our work sheds light on NLR activation mechanisms and expands understanding of NLR structural diversity.**

## INTRODUCTION

Nucleotide-binding and leucine-rich repeat (NLR) intracellular immune receptors are a key component of innate immunity across the tree of life (*1*–*4*). Upon recognition of pathogen-derived ligands, they initiate an array of immune responses to counteract infection. In plants, NLRs can be activated by pathogen-secreted virulence proteins, termed effectors, which pathogens deliver into host cells to modulate host physiology (*3*). A common theme for NLR activation in eukaryotes and prokaryotes is their oligomerization into higher-order immune complexes, such as plant resistosomes or mammalian and bacterial inflammasomes. These complexes initiate immune signaling via diverse mechanisms, often leading to different forms of programmed cell death (*1*, *5*). Some NLRs can function as single units, termed "singletons," with one NLR protein mediating both ligand/effector perception and subsequent downstream signaling and cell death execution (*6*). However, NLRs can also function as receptor pairs or in higher-order configurations termed NLR networks. In these cases, the paired NLRs have subfunctionalized: One NLR acts as a pathogen sensor that activates another NLR, known as helper, which mediates immune activation and disease resistance (*3*, *7*). While substantial progress has been made in recent years regarding the biochemical mechanisms of NLR activation, our understanding of the activation dynamics of paired and networked NLRs remains fragmentary. In particular, our knowledge of the structural biology of helper NLRs is still limited.

NLRs typically exhibit a tripartite domain architecture consisting of an N-terminal signaling domain, a central nucleotide-binding (NB) and oligomerization module, and C-terminal superstructure-forming repeats (*5*). In plant NLRs, the central module is termed NB-ARC (NB adaptor shared by APAF-1, plant R proteins, and CED-4) and is a defining feature of this protein family (*8*). The NB-ARC module can be subdivided into NB domain, helical domain 1 (HD1), and winged-helix domain (WHD) (*8*). The NB-ARC domain acts as a molecular switch, mediating conformational changes required for transitioning from resting to activated forms (*5*). In contrast, the N-terminal domain of plant NLRs is variable; it can broadly be used to classify these receptors into distinct groups, which tend to cluster together in NB-ARC–based phylogenetic analyses. In plants, coiled-coil (CC)–type and Toll–interleukin-1 receptor (TIR)–type N-terminal domains are the most widespread N-terminal domains (*5*, *8*).

Two plant CC-NLR inflammasome-like structures (resistosomes)—AtZAR1 and TmSr35 from *Arabidopsis* and wheat, respectively (*9*–*11*)—have been reported to date to be pentameric oligomers. Once activated, these pentameric CC-NLR resistosomes insert into the plasma membrane, mediating $Ca^{2+}$ influx, immune signaling, and programmed cell death (*10*, *12*). Both activated CC-NLR structures correspond to singleton NLRs that do not require other NLRs to function. Activated TIR-type sensor NLRs, such as Roq1 and RPP1, have been reported to assemble into tetrameric resistosomes that activate downstream helper NLRs via small-molecule production (*13*, *14*). In contrast, no structures of paired CC-type sensor NLRs or sensor-activated helper NLRs have been reported to date. Although activated helper NLRs have recently been reported to oligomerize in planta, whether they form tetrameric, pentameric, or alternative assemblies is unknown (*15*–*18*).

Plant CC-NLRs exhibit diverse N termini that match the phylogeny of the NB-ARC domain, indicating that they have a deep evolutionary origin (*3*, *8*). To date, two N-terminal CC domains have been defined in angiosperms besides the typical CC domain: RESISTANCE TO POWDERY MILDEW 8 (RPW8)–type ($CC_R$) and G10-type CC ($CC_{G10}$) (*3*, *8*). In addition, about 20% or so of the typical CC-type NLRs belong to the wider family of MADA-CC-NLRs, defined by a

[1]The Sainsbury Laboratory, University of East Anglia, Norwich Research Park, Norwich, UK. [2]Bioimaging Facility, John Innes Centre, Norwich Research Park, Norwich, UK. [3]Department of Life Sciences, Imperial College, London, UK. [4]Department of Biochemistry and Metabolism, John Innes Centre, Norwich Research Park, Norwich, UK.
*Corresponding author. Email: Madhu.Jogi@tsl.ac.uk (J.M.); Michael.Webster@jic.ac.uk (M.W.W.); Sophien.Kamoun@tsl.ac.uk (S.K.)

Downloaded from https://www.science.org on August 02, 2025

consensus sequence of their N-terminal α1 helices that assemble into the funnel-like membrane pore (*19*). Both AtZAR1 and TmSr35 can be generally classified as MADA-CC-NLRs. Overall, the N-terminal domain is thought to dictate the types of downstream signaling pathways and activities that take place following NLR activation. However, the structural diversity of these various N-terminal domains and whether they all activate into oligomeric resistosomes is unclear.

Asterids—the largest group of flowering plants—have a complex immune receptor network composed of a multitude of sensor CC-NLRs that can signal redundantly via downstream helper MADA-type CC-NLRs, the NRCs (NLRs required for cell death) (*20*, *21*). Sensor NLRs in this network include a number of agronomically important disease resistance (R) proteins that function against a variety of microbial pathogens and metazoan pests (*21*, *22*). Previously, our group proposed an activation-and-release model for sensor-helper pairs in the NRC network (*16*, *17*). In this model, effector perception by sensor NLRs leads to conformational changes that expose the central NB domain and enable it to activate downstream NRC helpers (*23*). This ultimately leads to NRC activation and immune signaling via the assembly of oligomeric resistosomes (*15*–*17*, *23*). More recently, our group also reported the structure of the resting state of the helper NLR NbNRC2 from *Nicotiana benthamiana* (NbNRC2), which accumulates as a homodimer before activation (*24*). NbNRC2 activation by the virus R protein Rx leads to conversion of the helper homodimer into an oligomeric resistosome (*24*). In parallel, Liu and colleagues (*25*) reported that a constitutively active mutant of the *N. benthamiana* NRC4 helper, NbNRC4$^{D478V}$, forms a hexameric homo-oligomer with $Ca^{2+}$ channel activity. Whether sensor-activated NRC helpers form hexameric homo-oligomeric assemblies remains to be determined.

Here, we report the structure of the sensor-activated helper NLR NbNRC2 purified from the model plant *N. benthamiana* determined by cryo–electron microscopy (cryo-EM). We show that perception of the Potato virus X coat protein (PVX CP) by Rx triggers the formation of homohexameric NbNRC2 resistosomes, distinct from the previously reported pentameric assemblies formed by singleton CC-NLRs. The NbNRC2 resistosome does not include the sensor NLR Rx, providing structural evidence for the previously proposed activation-and-release model (*17*). The structure allowed us to identify and validate the interaction interface between the NbNRC2 protomers in the hexamer and to pinpoint key residues mediating hexamer assembly. Last, we used the NbNRC2 hexamer structure to assess the ability of AlphaFold 3 to predict activated CC-NLR oligomers (*26*) and showed that it allows for confident modeling of the N-terminal α1 helices of NbNRC2 and other CC-NLRs, a feature that has not been well-resolved in most experimental structures determined to date. Overall, our work sheds light on the structural and biochemical mechanisms underpinning NLR activation and expands our understanding of NLR structural diversity.

## RESULTS

### Cryo-EM analysis reveals homohexameric resistosome structure of NbNRC2 activated with Rx and PVX CP

The *N. benthamiana* helper CC-NLR NbNRC2 exists as a homodimer at resting state and assembles into a higher-order oligomeric resistosome upon activation by Rx or other NRC-dependent sensor NLRs (*15*–*17*, *24*). The precise structural organization of the activated NRC resistosome is not known. In particular, whether it forms a pentameric assembly that resembles singleton CC-NLRs resistosomes has not been experimentally tested (*9*–*11*). To structurally characterize the activated NbNRC2 oligomer, we purified it from *N. benthamiana* following transient overexpression for cryo-EM analysis. We used an NbNRC2 variant with mutations in its N-terminal MADA motif (NbNRC2$^{EEE}$), which was previously identified to abolish cell death induction without compromising receptor activation and oligomerization (*17*, *19*). The C terminally 3x-FLAG–tagged NbNRC2$^{EEE}$ was activated in planta by coexpressing the sensor Rx and PVX CP and purified by FLAG-affinity purification (fig. S1). Analysis by negative stain electron microscopy revealed NbNRC2$^{EEE}$ oligomers that were primarily hexameric assemblies. Additional class averages indicated dimerization of the hexamer, producing dodecameric states in a subset of the particles (fig. S1A). The cryo-EM analysis of the sample yielded a reconstruction of the NbNRC2 hexameric resistosome, which was resolved to approximately 2.9-Å resolution with the application of C6 symmetry, into which a structural model was built (Fig. 1 and fig. S1, B to F).

### Overall structure of the NbNRC2 homohexamer reveals similarities and differences with respect to pentameric resistosomes

The Rx-activated NbNRC2 oligomer contains six protomers that are assembled into a star-shaped resistosome. The NbNRC2 resistosome therefore contains one more subunit than the previously reported pentameric resistosomes of the MADA-CC-NLRs AtZAR1 and TmSr35 (Fig. 1A) (*9*–*11*). The α1 helices (residues 1 to 26), which carry the MADA consensus sequence, were not resolved in the NbNRC2 homohexamer, indicating their flexible nature. In contrast, the rest of the CC domain (residues 27 to 133), NB (residues 156 to 303), HD1 (residues 315 to 376), WHD (residues 392 to 497), and LRR (residues 497 to 882) regions were resolved (Fig. 1, A and B, and table S1). Within the NbNRC2 resistosome, the arrangement of domains in each protomer is stabilized by interactions between the CC and LRR domains of the same subunit (Fig. 1C). Specifically, the α3 helix in the NbNRC2 resistosome contacts residues of the LRR and WHD domains. Part of the interaction involves contacts between two conserved motifs that were previously identified: the EDVID motif in the α3 helix and arginine residues from the LRR$^{R\text{-cluster}}$ (*10*, *11*). However, the NbNRC2 resistosome also contains features unlike the AtZAR1 and TmSr35 resistosomes. First, NbNRC2 contains an extended EDVID motif in which residues I81, K84, and L85 in the CC α3 helix interact with H590, W612, and Y589, respectively, in the LRR region (Fig. 1C). In addition, and unlike the TmSr35 resistosome, only two arginine residues contribute to interactions with the acidic residues from the EDVID motif. Specifically, arginine R519 in the LRR region mediates a bidentate salt bridge with the first two acidic residues of the EDVID motif (E73 and D74), and arginine R541 forms a salt bridge with the final aspartate of the EDVID motif (D77) (Fig. 1C). Two potential contacts were observed at the beginning of the α3 helix: Residues K66 and N70 likely interact with E495 and N496 in the WHD domain, respectively (Fig. 1C).

In the reconstruction, density was observed within the groove formed between the NB domain and HD1 domain of each protomer that is well modeled by a molecule of adenosine triphosphate (ATP) (Fig. 1D). The ATP phosphate groups are coordinated by NB domain residues T189, T190, K188, and R293, and the adenine base is within a hydrophobic pocket bordered by F156 and V356 (Fig. 1D). The presence of ATP at this position supports its proposed role in stabilization of the resistosome, shared with AtZAR1 and TmSr35 (*10*, *11*).

Downloaded from https://www.science.org on August 02, 2025

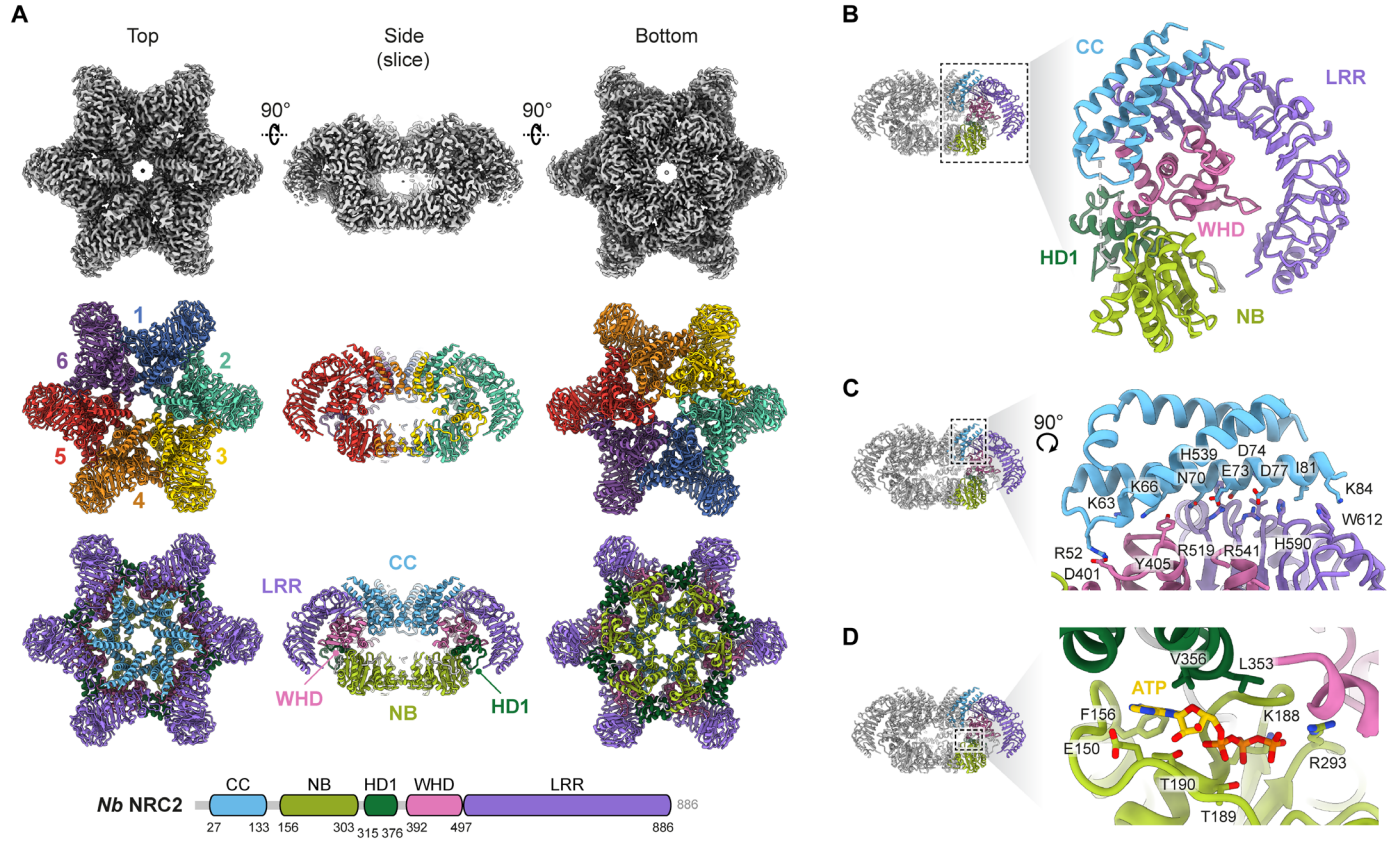


**Fig. 1. Cryo-EM structure of the NbNRC2 resistosome reveals a homohexameric oligomer.** (**A**) Cryo-EM structural analysis revealed that the sensor-activated NbNRC2 assembles into a homohexameric resistosome. The central panel shows the presence of six protomers of NbNRC2. The panel at the bottom displays the individual protomers, colored by different domains, in accordance with the domain organization (refer to the schematic below) as determined by the structural model. (**B**) For clarity, different domains within a single NbNRC2 protomer and their relative orientations to each other are represented separately. (**C**) Conserved motif EDVID from the α3 helix and its interacting residues from the $LRR^{R\text{-}cluster}$ are highlighted, one of the critical contact points important for stabilization of the NbNRC2 resistosome. (**D**) Structural analysis also confirmed the presence of an adenosine triphosphate (ATP) molecule within the groove formed between the NB domain and HD1 domain of each protomer.

Additional density in the cryo-EM map of the sensor-activated NbNRC2 hexameric resistosome was observed within the concave surface of the LRR domain around residues W426, K475, K691, N720, K722, K748, and K774 (fig. S1G), which better fits a nucleotide triphosphate. A recent study by Ma *et al.* (*27*) on the resting state of SlNRC2 reported inositol hexakisphosphate ($IP_6$) or inositol 1,3,4,5,6-pentakisphosphate ($IP_5$) bound at the same location. However, we could not find the density corresponding to $IP_6$ or $IP_5$ around these residues (fig. S1G).

## Multiple interprotomer interactions stabilize the NbNRC2 hexameric resistosome

The NbNRC2 resistosome is stabilized by multiple interfaces between adjacent protomers (Fig. 2A). The most extensive interaction that stabilizes the central part of the resistosome is formed by the embedding of each HD1 domain within a concave surface of the adjacent protomer lined by the NB, WHD, and LRR regions (Fig. 2B). Additional interactions occur between each adjacent CC domain, which form one pore, and each adjacent NB domain, which form the opposing pore. In the contact between CC domains, aspartate D40 in the α2 helix contacts glutamate E60 and lysine K64 of the α3 helix in the adjacent protomer (distances of 3.7 and 3.4 Å, respectively) (Fig. 2C). In addition, glutamine Q36 of the α2 helix contacts glutamate E60 (distance of 3.8 Å). These extensive electrostatic interactions between CC domains likely stabilize their position within the NbNRC2 resistosome.

At the interface between NB domains, aspartate D239 and cysteine C241 from one protomer contact threonine T234 and asparagine N225 at distances of 3.3 and 4.4 Å, respectively, in the other protomer (Fig. 2D). To assess the contribution of the contact between NB domains, we introduced mutations into key residues at the interface and assayed the mutants for activation of immunity and resistosome formation. NbNRC2 variants with single mutations in the interprotomer interface were unaltered in their ability to cause hypersensitive cell death (fig. S2). From a set of seven combinatorial mutations, we identified two variants that contained mutations of two residues that showed weak cell death activity following activation by Rx and PVX CP ($NbNRC2^{N225A/T234A}$ and $NbNRC2^{N225A/D239A}$) and a variant with mutation of three residues that displayed an almost complete loss of cell death activity ($NbNRC2^{N225A/T234A/D239A}$) (Fig. 2E and fig. S3). The protein abundance of double and triple NbNRC2 mutants was comparable to $NbNRC2^{WT}$, indicating that the lack of cell death is not due to these NbNRC2 variants accumulating poorly

Downloaded from https://www.science.org on August 02, 2025

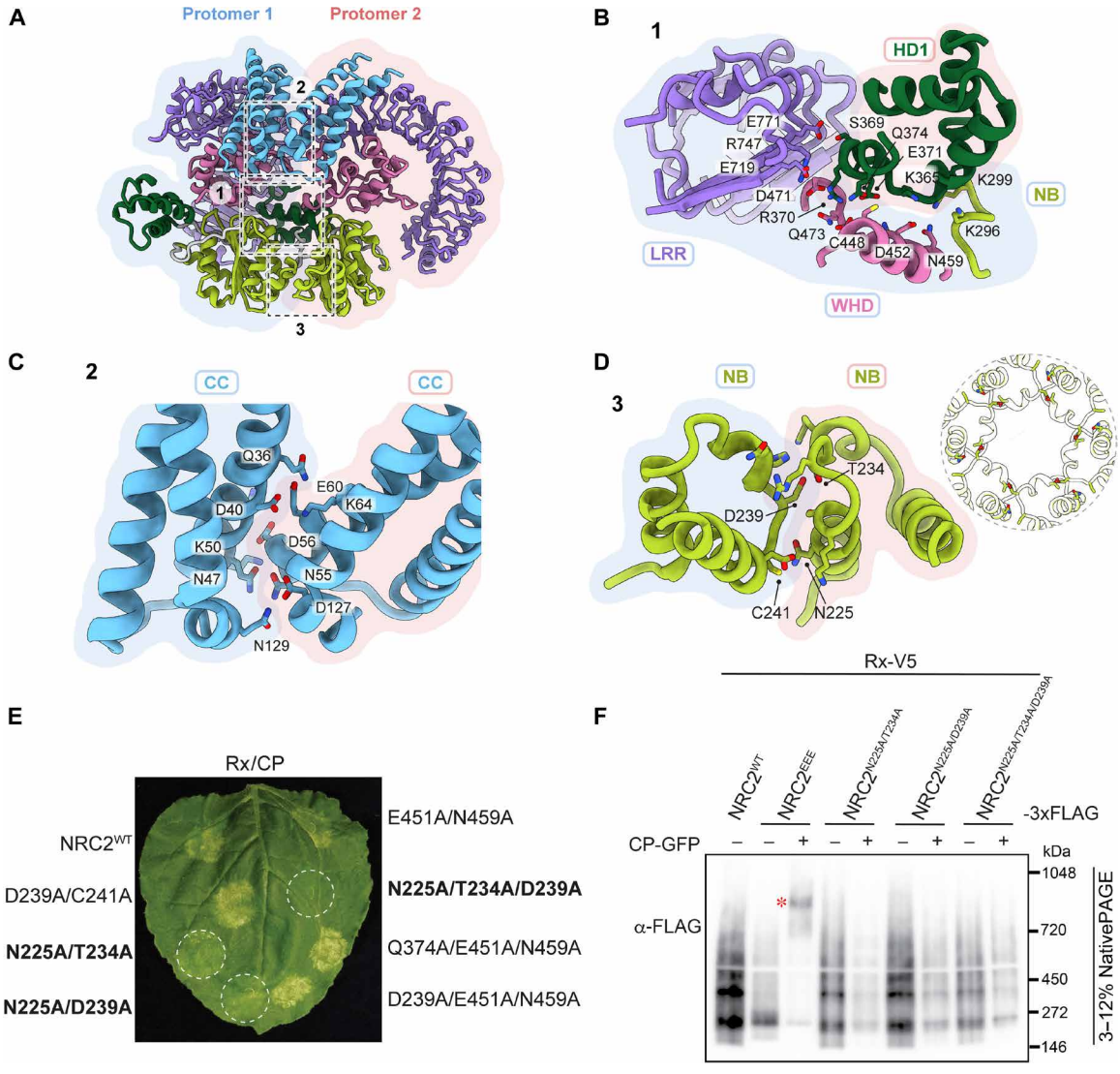


**Fig. 2. Interprotomer interactions stabilize the NbNRC2 resistosome.** (**A**) Multiple potential contacts between the two protomers of the NbNRC2 resistosome, highlighted in dashed boxes, typically contribute to its overall stability. (**B**) HD1 domain from one protomer establishes extensive interactions with the NB, WHD, and LRR domains of the adjacent protomer, stabilizing the NbNRC2 resistosome. (**C**) CC versus CC interactions between the two adjacent protomers specifically stabilize the NbNRC2 homohexamer from the topside. (**D**) Similarly, residues at the NB versus NB interface contribute to the stabilization of the resistosome from the underside. The inset shows the NB pore of the NRC2 resistosome and how it is well connected by the four crucial amino acids. Potential contact residues from all these interfaces are highlighted in stick representation. (**E**) Representative leaf picture from *N. benthamiana nrc2/3/4* knockout plants showing HR after coexpression of Rx/PVX CP with NRC2$^{WT}$ and its combinatorial variants. (**F**) BN-PAGE assay with inactive and activated Rx with NRC2$^{EEE}$ and the NRC2$^{WT}$ mutants, which exhibited weak or no hypersensitive cell death. Sensor-helper combinations shown were co-infiltrated together with green fluorescent protein (GFP) or CP-GFP. Total protein extracts were run in parallel on native and denaturing PAGE and immunoblotted with the antisera labeled on the left. SDS-PAGE blots are found in fig. S4. Approximate molecular weights (in kilodalton) of the proteins are shown on the left. An asterisk represents the higher-order oligomer state for NRC2$^{EEE}$ upon activation with Rx and PVX CP. The experiment was repeated three times with similar results. WT, wild type.

(fig. S3). As the cell death response was compromised, we were able to assess the oligomerization of the mutants upon Rx-mediated activation using blue native–polyacrylamide gel electrophoresis (BN-PAGE) assays, as previously reported (*16*, *17*). Unlike NbNRC2$^{EEE}$, the double mutants and the triple mutant did not form detectable higher-order resistosome-like complexes upon Rx-mediated activation (Fig. 2F).

From these results, we conclude that the residues at the NB domain interface, N225, T234, and D239 are critical to resistosome formation. It is notable that mutation of a small number of residues within the NB domain is sufficient to compromise hexamer formation given the extensive interprotomer interface that involves all domains of NbNRC2 (Fig. 2B). We conclude that contact between NB domains plays an important role in the oligomerization pathway and that the more extensive interactions between other domains are not stable in its absence. Furthermore, the contribution of the interaction between NB domains is comparable to the role of the interaction between the well-conserved EDVID motif from the α3 helix and the LRR$^{R\text{-cluster}}$ at the topside of the resistosomes.

Downloaded from https://www.science.org on August 02, 2025

### Comparison between resting state homodimer and activated hexamer of NbNRC2 reveals extensive NB-ARC conformational rearrangements

Our model allows us to examine the mechanism of resistosome formation by comparing the active hexameric resistosome to that of the dimeric resting state. We performed a comparative structural analysis assessing the conformation of NbNRC2 protomers in each state and the interactions between them that support oligomerization. We identified that NbNRC2 contains two structural modules that vary in their relative position between the hexameric and dimeric states (Fig. 3A). The first structural module comprises the NB and HD1 domains and the second comprises the WHD and LRR domains. The relative orientations of the domains within each module are mostly unchanged between the hexameric and dimeric states. By contrast, the two modules must undergo a rotation of approximately 180° with respect to each other to transition between the states (Fig. 3B and movie S1).

The transition between resting dimeric and active hexameric states involves additional changes. First, the linker between the HD1 and WHD domains that connects the structural modules is ordered in the dimeric state but disordered in the hexamer. Second, the extensive interactions between the WHD, HD1, and NB domains of a single

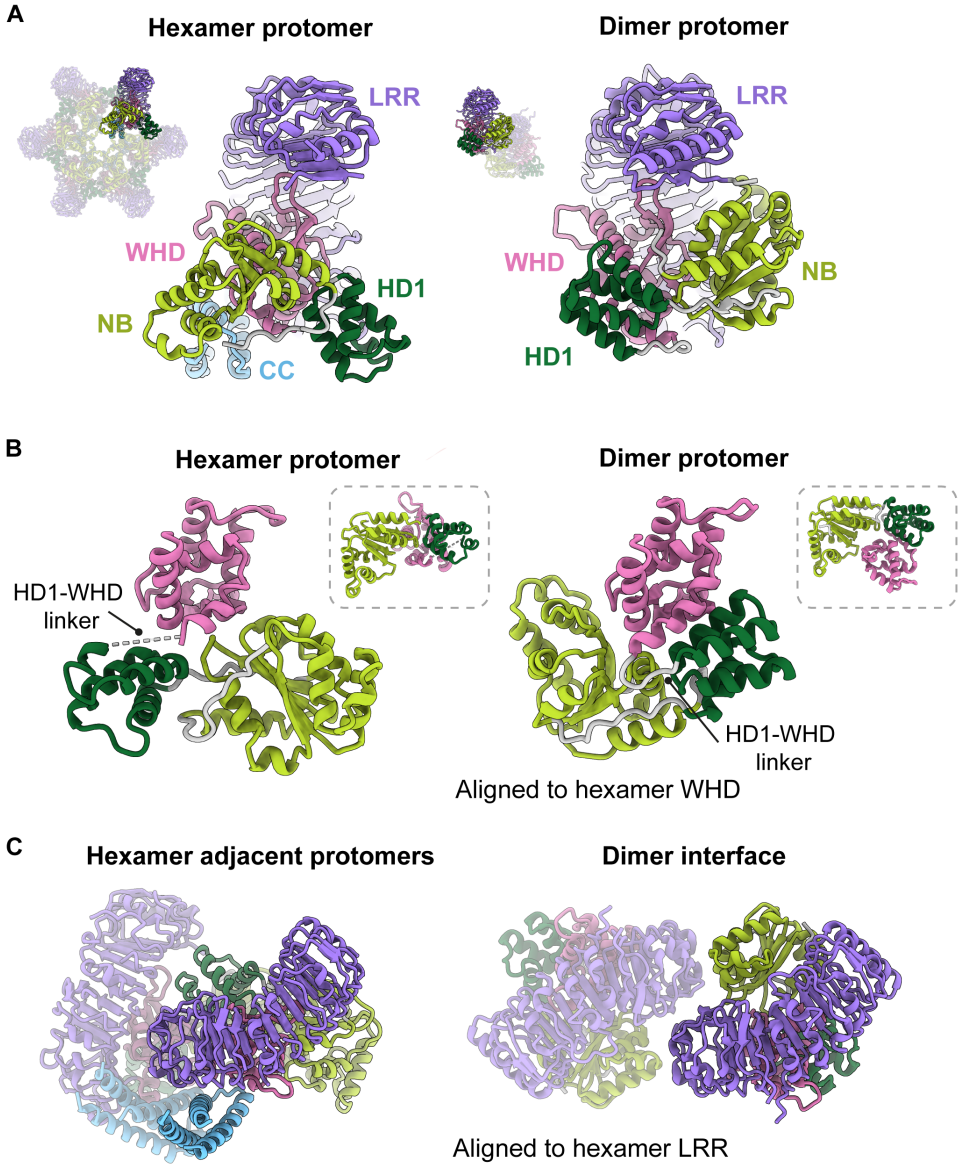


**Fig. 3. A protomer-level structural comparison between the NbNRC2 hexamer and dimer reveals major differences in the NB-ARC regions.** (**A**) Comparison of the individual protomers from the NbNRC2 hexamer (PDB ID: 9FP6) and dimer (PDB ID: 8RFH) complexes revealed crucial differences in the relative orientation of the NB, HD1, and WHD domains within the NB-ARC regions. The difference in the relative orientation of the NB and WHD domains, along with the contribution from the HD1-WHD linker region to this switch, was further highlighted by aligning to the hexamer WHD (**B**) and hexamer LRR region (**C**), independently. The insets (dashed boxes) in (B) are aligned to the hexamer NB to show that the NB-HD1 module moves as a rigid body. The missing density for the HD1-WHD linker from the hexamer protomer is indicated by a dashed line.

Downloaded from https://www.science.org on August 02, 2025

protomer in the dimeric state must be disrupted to allow the NB-HD1 module to rotate with respect to the WHD-LRR module (Fig. 3B and movie S1). Third, the CC domain is resolved in the hexamer but not the dimer state, suggesting that it is disordered or highly flexible in the dimeric state but partly ordered in the hexamer, except for the α1 helix. Last, the surfaces that form interprotomer interaction interfaces in the NbNRC2 homodimer are not in contact in the hexamer. The dimer interface involves contacts between the LRR and NB domains, and these domains have different orientations in the hexamer (Fig. 3C) (*16*). We conclude that the characterized homodimeric state undergoes substantial conformational rearrangements to form the active hexamer upon Rx-mediated activation, suggesting that intermediate conformations may occur.

### The NbNRC2 hexamer exhibits structural commonalities and differences with the previously reported MADA-CC-NLR pentameric resistosomes

NbNRC2 is a member of the MADA class of CC-NLRs like AtZAR1 and TmSr35. The finding that NbNRC2 forms a hexameric state upon activation, as recently reported for $NRC4^{D478V}$ (*25*), reveals unexpected diversity in MADA-CC-NLR oligomerization, given that AtZAR1 and TmSr35 are both pentameric. To investigate the structural basis of hexamer rather than pentamer formation, we compared the structures of characterized CC-NLR resistosomes (*9*–*11*). Despite substantial difference in overall resistosome architecture caused by the accommodation of an additional subunit, the conformation of individual NbNRC2 protomers closely resembles those of AtZAR1 and TmSr35 (Fig. 4A). In each resistosome, corresponding regions of the CC and NB domains support intersubunit interactions, but the residues at the interfaces vary considerably.

The relative positions of the domains that comprise the NB-ARC module differ between NbNRC2 and AtZAR1 in a way that is consequential to the stoichiometry of the complex (Fig. 4B). The interdomain angle within the CC-NB-ARC was measured to be 10° larger in NbNRC2 relative to AtZAR1. This widening of the NB-ARC has two consequences. First, the NB domains are pushed outward in NbNRC2 relative to their positions in AtZAR1 (Fig. 4C). This difference is important for the accommodation of an additional subunit in the NbNRC2 resistosome. Second, the cavity bordered by the LRR, WHD, and NB on the internal face of the protomer that interacts with the HD1 domain of the adjacent protomer (Fig. 2B) is substantially larger in NbNRC2 than AtZAR1. This allows the HD1 domain to insert further into the cavity and make more extensive contact. Last, a structural difference in the CC domain also contributes to the stoichiometry of the resistosome. The α4 helix of NbNRC2 contains a bend near residue L126, which is at the end closest to the resistosome core (Fig. 4D). This difference contributes toward the accommodation of an additional protomer as structural superposition showed the straight α4 helix of AtZAR1 would sterically overlap with the adjacent protomer in a hexameric configuration.

The presence of an additional protomer and the increased separation of the NB domain positions prompted us to examine whether the pores of the NbNRC2 resistosome are larger than those of pentameric resistosomes. We identified that NbNRC2 and TmSr35 have a one third wider CC pore (17 to 19 Å) compared to the AtZAR1 (12 Å) (Fig. 4E). The small CC pore of AtZAR1 is a consequence of the α4 helix, which is longer than that of TmSr35 and unbent unlike NbNRC2. On the opposing side, the NB pore of all three resistosomes has a similar width, although that of NbNRC2 is 3 Å larger (19 Å) than those of AtZAR1 and TmSr35 (16 Å) (Fig. 4E). Thus, the stoichiometry of the resistosome is not the only factor determining pore diameter. We additionally observed that the residues that line the pores of each resistosome are different across characterized resistosomes. Whereas the CC pore of NbNRC2 is hydrophobic due to a ring of leucine residues (L126), the CC pore of AtZAR1 is acidic due to a ring of glutamate residues (E130 and E134), and the CC pore of TmSr35 features both charged and uncharged residues (K132 and Q139). We conclude that the size and chemical composition of resistosome pores are unexpectedly variable, with potential consequences for their channel activity.

### AlphaFold 3 can predict a lipid-bound NbNRC2 resistosome with high confidence

Activated CC-NLR resistosomes insert themselves into membranes via a funnel-like structure formed by their N-terminal α1 helices, leading to the induction of cell death. The absence of the α1 helix and the incomplete pore in the NbNRC2 resistosome cryo-EM structure led us to use AlphaFold to generate a structural prediction for the missing region to obtain an integrated model that is more complete (*26*). First, we used the experimentally resolved NbNRC2 hexamer structure to assess the performance of AlphaFold 2, AlphaFold 3, and AlphaFold 3 with 50 oleic acid molecules as a stand-in for the plasma membrane (*26*, *28*, *29*). We focused on modeling the CC-NB-ARC portion of the full-length NbNRC2, which includes the oligomerizing domains. We analyzed the models based on different metrics such as predicted local distance difference test (pLDDT), predicted template modeling score (pTM), interface pTM (ipTM), predicted aligned error (PAE), minimum per-chain pTM, and chain-pair ipTM (*26*, *29*). AlphaFold 2, AlphaFold 3, and AlphaFold 3 with lipids, all generated high-confidence models with pTM and ipTMs of 0.7 and higher and structurally aligned with the experimental model with root mean square deviation (RMSD) values of lower than 1.8 Å (Fig. 5A and fig. S5, A and B). However, in the AlphaFold 2 model, the N-terminal α1 helix faced inward, whereas in both AlphaFold 3 predicted structures, the N-terminal α1 helix was facing outward and formed a full funnel-shaped structure (fig. S5, A and B). In the AlphaFold 3 model with 50 oleic acids, the N-terminal α1 helix showed confident interactions with the lipids and had a higher local confidence compared to the models without the lipids (Fig. 5B and fig. S5, A and B).

How does varying the NbNRC2 stoichiometry affect the confidence of the AlphaFold 3 predictions? To assess this, we repeated the process using a range of stoichiometries from four to eight NbNRC2 copies. For each stoichiometry, we generated 10 models with different seeds each time, all modeled with 50 oleic acid molecules (Fig. 5C). Hexamer models had the highest median pTM and ipTM confidence scores and aligned with the experimental NbNRC2 structure with RMSD values lower than 1.8 Å (Fig. 5C and fig. S6). Predictions for pentamers and heptamers were less confident across all metrics, while tetramers and octamers were of lower confidence and showed greater variability (Fig. 5C). All oligomeric forms consistently displayed complete funnel-like structures with the exception of tetramers. Tetramer models varied, with some forming complete funnels and others resembling incomplete hexameric-like resistosomes (fig. S7A).

To further assess the AlphaFold 3 models, we checked if the contact residues from the cryo-EM structure were also predicted in the AlphaFold 3 resistosome structures. On the basis of a 4.5-Å cutoff for contact, most residues involved in interactions in the cryo-EM

Downloaded from https://www.science.org on August 02, 2025

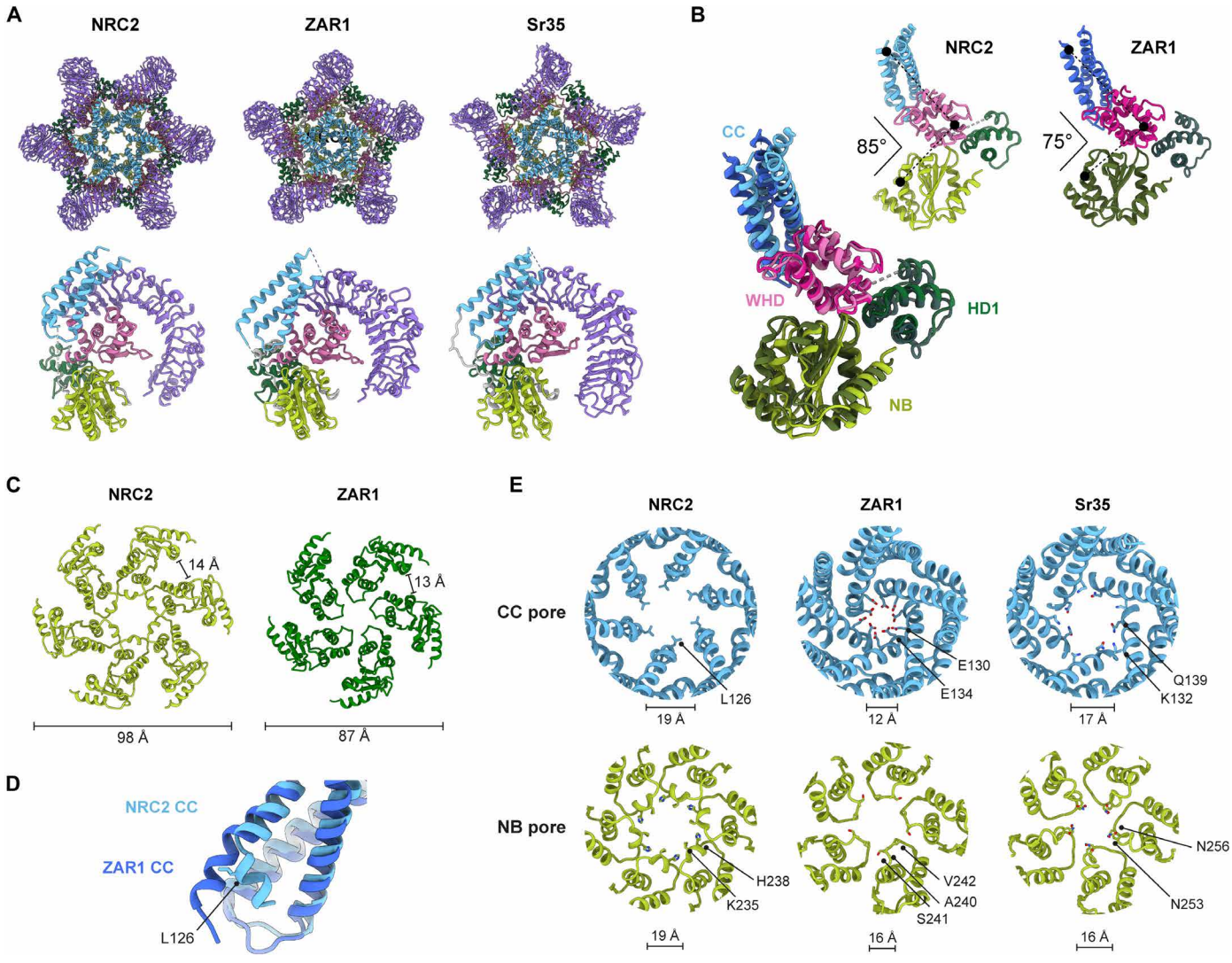


**Fig. 4. Comparison of NbNRC2, AtZAR1, and TmSr35 resistosomes reveals striking structural differences.** (**A**) Sensor-activated NbNRC2 assembles into a homohexameric resistosome, in contrast to AtZAR1 and TmSr35, which form pentameric resistosomes. The induvial protomers (colored by domains) from these resistosomes still share the same topology. (**B**) Structural superposition of the protomers from the NbNRC2 hexamer and the AtZAR1 pentamer revealed differences at the protomer level. Specifically, the angular distances between the domains within the individual protomers differ, potentially influencing the packing of protomers within the respective resistosomes. (**C**) Further, this arrangement results in an overall outward displacement of the 'NB' domains, creating a wider underside in the NbNRC2 resistosome while maintaining a nearly constant distance between the domains. (**D**) Structural superposition of the NbNRC2 and AtZAR1 CC domains revealed a "kink" in the α4 helix of the CC domain in the individual protomers from NbNRC2 resistosome. (**E**) Comparison of the CC and NB pores and the chemical nature of the pores in the NbNRC2, AtZAR1, and TmSr35 resistosomes. Distances indicated are measured between the $C^{\alpha}$ atoms of the two opposite residues highlighted in the respective resistosomes.

model were also predicted in the AlphaFold 3 model (Fig. 5D and data S2). However, the ability to predict the details of the interaction interface varied. While the interaction between adjacent CC domains was predicted approximately correctly, the residues at the interface between adjacent NB domains were dissimilar to those in the experimental structural model (Fig. 5E and fig. S7, B and C).

## AlphaFold 3 resistosome prediction of CC-NLR resistosomes reveals a diversity of N-terminal structures

The ability of AlphaFold 3 to predict the NbNRC2 resistosome stoichiometry and architecture with confidence prompted us to examine predicted models of other NLR proteins. We first modeled 11 representatives from the major NRC protein clades as pentamers and hexamers (*29*). Three of the 11 NRC proteins did not show confident models with SlNRC0, NbNRCX, and NbNRC7a having ipTM and pTM scores lower than 0.6 as both pentamers and hexamers (figs. S8 and S9). The remaining eight NRCs all had confidence values of 0.6 and higher for both pentamer and hexamers (figs. S8 and S9). In all 11 cases, hexamers had higher confidence values in all models compared to pentamers, although this difference was subtle (fig. S9). In addition, all hexamer models except NbNRC7a had minimum per-chain pTM scores of 0.7 and higher. In contrast, only eight of the 12 NRCs had minimum per-chain pTM scores of 0.7 and higher as pentamers (fig. S9).

Downloaded from https://www.science.org on August 02, 2025

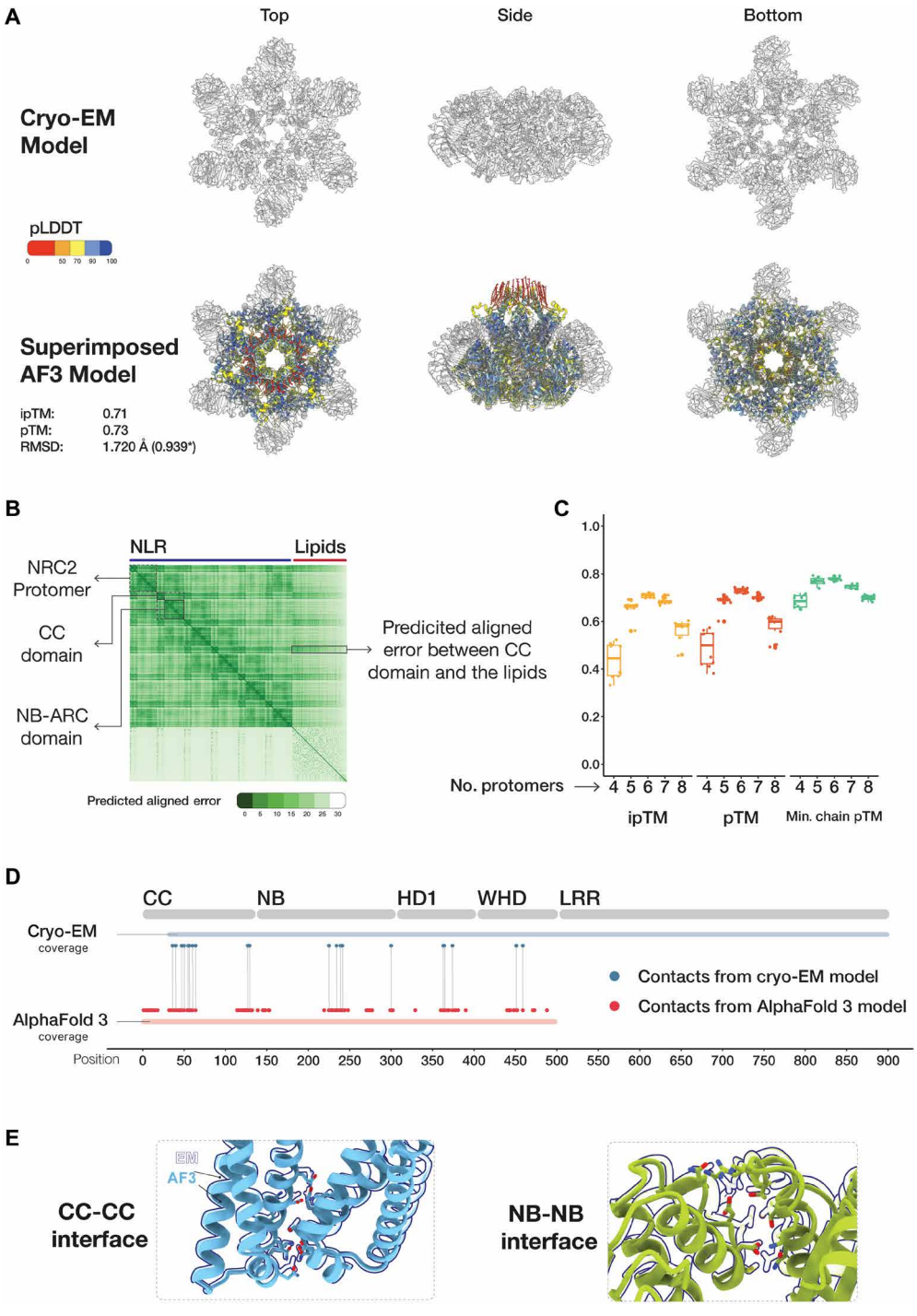


**Fig. 5. AlphaFold 3 can predict a high-confidence NbNRC2 resistosome.** (**A**) Superimposition of NbNRC2 predicted model with the cryo-EM structure. NbNRC2 AlphaFold 3 resistosome model fits into the cryo-EM structure (PDB ID: 9FP6) with an RMSD of 1.72 Å. Structures are colored by pLDDT values. The asterisk (*) indicates the RMSD value after pruning done by Matchmaker command from ChimeraX. (**B**) PAE plot of NbNRC2 AlphaFold 3 model. Representative single protomers, domains, and interactions between the CC domain and the lipids are shown. (**C**) ipTM, pTM, and minimum chain pTM confidence values of NbNRC2 predicted oligomers ($n = 10$). (**D**) NbNRC2 AlphaFold 3 resistosome model comprises overlapping contact regions as the cryo-EM structure. (**E**) Predicted NbNRC2 model superimposed on selected contact regions in the cryo-EM model.

Downloaded from https://www.science.org on August 02, 2025

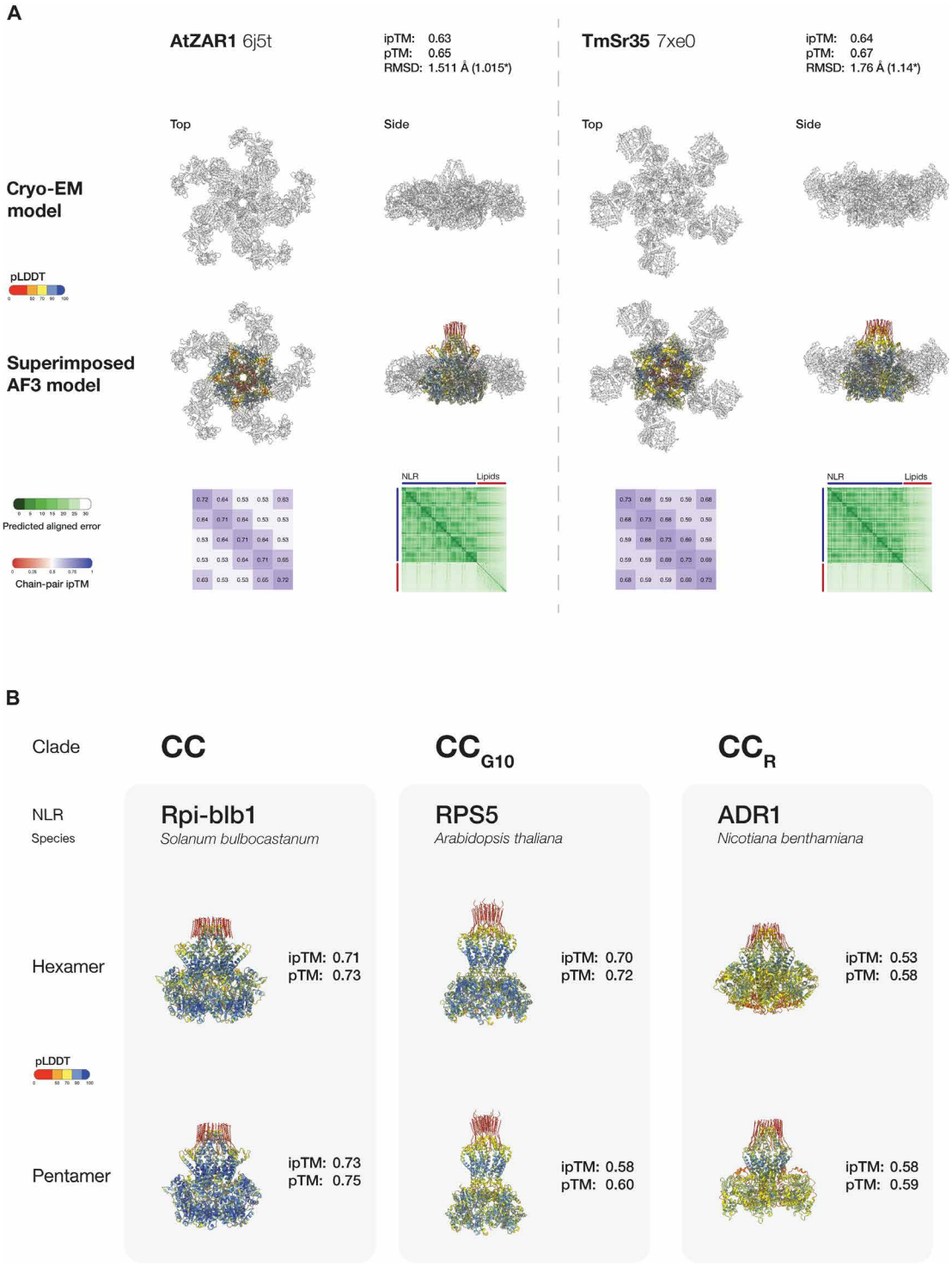


**Fig. 6. Other CC-type NLR resistosomes can be predicted confidently using AlphaFold 3.** (**A**) Superimposition of AtZAR1 and TmSr35 AlphaFold 3 predicted resistosome models on their available cryo-EM structures (PDB IDs: 6J5T and 7XE0) with PAE and chain-pair ipTM confidence plots. The asterisk (*) indicates the RMSD value after pruning done by Matchmaker command from ChimeraX. (**B**) Predicted AlphaFold 3 resistosome structures of SbRpi-blb1, AtRPS5, and NbADR1 as pentamers and hexamers. Structures are colored by pLDDT values. This approach revealed that the CC-type and $CC_{G10}$-type NLR clades each contain representatives with hexamer and pentamer resistosome configurations. In the CC-NLR clade, all NLRs modeled with ipTM, pTM, and minimum chain pTM values of 0.6 or higher (figs. S12 to S14 and S18). AtHrt1 was confidently predicted to be a hexamer, whereas AtRpm1 and SlPtr1 were more confident as hexamers than pentamers. OsPit, TaPm2a, StR3a, SbRpi-blb1, and BvRz2 all showed higher model confidence for pentamers (figs. S12 to S14). However, in StR3a and BvRz2, the CC domain and the N-terminal α helix were modeled with lower confidence than in the other resistosome models in either oligomeric form (figs. S13 and S14).

Downloaded from https://www.science.org on August 02, 2025

We also determined whether AlphaFold 3 can model the CC-NB-ARC portion of AtZAR1 and TmSr35, the two CC-NLRs with experimentally determined pentamer resistosome structures (*9*–*11*). We used stoichiometries of either five or six copies. Although not predicted with as high confidence as NbNRC2, the predicted pentamer models of AtZAR1 and TmSr35 aligned well to experimental models, with RMSD values of 1.51 and 1.76 Å, respectively (Fig. 6A). Each NLR had higher confidence for the pentameric form compared to the hexameric form, reflecting their experimentally validated resistosome configurations (fig. S10).

Given AlphaFold 3 performance in modeling CC-NLRs such as NbNRC2, AtZAR1, and TmSr35, we proceeded to model a set of phylogenetically diverse plant NLR proteins with unknown resistosome structures (fig. S11 and data S1). We chose eight CC-type, six $CC_{G10}$-type, and two $CC_R$-type NLRs and modeled them with AlphaFold 3 as pentamers and hexamers to assess if their resistosome structures could be predicted with high-confidence metrics and to determine which oligomeric configuration yielded better models (Fig. 6B).

$CC_{G10}$-NLRs showed variable model confidence for hexamers and pentamers. AtRPS5 had higher confidence as a hexamer (fig. S16), whereas CaPvr4, LsRGC2B, GmRsv3, and CmVat showed higher model confidence in their pentameric form (figs. S15 and S16). Compared to the rest of the $CC_{G10}$-NLRs, AtRPS2 was poorly modeled in both stoichiometries, with confidence values below 0.6 (figs. S15 and S18).

The two $CC_R$-NLRs modeled, NbADR1 and NbNRG1, did not yield high-confidence models as pentamers or hexamers, with confidence values below 0.6 in all cases (figs. S17 and S18). However, while the overall confidence values were low, they showed higher confidence as pentamers compared to hexamers.

## DISCUSSION

Here, we report the structure of a sensor-activated plant helper NLR determined by cryo-EM. We report that, following perception of the coat protein of PVX by the disease-resistance protein Rx, the helper CC-NLR NbNRC2 assembles into a hexameric resistosome that is different to the pentameric complexes formed by activated singleton MADA-type CC-NLRs (Fig. 1). The NbNRC2 resistosome does not contain Rx, providing structural evidence for the activation-and-release mechanism for sensor-helper pairs in the NRC immune receptor network (*17*). This indicates that this mode of activation of paired NLRs is markedly distinct from the heterocomplexes of metazoan-paired NLRs, such as NAIPs and NLRC4 (*17*, *30*). We conclude that paired and networked inflammasomes and resistosomes from various biological systems assemble through diverse mechanisms (*2*, *30*).

Our study provides insights into helper NLR activation by sensors, which involves oligomerization into a hexameric resistosome. This expands our current understanding of NLR structural diversity beyond tetrameric- and pentameric-activated oligomers. What is the functional relevance of the NbNRC2 hexamer? In previous studies, we showed that activated NbNRC2 and NbNRC4 oligomers accumulate as plasma membrane–associated puncta following activation by sensors, leading to cell death and disease resistance (*17*, *31*). Recently, the $NbNRC4^{D478V}$ oligomer was also shown to function as a calcium channel as has been shown for pentameric resistosomes of CC-NLRs AtZAR1 and TmSr35 (*10*, *12*, *25*). Considering that the NbNRC2 hexamer features a CC pore size that is one-third larger than AtZAR1 and different inner volumes (Figs. 3 and 4), it will be interesting to understand if these differences lead to altered ion channel dynamics compared to CC-NLR pentamers. Moreover, the extent to which the NbNRC2 hexamer serves as a channel for influx/efflux of other unknown immunogenic small molecules that cannot be channeled by smaller, pentameric assemblies remains to be determined. The relevance and consequences of resistosome pore size on downstream immune activation will be an exciting question to answer.

While we identified density corresponding to a nucleotide triphosphate around residues W426, K475, K691, N720, K722, K748, and K774 in the active NbNRC2 resistosome, a recent study by Ma *et al.* reported $IP_6$ or $IP_5$ bound at the same location in the resting-state structure of SlNRC2 (*27*). Mutation of these residues in SlNRC2 resulted in either reduced or complete loss of cell death or conductivity upon activation with Rx and PVX CP (*27*). Whether or not mutations at these positions affect hexamerization remains to be tested.

The NbNRC2 hexamer is the fourth NLR to be structurally characterized by cryo-EM using purification from the model plant *N. benthamiana*, underscoring the versatility of this emerging expression system for structural biology. The capacity to purify NLR protein complexes directly from plants and characterize them using cryo-EM promises to accelerate our understanding of immune receptor structural diversity (*13*, *24*, *25*). Whether other CC-NLRs assemble into hexamers remains to be determined. It is tempting to speculate that additional resistosome stoichiometries remain to be found.

Comparative analyses of the resting and activated forms of NbNRC2 revealed distinct interfaces involved in homodimerization compared to homohexamerization and extensive intramolecular rearrangements within each NbNRC2 protomer, particularly in the NB-ARC domain (Fig. 3). It will be interesting to determine whether there are subtle differences between the overall structure and the conformational changes of individual domains between NbNRC2 and other NRC hexamers (*25*). In the NbNRC2 hexamer, the homodimerization interface is largely surface exposed, suggesting that this interface needs to be disrupted to allow for resistosome formation (Fig. 3 and movie S1). However, whether its disruption leads to homodimer dissociation into individual monomers that then hexamerize is not clear. We could not detect the appearance of a monomeric NRC2 species in our BN-PAGE assays using hexamerization interface mutants unable to oligomerize (Fig. 2). Another alternative is that the NbNRC2 homodimer remains associated upon activation, but that the individual protomers in the homodimer undergo extensive conformational rearrangements that allow them to oligomerize. Three primed homodimers could assemble into a hexamer, and this could explain the absence of pentameric NRC2. A mechanism that involves trimerization of homodimers would provide a straightforward explanation for hexamer assembly. Future experiments will shed light on the precise dynamics of NRC homodimer conversion into hexamers.

So far, plant NLRs have been shown to assemble into tetrameric, pentameric, and now hexameric resistosomes (*3*, *5*). That the highly conserved NB-ARC domain of plant NLRs can form oligomeric assemblies of this different stoichiometry is intriguing and highlights its flexible nature. Further analyses, possibly assisted by AlphaFold 3, may help identify the molecular features within the NB-ARC and CC domains that determine resistosome stoichiometry, which may potentially allow for predicting the number of protomers in an activated NLR resistosome based solely on amino acid sequence. Similarly, we previously showed that the AtZAR1 α1 helix can functionally

Downloaded from https://www.science.org on August 02, 2025

complement cell death activity and disease resistance when swapped into NRCs (*19*, *32*). That the α1 helix from a pentamer-forming CC-NLR can still function just as well in the context of a hexamer-forming oligomer indicates that these N-terminal helices encode features at the amino acid level, which allow them to be quite versatile and capable of forming funnels with different number of units and pore sizes.

We found that AlphaFold 3 can predict the overall architecture of the NbNRC2 hexamer and a subset of the interaction interface residues with high confidence (Figs. 2 and 5). Moreover, we found that the inclusion of oleic acids in the prediction allowed it to confidently predict the N-terminal funnel formed by the α1 helices, which is not always resolved in experimental CC-NLR resistosome structures (Fig. 5 and fig. S7C) (*26*). We hypothesized that this approach could be effective for predicting membrane-bound protein structures as recently proposed (*28*). Our assessment using three experimental CC-NLR resistosome structures revealed that AlphaFold 3 can predict activated NRC hexamers and CC-NLR pentamers with high confidence. Including oleic acids in the prediction allowed for modeling of the N-terminal funnel formed by the α1 helices of the CC-NLR protomers with high confidence. Using this approach, we obtained confident predictions of N-terminal helices for a representative set of NLRs with coiled coil N termini, including canonical CC-type and $CC_{G10}$-type NLRs. This suggests that these NLRs are likely to assemble into resistosomes with diverse pore-like N-terminal structures. However, note that $CC_R$-NLRs and several CC-NLRs modeled did not yield high-confidence resistosome models. The full significance of these predictions will require further investigations.

The N-terminal funnels of activated CC-NLR resistosomes are often not resolved in experimental structures, either due to the mutations introduced in the α1 helices to abolish cell death or due to depletion of lipids during purification, which may play a key role in stabilizing these N-terminal funnels (*9*, *10*, *25*). In this sense, AlphaFold 3 can be used to fill out gaps in resistosome structures that have remained elusive due to technical limitations. These results exemplify how AlphaFold 3 can be used as a tool to study the structural diversity of activated NLRs, serving as a platform for hypothesis generation and NLR classification without the need for experimental structures. In ongoing work in our group, we have been using AlphaFold predictions to complement phylogenetic grouping and other data to triage NLRs into functional categories and prioritize them for functional analyses.

Ever since the first plant NLR resistosome structure was solved in 2019 (*11*), a multitude of key structural, biochemical, and cell biology studies have resulted in models for NLR activation, largely based on the initial AtZAR1 resistosome (*3*, *5*). This present study together with our recent work on the NbNRC2 resting-state homodimer (*24*) expands the current NLR paradigms beyond the monomer to pentamer model established for singleton CC-NLRs and indicates that paired helper NLRs function through distinct mechanisms. However, whereas we now have a clearer understanding of the beginning and final states of NRC activation, the precise dynamics of homodimer conversion into hexamers remains unanswered. How sensor NLRs trigger this process without becoming stably integrated into the helper oligomers is a key question that remains technically challenging to address due to the transient nature of sensor-NRC interactions (*33*). Another interesting question pertains to the contribution of lipids and the plasma membrane to resistosome assembly. NRCs and other CC-NLRs have been shown to shift from cytoplasm to plasma membrane–associated puncta upon activation (*17*, *31*). Whether resistosomes assemble in the cytoplasm and then insert into membranes, or whether primed intermediates first accumulate at the membrane and then oligomerize by the aid of phospholipids remains to be determined. Obtaining structures of additional NLRs in different states of activation in their membrane context will hopefully shed light on the precise contributions of membranes to immune receptor activation. In this context, AlphaFold 3 will surely contribute to tackling these questions and complementing experimental data.

In conclusion, while the pentameric AtZAR1 resistosome kicked-off a golden age for plant NLR biology, our understanding of NLR activation is moving beyond the AtZAR1 model. Further structures of NLRs covering a broader range of plant phylogeny will surely uncover more structural and functional diversity than previously anticipated, allowing us to advance our understanding of plant NLR activation beyond singleton NLRs.

## MATERIALS AND METHODS

### Plant growth conditions

*nrc2/3/4* CRISPR mutant *N. benthamiana* lines were grown in a controlled environment growth chamber with a temperature range of 22° to 25°C, humidity of 45 to 65%, and a 16-/8-hour light/dark cycle.

### Plasmid constructions

The Golden Gate Modular Cloning (MoClo) Kit (*34*) and the MoClo plant parts kit (*35*) were used for cloning, and all vectors are from this kit unless specified otherwise. PVX CP–enhanced green fluorescent protein (eGFP), Rx-6xHA, and $NbNRC2^{EEE}$-3xFLAG used in protein purification were all previously reported (*17*). NbNRC2 and NbNRC2 hexamerization mutants used in Fig. 2 were cloned into the binary vector pJK001c, with a 2x35*S* promoter (pICSL51288), 35*S* terminator (pICSL41414), and C-terminal 3xFLAG tag (pICSL5007) (*36*). Cloning design and sequence analysis were done using Geneious Prime (v2021.2.2; www.geneious.com).

### Transient protein expression in *N. benthamiana* by agroinfiltration

Effectors and NLR immune receptors of interest were transiently expressed according to previously described methods (*37*). Briefly, leaves from 4- to 5-week-old plants were infiltrated with suspensions of *Agrobacterium tumefaciens* GV3101 pM90 strains transformed with expression vectors coding for different proteins indicated. Final optical density of 600 ($OD_{600}$) of all *A. tumefaciens* suspensions was adjusted in infiltration buffer [10 mM MES, 10 mM $MgCl_2$, and 150 μM acetosyringone (pH 5.6)]. Final $OD_{600}$ used was 0.3 for all NRC2 variants used, 0.1 for Rx, and 0.1 for PVX CP, adding up to a total $OD_{600}$ of 0.5.

### Protein purification from *N. benthamiana*

Around 30 leaves of *nrc2/3/4* knockout *N. benthamiana* were agroinfiltrated as described above to transiently express $NbNRC2^{EEE}$-3xFLAG, Rx-V5, and PVX CP-eGFP. Tissue was harvested after 3 days and snap-frozen in liquid nitrogen. All samples were stored at −80 ° C until the protein was lastly extracted. The entire purification process was completed in the same day for each preparation. On the day of purification, the frozen tissue was ground into fine powder in

Downloaded from https://www.science.org on August 02, 2025

a mortar and pestle that was precooled with liquid nitrogen. A total of 20 g of ground powder was resuspended with extraction buffer [100 mM tris-HCl (pH 7.5), 150 mM NaCl, 1 mM $MgCl_2$, 1 mM EDTA, 10% glycerol, 10 mM dithiothreitol (DTT), 1x cOmplete EDTA-free protease inhibitor tablets (Sigma-Aldrich), and 0.2% (v/v) IGEPAL]. A total of 20 g of ground tissue was resuspended in ice-cold extraction buffer at a 1:4 (w/v) ratio (20 g of powder in 80 ml of extraction buffer). After vortexing and resuspending the powder in this buffer, the crude extract was spun down for 10 min at maximum speed. The supernatant was transferred to another tube and centrifuged again for 10 min at maximum speed. This second supernatant was filtered using Miracloth (Merck). A total of 200 µl of anti-FLAG beads were added to the supernatant and incubated at 4°C for 90 min. The tubes were in constant rotation to prevent the beads from sedimenting. The protein-bound beads were collected on an open column and washed with 10 ml of wash buffer [100 mM tris-HCl (pH 7.5), 150 mM NaCl, 1 mM $MgCl_2$ 1 mM EDTA, 10% glycerol, and 0.2% (v/v) IGEPAL]. The washed beads were collected in a 1.5-ml microfuge tube and eluted with the final isolation buffer in 200-µl volume [100 mM tris-HCl (pH 7.5), 150 mM NaCl, 1 mM $MgCl_2$, and 3% glycerol] supplemented with 3xFLAG peptide (0.5 mg/ml). The eluted protein was analyzed on the SDS-PAGE to assess sample quality and purity. About 2.4 mg/ml concentration was obtained for $NRC2^{EEE}$-3xFLAG from each purification, as determined by absorption at 280 nm. FLAG-eluted pure protein samples were used for cryo-EM studies.

### Negative staining

A 3.5 µl of purified $NRC2^{EEE}$ sample, diluted to 0.3 mg/ml, was applied to 400-mesh copper grids with continuous carbon (Agar Scientific) that was glow-discharged using a PELCO easiGlow (Ted Pella) for 30 s at 8 mA. After 30 s, the sample was blotted using Sartorius 292 filter paper and immediately washed with two consecutive drops of 100 µl of distilled water each. After washing, 3.5 µl of 2% (w/v) uranyl acetate stain in $H_2O$ was applied, and after 30 seconds, the excess stain was blotted off and air-dried. Grids were examined in a FEI Talos F200C transmission electron microscope operated at 200 keV, equipped with a Falcon 4i direct electron detector (Thermo Fisher Scientific). Fifty representative micrographs were recorded using EPU v3.4.0.5704 (Thermo Fisher Scientific) with a total dose of 20 $e^-/Å^2$, nominal magnification of 73 k×, and calculated pixel size of 1.7 Å. Particles were auto-picked using Cryo-SPARC (*38*) without any template. Two-dimensional (2D) classification of the auto-picked particles (~2500 particles) from these images revealed particles resembling the putative NRC2 hexamers.

### Cryo-EM sample preparation and data collection

Quantifoil R 2/1 on copper 300-mesh grids was used for cryo-EM grid preparation. A 3.5 µl of $NRC2^{EEE}$ sample (2.4 mg/ml) was applied over negatively glow-discharged Quantifoil R 2/1 grids coated with graphene oxide. The sample was applied inside the chamber of a Vitrobot Mark IV (Thermo Fisher Scientific) at 4°C and 90% humidity and vitrified in liquid ethane. Without graphene oxide coating, no particles were observed in vitreous ice, so graphene-coated grids were used. The cryo-EM images were collected on a FEI Titan Krios (Thermo Fisher Scientific) operated at 300 keV equipped with a K3 direct electron detector (Gatan) after inserting an energy filter with a slit width of 20 eV. Micrographs were collected with a total dose of 50 $e^-/Å^2$ and a nominal magnification of 105 kX, giving a magnified pixel size of 0.828 Å. Images were collected as movies of 50 fractions with defocus values ranging from −1.5 to −2.7 µm with 2 exposures per hole. A total of 6135 movies were collected for the image processing and 3D reconstruction using CryoSPARC (*38*, *39*).

The micrograph movies were imported into CryoSPARC and subjected to drift correction using MotionCor2 (*40*), and CTFFIND4.0 was used for fitting of contrast transfer function and defocus estimation. The Laplacian of Gaussian auto-picker in CryoSPARC was used for automatic reference-free particle picking (*38*, *39*). The particles were extracted in 256-pixel box and subjected to several rounds of 2D classification with a circular mask of 180 Å. The 2D classes revealed a clear hexamer with secondary structural features in different views. Clean 2D classes were selected (664,305 particles) and were subjected to 3D classification using an ab initio 3D model generated by Cryo-SPARC (*38*). The best 3D class revealing the protein fold consisted of 229,347 particles and was subjected to 3D refinement using Refine3D using that 3D class as a reference with a circular mask of 180 Å. Following examination of the C1 refined map, a C6 symmetry was applied. After particle polishing, CTF refinement, and postprocessing, the final average resolution was 2.9 Å as estimated by the Fourier shell correlation (FSC) (FSC = 0.143). The local resolution plot was calculated using PHENIX 3.0 (*41*). The final map revealed distinct domain boundaries of the NRC2 protein fold with clear secondary structural features, helical twists, and individual β strands and allowed us to place each NRC2 protomer and initiate model building at this resolution. A considerable number of particle views are down the short dimension, owing to graphene oxide backing. The final map revealed the CC, NB-ARC, and LRR domains of the NRC2 molecule.

### Model building and refinement

An initial models of the NRC2 monomer was generated with AlphaFold 2 (*29*) and fitted approximately within the density by structural alignment to a model of the entire NRC2 hexamer built using ModelAngelo (*42*). Iterations of manual adjustment in Coot, de novo model building, and real-space refinement in Phenix were performed with the consensus EM map (*41*, *43*). This model was validated using PHENIX and MolProbity (*41*, *44*). Figures were made using ChimeraX (*45*). The interface residues and the buried surface area were evaluated using PyMOL and the PISA server (*46*, *47*). A distance cutoff of 5 Å is used to define residues at the interface to accommodate all short- and long-range interacting residues. Further details on cryo-EM data processing statistics can be found in table S1.

### Extraction of total proteins for BN-PAGE and SDS-PAGE assays

Four- to 5-week-old plants were agroinfiltrated as described above with constructs of interest, and the leaf tissue was collected 2 days after agroinfiltration in experiments. The final $OD_{600}$ used was 0.3 for all NRC2–wild type or variants used, 0.1 for Rx, 0.1 for PVX CP, and 0.1 for GFP and a total $OD_{600}$ of 0.5. BN-PAGE was performed using the bis-tris NativePAGE system (Invitrogen) according to the manufacturer's instructions. Leaf tissue was ground using a Geno/Grinder tissue homogenizer, and total protein was subsequently extracted and homogenized extraction buffer. For NRC2, GTMN extraction buffer was used [10% glycerol, 50 mM tris-HCl (pH 7.5), 5 mM $MgCl_2$, and 50 mM NaCl] supplemented with 10 mM DTT, 1x protease inhibitor cocktail (Sigma-Aldrich), and

Downloaded from https://www.science.org on August 02, 2025

0.2% NP-40 substitute (Sigma-Aldrich). Samples were incubated in extraction buffer on ice for 15 min with short vortex mixing at every 2 min. Following incubation, samples were centrifuged at 5000*g* for 15 min, and the supernatant was used for BN-PAGE and SDS-PAGE assays.

### BN-PAGE assays

For BN-PAGE, samples extracted as detailed above were diluted as per the manufacturer's instructions by adding NativePAGE 5% G-250 sample additive, 4× sample buffer, and water. After dilution, samples were loaded and run on NativePAGE 3 to 12% bis-tris gels alongside either NativeMark unstained protein standard (Invitrogen) or SERVA Native Marker (SERVA). The proteins were then transferred to polyvinylidene difluoride membranes using NuPAGE transfer buffer using a Trans-Blot Turbo Transfer System (Bio-Rad) as per the manufacturer's instructions. Proteins were fixed to the membranes by incubating with 8% acetic acid for 15 min, washed with water, and left to dry. Membranes were subsequently reactivated with methanol to correctly visualize the unstained native protein marker. Membranes were immunoblotted as described below.

### SDS-PAGE assays

For SDS-PAGE, samples were diluted in SDS loading dye and denatured at 72°C for 10 min. Denatured samples were spun down at 5000*g* for 3 min, and supernatant was run on 4 to 20% Bio-Rad 4 to 20% Mini-PROTEAN TGX gels alongside a PageRuler Plus prestained protein ladder (Thermo Fisher Scientific). The proteins were then transferred to polyvinylidene difluoride membranes using Trans-Blot Turbo Transfer Buffer using a Trans-Blot Turbo Transfer System (Bio-Rad) as per the manufacturer's instructions. Membranes were immunoblotted as described below.

### Immunoblotting and detection of BN-PAGE and SDS-PAGE assays

Blotted membranes were blocked with 5% milk in tris-buffered saline plus 0.01% Tween 20 (TBS-T) for an hour at room temperature and subsequently incubated with desired antibodies at 4°C overnight. Antibodies used were anti-GFP (B-2) horseradish peroxidase (HRP) (Santa Cruz Biotechnology), anti-Myc (9E10) HRP (Roche), and anti-FLAG (M2) HRP (Sigma-Aldrich), all used in a 1:5000 dilution in 5% milk in TBS-T. To visualize proteins, we used Pierce ECL Western (32106, Thermo Fisher Scientific), supplementing with up to 50% SuperSignal West Femto Maximum Sensitivity Substrate (34095, Thermo Fisher Scientific) when necessary. Membrane imaging was carried out with an ImageQuant LAS 4000 or an ImageQuant 800 luminescent imager (GE Healthcare Life Sciences, Piscataway, NJ). Rubisco loading control was stained using Ponceau S (Sigma-Aldrich) or Ponceau 4R (AG Barr).

### Structural modeling and processing

ColabFold v1.5.5 was used to model NbNRC2a CC-NB-ARC (*29*, *48*). The AlphaFold 3 webserver (https://golgi.sandbox.google.com/) was used to model the CC-NB-ARC domains of 11 NRC helpers, 10 CC-NLRs, 6 $CC_{G10}$-NLRs, and 2 $CC_R$-NLRs with 50 oleic acids as a proxy for the plasma membrane (table S2) (*26*). The default seed was set to 1. NbNRC4c and NbNRG1 hexamers were modeled with seed 11. To replicate NbNRC2a oligomers, we generated nine additional models with randomized seed numbers, in addition to the default seed (table S2). From each modeling run, only the top-ranked model (model_0) was retained and processed. The ipTM, pTM, chain-pair ipTM, and minimum chain pTM values were extracted from the AlphaFold 3 JSON files containing model metadata using custom scripts and plotted in R. The AlphaFold 3 models matching the cryo-EM structures of NbNRC2a (9fp6), AtZAR1 (6j5t), and TmSr35 (7xe0) were aligned to the cryo-EM structures using the matchmaker function of ChimeraX with default options (*45*). The contact points from AlphaFold structures were extracted using the ChimeraX (AlphaFold contacts #1/a to #1/b distance of 4.5) (*45*). All structures were visualized using ChimeraX and assembled manually (*45*). All scripts are available at github.com/amiralito/NRC2Hexamer (*49*). AlphaFold predicted structures are deposited on Zenodo (*50*).

## Supplementary Materials

**The PDF file includes:**

Figs. S1 to S18
Table S1
Legend for movie S1
Legends for data S1 and S2

**Other Supplementary Material for this manuscript includes the following:**

Movie S1
Data S1 and S2

## REFERENCES AND NOTES


1. W.-C. Chou, S. Jha, M. W. Linhoff, J. P.-Y. Ting, The NLR gene family: From discovery to present day. *Nat. Rev. Immunol.* **23**, 635–654 (2023).
2. B. Sundaram, R. E. Tweedell, S. P. Kumar, T.-D. Kanneganti, The NLR family of innate immune and cell death sensors. *Immunity* **57**, 674–699 (2024).
3. M. P. Contreras, D. Lüdke, H. Pai, A. Toghani, S. Kamoun, NLR receptors in plant immunity: Making sense of the alphabet soup. *EMBO Rep.* **24**, e57495 (2023).
4. B. P. M. Ngou, P. Ding, J. D. G. Jones, Thirty years of resistance: Zig-zag through the plant immune system. *Plant Cell* **34**, 1447–1478 (2022).
5. A. Förderer, J. Kourelis, NLR immune receptors: Structure and function in plant disease resistance. *Biochem. Soc. Trans.* **51**, 1473–1483 (2023).
6. H. Adachi, L. Derevnina, S. Kamoun, NLR singletons, pairs, and networks: Evolution, assembly, and regulation of the intracellular immunoreceptor circuitry of plants. *Curr. Opin. Plant Biol.* **50**, 121–131 (2019).
7. C.-H. Wu, L. Derevnina, S. Kamoun, Receptor networks underpin plant immunity. *Science* **360**, 1300–1301 (2018).
8. J. Kourelis, T. Sakai, H. Adachi, S. Kamoun, RefPlantNLR is a comprehensive collection of experimentally validated plant disease resistance proteins from the NLR family. *PLOS Biol.* **19**, e3001124 (2021).
9. Y.-B. Zhao, M.-X. Liu, T.-T. Chen, X. Ma, Z.-K. Li, Z. Zheng, S.-R. Zheng, L. Chen, Y.-Z. Li, L.-R. Tang, Pathogen effector AvrSr35 triggers Sr35 resistosome assembly via a direct recognition mechanism. *Sci Adv.* **8**, eabq5108 (2022).
10. A. Förderer, E. Li, A. W. Lawson, Y.-N. Deng, Y. Sun, E. Logemann, X. Zhang, J. Wen, Z. Han, J. Chang, Y. Chen, P. Schulze-Lefert, J. Chai, A wheat resistosome defines common principles of immune receptor channels. *Nature* **610**, 532–539 (2022).
11. J. Wang, M. Hu, J. Wang, J. Qi, Z. Han, G. Wang, Y. Qi, H.-W. Wang, J.-M. Zhou, J. Chai, Reconstitution and structure of a plant NLR resistosome conferring immunity. *Science* **364**, eaav5870 (2019).
12. G. Bi, M. Su, N. Li, Y. Liang, S. Dang, J. Xu, M. Hu, J. Wang, M. Zou, Y. Deng, The ZAR1 resistosome is a calcium-permeable channel triggering plant immune signaling. *Cell* **184**, 3528–3541.e12 (2021).
13. R. Martin, T. Qi, H. Zhang, F. Liu, M. King, C. Toth, E. Nogales, B. J. Staskawicz, Structure of the activated ROQ1 resistosome directly recognizing the pathogen effector XopQ. *Science* **370**, eabd9993 (2020).
14. S. Ma, D. Lapin, L. Liu, Y. Sun, W. Song, X. Zhang, E. Logemann, D. Yu, J. Wang, J. Jirschitzka, Z. Han, J. E. Parker, J. Chai, Direct pathogen-induced assembly of an NLR immune receptor complex to form a holoenzyme. *Science* **370**, eabe3069 (2020).
15. H. K. Ahn, X. Lin, A. C. Olave-Achury, L. Derevnina, M. P. Contreras, J. Kourelis, C. H. Wu, S. Kamoun, J. D. Jones, Effector-dependent activation and oligomerization of plant NRC class helper NLRs by sensor NLR immune receptors Rpi-amr3 and Rpi-amr1. *EMBO J.* **42**, e111484 (2023).


Downloaded from https://www.science.org on August 02, 2025

16. M. P. Contreras, H. Pai, M. Selvaraj, A. Toghani, D. M. Lawson, Y. Tumtas, C. Duggan, E. L. H. Yuen, C. E. M. Stevenson, A. Harant, A. Maqbool, C.-H. Wu, T. O. Bozkurt, S. Kamoun, L. Derevnina, Resurrection of plant disease resistance proteins via helper NLR bioengineering. *Sci Adv.* **9**, eadg3861 (2023).
17. M. P. Contreras, H. Pai, Y. Tumtas, C. Duggan, E. L. H. Yuen, A. V. Cruces, J. Kourelis, H. K. Ahn, K. T. Lee, C. H. Wu, T. O. Bozkurt, L. Derevnina, S. Kamoun, Sensor NLR immune proteins activate oligomerization of their NRC helpers in response to plant pathogens. *EMBO J.* **42**, e111519 (2023).
18. J. M. Feehan, J. Wang, X. Sun, J. Choi, H.-K. Ahn, B. P. M. Ngou, J. E. Parker, J. D. Jones, Oligomerization of a plant helper NLR requires cell-surface and intracellular immune receptor activation. *Proc. Natl. Acad. Sci. U.S.A.* **120**, e2210406120 (2023).
19. H. Adachi, M. P. Contreras, A. Harant, C.-H. Wu, L. Derevnina, T. Sakai, C. Duggan, E. Moratto, T. O. Bozkurt, A. Maqbool, J. Win, S. Kamoun, An N-terminal motif in NLR immune receptors is functionally conserved across distantly related plant species. *eLife* **8**, e49956 (2019).
20. F.-J. Goh, C.-Y. Huang, L. Derevnina, C.-H. Wu, NRC immune receptor networks show diversified hierarchical genetic architecture across plant lineages. *Plant Cell* **36**, 3399–3418 (2024).
21. C.-H. Wu, A. Abd-El-Haliem, T. O. Bozkurt, K. Belhaj, R. Terauchi, J. H. Vossen, S. Kamoun, NLR network mediates immunity to diverse plant pathogens. *Proc. Natl. Acad. Sci. U.S.A.* **114**, 8113–8118 (2017).
22. L. Derevnina, M. P. Contreras, H. Adachi, J. Upson, A. Vergara Cruces, R. Xie, J. Skłenar, F. L. Menke, S. T. Mugford, D. MacLean, W. Ma, S. A. Hogenhout, A. Goverse, A. Maqbool, C.-H. Wu, S. Kamoun, Plant pathogens convergently evolved to counteract redundant nodes of an NLR immune receptor network. *PLOS Biol.* **19**, e3001136 (2021).
23. M. P. Contreras, H. Pai, R. Thompson, C. Marchal, J. Claeys, H. Adachi, S. Kamoun, The nucleotide-binding domain of NRC-dependent disease resistance proteins is sufficient to activate downstream helper NLR oligomerization and immune signaling. *New Phytol.* **243**, 345–361 (2024).
24. M. Selvaraj, A. Toghani, H. Pai, Y. Sugihara, J. Kourelis, E. L. H. Yuen, T. Ibrahim, H. Zhao, R. Xie, A. Maqbool, J. C. De la Concepcion, M. J. Banfield, L. Derevnina, B. Petre, D. M. Lawson, T. O. Bozkurt, C.-H. Wu, S. Kamoun, M. P. Contreras, Activation of plant immunity through conversion of a helper NLR homodimer into a resistosome. bioRxiv 572070 [Preprint] (2023).
25. F. Liu, Z. Yang, C. Wang, R. Martin, W. Qiao, J. E. Carette, S. Luan, E. Nogales, B. Staskawicz, The activated plant NRC4 immune receptor forms a hexameric resistosome. bioRxiv 571367 [Preprint] (2023).
26. J. Abramson, J. Adler, J. Dunger, R. Evans, T. Green, A. Pritzel, O. Ronneberger, L. Willmore, A. J. Ballard, J. Bambrick, Accurate structure prediction of biomolecular interactions with AlphaFold 3. *Nature* **630**, 493–500 (2024).
27. S. Ma, C. An, A. W. Lawson, Y. Cao, Y. Sun, E. Y. J. Tan, J. Pan, J. Jirschitzka, F. Kümmel, N. Mukhi, Oligomerization-mediated autoinhibition and cofactor binding of a plant NLR. *Nature* **632**, 869–876 (2024).
28. L. Abriata, "Sparks of Chemical Intuition"—and Gross Limitations!—in AlphaFold 3, *Medium*, 10 June 2024.
29. J. Jumper, R. Evans, A. Pritzel, T. Green, M. Figurnov, O. Ronneberger, K. Tunyasuvunakool, R. Bates, A. Žídek, A. Potapenko, Highly accurate protein structure prediction with AlphaFold. *Nature* **596**, 583–589 (2021).
30. L. Zhang, S. Chen, J. Ruan, J. Wu, A. B. Tong, Q. Yin, Y. Li, L. David, A. Lu, W. L. Wang, Cryo-EM structure of the activated NAIP2-NLRC4 inflammasome reveals nucleated polymerization. *Science* **350**, 404–409 (2015).
31. C. Duggan, E. Moratto, Z. Savage, E. Hamilton, H. Adachi, C.-H. Wu, A. Y. Leary, Y. Tumtas, S. M. Rothery, A. Maqbool, S. Nohut, T. R. Martin, S. Kamoun, T. O. Bozkurt, Dynamic localization of a helper NLR at the plant–pathogen interface underpins pathogen recognition. *Proc. Natl. Acad. Sci. U.S.A.* **118**, e2104997118 (2021).
32. J. Kourelis, M. P. Contreras, A. Harant, H. Pai, D. Lüdke, H. Adachi, L. Derevnina, C.-H. Wu, S. Kamoun, The helper NLR immune protein NRC3 mediates the hypersensitive cell death caused by the cell-surface receptor Cf-4. *PLOS Genet.* **18**, e1010414 (2022).
33. C.-Y. Huang, Y.-S. Huang, Y. Sugihara, H.-Y. Wang, L.-T. Huang, J. C. Lopez-Agudelo, Y.-F. Chen, K.-Y. Lin, B.-J. Chiang, A. Toghani, Functional divergence shaped the network architecture of plant immune receptors. bioRxiv 571219 [Preprint] (2023).
34. E. Weber, C. Engler, R. Gruetzner, S. Werner, S. Marillonnet, A modular cloning system for standardized assembly of multigene constructs. *PLOS ONE* **6**, e16765 (2011).
35. C. Engler, M. Youles, R. Gruetzner, T.-M. Ehnert, S. Werner, J. D. Jones, N. J. Patron, S. Marillonnet, A golden gate modular cloning toolbox for plants. *ACS Synth. Biol.* **3**, 839–843 (2014).
36. J. Kourelis, S. Malik, O. Mattinson, S. Krauter, P. S. Kahlon, J. K. Paulus, R. A. van der Hoorn, Evolution of a guarded decoy protease and its receptor in solanaceous plants. *Nat. Commun.* **11**, 1–15 (2020).
37. J. I. Bos, T. D. Kanneganti, C. Young, C. Cakir, E. Huitema, J. Win, M. R. Armstrong, P. R. Birch, S. Kamoun, The C-terminal half of Phytophthora infestans RXLR effector AVR3a is sufficient to trigger R3a-mediated hypersensitivity and suppress INF1-induced cell death in Nicotiana benthamiana. *Plant J.* **48**, 165–176 (2006).
38. A. Punjani, J. L. Rubinstein, D. J. Fleet, M. A. Brubaker, cryoSPARC: Algorithms for rapid unsupervised cryo-EM structure determination. *Nat. Methods* **14**, 290–296 (2017).
39. D. Kimanius, L. Dong, G. Sharov, T. Nakane, S. H. Scheres, New tools for automated cryo-EM single-particle analysis in RELION-4.0. *Biochem. J.* **478**, 4169–4185 (2021).
40. S. Q. Zheng, E. Palovcak, J.-P. Armache, K. A. Verba, Y. Cheng, D. A. Agard, MotionCor2: Anisotropic correction of beam-induced motion for improved cryo-electron microscopy. *Nat. Methods* **14**, 331–332 (2017).
41. P. V. Afonine, B. K. Poon, R. J. Read, O. V. Sobolev, T. C. Terwilliger, A. Urzhumtsev, P. D. Adams, Real-space refinement in PHENIX for cryo-EM and crystallography. *Acta Crystallogr. D Struct. Biol.* **74**, 531–544 (2018).
42. K. Jamali, L. Käll, R. Zhang, A. Brown, D. Kimanius, S. H. Scheres, Automated model building and protein identification in cryo-EM maps. *Nature* **628**, 450–457 (2024).
43. P. Emsley, B. Lohkamp, W. G. Scott, K. Cowtan, Features and development of Coot. *Acta Crystallogr. D Biol. Crystallogr.* **66**, 486–501 (2010).
44. C. J. Williams, J. J. Headd, N. W. Moriarty, M. G. Prisant, L. L. Videau, L. N. Deis, V. Verma, D. A. Keedy, B. J. Hintze, V. B. Chen, MolProbity: More and better reference data for improved all-atom structure validation. *Protein Sci.* **27**, 293–315 (2018).
45. E. F. Pettersen, T. D. Goddard, C. C. Huang, E. C. Meng, G. S. Couch, T. I. Croll, J. H. Morris, T. E. Ferrin, UCSF ChimeraX: Structure visualization for researchers, educators, and developers. *Protein Sci.* **30**, 70–82 (2021).
46. W. L. DeLano, Pymol: An open-source molecular graphics tool. *CCP4 Newsl. Protein Crystallogr.* **40**, 82–92 (2002).
47. E. Krissinel, K. Henrick, Inference of macromolecular assemblies from crystalline state. *J. Mol. Biol.* **372**, 774–797 (2007).
48. M. Mirdita, K. Schütze, Y. Moriwaki, L. Heo, S. Ovchinnikov, M. Steinegger, ColabFold: Making protein folding accessible to all. *Nat. Methods* **19**, 679–682 (2022).
49. A. Toghani, amiralito/NRC2Hexamer: Repository release (v1.0.1) (Zenodo, 2024).
50. A. Toghani, T. O. Bozkurt, S. Kamoun, AlphaFold 3 predicted NLR resistosome structures (Zenodo, 2024).

**Acknowledgements:** We thank D. Bubeck (Imperial College London) and R. Frijters (Rijk Zwaan) for useful comments and suggestions. We thank N. Lukoyanova (Birkbeck, University of London, London, UK) for support with cryo-EM imaging. M.P.C. thanks C. Rica and B. Variegatus for inspiration during the writing process. The cryo-EM data for this investigation were collected at ISMB EM facility, which is supported by the Wellcome Trust (202679/Z/16/Z and 206166/Z/17/Z). We thank all members of the TSL Support Services for the invaluable assistance. **Funding:** We received funding from the following sources listed: The Gatsby charitable foundation, Biotechnology and Biological Sciences Research Council (BBSRC) BB/P012574 (Plant Health ISP), BBSRC BBS/E/J/000PR9795, BBSRC BBS/E/J/000PR9796 (Plant Health ISP–Response), BBSRC BBS/E/J/000PR9797 (Plant Health ISP–Susceptibility), BBSRC BBS/E/J/000PR9798 (Plant Health ISP–Evolution), BBSRC BB/V002937/1, BBSRC BB/X016382/1, BBSRC BB/T006102/1, and BBSRC BB/X01102X/1; the European Research Council (ERC) 743165; and UK Research and Innovation (UKRI) Future Leaders Fellowship MR/X033481/1. The funders had no role in the study design, data collection and analysis, decision to publish, or preparation of the manuscript. **Author contributions:** Conceptualization: J.M., A.T., M.P.C., T.O.B., M.W.W., and S.K. Methodology: J.M., A.T., A.P., J.R., and M.W.W. Data curation: J.M., A.T., J.R., and M.W.W. Formal analysis: J.M., A.T., and M.W.W. Investigation: J.M., A.T., J.R., and M.W.W. Resources: S.K. and J.K. Writing—original draft: J.M., A.T., M.P.C, M.W.W., and S.K. Writing—review and editing: J.M., A.T., M.P.C., A.P., J.R., J.K., T.O.B., M.W.W., and S.K. Visualization: J.M., A.T., and M.W.W. Supervision: J.M., M.P.C., M.W.W., and S.K. Project administration: J.M., M.P.C., A.T., M.W.W., and S.K. Funding acquisition: M.W.W. and S.K. **Competing interests:** T.O.B. and S.K. receive funding from industry on NLR biology and cofounded a start-up company (Resurrect Bio Ltd.) on resurrecting disease resistance. M.P.C., J.K., and S.K. have filed patents on NLR biology. M.P.C. and J.K. have received fees from Resurrect Bio Ltd. The other authors declare that they have no competing interests. **Data and materials availability:** All data needed to evaluate the conclusions in the paper are present in the paper and/or the Supplementary Materials. Data related to the NbNRC2 hexamer structure can be found at PDB/EMDB, with PDB ID 9FP6 and EMDB ID EMD-50637, as well as in table S1. Datasets associated to AlphaFold 3 NLR oligomer predictions can be accessed on Zenodo (*50*). All scripts used to extract information from AlphaFold predicted structures are available at github.com/amiralito/NRC2Hexamer (*49*).

Submitted 22 June 2024
Accepted 3 October 2024
Published 6 November 2024
10.1126/sciadv.adr2594

**Correction (27 November 2024):** After publication, an error in the placement of text in the Fig. 5 caption was brought to the attention of the Editorial Office. The following paragraph was erroneously in the Fig. 5 caption and has been moved to the Results section: "How does varying the NbNRC2 stoichiometry...incomplete hexameric-like resistosomes (fig. S7A)." The XML and PDF versions of the article have been updated.

Downloaded from https://www.science.org on August 02, 2025

viruses

MDPI

*Article*

# Exploring the Multifunctional Roles of Odontoglossum Ringspot Virus P126 in Facilitating Cymbidium Mosaic Virus Cell-to-Cell Movement during Mixed Infection

**Shu-Chuan Lee [1], Hsuan Pai [1], Ying-Wen Huang [2], Meng-Hsun He [1], Yun-Lin Song [1], Song-Yi Kuo [2], Wen-Chi Chang [3], Yau-Heiu Hsu [2] and Na-Sheng Lin [1,*]**

1 Institute of Plant and Microbial Biology, Academia Sinica, Taipei 11529, Taiwan; shuchuanlee@gate.sinica.edu.tw (S.-C.L.); chuppadeju904@hotmail.com (H.P.); mhhe@gate.sinica.edu.tw (M.-H.H.); as0200594@gate.sinica.edu.tw (Y.-L.S.)
2 Graduate Institute of Biotechnology, National Chung Hsing University, Taichung 40227, Taiwan; ywhuang0101@gmail.com (Y.-W.H.); unchatbleu124@gmail.com (S.-Y.K.); yhhsu@nchu.edu.tw (Y.-H.H.)
3 College of Biosciences and Biotechnology, Institute of Tropical Plant Sciences, National Cheng Kung University, Tainan 70101, Taiwan; sarah321@mail.ncku.edu.tw
* Correspondence: nslin@sinica.edu.tw; Tel.: +886-2-2789-2897

**Abstract:** Synergistic interactions among viruses, hosts and/or transmission vectors during mixed infection can alter viral titers, symptom severity or host range. Viral suppressors of RNA silencing (VSRs) are considered one of such factors contributing to synergistic responses. Odontoglossum ringspot virus (ORSV) and cymbidium mosaic virus (CymMV), which are two of the most significant orchid viruses, exhibit synergistic symptom intensification in *Phalaenopsis* orchids with unilaterally enhanced CymMV movement by ORSV. In order to reveal the underlying mechanisms, we generated infectious cDNA clones of ORSV and CymMV isolated from *Phalaenopsis* that exerted similar unilateral synergism in both *Phalaenopsis* orchid and *Nicotiana benthamiana*. Moreover, we show that the ORSV replicase P126 is a VSR. Mutagenesis analysis revealed that mutation of the methionine in the carboxyl terminus of ORSV P126 abolished ORSV replication even though some P126 mutants preserved VSR activity, indicating that the VSR function of P126 alone is not sufficient for viral replication. Thus, P126 functions in both ORSV replication and as a VSR. Furthermore, P126 expression enhanced cell-to-cell movement and viral titers of CymMV in infected *Phalaenopsis* flowers and *N. benthamiana* leaves. Taking together, both the VSR and protein function of P126 might be prerequisites for unilaterally enhancing CymMV cell-to-cell movement by ORSV.

**Keywords:** odontoglossum ringspot virus (ORSV); cymbidium mosaic virus (CymMV); viral synergism; RNA silencing; viral suppressor of RNA silencing (VSR); *Phalaenopsis*

check for updates

**Citation:** Lee, S.-C.; Pai, H.; Huang, Y.-W.; He, M.-H.; Song, Y.-L.; Kuo, S.-Y.; Chang, W.-C.; Hsu, Y.-H.; Lin, N.-S. Exploring the Multifunctional Roles of Odontoglossum Ringspot Virus P126 in Facilitating Cymbidium Mosaic Virus Cell-to-Cell Movement during Mixed Infection. *Viruses* **2021**, *13*, 1552. https://doi.org/10.3390/v13081552

Academic Editor: Sylvie German-Retana

Received: 28 June 2021
Accepted: 2 August 2021
Published: 6 August 2021

**Publisher's Note:** MDPI stays neutral with regard to jurisdictional claims in published maps and institutional affiliations.

**Copyright:** © 2021 by the authors. Licensee MDPI, Basel, Switzerland. This article is an open access article distributed under the terms and conditions of the Creative Commons Attribution (CC BY) license (https://creativecommons.org/licenses/by/4.0/).

## 1. Introduction

Mixed infections by plant viruses are commonly found in nature and cause many important viral diseases [1]. The virus–virus and viruses–host interactions in co-infection scenarios may be antagonistic or synergistic depending on the combinations of viral strains, hosts, infection time-points and, in some cases, insect vectors [1,2]. The synergistic interactions arising from mixed infection may result in beneficial effects for one or all viral partners, potentially increasing viral titers and enhancing viral movement and/or symptoms in the host plants [3–8]. The pathological consequences of mixed viral infections are rather unpredictable, but may involve infection time-lapses beyond a threshold level [2]. The molecular mechanisms underlying viral synergism remain largely unclear. However, virus-encoded suppressors that counteract the plant RNA silencing surveillance system not only regulate gene expression for proper development in eukaryotes [9] but also serve in a major strategic role against virus infection [10,11]. Indeed, a few studies have shown that viral suppressors of RNA silencing (VSRs) are determinants of viral synergism.

For instance, in overexpressing the VSRs of potyviral helper component-proteinase (HC-Pro) [8,12], sweet potato chlorotic stunt virus RNase III [13], cucumber mosaic virus 2b [14] and tobacco mosaic virus (TMV) P126 replicase [15] increased host susceptibility and the accumulation of unrelated viruses.

Orchids are the largest Monocotyledon family, with more than 900 genera and 20,000 to 35,000 species [16]. More than 50 viruses have been reported to infect orchids [17]. Among them, the odontoglossum ringspot virus (ORSV) and cymbidium mosaic virus (CymMV) are two of the most prevalent orchid-infecting viruses worldwide [18,19]. Single infection with ORSV or CymMV causes orchids to display growth defects and diminished flower quality, whereas co-infection results in synergistic effects that exacerbate disease severity, which can erode the orchid's economic value [18–22] and even cause plant death [18,23,24].

ORSV and CymMV are taxonomically distinct viruses exhibiting different genome organizations and morphologies. ORSV is a *Tobamovirus*, with a genome size of ~6.6 kb and a tRNA-like structure at its 3′-terminus [25]. This single-stranded, positive-sense RNA genome has four open reading frames (ORFs) that encode P126 replicase and its readthrough product P183, movement protein (MP) and capsid protein (CP). The mutation of $Phe^{50}$ to $Ser^{50}$ in P126/183 of an ORSV infectious cDNA clone abolished ORSV replication [26]. Moreover, the ORSV replicase is responsible for host range restriction in *Nicotiana sylvestris* [27]. For other tobamoviruses, P126 was shown to act in a non-membrane-bound form as an VSR [28,29], but it may form a membrane-bound heterodimer with P183 for viral replication. P126 has methyltransferase (MET), non-conserved region (NON) and helicase (HEL) domains. The MET, HEL and a portion of the NON-domains of TMV P126 individually possess VSR activity and, notably, the VSR activities of the MET and HEL domains can operate independently from their enzymatic activities [30]. The P126 protein interferes with the RNA silencing pathway by binding to duplexes of small interfering RNAs (siRNAs), which may inhibit HEN1-mediated siRNA methylation and potentially sequesters them to prevent the RNA-induced silencing complex (RISC) formation [31,32]. By contrast, CymMV is a *Potexvirus*, with a poly(A)-tailed, single-stranded and positive-sense RNA genome of ~6.2 kb [33]. The CymMV genome comprises five ORFs that encode RNA-dependent-RNA polymerase (RdRp) for genome replication, three overlapping triple-gene-block proteins (TGBps) for cell-to-cell and long-distance movement and CP for virus encapsidation. The CymMV CP also contributes to viral movement within different hosts [34].

Synergistic ORSV and CymMV isolated from *Cattleya* exhibited enhanced replication upon co-infection of *Dendrobium* petal protoplasts relative to the single infection, displaying earlier and higher viral RNA titers [3]. Interestingly, transgenic plants expressing CymMV TGBps supported the cell-to-cell movement of a movement-deficient ORSV mutant, and the cell-to-cell movement-deficient CymMV was rescued in ORSV MP transgenic plants [6]. However, long-distance movement of a CymMV CP-deficient mutant could be rescued in ORSV CP transgenic plants, but CymMV CP transgenic plants were unable to restore systemic movement of an ORSV CP-deficient mutant [6]. Although *Phalaenopsis* orchids co-infected with ORSV and CymMV exhibited significant symptom intensification, unlike the viral synergism found in *Cattleya*, CymMV movement was unilaterally boosted by ORSV in co-inoculated *Phalaenopsis* [35]. Virus titers of CymMV and ORSV were similar upon single or co-infection of protoplasts from *Nicotiana benthamiana* leaves and *Phalaenopsis amabilis* flowers [35,36].

Here, we show that ORSV P126 is a VSR and our mutation analysis demonstrates that its VSR activity can operate independently of its virus replication activity. Moreover, the VSR and protein functions of ORSV P126 are required in order to facilitate CymMV cell-to-cell movement, enabling the unilateral synergism that enhances CymMV infection. Our findings provide insights into the mechanism underlying asymmetric synergism during CymMV and ORSV co-infection in *Phalaenopsis*.

## 2. Materials and Methods

### *2.1. Plants and Growth Conditions*

*N. benthamiana* and *Chenopodium quinoa* plants were grown at 28 °C with a 16 h/8 h light/dark photoperiod in a walk-in growth chamber. *Phalaenopsis* plants were purchased from Clone International Biotech Co. Ltd. (Pingtung, Taiwan). *Phalaenopsis* plants were first validated to be CymMV-free and ORSV-free by reverse transcription-polymerase chain reaction (RT-PCR) [37] before being subjected to virus inoculation.

### *2.2. RT-PCR Detection of CymMV and ORSV*

CymMV-free and ORSV-free *Phalaenopsis* plants were screened by multiplex RT-PCR by using primers for the amplification of CymMV, ORSV and an internal *nad5* control (Table S1) [37]. Briefly, the RT-PCR first-strand cDNA reaction was performed by using SuperScript™ III Reverse Transcriptase (Invitrogen, Carlsbad, CA, USA) and via simultaneous addition of three reverse primers: CymMV CP-R1, ORSV CP-R1 and mt-R1. PCR was then performed on cDNAs by using a multiplex primer set (including 2.5 μM mt-F2/mt-R1, 1.25 μM CymMV CP-F1/CymMV CP-R1 and 1.25 μM ORSV CPF1/ORSV CP-R1) and 2× SuperRed PCR Master Mix (Biotools Co. Ltd., New Taipei City, Taiwan) by following the manufacturer's instructions. The RT-PCR products were then analyzed by agarose gel electrophoresis.

### *2.3. Virus Isolation, Purification, Inoculation and RNA Extraction*

CymMV and ORSV isolated from diseased *Phalaenopsis* plants were maintained in *N. benthamiana* plants [35,36], and the virions were purified as described previously [38]. Purified virions were adjusted to 2 mg/mL and stored at −80 °C.

For single virus inoculation, plants were inoculated with 0.5 μg/leaf of CymMV or ORSV virions or with 1 μg of viral transcripts. For co-infection scenarios, a mixture of 0.5 μg/leaf CymMV and 0.5 μg ORSV virions was used to inoculate leaves of 3-week-old *N. benthamiana*, 5-week-old *C. quinoa* or 6-month-old acclimatized *Phalaenopsis*. The replication of the ORSV infectious clone OS4 and its P126 mutants was verified by inoculation of viral transcripts to *C. quinoa* or agro-infiltration of *Agrobacterium* carrying pkn, pkOS4, pkOS4-P126R, pkOS4-P126S or pkOS4-P126R to *N. benthamiana*.

Plant leaf total RNAs were extracted by TRIzol® Reagent following the manufacturer's instructions (Invitrogen, Carlsbad, CA, USA). RNA quality and quantity were assessed using a NanoDrop 1000 Spectrophotometer (ThermoFisher Scientific Inc., Wilmington, DE, USA) and samples were stored at −80 °C.

### *2.4. Plasmid Construction*

The full-length CymMV and ORSV genomes were directly amplified by RT-PCR from the total RNAs of orchids inoculated with wild isolate (wt) virions of CymMV and ORSV. Briefly, one microgram of total RNA was used for first-strand cDNA synthesis by using the SuperScript III reverse transcriptase (Invitrogen, Carlsbad, CA, USA) and primer ORSV-RP1 or CymMV-RP1, respectively. The first strand cDNAs were then used as templates for primer pairs—ORSV-FP1 and ORSV-RP1 for ORSV; CymMV-FP1 and CymMV-RP1 for CymMV—to synthesize the full-length genomes by PCR using Phusion Flash High-Fidelity PCR Master Mix (ThermoFisher Scientific Inc.). The amplified fragments were purified by using a QIAEX II Gel Extraction Kit (QIAGEN, Hilden, Germany), digested with *Sac*I and *Sma*I (for CymMV) or *Bam*HI and *Spe*I (for ORSV) and then cloned into pU119 vector at the corresponding sites to generate pUCy1 and pUOS4 constructs, respectively.

The full-length ORSV cDNA clones harboring the P126 M1104R/S/A mutation—pUOS4-P126R, pUOS4-P126S and pUOS4-P126A—were generated by using a QuikChange Site-Directed Mutagenesis Kit (Agilent Technologies, Santa Clara, CA, USA) and the primer pairs that are presented in Table S1. The full-length Cy1 fragment of pUCy1 was further PCR-amplified and subcloned into pkn binary vector [39] to generate pkCy1 plasmid. The same procedure was used to generate pkOS4, pkOS4-P126R, pkOS4-P126S and pkOS4-

P126A from pUOS4, pUOS4-P126R, pUOS4-P126S and pUOS4-P126A, respectively. Clones were confirmed by sequencing. The CymMV construct with a green fluorescent protein (GFP) reporter, pkCy1GFP, was generated by inserting the GFP gene downstream of the duplicated CymMV CP subgenomic promoter (−100 to +22 [40]). A 35S promoter-driven mCherry expression cassette was further amplified by PCR and inserted into the *Bgl*II site of pkn vector to obtain pkn::mCherry. The pkCy1GFP::mCherry construct was generated by subcloning the 2× 35S promoter-Cy1GFP expression cassette from pkCy1GFP into pkn::mCherry.

For transient expression assays, viral ORFs or mutants were PCR-amplified from pUCy1, pUOS4 or pUOS4 mutants and cloned between two *Sma*I sites or between the *Sma*I and *Bam*HI sites of the pBIN61 binary vector [41] with a HA sequence at their C-terminus. The ORSV P126 ORF mutants were generated by using a QuikChange Site-Directed Mutagenesis Kit (Agilent Technologies), with pBIN61-ORSV P126 and pBIN61-ORSV P126-R as templates. All primers used for cloning and detection are listed in Table S1. All clones described below were verified by restriction enzyme digestion and DNA sequencing. The VSR indicator, pBIN61-GFP (GFP) and the positive controls pBIN19-P19 and pBIN61-P25, which encode tomato bushy stunt virus (TBSV) P19 and potato virus X (PVX) P25 proteins, were gifts from Dr. David Baulcombe, University of Cambridge, UK.

### *2.5. In Vitro Transcription*

The plasmids of pUCy1 or pUOS4 were linearized by *Sma*I or *Spe*I digestion, respectively. Capped transcripts corresponding to the wt virus were synthesized through in vitro transcription by using T7 RNA polymerase (Promega, Madison, WI, USA) in the presence of the cap analogue m7G(5′)ppp(5′)G (New England Biolabs, Inc., Ipswich, MA, USA) under the reaction conditions recommended by the manufacturer.

### *2.6. Tissue Blotting and RNA Blot Analysis*

Tissue blotting to reveal virus infection and distribution in inoculated *Phalaenopsis* leaves was performed as described previously [35,42]. In brief, leaf slices from inoculated and adjacent non-inoculated tissues were printed onto Hybond™-$N^+$ membranes (GE Healthcare Life Sciences, Buckinghamshire, UK) and hybridized with riboprobes specific to CymMV/ORSV full-length CP genes by using the DIG Nucleic Acid Detection Kit (Sigma-Aldrich, St. Louis, MO, USA). Northern blot analysis was performed, as described previously [43,44], by using DIG-labeled probes targeted to the CP and 3′ UTR sequence of the pUCy1 and pUOS4 genomes.

### *2.7. Agrobacterium Infiltration and GFP Imaging*

The VSR activity assay for individual viral ORFs was performed as described previously [45] with some modifications. *Agrobacterium tumefaciens* harboring corresponding plasmids was grown overnight at 28 °C. The bacteria were then pelleted down and suspended in 0.1 volume of induction solution (10 mM $MgCl_2$ and 100 μM acetosyringone in sterile water) and incubated in the dark at room temperature for 4 hours. Equal volumes of *A. tumefaciens* cultures ($OD_{600}$ = 1) expressing positive sense-GFP, pBIN61-eGFP and *A. tumefaciens* cultures ($OD_{600}$ = 1) harboring pBIN61-viral ORF-HA expression vectors were mixed and co-infiltrated into the leaves of 3-week-old to 4-week-old *N. benthamiana*. Expression plasmids for the VSRs P19 encoded by TBSV (pBIN19-P19) and P25 encoded by PVX (pBIN61-p25) were used as positive controls, whereas empty vector (pBIN61) served as a negative control. The agroinfiltrated leaves were illuminated under a long-wavelength UV lamp (Black Ray model B 100 AP) and photographed at 4 days post-agroinfiltration (DPA). The GFP signal intensity was detected and measured by using an IVIS Lumina III LT in vivo Imaging System (XENOGEN Co., Alameda, CA, USA) [46]. All experiments were repeated three times. The images were processed electronically by using Adobe Photoshop CS5.

In order to measure CymMV cell-to-cell movement, cultures of *A. tumefaciens* carrying pBIN61 (vector), pBIN61-P126 or P126-derived mutants were induced and adjusted to $OD_{600}$ = 0.5 for infiltration. Two hours after infiltration, the bacterial ooze of *A. tumefaciens* carrying pkCy1GFP::mCherry was pinpricked into infiltrated leaves using a toothpick for infection. CymMV cell-to-cell movement was observed by using an IVIS Lumina III LT in vivo Imaging System (XENOGEN Co., Alameda, CA, USA) at 6 DPA and then quantified by using its Live Imaging software. Images were processed in ImageJ (NIH).

### 2.8. Western Blot Analysis

The leaf tissue from infiltration zones was ground in liquid nitrogen and resuspended (20 (*v/w*)) in 2× MURB buffer (100 mM sodium phosphate, pH 7.0, 50 mM MES, 2% (*w/v*) sodium dodecyl sulfate, 6 M Urea; and 1 mM sodium azide with freshly added 10% (*v/v*) β-mercaptoethanol). The protein samples were incubated at 55 °C for 15 min and then subjected to SDS-PAGE and immunoblot analysis. Anti-CymMV CP serum was used to detect CymMV, as described previously [17]. The detection of ORSV was performed by using anti-ORSV CP serum generated by immunizing rabbits with purified ORSV virions. The overexpression of ORSV P126 and derived mutant proteins were detected via their C-terminus HA tags by using the monoclonal anti-HA antibody produced in mice (Sigma-Aldrich, St. Louis, MO, USA). Plant actin was used as a protein loading control and was detected by using monoclonal anti-Actin (clone 10-B3, Sigma, St. Louis, MO, USA) and horseradish peroxidase (HRP)-linked secondary antibodies. GFP was detected using HRP-conjugated anti-GFP antibody (Abking Biotechnologies Inc., Taipei, Taiwan). Immunoreactivity was detected by using the Clarity™ Western ECL Substrate (Bio-Rad Laboratories, Inc., Hercules, CA, USA) as per the manufacturer's instructions. Blots were exposed to X-ray film for various time-periods. All experiments were repeated three times. The signal intensity was quantified in ImageJ.

### 2.9. Statistical Analysis

Statistical analysis was performed by one-way ANOVA and followed by a post-hoc test. The significant differences are marked as follows: *: $p < 0.05$; **: $p < 0.01$; ***: $p < 0.001$; ****: $p < 0.0001$; and ns: no significant difference.

## 3. Results

### 3.1. Construction of ORSV and CymMV Infectious cDNA Clones

The viral synergism caused by ORSV and CymMV isolated from *Phalaenopsis* [35,36] was confirmed by back-inoculation of purified virions to *Phalaenopsis* plants alone or mixed (Figure S1). In order to characterize the biological properties of *Phalaenopsis* ORSV and CymMV isolates, we generated their infectious cDNA clones. By aligning all eight full-length ORSV genome sequences currently available from the NCBI database, we used the conserved 5′ and 3′ sequences to design the primers ORSV-FP1 and ORSV-RP1 (Figure S2A) for the direct amplification of the complete ORSV genome from total RNA of infected *Phalaenopsis* leaves by RT-PCR. The amplified ORSV cDNA genome was linked to an upstream T7 promoter and a downstream restriction enzyme site (*Spe*I) (Figure S3A and Table S1). *Spe*I cleavage resulted in the correct 3′ terminus sequence of ORSV, thereby preventing the incorporation of any non-viral sequences that might adversely affect ORSV clone infectivity [47,48]. Infectivity of ORSV cDNA clones was verified by inoculating the in vitro synthesized ORSV RNA transcripts into *C. quinoa*. Inoculated *C. quinoa* leaves presented localized chlorotic lesions in which ORSV accumulation was detected by Western blot using anti-ORSV CP serum after 4 days post-inoculation (DPI) (Figure S3B,C). The infectious transcripts derived from ORSV cDNA clone, denoted OS4 hereafter, were inoculated into *C. quinoa* for virion purification. The CPs purified from OS4 or ORSV wild isolate (OR-wt) virions are ~17 kDa and are indistinguishable from one another (Figure S3D). The OS4 genome sequence comprises 6611 nucleotides in length and demonstrates 97–99% identity

relative to the ORSV genomes published in the NCBI database, and they display similar genome organizations (Figure S4A,B).

In order to generate CymMV infectious cDNA clones, we used the same strategy as for ORSV. The full-length CymMV genome was amplified using specific primers CymMV-FP1 and CymMV-RP1 and linked to an upstream T7 promoter and a downstream poly(A) tail; we designated this infectious cDNA clone as pUCy1 (Figure S3A and Table S1). Inoculation of in vitro synthesized pUCy1 RNA transcripts, denoted Cy1 hereafter, into *C. quinoa* leaves resulted in tiny lesions, which displayed detectable CymMV CP accumulation based on Western blot using anti-CymMV CP serum after 8 DPI (Figure S3B,C). The size of the CP protein from Cy1 virions purified from inoculated *C. quinoa* was ~25 kDa, i.e., indistinguishable from that of wild CymMV isolate (Cy-wt) (Figure S3D). Sequence analysis of pUCy1 revealed it was 6225 nucleotides long, excluding the poly(A) tail, and it exhibits 96–97% identity to most CymMV genomes published in the NCBI database and presents similar genome organization (Figure S4C,D).

### *3.2. Asymmetric Synergism of CymMV and ORSV Infection in N. benthamiana and Phalaenopsis Orchid*

Since OS4 and Cy1 derived from infected *Phalaenopsis* were shown to be infectious (Figure S3), we assayed synergistic interactions between OS4 and Cy1 in an experimental host, *N. benthamiana*. The infection of Cy1 alone resulted in tiny localized chlorotic/white lesions in the inoculated leaves (IL) of *N. benthamiana* at 14 DPI, but few lesions or no symptoms on systemic leaves (SL) were observed (Figure 1A). The growth of Cy1-inoculated *N. benthamiana* was comparable to mock-inoculated plants (Figure 1A). Accumulation of Cy1 CP could be detected in IL at 14 DPI and slightly in SL via Western blot using an antibody against CymMV CP (Figure 1B). RNA blotting confirmed Cy1 RNA accumulation in inoculated plants (Figure 1C). By contrast, OS4 did not cause visible symptoms on IL, but plants showed yellowing and distortion of SL and whole-plant growth defects at 14 DPI (Figure 1A). As for Cy1, there was a substantial accumulation of OS4 CP and RNA in both IL and SL based on Western blot and RNA blot analyses, respectively (Figure 1B,C). However, *N. benthamiana* co-infected with Cy1 and OS4 exhibited more severe symptoms in IL, SL, and whole-plant growth defects than presented upon single infection (Figure 1A). In co-infected leaves, Cy1 CP and Cy1 RNA were hyper-accumulated in IL relative to levels observed for single infection, indicating that Cy1 levels were enhanced by OS4 (Figure 1B,C). In SL, dramatic increases in Cy1 CP and Cy1 RNA levels were noted upon co-infection (Figure 1B,C). However, the levels of OS4 CP and RNA were similar regardless of single or co-infection (Figure 1B,C), which is consistent with our previous reports [35,36]. Thus, our infectious clones Cy1 and OS4 faithfully recapitulated the asymmetric synergistic effects of virion wild isolates from *Phalaenopsis* orchid, i.e., unilaterally enhanced CymMV accumulation and systemic movement due to ORSV, which result in enhanced disease symptoms during co-infection.

In order to further examine the viral synergism of Cy1 and OS4 in a natural host, we inoculated Cy1 and/or OS4 virions onto half a leaf-tip of *Phalaenopsis* leaves. After 10 DPI, no symptoms were observed for leaves inoculated solely with Cy1 or OS4 (Figure S5A), although tissue blots revealed accumulations of Cy1 and OS4 RNAs, respectively (Figure S5B). However, in contrast to symptomless single infection, co-infected orchid leaves presented necrotic, ring-like lesions (Figure S5A) and enhanced Cy1 movement relative to non-inoculated neighboring tissues at 10 DPI (Figure S5B), which is consistent with our findings from *N. benthamiana* (Figure 1). Thus, the Cy1 and OS4 faithfully represent the biological characteristics of Cy-wt and OR-wt from the *Phalaenopsis* orchid (Figures S1 and S5).

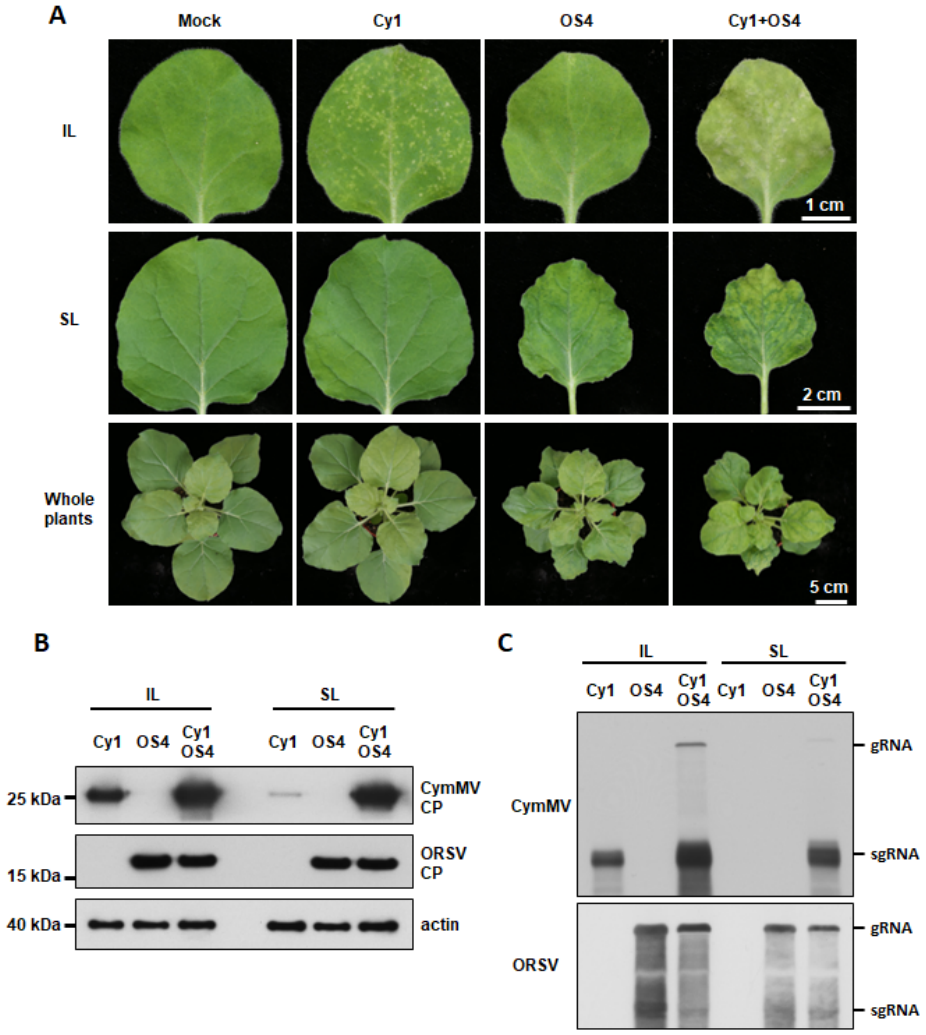


**Figure 1.** Cy1 and OS4 infectivity and synergism in inoculated *N. benthamiana* plants. (**A**) Symptoms and synergistic effects upon co-infection with Cy1 and OS4 virions. Eighteen-day-old *N. benthamiana* plants were individually inoculated with 0.5 μg/leaf of Cy1 or OS4 virions or co-inoculated with 1 μg/leaf of Cy1 and OS4 (0.5 μg/leaf each). Symptoms on inoculated leaves (IL), systemic leaves (SL) and whole plants were photographed at 14 DPI. (**B**) Immuno-detection of Cy1 and OS4 CPs from leaf extracts of inoculated plants at 14 DPI using antibodies against the CP of CymMV or ORSV. Actin was detected by using anti-Actin monoclonal antibody as a protein loading control. (**C**) RNA blots for assessing Cy1 and OS4 viral RNA accumulation. Total RNAs were extracted from leaves as in (**B**). RNA was detected by using DIG-labeled probes against the CP and 3′ UTRs of Cy1 or OS4, respectively.

### *3.3. Identification of ORSV-Encoded P126 as a VSR*

Several studies have shown that expression of VSRs can increase host susceptibility and virus titers of unrelated viruses [2,12–15]. Accordingly, we wondered if ORSV also encodes a VSR that could contribute to CymMV and ORSV synergism. We identified candidate ORSV VSRs by co-expressing GFP together with individual OS4-encoded proteins in an *Agrobacterium*-mediated expression system [45]. Two well-characterized VSRs, TBSV P19 and PVX P25 (P19 and P25 hereafter) were used as strong or moderate VSR controls, respectively, and an empty vector acted as a negative control (Figure 2A). The OS4 ORFs or protein domains, including the MET, NON, HEL and polymerase domain p54, were individually cloned into binary vector pBIN61 to generate transient-expressing protein constructs (Figure 2B). After the co-expression of GFP and individual HA-tagged viral proteins, the relative GFP signal intensity was measured at 4 DPA. As anticipated, the GFP signal was enhanced strongly by P19 and moderately by P25 (Figure 2C,D). Among the

ORSV constructs we tested, only P126 showed statistically significant VSR activity, which was comparable to P25 (Figure 2C,D). Moreover, P126 expression also increased the GFP protein accumulation as P19 and P25 did (Figure 2E). These results indicate that the ORSV P126 replicase is a VSR. When the viral proteins were co-expressed, all OS4 viral proteins, including P126 (Figure 2E), were detectable by Western blots, with the exception of the HEL and p54 proteins (Figure S6A). Thus, their VSR activities need to be examined further. In addition, we also assayed the potential VSR candidates among Cy1 ORFs. Although Cy1 RdRp, TGBp1, TGBp3 and CP were indeed expressed (Figure S6B), none of them exhibited significant VSR activity (Figure S6C). As Cy1 TGBp2 protein was not detected, its VSR activity could not be concluded.

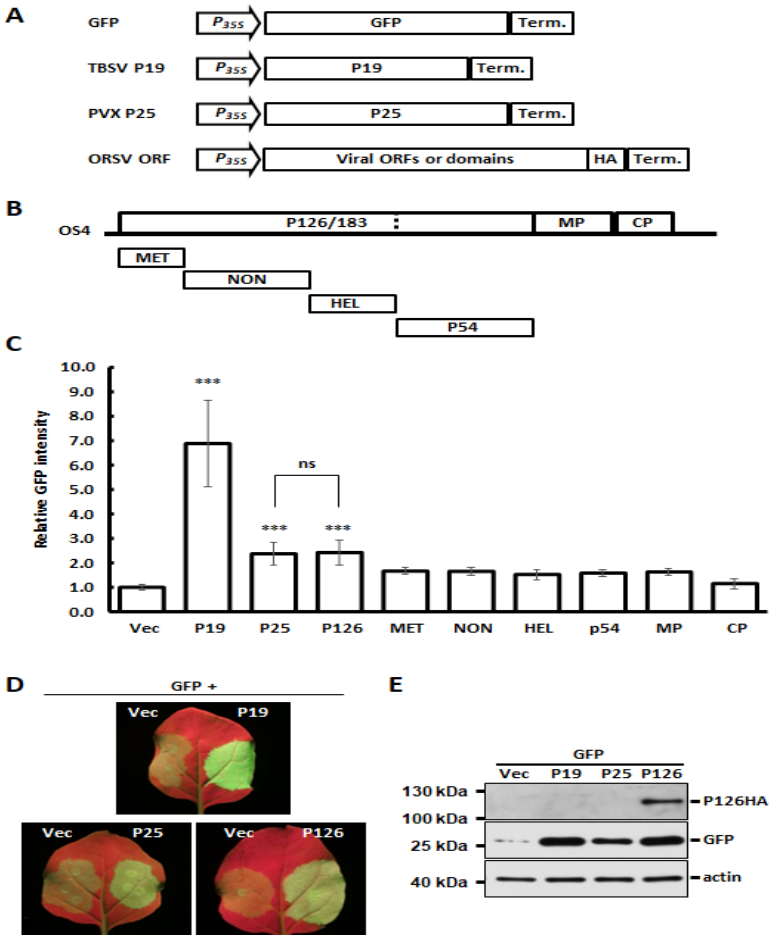


**Figure 2.** VSR assays of ORSV-encoded proteins and protein domains. (**A**) Schematics of expression cassettes for GFP (reporter), TBSV P19 and PVX P25 (VSR positive controls), as well as tested ORSV ORFs. (**B**) Individual ORFs and domains used for VSR assay. (**C**) Quantitative analysis of VSR activities. Overnight cultures of *Agrobacterium* carrying a corresponding plasmid were adjusted to final OD = 1. The co-infiltration of *N. benthamiana* leaves was performed by mixing *Agrobacterium* carrying pBIN61-GFP and *Agrobacterium* carrying plasmid positive for VSR or tested viral ORFs in a ratio of 1:1. GFP signals were detected and quantified using the IVIS Lumina III LT in vivo Imaging System at 4 DPA. Relative GFP intensity represents the mean of three independent experiments and was normalized to vector control. The significance was calculated by one-way ANOVA followed by post-hoc test and marked when $p < 0.001$ (***); ns: no significant difference. (**D**) Representative images of GFP signals as observed under hand-held UV lamp. (**E**) Accumulation of HA-tagged P126, GFP and actin in (**D**) was assessed by Western blotting by using antibodies against HA, GFP and actin, respectively.

### *3.4. Single Amino Acid Substitution Abolishes ORSV P126 VSR Activity*

The VSR activity of several *Tobamovirus* P126 mutants has previously been reported to be diminished or abolished [28–30]. We substituted several amino acids to alanine (A)—including Gly (G)$^{325}$, Leu (L)$^{348}$, Lys (K)$^{367}$, Glu (E)$^{601}$, Glu (E)$^{663}$ and Val (V)$^{742}$—which corresponded to tobamovirus replicase mutants exhibiting defective VSR activity (Figure S7A). We also mutated Met (M)$^{1104}$ to Arg (R), since a screening of ORSV cDNA clones had revealed this mutation eliminated ORSV replication. Several single (e.g., E$^{601}$A) and double (e.g., E$^{601}$A and M$^{1104}$R) mutants were generated (Figure S7B). Most of the ORSV P126 single mutants exhibited a similar level of VSR activity to parental P126 protein in terms of enhancing GFP accumulation, except for P126-R$^{1104}$ (P126R) (Figure 3 and Figure S7B). A further two single mutants, P126S and P126A representing the mutation of M$^{1104}$ to Ser or Ala, respectively, exhibited similar VSR activity (Figure 3A,C) to P126, despite P126A or P126S mutant protein levels being reduced relative to P126 (Figure 3B). Notably, the P126R protein level was barely detectable and that could be due to the protein instability (Figure 3B and Figure S7C). As expected, none of the P126R double mutants presented any VSR activity (Figure S7B).

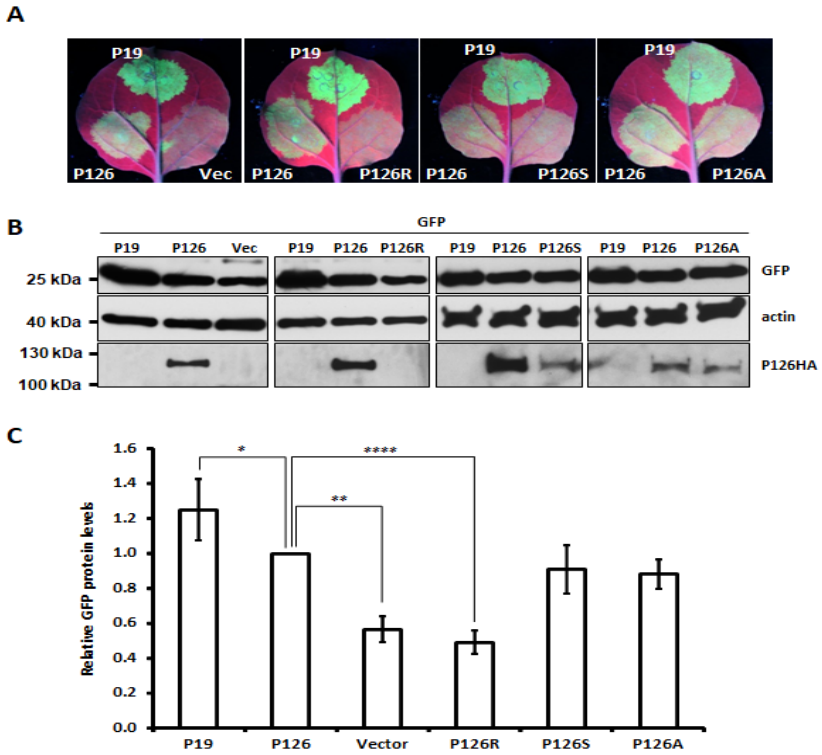


**Figure 3.** VSR activity of single amino acid substitution mutants of ORSV P126. (**A**) GFP signals upon co-expression with vector control (Vec), P19, P126 and derived P126 mutants. (**B**) Total protein was extracted from the infiltrated leaf discs and then subjected to Western blot in order to detect GFP, actin, P126 and mutant variants. (**C**) Relative GFP protein level was normalized with actin. The GFP level upon co-expression with P126 was set as 1. Vec: vector control. Data represent results from three different experiments. Significant differences are marked as follows: *: $p < 0.05$; **: $p < 0.01$; **** $p < 0.0001$ (one-way ANOVA followed by a post-hoc test).

### *3.5. ORSV P126 VSR Activity Uncouples ORSV Replication*

Since the full-length ORSV cDNA clone harboring the P126R mutation was unable to replicate, we wondered if the ORSV clones with the P126S and P126A mutations, which retained VSR activity, remained infectious. We generated the corresponding cDNA clones OS4-P126S and OS4-P126A and inoculated their transcripts or OS4 control onto *C. quinoa* leaves. We observed localized lesions at 5 DPI upon OS4 control inoculation but not for

the P126R, P126S or P126A mutants (Figure 4A). Moreover, only OS4 control-inoculated tissues exhibited substantial CP accumulation, whereas none of leaves inoculated with the mutants did (Figure 4B). The replication of OS4 and OS4-P126 mutants were further assayed on *N. benthamiana* by agro-infiltration. The accumulations of CP and viral RNAs were detected from OS4 but not from OS4-P126 mutants by Western and RNA blots at 2 and 8 DPA, respectively (Figure 4C,D), indicating that the amino acid substitution in P126 $M^{1104}$ abolished ORSV replication. Thus, P126 has two distinct roles in virus replication and RNAi suppression.

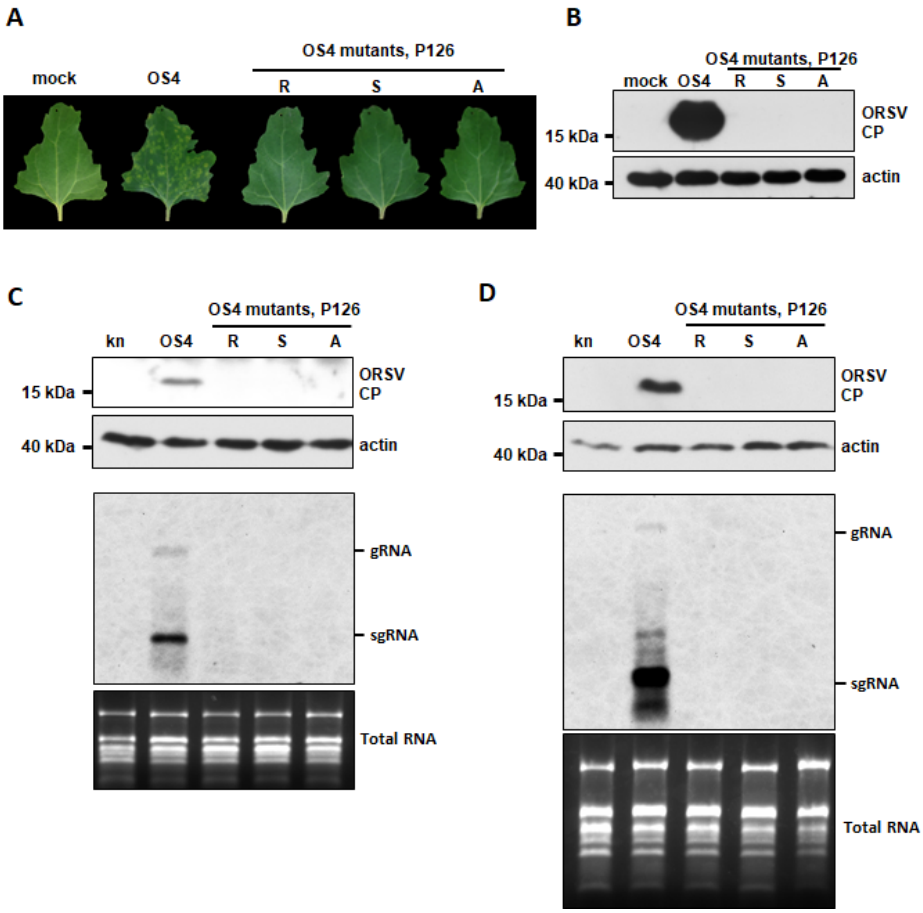


**Figure 4.** Replication of OS4 and its P126 mutants. (**A**) Symptoms of *C. quinoa* leaves inoculated with transcripts of OS4 and P126 mutants at 5 DPI. Mock represents leaves inoculated with phosphate buffer, which were used as a control. (**B**) Accumulation of ORSV CP in (**A**) as assessed by Western blot. Actin acted as a loading control. (**C**,**D**) Accumulations ORSV CP and viral RNAs in *N. benthamiana* at 2 DPA (**C**) and 8 DPA (**D**), respectively. *Agrobacterium* carrying pkn, pkOS4, pkOS4-P126-R, P126-S and P126-A mutants were adjusted to $OD_{600}$ = 1 and infiltrated into 17-day-old *N. benthamiana* leaves. Western blot detection of ORSV CP (upper two panels) and RNA blot for ORSV RNAs (lower two panels) were performed as described in Figure 1. Total RNA was used as RNA loading control.

### *3.6. ORSV P126 Is the Synergistic Determinant That Enhances CymMV Cell-to-Cell Movement*

Our previous studies demonstrated that the co-infection of *Phalaenopsis*-derived CymMV and ORSV isolates did not enhance viral accumulation at the single cell level [35,36]. However, we observed greatly enhanced accumulation of Cy1 in *N. benthamiana* IL and SL upon co-infection with OS4 (Figure 1B,C). In order to test if ORSV P126 synergistically enhances CymMV accumulation by increasing CymMV cell-to-cell movement, we generated a dual expression cassette, pkCy1GFPF::mCherry, that is driven by the 35S promoter for *Agrobacterium*-mediated transient expression (Figure 5A). The mCherry and GFP signals, representing the infection foci of *Agrobacterium* and Cy1GFP, respectively, could be

observed simultaneously after agro-infiltration of *N. benthamiana* leaves with *Agrobacterium* carrying pkCy1GFP::mCherry (Figure S8A,B). At 4 DPA, we observed that the mCherry signal was restricted to the infection site, whereas the expanded GFP signal represented cell-to-cell movement of Cy1GFP (Figure S8C).

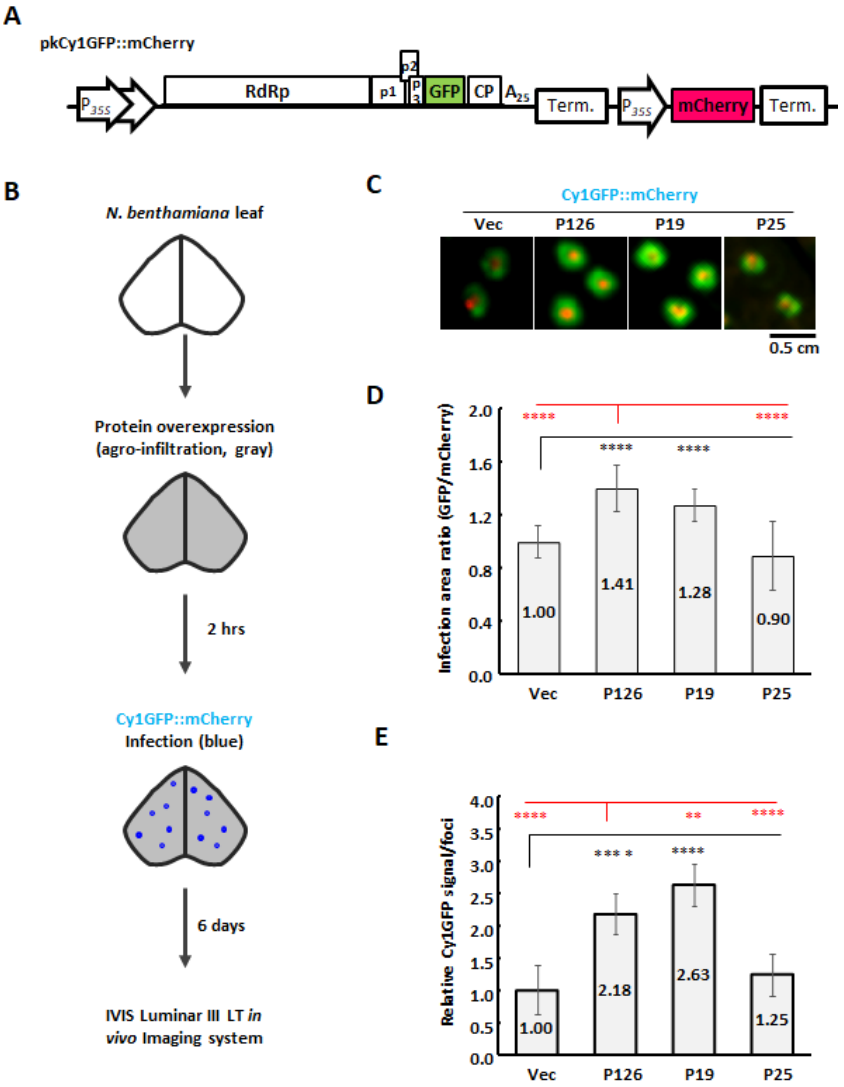


**Figure 5.** CymMV cell-to-cell movement and accumulation upon overexpressing VSRs in *N. benthamiana* leaves. (**A**) Schematic construct of pkCy1GFP::mCherry. (**B**) Flowchart for protein expression and CymMV inoculation. *Agrobacterium* carrying pBIN61 (Vec), pBIN61-P126 (P126), pBIN19-P19 (P19) or pBIN61-P25 (P25) were adjusted to $OD_{600}$ = 0.5 and then infiltrated into 17-day-old *N. benthamiana* leaves. After 2 hours post-agroinfiltration, the *Agrobacterium* ooze carrying pkCy1GFP::mCherry was collected on a toothpick and pinpricked onto the infiltrated leaves. (**C**) Representative images of *Agrobacterium* primary infection sites (mCherry in red) and Cy1GFP spreading infected cells (GFP in green) using the IVIS Lumina III LT in vivo Imaging System at 6 DPA. Images were processed in ImageJ. (**D**) Quantification of CymMV movement. According to (**C**), the ratio of coverage areas was measured by the expanded Cy1GFP signals (GFP) against primary infection site (mCherry). (**E**) Effects of VSRs on accumulation of Cy1GFP. The relative Cy1GFP signals were measured by the total GFP signals per infection foci and quantification was normalized to vector control (black star) or P126 (red star). Data represent three experimental replicates, each of which encompassed analysis of six infection foci. Significant differences are marked as follows: **: $p < 0.01$ and ****: $p < 0.0001$ (one-way ANOVA followed by post-hoc test).

In order to evaluate the function of P126 protein in CymMV cell-to-cell movement, we overexpressed P126 protein or vector control in *N. benthamiana* leaves, followed by agro-infection of Cy1GFP::mCherry by using a toothpick (Figure 5B). Expanded Cy1GFP signal could be observed at 6 DPA (Figure 5C) and the virus spreading was evaluated by measuring the relative signal areas of GFP/mCherry. By comparing the spread of Cy1GFP signal under P126 expression relative to vector control, we found that Cy1GFP cell-to-cell spread was enhanced by the expression of P126 to 1.41-fold (Figure 5D). Furthermore, the total detected GFP signals were used to evaluate the Cy1GFP titer of the infection foci. The results showed that the expression of P126 increased Cy1GFP titer to 2.18-fold compared with Vec (Figure 5E), indicating that P126 overexpression stimulates both cell-to-cell movement and viral titers. Moreover, similar results were also observed while assayed in *Phalaenopsis* flowers (Figure S9).

In order to further assay if any other VSRs have such enhancement for CymMV movement, TBSV P19 and PVX P25 were included in this assay. Despite that P19 and P25 have strong and moderate VSR activities, respectively, only TBSV P19 stimulated CymMV cell-to-cell movement (1.28-fold) and accumulation (2.63-fold) as P126 did, but P25 could not (Figure 5D,E). Interestingly, although P19 showed significantly stronger VSR activity than P126 (Figure 2C), its enhancement of CymMV cell-to-cell movement was inferior to P126 (Figure 5D).

Taken together, our findings demonstrate that the ORSV P126 expression alone was sufficient to increase CymMV accumulation by enhancing CymMV cell-to-cell movement. The P126S and P126A mutants retain comparable VSR activity relative to parental protein but lacked replicase activity. Thus, we conclude that ORSV P126 has multiple roles in virus infection, including viral replication, VSR and promoting CymMV movement during co-infection scenarios.

## 4. Discussion

Synergistic interactions among two or more viruses have complex consequences that can vary depending on the host, viral strains and infection timing among other factors [1,2]. ORSV and CymMV isolates from *Cattleya* orchids mutually enhanced viral RNA replication in orchid protoplasts upon mixed infection [3]. However, this synergistic interaction is restricted in *Phalaenopsis* orchids to a unilateral enhancement of CymMV movement rather than mutually bolstered replication [35,36]. These studies imply that divergences in synergistic interactions between ORSV and CymMV could be attributable to different virus isolates and orchid species. Here, the infectious ORSV and CymMV cDNA clones we generated from *Phalaenopsis*-derived isolates (termed OS4 and Cy1, respectively) not only displayed similar biological activities to wild-isolated viruses, but also recapitulated the synergism-induced phenotypes manifested upon co-infection, including symptom enhancement and increased CymMV titers in both natural (*Phalaenopsis*) and experimental (*N. benthamiana*) hosts. Moreover, titers and movement of Cy1 were enhanced by OS4 but not vice versa (Figure 1 and Figure S5). These outcomes indicate that our Cy1 and OS4 clones preserved all the functional features of viral single-infection and co-infection and that the unilateral benefits relative to Cy1 accumulation might be driven by factors and/or effects arising from OS4 co-infection.

VSRs not only facilitate viral infection by counteracting the RNA silencing element of plant immunity [10,49,50] but also contribute to synergism during mixed infections. Herein, we have identified the ORSV P126 replicase as a VSR (Figure 2), which is consistent with the replicases of other tobamoviruses [28,29]. Notably, despite potexvirus TGBp1 (P25) being a well-known VSR [28,29,51], none of the CymMV viral proteins we tested exhibited any significant VSR activity, not even CymMV TGBp1 (Figure S6C).

In order to test if the VSR activity of P126 is required for ORSV replication, we generated several P126 mutants (Figure 4). One such mutant, P126R, lacked VSR activity, most likely due to impaired protein stability given its low protein levels (Figures 3B and S7C). However, P126 mutants lacked virus replication ability in *N. benthamiana*, whether

they exhibited VSR activity (Figures 3 and 4). Thus, the VSR activity of the ORSV P126 replicase is not sufficient to support the successful viral infection in plants. Similar results have been reported for mutations that disrupted the helicase domain motifs of TMV 126/183 kDa proteins in that they inhibited virus replication but did not affect RNAi suppression [52]. Importantly, most host factors identified to date as interacting with tobamovirus P126 protein target the HEL domain in order to facilitate tobamovirus multiplication and pathogenicity [53]. Whether amino acid change at residue $M^{1104}$ alters interactions with host factors required for replication warrants further investigation. Since ORSV P183, which is the readthrough protein of P126, is consequently affected by P126 mutation, a role for it in replication deficiency cannot be excluded.

We have shown that the expression of OS4 P126 alone effectively promoted cell-to-cell movement and accumulation of Cy1 in inoculated leaves (Figure 5), indicating that one of the key underlying mechanisms of CymMV and ORSV synergism is dependent on promoting movement and accumulation of CymMV by ORSV P126. The P25, with comparable VSR activity as P126 (Figure 2C), however, did not enhance CymMV movement at all (Figure 5D). Interestingly, P19 displayed stronger VSR activity than P126 but showed relatively less efficiency than P126 to stimulate CymMV cell-to-cell movement (Figures 2C and 5D). This may be attributed to the function of P19 in increasing host susceptibility and resulting in increased accumulation of unrelated viruses [54]. Thus, the efficient promotion for viral synergism might be related to the compatible or specific interaction between virus and VSR protein rather than just VSR activity alone. Other viral VSRs, such as potyvirus P1/HC-Pro, crinivirus RNaseIII and cucumovirus 2b, have been characterized as mediating synergistic effects by increasing virus titers, long-distance movement and/or pathogenicity in addition to suppressing host RNA silencing responses [2,8,12,13]. Moreover, VSRs from a wide spectrum of viruses, including animal viruses, were demonstrated to complement cell-to-cell movement of a VSR-depleted turnip crinkle virus [55], but a role for TMV P126 in facilitating cell-to-cell movement of other viruses has yet to be revealed. Nevertheless, it has been shown that TMV P126 and/or P183 proteins are involved in the cell-to-cell movement of TMV [56,57]. Furthermore, intracellular trafficking of P126 alone or TMV viral replication complexes harboring P126 required the association of TMV P126 to microfilaments [58,59], suggesting that ORSV-promoted CymMV movement might also be modulated directly or indirectly via P126-microfilament interactions. The CymMV and ORSV viruses isolated from *Cattleya* orchids exhibited mutual replication enhancement [3], but *Phalaenopsis*-derived isolates only unilaterally enhanced CymMV movement [35,36]; this highlights the complexities and different layers of regulation between virus–virus and virus–host interactions.

**Supplementary Materials:** The following are available online at https://www.mdpi.com/article/10.3390/v13081552/s1, Figure S1: Infectivity of wild type isolates of ORSV and CymMV in *Phalaenopsis* orchids, Figure S2: Sequence alignments of ORSV and CymMV UTRs, Figure S3: Genome maps of viral cDNA clones, pUOS4 and pUCy1 and their infectivity in *C. quinoa*, Figure S4: Sequence analysis of ORSV and CymMV cDNA clones, Figure S5: Cy1 and OS4 infectivity and synergism in *Phalaenopsis* orchids, Figure S6: Accumulation of overexpressed viral proteins and VSR activity assay for CymMV proteins, Figure S7: VSR assays of ORSV P126 and its mutants, Figure S8: Expression cassettes used to determine the primary infection foci and cell-to-cell movement of CymMV-GFP, Figure S9: CymMV cell-to-cell movement upon overexpressing P126 in *Phalaenopsis* flowers, Table S1: Primers used in this study.

**Author Contributions:** Conceptualization, S.-C.L. and N.-S.L.; performed research, S.-C.L., H.P., Y.-W.H., M.-H.H. and Y.-L.S.; data analysis, S.-C.L., H.P. and W.-C.C.; resources, S.-Y.K. and Y.-H.H.; writing and editing, S.-C.L., N.-S.L. and Y.-H.H.; project administration, N.-S.L.; funding acquisition, N.-S.L. All authors have read and agreed to the published version of the manuscript.

**Funding:** This research was funded by the Institute of Plant and Microbial Biology, Academia Sinica, Taiwan, and the Innovative Translational Agricultural Research Program (AS-109-ITAR-L02).

**Institutional Review Board Statement:** Not applicable.

**Informed Consent Statement:** Not applicable.

**Acknowledgments:** We thank Mei-Jane Fang at the Plant Cell Biology Core Lab of Institute of Plant and Microbial Biology, Academia Sinica, for technical assistance. We also thank the DNA Sequencing Core Facility of the Institute of Biomedical Sciences, Academia Sinica, for DNA sequencing analysis. The core facility is funded by Academia Sinica Core Facility and Innovative Instrument Project (AS-CFII-108-115).

**Conflicts of Interest:** The authors declare no conflict of interest.

## References

1. Syller, J. Facilitative and antagonistic interactions between plant viruses in mixed infections. *Mol. Plant Pathol.* **2011**, *13*, 204–216. [CrossRef] [PubMed]
2. García-Cano, E.; Resende, R.O.; Fernandez-Munoz, R.; Moriones, E. Synergistic Interaction Between Tomato chlorosis virus and Tomato spotted wilt virus Results in Breakdown of Resistance in Tomato. *Phytopathology* **2006**, *96*, 1263–1269. [CrossRef]
3. Hu, W.-W.; Wong, S.-M.; Loh, C.-S.; Goh, C.-J. Synergism in replication of cymbidium mosaic potexvirus (CymMV) and odontoglossum ringspot tobamovirus (ORSV) RNA in orchid protoplasts. *Arch. Virol.* **1998**, *143*, 1265–1275. [CrossRef]
4. Karyeija, R.; Kreuze, J.; Gibson, R.; Valkonen, J. Synergistic Interactions of a Potyvirus and a Phloem-Limited Crinivirus in Sweet Potato Plants. *Virology* **2000**, *269*, 26–36. [CrossRef]
5. Vance, V.B. Replication of Potato virus-X RNA is altered in coinfections with Potato virus-Y. *Virology* **1991**, *182*, 486–494. [PubMed]
6. Ajjikuttira, P.; Loh, C.-S.; Wong, S.-M. Reciprocal function of movement proteins and complementation of long-distance movement of *Cymbidium mosaic virus* RNA by *Odontoglossum ringspot virus* coat protein. *J. Gen. Virol.* **2005**, *86*, 1543–1553. [CrossRef]
7. Rao, A.L.N.; Cooper, B.; Deom, C.M. Defective movement of viruses in the family Bromoviridae is differentially comple-mented in *Nicotiana benthamiana* expressing tobamovirus or dianthovirus movement proteins. *Phytopathology* **1998**, *88*, 666–672. [CrossRef]
8. Ryang, B.-S.; Kobori, T.; Matsumoto, T.; Kosaka, Y.; Ohki, S.T. Cucumber mosaic virus 2b protein compensates for restricted systemic spread of Potato virus Y in doubly infected tobacco. *J. Gen. Virol.* **2004**, *85*, 3405–3414. [CrossRef] [PubMed]
9. Hannon, G.J. RNA interference. *Nat. Cell Biol.* **2002**, *418*, 244–251. [CrossRef]
10. Ding, S.-W. RNA-based antiviral immunity. *Nat. Rev. Immunol.* **2010**, *10*, 632–644. [CrossRef]
11. Li, F.; Wang, A. RNA-Targeted Antiviral Immunity: More Than Just RNA Silencing. *Trends Microbiol.* **2019**, *27*, 792–805. [CrossRef] [PubMed]
12. Pruss, G.; Ge, X.; Shi, X.M.; Carrington, J.; Vance, V.B. Plant viral synergism: The potyviral genome encodes a broad-range pathogenicity enhancer that transactivates replication of heterologous viruses. *Plant Cell* **1997**, *9*, 859–868. [CrossRef] [PubMed]
13. Cuellar, W.; Kreuze, J.; Rajamäki, M.-L.; Cruzado, K.R.; Untiveros, M.; Valkonen, J.P.T. Elimination of antiviral defense by viral RNase III. *Proc. Natl. Acad. Sci. USA* **2009**, *106*, 10354–10358. [CrossRef] [PubMed]
14. Siddiqui, S.A.; Valkonen, J.; Rajamäki, M.-L.; Lehto, K. The 2b Silencing Suppressor of a Mild Strain of Cucumber mosaic virus Alone Is Sufficient for Synergistic Interaction with Tobacco mosaic virus and Induction of Severe Leaf Malformation in 2b-Transgenic Tobacco Plants. *Mol. Plant Microbe Interact.* **2011**, *24*, 685–693. [CrossRef] [PubMed]
15. Harries, P.A.; Palanichelvam, K.; Bhat, S.; Nelson, R.S. Tobacco mosaic virus 126-kDa Protein Increases the Susceptibility of Nicotiana tabacum to Other Viruses and Its Dosage Affects Virus-Induced Gene Silencing. *Mol. Plant Microbe Interact.* **2008**, *21*, 1539–1548. [CrossRef] [PubMed]
16. Stewart, J.; Griffiths, M. *Manual of Orchids*; Timber Press: Portland, OR, USA, 2005.
17. Chang, C.; Chen, Y.-C.; Hsu, Y.-H.; Wu, J.-T.; Hu, C.-C.; Chang, W.-C.; Lin, N.-S. Transgenic resistance to Cymbidium mosaic virus in Dendrobium expressing the viral capsid protein gene. *Transgenic. Res.* **2005**, *14*, 41–46. [CrossRef]
18. Zettler, F.W.; Ko, N.J.; Wisler, G.C.; Elliott, M.S.; Wong, S.M. Viruses of orchids and their control. *Plant Dis.* **1990**, *74*, 621–626. [CrossRef]
19. Wong, S.; Chng, C.; Lee, Y.; Tan, K.; Zettler, F. Incidence of cymbidium mosaic and odontoglossum ringspot viruses and their significance in orchid cultivation in Singapore. *Crop. Prot.* **1994**, *13*, 235–239. [CrossRef]
20. Moraes, L.A.; Krause-Sakate, R.; Pavan, M.A. Incidence and characterization of viruses infecting orchids in São Paulo state, Brazil. *Trop. Plant Pathol.* **2017**, *42*, 126–131. [CrossRef]
21. Liu, F.; Han, Y.; Li, W.; Shi, X.; Xu, W.; Lin, M. Incidence of Cymbidium mosaic virus and Odontoglossum ringspot virus affecting Oncidium orchids in Hainan Island, China. *Crop. Prot.* **2013**, *54*, 176–180. [CrossRef]
22. McMillan, R.T.; Palmateer, A.; Vendrame, W.A. Survey for Cymbidium mosaic and Odontoglossum ring spot viruses in domestic and international orchids. *Phytopathology* **2006**, *96*, S76.
23. Hu, J.S.; Ferreira, S.; Wang, M.; Xu, M.Q. Detection of *Cymbidium mosaic virus*, *Odontoglossum ringspot virus*, Tomato spotted wilt virus, and potyviruses infecting orchids in Hawaii. *Plant Dis.* **1993**, *77*, 464–468. [CrossRef]
24. Pearson, M.N.; Cole, J.S. Further Observations on the Effects of *Cymbidium mosaic virus* and *Odontoglossum ringspot virus* on the Growth of Cymbidium Orchids. *J. Phytopathol.* **1991**, *131*, 193–198. [CrossRef]
25. Ryu, K.H.; Park, W.M. The complete nucleotide sequence and genome organization of odontoglossum ringspot tobamovirus RNA. *Arch. Virol.* **1995**, *140*, 1577–1587. [CrossRef] [PubMed]

26. Wang, H.H.; Yu, H.H.; Wong, S.M. Mutation of Phe50 to Ser50 in the 126/183-kDa proteins of Odontoglossum ringspot virus abolishes virus replication but can be complemented and restored by exact reversion. *J. Gen. Virol.* **2004**, *85*, 2447–2457. [CrossRef]
27. Rabindran, S.; Robertson, C.; Achor, D.; Holt, C.A.; Dawson, W.O.; German-Retana, S. *Odontoglossum ringspot virus* host range restriction in Nicotiana sylvestris maps to the replicase gene. *Mol. Plant Pathol.* **2005**, *6*, 439–447. [CrossRef] [PubMed]
28. Ding, X.S.; Liu, J.; Cheng, N.-H.; Folimonov, A.; Hou, Y.-M.; Bao, Y.; Katagi, C.; Carter, S.A.; Nelson, R.S. The Tobacco mosaic virus 126-kDa Protein Associated with Virus Replication and Movement Suppresses RNA Silencing. *Mol. Plant Microbe Interact.* **2004**, *17*, 583–592. [CrossRef]
29. Kubota, K.; Tsuda, S.; Tamai, A.; Meshi, T. Tomato mosaic virus replication protein suppresses virus-targeted posttranscrip-tional gene silencing. *J. Virol.* **2003**, *77*, 11016–11026. [CrossRef]
30. Wang, L.-Y.; Lin, S.-S.; Hung, T.-H.; Li, T.-K.; Lin, N.-C.; Shen, T.-L. Multiple Domains of the *Tobacco mosaic virus* p126 Protein Can Independently Suppress Local and Systemic RNA Silencing. *Mol. Plant Microbe Interact.* **2012**, *25*, 648–657. [CrossRef]
31. Csorba, T.; Bovi, A.; Dalmay, T.; Burgyan, J. The p122 subunit of *Tobacco mosaic virus* replicase is a potent silencing suppressor and compromises both small interfering RNA- and microRNA-mediated pathways. *J. Virol.* **2007**, *81*, 11768–11780. [CrossRef]
32. Kurihara, Y.; Inaba, N.; Kutsuna, N.; Takeda, A.; Tagami, Y.; Watanabe, Y. Binding of tobamovirus replication protein with small RNA duplexes. *J. Gen. Virol.* **2007**, *88*, 2347–2352. [CrossRef] [PubMed]
33. Wong, S.M.; Mahtani, P.H.; Lee, K.C.; Yu, H.H.; Tan, Y.; Neo, K.K.; Chan, Y.; Wu, M.; Chng, C.G. *Cymbidium mosaic potexvirus* RNA: Complete nucleotide sequence and phylogenetic analysis. *Arch. Virol.* **1997**, *142*, 383–391. [CrossRef] [PubMed]
34. Lu, H.-C.; Chen, C.-E.; Tsai, M.-H.; Wang, H.-I.; Su, H.-J.; Yeh, H.-H. *Cymbidium mosaic potexvirus* isolate-dependent host movement systems reveal two movement control determinants and the coat protein is the dominant. *Virology* **2009**, *388*, 147–159. [CrossRef]
35. Pai, H.; Jean, W.; Lee, Y.; Chang, Y.A.; Lin, N. Genome-wide analysis of small RNAs from Odontoglossum ringspot virus and Cymbidium mosaic virus synergistically infecting Phalaenopsis. *Mol. Plant Pathol.* **2019**, *21*, 188–205. [CrossRef] [PubMed]
36. Chen, T.-Y.; Pai, H.; Hou, L.-Y.; Lee, S.-C.; Lin, T.-T.; Chang, C.-H.; Hsu, F.-C.; Hsu, Y.-H.; Lin, N.-S. Dual resistance of transgenic plants against Cymbidium mosaic virus and Odontoglossum ringspot virus. *Sci. Rep.* **2019**, *9*, 1–12. [CrossRef]
37. Lee, S.-C.; Chang, Y.-C. Multiplex RT-PCR detection of two orchid viruses with an internal control of plant nad5 mRNA. *Plant Pathol. Bull.* **2006**, *15*, 187–196.
38. Lin, N.S.; Chen, C.C. Association of Bamboo mosaic virus (BoMV) and BoMV-specific electron-dense crystalline bodies with chloroplasts. *Phytopathology* **1991**, *81*, 1551–1555. [CrossRef]
39. Liou, M.-R.; Huang, Y.-W.; Hu, C.-C.; Lin, N.-S.; Hsu, Y.-H. A dual gene-silencing vector system for monocot and dicot plants. *Plant Biotechnol. J.* **2013**, *12*, 330–343. [CrossRef] [PubMed]
40. Lu, H.-C.; Chen, H.-H.; Tsai, W.-C.; Chen, W.-H.; Su, H.-J.; Chang, D.C.-N.; Yeh, H.-H. Strategies for Functional Validation of Genes Involved in Reproductive Stages of Orchids. *Plant Physiol.* **2007**, *143*, 558–569. [CrossRef]
41. Bendahmane, A.; Farnham, G.; Moffett, P.; Baulcombe, D.C. Constitutive gain-of-function mutants in a nucleotide binding site-leucine rich repeat protein encoded at the Rx locus of potato. *Plant J.* **2002**, *32*, 195–204. [CrossRef] [PubMed]
42. Lin, N.S.; Hsu, Y.H.; Hsu, H.T. Immunological detection of plant viruses and a mycoplasma-like organism by direct tissue blotting on nitrocellulose membranes. *Phytopathology* **1990**, *80*, 824–828. [CrossRef]
43. Lin, N.S.; Lee, Y.S.; Lin, B.; Lee, C.W.; Hsu, Y.H. The open reading frame of bamboo mosaic potexvirus satellite RNA is not essential for its replication and can be replaced with a bacterial gene. *Proc. Natl. Acad. Sci. USA* **1996**, *93*, 3138–3142. [CrossRef]
44. Palani, P.V.; Lin, N.-S. Northern Analysis of Viral Plus- and Minus-Strand RNAs. *Curr. Protoc. Microbiol.* **2007**, *16*, 16E.3.1–16E.3.32.
45. Johansen, L.K.; Carrington, J.C. Silencing on the spot. Induction and suppression of RNA silencing in the Agrobacte-rium-mediated transient expression system. *Plant Physiol.* **2001**, *126*, 930–938. [CrossRef] [PubMed]
46. Stephan, D.; Slabber, C.; George, G.; Ninov, V.; Francis, K.P.; Burger, J.T. Visualization of plant viral suppressor silencing activity in intact leaf lamina by quantitative fluorescent imaging. *Plant Methods* **2011**, *7*, 25. [CrossRef] [PubMed]
47. Junqueira, B.R.T.; Nicolini, C.; Lucinda, N.; Orílio, A.F.; Nagata, T. A simplified approach to construct infectious cDNA clones of a tobamovirus in a binary vector. *J. Virol. Methods* **2014**, *198*, 32–36. [CrossRef]
48. Turpen, T.H.; Turpen, A.M.; Weinzettl, N.; Kumagai, M.H.; Dawson, W.O. Transfection of whole plants from wounds inocu-lated with *Agrobacterium tumefaciens* containing cDNA of Tobacco mosaic virus. *J. Virol. Methods* **1993**, *42*, 227–239. [CrossRef]
49. Qu, F.; Morris, T.J. Suppressors of RNA silencing encoded by plant viruses and their role in viral infections. *FEBS Lett.* **2005**, *579*, 5958–5964. [CrossRef]
50. Pumplin, N.; Voinnet, O. RNA silencing suppression by plant pathogens: Defence, counter-defence and counter-counter-defence. *Nat. Rev. Genet.* **2013**, *11*, 745–760. [CrossRef] [PubMed]
51. Voinnet, O.; Lederer, C.; Baulcombe, D.C. A Viral Movement Protein Prevents Spread of the Gene Silencing Signal in *Nicotiana benthamiana*. *Cell* **2000**, *103*, 157–167. [CrossRef]
52. Wang, X.; Kelman, Z.; Culver, J.N. Helicase ATPase activity of the *Tobacco mosaic virus* 126-kDa protein modulates replicase complex assembly. *Virology* **2010**, *402*, 292–302. [CrossRef]
53. Ishibashi, K.; Nishikiori, M.; Ishikawa, M. Interactions Between Tobamovirus Replication Proteins and Cellular Factors: Their Impacts on Virus Multiplication. *Mol. Plant Microbe Interact.* **2010**, *23*, 1413–1419. [CrossRef] [PubMed]
54. Russo, M.; Burgyan, J.; Martelli, G.P. Molecular Biology of Tombusviridae. *Adv. Clin. Chem.* **1994**, *44*, 381–428.
55. Powers, J.G.; Sit, T.L.; Qu, F.; Morris, T.J.; Kim, K.-H.; Lommel, S.A. A Versatile Assay for the Identification of RNA Silencing Suppressors Based on Complementation of Viral Movement. *Mol. Plant Microbe Interact.* **2008**, *21*, 879–890. [CrossRef] [PubMed]

56. Hirashima, K.; Watanabe, Y. RNA Helicase Domain of Tobamovirus Replicase Executes Cell-to-Cell Movement Possibly through Collaboration with Its Nonconserved Region. *J. Virol.* **2003**, *77*, 12357–12362. [CrossRef]
57. Hirashima, K.; Watanabe, Y. Tobamovirus Replicase Coding Region Is Involved in Cell-to-Cell Movement. *J. Virol.* **2001**, *75*, 8831–8836. [CrossRef]
58. Liu, J.; Blancaflor, E.; Nelson, R.S. The Tobacco Mosaic Virus 126-Kilodalton Protein, a Constituent of the Virus Replication Complex, Alone or within the Complex Aligns with and Traffics along Microfilaments. *Plant Physiol.* **2005**, *138*, 1853–1865. [CrossRef]
59. Kawakami, S.; Watanabe, Y.; Beachy, R.N. Tobacco mosaic virus infection spreads cell to cell as intact replication complexes. *Proc. Natl. Acad. Sci. USA* **2004**, *101*, 6291–6296. [CrossRef]

Molecular Plant Pathology

MOLECULAR PLANT PATHOLOGY (2020) 21(2), 188–205 DOI: 10.1111/mpp.12888

# Genome-wide analysis of small RNAs from Odontoglossum ringspot virus and Cymbidium mosaic virus synergistically infecting *Phalaenopsis*

HSUAN PAI[1], WEN-HAN JEAN[2], YUN-SHIEN LEE[3], YAO-CHIEN ALEX CHANG[4,*] AND NA-SHENG LIN [1,*]

[1]*Institute of Plant and Microbial Biology, Academia Sinica, Taipei, Taiwan, 11529*

[2]*Agricultural Biotechnology Research Center, Academia Sinica, Taipei, Taiwan, 11529*

[3]*Department of Biotechnology, Ming Chuan University, Tao-Yuan, Taiwan, 33348*

[4]*Department of Horticulture and Landscape Architecture, National Taiwan University, Taipei, Taiwan, 10617*

## SUMMARY

Cymbidium mosaic virus (CymMV) and Odontoglossum ringspot virus (ORSV) are the two most prevalent viruses infecting orchids and causing economic losses worldwide. Mixed infection of CymMV and ORSV could induce intensified symptoms as early at 10 days post-inoculation in inoculated *Phalaenopsis amabilis*, where CymMV pathogenesis was unilaterally enhanced by ORSV. To reveal the antiviral RNA silencing activity in orchids, we characterized the viral small-interfering RNAs (vsiRNAs) from CymMV and ORSV singly or synergistically infecting *P. amabilis*. We also temporally classified the inoculated leaf-tip tissues and noninoculated adjacent tissues as late and early stages of infection, respectively. Regardless of early or late stage with single or double infection, CymMV and ORSV vsiRNAs were predominant in 21- and 22-nt sizes, with excess positive polarity and underrepresented 5′-guanine. While CymMV vsiRNAs mainly derived from RNA-dependent RNA polymerase-coding regions, ORSV vsiRNAs encompassed the coat protein gene and 3′-untranslated region, with a specific hotspot residing in the 3′-terminal pseudoknot. With double infection, CymMV vsiRNAs increased more than 5-fold in number with increasing virus titres. Most vsiRNA features remained unchanged with double inoculation, but additional ORSV vsiRNA hotspot peaks were prominent. The potential vsiRNA-mediated regulation of the novel targets in double-infected tissues thereby provides a different view of CymMV and ORSV synergism. Hence, temporally profiled vsiRNAs from taxonomically distinct CymMV and ORSV illustrate active antiviral RNA silencing in their natural host, *Phalaenopsis*, during both early and late stages of infection. Our findings provide insights into offence–defence interactions among CymMV, ORSV and orchids.

* *Correspondence*: Email: nslin@sinica.edu.tw; alexchang@ntu.edu.tw

**Keywords:** anti-viral RNA silencing, Cymbidium mosaic virus, Odontoglossum ringspot virus, *Phalaenopsis*, small RNA sequencing, synergism, viral siRNA (vsiRNA).

## INTRODUCTION

The Orchidaceae is an immense family of more than 800 genera, about 28 000 native species and more than 110 000 cultivars (Christenhusz and Byng, 2016; Sheehan, 2003). Because of their elegant flowers with a fascinating array of colours, long blooming duration and adaptability for growing indoors, orchids, especially *Phalaenopsis*, have been popular in the ornamental market. However, among numerous orchid pests and diseases, viruses are the most troublesome and we have no efficient measures to control virus diseases. Virus infections can result in retarded growth of orchids, even though the plants appear symptomless (Chia and He, 1999; Zettler *et al.*, 1990); the hidden risk of latent symptom formation after shipment is a thorny problem (Inouye, 2008). Although large-scale cultivation by tissue culture propagation has become the trend in orchid production, mechanical transmission of orchid-infecting viruses via tissue propagation remains a major threat in the orchid industry (Ajjikuttira and Wong, 2009; Chang *et al.*, 2010).

Among more than 50 orchid-infecting viruses, Cymbidium mosaic virus (CymMV) and Odontoglossum ringspot virus (ORSV) are prevalent worldwide. The potexvirus CymMV has positive-sense single-stranded RNA ((+)-ssRNA) monopartite genome, consisting of five open reading frames (ORFs) encoding a 160-kDa RNA-dependent RNA polymerase (RdRp), three triple-gene-block proteins (TGBps) and a 24-kDa capsid protein (CP). The genomic RNA (gRNA) of about 6200-nt is 5′-capped and 3′-polyadenylated (Ajjikuttira and Wong, 2009; Wong *et al.*, 1997). ORSV, which belongs to the *Tobamovirus* genus, also harbours a (+)-ssRNA

© 2019 THE AUTHORS. *MOLECULAR PLANT PATHOLOGY* PUBLISHED BY BRITISH SOCIETY FOR PLANT PATHOLOGY AND JOHN WILEY & SONS LTD

This is an open access article under the terms of the Creative Commons Attribution-NonCommercial License, which permits use, distribution and reproduction in any medium, provided the original work is properly cited and is not used for commercial purposes.

monopartite genome of about 6600 nt. The ORF1 encodes 126- and 183-kDa readthrough RdRp proteins. Other ORFs encode a 34-kDa movement protein (MP) and 18-kDa CP (Ajjikuttira and Wong, 2009; Ryu and Park, 1995). The gRNA of ORSV has a 5′-capped structure but lacks the 3′-poly(A) tail. Instead, its 3′-untranslated region (3′-UTR) consists of a transfer RNA (tRNA)-like structure in the terminus and an upstream pseudoknot (PK) chain (Chng *et al*., 1996).

Both CymMV and ORSV are easily transmitted by mechanical wounding, with no recognized vectors in the field (Ajjikuttira and Wong, 2009). Although taxonomically distinct, these two viruses commonly feature coinfection in orchid nurseries, and the synergistic effects of CymMV and ORSV coinfection often result in intensified symptoms (Ajjikuttira *et al*., 2005; Hu *et al*., 1998; Wong *et al*., 1994). Rapid virus diagnostic techniques are well established (Ali *et al*., 2014; Hu and Wong, 1998; Lee *et al*., 2011; Seoh *et al*., 1998), but the molecular mechanism of this synergistic infection remains largely unknown.

RNA silencing plays a major role in the antiviral response in plants. It is triggered by double-stranded RNAs (dsRNAs) or self-folding RNAs that are processed into functional small RNAs (sRNAs) that are 21- to 24-nt long by RNase III-type Dicer-like proteins (DCLs). On virus infection, viral dsRNAs, such as replication intermediates or those with self-annealing hairpin structures, can serve as templates for DCL processing. Virus-derived small interfering siRNAs (vsiRNAs) usually accumulate at high levels in infected plants and are further recruited into an RNA-induced silencing complex (RISC), thereby guiding sequence-specific viral RNA cleavage. In addition, plant endogenous RdRps are involved in synthesizing dsRNAs from viral ssRNAs that serve as substrates for generation of secondary vsiRNAs, thus amplifying the antiviral cascade (Angell and Baulcombe, 1997; Blevins *et al*., 2006; Dougherty *et al*., 1994; Llave, 2010; Ruiz *et al*., 1998). Furthermore, siRNAs are mobile molecules and can spread throughout the plant via phloem (Molnar *et al*., 2010), so vsiRNAs may act as signal molecules and confer systemic antiviral silencing. Counteractively, viruses have evolved viral suppressors of RNA silencing (VSRs) to interfere with the host endogenous sRNA pathways and inhibit the antiviral activity (reviewed in Bivalkar-Mehla *et al*., 2011; Csorba *et al*., 2015; Szittya and Burgyan, 2013). In addition to viral RNAs, vsiRNAs may potentially target plant transcripts, thereby dysregulating plant development (Qi *et al*., 2009; Wang *et al*., 2004, 2012b). Collectively, the RNA silencing machinery plays an important role in regulating plant growth and also constitutes a multifaceted layer of defence and counterdefence interactions between viruses and plants.

With advances in high-throughput sequencing technologies, the composition of vsiRNAs has been analysed in different plant–virus pathosystems, focusing on vsiRNA profiling of single pairs of a host and a virus or several viruses in single-inoculated plants (Donaire *et al*., 2009; Li *et al*., 2016; Naveed *et al*., 2014), the vsiRNA pattern with tissue or host specificity (Herranz *et al*., 2015; Lin *et al*., 2010; Mitter *et al*., 2013; Ogwok *et al*., 2016; Xu *et al*., 2012), and the effect of double infection on vsiRNA profiles (Cuellar *et al*., 2015; Li *et al*., 2013; Tatineni *et al*., 2014; Xia *et al*., 2016). Thus, by analysing the cleaved products and combined with other genetic assays, vsiRNA profiles could reflect the mode of action and components involved in antiviral RNA silencing (Szittya *et al*., 2010; Zhang *et al*., 2015).

This study documented CymMV and ORSV synergism in *Phalaenopsis amabilis*. We correlated viral synergism with temporal vsiRNA accumulation in infected orchids, with emphasis on comparing profiles of (1) early and late stages of infection, and (2) infection of *Phalaenopsis* with CymMV and ORSV alone or together.

## RESULTS

### CymMV and ORSV infection synergism in *P. amabilis*

ORSV and CymMV commonly infect orchids. Although viral infection could be detected in systemically infected orchid leaves over 2–8 weeks post-inoculation (Chan *et al*., 2005; Liao *et al*., 2004; Lu *et al*., 2007, 2009), the time course of infection progression for ORSV and CymMV in inoculated leaves of *P. amabilis* remains unclear. In our preliminary study, we first collected sample strips from ORSV-inoculated leaves at 2, 4, 7, 11 and 30 days post-inoculation (dpi) by tissue blotting. RNA blots revealed that mechanical infection with ORSV in leaf-tip tissues gradually spread to noninoculated leaf-base tissue by 15 days. However, in a similar assay, the time course of CymMV infection was obscure because the signal could not be differentiated from background (data not shown). Nevertheless, 10 dpi was considered the time when ORSV or CymMV titres were substantially raised and confined mostly in inoculated areas; therefore, in this study we collected inoculated leaves at 10 dpi for infection assays.

To determine the synergism of ORSV and CymMV coinfection in *P. amabilis*, leaf-tip tissues in virus-free *Phalaenopsis* were inoculated with CymMV or ORSV alone or combined (Fig. 1A). Virus infection was first confirmed by tissue blotting with digoxygenin (DIG)-labelled riboprobes (Fig. 1B). Tissue was collected separately from inoculated and noninoculated areas for RNA analysis. At 10 dpi, tissue blotting revealed ORSV single infection confined to the inoculated area in most inoculations (Fig. 1B, Oi). Similar to ORSV inoculation, in more than half of the inoculations (32/60 leaves), CymMV accumulation was confined to the inoculated area at 10 dpi (Fig. 1B, Ci). The results suggest that the system could be used to collect tissues of different infection stages by spatial separation. To avoid confusion with the scattered tracts of infected tissues over the separation line, we excluded leaves with virus infection detected in noninoculated tissues from further analysis. Of note, single-infected leaves were symptomless, but chlorotic

© 2019 THE AUTHORS. *MOLECULAR PLANT PATHOLOGY* PUBLISHED BY BRITISH SOCIETY FOR PLANT PATHOLOGY AND JOHN WILEY & SONS LTD 

13643703, 2020, 2, Downloaded from https://bsppjournals.onlinelibrary.wiley.com/doi/10.1111/mpp.12888 by Test, Wiley Online Library on [02/08/2025]. See the Terms and Conditions (https://onlinelibrary.wiley.com/terms-and-conditions) on Wiley Online Library for rules of use; OA articles are governed by the applicable Creative Commons License

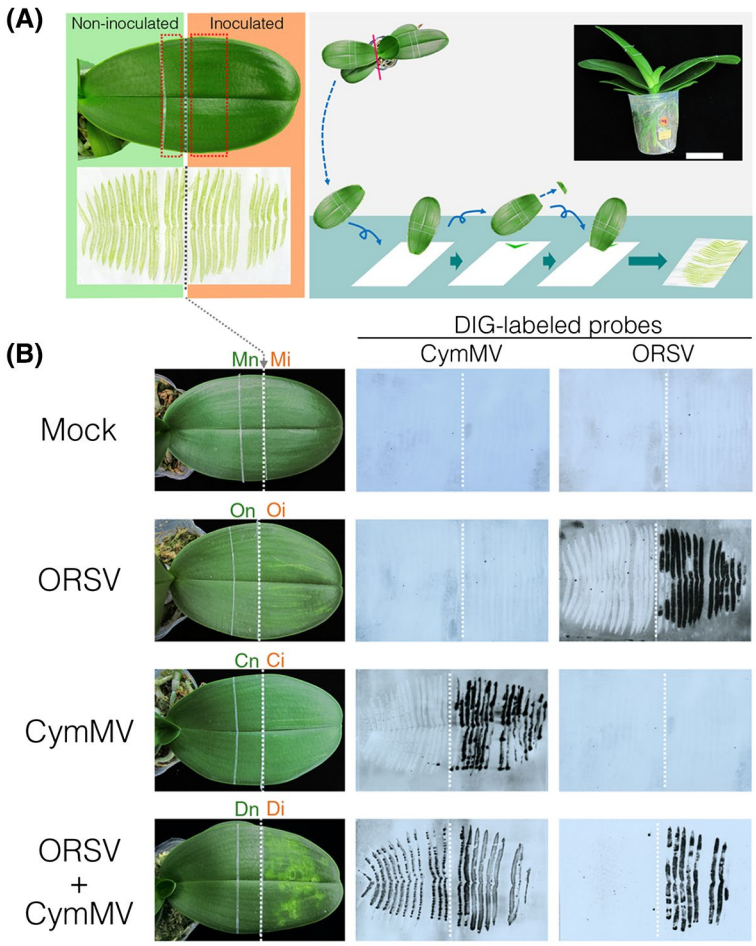


**Fig. 1** Symptoms and tissue blotting detection of ORSV and/or CymMV-infection in *Phalaenopsis*. (A) Diagrams of leaf-tip inoculation and tissue-blotting detection in the infection assays. *Phalaenopsis amabilis* was inoculated with virions in the tip-half of the inoculated leaf. Red rectangles indicate areas that were used for collecting inoculated and noninoculated tissues. Right panel illustrates the sampling procedure of tissue blotting: the whole inoculated leaf was cut off and sequentially sliced from the base (noninoculated) to tip (inoculated). Each cut was pressed on nylon membranes. (B) Phenotype and tissue-blotting detection of ORSV and CymMV from mock- and inoculated leaves at 10 dpi. Mock (M) tissues with buffer inoculation and adjacent tissues were designated Mi and Mn, respectively. Dashed lines separate inoculated (right) and noninoculated (left) areas corresponding to (A). Labels indicate inoculated (i, orange characters) or noninoculated (n, green characters) tissues of mock (M), ORSV (O), CymMV (C) or CymMV and ORSV double (D)-inoculated leaves. The blots were hybridized with digoxygenin (DIG)-labelled CymMV- and ORSV-CP gene-specific probes.

lesions and ringspots appeared in double-infected leaves and were restrained to inoculated areas at 10 dpi (Fig. 1B, Di). In all 60 double-inoculated leaves, ORSV infection was detectable only in inoculated areas (Fig. 1B, Di), without much difference from ORSV single infection (Fig. 1B, Oi). In contrast, double-infected leaves showed enhanced CymMV spreading to noninoculated tissues in 54/60 leaves (Fig. 1B, Dn).

To further confirm the viral accumulation, total RNA samples were separately extracted from inoculated (i) and noninoculated (n) tissues for northern blot analysis. Inoculated tissues of CymMV (C), ORSV (O) or CymMV mixed with ORSV (D, for 'double') were designated Ci, Oi and Di, respectively. Similarly, noninoculated adjacent tissues from corresponding inoculations were designated Cn, On and Dn. Mock (M) tissues with buffer inoculation and adjacent tissues were designated Mi and Mn, respectively (Fig. 1B). RNA blotting revealed much higher CymMV viral RNA accumulation in Di than Ci tissue (Fig. 2A), which suggests enhanced CymMV titres during coinfection with ORSV. ORSV accumulation was slightly reduced in double infection (Fig. 2A), which supports the tissue blotting results (Fig. 1B). Accordingly, sRNA blotting revealed a higher amount of CymMV vsiRNAs in Di than Dn or Ci tissues (Fig. 2B). Also, ORSV vsiRNA accumulation was higher in Di than in Dn tissues (Fig. 2B), so levels of vsiRNAs were associated with virus accumulation in infected tissues. Reverse transcription-PCR (RT-PCR) assay confirmed single or double infection in inoculated tissues and no virus in mock-inoculated tissues (Fig. 2C). Although CymMV and/or ORSV was undetectable in RNA blots (Figs 1B and 2A), RT-PCR reached higher sensitivity and



13643703, 2020, 2, Downloaded from https://bsppjournals.onlinelibrary.wiley.com/doi/10.1111/mpp.12888 by Test, Wiley Online Library on [02/08/2025]. See the Terms and Conditions (https://onlinelibrary.wiley.com/terms-and-conditions) on Wiley Online Library for rules of use; OA articles are governed by the applicable Creative Commons License

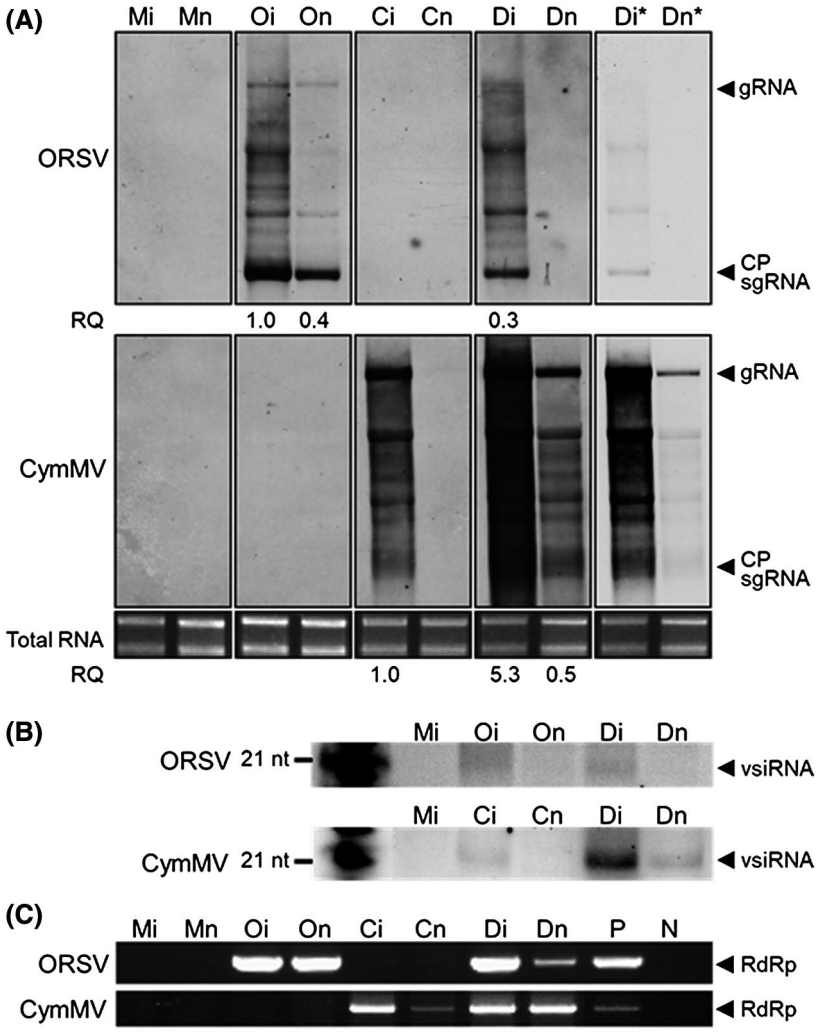


**Fig. 2** Accumulation of CymMV and ORSV RNA and vsiRNA in *Phalaenopsis*. Northern blot analysis of (A) viral RNA and (B) vsiRNA accumulation. Viral genomic RNA (gRNA), subgenomic RNA (sgRNA) and vsiRNA were detected with CymMV or ORSV CP- and RdRp-specific probes. Ethidium bromide-stained total RNA is shown as a loading control. Longer (left) and shorter (right, indicated with asterisk) exposure films of viral RNA northern blot are presented for Di and Dn. RQ, relative quantity. (C) Reverse transcription-PCR detection of virus infection at 10 days post-inoculation (dpi). Mi, Oi, Ci and Di: inoculated (i) tissues of mock (M)-, ORSV (O)-, CymMV (C)- and double (D)-inoculated plants. Mn, On, Cn and Dn: noninoculated (n) tissues of mock (M)-, ORSV (O)-, CymMV (C)- and double (D)-inoculated plants. P, CymMV and ORSV double-infected *Phalaenopsis* as a positive control; N, nontemplate negative control for PCRs.

revealed virus accumulation in noninoculated tissues (Fig. 2C, Cn, On and Dn), so the viruses had started invading these tissues at the initial stage of infection.

In summary, by leaf-tip inoculation, early (e.g. Cn and On tissues) and late (e.g. Ci, Oi and Di tissues) stages of infection could be distinguished at 10 dpi in noninoculated and inoculated tissues, respectively. Also, coinfection with CymMV and ORSV enhanced CymMV titres and spreading as well as symptom formation.

### Profiling sRNAs from virus-infected *P. amabilis*

To analyse the vsiRNA profiles, we purified each sRNA pool from samples as described previously, then used Illumina high-throughput sequencing. We generated 50 342 804 raw reads from eight sRNA libraries. After quality trimming and size filtering, more than 2.9 million clean reads of 18–25 nt sRNAs were retrieved for each library (Table 1). Identical sequences were grouped into unique reads (tags) for further characterization (Table S1). The size distribution of total sRNA tags was similar among the libraries: the 24-nt length was most prevalent and represented more than 50% of total unique reads (Fig. 3B). For the redundant reads, 21-nt sequences were predominant in all libraries, followed by 24-nt sequences (Fig. 3A). Notably, the proportion of 24-nt reads was overwhelmingly lowered due to the much reduced number of 24-nt tags in the Di library (Fig. 3B).

© 2019 THE AUTHORS. *MOLECULAR PLANT PATHOLOGY* PUBLISHED BY BRITISH SOCIETY FOR PLANT PATHOLOGY AND JOHN WILEY & SONS LTD 

13643703, 2020, 2, Downloaded from https://bsppjournals.onlinelibrary.wiley.com/doi/10.1111/mpp.12888 by Test, Wiley Online Library on [02/08/2025]. See the Terms and Conditions (https://onlinelibrary.wiley.com/terms-and-conditions) on Wiley Online Library for rules of use; OA articles are governed by the applicable Creative Commons License

**Table 1** Summary of total reads in sRNA libraries constructed from mock- and virus-inoculated *Phalaenopsis* tissues

| | Mi* | Mn | Oi | On | Ci | Cn | Di | Dn |
|---|---|---|---|---|---|---|---|---|
| Raw data input | | | | | | | | |
| Total reads | 5 384 213 | 5 230 602 | 11 447 603 | 6 911 927 | 5 049 276 | 5 680 202 | 5 326 905 | 5 312 076 |
| Adaptor and quality trimmed† | 5 056 536 | 4 933 398 | 11 094 651 | 6 737 444 | 4 739 283 | 5 375 120 | 5 082 378 | 5 066 946 |
| Low frequency filtered 18–25 nt reads‡ | 3 313 331 | 2 984 471 | 7 422 666 | 3 842 315 | 3 286 321 | 3 635 286 | 3 652 115 | 3 335 055 |
| Viral siRNAs | | | | | | | | |
| ORSV§ | 1 | 3 | 2 178 379 (29.34%) | 4577 (0.12%) | 50 | 87 | 439 373 (12.03%) | 237 (<0.01%) |
| CymMV | 5 | 12 | 3 | 1 | 176 757 (5.37%) | 759 (0.02%) | 961 229 (26.32%) | 258 119 (7.74%) |
| sRNAs from *Phalaenopsis* | | | | | | | | |
| *P. aphrodite* ESTs | 2 044 888 | 1 871 853 | 2 762 900 | 2 597 837 | 1 771 682 | 2 197 024 | 1 042 558 | 1 924 590 |
| Structure RNA (Rfam) | 179 345 | 171 235 | 452 767 | 327 299 | 134 762 | 157 086 | 251 479 | 182 899 |
| miRNA | 43 671 | 35 788 | 23 459 | 16 567 | 42 453 | 42 556 | 19 103 | 29 388 |
| Others | 1 045 421 | 905 580 | 2 005 158 | 896 034 | 1 160 527 | 1 237 774 | 938 373 | 939 822 |

*Mi, Oi, Ci and Di: inoculated (i) tissues of mock (M)-, ORSV (O)-, CymMV (C)- and double (D)-inoculated plants. Mn, On, Cn and Dn: noninoculated (n) tissues of mock (M)-, ORSV (O)-, CymMV (C)- and double (D)-inoculated plants.

†Trimming steps, including sequencing quality, adapter removal and filtering poly-A/T/C/G or N (null)-calling bases containing reads.

‡Reads with only one count are defined as low-frequency reads and filtered before further analysis.§The numbers in parentheses indicate the percentage of ORSV and CymMV vsiRNAs in clean (low-frequency filtered 18–25 nt) reads.



13643703, 2020, 2, Downloaded from https://bsppjournals.onlinelibrary.wiley.com/doi/10.1111/mpp.12888 by Test, Wiley Online Library on [02/08/2025]. See the Terms and Conditions (https://onlinelibrary.wiley.com/terms-and-conditions) on Wiley Online Library for rules of use; OA articles are governed by the applicable Creative Commons License

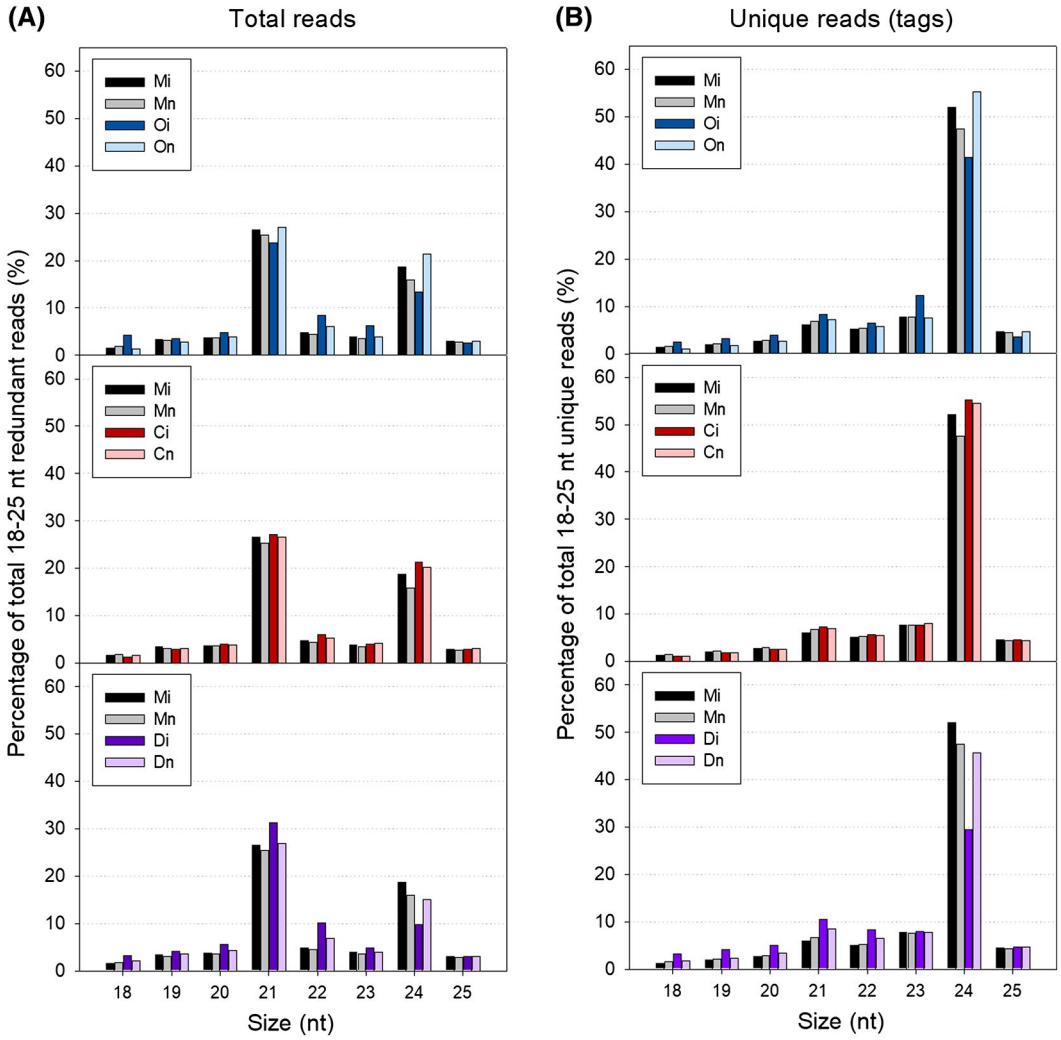


**Fig. 3** Size distribution of total sRNAs in mock- or virus-inoculated *Phalaenopsis*. Percentage and size distribution of 18- to 25-nt redundant (left) or unique (right) reads of total sRNAs are shown. Mi, Oi, Ci and Di: inoculated (i) tissues of mock (M)-, ORSV (O)-, CymMV (C)- and double (D)-inoculated plants. Mn, On, Cn and Dn: noninoculated (n) tissues of mock (M)-, ORSV (O)-, CymMV (C)- and double (D)-inoculated plants.

CymMV and ORSV vsiRNAs were identified after searching against the viral genome for both viruses (Fig. S1). To tolerate possible sequence variations evolved during virus replication, genome sequences from 11 CymMV and five ORSV strains deposited in GenBank were used for annotation. Also, we confirmed that no read could be mutually mapped to both CymMV and ORSV genomes. About 29.3% (2 178 379 reads) and 0.1% (4577 reads) of total annotated reads in the Oi and On libraries, respectively, were perfectly matched to the ORSV genomes (Table 1). A rather smaller proportion, about 5.4% and <0.1% total reads in the Ci and Cn libraries, respectively, were matched to the CymMV genomes (Table 1). As compared with Ci, CymMV vsiRNAs reached a much higher proportion, with 26.3% and 7.7% total reads in Di and Dn, respectively. In contrast, ORSV vsiRNAs contributed to 12.0% total reads (439 373 reads) for about 2-fold less accumulation than CymMV vsiRNAs in the Di library, and about 2.5-fold less accumulation than in the Oi library. Dn tissues showed an even larger gap between proportions of CymMV and ORSV vsiRNAs because less than 0.1% (237 reads) of total reads was identified as ORSV vsiRNAs. The more than 5-fold enrichment of CymMV vsiRNAs again demonstrated synergistic enhancement of CymMV accumulation.

## Size distribution, strand polarity and 5′-end nucleotide preference of CymMV and ORSV vsiRNAs

We analysed the size distribution, strand polarity and 5′-end nucleotide preference in CymMV and ORSV vsiRNA populations. In the single-infected Ci and Oi libraries, 21-nt vsiRNAs were predominant (63.4% for CymMV and 61.3% for ORSV), followed by the 22-nt class (21.9% for CymMV and 17.2% for ORSV; Fig. 4). The size distribution of CymMV and ORSV vsiRNAs in double-infected tissues (Di and Dn) showed similar patterns, with 21 nt as

© 2019 THE AUTHORS. *MOLECULAR PLANT PATHOLOGY* PUBLISHED BY BRITISH SOCIETY FOR PLANT PATHOLOGY AND JOHN WILEY & SONS LTD 

13643703, 2020, 2, Downloaded from https://bsppjournals.onlinelibrary.wiley.com/doi/10.1111/mpp.12888 by Test, Wiley Online Library on [02/08/2025]. See the Terms and Conditions (https://onlinelibrary.wiley.com/terms-and-conditions) on Wiley Online Library for rules of use; OA articles are governed by the applicable Creative Commons License

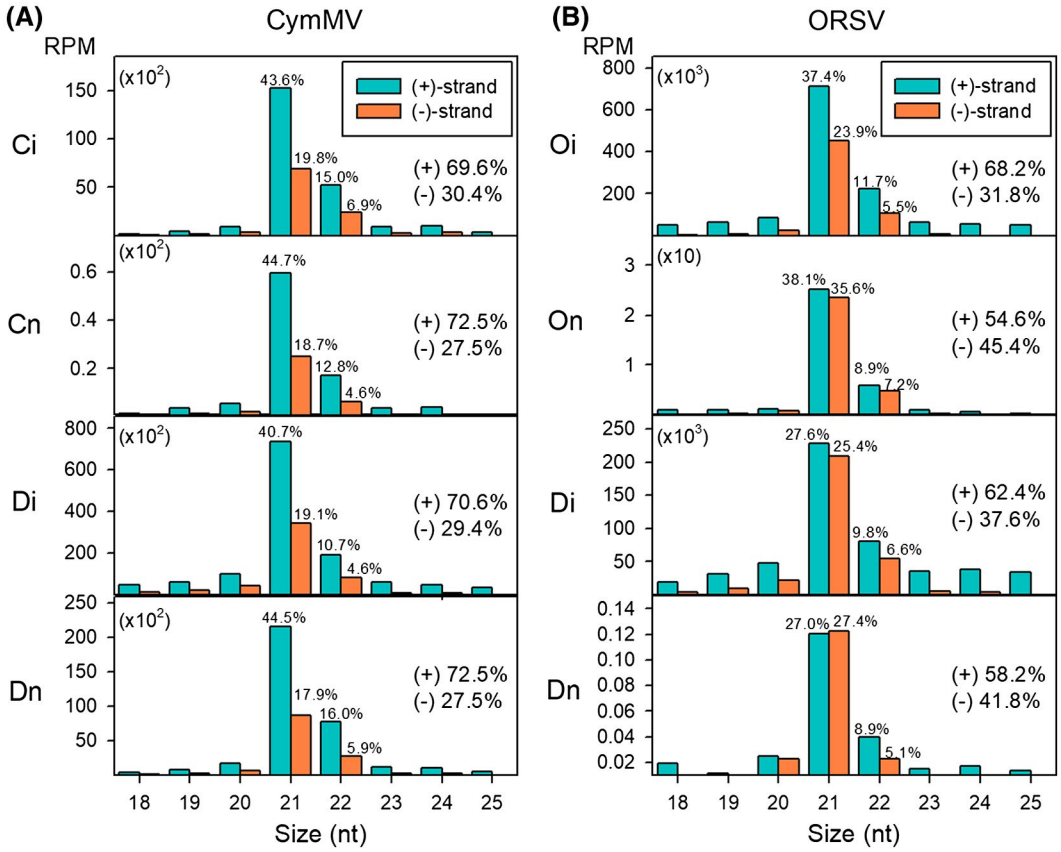


**Fig. 4** Abundance and size distribution of CymMV (A) and ORSV (B) vsiRNAs in inoculated *Phalaenopsis*. Blue and orange bars represent reads matched to (+) or (–) strands of viral genomic RNA, respectively. Percentages above the bar indicate the proportion in total CymMV or ORSV vsiRNAs within the library. The accumulation level is presented as reads per million (RPM). Oi, Ci and Di: inoculated (i) tissues of ORSV (O)-, CymMV (C)- and double (D)-inoculated plants. On, Cn and Dn: noninoculated (n) tissues of ORSV (O)-, CymMV (C)- and double (D)-inoculated plants.

the major size class (59.8% in Di and 62.4% in Dn for CymMV vsiRNAs, 53.0% in Di and 54.4% in Dn for ORSV vsiRNAs) and 22 nt as the second most abundant (Fig. 4). The 21- and 22-nt reads represented 81.4% (CymMV) and 76.5% (ORSV) of total vsiRNAs, which suggests that antiviral RNA silencing in *P. amabilis* may be mediated mainly by DCL4 and DCL2 proteins.

We observed asymmetrical distribution of vsiRNAs in sense-strand polarity among all the libraries except the On library, in which vsiRNAs were derived almost equally from both polarities and possessed only a modest enrichment (54.6%) of (+)-strand reads (Fig. 4B, On). The prevalence of sense-strands remained in CymMV and ORSV double-infected tissues Di and Dn, accounting for 70.6% to 72.5% of total CymMV vsiRNAs (Fig. 4A, Di/Dn) and 58.2% to 62.4% of total ORSV vsiRNAs (Fig. 4B, Di/Dn).

When grouped by the 5′-end nucleotide composition, generally C- and U-terminated CymMV vsiRNAs were prevalent in the 21- and 22-nt classes in the CymMV single-infected Ci and Cn libraries (Figs 5A and S2A). This 5′-end C and U dominance of CymMV vsiRNAs was likewise observed among the Ci, Cn, Di and Dn libraries. In contrast, ORSV vsiRNAs showed an even distribution of 5′ A, C and U in the 21- and 22-nt classes in the Oi and On libraries (Figs 5B and S2B), whereas the preference was slightly shifted to 5′ U and C dominance in the Di and Dn libraries (Figs 5B and S2B). For vsiRNA species with other sizes, the pattern for 5′-end nucleotide preference seemed biased from low vsiRNA reads (Fig. S2). Generally, CymMV and ORSV vsiRNAs were infrequently 5′ G, regardless of size classes in all the libraries (Figs 5 and S2).

Collectively, we found a prevalence of 21- and 22-nt size classes and (+)-strand polarity for both CymMV and ORSV vsiRNAs in all the libraries, regardless of infection stages with single or double viruses. These results suggest that CymMV and ORSV trigger common gene silencing machinery to generate similar vsiRNA profiles as the defence response in *Phalaenopsis*.

## Genome mapping, coverage and hotspots of CymMV and ORSV vsiRNAs

To study the vsiRNA origins across the entire viral genome, vsiRNAs were located according to their 5′-end sites along both positive and negative strands of the CymMV (AY571289) and ORSV (AY571290) genomes (Figs 6, S3 and S4). In the Di



13643703, 2020, 2, Downloaded from https://bsppjournals.onlinelibrary.wiley.com/doi/10.1111/mpp.12888 by Test, Wiley Online Library on [02/08/2025]. See the Terms and Conditions (https://onlinelibrary.wiley.com/terms-and-conditions) on Wiley Online Library for rules of use; OA articles are governed by the applicable Creative Commons License

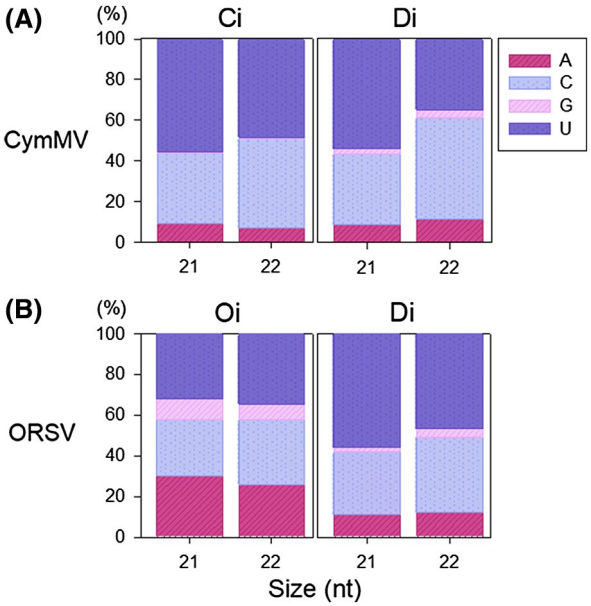


**Fig. 5** Nucleotide composition of 5′-end of CymMV (A) and ORSV (B) vsiRNAs in inoculated *Phalaenopsis*. The proportion of adenine (A), cytosine (C), guanine (G) and uridine (U) within each size class is shown. Oi, Ci and Di: inoculated (i) tissues of ORSV (O)-, CymMV (C)- and double (D)-inoculated plants.

library, the genome coverage was up to 91.0% and 98.8% for all sizes of CymMV and ORSV vsiRNAs, respectively. All the 21- to 24-nt size classes distributed continuously (Fig. S5) but with some genomic regions showing higher mapping frequencies. The CymMV vsiRNA distribution extensively encompassed the RdRp-coding region, and few were located in the TGBp- and CP-coding regions (Fig. 6A), and showed similar patterns in co-infection with ORSV or in early and late stages of infection (Figs 6A and S3). Northern blot hybridization confirmed the accumulation of RdRp-originated CymMV vsiRNAs in Ci, Di and Dn tissues (Fig. 2B). The origins of ORSV vsiRNAs had comparable patterns in the Oi and On libraries, with more ORSV vsiRNAs encompassing the region for the CP-coding sequence to 3′-UTR (Figs 6B and S4). A specific hotspot located in the 3′-UTR was observed, which was strikingly contributed by only one (+)-strand tag and accounted for 1.2% (26 801 reads, 2341.19 RPM) and 1.9% (88 reads, 12.73 RPM) of total ORSV-specific siRNAs in Oi and On, respectively. Further analysis revealed that the hotspot vsiRNA tag (5′-UCCACUUAAAUCGAAGGGUUG-3′) featured a conserved sequence among tobamovirus 3′-UTRs (Fig. S6A). The tobamovirus 3′-UTR contains a highly structured PK chain and ends with a tRNA-like structure (Zeenko *et al.*, 2002). Most tobamoviruses have only three PKs in the conserved domain, whereas ORSV 3′-UTR, about 412 nt long, contains three consecutive homologous regions and 11 PKs (Fig. S6B) (Ajjikuttira and Wong, 2009; Chng *et al.*, 1996; Gultyaev *et al.*, 1994). The two duplicated sequences also contain the hotspot sequence but with one base variation, substituting a G for a U at the 3′ end (5′-UCCACUUAAAUCGAAGGGUUU-3′). We have found vsiRNAs generated from the duplicated sequences, but the number of reads was much lower, with 785 reads and only one read in the Oi and On libraries, respectively (Fig. S6B).

Most surprisingly, the ORSV vsiRNA hotspot distribution showed a sharp difference between the double-infected (Di and Dn) and ORSV single-infected (Oi and On) libraries (Figs 6B and S4). Unique ORSV vsiRNA hotspots originated around the (–)-strand of the genome nucleotides 2260, 2643 and 4173 RdRp regions, comprising three prominent peaks in the Di library (Fig. 6B). Like the 3′-UTR hotspot, these peaks also featured a single major tag that represented 1.1% (1262.27 RPM), 1.6% (861.48 RPM) and 2.0% (1647.67 RPM) of the total ORSV vsiRNA pool, respectively. The hotspot tags represented <0.1% of the ORSV vsiRNAs in the Oi library. Likewise, the 3′-UTR hotspot vsiRNA found in the Oi library was retained in the Di library, but the abundance decreased greatly (308.99 RPM).

To evaluate the consistency of vsiRNA profiles in inoculated *Phalaenopsis*, sRNA libraries from another batch of mock- and CymMV/ORSV double-infected plants were constructed and analysed following the same pipeline. This time we obtained 20 777 593 raw reads from four libraries (Mi-2, Mn-2, Di-2 and Dn-2). In total, 10 997 553 clean reads were retained after quality and size filtering (Table S2). Although ORSV vsiRNAs accumulated to a higher level in the second batch of libraries with reduced (+)-strand predominance (Table S2 and Fig. S7), the other characteristics of vsiRNAs in the pool remained similar to the first profile. For instance, 21- and 22-nt size classes, (+)-strand polarity and 5′ U/C ends still prevailed in both CymMV and ORSV vsiRNA profiles (Fig. S7A,B). When mapping the vsiRNAs to viral genomes, conserved origins and peak pattern were almost the same, especially for CymMV vsiRNAs between the Di and Di-2 libraries (Fig. S7C). For ORSV vsiRNAs, although similar cleavage sites remained unchanged between the two batches, some slight variation in peaking level was observed (Fig. S7C). The alteration may relate to the discrepancy in ORSV vsiRNA accumulation level and the shift in (+):(–)-strand ratio. Nevertheless, the enrichment of (–)-polarity ORSV vsiRNA hotspots in double infection was validated by northern blots (Fig. S7D). From the two replicates, we have identified and confirmed the general characteristics and major cleavage sites of CymMV/ORSV vsiRNAs in *Phalaenopsis*.

## Potential roles of CymMV/ORSV vsiRNAs in manipulating viral pathogenesis in infected orchids

On the basis of sequence homology, previous studies have suggested vsiRNA-induced symptom formation via mediating host mRNA degradation (Navarro *et al.*, 2012; Shimura *et al.*, 2011). To search transcripts that could be targeted by CymMV or ORSV vsiRNAs, we examined possible pairings between vsiRNA tags and *P. aphrodite* EST sequences (Chao *et al.*, 2014). A global search for all the sequenced tags revealed 22 021 and 24 772 orchid transcripts as potential targets by CymMV or ORSV vsiRNAs,

© 2019 THE AUTHORS. *MOLECULAR PLANT PATHOLOGY* PUBLISHED BY BRITISH SOCIETY FOR PLANT PATHOLOGY AND JOHN WILEY & SONS LTD 

13643703, 2020, 2, Downloaded from https://bsppjournals.onlinelibrary.wiley.com/doi/10.1111/mpp.12888 by Test, Wiley Online Library on [02/08/2025]. See the Terms and Conditions (https://onlinelibrary.wiley.com/terms-and-conditions) on Wiley Online Library for rules of use; OA articles are governed by the applicable Creative Commons License

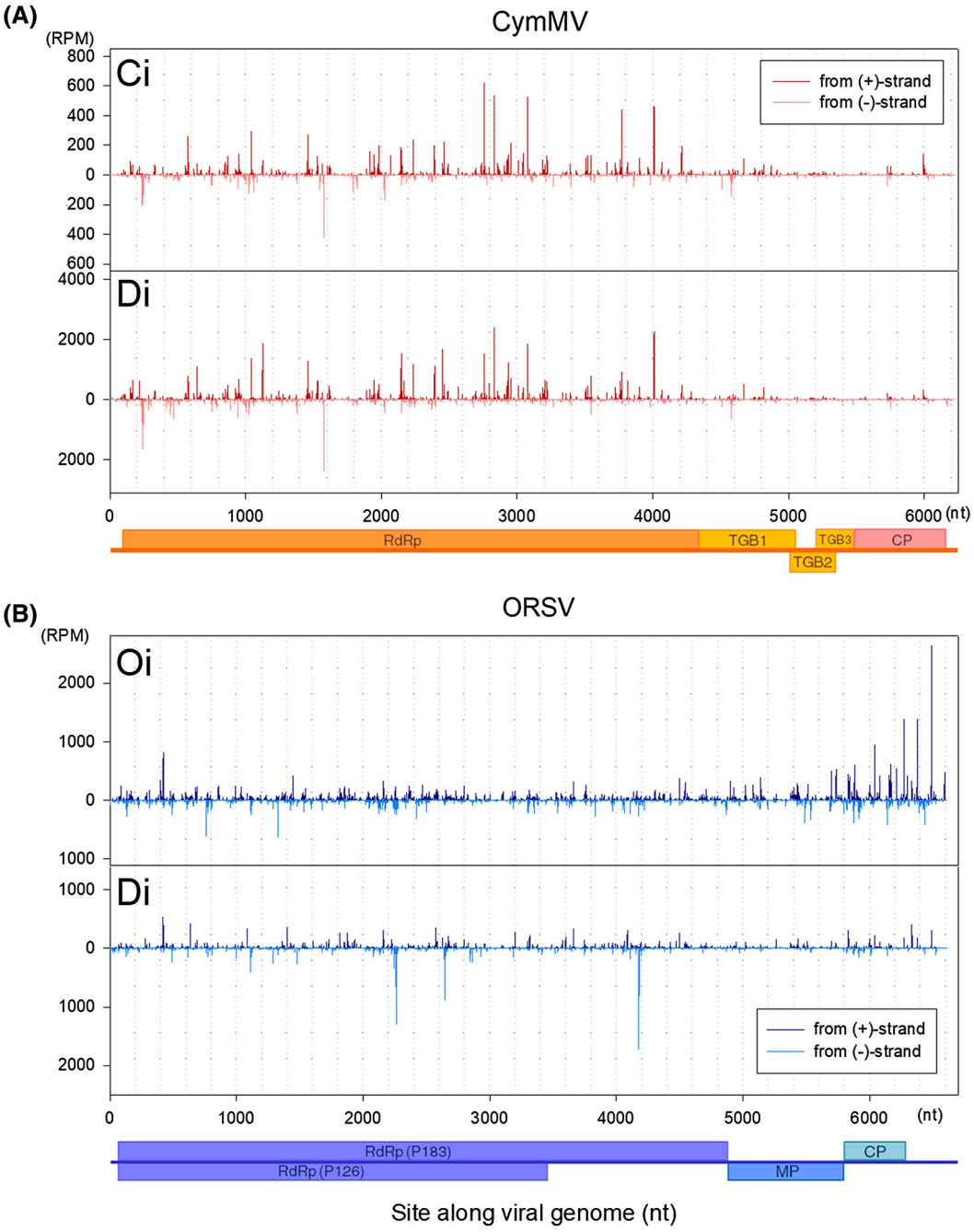


**Fig. 6** Distribution of vsiRNAs along CymMV (A) and ORSV (B) genome corresponding to reads from the CymMV (Ci), ORSV (Oi) and double inoculated (Di) inoculated tissue libraries. Upward dark-coloured and downward light-coloured lines represent (+) and (–) polarity reads, respectively. Genomic sites of RdRp, TGB (or MP) and CP gene coding regions are indicated below (numbers based on GenBank accession CymMV AY571289 or ORSV AY571290). The peak level is presented as reads per million (RPM).

respectively. Assuming that vsiRNA tags with prevalent reads may have higher impact on the expression of target genes, we focused on targets of the 20 most abundant vsiRNAs in the Oi, Ci and Di libraries. The filter highlighted 52 targets for 24 CymMV vsiRNAs and 68 for 28 ORSV vsiRNAs (Tables S3 and S4 and Fig. S8). We observed high overlapping between sets from the Ci and Di libraries for targets of CymMV vsiRNAs versus ORSV vsiRNAs (Fig. S8), which reflects that the ORSV vsiRNA hotspot shift may have a specific impact on host gene regulation in synergistic infections.



13643703, 2020, 2, Downloaded from https://bsppjournals.onlinelibrary.wiley.com/doi/10.1111/mpp.12888 by Test, Wiley Online Library on [02/08/2025]. See the Terms and Conditions (https://onlinelibrary.wiley.com/terms-and-conditions) on Wiley Online Library for rules of use; OA articles are governed by the applicable Creative Commons License

To evaluate our hypothesis, we performed gene ontology (GO) enrichment analyses for functional interpretation of the vsiRNA targets. The annotations for CymMV vsiRNA targets were mainly enriched in autophagy, metabolic activities and transmembrane transport terms regardless of single (Ci) or double (Di) infections (Tables S5 and S6). However, the annotation of targets of ORSV vsiRNAs in single infection (Oi) encompassed a broader range of biological processes, including protein translocation, endoplasmic reticulum (ER) response, molecule modification, response to environmental stimulus and others (Table S7). Another 34 novel targets were identified for dominant ORSV vsiRNAs in double infection (Di), and GO terms linked to transcription and protein modification prevailed (Table S8). Of note, EKC/KEOPS complex subunit bud32 and tryptophan aminotransferase-related protein 2 (TAR2) were potential targets of ORSV 3′-UTR hotspot vsiRNAs. Also, two of the topmost (–)-strand hotspot ORSV vsiRNAs target chloroplastic nudix hydrolase 23 (NUDX23) and serine/threonine-protein kinase NAK (Table S4).

### Differential expression of *P. amabilis* RNAi components in response to CymMV and ORSV infection

To identify the major components mediating vsiRNA generation, we determined transcript levels of *P. amabilis* DCL1/2/4, Argonaute proteins (AGOs) AGO1/4/5/10 and RNA-dependent RNA polymerases (RDRs) RDR1/2/6 with CymMV and ORSV single or double infection. All evaluated components except AGO4 and AGO10 were up-regulated with CymMV and ORSV double infection (Fig. 7). For single infections, AGO5, RDR1 and RDR6 expressions were readily induced by CymMV infection. Of note, several components including AGO4, AGO10, RDR2 and DCL4 were suppressed with ORSV single infection. These results show that the viruses have different effects on the RNAi genes, which may contribute to the varied profiles of CymMV and ORSV vsiRNAs.

## DISCUSSION

In this study, we recorded the synergistic effects of CymMV and ORSV double infection in *P. amabilis*. Consistent with previous studies (Hadley *et al*., 1987; Lawson and Brannigan, 1986; Pearson and Cole, 1991), chlorotic lesions and ringspots appeared at about 7 dpi and continued enlarging afterwards in double-inoculated tissues (Fig. 1B and data not shown). Northern blot analysis further revealed enhanced CymMV titres (Fig. 2A) as well as about 5-fold accumulation of CymMV vsiRNAs in double- versus single-infected (Di vs Ci) tissues. In contrast, the viral titres of ORSV did not increase in Di tissues with CymMV coinfection and were scarcely detected in the noninoculated (Dn) tissues by northern blot or RT-PCR (Fig. 2A,C). The results clearly demonstrate an asymmetric synergism between CymMV and ORSV in double-infected *Phalaenopsis*. Previously, Hu *et al* (1998) reported that both CymMV and ORSV accumulation could be detected in *Dendrobium* protoplasts at earlier time points on mixed inoculation. In addition, ORSV genomic RNA accumulation was accelerated in double-infected *Nicotiana benthamiana* (Ajjikuttira and Wong, 2009). Although we have observed intensified symptoms in mixed infected *Nicotiana* and orchid, both CymMV and ORSV titres reached similar levels between singly and doubly transfected protoplasts (Chen *et al*., 2019; Fig. S9). The discrepancy between our results and the other reports may be due to different virus strains in response to different host species. Their *Cattleya*-originated viral strains (Yu and Wong, 1998) differ from ours from *P. amabilis* with about 3% nucleotide variation (data not shown). This could be the result of coevolution between viruses and their natural hosts.

In reviewing asymmetric viral synergism, the classical example is potato virus Y (PVY) supporting potato virus X (PVX) accumulation (Vance, 1991). Similarly, PVX benefited more from mixed infection with tobacco mosaic virus (TMV) in tomato (Balogun *et al*., 2002). Of note, the accumulation of 'helper' viruses usually remained unchanged or slightly decreased in most combinations (Mascia and Gallitelli, 2016). This was also the case for ORSV in our study. TMV P126 protein has VSR activity that can increase the susceptibility of several viruses in *Nicotiana tabacum* (Harries *et al*., 2008). In addition, Ajjikuttira *et al.* (2005) demonstrated that the MPs and CPs were functionally interchangeable between CymMV and ORSV, with the exception of long-distance movement of ORSV RNA by CymMV CP. In other tobamoviruses, the VSR and the ability of MP to increase the size exclusion limit of plasmodesmata have been documented (Wang *et al*., 2012a; Wolf *et al*., 1989). Together with the result of unchanged CymMV and ORSV viral titres in protoplasts (Chen *et al*., 2019; Fig. S9), we suggest that enhanced CymMV movement may be the major force for synergism. Whether ORSV exerts helper components to pave the way for vigorous CymMV infection requires further investigation.

The production of vsiRNAs is a hallmark of antiviral RNA silencing in host plants. In *P. amabilis*, although CymMV and ORSV outcompete the defence response and render the plant susceptible, vsiRNAs generated by ribonuclease cleavage against CymMV and ORSV viral RNAs were readily detectable in inoculated (Ci, Oi and Di) as well as neighbouring noninoculated (Cn, On and Dn) tissues (Fig. 2B), which indicates that antiviral RNA silencing was activated in the early stage of infection as well. The profile revealed that CymMV and ORSV vsiRNAs shared common features including (1) the predominance of 21- and 22-nt classes, which mirrors the conserved roles of DCL4 and DCL2 homologues in *P. amabilis* antiviral RNA silencing, as in many other plants; (2) asymmetry in strand polarity, which indicates that the biosysnthesis of CymMV and ORSV vsiRNAs may involve self-annealing hairpin structures within viral ssRNA (Molnár *et al*., 2005) in addition to replicative intermediates and long dsRNA during viral replication (Ding, 2010); and (3) under-representation of guanine at the 5′-end nucleotide composition. The avoidance was clearly demonstrated because the base composition of ORSV genomic RNA is U (30.8%) > A (29.8%) > G (21.6%) > C (17.8%) (AY571290), and

© 2019 THE AUTHORS. *MOLECULAR PLANT PATHOLOGY* PUBLISHED BY BRITISH SOCIETY FOR PLANT PATHOLOGY AND JOHN WILEY & SONS LTD 

13643703, 2020, 2, Downloaded from https://bsppjournals.onlinelibrary.wiley.com/doi/10.1111/mpp.12888 by Test, Wiley Online Library on [02/08/2025]. See the Terms and Conditions (https://onlinelibrary.wiley.com/terms-and-conditions) on Wiley Online Library for rules of use; OA articles are governed by the applicable Creative Commons License

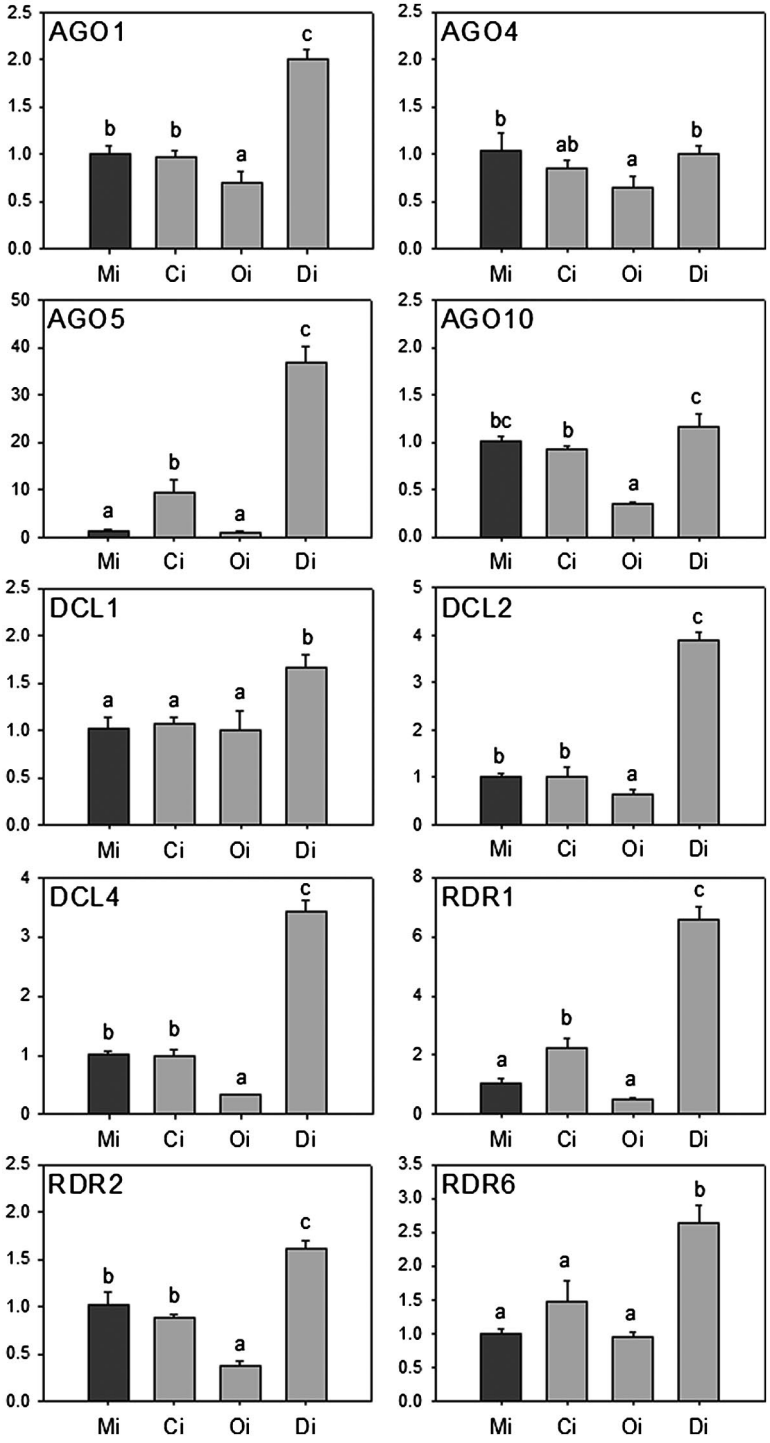


**Fig. 7** Expression of *Phalaenopsis amabilis* RNA silencing components with CymMV and/or ORSV infection. Quantitative reverse transcription PCR (RT-qPCR) analysis of mRNA accumulation of DCL1/2/4, RDR1/2/6 and AGO1/4/5/10. Mi, Ci, Oi and Di: inoculated tissues of mock (M)-, ORSV (O)-, CymMV (C)-, ORSV (O)- and double (D)-inoculated plants. Relative quantity (*y*-axis) was averaged from three biological replicates, presented as mean ± SD ($n = 3$). The average of mock (Mi) was arbitrarily set as one. Significant differences are marked with lower case letters at $P \leq 0.05$ (Student–Newman–Keuls test).

CymMV genome is proportioned as C (29.2%) > A (26.5%) > U (24.7%) > G (19.6%) (AY571289). No preferential vsiRNA size class was associated with strand polarity and 5′ nucleotide preference, so the bias was not introduced by different DCL processing. Moreover, the 5′-end nucleotide identity is a key determinant for sorting sRNAs into distinct AGO proteins (Czech and



13643703, 2020, 2, Downloaded from https://bsppjournals.onlinelibrary.wiley.com/doi/10.1111/mpp.12888 by Test, Wiley Online Library on [02/08/2025]. See the Terms and Conditions (https://onlinelibrary.wiley.com/terms-and-conditions) on Wiley Online Library for rules of use; OA articles are governed by the applicable Creative Commons License

Hannon, 2011; Kim, 2008), such as AGO1 preferring sRNAs with the 5′-terminal U, AGO2 and AGO4 the 5′ A, and AGO5 the 5′ C (Hu *et al*., 2011; Mi *et al*., 2008; Montgomery *et al*., 2008; Takeda *et al*., 2008). The absence of known 5′-G preferred AGO species may explain the avoidance of 5′-G vsiRNAs (Donaire *et al*., 2009). Furthermore, the 5′-A preference of ORSV vsiRNAs in single infection shifted to 5′-U and 5′-C dominance with double infection with CymMV, which coincided with up-regulation of AGO1 and AGO5 in double-infected tissues (Fig. 7). The results suggest that CymMV and ORSV vsiRNAs could be recruited into different AGO proteins with single or double infection.

For vsiRNA origins from viral genomes, the CymMV and ORSV vsiRNA profiles differed. In single-infected tissues, more hotspots resided in the RdRp of CymMV and the CP to 3′-UTR region of the ORSV genome (Fig. 6). We analysed the GC context of each viral segment but found no clear relevance (Table S9). This discrepancy may be due to higher accumulation of ORSV CP-expressed subgenomic RNA and more abundant CymMV gRNAs in the infected *P. amabilis* tissues, as shown on northern blots (Fig. 2A). ORSV single-infected tissues (Oi and On) showed a unique hotspot located in the 3′-UTR (Figs 6B and S4), which had one specific (+)-polarity tag. Modelling of the 3′-UTR secondary structure by Gultyaev *et al* (1994) revealed that the hotspot vsiRNA resided in the first PK structure upstream of the tRNA-like structure (Fig. S6B), which was not a typical double-strand structure expected to be preferentially cleaved by DCL enzymes. Of note, we also identified similar hotspot vsiRNAs in TMV-infected tobacco that shared a conserved sequence and structural origin with the ORSV PK vsiRNA (Fig. S6C). These observations suggest the accessibility of DCL dicing at the PK structure. The 3′-UTR of tobamoviruses plays a central role in viral replication (reviewed in Chujo *et al*., 2015), especially as the two PKs upstream of the tRNA-like structure are indispensable for full translation and infectivity (Leathers *et al*., 1993; Takamatsu *et al*., 1990). However, how the RNA structure or the recruited factors are involved in generating the abundant hotspot vsiRNAs remains to be explored.

In addition, we identified three prominent hotspot peaks in the negative polarity of the ORSV genome specifically in double-infected tissues (Figs 6B and S4). Similarly, the sweet potato begomovirus isolate StV1 asymmetrically benefitted from coinfection with crinivirus sweet potato chlorotic stunt virus (SPCSV), and a specific change in vsiRNAs derived from SPCSV but not StV1 was observed (Cuellar *et al*., 2015). Moreover, vsiRNAs hotspot distribution was increased in asymmetrical synergism between maize chlorotic mottle virus and sugarcane mosaic virus (Xia *et al*., 2016) or between brassica yellows virus and pea enation mosaic virus 2 (Zhou *et al*., 2017). These studies suggest possible roles of potent VSR activity in altering the hosts' RNA silencing machinery and leading to modified targeting to viral RNAs. In line with these hypotheses, vsiRNA profiles from wild-type or VSR-deficient CymRSV (Szittya *et al*., 2010) and tospoviruses (Margaria *et al*., 2015) revealed the influence of VSRs to DCL targeting of the viral genome. P25 of CymMV and P126 of ORSV are potential VSRs to suppress RNA silencing and affect vsiRNA generation. Along with DCL1/2/4 being highly induced in double-infected tissues (Fig. 7), the discrepancy in distribution of ORSV vsiRNA hotspots may be due to differences in the effects of VSRs and altered DCL accessibility to ORSV viral RNAs during interaction with CymMV.

In contrast to the viral RNA clearance activity of plant RNA silencing pathways, host transcripts could be targeted by vsiRNAs if the virus and host mRNAs share sequence complementarity (Navarro *et al*., 2012; Shimura *et al*., 2011; Smith *et al*., 2011). Our study predicted potential *Phalaenopsis* target genes of ORSV and CymMV vsiRNAs. For instance, targets of CymMV vsiRNAs include (1) serine/threonine kinases that harbour protein phosphorylation activity (Hardie, 1999) and several members reported to be involved in defence responses (Afzal *et al*., 2008; Rodriguez *et al*., 2010); (2) protochlorophyllide-dependent translocon component 52 involved in chlorophyll metabolism (Bartsch *et al*., 2008); and (3) autophagy-related proteins, which may contribute to antiviral responses or in turn facilitate viral replication (Clavel *et al*., 2017). On the other hand, EKC/KEOPS complex subunit bud32 and TAR2 were potential targets of the 3′-UTR ORSV hotspot vsiRNA. Novel targets such as NUDX23 and serine/threonine-protein kinase NAK were highlighted because unique ORSV vsiRNA hotspots were generated upon mixed infection with CymMV. EKC/KEOPS is a conserved complex for tRNA modification (Srinivasan *et al*., 2011) and TAR2 has been linked to local auxin production (Stepanova *et al*., 2008). Because tobamoviruses are tRNA-tailed, and the auxin-response pathway confers an age-dependent defence against TMV (Collum *et al*., 2016; Padmanabhan *et al*., 2008), regulation of these two host genes may affect ORSV pathogenesis. NUDX23 is a chloroplastic flavin pyrophosphohydrolase in *Arabidopsis* involved in the antioxidant response (Maruta *et al*., 2012). Another pyrophosphohydrolase, NUDT7, was identified as a negative regulator of the defence response against bacteria (Ge and Xia, 2008). Because viral symptoms appeared only in Di tissues at 10 dpi, combined with the presence of unique ORSV vsiRNA hotspots and high abundance of CymMV vsiRNAs, dysregulation of the novel targets of ORSV vsiRNAs and/or enhanced targeting of CymMV vsiRNAs to host transcripts may lead to synergized viral pathogenesis under mixed infection. We expect future work will uncover the association between CymMV/ORSV viral synergism and vsiRNA-mediated silencing of *Phalaenopsis* genes.

## EXPERIMENTAL PROCEDURES

### Plant materials, virus inoculation, tissue blot and total RNA isolation

Mericlone *P. amabilis* plants in 7.5-cm pots were purchased from I-hsin Biotechnology Inc. (Chia-yi, Taiwan). The plants were confirmed to be CymMV and ORSV-free by multiplex

© 2019 THE AUTHORS. *MOLECULAR PLANT PATHOLOGY* PUBLISHED BY BRITISH SOCIETY FOR PLANT PATHOLOGY AND JOHN WILEY & SONS LTD 

13643703, 2020, 2, Downloaded from https://bsppjournals.onlinelibrary.wiley.com/doi/10.1111/mpp.12888 by Test, Wiley Online Library on [02/08/2025]. See the Terms and Conditions (https://onlinelibrary.wiley.com/terms-and-conditions) on Wiley Online Library for rules of use; OA articles are governed by the applicable Creative Commons License

RT-PCR as described (Lee and Chang, 2006), then grown in walk-in chambers with a day/night temperature of 28/25 °C. CymMV and ORSV isolates were kindly provided by Dr Yau-Heiu Hsu (National Chung Hsing University, Taichung, Taiwan). After propagating in *N. benthamiana*, virions were purified as described (Lin and Chen, 1991; Lin *et al*., 1992). For inoculation assays, 1 μg of CymMV/ORSV or 0.5 μg of each CymMV and ORSV virions per leaf was inoculated on the first and second fully expanded leaves. Assuming the virus would spread along parallel veins, plants were mechanically inoculated with purified virions only at the tip halves. The mock-inoculated plants with 20 μL inoculation buffer (5 mM Tris-HCl, 1 mM EDTA, 5 mM phosphate buffer and 1 g/L bentonite, pH 8.0) were used as controls. At 10 dpi, we first used tissue blotting to reveal virus infection and distribution in the inoculated leaves, as illustrated in Fig. 1A (Lin *et al*., 1990). Slices from inoculated and adjacent noninoculated tissues were separately collected. The blots were then hybridized with riboprobes specific to CymMV/ORSV full-length CP genes by using the DIG Nucleic Acid Detection Kit (Sigma-Aldrich, St Louis, MO, USA). The collected leaves were classified by infection stage as revealed by tissue blotting. Tissues of the same category from three leaves were pooled for total RNA extraction by using TriPure Isolation Reagent (Sigma-Aldrich) following the manufacturers' instructions.

## Northern blot, sRNA detection and RT-PCR

Accumulation of viral RNA was examined by northern blot analysis as described (Lin *et al*., 1996; Palani and Lin, 2007), following the hybridization methods used for tissue blotting. The northern blot method for total vsiRNAs was according to Lin *et al* (2010). In brief, 25 μg total RNA was separated and electroblotted onto to Hybond-$N^+$ nylon membranes. The blots were hybridized with [$\gamma$ – $^{32}$P] cytidine triphosphate (CTP)-labelled, carbonate buffer-fragmented RNA probes CymMV-RdRp or ORSV-CP3UTR (Table S11). To determine relative vsiRNA abundance of different genomic regions, a series of *in vitro* transcripts corresponding to CymMV and ORSV genomic segments (Table S11) were first blotted onto nylon membranes. Small RNAs were enriched by using *miR*vana miRNA isolation kit (Invitrogen, Waltham, MA, USA) and the 5′-end labelled as described (Lin *et al*., 2010), then hybridized to the blots. Radioactive signals were recorded by using the phosphorimager Typhoon FLA7000 (GE Healthcare Life Sciences, Chicago, IL, USA).

For RT-PCR and RT-qPCR analyses, cDNA was reverse-transcribed from 1 μg total RNA by using the ToolsQuant II Fast RT Kit (Biotools, New Taipei City, Taiwan) with the primer pairs specific to CymMV/ORSV RdRp genes (CymRdRp-F, CymRdRp-R and OR-RdRp-F, OR-RdRp-R) to detect virus infection. To determine expression levels of *P. amabilis* RNA silencing components, putative DCLs/AGOs/RDRs sequences were retrieved from Orchidstra 2.0 (Chao *et al*., 2014; Su *et al*., 2011) and OrchidBase 3.0 (Cai *et al*., 2015) by name search. Phylogenetic analysis by using *Arabidopsis* and *Oryza sativa* references clearly grouped DCL1/2/3/4, AGO1/4/5/6/7/10 and RDR1/2/3/6 homologues in *Phalaenopsis*. The sequences were cloned from *P. amabilis* for primer design (data not shown). Real-time PCR for major antiviral components involved the SYBR Green PCR Master Mix (Applied Biosystems, Waltham, MA, USA) and QuantStudio 12K Flex System (Applied Biosystems). RT-qPCR reads were transformed into a relative expression index calculated by the $\Delta\Delta C_t$ algorithm (Livak and Schmittgen, 2001), with ubiquitin (primer pairs Pa-Ubi-2F and Pa-Ubi-2R) as a reference gene. The mean of Mi tissue replicates was set as the secondary standard. The primer sequences are shown in Table S10.

## sRNA deep-sequencing and bioinformatic annotation

The integrity of the RNA samples was checked by using Agilent 2100 Bioanalyzer (Agilent Technologies, Santa Clara, CA, USA) before being submitted to sRNA library construction. For each library, 10 μg total RNA was size-fractionated on 15% Tris-borate-EDTA urea polyacrylamide gel. sRNAs recovered from the gel bands corresponded to 18–30 nt of the marker. Construction of cDNA libraries involved the TruSeq Small RNA Sample Preparation protocol (Illumina, San Diego, CA, USA). Bar-coded libraries were pooled in a single channel of the flow cell and sequenced by using the Illumina HiSeq 2000 at Yourgene Bioscience (New Taipei City, Taiwan).

The raw sequencing reads were first processed by using Trimmomatic (Bolger *et al*., 2014). Customized Perl scripts were used to examine contamination from adapters, size markers, reads with N (null) or and poly-A/T/C/G callings. Clean reads were then grouped into unique reads (tags) by sequence identity. Low-frequency tags (i.e. tags with only one read in a single library that were not detected in any other libraries) and tags with sizes <18 nt or >25 nt were filtered out. CymMV- and ORSV-specific vsiRNAs were identified by alignment against viral genome sequences, which was conducted using Bowtie (Langmead, 2010). All the available CymMV/ORSV genome sequences were downloaded from GenBank (CymMV accessions AF016914, AY571289, JQ860108, HQ681906, EF125180, EF125179, EF125178, AM055720, AB197937, NC_001812, EU314803; ORSV accessions AY571290, DQ139262, NC_001728, KF855954, U34586). The nonredundant results from mapping to different isolates were summed as total mapped reads for CymMV/ORSV. To identify hotspots of vsiRNA origins, we selected the Taiwan isolates (CymMV AY571289 and ORSV AY571290) as representatives for genomic sites. The nonviral reads were further annotated with plant resources including databases for miRNAs (miRBase v. 21.0, Kozomara and Griffiths-Jones, 2013). The *P. aphrodite* transcriptome (Orchidstra 2.0), Rfam v. 10.1 (Nawrocki *et al*., 2015) and other local databases, with the hierarchy and criteria indicated in Fig. S1. For TMV vsiRNA profile, sRNA sequencing data collected by



13643703, 2020, 2, Downloaded from https://bsppjournals.onlinelibrary.wiley.com/doi/10.1111/mpp.12888 by Test, Wiley Online Library on [02/08/2025]. See the Terms and Conditions (https://onlinelibrary.wiley.com/terms-and-conditions) on Wiley Online Library for rules of use; OA articles are governed by the applicable Creative Commons License

Pecman *et al.* (2017) were downloaded from Sequence Read Archive accession SRX2672447. Sequence quality and size trimming were performed as described for *Phalaenopsis* libraries. TMV vsiRNAs were identified by a perfect match to the TMV reference genome NC_001367.

### Target gene prediction and GO enrichment analysis

Putative CymMV/ORSV vsiRNA targeting *Phalaenopsis* genes were predicted by using a scoring matrix (Weiberg *et al.*, 2013). Because of the huge diversity, we selected only predicted targets of the top 20 abundant CymMV and ORSV vsiRNAs with single (Ci and Oi) or double infection (Di) for further analysis. GO annotations for the *P. aphrodite* transcriptome were downloaded from Orchidstra 2.0. A statistical test based on a hypergeometric distribution was performed using Matlab to determine whether a certain category was significantly enriched. The enriched terms with $P \leq 0.05$ were summarized into major categories using the web tool REVIGO (Supek *et al.*, 2011).

### Protoplast isolation, virus transfection and western blot analysis

Flower protoplasts were isolated from *P. amabilis* petals and sepals using methods previously described (Lin *et al.*, 2018). In addition, the protoplasts were floated onto 20% sucrose gradient and centrifuged at 70 *g* for 5 min to remove oxalate crystals. Approximately $2 \times 10^5$ cells were transfected with 0.5 μg of CymMV/ORSV or 0.5 μg of each CymMV and ORSV virions by the PEG1450 method. The protoplasts were cultivated at 25 °C under light for 12 or 20 h before harvest. Virus accumulation was detected by western blots conducted with laboratory-generated rabbit anti-CymMV or anti-ORSV CP antiserum.

## ACKNOWLEDGEMENTS

This work was funded by the Institute of Plant and Microbial Biology, Academia Sinica, Taiwan, and the Innovative Translational Agricultural Research Program. We thank Dr Chun-Lin Su, Dr Ya-Ting Chao and the Bioinfomatics Core Facility at the Agricultural Biotechnology Research Center, Academia Sinica, for helpful discussions. The authors declare no conflicts of interest.

## REFERENCES

**Afzal, A.J., Wood, A.J. and Lightfoot, D.A.** (2008) Plant receptor-like serine threonine kinases: Roles in signaling and plant defense. *Mol. Plant-Microbe Interact.* **21**, 507–517.

**Ajjikuttira, P. and Wong, S.M.** (2009) Molecular biology of two orchid infecting viruses: cymbidium mosaic potexvirus and Odontoglossum ringspot tobamovirus. In: Orchid Biology: Reviews and Perspectives, X, (Kull, T., Arditti, J. and Wong, S., eds.), pp. 251–277. Netherlands: Springer.

**Ajjikuttira, P., Loh, C.S. and Wong, S.M.** (2005) Reciprocal function of movement proteins and complementation of long-distance movement of Cymbidium mosaic virus RNA by Odontoglossum ringspot virus coat protein. *J. Gen. Virol.* **86**, 1543–1553.

**Ali, R.N., Dann, A.L., Cross, P.A. and Wilson, C.R.** (2014) Multiplex RT-PCR detection of three common viruses infecting orchids. *Arch. Virol.* **159**, 3095–3099.

**Angell, S.M. and Baulcombe, D.C.** (1997) Consistent gene silencing in transgenic plants expressing a replicating Potato virus X RNA. *EMBO J.* **16**, 3675–3684.

**Balogun, O.S., Xu, L., Teraoka, T. and Hosokawa, D.** (2002) Effects of single and double infections with Potato virus X and Tobacco mosaic virus on disease development, plant growth, and virus accumulation in tomato. *Fitopatol. Bras.* **27**, 241–248.

**Bartsch, S., Monnet, J., Selbach, K., Quigley, F., Gray, J., von Wettstein, D., Reinbothe, S. and Reinbothe, C.** (2008) Three thioredoxin targets in the inner envelope membrane of chloroplasts function in protein import and chlorophyll metabolism. *Proc. Natl. Acad. Sci. USA.* **105**, 4933–4938.

**Bivalkar-Mehla, S., Vakharia, J., Mehla, R., Abreha, M., Kanwar, J.R., Tikoo, A. and Chauhan, A.** (2011) Viral RNA silencing suppressors (RSS): novel strategy of viruses to ablate the host RNA interference (RNAi) defense system. *Virus Res.* **155**, 1–9.

**Blevins, T., Rajeswaran, R., Shivaprasad, P.V., Beknazariants, D., Si-Ammour, A., Park, H.S., Vazquez, F., Robertson, D., Meins, F., Hohn, T. and Pooggin, M.M.** (2006) Four plant Dicers mediate viral small RNA biogenesis and DNA virus induced silencing. *Nucleic Acids Res.* **34**, 6233–6246.

**Bolger, A.M., Lohse, M. and Usadel, B.** (2014) Trimmomatic: a flexible trimmer for Illumina sequence data. *Bioinformatics*, **30**, 2114–2120.

**Cai, J., Liu, X., Vanneste, K., Proost, S., Tsai, W.C., Liu, K.W., Chen, L.-J., He, Y., Xu, Q., Bian, C., Zheng, Z., Sun, F., Liu, W., Hsiao, Y.-Y., Pan, Z.-J., Hsu, C.-C., Yang, Y.-P., Hsu, Y.-C., Chuang, Y.-C., Dievart, A., Dufayard, J.-F., Xu, X., Wang, J.-Y., Wang, J., Xiao, X.-J., Zhao, X.-M., Du, R., Zhang, G.-Q., Wang, M., Su, Y.-Y., Xie, G.-C., Liu, G.-H., Li, L.-Q., Huang, L.-Q., Luo, Y.-B., Chen, H.-H., Van de Peer, Y. and Liu, Z.-J.** (2015) The genome sequence of the orchid *Phalaenopsis equestris*. *Nat. Genet.* **47**, 65–72.

**Chan, Y.L., Lin, K.H., Liao, L.J., Chen, W.H. and Chan, M.T.** (2005) Gene stacking in *Phalaenopsis* orchid enhances dual tolerance to pathogen attack. *Transgenic Res.* **14**, 279–288.

**Chang, C.A., Chen, H.R. and Chiu, C.H.** (2010) Disinfection of Odontoglossum ringspot virus and Cymbidium mosaic virus from tools used during orchid cultivation. *Acta Hortic.* **878**, 381–388.

**Chao, Y.T., Su, C.L., Jean, W.H., Chen, W.C., Chang, Y.C. and Shih, M.C.** (2014) Identification and characterization of the microRNA transcriptome of a moth orchid *Phalaenopsis aphrodite*. *Plant Mol. Biol.* **84**, 529–548.

**Chen, T.Y., Pai, H., Hou, L.Y., Lee, S.C., Lin, T.T., Chang, C.H., Hsu, F.-C., Hsu, Y.-H. and Lin, N.-S.** (2019) Dual resistance of transgenic plants against Cymbidium mosaic virus and Odontoglossum ringspot virus. *Sci. Rep.* **9**, 10230.

**Chia, T.F. and He, J.** (1999) Photosynthetic capacity in *Oncidium* (Orchidaceae) plants after virus eradication. *Environ. Exper. Bot.* **42**, 11–16.

**Chng, C.G., Wong, S.M., Mahtani, P.H., Loh, C.S., Goh, C.J., Kao, M.C., Chung, M.C.-M. and Watanabe, Y.** (1996) The complete sequence of a Singapore isolate of Odontoglossum ringspot virus and comparison with other tobamoviruses. *Gene*, **171**, 155–161.

**Christenhusz, M.J.M. and Byng, J.W.** (2016) The number of known plants species in the world and its annual increase. *Phytotaxa*, **261**, 201–217.

**Chujo, T., Ishibashi, K., Miyashita, S. and Ishikawa, M.** (2015) Functions of the 5′- and 3′-untranslated regions of tobamovirus RNA. *Virus Res.* **206**, 82–89.

**Clavel, M., Michaeli, S. and Genschik, P.** (2017) Autophagy: a double-edged sword to fight plant viruses. *Trends Plant Sci.* **22**, 646–648.



13643703, 2020, 2, Downloaded from https://bsppjournals.onlinelibrary.wiley.com/doi/10.1111/mpp.12888 by Test, Wiley Online Library on [02/08/2025]. See the Terms and Conditions (https://onlinelibrary.wiley.com/terms-and-conditions) on Wiley Online Library for rules of use; OA articles are governed by the applicable Creative Commons License

**Collum, T.D., Padmanabhan, M.S., Hsieh, Y.C. and Culver, J.N.** (2016) Tobacco mosaic virus-directed reprogramming of auxin/indole acetic acid protein transcriptional responses enhances virus phloem loading. *Proc. Natl. Acad. Sci. USA*. **113**, E2740–2749.

**Csorba, T., Kontra, L. and Burgyan, J.** (2015) viral silencing suppressors: tools forged to fine-tune host-pathogen coexistence. *Virology*, **479–480**, 85–103.

**Cuellar, W.J., Galvez, M., Fuentes, S., Tugume, J. and Kreuze, J.** (2015) Synergistic interactions of begomoviruses with Sweet potato chlorotic stunt virus (genus *Crinivirus*) in sweet potato (*Ipomoea batatas* L.). *Mol. Plant Pathol.* **16**, 459–471.

**Czech, B. and Hannon, G.J.** (2011) Small RNA sorting: matchmaking for Argonautes. *Nat. Rev. Genet.* **12**, 19–31.

**Ding, S.W.** (2010) RNA-based antiviral immunity. *Nat. Rev. Immunol.* **10**, 632–644.

**Donaire, L., Wang, Y., Gonzalez-Ibeas, D., Mayer, K.F., Aranda, M.A. and Llave, C.** (2009) Deep-sequencing of plant viral small RNAs reveals effective and widespread targeting of viral genomes. *Virology*, **392**, 203–214.

**Dougherty, W.G., Lindbo, J.A., Smith, H.A., Parks, T.D., Swaney, S. and Proebsting, W.M.** (1994) RNA-mediated virus resistance in transgenic plants: exploitation of a cellular pathway possibly involved in RNA degradation. *Mol. Plant-Microbe Interact.* **7**, 544–552.

**Ge, X. and Xia, Y.** (2008) The role of AtNUDT7, a Nudix hydrolase, in the plant defense response. *Plant Signal Behav.* **3**, 119–120.

**Gultyaev, A.P., van Batenburg, E. and Pleij, C.W.** (1994) Similarities between the secondary structure of satellite Tobacco mosaic virus and tobamovirus RNAs. *J. Gen. Virol.* **75**, 2851–2856.

**Hadley, G., Arditti, M. and Arditti, J.** (1987) Orchids diseases - A compendium. In: Orchid Biology, Revies and Perspectives IV, (Arditti, J. ed.), pp. 263–322. Ithaca: Cornell University Press.

**Hardie, D.G.** (1999) Plant protein serine/threonine kinases: classification and functions. *Annu. Rev. Plant Physiol. Plant Mol. Biol.* **50**, 97–131.

**Harries, P.A., Palanichelvam, K., Bhat, S. and Nelson, R.S.** (2008) Tobacco mosaic virus 126-kDa protein increases the susceptibility of *Nicotiana tabacum* to other viruses and its dosage affects virus-induced gene silencing. *Mol. Plant-Microbe Interact.* **21**, 1539–1548.

**Herranz, M.C., Navarro, J.A., Sommen, E. and Pallas, V.** (2015) Comparative analysis among the small RNA populations of source, sink and conductive tissues in two different plant-virus pathosystems. *BMC Genom.* **16**, 117.

**Hu, W.W. and Wong, S.M.** (1998) The use of DIG-labelled cRNA probes for the detection of Cymbidium mosaic potexvirus (CymMV) and Odontoglossum ringspot tobamovirus (ORSV) in orchids. *J. Virol. Methods*, **70**, 193–199.

**Hu, W.W., Wong, S.M., Goh, C.J. and Loh, C.S.** (1998) Synergism in replication of Cymbidium mosaic potexvirus (CymMV) and Odontoglossum ringspot tobamovirus (ORSV) RNA in orchid protoplasts. *Arch. Virol.* **143**, 1265–1275.

**Hu, Q., Hollunder, J., Niehl, A., Korner, C.J., Gereige, D., Windels, D., Arnold, A., Kuiper, M., Vazquez, F., Pooggin, M. and Heinlein, M.** (2011) Specific impact of tobamovirus infection on the *Arabidopsis* small RNA profile. *PLoS ONE*, **6**, e19549.

**Inouye, N.** (2008) Viruses of Orchids: Symptoms, Diagnosis, Spread and Control. Netherlands: Blue Bird Publishers, p. 176.

**Kim, V.N.** (2008) Sorting out small RNAs. *Cell*, **133**, 25–26.

**Kozomara, A. and Griffiths-Jones, S.** (2013) miRBase: annotating high confidence microRNAs using deep sequencing data. *Nucleic Acids Res.* **42**, D68–D73.

**Langmead, B.** (2010) Aligning short sequencing reads with Bowtie. *Curr. Protoc. Bioinformatics*, **32**, 11.7.1–11.7.14.

**Lawson, R.H. and Brannigan, M.** (1986) Virus diseases of orchids. In: Handbook of Orchid Pests and Diseases, (Alec and Tillman, eds.). West Palm Beach, FL: American Orchid Society.

**Leathers, V., Tanguay, R., Kobayashi, M. and Gallie, D.R.** (1993) A phylogenetically conserved sequence within viral 3' untranslated RNA pseudoknots regulates translation. *Mol. Cell Biol.* **13**, 5331–5347.

**Lee, S.C. and Chang, Y.C.** (2006) Multiplex RT-PCR detection of two orchid viruses with an internal control of plant nad5 mRNA. *Plant Pathol. Bullet.* **15**, 187–196.

**Lee, M.S., Yang, M.J., Hseu, Y.C., Lai, G.H., Chang, W.T., Hsu, Y.H. and Lin, M.-K.** (2011) One-step reverse transcription loop-mediated isothermal amplification assay for rapid detection of Cymbidium mosaic virus. *J. Virol. Methods*, **173**, 43–48.

**Li, J., Andika, I.B., Shen, J., Lv, Y., Ji, Y., Sun, L. and Chen, J.** (2013) Characterization of Rice black-streaked dwarf virus- and Rice stripe virus-derived siRNAs in singly and doubly infected insect vector *Laodelphax striatellus*. *PLoS ONE*, **8**, e66007.

**Li, M., Li, Y., Xia, Z., Di, D., Zhang, A., Miao, H., Zhou, T. and Fan, Z.** (2016) Characterization of small interfering RNAs derived from Rice black streaked dwarf virus in infected maize plants by deep sequencing. *Virus Res.* **228**, 66–74.

**Liao, L.-J., Pan, I.C., Chan, Y.-L., Hsu, Y.-H., Chen, W.-H. and Chan, M.-T.** (2004) Transgene silencing in *Phalaenopsis* expressing the coat protein of Cymbidium mosaic virus is a manifestation of RNA-mediated resistance. *Mol. Breed.* **13**, 229–242.

**Lin, N.S. and Chen, C.C.** (1991) Association of Bamboo mosaic virus (BaMV) and BaMV-specific electron-dense crystalline bodies with chloroplasts. *Phytopathology*, **81**, 1551–1555.

**Lin, N.S., Hsu, Y.H. and Hsu, H.T.** (1990) Immunological detection of plant viruses and a mycoplasma-like organism by direct tissue blotting on nitrocellulose membranes. *Phytopathology*, **80**, 824–828.

**Lin, N.S., Huang, T.Z. and Hsu, Y.H.** (1992) Infection of barley protoplasts with Bamboo mosaic virus RNA. *Bot. Bull. Acad. Sin.* **33**, 271–275.

**Lin, N.S., Lee, Y.S., Lin, B.Y., Lee, C.W. and Hsu, Y.H.** (1996) The open reading frame of Bamboo mosaic potexvirus satellite RNA is not essential for its replication and can be replaced with a bacterial gene. *Proc. Natl. Acad. Sci. USA*. **93**, 3138–3142.

**Lin, K.Y., Cheng, C.P., Chang, B.C., Wang, W.C., Huang, Y.W., Lee, Y.S., Huang, H.-D., Hsu, Y.-H. and Lin, N.-S.** (2010) Global analyses of small interfering RNAs derived from Bamboo mosaic virus and its associated satellite RNAs in different plants. *PLoS ONE*, **5**, e11928.

**Lin, H.Y., Chen, J.C. and Fang, S.C.** (2018) A protoplast transient expression system to enable molecular, cellular, and functional studies in *Phalaenopsis* orchids. *Front. Plant Sci.* **9**, 843.

**Livak, K.J. and Schmittgen, T.D.** (2001) Analysis of relative gene expression data using real-time quantitative PCR and the $2^{-\Delta\Delta CT}$ method. *Methods*, **25**, 402–408.

**Llave, C.** (2010) Virus-derived small interfering RNAs at the core of plant–virus interactions. *Trends Plant Sci.* **15**, 701–707.

**Lu, H.C., Chen, H.H., Tsai, W.C., Chen, W.H., Su, H.J., Chang, D.C., and Yeh, H.-H.** (2007) Strategies for functional validation of genes involved in reproductive stages of orchids. *Plant Physiol.* **143**, 558–569.

**Lu, H.C., Chen, C.E., Tsai, M.H., Wang, H.I., Su, H.J. and Yeh, H.H.** (2009) Cymbidium mosaic potexvirus isolate-dependent host movement systems reveal two movement control determinants and the coat protein is the dominant. *Virology*, **388**, 147–159.

**Margaria, P., Miozzi, L., Rosa, C., Axtell, M.J., Pappu, H.R. and Turina, M.** (2015) Small RNA profiles of wild-type and silencing suppressor-deficient Tomato spotted wilt virus infected *Nicotiana benthamiana*. *Virus Res.* **208**, 30–38.

**Maruta, T., Yoshimoto, T., Ito, D., Ogawa, T., Tamoi, M., Yoshimura, K. and Shigeoka, S.** (2012) An *Arabidopsis* FAD pyrophosphohydrolase, AtNUDX23, is involved in flavin homeostasis. *Plant Cell Physiol.* **53**, 1106–1116.



13643703, 2020, 2, Downloaded from https://bsppjournals.onlinelibrary.wiley.com/doi/10.1111/mpp.12888 by Test, Wiley Online Library on [02/08/2025]. See the Terms and Conditions (https://onlinelibrary.wiley.com/terms-and-conditions) on Wiley Online Library for rules of use; OA articles are governed by the applicable Creative Commons License

**Mascia, T. and Gallitelli, D.** (2016) Synergies and antagonisms in virus interactions. *Plant Sci.* **252**, 176–192.

**Mi, S., Cai, T., Hu, Y., Chen, Y., Hodges, E., Ni, F., Wu, L., Li, S., Zhou, H., Long, C., Chen, S., Hannon, G.J. and Qi, Y.** (2008) Sorting of small RNAs into *Arabidopsis* argonaute complexes is directed by the 5' terminal nucleotide. *Cell*, **133**, 116–127.

**Mitter, N., Koundal, V., Williams, S. and Pappu, H.** (2013) Differential expression of Tomato spotted wilt virus-derived viral small RNAs in infected commercial and experimental host plants. *PLoS ONE*, **8**, e76276.

**Molnár, A., Csorba, T., Lakatos, L., Varallyay, E., Lacomme, C. and Burgyan, J.** (2005) Plant virus-derived small interfering RNAs originate predominantly from highly structured single-stranded viral RNAs. *J. Virol.* **79**, 7812–7818.

**Molnar, A., Melnyk, C.W., Bassett, A., Hardcastle, T.J., Dunn, R. and Baulcombe, D.C.** (2010) Small silencing RNAs in plants are mobile and direct epigenetic modification in recipient cells. *Science*, **328**, 872–875.

**Montgomery, T.A., Howell, M.D., Cuperus, J.T., Li, D., Hansen, J.E., Alexander, A.L., Chapman, E.J., Fahlgren, N., Allen, E. and Carrington, J.C.** (2008) Specificity of ARGONAUTE7-miR390 interaction and dual functionality in TAS3 trans-acting siRNA formation. *Cell*, **133**, 128–141.

**Navarro, B., Gisel, A., Rodio, M.E., Delgado, S., Flores, R. and Di Serio, F.** (2012) Small RNAs containing the pathogenic determinant of a chloroplast-replicating viroid guide the degradation of a host mRNA as predicted by RNA silencing. *Plant J.* **70**, 991–1003.

**Naveed, K., Mitter, N., Harper, A., Dhingra, A. and Pappu, H.R.** (2014) Comparative analysis of virus-specific small RNA profiles of three biologically distinct strains of Potato virus Y in infected potato (*Solanum tuberosum*) cv. Russet Burbank. *Virus Res.* **191**, 153–160.

**Nawrocki, E.P., Burge, S.W., Bateman, A., Daub, J., Eberhardt, R.Y., Eddy, S.R., Floden, E.W., Gardner, P.P., Jones, T.A., Tate, J. and Finn, R.D.** (2015) Rfam 12.0: Updates to the RNA families database. *Nucleic Acids Res.* **43**, D130–137.

**Ogwok, E., Ilyas, M., Alicai, T., Rey, M.E. and Taylor, N.J.** (2016) Comparative analysis of virus-derived small RNAs within cassava (*Manihot esculenta* Crantz) infected with Cassava brown streak viruses. *Virus Res.* **215**, 1–11.

**Padmanabhan, M.S., Kramer, S.R., Wang, X. and Culver, J.N.** (2008) Tobacco mosaic virus replicase-auxin/indole acetic acid protein interactions: reprogramming the auxin response pathway to enhance virus infection. *J. Virol.* **82**, 2477–2485.

**Palani, P.V. and Lin, N.S.** (2007) Northern analysis of viral plus- and minus-strand RNAs. *Curr. Protoc. Microbiol.* **4**, 16E.3.1–16E.3.32.

**Pearson, M.N. and Cole, J.S.** (1991) Further observations on the effects of Cymbidium mosaic virus and Odontoglossum ringspot virus on the growth of *Cymbidium* orchids. *J. Phytopathol.* **131**, 193–198.

**Pecman, A., Kutnjak, D., Gutierrez-Aguirre, I., Adams, I., Fox, A., Boonham, N. and Ravnikar, M.** (2017) Next generation sequencing for detection and discovery of plant viruses and viroids: Comparison of two approaches. *Front. Microbiol.* **8**, 1998.

**Qi, X., Bao, F.S. and Xie, Z.** (2009) Small RNA deep sequencing reveals role for *Arabidopsis thaliana* RNA-dependent RNA polymerases in viral siRNA biogenesis. *PLoS ONE*, **4**, e4971.

**Rodriguez, M.C., Petersen, M. and Mundy, J.** (2010) Mitogen-activated protein kinase signaling in plants. *Annu. Rev. Plant Biol.* **61**, 621–649.

**Ruiz, M.T., Voinnet, O. and Baulcombe, D.C.** (1998) Initiation and maintenance of virus-induced gene silencing. *Plant Cell*, **10**, 937–946.

**Ryu, K.H. and Park, W.M.** (1995) The complete nucleotide sequence and genome organization of Odontoglossum ringspot tobamovirus RNA. *Arch. Virol.* **140**, 1577–1587.

**Seoh, M.L., Wong, S.M. and Zhang, L.** (1998) Simultaneous TD/RT-PCR detection of Cymbidium mosaic potexvirus and Odontoglossum ringspot tobamovirus with a single pair of primers. *J. Virol. Methods*, **72**, 197–204.

**Sheehan, T.J.** (2003) What is an orchid? Characteristics unite more than 25,000 species and 110,000 hybrids into a family of amazing diversity. In: Orchids, (Sheehan, T.J., ed.), pp. 274–283. West Palm Beach, FL: American Orchid Society.

**Shimura, H., Pantaleo, V., Ishihara, T., Myojo, N., Inaba, J., Sueda, K., Burgyán, J. and Masuta, C.** (2011) A viral satellite RNA induces yellow symptoms on tobacco by targeting a gene involved in chlorophyll biosynthesis using the RNA silencing machinery. *PLoS Pathog.* **7**, e1002021.

**Smith, N.A., Eamens, A.L. and Wang, M.B.** (2011) Viral small interfering RNAs target host genes to mediate disease symptoms in plants. *PLoS Pathog.* **7**, e1002022.

**Srinivasan, M., Mehta, P., Yu, Y., Prugar, E., Koonin, E.V., Karzai, A.W. and Sternglanz, R.** (2011) The highly conserved KEOPS/EKC complex is essential for a universal tRNA modification, t6A. *EMBO J.* **30**, 873–881.

**Stepanova, A.N., Robertson-Hoyt, J., Yun, J., Benavente, L.M., Xie, D.Y., Dolezal, K., Schlereth, A., Jürgens, G. and Alonso, J.M.** (2008) TAA1-mediated auxin biosynthesis is essential for hormone crosstalk and plant development. *Cell*, **133**, 177–191.

**Su, C.L., Chao, Y.T., Alex Chang, Y.C., Chen, W.C., Chen, C.Y., Lee, A.Y., Hwa, K.T. and Shih, M.-C.** (2011) *De novo* assembly of expressed transcripts and global analysis of the *Phalaenopsis aphrodite* transcriptome. *Plant Cell Physiol.* **52**, 1501–1514.

**Supek, F., Bosnjak, M., Skunca, N. and Smuc, T.** (2011) REVIGO summarizes and visualizes long lists of gene ontology terms. *PLoS ONE*, **6**, e21800.

**Szittya, G. and Burgyan, J.** (2013) RNA interference-mediated intrinsic antiviral immunity in plants. *Curr. Top. Microbiol. Immunol.* **371**, 153–181.

**Szittya, G., Moxon, S., Pantaleo, V., Toth, G., Rusholme Pilcher, R.L., Moulton, V., Burgyan, J. and Dalmay, T.** (2010) Structural and functional analysis of viral siRNAs. *PLoS Pathog.* **6**, e1000838.

**Takamatsu, N., Watanabe, Y., Meshi, T. and Okada, Y.** (1990) Mutational analysis of the pseudoknot region in the 3' noncoding region of Tobacco mosaic virus RNA. *J. Virol.* **64**, 3686–3693.

**Takeda, A., Iwasaki, S., Watanabe, T., Utsumi, M. and Watanabe, Y.** (2008) The mechanism selecting the guide strand from small RNA duplexes is different among argonaute proteins. *Plant Cell Physiol.* **49**, 493–500.

**Tatineni, S., Riethoven, J.J., Graybosch, R.A., French, R. and Mitra, A.** (2014) Dynamics of small RNA profiles of virus and host origin in wheat cultivars synergistically infected by wheat streak mosaic virus and Triticum mosaic virus: virus infection caused a drastic shift in the endogenous small RNA profile. *PLoS ONE*, **9**, e111577.

**Vance, V.B.** (1991) Replication of potato virus X RNA is altered in coinfections with potato virus Y. *Virology*, **182**, 486–494.

**Wang, M.B., Bian, X.Y., Wu, L.M., Liu, L.X., Smith, N.A., Isenegger, D., Wu, R.-M., Masuta, C., Vance, V.B., Watson, J.M., Rezaian, A., Dennis, E.S. and Waterhouse, P.M.** (2004) On the role of RNA silencing in the pathogenicity and evolution of viroids and viral satellites. *Proc. Natl. Acad. Sci. USA.* **101**, 3275–3280.

**Wang, L.Y., Lin, S.S., Hung, T.H., Li, T.K., Lin, N.C. and Shen, T.L.** (2012a) Multiple domains of the Tobacco mosaic virus p126 protein can independently suppress local and systemic RNA silencing. *Mol. Plant-Microbe Interact.*, **25**, 648–657.

**Wang, M.B., Masuta, C., Smith, N.A. and Shimura, H.** (2012b) RNA silencing and plant viral diseases. *Mol. Plant-Microbe Interact.*, **25**, 1275–1285.

**Weiberg, A., Wang, M., Lin, F.M., Zhao, H., Zhang, Z., Kaloshian, I., Huang, H.-D. and Jin, H.** (2013) Fungal small RNAs suppress plant immunity by hijacking host RNA interference pathways. *Science*, **342**, 118–123.

**Wolf, S., Lucas, W.J., Deom, C.M. and Beachy, R.N.** (1989) Movement protein of tobacco mosaic virus modifies plasmodesmatal size exclusion limit. *Science*, **246**, 377–379.

**Wong, S.M., Chng, C.G., Lee, Y.H., Tan, K. and Zettler, F.W.** (1994) Incidence of cymbidium mosaic and odontoglossum ringspot viruses and their significance in orchid cultivation in Singapore. *J. Crop Prot.* **13**, 235–239.

© 2019 THE AUTHORS. *MOLECULAR PLANT PATHOLOGY* PUBLISHED BY BRITISH SOCIETY FOR PLANT PATHOLOGY AND JOHN WILEY & SONS LTD 

13643703, 2020, 2, Downloaded from https://bsppjournals.onlinelibrary.wiley.com/doi/10.1111/mpp.12888 by Test, Wiley Online Library on [02/08/2025]. See the Terms and Conditions (https://onlinelibrary.wiley.com/terms-and-conditions) on Wiley Online Library for rules of use; OA articles are governed by the applicable Creative Commons License

**Wong, S.M., Mahtani, P.H., Lee, K.C., Yu, H.H., Tan, Y., Neo, K.K., Chan, Y., Wu, M. and Chng, C.G.** (1997) Cymbidium mosaic potexvirus RNA: complete nucleotide sequence and phylogenetic analysis. *Arch. Virol.* **142**, 383–391.

**Xia, Z., Zhao, Z., Chen, L., Li, M., Zhou, T., Deng, C., Zhou, Qi and Fan, Z.** (2016) Synergistic infection of two viruses MCMV and SCMV increases the accumulations of both MCMV and MCMV-derived siRNAs in maize. *Sci. Rep.* **6**, 20520.

**Xu, Y., Huang, L., Fu, S., Wu, J. and Zhou, X.** (2012) Population diversity of Rice stripe virus-derived siRNAs in three different hosts and RNAi-based antiviral immunity in *Laodelphgax striatellus*. *PLoS ONE*, **7**, e46238.

**Yu, H.H. and Wong, S.M.** (1998) Synthesis of biologically active cDNA clones of Cymbidium mosaic potexvirus using a population cloning strategy. *Arch. Virol.* **143**, 1617–1620.

**Zeenko, V.V., Ryabova, L.A., Spirin, A.S., Rothnie, H.M., Hess, D., Browning, K.S. and Hohn, T.** (2002) Eukaryotic elongation factor 1A interacts with the upstream pseudoknot domain in the 3′ untranslated region of Tobacco mosaic virus RNA. *J. Virol.* **76**, 5678–5691.

**Zettler, F.W., Ko, N.J., Wisler, G.C., Elliott, M.S. and Wong, S.M.** (1990) Viruses of orchids and their control. *Plant Dis.* **74**, 621–626.

**Zhang, C., Wu, Z., Li, Y. and Wu, J.** (2015) Biogenesis, function, and applications of virus-derived small RNAs in plants. *Front. Microbiol.* **6**, 1237.

**Zhou, C.J., Zhang, X.Y., Liu, S.Y., Wang, Y., Li, D.W., Yu, J.L. and Han, C.-G.** (2017) Synergistic infection of BrYV and PEMV 2 increases the accumulations of both BrYV and BrYV-derived siRNAs in *Nicotiana benthamiana*. *Sci. Rep.* **7**, 45132.

## SUPPORTING INFORMATION

Additional supporting information may be found in the online version of this article at the publisher's web site:

**Fig. S1** Annotation pipeline of deep sequencing data. The pre-processed reads were used as queries to search against virus genome, *Phalaenopsis* transcriptome, Rfam, and miRBase using Bowtie algorithm. The criteria and hierarchy are indicated. Reads that not annotated as known categories (classified as "others" at first) were mapped to *P. aphrodite* expression tags (ESTs) again and allowed 1 mismatch in the second round.

**Fig. S2** Nucleotide composition of 5′-end of CymMV (A) and ORSV (B) vsiRNAs in inoculated *Phalaenopsis*. The proportion of adenine (A), cytosine (C), guanine (G) and uridine (U) within each size class. Libraries constructed from inoculated (i) or noninoculated (n) tissues of mock (M), ORSV (O), CymMV (C), or CymMV and ORSV double (D)-inoculated leaves are shown.

**Fig. S3** Distribution of vsiRNAs along CymMV genome corresponding to reads from libraries of CymMV-infected tissue. Upward dark-coloured and downward light-coloured lines represent (+) and (–)-polarity reads, respectively. Genomic sites of RdRp, TGB and CP gene coding regions are indicated below (numbers based on GenBank accession CymMV AY571289). Maps constructed from inoculated (i) or noninoculated (n) tissues with CymMV (C) single inoculation, or CymMV and ORSV double (D)-inoculated leaves are shown.

**Fig. S4** Distribution of vsiRNAs along ORSV genome corresponding to reads from libraries of ORSV-infected tissue. Upward dark-coloured and downward light-coloured lines represent (+) and (–)-polarity reads, respectively. Genomic sites of RdRp, MP and CP gene coding regions are indicated below (numbers based on GenBank accession ORSV AY571290). Maps constructed from inoculated (i) or noninoculated (n) tissues with ORSV (O) single inoculation, or CymMV and ORSV double (D)-inoculated leaves are shown.

**Fig. S5** Size-separated mapping of CymMV and ORSV vsiRNA hotspots. Peaks of (A) CymMV and (B) ORSV vsiRNA reads of 21-, 22-, or 24-nt classes are indicated in different-coloured lines.

**Fig. S6** Analyses of sequence conservation and vsiRNA generation frequency of ORSV 3′-UTR. (A) Alignment of the 3′-UTR of some tobamovirus model species registered in ICTVdb. Red line indicates the ORSV 3′-UTR hotspot vsiRNA sequence. (B) Location and frequency of 3′-UTR-originating (+)-strand ORSV vsiRNAs. The hotspot vsiRNAs and its homologous sequences are indicated in red and blue, respectively. Grey numbers indicating the ORSV genome sites (based on AY571290). Reads per million (RPM) index of cumulative reads in Di library are presented in single-nucleotide resolution with different colour scales. (C) Pseudoknot (PK)-origin TMV vsiRNA identified at the 3′-terminus of the viral genome. Red numbers indicate the top 12 abundant TMV vsiRNA hotspots including a PK-origin vsiRNA that shared a conserved sequence with the ORSV 3′-UTR hotspot vsiRNA. The 12$^{th}$ peak is constituted by eight vsiRNA species as listed above the map. The ranking of each vsiRNA tag is shown, and the conserved nucleotides are indicated in red. In addition, seq1008031 shared an identical sequence with the ORSV 3′-UTR hotspot vsiRNA but did not contribute to a prominent peak on the map. Mapping of seq1083806 to the PK structure is highlighted in pink. The diagram of TMV 3′-UTR structure is modified from Osman *et al* (2000).

**Fig. S7** Abundance and size distribution of CymMV and ORSVvsiRNAs in the second batch of libraries. (A) Abundance and size distribution of vsiRNAs. Green and orange bars represent reads matched to a (+)- or (–)-strand viral genomic RNA, respectively. Percentages above the bar indicate the proportion of total CymMV or ORSV vsiRNAs within the library. The accumulation level is presented by reads per million (RPM). (B) Nucleotide composition of 5′-end of vsiRNAs. Shows the proportion of adenine (A), cytosine (C), guanine (G) and uridine (U) within each size class. (C) Genomic distribution of the vsiRNAs. Upward dark-coloured and downward light-coloured lines represent (+) and (–)-polarity reads, respectively. Genomic sites of gene-coding regions are indicated below (numbers based on GenBank accession CymMV AY571289 and ORSV AY571290). Labels indicate libraries constructed from inoculated (Di-2) or noninoculated (Dn-2) tissues of CymMV and ORSV double-inoculated leaves. Maps from the first batch of sRNA sequencing (Di) are shown side by side to reveal consistency between the two batches. (D) The composition of CymMV and ORSV vsiRNAs originated from different genomic regions was validated by northern blot. The enriched sRNAs from CymMV/ORSV single- or double-infected total RNA samples were 5′-end labelled and hybridized to *in vitro* transcripts



13643703, 2020, 2, Downloaded from https://bsppjournals.onlinelibrary.wiley.com/doi/10.1111/mpp.12888 by Test, Wiley Online Library on [02/08/2025]. See the Terms and Conditions (https://onlinelibrary.wiley.com/terms-and-conditions) on Wiley Online Library for rules of use; OA articles are governed by the applicable Creative Commons License

corresponding to different genomic regions (indicated by 1-7, the genomic regions are listed in Table S11) on the blots.

**Fig. S8** Venn diagrams showing the overlap of the top 20 vsiRNA species and predicted targets in single- or double-inoculation libraries. The top 20 abundant vsiRNA species were largely overlapped between Ci and Di libraries (A), whereas the list was totally exclusive between Oi and Di (B). VsiRNAs that did not predict with targets were discarded from the analysis, so the total number for each library was <20. The high overlap of CymMV vsiRNA species between Ci and Di led to highly overlapped target accessions as shown in (C). Correspondingly, there were no identical targets for top 20 ORSV vsiRNAs between Oi and Di (D).

**Fig. S9** CymMV and ORSV accumulation in *Phalaenopsis amabilis* protoplasts. (A) Flower protoplasts were isolated from *P. amabilis* petals and sepals. (B) At 12 and 20 h, the transfected protoplasts were harvested for detecting CymMV and ORSV CPs by western blots using CymMV and ORSV CP antibodies. Mock (M), CymMV (C), ORSV (O), and CymMV plus ORSV double (D) transfection was indicated. Coomassie blue staining (CB) and actin detection are served as loading control.

**Table S1** Summary of total unique reads in sRNA libraries constructed from mock- and virus-inoculated *Phalaenopsis* tissues.

**Table S2** Summary of (A) total reads and (B) unique tags in sRNA libraries constructed from the second batch of mock- and virus-inoculated *Phalaenopsis* tissues.

**Table S3** List of *Phalaenopsis* transcripts that were predicted as targets of the 20 topmost abundant CymMV vsiRNAs.

**Table S4** List of *Phalaenopsis* transcripts that were predicted as targets of the 20 topmost abundant ORSV vsiRNAs.

**Table S5** List of enriched GO terms (Biological process) for potential targets of top 20 CymMV vsiRNAs in Ci library.

**Table S6** List of enriched GO terms (Biological process) for potential targets of top 20 CymMV vsiRNAs in Di library.

**Table S7** List of enriched GO terms (Biological process) for potential targets of top 20 ORSV vsiRNAs in Oi library.

**Table S8** List of enriched GO terms (Biological process) for potential targets of top 20 ORSV vsiRNAs in Di library.

**Table S9** GC context of CymMV and ORSV viral segments.

**Table S10** Primers used in this study.

**Table S11** Information of viral probes used in this study.

© 2019 THE AUTHORS. *MOLECULAR PLANT PATHOLOGY* PUBLISHED BY BRITISH SOCIETY FOR PLANT PATHOLOGY AND JOHN WILEY & SONS LTD 

13643703, 2020, 2, Downloaded from https://bsppjournals.onlinelibrary.wiley.com/doi/10.1111/mpp.12888 by Test, Wiley Online Library on [02/08/2025]. See the Terms and Conditions (https://onlinelibrary.wiley.com/terms-and-conditions) on Wiley Online Library for rules of use; OA articles are governed by the applicable Creative Commons License

SCIENTIFIC REPORTS

OPEN

# Dual resistance of transgenic plants against *Cymbidium mosaic virus* and *Odontoglossum ringspot virus*

Received: 19 May 2019
Accepted: 3 July 2019
Published online: 15 July 2019

Ting-Yu Chen[1], Hsuan Pai[1], Liang-Yu Hou[1], Shu-Chuan Lee[1], Tzu-Tung Lin[1], Chih-Hao Chang[1], Fu-Chen Hsu[1], Yau-Heiu Hsu[2] & Na-Sheng Lin[1]

**Taxonomically distinct *Cymbidium mosaic potexvirus* (CymMV) and *Odontoglossum ringspot tobamovirus* (ORSV) are two of the most prevalent viruses worldwide; when co-infecting orchids, they cause synergistic symptoms. Because of the huge economic loss in quality and quantity in the orchid industry with virus-infected orchids, virus-resistant orchids are urgently needed. To date, no transgenic resistant lines against these two viruses have been reported. In this study, we generated transgenic *Nicotiana benthamiana* expressing various constructs of partial CymMV and ORSV genomes. Several transgenic lines grew normally and remained symptomless after mixed inoculation with CymMV and ORSV. The replication of CymMV and ORSV was approximately 70–90% lower in protoplasts of transgenic lines than wild-type (WT) plants. Of note, we detected extremely low or no viral RNA or capsid protein of CymMV and ORSV in systemic leaves of transgenic lines after co-infection. Grafting experiments further revealed that CymMV and ORSV trafficked extremely inefficiently from co-infected WT stocks to transgenic scions, presumably due to RNA-mediated interference. This study reports the first successful creation of dual resistant transgenic lines against CymMV and ORSV. Our studies shed light on the commercial development of transgenic orchid production to combat the global viral threat.**

The Orchidaceae is the largest and most diverse family of flowering plants, about 28,000 species, distributed in about 763 genera[1]. Because of the fascinating array of colors, delicate flower shapes, and fragrant blooms, orchids have become popular and valuable ornamental plants in the market. However, orchids are susceptible to virus infection; at least 50 different viruses have been reported[2]. Of these, *Cymbidium mosaic virus* (CymMV) and *Odontoglossum ringspot virus* (ORSV) are the two most prevalent and economically important viruses affecting orchids worldwide[2].

CymMV usually causes mild mosaic chlorotic or necrotic sunken patches on leaves and necrosis on flowers, whereas ORSV induces chlorotic ringspots or necrosis in leaves and color breaking and/or distortion on flowers. However, sometimes orchids infected by either of the two viruses do not display any symptoms but still show reduced vigor, growth rates and flower quality. Mixed infection with CymMV and ORSV commonly occurs worldwide and induces synergistic severe symptoms, including necrotic ringspots in leaves and mottling, ridging, curling and distortion of flowers[3–5], leading to diminished flower size, quality and great economic loss.

CymMV, a *Potexvirus* member, has a single-stranded (ss) and positive-sense (+) RNA genome of about 6200 nucleotides (nts) consisting of five open reading frames (ORFs) and encoding a 160-kDa putative RNA-dependent RNA polymerase (RdRp) for viral replication, an overlapped tripe gene block (TGB) proteins (26, 13 and 10 kDa for TGBp1, TGBp2 and TGBp3, respectively) for movement and an 24-kDa capsid protein (CP)[6,7]. ORSV is a *Tobamovirus* member and has a ss, (+) RNA genome of about 6600 nts consisting of four ORFs and encoding a 126- and 183- readthrough RdRps, a 33-kD movement protein (MP) and an 18-kDa CP[8]. The CPs of CymMV and ORSV are expressed from their respective subgenomic RNAs. In addition, the CP of *Potexvirus* has been found required for cell-to-cell movement[9], whereas that of *Tobamovirus* is a host-specific determinant of long-distance movement in plants[10].

With mixed infection of CymMV and ORSV, the synergism of CymMV and ORSV in replication has been observed at the single-cell level in orchid protoplasts[4]. In addition, the complementation of MPs and CPs of

[1]Institute of Plant and Microbial Biology, Academia Sinica, 11529, Taiwan. [2]Graduate Institute of Biotechnology, National Chung Hsing University, Taichung, 40027, Taiwan. Correspondence and requests for materials should be addressed to N.-S.L. (email: nslin@sinica.edu.tw)

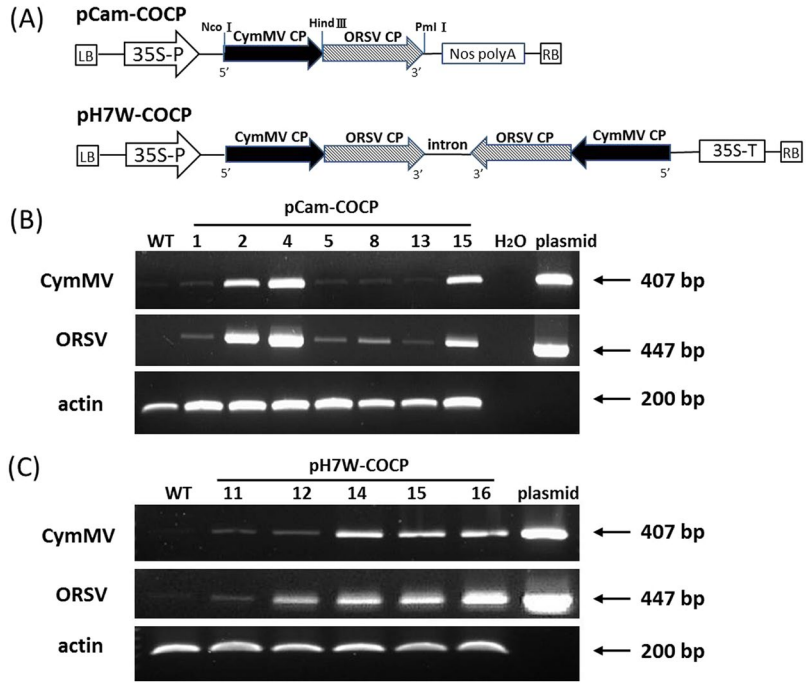


**Figure 1.** Physical map and analyses of transgenes in transgenic lines. (**A**) Schematic representation of pCam-COCP and pH7W-COCP constructs used for *N. benthamiana* transformation. (**B**,**C**) RT-PCR analysis of transgene expression in WT and transgenic pCam-COCP lines (**B**) and pH7W-COCP lines (**C**). The CymMV CP transcripts were detected by primer pair CyCP3 and CyCP6 with an expected size of 407 bp and ORSV CP transcripts by primer pair ORSV3 and ORSV4 of 447 bp. Plasmids pCam-COCP and pH7W-COCP were used for positive controls. The numbers on top of gel tracks indicate different transgenic lines. $H_2O$ and actin are negative and internal controls, respectively.

CymMV and ORSV in cell-to-cell movement has been reported[3]. Although no insect vector has been reported in the field, we lack efficient measures to control virus diseases as compared with other pests and pathogens.

Pathogen-derived resistance has become one of the most powerful strategies to control virus diseases[11]. Various transgenes have been used successfully to confer virus diseases, including viral protein genes (replicase, MP or CP genes), viral RNAs (sense-, antisense- or double-stranded RNAs), satellite RNAs, defective interfering RNAs, hairpin RNAs, artificial microRNAs (miRNAs), host-derived resistance genes, or various factors involved in host defense responses (review in[12]). Previously, CymMV CP expression in transgenic *Nicotiana benthamiana*[13], *Dendrobium*[14] and *Phalaenopsis*[15,16] could successfully protect plants against CymMV infection. Recently, Petchthai *et al.* (2018) using *Oryza sativa* miR528 as a backbone, expressed artificial miRNA (amiRNA) targeting replicase genes of CymMV and ORSV. AmiRNA transgenic *N. benthamiana* lines conferred high resistance to CymMV infection but weak resistance to ORSV infection[17]. No transgenic plants completely resistant to both CymMV and ORSV have been reported.

In this study, we used *N. benthamiana* as a model plant to express various constructs of CymMV and ORSV CP genes. Resistant transgenic lines showed a great reduction in CymMV and ORSV replication at the single-cell level as well as weak long-distance trafficking. This first successful example of dual resistance to CymMV and ORSV infection could be used to generate transgenic orchids.

## Results

**Plant transformation and transgene expression analysis.** Leaf discs of *N. benthamiana* were transformed with *Agrobacterium tumefaciens* strain GV3101 containing pCam-COCP or pH7W-COCP; schematic representations of plasmid constructs are shown in Fig. 1A. Initially, embryogenic calli were induced and selected on medium containing hygromycin to regenerate putative T0 transgenic lines. Seedlings exhibiting resistance to hygromycin were examined for transgene expression by reverse transcription-polymerase chain reaction (RT-PCR). The expected product sizes of 407 and 477 base pairs (bps) for CymMV and ORSV, respectively, were obtained from *N. benthamiana* lines containing pCam-COCP or pH7W-COCP (Fig. 1B,C). We obtained a total of 7 independent T2 homozygous lines from pCam-COCP and 13 lines from pH7W-COCP after segregation analysis.

**Assessment of CymMV and ORSV resistance in transgenic *N. benthamiana* plants.** To examine whether these *N. benthamiana* transgenic lines were resistant to viral infection, all RT-PCR positive lines were individually inoculated with an equal amount of CymMV and ORSV virions (C+O). At 20 days post-infection (dpi), only transgenic line 2 expressing pCam-COCP (designated pCam-COCP line 2 hereafter) showed no symptoms on systemic leaves (SL), but other lines showed mottling, ridging, curling on inoculated leaves (IL) and SL, with stunted

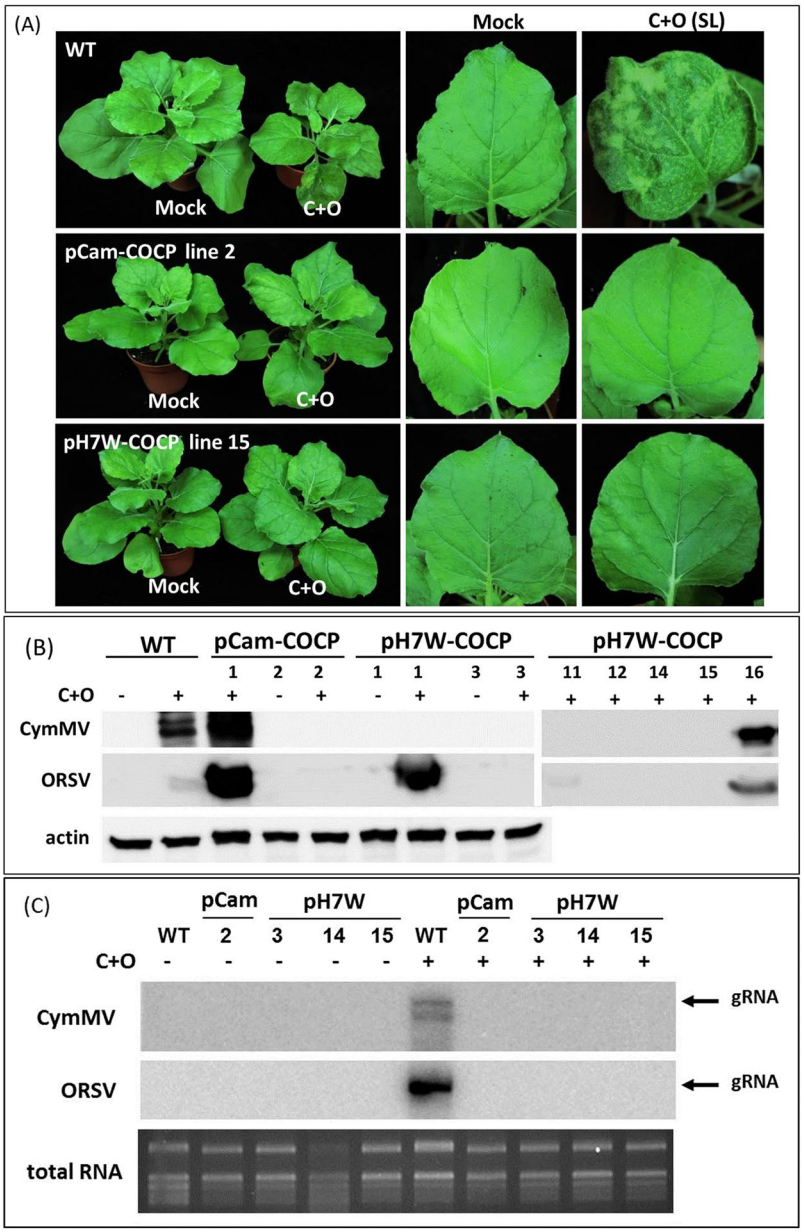


**Figure 2.** Assessment of CymMV and ORSV resistance in transgenic *N. benthamiana* plants. (**A**) Symptoms of WT and transgenic pCam-COCP line 2 and pH7W-COCP line 15 after inoculation with CymMV and ORSV virions (C+O). Photos were taken for whole plants and systemic leaves (SLs) at 20 dpi. (**B**) Western blot analysis of CymMV and ORSV capsid protein (CP) accumulation in SL of WT and transgenic lines inoculated with C+O at 20 or 26 dpi by antibodies against CymMV or ORSV CP, respectively. Actin was an internal control. (**C**) Northern blot analysis of viral RNA accumulation in WT and transgenic lines at 20 dpi with $^{32}$P-CTP labeled replicase probes for CymMV and ORSV. total RNA: EtBr staining of total RNA for equal loading. −: mock; +: C+O infection; gRNA: genomic RNA.

plant growth, as shown in the wild type (WT) plants (Fig. 2A). However, among the 13 transgenic lines expressing pH7W-COCP, several lines, such as 3, 14 and 15, exhibited no symptoms at 20 dpi after viral challenge (Fig. 2A).

We further performed enzyme-linked immunosorbent assay (ELISA) to measure the accumulation of CymMV and ORSV in WT and transgenic lines after C+O infection. As expected, the IL and SL of WT plants showed high ELISA values (>1.2) with C+O infection at 10 and 20 dpi, respectively. However, WT-mock-inoculated plants always showed low ELISA absorbance (<0.2), which can be considered a background level (Table 1). For transgenic lines expressing pCam-COCP, all lines had a slightly greater ELISA value (>2.0) than WT in IL for CymMV, but showed a wide range in SL. A background level was detected in SL of lines 2 and 15 for CymMV, with a similar low value for ORSV in line 2 but not in line 15 (Table 1). Thus, transgenic pCam-COCP line 2 could harbor CymMV and ORSV accumulation in IL but restricted viruses from moving to SL. In contrast, lines 1, 4, 5, 8 and 13 were permissive to a high accumulation of CymMV and ORSV in SL at 20 dpi (Table 1).

| Plants | | | CymMV level[b] | | ORSV level[b] | | Resistance[c] | |
|---|---|---|---|---|---|---|---|---|
| | Line | Infection[a] | IL[d] | SL[e] | IL | SL | CymMV | ORSV |
| WT | | mock | 0.16 ± 0.01 | 0.14 ± 0.01 | 0.18 ± 0.01 | 0.15 ± 0.01 | − | − |
| | | C+O | 1.68 ± 0.19 | 3.34 ± 0.17 | 1.87 ± 0.06 | 1.23 ± 0.33 | − | − |
| pCam-COCP | 1 | C+O | 2.75 ± 0.16 | 3.24 ± 0.17 | 0.92 ± 0.10 | 1.31 ± 0.06 | − | − |
| | 2 | C+O | 1.94 ± 0.35 | 0.22 ± 0.07 | 0.20 ± 0.03 | 0.17 ± 0.01 | + | ++ |
| | 4 | C+O | 2.02 ± 0.12 | 2.38 ± 0.25 | 0.76 ± 0.14 | 0.90 ± 0.34 | − | − |
| | 5 | C+O | 2.00 ± 0.11 | 2.04 ± 0.16 | 0.82 ± 0.22 | 1.05 ± 0.19 | − | − |
| | 8 | C+O | 2.09 ± 0.15 | 2.15 ± 0.18 | 0.73 ± 0.18 | 0.78 ± 0.39 | − | − |
| | 13 | C+O | 2.39 ± 0.35 | 2.60 ± 0.20 | 0.84 ± 0.18 | 1.25 ± 0.30 | − | − |
| | 15 | C+O | 2.79 ± 0.07 | 0.14 ± 0.02 | 0.93 ± 0.07 | 1.62 ± 0.15 | + | − |
| pH7W-COCP | 1 | C+O | 2.69 ± 0.09 | 0.12 ± 0.01 | 0.89 ± 0.09 | 1.41 ± 0.12 | + | − |
| | 3 | C+O | 1.45 ± 0.08 | 0.15 ± 0.01 | 0.17 ± 0.01 | 0.14 ± 0.01 | + | ++ |
| | 7 | C+O | 2.58 ± 0.24 | 2.24 ± 0.08 | 0.79 ± 0.38 | 1.68 ± 0.80 | − | − |
| | 8 | C+O | 2.40 ± 0.17 | 0.18 ± 0.01 | 0.36 ± 0.02 | 1.07 ± 0.35 | + | − |
| | 9 | C+O | 2.67 ± 0.25 | 0.26 ± 0.10 | 0.77 ± 0.08 | 2.21 ± 0.22 | − | − |
| | 10 | C+O | 1.98 ± 0.05 | 0.17 ± 0.02 | 0.49 ± 0.07 | 1.25 ± 0.73 | + | − |
| | 11 | C+O | 2.28 ± 0.44 | 0.17 ± 0.01 | 0.74 ± 0.10 | 2.71 ± 0.09 | + | − |
| | 12 | C+O | 2.24 ± 0.41 | 0.20 ± 0.02 | 0.58 ± 0.17 | 0.86 ± 0.14 | + | − |
| | 13 | C+O | 2.75 ± 0.22 | 0.22 ± 0.04 | 0.89 ± 0.14 | 1.06 ± 0.54 | − | − |
| | 14 | C+O | 1.72 ± 0.11 | 0.18 ± 0.03 | 0.14 ± 0.07 | 0.20 ± 0.09 | + | ++ |
| | 15 | C+O | 1.43 ± 0.07 | 0.16 ± 0.03 | 0.11 ± 0.02 | 0.19 ± 0.10 | + | ++ |
| | 16 | C+O | 2.10 ± 0.27 | 2.90 ± 0.67 | 1.03 ± 0.27 | 3.03 ± 0.51 | − | − |
| | 17 | C+O | 2.73 ± 0.21 | 2.08 ± 0.07 | 1.36 ± 0.24 | 3.37 ± 0.39 | − | − |

**Table 1.** ELISA values (mean ± standard deviation) for *Cymbidium mosaic potexvirus* (CymMV) and *Odontoglossum ringspot tobamovirus* (ORSV) accumulation in *N. benthmiana* wild-type (WT) and transgenic lines after challenge with CymMV and ORSV virions. [a]Mock: mock-inoculated; C+O: mechanical inoculation of mixed virions of CymMV (C) and ORSV (O). [b]ELISA value: the OD (A405 nm) value showing virus accumulation in inoculated leaves (IL) and systemic leaves (SL) after inoculation with C+O, which was obtained from three individual samples of each plant type. [c]"−": ELISA value > 2.0; "+": ELISA value for IL > 0.8, SL < 0.2; "++": ELISA value < 0.2 in both IL and SL. [d]IL: inoculated leaves at 10 dpi. [e]SL: systemic leaves at 20 dpi.

For transgenic lines expressing pH7W-COCP, CymMV detected in SL and ORSV in IL and SL of lines 3, 14 and 15 were close to WT-mock level of ELISA values (<0.2) (Table 1 and Fig. S1), so these three lines could be resistant to C+O co-infection. Among other lines, the IL of those lines showed higher ELISA value for CymMV and ORSV (both > 0.2) than the WT-mock level. Especially, the SL of lines 1, 8, 10, 11, 12 showed only low values for CymMV but high values for ORSV, which suggests that the five lines might be resistant to only CymMV but not ORSV. No other lines showed resistance to only ORSV (Table 1). Collectively, the efficiency of generate resistant lines from pH7W-COCP construct is higher than that from pCam-COCP. Moreover, differential resistance against CymMV and ORSV was noted between transgenic lines.

To further confirm the viral resistance in transgenic lines, we performed Western and Northern blot analyses. When the selected resistant transgenic lines described above were co-inoculated with C+O, on Western blot analysis, CymMV and ORSV CPs were not detectable in pCam-COCP line 2 with antibodies specific to CymMV or ORSV (Fig. 2B) nor in transgenic pH7W-COCP lines 3, 12, 14, and 15 at 20 or 26 dpi (Fig. 2B). Conversely, for lines showing severe symptoms after C+O co-inoculation, CymMV and ORSV CP levels were substantial in transgenic pCam-COCP line 1 and pH7W-COCP line 16, but pH7W-COCP line 1 and 11 were infected with ORSV only (Fig. 2B), which is consistent with ELISA results (Table 1 and Fig. S1). On Northern blot analysis, genomic RNAs of both CymMV and ORSV were again undetectable in resistant transgenic lines at 20 dpi (Fig. 2C), regardless of extraction from plants with or without C+O co-inoculation. All results indicate that transgenic pCam-COCP line 2 and pH7W-COCP lines 3, 14 and 15 are highly resistant to C+O co-infection.

**Virus accumulation is greatly reduced in protoplasts from resistant transgenic plants.** Successful virus infection involves several important steps: virus replication, cell-to-cell movement and long-distance movement in hosts. To determine whether the virus resistance occurred at the single-cell level, protoplasts were isolated from WT and transgenic lines and inoculated with C+O mediated by polyethylene glycol (PEG). On quantitative reverse transcription polymerase chain reaction (RT-qPCR) analysis, the accumulation of CymMV in protoplasts of transgenic lines, such as pCam-COCP line 2 and pH7W-COCP lines 3, 14 and 15, decreased from 63% to 92% as compared with the WT; ORSV accumulation decreased from 62% to 90% (Fig. 3A). Northern blot analysis also confirmed the reduced CymMV and ORSV RNA levels in transgenic protoplasts of pCam-COCP line 2 and pH7W-COCP line 3 (Fig. 3B). Although protoplasts of transgenic lines could be infected with CymMV and ORSV, only low replication efficiency of CymMV and ORSV were observed.

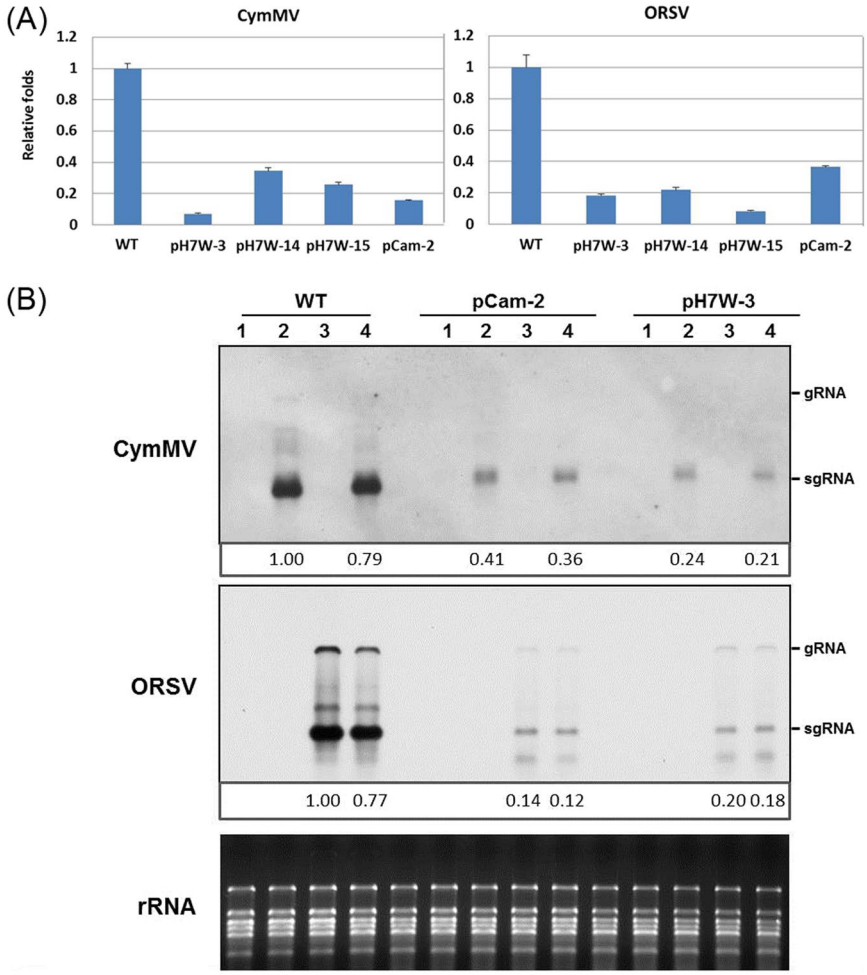


**Figure 3.** CymMV and ORSV RNA accumulation in protoplasts from WT and transgenic lines. (**A**) RT-qPCR analysis of CymMV and ORSV RNA in protoplasts of WT and transgenic lines after C+O infection at 18 hpi. Values are normalized against CymMV and ORSV RNA in protoplasts of WT plants infected with C+O. (**B**) Northern blot analysis of CymMV and ORSV in protoplasts from WT and transgenic lines transfected with C+O by DIG-labeled CP probes. Protoplasts were mock-inoculated with $H_2O$ (Lane 1), CymMV virions (Lane 2), ORSV virions (Lane 3), and mixed C+O (Lane 4). The relative accumulation of CymMV and ORSV in transgenic lines were shown compared with single virion inoculation in WT plants.

**Similar cell-to-cell movement efficiency between the leaves of WT and transgenic lines.** Given that the accumulation of CymMV and ORSV in protoplasts and IL was significantly lower in resistant transgenic lines than WT plants and almost no virus was detectable in SL of transgenic lines (Table 1 and Fig. S1), we considered that viral trafficking may be limited in transgenic lines. Therefore, we tested whether cell-to-cell movement was affected in transgenic lines by using eGFP or 2x.eGFP as reporters in bombardment assays. Leaves of WT and transgenic lines were bombarded with pCass-eGFP to assess cell-to-cell trafficking efficiency. Confocal microscopy revealed free eGFP fluorescence localized in single cells (65.2%) in more than half of the observed sites in the WT at 40 h post-bombardment; however, eGFP also moved to two or three cells at the sustainable level (>30%) (Table 2 and Fig. S2). Transgenic pH7W-COCP line 3 showed similar or slightly higher trafficking efficiency of eGFP (Table 2 and Fig. S2B). To create a larger fluorescent marker, we fused two tandem copies of eGFP to generate pCass-2x.eGFP. Although 2x.eGFP was restricted in nearly 80% of observed sites, WT and transgenic pH7W-COCP line 3 showed no significant difference in 2x.eGFP movement beyond more than 2 cells (Table 2 and Fig. S2C,D). Hence, the gating of plasmodesmata (PD) for cell-to-cell movement was similar in transgenic line and the WT.

**Long-distance movement of CymMV and ORSV was impeded in transgenic line.** To further determine whether the long-distance trafficking of the viruses was affected, we measured virus systemic movement in the WT and transgenic pH7W-COCP line 3 (pH7W-3) by tissue blotting analysis from rolled IL and stems harvested at 14 dpi. We found strong hybridization signals for CymMV and ORSV RNAs in IL, e.g. leaf 3 (L3), leaf 4 (L4) and stems between inoculated L4 and non-inoculated leaf L5 (S4) or stems between upper non-inoculated L5 and leaf L6 (S5) of the WT (Fig. 4A,B). In contrast, weak signals for ORSV RNA were obtained

| | WT | | pH7W-COCP line 3 |
|---|---|---|---|
| eGFP | 1 cell | 43/66 (65.2%) | 53/65 (81.5%) |
| | 2 cells | 15/66 (22.7%) | 10/65 (15.5%) |
| | >2 cells | 8/66 (12.1%) | 2/65 (3.0%) |
| 2x.eGFP | 1 cell | 38/51 (74.5%) | 46/57 (80.7%) |
| | 2 cells | 10/51 (19.6%) | 8/57 (14.0%) |
| | >2 cells | 3/51 (5.9%) | 3/57 (5.3%) |

**Table 2.** Cell-to-cell movement of eGFP and 2x.eGFP in leaves of *N. benthamiana* WT and transgenic pH7W-COCP line 3 at 40 hours after particle bombardment.

in the IL of transgenic pH7W-3, in agreement with ELISA results (Fig. S1). However, we found no detectable signals in both stems of S4 and S5 in transgenic pH7W-3 with CymMV or ORSV probes (Fig. 4B), indicating that the long-distance movement of CymMV and ORSV might be blocked in the transgenic line. To confirm the detection, we carried out a more sensitive assay such as RT-PCR. With this procedure, we detected CymMV and ORSV viral RNAs in both WT and transgenic pH7W-3, but a sharp difference in an extremely weak signal in non-inoculated leaf L5, S4 or S5 in transgenic line compared with the inoculated WT plants. These results further confirmed that CymMV and ORSV confined in the ILs with trafficking from IL to SL in an inefficient manner in resistant line.

Next, to explore the long-distance trafficking of CymMV and ORSV in transgenic lines again, we grafted transgenic pH7W-3 onto virus-infected WT plants (pH/WT). WT plants were first co-inoculated with C+O and served as stocks at 3 dpi, with transgenic pH7W-3 as scions (Fig. 5A). In parallel experiments, mock-inoculated WT scions or *Bamboo mosaic virus* (BaMV)-inoculated WT stocks served as controls. As expected, grafted control plants (WT/WT) with C+O infection showed severe leaf curling, chlorotic leaves and stunted growth at 17 dpi, which did not appear on grafted scion plants (pH/WT). In contrast, BaMV caused chlorotic and mosaic leaves on both grafted plants (WT/WT; pH/WT) (Fig. 5B).

CymMV and ORSV viral RNA accumulation was measured in IL of stocks at 11 dpi and scions at 17 dpi by RT-PCR (Fig. 5A). The accumulation of CymMV, ORSV or BaMV RNA was easily detected in stock leaves from grafted plants (pH/WT) or control plants (WT/WT) (Fig. 5C). However, CymMV and ORSV RNAs were nearly undetectable in grafted scion leaves (pH/WT) at 17 dpi (Fig. 5D). In contrast, BaMV RNA level was substantially detected in both grafted scions (WT/WT and pH/WT) at 17 dpi. Thus, CymMV and ORSV were not only limited in transport from WT stocks to transgenic scions, but such long-distance movement blocking were CymMV- and ORSV- specific.

**Virus-specific small interfering RNAs (vsiRNAs) production in transgenic line.** To evaluate if the viral resistance in transgenic line was resulted from gene silencing, we detected CymMV- and ORSV- specific vsiRNAs in inoculated WT and transgenic lines. RNA samples of C+O co-infected or mock-inoculated leaves of WT and transgenic pH7W-3 at 10 dpi were hybridized with CymMV and ORSV probes by northern blot analyses. Both CymMV and ORSV probes showed much stronger signals in the WT-inoculated leaves than in the transgenic lines, predominantly in 21 nt. Interestingly, both probes also detected abundant vsiRNAs from mock-inoculated transgenic line, which was absent in the mock-inoculated WT plants (Fig. 4D), suggesting transgene-derived vsiRNA production could trigger gene silencing for viral resistance in transgenic line during infection.

## Discussion

In this study, we successfully generated transgenic *N. benthamiana* plants expressing two different constructs, pCam-COCP or pH7W-COCP (Fig. 1A), that were able to confer resistance to both CymMV and ORSV (Table 1). Of note, more resistant lines against the two viruses were generated from transgenic lines with the pH7W-COCP transgene (Fig. 1B,C), which has a hairpin structure containing the full-length CP genes of CymMV and ORSV under control of the 35S promoter. Our finding agrees with the notion that double-stranded RNA is a powerful inducer in RNA silencing than either sense or antisense RNA alone[18]. In addition to double resistant lines, more lines were solely resistant to CymMV than ORSV (Table 1). The Tobamovirus-encoded P126 protein has been shown as a strong virus suppressor of RNA silencing (VSR); it affects gene silencing dose-dependently and also increases the plant susceptibility to several viruses[19]. In contrast, TGBp1 encoded by Potexvirus is usually a weak VSR[20]. This phenomena may explain why we could generate more resistant lines to CymMV but few to ORSV or both in our study. Previously, different strategies for designing transgenes have been attempted, including using the sense or antisense CymMV CP gene[14,21] and amiRNA targeting RdRp genes of CymMV and ORSV[17], but most transgenic studies have successfully conferred resistance to only CymMV. To date, no transgenic lines with resistance to ORSV or efficient dual resistance to both viruses have been reported.

Among all the transgenic lines we generated, the highly resistant lines pCam-COCP line 2 and pH7W-COCP lines 3, 14 and 15 were selected after virus resistance assays. These transgenic lines showed multilayer resistance during virus infection. First, both the accumulation of CymMV and ORSV was approximately 80% less in protoplasts of resistant lines than WT plants (Fig. 3), which represents the low replication efficiency at the single-cell level in transgenic lines. This less efficient virus replication could also result in lower viral accumulation in SL, as for some Geminivirus[22]. However, viral RNAs were nearly undetectable in SL of inoculated transgenic lines with C+O by ELISA (Table 1 and Fig. S1), Western blot analysis (Fig. 2B), Northern blot analysis (Fig. 2C), and

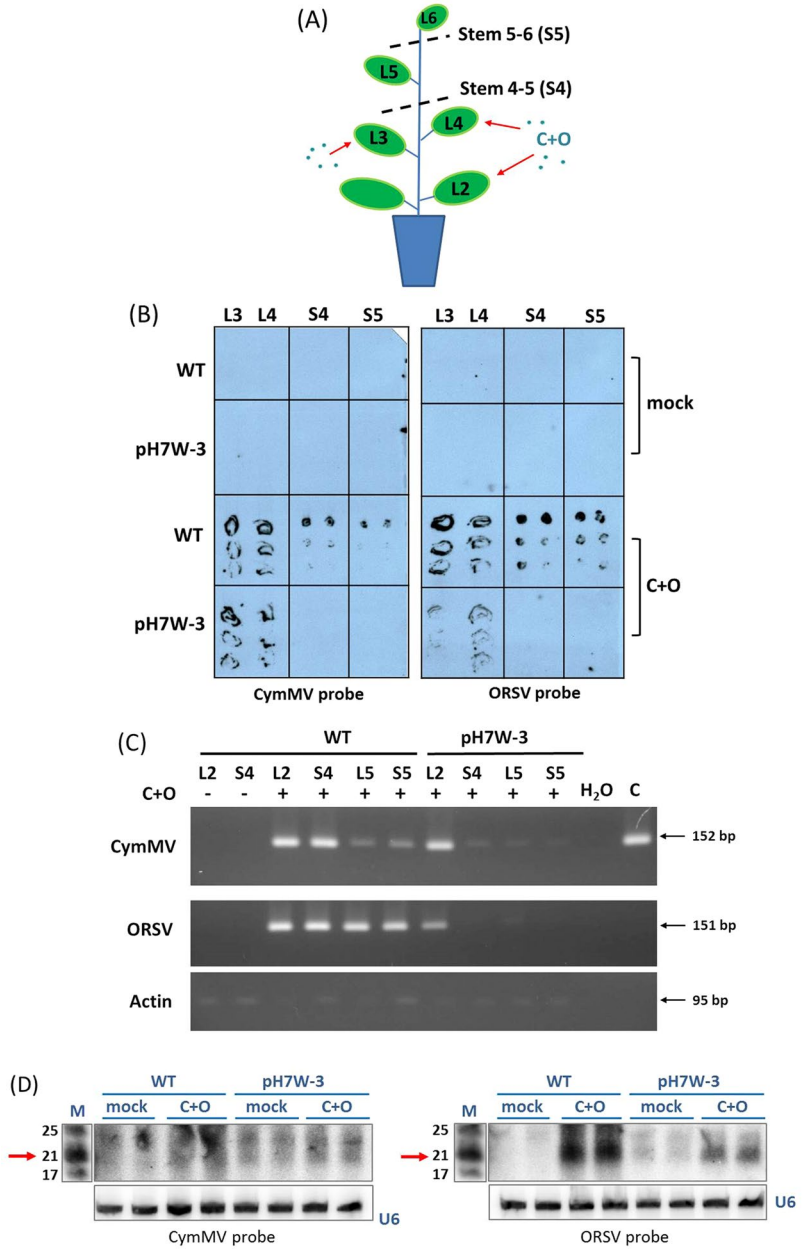


**Figure 4.** CymMV and ORSV viral RNA and siRNA accumulation in WT and transgenic plants inoculated with C+O. (**A**) Illustrations of sampling tissues in WT and transgenic line pH7W-COCP line3 (pH7W-3) after Leaf 3 (L3) and leaf 4 (L4) co-inoculated with C+O. L3, L4, Stem between L4 and L5 (S4), Stem between L5 and L6 (S5) and systemic leaf 5 (L5) were harvested for tissue blotting (**B**) and RT-PCR (C) at 14 dpi. (**B**) The tissue blots prepared from various tissues of WT and transgenic line were hybridized with DIG-labeled CymMV- and ORSV-specific CP probes. (**C**) Accumulation of CymMV and ORSV viral RNA in L2, S4, S5 and L5 of WT and transgenic line by RT-PCR at 14 dpi. CymMV RNA was detected by primer pair (CymMV RdRp-F and CymMV RdRp-R) of expected size 152 bp and ORSV RNA by primer pair (ORSV RdRp-F and ORSV RdRp-R) of 151 bp. Actin was used for loading controls. (**D**) Detection of the vsiRNAs in mock and C+O infected IL of WT and transgenic pH7W-3 at 10 dpi by [$\gamma$-$^{32}$P] CTP-labeled CymMV or ORSV CP probes. The lower panel shows hybridization of U6 probes as equal loading control. The positions of 21 nt RNA is indicated by arrows. M: marker; mock: water inoculation; C+O: inoculated with CymMV and ORSV.

RT-PCR (Fig. 4C). These results may suggest that virus long-distance movement is another defense layer against dual virus infection in transgenic line, although the PD gating ability was similar to WT plants (Fig. S2).

Tissue blotting further confirmed the lack of virus accumulation in vascular systems of resistant lines (Fig. 4B). For virus infection, the phloem-bundle sheath interface is a crucial barrier to several viruses entering into phloem long-distance trafficking during the virus–host interaction; these viruses include *Grapevine berry inner necrosis virus*[23], *Tomato aspermy virus*[24], *Red clover necrotic mosaic virus*[25] and *Cucumber mosaic virus*[26]. Hence, CymMV

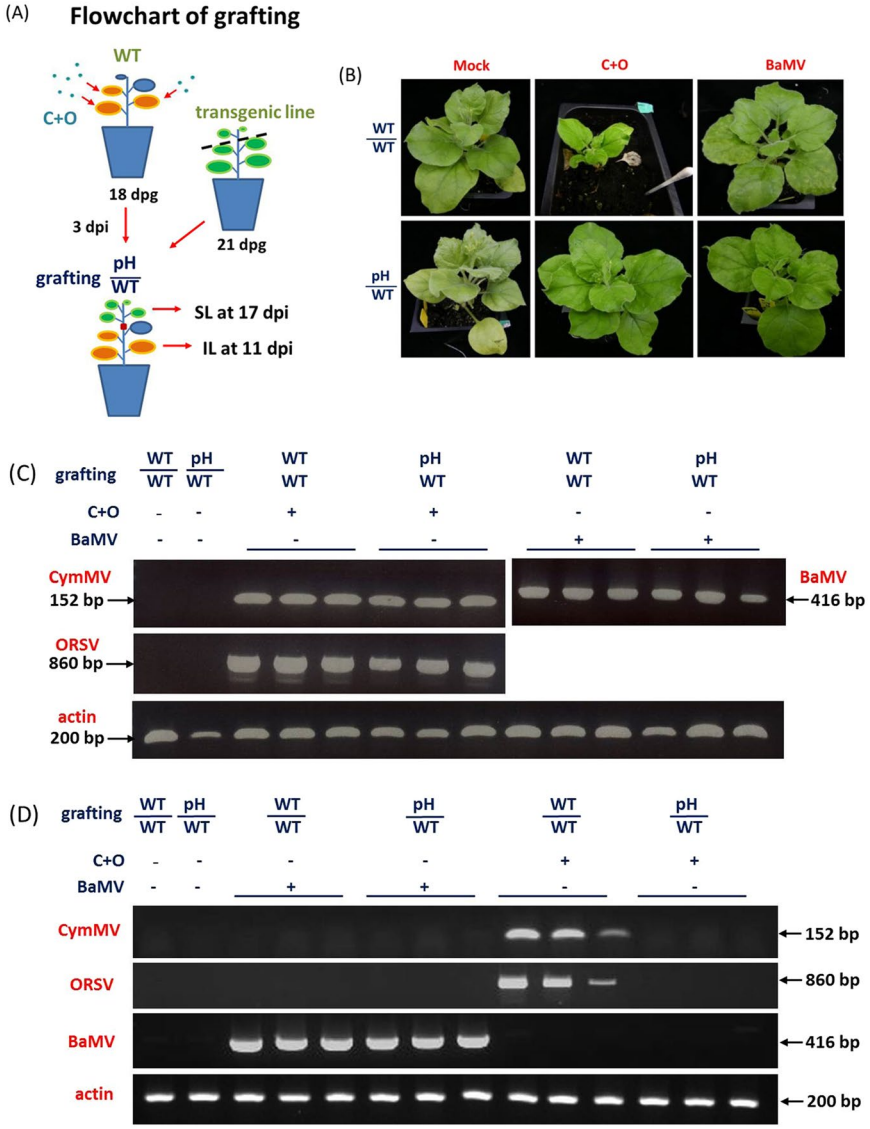


**Figure 5.** Long-distance movement of CymMV and ORSV in WT and transgenic pH7W-COCP line 3 (pH) by grafting assay. (**A**) Flowchart of grafting. (**B**) Symptoms of grafting plants inoculated with C+O at 17 dpi. (**C**,**D**) RT-PCR analysis of CymMV and ORSV RNA accumulation in grafted stock leaves at 11 dpi (**C**) and systemic scion leaves at 17 dpi (**D**). CymMV was detected by primer pair (CymMV RdRp-F and CymMV RdRp-R) of 152 bp; ORSV by primer pair (ORSV-RdRpPai-F and ORSV-RdRpPai-R) of 860 bp and BaMV by primer pair (BaMV-P2-F and BaMV-P2-R) of 416 bp, respectively. Actin was an internal control.

and ORSV may be restricted at the phloem-bundle sheath barrier. However, whether CymMV and ORSV are blocked at the parietal layer of the sieve element or whether CymMV and ORSV can invade phloem parenchyma cells, companion cells, or the sieve element through the bundle sheath in the IL of resistant transgenic lines remains to be determined.

In higher plants, RNA molecules including siRNAs, miRNAs, transfer RNAs, ribosomal RNAs and mRNAs could traffic via the phloem to distant tissues, which is essential for nutrient allocation, gene silencing, stress responses and plant development[27]. Grafting experiments revealed several *Arabidopsis* mobile RNAs[28] as well as small RNAs, including miRNAs, endogenous siRNAs or vsiRNAs[29], are able to transport to distant tissues non-autonomously. Our grafting results strongly support that CymMV and ORSV were restricted in infected WT stocks with transgenic lines expressing CymMV and ORSV CP genes as scions (Fig. 5); presumably CymMV- and ORSV-specific vsiRNAs play a major role in systemic silencing[30]. In contrast, with similar grafting, BaMV RNA trafficked efficiently toward transgenic scions (Fig. 5), so these vsiRNAs could determine the viral RNA specificity and trafficking efficiency for viral resistance in resistant lines. Several studies have also indicated that non-transgenic plants grafted onto resistant transgenic lines could result in transfer of resistance to scions, such as with *Prunus necrotic ringspot virus*[31], *Tomato spotted wilt virus*[32] and *Tobacco mosaic virus*[33]. In double scions grafted onto a rootstock previously infected with *Pepper golden mosaic virus*, the resistant intermediate tissue

delayed virus movement from the infected rootstock to the susceptible apex[34]. Such resistance is highly associated with early degradation of viral RNA by an siRNA mechanism[12].

Taken together, our studies demonstrate the nearly complete dual resistance to CymMV and ORSV in *N. benthamiana* transgenic plants without any growth penalty by RNA-mediated interference. This is the first report of the development of transgenic plants with double resistance to the two most prevailing viruses, CymMV and ORSV, that infect orchids. Our study provides the exciting prospect of using similar transgenes to generate resistant orchids.

## Methods

**Construction of plasmids.** We generated two constructs of transgenes for plant transformation. First, ORSV CP fragment was cloned from ORSV-infecting orchid total RNA. The first strand cDNA was synthesized with specific primer ORSV-CP-R, followed by PCR amplification with primers ORSV-CP-F and ORSV-CP-R (Table S1). *Xho*I and *Kpn*I –digested PCR product of ORSV CP fragment was then purified and cloned into pkylx7 vector in the cognate sites to generate pkylx-ORSVCP. To construct pkylx-COCP, the CymMV CP sequence was amplified by using pCYCP-11[14] as template with primers CyCP9 and CyCP10 (Table S1). The fragment was inserted upstream to ORSV CP fragment in pkylx-ORSVCP via *Hind*III to generate pkylx-COCP. The whole cassette including the 35S promoter, CymMV-ORSV CP fragment, and rbcs terminator was amplified by primers 35S-1 and rbcSR3 (Table S1). The amplicon was then ligated into pCambia1301 through *BamH*I and *Xba*I sites to generate pCam-COCP. Second, to construct pH7W-COCP, the CymMV-ORSV CP fragment was first amplified from pkylx-COCP by attB1-COCP and attB2-COCP primers (Table S1) and cloned into the entry vector pDONR$^{TM}$221, using BP clonase. The COCP fragment was then transferred into binary vector pH7GWI-WG2I in sense and antisense orientation by using Gateway LR recombination (Life technologies). The constructs pCam-COCP and pH7W-COCP were transformed into *A. tumefaciens* strain GV3101, respectively.

**Generation of transgenic plants.** Leaf discs of *N. benthamiana* were transformed with *A. tumefaciens* strain GV3101 containing pCam-COCP or pH7W-COCP as previously described[35], and hygromycin (20 mg/l) was used as a selection marker. Transgenic shoots regenerated from leaf discs of *N. benthamiana* were grown on Murashige and Skoog agar medium (Sigma-Aldrich) containing hygromycin. T0 plants were transferred to soil and generated seeds. Transgenic plants were verified by PCR with specific primers (for COCP1 and COCP2, amplified size 1170 bp; Table S1). Homozygous individuals were selected from T1 and T2 progenies by hygromycin resistance and confirmed by RT-PCR with specific primer pairs (CyCP3 and CyCP6; ORSV3 and ORSV4; Table S1) for CP transgenes.

**Plant growth, inoculation and grafting.** All WT and transgenic lines were grown at 28 °C in a walk-in plant growth chamber under a 16-h-light/8-h-dark cycle with white light (about 220 $\mu$mol/m$^2$/s$^1$). For each experiment, at least 4 plants from each transgenic line were co-inoculated with CymMV and ORSV virions (0.05 $\mu$g eacg/leaf) by gently rubbing virions onto 1 to 3 true leaves. For each construct transformation, 7 to 17 putative independent lines were assayed for resistance. Symptoms were observed visually till 20 dpi. The IL and SL were harvested at 10 and 20 or 26 dpi, respectively.

Grafting was performed as described[36] except that 18~21-day-old *N. benthamiana* plants were used. WT plants were first inoculated with a mixture of CymMV and ORSV or BaMV virions[37] as a control, then transgenic plants as scions were grafted onto infected WT plants at 3 dpi. The grafted plants were then incubated in a walk-in growth chamber for harvesting IL from stocks at 11 dpi and SL from scions at 17 dpi, and symptoms on grafted plants were continuously observed.

**ELISA and western blot analysis.** From WT and transgenic plants, total protein was extracted from IL and SL at 10 and 20 dpi, respectively, by using coating buffer (15 mM $Na_2CO_3$, 35 mM NaHCO3, pH 9.6). For ELISA, a protocol was modified from Lin *et al.*[38] () to measure the accumulation of CymMV and ORSV. Briefly, 96-microwell plates (Immuno 96 MicroWell plate, Nunc) were coated with total protein, then treated with the primary rabbit antibody for CymMV-CP or ORSV-CP (1:10,000 dilution) and secondary antibody, goat anti-rabbit immunoglobulin G conjugated with alkaline phosphatase (Applied Biological Materials, BC, Canada) (1:5,000 dilution). After the addition of substrate (p-nitrophenyl phosphate, 1 mg/mL), the absorbance at 405 nm was recorded by using an ELISA reader (PowerWave HT Microplate Spectrophotometer, BioTek Instruments, VT, USA) for 10 to 30 min.

For western blot analysis, proteins extracted from 0.1 g leaf of each sample were separated by 12% SDS-PAGE and transferred onto PVDF blotting membranes (GE Healthcare) as described[14]. Membranes were blocked with 5% milk in 1X PBS Buffer (Omics Bio) and incubated with the primary antibody for CymMV-CP or ORSV-CP (1:10,000 dilution) at 4 °C overnight, followed by the goat anti-rabbit IgG-HRP (1:5,000 dilution) and Western ECL substrate (Bio-Rad Laboratories, CA, USA).

**RNA analysis.** Total RNA was extracted from 0.1 g leaf tissues by using TRIzol (Invitrogen, CA, USA). To identify the transgene expression in the transgenic line, RT-PCR was used with specific primer pairs for the COCP transgene. An amount of 2 µg total RNA was reverse transcribed by using a SuperScript III kit (Life Technologies, CA, USA) with poly(T) primer. The primer pairs (CyCP3 and CyCP6; ORSV3 and ORSV4) (Table S1) were used to amplify 407-nt CymMV-CP and 447-nt ORSV-CP cDNA fragments. The RT-PCR products were monitored by electrophoresis on 1.5% agarose gel in TBE buffer (Tris-borate-EDTA) and visualized with SYBR Green I core reagent (Life Technologies).

To detect the accumulation of CymMV and ORSV in WT and transgenic line after infection or grafting, RNA was extracted from various tissues and reverse transcribed into cDNA as described above. The accumulation of CymMV, ORSV and BaMV was detected by RT-PCR with specific primer pairs (CymMV RdRpF and CymMV RdRpR; ORSV RdRp-F and ORSV RdRp-R; ORSV RdRpPai-F and ORSV RdRpPai-R; or BaMV-P2-F and BaMV-P2-R), respectively (Table S1).

For RT-qPCR, cDNA template was mixed with 2X SYBR Green PCR master mix (Applied Biosystems) with the Applied Biosystems QuantStudio 12 K Flex Real-Time PCR system (Life Technologies). Specific primers (CymMV RdRp-F and CymMV RdRp-R; ORSV RdRp-F and ORSV RdRp-R) (Table S1) were used to detect CymMV and ORSV. Normalization of CymMV and ORSV RNA accumulation was with Nb Actin gene expression amplified by Nb-actin-F and Nb-actin-R (Table S1).

For Northern blot analysis, RNA gel blot was analyzed as described[39], except that the membrane was hybridized with a DIG-labeled full-length CP probes or [$\gamma$-$^{32}$P] CTP-labeled replicase probes for CymMV (EF125180, 2404–3722 nt, 1319 bp) and ORSV (AY571290, 2411–3270 nt, 860 bp). For CymMV and ORSV vsiRNA detection, 10 $\mu$g total RNA was loaded for Northern blot analysis. The blots were probed with [$\gamma$-$^{32}$P] CTP-labeled, carbonate buffer-fragmented RNA transcripts corresponding to CP genes of CymMV (EF125180) or ORSV (AY571290). Probing of markers and other details were performed as previously described[40].

**Protoplast isolation and virus inoculation.** Protoplasts were isolated from WT and transgenic plants and inoculated as described[41]. Approximately $2 \times 10^5$ protoplasts were transfected with 0.6 $\mu$g each of CymMV and ORSV viral RNAs or virions by PEG method. Total RNA was extracted from protoplasts by using the Hybrid-R kit (Gene All Biotechnology, Korea) at 18 hours after transfection for analysis of viral RNA accumulation by RT-qPCR and Northern blot assay.

**Monitoring cell-to-cell movement efficiency.** To test whether cell-to-cell movement efficiency was affected in transgenic plants and the WT, we used eGFP and 2x.eGFP as reporters. The gold particles were coated with plasmid DNA by using a $CaCl_2$/spermidine precipitation technique[42]. An amount of 10 $\mu$l plasmid DNA (1 $\mu$g/$\mu$l, pCass-eGFP or pCass-2x.eGFP), 100 $\mu$l 2.5 M $CaC1_2$, 40 $\mu$l 0.1 M spermidine and 100 $\mu$l sterile gold particles (60 mg/ml, 1.0 $\mu$m diameter) were mixed with continuous agitation in 1.5 ml Eppendorf tubes, vortexed continuously for 1 min, then centrifuged (6000 rpm, 30 sec). The supernatant was removed and the pellet was resuspended in 200 $\mu$l absolute ethanol two or three times. The gold particles were resuspended in 100 $\mu$l absolute ethanol. Aliquots of 10 $\mu$l gene particle solution for each shot were used with GDS-80 for bombardment (Wealtec Bioscience Co.). The bombardment was set up with helium pressure 50 pounds per inch, vacuum 3.5 kgf/cm$^2$, and 7-cm target distance. Leaf segments from WT and transgenic plants were used for bombardment assay. The eGFP and 2x.eGFP expressions were observed periodically under a confocal laser scanning microscope (LSM880, Zeiss) after bombardment. Results are expressed as number of fluorescent cell units per bombardment. Each experiment was repeated three times.

**Tissue blotting.** WT and transgenic plants were first inoculated with mixed CymMV and ORSV. Sections were cut from fresh leaves and stem tissues 14 dpi by hand using a new razor blade. Tissue blots were made by pressing the newly cut surface onto Hybond$^{TM}$ -N$^+$ nylon membranes (GE Healthcare Life Sciences, Little Chalfont, UK) as described[43]. The blots were then hybridized with DIG-labeled RNA probes specific to CymMV or ORSV RdRp gene sequences by using the DIG Nucleic Acid Detection Kit (Sigma-Aldrich, MO, USA).

## References


1. Christenhusz, M. J. M. & Byng, J. W. The number of known plants species in the world and its annual increase. *Phytotaxa* **261**, 201–217, https://doi.org/10.11646/phytotaxa.261.3.1 (2016).
2. Zettler, F. W., Ko, N. J., Wisler, G. C., Elliott, M. S. & Wong, S. M. Viruses of Orchids and Their Control. *Plant Dis* **74**, 621–626, https://doi.org/10.1094/Pd-74-0621 (1990).
3. Ajjikuttira, P., Loh, C. S. & Wong, S. M. Reciprocal function of movement proteins and complementation of long-distance movement of Cymbidium mosaic virus RNA by Odontoglossum ringspot virus coat protein. *J Gen Virol* **86**, 1543–1553, https://doi.org/10.1099/vir.0.80772-0 (2005).
4. Hu, W. W., Wong, S. M., Goh, C. J. & Loh, C. S. Synergism in replication of cymbidium mosaic potexvirus (CymMV) and odontoglossum ringspot tobamovirus (ORSV) RNA in orchid protoplasts. *Arch Virol* **143**, 1265–1275 (1998).
5. Wong, S. M., Chng, C. G., Lee, Y. H., Tan, K. & Zettler, F. W. Incidence of Cymbidium Mosaic and Odontoglossum Ringspot Viruses and Their Significance in Orchid Cultivation in Singapore. *Crop Prot* **13**, 235–239, https://doi.org/10.1016/0261-2194(94)90084-1 (1994).
6. Kim, J. D., Koo, Y. B. & Chang, M. U. Genome characterization of a Korean isolate of cymbidium mosaic virus. *Mol Cells* **8**, 181–188 (1998).
7. Wong, S. M. *et al*. Cymbidium mosaic potexvirus RNA: complete nucleotide sequence and phylogenetic analysis. *Arch Virol* **142**, 383–391 (1997).
8. Chng, C. G. *et al*. The complete sequence of a Singapore isolate of odontoglossum ringspot virus and comparison with other tobamoviruses. *Gene* **171**, 155–161 (1996).
9. Chapman, S., Hills, G., Watts, J. & Baulcombe, D. Mutational analysis of the coat protein gene of potato virus X: effects on virion morphology and viral pathogenicity. *Virology* **191**, 223–230 (1992).
10. Hilf, M. E. & Dawson, W. O. The tobamovirus capsid protein functions as a host-specific determinant of long-distance movement. *Virology* **193**, 106–114, https://doi.org/10.1006/viro.1993.1107 (1993).
11. Abel, P. P. *et al*. Delay of Disease Development in Transgenic Plants That Express the Tobacco Mosaic-Virus Coat Protein Gene. *Science* **232**, 738–743, https://doi.org/10.1126/science.3457472 (1986).
12. Cillo, F. & Palukaitis, P. Transgenic resistance. *Adv Virus Res* **90**, 35–146, https://doi.org/10.1016/B978-0-12-801246-8.00002-0 (2014).
13. Chia, T. F., Chan, Y. S. & Chua, N. H. Characterization of cymbidium mosaic virus coat protein gene and its expression in transgenic tobacco plants. *Plant Mol Biol* **18**, 1091–1099 (1992).
14. Chang, C. *et al*. Transgenic resistance to Cymbidium mosaic virus in Dendrobium expressing the viral capsid protein gene. *Transgenic Res* **14**, 41–46 (2005).
15. Chan, Y. L. *et al*. Gene stacking in Phalaenopsis orchid enhances dual tolerance to pathogen attack. *Transgenic Res* **14**, 279–288 (2005).
16. Liao, L. J. *et al*. Transgene silencing in Phalaenopsis expressing the coat protein of Cymbidium Mosaic Virus is a manifestation of RNA-mediated resistance. *Mol Breeding* **13**, 229–242, https://doi.org/10.1023/B:Molb.0000022527.68551.30 (2004).

17. Petchthai, U., Yee, C. S. L. & Wong, S. M. Resistance to CymMV and ORSV in artificial microRNA transgenic Nicotiana benthamiana plants. *Sci Rep* **8**, 9958, https://doi.org/10.1038/s41598-018-28388-9 (2018).
18. Mansoor, S., Amin, I., Hussain, M., Zafar, Y. & Briddon, R. W. Engineering novel traits in plants through RNA interference. *Trends Plant Sci* **11**, 559–565, https://doi.org/10.1016/j.tplants.2006.09.010 (2006).
19. Harries, P. A., Palanichelvam, K., Bhat, S. & Nelson, R. S. Tobacco mosaic virus 126-kDa protein increases the susceptibility of Nicotiana tabacum to other viruses and its dosage affects virus-induced gene silencing. *Mol Plant Microbe Interact* **21**, 1539–1548, https://doi.org/10.1094/MPMI-21-12-1539 (2008).
20. Hsu, H. T., Hsu, Y. H., Bi, I. P., Lin, N. S. & Chang, B. Y. Biological functions of the cytoplasmic TGBp1 inclusions of bamboo mosaic potexvirus. *Arch Virol* **149**, 1027–1035, https://doi.org/10.1007/s00705-003-0254-y (2004).
21. Lim, S. H., Ko, M. K., Lee, S. J., La, Y. J. & Kim, B. D. Cymbidium mosaic virus coat protein gene in antisense confers resistance to transgenic Nicotiana occidentalis. *Mol Cells* **9**, 603–608 (1999).
22. Akad, F. *et al*. Making a friend from a foe: expressing a GroEL gene from the whitefly Bemisia tabaci in the phloem of tomato plants confers resistance to tomato yellow leaf curl virus. *Arch Virol* **152**, 1323–1339, https://doi.org/10.1007/s00705-007-0942-0 (2007).
23. Yoshikawa, N. *et al*. Interference of Long-Distance Movement of Grapevine berry inner necrosis virus in Transgenic Plants Expressing a Defective Movement Protein of Apple chlorotic leaf spot virus. *Phytopathology* **96**, 378–385, https://doi.org/10.1094/PHYTO-96-0378 (2006).
24. Thompson, J. R. & Garcia-Arenal, F. The bundle sheath-phloem interface of Cucumis sativus is a boundary to systemic infection by tomato aspermy virus. *Mol Plant Microbe In* **11**, 109–114, https://doi.org/10.1094/Mpmi.1998.11.2.109 (1998).
25. Wang, H. L., Wang, Y., Giesman-Cookmeyer, D., Lommel, S. A. & Lucas, W. J. Mutations in viral movement protein alter systemic infection and identify an intercellular barrier to entry into the phloem long-distance transport system. *Virology* **245**, 75–89, https://doi.org/10.1006/viro.1998.9154 (1998).
26. Wintermantel, W. M., Banerjee, N., Oliver, J. C., Paolillo, D. J. & Zaitlin, M. Cucumber mosaic virus is restricted from entering minor veins in transgenic tobacco exhibiting replicase-mediated resistance. *Virology* **231**, 248–257, https://doi.org/10.1006/viro.1997.8533 (1997).
27. Ham, B. K. & Lucas, W. J. Phloem-Mobile RNAs as Systemic Signaling Agents. *Annu Rev Plant Biol* **68**, 173–195, https://doi.org/10.1146/annurev-arplant-042916-041139 (2017).
28. Thieme, C. J. *et al*. Endogenous Arabidopsis messenger RNAs transported to distant tissues. *Nat Plants* **1**, 15025, https://doi.org/10.1038/nplants.2015.25 (2015).
29. Molnar, A. *et al*. Small silencing RNAs in plants are mobile and direct epigenetic modification in recipient cells. *Science* **328**, 872–875, https://doi.org/10.1126/science.1187959 (2010).
30. Chen, W. *et al*. A Genetic Network for Systemic RNA Silencing in Plants. *Plant Physiol* **176**, 2700–2719, https://doi.org/10.1104/pp.17.01828 (2018).
31. Zhao, D. & Song, G. Q. Rootstock-to-scion transfer of transgene-derived small interfering RNAs and their effect on virus resistance in nontransgenic sweet cherry. *Plant Biotechnol J* **12**, 1319–1328, https://doi.org/10.1111/pbi.12243 (2014).
32. Spano, R., Mascia, T., Kormelink, R. & Gallitelli, D. Grafting on a Non-Transgenic Tolerant Tomato Variety Confers Resistance to the Infection of a Sw5-Breaking Strain of Tomato spotted wilt virus via RNA Silencing. *PLoS One* **10**, e0141319, https://doi.org/10.1371/journal.pone.0141319 (2015).
33. Md Ali, E., Kobayashi, K., Yamaoka, N., Ishikawa, M. & Nishiguchi, M. Graft transmission of RNA silencing to non-transgenic scions for conferring virus resistance in tobacco. *PLoS One* **8**, e63257, https://doi.org/10.1371/journal.pone.0063257 (2013).
34. Garcia-Neria, M. A. & Rivera-Bustamante, R. F. Characterization of Geminivirus resistance in an accession of Capsicum chinense Jacq. *Mol Plant Microbe Interact* **24**, 172–182, https://doi.org/10.1094/MPMI-06-10-0126 (2011).
35. Horsch, R. B. *et al*. A Simple and General-Method for Transferring Genes into Plants. *Science* **227**, 1229–1231 (1985).
36. Chang, C. H. *et al*. The Nucleolar Fibrillarin Protein Is Required for Helper Virus-Independent Long-Distance Trafficking of a Subviral Satellite RNA in Plants. *Plant Cell* **28**, 2586–2602, https://doi.org/10.1105/tpc.16.00071 (2016).
37. Liou, M. R., Huang, Y. W., Hu, C. C., Lin, N. S. & Hsu, Y. H. A dual gene-silencing vector system for monocot and dicot plants. *Plant Biotechnol J* **12**, 330–343, https://doi.org/10.1111/pbi.12140 (2014).
38. Lin, K. Y., Hsu, Y. H., Chen, H. C. & Lin, N. S. Transgenic resistance to Bamboo mosaic virus by expression of interfering satellite RNA. *Mol Plant Pathol* **14**, 693–707, https://doi.org/10.1111/mpp.12040 (2013).
39. Alazem, M., Lin, K. Y. & Lin, N. S. The Abscisic Acid Pathway Has Multifaceted Effects on the Accumulation of Bamboo mosaic virus. *Mol Plant Microbe In* **27**, 177–189, https://doi.org/10.1094/Mpmi-08-13-0216-R (2014).
40. Lin, K. Y. *et al*. Global analyses of small interfering RNAs derived from Bamboo mosaic virus and its associated satellite RNAs in different plants. *PLoS One* **5**, e11928, https://doi.org/10.1371/journal.pone.0011928 (2010).
41. Lin, N. S., Huang, T. Y. & Hsu, Y. H. Infection of Barley Protoplasts with Bamboo Mosaic-Virus Rna. *Bot Bull Acad Sinica* **33**, 271–275 (1992).
42. Morgan, J. L. & Kerschensteiner, D. Coating gold particles with DNA (biolistics). *Cold Spring Harb Protoc* **2012**, 114–117, https://doi.org/10.1101/pdb.prot067066 (2012).
43. Lin, N. S., Hsu, Y. H. & Hsu, H. T. Immunological Detection of Plant-Viruses and a Mycoplasmalike Organism by Direct Tissue Blotting on Nitrocellulose Membranes. *Phytopathology* **80**, 824–828, https://doi.org/10.1094/Phyto-80-824 (1990).


## Acknowledgements

This work was supported by the Innovative Translational Agricultural Research Program of Academia Sinica (2014CP01, 2018PRE020). We thank M.-Z. Fang for sequencing and RT-qPCR. We also thank the Transgenic Plant Core Lab (http://transplant.sinica.edu.tw) for generating the transgenic plants and Live-Cell-Imaging Core Lab (https://ipmb.sinica.edu.tw/en/ipmb_core/30886704460717774) in the Institute of Plant and Microbial Biology, Academia Sinica, Taiwan, for technical assistance.

## Author Contributions

T.Y.C. and N.S.L. initiated and designed the experiments; Y.H.H. isolated the viral samples and prepared antiserum; F.C.H. constructed the transgenes; T.Y.C. did the transformation; T.Y.C., H.P., L.Y.H., C.H.C. and T.T.L. screened and characterized the transformants; S.C.L. did protoplast inoculation assay; T.Y.C. analyzed the data. T.Y.C., H.P., C.H.C., S.C.L. and N.S.L. wrote the manuscript; and all authors edited the manuscript.

## Additional Information

**Supplementary information** accompanies this paper at https://doi.org/10.1038/s41598-019-46695-7.

**Competing Interests:** The authors declare no competing interests.

**Publisher's note:** Springer Nature remains neutral with regard to jurisdictional claims in published maps and institutional affiliations.

**Open Access** This article is licensed under a Creative Commons Attribution 4.0 International License, which permits use, sharing, adaptation, distribution and reproduction in any medium or format, as long as you give appropriate credit to the original author(s) and the source, provide a link to the Creative Commons license, and indicate if changes were made. The images or other third party material in this article are included in the article's Creative Commons license, unless indicated otherwise in a credit line to the material. If material is not included in the article's Creative Commons license and your intended use is not permitted by statutory regulation or exceeds the permitted use, you will need to obtain permission directly from the copyright holder. To view a copy of this license, visit http://creativecommons.org/licenses/by/4.0/.

© The Author(s) 2019